Springer Proceedings in Physics 224

Ivan A. Parinov
Shun-Hsyung Chang
Yun-Hae Kim *Editors*

Advanced Materials

Proceedings of the International Conference on "Physics and Mechanics of New Materials and Their Applications", PHENMA 2018

Springer

Springer Proceedings in Physics

Volume 224

Indexed by Scopus. The series Springer Proceedings in Physics, founded in 1984, is devoted to timely reports of state-of-the-art developments in physics and related sciences. Typically based on material presented at conferences, workshops and similar scientific meetings, volumes published in this series will constitute a comprehensive up-to-date source of reference on a field or subfield of relevance in contemporary physics. Proposals must include the following:

- name, place and date of the scientific meeting
- a link to the committees (local organization, international advisors etc.)
- scientific description of the meeting
- list of invited/plenary speakers
- an estimate of the planned proceedings book parameters (number of pages/articles, requested number of bulk copies, submission deadline).

More information about this series at http://www.springer.com/series/361

Ivan A. Parinov · Shun-Hsyung Chang ·
Yun-Hae Kim
Editors

Advanced Materials

Proceedings of the International Conference on "Physics and Mechanics of New Materials and Their Applications", PHENMA 2018

Springer

Editors
Ivan A. Parinov
I. I. Vorovich Mathematics, Mechanics and Computer Sciences Institute
Southern Federal University
Rostov-on-Don, Russia

Shun-Hsyung Chang
Department of Microelectronics Engineering
National Kaohsiung University of Science and Technology
Kaohsiung, Taiwan

Yun-Hae Kim
Mechanical Engineering Department
Korea Maritime and Ocean University
Busan, Korea (Republic of)

ISSN 0930-8989 ISSN 1867-4941 (electronic)
Springer Proceedings in Physics
ISBN 978-3-030-19893-0 ISBN 978-3-030-19894-7 (eBook)
https://doi.org/10.1007/978-3-030-19894-7

This Springer imprint is published by the registered company Springer Nature Switzerland AG
The registered company address is: Gewerbestrasse 11, 6330 Cham, Switzerland

Preface

The modern trends in materials science and related techniques and technologies are caused by the fast development of theoretical, experimental and numerical methods, directed on researching and designing numerous promising materials, composites and structures. Existing requirements to scientific investigations take a great attention to the development of environmentally friendly materials. Industrial needs are aimed at the manufacture of devices, demonstrating very high accuracy of measurement, reliability and durability. These goods must operate under temperatures and pressures changing into broad limits, as well as in aggressive media. At the same time, the quality of these devices and technologies directly depends on the structure-sensitive properties and physico-mechanical characteristics of the materials and composites used. The study of modern physical processes, techniques and technologies is also impossible without creating materials and devices with optimal and outstanding properties.

This collection of 50 papers presents selected reports of the 2018 International Conference on "Physics, Mechanics of New Materials and Their Applications" (PHENMA-2018), which has been taken place in Busan, South Korea, during August, 9–11, 2018 (http://phenma2018.math.sfedu.ru). The conference was sponsored by the Busan Tourism Organization (South Korea), Ministry of Education and Science of Russian Federation, South Scientific Center of Russian Academy of Science, Russian Foundation for Basic Research, Ministry of Science and Technology of Taiwan, The Korean Society of Ocean Engineering (South Korea), New Century Education Foundation (Taiwan), Ocean & Underwater Technology Association (Taiwan), Unity Opto Technology Co. (Taiwan), Fair Well Fishery Co. (Taiwan), Woen Jinn Harbor Engineering Co. (Taiwan), Lorom Group (Taiwan), Longwell Co. (Taiwan), University of 17 Agustus 1945 Surabaya (Indonesia), University of 45, Surabaya (Indonesia), University of Islam Kadiri (Indonesia), University of Darul Ulum, Jombang (Indonesia), University of Maarif Hasyim Latif, Sidoarjo (Indonesia), PDPM Indian Institute of Information Technology, Design and Manufacturing (India), Don State Technical University (Russia), South Russian Regional Centre for Preparation and Implementation of International Projects.

The thematic of the PHENMA-2018 continued ideas of previous international symposia and conferences: PMNM-2012 (http://pmnm.math.rsu.ru), PHENMA-2013 (http://phenma.math.sfedu.ru), PHENMA-2014 (http://phenma2014.math.sfedu.ru), PHENMA-2015 (http://phenma2015.math.sfedu.ru), PHENMA-2016 (http://phenma2016.math.sfedu.ru) and PHENMA-2017 (http://phenma2017.math.sfedu.ru), whose results have been published in the following edited books *Physics and Mechanics of New Materials and Their Applications*, Ivan A. Parinov, Shun-Hsyung Chang (Eds.), Nova Science Publishers, New York, 2013, 444 p. ISBN: 978-1-626-18535-7; *Advanced Materials—Physics, Mechanics and Applications*, Springer Proceedings in Physics. Vol. 152. Shun-Hsyung Chang, Ivan A. Parinov, Vitaly Yu. Topolov (Eds.), Springer, Heidelberg, New York, Dordrecht, London, 2014, 380 p. ISBN: 978-3-319-03748-6; *Advanced Materials—Studies and Applications*, Ivan A. Parinov, Shun-Hsyung Chang, Somnuk Theerakulpisut (Eds.), Nova Science Publishers, New York, 2015, 527 p. ISBN: 978-1-634-63749-7; *Advanced Materials—Manufacturing, Physics, Mechanics and Applications*, Springer Proceedings in Physics, Vol. 175, Ivan A. Parinov, Shun-Hsyung Chang, Vitaly Yu. Topolov (Eds.). Heidelberg, New York, Dordrecht, London: Springer Cham. 2016, 707 p. ISBN: 978-3-319-26322-9, *Advanced Materials—Techniques, Physics, Mechanics and Applications*, Springer Proceedings in Physics, Vol. 193, Ivan A. Parinov, Shun-Hsyung Chang, Muaffaq A. Jani (Eds.). Heidelberg, New York, Dordrecht, London: Springer Cham. 2017, 627 p. ISBN: 978-3-319-56062-5; and *Advanced Materials—Proceedings of the International Conference on "Physics and Mechanics of New Materials and Their Applications", PHENMA 2017*, Springer Proceedings in Physics, V. 207, Ivan A. Parinov, Shun-Hsyung Chang, Vijay K. Gupta (Eds.). Heidelberg, New York, Dordrecht, London: Springer Cham. 2018, 640 p. ISBN: 978-3-319-78918-7, respectively.

The papers of the PHENMA-2018 are divided into four scientific directions: (i) Processing Techniques of Advanced Materials, (ii) Physics of Advanced Materials, (iii) Mechanics of Advanced Materials and (iv) Applications of Advanced Materials.

Into framework of the first direction is considered, in particular, the process for ammonia sensing using electrospun PVDF/PANI nanofiber chemiresistor. Then, there are studies of composition, activity, structure and stability of Pt Pt*M*/C electrocatalysts, and also the effects of mechanical activation, modifying with dopants and technologies on the structure, dielectric and relaxation properties of different ferro-piezoelectric ceramics, films and composites. Moreover, the influence of carbothermal synthesis on morphology and photoluminescence of ZnO nanorods and the resistance of organic coatings to acid media are studied. The first part is finished by considering the effects of high-voltage nanosecond pulses on the structural defects in dielectric minerals and activity of the mineral additives on physico-mechanical properties of concretes.

The physical topic is opened by the theoretical investigations of the method of density matrix in the theory of laser, critical current in strips based on the Josephson medium and the equations of state for light rare-gas crystals. Then, promising complex perovskite-like solid solutions $Bi_3Ti_{1-x}Sn_xNbO_9$ are studied as well as the properties of unipolarity arising in unpolarized ferroelectrics under stationary strain gradient. Moreover, structures of ferroelectrics-relaxors at various scales are investigated under morphotropic phase transitions. Optical properties of the niobate crystals and epitaxial films are present together with thermophysical properties of multiferroics. Other papers are devoted to investigations of micro-arc discharge in deep-sea water at high pressure, hydrogen in materials and new method for detecting ultra-low boron concentration in steel.

In the part of mechanics are present new mathematical and finite-element models (FEM) for harmonic vibrations of nanosized magnetoelectric bodies with coupled surface and interphase effects; the elastic properties of CNT-reinforced silver nanocomposite are also studied by FEM. The new approaches of thermoelasticity are developed to the diagnostics and protection of tribological devices and to study the composites with imperfect interfaces. 3D boundary-element dynamic analysis is applied to the poro-viscoelastic half-space with a cavity under vertical load. Moreover, there are considered nonstationary contact problem of thermoelasticity for a ring with a reinforcing layer on the friction surface and also the indentation process for sample with plastic layers. Other studies are devoted to forced oscillations of polymeric composite shells of revolution, to transverse isotropic plane-layered constructions under pulse impacts and to the wave propagating along waveguide. Finally, the local hydrogen embrittlement of metals is investigated.

The presented applications are touched to set of modern devices, manufactured on the base of novel approaches. In particular, resonant frequencies of ultrasonic vibrations of a medical scalpel are studied as well as tensoresistor sensor, based on layers of composite nanomaterials. Then, the issues of the optimization of modified ZnO films for ultraviolet surface acoustic wave photodetector are studied. Energy harvesting topic is studied on the examples of Archimedes wave swing harvester, circular PZT-actuator, cantilever-type piezoelectric generator with proof mass and piezoelectric-based harvester for rotating objects. Moreover, the surface roughness of aluminum alloy–coal bottom ash particle composites for bolts also is investigated as well as the effect of the hardened surface layer properties of the tribocontact parts. Finally, underwater transmission scheme for audio signals is present.

The book will be very useful for students of different levels of education, scientists and engineers, researching and developing nanomaterials and nanostructures, ferro-piezoelectrics, ferromagnetic and environmentally friendly materials and composites. The book also discusses theoretical and experimental problems, directed to study, modeling and designing of modern devices using advanced materials, which are suitable for wide applications in different scientific, technological and technical fields. The book includes new research results in the field of materials science, condensed matter physics, physical–mechanical theory,

numerical and physical modeling and experiment, methods of processing and developing advanced materials and composites, computational methods and various applications.

Rostov-on-Don, Russia — Ivan A. Parinov
Kaohsiung, Taiwan — Shun-Hsyung Chang
Busan, Korea (Republic of) — Yun-Hae Kim

Contents

Contributors

Muslimin Abdulrahim Department of Industrial Engineering, 17 Agustus 1945 University, Surabaya, Indonesia

K. G. Abdulvakhidov Southern Federal University, Rostov-on-Don, Russia

Abu Abubakarov Research Institute of Physics, Southern Federal University, Rostov-on-Don, Russia

Oleg Alekseevich Ageev Research and Education Centre «Nanotechnology», Southern Federal University, Taganrog, Russia

Sergei M. Aizikovich Research and Education Center "Materials", Don State Technical University, Rostov-on-Don, Russia

Anastasia Alekseenko Chemistry Department, Southern Federal University, Rostov-on-Don, Russia

A. Alexiev Institute of Mechanics, Bulgarian Academy of Sciences, Sofia, Bulgaria

Nataliya E. Anashkina N.V. Mel'nikov Institute of Comprehensive Exploitation of Mineral Resources, Russian Academy of Science, Moscow, Russian Federation

Konstantin Andryushin Research Institute of Physics, Southern Federal University, Rostov-on-Don, Russia

K. P. Andryushin Research Institute of Physics, Southern Federal University, Rostov-on-Don, Russia

Inna Andryushina Research Institute of Physics, Southern Federal University, Rostov-on-Don, Russia

I. E. Andzhikovich South Center of Russian Academy of Science, Rostov on Don, Russia

A. S. Anokhin Southern Scientific Center of the RAS, Rostov-on-Don, Russia

Rajashree S. Anwane Department of Physics, Rashtrasant Tukadoji Maharaj Nagpur University, Nagpur, India

A. G. Bakmaev H.I. Amirkhanov Institute of Physics of Daghestanian Scientific Center of the Russian Academy of Sciences, Makhachkala, Russia

E. Barkanov Riga Technical University, Riga, Latvia

Sergey Belenov Chemistry Department, Southern Federal University, Rostov-on-Don, Russia

M. V. Belodedov Bauman Moscow State Technical University (BMSTU), Moscow, Russia

Nikita A. Boldyrev Research Institute of Physics, Southern Federal University, Rostov-on-Don, Russia

Boris V. Bondarev Moscow Aviation Institute, Moscow, Russia

Igor Zh. Bunin N.V. Mel'nikov Institute of Comprehensive Exploitation of Mineral Resources, Russian Academy of Science, Moscow, Russian Federation

O. A. Bunina Faculty of Physics, Research Institute of Physics, Southern Federal University, Rostov-on-Don, Russia

N. I. Buravchuk I. I. Vorovich Mathematics, Mechanics and Computer Sciences Institute, Southern Federal University, Rostov-on-Don, Russia

S.-H. Chang National Kaohsiung University of Science and Technology, Kaohsiung city, Taiwan

Shun-Hsyung Chang Department of Microelectronic Engineering, National Kaohsuing University of Science and Technology, Kaohsiung, Taiwan, ROC

Valentine A. Chanturiya N.V. Mel'nikov Institute of Comprehensive Exploitation of Mineral Resources, Russian Academy of Science, Moscow, Russian Federation

M. I. Chebakov I. I. Vorovich Institute of Mathematics, Mechanics and Computer Sciences, Southern Federal University, Rostov-on-Don, Russia;
Rostov State Transport University, Rostov-on-Don, Russia

V. A. Chebanenko South Center of Russian Academy of Science, Rostov on Don, Russia;
South Scientific Center, Russian Academy of Sciences, Rostov-on-Don, Russia

A. V. Chernyshev Southern Federal University, Rostov-on-Don, Russia

A. V. Cherpakov Southern Federal University, Rostov-on-Don, Russia;
Don State Technical University, Rostov-on-Don, Russia

S. A. Danilchenko Rostov State Transport University, Rostov-on-Don, Russia;
I. I. Vorovich Mathematics, Mechanics and Computer Sciences Institute, Southern Federal University, Rostov-on-Don, Russia

S. I. Dudkina Research Institute of Physics, Southern Federal University, Rostov-on-Don, Russia

Svetlana Dudkina Research Institute of Physics, Southern Federal University, Rostov-on-Don, Russia

Vladimir Nikolayevich Dzhuplin Research and Education Centre «Nanotechnology», Southern Federal University, Taganrog, Russia

Victor A. Eremeyev Faculty of Civil and Environmental Engineering, Gdańsk University of Technology, Gdańsk, Poland;
I. I. Vorovich Institute of Mathematics, Mechanics and Computer Sciences, Southern Federal University, Rostov-on-Don, Russia

M. A. Evstigneeva Faculty of Physics, Research Institute of Physics, Southern Federal University, Rostov-on-Don, Russia

N. S. Filatova Physics Faculty, Research Institute of Physics, Southern Federal University, Rostov-on-Don, Russia

Kseniya Frolova Institute for Problems in Mechanical Engineering RAS, St. Petersburg, Russia

Hiroshi Furuta Department of Electronic and Photonic Systems Engineering, Kochi University of Technology, Kami, Kochi, Japan;
Center for Nanotechnology, Research Institute of KUT, Kochi University of Technology, Kami, Kochi, Japan

G. G. Gadjiev H.I. Amirkhanov Institute of Physics of Daghestanian Scientific Center of the Russian Academy of Sciences, Makhachkala, Russia

Vladislav Gamaleev Department of Electronic and Photonic Systems Engineering, Kochi University of Technology, Kami, Kochi, Japan

Andrew Geldash Research and Education Centre «Nanotechnology», Southern Federal University, Taganrog, Russia

T. E. Gerasimenko I. I. Vorovich Mathematics, Mechanics and Computer Sciences Institute, Southern Federal University, Rostov-on-Don, Russia

Alexander Gerasimenko National Research University of Electronic Technology, Zelenograd, Moscow, Russia;
I.M. Sechenov First Moscow State Medical University, Moscow, Russia

Irina Gerasimova Chemistry Department, Southern Federal University, Rostov-on-Don, Russia

E. V. Glazunova Southern Federal University, Rostov-on-Don, Russia

Ekaterina Glazunova Research Institute of Physics, Southern Federal University, Rostov-on-Don, Russia

Ievgen Ie. Gorbenko Lugansk Taras Shevchenko National University, Lugansk, Ukraine

V. K. Gupta Discipline of Mechanical Engineering, PDPM Indian Institute of Information Technology, Design and Manufacturing, Jabalpur, Jabalpur, Madhya Pradesh, India

O. V. Guryanova I. I. Vorovich Mathematics, Mechanics and Computer Sciences Institute, Southern Federal University, Rostov-on-Don, Russia

A. A. Gusev Institute of Solid State Chemistry and Mechanochemistry, SB RAS, Novosibirsk, Russia

Vladimir Guterman Chemistry Department, Southern Federal University, Rostov-on-Don, Russia

Akimitsu Hatta Department of Electronic and Photonic Systems Engineering, Kochi University of Technology, Kami, Kochi, Japan;
Center for Nanotechnology, Research Institute of KUT, Kochi University of Technology, Kami, Kochi, Japan

L. P. Ichkitidze National Research University of Electronic Technology (MIET), Zelenograd, Moscow, Russia;
I.M. Sechenov First Moscow State Medical University, Moscow, Russia

Levan Ichkitidze National Research University of Electronic Technology, Zelenograd, Moscow, Russia;
I.M. Sechenov First Moscow State Medical University, Moscow, Russia

Leonid Igumnov Research Institute for Mechanics, Lobachevsky State University of Nizhni Novgorod, Nizhny Novgorod, Russia

Aleksandr Ipatov Research Institute for Mechanics, Lobachevsky State University of Nizhni Novgorod, Nizhny Novgorod, Russia

V. A. Irkha Don State Technical University, Rostov-on-Don, Russia

V. P. Isupov Institute of Solid State Chemistry and Mechanochemistry, SB RAS, Novosibirsk, Russia

Niharika Jain Department of Conservative Dentistry and Endodontics, Hospital and Research Centre, Triveni Institute of Dental Science, Bilaspur, Chhattisgarh, India

Prashant K. Jain CAD/CAM Lab, Mechanical Engineering Discipline, PDPM, Indian Institute of Information Technology, Design and Manufacturing Jabalpur, Jabalpur, Madhya Pradesh, India

M. A. Jani University of 17 Agustus 1945 Surabaya, Surabaya, Indonesia

E. M. Kaidashev Southern Federal University, Rostov-on-Don, Russia

S. N. Kallaev H.I. Amirkhanov Institute of Physics of Daghestanian Scientific Center of the Russian Academy of Sciences, Makhachkala, Russia

A. S. Kamencev Southern Federal University, Rostov-on-Don, Russia

P. K. Kankar Discipline of Mechanical Engineering, PDPM Indian Institute of Information Technology, Design and Manufacturing, Jabalpur, Jabalpur, Madhya Pradesh, India;
CAD/CAM Lab, Mechanical Engineering Discipline, PDPM, Indian Institute of Information Technology, Design and Manufacturing Jabalpur, Jabalpur, Madhya Pradesh, India

Svetlana Kara-Murza Lugansk Taras Shevchenko National University, Lugansk, Ukraine

G. Ya. Karapetyan Southern Federal University, Rostov-on-Don, Russia

Nonna G. Kasparova Academy of Architecture and Art, Southern Federal University, Rostov-on-Don, Russia

V. E. Kaydashev Southern Federal University, Rostov-on-Don, Russia

S. V. Khasbulatov Research Institute of Physics, Southern Federal University, Rostov-on-Don, Russia

Lakshya Khurana Department of Mechanical Engineering, Manipal University Jaipur, Jaipur, India

E. V. Kirillova RheinMain University of Applied Sciences, Wiesbaden, Germany

Evgeniya Kirillova RheinMain University of Applied Sciences, Wiesbaden, Germany

L. I. Kiseleva South Scientific Center, Russian Academy of Sciences, Rostov-on-Don, Russia

Evgeny Kitsyuk Scientific Manufacturing Complex “Technological Centre”, Zelenograd, Moscow, Russia

Viktor Sergeevich Klimin Research and Education Centre «Nanotechnology», Southern Federal University, Taganrog, Russia

Pankaj Koinkar Department of Optical Science, Tokushima University, Tokushima, Japan

V. I. Kolesnikov Rostov State Transport University, Rostov-on-Don, Russia

Vladimir I. Kolesnikov Rostov State Transport University, Rostov-on-Don, Russia

E. M. Kolosova I. I. Vorovich Institute of Mathematics, Mechanics and Computer Sciences, Southern Federal University, Rostov-on-Don, Russia

Sanchit Kondawar Department of Electronics, Government College of Engineering, Jalgaon, India

Subhash B. Kondawar Department of Physics, Rashtrasant Tukadoji Maharaj Nagpur University, Nagpur, India

Elizaveta V. Koporulina N.V. Mel'nikov Institute of Comprehensive Exploitation of Mineral Resources, Russian Academy of Science, Moscow, Russian Federation

Nataliya Korchikova Lugansk Taras Shevchenko National University, Lugansk, Ukraine

S. P. Kubrin Faculty of Physics, Research Institute of Physics, Southern Federal University, Rostov-on-Don, Russia

Oleg V. Kudryakov Don State Technical University, Rostov-on-Don, Russia

Y. A. Kuprina Faculty of Physics, Research Institute of Physics, Southern Federal University, Rostov-on-Don, Russia

M. E. Kutepov Southern Federal University, Rostov-on-Don, Russia

L. E. Kuznetsova Southern Federal University, Rostov-on-Don, Russia

Dattatray J. Late Physical and Materials Chemistry Division, National Chemical Laboratory, Pune, India

Alla R. Lebedinskaya Academy of Architecture and Art, Southern Federal University, Rostov-on-Don, Russia

G. R. Li Shanghai Institute of Ceramics, Chinese Academy of Sciences, Shanghai, China

Chun-Kang Li Department of Electrical Engineering, National Taiwan Ocean University, Keelung, Taiwan, ROC

Chin-Feng Lin Department of Electrical Engineering, National Taiwan Ocean University, Keelung, Taiwan, ROC

Rui Lin Clean Energy Automotive Engineering Center, Tongji University, Shanghai, China

Svetlana Litvinchuk Research Institute for Mechanics, Lobachevsky State University of Nizhni Novgorod, Nizhny Novgorod, Russia

Igor A. Lubyagin Research and Education Center "Materials", Don State Technical University, Rostov-on-Don, Russia

A. G. Lutokhin Faculty of Physics, Research Institute of Physics, Southern Federal University, Rostov-on-Don, Russia

A. A. Lyapin I. I. Vorovich Institute of Mathematics, Mechanics and Computer Sciences, Southern Federal University, Rostov-on-Don, Russia

M.-R. M. Magomedov H.I. Amirkhanov Institute of Physics of Daghestanian Scientific Center of the Russian Academy of Sciences, Makhachkala, Russia

M. A. Malitskaya Faculty of Physics, Research Institute of Physics, Southern Federal University, Rostov-on-Don, Russia

Mastuki Department of Mechanical Engineering, 17 Agustus 1945 University, Surabaya, Indonesia

Vladislav Menschikov Chemistry Department, Southern Federal University, Rostov-on-Don, Russia

Vladislav Menshchikov Chemistry Department, Southern Federal University, Rostov-on-Don, Russia

Yuri F. Migal Rostov State Transport University, Rostov-on-Don, Russia

T. A. Minasyan Southern Federal University, Rostov-on-Don, Russia

I. P. Miroshnichenko Don State Technical University, Rostov-on-Don, Russia

Boris I. Mitrin Research and Education Center "Materials", Don State Technical University, Rostov-on-Don, Russia

Elizaveta Moguchikh Chemistry Department, Southern Federal University, Rostov-on-Don, Russia

Alexandr Nagaenko Research and Design Bureau "Piezopribor", Southern Federal University, Rostov-on-Don, Russia

Tejkaran Narolia PDPM IIITDM Jabalpur, Jabalpur, India

Anna Nasedkina Institute of Mathematics, Mechanics and Computer Science, Southern Federal University, Rostov-on-Don, Russia

Andrey Nasedkin Institute of Mathematics, Mechanics and Computer Science, Southern Federal University, Rostov-on-Don, Russia

Andrey V. Nasedkin I. I. Vorovich Institute of Mathematics, Mechanics and Computer Sciences, Southern Federal University, Rostov-on-Don, Russia

Rommel Nath Discipline of Mechanical Engineering, PDPM Indian Institute of Information Technology, Design and Manufacturing, Jabalpur, Jabalpur, Madhya Pradesh, India

Ankit Nayak CAD/CAM Lab, Mechanical Engineering Discipline, PDPM, Indian Institute of Information Technology, Design and Manufacturing Jabalpur, Jabalpur, Madhya Pradesh, India

Alexander V. Nazarenko Southern Scientific Center of the Russian Academy of Science, Rostov-on-Don, Russia

A. A. Nesterov Department of Chemistry, Southern Federal University, Rostov-on-Don, Russia

Alina Nevelskaya Chemistry Department, Southern Federal University, Rostov-on-Don, Russia

A. L. Nikolaev Southern Federal University, Rostov-on-Don, Russia;
Don State Technical University, Rostov-on-Don, Russia

P. A. Oganesyan I. I. Vorovich Mathematics, Mechanics and Computer Sciences Institute, Southern Federal University, Rostov-on-Don, Russia

Z. M. Omarov H.I. Amirkhanov Institute of Physics of Daghestanian Scientific Center of the Russian Academy of Sciences, Makhachkala, Russia

Mikhail N. Palatnikov Tananaev Institute of Chemistry, Subdivision of the Federal Research Centre, "Kola Science Centre of the Russian Academy of Sciences", Akademgorodok, Apatity, Murmansk Region, Russia

E. A. Panich Technology Institute "Piezopribor", Southern Federal University, Rostov-on-Don, Russia

Kirill Paperj Chemistry Department, Southern Federal University, Rostov-on-Don, Russia

Lyubov I. Parinova I. I. Vorovich Mathematics, Mechanics and Computer Sciences Institute, Southern Federal University, Rostov-on-Don, Russia

I. A. Parinov Institute of Mathematics, Mechanics and Computer Sciences, Southern Federal University, Rostov-on-Don, Russia

Ivan A. Parinov I. I. Vorovich Mathematics, Mechanics, and Computer Science Institute, Southern Federal University, Rostov-on-Don, Russia

A. A. Pavelko Research Institute of Physics, Southern Federal University, Rostov-on-Don, Russia

Alexey Pavelko Research Institute of Physics, Southern Federal University, Rostov-on-Don, Russia

A. V. Pavlenko South Scientific Center, Russian Academy of Sciences, Rostov-on-Don, Russia

Anatoly Pavlenko Southern Scientific Center of Russian Academy of Science, Rostov-on-Don, Russia;
Research Institute of Physics, Southern Federal University, Rostov-on-Don, Russia

Angelina Pavlets Chemistry Department, Southern Federal University, Rostov-on-Don, Russia

Vladimir Petukhov National Research University of Electronic Technology, Zelenograd, Moscow, Russia

Ekaterina A. Pilipenko A.A. Galkin Physics and Technology Institute, Donetsk, Ukraine

Vitali Podgaetski National Research University of Electronic Technology, Zelenograd, Moscow, Russia

Vladimir Polyanskiy Peter the Great Saint-Petersburg Polytechnic University, St. Petersburg, Russia;
Institute for Problems in Mechanical Engineering RAS, St. Petersburg, Russia

Nikolay N. Prokopiv Far Eastern State Transport University, Khabarovsk, Russia

E. P. Putri University of 17 Agustus 1945 Surabaya, Surabaya, Indonesia;
Khon Kaen University, Khon Kaen, Thailand

S. I. Raevskaya Faculty of Physics, Research Institute of Physics, Southern Federal University, Rostov-on-Don, Russia

I. P. Raevski Faculty of Physics, Research Institute of Physics, Southern Federal University, Rostov-on-Don, Russia

I. P. Raevsky Physics Faculty, Research Institute of Physics, Southern Federal University, Rostov-on-Don, Russia

Amirtham Rajagopal Department of Civil Engineering, Indian Institute of Technology, Hyderabad, India

L. A. Reznichenko Research Institute of Physics, Southern Federal University, Rostov-on-Don, Russia

Larisa Reznichenko Research Institute of Physics, Southern Federal University, Rostov-on-Don, Russia

Larisa A. Reznichenko Research Institute of Physics, Southern Federal University, Rostov-on-Don, Russia

E. V. Rozhkov Southern Federal University, Rostov on Don, Russia

Mariya V. Ryazantseva N.V. Mel'nikov Institute of Comprehensive Exploitation of Mineral Resources, Russian Academy of Science, Moscow, Russian Federation

Khizir Sadykov Research Institute of Physics, Southern Federal University, Rostov-on-Don, Russia;
Chechen State University, Grozny, Russia

V. G. Safronenko I. I. Vorovich Mathematics, Mechanics and Computer Sciences Institute, Southern Federal University, Rostov-on-Don, Russia

V. P. Sakhnenko Physics Faculty, Research Institute of Physics, Southern Federal University, Rostov-on-Don, Russia

S. V. Selishchev National Research University of Electronic Technology (MIET), Zelenograd, Moscow, Russia

Sergei Selishchev National Research University of Electronic Technology, Zelenograd, Moscow, Russia

Harjo Seputro Department of Mechanical Engineering, 17 Agustus 1945 University, Surabaya, Indonesia

Sergey Shevtsov Head of Aircraft Systems and Technologies Laboratory at the South Center of Russian Academy of Science, Rostov-on-Don, Russia

M. S. Shevtsova RheinMain University of Applied Sciences, Wiesbaden, Germany

L. A. Shilkina Research Institute of Physics, Southern Federal University, Rostov-on-Don, Russia

Lidia A. Shilkina Research Institute of Physics, Southern Federal University, Rostov-on-Don, Russia

Lidiya Shilkina Research Institute of Physics, Southern Federal University, Rostov-on-Don, Russia

Lydia Shilkina Research Institute of Physics, Southern Federal University, Rostov-on-Don, Russia

S. P. Shpanko Southern Federal University, Rostov-on-Don, Russia

E. N. Sidorenko Southern Federal University, Rostov-on-Don, Russia

Nikolay V. Sidorov Tananaev Institute of Chemistry, Subdivision of the Federal Research Centre, "Kola Science Centre of the Russian Academy of Sciences", Akademgorodok, Apatity, Murmansk Region, Russia

E. I. Sitalo Physics Faculty, Research Institute of Physics, Southern Federal University, Rostov-on-Don, Russia

V. P. Sizov Don State Technical University, Rostov-on-Don, Russia

A. S. Skaliukh I. I. Vorovich Mathematics, Mechanics and Computer Sciences Institute, Southern Federal University, Rostov-on-Don, Russia

Boris Sobol Department of Information Technologies, Don State Technical University, Rostov-on-Don, Russia

Arcady Soloviev Department of Theoretical and Applied Mechanics, Don State Technical University, Rostov-on-Don, Russia;
Institute of Mathematics, Mechanics and Computer Sciences, Southern Federal University, Rostov-on-Don, Russia

A. N. Soloviev Southern Federal University, Rostov-on-Don, Russia;
Department of Theoretical and Applied Mechanics, Don State Technical University, Rostov-on-Don, Russia

A. A. Solovieva Department of Theoretical and Applied Mechanics, Don State Technical University, Rostov-on-Don, Russia

E. A. Sosin Southern Federal University, Rostov-on-Don, Russia

Ashish Kumar Srivastava Department of Mechanical Engineering, Manipal University Jaipur, Jaipur, India

Pavel Syromyatnikov Southern Research Center of Russian Academy of Sciences, Rostov-on-Don, Russia

Alexander V. Syuy Far Eastern State Transport University, Khabarovsk, Russia

Natalia Tabachkova National University of Science and Technology «MISIS», Moscow, Russia

Nataliya Tabachkova National University of Science and Technology «MISIS», Moscow, Russia

Dmitry Telyshev National Research University of Electronic Technology, Zelenograd, Moscow, Russia;
I.M. Sechenov First Moscow State Medical University, Moscow, Russia

Natalya A. Teplyakova Tananaev Institute of Chemistry, Subdivision of the Federal Research Centre, "Kola Science Centre of the Russian Academy of Sciences", Akademgorodok, Apatity, Murmansk Region, Russia

Alexandr Tikhii Lugansk Taras Shevchenko National University, Lugansk, Ukraine

Roman A. Titov Tananaev Institute of Chemistry, Subdivision of the Federal Research Centre, "Kola Science Centre of the Russian Academy of Sciences", Akademgorodok, Apatity, Murmansk Region, Russia

Sergei Titov Research Institute of Physics, Southern Federal University, Rostov-on-Don, Russia

V. V. Titov Faculty of Physics, Research Institute of Physics, Southern Federal University, Rostov-on-Don, Russia

Victor Titov Research Institute of Physics, Southern Federal University, Rostov-on-Don, Russia

Gennady Tolmachev Southern Scientific Center of Russian Academy of Science, Rostov-on-Don, Russia

D. A. Tretyakov Peter the Great Saint-Petersburg Polytechnic University, Saint-Petersburg, Russia

Dmitriy Tretyakov Peter the Great Saint-Petersburg Polytechnic University, St. Petersburg, Russia

Dharmendra Tripathi Department of Mathematics, NIT Uttarakhand, Srinagar, India

Elena P. Troitskaya A.A. Galkin Physics and Technology Institute, Donetsk, Ukraine

Anatoliy Turik Research Institute of Physics, Southern Federal University, Rostov-on-Don, Russia

Zakhar Vakulov Research and Education Centre «Nanotechnology», Southern Federal University, Taganrog, Russia

Pavel Vasiliev Department of Information Technologies, Don State Technical University, Rostov-on-Don, Russia

I. A. Verbenko Research Institute of Physics, Southern Federal University, Rostov-on-Don, Russia

Iliya Verbenko Research Institute of Physics, Southern Federal University, Rostov-on-Don, Russia

Ilya A. Verbenko Research Institute of Physics, Southern Federal University, Rostov-on-Don, Russia

Vadim Volochaev Chemistry Department, Southern Federal University, Rostov-on-Don, Russia

Y. A. Yakovlev Institute for Problems in Mechanical Engineering RAS, Saint-Petersburg, Russia

Yuri Yakovlev Institute for Problems in Mechanical Engineering RAS, St. Petersburg, Russia

Yuriy I. Yurasov Research Institute of Physics, Southern Federal University, Rostov-on-Don, Russia;
Southern Scientific Center of the Russian Academy of Science, Rostov-on-Don, Russia;
Southern Scientific Centre RAS, Rostov-on-Don, Russia

M. A. Zaerko Physics Faculty, Research Institute of Physics, Southern Federal University, Rostov-on-Don, Russia

I. N. Zakharchenko Faculty of Physics, Research Institute of Physics, Southern Federal University, Rostov-on-Don, Russia

Yu. N. Zakharov Physics Faculty, Research Institute of Physics, Southern Federal University, Rostov-on-Don, Russia

Vladimir B. Zelentsov Research and Education Center “Materials”, Don State Technical University, Rostov-on-Don, Russia

D. A. Zhilin Southern Federal University, Rostov-on-Don, Russia

S. V. Zubkov Scientific Research Institute of Physics, Southern Federal University, Rostov-on-Don, Russia

Part I
Processing Techniques of Advanced Materials

Chapter 1
Facile Process for Ammonia Sensing Using Electrospun Polyvinylidene Fluoride/Polyaniline (PVDF/PANI) Nanofibers Chemiresister

Sanchit Kondawar, Dattatray J. Late, Rajashree S. Anwane, Subhash B. Kondawar, Pankaj Koinkar and Ivan A. Parinov

Abstract Electrospun polyvinylidene fluoride/polyaniline (PVDF/PANI) nanofibers chemiresister was fabricated by electrospinning and polymerization. As-fabricated PVDF/PANI nanofibers chemiresister was characterized by SEM, FTIR, TGA and DTG analyses. Cost effective with high accuracy microcontroller based sensor set up was designed for the measurement of change in resistance of chemiresister with respect to different concentrations of ammonia gas at various temperatures. The semiconducting behavior of the chemiresister was found to respond quickly towards ammonia gas. High sensitivity, fast response and recovery of PVDF/PANI nanofibers for ammonia gas at room temperature confirmed the chemiresister as potential candidate for ammonia sensing in environmental monitoring safety systems, chemical and automotive industries.

S. Kondawar (✉)
Department of Electronics, Government College of Engineering, Jalgaon 425001, India
e-mail: sanchitkondawar@yahoo.com

D. J. Late
Physical and Materials Chemistry Division, National Chemical Laboratory, Pune 411008, India

R. S. Anwane · S. B. Kondawar (✉)
Department of Physics, Rashtrasant Tukadoji Maharaj Nagpur University, Nagpur 440033, India
e-mail: sbkondawar@yahoo.co.in

P. Koinkar
Department of Optical Science, Tokushima University, Tokushima 7708506, Japan

I. A. Parinov
I. I. Vorovich Institute of Mathematics, Mechanics and Computer Science, Southern Federal University, Rostov-on-Don 344090, Russia

I. A. Parinov et al. (eds.), *Advanced Materials*, Springer Proceedings in Physics 224, https://doi.org/10.1007/978-3-030-19894-7_1

1.1 Introduction

Sensing of toxic gases has always been a subject of interest not only because it is of utmost importance as far as environment is concerned but also due to the continuous progress in the methods of preparation of new materials which can be used for sensing. Ammonia, hydrogen chloride, carbon monoxide, etc. are considered to be toxic for the living beings since inhalation of these gases may cause harmful and sometimes permanent damaging effects on the humans and the aquatic life. For the human safety and environmental monitoring requirements, there is considerable attention in recent years on sensors based on advanced materials for toxic gases [1]. Ammonia (NH_3) is not only hazardous for humans but also harm the aquatic life on a large scale since both the gases are soluble in water. The widespread use of ammonia in farms and industrial locations makes humans vulnerable to its exposure. Ammonia forms the very caustic ammonium hydroxide on contact with the available moisture in skin, eyes, oral cavity and respiratory tract. However, it may be extremely necessary to detect and quantify the low concentrations of ammonia in specific application areas since the human nose fails at such lower concentrations. For example in a chemical industry where several processes may be carried out at temperatures as high as 500 °C, leakage alarms are required to be installed to detect ammonia leakages in the range of 20 ppm to less than 1000 ppm within minutes of leakage. At present, much of the research work has been carried out for the detection of ammonia gases [2]. Several gas sensors have been developed in the past suitable for the specific application purpose. Sensor is a device that detects or senses the changes in the surrounding environment and records the information (changes) in a specific manner. As compared to the commercially available gas sensors mostly based on metal oxides and operated at high temperatures, the sensors fabricated from conducting polymers have added advantages [3, 4]. They have relatively high sensitivity and short response time, which makes them attractive commercially, especially when these features are ensured at or near room temperature. Since the nanostructure materials prepared in the form of thin films have large surface area to volume ratio, a porous surface morphology which allows for larger adsorption of gas molecules, nanoscale conducting polymers may be the right candidates for sensing application with high sensitivity, less response time at room temperature [5]. The nanofibers not only offer higher surface area to volume ratio but also inherent large aspect ratio, which makes it a quick sensor as compared to the thin films. Very low concentration of chemical vapours is sufficient to change the electrical properties of the sensing elements made of nanofibers. Conducting polymer nanofibers have superior sensing characteristics as well as flexibility in surface functionalities. In recent years, a number of processing techniques have been used to prepare conducting polymer nanofibers [6].

Although, there are various methods to fabricate nanofibers of the conducting polymers, electrospinning is simple, cost effective, convenient, versatile process to produce fibers with very large aspect ratio in mass scale [7–9]. Polyaniline (PANI) is one of the most extensively studied conducting polymer because it can be easily

synthesised and exhibits moderately high conductivity on doping. However, the polymer chains of polyaniline are short to be electrospun into long fine fibers. Therefore, another polymer with sufficiently long chain length is required to blend with polyaniline for electrospinning. Blends of conducting and non-conducting polymers are prepared to extract the desirable properties of the individual constituents which may be otherwise absent in them.

In the present study, PVDF/PANI blend nanofibers have been synthesized through electrospinning and dip-coating polymerization. The coating of conducting PANI on PVDF nanofibers ensures a change in the conductivity on exposure to ammonia gas thus enabling the use of prepared blend as a chemical gas sensor. Cost effective with high accuracy microcontroller based sensor set up was designed for the measurement of change in resistance of chemiresister made of PVDF/PANI blend nanofibers with respect to different concentrations of ammonia gas at various temperatures. The semiconducting behaviour of the chemiresister was found to respond quickly towards ammonia gas. High sensitivity, fast response and recovery of PVDF/PANI nanofibers for ammonia gas at room temperature confirmed the chemiresister as potential candidate for ammonia sensing in environmental monitoring safety systems.

1.2 Experimental

The 2.2 g PVDF was dissolved in 15 ml DMF and magnetically stirred for 1 h to get homogeneous solution. PVDF solution was then loaded into 5 ml disposable plastic syringe with the metallic needle of 0.5 mm diameter for electrospinning. During the electrospinning process at room temperature, the solution was fed to the tip using a computer controlled syringe pump at a flow rate of 0.2 ml/hr. 20 kV was applied to the needle of the syringe containing solution and the metallic plate wrapped with aluminium foil kept at a distance of 15 cm from the needle. The electrospun nanofibers were collected on the foil. After electrospinning, the non-woven membrane of PVDF nanofibers was dried at 80 °C. Further, as-prepared PVDF nanofibers were used for coating polyaniline to form PVDF/PANI blend nanofibers by dip-coating *in situ* chemical oxidative polymerization process. In the typical process of polymerization, 0.4 M aniline solution was prepared with 50 ml of 1 M HCl in deionized water. 0.45 M ammonium peroxydisulphate (APS) solution was prepared with 50 ml of 1 M HCl in deionizied water and mixed to aniline solution drop wise at 5 °C while stirring for 5 h. As-prepared PVDF nanofibers were inserted into the solution during polymerization using dip-coating technique. PANI was grown on PVDF nanofibers due to chemical oxidation of aniline and the solution turned dark green. PVDF/PANI nanofibers were washed with deionized water and dried at 80 °C in vacuum oven. The schematic of preparation and sensing application of PVDF/PANI blend nanofibers is shown in Fig. 1.1.

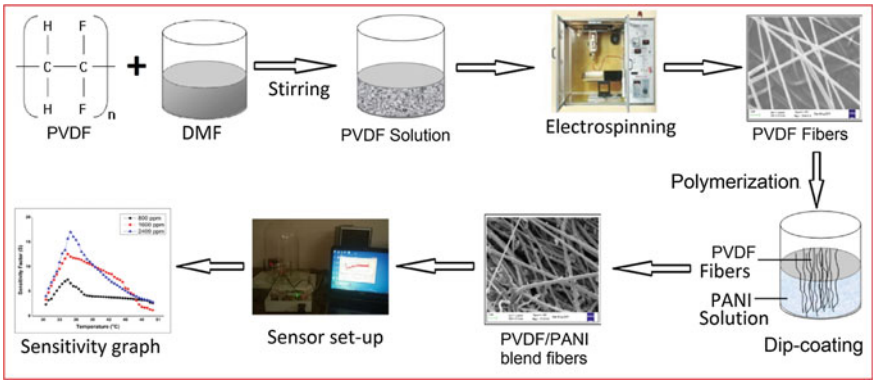

Fig. 1.1 Schematic of preparation and sensing application of PVDF/PANI nanofibers

1.3 Microcontroller Based Sensor Set up

A low cost microcontroller based electronic system was developed for measurement of sensor ohmic resistance. The instrument is capable of measuring resistance from few ohms up to 10 MΩ using selectable range to accommodate for verity of sensors and wide variation of sensor resistance with temperature and concentration of gas. To get a correlation between the sensor resistances at different temperature, a temperature measurement circuit based on LM35 is also included. The system helps to reduce testing time. The data is stored in the memory of the computer in excel format and is available for future use. The automated system has also eliminated manual interference and its limitation and disadvantages during tests. The basic block diagram of the developed instrument for resistance measurement of prepared samples is shown in Fig. 1.2.

Measurement of resistance is performed by passing a fixed current through the sensor and then measuring the voltage across it. The voltage is interpreted in the

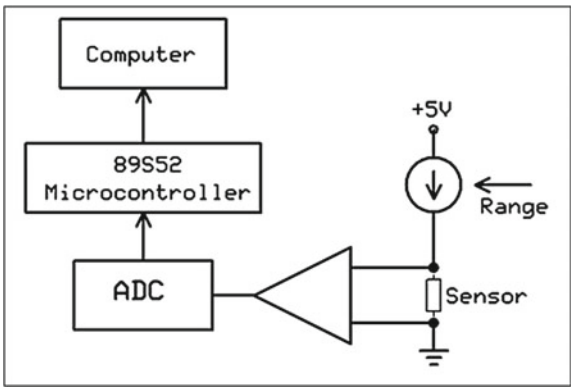

Fig. 1.2 Block diagram of microcontroller based resistance measurement circuit

form of sensor resistance. The upper limit of the developed instrument equal to 10 MΩ is limited by the noise pick up, the amplifier input currents and the accurate generation of fixed current of the current source. During the measurement of low resistance, a high current passes through the sensor, which causes the self-heating of the sensor and hence interferes with the accurate measurement of the gas concentration. A low current of 20 mA in lowest range is used to avoid self-heating. The resistance below 100 Ω is easily measured in this range.

Figure 1.3 depicts the circuit diagram of the resistance measurement and temperature measurement unit. Op-amp U1 along with Q1 forms a circuit, which delivers a constant current at the collector of the transistor. Non-inverting terminal of the op-amp is set at 2.048 V below 5 V. Since the op-amp along with the transistor is in closed loop, the voltage at inverting terminal of op-amp will also be at same voltage and is independent of any other parameter of the circuit. Hence, if 100 Ω-range is used then the range selector switch connects RA to inverting terminal of U1. Hence, the current of the current source is given by the equation:

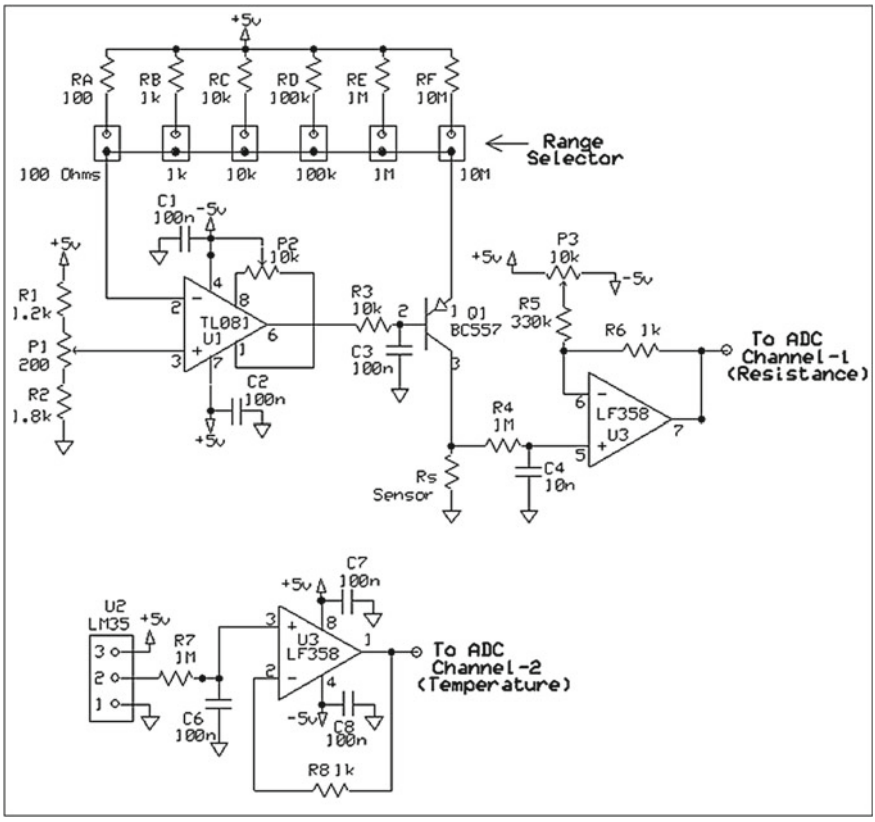

Fig. 1.3 Circuit diagram of the resistance and temperature measurement unit

$$I_{(100)} = \frac{2.048\,\text{V}}{100\,\Omega} = 20.48\,\text{mA} \tag{1}$$

Similarly, current for 1 K, 10 K, 100 K, 1 M and 10 M range will be 2.048 mA, 204.8μA, 20.48 μA, 2.048 μA, 0.2048 μA, respectively. When the above current passes through the sensor resistance, a voltage is generated proportional to the resistance of the sensor. Voltage so obtained across the sensor is applied to a buffer after passing through a low pass filter to remove unwanted noise. The measured voltage across the sensor is multiplied by a factor to directly give the value of the resistance of the sensor. A low cost 8 channel, 12 bit, SPI interface ADC from Microchip MCP3304 is used to convert analogue voltage into equivalent digital data. The reference voltage to MCP3304 is kept at 2.048 V so that to avoid calculation while processing in computer.

At the same time, temperature measurement is performed by using IC LM35, which gives output directly in °C and has a sensitivity of 10 mV/°C. The voltage from LM35 is applied to another channel of the ADC IC. The ADC is interfaced to microcontroller 89S52. The microcontroller controls all the operations measurement of sensor resistance, temperature and communication with the PC using serial to USB converters. The software is developed in visual basic. Figure 1.4 shows the front panel screen of test software. Provision is made for real time graphing of the sensor resistance and temperature with time. The data is recorded in PC in excel

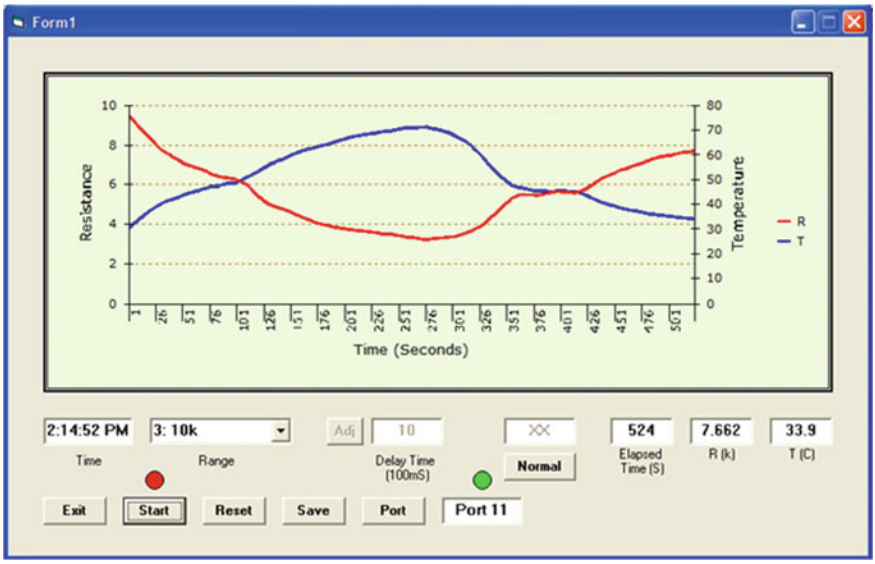

Fig. 1.4 Front panel screen of test software

format, which is later used to analyze the behavior of sensor for future analysis. The graph shown in GUI panel (see Fig. 1.4) is the measurement of resistance of a thermister with temperature change from 30° to 70° cycle.

1.4 Results and Discussion

SEM image and histogram of nanofibers of pure PVDF obtained to study the morphology and frequency distribution is shown in Fig. 1.5a. Uniformly long and thin nanofibers of pure PVDF can be seen in the SEM image whereas the corresponding histogram depicting frequency distribution of the nanofibers reveals that the average diameter of PVDF nanofibers was obtained equal to 280 nm. SEM image and histogram of the PVDF/PANI blend nanofibers is shown in Fig. 1.5b. The white coloured small clusters of PANI on PVDF fibers are seen in the SEM micrograph. The increase in the average diameter from 280 to 330 nm as well as the clustered coating confirms the successful formation of the desired blend.

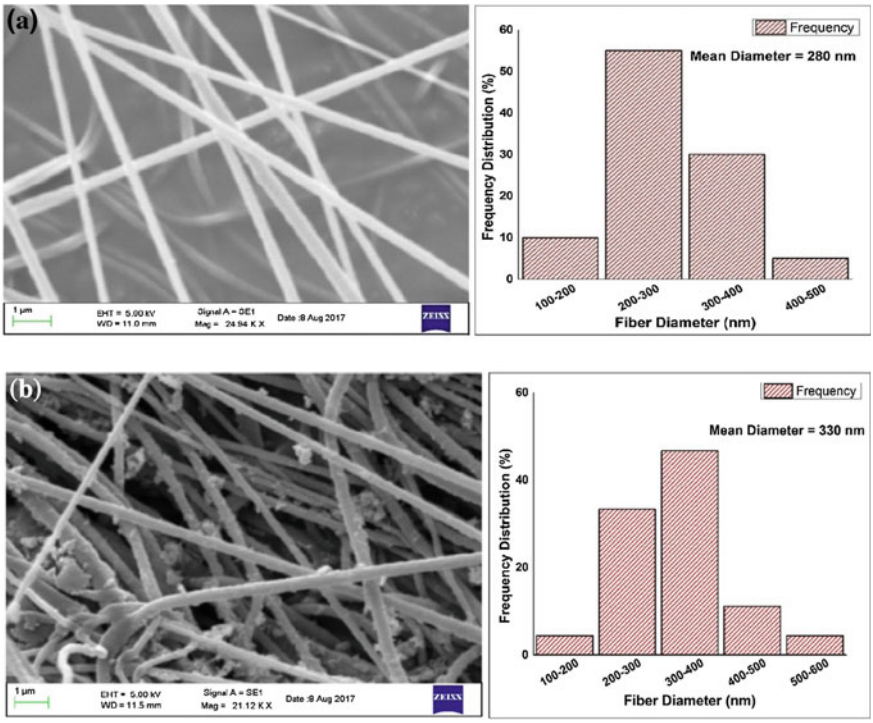

Fig. 1.5 **a** SEM image and histogram of PVDF nanofibers, **b** SEM image and histogram of PVDF/PANI blend nanofibers

FTIR of pure PVDF and PVDF/PANI nanofibers are shown in Fig. 1.6. The peaks at 2979.18 and 3017.76 cm^{-1} in the FTIR of pure PVDF correspond to the CH_2 symmetric and asymmetric vibrations, respectively. The CH_2 wagging vibration of PVDF is represent by the peak at 1401.34 cm^{-1}. The peak at 1230.64 cm^{-1} corresponds to the C–F stretch of the PVDF polymeric chain. The peaks at 841 and 875.72 cm^{-1} are related, respectively, to C–F stretching vibration and C–C–C asymmetrical stretching vibration of PVDF. In the FTIR of PVDF/PANI, the peaks at 1493.93 and 1584.59 cm^{-1} correspond to the stretch of benzene ring and quinine ring, respectively, confirming the presence of PANI in the blend. The bands in the range of 1200–1400 cm^{-1} are the C–N stretching bands of aromatic amine.

Thermogravimetric curves of electrospun pure PVDF and PVDF/PANI nanofibrous mat are depicted in Fig. 1.7. The corresponding DTG graphs are also shown in the same figure. Pure PVDF exhibits a very small weight loss before a major weight loss at 460 °C. The intense narrow peak of the corresponding DTG curve confirms the statement. The residual weight of PVDF is 31.6% at 610 °C.

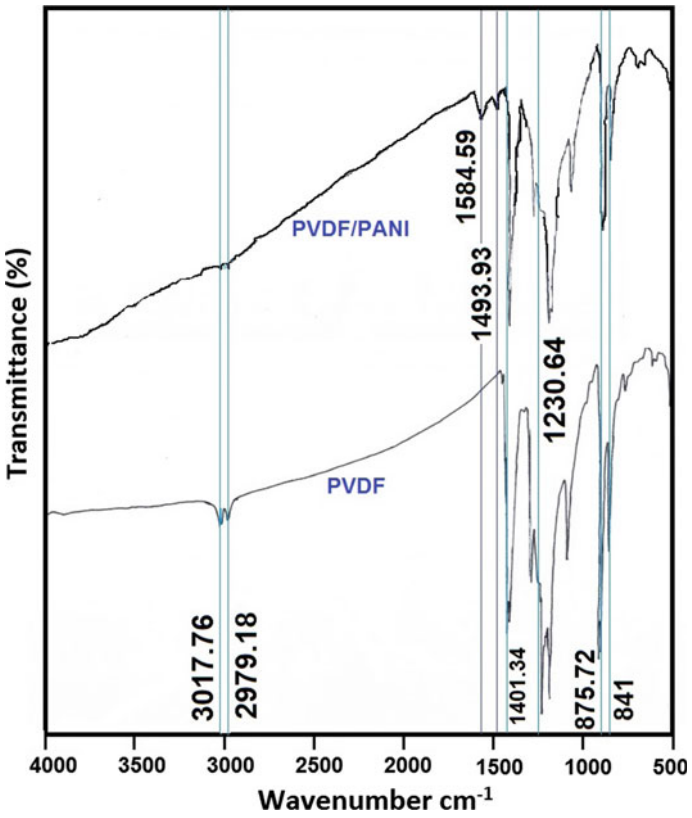

Fig. 1.6 FTIR spectra of pure PVDF and PVDF/PANI blend nanofibers

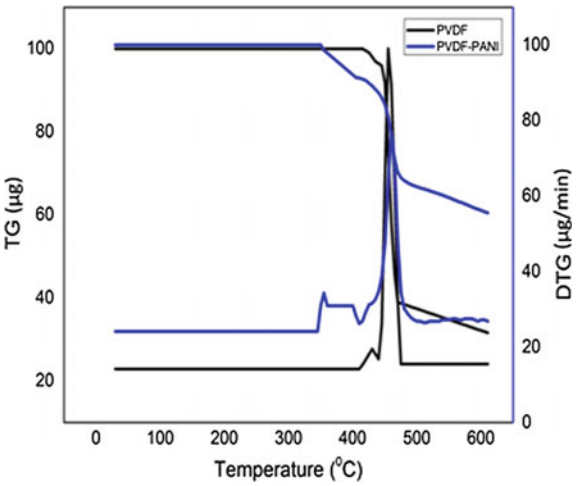

Fig. 1.7 Thermogravimetric curves of PVDF and PVDF/PANI blend nanofibers

The weight loss may be attributed to the decomposition of the polymer chains in PVDF [10–12]. The nanofibrous mats of PVDF/PANI degrade at a lower temperature than pure PVDF with somewhat similar profile to that of pure PVDF. The onset of decomposition at lower temperature may be due to the PANI coating on PVDF fibers. However, it can be very well stated that the decomposition of PANI coated on PVDF fibers is at higher temperature as compared to pure PANI. The loss in weight of PVDF/PANI blend at temperature from 350 to 400 °C may be attributed to the loss of moisture followed by the loss of dopant in the synthesised PANI. The corresponding DTG curve for PVDF/PANI blend confirms the TG analysis.

Figure 1.8 depicts the sensitivity factor of the PVDF/PANI blend for ammonia gas at different ppm concentrations. We can observe that the sensitivity factor again increases with the increasing concentration of NH_3 gas. The highest sensitivity was again obtained near room temperature. There is a slight variation in the operating temperature at different concentrations of the gas. When the blend is exposed to NH_3 gas, deprotonation takes place and the number of charge carriers in the PANI layer decreases thereby decreasing the conductivity of the blend. The sensitivity factor of PVDF/PANI blend was found equal to 7.36 for 800 ppm, 12.54 for 1600 ppm and 16.98 for 2400 ppm of NH_3 gas. The response and recovery of the PVDF/PANI blend sensor for NH_3 gas was calculated and the corresponding curve is shown in Fig. 1.9. The curve clearly confirms that the response (R_g/R_a) rises with increasing concentration of NH_3 gas. The smallest response time was found equal to 30 s for 800 ppm of ammonia gas and the highest recovery time was $\sim$3000 s for 2400 ppm of ammonia gas calculated for 90% change of the resistance. The very small response time indicates that ammonia molecules adsorbed quickly onto the PANI layer. However, they take very long to desorb from the blend, which is revealed from recovery time in minutes.

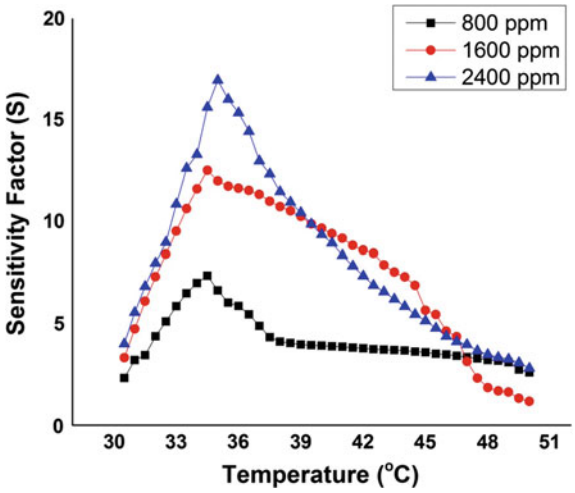

Fig. 1.8 Sensitivity of PVDF/PANI blend nanofibers for NH_3

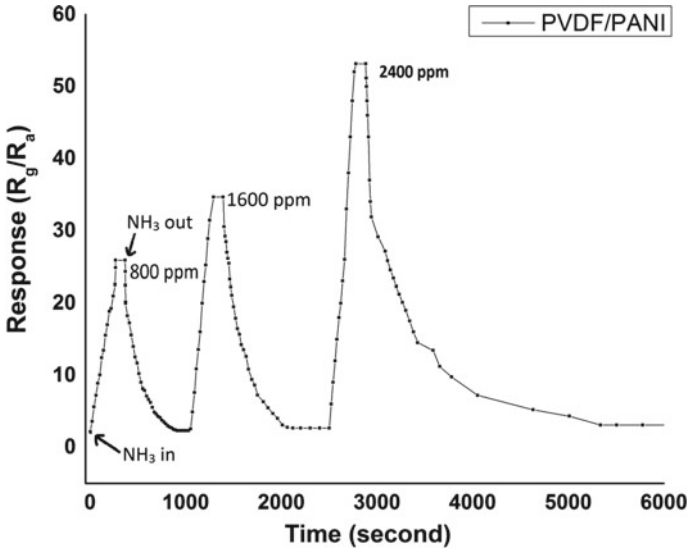

Fig. 1.9 Response and recovery of PVDF/PANI blend nanofibers for NH_3

The sensing mechanism that takes place at the molecular level due to the adsorption of NH_3 gas on the PANI layer is depicted in Fig. 1.10. When the sensor is exposed to the ammonia gas, deprotonation takes place. NH_3 molecules of gas take up the hydrogen atom from the PANI chain and form NH_4^+ ammonium ions. The emeraldine salt form of the PANI thus changes to the emeraldine base form with decrease in the number of carriers. This leads to the decrease in the number of

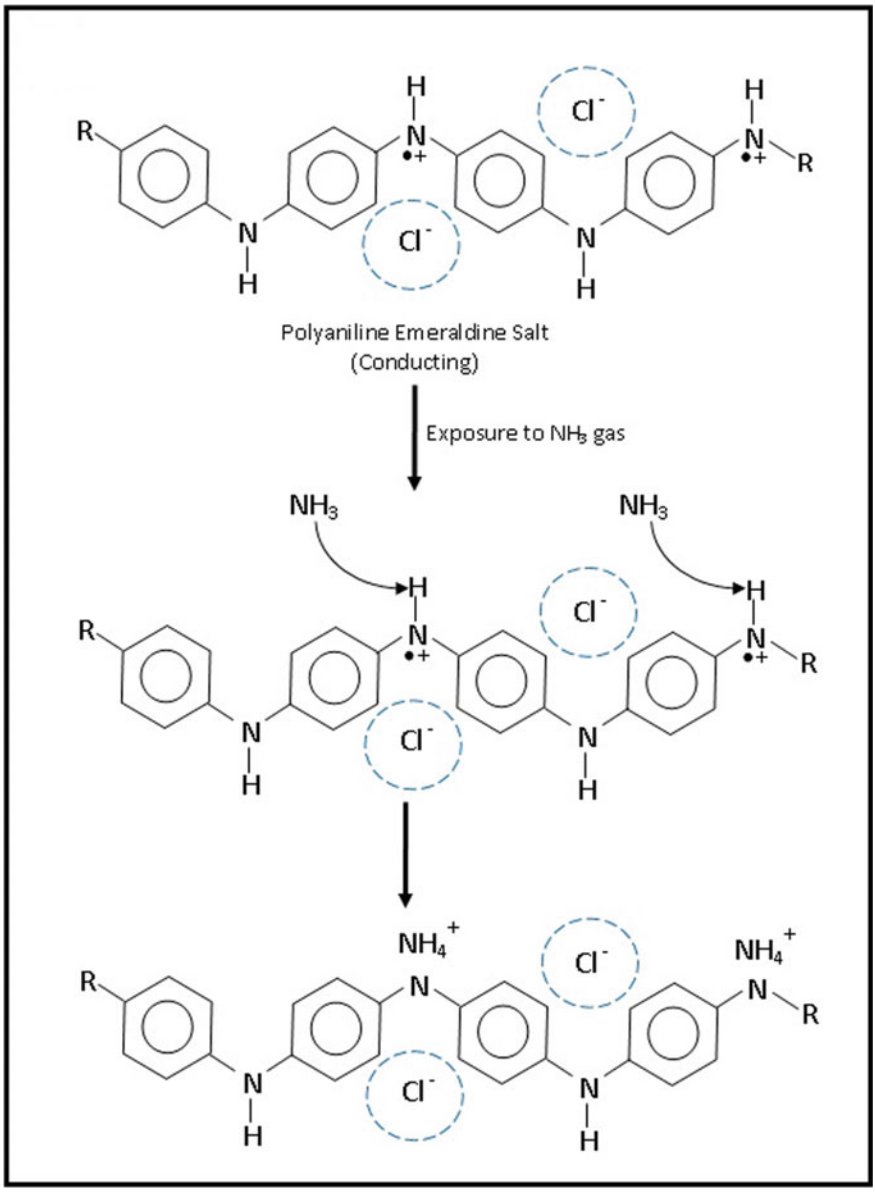

Fig. 1.10 Sensing mechanism of the PVDF/PANI blend nanofibers on exposure to NH_3 gas

polarons and the electrical resistivity of the sensor increases. Here too the sensitivity is found to increase with the increasing concentration of the NH_3 gas, which indicates that more NH_3 molecules diffuse into the fiber at higher concentration. The response and recovery time are defined as the time to reach 90% of the

resistance change during exposure and on removal of gas, respectively. The lower response time of the PVDF/PANI blend for NH_3 gas indicates the faster diffusion of the gas molecules into the fiber immediately upon exposure to the gas. This may be attributed to the difficulty of the adsorbed NH_3 molecules to desorb from the fiber. The response and recovery rate may be improved by fabricating a nanofibrous sheet of aligned nanofibers of PVDF, which will further increase the available surface area for PANI coating during dip-coating polymerization, thereby increasing the possibility of quick response and recovery. Attempts can be made to spin the PVDF nanofibers of reduced diameters by optimizing the affecting parameters. This will again result in increased specific surface area leading to quicker gas response and reversibility.

1.5 Conclusions

PVDF/PANI blend nanofibers have been synthesized successfully by electrospinning and dip-coating polymerization. The formation of PVDF/PANI blend is confirmed by SEM, FTIR and TGA-DTG analysis. A cost effective process of gas sensing by laboratory designed microcontroller based sensor set up is successfully installed and applied for PVDF/PANI blend as chemiresister for NH_3 gas, which showed increase in sensitivity with the increasing concentration of gas. The operating temperature of PVDF/PANI for NH_3 gas sensor was found to be near room temperature. These results, along with low response time, confirmed the possible use of the prepared material as a potential candidate for the sensing of NH_3 gas in the environmental monitoring safety systems, chemical industry, automotive industry and medical application areas.

References

1. S. Chen, G.A.C.S. Appl, Mater. Interfaces. **5**(14), 6473 (2013)
2. B. Lakard, S. Carquigny, O. Segut, T. Patois, S. Lakard, Metals **5**(3), 1371 (2015)
3. S.B. Kondawar, S.P. Agrawal, S.H. Nimkar, H.J. Sharma, P.T. Patil, Adv. Mater. Lett. **3**(5), 393 (2012)
4. C.C. Tang, R. Huang, Y.Z. Long, B. Sun, H.D. Zhang, C.Z. Gu, W.X. Wang, J.J. Li, Adv. Mater. Res. **562**, 308 (2012)
5. H.D. Zhang, C.C. Tang, Y.Z. Long, J.C. Zhang, R. Huang, J.J. Li, C.Z. Gu, Sens. Actuators A: Phys. **219**, 123 (2014)
6. S.M. Pethe, S.B. Kondawar, Adv. Mater. Lett. **5**(12), 728 (2014)
7. P.T. Patil, R.S. Anwane, S.B. Kondawar, Proc. Mater. Sci. **10**, 195 (2015)
8. H.J. Sharma, N.D. Sonwane, S.B. Kondawar, Fibers Polym. **16**(7), 1527 (2015)
9. Z.M. Huanga, Y.Z. Zhang, M. Kotaki, S. Ramakrishna, Compos. Sci. Technol. **63**(15), 2223 (2003)

10. C. Merlini, G.M. Barra, S.D.A. da Silva Ramôa, G. Contri, R. Almeida, M.A. d'Ávila, B.G. Soares, Front. Mater. **2**, 1 (2015)
11. Z. Zhong, Q. Cao, B. Jing, X. Wang, X. Li, H. Deng, Mater. Sci. Eng. B **177**(1), 86 (2012)
12. V.K. Thakur, E.J. Tan, M.F. Lin, P.S. Lee, J. Mater. Chem. **21**, 3751 (2011)

Chapter 2
Activity and Stability of Pt/C and Pt*M*/C Electrocatalysts: In Search of a Compromise

Anastasia Alekseenko, Sergey Belenov, Vladimir Guterman, Rui Lin, Natalia Tabachkova, Vadim Volochaev, Elizaveta Moguchikh, Angelina Pavlets, Kirill Paperj and Vladislav Menschikov

Abstract Carbon supported Pt–Cu and Pt–Co electrocatalysts with increased platinum content on the surface layer of nanoparticles were synthesized by different chemical methods. The compositions, microstructures and electrochemical behaviors of these electrocatalysts were studied using the X-ray diffraction, thermogravimetry, X-ray fluorescence analysis, TEM and cyclic voltammetry. During stability tests (1000 voltammetric cycles in $HClO_4$ solution) the values of electrochemically active surface area (ESA) for Pt–Cu/C catalysts reduced by 34%. Commercial Pt/C catalyst HiSPEC 3000 decreased ESA value by 70% (from 102 to 30 m^2g^{-1} (Pt)) in the similar tests. High stability of the prepared Pt–Cu/C catalysts combined with the high ESA values and ORR activity may be due to the fact that despite a comparatively large size of nanoparticles most of them have a core-shell or hollow (nanoporous) structure. The obtained result demonstrates a great potential for using bimetallic catalyst systems with an uneven surface distribution of metals in nanoparticles as electrocatalysts in low temperature fuel cells and show the way for combining high activity and durability of electrocatalysts.

A. Alekseenko (✉) · S. Belenov · V. Guterman · V. Volochaev · E. Moguchikh · A. Pavlets · K. Paperj · V. Menschikov
Chemistry Department, Southern Federal University, Rostov-on-Don, Russia
e-mail: an-an-alekseenko@yandex.ru

R. Lin
Clean Energy Automotive Engineering Center, Tongji University, Shanghai, China

N. Tabachkova
National University of Science and Technology «MISIS», Moscow, Russia

I. A. Parinov et al. (eds.), *Advanced Materials*, Springer Proceedings in Physics 224, https://doi.org/10.1007/978-3-030-19894-7_2

2.1 Introduction

Carbon-supported platinum (Pt/C) catalysts are widely used in low temperature fuel cells [1–3]. High costs of platinum, as well as Pt/C degradation during the operation of a fuel cell, hamper the commercialization of PEMFC and DMFC [2, 4]. The cost of the catalyst layer, according to some estimates [5], is from 30 to 40% of the membrane-electrode assembly. At the same time, a two-fold increase in the effective period of work of the catalytic layer in a fuel cell is identical to a two-fold reduction of platinum content in the catalyst. At the present time one of the targets of the scientific community is to develop new types of catalysts that combine high activity and stability during the operation of a fuel cell [1–3, 6].

Lately the interest in Pt bimetallic nanoparticle catalysts (Pt*M* with *M* = Co, Cu, Ni, etc.) has greatly increased due to the improved ORR activity, decreased Pt loading and reduced material cost [1–3, 7–18]. Increased tolerance of anode catalysts to CO impurities or intermediates oxidation of organic compounds is achieved by platinum alloying with Ru, Sn, Mo [1, 2, 19].

Unfortunately, there are some ambiguous issues with the application of catalysts with the two-component metal nanoparticles. One of them is the dissolution of an alloying component which leads to the degradation of the polymeric membrane of a fuel cell (decrease of proton conductivity). From this point of view, the solution for this problem could be creation of catalysts based on the *M*-core—Pt-shell architecture of bimetallic nanoparticles, where *M* is an inexpensive transition *d*-metal [1–3, 6, 20–22]. In this case reduction in the nanoparticle size ceases to be the major factor in ensuring high activity (high surface area) of the noble metal in the catalyst.

The electrocatalytic activity of P/C and Pt-*M*/C catalysts largely depends on their surface properties, the nanoparticle shape, size and the size distribution of nanoparticles, as well as chemical composition [1–3, 9–11]. Multi-level structural organization of Pt/C and Pt-*M*/C catalysts is determined by the shape and size of carbon particles, the spatial (on the surface and in the pores of the support particles) and size distribution of metal nanoparticles [1, 3, 23]. An interesting but scantily explored is the approach associated with an attempt to produce the catalyst containing hollow-nanoparticles of platinum or bimetallic nanoparticles with a core-shell architecture [1–3, 6, 20, 21]. In the last case the catalysis occurs on the platinum surface of nanoparticles, their cores being an inexpensive non-precious metal.

Degradation of Pt/C and Pt_xM/C catalysts during PEMFC operation is more expressed on the oxygen electrode. It is due to different reasons. Firstly, small Pt particles may dissolve in the ionomer phase and re-deposit on the surface of large particles, leading to the particle growth. This phenomenon is known as Ostwald ripening [24]. Corrosion of the carbon support mostly in the vicinity of the platinum/carbon interface is the second reason [25–28]. The result is a complete loss of contact with the carrier for a part of nanoparticles, facilitation of their movement across the surface, followed by aggregation of nanoparticles [24–28].

Finally, it is the corrosion of platinum [29] that can be followed by subsequent reduction of Pt^{2+} ions to the metal nanoparticles inside polymer membrane [30].

There are various methods for evaluating stability of the Pt-contained electrocatalyst. Nevertheless, the most common electrochemical method to assess the stability of Pt/C electrocatalysts is the registration of a large number of cyclic voltammograms (CV) (100–5000 cycles) [9, 18, 31–35]. Conditions for electrochemical stability measurement such as the sweep rate, the number of cycles and the potential range were described by different authors.

Analysis of publications devoted to the preparation and study of the catalysts with high functional characteristics [15, 30–36] shows that their authors mostly focus attention on achieving high activity or high stability of materials. The point is that high values of the ESA, which are a prerequisite for achieving high mass activity of the catalysts, adversely affect the corrosion-morphological stability of materials. At the same time, the question of the "ideal" microstructure, that provides an optimal combination of activity and stability, is still difficult to answer. The preparation of such catalysts is a pressing technological challenge.

In this paper a comparative study of durability for some of the Pt*M*/C and *M*@Pt/C electrocatalysts obtained in our research was performed. For comparison, the samples of commercial catalysts were also studied. It was important to evaluate the possibility of obtaining materials that combine high catalytic activity and stability, as well as to study the effect of composition and fine structure of nanoparticles on their functional characteristics.

2.2 Experimental Part

2.2.1 Preparation of Cu@Pt/C and Co@Pt/C Catalysts

Preparation of Pt–Cu/C electrocatalyst was carried out in two stages as described in [16]. At the first stage we reduced Cu^{2+} in the carbon (Vulcan XC72) suspension, containing $CuSO_4$ and NH_3 solution at pH = 10. Then, a Cu/C slurry in $H_2PtCl_6 \cdot nNH_3$ solution (pH = 10) was prepared and Pt (IV) was reduced. An excess of aqueous solution of 0.5 M $NaBH_4$ was used as a reducing agent. A mixture of water and ethylene glycol (1:1) was used as a solvent to prepare the suspensions. The choice of sequential chemical reduction of metals was due to the requirement of obtaining bimetallic nanoparticles with Cu-core—Pt-shell structure [16]. A PtCo/C electrocatalyst was synthesized by the two-step reduction method [18].

Formation of a secondary platinum shell preferably on the surface of the preformed copper "cores" rather than formation of separate platinum nanoparticles on the active sites of the carbon support may be a consequence of a much better matching of crystal lattice structures for Cu and Pt than for Pt and C, as well as a more intense interatomic interaction in the Pt–Cu system. The materials obtained

were named according to their chemical Pt_xM/C composition. Commercial Pt/C catalyst with 20% Pt (HiSPEC 3000, Johnson Matthey) was studied for comparison.

2.2.2 Characterization of the Catalysts Structure

X-ray powder diffraction analysis for Pt/C materials was performed at ARL X'TRA (Thermo Scientific, Switzerland) diffractometer (CuKa radiation, $\lambda = 0.154056$ nm, 40 kV and 30 mA). The diffraction data were recorded at room temperature in the range $15° \leq 2\theta \leq 90°$, step size 0.02° 2θ, the exposure time of 0.5° per second. An average crystallite size was calculated according to the Scherrer equation [37] by XRD data as referred <111> peak, which corresponds to $2\theta = 39.9°$. Background subtraction was performed via comparison of the diffractogram for the pure pattern of the substrate and the final diffractogram of the material.

Microphotographs of the synthesized materials were obtained using a JEM-2100 (JEOL, Japan) microscope operated at an accelerating voltage of 200 kV and resolution of 0.2 nm. To conduct electron-microscopic studies a drop of a specially prepared catalyst ink (about 0.5 mg of the catalyst being dispersed ultrasonically in 1 ml of isopropanol for 5 min) was applied on a copper grid covered with a thin layer of amorphous carbon film and then dried for about 20 min at room temperature.

2.2.3 Electrochemical Measurements

Electrochemical measurements were performed at 25 ± 2 °C using a conventional three-electrode cell. A 0.1 M $HClO_4$ solution saturated by Ar at standard pressure was used as an electrolyte. The glassy carbon electrodes with the electrocatalyst powder applied on them were used as working electrodes. The platinum wire was employed as the counter electrode and the Ag/AgCl saturated electrode was used as a reference electrode. All the potentials throughout this paper are reported versus the standard hydrogen electrode (SHE).

The Pt–Cu/C slurry (the so-called "catalyst ink") was prepared for applying the catalyst to the edge of a rotating disk electrode. The catalytic ink consisted of a dispersed suspension of 0.006 g of electrocatalyst in a mixture, prepared by mixing 900 μl of isopropanol and 100 μl of a 0.05% Nafion solution. The obtained suspension was sonicated during 10 min and then mixed by a magnetic stirrer during 10 min. An aliquot (6 μl) of catalytic ink was dropped onto the surface of a glassy carbon electrode with the geometric surface 0.196 cm^2 (diameter 5 mm) and dried at room temperature for 10 min to form a thin catalyst layer on the electrode

surface. Then, to further binding of the catalyst layer, a 7 µl of 0.05% Nafion solution was applied and dried.

Voltammetric cycling was performed using AFCBP1 potentiostate and an electrode rotator AFMSRE (Pine Research Instrumentation, Inc., USA). For displacement of oxygen from 0.1 M $HClO_4$, pure argon was bubbled for 30 min before and during the process of cyclic voltammograms registration.

Active surface area of the electrode (ESA) was determined by the quantity of electricity expended for electrochemical adsorption/desorption of atomic hydrogen with the input of a double layer region, as described in [16]. Preliminary 100 standardized cycles were registered in the potential range of −0.03 to 1.12 V at 200 mV s^{-1}. The second cyclic voltammogram was recorded at a potential scan rate of 20 mV s^{-1} and then used to calculate ESA. Direct calculation of the amount of electricity was carried out by integrating the corresponding "hydrogen" CV region in the "current–time" coordinates, using AfterMath software (Pine Research Instrumentation Co.). Meanwhile we also took into account the background current which was spent on the charge/discharge of the electrical double layer [16].

Measurements of stability were performed under the following program: I—registration of 100 cycles potential sweep in the range of 0.60–1.40 V at 100 mV s^{-1}; II—registration of 2 cycles with potential sweep rate of 20 mV s^{-1} in the range from −0.033 to 1.197 V. This program was repeated 10 times.

Linear sweep voltammetry (LSV) measurement was performed to evaluate the activity of catalytic materials in the oxygen electroreduction reaction (ORR). In this case, after ESA measurements, a 0.1 M $HClO_4$ solution was saturated with oxygen at atmospheric pressure for 50 min. Then, while continuing oxygen purging, the potential of the working electrode was changed from 0.020 to 1.2 V with a sweep rate of 20 mV s^{-1} at 1600 rpm. To compare the activity of the tested catalysts the measured currents were normalized by the mass of platinum (A g^{-1} (Pt)) and/or on the ESA of the catalyst (mA cm^{-2} (Pt)).

2.3 Results and Discussion

2.3.1 Composition and Microstructure of Pt/C and Pt-M/C Materials

According to the XRD-study (Fig. 2.1) all obtained materials contained metal nanoparticles with a face-centered cubic structure. The values of the reflection maximum for the Pt-*M*/C samples were shifted to higher values of 2θ, compared to the phase of pure platinum ($2\theta = 39.9°$) (Fig. 2.1). The maximum shift of the peak was observed for the $Pt_{0.8}Cu$/C material (Fig. 2.1, curve 3). Reflections corresponding to copper, cobalt or its oxides were not observed on the diffractograms. According to the calculation by the Scherrer equation, the largest average size of metal nanoparticles was determined for $Pt_{1.3}Cu$/C material (Table 2.1).

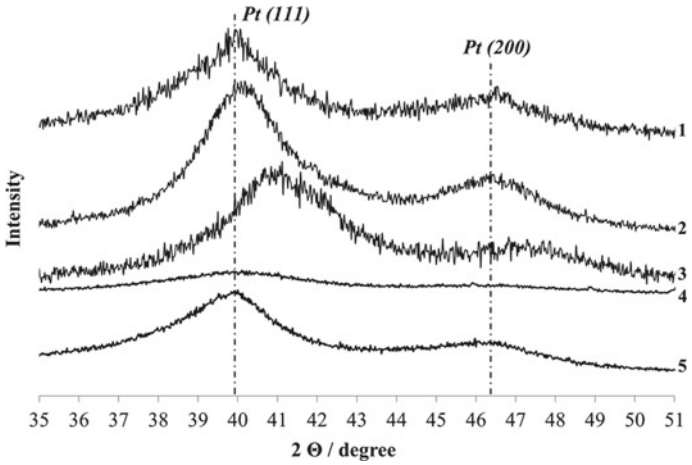

Fig. 2.1 XRD patterns of the Pt/C and Pt-*M*/C catalysts. 1—Pt_3Co/C, 2—$Pt_{1.3}Cu$/C, 3—$Pt_{0.8}Cu$/C, 4—Pt_3Cu/C, 5—commercial Pt/C catalyst (HiSPEC 3000)

Table 2.1 Some characteristics of commercial Pt/C catalysts HiSPEC 3000, Pt–Cu/C and Pt–Co/C catalysts

Sample	Metals loading, ω, % (TG)	ESA, $m^2\ g^{-1}$ (Pt)	$D_{(111)}$, nm (XRD)	D_{aver}, nm (TEM)	J_{spec}, A m^{-2} (Pt) (E = 0.8 V)	J_{mass}, A g^{-1} (Pt) (E = 0.8 V)	Stability (ESA_{1000}/ESA_0), %
HiSPEC 3000	20	102	2.2	2.0 [38]	0.21	21.1	30
$Pt_{1.3}Cu$	31	43	4.8	5.3	0.29	12.6	66
Pt_3Cu	20	72	1.7	3.4	0.21	15.1	48
$Pt_{0.8}Cu$	16	75	2.5	3.8	0.23	17.3	40
Pt_3Co	20	68	2.3	3.2	0.17	13.7	51

Unfortunately, the results of the X-ray analysis neither confirm, nor deny the formation of nanoparticles with the core-shell structure. The resulting diffractogram can match nanoparticles of two-component PtCu solid solution with an average crystallite size of about 4.2 nm. PtCu nanoparticles with a core-shell structure could give the same diffractogram. In the last case the observed reflections are the imposition (superposition) of the reflections for two phases: platinum and copper, or solid solutions thereof.

The chemical composition of the metal component for the PtCu materials was between $Pt_{0.8}Cu$ and Pt_3Cu (Table 2.1).

Transmission electron microscopy is one of the direct methods that could confirm the existence of core-shell nanoparticles in the synthesized *M*@Pt/C electrocatalysts. The criterion of a different nature of atoms in the shell and in the core, in

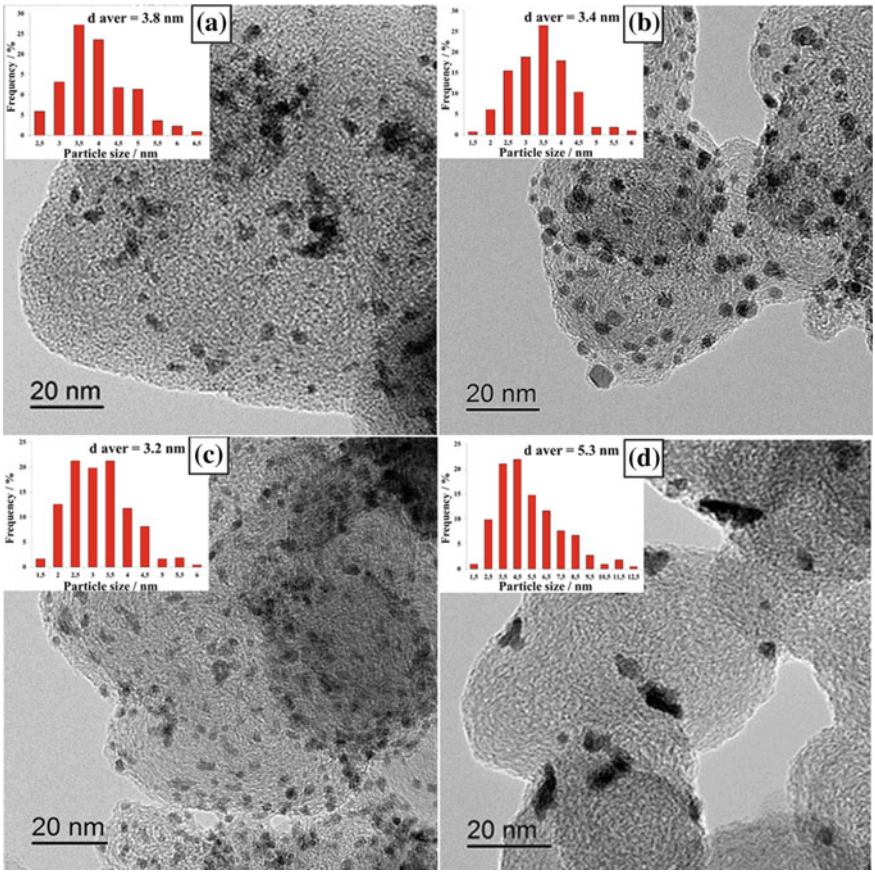

Fig. 2.2 Transmission electron microscopy photographs of $Pt_{0.8}Cu/C$ (**a**), Pt_3Cu/C (**b**), Pt_3Co/C (**c**) and $Pt_{1.3}Cu/C$ (**d**) catalysts

the first place, is a different brightness (contrast) of the corresponding areas of the nanoparticles in the photographs. Obviously, it is easy to identify the structure of the core-shell by electron-microscopic study only for large nanoparticles. Maybe this is the reason, why the existence of such structure is well established only for some nanoparticles (Fig. 2.2d).

For all studied materials an average nanoparticle size, measured by TEM (Fig. 2.2), is larger than the size of crystallites calculated by XRD ($D_{(111)}$) (Table 2.1). This often happens when comparing the nanoparticle sizes, determined by different methods. In addition, we note that the calculation of the crystallite size on the base of half-width of the XRD-peak may produce a mistake in the case of core-shell nanoparticles, if the peak is a superposition of reflections of two phases.

2.3.2 Electrochemical Measurements

2.3.2.1 ESA Determination

Cyclic voltammetry is a common method for investigation of supported Pt/C and Pt-*M*/C electrocatalysts. It is a well-known fact that cleaning the platinum surface from contamination occurs in the course of repetitive potential sweep cycles. As a result, stabilization of the current values at the cyclic voltammogram is observed. The active surface area of Pt/C and Pt-*M*/C materials was measured after 100 cycles of potential sweep. During the repetitive CV process the majority of investigated electrocatalysts was characterized by the following common features (Fig. 2.3):

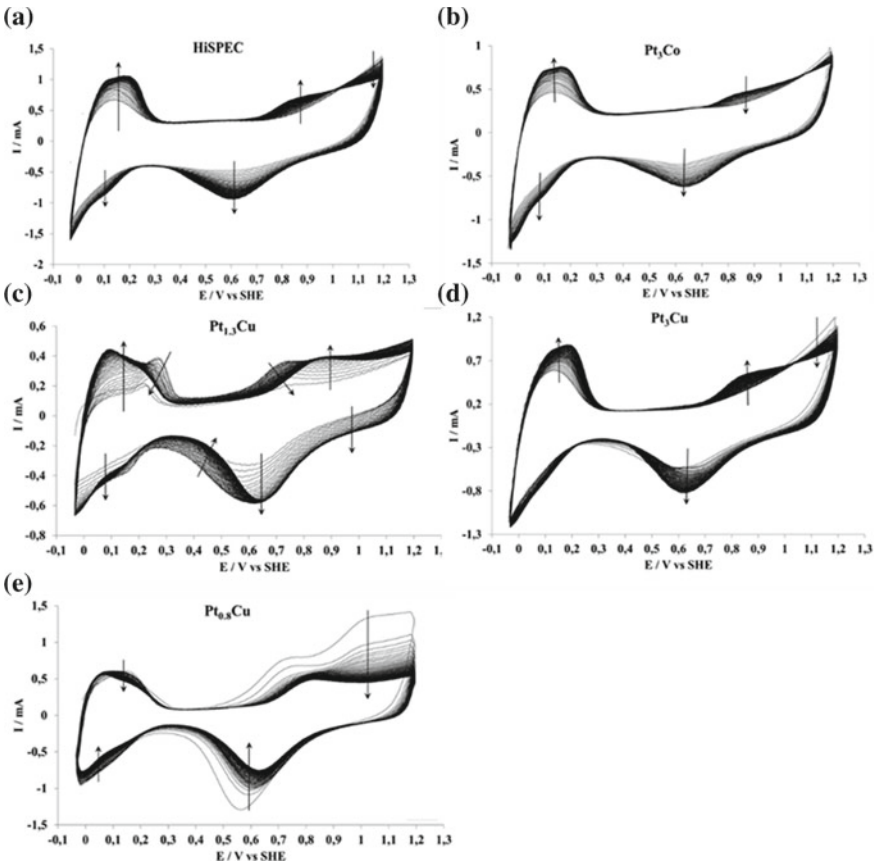

Fig. 2.3 100 CV curves of pre-treatment for **a** Pt/C HiSPEC 3000, **b** Pt_3Co/C, **c** $Pt_{1.3}Cu$/C, **d** Pt_3Cu/C and **e** $Pt_{0.8}Cu$/C electrocatalysts in 0.1 M $HClO_4$ saturated by Ar at room temperature; a scan rate is 200 mV s^{-1}

(i) a gradual increase in the quantity of electricity, which corresponded to hydrogen adsorption/desorption (the potential range of 0.03–0.3 V);
(ii) a decrease of the anodic current in the range of potentials, which corresponded to the oxidation of platinum (the potential range of 0.7–1 V);
(iii) an increase in the cathodic current peak, which corresponded to the electroreduction of the oxidized platinum surface (the potential range of 0.6–0.7 V).

At the same time, electrocatalysts with high copper content ($Pt_{1.3}Cu/C$ and $Pt_{0.8}Cu/C$) demonstrate some features of electrochemical behavior (Fig. 2.3c, e). Thus, the anodic maximum of ~0.28 V, caused by copper dissolution, is recorded for $Pt_{1.3}Cu/C$ CVs. Apparently, this electrocatalyst comprises a significant number of nanoparticles with defective platinum shell, which does not protect the core in copper-rich materials (Fig. 2.3c). During the standardizing cycling such nanoparticles could be transformed to standard or hollow Pt-nanoparticles. The number of defective nanoparticles in the $Pt_{1.3}Cu/C$ was not very big, hereupon the peak of copper anodic dissolution on cyclic voltammograms disappeared after 10–15 cycles. A similar situation was recently observed in [16] for core-shell $Cu@Pt_{0.8}/C$ electrocatalyst.

Features of $Cu@Pt_{0.8}/C$ electrocatalyst behavior, consisting in the progressive decrease and subsequent stabilization of electric current values in the oxygen region of CV (Fig. 2.3e), in our opinion, may be due to the influence of copper (I) oxide formed during the synthesis and its gradual dissolution during the cycling process.

The ESA values of Pt–Cu/C catalysts (43–75 $m^2\ g^{-1}$(Pt)) calculated by hydrogen adsorption/desorption areas of CVs (Fig. 2.4) were lower than those for commercial Pt/C catalyst HiSPEC 3000 (102 $m^2\ g^{-1}$(Pt)). This fact may be connected both with a large size of Pt–Cu nanoparticles in comparison with

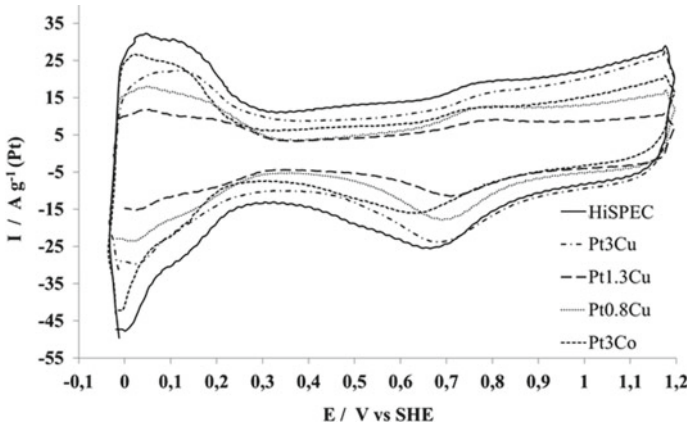

Fig. 2.4 CV curves for different Pt/C and Pt*M*/C catalysts in 0.1 M $HClO_4$ saturated by Ar at room temperature; a scan rate is 20 mV s^{-1}

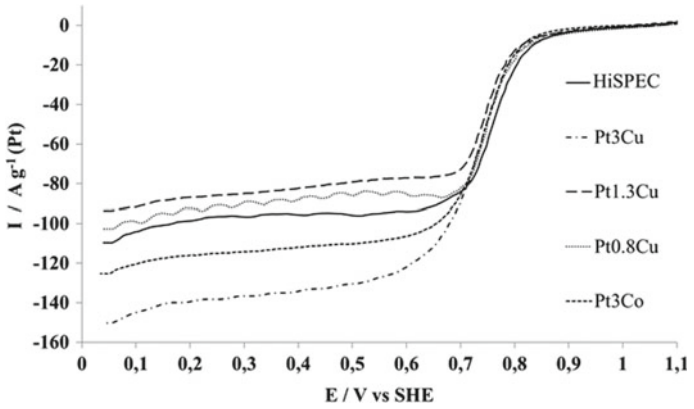

Fig. 2.5 LSV curves for different Pt/C and Pt*M*/C catalysts in 0.1 M $HClO_4$ saturated by O_2 at room temperature; a scan rate is 20 mV s^{-1}, rotating speed is 1600 rpm

Pt-nanoparticles in the HiSPEC 3000 and a higher degree of agglomeration for particles in Pt–Cu/C catalysts (Fig. 2.2a, d).

Comparison of cathodic potentiodynamic curves for the studied samples (Fig. 2.5) shows that mass-activities of Pt-*M*/C catalysts in ORR are slightly different. But in general, the commercial Pt/C catalysts exhibit a somewhat greater mass-activity in ORR (Table 2.1). At the same time, specific-activity of $Pt_{1.3}Cu$ catalyst is higher compared to specific-activity of HiSPEC 3000.

2.3.2.2 Durability of Electrocatalysts

The study of the nature of changes in the catalysts ESA in the process of a long-term cycling (see Sect. 2.2) (Fig. 2.6) has allowed researchers to compare their durability [39].

Note some special changes in the CV shape for different samples during the stress test. The values of cathodic and anodic currents corresponding to the areas of adsorption/desorption of hydrogen and formation/reduction of oxides on the platinum surface, respectively, vastly reduced during the cycling for the Pt/C catalyst (Fig. 2.6a) and in significantly smaller degree for Pt_3Cu and $Pt_{0.8}Cu$/C catalysts (Fig. 2.6d, e). This fact means the decrease of ESA value during the corrosion test, which may be caused by different reasons (mechanisms of degradation): agglomeration of metal nanoparticles, metal corrosion and Pt re-deposition from small NPs on big NPs, carbon support oxidation, and separation of nanoparticles from the support [40, 41].

In contrast, the values of cathodic and anodic currents for Pt_3Co/C and $Pt_{1.3}Cu$ catalysts slightly increased during CV cycling (Fig. 2.6b, c). On the other hand, an increase of electric current values in the double-layer region of CV (voltage range from 0.25 to 0.55 V) (Fig. 2.6b–d), which may be associated with the development

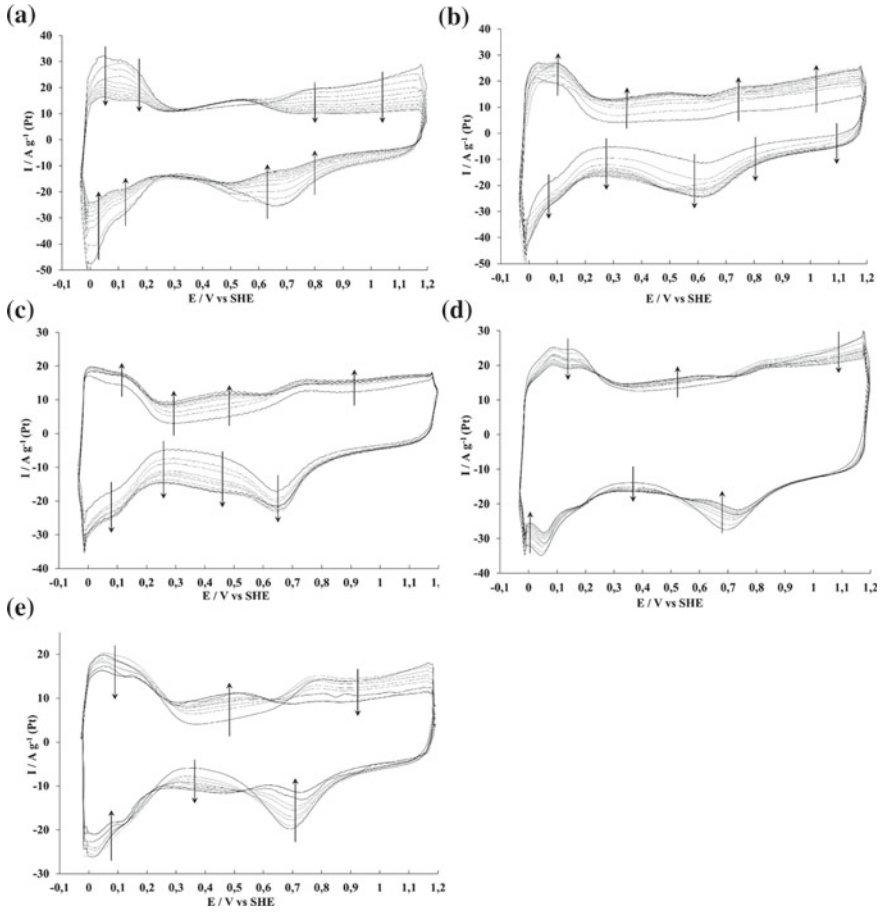

Fig. 2.6 Regularly repeated CV profiles for **a** commercial Pt/C material HiSPEC3000, **b** Pt_3Co/C, **c** $Pt_{1.3}Cu/C$, **d** Pt_3Cu/C and **e** $Pt_{0.8}Cu/C$ during 1000 stress-tests in de-aerated 0.1 M $HClO_4$ at room temperature; scan rate is 20 mV s^{-1} (see further explanation in Sect. 2.2)

of the carbon surface during the cycling, is typical for Pt-*M*/C catalysts [42]. It is of interest, that electric current values in the double-layer region of CV remained practically unchanged during stress-tests for Pt/C catalyst HiSPEC 3000 (Fig. 2.6a). Thus, CV behavior of different catalysts in the process of cycling demonstrates some differences, which are difficult to systematize.

Despite the above differences in the nature of CV changes, ESA reduction during the cycling was observed for all of the studied catalysts (Fig. 2.7). The higher the initial ESA value of the material is, the higher the catalyst degradation rate becomes (Fig. 2.7, inset). First of all, this is due to the decrease in the thermodynamic stability of the nanoparticles with a decrease in their size. Unfortunately, the small size of nanoparticles is the main reason of high ESA and, consequently, of high

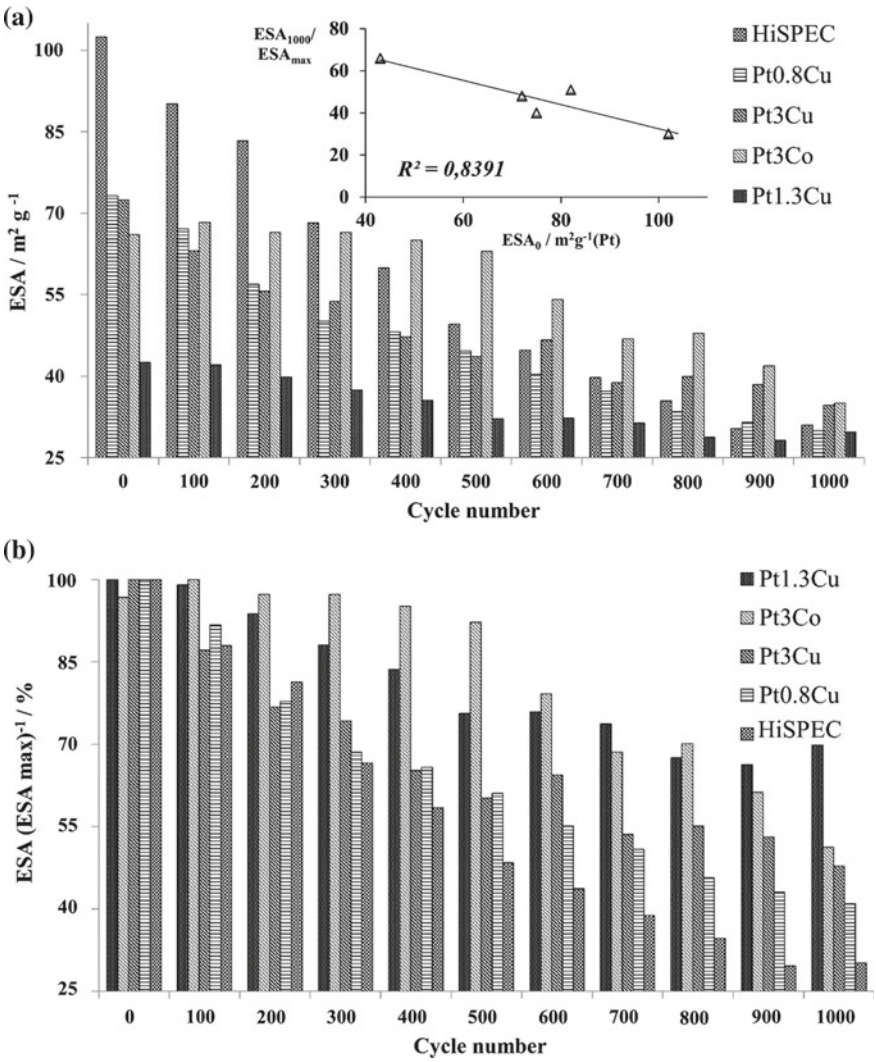

Fig. 2.7 Histograms of **a** change in the ESA value and **b** change of the degradation degree (ESA/ESA_{max}) during the stress-test for different catalysts in de-aerated 0.1 M $HClO_4$ at room temperature; insert—the dependence of ESA_{1000}/ESA_{max} on initial values of the catalyst ESA (see further explanation in Sect. 2.2)

mass-activity [16, 43]. $Pt_{1.3}Cu/C$ sample with an average size of nanoparticles (crystallites) about 4.8 nm according to XRD, and a relatively small initial ESA of 43 $m^2\ g^{-1}$(Pt) demonstrated the highest stability. Pt_3Co/C catalyst, which demonstrated 49% degradation, has shown the highest ESA value of 35 $m^2\ g^{-1}$(Pt) after

the stress-test. It is interesting to note, that the process of ESA decrease for the catalyst proceeds nonmonotonically (Fig. 2.7a, b): during the first 500 cycles ESA decreased by only 8%, while for the next 500 cycles it dropped to 41%).

2.4 Conclusions

Bimetallic Pt_xCu/C ($0.8 \leq x \leq 3$) and Pt_3Co/C electrocatalysts with a non-uniform distribution of components in the nanoparticles, namely, higher platinum content of the surface layer, were prepared by a successive chemical reduction of Cu^{2+} or Co^{2+}, and then of Pt (IV) compounds from solutions. ESA of the prepared catalysts was from 43 to 75 $m^2\ g^{-1}$ (Pt). The specific catalytic activity of the synthesized PtM/C catalysts in ORR is close to that of a commercial Pt/C sample HiSPEC 3000. All PtM/C electrocatalysts showed significantly high stability during the repeated (over 1000 cycles) voltammetric cycling in comparison to HiSPEC 3000 Pt/C catalyst. The main but not the only reason, which improved stability of PtM/C electrocatalysts, were the increased nanoparticles size and reduced platinum ESA in these materials compared to the commercial Pt/C sample. Pt_3Co/C electrocatalyst has demonstrated a non-monotonic change of ESA during the stress-test, after the first 500 cycles ESA has reduced only by 8%.

We believe that the combination technique for successive reduction of *d*-metal and platinum, followed by post-treatment of the pristine Pt-*M*/C material, would allow us to obtain the catalysts that are comparable with the commercial Pt/C catalyst in specific activity in the ORR reaction but superior in the corrosion—morphological stability during MEA exploitation.

Acknowledgements This research was supported by the Ministry of Education and Science of the Russian Federation (project No. 13.3005.2017/4.6).

References

1. N. Junga, D.Y. Chung, J. Ryua, S.J. Yoo, Y. Sung, Nano Today **9**, 433 (2014)
2. O.T. Holto, J.W. Stevenson, Platinum Met. Rev. **4**, 259 (2013)
3. R.N. Singh, R. Awasthi, C.S. Sharma, Int. J. Electrochem. Sci. **9**, 5607 (2014)
4. Ch. He, S. Desai, G. Brown, S. Bollepalli, Electrochem. Soc. Interface **14**, 41 (2005)
5. H. Yang, Angew. Chem. Int. Ed. **50**, 2674 (2011)
6. A.B. Yaroslavtsev, Y.A. Dobrovolsky, N.S. Shaglaeva, L.A. Frolova, E.V. Gerasimova, E.A. Sanginov, Russ. Chem. Rev. **81**, 191 (2012)
7. D. Thompsett, in *Handbook of Fuel Cells—Fundamentals, Technology and Applications*, ed. by W. Vielstic (Wiley, New York, 2003), p. 476
8. C. Xu, Yu. Liu, J. Wang, H. Geng, H. Qiu, ACS Appl. Mater. Interfaces. **3**, 4626 (2011)
9. Zh Xu, H. Zhang, S. Liu, B. Zhang, H. Zhong, D.S. Su, Int. J. Hydrogen Energy **37**, 17978 (2012)
10. L. Xiong, A.M. Kannan, A. Manthiram, Electrochem. Commun. **4**, 898 (2002)

11. V. Stamenkovic, B. Fowler, B.S. Mun, G.F. Wang, P.N. Ross, C.A. Lucas, N.M. Markovic, Science **315**, 493 (2007)
12. L. Ou, Comput. Theor. Chem. **104**, 869 (2014)
13. G. Pérez, E. Pastor, C.F. Zinola, Int. J. Hydrogen Energy **34**, 9523 (2009)
14. Ch. Wang, M. Chi, D. Li, D. Strmcnik, D. Vliet, G. Wang, J. Am. Chem. Soc. **133**, 14396 (2011)
15. F. Godínez-Salomón, M. Hallen-López, O. Solorza-Feria, Int. J. Hydrogen Energy **37**, 14902 (2012)
16. V.E. Guterman, S.V. Belenov, AYu. Pakharev, M. Min, NYu. Tabachkova, Int. J. Hydrogen Energy **41**, 1609 (2016)
17. D.A. Cantane, F.E.R. Oliveira, S.F. Santos, F.H.B. Lima. Appl. Catal. B **136**, 351 (2013)
18. R. Lin, T. Zhao, M. Shang, J. Wang, W. Tang, V.E. Guterman, J. Power Sources **293**, 274 (2015)
19. E. Antolini, Appl. Catal. B, **74**, 337 (2007)
20. X. Ge, L. Chen, J. Kang, T. Fujita, A. Hirata, Adv. Funct. Mater. **23**, 4156 (2013)
21. G.E. Ramirez-Caballero, P.B. Balbuena, Chem. Phys. Lett. **456**, 64 (2008)
22. V.V. Pryadchenko, V.V. Srabionyan, E.B. Mikheykina, L.A. Avakyan, V.Y. Murzin, Y.V. Zubavichus, I. Zizak, V.E. Guterman, L.A. Bugaev, J. Phys. Chem. **109**, 3217 (2015)
23. I. Leontyev, A. Kuriganova, Y. Kudryavtsev, B. Dkhil, N. Smirnova, Appl. Catal. A **431**, 120 (2012)
24. J.C. Meier, C. Galeano, I. Katsounaros, J. Witte, H.J. Bongard, Beilstein J. Nanotechnol. **5**, 44 (2014)
25. J.F. Wu, X.Z. Yuan, J.J. Martin, H.J. Wang, J.J. Zhang, J. Shen, J. Power Sources **184**, 104 (2008)
26. J. Wang, G. Yin, Y. Shao, S. Zhang, Z. Wang, Y. Gao, J. Power Sources **171**, 331 (2007)
27. D.A. Stevens, J.R. Dahn, Carbon **43**, 179 (2005)
28. S.N. Stamatin, M. Borghei, S.M. Andersen, S. Veltze, V. Ruiz, Int. J. Hydrogen Energy **39**, 8215 (2014)
29. S. Horn, W.C. Sheng, S. Chen, P.J. Ferreira, E.F. Holby, D. Morgan, Top. Catal. **46**, 285 (2007)
30. X. Yu, S. Ye, J. Power Sources **172**, 145 (2007)
31. F. Xu, M. Wang, Q. Liu, H. Sun, S. Simonson, J. Electrochem. Soc. **157**, 1138 (2010)
32. W.M. Chen, Q. Xin, G.Q. Sun, Q. Wang, Q. Mao, H.D. Su, J. Power Sources **180**, 199 (2008)
33. A.S. Arico, A. Stassi, E. Modica, R. Ornelas, I. Gatto, E. Passalacqua, V. Antonucci, J. Power Sources **178**, 525 (2008)
34. Y.C. Park, K. Kakinuma, M. Uchida, D.A. Tryk, T. Kamino, Electrochim. Acta **91**, 195 (2013)
35. K.C. Neyerlin, R. Srivastava, C.F. Yu, P. Strasser, J. Power Sources **186**, 261 (2009)
36. I.N. Leontyev, S.V. Belenov, V.E. Guterman, P. Haghi-Ashtiani, A.P. Shaganov, J. Phys. Chem. C **115**, 5429 (2011)
37. T.A. Lastovina, V.E. Guterman, S.S. Manokhin, Int. Sci. J. Altern. Energy Ecol. **9**, 111 (2012)
38. Y.-Ch. Chiang, Ch.-Ch. Liang, Ch.-P. Chung, Materials **8**, 6484 (2015)
39. D.A. Ohma, K. Shinohara, A. Iiyama, T. Yoshida, Catalyst **41**, 775 (2011)
40. Y. Zhang, S. Chen, Y. Wang, W. Ding, R. Wu, J. Power Sources **273**, 62 (2015)
41. I. Katsounaros, S. Cherevko, A.R. Zeradjanin, K.J.J. Mayrhofer, Angew. Chem. Int. Ed. **53**, 102 (2014)
42. H. Wu, D. Wexler, G. Wang, H. Liu, J. Solid State Electrochem. **16**, 1105 (2012)
43. V.E. Guterman, T.A. Lastovina, S.V. Belenov, N.Y. Tabachkova, V.G. Vlasenko, I.I. Khodos, E.N. Balakshina, J. Solid State Electrochem. **18**, 1307 (2014)

Chapter 3
Composition, Structure and Stability of PtCu/C Electrocatalysts with Non-uniform Distribution of Metals in Nanoparticles

Sergey Belenov, Vladimir Guterman, Nataliya Tabachkova, Vladislav Menshchikov, Alina Nevelskaya and Irina Gerasimova

Abstract Carbon supported Pt–Cu electrocatalyst with increased platinum content in the surface layer of nanoparticles was synthesized by a sequential chemical reduction of Cu (II) and Pt (IV) compounds from their solutions. A subsequent thermo-treatment and the combination of thermo- and corrosion treatment of the catalyst resulted in a slight increase in an average crystallite size, but had not an essential negative impact on the electrochemically active surface area (ESA) value. During stability tests (1000 voltammetric cycles), the values of ESA for pristine and post-treated Pt–Cu/C catalysts decreased by 15–20% from 61–65 to 56 m^2g^{-1} (Pt). In similar tests of commercial Pt/C catalyst TEC10v30e an ESA value decreased by 56% from 80 to 36 m^2g^{-1} (Pt). High stability of the prepared Pt–Cu/C catalysts in combination with high ESA values and oxygen reduction reaction activity may be since, despite the comparatively large size of nanoparticles, the majority of them have a core-shell or hollow structure. The obtained result demonstrates the prospect of using bimetallic catalyst systems with an uneven surface distribution of metals in nanoparticles as electrocatalyst in low temperature fuel cells and shows a way of combining high activity and durability of the electrocatalyst.

3.1 Introduction

Carbon-supported platinum catalysts are the main components of the catalyst layer in low temperature fuel cells (LTFC) of different types. To reduce the cost of power, produced by LTFC, it is necessary to significantly reduce the noble metal loading in the catalyst layer, without reducing the catalyst specific characteristics and stability

S. Belenov (✉) · V. Guterman · V. Menshchikov · A. Nevelskaya · I. Gerasimova
Chemistry Department, Southern Federal University, Rostov-on-Don, Russia
e-mail: sbelenov@sfedu.ru

N. Tabachkova
National University of Science and Technology «MISIS», Moscow, Russia

I. A. Parinov et al. (eds.), *Advanced Materials*, Springer Proceedings in Physics 224, https://doi.org/10.1007/978-3-030-19894-7_3

[1–3]. It can be accomplished by partial substitution of platinum by other less expensive metals [1–5]. Unfortunately, the use of catalysts, based on nanoparticles of two-component platinum-metallic solid solutions, has problems associated with the selective dissolution of the alloying component [2, 5, 6]. Catalysts based on the *M*-core–Pt-shell structure of the bimetallic nanoparticles, where *M* is an inexpensive transition *d*-metal, may be an effective solution to these problems [7–16]. In this case, the reduction of the nanoparticle size ceases to be a major factor in ensuring high activity (high surface area, m^2g^{-1} of the noble metal) of the catalyst. The thickness and continuity of the shell, stability of the core-shell structure during the operation, and the influence of the metal core on the catalytic activity of the shell are becoming crucial factors. It should be highlighted that the selective dissolution of the least stable component from the nanoparticle core in the case of violation of platinum shell integrity can lead to the formation of the so-called hollow platinum nanoparticles, the latter being very promising for the catalysis [17–21].

Synthesis in the plurality of metal nanoparticles, which are characterized by an uneven distribution of the components in each nanoparticle, is very challenging [22]. The task of producing nanoparticles, the architecture of which remains unchanged during the operation of the catalyst, is even more difficult [3, 15, 18, 23–27]. There are a number of physico-chemical methods of investigation to demonstrate the details of nanoparticle architecture [3, 9, 13, 22, 24, 28–33]. Unfortunately, the complexity of these methods can make the analysis and interpretation of experimental data rather complicated.

The main approaches used for the synthesis of nanoparticles with a core-shell structure, to a first approximation, can be divided into two types: (i) sequential formation of the core and the shell of nanoparticle [22, 34, 35] and (ii) preparation of bimetallic nanoparticles with subsequent treatment [23, 28, 36], which leads to the formation of a thin shell of platinum. Upon preparation of Pt—*M* core-shell nanoparticles a real "core" is not always uniformly coated by platinum, moreover the thickness of the shell can be varied for nanoparticles ("cores") of different sizes [36, 37]. Thus, even when trying to obtain similar types of nanoparticles with a core-shell structure, the formation of a complex mixture of nanoparticles of different size and structure—from the solid solutions to core-shell structures—seems to be quite possible in real systems.

Apparently, the structure of the nanoparticles with a complex architecture can vary over time due to the processes of mutual diffusion of atoms of different metals [25], and/or due to segregation of one of the metal components on the surface of nanoparticles [23, 28]. All these effects cause changes in the composition and structure of the nanoparticles and, consequently, affect the catalytic activity of the material during operation. It must be emphasized that we have not found any publications, which carried out a comparative evaluation of the stability for catalysts containing nanoparticles of Pt-based solid solution, and bimetallic catalysts based on core-shell nanoparticles. At the same time, the number of papers devoted to assessing the stability of Pt/C and Pt-alloy/C catalysts is very large. For example, the review by Shengsheng Zhang et al. [38] analyzed the results of more than 120 articles devoted to the evaluation of various aspects of the stability of the catalysts.

The common reasons of the degradation of Pt/C and Pt-*M*/C catalysts are well understood by researchers and in a simplified form can be summarized as follows [38–40]: detachment of NPs from carbon support, NPs migration from the carbon support and thereafter overlapping, dissolution and re-precipitation of platinum, oxidation of carbon support in the zone of contact with platinum.

There are several express-methods proposed for evaluating the stability of platinum catalysts [41–44]: soaking in hot solutions of various acids [5, 23], thermo-treatment in air [45, 46], electrochemical testing. In view of the test conditions, these methods can be used for rapid evaluation of catalyst stability in the different modes of operation of the fuel cell. For example, it is possible to use load cyclic voltammetry to simulate start–stop conditions of a PEMFC, thus enabling an investigation into how specific operational conditions affect degradation [38, 39]. The most common electrochemical methods to assess the stability of platinum-carbon electrocatalysts should include the registration of a large number of cyclic voltammograms (CV) (100–5000 cycles) [31, 47–50], and prolonged potentiostatic measurements [51, 52]. Questions of the sweep rate, potential range and the number of cycles to be carried out to assess the durability of catalysts are considered by different authors in different ways. Generally, the narrower the range of potential cycling, the greater the number of cycles carried out for evaluating the durability of the catalyst must be.

Concluding the review of the literature, we would like to point out two important aspects of research in the area of materials preparation and of functional characteristics of electrocatalysts for LTFC. First, despite a large number of papers devoted to the preparation and study of metal nanoparticles of a core-shell structure, the problem of developing an efficient and reliable method for obtaining active and stable catalyst-based bimetallic nanoparticles with a core-shell structure has not been solved yet. Moreover, development of methods for synthesis and post-treatment of metal nanoparticles of the core-shell structure, which would ensure the stability of the structure during catalyst operation combined with high activity of the catalyst, is still an urgent task.

Second, the evolution of core-shell electrocatalysts, and their ability to preserve the complex structure of bimetallic nanoparticles in the process of operation remain important and scarcely explored issues. Long term cycling voltammetry is the most common and informative express-method to evaluate the stability of electrocatalysts.

The aim of this article is to study the electrochemical performance and the stability of the structural characteristics of Pt–Cu/C electrocatalyst, prepared by successive chemical reductions of Cu (II) and Pt (IV) from solutions of their compounds. Also it was important to assess the possibility of a positive effect of the thermal and corrosion post-treatment of the catalyst on its stability and catalytic activity in the oxygen reduction reaction (ORR). We consider it possible to use in this case a voltammetric cycling within a wide range of potential values (from 0.6 to 1.4 V) to assess the structural stability of the catalyst by comparing it with a commercial Pt/C catalyst TEC10v30e (TKK, Japan) as a reference sample.

3.2 Research Method

3.2.1 Preparation and Post-treatment of Cu@Pt/C Catalyst

Preparation of Pt–Cu/C electrocatalyst was carried out in two stages. First, we reduced Cu^{2+} in the carbon (Vulcan XC72) suspension based on $CuSO_4$ and NH_3 solution at pH = 10. Then, a Cu/C slurry in $H_2PtCl_6 \cdot nNH_3$ solution (pH = 10) was prepared and Pt (IV) was reduced. As the reducing agent, an aqueous solution of 0.5 M $NaBH_4$, the excess of which was injected into the previously prepared suspension containing the precursors of copper and platinum, was used. A mixture of water and ethylene glycol (1:1) was used as a solvent for the preparation of suspensions. This sequential chemical reduction of metals was due to the desire to obtain bimetallic nanoparticles, a significant proportion of which would have a Cu-core—Pt-shell structure.

The possibility to obtain Pt–Cu/C catalysts based on core-shell nanoparticles using similar methods of synthesis, previously has been demonstrated in [53]. The formation of a secondary platinum shell preferably on the surface of preformed copper "cores", rather than the formation of separate platinum nanoparticles on the active sites of the carbon support, may be a consequence of a much better matching of crystal lattice structures for Cu and Pt, than for Pt and C, as well as enabling a more intense interatomic interaction in the system Pt–Cu.

A composition of Pt–Cu/C material, calculated by the amount of precursors, corresponds to a 30% mass loading of metals with an atomic ratio 1:1. Part of the resulting Pt–Cu/C catalyst was heated at 250 °C for 1 h in an atmosphere of Ar. In the following, the notation CP_{therm} for this sample is used. A part of the CP_{therm} material was exposed to post-treatment, during which the material was maintained at room temperature in 1 M HNO_3 for 1 h and then was washed and dried. For this sample, the notation CP^{cor}_{therm} is used.

3.2.2 Characterization of the Catalysts

Diffraction patterns for the Pt/C materials were obtained using an ARL X'TRA (Thermo Scientific, Switzerland) diffractometer with CuKa radiation (λ = 0.154056 nm), operation at 40 kV and 30 mA. The average crystallite size was calculated according to the Scherrer equation [54] using XRD data concerned with 111 peak, corresponding to $2\theta = 39.9°$.

XPS method was used for the determination composition of surface layer of Pt–Cu nanoparticles. XPS data were obtained with Axis Ultra DLD (Kratos) spectrometer, which used monochromatic Al Kα radiation with energy of analyzer transmission 20 eV. Atomic ratios of elements in the catalysts were calculated from the integrated areas of the Pt 4f and Cu 2p photoelectron peaks.

Microphotographs of the synthesized materials were obtained using a JEM-2100 (JEOL, Japan) microscope operated at an accelerating voltage of 200 kV and

resolution of 0.2 nm. To conduct electron-microscopic studies a drop of specially prepared catalyst ink (about 0.5 mg of the catalyst was dispersed ultrasonically in 1 ml of isopropanol for 5 min) was applied on a copper grid covered with a thin layer of amorphous carbon film (to fix the microparticles on the surface) and dried for about 20 min in an air atmosphere at room temperature.

3.2.3 Electrochemical Measurements

Electrochemical measurements were performed at room temperature 25 ± 2 °C using a conventional three-electrode cell. A 0.1 M $HClO_4$ solution saturated with Ar at atmospheric pressure was used as an electrolyte. The glassy carbon electrodes with an applied layer of electrocatalyst powder were used as the working electrodes. The platinum wire was employed as the counter electrode, the Ag/AgCl/KCl saturated electrode applied as the reference electrode. All potentials in this work are referenced *versus* a standard hydrogen electrode.

The Pt–Cu/C slurry (the so-called "catalyst ink") was prepared for applying the catalyst on the end of the rotating disk electrode. The catalytic ink consisted of a dispersed suspension of 0.006 g of electrocatalyst in a mixture, which was prepared by mixing 900 µl of isopropanol and 100 µl of a 0.05% Nafion solution. The resulting suspension was sonicated during 10 min and then mixed by magnetic stirrer for 10 min. An aliquot (6 µl) of catalytic ink dropped to the surface of a glassy carbon electrode with geometric surface 0.196 cm^2 (diameter 5 mm) and dried at room temperature for 10 min to form a thin catalyst layer on the electrode surface. Then, to further the binding of the catalyst layer, a 7 µl of 0.05% Nafion solution was applied and dried.

The active surface area (ESA) was determined by the quantity of electricity expended for electrochemical adsorption/desorption of atomic hydrogen with input of double layer region, as described in [55–57]. Measurements were performed under the following program: I—registration of 100 cycles with potential sweep in the range of 0.597 to 1.397 V at 100 mV s^{-1}; II—registration of 2 cycles with potential sweep rate of 20 mV s^{-1} in the range from −0.033 to 1.197 V. This program was repeated 10 times. A second cyclic voltammogram, which was recorded at a potential scan rate of 20 mV s^{-1}, was used to calculate ESA. Direct calculation of the quantity of electricity was carried out by integrating the corresponding "hydrogen" CV region in the "current–time" coordinates using AfterMath software (Pine Research Instrumentation Co.), considering the background current, which was spent on charge/discharge of the electrical double layer [55].

A linear sweep voltamperometry (LSV) measurement was performed to evaluate the activity of catalytic materials in the oxygen electroreduction reaction (ORR). In this case, after ESA measurements, a 0.1 M $HClO_4$ solution was saturated with oxygen at atmospheric pressure for 60 min. Then, while continuing to purge oxygen, the potential of the working electrode was changed from 1.197 to 0.020 V with a sweep rate of 20 mV s^{-1} at different speeds of disc electrode rotation

(400, 600, 1000, 1400, 1800 and 2400 rpm). To compare the activity of the tested catalysts, measured currents were normalized by the mass of platinum (A g^{-1} (Pt)) and/or on the ESA of the catalyst (mA cm^{-2} (Pt)).

3.3 Results and Discussion

3.3.1 Composition and Microstructure of Pt–Cu/C Materials

According to the XRD-study (Fig. 3.1) Pt–Cu/C material obtained (CP) contains metal nanoparticles with a face-centered cubic structure. The values of the reflection maximum for the sample are shifted to higher values of 2θ, compared with the phase of pure platinum (2θ = 39.9°) (Fig. 3.1, curve 1). Reflections corresponding to copper or its oxides are not observed on the diffractogram. Unfortunately, the results of X-ray analysis cannot confirm the formation of core-shell nanoparticles. The resulting diffractogram can match nanoparticles of two-component PtCu solid solution with an average crystallite size of about 4.2 nm. PtCu nanoparticles with a core-shell structure can show the same diffractogram. In this case, observed reflections are the imposition (superposition) of the reflections for two phases: platinum and copper, or solid solutions thereof.

Thermo-treatment of the pristine PtCu/C material in an inert atmosphere not influenced substantially by the position of the reflection maxima in the diffractogram (Fig. 3.1, Table 3.1), however, led to their slight broadening (Fig. 3.1, curve 2),

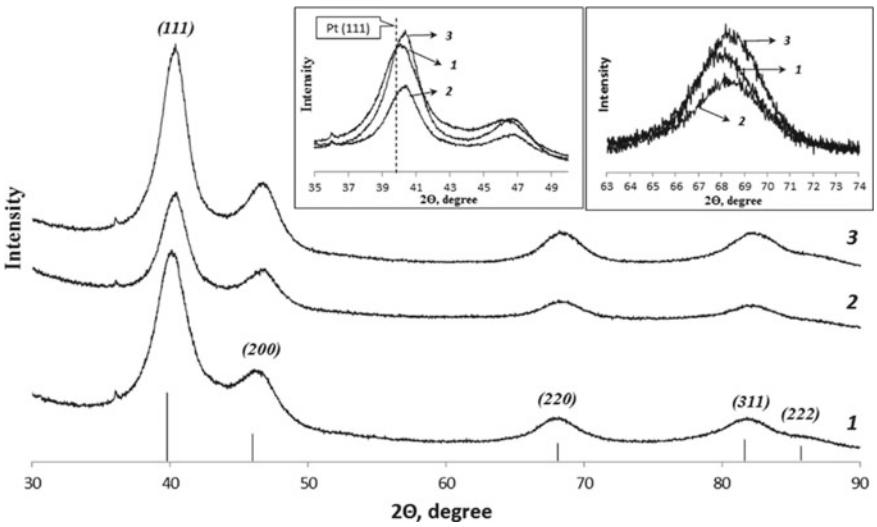

Fig. 3.1 XRD patterns of the PtCu/C catalysts. 1—pristine ("as prepared") sample, 2—after thermo-treatment (250 °C, 1 h), 3—after thermo- and acid- (1 h in 1 M HNO_3) treatment

Table 3.1 Some characteristics of commercial TEC10v30e catalyst and prepared PtCu/C catalyst before and after treatment

Sample	Metals Loading, ω, % (TG)	$D_{(111)}$, nm	Lattice Parameter (a), nm	ESA, $m^2\ g^{-1}$ Pt	EDX Composition[a]	XPS Composition[b]
CP	29	4.2	0.3891(2)	61	1.9	–
CP_{therm}	29	4.6	0.3884(2)	65	2.0	–
CP^{cor}_{therm}	23	3.9	0.3887(5)	63	3.9	11.1
TEC10v30e	28	3.3	0.3987(6)	80	–	–

[a]*x*-value of Pt_xCu material
[b]*x*-value at the surface of Pt_xCu

presumably because of the increased average size of the crystallites to about 4.6 nm (Table 3.1). Note that the diffractogram of thermo-treated PtCu/C (sample CP_{therm}) also does not show maxima corresponding copper oxides.

The chemical composition of the metal component for the CP_{therm} material is close to Pt_2Cu, which almost corresponds to the composition of the pristine CP material (Table 3.1). At the same time, the sample, which was sequentially thermo- and acid treated—CP^{cor}_{therm}, comprises a reduced amount of copper as compared with the original CP catalyst (Table 3.1). The exposition of Pt_2Cu/C in a solution of nitric acid resulted in partial dissolution of copper to the $Pt_{3.9}Cu$ composition. The half-width of the <111> maximum on the diffractogram (Fig. 3.1, curve 3), for which the average crystallite size (Table 3.1) was calculated, was virtually unchanged after this treatment.

It should be highlighted also that the metal loading does not change in the sample after a thermal treatment (CP_{therm}), but decreases through further acid treatment from 29 to 23 wt% (Table 3.1). It is caused mainly by copper dissolution in nitric acid. Furthermore, a separation of some Pt or Pt–Cu nanoparticles from the carbon surface can occur during acid treatment. Thus, heat treatment of Pt_2Cu/C material leads to a slight increase in the average crystallite size, and subsequent treatment in acid that is to an even greater decrease in the size of the crystallites and the partial dissolution of the metal. It causes a decrease of metals loading in the sample to 23% and the change in the composition of metal component from Pt_2Cu to $Pt_{3.9}Cu$. Taking into account the high reactivity of the copper nanoparticles with respect to the solution of nitric acid, it can be assumed that the acid treatment leads to the dissolution of copper from nanoparticles with core-shell structure in the situation where the platinum shell is not continuous and therefore does not protect the core from corrosion. Additionally, a leaching (selective dissolution) of copper atoms from the surface layers of nanoparticles should occur when nanoparticles of a solid solution of Pt_xCu react with an acid [22, 25], as it was in the case of different Pt—*M* alloys [23, 28]. The formation of a secondary core-shell structure is a consequence of copper dissolution. In contrast to the primary core-shell structures, the core in such nanoparticles is a solid solution of copper in platinum. Apparently, CP^{cor}_{therm} material comprises nanoparticles of three types: (i) Cu-core–Pt-shell

particles with continuous platinum shell; (ii) secondary structure of Pt–Cu-core–Pt-shell, and (iii) hollow platinum nanoparticles formed by the dissolution of the copper core from the imperfect structures of the first type, which got a "leaky" shell in the pristine state. The X-ray photoelectron spectroscopy confirmed the assumption that a certain fraction of particles in the material CP^{cor}_{therm} had a core-shell structure: a concentration of copper on the surface of the nanoparticles in the material is much lower than the bulk concentration (Table 3.1). On the other hand, the results of XPS cannot predict the presence of only the particles with core-shell structure because copper atoms are also present on the surface.

Transmission electron microscopy, perhaps, is the only direct method that can confirm the existence of core-shell nanoparticles in the synthesized Cu@Pt/C electrocatalysts. The criterion of a different nature of the atoms in the shell and in the core, in the first place, is a different brightness (contrast) of the respective areas of the nanoparticles in the photograph. Obviously, to identify the structure of the core-shell by electron-microscopic study is easier for large nanoparticles. Maybe this is the reason, why the existence of such a structure is well established only for some nanoparticles (Fig. 3.2d).

The study of the microstructure of pristine and post-treated Pt–Cu/C electrocatalysts cannot predict possible differences in the values of their ESA. The ESA of the metal (platinum) in post-treated materials, in principle, could be either higher or lower than that in the pristine CP electrocatalyst. It should depend both on the proportion of nanoparticles with a different structure (core-shell, solid solution, single phase nanoparticles) in the initial material and from the influence of the post-treatment to the composition, structure, and degree of agglomeration of the nanoparticles. Possible ways of evolution of the structure of nanoparticles in the result of catalyst post-treatment are displayed schematically in Fig. 3.3.

3.3.2 Electrochemical Measurements

3.3.2.1 Voltammetric Study and Definition of Electrocatalyst ESA

As already mentioned in Sect. 2.2, to determine the ESA for PtCu/C materials CP, CP_{therm} and CP^{cor}_{therm} known technique was used. It was based on the analysis of the CV shape and determining the amount of electricity that has been spent on the adsorption/desorption of atomic hydrogen. The commercial Pt/C catalyst TEC10v30e was studied under the same conditions as the reference catalyst. The characteristic shape of the platinum CV associated with the presence of three regions: (i) the oxygen region (formation and reduction of oxides on the surface), (ii) double-layer region (charging/discharging of the electric double layer) and (iii) the hydrogen region (adsorption and desorption of hydrogen atoms on the platinum surface) [55, 57]. It is known [58] that in the process of repetitive cycles of potential sweeps the Pt surface is cleaned from impurities with subsequent stabilization of current values. At the same time, changes of CV during cycling can be

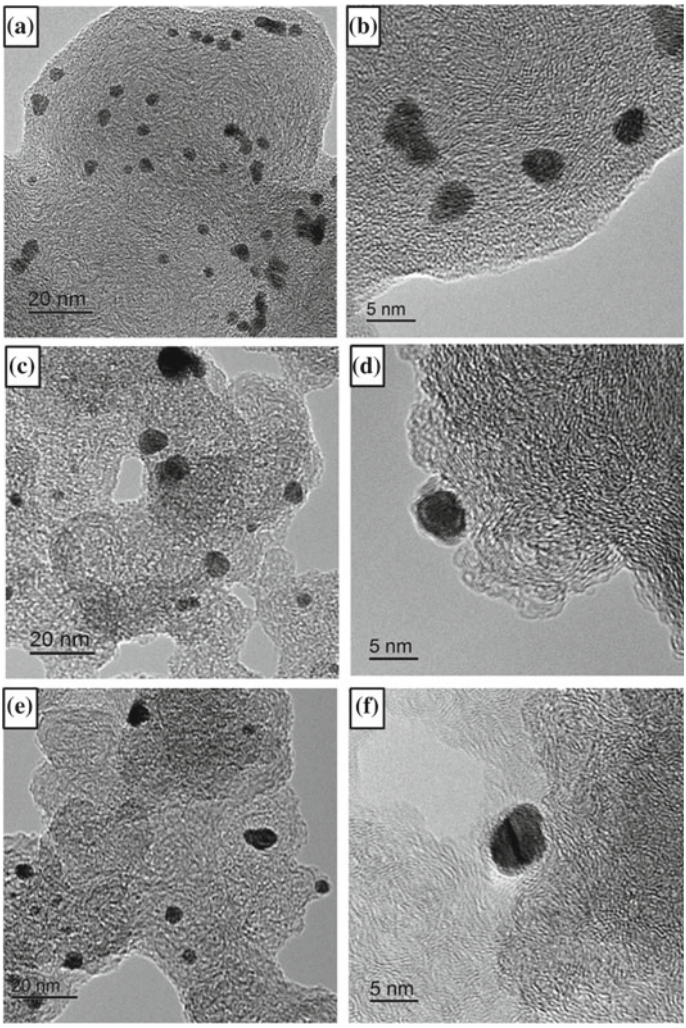

Fig. 3.2 Transmission electron microscopy photographs of the surface for $Cu_{0.9}Pt_{0.1}$@Pt/C electrocatalysts CP (**a**, **b**), CP_{therm} (**c**, **d**) and CP^{cor}_{therm} (**e**, **f**)

associated with the degradation of the electrocatalyst (decreasing of the current) or the development of the surface (growth of the currents). Therefore, a comparative analysis of changes in CV during cycling allows us to draw some conclusions about the nature of the dissolution of less noble components from the surface of the multicomponent nanoparticles [58].

Cyclic voltammograms of PtCu/C materials CP, CP_{therm} and CP^{cor}_{therm}, as well as of commercial Pt/C electrocatalyst TEC10v30e, recorded during the first 100 cycles, are shown in Fig. 3.4. In all cases, a gradual increase in the quantity of

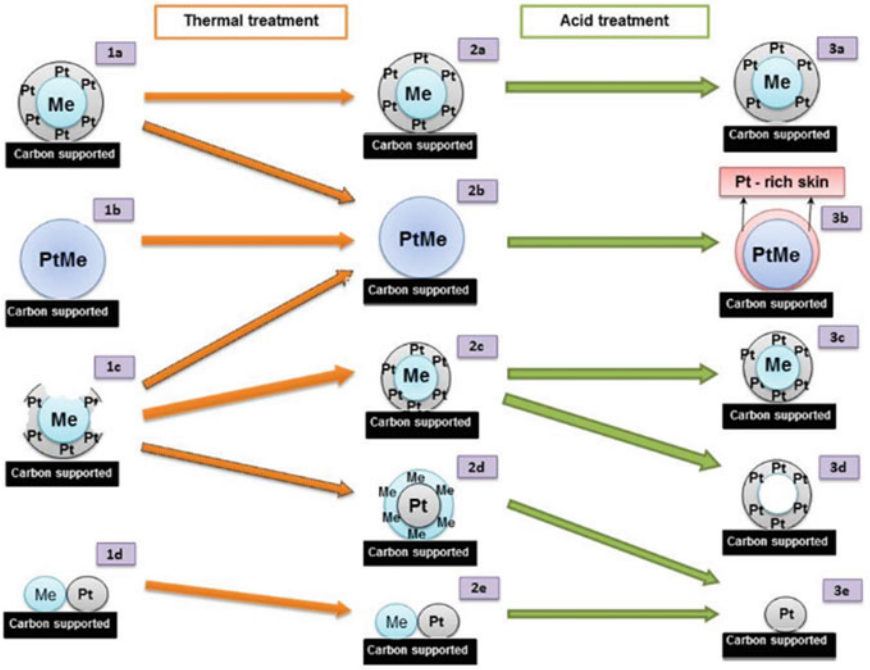

Fig. 3.3 Diagram of the possible evolution of bimetallic nanoparticles in the result of post-treatment. The structure of the nanoparticles: core-shell (1a, 2a, 3a, 2c, 3c), solid solution (1b, 2b), the secondary core-shell nanoparticles (3b), core-shell with defective shell (1c), hollow nanoparticles (3d), metal particles of various phases (1d, 2e), platinum nanoparticles (3e)

electricity, which expends to the adsorption/desorption of hydrogen (the potential range from 0 to 0.2 V) and an increase in the anodic and cathodic currents in the ranges of potentials, corresponding to the oxidation of platinum (0.7–1.0) and electroreduction of oxygen on the oxidized surface (from about 0.8 to 0.5), are observed during cycling. A shape of CV (electric current values) stabilizes after about 10–15 cycles for PtCu/C materials and about 20–30 cycles for the Pt/C catalyst. Note that none of the series of the current–voltage curves are observed anodic peaks in the potential range of 0.2–0.3 and 0.6–0.8 V, corresponding to the dissolution of pure copper or copper from a solid solution with platinum [31, 59]. It means that intensive dissolution of copper from the surface of the catalyst does not occur during the standardization process of PtCu/C electrode.

The active surface area of PtCu/C materials was measured after 100 cycles of potential sweeps (Fig. 3.4). It was found that the ESA values of pristine catalyst and the ESA for the samples after thermo- and consistent thermo- and acid-treatment were similar to each other (Table 3.1). At the same time, the ESA values of PtCu/C catalysts (60–65 $m^2\ g^{-1}$ Pt) were lower than that for the commercial Pt/C catalyst TEC10v30e (80 $m^2\ g^{-1}$ Pt). This fact can be connected both with the large size of

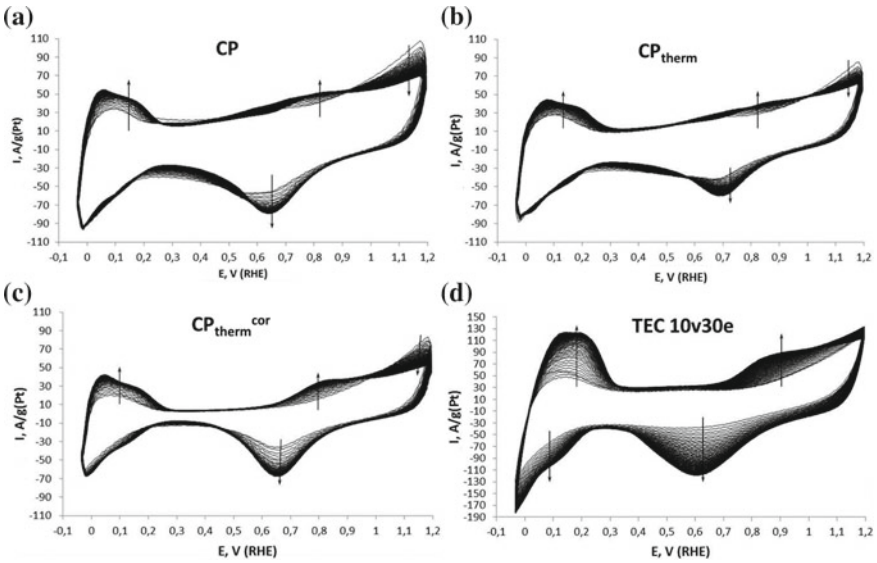

Fig. 3.4 100 CV profiles of (1) PtCu/C as prepared, (2) PtCu/C after thermos-treatment, (3) PtCu/C after thermo- and acid treatment and (4) commercial Pt/C material TEC10v30e in deaerated 0.1 M $HClO_4$ at room temperature with a scan rate of 200 mV s^{-1}

Pt–Cu nanoparticles in comparison with platinum nanoparticles in the commercial catalyst, and with a higher degree of particle agglomeration in PtCu/C catalysts.

3.3.2.2 Durability of Pt–Cu/C Electrocatalysts

The study of the nature of changes in the ESA of catalysts in the process of long-term cycling (see Sect. 2.2) has allowed comparison of their morphological stability. All PtCu/C samples demonstrated a small increase in the active surface area with the maximum after the first 100–200 cycles (the maximum value of the ESA was taken as 100%). Upon subsequent cycling, the gradual decrease in the ESA value was observed (Fig. 3.5a, c). The ESA of the commercial Pt/C material TEC10v30e monotonically decreased during all 1000 cycles (Fig. 3.5d). The ESA of each PtCu/C electrode decreased after 1000 cycles by about 15–20% of the maximum value and in absolute terms amounted to 54–56 m^2 g^{-1} Pt. The ESA of the commercial Pt/C material TEC10v30e decreased by 56% from its maximum value (from 80 to 35 m^2 g^{-1} Pt) after a similar test. Thus, the commercial Pt/C catalyst degraded considerably faster in comparison with prepared PtCu/C catalysts.

We note some characteristics of the electrochemical behavior of the catalysts during cycling. An increase of current values in the double-layer region (voltage range from 0.25 to 0.55 V) (Fig. 3.5a–c), which may be associated with the development of the surface of the carbon support during cycling, is typical for

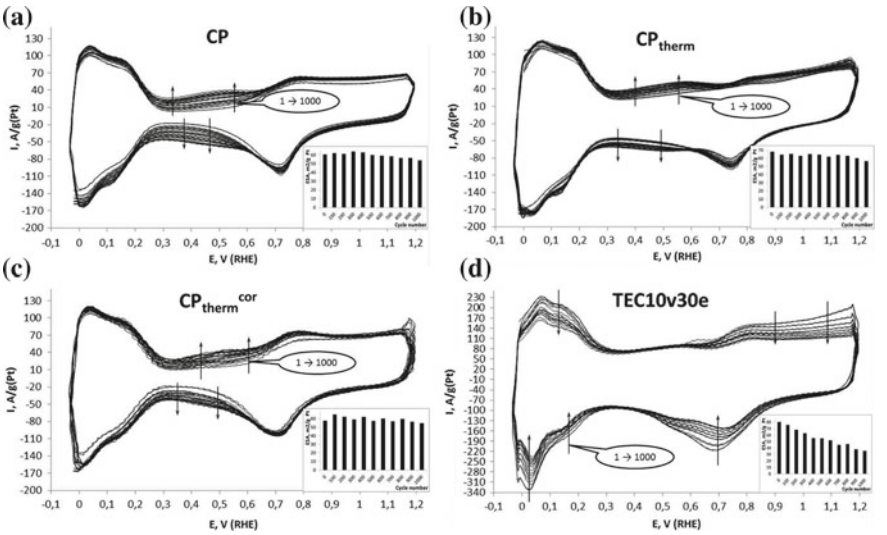

Fig. 3.5 CV profiles for regularly repeated with a scan rate of 20 mV s^{-1} cycles of (1) PC, (2) PC_{therm}, (3) PC^{cor}_{therm}, and (4) commercial Pt/C material TEC10v30e during 1000 corrosion tests in de-aerated 0.1 M $HClO_4$ at room temperature

PtCu/C materials. In contrast, current values in the double-layer region for commercial Pt/C material TEC10v30e remained practically unchanged during corrosion tests. On the other hand, the values of cathodic and anodic currents corresponding to the areas of absorption/desorption of hydrogen and to the formation/reduction of oxides on the platinum surface, markedly reduced during cycling (Fig. 3.5d) in the case of the Pt/C catalyst, while for PtCu/C catalysts the values are stable or even slightly increased (Fig. 3.5a–c). These curves demonstrate a higher stability of electrode characteristics for PtCu/C catalysts compared to a referenced Pt/C catalyst TEC10v30e.

3.3.2.3 Oxygen Reduction Reaction

Comparison of LSV curves for the studied samples (Fig. 3.6) shows that a specific activity of Pt–Cu/C catalyst in the ORR in the potential range of 0.75–0.8 V increases by 3.5–5 times after the thermo-treatment (Table 3.2). Subsequent treatment of the CP_{therm} sample in the acid does not lead to a significant change of specific activity for CP^{cor}_{therm} catalyst. At potentials range of 0.75–0.78 V, CP_{therm}, CP^{cor}_{therm} and commercial Pt/C catalysts exhibit close values of activity (Table 3.2). At the same time, when the potential is 0.8 V, the commercial catalyst exhibits a higher mass activity, compared to copper-based CP_{therm} and CP^{cor}_{therm} catalysts (Table 3.2, Fig. 3.6).

The determination of the number of electrons involved in reactions was made for all the investigated materials. The study was conducted on a rotating disk

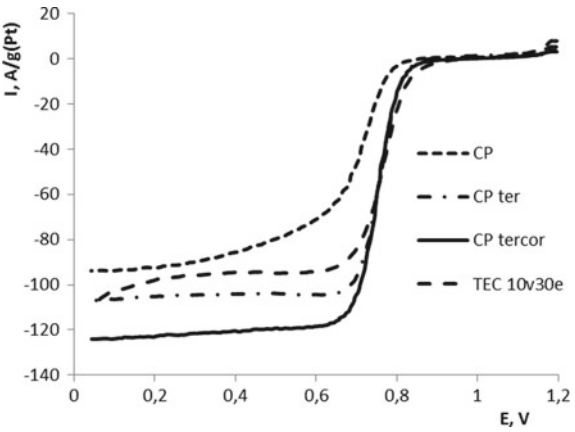

Fig. 3.6 LSV curves for (1) PC, (2) PC_{therm}, (3) PC_{therm}^{cor} and (4) commercial Pt/C catalysts in 0.1 M $HClO_4$ saturated by O_2 at room temperature; scan rate = 20 mV s^{-1}, rotating speed = 1000 rpm

Table 3.2 Features of catalysts obtained from the results of electrochemical studies

Sample	ESA, m^2 g^{-1} (Pt)	D_{aver}, nm	Stability[a], % from maximum	j_{mass}, A g^{-1} (Pt)		J_{spec}, A m^{-2} (Pt)		n
				Potential, V				
				0.75	0.8	0.75	0.8	
CP	61	4.2	85	16.6	3.0	0.27	0.05	3.6
CP_{therm}	65	4.6	80	58.	14.9	0.90	0.22	4.1
CP_{therm}^{cor}	63	3.9	84	58.9	14.7	0.93	0.23	3.9
TEC10v30e	80	2.4	44	58.0	21.5	0.72	0.27	4.1

[a]The electrochemically active surface area after 1000 cycles to a maximum ESA, %

electrode. A Koutecky–Levich equations were used for the calculation, as described in [55, 58].

The calculated value of n was close to the characteristic for pure platinum value $n = 4$ for all the samples (Table 3.2). At the same time, for the CP catalyst the number of electrons $n = 3.6$ is somewhat lower than that for the other samples. This may be a consequence of concurrent side reactions, including the 2-electron reaction of oxygen electroreduction to hydrogen peroxide, on this catalyst. This behavior may be due to the higher surface concentration of copper in the CP material, compared with CP_{therm} and CP_{therm}^{cor} catalysts.

3.4 Conclusion

Bimetallic PtCu/C electrocatalysts (CP, CP_{therm}, and CP_{therm}^{cor}) with a non-uniform distribution of the components in the nanoparticles, namely a higher platinum content of the surface layer, were prepared by the successive chemical reduction of Cu (II), and then Pt (IV) compounds from solutions using the following

thermo- and corrosion treatments. The ESA of prepared catalysts was approximately 60–65 $m^2\ g^{-1}$ (Pt), which is less than that for the commercial Pt/C catalyst TEC10v30e ($\sim 80\ m^2\ g^{-1}$ (Pt)), which was used for comparison.

It has been established that the thermo- and following acid treatment of PtCu/C catalyst do not affect the value of the electrochemically active surface area of the metal, but after acid treatment, the material loses a substantial amount of copper. All PtCu/C electrocatalysts showed significantly greater stability during repeated (over 1000 cycles) voltammetric cycling in comparison with a commercial Pt/C catalyst. Cyclic voltammograms of Pt–Cu/C catalysts show a shape—the same as for supported Pt/C catalysts, and the electroreduction of oxygen in these materials occurs at a characteristic for platinum 4-electron mechanism. The specific catalytic activity of the post-treated PtCu/C catalysts in the ORR is not inferior to that of a standard Pt/C sample.

Features of the electrochemical behavior of the prepared PtCu/C materials may be due to the presence of a significant number of nanoparticles with Cu-core–Pt-shell structure. In the case of CP^{cor}_{therm} catalyst, which was treated in nitric acid, a part of core-shell nanoparticles, presumably converted into hollow nanoparticles, which also exhibit high stability and catalytic activity in the ORR.

Thus, a combination of a technique for successive reduction of copper and platinum, and subsequent treatment of the pristine PtCu/C material produces catalysts that are comparable with the commercial Pt/C catalyst in a specific activity in the ORR reaction, but superior to it in the corrosion—morphological stability.

Acknowledgements This research was performed into framework of financing by the Ministry of Education and Science of the Russian Federation (project No. 13.3005.2017/4.6)

References

1. M. Bron, C. Roth, in *New and Future Developments in Catalysis*, ed. by S.L. Suib (Elsevier, 2013), p. 271
2. A.B. Yaroslavtsev, Y.A. Dobrovolsky, N.S. Shaglaeva, L.A. Frolova, E.V. Gerasimova, E.A. Sanginov, Russ. Chem. Rev. **81**, 191 (2012)
3. D. Thompsett (ed.), *Pt Alloys as Oxygen Reduction Catalysts*, 6 (2010)
4. V.S. Bagotsky. *Fuel Cells: Problems and Solutions*, 41 (2012)
5. H.A. Gasteiger, S.S. Kocha, B. Sompalli, F.T. Wagner, Appl. Catal. B Environ. **56**, 9 (2005)
6. E. Antolini, Appl. Catal. B Environ. **74**, 337 (2007)
7. D.A. Cantane, F.E.R. Oliveira, S.F. Santos, F.H.B. Lima, Appl. Catal. B Environ. **136**, 351 (2013)
8. F. Godinez-Salomon, M. Hallen-Lopez, O. Solorza-Feria, Int. J. Hydrogen Energy **37**, 14902 (2012)
9. S.V. Belenov, V.A. Volochaev, V.V. Pryadchenko, V.V. Srabionyan, D.B. Shemet, N. Yu. Tabachkova, V.E. Guterman, Russ. Nanotechnol. **12**(3–4), 147 (2017) (In Russian)
10. H. Zhu, M. Luo, S. Zhang, L. Wei, F. Wang, Z. Wang, Y. Wei, K. Han, Int. J. Hydrogen Energy **38**, 3323 (2013)
11. L. Nguyen Viet, Y. Yang, T. Cao Minh, M. Nguyen Van, Y. Cao, M. Nogami. *Nano Energy* **2**, 636 (2013)

12. A.A. Alekseenko, V.E. Guterman, S.V. Belenov, V.S. Menshikov, N.Y. Tabachkova, O.I. Safronenko, E.A. Moguchikh, Int. J. Hydrogen Energy **43**(7), 3676 (2018)
13. Y.M. Chen, F. Yang, Y. Dai, W.Q. Wang, S.L. Chen, J. Phys. Chem. C **112**, 1645 (2008)
14. J. Zhang, F.H.B. Lima, M.H. Shao, K. Sasaki, J.X. Wang, J. Hanson, R.R. Adzic, J. Phys. Chem. B **109**, 22701 (2005)
15. V.V. Pryadchenko, V.V. Srabionyan, A.A. Kurzin, N.V. Bulat, D.B. Shemet, L.A. Avakyan, S.V. Belenov, V.A. Volochaev, I. Zizak, V.E. Guterman, L.A. Bugaev, Appl. Catal. A General **525**, 226 (2016)
16. Z.D. Wei, Y.C. Feng, L. Li, M.J. Liao, Y. Fu, C.X. Sun, Z.G. Shao, P.K. Shen, J. Power Sources **180**, 84 (2008)
17. D.A. Cantane, F.E.R. Oliveira, S.F. Santos, F.H.B. Lima, Appl. Catal. B Environ. **136**, 351 (2013)
18. X. Zhou, Y. Gan, J. Du, D. Tian, R. Zhang, C. Yang, Z. Dai, J. Power Sources **232**, 310 (2013)
19. Y. Zhang, C. Ma, Y.M. Zhu, R. Si, Y. Cai, J.X. Wang, R.R. Adzic, Catal. Today **202**, 50 (2013)
20. M.R. Kim, D.K. Lee, D.J. Jang, Appl. Catal. B Environ. **103**, 253 (2011)
21. L. Dubau, J. Durst, F. Maillard, L. Guetaz, M. Chatenet, J. Andre, E. Rossinot, Electrochim. Acta **56**, 10658 (2011)
22. Z.M. Peng, H. Yang, Nano Today **4**, 143 (2009)
23. N. Travitsky, T. Ripenbein, D. Golodnitsky, Y. Rosenberg, L. Burshtein, E. Peled, J. Power Sources **161**, 782 (2006)
24. D.L. Wang, H.L.L. Xin, R. Hovden, H.S. Wang, Y.C. Yu, D.A. Muller, F.J. DiSalvo, H.D. Abruna, Nat. Mater. **12**, 81 (2013)
25. A. Marcu, G. Toth, R. Srivastava, P. Strasser, J. Power Sources **208**, 288 (2012)
26. L. Dubau, F. Maillard, M. Chatenet, J. Andre, E. Rossinot, Electrochim. Acta **56**, 776 (2010)
27. F. Maillard, L. Dubau, J. Durst, M. Chatenet, J. Andre, E. Rossinot, Electrochem. Commun. **12**, 1161 (2010)
28. C. Wang, M.F. Chi, D.G. Li, D. Strmcnik, D. van der Vliett, G.F. Wang, V. Komanicky, K.C. Chang, A.P. Paulikas, D. Tripkovic, J. Pearson, K.L. More, N.M. Markovic, V.R. Stamenkovic, J. Am. Chem. Soc. **133**, 14396 (2011)
29. R.F. Wang, H. Wang, B.X. Wei, W. Wang, Z.Q. Lei, Int. J. Hydrogen Energy **35**, 10081 (2010)
30. F. Xu, M.-X. Wang, Q. Liu, H.-F. Sun, S. Simonson, N. Ogbeifun, E.A. Stach, J. Xie, J. Electrochem. Soc. **157**, B1138 (2010)
31. G. Gupta, D.A. Slanac, P. Kumar, J.D. Wiggins-Camacho, X. Wang, S. Swinnea, K.L. More, S. Dai, K.J. Stevenson, K.P. Johnston, Chem. Mater. **21**, 4515 (2009)
32. V.R. Stamenkovic, B.S. Mun, M. Arenz, K.J.J. Mayrhofer, C.A. Lucas, G. Wang, P.N. Ross, N.M. Markovic, Nat. Mater. **6**, 241 (2007)
33. Z.L. Wang, J. Phys. Chem. B **104**, 1153 (2000)
34. H. Zhu, M.C. Luo, S. Zhang, L.L. Wei, F.H. Wang, Z.M. Wang, Y.S. Wei, K.F. Han, Int. J. Hydrogen Energy **38**, 3323 (2013)
35. M. Ammam, E.B. Easton, J. Power Sources **222**, 79 (2013)
36. Z. Peng, H. Yang, Nano Today **4**, 143 (2009)
37. V.V. Pryadchenko, S.V. Belenov, D.B. Shemet, V.A. Volochaev, V.V. Srabionyan, L. A. Avakyan, N.Yu. Tabachkova, V.E. Guterman, L. A. Bugaev. Fizika Tverdogo Tela, **59**(8), 1642 (2017) (In Russian)
38. S. Zhang, X.-Z. Yuan, J.N.C. Hin, H. Wang, K.A. Friedrich, M. Schulze, J. Power Sources **194**, 588 (2009)
39. J. Speder, A. Zana, I. Spanos, J.J.K. Kirkensgaard, K. Mortensen, M. Hanzlik, M. Arenz, J. Power Sources **261**, 14 (2014)
40. A. Zana, J. Speder, N.E.A. Reeler, T. Vosch, M. Arenz, Electrochim. Acta **114**, 455 (2013)
41. J.F. Wu, X.Z. Yuan, J.J. Martin, H.J. Wang, J.J. Zhang, J. Shen, S.H. Wu, W. Merida, J. Power Sources **184**, 104 (2008)

42. Y. Shao-Horn, W.C. Sheng, S. Chen, P.J. Ferreira, E.F. Holby, D. Morgan, Topics Catal. **46**, 285 (2007)
43. Y.Y. Shao, G.P. Yin, Y.Z. Gao, J. Power Sources **171**, 558 (2007)
44. E. Antolini, J.R.C. Salgado, E.R. Gonzalez, J. Power Sources **160**, 957 (2006)
45. V.V. Pryadchenko, S.V. Belenov, D.B. Shemet, V.V. Srabionyan, L.A. Avakyan, V.A. Volochaev, A.S. Mikheykin, K.E. Bdoyan, I. Zizak, V.E. Guterman, L.A. Bugaev, J. Phys. Chem. C **122**, 17199 (2018)
46. S.C. Zignani, E. Antolini, E.R. Gonzalez, J. Power Sources **182**, 83 (2008)
47. V.E. Guterman, S.V. Belenov, A.A. Alekseenko, R. Lin, N.Yu. Tabachkova, O.I. Safronenko. *Electrocatalysis*, **9**(5), 550 (2018)
48. A.S. Arico, A. Stassi, E. Modica, R. Ornelas, I. Gatto, E. Passalacqua, V. Antonucci, J. Power Sources **178**, 525 (2008)
49. Y.-C. Park, K. Kakinuma, M. Uchida, D.A. Tryk, T. Kamino, H. Uchida, M. Watanabe, Electrochim. Acta **91**, 195 (2013)
50. K.C. Neyerlin, R. Srivastava, C.F. Yu, P. Strasser, J. Power Sources **186**, 261 (2009)
51. H.R. Colon-Mercado, B.N. Popov, J. Power Sources **155**, 253 (2006)
52. H.R. Colon-Mercado, H. Kim, B.N. Popov, Electrochem. Commun. **6**, 795 (2004)
53. V.E. Guterman, S.V. Belenov, AYu. Pakharev, M. Min, NYu. Tabachkova, E.B. Mikheykina, L.L. Vysochina, T.A. Lastovina, Int. J. Hydrogen Energy **41**(3), 1609 (2016)
54. J.I. Langford, A.J.C. Wilson, J. Appl. Cryst. **11**, 102 (1978)
55. U.A. Paulus, A. Wokaun, G.G. Scherer, T.J. Schmidt, V. Stamenkovic, N.M. Markovic, P.N. Ross, Electrochim. Acta **47**, 3787 (2002)
56. V.E. Guterman, T.A. Lastovina, S.V. Belenov, N.Y. Tabachkova, V.G. Vlasenko II, E.N.Balakshina Khodos, J. Solid State Electrochem. **18**, 1307 (2014)
57. H. Schulenburg, J. Durst, E. Muller, A. Wokaun, G.G. Scherer, J. Electroanal. Chem. **642**, 52 (2010)
58. M.K. Jeon, Y.A. Zhang, P.J. McGinn, Electrochim. Acta **55**, 5318 (2010)
59. K. Shirlaine, Y. Chengfei, P. Strasser, ECS Trans. **11**, 205 (2007)

Chapter 4
The Effect of Mechanical Activation on the Structure and Dielectric Properties of $PbYb_{1/2}Nb_{1/2}O_3$–$PbFe_{1/2}Nb_{1/2}O_3$ Solid Solution Ceramics

I. P. Raevski, A. A. Gusev, V. P. Isupov, M. A. Evstigneeva, S. I. Raevskaya, A. G. Lutokhin, S. P. Kubrin, I. N. Zakharchenko, Y. A. Kuprina, V. V. Titov, M. A. Malitskaya, G. R. Li and O. A. Bunina

Abstract Recently we have found out that high-energy mechanical activation during mechanochemical synthesis stimulates disordering of Yb^{3+} and Nb^{5+} cations in the $PbYb_{1/2}Nb_{1/2}O_3$ (PYN) ceramics. However, one could expect a contamination of thus obtained ceramics by iron as the planetary mill AGO-2 with both jars and balls made of the stainless steel was used for mechanical activation. To elucidate the effect of iron doping on the compositional ordering of PYN, in the present work several $(1 - x)$PYN–$x$$PbFe_{1/2}Nb_{1/2}O_3$ (PYN–xPFN) solid solution compositions have been fabricated by both the usual solid-state synthesis and by high-energy mechanochemical synthesis and their structure and properties were compared. Basing on these data the (x, T)-phase diagrams for the PYN – xPFN solid solutions fabricated by both methods were constructed. It was found out that the difference in the lattice parameters values and dielectric properties of ceramics fabricated by different methods are partially due to the formation of the (1–x)PYN–xPFN solid solutions with PFN content larger than nominal one and partially due to the effect of high-energy mechanical activation.

I. P. Raevski (✉) · M. A. Evstigneeva · S. I. Raevskaya · A. G. Lutokhin · S. P. Kubrin · I. N. Zakharchenko · Y. A. Kuprina · V. V. Titov · M. A. Malitskaya · O. A. Bunina
Faculty of Physics, Research Institute of Physics, Southern Federal University, 344090 Rostov-on-Don, Russia
e-mail: igorraevsky@gmail.com

A. A. Gusev · V. P. Isupov
Institute of Solid State Chemistry and Mechanochemistry, SB RAS, 630128 Novosibirsk, Russia

G. R. Li
Shanghai Institute of Ceramics, Chinese Academy of Sciences, 200050 Shanghai, China

I. A. Parinov et al. (eds.), *Advanced Materials*, Springer Proceedings in Physics 224, https://doi.org/10.1007/978-3-030-19894-7_4

4.1 Introduction

Lead-ytterbium niobate $PbYb_{1/2}Nb_{1/2}O_3$ (PYN) belongs to a large family of the so-called 1:1 ternary perovskite oxides $PbB^{3+}_{1/2}M^{5+}_{1/2}O_3 (B^{3+} = Fe, Mn, Sc, In, Yb, Tm, Ho; M^{5+} = Nb, Ta, Sb)$ [1–4]. Similar to 1:2 perovskites $PbB^{2+}_{1/3}M^{5+}_{2/3}O_3$ $\left(B^{2+} = Mg, Zn; M^{5+} = Nb, Ta\right)$ [5–11] both ceramics and single crystals of 1:1 perovskites $PbB^{3+}_{1/2}M^{5+}_{1/2}O_3$ and especially solid solutions on their base are extensively studied nowadays as they exhibit outstanding dielectric, piezoelectric, electrostrictive, pyroelectric, electrocaloric and magnetoelectric properties [12–37]. About 40 years ago, it was discovered that one can change the distribution of the B^{3+} and M^{5+} cations in 1:1 perovskites $PbB^{3+}_{1/2}M^{5+}_{1/2}O_3$ over the octahedral sites of the perovskite lattice and such compositional ordering has a large impact on the properties of these materials and on the temperatures of both ferroelectric and magnetic phase transitions [38–56]. To characterize the degree of such compositional or chemical ordering a long-range order parameter (S) is used. It is defined as $S = 2p - 1$, where p is an occupation probability of either B^{3+} or M^{5+} ions in their "own" sublattice [2, 38–40].

The known methods of varying the ordering degree in $PbB'_nB''_{1-n}O_3$ perovskites are a long-time annealing at temperatures below the temperature T_{OD} of the order-disorder phase transition [2, 38–40], varying of the crystallization conditions [45–48] and Li-doping [49, 50]. However in the case of PYN substantial changes of the ordering degree were achieved only by the latter two methods (Fig. 4.1).

Recently it was found out that high-energy mechanical activation appears to be one of the more effective methods of changing the ordering degree of $PbB'_nB''_{1-n}O_3$ perovskites [54, 57–63]. Our studies revealed the possibility of substantial suppression of relaxor properties of $PbFe_{1/2}Ta_{1/2}O_3$ (PFT) and $PbMg_{1/3}Nb_{2/3}O_3$

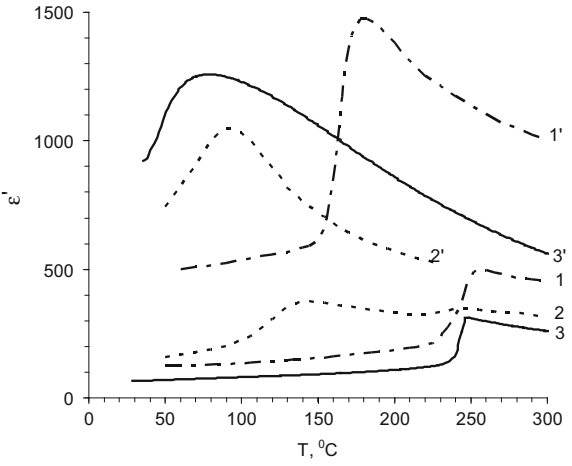

Fig. 4.1 Temperature dependencies of the real part of dielectric permittivity ε' measured at 1 MHz for the most ordered (curves 1–3) and most disordered (curves 1′–3′) $PbYb_{1/2}Nb_{1/2}O_3$ samples fabricated by different methods: 1, 1′—single crystals [56]; 2, 2′—Li-doped ceramics [55, 56]; 3, 3′—ceramics, sintered from the mechanochemically synthesized powders [63]

ceramics by this method [59–61]. This effect is believed to be caused by the local order-disorder processes. Such assumption is supported by the changes in the temperature of magnetic phase transition in PFT and $PbFe_{1/2}Nb_{1/2}O_3$ (PFN) fabricated by mechanochemical synthesis [24]. Using high-energy mechanical activation, we managed to obtain for the first time the disordered modification of ceramic PYN without the use of any additives [62, 63]. We used for mechanical activation a high-energy planetary-centrifugal mill AGO-2 with both jars and balls made of the stainless steel and a contamination of the processed powder with iron took place as was evidenced by the change of the color of ceramics. So one could expect the formation of the $(1 - x)$PYN–$x$$PbFe_{1/2}Nb_{1/2}O_3$ (PYN–xPFN) solid solution during sintering.

The scope of the present work was to elucidate the effect of iron doping on the properties of PYN. For this purpose we carried out a comparative study of the structure and dielectric permittivity of several PYN–xPFN solid solution compositions fabricated by either the usual solid-state synthesis or by high-energy mechanochemical synthesis.

4.2 Experimental

Ceramic samples of $(1 - x)$PYN–$x$$PbFe_{1/2}Nb_{1/2}O_3$ (PYN–xPFN) solid solutions were fabricated by sintering the PYN–xPFN powders synthesized using two technological routes. Route I included a usual solid state synthesis at 850 °C for 4 h of PYN–xPFN compositions from high-purity Yb_2O_3, Fe_2O_3, Nb_2O_5 and PbO oxides thoroughly mixed in a mortar. Route II included the preliminary synthesis of $YbNbO_4$ precursor via the 20 minutes-long high-energy mechanochemical synthesis and subsequent mechanical activation of the mixture of this precursor with PbO. In order to compensate PbO losses during sintering 3 wt% excess of PbO was added to the nominally stoichiometric compositions both in Route I and Route II. High-energy mechanical activation was carried out using planetary-centrifugal mill AGO-2 with the rotation speed of the supporting disc 690 rpm. A mixture of powdered reagents (10 grams) was placed into a steel jar together with steel balls 8 mm in diameter. The ratio of powder to balls weight was 1:20. After each five minutes of activation, the mill was stopped, the jars were opened, the powder was taken out and homogenized in a mortar. Then the activation was continued. The disc-shaped samples for sintering were pressed at 1000 kg/cm^2 without using any plasticizer. They had a diameter of 10 mm and a thickness of about 3 mm. Sintering of the samples was carried out in an electric furnace at 800–1150 °C for 2 h. The pressed samples were placed into the sealed alumina crucibles filled with $PbZrO_3$ powder. This powder created a buffer atmosphere suppressing the PbO evaporation during sintering. The density of thus obtained ceramics measured by the Archimedes method was about 92–96% of the theoretical one. X-ray diffraction (XRD) studies were performed at room temperature in the 2Θ-interval of 20°–80° using the DRON-3 diffractometer and filtered Cu-Kα radiation.

Studies of dielectric permittivity were carried out with the help of the Novocontrol (Alpha-A) and Weine-Kerr 6500 impedance analyzers. The electrodes for measurements were deposited by firing on the silver past at 500 °C.

4.3 Results and Discussion

Our preliminary studies have shown (Fig. 4.2) that ceramic samples of PYN–*x*PFN compositions with $x \geq 0.2$ fabricated by both technological routs exhibit high dielectric losses and enhanced frequency dispersion of the real part of dielectric permittivity ε' values, which masks the $\varepsilon'(T)$ maximum at low frequencies. Such properties are typical of PFN, $PbFe_{1/2}Ta_{1/2}O_3$ and other ternary Fe-containing perovskites and are due to high conductivity [64, 65]. In order to obtain reliable results we used the Li-doping which is known as an effective method of lowering the conductivity of PFN and similar compounds [64–68].Thus all the compositions studied were doped with 1 wt% of Li_2CO_3 As one can see in the inset (a) in Fig. 4.2, such doping enabled us to obtain PYN–*x*PFN ceramics with a very small frequency dispersion of the ε' values above the $\varepsilon'(T)$ maximum.

XRD studies of the polished surfaces of the PYN–*x*PFN ceramic samples carried out at room temperature have shown that for all the compositions studied the main

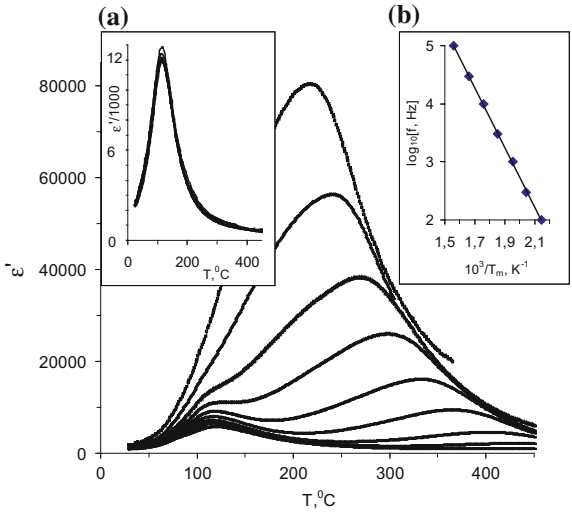

Fig. 4.2 Temperature dependencies of the real part of dielectric permittivity ε' for the 0.8PYN–0.2PFN ceramics sintered from mechanochemically synthesized powders and measured at different frequencies f (Hz): $1–10^3$, $2–10^{3.5}$, $3–10^4$, $4–10^{4.5}$, $5–10^5$, $6–10^{5.5}$, $7–10^6$. The inset (a) shows the $\varepsilon'(T)$ curves measured at the same frequencies for 0.8PYN–0.2PFN ceramics doped with 1 wt% of Li_2CO_3. The inset (b) shows Arrhenius plot of the frequency shift for the high-temperature $\varepsilon'(T)$ relaxation maximum for undoped 0.8PYN–0.2PFN ceramics

phase appeared to be a perovskite one. The admixture of the parasitic pyrochlore phase, estimated from the ratio of relative intensities of the (222) pyrochlore reflex and the (110) perovskite reflex [69] did not exceed 5–10%. No one of the samples studied exhibited the splitting of the main perovskite reflections, corresponding to the orthorhombic distortion of the unit cell, characteristic of the ordered PYN [3, 4, 15, 28, 55, 58, 62, 63, 70].

The concentration dependences of the mean pseudocubic lattice parameter $\tilde{a} = V^{1/3}$ for the $(1 - x)$PYN–xPFN ceramic compositions fabricated either via the usual solid state synthesis or sintered from the mechanochemically synthesized powders are shown in Fig. 4.3. For both fabrication routes, the $\tilde{a}$ values decrease as the PFN content x grows. One can see that in the whole concentration range the $\tilde{a}$ values for the samples fabricated via the usual solid-state synthesis are larger, than for the samples sintered from the mechanochemically synthesized powders. Though this difference becomes smaller as the PFN content x grows, it does not disappear even for pure PFN. Thus one can conclude that smaller $\tilde{a}$ values for the samples fabricated via the Route II are partially due to the formation of the (1–x)PYN–xPFN solid solutions and partially due to the effect of high-energy mechanical activation.

Figures 4.4 and 4.5 show the temperature dependencies of the real part of dielectric permittivity ε' for some (1–x)PYN–xPFN samples fabricated by technological routes I and II and sintered at 1000–1050 °C. One can see that for all the compositions studied the $\varepsilon'(T)$ curves are rather diffused independently of the technological route used for their fabrication. The values of the temperature T_m of the $\varepsilon'(T)$ maximum are also comparatively low. It is known that in the highly-ordered state PYN has a sharp antiferroelectric phase transition at 280–300 °C [3, 4, 15, 28, 58] while disordering causes the lowering of T_m down to 60–75 °C accompanied by a dramatic diffusion of the $\varepsilon'(T)$ maximum [55, 56, 62, 63]. Thus diffuse $\varepsilon'(T)$ curves and low T_m values imply that all the (1–x)PYN–xPFN samples studied are highly disordered irrespectively of the technological route used for their fabrication.

Figure 4.6 shows the effect of the sintering temperature on the $\varepsilon'(T)$ curves of the 0.9PYN–0.1PFN ceramics sintered from the mechanochemically synthesized powders. One can see that the sample sintered at 1100 °C, i.e. close to the

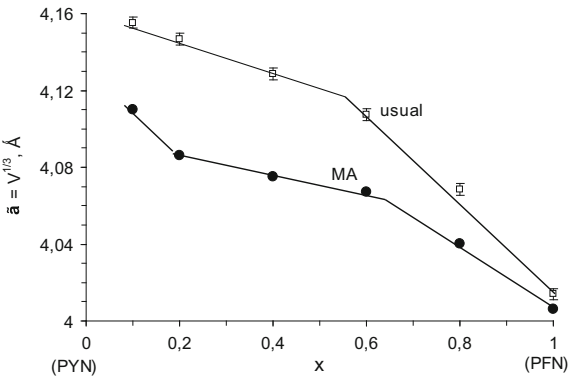

Fig. 4.3 Concentration dependence of the mean lattice parameter $\tilde{a} = V^{1/3}$ for the Li-doped $(1 - x)$PYN–xPFN ceramics fabricated either via the usual solid state synthesis (empty symbols) or sintered from the mechanochemically synthesized powders (filled symbols)

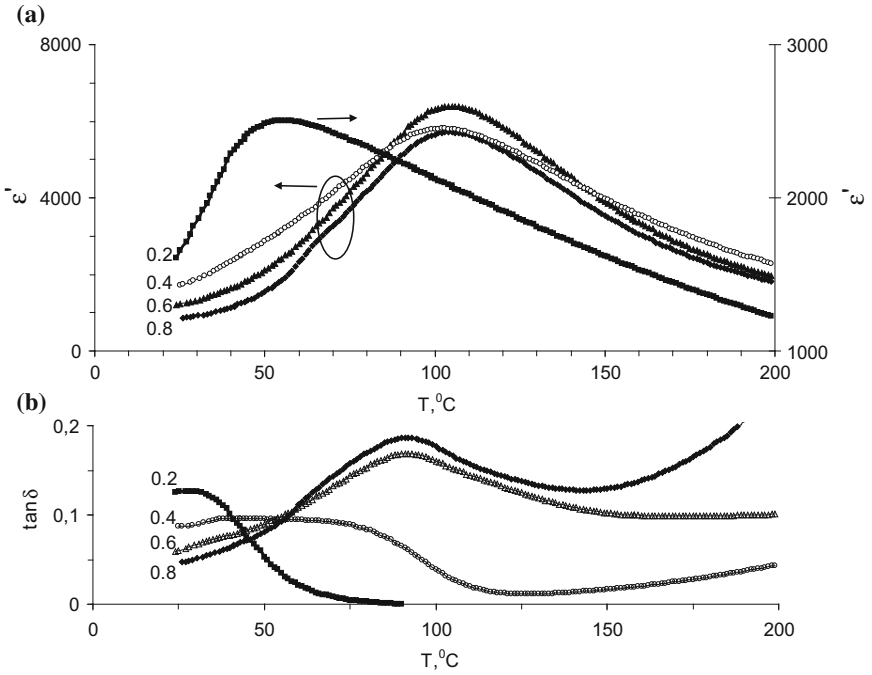

Fig. 4.4 Temperature dependencies of the real part of dielectric permittivity ε' (**a**) and loss tangent tan δ (**b**) measured at 1 kHz for the Li-doped $(1 - x)$PYN–xPFN ceramics sintered from the mechanochemically synthesized powders. Numbers at the curves correspond to x values

temperature T_{OD} of the order-disorder phase transition (for Li-doped PYN ceramics T_{OD} is about 1130 °C [55]) has a substantially higher $\varepsilon'(T)$ maximum and larger frequency shift of T_m as compared to the sample sintered at 800 °C. At the same time T_m value of the sample sintered at 800 °C is higher than that of the sample sintered at 1100 °C. All these facts imply that the sample sintered at 800 °C has somewhat higher degree of ordering than the one sintered at 1100 °C. However, the diffusion of the $\varepsilon'(T)$ maximum estimated using the parameter W2/3 M-H defined as the difference between T_m and the temperature where ε' falls above T_m to the 2/3 of the maximum value [71–73] is practically the same (W2/3 M-H $\approx$ 90 K) for both samples. This value of W2/3 M-H is larger than that for the disordered Li-doped PYN ceramics (W2/3 M-H $\approx$ 65 K) obtained by usual method [55, 56]. Larger diffusion of the $\varepsilon'(T)$ maximum as compared to ceramics obtained by usual method appears to be typical of ferroelectric ceramics sintered from the mechanochemically synthesized powders [57, 59, 63, 64, 68, 74]. This enhanced diffusion of the $\varepsilon'(T)$ maximum seems to be due to higher concentration of defects created in the course of high-energy mechanical activation as well as for spatial inhomogeneities of the compositional ordering degree typical of both single crystals and ceramics of ternary perovskites [75, 76, 79–81].

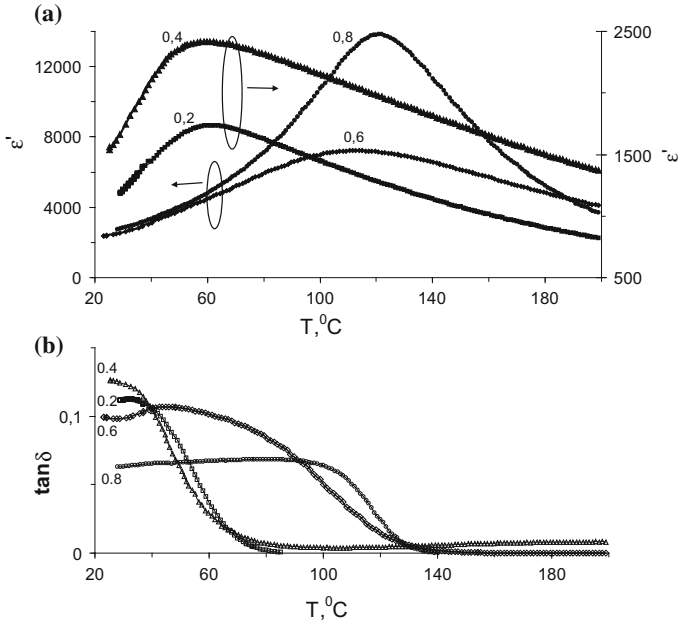

Fig. 4.5 Temperature dependencies of the real part of dielectric permittivity ε' (**a**) and loss tangent tan δ (**b**) measured at 1 kHz for the Li-doped $(1 - x)$PYN–xPFN ceramics fabricated via the usual solid state synthesis. Numbers at the curves correspond to x values

For both 0.9PYN–0.1PFN samples shown in Fig, 4.6 the increase of T_m with the frequency f does not follow the Arrhenius law, evidencing the non-Debye character of relaxation (Fig. 4.7a). However, as one can see in Fig. 4.7b, the frequency shift of T_m for both these samples is well fitted with the empirical Vogel–Fulcher law typical of relaxors [77–79]:

$$f = f_0 \exp[-W/k(T_m - T_0)]$$

Here f_0 is an attempt frequency, W is the activation energy and T_0 is the so-called Vogel–Fulcher temperature, associated with the freezing of polar nanoregions and transition into the dipole-glass state [77]. For both 0.9PYN–0.1PFN samples studied $f_0 \approx 10^{11}$ Hz. The Vogel–Fulcher activation energy W for the 0.9PYN–0.1PFN sample sintered at 800 °C (0.013 eV) is smaller than that for the sample sintered at 1100 °C (0.041 eV) in good correlation with much larger frequency shift of T_m of the latter one. It is worth noting that W values of both 0.9PYN–0.1PFN samples studied are smaller than that of the canonical relaxor $PbMg_{1/3}Nb_{2/3}O_3$ ($W \approx 0.07$ eV [77, 79]).

Besides the $\varepsilon'(T)$ maximum at the ferroelectric or antiferroelectric phase transition, in the majority of the (1–x)PYN–xPFN samples studied a high-temperature relaxation $\varepsilon'(T)$ maxima are observed above T_m. In contrast to undoped ceramics

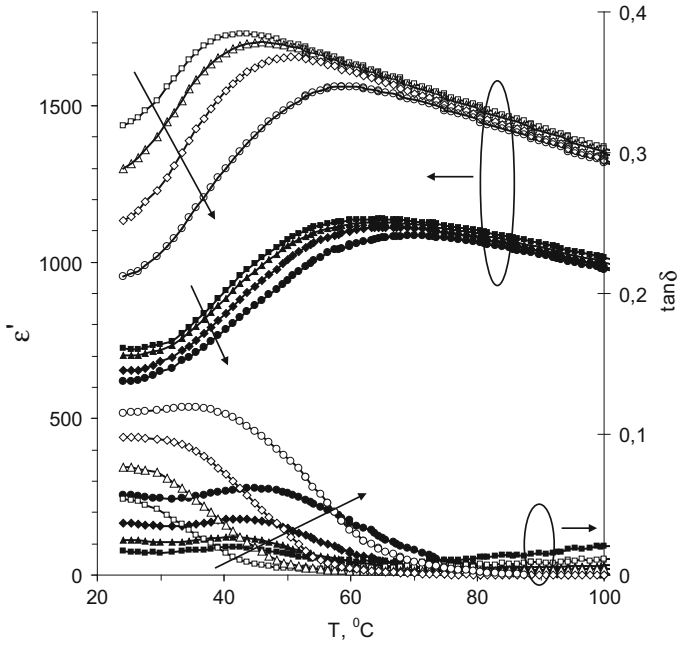

Fig. 4.6 Temperature dependencies of the real part of dielectric permittivity ε' and loss tangent tan δ for the 0.9PYN–0.1PFN ceramics sintered from the mechanochemically synthesized powders at 1100 °C (empty symbols) and at 800 °C (filled symbols) measured at different frequencies f (Hz): 10^3, 10^4, 10^5, 10^6. The arrows show the direction of the frequency increase

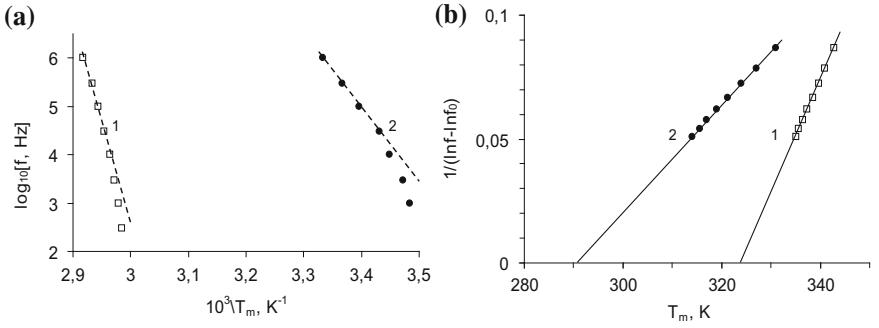

Fig. 4.7 **a** Nonlinear dependencies of the temperatures T_m of the $\varepsilon'(T)$ maximum on frequency f in the Arrhenius coordinates for the 0.9PYN–0.1PFN ceramics sintered from mechanochemically synthesized powders at 800 °C (curve 1) and at 1100 °C (curve 2), illustrating the non-Debye character of relaxation; **b** dependencies of $(\ln f_0 - \ln f)^{-1}$ on T_m for the same samples as in the panel (a), illustrating the applicability of the Vogel–Fulcher law for fitting the frequency shift of their $\varepsilon'(T)$ maxima

(Fig. 4.2) these maxima in the Li-doped samples are much lower that the ε' (T) maximum corresponding to the phase transition and they are usually observed well above T_m. The frequency shift of the temperature of these maxima appears to be linear in the Arrhenius coordinates (see the inset (b) in Fig. 4.2), i.e. this relaxation obeys the Debye law. Similar high-temperature Debye-like relaxation was reported previously for a large number of binary and ternary perovskites as well as for their solid solutions [44, 61–65, 80–87]). Three ranges of the activation energy of relaxation, namely 0.4–0.8 eV, 1.0–1.2 eV and 1.45–1.7 eV, were observed for the (1–x)PYN–xPFN compositions studied, irrespectively of the method they were fabricated (either mechanochemical synthesis or usual solid state synthesis). These relaxation processes seem to be due to the presence of oxygen vacancies, which are the most probable intrinsic point defects in perovskites [88, 89]. Activation energies of about 0.4–0.8 eV corroborate well the values of the energy of the second level of the oxygen vacancy reported for a large number of perovskite oxides [88, 89]. Activation energies of about 1.0–1.2 eV and 1.5 eV, are usually attributed to the short-range [80] and long-range [83] hopping of the doubly-ionized oxygen vacancies, respectively.

Figure 4.8 shows the concentration dependences of the temperatures T_m of the ε' (T) maximum for the Li-doped (1–x)PYN–xPFN ceramics fabricated by both technological routes used. They look very similar, and exhibit a deep minimum at $x \approx 0.15$–0.25 (curves 1 and 1′). These data corroborate the literature data which are available only for (1–x)PYN–xPFN compositions from the $0 \leq x \leq 0.2$ range (curve 1″) [90]. It is worth noting that the minimum of the $T_m(x)$ dependence for the ceramics fabricated via the usual solid state synthesis (curve 1) is much more

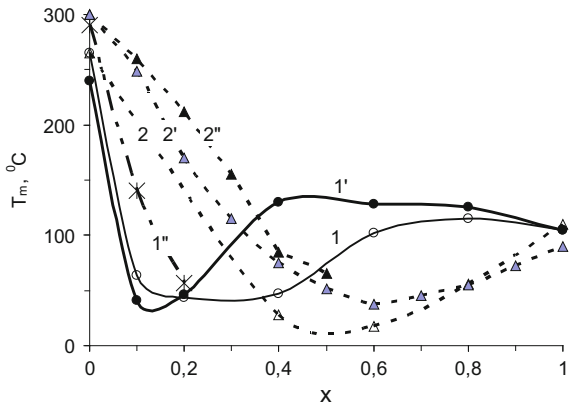

Fig. 4.8 Concentration dependences of the temperatures T_m of the $\varepsilon'(T)$ maximum for the Li-doped (1 − x)PYN–xPFN ceramics fabricated either via the usual solid state synthesis (curve 1) or sintered from the mechanochemically synthesized powders (curve 1′). For comparison the $T_m(x)$ dependences for undoped (1 − x)PYN–xPFN ceramics (curve 1″ [90]), and (1 − x)PYN–xPbSc$_{1/2}$Nb$_{1/2}$O$_3$ ceramics (2, 2′, 2″) plotted using the data of [41], [91] and [92], respectively, are also shown

diffused and shifted to larger x values as compared to ceramics sintered from the mechanochemically synthesized powders (curve 1′). This difference seems to be due to PFN content larger than the nominal one in the samples sintered from the mechanochemically synthesized powders as they are contaminated by iron during mechanical activation. For comparison the $T_m(x)$ dependences for a solid solution of PYN with $PbSc_{1/2}Nb_{1/2}O_3$ which is very similar to PFN are plotted (curves 2, 2′, 2″) using the data of [41], [91] and [92], respectively. These dependences are qualitatively the same as those for (1–x)PYN–xPFN. The ordered PYN is an antiferroelectric and the decrease of T_m of the antiferroelectric, when it is diluted by a ferroelectric is well documented in the literature [85, 93]. One more reason for lowering of T_m at small x values is the decrease of the ordering degree.

4.4 Summary

Several ceramic compositions of $(1 - x)Pb(Yb_{1/2}Nb_{1/2})O_3$–$xPbFe_{1/2}Nb_{1/2}O_3$ (PYN–xPFN) solid solution have been fabricated by both the usual solid-state synthesis and by high-energy mechanochemical synthesis and their structure and dielectric permittivity were compared in order to estimate the effect of iron doping and that of high-energy mechanical activation on the properties of PYN–xPFN. Based on these data the (x, T)-phase diagrams for the PYN–xPFN solid solutions fabricated by both methods were constructed. The concentration dependences of the temperature T_m of the $\varepsilon'(T)$ maximum for both types of the samples appeared to be very similar. However, the minimum of the $T_m(x)$ dependence for ceramics, fabricated via the usual solid-state synthesis, is much more diffused and shifted to larger x values as compared to ceramics sintered from the mechanochemically synthesized powders. This difference seems to be due to PFN content larger than the nominal one in the samples sintered from the mechanochemically synthesized powders as they are contaminated by iron in the course of mechanical activation. The lattice parameter values for the samples fabricated via the usual solid-state synthesis are larger than for the samples sintered from the mechanochemically synthesized powders. Though this difference becomes smaller as the PFN content x grows, it does not disappear even for pure PFN implying that it is partially due to the formation of the $(1 - x)$PYN–xPFN solid solutions and partially due to the effect of high-energy mechanical activation.

Acknowledgements This work was supported in part by the Ministry of Education and Science of the Russian Federation (research project No. 3.1649.2017/4.6) and by the Russian Foundation for Basic Research (grant No 17-03-01293_a). IPR acknowledges the support from the CAS President's International Fellowship Initiative through the project 2018VEA0011.

References

1. V.A. Isupov, Ferroelectrics **289**, 131 (2003)
2. A.A. Bokov, I.P. Rayevsky, Ferroelectrics **90**, 125 (1989)
3. V.V. Kochetkov, YuN Venevtsev, Izv. Akad. Nauk SSSR. Neorg. Mater. **15**, 1833 (1979)
4. A.N. Salak, N.P. Vyshatko, V.M. Ferreira, N.M. Olekhnovich, A.D. Shilin, Mater. Res. Bull. **38**, 453 (2003)
5. E. Dul'kin, I.P. Raevski, S.M. Emel'yanov, Phys. Solid State **45**, 158 (2003)
6. E. Dul'kin, E. Mojaev, M. Roth, I.P. Raevski, S.A. Prosandeev, Appl. Phys. Lett. **94**, 252904 (2009)
7. S.I. Raevskaya, YuN Zakharov, A.G. Lutokhin, A.S. Emelyanov, I.P. Raevski, M.S. Panchelyuga, V.V. Titov, S.A. Prosandeev, Appl. Phys. Lett. **93**, 042903 (2008)
8. S. Prosandeev, I.P. Raevski, M.A. Malitskaya, S.I. Raevskaya, H. Chen, C.C. Chou, B. Dkhil, J. Appl. Phys. **114**, 124103 (2013)
9. S. Zhang, F. Li, J. Appl. Phys. **111**, 031301 (2012)
10. V.V. Shvartsman, A.L. Kholkin, I.P. Raevski, S.I. Raevskaya, F.I. Savenko, A.S. Emelyanov, J. Appl. Phys. **113**, 187208 (2013)
11. V.I. Aleshin, I.P. Raevski, J. Alloys Compnds **587**, 138 (2014)
12. A. Sternberg, L. Shebanovs, J.Y. Yamashita, M. Antonova, M. Livinsh, Ferroelectrics **241**, 51 (2000)
13. I.K. Bdikin, J. Gracio, D.A. Kiselev, I.P. Raevski, S.I. Raevskaya, S.A. Prosandeev, A.L. Kholkin, J. Appl. Phys. **110**, 052002 (2011)
14. E.I. Sitalo, I.P. Raevski, A.G. Lutokhin, A.V. Blazhevich, S.P. Kubrin, S.I. Raevskaya, YuN Zakharov, M.A. Malitskaya, V.V. Titov, I.N. Zakharchenko, IEEE Trans. Ultrason. Ferroelect. Freq. Contr. **58**, 1914 (2011)
15. A. Kania, J. Cryst. Growth **310**, 2767 (2008)
16. Y.N. Zakharov, S.I. Raevskaya, A.G. Lutokhin, V.V. Titov, I.P. Raevski, V.G. Smotrakov, V. V. Eremkin, A.S. Emelyanov, A.A. Pavelko, Ferroelectrics **399**, 20 (2010)
17. I.P. Raevski, V.V. Titov, M.A. Malitskaya, E.V. Eremin, S.P. Kubrin, A.V. Blazhevich, H. Chen, C.-C. Chou, S.I. Raevskaya, I.N. Zakharchenko, D.A. Sarychev, S.I. Shevtsova, J. Mater. Sci. **49**, 6459 (2014)
18. E.I. Sitalo, YuN Zakharov, A.G. Lutokhin, S.I. Raevskaya, I.P. Raevski, M.S. Panchelyuga, V.V. Titov, L.E. Pustovaya, I.N. Zakharchenko, A.T. Kozakov, A.A. Pavelko, Ferroelectrics **389**, 107 (2009)
19. N. Yasuda, H. Inagaki, Japan. J. Appl. Phys. **5**, L2050 (1991)
20. V.V. Laguta, A.N. Morozovska, E.I. Eliseev, I.P. Raevski, S.I. Raevskaya, E.I. Sitalo, S.A. Prosandeev, L. Bellaiche, J. Mater. Sci. **51**, 5330 (2016)
21. D.A. Sanchez, N. Ortega, A. Kumar, G. Sreenivasulu, R.S. Katiyar, J.F. Scott, D.M. Evans, M. Arredondo-Arechavala, A. Schilling, J.M. Gregg, J. Appl. Phys. **113**, 074105 (2013)
22. V.V. Laguta, V.A. Stephanovich, I.P. Raevski, S.I. Raevskaya, V.V. Titov, V.G. Smotrakov, V.V. Eremkin, Phys. Rev. B **95**, 014207 (2017)
23. Y. Yamashita, K. Harada, Y. Hosono, S. Natsume, N. Ichinose, J. Jpn, Appl. Phys. **37**, 5288 (1998)
24. A.A. Gusev, S.I. Raevskaya, V.V. Titov, V.P. Isupov, E.G. Avvakumov, I.P. Raevski, H. Chen, C.-C. Chou, S.P. Kubrin, S.V. Titov, M.A. Malitskaya, D.A. Sarychev, V.V. Stashenko, S.I. Shevtsova, Ferroelectrics **496**, 231 (2016)
25. A.A. Gusev, S.I. Raevskaya, I.P. Raevski, V.P. Isupov, E.G. Avvakumov, S.P. Kubrin, H. Chen, V.V. Titov, T.A. Minasyan, C.-C. Chou, S.V. Titov, M.A. Malitskaya, Ferroelectrics **496**, 250 (2016)
26. M. Maryško, V.V. Laguta, I.P. Raevski, R.O. Kuzian, N.M. Olekhnovich, A.V. Pushkarev, YuV Radyush, S.I. Raevskaya, V.V. Titov, S.P. Kubrin, AIP Adv. **7**, 056409 (2017)
27. S.I. Raevskaya, S.P. Kubrin, I.P. Raevski, C.-C. Chou, H. Chen, V.V. Titov, M.A. Malitskaya, D.A. Sarychev, I.N. Zakharchenko, Ferroelectrics **509**, 64 (2017)

28. S. Zhang, P.W. Rehrig, C. Randall, T.R. Shrout, J. Cryst. Growth **234**, 415 (2002)
29. K. Kouril, V. Chlan, H. Štepánková, R. Reznícek, K. Ulicná, V.V. Laguta, I.P. Raevski, Acta Phys. Polonica A. **127**, 234 (2015)
30. N.S. Druzhinina, YuI Yuzyuk, I.P. Raevski, M. El Marssi, V.V. Laguta, S.I. Raevskaya, Ferroelectrics **438**, 107 (2012)
31. Y.I. Yuzyuk, I.P. Raevski, S.I. Raevskaya, N. Lemee, M.G. Karkut, W. Peng, M. El Marssi, H. Chen, J. Alloys Compnds. **695**, 1821 (2017)
32. I.P. Raevski, S.P. Kubrin, S.I. Raevskaya, V.V. Stashenko, D.A. Sarychev, M.A. Malitskaya, M.A. Seredkina, V.G. Smotrakov, I.N. Zakharchenko, V.V. Eremkin, Ferroelectrics **373**, 121 (2008)
33. S.A. Prosandeev, I.P. Raevski, S.I. Raevskaya, H. Chen, Phys. Rev. B. **92**, 220419(R) (2015)
34. A.T. Kozakov, A.G. Kochur, A.V. Nikolskii, I.P. Raevski, S.P. Kubrin, S.I. Raevskaya, V.V. Titov, M. A. Malitskaya, I.N. Zakharchenko, S.I. Shevtsova, J. Mater. Sci. **52**, 10140 (2017)
35. S.I. Raevskaya, S.P. Kubrin, A.V. Pushkarev, N.M. Olekhnovich, Y.V. Radyush, V.V. Titov, M.A. Malitskaya, I.N. Zakharchenko, H. Chen, C-C. Chou, I.P. Raevski , Ferroelectrics. **509**, 40 (2017)
36. I.P. Raevski, S.P. Kubrin, V.V. Laguta, M. Marysko, H. Chen, S.I. Raevskaya, V.V. Titov, C.-C. Chou, A.V. Blazhevich, E.I. Sitalo, D.A. Sarychev, T.A. Minasyan, A.G. Lutokhin, YuN Zakharov, L.E. Pustovaya, I.N. Zakharchenko, M.A. Malitskaya, Ferroelectrics **475**, 20 (2015)
37. I.P. Raevski, S.P. Kubrin, S.I. Raevskaya, S.A. Prosandeev, D.A. Sarychev, M.A. Malitskaya, V.V. Stashenko, I.N. Zakharchenko, Ferroelectrics **398**, 16 (2010)
38. C.G.F. Stenger, F.L. Scholten, A.J. Burggraaf, Solid State Commun. **32**, 989 (1979)
39. N. Setter, L.E. Cross, J. Appl. Phys. **51**, 4356 (1980)
40. A.A. Bokov, I.P. Raevskii, V.G. Smotrakov, Fizika Tverd. Tela. **26**, 2824 (1984)
41. A.A. Bokov, I.P. Raevski, VYu. Shonov, Inorg. Mater. **26**, 2033 (1990)
42. A.A. Bokov, I.P. Raevsky, V.G. Smotrakov, S.M. Zaitsev, Kristallografiya **32**, 1301 (1987)
43. I.P. Raevski, S.A. Prosandeev, S.M. Emelyanov, F.I. Savenko, I.N. Zakharchenko, O.A. Bunina, A.S. Bogatin, S.I. Raevskaya, E.S. Gagarina, E.V. Sahkar, L. Jastrabik, Integr Ferroelectr. **53**, 475 (2003)
44. I.P. Raevskii, V.V. Eremkin, V.G. Smotrakov, M.A. Malitskaya, S.A. Bogatina, L.A. Shilkina, Crystallogr. Rep. **47**, 1007 (2002)
45. I.P. Raevski, S.A. Prosandeev, S.M. Emelyanov, V.G. Smotrakov, V.V. Eremkin, I.N. Zakharchenko, S.I. Raevskaya, E.S. Gagarina, F.I. Savenko, E.V. Sahkar, Ferroelectrics **298**, 267 (2004)
46. P.K. Davies, H. Wu, A.Y. Borisevich, I.E. Molodetsky, L. Farber, Annu. Rev. Mater. Res. **38**, 369 (2008)
47. V.A. Shuvaeva, I. Pirog, Y. Azuma, K. Yagi, K. Sakaue, H. Terauchi, I.P. Raevskii, K. Zhuchkov, MYu. Antipin, J. Phys.: Condens. Matter **15**, 2413 (2003)
48. A.A. Bokov, N.P. Protsenko, Z.-G. Ye, J. Phys. Chem. Sol. **61**, 1519 (2000)
49. I.P. Raevskii, D.A. Sarychev, S.A. Bryugeman, L.A. Reznichenko, L.A. Shilkina, O.N. Razumovskaya, V.S. Nikolaev, N.P. Vyshatko, A.N. Salak, Crystallogr. Rep. **47**, 1012 (2002)
50. S.P. Kubrin, S.I. Raevskaya, S.A. Kuropatkina, I.P. Raevski, D.A. Sarychev, Ferroelectrics **340**, 155 (2006)
51. V.V. Laguta, V.A. Stephanovich, M. Savinov, M. Marysko, R.O. Kuzian, N.M. Olekhnovich, A.V. Pushkarev, YuV Radyush, I.P. Raevski, S.I. Raevskaya, S.A. Prosandeev, New J. Phys. **16**, 11304 (2014)
52. I.P. Raevski, N.M. Olekhnovich, A.V. Pushkarev, Y.V. Radyush, S.P. Kubrin, S.I. Raevskaya, M.A. Malitskaya, V.V. Titov, V.V. Stashenko, Ferroelectrics **444**, 47 (2013)
53. I.P. Raevski, A.V. Pushkarev, S.I. Raevskaya, N.M. Olekhnovich, Y.V. Radyush, S. P. Kubrin, H. Chen, C.-C. Chou, D.A. Sarychev, V.V. Titov, M.A. Malitskaya, Ferroelectrics **501**, 154 (2016)

54. H. Uršič, A. Benčan, G. Dražič, G. Esteves, J.L. Jones, T.-M. Usher, T. Rojac, S. Drnovšek, M. Deluca, J. Jouin, V. Bobnar, G. Trefalt, J. Holc, B. Malič, J. Mater. Chem. C. **3**, 10309 (2015)
55. A.A. Bokov, V.Y. Shonov, I.P. Rayevsky, E.S. Gagarina, M.F. Kupriyanov, J. Phys. Condens. Matter **31**, 5491 (1993)
56. I.P. Raevski, V.Y. Shonov, M.A. Malitskaya, E.S. Gagarina, V.G. Smotrakov, V.V. Eremkin, Ferroelectrics. **235**, 205 (1999)
57. X. Gao, J. Xue, J. Wang, Mater. Sci. Eng. B **99**, 63 (2003)
58. C. Cochard, F. Karolak, C. Bogicevic, O. Guedes, P.-E. Janolin, Adv. Mater. Sci. Eng. **2015**, 408101 (2015)
59. A.A. Gusev, S.I. Raevskaya, V.V. Titov, E.G. Avvakumov, V.P. Isupov, I.P. Raevski, H. Chen, C.-C. Chou, S.P. Kubrin, S.V. Titov, M.A. Malitskaya, A.V. Blazhevich, D.A. Sarychev, V.V. Stashenko, S.I. Shevtsova, Ferroelectrics **475**, 41 (2015)
60. M. Savinov, P. Bednyakov, S.I. Raevskaya, A.A. Gusev, V.P. Isupov, I.P. Raevski, V.V. Titov, H. Chen, S.A. Kovrigina, C.-C. Chou, T.A. Minasyan, M.A. Malitskaya, Ferroelectrics **509**, 80 (2017)
61. S.I. Raevskaya, A.A. Gusev, V.P. Isupov, S.P. Kubrin, I.P. Raevski, V.V. Titov, H. Chen, Ferroelectrics **525**, 37 (2018)
62. I.P. Raevski, A.A. Gusev, V.P. Isupov, S.I. Raevskaya, V.V. Titov, H. Chen, Ferroelectrics **525**, 54 (2018)
63. I.P. Raevski, YuA Kuprina, I.N. Zakharchenko, A.A. Gusev, V.P. Isupov, O.A. Bunina, V.V. Titov, S.I. Raevskaya, M.A. Malitskaya, A.V. Blazhevich, S.V. Orlov, E.I. Sitalo, Springer Proc. Phys. **207**, 209 (2018)
64. I.P. Raevski, S.P. Kubrin, S.I. Raevskaya, S.A. Prosandeev, M.A. Malitskaya, V.V. Titov, D. A. Sarychev, A.V. Blazhevich, I.N. Zakharchenko, IEEE Trans. Ultrason. Ferroelect. Freq. Contr. **59**, 1872 (2012)
65. A.V. Pavlenko, N.A. Boldyrev, L.A. Reznichenko, I.A. Verbenko, G.M. Konstantinov, L.A. Shilkina, Inorg. Mater. **50**, 750 (2014)
66. D. Bochenek, P. Kruk, R. Skulski, P. Wawrzała, J. Electroceram. **26**, 8 (2011)
67. I.P. Raevskii, S.T. Kirillov, M.A. Malitskaya, V.P. Filippenko, S.M. Zaitsev, L.G. Kolomin, Inorg. Mater. **24**, 217 (1988)
68. A.A. Gusev, I.P. Raevski, E.G. Avvakumov, V.P. Isupov, S.I. Raevskaya, H. Chen, V.V. Titov, C.-C. Chou, S.P. Kubrin, S.V. Titov, M.A. Malitskaya, Ferroelectrics **475**, 61 (2015)
69. I.P. Raevski, S.P. Kubrin, S.A. Kovrigina, S.I. Raevskaya, V.V. Titov, A.S. Emelyanov, M.A. Malitskaya, I.N. Zakharchenko, Ferroelectrics **397**, 96 (2010)
70. J.R. Kwon, W.K. Choo, J Phys. Condens. Matter, **3,** 2147 (1991)
71. C. Lei, A.A. Bokov, Z.-G. Ye, J. Appl. Phys. **101**, 084105 (2007)
72. S.I. Raevskaya, A.G. Lutokhin, A.M. Pugachev, I.P. Raevski, V.V. Titov, YuN Zakharov, D. V. Suzdalev, E.M. Panchenko, S.A. Prosandeev, Ferroelectrics **440**, 59 (2012)
73. S.I. Raevskaya, V.V. Titov, I.P. Raevski, A.G. Lutokhin, Y.N. Zakharov, V.Y. Shonov, A.V. Blazhevich, E.I. Sitalo, H. Chen, C-C. Chou, S.A. Kovrigina, M.A. Malitskaya, Ferroelectrics. **475**, 31 (2015)
74. Z. Branković, G. Branković, V. Vukotić, R. Tararam, J.A. Varela, Metall. Mater. Trans. A **39**, 875 (2008)
75. A.A. Bokov, M.A. Malitskaya, I.P. Raevskii, VYu. Shonov, Fizika Tverdogo Tela. **32**, 2488 (1990)
76. A.S. Bogatin, A.A. Bokov, I.P. Rayevsky, V.P. Filippenko, Ferroelectrics **118**, 232 (1990)
77. D. Viehland, S. Jang, L.E. Cross, M. Wuttig, Philos. Mag. B **64**, 335 (1991)
78. I.P. Raevski, V.V. Eremkin, V.G. Smotrakov, E.S. Gagarina, M.A. Malitskaya, Phys. Solid State **42**, 161 (2000)
79. F. Chu, I.M. Reaney, N. Setter, Ferroelectrics **151**, 343 (1994)
80. M. Puri, S. Bahel, I.P. Raevski, S.B. Narang, J. Mater. Sci. Mater. El. **27**, 1077 (2016)
81. V. Bobnar, H. Uršič, G. Casar, S. Drnovšek, Phys. Status Solidi B **250**, 2232 (2013)

82. I.P. Raevski, S.A. Kuropatkina, S.P. Kubrin, S.I. Raevskaya, V.V. Titov, D.A. Sarychev, M. A. Malitskaya, A.S. Bogatin, I.N. Zakharchenko, Ferroelectrics **379**, 272 (2009)
83. C. Ang, Z. Yu, L.E. Cross, Phys. Rev. B. **62**, 228 (2000)
84. I.P. Raevski, S.P. Kubrin, S.I. Raevskaya, D.A. Sarychev, J.-L. Dellis, Ferroelectrics **371**, 113 (2008)
85. S.I. Raevskaya, L.A. Reznitchenko, V.V. Titov, I.P. Raevski, M.A. Malitskaya, I.N. Zakharchenko, J.-L. Dellis, Ferroelectrics **371**, 63 (2008)
86. I.P. Raevski, L.A. Reznitchenko, M.A. Malitskaya, L.A. Shilkina, S.O. Lisitsina, S.I. Raevskaya, E.M. Kuznetsova, Ferroelectrics **299**, 95 (2004)
87. I.P. Rayevsky, A.A. Bokov, A.S. Bogatin, S.M. Emelyanov, M.A. Malitskaya, O.I. Prokopalo, Ferroelectrics **126**, 191 (1992)
88. S.A. Prosandeev, A.V. Fisenko, A.V. Riabchinski, I.A. Osipenko, I.P. Raevski, N. Safontseva, J. Phys. Condens. Matter **8**, 6705 (1996)
89. I.P. Raevski, S.M. Maksimov, A.V. Fisenko, S.A. Prosandeev, I.A. Osipenko, P.F. Tarasenko, J. Phys. Condens. Matter **10**, 8015 (1998)
90. B.J. Kuh, D.C. Choi, W.K. Choo, Ferroelectrics **223**, 187 (1999)
91. J.-H. Kim, W.K. Choo, Ferroelectrics **270**, 69 (2002)
92. M. Dambekalne, M. Kalnberga, M. Livinsh, K. Bormanis, Key Eng. Mater. **264–268**, 1353 (2002)
93. M.P. Ivliev, I.P. Raevskii, L.A. Reznichenko, S.I. Raevskaya, V.P. Sakhnenko, Phys. Solid State **45**, 1984 (2003)

Chapter 5
Features of Obtaining Solid Solutions of the Quasi-Binary System $(1-x)(Na_{0.5}K_{0.5})NbO_3-xPb(Ti_{0.5}Zr_{0.5})O_3$

Konstantin Andryushin, Ekaterina Glazunova, Lidiya Shilkina, Inna Andryushina, Svetlana Dudkina, Iliya Verbenko and Larisa Reznichenko

Abstract The possibility of obtaining solid solutions (SSs) of the quasi-binary system $(1-x)(Na_{0.5}K_{0.5})NbO_3–xPb(Ti_{0.5}Zr_{0.5})O_3$ using various technological procedures was investigated. The effects of mechanical activation on phase formation and sintering temperature of solid solutions are shown. The optimal technological regulations that ensure the impermeability and high relative density of ceramics, promising for microelectronics (converters operating in receive mode, devices operated for the load) are identified.

5.1 Introduction

This work is a continuation and development of complex studies of multi- element compositions based on lead-containing and lead-free compounds that form a four-component SS system of the form (Na, Li) NbO_3–Pb (Ti, Zr) O_3, undertaken in [1–3]. The results of an experimental study of phase formation processes in a similar four-component system in which, instead of $LiNbO_3$, $KNbO_3$ was introduced, which was manufactured by solid-phase synthesis using four different methods followed by sintering using conventional ceramic technology (without external pressure, as in [1, 2]). The difficulty of making ceramics, which consists of lead and niobium, lies in the fact that already at the first synthesis stage, in addition to the main perovskite phase, an impurity phase with a pyro-chlorine type structure is formed. Subsequent sintering of ceramics according to conventional ceramic technology at temperatures that provide high density usually leads to an increase in the content of the pyro-chlorine phase. This is explained by the fact that, according to their crystal-chemical characteristics, the elements that make up the SS under

K. Andryushin (✉) · E. Glazunova · L. Shilkina · I. Andryushina · S. Dudkina · I. Verbenko · L. Reznichenko
Research Institute of Physics, Southern Federal University, Rostov-on-Don, Russia
e-mail: kpandryushin@gmail.ru

I. A. Parinov et al. (eds.), *Advanced Materials*, Springer Proceedings in Physics 224, https://doi.org/10.1007/978-3-030-19894-7_5

study do not satisfy the conditions under which the formation of substitution SS is possible: the difference in ionic radii should not exceed 15% relative to a smaller value and the difference in electro negativities (EN) should not exceed 0.4 according to Pauling [4]. If these conditions are violated, only limited solubility or even micro isomorphism is possible. In the data SS ΔR (K–Na) = 36%, ΔR (Pb–Na) = 28% (ionic radii according to Belov–Bokiy [5]), ΔEN (Pb–Na) = 1.4, ΔEN (Pb–K) = 1.5 [6]. It is possible to manufacture pure ceramics using hot pressing molding, but this significantly increases the energy costs and the cost of the final product.

The objective point of the work is the development of poly functional materials based on media with fundamentally different macro responses promising for microelectronics (converters operating in the receive mode, devices operating for the load).

5.2 Materials and Methods

The objects of study were the SS of composition $(1 - x)(Na_{0.5}K_{0.5})NbO_3$–$xPb(Ti_{0.5}Zr_{0.5})O_3$, where $0.0 \leq x \leq 1.0$, $\Delta x = 0.2$, made by two-step synthesis, followed by sintering using conventional ceramic technology. As a source of raw materials, we used $NaHCO_3$ (cc), $KHCO_3$ (c.f.a.), Nb_2O_5 (c), PbO (c), TiO_2 (c.f.a.), ZrO_2 (c) of the supplier from Rostov-on-Don LLC ROSTEKHNOHIM (where "cc" is chemical clean, "c" is clean," c.f.a." is clean for analysis).

The conditions of synthesis and sintering were selected on a series of samples according to the results of X-ray phase analysis and measurements of the relative density of ceramic samples. Probes were made in the form of tablets with a diameter of 10 mm and a thickness of 1 mm. The content of impurity phases was estimated by the relative intensity of their strong line $I_{rel} = I/I_1 \times 100$, where I and I_1 are the intensities at the maximum of the lines of the impurity and perovskite phases, respectively. Experimental density was measured by hydrostatic weighing in octane. The X-ray density was calculated using the formula: $\rho_{X\text{-ray}} = 1.66 \times M/V$, where M is the molecular weight per cell, V is the cell volume. The relative density was determined by the formula $\rho_{rel} = (\rho_{exp}/\rho_{X\text{-ray}}) \times 100$, %. Mechanical activation was carried out in a spherical planetary mill AGO-2 for 20 min.

5.3 Results and Discussion

As mentioned above, the SS of the composition $(1 - x)(Na_{0.5}K_{0.5})NbO_3$–$xPb(Ti_{0.5}Zr_{0.5})O_3$, $\Delta x = 0.2$ was manufactured in four ways. In the first case, samples were obtained from $NaHCO_3$ (cc), $KHCO_3$ (c.f.a.), Nb_2O_5 (c), PbO (c), TiO_2 (c.f.a.), ZrO_2 (c) by the method of two-stage solid-phase synthesis, followed by sintering using conventional ceramic technology.

X-ray showed that after the first synthesis all samples have a perovskite-type structure, but contain pyro-chlorine impurities. Table 5.1 shows the results of X-ray analysis of probes at all synthesis temperatures of SS and composition at the selected temperature. Isothermal aging at all stages of the synthesis was 4 h. From Table 5.1, it is clear that the best result was obtained under the following synthesis conditions: T_1 = (1173–1223)K, τ_1 = 4 h, T_2 = (1248–1273)K, τ_2 = 4 h, depending on the composition.

Table 5.2 shows the relative density of ceramic probes at all sintering temperatures. The table shows that it was not possible to obtain high-density ceramics without using additional treatment of the synthesized material. Using the example of the composition $Na_{0.1}K_{0.1}Pb_{0.8}Nb_{0.2}Ti_{0.4}Zr_{0.4}O_3$, it was shown that the use of mechanical activation of powders that passed 2 stages of the synthesis in a spherical planetary mill for 15 min (high-energy grinding, frequency is 1800 rpm) allowed one to increase the ceramic density ρ_{rel} to 94%.

In the second case, samples from the precursors, which were the extreme components of the system: $(Na_{0.5}K_{0.5})NbO_3$ and Pb $(Ti_{0.5}Zr_{0.5})O_3$ were obtained at T_1 = 1223 K, τ_1 = 4 h, T_2 = 1273 K, τ_2 = 4 h and T_1 = 1143 K, τ_1 = 6 h, T_2 = 1223 K, τ_2 = 6 h, respectively.

Table 5.3 shows the results of X-ray analysis of probes at all temperatures of synthesis of SS and composition at the selected temperature, manufactured by the second method. Isothermal aging at all stages of the synthesis was also 4 h.

In the third case, the powders that passed the 2 stages of the synthesis were subjected to mechanical activation in a ball planetary mill for 15 min (high-energy grinding in AGO-2 drums, frequency is 1800 rpm) in order to reduce impurity phases and increase the relative density ρ_{rel} ceramics.

Table 5.4 shows the relative densities of ceramic probes at all sintering temperatures. The table shows that the use of additional mechanical activation processing of the synthesized material led to a significant decrease in sintering temperatures.

Table 5.5 shows the relative density of the samples obtained with using mechanical activation and without it, at all sintering temperatures. The table shows that using of mechanical activating grinding increases the relative density of ceramics, but it is not possible to achieve a density of more than 86%.

In the fourth case, we studied the effect of the Nb_2O_5 polymorphism on the phase formation and properties of ceramics on the example of the SS with x = 0.2. The significant role of niobium pentaoxide in the formation of the properties of niobate ferroelectric ceramics (NFCs) is due to the fact that it is the most thermally stable reagent of the NFCs involved in the synthesis, covered by the reaction products and is contained in the mixtures in the largest amounts. A significant influence on the properties of the obtained NFCs has a phase composition of Nb_2O_5. Commercially available niobium oxide is almost always multiphase, which can have a significant impact on the final properties of the obtained ferroelectric materials [7].

For the study, we preliminarily compared the phase composition of the plant Nb_2O_5 (LLC ROSTEKHNOHIM) qualification (“c”) and after calcination at

Table 5.1 X-ray results, I_{rel}, SS $(1 - x)(Na_{0.5}K_{0.5})NbO_3$–$xPb(Ti_{0.5}Zr_{0.5})O_3$, at all synthesis temperatures

$(Ba_{0.95}La_{0.05})_{1-x}Sr_xTiO_3$	Probes				Composition	
First synthesis	T_1 = 1073 K	T_1 = 1173 K	T_1 = 1198 K	T_1 = 1223 K	T_1 = 1173 K	T_1 = 1223 K
	The relative intensity of the lines of impurity compounds					
$(Na_{0.5}K_{0.5})NbO_3$	–	9	–	9	–	3
$Na_{0.4}K_{0.4}Pb_{0.2}Nb_{0.8}Ti_{0.1}Zr_{0.1}O_3$	12	8	–	–	8	–
$Na_{0.3}K_{0.3}Pb_{0.4}Nb_{0.6}Ti_{0.2}Zr_{0.2}O_3$	0	<1	–	–	7	–
$Na_{0.2}K_{0.2}Pb_{0.6}Nb_{0.4}Ti_{0.3}Zr_{0.3}O_3$	7	10	–	–	<1	–
$Na_{0.1}K_{0.1}Pb_{0.8}Nb_{0.2}Ti_{0.4}Zr_{0.4}O_3$	30	13	9	0[a]	–	<1[a]
$Pb(Ti_{0.5}Zr_{0.5})O_3$	–	0	–	0	–	3
Second synthesis	T_2 = 1248 K		T_2 = 1273 K		T_2 = 1248 K	T_2 = 1248 K
	The relative intensity of the lines of impurity compounds					
$(Na_{0.5}K_{0.5})NbO_3$	–		<1		–	<1
$Na_{0.4}K_{0.4}Pb_{0.2}Nb_{0.8}Ti_{0.1}Zr_{0.1}O_3$	5		<1		–	0
$Na_{0.3}K_{0.3}Pb_{0.4}Nb_{0.6}Ti_{0.2}Zr_{0.2}O_3$	7		5		–	0
$Na_{0.2}K_{0.2}Pb_{0.6}Nb_{0.4}Ti_{0.3}Zr_{0.3}O_3$	0		–		<1	–
$Na_{0.1}K_{0.1}Pb_{0.8}Nb_{0.2}Ti_{0.4}Zr_{0.4}O_3$	0[a]		–		0[a]	–
$Pb(Ti_{0.5}Zr_{0.5})O_3$	–		0		–	0

[a]Mechanical activation

Table 5.2 Relative density, % SS $(1 - x)(Na_{0.5}K_{0.5})NbO_3 - xPb(Ti_{0.5}Zr_{0.5})O_3$ at different sintering temperatures

$(1 - x)(Na_{0.5}K_{0.5})NbO_3$–$xPb(Ti_{0.5}Zr_{0.5})O_3$	Probes			
$T_{sint.}$ (2 h), K	1373	1473	1523	1573
$(Na_{0.5}K_{0.5})NbO_3$	69.84	55.21	melt	–
$Na_{0.4}K_{0.4}Pb_{0.2}Nb_{0.8}Ti_{0.1}$ $Zr_{0.1}O_3$	67.35	81.61	66.22	–
$Na_{0.3}K_{0.3}Pb_{0.4}Nb_{0.6}Ti_{0.2}$ $Zr_{0.2}O_3$	62.13	73.92	70.43	–
$Na_{0.2}K_{0.2}Pb_{0.6}Nb_{0.4}Ti_{0.3}$ $Zr_{0.3}O_3$	62.97	61.02	65.22	–
$Na_{0.1}K_{0.1}Pb_{0.8}Nb_{0.2}Ti_{0.4}$ $Zr_{0.4}O_3$	–	93.65[a]	93.78[a]	87.03[a]
$Pb(Ti_{0.5}Zr_{0.5})O_3$	69.29	78.72	–	–

[a]Mechanical activation

Table 5.3 X-ray results, I_{rel}, SS $(1 - x)(Na_{0.5}K_{0.5})NbO_3$–$xPb(Ti_{0.5}Zr_{0.5})O_3$ at all synthesis temperatures

$(Ba_{0.95}La_{0.05})_{1-x}Sr_xTiO_3$	Probes			Composition
First synthesis	T_1 = 900 °C			T_1 = 900 °C
	The relative intensity of the lines of impurity compounds			
$Na_{0.4}K_{0.4}Pb_{0.2}Nb_{0.8}Ti_{0.1}Zr_{0.1}O_3$	0			0
$Na_{0.3}K_{0.3}Pb_{0.4}Nb_{0.6}Ti_{0.2}Zr_{0.2}O_3$	8			9
$Na_{0.2}K_{0.2}Pb_{0.6}Nb_{0.4}Ti_{0.3}Zr_{0.3}O_3$	8			10
$Na_{0.1}K_{0.1}Pb_{0.8}Nb_{0.2}Ti_{0.4}Zr_{0.4}O_3$	8			8
Second synthesis	T_2 = 950 °C	T_2 = 970 °C	T_2 = 1000 °C	T_2 = 970 °C
	The relative intensity of the lines of impurity compounds			
$Na_{0.4}K_{0.4}Pb_{0.2}Nb_{0.8}Ti_{0.1}Zr_{0.1}O_3$	0	0	0	0
$Na_{0.3}K_{0.3}Pb_{0.4}Nb_{0.6}Ti_{0.2}Zr_{0.2}O_3$	12	10	9	8
$Na_{0.2}K_{0.2}Pb_{0.6}Nb_{0.4}Ti_{0.3}Zr_{0.3}O_3$	12	10	15	10
$Na_{0.1}K_{0.1}Pb_{0.8}Nb_{0.2}Ti_{0.4}Zr_{0.4}O_3$	10	10	14	10

Table 5.4 Relative density, % SS $(1 - x)(Na_{0.5}K_{0.5})NbO_3$–$xPb(Ti_{0.5}Zr_{0.5})O_3$ at different sintering temperatures

$(1 - x)(Na_{0.5}K_{0.5})NbO_3$–$xPb(Ti_{0.5}Zr_{0.5})O_3$	Probes					
T_{sint} (2 h.), K	1423	1453	1473	1498	1523	1573
$(Na_{0.5}K_{0.5})NbO_3$	68.96	–	melt	–	melt	melt
$Na_{0.4}K_{0.4}Pb_{0.2}Nb_{0.8}Ti_{0.1}Zr_{0.1}O_3$	–	–	75.42	76.92	66.98	melt
$Na_{0.3}K_{0.3}Pb_{0.4}Nb_{0.6}Ti_{0.2}Zr_{0.2}O_3$	–	65.28	65.12	–	73.59	melt
$Na_{0.2}K_{0.2}Pb_{0.6}Nb_{0.4}Ti_{0.3}Zr_{0.3}O_3$	–	–	62.52	79.91	83.51	melt
$Na_{0.1}K_{0.1}Pb_{0.8}Nb_{0.2}Ti_{0.4}Zr_{0.4}O_3$	–	–	70.27	83.38	85.14	melt
$Pb(Ti_{0.5}Zr_{0.5})O_3$	–	–	81.02	79.81	66.02	melt

Table 5.5 Relative density of SS $(1 - x)(Na_{0.5}K_{0.5})NbO_3$–$xPb(Ti_{0.5}Zr_{0.5})O_3$

$(1 - x)(Na_{0.5}K_{0.5})NbO_3$–$xPb(Ti_{0.5}Zr_{0.5})O_3$		I_{rel}, %	Relative density of ceramics without mechanical activation, %					
No.	x		1398 K	1448 K	1458 K	1473 K	1498 K	1523 K
1	0	0	68.51	–	–	melt	–	–
2	0.2	0	–	56.00	72.6	76.8	70.94	66.60
3	0.4	0	–	–	75.91	75.42	–	70.41
$(1 - x)(Na_{0.5}K_{0.5})NbO_3$–$xPb(Ti_{0.5}Zr_{0.5})O_3$		I_{rel}, %	Relative density of ceramics, with mechanical activation, %					
No.	x		1398 K	1448 K	1458 K	1473 K	1498 K	1523 K
1	0	0	85.37	77,8	–	melt	–	–
2	0.2	0	–	79.10	77.40	77.90	76.23	melt
3	0.4	0	–	78.6	85.05	81.90	81.25	77.20

temperatures of 1373 K and 1473 K with an exposure of 2 h. The X-ray phase analysis showed that the factory Nb_2O_5 consists of three modifications: L-phases (PDF set 27, card 1003), β-phases (PDF set 9, card 862) and high-temperature αB-phase (PDF set 16, card 53). After heat treatment at both temperatures, the niobium pentaoxide became single phase –αW.

With each niobium oxide: factory, annealed at 1373 K, annealed at 1473 K; SSs of the studied system were made with $x = 0.2$; we denote them No. 1, No. 2 and No. 3, respectively. All SSs were obtained under the following synthesis conditions: $T_1 = 1173$ K, $T_2 = 1223$ K, $\tau_{1,2} = 4$ h. Table 5.6 shows the results of X-ray synthesized SSs.

It can be seen (Table 5.6) that the use of thermally treated niobium pentaoxide in the manufacture of NFCs results in the production of a pure product at the first stage of the synthesis.

After the synthesis, all the compositions were divided into two parts and sintered in two ways: using conventional ceramic technology and using mechanical activation grinding before sintering.

Table 5.6 The results of X-ray analysis of the SS $(1 - x)(Na_{0.5}K_{0.5})NbO_3$–$xPb(Ti_{0.5}Zr_{0.5})O_3$ using three types of niobium pentaoxide after synthesis

No.	Synthesis	
	$T_1 = 1173$ K	$T_2 = 1223$ K
	I_{rel}, %	
1	8	<1
2	0	0
3	0	0

Table 5.7 Results of the X-ray, *I*, TP $Na_{0.4}K_{0.4}Pb_{0.2}Nb_{0.8}Ti_{0.1}Zr_{0.1}O_3$

№	I_{rel}, %	Sintering					
		Without mechanical activation			With mechanical activation		
		Relative density, %					
		1175 °C	1200 °C	1225 °C	1175 °C	1200 °C	1225 °C
1	0	56,00	76.8	70.94	79.10	77.90	76.23
2	0	53.80	67.00	57.4	73.80	75.7	65.80
3	0	56.00	63.60	60.2	74.5	77.4	65.50

Table 5.7 shows the relative densities of samples obtained using mechanical activation and without using mechanical activation at all sintering temperatures.

After analyzing the data of Table 5.7, one can say that mechanical activation (when using thermally treated Nb_2O_5) does not increase the density of ceramics.

5.4 Conclusion

The optimal technological procedures for manufacturing the SSs of the quasi-binary system $(1 - x)(Na_{0.5}K_{0.5})NbO_3$–$xPb(Ti_{0.5}Zr_{0.5})O_3$ have been developed. It has been established that the use of monoxide gives a better result than obtaining the above-mentioned SSs from precursors. It was also revealed that high-density ceramics of SS of the four-component system $(1 - x)(Na_{0.5}K_{0.5})NbO_3$–$xPb(Ti_{0.5}Zr_{0.5})O_3$ can be obtained using mechanical activation of powders that have passed through two stages of the synthesis. The influence of Nb_2O_5 polymorphism on phase formation and properties of ceramics has been established, and a conclusion has been made in favor of using Nb_2O_5 without preliminary heat treatment.

Acknowledgements The work was funded by the Ministry of Education and Science of the Russian Federation projects Nos. 3.6371.2017/8.9, 3.6439.2017/8.9 (the basic part of the state task); Grant of Russian Foundation for Basic Research No. 18-32-00552 mol_a; Scholarship of President of Russian Federation No. SP-4674.2018.1. Equipment of the Centers «Electromagnetic, Electromechanical and Thermal Properties of Solids» of SFedU was used.

References

1. S.I. Dudkina, N.A. Boldyrev, I.N. Andryushina, L.A. Shilkina, K.P. Andryushin, I.A. Verbenko, L.A. Reznichenko, E.F. Vajnshtejn, Constr Composite Mater **2**(42) (2016) (in Russian)
2. S.I. Dudkina, K.P. Andryushin, I.N. Andryushina, N.A. Boldyrev, L.A. Shilkina, I.A. Verbenko, L.A. Reznichenko. in: *Proceedings of the 2016 International Conference on "Physics, Mechanics of New Materials and Their Applications",* ed. by I.A. Parinov, S.-H. Chang, M.A. Jani. (Nova Science Publishers, New York, 23 2017) (Chapter 4)

3. L.A. Reznichenko,, I.A. Verbenko, L.A. Shilkina, A.V. Pavlenko, S.I. Dudkina, I.N. Andryushina, K.P. Andryushin, A.G. Abubakarov, T.V. Krasnyakova. in: *Advanced Materials—Proceedings of the International Conference on "Physics, Mechanics of New Materials and Their Applications", PHENMA 2017*, ed. by I.A. Parinov, S.-H. Chang, V. K. Gupta (Springer Nature, **207**, 3 2018)
4. V.S. Urusov. *Theoretical Crystal Chemistry*. (Moscow State University Press, Moscow, 1987), p. 275 (in Russian)
5. G.B. Boky, *Introduction to Crystal Chemistry*. (Moscow State University Press, Moscow, 1954), p. 491 (in Russian)
6. J. Emsley, *The Elements,* 2nd edn. (Clarendon Press, Oxford, 1991), p. 260 (in Russian)
7. V.V. Titov. *PhD Thesis on Physical and Mathematical Sciences*. Rostov-on-Don. (Rostov State University, 2003) p. 144 (in Russian)

Chapter 6
Effects of Modifying with Simple (MnO_2, CuO) and Combined (MnO_2 + NiO, Bi_2O_3 + Fe_2O_3) Dopants of Multi-Element Media Based on Alkali Niobates

Khizir Sadykov, Konstantin Andryushin, Abu Abubakarov, Anatoliy Turik, Alexey Pavelko, Lidiya Shilkina, Alexandr Nagaenko, Svetlana Dudkina, Iliya Verbenko, Inna Andryushina and Larisa Reznichenko

Abstract The features of the crystal structure, grain structure, dielectric, piezoelectric, ferroelastic characteristics of media based on sodium-potassium niobates and modified simple and combined oxides of various elements were studied. It was established that the solid solutions studied were inhomogeneous and actually consist of several low-symmetry phases with close cell parameters. It was shown that in the behavior of macroparameters, a difference was observed in various ways of introducing additives. Regularities in the formation of correlation relationships was established for electrophysical properties presenting the areas of application of the solid solutions under analysis, taking into account their crystallochemical specifics and thermodynamic background. The developed materials are promising for applications in devices operating in power modes (piezotransformers, piezomotors, high- voltage generators). The manifestation of the ferrosoft properties of solid solutions with the introduction of MnO_2 can also be useful for use in low-frequency receiving devices (hydrophones, microphones, seismic receivers).

K. Sadykov · K. Andryushin · A. Abubakarov · A. Turik · A. Pavelko · L. Shilkina · S. Dudkina · I. Verbenko · I. Andryushina · L. Reznichenko
Research Institute of Physics, Southern Federal University, Rostov-on-Don, Russia

K. Sadykov (✉)
Chechen State University, Grozny, Russia
e-mail: hizir-2010@mail.ru

A. Nagaenko
Research and Design Bureau "Piezopribor", Southern Federal University, Rostov-on-Don, Russia

I. A. Parinov et al. (eds.), *Advanced Materials*, Springer Proceedings in Physics 224, https://doi.org/10.1007/978-3-030-19894-7_6

6.1 Introduction

Recently, there are the current trends of the complete replacement of the known Pb-containing world piezo-technical brands on materials without toxic elements. The last materials are also obtained using technologies that allow mass production. The requirements of the maximum approximation of all their basic characteristics are similar to those in compositions based on $PbZr_{1-x}Ti_xO_3$ (PZT) systems. Among these objects, complex multielement (and multicomponent) media based on alkali metal niobates with unique physical properties (low specific weight and permittivity, high Curie temperatures and sound velocity, a wide range of mechanical Q and piezoelectric activity) are priority [1]. This makes them practically indispensable as the base of sensitive elements of microwave technology.

In order to preserve sufficiently high electrophysical parameters in the transition to conventional ceramic technology (CCT), one of the most effective methods of forming the physical properties of ferroelectrics is the introducing small (no more than 5 mass%) additions of monooxides of various elements (modification) [2–5]. This allows, with the preservation of the specific properties of the original objects by modifying their composition to vary the values of certain parameters in the desired direction.

The purpose of the present work is to consider the effect on the macro-responses in solid solutions (SS) based on (Na, K)NbO_3 of small changes in the cation-anion composition when modifying objects with simple and combined oxides, the conditions of preparation and morphology of the samples, nano-microstructure, taking into account the crystal-chemical parameters cations, included in the composition of SS, and the characteristics of the chemical bond.

6.2 Materials and Methods

SS on the base of a multielement composition of $0.98(Na_{0.54}K_{0.46})(Nb_{0.9}Ta_{0.1})O_3$—$x$LiSbO$_3$ (x = 0.02, 0.04, 0.06) including modified with simple (MnO_2, CuO) and combined (MnO_2 + NiO, Bi_2O_3 + Fe_2O_3) oxides was considered according to the scheme shown in Fig. 6.1.

The samples were produced by two-stage solid-phase synthesis followed by sintering in conventional ceramic technology with variation in sintering temperature. The synthesis temperatures T_1 = (880–890) °C, T_2 = (890–900) °C, the isothermal holding time $\tau_1 = \tau_2$ = 6 h; sintering at temperatures $T_{sint.}$ = (1155–1200) °C (depending on the composition), for (1.0–1.5) h.

The X-ray studies were carried out using the powder diffraction method using DRON-3 and ADP (FeK_α- radiation; Mn-filter; FeK_β- radiation, Bragg-Brentano geometry). The bulk and ground ceramic objects were examined, which allowed the exclusion of the influence of surface effects, stresses and textures arising in the

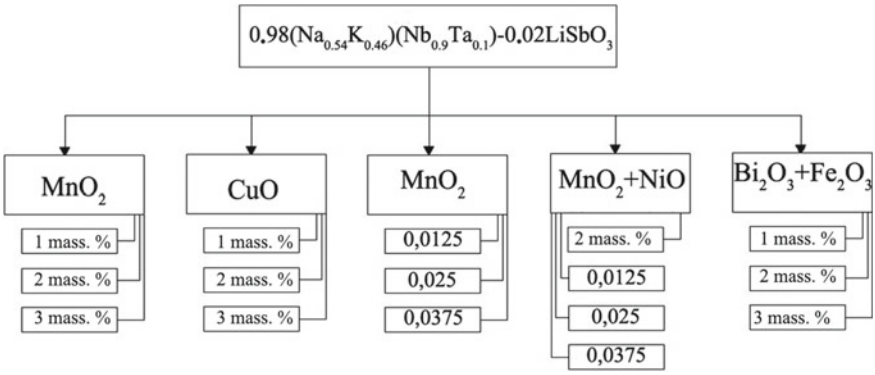

Fig. 6.1 Scheme for modifying SS of a multicomponent system based on (Na,K)NbO_3 (c/c is superstoichiometric, c is stoichiometric)

process of preparation of the ceramics. The structural parameters were calculated in accordance with the standard procedure [6].

A scanning electron microscope JSM-6390L (Japan) with a microanalyzer system from Oxford Instruments (UK) was used to study the microstructure of the chips. The resolution of the microscope is up to 1.2 nm with an accelerating voltage of 30 kV (image in secondary electrons), the limits of the accelerating voltage are from 0.5 to 30 kV, the increase is from ×10 to × 1,000,000, the beam current is up to 200 nA.

Dielectric, piezoelectric and elastic parameters of the SSs at room temperature were measured by the resonance- antiresonance method [7] of OST [8]. In doing this, we determined the relative dielectric permittivities of poled ($\varepsilon_{33}^{T}/\varepsilon_0$) and unpoled ($\varepsilon/\varepsilon_0$) samples, the dielectric losses at a low electric field (loss tangent, tgδ), Curie temperature (T_C), the piezoelectric modulus ($|d_{31}|$, d_{33}), the electromechanical coupling factor of a planar mode of vibration (K_p), ferroelectric coefficients (ferrosensitivity) ($|g_{31}|$, g_{33}), the mechanical quality factor ($Q_м$), the Young's modulus $\left(Y_{11}^{E}\right)$ and the sound speed $\left(V_1^{E}\right)$.

The measurement error was: linear $\Delta a = \Delta b = \Delta c = \pm$ (0.002–0.004) Å; angular $\Delta\alpha = 3'$; volume $\Delta V = \pm 0.05$ Å^3; electrophysical $\Delta\varepsilon/\varepsilon_0$, $\Delta\varepsilon_{33}^{T}/\varepsilon_0 \leq \pm$ 1.5%, $\Delta K_p \leq \pm 2.0\%$, $\Delta|d_{31}| \leq \pm 4.0\%$, $\Delta d_{33} \leq \pm 10\%$, $\Delta Q_m = \leq \pm 12\%$; $\Delta Y_{11}^{E} \leq \pm 0.7\%$.

6.3 Results and Discussion

The X-ray phase analysis has shown that SS of composition 0.98($Na_{0.54}K_{0.46}$)($Nb_{0.9}Ta_{0.1}$)O_3–xLiSbO_3 have a rhombic symmetry with a monoclinic perovskite cell R(M). The large width of the X-ray lines, the asymmetry and the apparent

splitting of the 200 and 020 lines indicate that they are inhomogeneous and actually consist of several low-symmetry phases with close cell parameters. Taking into account the complex formula composition of the investigated SS, one can expect that in addition to the main phase (R(M)) with a small angle β, characteristic for SS $Na_{0.54}K_{0.46}NbO_3$, there can be a R(M) phase with a large angle β corresponding to SS $Na_{1-x}Li_xNbO_3$ at a low Li content.

Figure 6.2 shows fragments of microstructures of the studied objects. The change in the character of the polycrystallinity of the modified ceramics is evident: the decrease in the average size of grains and the broadening of the intercrystalline interlayers up to the violation of intergranular connectivity and the development of bimodal structures; intensification of the processes of secondary discontinuous recrystallization with anisotropic excessive growth of ideomorphic grains to giant

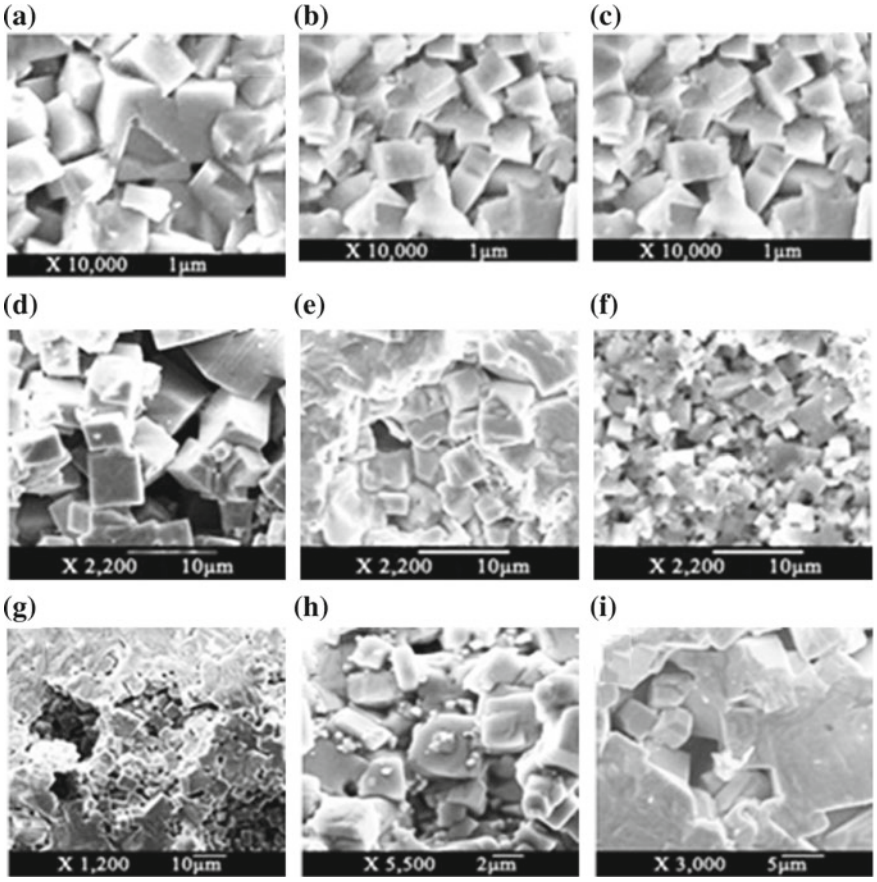

Fig. 6.2 Fragments of microstructures of SS: without modifier $x = 0.02$ (**a**), 0.04 (**b**), 0.06 (**c**); with modifier (superstoichiometric, 1 mass%) MnO_2 (**d**), CuO (**e**), $Bi_2O_3 + Fe_2O_3$ (**f**); with bimodal grain structure of modified ceramics (**g**–**k**)

sizes, which is a consequence of the transition from solid-phase to liquid-phase structure formation.

The causes of the latter are the liquid phases of eutectic origin formed during synthesis and sintering, the possibility of their occurrence being allowed at certain cation-anion ratios and temperatures by phase equilibrium in the systems Mn–O, Cu–O, Bi–O, $Bi_2O_3 + Fe_2O_3$; polymorphism of the initial reagents—Sb_2O_5 (Sb_2O_3), undergoing a number of phase transformations during the heat treatment of the charges with a change in the oxidation state Sb: $Sb_2O_5 \overset{600\,K}{\rightarrow} Sb_6O_{13} \overset{940\,K}{\rightarrow} SbO_2$; $Sb_2O_3 \underset{air.}{\overset{400\,K}{\rightarrow}} SbO_2$; the development of crystal-chemical disorder due to the possibility of placing Li in the *A*- and *B*-positions of the perovskite and perovskite-like structures; a considerable disparity (22–34%) of the radii of the substituting ion Sb^{5+} (0.52 Å), Sb^{3+} (0.90 Å) and replaceable Nb^{5+} (0.66 Å), Nb^{4+} (0.67 Å), Ta^{5+} (0.66 Å) ions exceeding the permissible (10–15%) to maintain the stability of the crystal structure. The appearance of the Hedwall effect, associated with the first circumstance that is increase in the reactivity of solids during or as a result of polymorphic transformations. This, in turn, stimulates the recrystallization processes, causing the simultaneous formation of many centers of primary recrystallization of reduced mass, due to which from each embryo of the future grain pattern grow smaller crystallites. The second and third causes destabilize the structure in conditions of its high heterogeneity, which also provokes the formation of several primary clusters and, as in the first case, leads to a restraint in the growth of grains. The development of the bimodal grain structure of SS is associated with the heterogeneity of the structure characterized by fluctuations in the composition, density of ceramics, and unevenness of the grain pattern.

Figures 6.3, 6.4 and 6.5 shows the dielectric, piezoelectric and ferroelastic properties of SS based on $0.98(Na_{0.54}K_{0.46})(Nb_{0.9}Ta_{0.1})$—$0.02LiSbO_3$ modified by MnO_2 (samples of different morphology and obtained for different $T_{sint.}$ were studied).

One can clearly see a fundamental difference in the behavior of macroparameters in various ways of introducing additives. Thus, in the case of stoichiometric modification, the characteristics under analysis are significantly inferior to those in SS with superstoichiometrically introduced MnO_2. The influence of technological factors ($T_{sint.}$, sample diameter) turned out to be ambiguous for each of the parameters, regardless of the type of SS doping. The observed, of course, is related to the phase state of the SS under consideration, as well as to their grain structure (enlarged and more inhomogeneous with stoichiometric MnO_2).

The addition of NiO to MnO_2 (Fig. 6.6) does not change the dynamics of the behavior of the electrophysical properties of the SS in principle, which is indicative of the suppressive role of MnO_2 in the tandem MnO_2 + NiO, which is undoubtedly associated with the crystallochemical features of nickel, and with the characteristics forming chemical bonds (less covalent than in the case of MnO_2). It is very similar to the observed behavior of electrophysical properties of SS modified by copper (Figs. 6.7, 6.8 and 6.9).

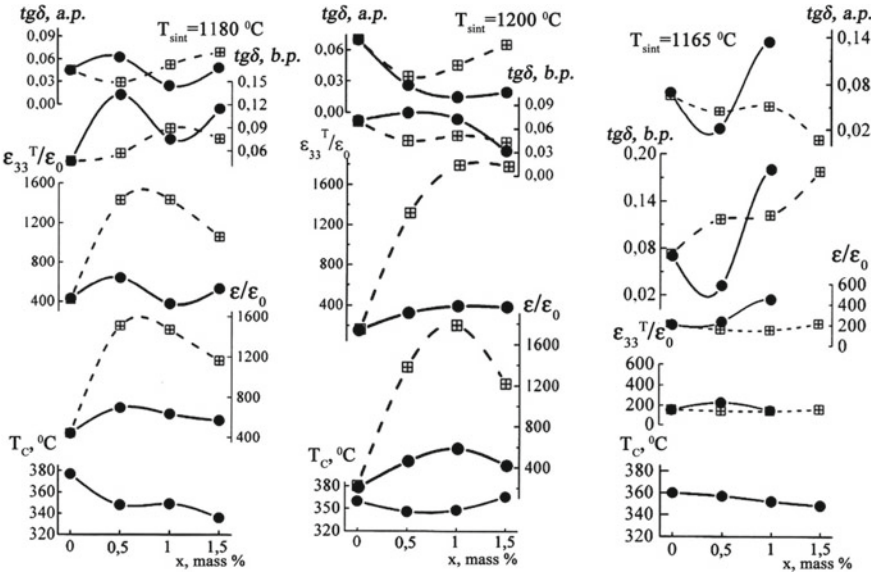

Fig. 6.3 Dependences of dielectric properties of SS on the base of $0.98(Na_{0.54}K_{0.46})(Nb_{0.9}Ta_{0.1})$–$0.02LiSbO_3$, modified by MnO_2 (modifier introduction method: on the left **a** superstoichiometric ($T_{sint.}$ = 1180 °C, $T_{sint.}$ = 1200 °C), on the right **b** stoichiometric ($T_{sint.}$ = 1165 °C), solid lines—samples with Ø 10 mm, dotted—Ø 20 mm)

The reason is probably that all the above-described SSs crystallize with the participation of the liquid phase, and this has a decisive influence on the formation of macro-responses, leveling the characteristics of each of their modifiers. Nevertheless, we note that with the introduction of MnO_2 and CuO, Q_m, $\varepsilon_{33}^T/\varepsilon_0$, tg$\delta$ increase sharply, while piezoelectric activity remains practically at the initial level. The increase in Q_m is probably the result of the following: manganese and copper cations have small ionic radii and a sufficiently high charge, which suggest their partial incorporation into the crystal lattice in the place of niobium according to the following schemes:

$$(Na_{1-x}K_x)\left(Nb_{1-y}M^{4+}{}_y\right)O_{3-y/2}\Upsilon_{y/2}(M{-}Mn;\ \Upsilon - \text{vacancy})$$
$$(Na_{1-x}K_x)\left(Nb_{1-y}M^{2+}{}_y\right)O_{3-3y/2}\Upsilon_{3y/2}(M{-}Cu;\ \Upsilon - \text{vacancy}).$$

This contributes to the formation of anion-deficient structures, which is accompanied by the formation of vacancies in the oxygen sublattice and a violation of the symmetry of the anionic environment of the *B*-cation, which contributes to the increase in the dipole moment and, as a consequence, to the growth of the ferrohardness (FH) of ceramics. The latter characterizes the addition of MnO_2 as a FP additive. On the other hand, increases of $\varepsilon_{33}^T/\varepsilon_0$ and tgδ indicate that the modifiers are soft. Such a "softening" of the SS may be a consequence of the following

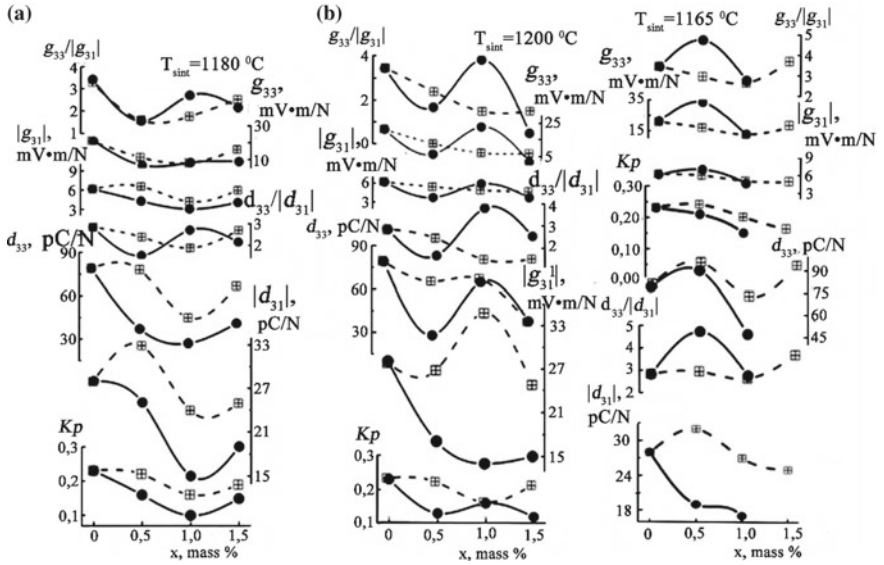

Fig. 6.4 Dependences of ferroelectric properties of SS on the base of $0.98(Na_{0.54}K_{0.46})(Nb_{0.9}Ta_{0.1})$–$0.02LiSbO_3$, modified by MnO_2 (modifier introduction method: on the left **a** superstoichiometric ($T_{sint.}$ = 1180 °C, $T_{sint.}$ = 1200 °C), on the right **b** stoichiometric ($T_{sint.}$ = 1165 °C), solid lines—samples with Ø 10 mm, dotted—Ø 20 mm)

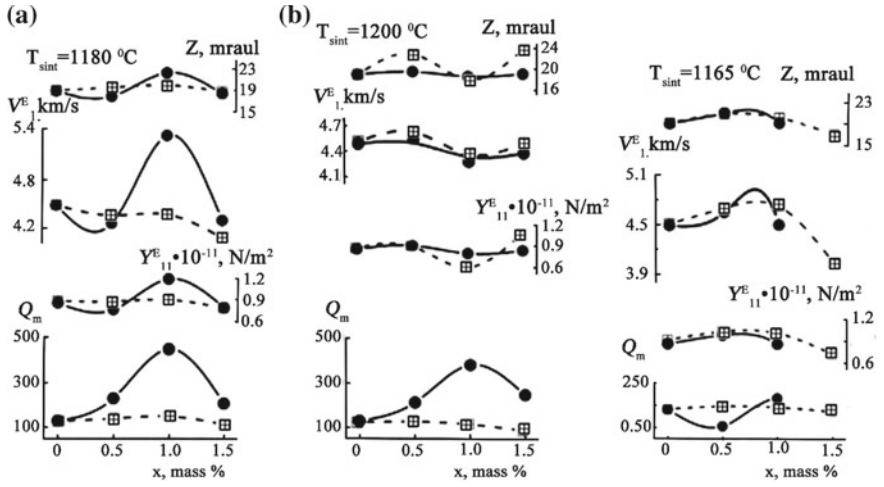

Fig. 6.5 Dependences of ferroelastic properties of SS on the base of $0.98(Na_{0.54}K_{0.46})(Nb_{0.9}Ta_{0.1})$–$0.02LiSbO_3$, modified by MnO_2 (modifier introduction method: on the left **a** superstoichiometric ($T_{sint.}$ = 1180 °C, $T_{sint.}$ = 1200 °C), on the right **b** stoichiometric ($T_{sint.}$ = 1165 °C), solid lines—samples with Ø 10 mm, dotted—Ø 20 mm)

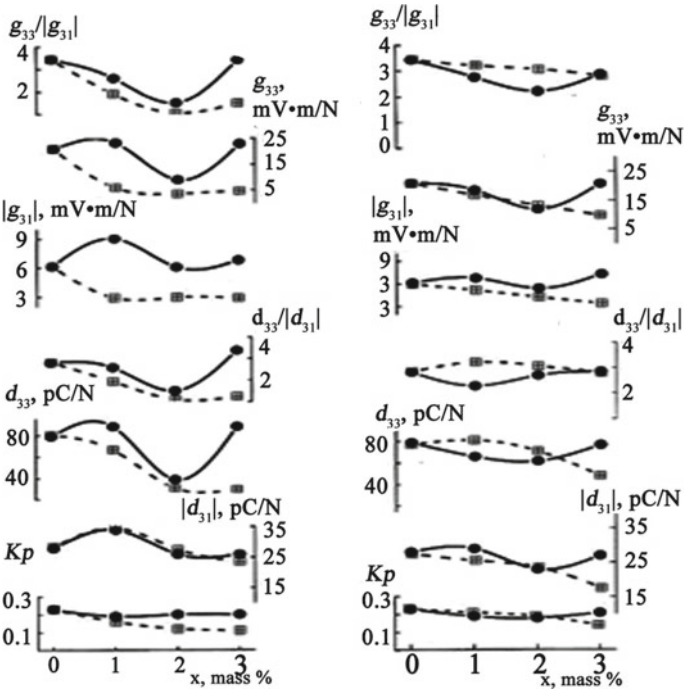

Fig. 6.6 Dependences of dielectric (**a**), piezoelectric (**b**), ferroelastic (**c**) properties of SS on the base of $0.98(Na_{0.54}K_{0.46})(Nb_{0.9}Ta_{0.1})$–$0.02LiSbO_3$, modified in combination MnO_2 + NiO, solid lines—samples with Ø 10 mm, dotted—Ø 20 mm)

circumstances. X-ray diffraction data show that, as the systems saturate with modifiers, δ (uniform strain parameter) decreases, and $\bar{D}$ (the average grain size) increases [8], indicating more favorable conditions for the diffusion and recrystallization processes [8].

The increase of $\varepsilon_{33}^{T}/\varepsilon_0$ at low δ is the effect of the inverse dependence of the dielectric macro-response on spontaneous polarization (spontaneous deformation, expressed through the structural parameter δ). With decreasing δ, the growth of the mobility of the domain walls and, as a consequence, the growth of $\varepsilon_{33}^{T}/\varepsilon_0$ [9] is associated. Thus, in the same way as in [10, 11], we noted an interesting feature of the result of the action of Mn (and Cu) on the initial SS: the modifiers simultaneously exhibit both FH and ferro-soft (FS) qualities, which is related to their crystallochemical features.

Figure 6.10 shows the dependence of the electrophysical properties of SS modified with the combined Bi_2O_3 + Fe_2O_3 modifier. It is clearly seen that as the content of the modifier increases (x = 1.0 mass%), the piezoelectric parameters increase sharply, then, with further increase of its concentration to x = 2.0 mass%, the piezoelectric activity decreases and its small growth exists at x = 3.0 mass%.

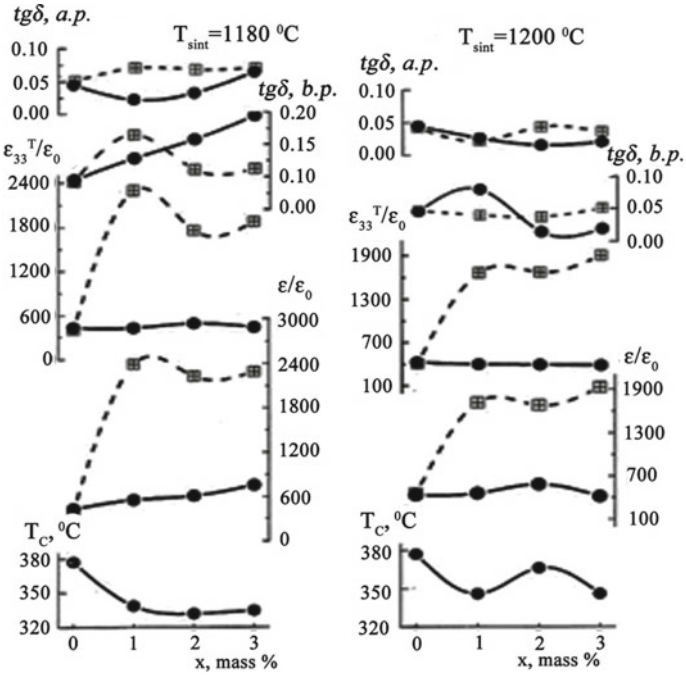

Fig. 6.7 Dependences of dielectric properties of SS on the base of $0.98(Na_{0.54}K_{0.46})(Nb_{0.9}Ta_{0.1})$–$0.02LiSbO_3$ superstoichiometric modified by CuO (solid lines—samples with Ø 10 mm, dotted—Ø 20 mm)

Electromechanical properties change as follows: the values of ${V_1}^E, Z, {Y_{11}}^E$ first increase (x = 1.0 mass%), and then decrease x = (2.0–3.0) mass%, Q_m, on the contrary, decreases at x = 1.0 mass% and increases in the interval x = (2.0–3.0) mass%. This behavior is typical for ferroelectric SS in the region of the morphotropic phase boundary and, obviously, is a consequence of the tetragonal-monoclinic transition [12].

Figure 6.11 shows a comparison of the results of the effects of all the additives described above on the matrix base. It can be seen that the simple modifier MnO_2 and the combined $Bi_2O_3 + Fe_2O_3$ are most effective. Introduced superstoichiometrically these additives enhance the piezoelectricity of the initial compositions (their mechanical Q-factor), which is of no small importance for the applications of the materials in devices operating in power regimes (piezotransformers, piezo-motors, high-voltage generators). The manifestation of FS properties in MnO_2 can also be useful for use such media in low-frequency receiving devices (hydrophones, microphones, seismic receivers).

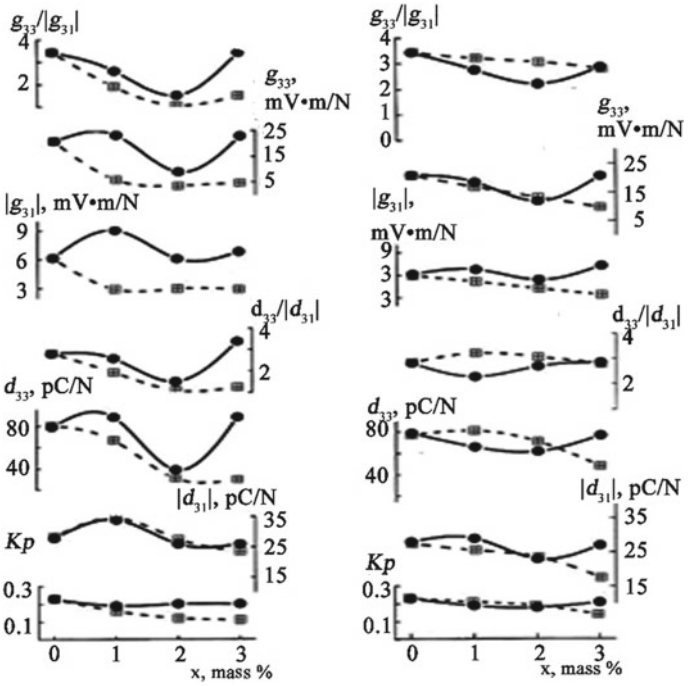

Fig. 6.8 Dependences of piezoelectic properties of SS on the base of $0.98(Na_{0.54}K_{0.46})(Nb_{0.9}Ta_{0.1})$–$0.02LiSbO_3$ superstoichiometric modified by CuO (solid lines—samples with Ø 10 mm, dotted—Ø 20 mm)

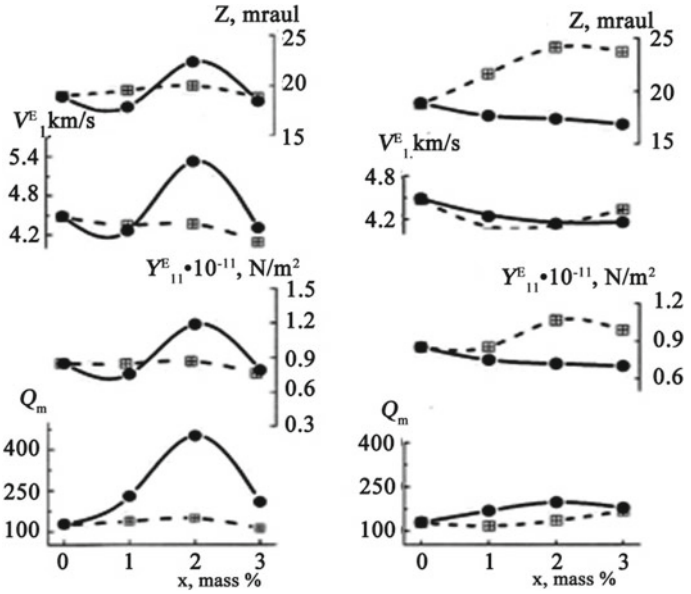

Fig. 6.9 Dependences of ferroelastic properties of SS on the base of $0.98(Na_{0.54}K_{0.46})(Nb_{0.9}Ta_{0.1})$–$0.02LiSbO_3$ superstoichiometric modified by CuO (solid lines—samples with Ø 10 mm, dotted—Ø 20 mm)

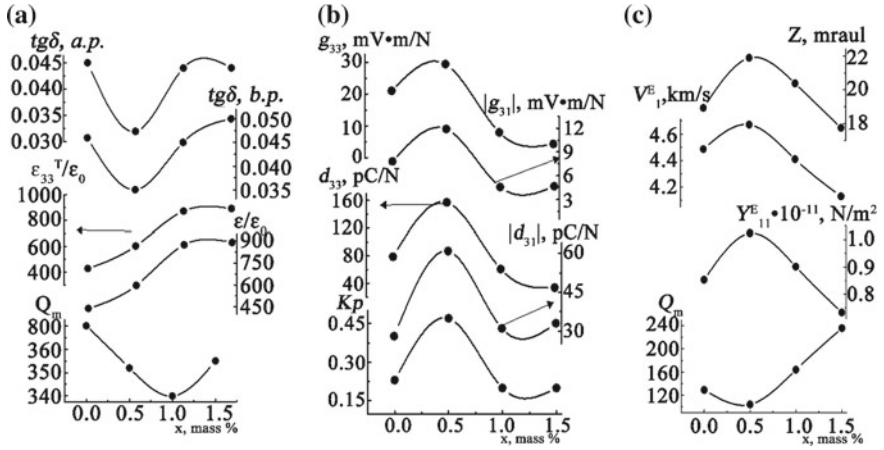

Fig. 6.10 Dependences of dielectric **a**, piezoelectric **b** and ferroelastic **c** properties of SS on the base of $0.98(Na_{0.54}K_{0.46})(Nb_{0.9}Ta_{0.1})$–$0.02LiSbO_3$ superstoichiometric modified by Bi_2O_3 + Fe_2O_3 ($T_{sint.}$ = 1180 °C) (solid lines—samples with Ø 10 mm, dotted—Ø 20 mm)

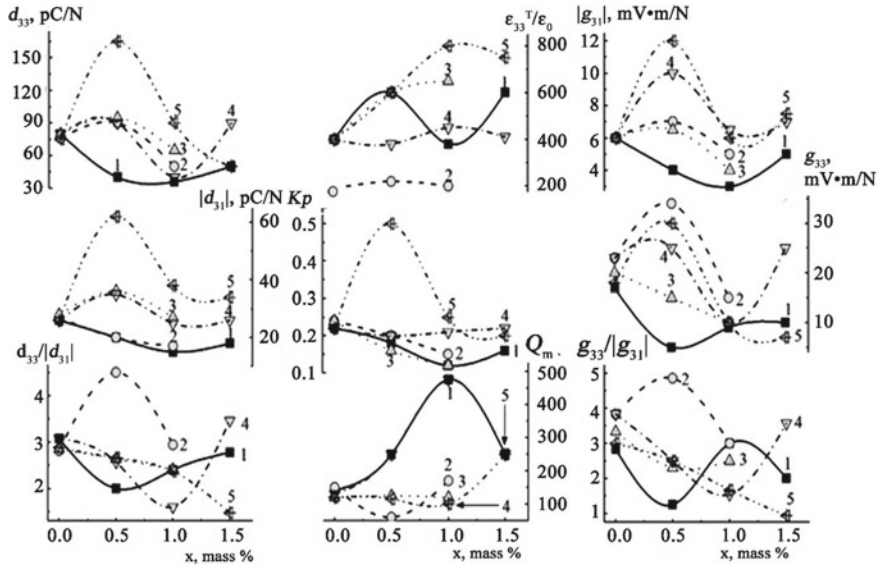

Fig. 6.11 Dependences of dielectric, piezoelectric and ferroelastic properties of SS on the base of $0.98(Na_{0.54}K_{0.46})(Nb_{0.9}Ta_{0.1})$–$0.02LiSbO_3$ superstoichiometric modified by MnO_2 (1), superstoichiometric MnO_2 (2), combined MnO_2 + NiO (3), superstoichiometric CuO (4), superstoichiometric Bi_2O_3 + Fe_2O_3 (5)

6.4 Conclusion

The influence of SS modification on the base of a multielement composition of 0.98 $0.98(Na_{0.54}K_{0.46})(Nb_{0.9}Ta_{0.1})O_3$–$x$LiSb$O_3$ (x = 0.02, 0.04, 0.06), including simple (MnO_2, CuO) and combined (MnO_2 + NiO, Bi_2O_3 + Fe_2O_3) oxides was investigated.

It is established that the investigated SSs are inhomogeneous and actually consist of several low-symmetry phases with close cell parameters.

It is shown that in the behavior of macroparameters, a difference is observed in various ways of introducing additives. Thus, in the case of stoichiometric modification, the characteristics under analysis are significantly inferior to those in SS with superstoichiometrically introduced MnO_2. The influence of technological factors ($T_{sint.}$, diameter of the samples) was also ambiguous for each of the parameters, regardless of the type of doping.

The greatest efficiency of a simple modifier of MnO_2 and a combined Bi_2O_3 + Fe_2O_3 was revealed. Introduced super stoichiometrically, these additives enhance the piezoactivity of the starting compositions, their mechanical quality factor. This makes promising for using of developed materials in devices operating in power regimes (piezotransformers, piezomotors, high-voltage generators). The manifestation of FS properties in MnO_2 can also be useful for use such media in low-frequency receiving devices (hydrophones, microphones, seismic receivers).

Acknowledgements The work was funded by: the Ministry of Education and Science of the Russian Federation projects Nos. 3.6371.2017/8.9, 3.6439.2017/8.9 (the basic part of the state task); Grant of Russian Foundation for Basic Research No. 18-32-00552 mol_a; Scholarship of President of Russian Federation No. SP-4674.2018.1. The equipment of the Centers "Electromagnetic, Electromechanical and Thermal Properties of Solids" and "High Technologies" of SFedU was used.

References

1. L.A. Reznichenko, *Doctor of Physical and Mathematical Sciences Thesis*. Rostov State University Press, Rostov-on-Don, 20024, 61 p. (In Russian)
2. Z.Y. Shen, Z. Zhen, K. Wang, J.F. Li, J. Am. Ceram. Soc. **52**, 1748 (2009)
3. Y. Gao, J. Zhang, Y. Qing, Y. Tan, Z. Zhang, X. Hao. J. Am. Ceram. Soc. **94**, 2968 (2011)
4. Y. Qin, J. Zhang, Y. Tan, W. Yao, C. Wang, S. Zhang, J. Eur. Ceram. Soc. **34**(16), 4177 (2014)
5. J.-F. Li, K. Wang, F.-Y. Zhu, L.-Q. Cheng, F.-Z. Yao, J. Am. Ceram. Soc. **96**(12), 3677 (2013)
6. E.G. Fesenko, *The Perovskite Family and Ferroelectricity* (Atomizdat, Moscow, 1972), p. 248. (In Russian)
7. IEEE Standard on Piezoelectricity ANSI/IEEE Std 176-1987, (New-York, 1988). https://doi.org/10.1109/ieeestd.1988.79638
8. L.A. Reznichenko, A.Y. Danziger, O.N. Razumovskaya, L.S. Ivanova, S.I. Dudkina, L.A. Shilkina, V.A. Servuly, V.P. Sakhnenko. in *Proceedings of the International Scientific and*

Practical Conference Fundamental problems of piezoelectronics "Piezotechnika-95". MP "Book", Rostov State University, **2**, 182 (1995) (In Russian)
9. E.G. Fesenko, A.Y. Danziger, O.N. Razumovskaya, *New Piezoceramic Materials* (Rostov State University Press, Rostov-on-Don, 1983), p. 156. (In Russian)
10. L.G. Gusakova, N.A. Spiridonov, D.V. Kuzenko, N.G. Kisel, V.M. Ischuk, S*cientific Papers of Donetsk National Technical University. Avg. Chemistry and Chemical. Technology.* Iss. 15, 86 (2010) (In Ukrainian)
11. L.G. Gusakova, V.M. Pogibko, N.A. Spiridonov, V.M. Ishchuk, N.G. Kisel, Nanosystems. Nanomater. Nanotechnol. **10**(2), 303 (2012). (In Ukrainian)
12. Kh.A. Sadykov, I.A. Verbenko, L.A. Shilkina, A.G. Abubakarov, A.A. Pavelko, G.M. Konstantinov, L.A. Reznichenko. in *Proceedings of the Fourth International Youth Symposium Physics of Lead-free Piezoactive and Related Materials (Analysis of the Current State and Development Prospects) (LFPM-2015) September 2–6, 2015*, vol. 2 (Rostov-on-Don—Tuapse, Russia, 2015) (In Russian), p. 184

Chapter 7
Influence of Mn_2O_3 Modification on the Structural, Microstructural, Dielectric, and Relaxation Characteristics of the $(1 - x)BiFeO_3$–$xPbTiO_3$ Ceramics

Nikita A. Boldyrev, Yuriy I. Yurasov, Lidia A. Shilkina, Alexander V. Nazarenko and Larisa A. Reznichenko

Abstract We obtained pure and modified overstoichiometrically by 0.5 mass. % of the manganese (III) oxide samples of binary system solid solutions $(1 - x)BiFeO_3 - xPbTiO_3$ ($x = 0.30$) using the solid-state reaction technique with further sintering according to common ceramic technology. We established the formation patterns of their crystalline structure, microstructure, dielectric and relaxation characteristics in a wide range of temperatures and frequencies. Dielectric relaxation phenomena was described by using Havriliak-Negami approximation model with considering the singular term. This research suggests an explanation for the observed effects.

7.1 Introduction

Multiferroics are the materials with coexisting electric and magnetic orderings in a wide range of temperatures above room temperature. Bismuth ferrite, $BiFeO_3$ (BFO) is representative for this class of objects (Curie temperature, $T_C = 1123$ K, Neel temperature, $T_N = 643$ K) and currently being considered as the base for many magnetoelectric structures [1]. But complicated preparation conditions, high electrical conductivity and, as a consequence, impossibility of creating a polarized state, do not allow using this material in engineering. Creation of solid solutions based on BFO with stable piezoelectric characteristics [2], magnetodielectric and

N. A. Boldyrev (✉) · Y. I. Yurasov · L. A. Shilkina · L. A. Reznichenko
Research Institute of Physics, Southern Federal University,
194, Stachki Avenue, 344090 Rostov-on-Don, Russia
e-mail: nboldyrev@sfedu.ru

Y. I. Yurasov · A. V. Nazarenko
Southern Scientific Center of the Russian Academy of Science,
41, Chekhov Avenue, 344006 Rostov-on-Don, Russia

I. A. Parinov et al. (eds.), *Advanced Materials*, Springer Proceedings in Physics 224, https://doi.org/10.1007/978-3-030-19894-7_7

magnetoelectric effects [3] can solve this problem. Lead titanate ($PbTiO_3$) is a high-temperature ferroelectric compound with a perovskite-type structure, which is the main component of a number of industrially used ferro-piezoelectric materials. System $(1 - x)BiFeO_3 - xPbTiO_3$ was studied for the first time in the 1960–70s [4]. However, the literature contains quite contradicting data on its properties [5, 6]. Earlier [7, 8], we also carried out a complex study of this system aimed at establishing the regularities in the formation of structural, dielectric, and magnetic structures in them. This work is aimed at studying the influence of modification on the structural and dielectric characteristics of the solid solutions of this system with $x = 0.30$. Concentration selection was due to the presence of the morphotropic region (MR) in the concentration interval $0.2 < x < 0.4$. MR is traditionally considered the region of optimal properties. Our earlier studies [9] have shown, that modification (in particular, by Mn-containing compounds) often leads to the appearance of relaxor properties in ceramics and to the enhancement of processes, associated with Maxwell-Wagner polarization and relaxation. To describe these phenomena, Havriliak-Negami formula is the most general model for approximation of relaxation in ferroelectric materials (1) [10, 11]. We can obtain the Debye ($\alpha = 0$, $\beta = 1$), Cole-Cole ($0 \leq \alpha \leq 1$, $\beta = 1$) and Davidson-Cole ($\alpha = 0$, $0 \leq \beta \leq 1$) laws in the formula (1) by varying the parameters α and β within range [0; 1]:

$$\varepsilon^* = \varepsilon_\infty + \frac{\varepsilon_S - \varepsilon_\infty}{\left(1 + (i\omega\tau)^{1-\alpha}\right)^\beta} \tag{1}$$

where $\varepsilon^* = \varepsilon' - i\varepsilon''$ is the complex dielectric permittivity; $\omega = 2\pi f$ is the angular frequency [rad/s]; ε_s are the values of ε at $\omega \to 0$ (low frequency region); ε_∞ are the values of ε at $\omega \to \infty$ (high frequency region); τ is the most probable relaxation time [s].

It was noted in [12, 13] that for "strong" and "weak" relaxations the electrical conductivity introduces an additional contribution to the imaginary part of the dielectric constant. This affects the form of the frequency or temperature dependences of the dielectric loss tangent, tan δ, or the imaginary part of the complex dielectric permittivity ε''. It makes difficult to calculate the activation energies using these parameters [14]. In [12, 13] the authors proposed a method for eliminating the effect through conductivity by introducing into the imaginary part ε'' singular term:

$$\varepsilon'' = \varepsilon'' + \frac{\gamma_{st}}{\omega\varepsilon_0}, \tag{2}$$

where ε_0 is a dielectric constant $\approx 8.85 \times 10^{-12}$ [$C^2/(N \cdot m^2)$]; γ_{st} is the electrical conductivity at $\omega \to 0$ ($\gamma'_{\omega \to 0}$). When the relaxators and charge carriers do not interact, this approach describes the relaxation processes with sufficient accuracy. In this paper, we carried out approximation of relaxation processes in $(1 - x)BiFeO_3 - xPbTiO_3$ ceramics using this model.

7.2 Methods of Obtaining and Examination of Samples

Pure (BFPT) and modified overstoichiometrically by 0.5 mass. % of Mn_2O_3 (BFPTM) samples of the binary system $(1 - x)BiFeO_3 - xPbTiO_3$ ($x = 0.30$) were obtained in two steps: by solid-state reaction technique, with further sintering and intermediate grinding at temperatures $T_1 = 1123$ K, $T_2 = 1143$ K and holding times $\tau_1 = \tau_2 = 10$ h, respectively. The sintering of the ceramic templates was performed at $T_{sin} = 1243$ K during $\tau_{sin} = 2$ h.

X-ray studies were conducted using a diffraction meter DRON-3 (Bragg-Brentano focusing, filtered $Co_{K\alpha}$-radiation). Calculations of the cell parameters (a, b, c are linear constants, α is a angular constant, V_{exp} is the volume) were performed according to the standard technique [15]. The accuracy of the measurements of structural parameters in single-phase solid solutions were the following: $\Delta a = \Delta b = \Delta c = \pm(0.002–0.004)$ Å, $\Delta\alpha = \pm 0.05°$, $\Delta V = \pm 0.05$ Å^3. In the MR of the studied system, the diffraction lines were very broad, hence the average cell parameters were calculated. The theoretical volume of the perovskite cell (V_{theor}) was calculated for substitutional solid solution in positions A and B according to the [16].

The study of the grain structure of the objects was carried out using the KEYENCE VK-9700 color laser scanning 3D microscope. Temperature dependencies of relative complex dielectric permittivity $\varepsilon^*/\varepsilon_0 = \varepsilon'/\varepsilon_0 - i\ \varepsilon''/\varepsilon_0$ ($\varepsilon'/\varepsilon_0$ and $\varepsilon''/\varepsilon_0$ are the real and imaginary parts of $\varepsilon^*/\varepsilon_0$, respectively; ε_0 is a dielectric constant) at $T = (300–1000)$ K in the frequency range $f = (75$ kHz–2 MHz) were obtained using an impedance analyzer Agilent 4285A. Preliminary approximation of the models of relaxation processes in dielectric spectra was carried out by the formulae (1) and (2) with the help of the specialized software [17].

7.3 Results and Discussion

All the investigated solid solutions belong to the MR of the binary system $(1 - x)$ $BiFeO_3 - xPbTiO_3$, whose composition is characterized by the coexistence of rhombohedral (Rh) and tetragonal (T) phases. The samples crystallize in a perovskite-type structure, the phase composition and parameters of the crystal lattice are shown in Table 7.1. As can be seen from Table 7.1, samples do not contain impurity phases.

It can be seen that the structural parameters of BFPT and BFPTM differ significantly in the T-phase. Thus, in the modified sample the cell volume decreased by 0.51 Å^3, and the degree of distortion of the cell c/a decreased by 0.01 relative to BFPT. This suggests that manganese is embedded in the crystal lattice of both phases. It can be possible in the case where Mn^{3+}, increasing the degree of oxidation to Mn^{4+} replaces B-cations (R of $Mn^{3+} = 0.70$ Å, R of $Mn^{4+} = 0.52$ Å, R of $Ti^{4+} = 0.64$ Å, R of $Fe^{3+} = 0.67$ Å). Also in [18] it was shown that Pb^{2+} in an

Table 7.1 Phase composition and parameters of the unit cell in the Rh and T phases in BFPT and BFPTM ceramics

	Phase composition	a_{Rh}, Å	α_{Rh}, degr.	V_{Rh}, Å^3	a_T, Å	c_T, Å	V_T, Å^3	μ_T, %
BFPT	Perovskite-type MR Rh + T	3.9645	89.68	62.31	3.8466	4.4119	65.28	20
BFPTM	Perovskite-type MR Rh + T	3.9671	89.59	62.433	3.8466	4.3776	64.773	18

amount of ~2.5 at. % can be placed in oxygen octahedra (*B*-positions) of a structure with a crystallographic shift of the ReO_3 type, which includes a perovskite-type structure.

Figure 7.1 shows the X-ray lines $(110)_k$, illustrating the ratios between the Rh- and T-phases. It can be seen that in BFPTM (lower X-ray diffraction) the T-phase concentration is lower than in BFPT. It indicates that the modification by Mn_2O_3 shifts the phase diagram towards $BiFeO_3$.

Figure 7.2 shows microphotographs of the chips of the studied ceramics. As can be seen from the figure, both pure and modified samples are characterized by a loose microstructure with small grains. It was shown [7] that a similar microstructure is observed in ceramics of the composition $(1 - x)BiFeO_3 - xPbTiO_3$ ($0.20 \leq x \leq 0.40$, $\Delta x = 0.10$). It may be due to the presence of MR approximately in this concentration interval in the solid solutions of the binary system $(1 - x)BiFeO_3 - xPbTiO_3$.

Figure 7.3 shows the temperature dependences $\varepsilon'/\varepsilon_0$ and tan δ from 300 to 950 K in the frequency range (75 kHz–1.2 MHz). It can be seen from the figure that both dependencies $\varepsilon'/\varepsilon_0(T)$ have the diffuse maxima with weak frequency dispersion associated with the phase transition from ferroelectric to the paraelectric phase. The observed frequency dispersion can be associated with a change in the degree of oxidation of transition metal ions (Fe, Ti), as well as with heterovalent cation substitution in both *A*- ($Bi^{3+} \rightarrow Pb^{2+}$) and *B*- ($Fe^{3+} \rightarrow Ti^{4+}$) positions in this solid solution.

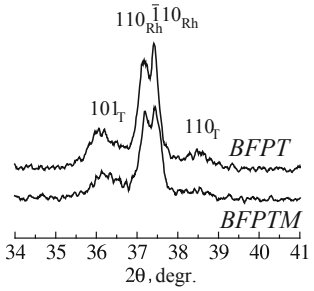

Fig. 7.1 X-ray lines $(110)_k$ of the investigated objects

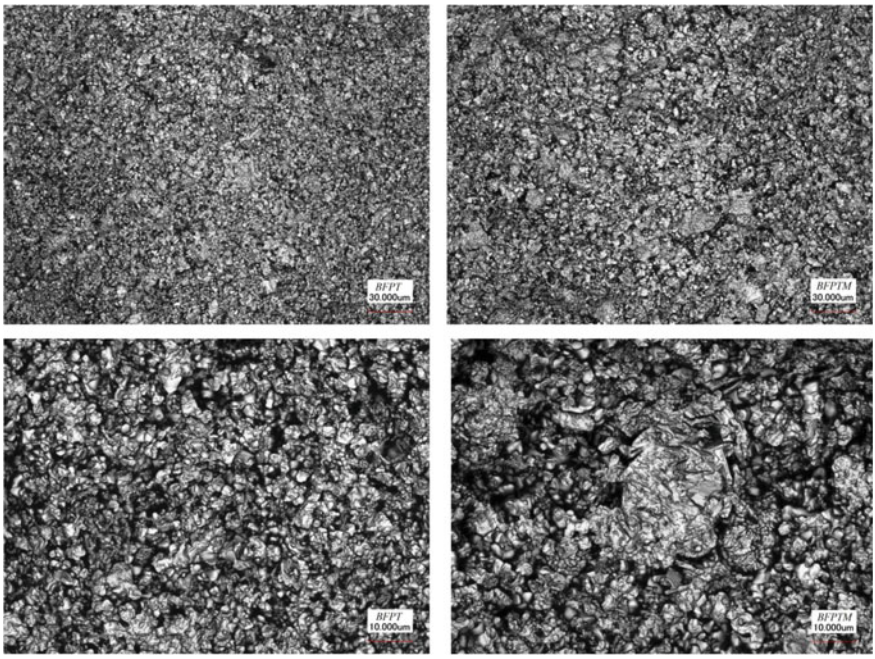

Fig. 7.2 Microphotographs of the chips surface of the studied samples

The modification have led to a shift of the Curie temperature to the low-temperature region (from 857 to 819 K) and to decrease in the $\varepsilon'/\varepsilon_{0max}$ values at $T = T_K$ by almost 25% (Fig. 7.4). Also, the anomaly is observed on the tan $\delta(T)$ dependencies in the temperature range (350–500 K). This anomaly manifests itself in a strong frequency dispersion of the local maxima of tan δ. Additional extremes have a relaxation character, which are described fairly well by the models of Cole-Cole, Havriliak-Negami, etc.

We used the Havriliak-Negami approximation model for describing this process. Figure 7.5 shows the dependences $\varepsilon'/\varepsilon_0(f)$, $\varepsilon''/\varepsilon_0(f)$, tan $\delta(f)$ and $\gamma'(f)$ of pure and modified samples in the temperature range (405–469 K). When the temperature was raised, we used the Gavriliac-Negami formula (1) with allowance for the singular term (2) to improve the convergence.

As can be seen from the figures, the character of the presented dependences corresponds to a "weak" relaxation process [19, 20] in temperature range (405–469 K). The introduction of the Mn_2O_3 have led to a decrease in the values of ε_∞ and ε_S.

The corrected Havriliak-Negami model with singular term of the electrical conductivity makes it possible to obtain a satisfactory convergence of the approximated curves and experimental points at $T \geq 421$ K. According to [21], for such model the Maxwell-Wagner polarization and relaxation in an inhomogeneous system can be the physical base. This system consists of approximately isodiametric

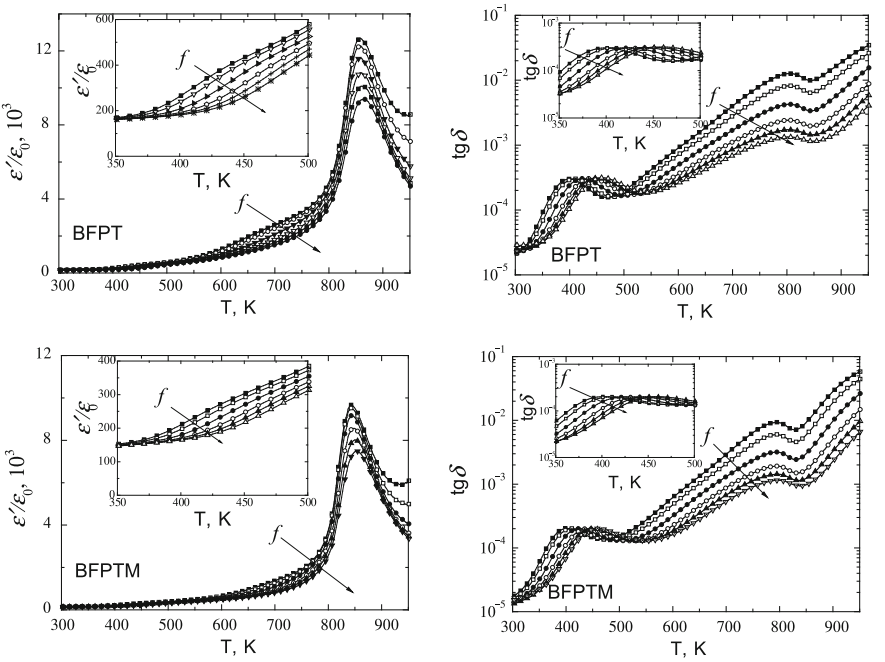

Fig. 7.3 Temperature dependencies of $\varepsilon'/\varepsilon_0$ and tan δ from 300 to 950 K in the frequency range (75 kHz–1.2 MHz)

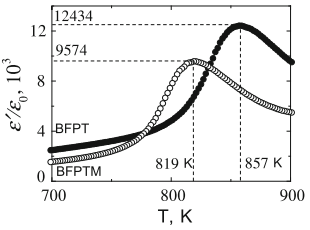

Fig. 7.4 Temperature dependencies of $\varepsilon'/\varepsilon_0$ from 700 to 900 K on the frequency 100 kHz

grains of ceramics, surrounded by thin layers (shells) with a small or large conductivity and a dielectric permittivity different from grains. The variation of dielectric permittivity, conductivities and thicknesses of grains and shells leads to a wide distribution of relaxation times and causes large values of the dielectric permittivity and conductivity in the samples. In addition to the equiprobable distribution of relaxation times in the case of Maxwell-Wagner relaxation, it is also possible to distribute the relaxation times around the most probable or least probable value.

Figure 7.6 shows the temperature dependencies of the most probable relaxation time τ, singular term γ'_{st}, coefficients α, β, ε_S and ε_∞ in the studied samples. The relaxation time in both compositions decreases with increasing temperature, while γ'_{st} increases. Such behavior of these characteristics can be associated with an increase of the contribution of the electrical conductivity with increasing temperature. The behavior of the relaxation time τ corresponds to the following law:

$$\tau = \tau_0 e^{\frac{E_A}{kT}}, \tag{3}$$

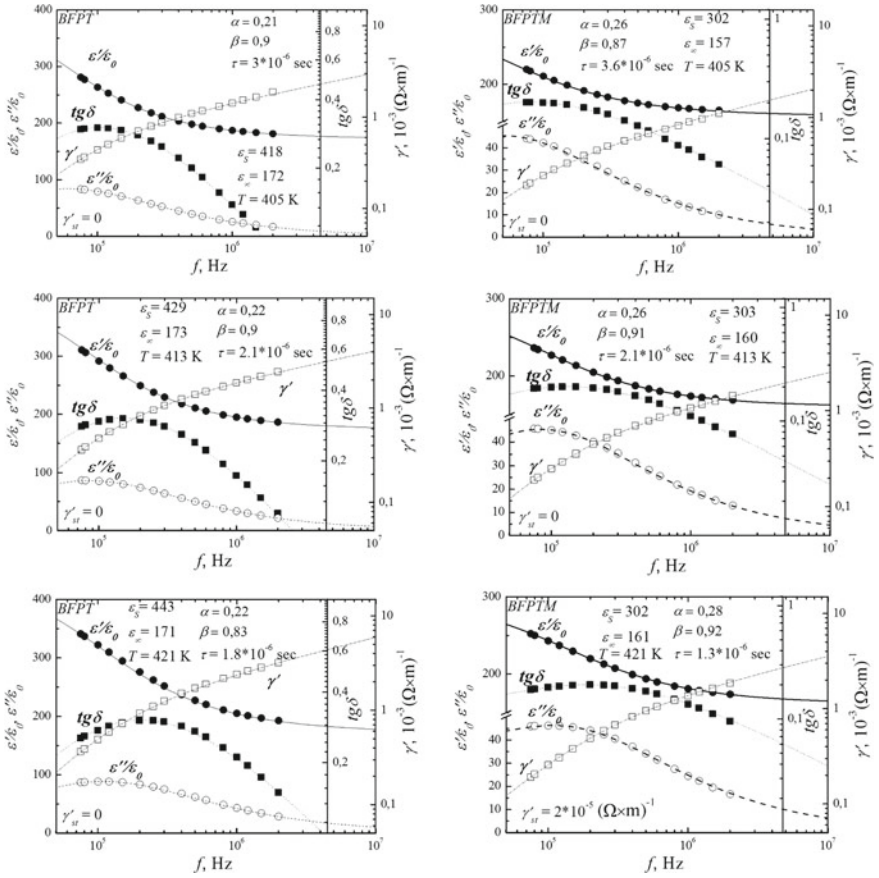

Fig. 7.5 Dependencies $\varepsilon'/\varepsilon_0(f)$, tan $\delta(f)$, $\gamma'/f)$ (a) and $\varepsilon''/\varepsilon_0$ ($\varepsilon'/\varepsilon_0$) pure and modified samples in the (405–469 K) temperature range; the dots represent the experimental data, the lines represent the calculated data

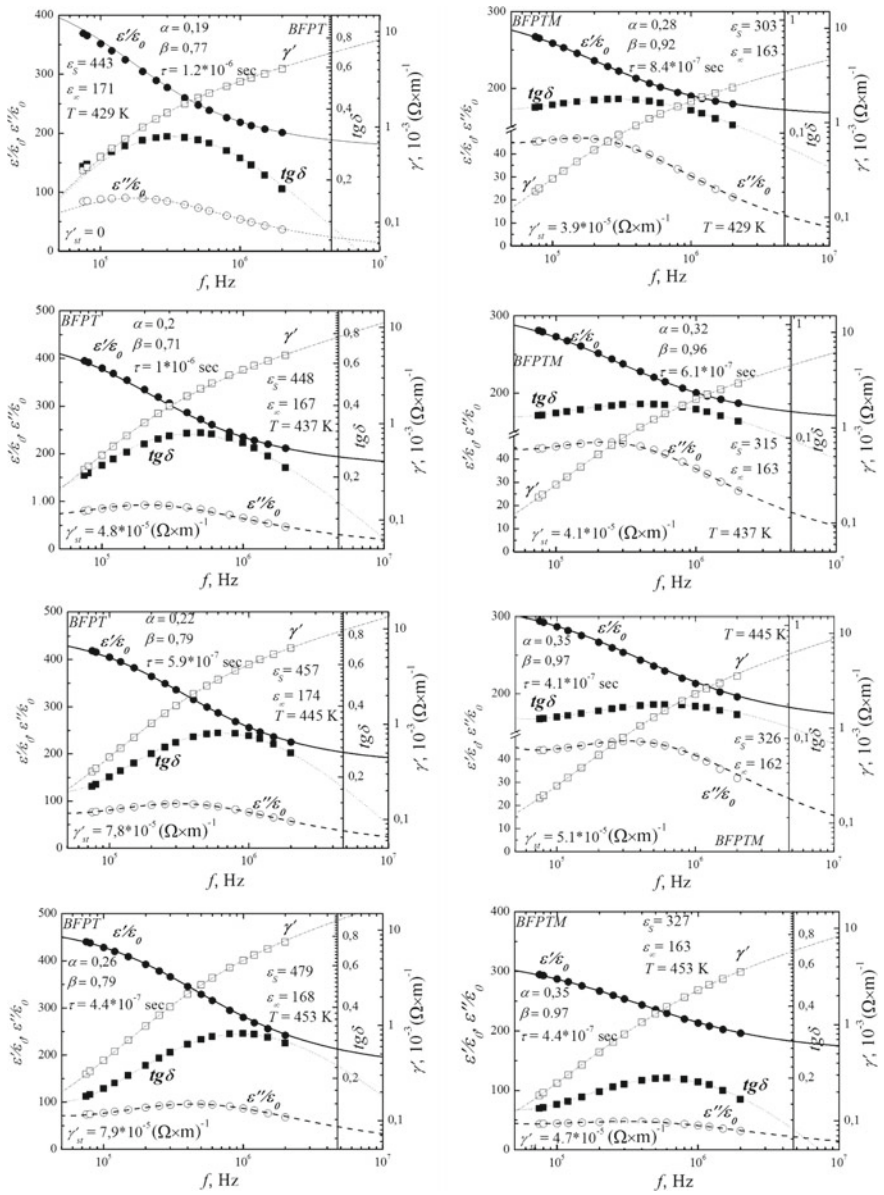

Fig. 7.5 (continued)

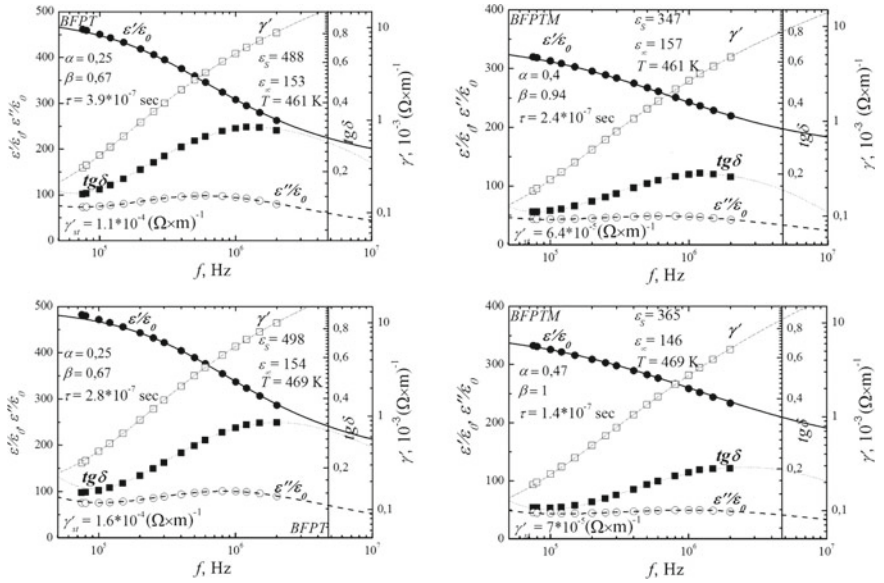

Fig. 7.5 (continued)

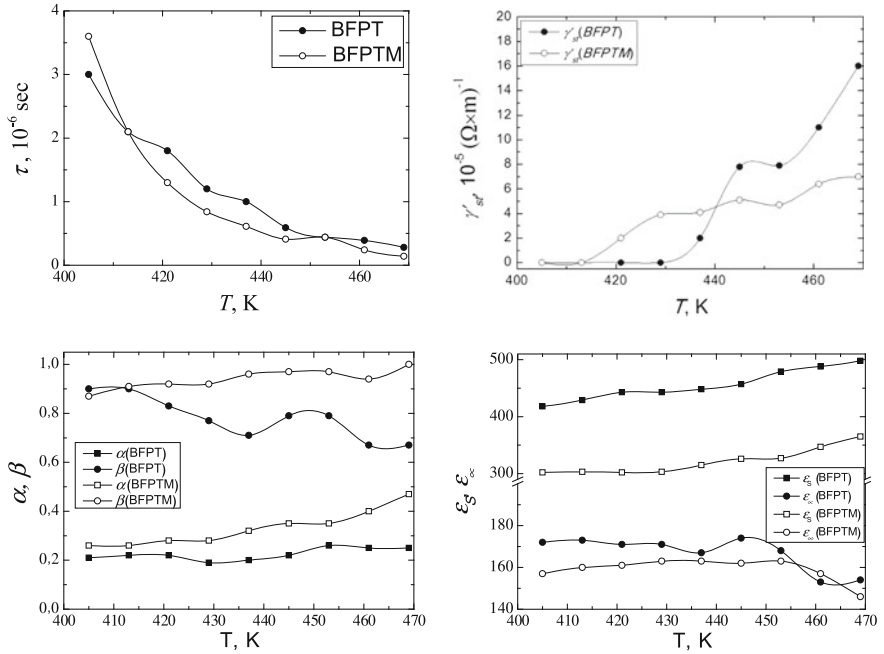

Fig. 7.6 Temperature dependencies of the most probable relaxation time τ, singular term γ'_{st}, coefficients α, β, ε_S and ε_{∞} in the studied samples

where E_A is the activation energy of the potential barrier; τ_0 is a pre-exponential factor (the time for one attempt to overcome the barrier); k is a Boltzmann constant. The calculated E_A and τ_0 values using (3) are: $E_A = 0.615$ eV, $\tau_0 = 7\times10^{-14}$ s for BFPT and $E_A = 0.764$ eV, $\tau_0 = 0.1\times10^{-14}$ s for BFPTM. Such energy values indicate the ionic mechanism of the electrical conductivity.

It should be noted that some relaxation characteristics of BFPT have the extremum in the region of $\sim$450 K. The nature of this anomaly will be investigated in our future works.

7.4 Conclusion

Pure and modified overstoichiometrically by 0.5 mass. % of the manganese (III) oxide samples of binary system solid solutions $(1 - x)BiFeO_3 - xPbTiO_3$ ($x = 0.30$) were obtained by using the solid-state reaction technique with further sintering according to common ceramic technology. It was found that the modification of this solid solution by manganese (III) oxide leads to a shift in the phase diagram of the $0.7BiFeO_3$–$0.3PbTiO_3$ ceramic towards $BiFeO_3$, a strong shift of the Curie point to the low-temperature region, and a decrease in the maximum value on the $\varepsilon'/\varepsilon_0(T)$ dependencies. It was established that the anomalies in the dependences of tan $g\delta(T)$ in the temperature range (350–500 K) are "weak" relaxation processes that are well approximated by the Havriliak-Negami model with singular term of the electrical conductivity. Calculating values potential barrier activation energy (0.615 and 0.764 eV) indicates the ionic mechanism of the electrical conductivity.

Acknowledgements This work was financially supported by the Ministry of Education and Science of the Russian Federation: themes Nos. 3.6371.2017/8.9, 3.6439.2017/8.9 and with the financial support of the Russian Foundation for Basic Research in the framework of a scientific project No. 17-08-01724, using the equipment of the Center for Collective Use "Electromagnetic, Electromechanical and Thermal Properties of Solids", Research Institute of Physics, Southern Federal University.

References

1. A.P. Pyatakov, A.K. Zvezdin, Phys. Usp. **55**(6), 557 (2012)
2. L. Fan, J. Chen, S. Li, H. Kang, L. Liu, L. Fang, X. Xing, Appl. Phys. Lett. **37**(2), 022905 (2013)
3. K. Manish, S. Shankar., O.P. Thakur, A.K. Ghosh, J. Mater. Sci.: Mater. Electron. **26**, 1427 (2015)
4. Y.Y. Tomashpol'skii, N.Y. Venevtsev, Crystallogr. Rep. **6**(16), 1037 (1971)
5. D.I. Woodward, I.M. Reaney, Eitel, C.A. Randall. J. of Appl. Phys. **5**(94), 3313 (2003)
6. T.L. Burnett, T.P. Comyn, A.J. Bell, E. Condliffe, G. Lloyd, J. Phys: Conf. Ser. **26**, 239 (2006)

7. N.A. Boldyrev, A.V. Pavlenko, L.A. Shilkina, G.M. Konstantinov, A.V. Turik, E.I. Sitalo, A.A. Amirov, V.V. Rodionova, R.A. Chichay, L.A. Reznicenko, in *Advanced Materials—Techniques, Physics, Mechanics and Applications*, ed. by I.A. Parinov, S.-H. Chang, M.A. Jani. Springer Proceedings in Physics, vol. 193 (2017), p. 25
8. N.A. Boldyrev, A.V. Pavlenko, L.A. Shilkina, L.A. Reznichenko, A.I. Miller, Bull. Russ. Acad. Sci.: Phys. **80**(6), 733 (2016)
9. A.V. Pavlenko, N.A. Boldyrev, L.A. Reznichenko, I.A. Verbenko, G.M. Konstantinov, L.A. Shilkina, Inorg. Mater. **52**(1), 76 (2016)
10. R.H. Cole, Discuss. Far. Soc. **23**, 31 (1957)
11. R. Zorn, J. Polym. Sci. Part B. **37**(10), 1043 (1999)
12. A.S. Bogatin, I.V. Lisitsa, S.A. Bogatina, Tech. Phys. Lett. **28**(9), 779 (2002)
13. A.S. Bogatin, Phys. Solid State **54**(1), 62 (2012)
14. N.P. Bogoroditskiy et al., *Theory of dielectrics* (Energia, Moscow, 1965)
15. E.G. Fesenko, *Perovskite Family and Ferroelectricity*, Moscow, Atomizdat (1972)
16. N.V. Dergunova, V.P. Sakhnenko, E.G. Fesenko, Crystallogr. Rep. **1**(23), 94 (1978)
17. Y.I. Yurasov, *Automatic Measuring Bench of Electrophysical Parameters of Ferro-Piezomaterials in a wide Range of Temperatures and Frequencies*. Patent of the Russian Federation, No. 66552 (2007)
18. L.A. Shilkina, L.A. Reznichenko, O.N. Razumovskaya, S.I. Dudkina, V.G. Vlasenko, S.I. Shevtsova, K.A. Guglev, A.T. Kozakov, A.V. Nikol'skii, Phys. Solid State, **58**(1), 115 (2016)
19. A.S. Bogatin, A.V. Turik, S.A. Kovrigina, V.N. Bogatina, E.V. Andreev, Bull. Russ. Acad. Sci.: Phys. **74**(8), 1066 (2010)
20. A.S. Bogatin, Bull. Russ. Acad. Sci.: Phys. **75**(8), 1128 (2011)
21. I.P. Raevski, S.A. Prosandeev, A.S. Bogatin, M.A. Malitskaya, L. Jastrabik, J. Appl. Phys. **93**, 4130 (2003)

Chapter 8
Technology and Electrophysical Parameters of Piezocomposites with a Connection Type 2–0–2

A. A. Nesterov and E. A. Panich

Abstract Possible ways for increasing the strength characteristics and volumetric piezo-parameters of composite materials with the 2–2-type connectivity due to a change in the type of their active elements are discussed. It is shown that the transition from the active element in the form of dense ceramic plates to the active element in the form of a thin porous piezoceramic enables us to shift the maximum values of the volumetric piezo-parameters of composite materials towards the larger volume fractions of the active elements in the system. In addition, these changes also promote an increase of the maximum achievable volumetric piezo-parameters values and mechanical strength of the samples.

8.1 Introduction

The active elements (AEs) of composite piezoelectric materials (CPMs) with the 1–3-type and 2–2-type connectivity are a combination of rods (of various geometries) or thin ceramic plates. The AEs can be made of powders of a ferroelectric component with different composition. In general, the CPMs of these types are a system formed by the parallel arranged (relative to each other) AEs, which are surrounded by a polymer matrix [1–3]. The practical attractiveness of these CPMs consists in improving the effectiveness of acoustic piezo transducers, ultrasonic sensors of medical diagnostics, sensors of emission control, flaw detectors and other piezoelectric devices [4–6]. CPMs demonstrate a combination of low mechanical quality factor, high values of the electromechanical coupling factors, low acoustic impedance and low permittivity [4–6]. The features of these CPMs are: (i) unevenness of mechanical stresses in the system, associated with the various mechanical properties of ceramics and polymer, and (ii) anisotropy of mechanical,

A. A. Nesterov (✉)
Department of Chemistry, Southern Federal University, Rostov-on-Don, Russia
e-mail: lanesan2448@ya.ru

E. A. Panich
Technology Institute “Piezopribor”, Southern Federal University, Rostov-on-Don, Russia

I. A. Parinov et al. (eds.), *Advanced Materials*, Springer Proceedings in Physics 224,
https://doi.org/10.1007/978-3-030-19894-7_8

dielectric and piezoelectric properties, which is determined by the axial arrangement of the AEs in the materials [7–9]. The manufacturing techniques of the 1–3-type and 2–2-type CPMs can be applied at a wide variation of the volume fraction of the piezoactive component, the geometry of the AE, the features of their mutual arrangement, the mechanical properties of the matrix, etc. All this makes it possible to vary the parameters of the CPMs in a very wide range, and, consequently, to achieve maximum efficiency of materials for piezoelectric converters suitable for various applications. The ideal option for the CPMs of the types considered is a polymer matrix, whose volume compressibility is significantly higher than that of the AE, and if this polymer matrix has high adhesion energy in relation to the ferroelectric phase. In this case, the mechanical stress applied to the CPMs is concentrated on the AE almost completely. This fact, in combination with a low dielectric permittivity of the CPMs, leads to an increase of piezoelectric sensitivity of these composite materials (g_{ij}). Thus, the polymer phase in CPMs acts as a kind of antenna for mechanical oscillations arising in the external environment and contributes to a decreasing dielectric permittivity of the sample. It should be noted, that the known CPM technologies of these types do not provide high reproducibility of their electrophysical parameters (EPPs). The scale of this problem increases with the increasing the porosity of the polymer matrix.

In the literature, the problems of the effect of the volume content of the ferroelectric component in the 1–3-type and 2–2-type composites, the geometry of the AE, and the properties of the polymer matrix on the values of the EPPs of the samples are considered in detail [5–9]. At the same time, high values of the volumetric piezo-parameters are achieved in these CPMs only at the volume fraction of the AE from 0.1 to 0.2 at condition that the AE is located in a volume-compressible polymer matrix. Therefore, high-effective piezocomposite materials of these types have a low value of the relative dielectric permittivity at constant mechanical stress $\varepsilon_{33}^{T}/\varepsilon_{o}$, which makes it difficult to reconcile piezoelectric converters made on their base with other components of piezoelectric systems.

In addition, the low volume fraction of the AE in high-effective CPMs of the 1–3- and 2–2-types predetermines their low mechanical strength. In the same way, the fact of low convergence of the experimental and theoretically calculated values of the bulk parameters of the CPM of a specific type is noteworthy. In addition, it should be noted that the technological reproducibility of the EPPs of these materials is low (especially for CPMs with a foamed polymer matrix). In particular, for approximately equal values of $\varepsilon_{33}^{T}/\varepsilon_{o}$, the values of the volumetric piezoelectric module (d_{v}) of samples within a single batch can vary from 80 to 250 pC/N (for a fixed composition of the ferroelectric component, as well as geometry and volume fraction of active elements). At the same time, the yield of high-effective materials (within the same batch), as a rule, does not reach 40% [4, 5, 7–9]. One of the reasons for the low reproducibility of samples of this type is the lack of technologies that ensure the formation of a strong contact between the AE and the polymer matrix.

8.2 Problem Formulation

In the present work, we consider: (i) technology for the production of the 2–0–2 composite (ferroelectric phase/air/polymer), and (ii) influence of the magnitude of the porosity of the AEs and their volume fraction on the set of dielectric and piezoelectric parameters of the studied PCMs.

8.3 Experimental Part

With a view to increase the adhesion energy between the ferroelectric component and binder in the 2–2-type CPM, we manufactured active elements in the form of porous ceramic parallelepipeds, (120–150) $\times$ 10^{-6} m in thickness, 10 mm long, and 5 mm high. For the production of these AEs, the method for casting plates was applied. The casting suspension consists of (i) ultrafine powders of a phase with the composition $Pb_{0.96}Bi_{0.04}Ti_{0.43}Zr_{0.51}Cd_{0.02}Ni_{0.02}W_{0.02}O_3$ (manufactured in the framework of the "chemical assembly" method [10]), and (ii) a binder that is a composition (polyvinyl butyral, benzoic acid and non-ionic surfactant and solvent – ethanol + ethyl acetate). The produced raw films to be (120–150) $\times$ 10^{-6} m thick, after their rolling, they were cut into strips with a width of 10.2–10.3 mm and a height of 5.2 mm. For carrying out the drying operation, the strips were placed on the ceramic substrates of zirconium oxide, the surface of which was coated with a powder of this oxide. After drying (on the same substrates), a polythermal firing of the samples was carried out in the temperature range from 25 to 950 °C. The powder of benzoic acid was used as a pore-forming agent in the manufacture of porous AE. Evaporation that contributes to the formation of pores, enabled us to vary the porosity of produced the ceramic films in the range from 12 to 65 vol.% (Fig. 8.1).

The parallel surfaces of the AE (average size: 10 mm $\times$ 0.11 mm) were metallized by burning a "silver" paste (the distance from the first electrode to the second electrode was 4 mm). The electrodes of the individual AEs were connected in parallel using a copper bus, and the manufactured cassettes were poled in air (E_p = 2 kV/mm at 80 °C). The cassettes were glued by using the silicon-organic binder Pentelast®-710 (that was selected by taking into account its adhesion, thermal, mechanical, electrical and dielectric properties), onto a band of porous material previously prepared, and based on the same binder. The thickness of the porous polymer tape varied depending on the technological task, from 0.1 to 0.5 mm. The CPM samples were made in the form of the rectangular parallelepiped with the sizes 10 mm $\times$ 10 mm $\times$ 5 mm. The change in the volume fraction of the plates in the PCM was achieved due to a change in the distance between them (on decreasing or increasing) and the thickness of the porous polymer layers. The CPM samples were collected in the technology mold. The samples, after the binder was completely cured, were removed from the technological mold in which they were

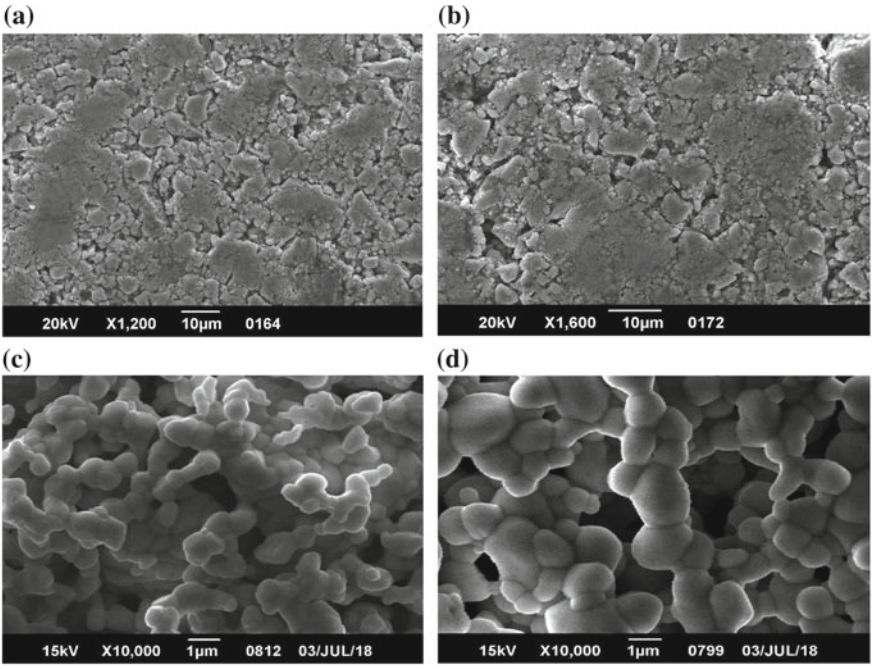

Fig. 8.1 Surfaces: **a**, **b** of initial rolled films, and **c**, **d** porous ceramic films, with total porosity: **c** 28 vol.%; **d** 55 vol.%. (JSM-6390LA)

assembled. The AE electrodes were released from the polymer, and copper bus bars were superimposed on them using conductive glue based on the same binder. The copper bus bars play the role of the electrodes on the CPM (2–0–2 connectivity, ferroelectric component/air/polymer). After the electrode formation process was completed, the CPM samples were sealed by coating them with a non-porous polymer. Studies of the EPP of the CPMs were carried out in accordance with the RF Standard (OST 110444-87—Piezoceramic materials). The magnitudes of the dielectric loss tangent tan δ and the permittivity $\varepsilon_{33}^{T}/\varepsilon_{o}$ of the CPM were determined at room temperature using the TSENZURKA-M equipment (Production of the SRDI "Piezopribor"). Using the same setup, the values of the transverse piezoelectric modulus d_{31} were determined (dynamical method), while the values of the longitudinal piezoelectric modulus d_{33} of the samples were found by means of the quasi-static method ("Piezo d_{33} TestSystem", Production of the APC International, Ltd., USA). Using the "Pascal" research equipment and "Membrane" (Production of the SRDI "Piezopribor"), the value of the volumetric piezoelectric sensitivity γ of the CPM was found. The value of the coefficient of the volumetric piezoelectric sensitivity g_v ($g_v = \gamma/h$, where h is the height of the piezoelement) was calculated from the γ values. The value of the d_v was calculated by using the relation $g_v = d_v/\varepsilon_{33}^{T}$. The EPP of these CPMs is shown in Figs. 8.2 and 8.3 wherein the

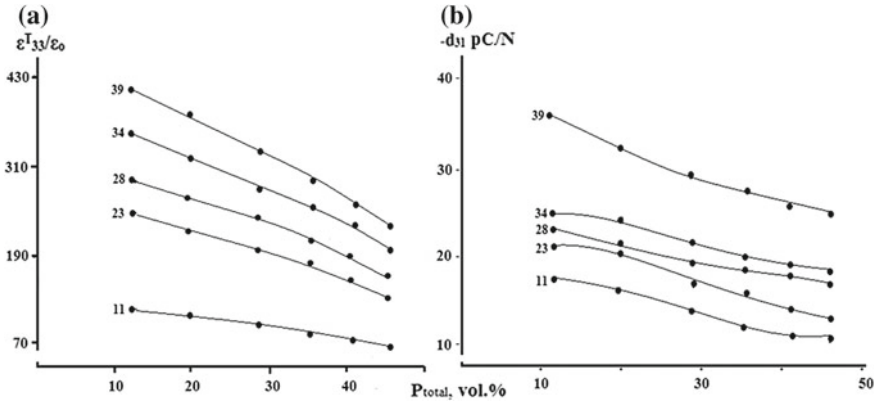

Fig. 8.2 Change in the values: **a** dielectric permittivity $\varepsilon_{33}^{T}/\varepsilon_{o}$; **b** transverse piezoelectric modulus d_{31} of CPM, with a change in the porosity and volume fraction of the AE

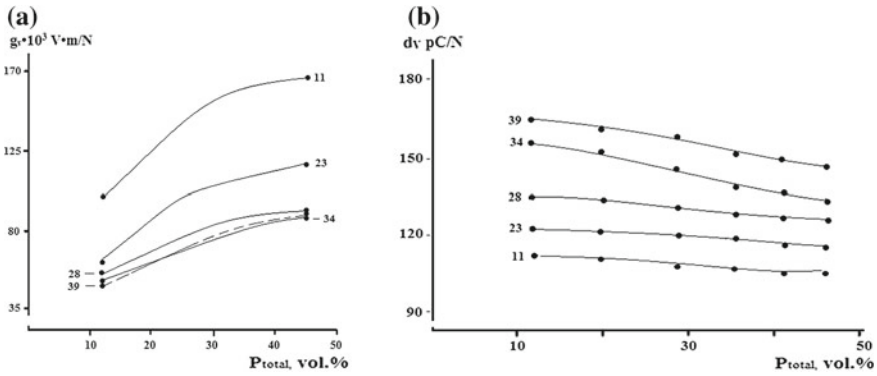

Fig. 8.3 Changes in the values of volumetric piezoparameters: **a** piezomodule (d_v); **b** the volume piezo sensitivity (g_v) of the CPM with a change in the porosity and volume fraction of the AE

change in the total porosity of the AE is shown along the abscissa axis, and the volume fraction ($\tilde{v}$) of the AE in the samples is indicated by the figures for the individual lines.

As follows from the results shown in Fig. 8.2, regardless of the volume fraction of AE in the samples, the increase in the porosity of the plates leads to a decrease in the dielectric permittivity, $\varepsilon_{33}^{T}/\varepsilon_{o}$ and the absolute value of the transverse piezoelectric modulus, d_{31}. At the same time, the increase in the volume fraction of plates in the system (with a fixed porosity) contributes to a decrease in the values of these ESPs. The values of the longitudinal piezoelectric modulus d_{33}, with increasing porosity of the plates, are reduced slightly (when a percentage of volume fraction of plates in the system are fixed). The formation of the values d_v is determined by two

factors as follows: the increase in the porosity of the plates should lead to increasing the values of this piezoelectric coefficient d_v, while the increase in the number of plates, due to their mutual reinforcement, should reduce the d_v value. In this connection, the magnitude of the d_v of the CPM under consideration, with a fixed volume fraction of the plates in the system, undergoes minor variations (Fig. 8.3). In connection with the indicated character of the change in d_v and taking into account decreasing the dielectric permittivity of the samples, as their porosity increases, the values of the volume piezoelectric susceptibility of the CPM type 2-0-2 are increase with increasing porosity of the plates and decrease with increasing their volume fraction in the system (Fig. 8.3).

The next parameter to be under discussion, is the reception factor (or squared figure of merit) $d_v g_v$, reaching its maximum values (up to 17.6×10^{-3} V m/N) for the CPM samples having a volume fraction of the AE in the range from 10 to 30 vol.%. The indicated values of the reception factor can be achieved for materials having different combinations of the values of the parameters g_v and d_v. For example, CPMs with the volume fraction of the AE from 0.10 to 0.15 are characterized by the minimum values of $\varepsilon_{33}^T/\varepsilon_o$ and d_v, but their values of g_v are maximum. Whereas samples with the volume fraction of the AE from 0.20 to 0.30 have higher values of $\varepsilon_{33}^T/\varepsilon_o$ and d_v, but their g_v values are minimal (for a fixed porosity of ceramic plates). This fact is of great practical importance, since it allows, in the design of transducers, to select a CPM in accordance with the required output signal type (for the specific type of the transducer).

Another way to increase the g_v and d_v values of the CPM is the chemical activation of the surface of *porous AE*s. For this, the AE, before assembling the CPM samples, is treated with solutions of substances whose molecules have two functional groups. One of these groups forms strong bonds to ions located on the surface of the ceramic plates, and the second group forms bonds to polymer molecules of the binder. This technique leads to increasing the energy of adhesion between ceramic plates and polymers several times. In this work, we used chlorosilanes as surface activators (coupling agents). This made it possible to increase the d_{33} and d_v values of the samples by 12–22% (but the values of $\varepsilon_{33}^T/\varepsilon_o$ and d_{31} of the CPM are, practically, unchanged). The effect of this method on the d_{33} and d_v values increases with increasing porosity of the ceramic plates. The indicated changes in the values of d_{33}, $\varepsilon_{33}^T/\varepsilon_o$, and d_{31} of the samples contribute to the growth of the values of not only the bulk piezo module, but also the volume piezo sensitivity and the reception factor.

8.4 Conclusion

In the result, of the research, a technological complex was created, including:

(i) low-temperature technologies for the production of ultra-disperse powders of the ferroelectric phase of the PZT system [10];

(ii) technologies for the production of the AE of the 2–0–2 CPM with porosity from 10 to 65 vol. %;
(iii) PCM with the 2–0–2 connectivity type, with a varying volume fraction of rods. The creation of such a technological complex leads to an increase in the reproducibility of the EPR of the PCM of the studied type.

Our research also made it possible to reveal the effect of the magnitude of the porosity of the AE and their volume fraction, on the values EPP of the CPM, and to establish the role of the surface activation of the plates AE when shaping the values of these parameters. The use of low-temperature technologies (synthesis of ultra-disperse powders of lead-containing ferroelectric phases, AE sintering) facilitated, in comparison to the known technologies, an increase in the ecological security of the CPM technologies of this type.

Acknowledgements The authors would like to thank Prof. Dr. A.E. Panich and Prof. Dr. V.Y. Topolov (Southern Federal University, Rostov-on-Don, Russia) for their continuing interest in the research problems. Special thanks are extended to Prof. Dr. V.Y. Topolov for his reading and improvement of the manuscript. In this paper, the results on the research project No. 11.5814.2017/8.9 in the internal grant Southern Federal University in the field of scientific activity are present. This research has been performed using the equipment of the Centre of Collective Use 'High Technologies' at the Southern Federal University.

References

1. R. Newnham, D. Skinner, L. Cross, Mater. Res. Bull. **13**(5), 525 (1978)
2. S. Huang, M. Sun, M. Zhou et al., Mater. Manuf. Processes **30**(2), 179 (2015)
3. K.A. Kliker, W.A. Schulze, J.V. Biggers, J. Am. Ceram. Soc. **65**(12), 208 (1982)
4. E.K. Akdogan, IEEE Trans. Ultrason., Ferroelec., a. Freq. Contr. **52**(5), 746 (2005)
5. L.P. Khoroshun, B.P. Maslov, P.V. Leschenko, *Prediction of Effective Properties of Piezoactive Composite Materials.* Kiev, Naukova Dumka, 208 p. (1989) (in Russian)
6. V.Y. Topolov, C.R. Bowen. *Electromechanical Properties in Composites Based on Ferroelectrics* (London, Springer, 2009), 202 p
7. J.E. Smay, J. Appl. Phys. **92**(10), 6119 (2002)
8. C.J. Dias, D.K. Das-Gupta, Ferroelectrics **157**, 405 (1994)
9. V.Y. Topolov, P. Bisegna, C.R. Bowen, *Piezoactive Composites. Orientation Effects and Anisotropy Factors»* (Berlin, Springer, 2014), 169 p
10. A.A. Nesterov, K.S. Masurenkov, E.V. Karyukov, Russ. J. Appl. Chem. **82**(3), 374 (2009)

Chapter 9
Morphology and Photoluminescence of Zinc Oxide Nanorods Obtained by Carbothermal Synthesis at Different Temperatures

A. L. Nikolaev, E. M. Kaidashev and A. S. Kamencev

Abstract The effect of the temperature of carbothermal synthesis on the morphology and oxygen vacancies concentration in ZnO nanorods (NRs) grown at temperatures from 900 to 1100 °C with and without the thin film ZnO sublayer on Si substrates was investigated. An estimation of the number of adsorption centers in the obtained samples was carried out by analyzing the luminescence spectra. The NRs with the maximum concentration of oxygen vacancies were synthesized at 1100 °C using the ZnO sublayer. Such NRs are more suitable for use in gas sensors. We made the CO sensor as follows: ZnO NRs were removed by ultrasound and placed on an 2D-array of Au square micro-islands. The sensor based on NRs coated with Au nanoparticles (NPs) showed a maximum sensitivity of 535% to 100 ppm CO at room temperature. The response time was 40 s and the recovery time was 45 s. Thus, coating zinc oxide NRs with Au NPs substantially effective reduce the maximum sensitivity temperature of the sensor. NRs with a minimum concentration of oxygen vacancies were synthesized at 925 °C without ZnO sublayer. Such NRs are more suitable for the use in UV photodetectors and photodiodes.

9.1 Introduction

Zinc oxide NRs are often used as active elements of gas sensors, photodetectors, ultraviolet diodes, nanolasers, solar cells and other nanoelectronic devices [1, 2]. Unlike photosensitivity, the gas sensitivity of ZnO NRs increases with the concentration of oxygen vacancies on the nanorod surface [3]. Thus, obtaining NRs

A. L. Nikolaev (✉) · E. M. Kaidashev · A. S. Kamencev
Southern Federal University, Rostov-on-Don 344090, Russia
e-mail: andreynicolaev@eurosites.ru

A. L. Nikolaev
Don State Technical University, Rostov-on-Don 344000, Russia

I. A. Parinov et al. (eds.), *Advanced Materials*, Springer Proceedings in Physics 224, https://doi.org/10.1007/978-3-030-19894-7_9

ZnO with the maximum and minimum concentrations of oxygen vacancies is an important task. The number of oxygen vacancies can be controlled by changing the parameters of carbothermal synthesis and by using a thin-film sublayer.

Normally the gas sensors based on zinc oxide have a number of disadvantages. First of them is a high operating temperature. Maximum sensitivity is achieved at temperatures from 250 to 350 °C. The second major problem is the low sensitivity of sensors based on zinc oxide films. The first problem can be solved by decorating NRs with Au NPs. The second problem can be solved by using zinc oxide NRs as an active element of such devices.

The result of the study will be the technique of obtaining an energy efficient structure with high gas sensitivity characteristics. Such structures will find their application both in everyday life (household kitchen sensors of carbon monoxide), systems of fire safety, in mechanical engineering (control of harmful exhausts in the exhaust manifold of internal combustion engines), metallurgy and oil refining industry, where the requirements of "environmental friendliness" are increasing every year and in many other areas of human activity.

9.1.1 Research Purpose

The main aim of this work is to study the luminescence spectra and morphology of zinc oxide NRs obtained by carbothermal synthesis at different temperatures (900–1100 °C) with and without a thin-film ZnO sublayer on Si (001). We also develop a highly efficient gas sensor based on ZnO NRs with the maximum concentration of oxygen vacancies to verify the obtained results.

9.1.2 Research Scope

In this study, we consider the following circumscriptions of the problem:

- ZnO NRs growth by carbothermal synthesis
- PL spectra study
- Scanning electron microscopy study of prepared at different temperatures samples
- Influence of ZnO thin film sublayer on O vacancies density and NRs morphology
- Development of gas sensor based on ZnO NRs
- Influence of Au NPs decoration to gas sensing properties of prepared NRs.

9.2 Research Method

Thin film ZnO sublayer was deposited by PLD on Si (001) substrate. The PLD technique is schematically shown in Fig. 9.1 [4]. Also, gold NPs were deposited by PLD on ZnO or Si surface. These particles played a role of catalyst for ZnO NRs growth (Fig. 9.2).

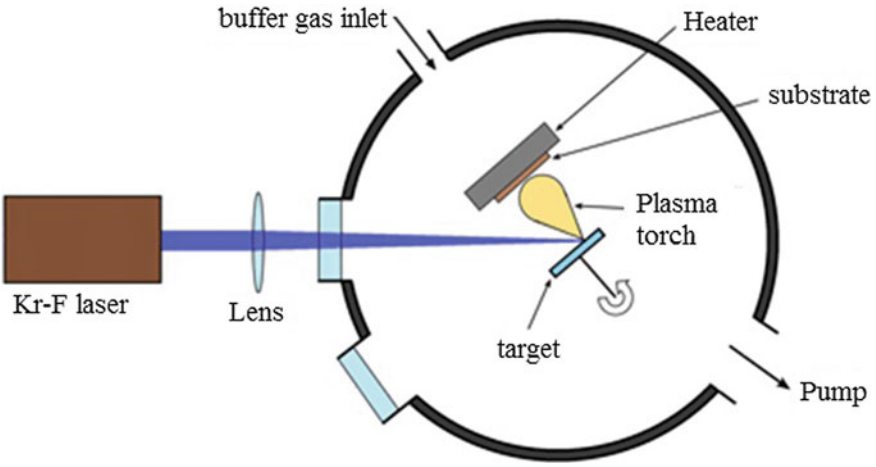

Fig. 9.1 PLD chamber

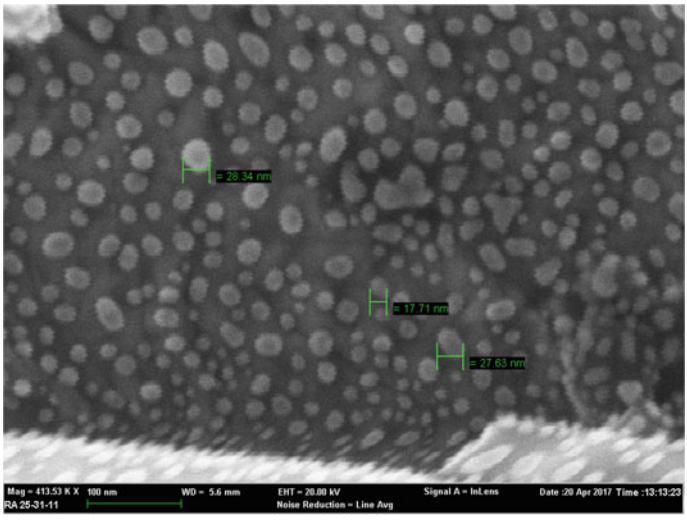

Fig. 9.2 SEM image of Au NPs on ZnO thin film sublayer

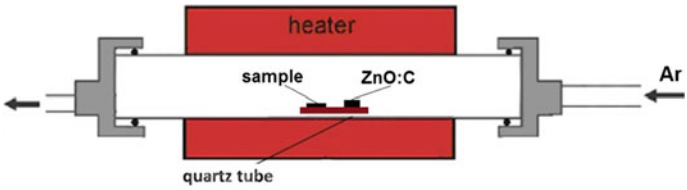

Fig. 9.3 Chamber of carbothermal synthesis

We obtained zinc oxide NRs by carbothermal synthesis (Fig. 9.3) on Si substrates at various temperatures [5]. Before the synthesis, the chamber was evacuated several times and filled with argon. During the synthesis, argon fulfilled transport function. Ar flow was 20 sccm, the pressure was normal. The precursor (1:1 by weight of ZnO:C) was 1 cm from the substrate in the direction of argon flow. The synthesis temperature stabilized with an accuracy of 0.1 °C. The heater in each case had the same heating rate of 0.5 °C per second or 30 °C per minute. ZnO NRs array was grown during 40 min.

The morphology of the zinc oxide NRs grown at different temperatures was investigated by scanning electron microscopy. PL spectra were obtained by a solar TII monochromator. PL measurements were carried out under excitation by 325 nm He–Cd laser beam at room temperature.

We made the CO sensor as follows: ZnO NRs were removed by ultrasound and placed on an 2D array of Au square micro-islands, which were previously deposited on the α-Al_2O_3 substrate by PLD.

To achieve better electrical contact, we annealed NRs upon their deposition on Au islands in high vacuum $\sim 10^{-5}$ mbar at 500 °C. The resulting NRs and micro-platforms structure is shown in Fig. 9.4.

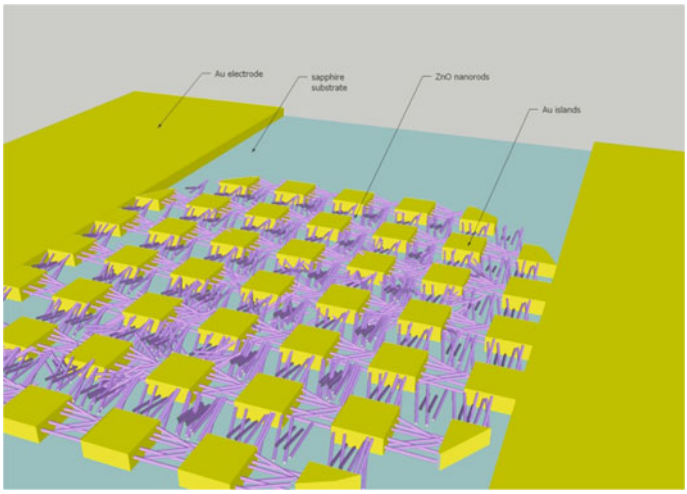

Fig. 9.4 CO sensor based on ZnO NRs

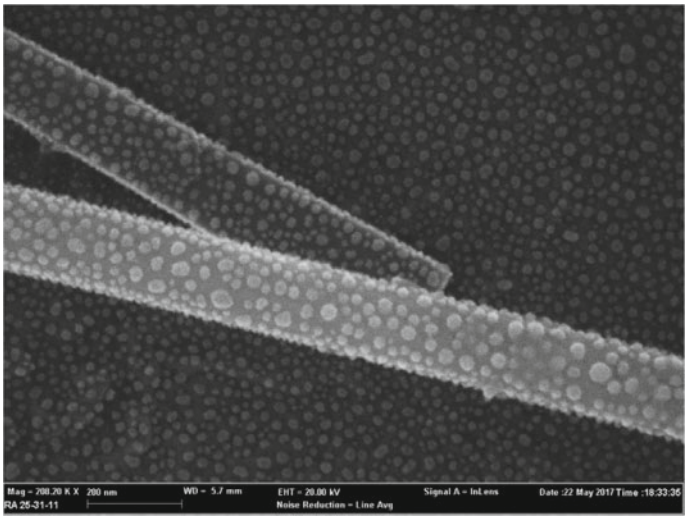

Fig. 9.5 SEM image of Au NPs on ZnO nanorod surface

Au NPs were obtained by PLD technique in an argon atmosphere at room temperature (Fig. 9.5) [6]. Ar pressure was 70 Pa, power density of the laser radiation was 2 J/cm^2, target-substrate distance was 3 cm.

Gas sensitivity was measured at temperatures from room to 250 °C. The concentration of carbon monoxide was 100 ppm, gas flow was 0.3 l/min.

9.3 Results and Discussion

9.3.1 Morphology of ZnO NRs Obtained by Carbothermal Synthesis at Different Temperatures

The shape and size of NRs directly depend on the crystal perfection of zinc oxide, caused by the synthesis parameters. The horizontal cut of ZnO nanorod with a good crystal structure is a right hexagon. By changing the temperature of carbothermal synthesis, one can change the growth dynamics of NRs, the stoichiometric composition of zinc oxide and, consequently, the size and shape of the NRs.

On a sample grown without a sublayer, we see a large number of disoriented objects resembling planes (Fig. 9.6b). As the synthesis temperature increases to 1000 °C, the length of the rods increases gradually on samples with a sublayer. The diameter of the NRs decreases (Fig. 9.6a, c, e). While on samples without a

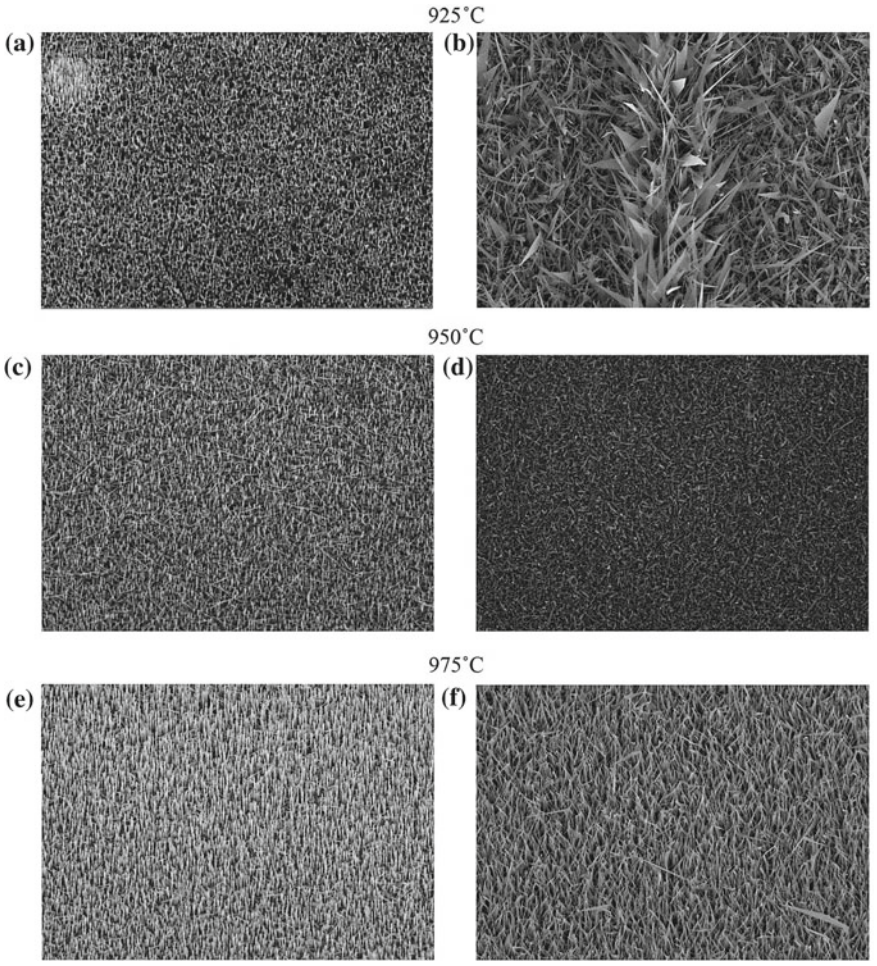

Fig. 9.6 SEM images of ZnO NRs obtained with sublayer at 925, 950 and 975 °C (**a**, **c** and **e**, respectively); SEM images of ZnO NRs obtained without sublayer at 925, 950 and 975°C (**b**, **d** and **f**, respectively)

sublayer of zinc oxide, we observe a decrease in the number of planes and an increase in the number of disoriented NRs up to 1000 °C (Figs. 9.6b, d, f and 9.7b).

At higher temperatures, the growth of the rods practically stops (Fig. 9.7d, f). However in samples with a sublayer, the growth of the rods continues and the tendency of diameter decrease and increase in the length becomes more obvious (Fig. 9.7c, e).

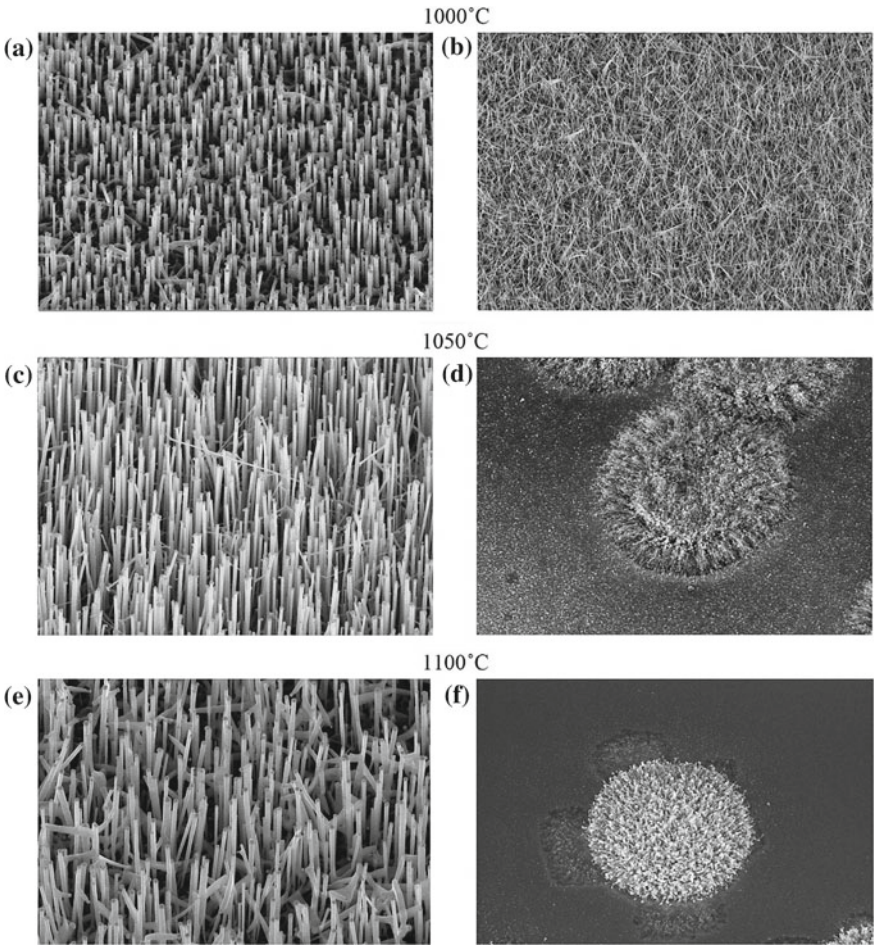

Fig. 9.7 SEM images of ZnO NRs obtained with sublayer at 1000, 1050 and 1100 °C (**a**, **c** and **e**, respectively); SEM images of ZnO NRs obtained without sublayer at 1000, 1050 and 1100 °C (**b**, **d** and **f**, respectively)

9.3.2 PL Spectra of Prepared NRs

PL measurements were carried out under excitation by 325 nm He–Cd laser beam at room temperature [7]. The PL spectrum of pure zinc oxide with an ideal crystal structure has one narrow peak at 375 nm wavelength.

However in the spectra of real samples, so-called "green luminescence" often appears. The nature of green luminescence has remained controversial for decades. In early studies, it was explained with copper impurities [8] , but were later presented strong evidence in favor of point defects such as isolated oxygen vacancies

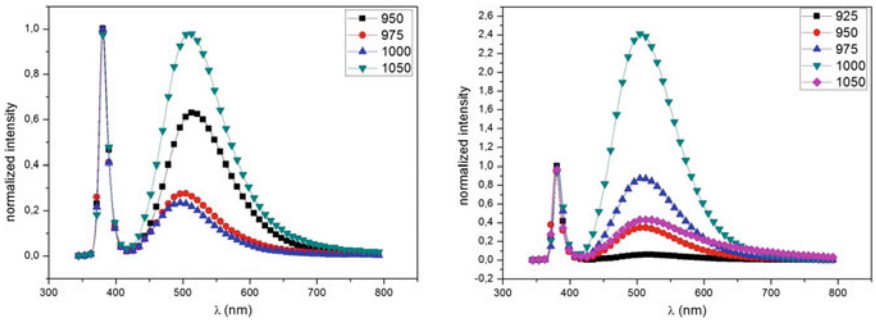

Fig. 9.8 PL spectra of NRs obtained by carbothermal synthesis at various temperatures with (**a**) and without (**b**) ZnO rh in film sublayer

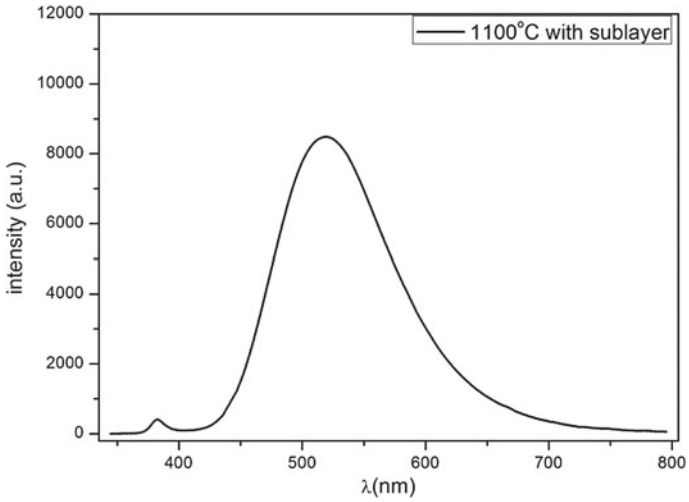

Fig. 9.9 PL spectrum of NRs obtained by carbothermal synthesis at 1100 °C with ZnO thin film sublayer

(∼510 nm) or complexes of oxygen vacancies (∼525 nm), which are major contributors to gas-sensing properties of ZnO NRs [1–3].

It was shown that the growth of green luminescence intensity occurs in direct ratio to the synthesis temperature growth up to 1050 °C on samples without a thin-film sublayer (Fig. 9.8). At temperatures higher than 1050 °C, horizontal growth begins to predominate over the vertical one. At the same time, the NRs grew even at 1100 °C on samples with a thin-film sublayer.

The NRs with the maximum concentration of oxygen vacancies were synthesized at 1100 °C using the ZnO sublayer (Fig. 9.9). Such NRs are more suitable for use in gas sensors than rods obtained under other conditions. NRs with a minimum

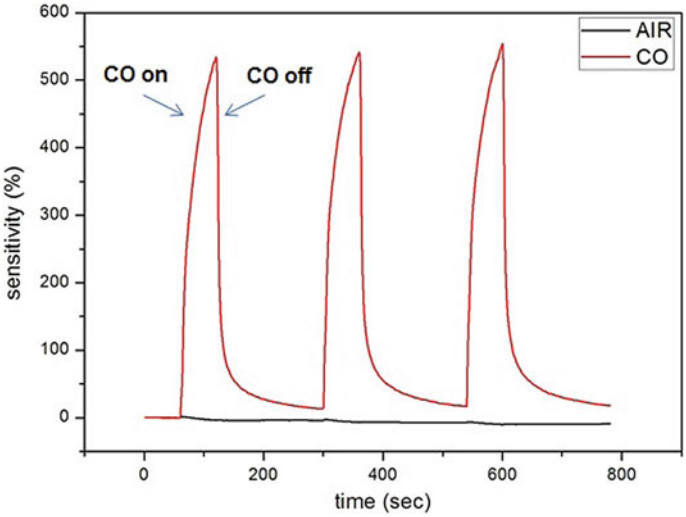

Fig. 9.10 Gas sensitivity of as prepared sensors to 100 ppm CO at room temperature

concentration of oxygen vacancies were synthesized at 925 °C without ZnO sublayer. Such NRs are more suitable for the use in UV photodetectors and photodiodes [9].

9.3.3 Gas Sensing Properties of ZnO NRs

Previous results made it possible for our team to construct the gas sensor using the NRs, obtained by the technology described. NRs, synthesized at 1100 °C by carbothermal technique, were selected to create the sensor.

The resistive response of the 2D network of ZnO sensor (Fig. 9.4) at room temperature exposed to a CO gas flow 0.3 l/min (100 ppm) is shown in Fig. 9.1d. The sensors resistance changed for more than $\sim$500% during $\sim$40 s and shown a saturation, when the CO flow was blocked. It takes $\sim$45 s before resistance drops to initial value (Fig. 9.10).

The sensitivity was calculated as

$$\text{Sensitivity} = ((R_a - R_b)/R_a) \times 100\% \tag{9.1}$$

where R_a and R_b are the sensor resistance in the presence of CO and in clean air, respectively.

The deposition of Au NPs gradually enhances sensitivity of ZnO NRs toward CO. The effect of Au particles is the most pronounced at room temperature (Fig. 9.11a), and becomes negligible at 100 °C. Hydroxyl groups on the ZnO surface react with CO adsorbed on ZnO/Au boundary, which increase the sensor

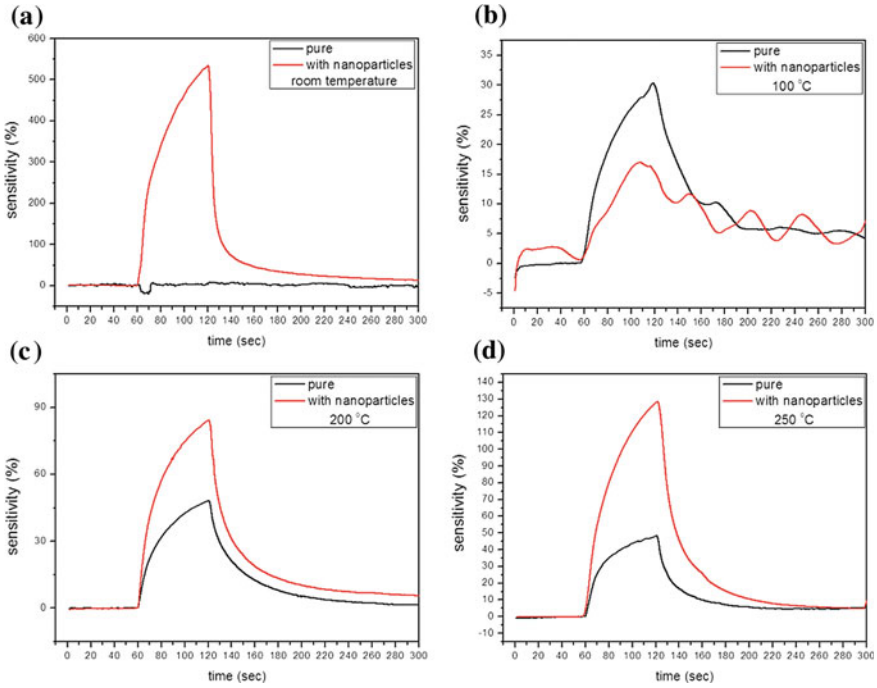

Fig. 9.11 Response of the sensors on 100 ppm CO at room temperature (**a**), 100 °C (**b**), 200 °C (**c**) and 250 °C (**d**)

response. At elevated temperature, the hydroxyl groups are readily desorbed from the ZnO surface [3]. However, at temperatures close to 100°C O_2- species localized at oxygen vacancies on ZnO [10] also become active for catalytic CO oxidation (Fig. 9.11b).

While the most part of the ZnO surface is blocked by Au, the less number of O_2- are chemisorbed on sensor. It reduces related mechanism of CO oxidation at elevated temperature.

At higher temperatures, oxygen species O− and O_2- [10] are responsible for the gas sensitivity. Under these conditions, Au successfully catalyzes CO oxidation process. This can be seen by a marked increase in sensor response with gold particles relative to the sensor with clean NRs (Fig. 9.11 c, d).

9.4 Conclusion

The results obtained made it possible to conclude that an increase in the synthesis temperature entails an increasing the number of oxygen vacancies in zinc oxide NRs, and a thin-film sublayer helps to obtain more crystalline perfect structures at

high synthesis temperatures and to increase the maximum possible synthesis temperature of ZnO NRs.

The sensor based on NRs coated with Au NPs showed a maximum sensitivity of 535% at room temperature. The response time was 40 s and the recovery time was 45 s. Thus, coating zinc oxide NRs with Au NPs substantially effective reduce the maximum sensitivity temperature of the sensor.

Acknowledgements This research work is supported by Ministry of Science and Higher Education of the Russian Federation project No.16.5405.2017/8.9, No.9.1481.2017/4.6 and RFBR according to the research project No. 16-58-52013 MNT_a.

References

1. T.J. Hsueh, Y.W. Chen, S.J. Chang, S.F. Wang, C.L. Hsu, Y.R. Lin, T.S. Lin, I.C. Chen, Electrochem. Soc. **154**, H153 (2007)
2. N.D. Khoang, H.S. Hong, D.D. Trung, N.D. Hoa, D.D. Thinh, N.V. Hieu, Sens. Actuators, B **181**, 529 (2013)
3. Matthew S. Ide, Robert J. Davis, Acc. Chem. Res. **47**(3), 825 (2014)
4. E.M. Kaidashev, M. Lorenz, H. Wenckstern, A. von, Rahm, H.C. Semmelback, K.H. Han, G. Bendorf, C. Bundesmann, H. Hochmuth, M. Grundmann, Appl. Phys. Lett. **82**, 3901 (2003)
5. N.V. Lyanguzov, D.A. Zhilin, E.M. Kaidashev, in *Advanced Materials—Physics, Mechanics and Applications*, ed. by S.-H. Chang, I.A. Parinov, V.Y. Topolov. Springer Proceedings in Physics, vol. 152 (Springer Cham, Heidelberg, New York, Dordrecht, London, 2014), p. 37
6. A.L. Nikolaev, G.Y. Karapetyan, D.G. Nesvetaev, N.V. Lyanguzov, V.G. Dneprovski, E.M. Kaidashev, in *Advanced Materials—Physics, Mechanics and Applications*, ed. by S.-H. Chang, I.A. Parinov, V.Y. Topolov. Springer Proceedings in Physics, vol. 152 (Springer Cham. Heidelberg, New York, Dordrecht, London, 2014), p. 27
7. A.S. Bugaev, V.B. Kireev, E.P. Sheshin, A.J. Kolodyazhnyj, Cathodoluminescent light sources: status and prospects. Usp. Fiz. Nauk. **185**(8), 853–883 (2015)
8. Shoou-Jinn Chang, Ting-Jen Hsueh, Cherng Chen, Bohr-Ran Huang, Nanotechnology **19** (17), 175502 (2008)
9. D.A. Zhilin, N.V. Lyanguzov, V.I. Pushkariov, L.A. Nikolaev, V.E. Kaydashev, E.M. Kaidashev, *Advanced Materials—Studies and Applications*, ed. by, I.A. Parinov, S.-H. Chang, S. Theerakulpisut (Nova Science Publishers, New York, 2015), p. 57
10. Sanggahaleh Ali, Mohammad Halali, Appl. Surf. Sci. 2555, 8202 (2009)

Chapter 10
Polarization of Thin $LiNbO_3$ Films Formed by Pulsed Laser Deposition

Zakhar Vakulov, Andrew Geldash, Vladimir Nikolayevich Dzhuplin, Viktor Sergeevich Klimin and Oleg Alekseevich Ageev

Abstract This work shows the results of influence of deposition time on $LiNbO_3$ thin film properties fabricated by pulsed laser deposition (PLD). It has been show that by increasing deposition time from 90 to 360 min, the films thickness increased from 66.2 to 198 nm. Wherein surface roughness and grain size of the films changed from 3.25 to 16.95 nm and from 78 to 234 nm, respectively. It has established that the films, fabricated under deposition time of 180 and 270 min, are ferroelectrics since the dependence of the polarization on the field strength for these films has hysteresis. Moreover, with the increasing in mobility of charge carriers from 75.553 to 131.033 $cm^2/(V\ s)$, the value of residual polarization decreased from 322 to 243 $\mu C/cm^2$. Increasing charge carrier concentration from 7.325×10^{17} cm^{-3} to 3.24×10^{19} cm^{-3} results in rising the dielectric loss tangent from 0.35 to 70. With further increasing of the concentration up to 7.918×10^{19} cm^{-3} results in decreasing the dielectric loss tangent to 5.6. Obtained results could be used in designing and manufacturing of piezoelectric transducers, acousto-optics elements, and SAW devices.

10.1 Introduction

Due to unique combination of electro-optic, acousto-optic, ferroelectric and piezoelectric properties lithium niobate ($LiNbO_3$) are widely used under development of acousto-optics and piezoelectric devices [1–3]. Some research groups use thin cuts of $LiNbO_3$ single crystal with definite crystal orientation under developing integrated optics devices [4, 5]. Despite the advantages of this method are obvious (using of single-crystal slices), such disadvantages as high surface roughness of slices, difficulties under doping operation, and expensive process of obtaining cuts

Z. Vakulov (✉) · A. Geldash · V. N. Dzhuplin · V. S. Klimin · O. A. Ageev
Research and Education Centre «Nanotechnology», Southern Federal University, Taganrog, Russia
e-mail: zvakulov@sfedu.ru

I. A. Parinov et al. (eds.), *Advanced Materials*, Springer Proceedings in Physics 224, https://doi.org/10.1007/978-3-030-19894-7_10

from $LiNbO_3$ single crystal make it difficult to integrate this method with existing technologies of micro- and nanoelectronics. Using of $LiNbO_3$ films will beneficial to overcome these issues [6].

Planar structures have small scale, the possibility of rapid electronic control and low power consumptions compare to hybrid devices. In addition, using the integral technology of microelectronics will avoid implementation in their construction of mechanical moving parts, which will significantly improve reliability and reduce costs. Nevertheless, at the current stage of technological development it is challenging to fabricate devices based on ferroelectric films due to vide variety of design approaches, used materials, and fabrication methods. In addition, using the multi-component oxides with high crystallization temperature under fabrication of the devices by integral technology leads to necessity of developing dozens accompanying operations. Therefore, despite significant progress in this area, the fabrication issue of ferroelectric thin-film structures with target properties, technological compatibility, and reproducibility cannot considered completely solved.

Currently, $LiNbO_3$ films can be obtained by molecular beam epitaxy [7], MOCVD [8], RF-magnetron sputtering [9], sol-gel method [10] and pulsed laser deposition (PLD) [11]. Using of PLD technique is allow one to fabricate $LiNbO_3$ films with target stoichiometric composition, and control structural-phase properties in a wide range [12–14].

Despite the modern stage of the development of piezoelectrics and acoustooptics is characterized by the creation of a large number of functional devices, the practical using of $LiNbO_3$ films in micro- and nanoelectronics is substantially limited due to the lack of compatible technology for obtaining thin ferroelectric films. Thus, the purpose of this work is studying the effect of deposition time on the properties of thin $LiNbO_3$ films fabricated by PLD.

10.2 Materials and Methods

For fabrication of thin $LiNbO_3$ films, nanotechnological cluster complex NANOFAB NTK-9 (NT–MDT, Russia), comprising PLD module Pioneer 180 (Neocera Co., USA) was used. The ablation of $LiNbO_3$ target (Kurt J. Lesker Co., USA) was carried out by KrF excimer laser (λ = 248 nm) with energy density at the target surface of 2.0 J/cm^2 and a repetition rate of 10 Hz. Target-substrate distance and substrate temperature were 100 mm and 600 °C, respectively. Deposition duration was changed from 90 to 360 min. $LiNbO_3$ thin films were deposited on silicon substrates (1×1 cm^2). All substrates were subjected to preliminary purification in inorganic solvents to remove surface contamination.

The morphology of obtained films was studied on Ntegra probe nanolab in semi-contact mode (NT–MDT, Russia) and using a scanning electron microscope Nova NanoLab 600 (FEI Co., Netherlands). Measurements of the polarization characteristics were carried out using the Sawyer-Tower method.

10.3 Results and Discussion

Figure 10.1 shows the dependence of $LiNbO_3$ films thickness on deposition time.

It has been established that increasing deposition duration from 90 to 360 min, the thickness of $LiNbO_3$ films increases from 66.2 to 198 nm. Figure 10.2 shows AFM images and cross-sectional profile of obtained $LiNbO_3$. Figure 10.3 shows the dependences of surface roughness and grain size of $LiNbO_3$ films on deposition time. It was found that increasing deposition time from 90 to 270 min the films acquire a rougher surface. Average surface roughness increased from 3.25 to 16.95 nm. Increasing in the roughness may be associated with growing of mechanical stresses in the films.

Figure 10.4 shows SEM images of $LiNbO_3$ fabricated under different deposition time.

Figure 10.5 shows the dependences of polarization on electric field strength. For deposition time from 180 to 270 min, the dependencies of polarization on electric field strength have hysteresis. This fact characterized these films as ferroelectrics. The obtained dependences characterize the samples fabricated under deposition time of 180 and 270 min, as films with spontaneous polarization, whereas a sample fabricated under deposition time of 90 min exhibits relaxation polarization.

It is established that increasing mobility of charge carrier from 75.553 to 131.033 (cm^2/V s), the value of residual polarization decreases from 322 to 243 μC/cm^2. Increasing charge carrier concentration from 7.325×10^{17} cm^{-3} to 3.24×10^{19} cm^{-3} results in increasing of dielectric loss tangent from 0.35 to 70. Further increasing the concentration up to 7.918×10^{19} cm^{-3} results to decreasing the dielectric loss tangent down to 5.6.

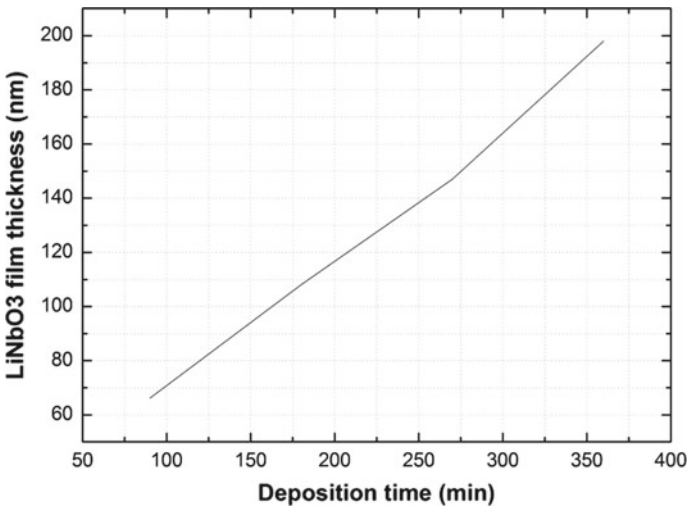

Fig. 10.1 Dependence of $LiNbO_3$ films thickness on deposition time

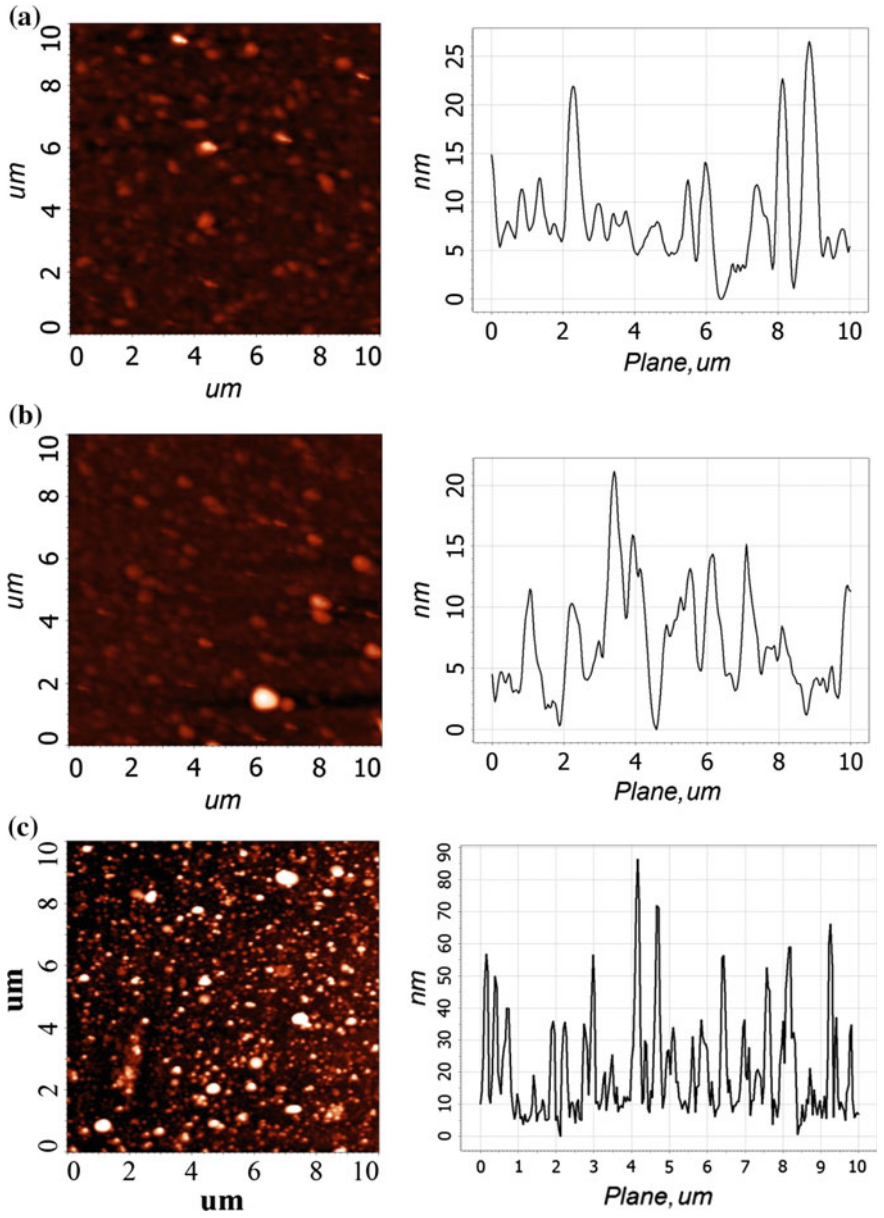

Fig. 10.2 AFM images and cross-sectional profiles of $LiNbO_3$ films fabricated under different deposition time: 90 min (**a**), 180 min (**b**), and 270 min (**c**)

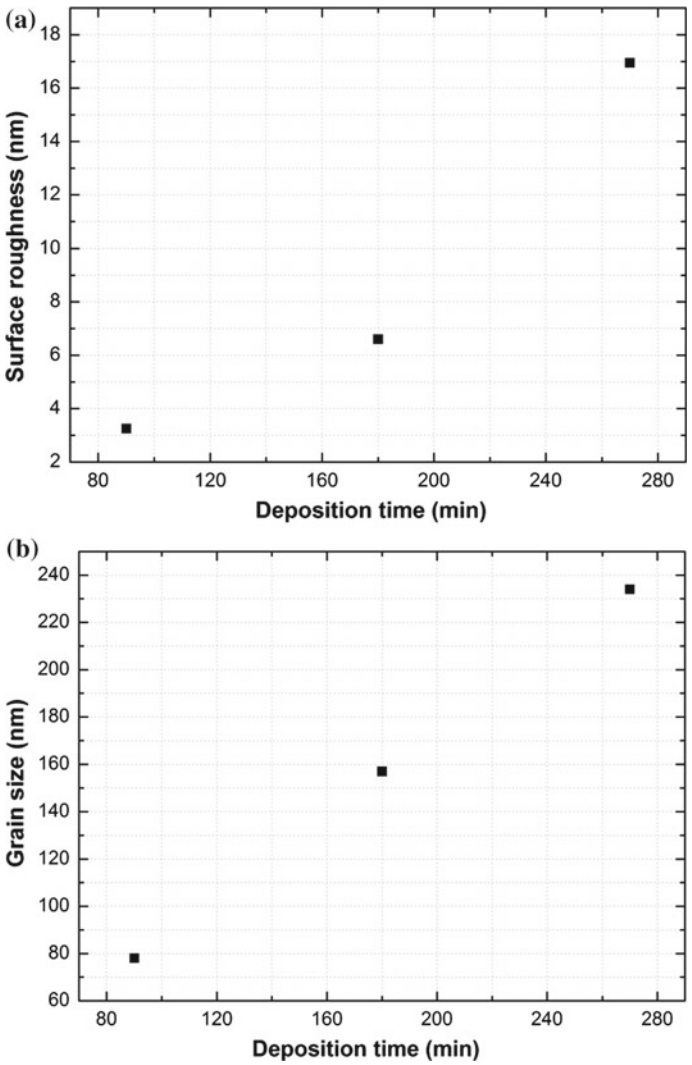

Fig. 10.3 Dependences of $LiNbO_3$ films surface roughness (**a**) and grain size (**b**) on deposition time

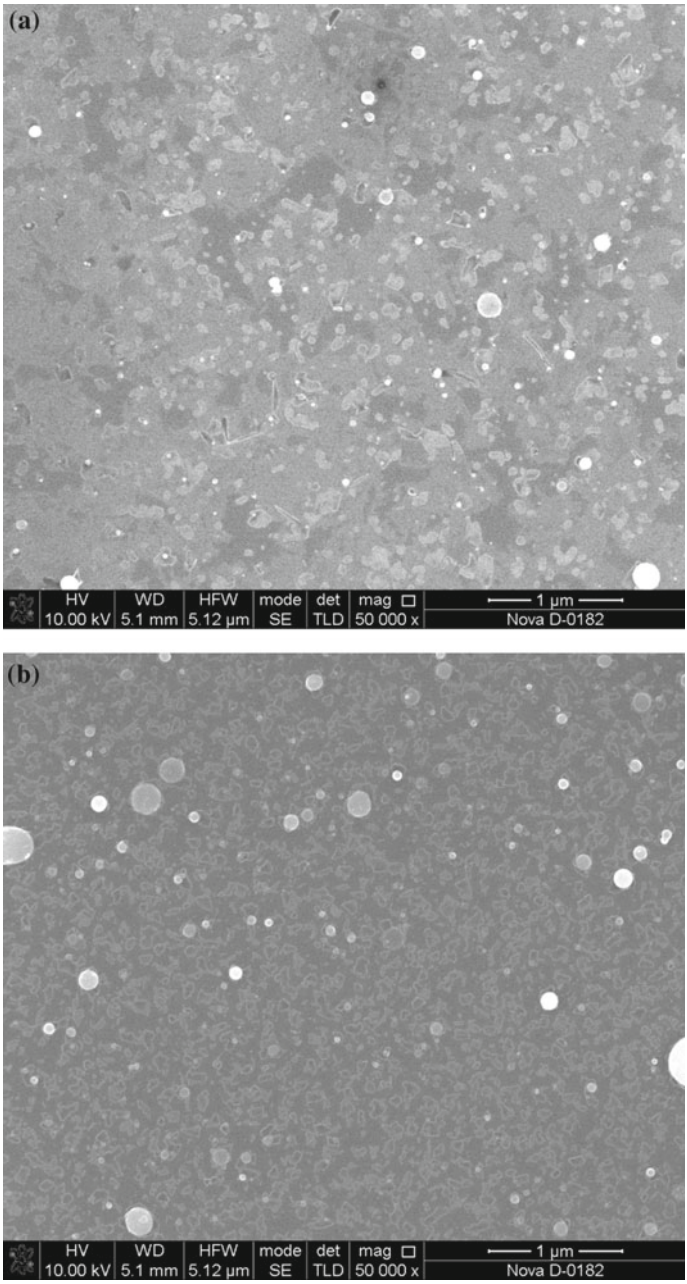

Fig. 10.4 SEM images of $LiNbO_3$ films fabricated under different deposition time: 180 min (**a**) and 360 nm (**b**)

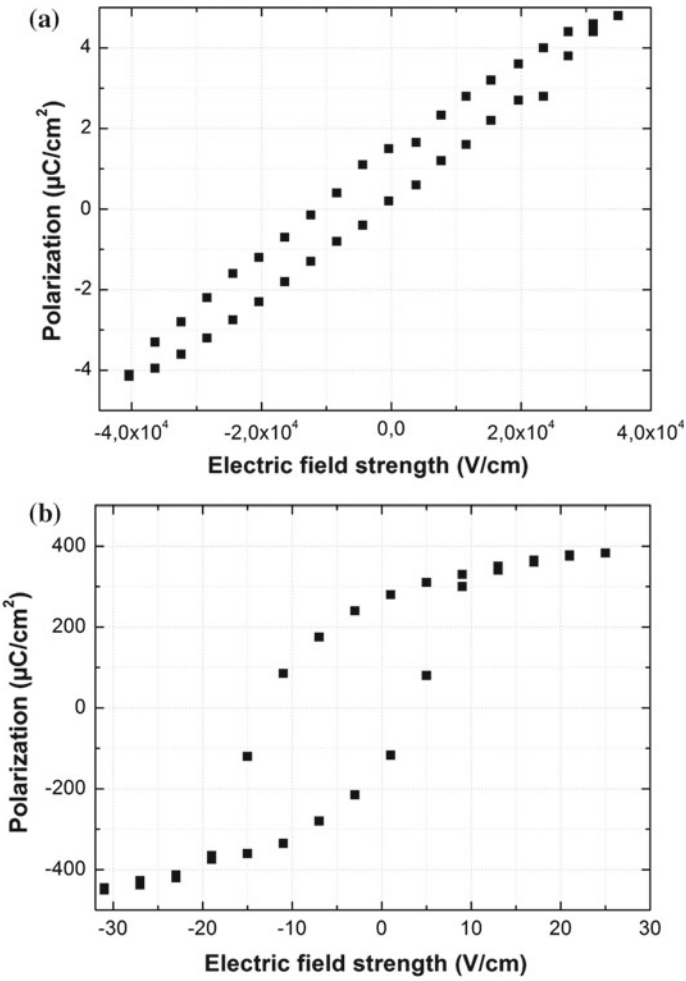

Fig. 10.5 Dependencies of polarization on electric field strength for $LiNbO_3$ films, fabricated under different deposition time: 90 min (**a**), 180 min (**b**)

10.4 Conclusion

It has been shown that increasing the deposition time from 90 to 270 min results in increasing in surface roughness and grain size from 3.25 to 16.95 nm and from 78 to 234 nm, respectively. It is established that the films fabricated under deposition time of 180 and 270 min are ferroelectrics since the dependence of the polarization on the field strength for these films has hysteresis. The dependence of sample fabricated under deposition time of 90 min has the shape of an ellipse. Thus, for films fabricated with deposition time 180 − 270 min are characterized by

spontaneous polarization whereas for the sample, fabricated under deposition time of 90 nm, a relaxation polarization is observed. It is established that increasing mobility of charge carrier from 75.553 to 131.033 $cm^2/(V\ s)$, the value of residual polarization decreases from 322 to 243 $\mu C/cm^2$. Increasing charge carrier concentration from $7.325 \times 10^{17}\ cm^{-3}$ to $3.24 \times 10^{19}\ cm^{-3}$ the value of the dielectric loss tangent increases from 0.35 to 70. With further increasing of the concentration up to $7.918 \times 10^{19}\ cm^{-3}$ results in decreasing of dielectric loss tangent to 5.6.

Obtained results can be used as technological base for the development and manufacture of integrated acousto-optic and piezoelectric devices, as well as sensitive elements of sensors using various effects of surface acoustic waves.

Acknowledgements This work was financially supported by the Russian Foundation for Basic Research (project No. 18-29-11019 mk) and Southern Federal University (project No. VnGr-07/2017-02). The work was done on the equipment of the Research and Education Centre «Nanotechnology» and Collective Use Centre «Nanotechnology» , Southern Federal University.

References

1. M. Elhosni, S. Petit-Watelot, M. Hehn, S. Hage-Ali, K.A. Aissa, D. Lacour, A. Talbi, O. Elmazria, Procedia Eng. **120**, 870 (2015)
2. M.A.A. Ganji, R. Asadi, Sens. Actuator A-Phys. **280**, 521 (2018)
3. M. Hossein-Zadeh, A.F.J. Levi, Solid State Electron. **49**, 1428 (2005)
4. P. Mackwitz, M. Rüsing, G. Bert, A. Widhalm, K. Müller, A. Zrenner, Appl. Phys. Lett. **108**, 152902 (2016)
5. L. Cai, R. Kong, Y. Wang, H. Hu, Opt. Express **23**, 29211 (2015)
6. W.C. Shih, X.Y. Sun, Physica B Condens. Matter. **405**, 1619 (2010)
7. C. Dubs, J.P. Ruske, J. Kräußlich, A. Tünnermann, Opt. Mater. **31**, 1650 (2009)
8. A. Bartasyte, V. Plausinaitiene, A. Abrutis, S. Stanionyte, S. Margueron, V. Kubilius, P. Boulet, S. Huband, P.A. Thomas, Mater. Chem. Phys. **149–150**, 622 (2015)
9. K.B.R. Varma, K.S. Harshavardhan, K.J. Rao, C.N.R. Rao, Mater. Res. Bull. **20**, 315 (1985)
10. S. Satapathy, C. Mukherjee, T. Shaktawat, P.K. Gupta, V.G. Sathe, Thin Solid Films **520**, 6510 (2012)
11. Z.E. Vakulov, E.G. Zamburg, D.A. Golosov, S.M. Zavadskiy, A.V. Miakonkikh, I.E. Clemente, K.V. Rudenko, A.P. Dostanko, O.A. Ageev, Bull. Russ. Acad. Sci. Phys. **81**, 1476 (2017)
12. S. Kilburger, R. Chety, E. Millon, Ph Di Bin, C. Di Bin, A. Boulle, R. Guinebretière, Appl. Surf. Sci. **253**, 8263 (2007)
13. S. Kilburger, E. Millon, P. Di Bin, A. Boulle, R. Guinebretière, C. Di Bin, Thin Solid Films **518**, 4654 (2010)
14. X. Wang, Y. Liang, S. Tian, W. Man, J. Jia, J. Cryst. Growth **375**, 73 (2013)

Chapter 11
The Resistance of Organic Coatings to Acid Media

S. P. Shpanko, E. N. Sidorenko, L. E. Kuznetsova and E. A. Sosin

Abstract The chapter presents the results of research of organic films, obtained by applying a self-organization method from an inhibited solution of sulphuric acid. The inhibitor used was an organic compound of imidazole class modified with thiocyanate anions. Acid post processing of the inhibited specimens was performed in sulphuric and hydrochloric acid solutions. It was found that organic coatings are more stable in the hydrochloric acid medium at a lower concentration of thiocyanate anions. A suggestion was made about the formation of a uniform film of complexon on the steel surface at a sufficient concentration of potassium thiocyanate that interferes the adsorption of the organic inhibitor molecule.

11.1 Introduction

Another important feature of inhibitors, beside the one that they protect metal products in aggressive media, is stability of phase films after the products are removed from a preliminary adsorption solution. The adsorption protective coatings, formed at the metal-inhibited electrolyte interface, are complex self-organizing molecular layers whose composition and morphology are determined by the conditions of their formation.

The formation of stable organic films in aggressive media, especially acid, is a most vital challenge of the physico-chemical science of the properties and applications of organic materials. Despite the latest systematic research [1–3], the scientific background of the stability of electrophysical properties of films based on organic matter has never been studied enough. The studies aimed at modifying coatings with a variety of components, not only organic, are especially promising.

S. P. Shpanko (✉) · E. N. Sidorenko · L. E. Kuznetsova · E. A. Sosin
Southern Federal University, 344006 Rostov-on-Don, Russia
e-mail: spsha@mail.ru

I. A. Parinov et al. (eds.), *Advanced Materials*, Springer Proceedings in Physics 224, https://doi.org/10.1007/978-3-030-19894-7_11

This chapter aims at studying the stability and physico-chemical properties of organic films, based on the heterocyclic compound of imidazole class and its compositions with thiocyanate anions in acid media.

11.2 Research Methods

The organic coatings on the surface of steel grade St3 (C-0.2, Mn-0.5, Si-0.15, P-0.04, S-0.05, Ni, Cu-up to 0.03%) were obtained by self-organization from an inhibited solution of 1 M H_2SO_4. The surface-active agent (SAS) under study was a derivative of benzimidazole-dihydrochloride1-(3,4-dichlorphenyl)-2{2-imino-3 [2-piperedines-1-il) ethyl]-2,3-dihydro-1 1H-behzimidazole-1-il} ethanol and its combinations with thiocyanate anions introduced as potassium salt. The SAS concentration (C_{SAS}) was maintained as constant 1 mmol/l, the concentration of KNCS (C_{KNCS}) varied from 30 to 90 mmol/l. The acid post-processing of the inhibited specimens was made in 1 M H_2SO_4 media and HCl (background solutions). The film protective properties were estimated as the residual degree of protections (RDP, Z_t).

To achieve this, the defatted samples were weighed and kept in inhibited H_2SO_4 solutions for 3 days. After that, the samples were unloaded, rinsed with distilled water and placed in background solutions. Weight losses were determined for a period t that varied from 1 to 120 h. The same solutions were used for the specimens without films. After a certain period, the specimens were taken out to determine their residual degree of protection Z_t for time t: $Z_t = (\Delta m_{0,t} - \Delta m_{i,t})/\Delta m_{0,t}$, where $\Delta m_{0,t}$ and $\Delta m_{i,t}$ are the weight losses in time t from the moment of submersion of the steel electrodes in the background solutions, for the specimens that were non-processed and processed in the inhibitor.

DEL measurements of the inhibited electrodes were made in inert atmosphere on an AC bridge P-5021 in 1 M H_2SO_4 at the AC frequency of 1 kHz. The time of film formation was one hour. Additional frequency measurements of the films electric capacity in air, depending on formation time 1, 3, and 5 day-night periods were made using the E7-20 immitance meter.

To determine the mechanism of protective action of organic films, electrochemical measurements were made on inhibited electrodes in 1 M HCl. The working electrode is a steel electrode with a film, the counter electrode is made of Pt, the reference electrode is silver chloride. The currentless potential was measured (corrosion potential E_{corr}). After that, direct current was put through the cell, after which the cathode and anode potentials were registered. The background curves were taken at the film-free electrodes after they had been processed in pure sulphuric acid during 24 h.

The time of acid post-processing of the inhibited samples was chosen individually, taking into account the specificity of the methods used.

11.3 Results and Discussion

It is well known [4] that the adsorption protective films at the metal-inhibited electrolyte solution interface are formed in several stages. The first stage shows the formation of a chemisorption layer on the metal surface that features chemical bond of the inhibitor's adsorbed molecules and the metal surface. This adsorption layer is most durable. Next, due to electrostatic forces there starts a formation of a layer of physically sorbed molecules. This layer is a less durable. It is also possible that the organic layer is formed thanks to the least durable bond of intermolecular (Van der Waals) forces. The force of the adsorption bond is weaker at the row: chemisorption–physical adsorption–intermolecular interaction and it strongly depends on various factors, i.e. time of film formation, nature, composition and concentration of the inhibitor, nature of the background solution.

11.3.1 Resistance of Organic Coatings to Acids

Organic coatings are extremely unstable in H_2SO_4. After 3 h, Z_t drops to 18–20%. Moreover, the increase KCNS leads to a sharp decrease in Z_t (Fig. 11.1a).

The residual degree of protection of inhibited specimens in HCl is much higher than in H_2SO_4 and is 68–78% (Fig. 11.1b). The changes in C_{KNCS} at film formation produce a negligible effect on its protective properties. An increase in C_{KCNS} slightly decreases the film Z_t. It is possible to highlight a few areas in the kinetic dependencies. **I** is the 1st film stability area (t = 1–3 h). Organic coatings are resistant to HCl. The maximal degree of protection amounts to 78 and 75%. **II** is the

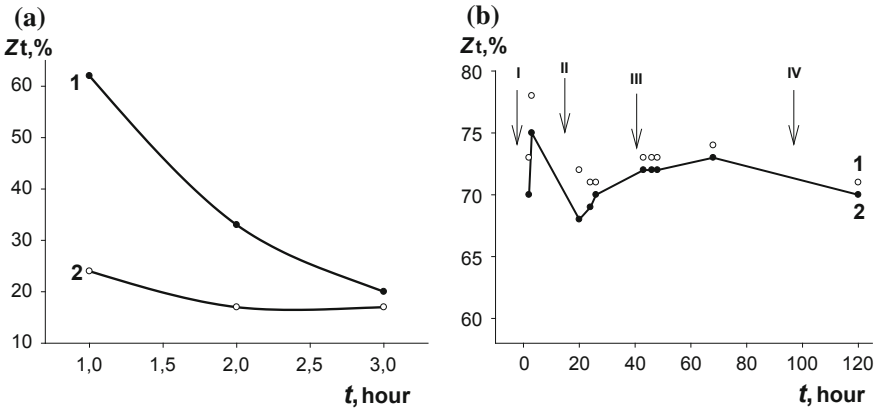

Fig. 11.1 Dependence of the residual degree of protection of the inhibited Z_t specimen on the time t of acid post-processing in 1 M H_2SO_4 (**a**) and in 1 M HCl (**b**) at different C_{KNCS} at film formation: 1–30 mmol/l, 2–90 mmol/l

area with disrupted film stability (t = 3–20 h). Organic coatings begin to disintegrate due to the destruction of the external intermolecular layer. The degree of protection drops to 65–68%. **III** is the second area of film stability (t = 24–68 h). The degree of protection increases and takes values of 72–73%. **IV** is the area of destruction of the second stable state of the film (t = 68–120 h). In this time spectrum, coating destruction increases, because the layer that was formed due to electrostatic forces is destructed. One may suggest that this residual degree of protection is supported by the chemisorption layer of the inhibitor that was stabilized with HCl anions.

The high resistance of the film to hydrochloric acid might be caused by the anions of chorine, penetrating through the pores of the adsorption layer to the steel surface. Their further adsorption at the active centers of metal oxidation creates a potential obstacle to metal cations' transfer from the crystal lattice to the solution.

11.3.2 Measurements of the Capacity of the Double Electric Layer (DEL)

The stability of phase films may be controled by their DEL absolutely capacity value and its changing value in time dC/dt (desorption rate).

The lower the DEL capacity by its absolute value and the lower is the rate of desorption of SAS from the surfaces of inhibited specimens, the higher stability they have in a given medium. This approach of the evaluation of phase layer stability has been discussed in [5]. The background solution here was 1 M H_2SO_4 (Fig. 11.2).

We have established (Fig. 11.2, Table 11.1) that films, obtained in the presence of a mixed inhibitor are less penetrable to corrosive medium. This is supported by the lower values of DEL capacity (Fig. 11.2) and of the rate of the SAS molecules desorption (Table 11.1). Moreover, the lower the KNCS concentration in the mixed inhibitor at forming the coating, the more resistant it is in acid medium.

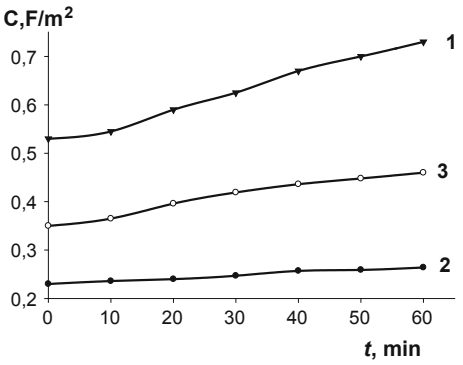

Fig. 11.2 Dependence of DEL capacity C on inhibited electrodes on the time t of acid post-processing i; the composition of adsorbate during film formation: 1—SAS and SAS + KNCS at C_{KNCS}; 2—30 mmol/l; 3—90 mmol/l

Table 11.1 Experimentally obtained rate values of the desorption of SAS molecule from the $\Delta C/\Delta t$ steel surface for adsorbates of different content at film formation

$\Delta C/\Delta t \cdot s \times 10^3$, F/m^2 min		
SAS	SAS + KNCS C_{KNCS} = 30 mmol/l	SAS + KNCS C_{KNCS} = 90 mmol/l
3.3	0.5	1.8

11.3.3 Electrochemical Measurements

In order to determine the mechanism of the protective effect of films in HCl, we did some electrochemical measurements with the results shown in Fig. 11.3 and Table 11.2.

Organic films increase the polarization of cathode and anode reactions and the polarizability of the cathode reaction (Fig. 11.3). As a result, the rates of cathode and anode reactions drop 7-fold as compared to the background. This makes us suggest the mixed nature of the anode-cathode mechanism of the protective effect of organic films. However, a slight increase in the current-free potential of the inhibited specimens (E_{corr}) as compared to the specimens without film (Table 11.2) shows a greater slowdown of the anode reaction.

The impact of thiocyanate ions on the degree of protection of an organic compound depends on their concentration [6]. At a low concentration of KNCS (C_{KNCS} < 5 mmol/l) anions NCS^- adsorbed on the positive surface of the steel, recharge it, contributing to the electrostatic adsorption of bulk organic salt cations. The degree of protection grows from 77 to 96%. A further increase in C_{KNCS}, however, leads to a decrease in the protection effect. We may suggest that at a sufficient concentration of NCS^- there appear favorable conditions of forming a strong bond between the chemisorption layer of complexions of Fe–NCS^-–SAS type and the iron surface. The higher C_{KNCS}, the better screening the surface of the

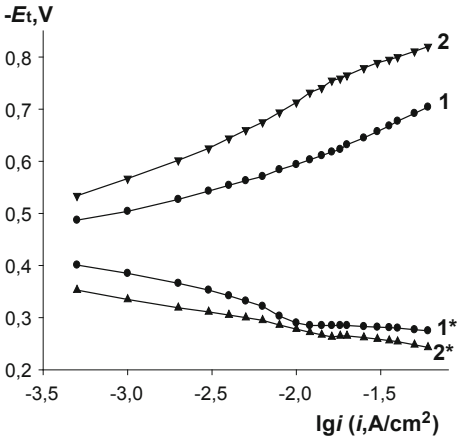

Fig. 11.3 Cathode (2) and anode (2*) polarization curves in 1 M HCl for St3 with film settled in the presence of admixed in inhibitor SAS + KNCS (C_{KNCS} = 30 mmol/l); 1, 1* are the background polarization curves on St3 without film

Table 11.2 St3 potentials without films (background) and with a film settled in the presence of SAS + KNCS mixed inhibitor at C_{KNCS} = 30 mmol/l, Tafel constants $в_к$ and $в_A$, the rates of reactions of cathode $i_к$ and anode i_A

Nature of medium	$-E_{corr}$ (V)	$в_к$	$в_A$	$i_к$ (mA/cm^2)^2) (E_K = −0.6 V)	i_A (mA/cm^2) (E_A = −0.33 V)
Background 1 M HCl	0.465	0.09	0.08	12.0	6.9
SAS + KNCS	0.426	0.100	0.078	1.9	1.0

specimens with a polymer film occurs. As a result, the adsorption of inhibitor molecules is difficult, which is inevitably accompanied by a decrease in the degree of protection. The residual degree of protection of coatings also decreases along with the growth of the concentration of thiocyanate anions.

11.3.4 Surface Morphology

The formation of the polymer film of the complexon impacts the morphology of the inhibited specimen surface. In fact, Fig. 11.4 shows that adding NCS anions to the organic inhibitor facilitates the forming on the steel surface of a volumetric coating with some changes in the shape and size of the crystallite cells (Fig. 11.4a, b). At that, the protection effect sharply increases. The increased C_{KNCS}, however, substantially changes the relief of the surface. The new film features a more homogeneous spread and size of the cells that cover virtually a whole the surface of the electrode (Fig. 11.4c).

We suggest that it is at the concentration of KNCS 90 mmol/l the entire surface of the specimen is covered with the polymer film of the complexon that impedes the adsorption of the organic inhibitor molecule. As a result, the residual degree of protection of the coating is reduced.

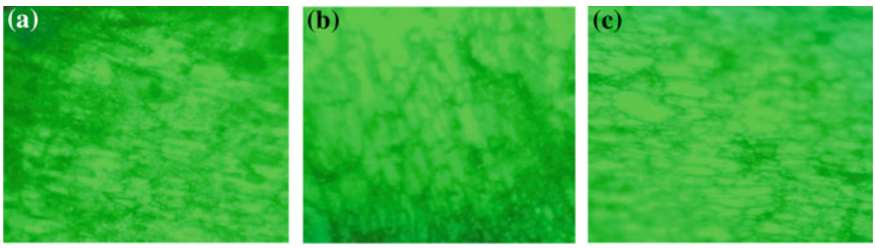

Fig. 11.4 Morphology of the surface of the inhibited specimens depending on the composition of the adsorbat: (**a**) SAS, SAS + KNCS; (**b**) at C_{KNCS} = 30 mmol/l; (**c**) at C_{KNCS} = 90 mmol/l; the formation time is 3 day-night periods

11.3.5 Frequency Measurements of the Films Electrical Capacity

The electric capacities of the films are negative, disregarding the duration of their formation or the C_{KNCS} concentration in the mixed inhibitor, which proves both the non-ordered structures of the organic coatings and the hopping nature of the transfer of charge carriers.

The dependence of the film electric capacity on C_{KNCS} is determined by the time of film formation. At measurement at the fixed frequency of the electric capacities of the films, formed for one day, their modules are inversely proportional C_{KNCS} concentrations. Prolongation of the SAS adsorption time to three 24-h periods increases the film electric capacities in the low frequency spectrum (10^2–10^3 Hz) by 1–2 orders, and they actually become comparable. With a further prolongation up to five 24-h periods, their capacities unevenly drop, so that the films produced in the presence of a mixed inhibitor with high C_{KNCS} concentration show higher capacity. This change in the dependence between film electric capacity and C_{KNCS} concentration at the growth of SAS adsorption time may be related to the formation on the steel surface of a chemisorption coating of complexons, the properties of which depend on the time of formation and on C_{KNCS} concentration in the mixed inhibitor in the process of film formation.

Thus, the residual protective properties of organic coatings are substantially dependent both on the nature of the background solution at acid post-processing of inhibited specimens and also on the concentration of thiocyanate ions in the mixed inhibitor in the film formation process. There has been noticed an increase in the stability of coatings in the HCl medium at the lower concentration of thiocyanate ions. A suggestion was made on the formation of a uniform polymer film of complexons on the steel surface, caused by the C_{KNCS} increased value in the mixed inhibitor that strongly affected the stability and electric properties of organic coatings.

References

1. S.P. Shpanko, E.N. Sidorenko, A.F. Semenchev, N.V. Lyanguzov, V.A. Anisimova, Prot. Metals Phys. Chem. Surf. **53**(2), 335 (2017)
2. S.P. Shpanko, E.N. Sidorenko, Y.V. Kabirov et al. in *Proceedings of the 2016 International Conference on Physics and Mechanics of New Materials and Their Applications*, ed. by I.A. Parinov, S.-H. Chang, M.A. Jani (Nova Science Publishers, New York, 2017), 345
3. E.N. Sidorenko, S.P. Shpanko, V.B. Shirokov, N. V. Voitenko, A.V. Mikhailishin. in *International Conference on "Physics and Mechanics of New Materials and Their Applications" (PHENMA 2017)*, Jabalpur, India, October 14–16, 2017, 236 (2017)
4. N.A. Belousova, V.P. Grigoryev, E.V. Plekhanova, S.P. Shpanko, in *Corrosion: Materials, Protection*, vol. 8, 13 (2015) (in Russian)

5. I.L. Rosenfeld, F. I. Rubinshtein, K.A. Zhigalova in *Protection of Metals from Corrosion with Paint Coatings*. Moscow, Chemistry, 224 p. (1987) (in Russian)
6. S.P. Shpanko, E.N. Sidorenko, L.E. Kuznetsova in *International Conference on "Physics and Mechanics of New Materials and Their Applications" (PHENMA 2018)*, Busan, South Korea, August 9–11, 2018, 318 (2018)

Chapter 12
Effect of High-Voltage Nanosecond Pulses on the Structural Defects and Technological Properties of Naturally Occurring Dielectric Minerals

Igor Zh. Bunin, Valentine A. Chanturiya, Mariya V. Ryazantseva, Nataliya E. Anashkina and Elizaveta V. Koporulina

Abstract To demonstrate the effectiveness of applying pulsed energy impacts in the processing of refractory tungsten (tungsten molybdenum, scheelite quartz) ores, the composition change mechanism was examined of the structural defects of the crystal lattice and optical spectroscopic properties of scheelite, fluorite, and calcite, as well as of the structural chemical, mechanical (microhardness), electrical, physicochemical, and process (flotation) properties of calcium minerals and quartz, when exposed to high-power (high-voltage) nanosecond electromagnetic pulses (HPEMP). With this aim, X-ray fluorescence spectroscopy, infrared Fourier spectroscopy (FTIR), X-ray photoelectron spectroscopy (XPS), scanning probe microscopy, methods based on Hammett indicator adsorption from aqueous media, electrophoretic light scattering (zeta potential), microhardness, contact angle measurements, and other methods were applied. The non-thermal effects of HPEMP caused a change in the concentration (content) of structural defects, softening of the surface (a relative decrease in the microhardness of the minerals by 30–67%), directional changes in the electrical properties and hydrophobicity of the surface, as well as an increase in the flotation activity of calcium minerals by 5–12% and a decrease in the flotation ability of quartz by 7–11%.

I. Zh. Bunin (✉) · V. A. Chanturiya · M. V. Ryazantseva · N. E. Anashkina · E. V. Koporulina
N.V. Mel'nikov Institute of Comprehensive Exploitation of Mineral Resources, Russian Academy of Science, 4 Kryukovsky Tupik, Moscow 111020, Russian Federation
e-mail: bunin_i@mail.ru

I. A. Parinov et al. (eds.), *Advanced Materials*, Springer Proceedings in Physics 224, https://doi.org/10.1007/978-3-030-19894-7_12

12.1 Introduction

Both in Russia and globally, due to a significant deterioration of mineral feeds reducing ore grades by a factor of 1.5–2.5, combined with disseminated ore minerals, an urgent need exists for fundamentally new, highly efficient, energy-saving methods and processes aimed at making mineral concentration circuits more complete and comprehensive [1]. Presently, non-conventional (non-mechanical) methods are being developed based on physicochemical, electrochemical, and pulsed energy impacts on complex earth materials (geomaterials) and aqueous slurries [1, 2] to improve the efficiency of disintegration and liberation processes of disseminated mineral complexes containing non-ferrous, rare earth, and noble metals, to recover valuable minerals, and to enhance the contrast of the structural chemical and process properties of refractory mineral feeds.

An urgent problem in scheelite (molybdenum scheelite) ore processing is to develop methods for improving the grade of scheelite concentrates with a content of WO_3 up to 50–80%. The minerals complicating the recovery of salable scheelite concentrates are primarily calcite and apatite, which is due to the proximity of their flotation properties to those of scheelite. At a sodium oleate concentration in the solution of 0.99×10^{-3} mol/l, the contact angle is 65° in scheelite, 64° in apatite, and 65° in calcite. The density of calcium ions per unit surface of the elementary mineral cell is 0.033 in scheelite, 0.022 + 0.034 in apatite (on the surface of apatite, calcium cations of two varieties co-exist), 0.05 in calcite [3]. The collector anion sorption takes place on the Ca^{2+} cation common for calcite and apatite, whose magnitude determines the recovery of the mineral into the concentrate. It is well known that a depressor (liquid glass) can be added to amplify the difference in the degree of collector adsorption at high concentrations in the solution typical of industrial processes.

Quartz, being one of the most abundant minerals in the earth's crust, is often associated with other minerals, such as feldspar, talc, pyrite, hematite, smithsonite, and apatite. Because of its unique physical and physicochemical properties, quartz is widely used in the manufacture of glass, ceramics, refractory and optical materials. The crystal lattice of quartz is characterized by an ion-covalent bond type. The two varieties of quartz (low-temperature α and high-temperature β) slightly differ in their crystalline structure. In α- and β-quartz, the width of the band gap is $\sim$8.8 and 8.82 eV, the width of the lower conduction band is $\sim$9 and 11 eV, respectively [4]. Quartz has natural hydrophilic properties and resists only flotation by anionic surfactants; the hydrophobicity of the mineral can be enhanced by adding multivalent cations (heavy metal ions) to the flotation circuit or by modifying the structural and chemical properties of the quartz surface by pretreatment using energy impacts.

12.1.1 Research Purpose

The effectiveness and mechanism were examined behind the effects of non-thermal impact of high-power (high-voltage) nanosecond electromagnetic pulses (HPEMP [5, 6]) on the structural defects, functional and chemical composition of the surface, microhardness, electrical and processing (flotation) properties of naturally occurring dielectric minerals—calcium minerals (calcite, scheelite, fluorite) and quartz.

12.1.2 Research Scope

In this paper, we studied the following aspects of the research problem:

(i) a comprehensive methodological approach to studying changes in the structural chemical, mechanical, electrical, physicochemical, and processing properties of naturally occurring dielectric minerals under the influence of high-voltage nanosecond pulses;
(ii) the mechanism behind the effect of HPEMP on the content (quantity) and composition of intrinsic crystal lattice defects, as well as the optical and spectroscopic properties of calcium minerals;
(iii) changes in the functional and chemical composition (surfactant adsorption centers) and surface softening (formation of surface defects, decrease in microhardness) of calcium minerals and quartz as a result of exposure to nanosecond HPEMP for achieving a controlled change in electrical properties, hydrophilic-hydrophobic surface balance, and flotation activity of minerals;
(iv) rational modes and conditions of electromagnetic pulsed treatment of geomaterials to improve the flotation efficiency of calcium minerals and the process properties of quartz.

12.2 Experimental

12.2.1 Materials and Research Technique

Structural chemical, electrical, mechanical, and processing (technological, namely, flotation) properties of calcium minerals were studied in monomineral fractions of scheelite, fluorite, and calcite from Tyrnyauz deposit, Russia. The content of chemical elements in the mineral samples (Table 12.1) was analyzed using inductively coupled plasma optical emission spectrometry (ICP-OES, optical emission spectrometer ICPE-9000) and X-ray fluorescence analysis (XRF, XRF spectrometer ARL ADVANT'X, Thermo Scientific).

Table 12.1 Chemical composition of calcium minerals, wt %

Minerals	Ca	W	F	Si	Fe	Al	Mg	Sr	Ba	S	Pb	Mn
Scheelite $CaWO_4$	57.11	14.08	0.29	0.52	0.42	0.43	0.06	N/d	N/d	0.48	0.15	N/d
Fluorite CaF_2	53.50	N/d	39.58	0.15	0.01	0.15	N/d	0.03	0.03	N/d	N/d	N/d
Calcite $CaCO_3$	40.68	N/d	0.85	0.11	0.10	0.05	0.03	0.01	0.02	N/d	N/d	0.002

The changes in the functional chemical composition of the surface, in the physicochemical, mechanical, electrophysical, and process properties of rock minerals under the influence of high-voltage nanosecond pulses was studied in samples of milk white gangue quartz (% wt: SiO_2 99.11, Al_2O_3 0.61, C 0.08, K_2O 0.07, Na_2O 0.05; the content of minor impurities not specified) and ferruginous quartz (Lebedinsky Mining and Concentrator Project, Russia).

Mineral samples represented by ground (powder) samples (1 g subsamples) and polished thin sections ($10 \times 10 \times 4.5$ mm^3) were treated with high-power (high-voltage) nanosecond electromagnetic pulses (HPEMP) in air under standard conditions using a high-voltage video pulse generator with a capacitive energy storage [7]. Before the treatment, the mineral subsamples were placed on a thin dielectric substrate presenting a flat dielectric barrier on the side of a flat-grounded electrode to create conditions close to the conditions existing at the generation of a pulsed nanosecond dielectric barrier discharge at atmospheric pressure [8]. Then the samples were moistened with distilled water at a S:L ratio of 5:1 according to the recommendations in [9]. The powder samples were moistened to improve the effectiveness of the electromagnetic pulsed impacts [7, 9, 10] and to recreate the industrial process conditions. After the HPEMP treatment, the mineral samples were air dried and kept in a rarefied atmosphere before carrying out analytical studies. The mineral thin sections were placed directly on the working surface of a grounded electrode (duralumin) maintaining a small ($\sim$0.1–0.2 mm) air gap between the top surface of the thin section and the surface of the active electrode (alloy steel). The linear dimensions of the active and grounded electrodes of the pulse generator were much larger than the dimensions of the treated samples.

The nanosecond pulse generator operates at a frequency of 100 Hz (pulse repetition rate), the output pulse amplitude is $\sim$25 kV, the duration of the leading edge of the pulse corresponds to the arrester's time to flashover and varies from pulse to pulse within 2–5 ns, and the pulse duration is the combined arrester's time to flashover and its extinction time and varies within 4–10 ns. Video pulses of a bipolar shape are generated, pulse energy $\sim$0.1 J, electric field strength in the interelectrode gap $(0.5–1) \times 10^7$ V/m, time range of the pulsed treatment of the mineral samples t_{treat} = 10–150 s, i.e. $N_{imp} \sim (1–15) \times 10^3$ HPEMP.

The structure (shape) of the generated pulses is characterized by the following features [11]: (i) the video pulse envelope has one or multiple field oscillations; the form of the oscillations is non-sinusoidal; (ii) the leading and trailing edges of the

pulse are asymmetric; (iii) the distances between the zero intercepts of the pulse envelope are unequal; (iv) the signal has no carrier frequency. It should be noted that experiments with nanosecond electromagnetic pulsed treatment of natural and man-made materials are classified as the so-called non-thermal impacts, since the energy of a single pulse ($\sim$0.1 J) and of the whole series of pulses is low and is not capable of substantially elevating the temperature of the sample as a whole [12]. However, for a time much shorter than the characteristic measurement time of the thermophysical properties of mineral components (geomaterials) making up the sample, the local temperature during the electromagnetic pulsed treatment may elevate [12, 13].

To analyze the structural defects of calcium minerals, identify structural impurities and intrinsic defects of the crystal lattice, X-ray fluorescent spectroscopy was used. The study was carried out using a setup by VIMS, Moscow, composed of an X-ray generator based on Iris-3m (NPP Burevestnik, Russia) and an X-ray tube 5BHV7 (NPP Svetlana-Rentgen, Russia); anode voltage 35 kV, anode current 30 mA. The monochromator MDR 23 (NPP LOMO, Russia) with computer control and a registration system based on a photon count was used in the study.

IR-spectra of the minerals were recorded in the inverse wavelength range from 4000 to 400 cm^{-1} with a spectral resolution of 4 cm^{-1} using the IR Fourier spectrometer IR-Affinity by Shimadzu and the attachment Diffuse IR by Pike Technologies. For each sample, at least five spectral curves were recorded with 50 scans in each spectrum. X-ray photoelectron spectroscopy (XPS, Kratos Axis Ultra DLD spectrometer with monochromatic X-ray generator AlK_α) was used to study the chemical (phase) composition of the surfaces of fluorite particles.

Acid-base centers (functional chemical composition) on the mineral surfaces were studied using the adsorption method of Hammett indicators from aqueous media [14, 15]. A summary of the indicators, values of the protolytic equilibria constant pK_α, working concentrations of the solutions, and the spectrophotometric measurement method (spectrophotometer Shimadzu UV-1700) of the optical density of standard aqueous solutions of acid-base indicators at wavelengths corresponding to the maxima of their optical absorption are given in [16].

Electrokinetic potential (zeta potential; ζ, mV) of the calcium minerals (particle size finer than 10 μm) before and after the HPEMP treatment was studied by the dynamic (electrophoretic) light scattering method using the universal system Zetasizer Nano ZS by Malvern Instruments. Measurements were made in an aqueous medium at pH = 10.5. To measure the electrokinetic potential of quartz, the dedicated particle ζ-potential analyzer Microtrac ZETA-check was used. The particles finer than 30 μm were mixed with distilled water at pH = 5.5–6.

Kelvin probe force microscopy (SPM–AFM, KPFM) was used to study the effects of HPEMP on the morphology and electrostatic potential (V, V) of the thin section surfaces of the calcium minerals. Potential measurements were carried out in air under standard conditions using the NTEGRA Prima atomic-force microscope (NT-MDT, Zelenograd, Russia) and silicon ACM cantilevers of the series NSM10/TiN with a conductive TiN coating on the needle side.

Microhardness of the minerals before and after the electromagnetic pulse treatment was determined by the Vickers method (*HV*, MPa) according to Russian GOST-2999-75 (ISO 6507-1:2005) in polished thin sections using the microhardness meter PMT-3M (LOMO, Russia); indenter load is 100 g (scheelite, fluorite, calcite), 200 g (quartz), loading time is 10–15 s.

The change in the hydrophilic-hydrophobic state of the surface of calcite and quartz as a result of electromagnetic pulse treatment of the minerals was evaluated by the change in the contact angle (water contact angle) of the thin section surface by the sessile drop method using a microscope with the digital camera Moticam 2300 and the software suite Motic Image Plus 2.0 ML for image input and processing. A drop of distilled water with a diameter of no larger than 2–3 mm was placed on the surface of the thin section and held at standard conditions for 40 s until the drop profile was recorded. To determine the contact angle, the image analysis software ImageJ with plugins DropSnake and LB-ADSA plugins was used [17].

Flotation agent treatment of the calcium minerals with a particle size of −80 + 50 μm (subsample 1 g, pH = 10, exposure time of the mineral to water 1 min, to liquid glass (100 g/t) 3 min, to sodium oleate (300 g/t) 3 min, flotation time 1.5 min) was selected to obtain the highest possible recovery in the flotation of scheelite in the initial state (without HPEMP treatment).

In the flotation tests of quartz, a lab-scale flotation cell with a capacity of 20 cm^3 was used. The exposure time of the mineral to the agents was 1 min, flotation froth removal time was 1.5 min. Milk white quartz samples were floated in the presence of an anionic collector (sodium oleate, 200 g/t), also in combination with a depressant (liquid glass, 200 g/t). In the flotation of the ferruginous quartz variety (Lebedinsky Mining and Concentrator Project), a cation collector (amine 200 g/t) was added, with starch (200 g/t) as a depressant. The pH of the medium was adjusted by adding an aqueous solution of sodium hydroxide (pH = 9.5–10.0). The experimental error was under 3%.

12.3 Results and Discussions

12.3.1 Effect of HPEMP on the Optically Active Defects in Calcium Minerals

The findings of X-ray fluorescent spectroscopy of calcium minerals attest to the effectiveness of high-voltage nanosecond pulses on the intrinsic (point) defects of the crystal lattice of calcium minerals and on their structural sensitive, including optical and spectroscopic properties.

In the X-ray fluorescence spectra of *scheelite* (Fig. 12.1a), a broad band with a maximum of 480 nm associated with at least four types of fluorescence centers was

identified, namely $\left\{\left[W^{5+}O_4\right]'_2V_A^{\bullet\bullet}\right\}^x$, $\left\{\left[W^{5+}O_4\right]'V_A^{\bullet\bullet}\right\}'$, $\left[W^{5+}O_4\right]'$, $\left\{\left[W^{5+}O_4\right]'''V_A^{\bullet\bullet\bullet}\right\}'$. Under the influence of high-voltage nanosecond pulses ($t_{treat} \sim$ 10–150 s), deterioration ("destruction") was observed of the fluorescence centers of this type, as evidenced by the extinction of this spectral band and a decrease in its integrated intensity by a factor of 1.3–1.4 (Fig. 12.1a). This nature of the change in the spectral curve indicates, apparently, the implementation of the mechanism of non-radiative relaxation of excited states of anionic complexes $[WO_4]^{2-}$, accompanied by the migration of energy from the excited groups to the fluorescent extinction centers also formed under the influence of HPEMP. By the

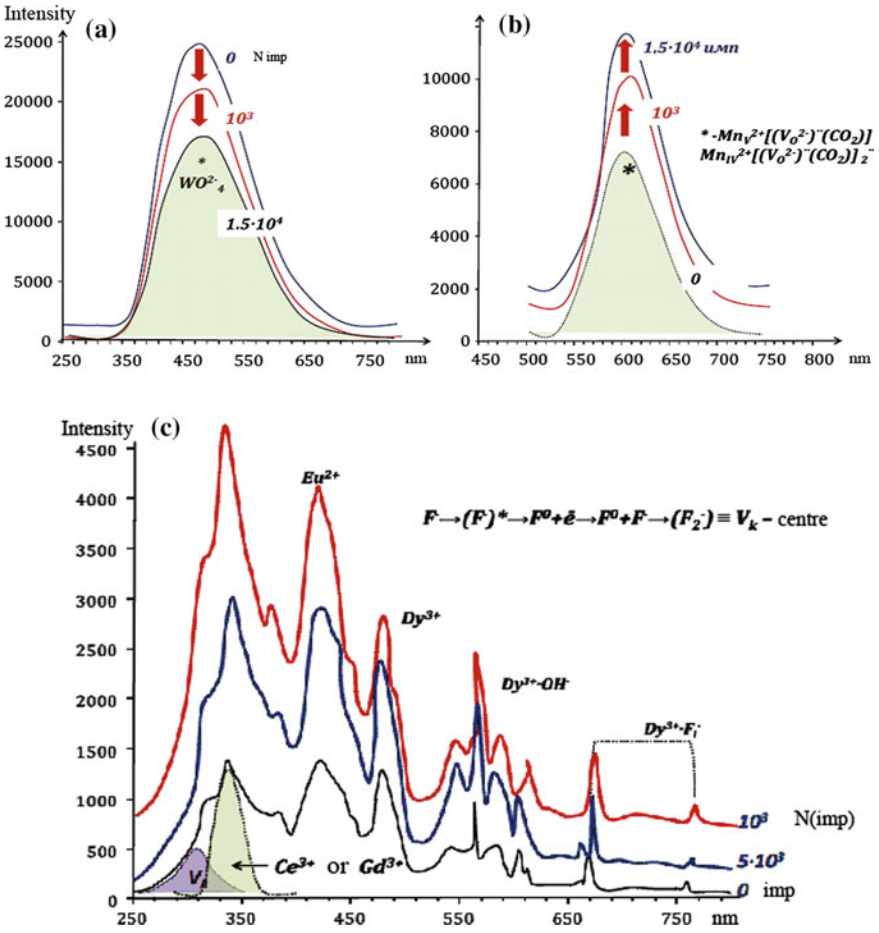

Fig. 12.1 X-ray fluorescence spectra of **a** scheelite, **b** calcite, and **c** fluorite before and after the influence of high-voltage nanosecond pulses ($t_{treat} \sim 10^3$–150 s)

method of IR Fourier spectroscopy (diffuse reflection mode), it was found in [18] that, as a result of short-term ($t_{treat} \sim 10$ s) electromagnetic pulse treatment of scheelite samples, a sharp increase was achieved in the area of the doublet 775 + 818 cm^{-1}, relating to the stretch vibration of the W–O anionic complex $[WO_4]^{2-}$.

It was shown that, in *calcite*, the non-thermal effect of nanosecond HPEMP ($t_{treat} \sim 10$–150 s) caused an increase in the intensity of the X-ray fluorescence band at 600 nm (Fig. 12.1b), determining the emission of impurity ions Mn^{2+}, isomorphically substituting Ca^{2+} and present in internodes and coordinated with oxygen vacancies. The observed change in the spectrum indicates the transformation of the original crystalline structure of the mineral, associated in this case with the accumulation of defects of the type $Mn_V^{2+}\left[\left(V''_{O^{2-}_{(I)}}\right)(CO_2)\right]^{\bullet\bullet}$, $Mn_{VI}^{2+}\left[\left(V''_{O^{2-}_{(II)}}\right)(CO_2)\right]^{\bullet\bullet}$. According to [19], in calcite, Mn_V^{2+}-centers transform into Mn_{VI}^{2+}-centers due to a change in the position of the oxygen vacancies $(V_{O^{2-}})^{\bullet\bullet}$ and the radical (CO_2), which is more likely at a high temperature (roasting). In this case, some types of center transformations can occur as a result of thermostimulated diffusion of the vacancies $(V_{O^{2-}})^{\bullet\bullet}$, $(V_{CO_2})^{x}$, $(V_{CO_3^{2-}})^{\bullet\bullet}$ and lead to dissociation of associative fluorescence centers in calcite [19]. According to IR Fourier spectroscopy [18], as a result of the electromagnetic pulsed treatment ($t_{treat} \sim 10$–100 s) of the calcite samples, the integrated intensity of the absorption band in the IR spectrum was consistently reduced at 1400 cm^{-1}, corresponding to the stretch vibration of the CO_3^{2-} ion in the mineral structure.

In the X-ray fluorescence spectra of *fluorite*, a series of bands with maxima at 4.25 eV (V_k-center), 3.62 eV (Ce^{3+}), 2.88 eV (Eu^{2+}), 2.7 eV (Dy^{3+}), 2.18 eV ($Dy^{3+} \cdot OH^-$), 1.8 eV, 1.6 eV ($Dy^{3+} \cdot F_i^-$) was observed [19, 20]. Electromagnetic pulsed treatment of the mineral resulted in a general increase in the fluorescence intensity without changes in the symmetry of the individual bands and the spectral curve profile (Fig. 12.1c).

The strongest increase (by a factor of 2.1–2.2) of the integrated band intensities was achieved in the result of HPEMP during the first $t_{treat} \sim 10$ s. Increasing the residence (treatment) time to $t_{treat} \geq 30$ s caused a decrease in the areas of these bands of the spectrum. Nevertheless, the numerical values of the areas of the sample bands after the pulsed treatment ($t_{treat} \geq 30$ s) exceeded the corresponding values for the sample in the initial (untreated by HPEMP) state by a factor of 1.5–1.7 (Fig. 12.1c). Apparently, in the evolution process of the optically active centers in naturally occurring fluorite under the influence of pulsed energy impacts, in the initial stage of treatment at $t_{treat} \sim 10$ s auto-localized holes (V_k centers) first formed and then, with an increase in the dose of electromagnetic radiation ($t_{treat} > 30$ s, $N_{imp} = 3 \times 10^3$) were partially annihilated. There was also a simbatic with V_k centers change in the number of centers associated with the emission of Ce^{3+}, Eu^{2+}, Dy^{3+}, $Dy^{3+} \cdot OH^-$, and $Dy^{3+} \cdot F_i^-$. Analysis of XPS profile of fluorine

F1*s* showed [18] that a $t_{treat} \sim 10$ s electromagnetic pulsed treatment of fluorite caused an increase in the surface concentration of the interstitial fluorine F_i^- from 5.36 to 8.12%. With an increase in the treatment time to $t_{treat} = 30$, 50, and 100 s, the atomic concentration of structural defects of the type F_i^- changed nonlinearly and was 6.37, 1.47, and ~4.0% at., respectively.

According to atomic force microscopy data (scan size 20 × 20 μm), in the result of a HPEMP treatment for $t_{treat} \sim 30$–50 s, there was an increase in the height of the relief and surface roughness of the minerals, namely in the arithmetic mean R_a and standard R_q deviation of the surface profile of the samples by a factor from 3.7 to 4 in fluorite and from 1.8 to 2 in calcite.

The identified changes in the surface spectroscopic properties and morphology of calcium minerals are most likely a manifestation of a specific non-thermal activation mechanism of diffusion processes caused by the microwave field [21]. It should be noted that for video pulse duration for 5 ns, the average frequency is $(\Delta\omega\tau \approx 2\pi)$ $\bar{f} = \tau^{-1} \approx 2 \times 10^8$ Hz and the average wavelength is $\bar{\lambda} = c/\bar{f} \approx$ 150 cm (the boundary between the meter and decimeter wave regions, the VHF-UHF band) [22]. Nevertheless, according to [21], the microwave action on the crystal creates an additional driving force enhancing mass transfer in the crystal, leading to accumulation, interaction, and annihilation of structural defects and impurities in the crystals. In addition, polarization (possibly, migratory (interlayer) or structural high-voltage polarization) of naturally occurring dielectric minerals in strong electric fields, which causes distortions in the crystal lattice, changes in hardness, and rupture of chemical bonds, can cause the formation of structural defects in the crystals.

12.3.2 Changes in the Functional Chemical Composition of Mineral Surfaces Under the Action of HPEMP

Hammett indicators [14–16, 23] with the lowest (typically, negative) values pK_α are selectively adsorbed at active centers of the primary Lewis type (electron donors) containing an unshared electron pair and capable of capturing protons during the hydrolytic dissociation of the water molecule [23]. With an increase in pK_α of the indicators, their selective adsorption occurs at Bronsted acidic centers ($pK_\alpha = 0$–7, surface OH groups with a tendency to proton cleavage), Bronsted basic (7–14, surface OH groups with a tendency to cleavage of the entire hydroxide), and Lewis acid centers ($pK_\alpha \geq 14$, atoms with a free orbital, capable of capturing hydroxyl with dissociative adsorption of water; electron acceptors) [23].

Using the adsorption method of Hammett color indicators, it was found that, in the result of exposure to high-voltage nanosecond pulses, the electron donor capacity of the fluorite surface enhanced and the acceptor properties of the scheelite surface improved. For instance, short-term pulsed treatment of *fluorite* ($t_{treat} = 10$ s) led to a decrease in the content of centers with $pK_\alpha = -4.4$ (Lewis primary centers)

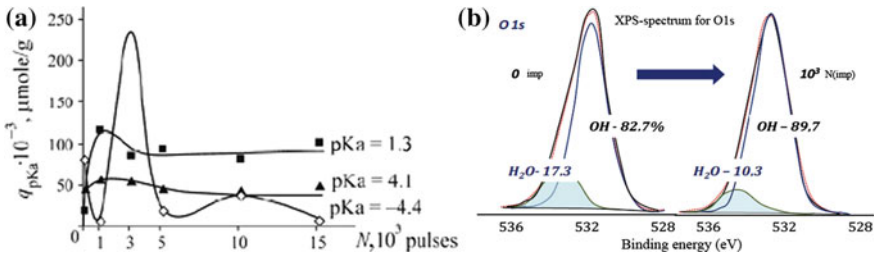

Fig. 12.2 **a** Number of adsorption centers at the surface of fluorite versus of $N_{imp} \sim (1–15) \times 10^3$ HPEMP; **b** higher resolution O1*s* of oxygen photoelectron spectra of surface of fluorite particles

by more than an order of magnitude (from 83.2×10^{-3} to 8.2×10^{-3} μmol/g) and a 5.5-fold increase in the number of centers with $pK_\alpha = 1.3$ (from 21.9×10^{-3} to 118.6×10^{-3} μmol/g; Bronsted acidic centers) (Fig. 12.2a), which indicates an increase in the electron donor capacity of the mineral surface.

Analysis of the oxygen XPS profile O1*s* (E_{be}(BE) = 531.7 eV) showed (Fig. 12.2b) that a $t_{treat} \sim 10$ s electromagnetic pulsed treatment of fluorite resulted in hydroxylation of the surface of mineral particles due to adsorption of products of radiolytic decomposition of physically sorbed water at the active sites of the mineral surface (E_{be} = 533.13 eV). The concentration of oxygen atoms associated with surface water decreased from 17.3 to 10.3% at., and the concentration of oxygen associated with hydroxyl groups increased from 12.1 to 14.1% at.

Increasing the time of pulsed treatment of fluorite to t_{treat} = 30 s caused the opposite effect (Fig. 12.2a) that is a major (by a factor of 3, compared to the initial sample) increase in the number of centers with $pK_\alpha = -4.4$ and a decrease in the content of centers with $pK_\alpha = 1.3$. This effect is, apparently, due to the processes of defect formation and deprotonation (adsorbed water molecules and hydroxyl groups) and/or dehydroxylation of the centers with $pK_\alpha = 4.1$ and 1.3. Continuous pulsed treatment of fluorite (t_{treat} = 50 s) caused a decrease in the content of centers with $pK_\alpha = -4.4$ by at least a factor of 11, indicating an increase in the donor capacity of the mineral surface.

The main changes in the acid-base properties of the *scheelite* surface under the action of HPEMP (t_{treat} = 150 s) are primarily associated with an increase in the number of Bronsted centers of the main type with $pK_\alpha = 12.8$ by a factor of 4.8–6 (from 5.5×10^{-3} in the initial state to 33.1×10^{-3} μmol/g). The content of acidic and neutral centers (pK_α = 1.3, 6.4, 7.3, and 8.8) did not change significantly during the treatment. This change in the acid-base properties indicates an increase in the acceptor capacity of the mineral surface.

Changes in the functional chemical composition of the *calcite* surface when exposed to HPEMP are mainly characterized by an antibate change in the number of centers with $pK_\alpha = 12.8$ and $pK_\alpha = 1.3$ depending on t_{treat}. Mutual transformation (transmutation) at $t_{treat} \leq 30$ s of Bronsted base and acid centers resulted in a weaker donor capacity and stronger acceptor properties of the mineral surface and

then, as the treatment time increased to $t_{treat} > 30$ s, recovery and strengthening of the donor capacity. At $t_{treat} \leq 50$ s, there was also an increase in the number of centers with $pK_\alpha = 4.1$ and $pK_\alpha = -4.4$, which can be associated with the processes of generation, accumulation, and annihilation of structural defects.

Analysis of the distribution of adsorption centers (active surface centers) by the magnitude of pK_α in gangue *quartz* in the initial state showed that the mineral surface was dominated by the main Lewis centers ($pK_\alpha = -4.4$). Smaller concentrations were also found of Bronsted acid ($pK_\alpha = 1.3$; 2.1; 4.1; 5.0; 6.0), neutral ($pK_\alpha = 7.3$), and basic ($pK_\alpha = 8.8$ and 12.8) centers. HPEMP treatment of the mineral ($t_{treat} = 30$–150 s) led to a decrease in the number (concentration, nmol/g) of the main Lewis centers with $pK_\alpha = -4.4$ by a factor of 1.2 (from 145.5 nmol/g in the initial state to ~120–115 nmol/g), a slight increase in the number of Bronsted acidic centers with $pK_\alpha = 5.0$, and a decrease in the number of Bronsted main centers ($pK_\alpha = 12.8$) from 20.7 nmol/g (in the initial state) to ~10.0 nmol/g ($t_{treat} = 10$ s) and further to ~5.5 nmol/g ($t_{treat} = 50$–100 s). In [24], as a result of treatment with an accelerated electron stream (dose 25–50 kGy) of moistened quartz glass, a decrease was observed in the content of active centers with $pK_\alpha = 14.2$ due to oxidation of silicon and formation of additional Si–O–Si bonds.

According to the IR Fourier spectroscopy data, under the action of HPEMP, the functional (hydrated) surface cover of the quartz particles changed, namely, the hydration level of the surface increased, which indicates a change in the energy state of the quartz surface. The IR spectra of quartz underwent appreciable profile transformations in the region corresponding to the stretch vibration of the O–H bond (3000–3700 cm^{-1}). For instance, in the spectrum of the untreated sample, an absorption band at 3650 cm^{-1} characteristic of OH groups was observed. According to [25, 26], this band can also be attributed to the existence on the mineral surface of single molecules of adsorbed water. Electromagnetic pulsed treatment of quartz ($t_{treat} = 10$ and 30 s) caused the appearance in the IR spectrum of a broad band in the spectral range of 3000–3700 cm^{-1}, which is typical of the so-called "polymers" of water (liquid-like) [25, 27]. Apparently, according to [28], the primary adsorption centers (of water molecules) were the silicon atoms in the most deformed and hydrated surface SiO_4 tetrahedra.

12.3.3 *Effect of Repetitive High-Voltage Nanosecond Pulses on Microhardness, Physicochemical and Flotation Properties of Minerals*

Microstructural changes in the surface layer of minerals caused by HPEMP resulted in an effective softening of their surface (Table 12.2): the maximum relative change (decrease) in microhardness ($\Delta HV = (HV_{0i} - HV_i)/HV_{0i}$, %, where HV_{0i} is microhardness of the samples in the initial state; HV_i is microhardness of the i-th sample after exposure to HPEMP) was observed after a $t_{treat} \sim 150$ s treatment and

Table 12.2 Effect of high-voltage nanosecond pulses (HPEMP) on microhardness *HV*, electrokinetic potentials ζ, water contact angle θ, and flotation ability (recovery, ε) of calcite/fluorite/scheelite/white gangue quartz

HPEMP treatment time, s	*HV*, MPa	ζ-potential, mV	$\theta°$ (calcite/quartz)	ε, %
0	790/876/2087/1425	−17.2/8.8/−20.6/−93.9	79.1/49.2	69/81/79/57
10	651/646/–/1344	−22.0/−6.1/−25.4/−98.7	84.0/50.5	74/88/77/53
50	366/538/1017/1229	−18.0/−9.4/−25.9/−102.2	80.5/43.4	77/88/91/50
100	297/425/–/1171	−14.4/−16.5/−26.8/−98.7	73.6/42.7	78/79/83/57
150	265/410/–/1013	−14.8/–/–/−102.4	73.2/38.5	75/78/89/57

was 66.5% (from 790 to 265 MPa) in calcite (Mohs hardness 3), 53.2% (from 876 to 410 MPa) in fluorite (hardness 4), 51.3% (from 2087 to 1017 MPa) in scheelite (Mohs hardness 5), and 29% (from 1424.6 to 1013.1 MPa) in quartz (Mohs hardness 7).

In general, noteworthy is the fact that under the action of nanosecond HPEMP, the relative change in the microhardness (ΔHV) and rate of change in the microhardness (*HV*) of dielectric minerals are, among other things, most likely determined by the mineral hardness (nature of chemical bonds, energy, valence), are the highest in minerals with a relatively low hardness (Mohs hardness), and in a number of cases are achieved at relatively low doses of electromagnetic pulsed radiation.

The electrokinetic potential of scheelite is negative throughout the pH range [19], which is largely due to the presence of surface defects carrying adsorbed oxygen and excess negative charges. In acidic media, intensive leaching of excess calcium ions occurs from the surface of scheelite, as a result of which complex ions and oxygen ions bearing negative charges are exposed on the surface of the mineral, for example, on the faces of pinacoid (001) [19]. The zeta potential of calcite in the pH range of 7–12.5 can be either positive in minerals of inorganic origin because of the excess of Ca^{2+} (or deficiency of CO_3^{2-}) or negative in calcite of biogenic origin due to the excess of CO_3^{2-} ions and organic substances (or deficiency of Ca^{2+}) [19]. The electrokinetic potential of type I fluorite (according to the classification in [19]) is positive over a broad range of pH values, which is due to the structure of the cleavage surface of crystals characterized by an elevated share of defects presence of positively attached adsorption centers. Apparently, in fluorite with a relatively low concentration of defects (type II, according to [19]), the zeta potential in an acid medium is negative, and an increase of pH to 7 leads to a decrease in the negative value of the potential to −2.62 mV, which remains unchanged to pH = 12 [19, 29].

The action of nanosecond high-voltage pulses caused a change in the charge state of the particle surface of calcium minerals and quartz (Table 12.2). In calcite, scheelite, and quartz, the absolute value of the zeta potential of the particles increased in the region of negative values. In calcite, the following changes were observed in the ζ-potential: −17.2 mV (reference sample), −22.0 mV (t_{treat} = 10 s);

in scheelite: −20.6 mV (reference sample), ∼−26.0 mV (t_{treat} = 30–100 s). In quartz, the maximum deviation of the ζ-potential from the initial value (−94 mV before the HPEMP treatment) was observed at t_{treat} = 50 and 150 s (−102 mV) and was ∼9%. Due to the overcharging of the surface of fluorite particles (apparently, type I mineral with a high defect content) as a result of HPEMP action, a shift of the electrokinetic potential of the mineral was recorded (8.8 mV in the reference sample) to the negative range (Table 12.2): −6.1 mV (t_{treat} = 10 s), −9.4 mV (t_{treat} = 50 s), −16.5 mV (t_{treat} = 100 s).

The effect of HPEMP on the electrostatic potential value (V, V) of the surface of the thin sections (KPFM method) is generally consistent with the trend of change in the ζ-potential of the mineral particles that is a decrease in the electrostatic potential of the fluorite (from 9.8 to 0.5 V) and scheelite (from 1.1 to −0.1 V) surface with the transition of scheelite V into the negative range, presumably due to the injection of charge carriers (electrons) from electrodes (and/or during the development of discharges between mineral particles) into dielectric minerals under the influence of electric fields of high tension (10^7–10^9 V/m), the capture of electrons by deep traps, and the formation of a space charge in crystals [30].

The change in the flotation activity of minerals was measured by the change in the contact angle ($\theta°$) of the surface of calcite and quartz thin sections and by the yield (recovery) of mineral particles into the flotation froth. It should be noted that calcite is a rock-forming mineral complicating the recovery of salable scheelite concentrates from the run-of-mine ore.

Short pulsed treatment of calcite (t_{treat} = 10 s) and quartz (t_{treat} = 10–30 s) caused an increase in the hydrophobicity of the mineral surface (Table 12.2): specifically, the contact angle of the calcite surface increased from 79° to 84° and in quartz $\theta°$ increased from 49° to 51°. With an increase in the dose of electromagnetic radiation (t_{treat} = 30–150 s), there was a gradual decrease in the contact angle from 79–80° to 73° in calcite and from 49–51° to 38° in quartz, which indicates a decrease in the hydrophobicity of the mineral surface with an increase in t_{treat}.

In monomineral flotation of calcite, fluorite, and scheelite, the optimal parameters were found of the preliminary HPEMP treatment (t_{treat} = 30–50 s) and the reagent treatment has been optimized for scheelite recovery, resulting in a 10–12% (from 79 to 91%) higher recovery of scheelite, 6% higher recovery of fluorite, and 8% higher recovery of calcite (Table 12.2).

Optical centers in crystals are known to act as (type as) adsorption centers [19], and an increase in the concentration of positively charged defects or a decrease in the concentration of negatively charged defects can cause an increase in the flotation activity of minerals and vice versa [19]. Apparently, the observed effect of electromagnetic pulsed destruction of scheelite fluorescence centers associated with negatively charged defects in the form of anionic complexes with a partially reduced central ion $\left\{\left[W^{5+}O_4\right]^{3-}\right\}^{/}$ and anion vacancies $V_A^{\bullet\bullet}$ [19] causes an increase in the sorption and flotation activity of the mineral at t_{treat} = 30–50 s.

Table 12.2 shows the effect of pulsed energy impacts on the flotation of pure milk white gangue quartz. In the result of a prolonged (t_{treat} = 100–150 s)

preliminary pulsed treatment of the gangue quartz samples, the flotation activity of the mineral in the presence of sodium oleate ($NaC_{18}H_{33}O_2$) was deteriorated by 10–11%. Adding liquid glass in combination with a fatty acid collector neutralizes the depressing effect of the preliminary pulsed treatment of t_{treat} = 100–150 s, and a decrease in the mineral yield into the flotation froth by ~7% was recorded in the result of HPEMP treatment of the mineral in the range t_{treat} = 30–50 s.

HPEMP treatment of ferruginous quartz from Lebedinsky Mining and Concentrator Project decreased the flotation activity of the mineral in the presence of an amine (cationic collector, 200 g/t) and starch (depressant, 200 g/t). In this case, the yield of the mineral into the flotation froth was decreased by ~6% (from 56.9 to 50.8%) at t_{treat} = 30 s.

12.4 Conclusions

In the result of the studies carried out using state-of-the-art precision physical and chemical analysis methods, the mechanism was identified behind the non-thermal action of high-voltage nanosecond pulses on the state of structural defects, functional chemical composition, and acid-base properties of the surface, as well as on the structurally sensitive (microhardness, optical, spectroscopic, electrical, physicochemical) and processing (flotation) properties of calcium minerals and quartz.

For the first time ever, the effect was described of a change in the composition and concentration of structural optically active defects in crystals of calcium minerals in the result of HPEMP treatment, namely: (i) accumulation of structural defects in calcite and fluorite; (ii) breakdown of scheelite fluorescence centers, associated with negatively charged defects, causing (among other factors) an increase in the sorption and flotation activity of the mineral at t_{treat} = 30–50 s.

In the result of the electromagnetic pulsed treatment, effective softening of the minerals (a relative change in the microhardness by 30–67%), directional change in electrical properties, hydrophobicity of the surface, as well as an increase in the flotation activity of calcium minerals by 5–12% and a decrease in the flotation ability of quartz by 7–11% were observed.

The findings attest to the possibility in principle and effectiveness of using pulsed energy impacts to achieve directed changes in the structurally sensitive (optical, spectroscopic, mechanical, electrical, physicochemical) and processing (technological, flotation) properties of naturally occurring dielectric minerals.

Acknowledgements This work was supported by the RF President's grant for the state support of leading scientific schools of the Russian Federation, Academician V.A. Chanturia's School NSh-7608.2016.5.

References

1. V.A. Chanturiya, Gorn. Zh. (Min. J.) (11), 7 (2017). (in Russian)
2. I.Zh. Bunin, M.V. Ryazantseva, A.L. Samusev, I.A. Khabarova, Gorn. Zh. (Min. J.) (11), 77 (2017). (in Russian)
3. E.D. Shepeta, L.A. Samatova, S.A. Kondrat'ev, J. Min. Sci. **48**(4), 746 (2012)
4. Y.P. Li, W.Y. Ching, Phys. Rev. B **31**(4), 2172 (1985)
5. V.A. Chanturiya, Y.V. Gulyaev, V.D. Lunin, I.Zh. Bunin, V.A. Cherepenin, V.A. Vdovin, A. V. Korzhenevsky, Trans. Russ. Akad. Sci. **366**(5), 680 (1999)
6. I.Zh. Bunin, N.S. Bunina, V.A. Vdovin, P.S. Voronov, Y.V. Gulyaev, A.V. Korzhenevsky, V.D. Lunin, V.A. Chanturiya, V.A. Cherepenin, Bull. Russ. Acad. Sci. Phys. **65**(12), 1950 (2001)
7. I.Zh. Bunin, *Theoretical Fundamentals of Nanosecond Electromagnetic Impulse Effects on Disintegration and Exposure of Finely Dispersed Mineral Complexes and Precious Metal Recovery from Ores*, Dr. Tech. Sci. Thesis, Moscow, 2009. (in Russian)
8. R. Brandenburg, Plasma Sources Sci. Technol. **26**(5), 053001 (2017)
9. V.A. Chanturiya, Y.V. Gulyaev, I.Zh. Bunin, V.A. Vdovin, A.V. Korzhenevsky, V.D. Lunin, V.A. Cherepenin, Trans. Russ. Akad. Sci. **379**(3), 372 (2001)
10. V.A. Chanturiya, Y.V. Gulyaev, I.Zh. Bunin et al., J. Min. Sci. **37**(4), 427 (2001)
11. A.B. Shvartsburg, Phys. Usp. **41**(1), 77 (1998)
12. V.A. Cherepenin, Phys. Usp. **49**(10), 1097 (2006)
13. V.A. Chanturiya, I.Zh. Bunin, A.T. Kovalev, Bull. Russ. Acad. Sci. Phys. **72**(8), 1053 (2008)
14. L.P. Hammett, *Physical Organic Chemistry. Reaction Rates, Equilibria and Mechanisms* (McGraw-Hill Book Company, New York, London, Mexico, Panama, Sydney, Toronto, 1970)
15. K. Tanabe, *Solid Acids and Bases. Their Catalytic Properties* (Academic Press, Kodansha, Tokyo, New York, London, 1970)
16. M.V. Ryazantseva, I.Zh. Bunin, J. Min. Sci. **51**(5), 140 (2015)
17. A.F. Stalder, T. Melchior, M. Müller, D. Saged, Th. Bluc, M. Unserd, Colloids Surf. A Physicochem. Eng. Asp. **364**(1–3), 72 (2010)
18. I.Zh. Bunin, V.A. Chanturiya, M.V. Ryazantseva, E.V. Koporulin, N.E. Anashkina, Bull. Russ. Acad. Sci. Phys. **82**(5), 561 (2018)
19. L.A. Barsky, O.V. Kononov, L.I. Ratmirova, *Selective Flotation of Calcium-bearing Minerals* (Nedra, Moscow, 1979). (in Russian)
20. O.A. Krasilschikova, A.N. Taraschan, A.N. Platonov, *Color and Luminescence of Natural Fluorite* (Naukova Dumka, Kiev, 1986). (in Russian)
21. N.S. Zayats, R.V. Konakova, V.V. Milenin, G.V. Milenin, R.A. Red'ko, S.N. Red'ko, Tech. Phys. Russ. J. Appl. Phys. **60**(3), 432 (2015)
22. V.V. Kulagin, A.V. Sokolov, V.A. Cherepenin, *Monopulse Location Using Powerful Nanosecond Microwave Pulses* (1999). http://www.cplire.ru/joined/win/lection5/text.html
23. N.V. Zakharova, M.M. Sychov, V.G. Korsakov, S.V. Mjkin, Condens. Media Interphase Borders **13**(1), 56 (2011). (in Russian)
24. V.E. Kurochkin, A.N. Krasovsky, I.V. Vasiljeva, S.V. Myakin, A.L. Zagranichek, AYu. Shmykov, Sci. Instrum. **18**(2), 3 (2008). (in Russian)
25. I.I. Plyusnina, *Infrared Spectra of Minerals* (Moscow State University Press, Moscow, 1977). (in Russian)
26. V.C. Farmer, *The Infrared Spectra of Minerals* (Mineralogical Society, London, 1974)
27. K. Nakamoto, *Infrared Spectra of Inorganic and Coordination Compounds* (Mir, Moscow, 1966). (in Russian)
28. B.J. Saikia, G. Parthasarathy, N.C. Sarmah, Bull. Mater. Sci. **31**(5), 775 (2008)
29. V.A. Chanturiya, S.A. Kondrat'ev, J. Min. Sci. **50**(1), 163 (2014)
30. V.A. Zakrevsii, N.T. Sudar, Phys. Solid State **47**(5), 961 (2005)

Chapter 13
The Influence of the Activity of the Mineral Additives on Physico-mechanical Properties of Concrete Compositions

N. I. Buravchuk, O. V. Guryanova, M. A. Jani and E. P. Putri

Abstract It has been experimentally proved that by introducing hydraulic additives of ashes or burnt rocks, it is possible to regulate the properties of concrete compositions. Characteristics of ashes and burned mine rocks are given. Technological methods of changing the activity of additives (ash, burnt rocks) are shown. The influence of the activity of ash and burnt rocks on the hardening of concrete compositions and the physical and mechanical properties of concrete has been studied.

13.1 Introduction

Obviously, concrete remains the most common building material. This material has great opportunities to meet the requirements for both low-rise and high-rise constructions. This is due to the great opportunities to regulate the properties of this material, depending on its purpose. Using various fillers, mineral additives, astringent and technological methods of manufacture, it is possible to obtain concrete compositions with predetermined properties and performance characteristics intended for long-term operation under conditions of increased loads, temperature differences and the action of corrosive media. A special role in managing the properties of concrete compositions belongs to mineral hydraulic additives.

N. I. Buravchuk (✉) · O. V. Guryanova (✉)
I. I. Vorovich Mathematics, Mechanics and Computer Sciences Institute, Southern Federal University, Rostov-on-Don, Russia
e-mail: burav@math.rsu.ru

O. V. Guryanova
e-mail: oguryanova@sfedu.ru

M. A. Jani · E. P. Putri
University of 17 Agustus 1945 Surabaya, Surabaya, Indonesia

E. P. Putri
Khon Kaen University, Khon Kaen, Thailand

I. A. Parinov et al. (eds.), *Advanced Materials*, Springer Proceedings in Physics 224, https://doi.org/10.1007/978-3-030-19894-7_13

Research of scientists and practitioners is aimed at improving the technology of production of concrete compositions with the aim to improve their properties, to increase durability while reducing the material intensity and cost. In this regard, the priority in the technology of concrete compositions is the use of products from technogenic raw materials. It can be fillers, finely dispersed fillers, active additives. The most acceptable way is the use of mineral additives that allow us to regulate the properties of concrete: increase strength, density, durability and other physical and mechanical properties and performance characteristics while reducing the consumption of binders, aggregates from natural raw materials. Utilization of technogenic raw materials is a major environmental problem, as dozens of man-caused waste from the mining, metallurgical, coal industries, heat energy waste, etc. accumulate on the earth's surface. The main way to solve this problem is the use of technogenic raw materials in building materials technology and road construction. In this direction, there are [1–10] technical solutions of many researchers. However, most of these studies do not find practical implementation. One of the main reasons for this situation is the instability of waste properties, as well as the absence of processing complexes for waste enrichment and the production of conditioned products that meet the requirements of regulatory documents for use in building materials technology, road construction and other general construction works in technogenic deposits.

13.1.1 Research Purpose

The purpose of this work is to study the effect of the activity of mineral additives from fly ash from the burning of coals and burned mine rocks on the physico-mechanical properties of concrete compositions.

13.1.2 Research Scope

We studied:

(i) composition and properties of fly ash and burned mine rocks;
(ii) ways to increase the activity of fly ash and burned mine rocks;
(iii) the influence of the activity of additives from fly ash and burned mine rocks on the physical and mechanical properties of concrete;
(iv) features of the formation of the structure and properties of cement stone with additives of ash, burned mine rocks.

13.2 Research Method

The object of research was burned mine rocks and fly ash, accumulated in dumps in the territory of the Rostov region (Russia). Preliminary preparation of the objects of investigation consisted of crushing and grinding. The fineness of the grinding was 350 m^2/kg.

Analytical and laboratory studies were performed to obtain information on the chemical and material composition of the raw materials, activity and the physical and mechanical properties of dispersed fly ash and burned rock. Then, technological tests were carried out for studying the effect of the activity of mineral additives on the main technical characteristics of concrete compositions. Methods of physical and chemical analysis have studied the effects of ash additives and burned rock on hardening and the properties of cement stone. Carrying out a complex of physic-ochemical and technological research makes it possible to determine the effectiveness and expediency of using products from technogenic raw materials to regulate the properties of concrete compositions.

13.3 Results and Discussion

13.3.1 Characteristics of Ashes and Burnt Mine Rocks

The objects of investigation of this work are burnt mine rocks and dry fly ash (fly ash). These are the products of thermal impact on coal-bearing rocks and mineral constituents of coal. The conditions for the formation of these materials are different.

Fly ash is a finely dispersed product of high-temperature processing of the mineral part of coals. It is formed when they are burned in a pulverized state in boiler furnaces and precipitated by trapping devices from chimneys. Burnt mine rocks are products of prolonged self-baking of overburden and enclosing rocks during coal mining. Under the influence of atmospheric oxygen, spontaneous burnout of organic substances and sulfur takes place, which lasts for dozens of years. In burnt mine rocks, the content of carbonaceous impurities does not exceed 5.0%. Burnt mine rocks of a homogeneous composition with a dense structure and a smooth stone surface are characterized by increased mechanical strength, resistance to abrasion, thermal and atmospheric influences. According to the chemical, granulometric and phase-mineralogical composition of ash and burnt rocks are in many aspects identical to natural mineral raw materials. They contain crystalline, amorphous and organic substances. The amorphous component of the ash is represented by a glass phase and an amorphous clay substance—metakaolinite, amorphous silica and alumina. In the study of waste by the methods of physical and

Table 13.1 Chemical composition of technogenic raw material

Sample	SiO_2	Al_2O_3	Fe_2O_3	CaO	MgO	SO_3	TiO_2	$K_2O + Na_2O$	P_2O_5	p.p. p[a]
Fly ash	56.74	21.53	6.43	2.15	1.88	0.69	0.96	2.84	0.15	6.56
Burnt mine rocks	59.87	19.08	5.23	2.25	1.71	2.04	1.42	2.95	0.12	4.93

[a]p. p. p.—loss on ignition

chemical analysis, it was established that the crystalline phase includes the slightly modified grains of the minerals of the initial fuel: quartz and its modifications, feldspars and other thermally stable minerals. There are crystalline neoplasms that have arisen during fuel combustion (mullite, hematite, magnetite, calcium silicates, etc.). Unburned fuel particles are present as impurities. They are different from the initial state and are in the form of coke, semicoke and graphitized carbonaceous matter. Coking products (semi-coke and coke residues) are resistant to oxidation and are durable when exposed to moisture and temperature changes.

Table 13.1 shows the averaged data on the chemical composition of these wastes. The chemical composition of the investigated objects is mainly represented by oxides of silicon, aluminum and iron, and modulo basicity, taking into account the ratio of alumina and silica, the technogenic raw material in question is acidic, with a high content of coloring oxides. The composition of the waste and its properties are not stable. This is one of the main restrictions to the widespread use of this technogenic raw material. However, with the observance of the recommended technological methods in the preparation and processing of waste from them, high-quality products can be obtained.

13.3.2 Activity of Ashes and Burning Mine Rocks

In the manufacture of concrete compositions, hydraulic additives are widely used, both in the concrete mix and in the cement composition. The provision of the required physical and mechanical properties of concrete largely depends on the composition and physical state of the mineral additives used.

An important property of ashes and burnt mine rocks, as mineral additives from technogenic raw materials, is the ability to exhibit hydraulic activity. The presence of components in the composition of the burnt mine rocks and fly ash, associated with their activity, is related to their origin. In the process of thermal exposure, the molecular bonds of aqueous aluminosilicates and other minerals, the dehydration of clay minerals, and the appearance of metakaolinite and a number of active modifications of aluminum oxides, soluble or active forms of silicic acid, iron oxides occur. The presence of these substances determines the manifestation of the physico-chemical and pozzolanic activity of this burnt mine rocks. With weathering in the grains of rocks, the microcracks arise. These factors lead to the appearance in

the products of thermal action and deleting some energy potential. Burnt mine rocks exhibit the properties of active clay, and ash shows characteristics a medium-active silicate-ferruginous additive. Such materials do not harden themselves and being to shut by water, they do not grasp and do not pass into a stone-like state. However, they are able to exhibit pozzolanic activity and to interact with inorganic and organic astringents.

A simple expression of the hydraulic activity of mineral additives is the clay-iron modulus equal to the ratio of Σ (Al_2O_3 + Fe_2O_3) to the amount of SiO_2. Based on the value of this modulus, in accordance with the classification of Knigina [6, 11], the investigated ash and burnt mine rocks refer to active and highly active argillites and siltstones. The clay-iron modulus is >0.4. A characteristic index for burning mine rocks and ash is adsorption activity, which largely depends on their dispersion. The adsorption activity of ash and burning mine rocks in the initial state, estimated from the change in optical density during the adsorption of methylene blue [12], is within the range 0.022–0.031 [13]. The effectiveness of the action of ash or burnt mine rock on the properties of concrete largely depends on the dispersion and the state of the surface of the additives. In the experiment, the ash or burned mine rock was introduced into the concrete mix as follows:

1. finely dispersed additive instead of part of cement;
2. activated additive obtained by co-grinding ash or burnt mine rocks with cement;
3. activated additive obtained by co-grinding ash or burnt mine rocks with cement and alkali-containing component.

Preparation of ash and burnt mine rocks was carried out in a vibrating mill MV-400-EKS. The specific surface of the finished product varied between 350 and 450 m^2/kg. As an alkali-containing additive, solid wastes of spent electrolyser solution of sodium hydroxide production were used. The content of the alkali-containing additive may be from 5 to 10% of the weight of the ash, the burnt mine rocks or a mixture thereof. The change in adsorption activity of ash, burnt rock and their mixture after grinding with cement and alkaline additive is given in Table 13.2 The characteristic of adsorption activity is a change in the optical density of the methylene blue dye (initial concentration) before treatment with the dye and after treatment (final concentration of the dye):

Table 13.2 Adsorption activity of mineral additives (ΔD)

№ p/p	Physical state of mineral additives	Evaluation of adsorption activity by using ΔD		
		Fly ash	Burnt mine rocks	$\frac{\text{fly ash}}{\text{burnt mine rocks}} = 1:1$
1	Initial	0.031	0.022	0.05
2	After grinding with cement	0.119	0.097	0.26
3	After grinding with cement and alkaline additive	0.176	0.158	0.62

$$\Delta D = D_1 - D_2,$$

where D_1 is the dye density of the initial concentration before processing the sample of the rock and D_2 is the density of the dye after treatment of the sample of the rock.

In a joint grinding of fly ash, burnt mine rocks or their mixture with cement, cement and alkaline additives, the mechanochemical activation is enhanced, which manifests itself in an increase in the specific surface and adsorption activity of the mineral additive. The adsorption activity of the additives during co-grinding with cement is increased by 4–5 times, with cement and alkaline additives more than 5 times. The greatest effect of activation is achieved in a mixture, consisting of finely divided ash and burnt mine rocks. In this case, the activation is enhanced due to the pronounced synergetic effect of the joint influence of ash and burnt mine rocks, which is confirmed by an increase in the adsorption activity (ΔD) of the mixture of the mineral additive by 12.5 times. Mechanochemical activation of ash, burnt mine rocks or their mixture was the base for obtaining an efficient and economical binder [14] based on technogenic raw materials. Figure 13.1 shows the change in the strength of the binder, depending on the ratio of cement and ash and the physical state (degree of activation) of the additive.

Activation of ash or burnt mine rocks allows obtaining a cement grade of at least 300, with cement savings of more than 20%. It follows from Fig. 13.1 the binder has the greatest strength, containing activated ash after grinding with cement and alkaline additive. For the activated burnt mine rocks the same dependence is observed. The difference is only in quantitative indicators of strength, they are slightly lower in comparison with ash. To assess the effect of additives of ash or burnt mine rocks, depending on their activity, samples of concrete compositions in the form of cubes $10 \times 10 \times 10$ cm^3 were made. Hardening of the samples was carried out in conditions of natural curing and steam curing regime: (i) pre-exposure samples for 5–6 h, (ii) the temperature rising to 90 °C for 3 h, (iii) isothermal holding at this temperature for 8 h, (iv) lowering the temperature for 3 h.

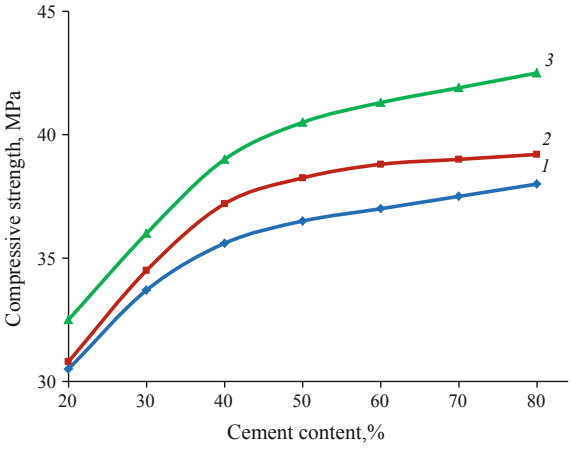

Fig. 13.1 Dependence of the strength of astringents on the composition: *1*—ash; *2*—activated ash with cement; *3*—activated ash with cement and alkaline additive

The diagram (Fig. 13.2) and Fig. 13.3 show the nature of the change in the strength of concrete containing activated fly ash in respect to the initial strength of concrete. The amount of additive added was 20% of the weight of the cement.

The obtained strength results indicate that, depending on the physical state and activity of the additive, the initial grades of concrete (concrete class) increase, namely: M100 → M200; M150 → M300; M200 → M350; M300 → M550. The same dependence was also found for burnt mine rocks concrete, the difference only

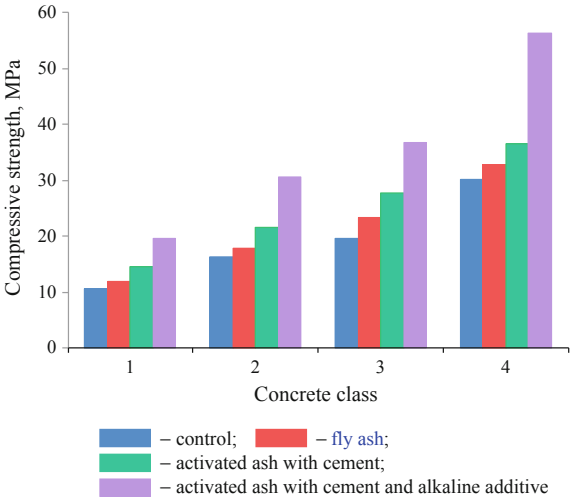

Fig. 13.2 Effect of ash activity on the strength of concrete compositions: 1—B7.5; 2—B12.5; 3—B15; 4—B22.5. —control; —fly ash; — activated ash with cement; —activated ash with cement and alkaline additive

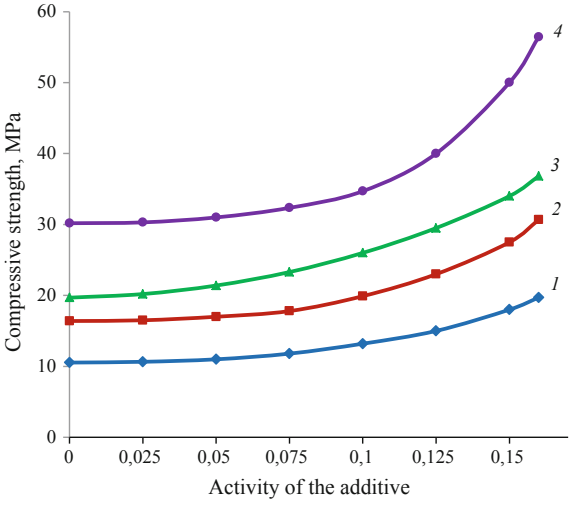

Fig. 13.3 Change in strength of concrete depending on the activity of the additive: (class of concrete: *1*—B7.5; *2*—B12.5; *3*—B20; *4*—B22.5)

in absolute values of strength. Economy of cement by using fly ash as a finely dispersed additive (initial ash) was 20%, as activated additive was from 30 to 50%, and by using burnt mine rocks as additive—from 15 to 40%.

13.3.3 Physical and Mechanical Properties of Concretes with Activated Additives

As an example, the results on the use of fine-dispersed ash and burnt mine rocks in concretes are shown (Table 13.3). In the result of the research, it was found that fine-dispersed ash and burnt mine rocks in concrete are also an active additive strengthening the hydration process, fine aggregate, plasticizer, microfiller, improving the structure of concrete, increasing the density of cement stone. For concrete containing finely dispersed additives, it is characteristic to increase the volume of mixed cement-ash (cement-rock) dough, which for moderately hard mixtures is 320–380 L/m^3, for mobile equals to 420–470 L/m^3. This is reflected in the rheological properties of concrete mixtures: plasticity, connectivity, water retention capacity is improved, homogeneity, workability of the concrete mixture is improved. Thus, the workability of a mixture with fine additives is significantly improved and sedimentation phenomena are absent. The quality of product surfaces is improved by reducing the number of large shells and pores. Visual control of the compacting of the concrete mix allows us to conclude that mixtures with ash have better molding properties than for concretes without ash. The plasticizing effect of the ground burnt mine rocks is lower than that of ash.

This is mainly due to the shape, porosity and roughness of the surface of the particles of the burnt mine rocks. It was found that to provide high strength properties of concrete, it is necessary to use finely dispersed additives with a specific surface of 500–600 m^2/kg. This conclusion agrees with the statement of [15] that the optimum dispersity of the mineral additive to cement should exceed the dispersity of the clinker mineral (cement) by 120–200 m^2/kg.

Concretes containing ash or burnt mine rocks formations have high bending strengths. Figure 13.4 shows the dependence of the strength of ash concrete in bending from the compressive strength.

Additions of ash or burnt mine rocks have an additional plasticizing effect. Especially it is characteristic for fly ash. Samples made of concrete with the addition of ash, burnt mine rocks had a smooth surface without shells and large pores.

Table 13.3 Physical and mechanical properties of concretes with technogenic additives

Class of concrete, (mark) sediment of the cone	Strength, MPa				Mark		Bulk weight, kg/m^3	Saving of cement, %
	Steaming[a]		Normal hardening, 28 days		Frost resistance	Water-tightness		
	R_c	R_b	R_c	R_b				
Concrete with ash								
B7.5; (M100) OK 3–4 cm	8.1	0.84	12.05	1.27	F 50	W2	2280	50
B10; (M150) OK 3–4 cm	11.3	2.24	18.74	3.26	F50	W2	2250	50
B15; (M200) OK 3–4 cm	15.7	3.50	22.43	5.12	F75	W4	2210	50
B20; (M250) OK 3–4 cm	18.2	4.06	26.02	5.83	F100	W4	2240	30
B22.5; (M300) OK 1–3 cm	22.6	4.55	32.29	6.51	F200	W6	2230	30
B30; (M400) OK 4–6 cm	29.8	5.20	41.52	7.44	F300	W8	2220	25
B35; (M450) OK 1 cm	33.4	5.38	47.71	7.85	F300	W10	2230	25
Concrete with burnt mine rocks								
B7.5; (M100) OK 3–4 cm	7.8	0.64	11.67	0.94	F50	W2	2200	20
B10; (M150) OK 3–4 cm	10.8	1.48	15.98	2.15	F50	W2	2230	50
B15; (M200) OK 3–4 cm	14.6	2.38	21.47	3.43	F75	W2	1990	15
B20; (M250) OK 1–3 cm	17.9	3.08	26.43	4.47	F100	W4	2130	15
B22,5; (M300) OK 4–6 cm	21.5	3.52	31.84	5.12	F200	W6	2150	15
B30; (M400) OK 4–6 cm	28.0	4.06	39.27	5.83	F250	W8	2180	10
B35; (M450) OK 1 cm	32.8	4.27	46.13	6.17	F250	W10	2210	10

[a]After steaming, the strength of concrete is at least 70% of the design

13.3.4 Structurization in Concretes with Activated Additives of Ash, Burnt Mine Rocks

The principles of the physicochemical mechanics of disperse systems [16, 17] are the theoretical base for the methods of obtaining concrete compositions. The base of these principles is the creation of conditions for directed structuring and formation

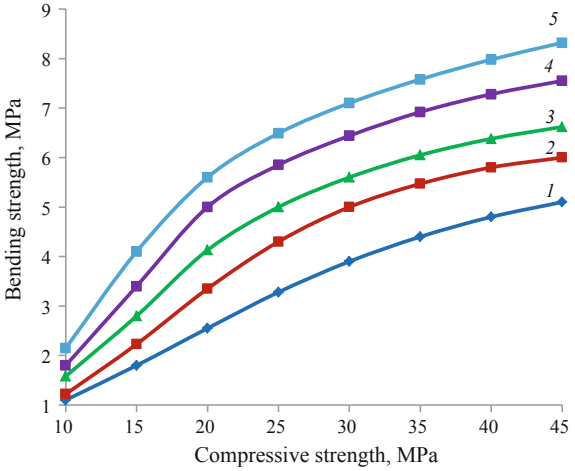

Fig. 13.4 Dependence of the strength of concrete compositions in bending on the compressive strength (class of concrete: *1*—B7.5; *2*—B12.5; *3*—B20; *4*—B22.5)

of compositions of a given structure and properties. One of the ways of controlling the structure formation of a disperse system is the introduction of dispersed mineral additives. To increase the number of new growth in a colloidal, and then in a crystalline form, it is necessary to enrich the phase composition with substances capable of reacting with the active part of the cement. Such substances are ash and burnt mine rocks. By assessing the effect of mineral additives of fly ash, burnt mine rocks or their mixture on the properties of binder, concrete, it is necessary to take into account the presence on the surface of mineral materials not only the finest colloidal films of oxides and hydroxides and amorphous silica and other active components, but also the state of the particle surface. It is known that on the surface of mineral materials there are acidic and basic centers of Lewis and Brönsted type [18, 19], which largely determine its activity. The genesis of ash and burnt mine rocks is associated with high temperatures. This contributes to the corrosion and destruction of the surface, the dispersion of particles, the appearance of microcracks and micropores, the violation of the crystal lattice and the opening of active sites. Additional activation of the surface occurs when forcibly shredding waste in mills of different action or disintegrators, both alone and in admixture with additives. The study of the hardening of concretes with additives has shown that both clinker components of cement and mineral additions of ash or burnt mine rocks take part in the structure formation. This point of view is also confirmed by the results of other authors [20–23]. Under identical conditions of hardening, due to the presence of glass phase, fly ash shows a more active participation in the structure formation in comparison with the burnt mine rocks. This can be judged by the greater intensity of neoplasm lines in X-ray diffraction studies. However, the phase composition of the neoplasms is basically identical, the difference is only in the quantitative content. Fine particles of fly ash or burnt mine rocks, affecting the process of hydration of cement, perform also the role of microfiller. At the stage of structure formation, a large number of new phase nuclei form on their surface, as on the substrate, and the

nuclei grow in the pore space of the cement stone. There is a filler consolidation and hardening of cement stone. This helps to create a more dense structure of the hardening composition. In such a system, internal stresses and cracking reduce. In the result of the intensifying effect of additions of fly ash or burned rock with pozzolanic activity on the cement and its hydration products, additional structural bonds form in the contact zone of the particles.

The resulting additional connections fill the voids and pores of the contact zone. As a result, the porous structure of the artificial stone changes: the number of fine pores and capillaries increases. Indirectly, the decrease in the porosity of the cement stone can be judged by the value of water absorption. Binders, containing as an additive fly ash or burnt mine rocks, the water absorption was 2–3%.

The adsorbed water in such micropores will be in the film state. It has an oriented structure and changed properties [24, 25]. The increase in the number of fine pores has a positive effect on strength, frost resistance and water resistance, deformability of concrete, which is confirmed experimentally. The introduction of ash additives, burnt mine rocks with pozzolanic activity, increases the efficiency of using cement by binding free calcium hydroxide to low-basic calcium hydrosilicates, such as C_3SH_2, C_3SH (A), C_4H_{13}, and hydroaluminates C_3AH_6, C_4AH_{13}. Investigations of the authors [26, 27] have established that crystals of low-basic calcium hydrosilicates possess the greatest strength. The content of free calcium hydroxide in the presence of additives of ash, burnt mine rocks decreases in comparison with the control, which is confirmed by radiographic studies. On X-ray diffraction patterns with the addition of ash and burnt mine rocks, the value of the $Ca(OH)_2$ peak decreased, which indicates a more complete binding of calcium hydroxide by active components of ash and burnt mine rocks.

By hardening, a coagulation structure first appears, the strength of which is provided by intermolecular forces. Interlayers of water weaken these forces. These structures are weak. They are thixotropic and restore their mechanical properties, disturbed by shaking. As the hydration processes deepen, the volume of neoplasms increases. This leads the system to cramped conditions (supersaturation), to compaction of the gel phase, to contacting the particles. Coagulation structures are transformed into coagulation-condensation structures with the formation of crystalline substances that harden with time to compounds with the crystallization-condensation type of the structure.

The high strength of such structures is due to strong ionic and covalent bonds. These structures are typical for hardened cement and concrete. Figure 13.5 shows the microstructure of binders. The cement stone of mixed finely ground astringent is distinguished by its density and strength, due to the optimal combination of the structural and dimensional parameters of the mixture and the high adhesion strength of the neoplasms. Cement stone, formed by small crystalline calcium hydrosilicates, due to increased contacts between them, has a dense structure of increased strength.

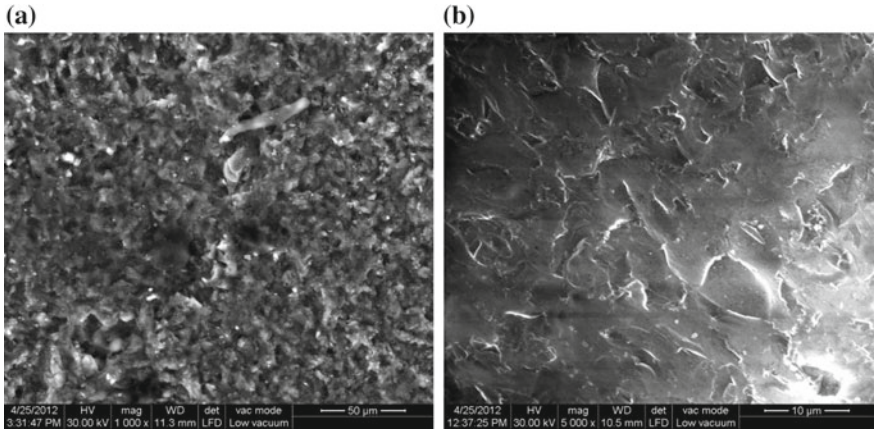

Fig. 13.5 Microstructure of mixed binder: **a** astringent with burnt mine rocks (×1000), **b** astringent with fly ash (×5000)

13.4 Conclusion

Despite the results achieved in the field of application of ash, burnt mine rocks, there are a number of directions that require additional research:

(i) detailed study of the energy state of the active components and peculiarities of their manifestation of pozzolanic properties,
(ii) optimization of the amount of natural raw materials replaced in dependence on the activity and physical and mechanical properties of the waste,
(iii) development of new economical ways of producing mixed cements,
(iv) development of normative documentation aimed at expanding the scope of application of these materials,
(v) development of methods for assessing the effectiveness of the use of ashes and burnt mine rocks in the technology of building materials.

The solution of these problems will result to improved technologies for using fly ash and burned mine rocks, increasing their utilization, cleaner environment, liberated land areas, saving raw materials and energy resources.

Acknowledgements This research was carried out within the framework of financing of the Ministry of Education and Science of the Russian Federation for the project No. BCH0110-11/2017-20.

References

1. A.V. Volzhensky, I.A. Ivanov, B.N. Vinogradov, *The Use of Ash and Fuel Slags in the Production of Building Materials* (Stroyizdat, Moscow, 1984), 255 p. (in Russian)
2. Y.M. Bazhenov, L.A. Alimov, B.B. Voronin, Izv. Univ. Build. **4**, 68 (1997) (in Russian)
3. N.I. Buravchuk, K.I. Rutkov, *Processing and Use of Coal Mining Waste and Incineration* (SKNC VSh Press, Rostov-on-Don, 1997), 224 p. (in Russian)
4. N.I. Buravchuk, V.M. Budnitsky, V.F. Brazhnikov et al., *Resource Saving in the Technology of Binders and Concretes* (Rostov-on-Don, 1999), 176 p. (in Russian)
5. L.I. Dvorkin, O.L. Dvorkin. *Building Materials from Industrial Waste* (Phoenix, Rostov-on-Don, 2007), 368 p. (in Russian)
6. G.I. Knigina, *Building Materials from Burned Mine Rocks* (Moscow, 1966), 206 p. (in Russian)
7. T.E. Mikheeva, *Investigation of Burned Mine Rocks with the Aim of Obtaining Corrosion-Resistant Slurry Mortars*. Ph.D. Thesis, Kharkov, 1982 (in Russian)
8. V.I. Solomatov, Build. Mater. Equip. Technol. 21st Century **1**, 28 (2000) (in Russian)
9. K.N. Trubetskoi, V.N. Umanets, Min. Mag. **1**, 12 (1992) (in Russian)
10. P.P. Gedeonov, L.V. Yudin, Build. Mater. **2**, 16 (1994) (in Russian)
11. G.I. Knigina, E.A. Kucherova, N.S. Zhitova, Izv. Vuzov. Constr. Architect. **3**, 71 (1978) (in Russian)
12. G.I. Knigina, News High. Educ. Inst. Constr. Architect. **2**, 82 (1962)
13. N.I. Buravchuk, O.V. Guryanova, M.A. Jani, E.P. Putri, in *Advanced Materials—Proceedings of the International Conference on "Physics and Mechanics of New Materials and Their Applications", PHENMA 2017*, ed. by I.A. Parinov, S.-H. Chang, V.K. Gupta. Springer Proceedings in Physics, vol. 207 (Springer, Cham, Heidelberg, New York, Dordrecht, London, 2018), pp. 161–169, 605
14. N.I. Buravchuk, O.V. Guryanova, *The Way of Obtaining Binder for Concrete and Mortar*. Positive Decision of 03.07.2018 on Russian Patent on Inventory (application No. 2017132779, 19.09.2017) (in Russian)
15. E.G. Velichko, J.S. Belyakova, Build. Mater. **3**, 27 (1966) (in Russian)
16. P.A. Rebinder, B.B. Segalov, V.A. Amelina, in *Proceedings of International Congress on Chemistry of Cement*, vol. 2, issue 1 (Stroyizdat, Moscow, 1976), p. 58 (in Russian)
17. P.A. Rebinder, *Surface Phenomena in Disperse Systems. Physico-chemical Mechanics* (Nauka, Moscow, 1979), 384 p. (in Russian)
18. R. Ailer, *Chemistry of Silica*, vol. 2 (Mir, Moscow, 1982), 712 p. (in Russian)
19. K. Tanabe, *Solid Acids and Bases* (Mir, Moscow, 1973), 183 p. (in Russian)
20. G.I. Knigina, *Use of Fossils as Building Materials* (Tomsk, 1963), p. 79 (in Russian)
21. V.V. Vlasov, Izv. Univ. Build. **5**, 42 (1997) (in Russian)
22. A.N. Ryazanov, P.E. Krytsya, Naukovii visnik NAU **2**, 3 (2009) (in Ukrainian)
23. M.I. Ukhanova, E.B. Khobotova, S.N. Tolmachev, in *Abstract International Scientific and Technological Conference Physico-chemical Problems in the Technology of Refractory Nonmetallic and Silicate Materials*, Caravel, p. 153 (2010) (in Russian)
24. G.N. Zatsepina, *Physical Properties and Structure of Water* (Moscow State University, Moscow, 1987), 170 p. (in Russian)
25. B.V. Deryagin, Z.M. Zorin, V.D. Sobolev et al., *Bound Water in Disperse Systems*, issue 5 (Moscow State University Press, Moscow, 1980), p. 4 (in Russian)
26. V.V. Timashev, *Cement* **2**, 6 (1978) (in Russian)
27. L.I. Sychev, V.P. Sokolov, V.V. Timashev et al., in *Proceedings of Moscow Chemical Technologic Institute*, vol. 98, p. 112 (1977) (in Russian)

Part II
Physics of Advanced Materials

Chapter 14
New Theory of Laser. Method of Density-Matrix

Boris V. Bondarev

Abstract This paper is based on the Lindblad equation for the statistical operator and the equation for the density matrix, which are equivalent to each other. These equations contain a dissipative operator and a dissipative matrix. Described equations are applied here for the formation of the equations which characterize the operation of the laser. First, the Hamiltonian was given by means of a unitary transformation into a diagonal form. Then a dissipative matrix was found, which characterizes the operations of thermodynamic transitions of the atom between the energy levels, pumping and attenuation operations. By using the diagonal of the Hamiltonian, dissipative matrix equations are obtained, which describe the continuous work of the laser. From the kinetic equation for the radiation, the spectral density of the radiation energy at the laser output is found.

14.1 Introduction

In 1964, N. G. Basov, A. M. Prokhorov, H. I. H. Townes won the Nobel prize. They were awarded this prize for fundamental research in the field of quantum electronics. These studies led to the creation of masers and lasers [1, 2]. In books [3, 4], the formulas describing modern lasers are given.

Consider the principle of the operation of quantum generator-laser. The main element of the quantum generator is the active medium, i.e. the substance in which the inverse population of levels is created. The active medium is usually in the form of a long cylinder (see Fig. 14.1).

At the ends of the cylinder perpendicular to its axis are two plane-parallel mirrors, one at each end. The purpose of these mirrors is to increase the length of the path on which the radiation is amplified by repeatedly passing the beam through the active medium. Mirrors form a so-called resonator. Between them there is a standing electromagnetic wave. One of the mirrors is made translucent. Through

B. V. Bondarev (✉)
Moscow Aviation Institute, Moscow, Russia
e-mail: bondarev.b@mail.ru

I. A. Parinov et al. (eds.), *Advanced Materials*, Springer Proceedings in Physics 224, https://doi.org/10.1007/978-3-030-19894-7_14

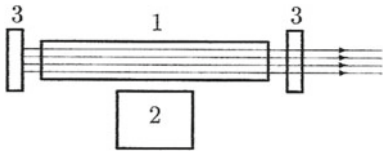

Fig. 14.1 Quantum generator circuitry: 1—active substance; 2—pumping device; 3—mirrors

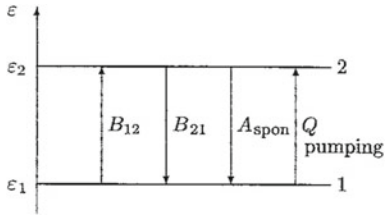

Fig. 14.2 Two-level scheme of interaction of an atom with radiation

this mirror, the resonator emits electromagnetic radiation in the form of a narrow, almost non-divergent beam. The process in which the active medium is transmitted in some way energy and creates an inversion of the population levels, called pumping. Pumping energy can be obtained in the form of light, electric current, energy of chemical or nuclear reactions, thermal or mechanical energy.

Various methods have been proposed to create population inversion of energy levels. The most convenient and widespread method is the two-level Bass and Prokhorov method proposed in 1955. Atoms or molecules of the active substance are affected in some way intensively so that electrons in them pass from the ground state $\varphi_1(r)$ with energy ε_1 to the excited state $\varphi_2(r)$ with energy ε_2 (see Fig. 14.2).

As a result, a sufficiently intense pumping saturation is achieved, in which the number of N_2 electrons in the state $\varphi_2(\boldsymbol{r})$ becomes equal to the number of N_1 electrons in the ground state $\varphi_1(\boldsymbol{r})$. At the same time for a couple of levels ε_1 and ε_2 occurs population inversion ($N_1 > N_2$). Only a small part of the energy transmitted to the active medium during pumping is converted into the energy of the generated radiation. Most of this energy goes into heat. The active medium is very hot and sometimes it has to be intensively cooled.

14.2 The Lindblad Equation and the Equation for Density Matrix

In quantum mechanics, the most general description of the system is the statistical operator $\hat{\varrho}$. The statistical operator at any given time must be normalized $\mathrm{Tr}\,\hat{\varrho} = 1$, self-adjoint $\hat{\varrho}^* = \hat{\varrho}$, and positive definite. The statistical operator $\hat{\varrho} = \hat{\varrho}(t, q)$ depends on the time t and the quantum coordinate of the q system. The equation that describes the Markov process was obtained by Lindblad [5]. This equation looks as

$$\mathrm{i}\hbar\dot{\hat{\varrho}} = [\widehat{H}\hat{\varrho}] + \mathrm{i}\hbar\widehat{D}, \tag{2.1}$$

where $\widehat{H}$ is the Hamiltonian of the system,

$$\widehat{D} = \sum_{jk} C_{jk}\left\{\left[\hat{a}_j\hat{\varrho}, \hat{a}_k^+\right] + \left[\hat{a}_j, \hat{\varrho}\hat{a}_k^+\right]\right\}, \tag{2.2}$$

C_{jk} is a some number, $\hat{a}_j$ is an arbitrary operator. The $\widehat{D}$ operator is called the dissipative operator. This statement can be written as

$$\widehat{D} = \sum_{jk} C_{jk}\left\{2\hat{a}_j\hat{\varrho}\hat{a}_k^+ - \hat{a}_k^+\hat{a}_j\hat{\varrho} - \hat{\varrho}\hat{a}_k^+\hat{a}_j\right\}. \tag{2.3}$$

The density matrix $\varrho_{nn'}(t)$ is related to the operator $\hat{\varrho}(t,q)$ by the formula

$$\varrho_{nn'}(t) = \int \varphi_n^*(t,q)\hat{\varrho}(t,q)\varphi_{n'}(t,q)\mathrm{d}q. \tag{2.4}$$

This formula specifies the density matrix $\varrho_{nn'}(t)$ in the n-representation. The wave function $\varphi_n(t,q)$ can be found from the Schrödinger equation:

$$\mathrm{i}\hbar\dot{\varphi}_n = \widehat{H}\varphi_n. \tag{2.5}$$

The equation for the density matrix was derived from the Liouville–von Neumann equation in [6, 7]. This equation is similar to the Lindblad equation and has the form:

$$\begin{aligned}\mathrm{i}\hbar\dot{\varrho}_{nn'} = &\sum_m (H_{nm}\varrho_{mn'} - \varrho_{nm}H_{mn'}) \\ &+ \mathrm{i}\hbar\left\{\sum_{mm'}\gamma_{nm,m'n'}\varrho_{mm'} - 1/2\sum_m(\gamma_{nm}\varrho_{mn'} + \varrho_{nm}\gamma_{mn'}\right\},\end{aligned} \tag{2.6}$$

where H_{nm} are the matrix elements of the Hamiltonian $\widehat{H}$ system, $\gamma_{nm,m'n'}$ is the some matrix,

$$\gamma_{nn'} = \sum_m \gamma_{mn',nm}. \tag{2.7}$$

Equation (2.6) can be written as

$$\mathrm{i}\hbar\dot{\varrho}_{nn'} = \sum_m (H_{nm}\varrho_{mn'} - \varrho_{nm}H_{mn'}) + \mathrm{i}\hbar D_{nn'}, \tag{2.8}$$

where $D_{nn'}$ is the dissipative matrix, which will now be equal to

$$D_{nn'} = \sum_{mm'} \gamma_{nm,m'n'} \varrho_{mm'} - 1/2 \sum_{m} (\gamma_{nm} \varrho_{mn'} + \varrho_{nm} \gamma_{mn'}). \tag{2.9}$$

By comparing this formula with formula (2.3), we establish that

$$\gamma_{nm,m'n'} = 2 \sum_{jk} C_{jk} a_{nm,j} a^{+}_{m'n',k}, \tag{2.10}$$

where $a_{nm,j}$ are the matrix elements of the $\hat{a}_j$ operator.

The diagonal element $\varrho_{nn'}$ is the probability w_n that the system is in the state n. This value satisfies the normalization condition

$$\sum_{n} \varrho_{nn} = 1. \tag{2.11}$$

In addition, the density matrix ϱ_{nm} satisfies the following condition:

$$\varrho^{*}_{nm} = \varrho_{mn}. \tag{2.12}$$

The same condition is subject to the Hamiltonian:

$$H^{*}_{nm} = H_{mn}. \tag{2.13}$$

Let us consider the case when the density matrix ϱ_{nm} at an arbitrary time t is in diagonal condition:

$$\varrho_{nm} = w_n \delta_{nm}, \tag{2.14}$$

where δ_{nm} is a Kronecker symbol. Then from (2.6) we obtain

$$\dot{w}_n = \sum_{m} (p_{nm} w_m - p_{mn} w_n), \tag{2.15}$$

where

$$p_{nm} = \gamma_{nm,mn} = 2\pi/\hbar \sum_{NM} \left| v_{nN,mM} \right|^2 W_M \delta(\varepsilon_n - \varepsilon_m + E_N - E_M) \tag{2.16}$$

is the probability of the transition of the system per unit time from the state m to the state n,

$$W_N = v \exp(-\beta E_N)$$

is the probability that the environment is in an equilibrium state with quantum numbers N, and E_N presents its energy in this state, v is the normalization factor, $\beta = 1/(k_B T)$ is the inverse temperature; $\upsilon_{nN,mM}$ are the matrix elements of the

system interaction with its environment. Formula (2.16) is the *Golden rule of Fermi*. Judging by the Fermi rule, the probability of transition p_{nm} can always be represented as

$$p_{nm} = p_{nm}^{(o)} \mathrm{e}^{-\beta(\varepsilon_n - \varepsilon_m)/2}, \tag{2.17}$$

$$p_{nm}^{(o)} = p_{mn}^{(o)}. \tag{2.18}$$

14.3 The Equation for the Density Matrix of the First Order Approximation

In [8], it was shown that (2.1) for the statistical operator $\hat{\varrho}$ was obtained in the first approximation by using the Hamiltonian of the interaction between the system and the thermostat. Therefore, this equation can be written as follows:

$$\mathrm{i}\hbar\dot{\hat{\varrho}} = [\widehat{H}\hat{\varrho}] + \lambda \mathrm{i}\hbar\widehat{D}(\hat{\varrho}) + \cdots, \tag{3.1}$$

here λ is an order parameter, $\widehat{D}(\hat{\varrho})$ is a dissipative operator. We write the statistical operator $\hat{\varrho}$ as follows:

$$\hat{\varrho} = \hat{\varrho}^{(o)} + \lambda\hat{\varrho}^{(1)} + \cdots, \tag{3.2}$$

where $\hat{\varrho}^{(o)}$, $\hat{\varrho}^{(1)}$, … are approximations of the density matrix.

Substitute the operator (3.2) in (3.1). We will have

$$\begin{aligned} \mathrm{i}\hbar\left(\dot{\hat{\varrho}}^{(o)} + \lambda\dot{\hat{\varrho}}^{(1)} + \cdots\right) = &\left[\hat{H}, \hat{\varrho}^{(o)} + \lambda\hat{\varrho}^{(1)} + \cdots\right] \\ &+ \lambda\mathrm{i}\hbar\widehat{D}\left(\hat{\varrho}^{(o)} + \lambda\hat{\varrho}^{(1)} + \cdots\right). \end{aligned} \tag{3.3}$$

If the parameter of order $\lambda = 0$, we obtain an equation for the unperturbed statistical operator $\hat{\varrho}^{(o)}$:

$$i\hbar\dot{\hat{\varrho}}^{(o)} = \left[\hat{H}\hat{\varrho}^{(o)}\right]. \tag{3.4}$$

The first parameter of order $\lambda = 1$ gives

$$\mathrm{i}\hbar\dot{\hat{\varrho}}^{(1)} = \left[\widehat{H}\hat{\varrho}^{(1)}\right] + \mathrm{i}\hbar\widehat{D}\left(\hat{\varrho}^{(o)}\right), \tag{3.5}$$

So, the operator $\hat{\varrho}$ satisfies this system of equations.

14.4 The Equation for the Zero-Order Density Matrix

For a two-level scheme at the first level there are g_1 wave functions $\varphi_n(\boldsymbol{r})$, and at the level 2 there are g_2 wave functions $\varphi_m(\boldsymbol{r})$. We now believe that all functions $\varphi_n(\boldsymbol{r})$ are equal to approximately one functions $\varphi_1(\boldsymbol{r})$ and all functions $\varphi_m(\boldsymbol{r})$ are equal to one function $\varphi_2(\boldsymbol{r})$:

$$\varphi_n(\boldsymbol{r}) \approx \varphi_1(\boldsymbol{r}), \quad \varphi_m(\boldsymbol{r}) \approx \varphi_2(\boldsymbol{r}).$$

Consider (2.6) of the density matrix $\varrho_{\alpha\alpha'}$ for a two-level scheme of interaction of an atom with radiation. Here α and α' are quantum numbers of states. In this case, the density matrix will be square with a side equal to two: ϱ_{11}, ϱ_{12}, ϱ_{21} and ϱ_{22}. Here, the quantum numbers α, β, α' and β' are equal to only two values 1 and 2.

The density matrix normalization condition (2.11) in our case will look as

$$\sum_n \varrho_{nn} + \sum_m \varrho_{mm} = 1.$$

This equation will have the following form:

$$g_1\varrho_{11} + g_2\varrho_{22} = 1. \tag{4.1}$$

We obtain the Hamiltonian of the system in the diagonal representation. The $\widehat{H}$ operator in the simplest representation can look as

$$\widehat{H} = \widehat{H}_o + \widehat{V}, \tag{4.2}$$

where $\widehat{H}_o$ is the Hamiltonian that has matrix elements of the form:

$$H^{(o)}_{\alpha\beta} = \varepsilon^{(o)}_{\alpha}\delta_{\alpha\beta},$$

$\varepsilon^{(o)}_{\alpha}$ is the power of the atom; the dipole operator $\widehat{V}$ of the interaction of radiation and fixed atom has the form:

$$\widehat{V} = -\widehat{\boldsymbol{d}} \cdot \boldsymbol{E},$$

$\widehat{\boldsymbol{d}} = \widehat{\boldsymbol{d}}(\boldsymbol{r})$ is the operator of the electric dipole moment of an atom, $\boldsymbol{E} = \boldsymbol{E}(t)$ is the electric field intensity vector. Thus, the interaction operator depends only on the coordinate $\boldsymbol{r}$ and time t: $\widehat{V} = \widehat{V}(\boldsymbol{r}, t)$. Since the Hamiltonian satisfies the condition $H^*_{\alpha\beta} = H_{\beta\alpha}$. The $\widehat{V}$ operator must also obey this condition: $V^*_{\alpha\beta} = V_{\beta\alpha}$, where $V_{\alpha\beta}$ are the matrix elements of the $\widehat{V}$ operator, where we put

$$V_{11} = 0, \quad V_{22} = 0.$$

Thus, the matrix elements of the Hamiltonian will be equal:

$$H_{\alpha\beta} = \varepsilon_{\alpha}^{(o)}\delta_{\alpha\beta} + V_{\alpha\beta}. \tag{4.3}$$

If the electric field strength is

$$\boldsymbol{E} = \boldsymbol{E}_o \cos \omega t,$$

where ω is the frequency of the electric field. Then the matrix elements of the dipole interaction operator will be equal

$$V_{\alpha\beta} = V_{\alpha\beta}^{(o)} \cos \omega t, \quad V_{\alpha\beta}^{(o)} = -\left(\widehat{\boldsymbol{d}} \cdot \boldsymbol{E}_o\right)_{\alpha\beta} = -\boldsymbol{d}_{\alpha\beta} \cdot \boldsymbol{E}_o,$$

where

$$\boldsymbol{d}_{\alpha\beta} = \int \varphi_{\alpha}^{*}(\boldsymbol{r})\widehat{\boldsymbol{d}}\varphi_{\beta}(\boldsymbol{r})\mathrm{d}\boldsymbol{r}. \tag{4.4}$$

The electric field strength $\boldsymbol{E}$ describes the effect of radiation on the atom.

Taking into account (4.4) put the matrix:

$$V_{\alpha\beta}^{(o)} = -\boldsymbol{d} \cdot \boldsymbol{E}_o, \quad \boldsymbol{d}_{12} = \int \varphi_1^{*}(\boldsymbol{r})\widehat{\boldsymbol{d}}\varphi_2(\boldsymbol{r})\mathrm{d}\boldsymbol{r} = \boldsymbol{d}.$$

Then

$$V_{12} = V_{21}^{*} = -\boldsymbol{d} \cdot \boldsymbol{E}_o \cos \omega t = -\hbar\Omega \cos \omega t, \tag{4.5}$$

where

$$\Omega = \boldsymbol{d} \cdot \boldsymbol{E}_o/\hbar \tag{4.6}$$

here Ω is the Rabi frequency.

Consider the zero approximation of the equation for the statistical operator:

$$\mathrm{i}\hbar\dot{\hat{\varrho}}^{(o)} = \left[\widehat{H}\hat{\varrho}^{(o)}\right].$$

We will have

$$\mathrm{i}\hbar\dot{\varrho}_{\alpha\alpha'}^{(o)} = \sum_{\beta}\left(H_{\alpha\beta}\varrho_{\beta\alpha'}^{(o)} - \varrho_{\alpha\beta}^{(o)}H_{\beta\alpha'}\right), \tag{4.7}$$

where $\varepsilon_1^{(o)}$ and $\varepsilon_2^{(o)}$ are the energies at the first and second levels. Substitute Hamiltonian (4.3) and matrix elements (4.5) in (4.7) and get

$$\begin{aligned} \mathrm{i}\dot{\varrho}_{11}^{(o)} &= -\Omega\left(\varrho_{21}^{(o)} - \varrho_{12}^{(0)}\right)\cos\omega t, \\ \mathrm{i}\dot{\varrho}_{12}^{(o)} &= -\omega_o\varrho_{12}^{(o)} + \Omega\left(\varrho_{11}^{(o)} - \varrho_{22}^{(o)}\right)\cos\omega t. \end{aligned} \tag{4.8}$$

where

$$\hbar\omega_o = \varepsilon_2^{(o)} - \varepsilon_1^{(o)} \tag{4.9}$$

ω_o is the frequency of transition between levels when the electric field is absent. We supplement these equations with normalization conditions (2.11) and self-conjugation conditions (2.12).

14.5 The Diagonal Hamiltonian

The eigenvalue of the atom energy can simply be found if we know the Hamiltonian $\widetilde{H}_{\kappa\kappa'}$ which is in diagonal form:

$$\widetilde{H}_{\kappa\kappa'} = \varepsilon_\kappa\delta_{\kappa\kappa'}, \tag{5.1}$$

where ε_κ is the desired eigenvalue of the energy of the atom.

In order to pass from the Hamiltonian (4.3):

$$H_{\alpha\beta} = \varepsilon_\alpha^{(o)}\delta_{\alpha\beta} + V_{\alpha\beta},$$

to the diagonal Hamiltonian $\widetilde{H}_{\kappa\kappa'}$, it is necessary to find the unitary matrix $U_{\alpha\kappa}$, which satisfies the condition:

$$\sum_\alpha U_{\alpha\kappa}U_{\alpha\kappa'}^* = \delta_{\kappa\kappa'}. \tag{5.2}$$

This transition from α-representation to κ-representation is carried out by the formula:

$$\widetilde{H}_{\kappa\kappa'} = \sum_{\alpha\beta} U_{\alpha\kappa}\cdot H_{\alpha\beta}U_{\beta\kappa'}^*. \tag{5.3}$$

In this case, the unitary matrix has the form:

$$U_{\alpha\kappa}=\left\| \begin{matrix} \cos\vartheta & -\sin\vartheta \\ \sin\vartheta & \cos\vartheta \end{matrix} \right\|. \tag{5.4}$$

When the electric field is absent, the Hamiltonian $\widehat{H}$ will be equal to $H_{\alpha\beta}=\varepsilon_{\alpha}^{(o)}\delta_{\alpha\beta}$. At the same time $\vartheta = 0$. Therefore, the unitary matrix is

$$U_{\alpha\kappa}^{(o)}=\left\| \begin{matrix} 1 & 0 \\ 0 & 1 \end{matrix} \right\|=\delta_{\alpha\kappa}.$$

The matrix elements of the Hamiltonian $\widehat{H}$ are

$$H_{11}=\varepsilon_1^{(o)},\quad H_{12}=-\hbar\Omega\cos\omega t,\quad H_{21}=-\hbar\Omega\cos\omega t,\quad H_{22}=\varepsilon_2^{(o)}. \tag{5.5}$$

We compute the diagonal Hamiltonian $\widetilde{H}_{\kappa\kappa'}$:

$$\widetilde{H}_{\kappa\kappa'}=\left\| \begin{matrix} a & -b \\ b & a \end{matrix} \right\| \left\| \begin{matrix} \varepsilon_1^{(o)} & -\hbar\Omega\cos\omega t \\ -\hbar\Omega\cos\omega t & \varepsilon_2^{(o)} \end{matrix} \right\| \left\| \begin{matrix} a & b \\ -b & a \end{matrix} \right\|,$$

where

$$a=\cos\vartheta,\quad b=\sin\vartheta. \tag{5.6}$$

The matrix elements of the Hamiltonian $\widetilde{H}_{\kappa\kappa'}$ will be

$$\begin{aligned}
\widetilde{H}_{11} &= \left(\varepsilon_1^{(o)}a+\Omega b\cos\omega t\right)a+\left(\hbar\Omega a\cos\omega t+\varepsilon_2^{(o)}b\right)b=\varepsilon_1,\\
\widetilde{H}_{12} &= \left(\varepsilon_1^{(o)}a+\hbar\Omega b\cos\omega t\right)b-\left(\hbar\Omega a\cos\omega t+\varepsilon_2^{(o)}b\right)a=0,\\
\widetilde{H}_{21} &= \left(\varepsilon_1^{(o)}b-\hbar\Omega a\cos\omega t\right)a+\left(\hbar\Omega b\cos\omega t-\varepsilon_2^{(o)}a\right)b=0,\\
\widetilde{H}_{22} &= \left(\varepsilon_1^{(0)}b-\hbar\Omega a\cos\omega t\right)b-\left(\hbar\Omega b\cos\omega t-\varepsilon_2^{(0)}a\right)a=\varepsilon_2.
\end{aligned}$$

Here we have two equations. These equations are identical:

$$\omega_o ab+\Omega\left(a^2-b^2\right)\cos\omega t=0.$$

By substituting expressions (5.6) into last equation we obtain an equation with one unknown ϑ:

$$\omega_o\cos\vartheta\sin\vartheta+\Omega\left(\cos^2\vartheta-\sin^2\vartheta\right)\cos\omega t=0.$$

Solve this equation with parameter ϵ:

$$\mathrm{tg}^2\vartheta - 2\mathrm{tg}\vartheta - \epsilon = 0, \tag{5.7}$$

where

$$\epsilon(\mathrm{t}) = 2\Omega\cos\omega t/\omega_o. \tag{5.8}$$

The solution of this equation is

$$\mathrm{tg}\,\vartheta = \left(1 - \sqrt{1+\epsilon^2}\right)/\epsilon.$$

The parameter ϵ is extremely small. Therefore, we decompose the function into a series:

$$\sqrt{1+\epsilon^2} = 1 + \epsilon^2/2 + \ldots$$

Herewith

$$\mathrm{tg}\vartheta = -\epsilon/2 + \ldots = -\Omega\cos\omega t/\omega_o + \ldots$$

Now we write down the eigenvalues of the atom's energy:

$$\varepsilon_1 = \varepsilon_1^{(o)}a^2 + \varepsilon_2^{(o)}b^2 + \hbar\Omega ab\cos\omega t,$$
$$\varepsilon_2 = \varepsilon_2^{(o)}a^2 + \varepsilon_1^{(o)}b^2 - \hbar\Omega ab\cos\omega t.$$

We express here a and b through the angle ϑ by formulas (5.6):

$$\begin{aligned}\varepsilon_1 &= \varepsilon_1^{(o)}\cos^2\vartheta + \varepsilon_2^{(o)}\sin^2\vartheta + \hbar\Omega\cos\vartheta\sin\vartheta\cos\omega t,\\ \varepsilon_2 &= \varepsilon_2^{(0)}\cos^2\vartheta + \varepsilon_1^{(0)}\sin^2\vartheta - \hbar\Omega\cos\vartheta\sin\vartheta\cos\omega t.\end{aligned} \tag{5.9}$$

Thus, we obtain a diagonal Hamiltonian:

$$\widetilde{H}_{\kappa\kappa'} = \varepsilon_\kappa(t)\delta_{\kappa\kappa'}. \tag{5.10}$$

14.6 The Density Matrix in the κ-Representation

The zero density matrix will correspond to the equation:

$$\mathrm{i}\hbar\dot{\hat{\varrho}}^{(o)} = \left[\hat{H}\hat{\varrho}^{(o)}\right].$$

In the κ-representation, this equation will look as

$$\mathrm{i}\hbar\dot{\tilde{\varrho}}_{\kappa\kappa'} = \sum_{\kappa''}\left(\widetilde{H}_{\kappa\kappa''}\tilde{\varrho}_{\kappa''\kappa'} - \tilde{\varrho}_{\kappa\kappa''}\widetilde{H}_{\kappa''\kappa'}\right). \tag{6.1}$$

Substituting the Hamiltonian $\widetilde{H}_{\kappa\kappa'}$ in the κ-representation here, we obtain

$$\mathrm{i}\hbar\dot{\tilde{\varrho}}_{\kappa\kappa'} = [\varepsilon_\kappa(t) - \varepsilon_{\kappa'}(t)]\tilde{\varrho}_{\kappa\kappa'}. \tag{6.2}$$

Or more

$$\dot{\tilde{\varrho}}_{11} = 0, \quad \mathrm{i}\hbar\dot{\tilde{\varrho}}_{12} = -[\varepsilon_2(t) - \varepsilon_1(t)]\tilde{\varrho}_{12}. \tag{6.3}$$

The second equation can be written as follows

$$\mathrm{d}\tilde{\varrho}_{12}/\tilde{\varrho}_{12} = \mathrm{i}/\hbar[\varepsilon_2(t) - \varepsilon_1(t)]\mathrm{d}t. \tag{6.4}$$

By integrating, we obtain

$$\ln\tilde{\varrho}_{12} = \mathrm{i}/\hbar\int[\varepsilon_2(t) - \varepsilon_1(t)]\mathrm{d}t. \tag{6.5}$$

Using the formula (5.9), we find the difference of energy eigenvalues:

$$\varepsilon_2(t) - \varepsilon_1(t) = \hbar(\omega_o\cos 2\vartheta - \Omega\sin 2\vartheta\cos\omega t). \tag{6.6}$$

Express cos 2ϑ and sin 2ϑ via tg ϑ:

$$\cos 2\vartheta = \left(1 - \mathrm{tg}^2\vartheta\right)/\left(1 + \mathrm{tg}^2\vartheta\right), \quad \sin 2\vartheta = 2\mathrm{tg}\vartheta/\left(1 + \mathrm{tg}^2\vartheta\right).$$

Substituting the formula tg ϑ here, we will have

$$\cos 2\vartheta = \left[1 - (\epsilon/2)^2\right]/\left[1 + (\epsilon/2)^2\right], \quad \sin 2\vartheta = -\epsilon/\left[1 + (\epsilon/2)^2\right].$$

Expand these functions in powers of ϵ:

$$\cos 2\vartheta = 1 - \epsilon^2/2 + \ldots, \quad \sin 2\vartheta = -\epsilon + \ldots$$

Substituting these formulas in (6.6) gives

$$[\varepsilon_2(t) - \varepsilon_1(t)]/(\hbar\omega_o) = 1 + 2(\Omega\cos\omega t/\omega_o)^2. \tag{6.7}$$

Using this function in the integral (6.5), we will have

$$\ln\tilde{\varrho}_{12} = \mathrm{i}\int\left[\omega_o + 2(\Omega\cos\omega t)^2/\omega_o\right]\mathrm{d}t.$$

Finally we obtain

$$\tilde{\varrho}_{12} = C_{12}\mathrm{e}^{\mathrm{i}\psi(t)}, \tag{6.8}$$

where

$$\psi(\mathrm{t}) = \left(\omega_o + \Omega^2/\omega_o\right)t + \Omega^2/(2\omega_o\omega)\sin 2\omega t. \tag{6.9}$$

Other solutions of the system (6.2) will have the form:

$$\tilde{\varrho}_{11} = C_{11}, \quad \tilde{\varrho}_{21} = C_{12}^{*}\mathrm{e}^{-\mathrm{i}\psi(t)}, \quad \tilde{\varrho}_{22} = C_{22}. \tag{6.10}$$

The eigenvalues of the energy ε_1 and ε_2 are found absolutely exactly and are given by formulas (5.9). To express them in time, write $\cos^2\vartheta$ and $\sin^2\vartheta$ using $\mathrm{tg}^2\vartheta$:

$$\cos^2\vartheta = 1/\left(1 + \mathrm{tg}^2\vartheta\right) \sim 1 - \mathrm{tg}^2\vartheta \sim 1 - \epsilon^2/4, \quad \sin^2\vartheta = \mathrm{tg}^2\vartheta/\left(1 + \mathrm{tg}^2\vartheta\right) \sim \epsilon^2/4.$$

It can be seen that $\sin\vartheta$ has a negative value:

$$\cos\vartheta\sin\vartheta = -\epsilon/2.$$

Let us put these formulas into formulas (5.9):

$$\varepsilon_1 = \varepsilon_1^{(o)} - \hbar\omega_o(\Omega\cos\omega t/\omega_o)^2, \quad \varepsilon_2 = \varepsilon_2^{(o)} + \hbar\omega_o(\Omega\cos\omega t/\omega_o)^2, \tag{6.11}$$

The eigenvalue difference will be proportional to the frequency $\tilde{\omega}$:

$$\varepsilon_2 - \varepsilon_1 = \hbar\tilde{\omega}, \tag{6.12}$$

which is equal to

$$\tilde{\omega}(\mathrm{t}) = \omega_o + 2(\Omega\cos\omega t)^2/\omega_o. \tag{6.13}$$

We see that the probabilities (6.10) remain constant because they do not take into account the pumping and attenuation operations. These phenomena are present in the second term of $\mathrm{i}\hbar\,\widehat{D}(\hat{\varrho})$ (2.1) and (2.6) for the density matrix, which demonstrates dissipative effects.

14.7 Kinetics of Quantum Transitions

In a two-level scheme, the numbers N_1 and N_2 of atoms in which the electrons are in states φ_1 and φ_2 can change over time: $N_1 = N_1(t)$ and $N_2 = N_2(t)$, but their sum will remain constant:

$$N_1 + N_2 = N, \tag{7.1}$$

where N is the total number of atoms.

Consider a system of non-interacting atoms in which a valence electron can make quantum transitions from one stationary state to another. Such transitions will have four options. First, the laser works if it receives some kind of energy. This process is called pumping. As a result of pumping, electrons are forced to move from the state φ_1 to the state φ_2 with a higher energy ε_2. Second, the community of the atoms in the state φ_1 with energy ε_1 can pass into a state φ_2 with more energy ε_2 in the absorption of photons by atoms. Third, a spontaneous transition of an electron from the state φ_2 to the state φ_1 with a lower energy ε_1 with the emission of a photon is possible. Finally, an atom can move from the state φ_2 to the state φ_1, making a forced (induced) transition (caused by a passing photon) between these states with the emission of another photon. At these transitions, the number of atoms $N_1(t)$ will change with time according to a law called the kinetic equation:

$$\mathrm{d}N_1/\mathrm{d}t = -[Q + B_{12}W(\omega)]N_1 + \left[A^{(\text{СПОН})} + B_{21}W(\omega)\right]N_2, \tag{7.2}$$

where

$$\mathrm{d}N_{12}^{(\text{pump})} = QN_1(t)\mathrm{d}t \tag{7.3}$$

is the number of atoms that are formed during the time $\mathrm{d}t$ in the process of pumping, Q is a factor of the pumping;

$$\mathrm{d}N_{12}^{(\text{absor})} = B_{12}W(\omega)N_1(t)\mathrm{d}t \tag{7.4}$$

is the number of atoms in which the electron makes the transition in the absorption of a photon, B_{12} is a coefficient, $W(\omega)$ is the spectral density of the radiation energy, the frequency ω of the photon is determined by the formula $\omega = (\varepsilon_2 - \varepsilon_1)/\hbar$;

$$\mathrm{d}N_{21}^{(\text{spon})} = AN_2(t)\mathrm{d}t \tag{7.5}$$

is the number of atoms in which an electron makes a spontaneous transition with the emission of a photon, A is a coefficient, called the probability of spontaneous transition of an atom;

$$dN_{21}^{(ind)} = B_{21}W(\omega)N_2(t)dt, \tag{7.6}$$

is the number of atoms in which an electron makes a transition caused by a passing photon with the emission of a second photon, B_{21} is a coefficient. Factors B_{12}, B_{21} and A are called Einstein coefficients.

When the active medium of the laser is at rest, the dependence $W(\omega)$ must be described by the Planck formula:

$$W^{(Planck)}(\omega) = \hbar\omega^3/\left(\pi^2c^3\right)\left(e^{\beta\hbar\omega} - 1\right).$$

It was proved that the Einstein coefficients are coupled by the relations:

$$B_{12} = B_{21}, \quad A/B_{12} = \hbar\omega^3/\left(\pi^2c^3\right).$$

Given these equations, (7.2) is written as

$$dN_1/dt = -[Q + BW(\omega)]N_1 + [A + BW(\omega)]N_2. \tag{7.7}$$

This is a phenomenological equation, which was derived only for reasons of justice, but without the participation of quantum laws.

14.8 Transition Density Matrix from the κ-Representation in the Initial α -Representation

The transition of the density matrix from the κ-representation to the α-representation is carried out by means of a unitary transformation:

$$\varrho_{\alpha\beta}^{(o)} = \sum_{\kappa\kappa'} U_{\alpha\kappa}\tilde{\varrho}_{\kappa\kappa'}U_{\beta\kappa'}^{*}, \tag{8.1}$$

where we have already found the unitary matrix $U_{\alpha\kappa}$.

The density matrix $\hat{\varrho}_{\kappa\kappa'}$ is

$$\tilde{\varrho}_{\kappa\kappa'} = \begin{Vmatrix} \tilde{\varrho}_{11} & \tilde{\varrho}_{12} \\ \tilde{\varrho}_{21} & \tilde{\varrho}_{22} \end{Vmatrix}. \tag{8.2}$$

Calculate the density matrix (8.1):

$$\varrho_{\alpha\beta}^{(o)} = \begin{Vmatrix} \cos\vartheta & -\sin\vartheta \\ \sin\vartheta & \cos\vartheta \end{Vmatrix} \begin{Vmatrix} \tilde{\varrho}_{11} & \tilde{\varrho}_{12} \\ \tilde{\varrho}_{21} & \tilde{\varrho}_{22} \end{Vmatrix} \begin{Vmatrix} \cos\vartheta & \sin\vartheta \\ -\sin\vartheta & \cos\vartheta \end{Vmatrix}. \tag{8.3}$$

Finally we will have

$$\begin{aligned}
\varrho_{11}^{(o)} &= \tilde{\varrho}_{11}\cos^2\vartheta + \tilde{\varrho}_{22}\sin^2\vartheta - (\tilde{\varrho}_{12}+\tilde{\varrho}_{21})\cos\vartheta\sin\vartheta,\\
\varrho_{12}^{(o)} &= (\tilde{\varrho}_{11}-\tilde{\varrho}_{22})\cos\vartheta\sin\vartheta + \tilde{\varrho}_{12}\cos^2\vartheta - \tilde{\varrho}_{21}\sin^2\vartheta,\\
\varrho_{21}^{(o)} &= (\tilde{\varrho}_{11}-\tilde{\varrho}_{22})\cos\vartheta\sin\vartheta - \tilde{\varrho}_{12}\sin^2\vartheta + \tilde{\varrho}_{21}\cos^2\vartheta,\\
\varrho_{22}^{(o)} &= \tilde{\varrho}_{11}\sin^2\vartheta + \tilde{\varrho}_{22}\cos^2\vartheta + (\tilde{\varrho}_{12}+\tilde{\varrho}_{21})\cos\vartheta\sin\vartheta.
\end{aligned} \tag{8.4}$$

The sum $\hat{\varrho}_{12}+\hat{\varrho}_{21}$ is equal to the doubled real part of the value $\hat{\varrho}_{12}$:

$$\tilde{\varrho}_{12}+\tilde{\varrho}_{21} = \tilde{\varrho}_{12}+\tilde{\varrho}_{12}^{*} = 2\,\mathrm{Re}\,\tilde{\varrho}_{12}. \tag{8.5}$$

Substitute in formula (8.5) (8.4) and approximate equations for ϑ. Given the formula (5.8) for the parameter ϵ, we will have

$$\begin{aligned}
\varrho_{11}^{(o)} &= \tilde{\varrho}_{11} + (\tilde{\varrho}_{22}-\tilde{\varrho}_{11})\xi^2(\mathrm{t}) + 2\,\mathrm{Re}\,\tilde{\varrho}_{12}\xi(\mathrm{t}),\\
\varrho_{12}^{(o)} &= \tilde{\varrho}_{12} + (\tilde{\varrho}_{22}-\tilde{\varrho}_{11})\xi(\mathrm{t}) - 2\,\mathrm{Re}\,\tilde{\varrho}_{12}\xi^2(\mathrm{t}),\\
\varrho_{21}^{(o)} &= \tilde{\varrho}_{21} + (\tilde{\varrho}_{22}-\tilde{\varrho}_{11})\xi(\mathrm{t}) - 2\,\mathrm{Re}\,\tilde{\varrho}_{12}\xi^2(\mathrm{t}),\\
\varrho_{22}^{(o)} &= \tilde{\varrho}_{22} - (\tilde{\varrho}_{22}-\tilde{\varrho}_{11})\xi^2(\mathrm{t}) - 2\,\mathrm{Re}\,\tilde{\varrho}_{12}\xi(\mathrm{t}),
\end{aligned} \tag{8.6}$$

where

$$\xi(\mathrm{t}) = \epsilon/2 = \Omega\cos\omega t/\omega_o. \tag{8.7}$$

The matrix (8.6) can never be diagonal if the external electric field acts on the atom [$\xi(\mathrm{t}) \neq 0$].

14.9 Dissipative Matrix

Now we need to find out what the matrix $\gamma_{nm,m'n'}$ looks like. The easiest way is to use the formula (2.10). Let this formula contains the operator $\hat{a}_j$ then this matrix looks as

$$\gamma_{nm,m'n'} = \sum_j C_j a_{nm,j} a^{+}_{m'n',j}, \tag{10.1}$$

where $a_{nm,j}$ are the matrix elements of the operator $\hat{a}_j$, C_j are constants. With this operator, we can write the dissipative operator using the Lindblad equation (2.3):

$$\widehat{D} = 1/2 \sum_j C_j \left(2\hat{a}_j \hat{\varrho} a_j^+ - a_j^+ \hat{a}_j \hat{\varrho} - \hat{\varrho} a_j^+ \hat{a}_j \right), \tag{9.2}$$

and the dissipative matrix will look as

$$D_{nn'} = \sum_{mm'} \gamma_{nm,m'n'} \varrho_{mm'} - 1/2 \sum_m (\gamma_{nm} \varrho_{mn'} + \varrho_{nm} \gamma_{mn'}), \tag{9.3}$$

Now we need to give physical meaning to $\hat{a}_j$ operators.

Let the duplex arrangement, the operator $\hat{a}_1$ is equal to

$$\hat{a}_1 = \left\| \begin{matrix} 0 & a_{12} \\ a_{21} & 0 \end{matrix} \right\|. \tag{9.4}$$

Substitute this operator in the formula (9.3) and write the dissipative matrix in elements:

$$\begin{aligned} D_{11}^{(1)} &= 1/2 C_1 \sum_{mm'} \left(2a_{1m} \varrho_{mm'} a_{m'1}^+ - a_{1m}^+ a_{mm'} \varrho_{m'1} - \varrho_{1m} a_{mm'}^+ a_{m'1} \right) \\ &= 1/2 C_1 \left(2a_{12} \varrho_{22} a_{21}^+ - a_{12}^+ a_{21} \varrho_{11} - \varrho_{11} a_{12}^+ a_{21} \right) \\ &= C_1 \left(a_{12}^2 \varrho_{22} - a_{21}^2 \varrho_{11} \right), \end{aligned} \tag{9.5}$$

$$\begin{aligned} D_{12}^{(1)} &= 1/2 C_1 \sum_{mm'} \left(2a_{1m} \varrho_{mm'} a_{m'2}^+ - a_{1m}^+ a_{mm'} \varrho_{m'2} - \varrho_{1m} a_{mm'}^+ a_{m'2} \right) \\ &= 1/2 C_1 \left(2a_{12} \varrho_{21} a_{12}^+ - a_{12}^+ a_{21} \varrho_{12} - \varrho_{12} a_{21}^+ a_{12} \right) \\ &= 1/2 C_1 \left[2a_{12} a_{21} \varrho_{21} - \left(a_{12}^2 + a_{21}^2 \right) \varrho_{12} \right], \end{aligned} \tag{9.6}$$

where

$$a_{12}^2 = p_{12}, \quad a_{21}^2 = p_{21}. \tag{9.7}$$

According to formulas (2.17) and (2.18), we have

$$p_{12} = p_{12}^{(o)} e^{-\beta(\varepsilon_1 - \varepsilon_2)/2}, \quad p_{21} = p_{21}^{(o)} e^{-\beta(\varepsilon_2 - \varepsilon_1)/2}, \tag{9.8}$$

$$p_{12}^{(o)} = p_{21}^{(o)} = p. \tag{9.9}$$

Let the matrix $\hat{a}_2$ has the form:

$$\hat{a}_2 = \left\| \begin{matrix} 0 & a_1 \\ a_2 & 0 \end{matrix} \right\|. \tag{9.10}$$

The dissipative matrix will now be as follows:

$$D_{11}^{(2)} = C_2\left(a_1^2\varrho_{22} - a_2^2\varrho_{11}\right). \tag{9.11}$$

$$D_{12}^{(2)} = 1/2C_2\left[2a_1a_2\varrho_{21} - \left(a_1^2 + a_2^2\right)\varrho_{12}\right]. \tag{9.12}$$

Let us to denote

$$a_1^2 = \gamma_1, \quad a_2^2 = \gamma_2. \tag{9.13}$$

If the matrix $\hat{a}_3$ is

$$\hat{a}_3 = \left\| \begin{matrix} 0 & a \\ a & 0 \end{matrix} \right\|. \tag{9.14}$$

The third dissipative matrix according to the formulas (9.11) and (9.12) will be

$$D_{11}^{(3)} = C_3a^2(\varrho_{22} - \varrho_{11}). \tag{9.15}$$

$$D_{12}^{(3)} = C_3a^2(\varrho_{21} - \varrho_{12}). \tag{9.16}$$

If the matrix $\hat{a}_4$ is diagonal, i.e. has the form:

$$a_{nm} = b_n\delta_{nm}, \tag{9.17}$$

that dissipative matrix will be

$$D_{nn'}^{(4)} = 1/2\, C_4\left(2b_nb_{n'} - b_n^2 - b_{n'}^2\right)\varrho_{nn'}. \tag{9.18}$$

In particular

$$\begin{aligned} D_{nn}^{(4)} &= 0, \\ D_{12}^{(4)} &= 1/2C_4\left(2b_1b_2 - b_1^2 - b_2^2\right)\varrho_{12}, \\ D_{21}^{(4)} &= 1/2C_4\left(2b_2b_1 - b_2^2 - b_1^2\right)\varrho_{21}. \end{aligned} \tag{9.19}$$

We can put

$$D_{12}^{(4)} = -\Gamma_{\varrho_{12}}, \quad D_{21}^{(4)} = -\Gamma\varrho_{21}. \tag{9.20}$$

where

$$\Gamma = 1/2C_4\left(b_1^2 + b_2^2 - 2b_1b_2\right).$$

Collect all four options dissipative matrices together. Putting $C_1 = 1$, $C_2 = -2$ and $C_3 = 1$, we obtain

$$D_{11} = \left(p_{12} + \gamma_1 + a^2\right)\varrho_{22} - \left(p_{21} + \gamma_2 + a^2\right)\varrho_{11}, \tag{9.21}$$

$$\begin{aligned} D_{12} = {} & 1/2\left[2\sqrt{p_{12}p_{21}}\varrho_{21} - (p_{12} + p_{21})\varrho_{12}\right] \\ & + (\gamma_1 + \gamma_2)\varrho_{12} - 2\sqrt{\gamma_1\gamma_2}\varrho_{21} + a^2(\varrho_{21} - \varrho_{12}) - \Gamma\varrho_{12}. \end{aligned} \tag{9.22}$$

14.10 The Equation for the Density Matrix in κ –Representation

We write the equation for the density matrix in κ-representation, where the Hamiltonian is diagonal, i.e. has the form:

$$\widetilde{H}_{\kappa\kappa'} = \varepsilon_\kappa(t)\delta_{\kappa\kappa'}, \tag{10.1}$$

Energy eigenvalues $\varepsilon_\kappa(t)$ are determined by the formula (6.11).

The equation looks as

$$\mathrm{i}\hbar\dot{\varrho}_{\kappa\kappa'} = \sum_{\kappa''}\left(\widetilde{H}_{\kappa\kappa''}\varrho_{\kappa''\kappa'} - \varrho_{\kappa\kappa'}\widetilde{H}_{\kappa''\kappa'}\right) + \mathrm{i}\hbar D_{\kappa\kappa'}. \tag{10.2}$$

Substituting here the formula (6.11), we obtain

$$\mathrm{i}\hbar\dot{\varrho}_{\kappa\kappa'} = [\varepsilon_\kappa(t) - \varepsilon_{\kappa'}(t)]\varrho_{\kappa\kappa'} + \mathrm{i}\hbar D_{\kappa\kappa'}. \tag{10.3}$$

Write using formulas (9.21) and (9.22) equations for density matrix ϱ_{11} and ϱ_{12}:

$$\dot{\varrho}_{11} = \left(p_{12} + \gamma_1 + a^2\right)\varrho_{22} - \left(p_{21} + \gamma_2 + a^2\right)\varrho_{11}, \tag{10.4}$$

$$\begin{aligned} \dot{\varrho}_{12} = {} & \mathrm{i}\tilde{\omega}\varrho_{12} + 1/2\left[2\sqrt{p_{12}p_{21}}\varrho_{21} - (p_{12} + p_{21})\varrho_{12}\right] \\ & + (\gamma_1 + \gamma_2)\varrho_{12} - 2\sqrt{\gamma_1\gamma_2}\varrho_{21} + a^2(\varrho_{21} - \varrho_{12}) - \Gamma\varrho_{12}. \end{aligned} \tag{10.5}$$

These equations should be supplemented by the following equations:

$$\varrho_{21} = \varrho_{12}^*, \tag{10.6}$$

$$\dot{\varrho}_{11} + \dot{\varrho}_{22} = 0. \tag{10.7}$$

14.11 Kinetic Equation and the Equation for the Density Matrix

Now we write (7.7) using probabilities w_1 and w_2. The number of atoms of N_1 and N_2 are associated with these probability ratios:

$$N_1 = Ng_1 w_1, \quad N_2 = Ng_2 w_2. \tag{11.1}$$

Equation (7.7) would look like this:

$$g_1 \dot{w}_1 = -(Q + BW)g_1 w_1 + (A + BW)g_2 w_2. \tag{11.2}$$

Substituting the density matrix instead of the probabilities into this equation:

$$W_{\kappa\kappa} \leftrightarrow \varrho_{\kappa\kappa},$$

we will have a kinetic equation expressed in terms of the density matrix:

$$\dot{\varrho}_{11} = -(Q + BW)\varrho_{11} + (A + BW)\varrho_{22}. \tag{11.3}$$

Now consider (10.4) obtained by us from the equation for the matrix. Equations (10.4) and (11.3) are remarkably similar. First of all, we need to put

$$\gamma_2 = Q, \tag{11.4}$$

and the values γ_1 and a^2 should be considered as

$$\gamma_1 = A, \quad a^2 = BW. \tag{11.5}$$

Substitute these values in (10.4). Finally, we will have

$$\dot{\varrho}_{11} = p_{12}\varrho_{22} - p_{21}\varrho_{11} - (Q + BW)\varrho_{11} + (A + BW)\varrho_{22}, \tag{11.6}$$

We proved that the phenomenological equation (7.7) coincides with the equation obtained by the quantum mechanical method.

Let us write down (11.6) in more detail:

$$\begin{aligned}\dot{\varrho}_{11} = {} & p\left(e^{\beta\hbar\tilde{\omega}/2}\varrho_{22} - e^{-\beta\hbar\tilde{\omega}/2}\varrho_{11}\right) \\ & + [A + BW(t, \tilde{\omega})]\varrho_{22} - [Q + BW(t, \tilde{\omega})]\varrho_{11}.\end{aligned} \tag{11.7}$$

We add this equation to the normalization condition:

$$\varrho_{11} + \varrho_{22} = 1. \tag{11.8}$$

Let us write down (10.5), substituting dissipative constants into it:

$$\begin{aligned}\dot{\varrho}_{12} = {} & \mathrm{i}\tilde{\omega}\varrho_{12} + 1/2\left[2\sqrt{p_{12}p_{21}}\varrho_{21} - (p_{12}+p_{21})\varrho_{12}\right] \\ & + (Q+A)\varrho_{12} - 2\sqrt{QA}\varrho_{21} + BW(\varrho_{21} - \varrho_{12}) - \Gamma\varrho_{12}.\end{aligned} \tag{11.9}$$

This equation is supplemented by the condition:

$$\varrho_{21} = \varrho_{12}^{*}, \tag{11.10}$$

Equations (11.7) and (11.9) form the basis of the new laser theory.

14.12 Kinetics of Radiation

The spectral density of the radiation energy $W(t, \tilde{\omega})$ obeys the equation:

$$\mu \mathrm{d}W/\mathrm{d}t = (A + BW)\varrho_{22} - BW\varrho_{11}. \tag{12.1}$$

The constant μ appeared here only to equalize the dimensions of the left and right sides of this equation. The energy density of the radiation has the form:

$$W(t, \tilde{\omega}) = W^{(\mathrm{Planck})}(\tilde{\omega}) + \Delta(t, \tilde{\omega}), \tag{12.2}$$

where $\Delta(t, \tilde{\omega})$ is the spectral density of the radiation energy, which occurs as a result of laser operation. When population inversion ($N_2 > N_1$) occurs for a pair of levels ε_1 and ε_2, it is natural to assume the validity of the inequality:

$$\Delta(t, \omega) > W^{(\mathrm{Planck})}(\omega) \tag{12.3}$$

for beams directed along the laser axis. Now from (12.1) we obtain the equation for density $\Delta(t, \omega)$:

$$\mu \mathrm{d}\Delta/\mathrm{d}t = (A + B\Delta)\varrho_{22} - B\Delta\varrho_{11}. \tag{12.4}$$

In the laser, there are two radiations that propagate along the axis in different directions. These radiations are characterized by energy densities Δ^{+} and Δ^{-}. The density Δ^{+} refers to the radiation flying to the right along the laser axis, and the density Δ^{-} flies to the left. These density equal density Δ:

$$\Delta^+ + \Delta^- = \Delta. \tag{12.5}$$

Now we write the equations for densities Δ^+ and Δ^- as follows:

$$\mu \, \mathrm{d}\Delta^+/\mathrm{d}t = \left(A + B\Delta^+\right)\varrho_{22} - B\Delta^+\varrho_{11}, \tag{12.6}$$

$$\mu \, \mathrm{d}\Delta^-/\mathrm{d}t = (A + B\Delta^-)\varrho_{22} - B\Delta^-\varrho_{11}. \tag{12.7}$$

When the laser is in continuous operation, it is convenient to express the energy densities Δ^+ and Δ^- through the x coordinate. Let the x-axis is directed from the left end of the laser, where $x = 0$, to the right (see Fig. 14.1). Then the time t for which the radiation going to the right passes the path x will be equal to

$$t = x/\mathrm{c}. \tag{12.8}$$

At the right end $x = l$, where l is the length of the active medium. Substitute the time (12.8) in (12.6). Now this equation will depend on x: $\Delta^+ = \Delta^+(x)$ and will look as

$$\mathrm{c}\mu \mathrm{d}\Delta^+/\mathrm{d}x = \left(A + B\Delta^+\right)\varrho_{22} - B\Delta^+\varrho_{11}. \tag{12.9}$$

Reflected from the right mirror, the radiation flies to the left. Now the time t, in which the radiation passes to the point x, will be

$$t = (l - x)/\mathrm{c}^*. \tag{12.10}$$

Substituting this time in (12.7), we will have

$$-\mathrm{c}\mu \mathrm{d}\Delta^-/\mathrm{d}x = (A + B\Delta^-)\varrho_{22} - B\Delta^-\varrho_{11}, \tag{12.11}$$

where $\Delta^- = \Delta^-(x)$.

For densities $\Delta^+(x)$ and $\Delta^-(x)$, there are boundary conditions. Let us assume that in the left mirror the light is reflected completely. This means that

$$\Delta^-(0) = \Delta^+(0). \tag{12.12}$$

In the right mirror light is reflected partially with coefficient reflection R:

$$\Delta^-(l) = R\Delta^+(l). \tag{12.13}$$

From the right of the mirror, the light with the spectral density of energy comes, which is equal to

$$\Delta^{+}_{\text{output}}(l) = (1 - R)\Delta^{+}(l). \tag{12.14}$$

14.13 Solving the Equation for the Diagonal Elements of the Density Matrix, When B = 0

In this case, (11.7) takes the form:

$$\dot{\varrho}_{11} = p\left(\mathrm{e}^{\beta\hbar\tilde{\omega}/2}\varrho_{22} - \mathrm{e}^{-\beta\hbar\tilde{\omega}/2}\varrho_{11}\right) + A \quad \varrho_{22} - Q\varrho_{11}, \tag{13.1}$$

where $\varrho_{11} + \varrho_{22} = 1$. Denote

$$\phi = \beta\hbar\omega_O/2. \tag{13.2}$$

Then

$$\mathrm{e}^{\beta\hbar\tilde{\omega}/2} + \mathrm{e}^{-\beta\hbar\tilde{\omega}/2} = 2\,\mathrm{ch}\,\phi,$$

where

$$\mathrm{ch}\,\phi = \left(\mathrm{e}^{\phi} + \mathrm{e}^{-\phi}\right)/2$$

is the hyperbolic cosine.

In the adopted designation, (13.1) would be

$$\dot{\varrho}_{11} = -(2p\,\mathrm{ch}\,\phi + A + Q)\varrho_{11} + p\mathrm{e}^{\phi} + A. \tag{13.3}$$

The general solution of this equation is given by the formula

$$\varrho_{11} = \mathrm{Ce}^{-(2p\,\mathrm{ch}\,\phi + A + Q)t} + \left(p\mathrm{e}^{\phi} + A\right)/(2p\,\mathrm{ch}\,\phi + A + Q). \tag{13.4}$$

The stationary solution will be

$$\begin{aligned} \varrho_{11} &= \left(p\mathrm{e}^{\phi} + A\right)/(2p\,\mathrm{ch}\,\phi + A + Q), \\ \varrho_{22} &= 1 - \varrho_{11}. \end{aligned} \tag{13.6}$$

The inverse population of $\varrho_{22} > \varrho_{11}$ levels will be observed if

$$Q > A + 2p\,\mathrm{sh}\,\phi. \tag{13.6}$$

14.14 Solution of Equations for the Spectral Density of Radiation Energy

Solution of equations for the spectral density of radiation epicduel these equations in the following way

$$c\mu d\Delta^+/dx = B(\varrho_{22} - \varrho_{11})\Delta^+ + A\varrho_{22}, \tag{14.1}$$

$$-c\mu d\Delta^-/dx = B(\varrho_{22} - \varrho_{11})\Delta^+ + A\varrho_{22}. \tag{14.2}$$

This will be only a zero solution to this problem.

Now substitute the diagonal elements of the density matrix in the κ-representation defined by the formulas (8.6) into the formula (14.1). Leaving only the first members, we will have

$$\varrho_{11}^{(o)} = \tilde{\varrho}_{11} + 2\,\mathrm{Re}\,\tilde{\varrho}_{12}\xi(t), \quad \varrho_{22}^{(o)} = \tilde{\varrho}_{22} - 2\,\mathrm{Re}\,\tilde{\varrho}_{12}\xi(t), \tag{14.3}$$

Substitution (14.3) gives a new equation:

$$c\mu d\Delta^+/dx = B[\varrho_{22} - \varrho_{11} - 4\,\mathrm{Re}\,\varrho_{12}\xi(t)]\Delta^+ + A[\varrho_{22} - 2\,\mathrm{Re}\,\varrho_{12}\xi(t)]. \tag{14.4}$$

Now, to find the non-diagonal density matrix ϱ_{12}, let us turn to (11.9). Let us simplify this equation, leaving only the first two terms in the right part of the equation:

$$\dot{\varrho}_{12} = i\tilde{\omega}\varrho_{12} - \Gamma\varrho_{12}. \tag{14.5}$$

Now, using the second formula (8.6), substitute the density matrix in κ-representation. Leaving in this formula only the first degree $\xi(t)$, we will have

$$\varrho_{12} = \tilde{\rho}_{12} + (\tilde{\varrho}_{22} - \tilde{\varrho}_{11})\xi(t). \tag{14.6}$$

The frequency $\tilde{\omega}$ of laser radiation is related to the frequency ω_o, when the electric field is absent, see formula (9.17):

$$\tilde{\omega}(t) = \omega_o + 2\Omega^2 \cos^2 \omega t/\omega_o. \tag{14.7}$$

Substituting formulas (14.6) and (14.7) into (14.5), we obtain a new equation:

$$\dot{\varrho}_{12} = \left[i\left(\omega_o + 2\Omega^2 \cos^2 \omega t/\omega_o\right) - \Gamma\right][\varrho_{12} + (\varrho_{22} - \varrho_{11})\Omega \cos \omega t/\omega_o]. \tag{14.8}$$

Solving these equations, we find the spectral density of the radiation energy at the output of the laser:

$$\begin{aligned}\Delta_{\text{output}}(l) &= (1-R)\Delta^{+}(l) \\ &= (1-R)\left(\mathrm{e}^{2\alpha l}-1\right)/\left(1-R\,\mathrm{e}^{2\alpha l}\right) \\ &\quad \left\{F+\Omega^2 M(l)/\left[2\mu\omega_o^2\left(\delta\omega^2+\Gamma^2\right)\right]\right\},\end{aligned} \tag{14.9}$$

where α, F and $M(l)$ are coefficients,

$$\delta\omega = \omega - \omega_o.$$

14.15 Conclusion

In this paper it is shown that the density matrix method is applicable to the theory of lasers. A new diagonal Hamiltonian was introduced, whose elements had eigenvalues of the atom's energy. A unitary matrix was used for this purpose. We obtained the matrix whose elements characterize the thermodynamic transitions and operations of the pumping and damping. Equations (11.7) and (11.9) describing the density matrix were obtained, too. Moreover, the equations for the spectral densities of the radiation energies generated by the laser were obtained. The solution of these equations makes it possible to find the spectral density of the radiation energy coming out of the laser. Equations (11.7), (11.9), (12.6) and (12.7) form the basis of the new laser theory.

References

1. N.G. Basov, A.M. Prokhorov. UFN **57**, 485 (1955); UFN **93**, 572 (1967)
2. J.P. Gordon, H.J. Zeiger, C.H. Townes, Phys. Rev. **99**, 1264 (1955)
3. L. Allen, J. Eberly. *Optical Resonance and Two-Level Atoms* (Mir, Moscow, 1978)
4. V.G. Minogin, *Laser Physics* (MIPT, Moscow, 2010)
5. G. Lindblad, Commun. Math. Phys. **48**, 119 (1976)
6. B.V. Bondarev, *Density Matrix Method in Quantum Cooperative Process Theory*, 2nd edn. (Sputnik+, Moscow, 2013)
7. B.V. Bondarev, Theor. Math. Phys. **100**, 33 (1994)
8. B.V. Bondarev, Appl. Math. **8**, 1529 (2017)

Chapter 15
Critical Current in Strips Based on the Josephson Medium

M. V. Belodedov, L. P. Ichkitidze and S. V. Selishchev

Abstract The penetration of the magnetic field into massive samples of high-temperature superconductors (HTSC) is traditionally considered from the standpoint of electrodynamics of superconductors of the second kind, although HTSC is a multiple Josephson medium. By averaging the microscopic parameters of such a medium its material equation is derived in the work. The vortex solutions of the resulting equations are modeled and the conclusion is drawn that magnetic vortices carrying single quanta of magnetic flux must be realized in HTSCs. On the base of the proposed phenomenological equation, modelling of high-temperature superconductor strips is carried out and the conclusion is drawn about the inexpediency of using wide strip.

15.1 Introduction

The response to the external magnetic field and the nature of its penetration is the main distinguishing feature of various superconducting media that attract the interest of researchers at all times, from the discovery of superconductivity. The process of magnetic field penetration into superconductors of the second kind, which are practically all superconducting alloys and compounds, is extremely complicated and confusing. As was first shown in [1], the field penetrates into them in the form of single vortices, each of which carries a separate quantum of the magnetic flux $\Phi_0 = hc/2e = 2.07 \times 10^{-7}$ G $\times$ cm^2 . The name "vortex" was fixed

M. V. Belodedov
Bauman Moscow State Technical University (BMSTU), 5/1, 2nd Baumanskaya Street, Moscow 105005, Russia

L. P. Ichkitidze (✉) · S. V. Selishchev
National Research University of Electronic Technology (MIET), 1, Shokin Square, Zelenograd, Moscow 124498, Russia
e-mail: leo852@inbox.ru; ichkitidze@bms.zone

L. P. Ichkitidze
I.M. Sechenov First Moscow State Medical University, Moscow 119991, Russia

I. A. Parinov et al. (eds.), *Advanced Materials*, Springer Proceedings in Physics 224, https://doi.org/10.1007/978-3-030-19894-7_15

these formations due to the fact that their normal (non-superconducting) core is surrounded by vortex superconducting currents shielding from magnetic field the rest of the array of superconductor. A beautiful analogue of the Abrikosov vortex is the Josephson vortex [2], which is observed in distributed Josephson transitions. As in the Abrikosov vortex, in the Josephson vortex there is a concentration of the magnetic field screened from penetration into the interior of the superconductor by London surface currents, and into the depth of the distributed transition by Josephson currents. Unlike Abrikosov, the Josephson vortex has not a normal core, but it also contains only a single quantum of magnetic flux.

With the discovery of high-temperature superconductors [3], the urgency of studying granular superconductors, which are a medium consisting of a large number of superconducting granules of small size, forming Josephson junction in contacts in with each other, has sharply increased. A qualitative picture of the penetration of a magnetic field into such a medium was proposed in [4]. It consists in the fact that the magnetic field penetrates into the space between the granules as a distributed transition and a Josephson vortex there, but since such transitions are many and they are connected in a random way, such a vortex forms a two-dimensional structure that captures a large number of granules. Such a vortex was called “hypervortex”. The exact properties and parameters of hypervortex (size, shape, contained magnetic flux) were not determined in [4], despite this, the overwhelming majority of researchers [5] hold the view that hypervortex is completely analogous to ordinary Abrikosov vortex, with the exception of the absence of a normal core and significantly larger sizes (which leads to significantly smaller values of the critical fields).

In this paper we propose a model for the formation of magnetic vortices in a granular superconductor and estimates of their main parameters are given. The vortex-free penetration of the magnetic field into a granular Josephson medium is also considered and estimates of the dependence of the maximum possible current through the HTSC wires from the external magnetic field are made.

15.2 The Material Equation of a Granular Superconductor

We will consider a granular superconductor as a multiple Josephson medium formed by superconducting granules and Josephson junctions at their contacts. We denote by $\theta(\vec{r}, t)$ the phase of the wave function of superconducting electrons. Assuming that the size of the granules significantly higher the London penetration depth, the function $\theta(\vec{r}, t)$ inside the granules is related to the vector-potential of the magnetic field by the Ginzburg-Landau equation [6]:

$$\nabla\theta = \frac{2\pi}{\Phi_0}\vec{A},$$

and undergoes a discontinuity at the Josephson junction between the granules. We construct a smooth function that coincides with $\theta(\vec{r},t)$ at the centers of the granules. It is obviously for any closed contour the condition:

$$\oint \nabla\tilde{\theta}(\vec{r})\mathrm{d}l = 2\pi m, \quad \mathrm{m-integer}. \tag{15.1}$$

It follows from the condition (15.1) that the rotor of the function $\theta(\vec{r},t)$ is zero almost everywhere, with the possible exception of individual points, where it is equal to $2\pi m$:

$$\mathrm{rot}\left(\nabla\tilde{\theta}\right) = \begin{cases} 0 & \text{almost everywhere;} \\ 2\pi m & \text{at individual points.} \end{cases} \tag{15.2}$$

Let us calculate the phase difference on the Josephson transition with the coordinates $\vec{r}_0$, formed by the granules whose centers have the coordinates $\vec{r}_i$ and $\vec{r}_j$:

$$\begin{aligned}\varphi_{i,j} &= \theta(\vec{r}_i) + (\vec{r}_0 - \vec{r}_i)\nabla\theta - \left(\theta\left(\vec{r}_j\right) + \left(\vec{r}_0 - \vec{r}_j\right)\nabla\theta\right) \\ &= \theta(\vec{r}_i) - \theta\left(\vec{r}_j\right) + \nabla\theta\left(\vec{r}_j - \vec{r}_i\right) = \tilde{\theta}(\vec{r}_i) - \tilde{\theta}\left(\vec{r}_j\right) - \frac{2\pi}{\Phi_0}\vec{A}\left(\vec{r}_j - \vec{r}_i\right) \\ &= \left(\nabla\tilde{\theta} - \frac{2\pi}{\Phi_0}\vec{A}\right)\left(\vec{r}_j - \vec{r}_i\right) = \left(\nabla\tilde{\theta} - \frac{2\pi}{\Phi_0}\vec{A}\right)a_{i,j},\end{aligned}$$

where $a_{i,j}$ is a vector connecting the centers of the granules under consideration.

Consider the vector quantity $\vec{F} = \vec{A} - \frac{2\pi}{\Phi_0}\nabla\tilde{\theta}$. This value determines the phase difference at the Josephson junction:

$$\varphi = -\frac{2\pi}{\Phi_0}\vec{F}\vec{a}, \tag{15.3}$$

where $\vec{a}$ is the vector connecting the centers of the granules forming the Josephson junction. On the other hand, the magnetic field $\vec{B}$ can be expressed through the rotor of the vector $\vec{F}$ almost everywhere except for individual points (15.2):

$$\mathrm{rot}\vec{F} = \mathrm{rot}\left(\vec{A} - \frac{2\pi}{\Phi_0}\nabla\tilde{\theta}\right) = \vec{B} - \frac{2\pi}{\Phi_0}\mathrm{rot}\left(\nabla\tilde{\theta}\right). \tag{15.4}$$

Let us apply the resistive model to the considered transition [6]:

$$I = I_c \sin\varphi - \frac{\Phi_0}{2\pi c}\left(\frac{1}{R}\dot{\varphi} + C\ddot{\varphi}\right),$$

where I is the current through the junction, I_c is the value of its critical current, R and C are its active resistance and capacitance.

Taking into account (15.3), the last expression can be written in the form:

$$I = -I_c \sin\left(\frac{2\pi}{\Phi_0}\vec{F}\vec{a}\right) - \frac{\vec{a}}{Rc}\left(\dot{\vec{F}} + RC\ddot{\vec{F}}\right). \tag{15.5}$$

Consider a volume V, containing a large number of granules (and correspondingly, a large number N of Josephson junctions formed between them), but at the same time small enough to put $\vec{A} = \text{const}$ inside it. We assume that the currents I_k flow each on the segment $\vec{a}_k$. To calculate the average current density in the volume V assume that a conductor of the length $\vec{a}_k$ has the cross-sectional area S_k and therefore a current with density $\vec{j}_k = \frac{\vec{a}_k}{a_k}\frac{I_k}{S_k} = \vec{a}_k\frac{I_k}{a_k S_k} = \frac{\vec{a}_k I_k}{V_k}$ flows inside it. The average current density in the volume V is thus equal to:

$$\vec{j} = \frac{1}{V}\sum_{k=1}^{N}\vec{j}_k V_k = \frac{1}{V}\sum_{k=1}^{N} I_k\vec{a}_k = \frac{1}{V}N\langle I\vec{a}\rangle = \rho\langle I\vec{a}\rangle, \tag{15.6}$$

where ρ denotes the average concentration of Josephson junctions.

The expression obtained includes the value $\langle I\vec{a}\rangle$:

$$\begin{aligned}\langle I\vec{a}\rangle &= -\left\langle \vec{a}\left(I_c \sin\left(\frac{2\pi}{\Phi_0}\vec{F}\vec{a}\right) + \frac{\vec{a}}{Rc}\left(\dot{\vec{F}} + RC\ddot{\vec{F}}\right)\right)\right\rangle \\ &= \left\langle I_c\vec{a}\sin\left(\frac{2\pi}{\Phi_0}\vec{F}\vec{a}\right)\right\rangle - \left\langle \frac{1}{Rc}\vec{a}\left(\vec{a}\left(\dot{\vec{F}} + RC\ddot{\vec{F}}\right)\right)\right\rangle.\end{aligned}$$

When calculating the given average values, it is natural to assume that the values I_c, R and C are statistically independent, so in the last expression they can be replaced by the mean values denoted by the same symbols:

$$\langle I\vec{a}\rangle = -I_c\left\langle \vec{a}\sin\left(\frac{2\pi}{\Phi_0}\vec{F}\vec{a}\right)\right\rangle - \frac{1}{Rc}\left\langle \vec{a}\left(\vec{a}\dot{\vec{F}}\right)\right\rangle - \frac{C}{c}\left\langle \vec{a}\left(\vec{a}\ddot{\vec{F}}\right)\right\rangle. \tag{15.7}$$

To calculate the average values in expression (15.7), assume that all directions of the vector $\vec{a}$ are equal, and its modulus has the distribution $w(a)$. We carry out averaging in a spherical coordinate system with the z-axis directed along the vector $\vec{F}$, the polar angle γ and the azimuthal angle ϕ. When the above assumptions are fulfilled, the mean values of expression (15.7) are determined only by the distribution law of the z-component of the vector $\vec{a}$:

$$\begin{aligned}
&\left\langle \vec{a}\sin\left(\tfrac{2\pi}{\Phi_0}\vec{F}\vec{a}\right)\right\rangle = \tfrac{\vec{F}}{F}\int\limits_{-\infty}^{\infty} a_z \sin\left(\tfrac{2\pi}{\Phi_0}Fa_z\right)w(a_z)\mathrm{d}a_z;\\
&\left\langle \vec{a}\left(\vec{a}\dot{\vec{F}}\right)\right\rangle = \tfrac{\dot{\vec{F}}}{F}\int\limits_{-\infty}^{\infty} a_z\left(\dot{F}a_z\right)w(a_z)\mathrm{d}a_z = \dot{\vec{F}}\int\limits_{-\infty}^{\infty} a_z^2 w(a_z)\mathrm{d}a_z;\\
&\left\langle \vec{a}\left(\vec{a}\ddot{\vec{F}}\right)\right\rangle = \ddot{\vec{F}}\int\limits_{-\infty}^{\infty} a_z^2 w(a_z)\mathrm{d}a_z.
\end{aligned} \tag{15.8}$$

It should be noted that in this case, the distribution law of the z-component of the vector $\vec{a}$, $w(a_z)$ is related to the distribution law of its modulus $w(a)$ by the relation:

$$w(a_z) = \int\limits_{a_z}^{\infty} \frac{w(a)}{2a}\mathrm{d}a. \tag{15.9}$$

Let us consider some of the most typical types of vector $\vec{a}$ distribution and the corresponding distribution laws $w(a_z)$.

1. The absolute value of the vector $\vec{a}$ is equal to $\bar{a}$. This means that all granules in the medium under consideration have a diameter $\bar{a}$. In this case $w(a_z) = 1/(2\bar{a})$ and expressions (15.8) take the form:

$$\begin{aligned}
&\left\langle \vec{a}\sin\left(\tfrac{2\pi}{\Phi_0}\vec{F}\vec{a}\right)\right\rangle = \tfrac{\vec{F}}{F}\times\bar{a}\left[\left(\tfrac{\Phi_0}{2\pi F\bar{a}}\right)^2\sin\left(\tfrac{2\pi}{\Phi_0}F\bar{a}\right) - \tfrac{\Phi_0}{2\pi F\bar{a}}\cos\left(\tfrac{2\pi}{\Phi_0}F\bar{a}\right)\right];\\
&\left\langle \vec{a}\left(\vec{a}\dot{\vec{F}}\right)\right\rangle = \tfrac{1}{3}\dot{\vec{F}}\bar{a}^2;\\
&\left\langle \vec{a}\left(\vec{a}\ddot{\vec{F}}\right)\right\rangle = \tfrac{1}{3}\ddot{\vec{F}}\bar{a}^2.
\end{aligned} \tag{15.10a}$$

2. The vector modulus $\vec{a}$ has a uniform distribution with an average value $\bar{a}$, where $0 \le a \le 2\bar{a}$. Using (15.9), it is not difficult to get that in this case $w(a_z) = \frac{1}{4\bar{a}}\ln\left|\frac{2\bar{a}}{a_z}\right|$ at $0 \le |a_z| \le 2\bar{a}$. Expressions (15.8) take the form:

$$\begin{aligned}
&\left\langle \vec{a}\sin\left(\tfrac{2\pi}{\Phi_0}\vec{F}\vec{a}\right)\right\rangle = \tfrac{\vec{F}}{F}\times\tfrac{\bar{a}}{2}\left(\tfrac{\Phi_0}{2\pi F\bar{a}}\right)^2\left[\mathrm{Si}\left(\tfrac{2\pi}{\Phi_0}F\bar{a}\right) - \sin\left(\tfrac{2\pi}{\Phi_0}F\bar{a}\right)\right];\\
&\left\langle \vec{a}\left(\vec{a}\dot{\vec{F}}\right)\right\rangle = \tfrac{4}{9}\dot{\vec{F}}\bar{a}^2;\\
&\left\langle \vec{a}\left(\vec{a}\ddot{\vec{F}}\right)\right\rangle = \tfrac{4}{9}\ddot{\vec{F}}\bar{a}^2.
\end{aligned} \tag{15.10b}$$

where Si denotes the integral sine function: $\mathrm{Si}(x) = \int_0^x \frac{\sin(x)}{x}\mathrm{d}x$.

3. The diameter of the granules has a uniform distribution, which corresponds to $w(a) = a/\bar{a}^2$ at $0 \le a \le \bar{a}$ and $w(a) = 2/\bar{a} - a/\bar{a}^2$ at $\bar{a} \le a \le 2\bar{a}$. In this case, the distribution law of the z-component of the vector $\vec{a}$ has the form:

$$w(a_z) = \begin{cases} \frac{1}{\bar{a}}\left(\ln 2 - \left|\frac{a_z}{2\bar{a}}\right|\right) & \text{at } 0 \le |a_z| \le \bar{a} \\ \frac{1}{\bar{a}}\left(\ln\left|\frac{2\bar{a}}{a_z}\right| + \left|\frac{a_z}{2\bar{a}}\right| - 1\right) & \text{at } |a_z| \ge \bar{a} \end{cases}$$

which corresponds to the following form of expressions (15.8):

$$\begin{aligned} \left\langle \vec{a}\sin\left(\frac{2\pi}{\Phi_0}\vec{F}\vec{a}\right)\right\rangle &= \frac{\vec{F}}{F}\times 2\bar{a}\left(\frac{\Phi_0}{2\pi F\bar{a}}\right)^3\left[\frac{2\pi}{\Phi_0}F\bar{a}\left(\mathrm{Si}\left(2\frac{2\pi}{\Phi_0}F\bar{a}\right)\right)\right. \\ &\quad \left. -\mathrm{Si}\left(\frac{2\pi}{\Phi_0}F\bar{a}\right)+2\cos^2\left(\frac{2\pi}{\Phi_0}F\bar{a}\right)-2\cos\left(\frac{2\pi}{\Phi_0}F\bar{a}\right)\right]; \\ \left\langle \vec{a}\left(\vec{a}\dot{\vec{F}}\right)\right\rangle &= \frac{7}{18}\dot{\vec{F}}\bar{a}^2; \\ \left\langle \vec{a}\left(\vec{a}\ddot{\vec{F}}\right)\right\rangle &= \frac{7}{18}\ddot{\vec{F}}\bar{a}^2. \end{aligned} \tag{15.10c}$$

4. The absolute value of the vector $\vec{a}$ has a Maxwell distribution with an average value $\bar{a}$:

$$w(a) = \frac{32}{\bar{a}^3\pi^2}a^2\exp\left(-\frac{4a^2}{\bar{a}^2\pi}\right).$$

In this case, the z-component of this vector $\vec{a}$ is distributed to the normal low:

$$w(a_z) = \frac{2}{\bar{a}\pi}\exp\left(-\frac{4a_z^2}{\bar{a}^2\pi}\right),$$

and the expressions (15.8) take the form:

$$\begin{aligned} \left\langle \vec{a}\sin\left(\tfrac{2\pi}{\Phi_0}\vec{F}\vec{a}\right)\right\rangle &= \tfrac{\vec{F}}{F}\times\bar{a}\tfrac{\pi}{8}\left(\tfrac{2\pi}{\Phi_0}F\bar{a}\right)\exp\left[-\tfrac{\pi}{16}\left(\tfrac{2\pi}{\Phi_0}F\bar{a}\right)^2\right]; \\ \left\langle \vec{a}\left(\vec{a}\dot{\vec{F}}\right)\right\rangle &= \tfrac{\pi}{8}\dot{\vec{F}}\bar{a}^2; \\ \left\langle \vec{a}\left(\vec{a}\ddot{\vec{F}}\right)\right\rangle &= \tfrac{\pi}{8}\ddot{\vec{F}}\bar{a}^2. \end{aligned} \tag{15.10d}$$

It should be noted that the case of the normal granule size distribution coincides with the case considered.

The relations (15.6), (15.7) and (15.8) give the base to write the material equation of the medium in question:

$$\vec{j} = -\frac{\vec{F}}{F} I_c \rho \bar{a} M(F) - \frac{\rho}{Rc} \eta \dot{\vec{F}} \bar{a}^2 - \frac{C\rho}{c} \eta \ddot{\vec{F}} \bar{a}^2, \tag{15.11}$$

where the $M(F)$ dependence is determined by the law of distribution of granules in size:

$$M(F) = \frac{1}{\bar{a}} \int_{-\infty}^{\infty} a_z \sin\left(\frac{2\pi}{\Phi_0} F a_z\right) w(a_z)\, \mathrm{d}a_z$$

and in the four cases considered, in accordance with the expressions (15.10a)–(15.10d) has the form:

1. $M(F) = \left(\frac{\Phi_0}{2\pi F \bar{a}}\right)^2 \sin\left(\frac{2\pi}{\Phi_0} F \bar{a}\right) - \frac{\Phi_0}{2\pi F \bar{a}} \cos\left(\frac{2\pi}{\Phi_0} F \bar{a}\right)$;
2. $M(F) = \frac{1}{2}\left(\frac{\Phi_0}{2\pi F \bar{a}}\right)^2 \left[\mathrm{Si}\left(2\frac{2\pi}{\Phi_0} F \bar{a}\right) - \sin\left(2\frac{2\pi}{\Phi_0} F \bar{a}\right)\right]$;
3. $M(F) = 2\left(\frac{\Phi_0}{2\pi F \bar{a}}\right)^3 \left[\frac{2\pi}{\Phi_0} F \bar{a}\left(\mathrm{Si}\left(2\frac{2\pi}{\Phi_0} F \bar{a}\right) - \mathrm{Si}\left(\frac{2\pi}{\Phi_0} F \bar{a}\right)\right)\right.$
$\left. + 2\cos^2\left(\frac{2\pi}{\Phi_0} F \bar{a}\right) - 2\cos\left(\frac{2\pi}{\Phi_0} F \bar{a}\right)\right]$;
4. $M(F) = \frac{\pi}{8}\left(\frac{2\pi}{\Phi_0} F \bar{a}\right) \exp\left[-\frac{\pi}{16}\left(\frac{2\pi}{\Phi_0} F \bar{a}\right)^2\right]$,

and is graphically represented in Figs. 15.1 and 15.2.

The coefficient η, determined by the same distribution law:

$$\eta = \frac{1}{\bar{a}^2} \int_{-\infty}^{\infty} a_z^2 w(a_z) \mathrm{d}a_z,$$

in the cases considered, has the following meanings:

1. $\eta = 1/3$;
2. $\eta = 4/9$;
3. $\eta = 7/18$;
4. $\eta = \pi/8$.

It is not difficult to show that the dependence $M(F)$ for small values of F tends to linear:

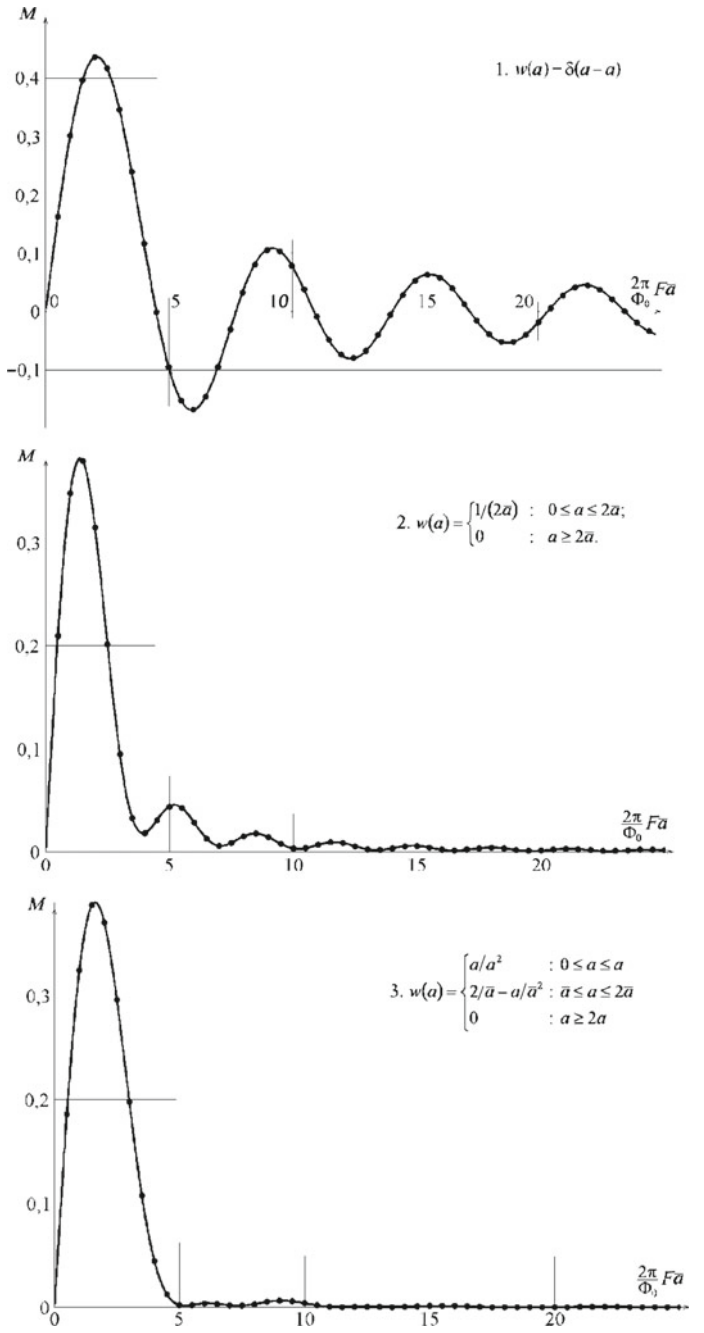

Fig. 15.1 Dependence $M(F)$ for different types of distribution a; the dots mark the results of direct calculation of $\langle \vec{a} \sin(2\pi \vec{F}\vec{a}/\Phi_0) \rangle$ by $10^8 \ldots 10^9$ implementations

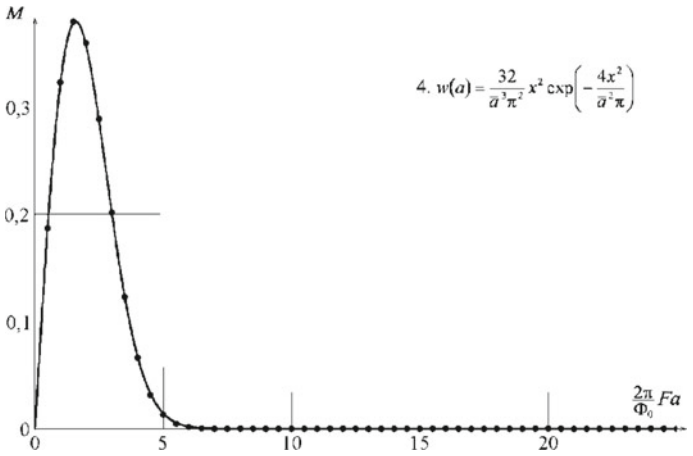

Fig. 15.1 (continued)

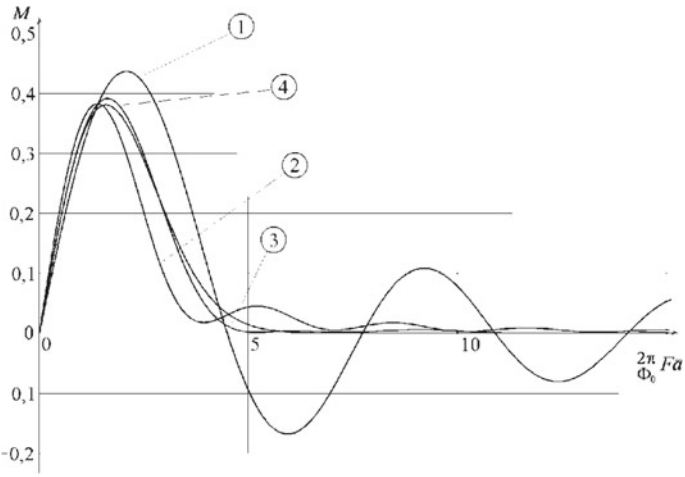

Fig. 15.2 Comparison of material dependences of granular superconducting media with different laws of distribution of granules in size: 1—(15.10a); 2—(15.10b); 3—(15.10c); 4—(15.10d)

$$\lim_{F\to 0} M(F) = \lim_{F\to 0} \frac{1}{\bar{a}} \int_{-\infty}^{\infty} a_z \sin\left(\frac{2\pi}{\Phi_0} F a_z\right) w(a_z)\, \mathrm{d}a_z$$

$$= \frac{1}{\bar{a}} \frac{2\pi}{\Phi_0} F \int_{-\infty}^{\infty} a_z^2 w(a_z)\, \mathrm{d}a_z = F \frac{2\pi}{\Phi_0} \eta \bar{a},$$

which implies that for small values of F in the stationary case, the material equation (15.11) takes the form:

$$j = -\frac{\vec{F}}{F}\frac{2\pi}{\Phi_0} I_c \rho \bar{a}^2 \eta F. \tag{15.12}$$

15.3 Penetration of a Weak Magnetic Field into a Granular Superconductor. Phenomenological Constants

We consider the problem of penetration of a magnetic field into a semi-infinite $(x > 0)$ medium of the type under consideration. Taking into account the Maxwell equation $\mathrm{rot}\,\mathrm{rot}\,\vec{A} = \mathrm{rot}\,\mathrm{rot}\,\vec{F} = \frac{4\pi\mu}{c}\vec{j}$ and the material equation (15.12), the penetration of the magnetic field into the medium is described by the equation:

$$\nabla^2 \vec{F} = \vec{F}\frac{2\pi}{\Phi_0}\frac{4\pi\mu}{c} I_c \rho \bar{a}^2 \eta,$$

which has the solution: $F = F_0 \exp(-x/\lambda_M)$, where the λ_M designates the characteristic penetration depth of the magnetic field:

$$\lambda_M = \sqrt{\frac{\Phi_0}{2\pi}\frac{c}{4\pi\mu I_c \rho \bar{a}^2 \eta}}.$$

In the last expressions, the value μ has the meaning of the magnetic permeability of the medium due solely to the Meissner currents of the individual granules.

The material equation (15.11), provided that the magnetic field is small, leads to the equation:

$$\nabla^2 \vec{F} = \frac{1}{\lambda_M^2}\vec{F} + \frac{1}{v_M^2}\frac{1}{RC}\dot{\vec{F}} + \frac{1}{v_M^2}\ddot{\vec{F}},$$

where a new parameter, $v_M = \frac{c}{2\bar{a}\sqrt{\pi\mu C \rho \eta}} = \lambda_M \sqrt{\frac{2\pi}{\Phi_0}\frac{cI_c}{C}}$, having a velocity dimension is introduced.

Thus, the multiple Josephson medium is described by the material equation:

$$\vec{j} = \frac{\vec{F}}{F} I_c \rho \bar{a} M(F) - \frac{c}{4\pi\mu}\frac{1}{v_M^2}\frac{1}{RC}\dot{\vec{F}} - \frac{c}{4\pi\mu}\frac{1}{v_M^2}\ddot{\vec{F}}, \tag{15.13}$$

and the distribution of the magnetic field in it obeys the equation:

$$\nabla^2\vec{F} = \frac{\vec{F}}{F}\frac{1}{\bar{a}\eta}\frac{\Phi_0}{2\pi}\frac{1}{\lambda_M^2}M(F) + \frac{1}{v_M^2}\frac{1}{RC}\dot{\vec{F}} + \frac{1}{v_M^2}\ddot{\vec{F}}. \tag{15.14}$$

Figure 15.2 demonstrates that granular media with essentially different laws of granule size distribution are described by approximately the same material equations, especially at the initial part of the dependence. A somewhat isolated position occupies only the "excessively ideal" case of granules of the same size.

15.4 Magnetic Vortices in a Granular Superconductor

Let us consider stationary radially symmetric solutions of (15.14). We will assume here that the magnetic field has only the component $B_z = B$, constant with respect to the z coordinate, that is, in the polar coordinate system, the vector $\vec{F}$ has only the component $F_\varphi = F$. Equation (15.14) under the accepted conditions will have the form:

$$\frac{\mathrm{d}}{\mathrm{d}r}\left(\frac{1}{r}\frac{\mathrm{d}}{\mathrm{d}r}(rF)\right) = \frac{1}{\bar{a}\eta}\frac{\Phi_0}{2\pi}\frac{1}{\lambda_M^2}M(F),$$

where the magnetic field is related to the value F by the relation:

$$B = \frac{1}{r}\frac{\mathrm{d}}{\mathrm{d}r}(rF)$$

everywhere except the point $r = 0$.

After the introduction of dimensionless quantities:

$$\tilde{r} = \frac{r}{\lambda_M}, \quad \tilde{F} = \frac{2\pi}{\Phi_0}F\bar{a}, \quad \tilde{B} = \frac{2\pi\bar{a}\lambda_M}{\Phi_0}B$$

the last equations are substantially simplified:

$$\begin{aligned} &\frac{\mathrm{d}}{\mathrm{d}\tilde{r}}\left(\frac{1}{\tilde{r}}\frac{\mathrm{d}}{\mathrm{d}\tilde{r}}\left(\tilde{r}\tilde{F}\right)\right) = \frac{1}{\eta}M\left(\tilde{F}\right); \\ &\tilde{B} = \frac{1}{\tilde{r}}\frac{\mathrm{d}}{\mathrm{d}\tilde{r}}\left(\tilde{r}\tilde{F}\right). \end{aligned} \tag{15.15}$$

In the four cases considered, the first of (15.15) takes the form:

$$
\begin{aligned}
&1.\ \frac{\mathrm{d}}{\mathrm{d}\tilde{r}}\left(\frac{1}{\tilde{r}}\frac{\mathrm{d}}{\mathrm{d}\tilde{r}}\left(\tilde{r}\tilde{F}\right)\right)=\frac{3}{\tilde{F}^2}\left[\sin\left(\tilde{F}\right)-\tilde{F}\cos\left(\tilde{F}\right)\right];\\
&2.\ \frac{\mathrm{d}}{\mathrm{d}\tilde{r}}\left(\frac{1}{\tilde{r}}\frac{\mathrm{d}}{\mathrm{d}\tilde{r}}\left(\tilde{r}\tilde{F}\right)\right)=\frac{9}{8}\frac{1}{\tilde{F}^2}\left[\mathrm{Si}\left(2\tilde{F}\right)-\sin\left(2\tilde{F}\right)\right];\\
&3.\ \frac{\mathrm{d}}{\mathrm{d}\tilde{r}}\left(\frac{1}{\tilde{r}}\frac{\mathrm{d}}{\mathrm{d}\tilde{r}}\left(\tilde{r}\tilde{F}\right)\right)=\frac{36}{7}\frac{1}{\tilde{F}^3}\left[\tilde{F}\left(\mathrm{Si}\left(2\tilde{F}\right)-\mathrm{Si}\left(\tilde{F}\right)\right)+2\cos^2\left(\tilde{F}\right)-2\cos\left(\tilde{F}\right)\right];\\
&4.\ \frac{\mathrm{d}}{\mathrm{d}\tilde{r}}\left(\frac{1}{\tilde{r}}\frac{\mathrm{d}}{\mathrm{d}\tilde{r}}\left(\tilde{r}\tilde{F}\right)\right)=\tilde{F}\exp\left(-\frac{\pi}{16}\tilde{F}^2\right).
\end{aligned}
\tag{15.16}
$$

We integrate the quantity F along a closed circular contour centered at the point $r = 0$ and with radius r, taking into account the relation (15.4):

$$
\begin{aligned}
\oint \vec{F}\mathrm{d}\vec{l}=\oint\left(\vec{A}-\frac{\Phi_0}{2\pi}\nabla\tilde{\theta}\right)\mathrm{d}\vec{l}&=\oint\vec{A}\mathrm{d}\vec{l}-\frac{\Phi_0}{2\pi}\oint\nabla\tilde{\theta}\mathrm{d}\vec{l}\\
&=\int\limits_S \mathrm{rot}\vec{A}\mathrm{d}s-n\Phi_0=nr^2B-n\Phi_0,
\end{aligned}
$$

where n is any integer. Because $\oint \vec{F}\mathrm{d}\vec{l}=2\pi rF$, the last expression with the aspiration of r to zero leads to the condition:

$$
\lim_{r\to 0}(Fr)=n\frac{\Phi_0}{2\pi},
$$

which for dimensionless quantities takes the form:

$$
\lim_{r\to 0}\left(\tilde{F}\tilde{r}\right)=n\frac{\bar{a}}{\lambda_M}. \tag{15.17a}
$$

The obtained condition, together with condition:

$$
\lim_{r\to\infty}\left(\tilde{B}\right)=0 \tag{15.17b}
$$

can be used to search for solitary vortex solutions to (15.16). The families of solutions of (15.16) with reduced boundary conditions (15.17) for the case of $\bar{a}/\lambda_M = 0.1$ and for various values of n are shown in Fig. 15.3. Different values of n correspond to different values of the magnetic field strength at the center of the vortex and the total magnetic flux contained in the vortex.

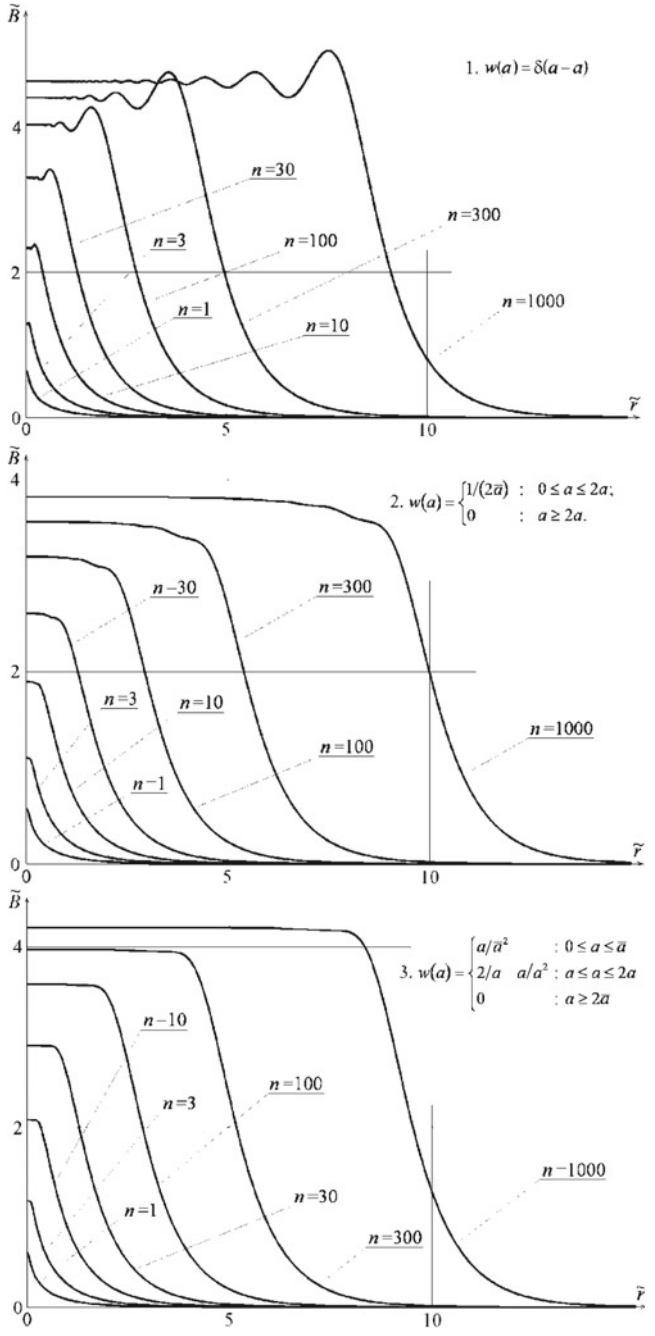

Fig. 15.3 Families of solutions of (15.16) with boundary conditions (15.17) for $\bar{a}/\lambda_M = 0.1$ and different values of the parameter n

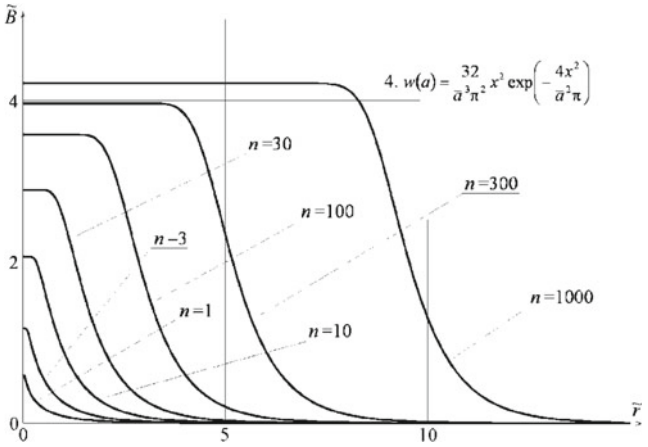

Fig. 15.3 (continued)

The most important practical significance is the question of the magnetic flux contained in a single vortex. To answer this question, it is sufficient to integrate the solutions obtained (Fig. 15.3):

$$\Phi = 2\pi \int_0^\infty B(r)\, r\mathrm{d}r = \Phi_0 \frac{\lambda_M}{\bar{a}} \int_0^\infty \tilde{B}(\tilde{r})\, \tilde{r}\mathrm{d}\tilde{r}. \tag{15.18}$$

The results of integration for different values of the parameters n and $\lambda_M/\bar{a}$ at various laws for the distribution of a are given in Table 15.1.

Despite the relatively low accuracy of calculations—a difference scheme of the first order of accuracy was used to solve the differential equation (15.16), and the integration (15.18) was carried out by the trapezoid method—the results of Table 15.1 allow us to draw a sufficiently expected conclusion: the magnetic flux contained in the vortex does not depend either from the law of granule size distribution (at least within the four distribution laws considered) nor on the parameter $\bar{a}/\lambda_M$, and is a multiple of the magnetic flux quantum Φ_0.

In order to determine which of the set of solutions of Fig. 15.3 (for a given material equation $M(F)$) is realized in practice, it is necessary to calculate their total energy, that is composed of the energy of the magnetic field and the internal energy of the Josephson junctions. A single transition has the energy [6]:

$$E_\mathrm{J} = \frac{\Phi_0}{2\pi} I_\mathrm{c}(1 - \cos\varphi),$$

Table 15.1 Magnetic flux contained in the vortex (in Φ_0 units) for different values of the parameters n and $\lambda_M/\bar{a}$

$\lambda_M/\bar{a}$	n					
	1	3	10	30	100	300
1. $w(a) = \delta(a - \bar{a})$						
3	1.0017	2.9998	10.0002	30.0001	99.9985	299.8948
10	0.9981	3.0026	9.9992	30.0002	99.9902	300.0020
30	1.0117	2.9943	10.0164	29.9974	100.0019	300.2763
100	0.9529	2.9774	9.9819	30.0262	99.9914	300.0020
2. $w(a) = \frac{1}{\bar{a}}$						
3	1.0006	2.9995	10.0009	29.9999	99.9972	299.7107
10	0.9959	3.0058	9.9982	29.9985	99.9997	299.9925
30	1.0110	2.9876	10.0055	29.9904	100.0090	299.9990
100	1.0409	3.0358	9.9584	30.0574	99.9637	299.9845
3. $w(a) = \begin{cases} \frac{a}{\bar{a}^2} & \text{for } 0 \le a \le \bar{a}; \\ \frac{2}{\bar{a}} - \frac{a}{\bar{a}^2} & \text{for } \bar{a} \le a \le 2\bar{a} \end{cases}$						
3	0.9992	2.9995	10.0005	30.0005	99.9979	299.8287
10	0.9992	3.0005	9.9983	30.0016	100.0016	299.9947
30	1.0008	3.0030	10.0003	29.9949	100.0045	300.0052
100	1.0152	3.0190	9.9927	30.0051	99.9819	299.5572
4. $w(a) = \frac{32}{\bar{a}^3\pi^2} a^2 \exp\left(-\frac{4a^2}{\bar{a}^2\pi}\right)$						
3	1.0003	3.0000	10.0005	29.9997	99.9954	299.8255
10	1.0014	2.9977	9.9998	29.9995	99.9983	299.9884
30	1.0099	3.0042	10.0027	29.9992	100.0045	299.9964
100	1.0077	3.0398	10.0139	29.9767	99.9976	299.9949

Simulation was carried out for different laws of distribution $w(a)$

therefore, the considered medium [taking into account the relation (15.3)] has a density of Josephson energy:

$$W_J = \frac{\Phi_0}{2\pi} I_c \rho \left(1 - \left\langle \cos\left(\frac{2\pi}{\Phi_0} \vec{F}\vec{a}\right)\right\rangle\right). \tag{15.19}$$

The last expression, taking into account the assumptions made earlier by deriving the relations (15.8), takes the form:

$$W_J = \frac{\Phi_0}{2\pi} I_c \rho \left(1 - \left\langle \cos\left(\frac{2\pi}{\Phi_0} F a_z\right)\right\rangle\right),$$

that makes it possible to obtain expressions for the density of the Josephson energy for the four considered laws of grain size distribution:

1. $W_J = \frac{\Phi_0}{2\pi} I_c \rho \left(1 - \frac{\Phi_0}{2\pi F\bar{a}} \sin\left(\frac{2\pi}{\Phi_0} F\bar{a}\right)\right)$;
2. $W_J = \frac{\Phi_0}{2\pi} I_c \rho \left(1 - \frac{\Phi_0}{4\pi F\bar{a}} \mathrm{Si}\left(\frac{4\pi}{\Phi_0} F\bar{a}\right)\right)$;
3. $W_J = \frac{\Phi_0}{2\pi} I_c \rho \left(1 - \left(\frac{\Phi_0}{2\pi F\bar{a}}\right)^2 \left(1 + \cos\left(2\frac{2\pi}{\Phi_0} F\bar{a}\right) - 2\cos\left(\frac{2\pi}{\Phi_0} F\bar{a}\right)\right)\right.$
$\left. -2\left(\frac{\Phi_0}{2\pi F\bar{a}}\right)\left(\mathrm{Si}\left(2\frac{2\pi}{\Phi_0} F\bar{a}\right) - \mathrm{Si}\left(\frac{2\pi}{\Phi_0} F\bar{a}\right)\right)\right)$;
4. $W_J = \frac{\Phi_0}{2\pi} I_c \rho \left(1 - \exp\left(-\frac{\pi}{16}\left(\frac{2\pi}{\Phi_0} F\bar{a}\right)^2\right)\right)$.

These dependencies are shown in Fig. 15.4, which demonstrates that the dependence of the energy density of Josephson junctions on the magnetic field varies slightly with the variation of the size distribution law of granules, just as in the case of material dependence (Fig. 15.2).

The total vorticity energy per unit length along the z coordinate is made up of the energy of the magnetic field and the energy of the Josephson junctions (15.19):

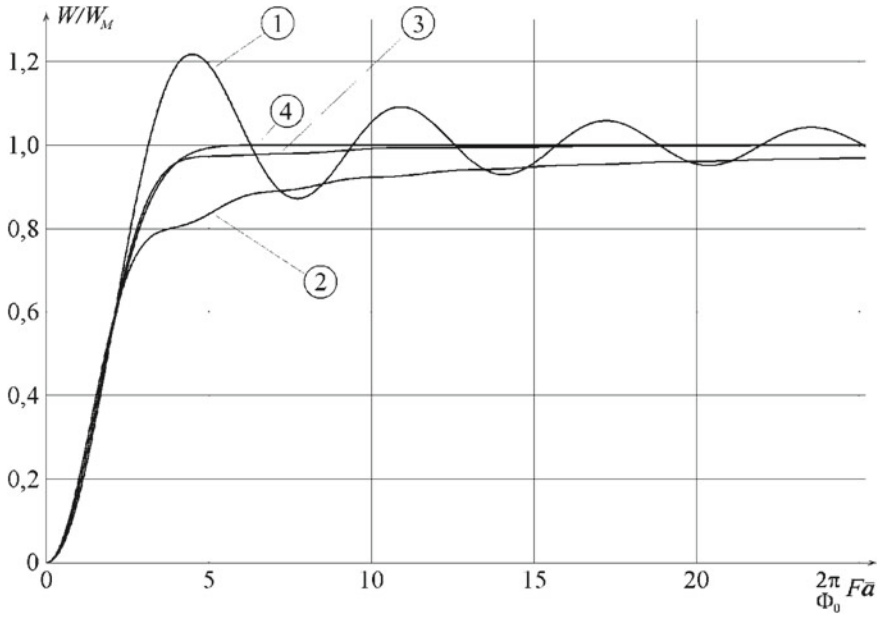

Fig. 15.4 Dependence of the energy density of Josephson junctions on the vector potential of the magnetic field (in $W_M = (\Phi_0/2\pi) I_c \rho$ units) for various laws of grain size distribution according to the formulas: 1—(15.10a); 2—(15.10b); 3—(15.10c); 4—(15.10d)

$$E = \int\limits_V \frac{B^2(r)}{8\pi\mu}\mathrm{d}x\,\mathrm{d}y + \int\limits_V W_\mathrm{J}(r)\mathrm{d}x\,\mathrm{d}y$$
$$= \frac{1}{4\mu}\int\limits_0^\infty rB^2(r)\mathrm{d}r + \frac{1}{c}\Phi_0 I_\mathrm{c}\rho\int\limits_0^\infty r\left(1 - \left\langle\cos\left(\frac{2\pi}{\Phi_0}Fa_z\right)\right\rangle\right)\mathrm{d}r,$$

and for dimensionless quantities has the form:

$$E = \frac{B_M^2\lambda_M^2}{4\mu}\left[\int\limits_0^\infty \tilde{r}\tilde{B}^2(\tilde{r})\mathrm{d}\tilde{r} + \mu\frac{1}{\eta}\int\limits_0^\infty \tilde{r}\left(1 - \left\langle\cos\left(\frac{2\pi}{\Phi_0}Fa_z\right)\right\rangle\right)\mathrm{d}\tilde{r}\right]. \tag{15.20}$$

Magnetic vortices containing n magnetic flux quanta will be realized in practice only if the ratio of their total energy to the parameter n has a minimum value. Figure 15.5 shows the dependence of the magnitude of the magnetic component of the specific total energy:

$$\tilde{E}_M = \frac{1}{n}\int\limits_0^\infty \tilde{r}\tilde{B}^2(\tilde{r})\mathrm{d}\tilde{r} \tag{15.21}$$

and its Josephson component

$$\tilde{E}_\mathrm{J} = \frac{1}{n}\frac{1}{\eta}\int\limits_0^\infty \tilde{r}\left(1 - \left\langle\cos\left(\frac{2\pi}{\Phi_0}Fa_z\right)\right\rangle\right)\mathrm{d}\tilde{r} \tag{15.22}$$

on the parameter n.

The dependences (15.21) and (15.22) increase monotonically with the growth of the integer parameter n, from which it follows that the specific total energy of the vortices

$$E = \frac{B_M^2\lambda_M^2}{4\mu}\left(\tilde{E}_M + \mu\tilde{E}_\mathrm{J}\right)$$

also increases monotonically with the increasing of n. This means that the minimum of the specific total energy is realized at the smallest value $n = 1$, corresponding, as has been shown, to vortices carrying single quanta of the magnetic flux.

Thus, in a granular superconductor, regardless of the law of grain size distribution, one-quantum magnetic vortices should be observed.

In view of the weak dependence of the proposed material equation on the law of distribution of granules by size, we will further consider the case 4—Maxwellian size distribution of granules:

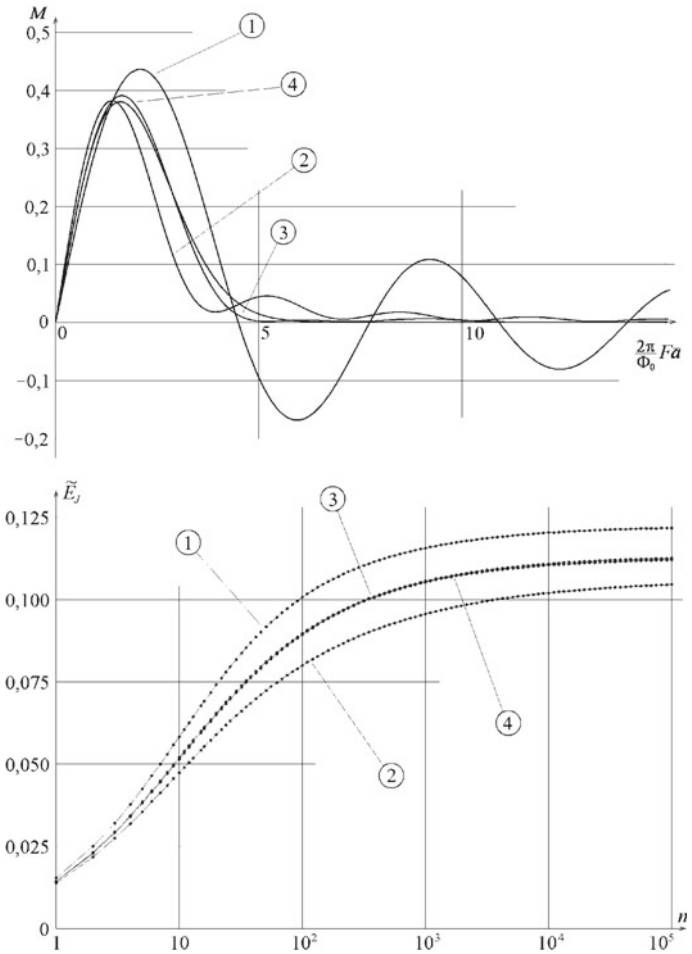

Fig. 15.5 Dependence of the magnetic and Josephson components of the specific total vortex energy on the parameter n. Dependences are given for the four laws of the distribution of the parameter a considered: 1—(15.10a); 2—(15.10b); 3—(15.10c); 4—(15.10d)

$$M(F) = \frac{\pi}{8}\left(\frac{2\pi}{\Phi_0}F\bar{a}\right)\exp\left[-\frac{\pi}{16}\left(\frac{2\pi}{\Phi_0}F\bar{a}\right)^2\right];$$

$$\vec{j} = -\frac{\vec{F}}{F}I_c\rho\bar{a}M(F) - \frac{\rho\pi\bar{a}^2}{8Rc}\dot{\vec{F}} - \frac{C\rho\pi\bar{a}^2}{8c}\ddot{\vec{F}},$$

which in the stationary case takes the form:

$$\vec{j} = -\frac{\vec{F}}{F} I_c \rho \bar{a} \frac{\pi}{8} \left(\frac{2\pi}{\Phi_0} F \bar{a} \right) \exp\left[-\frac{\pi}{16} \left(\frac{2\pi}{\Phi_0} F \bar{a} \right)^2 \right].$$

Thus, the penetration of a magnetic field into the medium under consideration in stationary case can be modeled using of phenomenological material equation:

$$\vec{j} = -\frac{c}{4\pi\mu} \nabla^2 \vec{F} = -\frac{c}{4\pi\mu} \times \frac{\vec{F}}{\lambda_M^2} \exp\left[-\frac{\pi}{16} \left(\frac{2\pi}{\Phi_0} F\, \bar{a} \right)^2 \right], \tag{15.23}$$

where the vector quantity $\vec{F}$ practically everywhere (except for individual points being the centers of "hypervortices") coincides with the vector potential of the magnetic field $\vec{A}$.

Let us consider some applications of the proposed material equation (15.23) for modeling the vortex-free penetration of a magnetic field into a Josephson medium.

15.5 Penetration of a Homogeneous Magnetic Field into a Semi-infinite Medium

Suppose, for definiteness, the semi-infinite medium occupies the space $x \geq 0$, and the magnetic field in the space $x < 0$ is directed along the y-axis and has the value B_0. In this case, the material equation (15.23) takes the form:

$$\frac{\mathrm{d}^2}{\mathrm{d}x^2} A = \frac{A}{\lambda_M^2} \exp\left[-\frac{\pi}{16} \left(\frac{2\pi}{\Phi_0} A\, \bar{a} \right)^2 \right] \tag{15.24}$$

and for dimensionless quantities

$$\tilde{x} = \frac{x}{\lambda_M}, \quad \tilde{A} = \frac{2\pi}{\Phi_0} A \bar{a}, \quad \tilde{B} = \frac{2\pi \bar{a} \lambda_M}{\Phi_0} B = \frac{\mathrm{d}\tilde{A}}{\mathrm{d}\tilde{x}}, \quad \tilde{j} = \frac{8}{I_c \rho \pi \bar{a}} j = -\tilde{A} \exp\left(-\frac{\pi}{16} \tilde{A}^2 \right) \tag{15.25}$$

it will look as

$$\frac{\mathrm{d}^2}{\mathrm{d}\tilde{x}^2} \tilde{A} = \tilde{A} \exp\left[-\frac{\pi}{16} \tilde{A}^2 \right]. \tag{15.26}$$

Vortex-free penetration of the magnetic field requires (15.26) to have a solution under boundary conditions:

$$\tilde{B}\big|_{\tilde{x}=0} = \frac{d\tilde{A}}{d\tilde{x}}\bigg|_{\tilde{x}=0} = \frac{2\pi\bar{a}\lambda_M}{\Phi_0} B_0 \text{ and } \lim_{\tilde{x}\to\infty} \tilde{A}(\tilde{x}) = 0. \tag{15.27}$$

Numerical simulation of (15.26) with boundary conditions (15.27) allows us to conclude that the maximum value of the external magnetic induction, for which there are no "hypervortices" and $\lim_{\tilde{x}\to\infty} \tilde{B}(\tilde{x}) = 0$, is

$$\left(\tilde{B}\big|_{\tilde{x}=0}\right)_{\max} = 2.256903\ldots,$$

which corresponds to the first critical field of the medium in question:

$$B_{c1} \approx 2.256903 \frac{\Phi_0}{2\pi\bar{a}\lambda_M}. \tag{15.28}$$

15.6 Simulation of Current Flow Through Strip Wires

Of great practical interest is the problem of the flow of a superconducting current through a strip-line. Consider such a line lying in the xy-plane with a thickness D and a width b, directed along the y-axis. Let the magnetic field be directed along the z-axis and has the value of $B = \mathrm{d}A/\mathrm{d}x$. The current density in the strip (under the condition that there are no vortices) is determined by the vector potential of the magnetic field (15.23):

$$j(x) = -\frac{c}{4\pi\mu}\frac{\mathrm{d}^2 A}{\mathrm{d}x^2},$$

whose distribution of along the coordinate x obeys (15.26):

$$\frac{\mathrm{d}^2}{\mathrm{d}\tilde{x}^2}\tilde{A} = \tilde{A}\exp\left[-\frac{\pi}{16}\tilde{A}^2\right].$$

A definite solution of (15.26) is possible only if there two boundary conditions. The first of them in the absence of an external magnetic field is obvious – the values of the magnetic field at the edges of the strip should be opposite in sign:

$$B\left(\frac{b}{2}\right) = -B\left(-\frac{b}{2}\right),$$

which corresponds to:

$$\left.\frac{d\tilde{A}}{d\tilde{x}}\right|_{\tilde{x}=-\frac{b}{2}} = -\left.\frac{d\tilde{A}}{d\tilde{x}}\right|_{\tilde{x}=\frac{b}{2}}. \tag{15.29}$$

The second boundary condition can be, for example, the condition:

$$\tilde{A}(\tilde{x})\big|_{\tilde{x}=0} = \tilde{A}_0. \tag{15.30}$$

Equation (15.26) with boundary conditions (15.29) and (15.30) can be solved by standard Runge-Kutta method.

A typical form of $\tilde{j}(\tilde{x})$ distributions with boundary condition (15.29) for different values of the $\tilde{A}_0$ constant in strips of different widths is shown in Fig. 15.6. In narrow strip es with a widths of the order of or less than λ_M a practically uniform distribution of the current is observed, in wide (several λ_M)—all the current is concentrated only on the edges of a strip 1–2 λ_M wide.

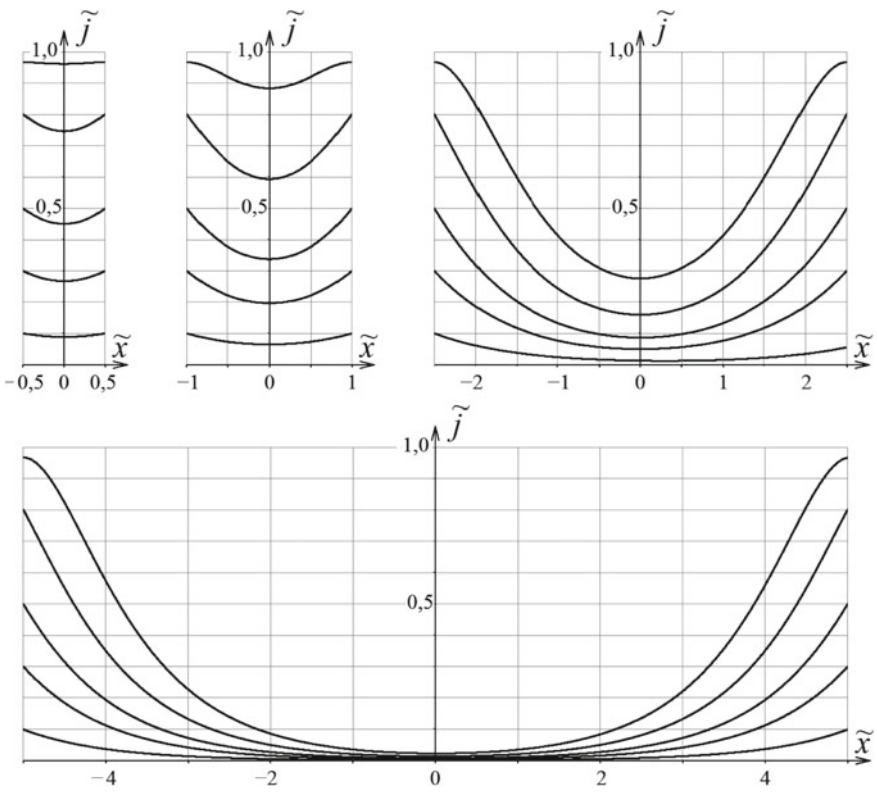

Fig. 15.6 Current distribution in strips of different widths for various values of the total current (from zero to the maximum value). Dimensionless units (15.25) are used

When modeling the flow of current through strips in an external magnetic field with induction $\tilde{B}_0$, perpendicular to the plane of the strip, the picture becomes more complicated. It is logical to assume that the current distribution along the width of the strip remains symmetrical. In this case, the changes in the magnetic field caused by the current of the strip at the opposite edges of the strip will be the same in magnitude, and opposite in sign, so the ratio must be expected:

$$\left(\tilde{B}\Big|_{\tilde{x}=-\frac{b}{2}}+\tilde{B}\Big|_{\tilde{x}=\frac{b}{2}}\right)/2=\left(\frac{\mathrm{d}\tilde{A}}{\mathrm{d}\tilde{x}}\Big|_{\tilde{x}=-\frac{b}{2}}+\frac{\mathrm{d}\tilde{A}}{\mathrm{d}\tilde{x}}\Big|_{\tilde{x}=\frac{b}{2}}\right)/2=\tilde{B}_0. \tag{15.31}$$

Thus, specifying two values $\tilde{A}_0$ and $\tilde{B}_0$ means setting two boundary conditions (15.30) and (15.31) and, thus, completely determines the solution of (15.26) and the current density distribution over the width of the strip $\tilde{j}(x)$. The distribution of the current density over the width of the strip makes it possible to calculate the total current through the strips:

$$\tilde{I}_{\mathrm{tot}}=D\int\limits_{-b/2}^{b/2}\tilde{j}(\tilde{x})\mathrm{d}\tilde{x}.$$

The numerical solution of (15.26) with boundary conditions (15.30) and (15.31) make it possible to obtain a tabular dependence $\tilde{I}_{\mathrm{tot}}\left(\tilde{A}_0,\tilde{B}_0\right)$. If one poses the problem of determining the maximum current through strips for a given external magnetic field, it is necessary to find the maximum value of $\tilde{I}_{\mathrm{tot}}$ in the set of all values of the constant $\tilde{A}_0$:

$$\tilde{I}_{\max}\left(\tilde{B}_0\right)=\max_{\tilde{A}_0}\left[\tilde{I}_{\mathrm{tot}}\left(\tilde{A}_0,\tilde{B}_0\right)\right]=\max_{\tilde{A}_0}\left(D\int\limits_{-b/2}^{b/2}\tilde{j}(\tilde{x})\big|_{\tilde{A}_0,\tilde{B}_0}\mathrm{d}\tilde{x}\right). \tag{15.32}$$

Obtained by the described method using the second-order Runge-Kutta method, the values of the maximum current through the strips for different values of the external magnetic field B_0 for strips of different widths are shown in the graphs of Fig. 15.7.

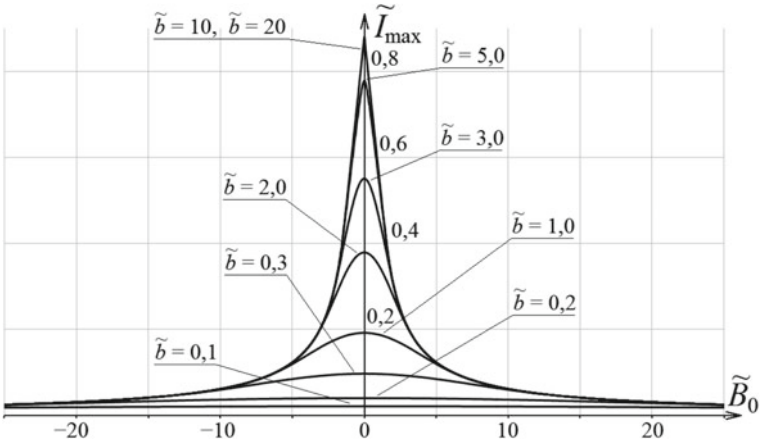

Fig. 15.7 Dependence of the maximum superconducting current through the Josephson medium strips on the external magnetic field for strips of different width (in units λ_M); $\tilde{B}_0$ is measured in units of $\Phi_0/(2\pi\bar{a}\lambda_M)$, $\tilde{I}_{max}$—in units of $I_c\rho D\bar{a}\lambda_M\pi/8$

15.7 Conclusion

In the framework of the classical model of electrodynamics of superconductors, the phenomenological material equation of Josephson medium (granular superconductors, HTSC ceramics) is obtained, the conclusion of which is:

- granular media with significantly different size distribution laws for granules are described by approximately the same material equations, a somewhat isolated situation only takes an "excessively ideal" case of granules of the same size;
- the depth of penetration into the Josephson medium of a weak magnetic field λ_M practically independent of the shape of superconducting granules and the laws of their size distribution and is determined only by the volume concentration of Josephson junction s, the average value of their critical current and the average size of the granules $\bar{a}$;
- a magnetic field with an indication exceeding the value of the first critical field of the medium, inversely proportional to the $\bar{a}\lambda_M$, penetrates into the medium in the form of vortices (hypervortices);
- the magnetic flux contained in the hypervortex does not depend on the law of grain size distribution (at least within the limits of four distribution laws considered), nor on the parameters $\bar{a}$, λ_M, and is equal to the magnitude of the magnetic flux quantum Φ_0;
- in the strip wire from the Josephson medium, a "size effect" is observed in the fields lesser than the first critical field, the density of the critical current decreases, and the slope of the dependence of the critical current on the magnetic field increases with the growth of the strip width, just as it is observed in films from a traditional superconductor [6].

The above results allow us to formulate recommendations for the designing of power wires based on granular superconductors (including those based on HTS-ceramics): to achieve the maximum possible current, it is advisable to make strips in the form of a kind of "litzwire", that is, bundles of separate (without mutual superconducting contact) filaments of width not exceeding λ_M. In this case, the gaps between the strips must be made sufficiently wide, much larger than the width of the individual thin strips.

The strong dependence of the critical current of a wide (several λ_M wide) band on a weak magnetic field indicates a high magnetic sensitivity of the Josephson medium. This dependence is also reflected in the presence of magnetoresistive effect, which is often fixed in samples of HTSP ceramics, both massive [7, 8] and film [9–11].

It can be assumed that with the improvement of the method for preparing a Josephson medium (high concentration of Josephson junctions and the values of their critical currents) magnetosensitive elements based on them can be used as sensors of a weak magnetic field. It is expected that by sensitivity they will be at the level of SQUIDs, surpassing them in simplicity of processing, reliability and cheapness. The creation of such sensors of a weak magnetic field opens great prospects in many areas of science and technology, including medical applications. In particular, for non-invasive control of an auxiliary pump of the left ventricle of the heart [12], for the creation of a system for the wireless transmission of electric energy in the human body [13], or for the control of the transportation of magnetic particles intended for various functions (diagnosis, drug delivery, treatment) [14, 15].

Acknowledgements This work was supported by the Ministry of Science and Higher Education of the Russian Federation (project no. 3.7829.2017/8.9). The work was done with the involvement of the Center by the collective use of "Microsystem technology and electronic component base MIET" and the Center for Technological Initiative MIET "Sensory".

References

1. A.A. Abrikosov, JETP **5**(6), 1174 (1957)
2. R.A. Ferrel, R.S. Prange, Phys. Rev. Letts. **10**(11), 479 (1963)
3. J.G. Bednorz, K.A. Muller, Z. Phys. **64**, 189 (1986)
4. E.B. Sonin, Lett. JETP **47**(8), 415 (1988)
5. E.B. Sonin, A.K. Tagantev, JETP **68**(3), 572 (1989)
6. V.V. Shmidt, *Introduction to Physics of Superconductors*, 2nd edn. (MCNMO, Moscow, 2000), 402 p. (in Russian)
7. D.A. Balaev, S.I. Popkov, E.I. Sabitova, S.V. Semenov, K.A. Shaykhutdinov, A.V. Shabanov, M.I. Petrov, J. Appl. Phys. **110**(9), 093918 (2011)
8. D.A. Balaev, S.V. Semenov, M.I. Petrov, J. Supercond. Novel Magn. **27**, 1425 (2014)
9. L.P. Ichkitidze, Bull. Russian Acad. Sci. Phys. **71**(8), 1145 (2007)
10. L.P. Ichkitidze, Physica C **460–462**(2), 781 (2007)
11. L.P. Ichkitidze, Physica C **435**, 140 (2006)

12. D. Telyshev, M. Denisov, A. Pugovkin, I. Nesterenko, S. Selishchev, Artif. Organs **42**(4), 432 (2018)
13. R.R. Aubakirov, A.A. Danilov, V.O. Shipunova, Biomed. Eng. **51**(6), 449 (2018)
14. I.V. Zelepukin, A.B. Mirkasymov, P.I. Nikitin, M.P. Nikitin, S.M. Deyev, Acta Nature. **9**(4), 58 (2017)
15. A.A. Tregubov, I.L. Sokolov, A.V. Babenyshev, P.I. Nikitin, V.R. Cherkasov, M.P. Nikitin, J. Magn. Magn. Mater. **449**(4), 590 (2018)

Chapter 16
Ab Initio Theory of the Equations of State for Light Rare-Gas Crystals

Ievgen Ie. Gorbenko, Elena P. Troitskaya, Ekaterina A. Pilipenko, Ilya A. Verbenko and Yuriy I. Yurasov

Abstract Nonempirical equations of state of compressed Ne and Ar crystals are studied on the base of the earlier-obtained ab initio adiabatic potential. The paired and three-body short-range repulsive potentials are calculated by the Hartree-Fock method on the base of localized functions with their exact mutual orthogonalization and do not contain experimentally determined parameters. The theory is compared with the experiment and results of calculations by other authors. Analysis of the proposed equations of state for large compressions has shown the importance of taking into account the three-body interaction and the terms of the higher order in the overlap integral in compressed Ne and the sufficiency of the quadratic approximation in the orthogonalization of functions in Ar.

16.1 Introduction

The properties of rare-gas crystals (RGC) at high pressure are of great interest because they provide an ideal system due to their closed-shell electronic configurations, allowing fruitful comparisons between experiments and theory. So they are often used as model objects for studying a number of fundamental problems of solid-state physics corresponding to lattice dynamics, many-electron effects, phase transformations, and for the development and improvement of new computational methods.

I. Ie. Gorbenko (✉)
Lugansk Taras Shevchenko National University, Lugansk, Ukraine
e-mail: e_g81@mail.ru

E. P. Troitskaya · E. A. Pilipenko
A.A. Galkin Physics and Technology Institute, Donetsk, Ukraine

I. A. Verbenko · Y. I. Yurasov
Research Institute of Physics, Southern Federal University, Rostov-on-Don, Russia

Y. I. Yurasov
Southern Scientific Centre RAS, Rostov-on-Don, Russia

I. A. Parinov et al. (eds.), *Advanced Materials*, Springer Proceedings in Physics 224, https://doi.org/10.1007/978-3-030-19894-7_16

Special attention is paid to studying the elastic properties of compressed RGC, since they are excellent materials as a hydrostatic pressure medium in high-pressure experiments using a diamond-anvil cell (DAC) [1]. This application of RGC is limited by the metallization pressure, which grows in the series Xe, Kr, Ar, and Ne. Now, the metallization pressure for Xe, $p_m = 132$ GPa [2], is experimentally known. The pressure created in DAC is 300 GPa [1] and goes on increasing; therefore, studying properties of light RGC (in particular Ne and Ar) at high pressures is of scientific and practical interest.

For the analysis of data on the state of a crystal subjected to large compression, it is necessary to develop a general equation of state (EOS), which relates finite deformations of a crystal to external stresses.

At room temperature, the equation of state of crystalline Ne was experimentally studied using the DAC technique in [3] up to $p = 14.4$ GPa; in [4], up to $p = 110$ GPa; and, in [5], up to $p = 208$ GPa. In [6], published in 2010, the structure and equations of state of neon under a pressure of up to 237 GPa were studied.

Theoretical descriptions of isotherms in a wide range of pressures are based on semi-empirical equations of state with parameters determined at normal pressure [7–15]. The most successful of them is the Vinet's equation of state [8], which requires the knowledge of four parameters: (i) the isothermal bulk modulus at zero pressure; (ii) its derivative with respect to pressure; (iii) the volume at $p = 0$, and (iv) thermal expansion at $p = 0$. The reliability of these equations is limited by the pressure up to which the experimental values and relationships used in deriving them are valid. In the range of pressures not yet available to the experiment, ab initio EOS have a predictive value.

Ab initio calculations of the equation of state of an RGC, based on the density functional theory (DFT) in the local density approximation (LDA) or generalized gradient approximation (GGA) for the exchange-correlation potential, yield results close to the experiment [16–18]. However, the DFT–LDA results are slightly underestimated in comparison to the experimental data, and the DFT–GGA results, on the contrary, overestimated [17]. The density-functional theory is currently not capable to account for two dispersive types of interactions in the long range and overlap effects in the short range to sufficiently high accuracy [19, 20]. At the same time, the quantum theoretical treatment of rare-gas crystals involves the correct description of dispersive type of interactions (van der Waals), overlap and repulsive effects resulting from the lattice dynamics [21]. As shown in [21], the quantum Monte Carlo method (QMC) gives an adequate description of the van der Waals interaction and the EOS calculated by this method is in a good agreement with the experimental results. In [22, 23] the equation of state $p(V, T)$ for solid Ne and Ar was obtained from a quantum theoretical treatment using two-, three-, and four-body forces, and an anharmonic treatment for lattice vibrations and temperature effects within the Einstein approximation. Presented results are within the experimental uncertainty for the available pressure-temperature range.

In [24], based on ab initio calculations of the adiabatic potential, a nonempirical equation of state was obtained. The energy of the pair short-range repulsive

potential was calculated in the Hartree-Fock approximation on the base of localized functions with their exact mutual orthogonalization and cluster expansion for the orthogonalization matrix. In this method, the orthogonalization matrix is calculated by summing certain subsequences of the series in S. This makes it possible to remove the restriction $S \neq 1$ and obtain the EOS and other characteristics of the crystals for relative compressions $u = \Delta V/V_0$ ($\Delta V = V_0 - V(p)$, $V_0 = V$ for $p = 0$) close to unity.

In [25] short-range many-body forces due to overlapping of the electron shells of an atom were studied. In this work, on the base of the obtained nonempirical EOS of light rare-gas crystals (Ne and Ar), the role of three-body interaction has been investigated at high pressures.

16.2 General Form of the Equation of State

In the most general case, the equation of state of a body will be understood as a relationship between the stress tensors t_{ij} and distortion tensor u_{ij} at a given temperature (or entropy; see, e.g., [26, pp. 25–27]):

$$t_{ij}(x) = \rho(x)\left[\frac{\partial F(T,x')}{\partial u'_{ij}}\right]_{T,u'=0} \tag{16.1}$$

where $\rho(x)$ is the density of matter in an arbitrary stressed state $\{x\}$ and $F(T, x')$ is the free energy of a unit of mass at a temperature T in the state $\{x'\}$ infinitesimally different from $\{x\}$.

The free energy $F(x)$ is a function of the distortion tensor, $F(T, x) = F(T, X, u_{ij})$, describing the transition from the initial state $\{X\}$ to the state $\{x\}$. In the general case, in any microscopic model, the free energy is a function of the volume of a unit cell Ω and vectors of the direct ($\mathbf{R}$) and reciprocal ($\mathbf{g}$) lattices $F(T, x) = F(\Omega, \mathbf{R}, \mathbf{g})$. Equation of state (16.1) takes the form:

$$\Omega\frac{\partial F}{\partial \Omega} - \sum_{\mathbf{g}} g_\alpha \frac{\partial F}{\partial g_\alpha} + \sum_{\mathbf{R}} R_\alpha \frac{\partial F}{\partial R_\alpha} = \Omega t_{\alpha\alpha}. \tag{16.2}$$

For hcp (or fcc) crystals, the free energy depends only on two parameters: the cell volume Ω and the ratio c/a, and the equation of state takes the form:

$$p = -\frac{\partial F(T,\Omega,c/a)}{\partial \Omega}, \quad \frac{\partial F(T,\Omega,c/a)}{\partial (c/a)} = 0. \tag{16.3}$$

For a cubic crystal, $c/a \equiv 1$, and the second equation in (16.3) becomes an identity. Let us derive the equation of state $p(u)$ at $T = 0$, which is suitable for large

hydrostatic compressions. The expression for the energy of the crystal U is obtained in the form (for details of the calculation, see [27, 28]):

$$U = \min \overline{H}$$
$$= \text{const} + \sum_{l} \left\{ \begin{array}{l} \frac{\left(\mathbf{P}^{l}\right)^{2}}{2\alpha} + \frac{1}{2}\sum\limits_{\alpha\beta}^{9} \frac{1}{2\beta_{44}} \left(Q^{l}_{\alpha\beta}\right)^{2} + \boldsymbol{\beta}^{l} \cdot \mathbf{P}^{l} + \frac{1}{2}\sum\limits_{\alpha\beta} D^{l}_{\alpha\beta} Q^{l}_{\alpha\beta} \\ \quad - \frac{1}{2}\sum\limits_{l'} \left[\frac{C}{\left|\mathbf{r}^{ll'}\right|^{6}} + \frac{C'}{\left|\mathbf{r}^{ll'}\right|^{8}} + \frac{C''}{\left|\mathbf{r}^{ll'}\right|^{10}} \right] \\ \quad + \frac{1}{2}\sum\limits_{l'} \mathrm{K}\left(\mathbf{P}^{l}, Q^{l}_{\alpha\beta}, \mathbf{P}^{l'}, Q^{l'}_{\alpha\beta}\right) + \frac{1}{2}\sum\limits_{l'}^{n.n.} U_{\mathrm{sr}}\left(\left|\mathbf{r}^{l} - \mathbf{r}^{l'}\right|\right) \end{array} \right\}. \tag{16.4}$$

In this expression, $\mathbf{P}^{l}$ and $Q^{l}_{\alpha\beta}$ are the dipole and quadrupole moments of the atom, induced by the motion of the nuclei at the site $\mathbf{l}$. The first four terms describe the deformation of the electron shells (α and β_{44} are the dipole and quadrupole polarizability coefficients). The following three terms give the van der Waals forces. K is the Coulomb (in the classical sense) interaction of all dipoles $\mathbf{P}^{l}$ and quadrupoles $Q^{l}_{\alpha\beta}$ with each other. The last term is the short-range forces.

Fluctuation deformations of the electron shells of atoms in the dipole approximation do not contribute to the elastic constants of the first (EOS) and second orders. They influence only the elastic higher orders constants, starting from the fourth order in the displacements of the nuclei (see [24] and references therein). The contribution of the deformation of the electron shells of an atom in the quadrupole approximation to the elastic moduli of the second order is considered in detail in [29–31]. Therefore, the short-range forces are defined by the formula

$$E^{l}_{\mathrm{sr}} = \frac{1}{2}\sum_{l'}^{n.n.} U_{\mathrm{sr}}\left(\left|\mathbf{r}^{l} - \mathbf{r}^{l'}\right|\right) = \sum_{l'} \left\langle 00 \middle| \widehat{H}^{ll'}_{\mathrm{sr}} \middle| 00 \right\rangle \tag{16.5}$$

In the one-electron approximation, the many-electron wave functions of the atoms $|0\rangle = \psi^{l}_{0}(\mathbf{r}_1, \mathbf{r}_2, \ldots)$ can be represented as determinants constructed on the wave functions of electrons of an isolated atom and satisfying the Hartree-Fock equation (the Hartree-Fock approximation).

16.3 Many-Body Short-Range Interaction in the Hartree-Fock Approximation

The expression for the energy of a crystal consisting of neutral atoms, written in the Hartree-Fock approximation via the one-electron density matrix $\rho(\mathbf{r}|\mathbf{r}'; \{\mathbf{l}\})$, where

$\mathbf{r}$ is the coordinate of an electron and $\{\mathbf{l}\}$ is the position of the nuclei in the lattice, has the form [32]:

$$E_{\mathrm{sr}}^{l} = T_{\mathrm{e}} + U_{\mathrm{C}} + U_{\mathrm{ex}} + U_{\mathrm{en}} + U_{\mathrm{nn}}, \tag{16.6}$$

where $T_{\mathrm{e}}(\{\mathbf{l}\})$ is the kinetic energy of electrons of the crystal; $U_{\mathrm{C}}(\{\mathbf{l}\})$ and $U_{\mathrm{ex}}(\{\mathbf{l}\})$ are the energies of the electron-electron Coulomb and exchange interactions; and U_{en} and U_{nn} are the energies of the electron-nucleus and nucleus-nucleus interactions.

On the base of atomic orbitals exactly orthogonalized to each other according to Lövdin, the density matrix $\rho(\mathbf{r}'|\mathbf{r};\{\mathbf{l}\})$ takes the form [25, 32]:

$$\rho(\mathbf{r}'|\mathbf{r};\{\mathbf{l}\}) = 2\sum_{\mathbf{l}s}\left\{\varphi_s(\mathbf{r}'-\mathbf{l})\varphi_s^*(\mathbf{r}-\mathbf{l}) - \sum_{\mathbf{l}'s'}\varphi_{s'}(\mathbf{r}'-\mathbf{l}')P_{s's}^{\mathbf{l}'\mathbf{l}}\varphi_s^*(\mathbf{r}-\mathbf{l})\right\},$$
$$\mathbf{P} = \mathbf{I} - (\mathbf{I}+\mathbf{S})^{-1}, \tag{16.7}$$

where $\varphi_s(\mathbf{r}-\mathbf{l}) = |\mathbf{l}s\rangle$ is the wave function of an electron of an isolated atom (atomic orbital) centered at the site $\mathbf{l}$ of the crystal lattice in the state number s ($\mathbf{l}$ and $\mathbf{l}'$ run through all N nodes), $\mathbf{P}$ is the orthogonalization matrix, $\mathbf{I}$ is the unit matrix, and $\mathbf{S}$ is the matrix of overlap integrals with the elements:

$$S_{s's}^{\mathbf{l}'\mathbf{l}} = \langle \mathbf{l}'s'|\mathbf{l}s\rangle \quad \text{at } \mathbf{l}\neq\mathbf{l}';\ S_{s's}^{\mathbf{l}'\mathbf{l}} = 0 \quad \text{at } \mathbf{l}=\mathbf{l}'. \tag{16.8}$$

The expression for the energy of short-range repulsion of crystal atoms, written via the orbitals of electrons of isolated atoms, $|\mathbf{l}s\rangle$, and the orthogonalization matrix, is as follows [25]:

$$E_{\mathrm{sr}} = E^{(0)} + \Delta E(\mathbf{P}) + \Delta E\left(\mathbf{P}^2\right), \tag{16.9}$$

where $E^{(0)}$ is the energy of the interatomic interaction with neglect of the orthogonalization of the orbitals of neighboring atoms, $\Delta E(\mathbf{P})$ is the orthogonalization correction linear in $\mathbf{P}$, and $\Delta E(\mathbf{P}^2)$ is the correction quadratic in $\mathbf{P}$. In expression (16.9) for E_{sr},

$$E^{(0)} = \sum_{\mathbf{l}} E_a^{\mathbf{l}} + {\sum_{\mathbf{l},\mathbf{m}}}'\left\langle \mathbf{l}s\middle| V_{\mathrm{en}}^{\mathbf{m}} + V_0^{\mathbf{m}} + V_{\mathrm{ex}}^{\mathbf{m}}\middle|\mathbf{l}s\right\rangle. \tag{16.10}$$

Here, the prime in the sign of the sum means that $\mathbf{m}\neq\mathbf{l}$. Henceforth, $\mathbf{l}\neq\mathbf{l}'\neq\mathbf{m}$ and $\mathbf{l}\neq\mathbf{l}'\neq\mathbf{m}\neq\mathbf{m}'$.

The first term in (16.10) represents the sum of the energies of isolated atoms $E_a^{\mathbf{l}}$, which does not depend on the interatomic distances in the crystal. It can be included

in the reference point for energy. The second term in (16.10) consists of two-center integrals: matrix elements of the electron-ion interaction potential $V_{\text{en}}^{\mathbf{m}}$, the potential of a neutral isolated atom $V_0^{\mathbf{m}}$, and the exchange interatomic interaction potential $V_{\text{ex}}^{\mathbf{m}}$, constructed on the atomic orbitals $|\mathbf{l}s\rangle$.

Expressions (16.9) for the crystal energy contain different types of multicenter integrals corresponding to different types of interatomic forces in a crystal. Term $E^{(0)}$ (16.10) contains only pair forces, i.e., two-center integrals, and the correction $\Delta E(\mathbf{P})$ contains two- and three-center integrals. The correction $\Delta E(\mathbf{P}^2)$ contains one- to four-center integrals.

Then, expression (16.9) for the energy E_{sr} of electrons in the crystal can be written in the form of an expansion in powers of the overlap integral S:

$$E_{\text{sr}} = E^{(0)}\left(S^2\right) + W_2\left(S^2\right) + W_3\left(S^3\right) + W_4\left(S^4\right) + W_5\left(S^5\right) + W_6\left(S^6\right). \tag{16.11}$$

Here, W_2 is the orthogonalization correction quadratic in S:

$$W_2 = -2\sum_{\mathbf{ll}'}{}' \sum_{ss'} P_{ss'}^{\mathbf{ll}'} \left\langle \mathbf{l}'s' \middle| V_0^{\mathbf{l}'} + V_{\text{ex}}^{\mathbf{l}'} \middle| \mathbf{l}s \right\rangle - \sum_{\mathbf{lm}}{}' \sum_{ss'tt'} P_{ss'}^{\mathbf{ml}} P_{tt'}^{\mathbf{lm}} \langle \mathbf{l}s'\mathbf{m}t'|v_{\text{C}}|\mathbf{m}s\mathbf{l}t\rangle, \tag{16.12}$$

where $\langle \mathbf{l}s'\mathbf{m}t'|v_{\text{C}}|\mathbf{m}s\mathbf{l}t\rangle = \int \varphi_{s'}^*(\mathbf{r}-\mathbf{l})\varphi_{t'}^*(\mathbf{r}'-\mathbf{m})v_{\text{C}}(\mathbf{r}-\mathbf{r}')\varphi_s(\mathbf{r}'-\mathbf{m})\quad \varphi_t(\mathbf{r}-\mathbf{l})\,\mathrm{d}\mathbf{r}\mathrm{d}\mathbf{r}'$, $v_{\text{C}}(\mathbf{r}-\mathbf{r}') = \frac{e^2}{|\mathbf{r}-\mathbf{r}'|}$, and e is the charge of an electron.

The correction W_2 contains only two-center integrals and corresponds to two-body interactions in the crystal. The term W_3 is a correction of the third degree in S, containing three-center integrals:

$$\begin{aligned} W_3 = &-2\sum_{\mathbf{ll}'}\sum_{ss'} P_{ss'}^{\mathbf{ll}'}(I-S)_{s's}^{\mathbf{l}'\mathbf{l}}\varepsilon_{\mathbf{l}s} - 2\sum_{\mathbf{ll}'}{}'\sum_{ss'} P_{ss'}^{\mathbf{ll}'}\left\langle \mathbf{l}'s' \middle| \sum_{\mathbf{m}\neq\mathbf{l},\mathbf{m}\neq\mathbf{l}'} \left(V_0^{\mathbf{m}} + V_{\text{ex}}^{\mathbf{m}}\right) \middle| \mathbf{l}s \right\rangle \\ &- 2\sum_{\mathbf{ll}'\mathbf{m}}{}'\sum_{ss'tt'} P_{ss'}^{\mathbf{ll}'} P_{tt'}^{\mathbf{l}'\mathbf{m}} \langle \mathbf{l}'s'\mathbf{m}t'|v_{\text{C}}|\mathbf{l}s\mathbf{l}'t\rangle, \end{aligned} \tag{16.13}$$

where $\varepsilon_{\mathbf{l}s}$ is the energy of the Hartree-Fock orbital $\varphi_s(\mathbf{r}-\mathbf{l})$.

Expressions for W_4–W_6 are not presented here due to their cumbersomeness (see [25]).

16.4 Nonempirical Two-Body and Three-Body Short-Range Repulsive Potential for RGC

In [33], the energy was calculated in the direct space with the following approximations: (i) atomic orbitals at different sites are orthogonalized up to S^2, inclusively; (ii) only the largest overlap integral $S = S^{l}_{np_z} S^{l'}_{np_z}$ (n = 2 and 3 for Ne and Ar) is assumed to be nonzero; (iii) from all the multicenter matrix elements, two-center elements and paired interactions between atoms are distinguished; (16.4) everywhere, the nearest-neighbor approximation is used.

Beyond approximations (i) and (iii), the exact Lövdin's orthogonalization in W_2 (16.12) and the three-body interaction W_3 (16.13) can be used.

In [24], the short-range repulsion potential $V_{\mathrm{sr}} = E^{(0)} + W_2$ for Ne is calculated from the first principles in the Hartree-Fock approximation and on the base of exactly orthogonalized atomic orbitals with the help of the Abarenkov-Antonova cluster expansion (CE), which was originally proposed for calculating the electron density matrix in ionic crystals [34]. The lowest order of the cluster expansion is the two-body clusters approximation, which selectively takes into account the terms of all orders in S, since it contains matrix (16.7).

In the calculations, the Clementi-Roetti tables of atomic orbitals [35] were used. For the argon crystal, it is sufficient to perform the orthogonalization of the atomic orbitals in the S^2 approximation [24].

The dependence $V_{\mathrm{sr}} = E^{(0)} + W_2$ (16.10) and (16.12) on the interatomic distance in the crystal is interpolated by the method of least squares in the form of a convenient expression (with an error of 1%):

$$V_{\mathrm{sr}} = E^{(0)} + W_2 = V_{\mathrm{sr}}(y) = \left(A_4 y^4 + A_3 y^3 + A_2 y^2 + A_1 y + A_0\right) \exp(-\alpha y), \quad (16.14)$$

where $y = r/r_0 - 1, r_0 = a\sqrt{2}$ is the distance between the nearest neighbors in an uncompressed crystal.

In model M4, A_i and α are calculated using the exact orthogonalization of atomic orbitals W_2(CE) (16.12) and in the first-neighbors approximation. In models M2 and M1, the pair short-range potential is calculated at atomic orbitals orthogonalized in the approximation S^2 ($W_2(S^2)$); the first neighbors are taken into account. The results of the calculations are presented in [24, 36].

The energy of attraction between two atoms was calculated in [33] and is represented in the form:

$$V_{\mathrm{lr}}(y) = -\frac{C}{r^6}[1 + f(y)], \quad f(y) = A \exp(-\beta y), \quad (16.15)$$

where C is the van der Waals constant and $f(y)$ is a function caused by the overlap of the electron shells of the atoms [24, 33].

The two-center Coulomb integrals entering into W_3 (16.13) were also calculated exactly on the base of the tables from [35]. The regularities found in this case were

used for approximating three- and four-center integrals by the products of the corresponding overlap integrals.

Then, if atoms l, l', and l'' form an equilateral triangle and $S \neq 1$, expression (16.13) for W_3 can be reduced to the form [25]:

$$W_3 = -\sum_{ll'l''} \left(S\left(r^{ll''}\right)\right)^2 f(r_1), \quad f(r_1) = \frac{S(r_1)}{r_1}, \quad r_1 = \left|\mathbf{r}^{l'} - \frac{1}{2}\mathbf{r}^{ll''}\right|, \qquad (16.16)$$

where $S = S^{ll'}_{np_z np_z}$ is the largest of the overlap integral between the outer np-electron orbitals. In contrast to the pair potential $W_2\left(r^{ll'}\right)$, the tree-body potential W_3 depends not only on $r^{ll'}$ and $r^{ll''}$ but also on $\left(\mathbf{r}^{ll'} \cdot \mathbf{r}^{ll''}\right)$.

As shown in Fig. 16.1, our short-range potentials for Ne (the pair potential $V_{sr}(S^2) = E^{(0)} + W_2$ and, the potential $V_{sr}(S^3) = E^{(0)} + W_2 + W_3$ with allowance for the three-body interaction) are in a good agreement with the corresponding best empirical potentials [12, 37, 38] in a wide range of compressions up to $u = 0.8$ ($R = a\sqrt{2} = 3.5$ a.u.). However, we see that their first derivatives are significantly different, starting from compressions $u \approx 0.6$, corresponding to a pressure $p \approx 30$ GPa.

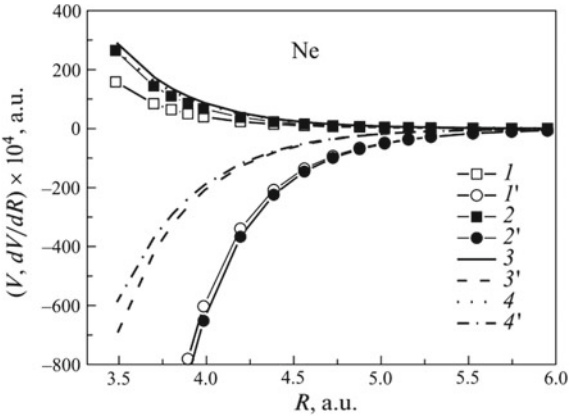

Fig. 16.1 Interatomic short-range potentials and their derivatives for Ne: (*1*) nonempirical pair short-range potential $V_{sr} = E^{(0)} + W_2$, calculated in model M4 [24]; (*1′*) its first derivative with respect to distance; (*2*) nonempirical total potential $V_{sr} = E^{(0)} + W_2 + W_3$ with allowance for the three-body interaction; (*2′*) its first derivative with respect to distance; (*3*) short-range part of the Aziz-Slaman pair empirical potential U_p [37]; (*3′*) its first derivative with respect to distance; (*4*) the empirical total potential including the short-range parts of the Aziz-Slaman pair potential and the Slater-Kirkwood three-body potential [12, 37, 38] $U = U_p - |U_{tr}| = U_p - A\exp\left[-\alpha_{tr}\left(3a\sqrt{2}\right)\right] \times \left(1 + 3\cos^3\frac{\pi}{3}\right)$; (*4′*) first derivative of the total potential with respect to distance

16.5 Calculation and Discussion of the Equations of State of Light Rare-Gas Crystals

In the general case, at a finite temperature T, equation of state (16.3) can be represented in the form:

$$p(T,V) = p_{\text{stat}}(V) + p_{\text{e}}^{*}(T,V) + p^{*}(T,V) + p_{\text{zp}}(V) + p_{\text{na}}(T,V). \qquad (16.17)$$

The pressure p_{stat} is the pressure created in the lattice at rest, $p_{\text{stat}} = p_{\text{sr}} + p_{\text{lr}}$, where p_{sr} and p_{lr} are the corresponding derivatives (with the opposite sign) with respect to the volume of the short-range, V_{sr}, and long-range V_{lr}, interaction potentials. The pressure p_{e}^{*} of the conduction-electron gas is small due to the smallness of T compared to the fundamental gap. The thermal phonon pressure $p^{*} \sim (T/\theta)^2 (\theta = \theta(p)$ is the Debye temperature) is small too. The ratio (T/θ) is always small at high pressures, since θ sharply increases with increasing pressure. For the same reason, the contributions of the electron-phonon and anharmonic interactions, entering into the nonadiabatic part of the pressure, p_{na}, are small.

Thus, all that remains are the contributions of the zero-point vibration, which are independent of T, from the harmonic, p_{zp}, and anharmonic, p_{na} $(T = 0)$ parts of the energy. By the definition [26],

$$p_{\text{zp}} = -\frac{\partial}{\partial \Omega} \sum_{\mathbf{q}\lambda} \hbar \omega_{\mathbf{q}\lambda} = \frac{\hbar}{2\Omega N} \sum_{\mathbf{q}\lambda} \omega_{\mathbf{q}\lambda} \gamma_{\mathbf{q}\lambda},$$

where $\omega_{\mathbf{q}\lambda}$ and $\gamma_{\mathbf{q}\lambda}$ are the frequency and Grüneisen microscopic parameter of a phonon with a wave vector $\mathbf{q}$ and polarization λ. Estimates show (see the approximate formula for γ in [39]) that the Grüneisen parameter is small (in comparison with the scale of the variation in pressure) and varies with the volume as a logarithm. The phonon frequencies vary stronger than $\gamma_{\mathbf{q}\lambda}$ but weaker than by the linear law [26]. Therefore, zero-point pressure is insignificant compared to p_{stat} and its relative contribution decreases with increasing compression. For example, it was shown in [22] that the contributions of zero-point vibrations in Ne at 6 and 600 GPa are 10 and 1%, respectively. This is also clearly seen from the approach of isotherms with increasing pressure, observed experimentally in many works (see, e.g., [39]). The pressure p_{na} $(T = 0)$ has a similar behavior, but it is even smaller due to the presence of phonon frequencies in the denominators of the integrals [26].

Finally, it can be concluded that, at large compressions, the decisive contribution comes from the static lattice at $T = 0$. For the RGC (cubic crystal), the binding energy with allowance for the second neighbors and the three-body short-range repulsion takes the form:

$$E_{\text{coh}} = 6E_{\text{sr}}\left(a\sqrt{2}\right) + 3E_{\text{sr}}(2a) + W_3(a) - \frac{1}{2a^6}\left[F_6(0,0)C + \frac{1}{a^2}F_8(0,0)C' + \frac{1}{a^4}F_{10}(0,0)C''\right], \tag{16.18}$$

where $E_{\text{sr}} = E^{(0)} + W_2$ and $F_n(0, 0)$ represent lattice sums of $1/r^n$ (n = 6, 8, 10) and are equal to 1.80674, 0.80001, and 0.38472, respectively [28].

Then, the EOS takes the form;

$$p = -\frac{\partial E}{\partial \Omega} = -\frac{e^2}{2a^4}[H(a) + 2F + \delta H - 2R_t + 0.30112B + 0.13335B' + 0.06412B''], \tag{16.19}$$

where $R_t = -\frac{a}{6e^2}\frac{dW_3(a)}{da}$; $W_3(a) = -24S^2\left(a\sqrt{2}\right)f\left(\frac{\sqrt{6}}{2}a\right)$; $B = \frac{6C}{a^5e^2}$; $B' = \frac{8C'}{a^7e^2}$, and $B'' = \frac{10C''}{a^9e^2}$.

In models M2 and M4, it is assumed that $C \to C[1 + f(y)]$, according to (16.15),

$$H(a) = \frac{2ax}{a^2}\frac{\mathrm{d}V_{\text{sr}}}{\mathrm{d}r} - AB\frac{6+\beta x}{24}\exp[-\beta(x-1)], \quad x = \frac{r}{r_0},$$
$$F = H(2a),$$
$$\delta H = -\frac{16a^3}{e^2}S(r_0)[2S_2(r_0)f(r_1) + 3S(r_0)f_2(r_1) - 2S_1(r_0)f_1(r_1)].$$

S_i and f_i are expressed via the first and second derivatives of the overlap integral $S\left(r^{II''}\right)$ with respect to the absolute value of the argument [40, 41].

For Ne and Ar, isotherms for large compressions were calculated in [24] with a pair nonempirical short-range potential.

Figures 16.2 and 16.3 present the equations of state of Ne and Ar crystals, calculated by Formula (16.19) (with the parameters from Table 16.1 for Ne), experimental values [4, 5, 42], and results of calculations by other authors [8, 16, 43]. For comparison, we present the results of calculations from [24]. For Ne and Ar crystals, at small compressions $u \leq 0.45$, the results of our EOS calculation in all models and the calculations by other authors agree with the experiment.

As can be seen from Fig. 16.2, for compressions $0.45 \leq u \leq 0.65$, the results of EOS calculations in the M2 model with a short-range potential $V_{\text{sr}} = E^{(0)} + W_2(S^2) + W_3(S^3)$ lie above the experimental data and, increasing pressure, the error increases. For the same compression interval, the results of EOS calculations in model M4 with the potential $V_{\text{sr}} = E^{(0)} + W_2(\text{CE}) + W_3(S^3)$, ($W_2$(CE) takes into account the exact orthogonalization of the wave function by Formula (16.12) with the help of the Abarenkov-Antonova cluster expansion [34]) are

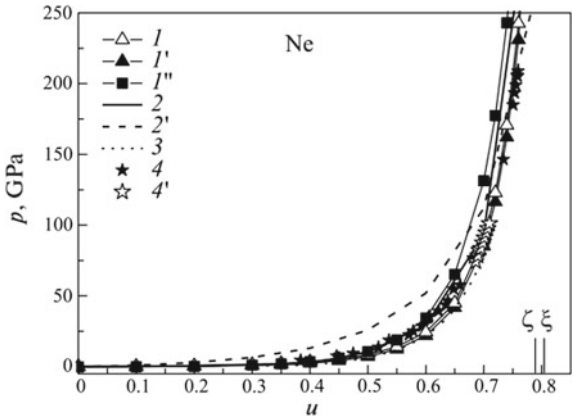

Fig. 16.2 Equations of state for crystalline Ne: (*1*) EOS calculation in the M4 model on the base of pair potential [24]; (*1′*) present EOS calculation in model M4 with allowance for the three-body interaction; (*1″*) present EOS calculation in model M2 with allowance for the three-body interaction; (*2*) and (*2′*) EOS empirical calculation by Vinet [8] and Poirier [43], respectively; (*3*) ab initio EOS calculation using DFT–LDA [16]; experiment (*4*) [5] and (*4′*) [4]; the vertical lines indicate the calculated values of the compression of metallization: ζ calculation in [44] (the corresponding pressure p_m = 740 GPa), ξ calculation in [45] ($p_m \approx 1$ TPa)

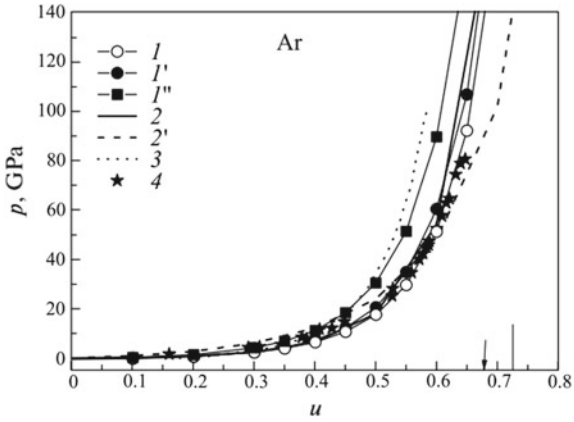

Fig. 16.3 Equations of state for crystalline Ar: (*1*) EOS calculation in the M1 model on the base of the pair potential; (*1′*) present EOS calculation in model M1 with allowance for the three-body interaction; (*1″*) present EOS calculation in model M2 with allowance for the three-body interaction; (*2*, *2′*, *3*) the same as in Fig. 16.2; (*4*) experiment [42]; the arrow indicates the calculated compression value of the fcc–hcp structural transition [46] (p = 220 GPa); the vertical line indicates the calculated value of the compression of metallization [46] (p_m = 510 GPa)

Table 16.1 Dimensionless parameters of two- and three-body interaction s for Ne as a function of compression

$\frac{\Delta V}{V_0}$	$H \times 10^2$		$\delta H \times 10^2$	$F \times 10^2$		$R_t \times 10^2$	$B \times 10^2$	$B' \times 10^2$	$B'' \times 10^2$
	$V_{sr}(S^2)$	V_{sr}(CE)		$V_{sr}(S^2)$	V_{sr}(CE)				
0	−1.278	−1.320	−0.024	−0.134	−0.133	0.010	4.244	2.500	0.900
0.1	−1.863	−1.873	−0.041	−0.197	−0.197	0.018	5.058	3.197	1.235
0.2	−2.833	−2.738	−0.072	−0.301	−0.302	0.032	6.156	4.208	1.758
0.3	−4.533	−4.147	−0.131	−0.483	−0.486	0.060	7.690	5.746	2.624
0.4	−7.719	−6.584	−0.252	−0.827	−0.834	0.118	9.943	8.234	4.167
0.5	−14.213	−11.190	−0.510	−1.542	−1.558	0.250	13.473	12.599	7.200
0.6	−28.972	−21.163	−1.107	−3.241	−3.272	0.567	19.543	21.206	14.062
0.7	−68.004	−48.031	−2.613	−8.191	−8.169	1.417	31.566	41.495	33.333
0.8	−199.12	−151.36	−6.742	−28.582	−27.452	3.974	62.045	106.88	112.5

slightly below the experimental values and the contribution of the three-body interaction is almost unnoticeable. At compressions $u \geq 0.65$, the best agreement with the experiment is demonstrated by the EOS calculations in the M4 model with allowance for the three-body interaction.

The allowance for the three-body interaction in EOS for Ne is difficult to classify visually; therefore, we calculated the relative error for 14 experimental points in different models (see Table 16.2). As it turned out, the best results (an error of 2.6%) for compressions $0.518 \leq u \leq 0.606$ are obtained in the EOS calculation using the pair potential and exactly orthogonalized wave functions [W_2(CE)] with allowance for the second neighbors and the three-body interaction. For compressions $0.696 \leq u \leq 0.758$, the pair potential W_2(CE) and three-body interaction are needed and the first neighbors are sufficient (an error of 5.8%). In fact, this means that our results in both cases fall within the experimental error.

In Ar (Fig. 16.3), the EOS is described best in the simplest M1 model ($A = \beta = 0$, taking into account only the first neighbors) on the base of the pair, $V_{sr}(S^2) = E^{(0)} + W_2$, or three-body, $V_{sr}(S^3) = E^{(0)} + W_2 + W_3$, short-range repulsive potentials. These results are close to one another, but, in the compression range $0.45 \leq u \leq 0.65$, the calculation with the pair potential lies slightly below the experimental values, and taking into account the contribution of the three-body interaction improves the agreement with the experiment. For $u \geq 0.6$, the EOS calculations based on the pair potential V_{sr} agree with the experiment slightly better.

For light rare-gas crystals, the EOS calculations by Vinet et al. [8] and other authors [7, 12, 13] using four and more experimental parameters are in a good agreement with the experimental data (except for [43]). Ab initio DFT–LDA calculations [16] are also close to the experiment (somewhat lower) for neon and argon in a wide range of pressures.

16.6 Conclusion

In [24], an analysis of a number of semi-empirical equations of state in application to a strongly compressed crystal (in the megabar pressure range) was given. The best agreement with the available experiment is demonstrated by Vinet's equation of state [8] for Ne up to compression $u \leq 0.7$, and up to compressions $u \leq 0.6$ for Ar. At stronger compressions, an appreciable deviation (overestimation) from the experiment is observed for RGC. To improve the agreement between theory and experiment for large compressions, the authors of [43] proposed a new equation of state based on the Birch-Murnaghan EOS [7]. The equation of state in [43] is derived using the Henky logarithmic stress and, in the authors' opinion, must be equivalent to the Vinet-type EOS [8] at small deformations but behave better at large ones. As can be seen from Figs. 16.2 and 16.3, one can agree with this in the case of Ar, but not in the case of Ne. In [11], five phenomenological equations of

Table 16.2 Equation of state for solid Ne in different models at high pressure[a]

Ne									
u	p_{exp} [5]	$V_{sr} = E^{(0)} + W^2(S^2)$		$V_{sr} = E^{(0)} + W^2(S^2) + W^3(S^3)$		$V_{sr} = E^{(0)} + W^2(CE)$		$V_{sr} = E^{(0)} + W^2(CE) + W^3(S^3)$	
		p	γ	p	γ	p	γ	p	γ
0.5181	13.6	18.871	38.76	17.398	27.93	14.459	6.32	12.986	4.51
0.5472	17.9	25.773	43.99	24.044	34.32	19.447	8.64	17.718	1.02
0.5707	22.5	33.496	48.87	31.515	40.07	25.000	11.11	23.018	2.30
0.5780	25.1	36.386	44.96	34.317	36.72	27.074	7.86	25.005	0.38
0.5940	28.6	43.841	53.29	41.559	45.31	32.421	13.36	30.139	5.38
0.6041	34.7	49.372	42.28	46.942	35.28	36.389	4.87	33.959	2.14
0.6060	35.7	50.564	41.64	48.103	34.74	37.245	4.33	34.784	2.57
0.6219	39.3	61.342	56.09	58.610	49.13	44.989	14.48	42.257	7.52
0.6984	91.2	170.803	87.28	165.695	81.68	88.216	3.27	83.108	8.87
0.7340	146.5	294.121	100.77	286.311	95.43	154.355	5.36	146.546	0.03
0.7509	185	387.735	109.59	377.688	104.16	205.941	11.32	195.895	5.89
0.7535	193.4	405.320	109.58	394.834	104.15	215.745	11.55	205.258	6.13
0.7555	199	419.563	110.84	408.709	105.38	223.709	12.42	212.855	6.96
0.7580	206.1	437.452	112.25	426.143	106.77	133.743	13.41	222.434	7.93

[a]Relative error is $\gamma = \left(\left|p_{theor} - p_{exp}\right|/p_{exp}\right) \cdot 100\%$; pressure p is given in GPa; γ is given in %

state were analyzed for solids (Ne, Ar, Cu, Al, LiH, and MgO) under very strong compressions; the EOS from [43] was most criticized—both the method of obtaining it and the calculation results.

The equations of state of the RGC, obtained in [24] on the base of a pair Hartree-Fock short-range repulsion describe well the available experiments. As shown in [24], in order to construct the potential of Ne, it is necessary to consider the pair terms of higher degrees in S (model M4), while, for the other crystals, it suffices to take into account only the terms $\sim S^2$ (models M1 and M2). This is explained by the fact that the potential V_{sr}, consisting of a large number of both positive and negative terms:

$$V_{\mathrm{sr}} = V_{\mathrm{sr}}^{+} + V_{\mathrm{sr}}^{-},$$

for Ar crystal is 40–50% of V_{sr}^{+}, whereas the ratio $V_{\mathrm{sr}}/V_{\mathrm{sr}}^{+}$ for neon is 20–25%. Thus, for Ar crystal, the terms with higher degrees of S are compensated and give small corrections, whereas, for the potential of Ne, their contribution is comparable with the terms $\sim S^2$.

The example of Ar shows that taking into account the three-body interaction gives overestimated results of EOS calculations for $u \geq 0.6$ and deteriorates the agreement with experiment as compared to the calculation based on the pair potential $W_2(S^2)$ (model M1). Probably, in this case, if the character of interaction is taken into account more accurately, it is desirable, as for Ne, that the pair potential be calculated more accurately using the cluster expansion for the orthogonalization matrix (model M4). However, there is no need to complicate the calculations, and it can be generally concluded that it is preferable to calculate the EOS for Ar and heavy RGCs on the base of effective pair potentials, as was shown in [24].

As before, on the base of calculations of the volume-dependent elastic moduli [40, 41, 47] and phonon frequencies [47], from the results of this paper, it is clear that the three-body interaction due to the overlapping of the electron shells of the atom remains small against the background of the pair potentials even at high pressures.

In conclusion, it should be noted that the equations of state (the first-order elastic modulus), in contrast to the second-order elastic moduli, does not contain terms describing the deformation of the electron shells, which are present in the adiabatic potential (16.4). Apparently, this explains a rather successful description of the EOS of RGC by the DFT methods on the base of empirical potentials and empirically established dependences between different thermodynamic quantities. However, taking into account the deformation of the electron shells in the dipole and quadrupole approximations is fundamentally important in calculations of phonon frequencies, shear elastic moduli, and, of course, in the deviation from the Cauchy relations [47]. In all these cases, the contributions from the three-body interaction and the deformation of the electron shells enter with different signs and in different proportions; therefore, the adequate description of the entire set of dynamic properties over a wide range of pressures by means of a single parameter (as in different

empirical models of three-body interaction) or by adding additional terms to the adiabatic potential (e.g., zero-point vibration in the Lundquist potential) is hardly possible.

Acknowledgements The work was supported by the Ministry of Education and Science of the Russian Federation: projects Nos. 3.6371.2017/8.9, 3.6439.2017/8.9 (the basic part of the state task). The equipment of the Center of Research Institute of Physics SFedU was used.

References

1. R.J. Hemley, H.K. Ashcroft, Phys. Today **51**, 26 (1998)
2. K.A. Goettel, J.H. Eggert, I.F. Silvera, W.C. Moss, Phys. Rev. Lett. **62**, 665 (1989)
3. L.W. Finger, R.M. Hazen, G. Zou, H.K. Mao, P.M. Bell, Appl. Phys. Lett. **39**, 892 (1981)
4. R.J. Hemley, C.S. Zha, A.P. Jephcoat, H.K. Mao, L.W. Finger, D.E. Cox, Phys. Rev. B **39**, 11820 (1989)
5. A. Dewaele, F. Datchi, P. Loubeyre, M. Mezouar, Phys. Rev. B **77**, 094106 (2008)
6. K. Takemyra, T. Watanuki, K. Ohwada, A. Machida, A. Ohmura, K. Aoki, J. Phys. Conf. Ser. **215**, 012017 (2010)
7. F. Birch, J. Geophys. Res. **57**, 227 (1952)
8. P. Vinet, J.H. Rose, J. Ferrante, L.R. Smidth, J. Phys. Condens. Matter **1**, 1941 (1989)
9. M. Kumar, Phys. B **212**, 391 (1995)
10. Z.H. Fang, Phys. Rev. B **58**, 20 (1998)
11. S. Gaurav, B.S. Sharmu, S.B. Sharma, S.C. Upadhyaya, Phys. B **322**, 328 (2002)
12. Y.A. Freiman, S.M. Tretyak, J. Low Temp. Phys. **33**, 719 (2007)
13. S. Gupta, S.C. Goyal, Sci. China Ser. D Earth Sci. **52**, 1599 (2009)
14. P. Bonnet, Phys. B **492**, 50 (2016)
15. P. Loubeyre, Phys. Rev. B **37**, 5432 (1988)
16. T. Tsuchiya, K. Kawamura, J. Chem. Phys. **117**, 5859 (2002)
17. Y. He, X. Tang, Y. Pu, Phys. B **405**, 4335 (2010)
18. M.G. Medvedev, I.S. Bushmarinov, J. Sun, J.P. Perdew, K.A. Lyssenko, Science **355**, 49 (2017)
19. F.O. Kannemann, A.D. Becke, J. Chem. Theory Comput. **5**, 719 (2009)
20. N. Gaston, P. Schwerdtfeger, Phys. Rev. B **74**, 024105 (2006)
21. N.D. Drummond, R.J. Needs, Phys. Rev. B **73**, 024107 (2006)
22. P. Schwerdtfeger, A. Hermann, Phys. Rev. B **80**, 064106 (2009)
23. P. Schwerdtfeger, K.G. Steenbergen, E. Pahl, Phys. Rev. B **95**, 214116 (2017)
24. E.V. Zarochentsev, E.P. Troitskaya, Phys. Solid State **43**, 1345 (2001)
25. E.P. Troitskaya, V.V. Chabanenko, I.V. Zhikharev, Ie.Ie. Gorbenko, Phys. Solid State **53**, 1634 (2011)
26. V.G. Bar'akhtar, E.V. Zarochentsev, E.P. Troitskaya, *Theory of Adiabatic Potential and Atomic Properties of Simple Metals* (Gordon and Breach, London, 1999), 317 p.
27. K.B. Tolpygo, E.P. Troitskaya, Sov. Phys. Solid State **13**, 939 (1971)
28. O.N. Bolonin, K.B. Tolpygo, Sov. Phys. Solid State **15**, 1124 (1973)
29. E.P. Troitskaya, V.V. Chabanenko, I.V. Zhikharev, Ie.Ie. Gorbenko, E.A. Pilipenko, Phys. Solid State **54**, 1254 (2012)
30. E.P. Troitskaya, V.V. Chabanenko, I.V. Zhikharev, Ie.Ie. Gorbenko, E.A. Pilipenko, Phys. Solid State **55**, 389 (2013)
31. E.P. Troitskaya, V.V. Chabanenko, E.A. Pilipenko, I.V. Zhikharev, Ie.Ie. Gorbenko, Phys. Solid State **55**, 2335 (2013)

32. I.V. Abarenkov, I.M. Antonova, V.G. Bar'yakhtar, V.L. Bulatov, E.V. Zarochentsev, *Computational Physics Methods in Solid State Theory. Electronic Structure of Ideal and Defect Crystals* (Naukova Dumka, Kiev, 1991), 450 p. (in Russian)
33. V.L. Dorman, E.V. Zarochentsev, E.P. Troitskaya, Sov. Phys. Solid State **23**, 925 (1981)
34. I.V. Abarenkov, K.B. Antonova, Sov. Phys. Solid State **20**, 326 (1978)
35. F. Clementi, C. Roetti, At. Data Nucl. Data Tables **14**, 177 (1974)
36. E.A. Pilipenko, E.P. Troitskaya, Ie.Ie. Gorbenko, Phys. Solid State **60**, 153 (2018)
37. R.A. Aziz, M.J. Slaman, J. Chem. Phys. **130**, 187 (1989)
38. I.F. Silvera, V.V. Goldman, J. Chem. Phys. **69**, 4209 (1978)
39. M. Taravillo, V.G. Baonza, J. Nunez, M. Caceres, Phys. Rev. B **54**, 7034 (1996)
40. V.N. Varyukhin, E.P. Troitskaya, V.V. Chabanenko, Ie.Ie. Gorbenko, E.A. Pilipenko, Phys. Status Solidi B **251**, 774 (2014)
41. V.N. Varyukhin, E.P. Troitskaya, Ie.Ie. Gorbenko, E.A. Pilipenko, V.V. Chabanenko, Phys. Status Solidi B **252**, 709 (2015)
42. M. Ross, H.K. Mao, P.M. Bell, J.A. Xu, J. Chem. Phys. **85**, 1028 (1986)
43. J.P. Poirier, A. Tarantola, Phys. Earth Planet. Inter. **109**, 1 (1998)
44. E.V. Zarochentsev, E.P. Troitskaya, Phys. Solid State **44**, 1370 (2002)
45. N.H. March, *Advances in High Pressure Research*, vol. 3, ed. by R.S. Bradley (Academic, New York, 1969), p. 241
46. I. Kwon, L.A. Collins, J.D. Kress, N. Troullier, Phys. Rev. B **52**, 165 (1995)
47. E.P. Troitskaya, Ie.Ie. Gorbenko, E.A. Pilipenko, J. Low Temp. Phys. **42**, 411 (2016)

Chapter 17
Crystal Structure and Dielectrical Properties of Complex Perovskite-like Solid Solutions $Bi_3Ti_{1-x}Sn_xNbO_9$ (x = 0.0, 0.1, 0.35)

S. V. Zubkov

Abstract Bi_3TiNbO_9 (BTN) is an important member of the Aurivillius bismuth layer-structured ferroelectric compounds, consisting of $[Bi_2O_2]^{2+}$ layers between which $[BiTiNbO_7]^{2-}$ layers are inserted. Aurivillius type $Bi_3Ti_{1-x}Sn_xNbO_9$, n = 2 (abbreviated as BSTN, where x = 0.0, 0.1, 0.35) ceramics were prepared by a conventional solid-state reaction route. X-ray diffraction confirmed that the material has a pure two-layer Aurivillius structure with unit cell parameters and adopts the space group $A2_1am$.

17.1 Introduction

The bases of many high-temperature ferroelectric piezoceramic materials are Bi-containing compounds with a layered perovskite-like structure, which causes their high Curie temperature [1]. In 1949, Aurivillius by studying the Bi_2O_3–TiO_2 system, established the formation of a $Bi_4Ti_3O_{12}$ oxide with a perovskite-like structure. In 1950, Aurivillius investigated the crystal structure of tantalate niobates $ABi_2Nb_2O_9$, ABi_2Np_2 (A = Ca, Sr, Pb, Ba), Bi_3TiNbO_9, and $Bi_4Ti_3O_{12}$, consisting of perpendicular [001] perovskite layer and layers of $Bi^{2+}O^{2+}$ [2–4]. At about the same time, Smolensky [5], showed that crystalline structures, having in their composition ions of small size and high charge (Ta, Nb, Ta, etc.) inside oxygen octahedral, connected through angles forming continuous oxygen-metal-oxygen chains, are favorable for ferroelectricity. Further Smolensky found that $PbBi_2Nb_2O_9$ is a new ferroelectric with T_C = 520 °C [6]. In 1960, Ismailzade studied the crystal structure of polycrystalline samples of $CaBi_2Nb_2O_9$, $CaBi_2Ta_2O_9$, Bi_3TiNbO_9 and $PbBi_2Nb_2O_9$, investigating the nature of the spontaneous polarization of these compounds [7]. In further Aurivillius and Subbarao obtained and studied [8–11],

S. V. Zubkov (✉)
Scientific Research Institute of Physics, Southern Federal University, Rostov-on-Don, Russia
e-mail: svzubkov61@mail.ru

I. A. Parinov et al. (eds.), *Advanced Materials*, Springer Proceedings in Physics 224, https://doi.org/10.1007/978-3-030-19894-7_17

several dozen phases of perovskite-like bismuth oxides, which received its own name, the Aurivillius phase. To date, hundreds of publications have been issued on the properties and structure of APs (Aurivillius phases) of various compositions.

There are several perovskite-like oxides with a layered microstructure: Dion–Jacobson (DJ) phases ($[A_mB_mO_{3m+2}]$), Ruddlesden–Popper phases (RP) ($[A_{m+1}B_mO_{3m+1}]$), APs ($[A_{m-1}Bi_2B_mO_{3m+3}]$), where m is the number of perovskite layers.

APs $A_{m-1}Bi_2B_mO_{3m+3}$ form a tetragonal lattice in the high-temperature paraelectric phase, in the ferroelectric state they have deformation components (and, as a consequence, spontaneous polarization) along the c-axis and along the rhombic axis b_0 dividing the angle between a_i and b_i in half and can be monoclinic, rhombic or tetragonal. Ions A in a position with a cubo-octahedral environment are occupied by one-, two-, and trivalent cations of large radius (Na^+, K^+, Ca^{2+}, Sr^{2+}, Ba^{2+}, Pb^{2+}, Bi^{3+}, Y^{3+}, Ln (lanthanides), and Ac (actinides)), and B positions within oxygen octahedra occupy highly charged ($\geq 3+$) cations with small radii (Ti^{4+}, Cr^{3+}, Ga^{3+}, Mn^{4+}, Fe^{3+}, Nb^{5+}, Mo^{6+}, Co^{3+}, Ta^{4+}, W^{6+}, Ir^{4+}, etc.) [12]. The value of m is determined by the number of perovskite $[A_{m-1}B_mO_{3m+1}]^{2-}$ layers, located between the fluorite-like layers of $[Bi_2O_2]^{2+}$ and can take integer or half-integer values in the interval of m = 1–5. If m is a half-integer number, then an alternation of perovskite layers with m differing by 1 is observed in the lattice. The structure of the APs above the Curie point is tetragonal and belongs to space group I4/mmm. The type of space group below the Curie point depends on the value of the number m. For odd m, the space group of the ferrophase is B2cb or $Pca2_1$, for even, it is $A2_1am$, Fmm2, Fmmm, and for half-target, it is Cmm2 or I2cm. Positions A and B may be occupied by the same or several different atoms. The substitution of atoms in positions A and B has a significant impact on the electrophysical characteristics of APs. The perovskite-like elementary cell of the APs has a structural fragment in which six X=O ions form a crystallographic polyhedron in the form of an octahedron around the smaller cation B, and eight large cations A can form a cube. Twelve oxygen ions form a cubo-octahedron. For each X=O, the nearest neighbors will be both A and B, located as a tetragonal bipyramid and having different sizes and properties. Four A form the base of the bipyramid with sides equal to the parameter of the unit cell a. Two B ($R_B < R_A$) are located on a perpendicular to the center of the base of the bipyramid on both sides at distances $a/2$.

A more detailed study of the laws of variations at the Curie temperature of APs from parameters such as the radii and electronegativity of A- and B-ions, as well as from the parameters of the cell, was carried out in [13]. Some anomalies of the properties of layered ferroelectrics $A_{m-1}Bi_2B_mO_{3m+3}$ were also considered [14]. In particular, it has been shown that Bi_2O_2 layers exert a pulling effect on the layered structure of these compounds, but the strength of this effect decreases as the number of perovskite layers increases. In addition, it was shown that Curie temperatures pass through a maximum as the distortions of the pseudo-perovskite cell grow in the perovskite-like layer, and the position of the maximum varies with the number of perovskite layers m. The study of the structural features of the

$Bi_{m+1}Fe_{m-3}Ti_3O_{3m+3}$ APs in the Bi_2O_3–Fe_2O_3–TiO_2 system showed the presence of abrupt structural changes with an increase in the thickness of the perovskite-like layer to ~2 nm ($m \approx 5$). With an increase in the thickness of the perovskite-like block to ~3.7 nm ($m \approx 9$), APs become unstable. This correlates with the alignment of the values of the effective charges of the octahedrally surrounded ions in two structurally inequivalent positions of the perovskite-like block. The APs instability also correlates with a decrease in the order in the distribution of Fe^{3+} and Ti^{4+} ions to their completely disordered distribution at $m \approx 9$ between the inner and outer layers of the perovskite-like block and the approximate average thickness of the perovskite-like layer to the corresponding parameter of the $BiFeO_3$ compound [15, 16].

In ferroelectric compounds of the perovskite family, as well as laminates, such as APs, the properties are closely related to small distortions of the ideal high-symmetry structure. In this regard, obtainment and analyze of information about such distortions can provide the key to understanding the nature of ferroelectricity in these materials and developing ways to obtain new materials with desired properties.

In the last ten years, the structure of APs with $m = 2$ has been intensively studied in order to identify patterns of their structure. Almost all connections (16) of these series, described in the literature, at room temperature have an orthorhombic cell with space group $A2_1am$ and similar parameters of unit cell. The exception is $BaBi_2Ta_2O_9$, which was clarified in the high-symmetry space group I4/mmm, and its cell parameters were: a = 3.92650 (8) Å and c = 25.5866 (8) Å [17].

In a number of studies, a series of comparative investigations have been carried out in APs with various atoms at position A [18–23]. In the course of these studies, some features of the structure were revealed, to some extent characteristic of all APs. Thus, atoms, located at the A- and B-positions are displaced along the c-axis towards the oxygen atoms lying in the fluorite-like layers. As the distance from the fluorite-like layers increases, this shift becomes smaller. This expansion of the cation sublattice is combined with the compression of the anion sublattice, which leads to the formation of short B–O bonds. The shift of cations at position of A also occurs along the polar a-axis. For example, on the base of powder diffraction patterns, the structures of three APs of the $ABi_2Ta_2O_9$ series are refined, where A = Ca, Sr, Ba [18]. The study shows that it is possible to trace the influence of the A-cation magnitude on the degree of structural distortions. The results clearly show how the distortion of TaO_6 octahedra increases as the size of the cation decreases at position of A. A similar comparative study for $Bi_{2.5}Na_{0.5}Nb_2O_9$ and $Bi_{2.5}K_{0.5}Nb_2O_9$ was described in [19]. Later, two other compounds of this series were investigated: $Bi_{2.5}Na_{0.5}Ta_2O_9$ [20] and $Bi_{2.5}Ag_{0.5}Nb_2O_9$ [21]. Here there is the same pattern as in the previous case, and the rhombic distortion increases in the sequence A = K → Ag → Na.

17.2 Experimental

Polycrystalline APs samples were synthesized by solid solutions reaction of the corresponding oxides of Bi_2O_3, TiO_2, Nb_2O_5 and SnO_2. After weighing and preliminary grinding of the starting compounds, the APs synthesis was carried out at a temperature of 870 °C (for 2 h), then a forth grinding and roasting were synthesized at a temperature of 1100 °C (for 8 h), followed by grinding with the addition of a binder. Then pellets with a diameter of 10 mm and a thickness of 1–1.5 mm were pressed and finally burnt at a temperature of 1100 °C (for 6 h).

X-ray diffraction spectra of the powder were obtained on a DRON-3 M diffractometer with Cu X-ray tube. CuKα1, α2-radiation was selected from the total spectrum using a Ni filter. The diffraction patterns were measured in the range of 2θ-angles from 10 to 60° with a scan step of 0.04° and an exposure of 20 s per point. The analysis of the profiles of the diffraction patterns, the determination of the positions of the lines, their indexing (*hkl*), and refinement of the unit cell parameters were performed with the PCW 2.4 program [13].

To perform the electric measurements, the APs samples were pressed in the form of ~1 mm thick discs with 10 mm in diameter, and then Ag–Pd electrodes were deposited on the plane surfaces of the discs. The measurements were carried out using an E7-20 immittance meter in the frequency range 100 kHz–1 MHz at temperatures in the range from room temperature to 960 °C.

17.3 Results and Discussion

The X-ray diffraction patterns of all $Bi_3Ti_{1-x}Sn_xNbO_9$, $n = 2$ ($x = 0.0, 0.1, 0.35$) solid solutions under study correspond to single phase APs with $m = 2$ of the orthorhombic system with space group A21am (36). It determines that all the APs obtained crystallize in orthorhombic system with the space group of the unit cell A21am (36). The unit cell parameters, refined on the base of the X-ray diffraction data and the volumes and parameters of the orthorhombic and tetragonal deformations, calculated on their base are present in Fig. 17.1 and Table 17.1.

This is due to the fact that at high temperatures the dominant charge carrier in the APs represents internal defects, the formation of which requires high activation energies. At low temperatures, the conductivity is mainly due to impurity defects, which have substantially lower activation energies. It should be noted that the activation energies of all $Bi_3Ti_{1-x}Sn_xNbO_9$, $n = 2$ ($x = 0.0, 0.1, 0.35$) series compounds are close in low temperature ranges, and this indicates that the conductivity in this range does not change. At the same time, changes occur in the high-temperature region indicating the appearance of new charges carriers.

The temperature dependences of the dielectric constants, as shown in Fig. 17.2a, b present peaks at 932 and 933 °C for $Bi_3Ti_{0.9}Sn_{0.1}NbO_9$ and $Bi_3Ti_{0.65}Sn_{0.35}NbO_9$, respectively. The phase transition at higher temperatures is a true ferroelectric-

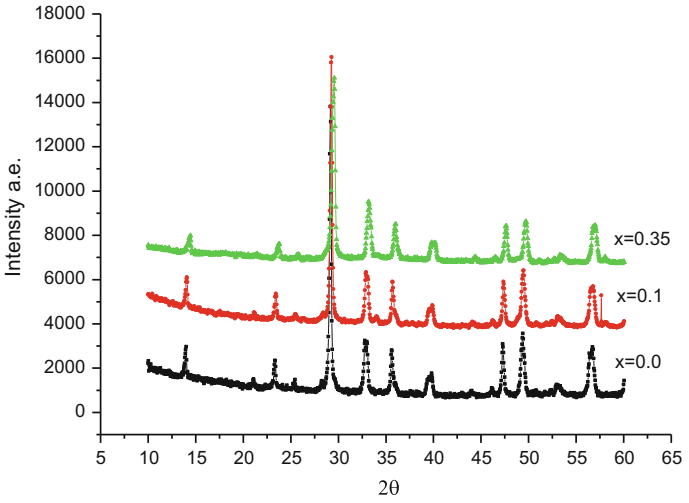

Fig. 17.1 X-ray diffraction patterns of the Bi_3TiNbO_9, $Bi_3Ti_{0.9}Sn_{0.1}NbO_9$, $Bi_3Ti_{0.65}Sn_{0.35}NbO_9$

Table 17.1 Unit cell parameters *a*, *b*, *c* and volume *V*, relative permittivity $\varepsilon/\varepsilon_0$, measured at frequency of 100 kHz

No.	Compounds	*a*, Å	*b*, Å	*c*, Å	*V*, Å^3	$\varepsilon/\varepsilon_0$
1	Bi_3TiNbO_9	5.4399	5.3941	25.099	736.4	340
2	$Bi_3Ti_{0.9}Sn_{0.1}NbO_9$	5.4369	5.4026	25.099	737.2	2100
3	$Bi_3Ti_{0.65}Sn_{0.35}NbO_9$	5.446	5.4194	25.0585	739.547	1100

paraelectric phase transition. As shown this study, the dependence of Curie temperature on the parameter *x* is close to linear, which is typical for solid solutions of the APs.

The temperature dependences of tanδ (Fig. 17.2 c, d) for the APs under study show a sharp increase in the dielectric loss at high temperatures (>600–700 °C). This increase is due to a large number of charge carriers, whose concentration increases sharply at high temperatures due to formation of oxygen vacancies. Moreover, the values of tanδ taken at a certain temperature, e.g., T_C, differ several times for different APs under study, and this fact indicates on different degrees of defects of the crystal structure of the APs.

Based on the dependence of lnσ *versus* $1/kT$, we found the activation energy of the charge carriers E_a for the full series of APs (Table 17.1). Figure 17.3 shows a typical $\ln\sigma = f(1/kT)$ dependence for $Bi_3Ti_{3-x}Sn_{0.1}NbO_9$, and we clearly see that there are three temperature ranges, in which the activation energies differ significantly.

Table 17.2 presents values of the temperature of relative permittivity $\varepsilon/\varepsilon_0$ peak (T_p), mean values of the tetragonal period (a_t), thickness of a single perovskite-like

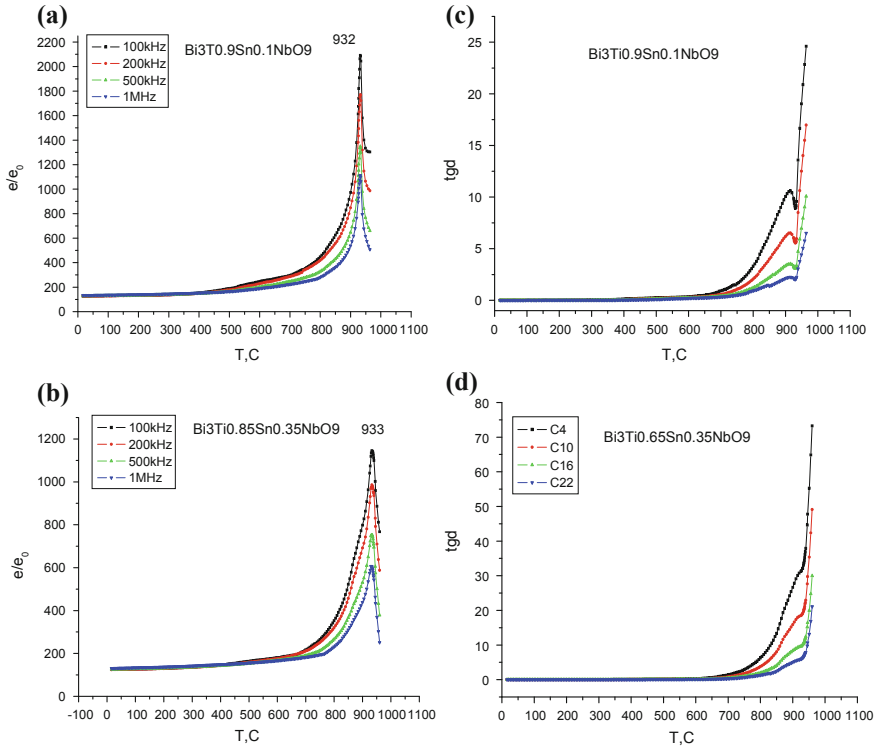

Fig. 17.2 Temperature dependences of the relative permittivity $\varepsilon/\varepsilon_0(T)$ (**a**, **b**) and loss tangent tg$d$ (**c**, **d**) for $Bi_3Ti_{1-x}Sn0.1_xNbO_9$ (x = 0.1, 0.35)

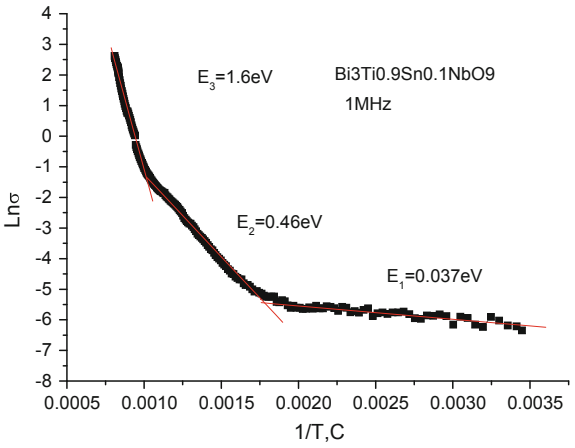

Fig. 17.3 Dependence of $\ln\sigma$ on $1/kT$ for the $Bi_3Ti_{3-x}Sn_{0.1}NbO_9$ sample

Table 17.2 Values of the temperature of relative permittivity peak (T_p), tetragonal period (a_t), thickness of a single perovskite-like layer (c), deviation of the cell from the cubic form (Δc), rhombic deformation (Δb_0), factor of tolerance (t)

	Compound	T_p, °C	$a_t = (a_0 + b_0)/2\sqrt{2}$, Å	c_l, Å	$\Delta c = (c - a_t)/a_t$	$\Delta b_0 = (b_0 - a_0)/a_0$	t
1	Bi_3TiNbO_9	920	3.83	3.765	−1.71	0.84	0.95
2	$Bi_3Ti_{0.9}Sn_{0.1}NbO_9$	932	3.832	3.765	−1.76	0.63	0.94
3	$Bi_3Ti_{0.65}Sn_{0.35}NbO_9$	933	3.84	3.759	−2.15	0.49	0.944

layer (c_l), deviation of the cell from the cubic form (Δc), rhombic deformation (Δb_0) , factor of tolerance (t). The thickness of a single perovskite-like layer c_l (the height of the octahedron along the c-axis) is calculated from the formula $c_l = 3c_{pl}/(8 + 6\ m)$, where c_{pl} is the thickness of the perovskite-like layer, m is the number of layers. The relative elongations of the pseudocubic cell in the perovskite-like layer along the c-axis are given, too; $\Delta c = (c - a_t)/a_t$ is the deviation of this cell from the cubic form. The sign of minus shows, that the elongation is shortening along the c-axis. By comparing a_t and c from Table 17.2, we see that value of c is usually less than a_t. In this case, pseudocubic cells of the perovskite-like layer are cubes, compressed along the c-axis.

17.4 Conclusion

Doping in layer-structured SBN ceramics was found to have significant influences on dielectric and electric properties. Depending on the ionic radii of dopants, the lattice constant and Curie temperature either increase or decrease with and increasing amount of dopants. Dielectric constants initially increase with a small amount of dopant, regardless of the types of dopants, and reach a maximum at a doping level between 2.5 and 15 at.%. It was also found that doping resulted in a reduced tangent loss and bulk conductivity at temperatures ranging from room temperature to 600 °C, regardless of the types of dopants at the doping level (<10 at.%) studied in this research.

Synthesized compounds have the highest temperature of the phase transition in a series of bismuth-titanium-niobate compounds of the APs. These factors indicate that BSTN ceramics is a promising candidate for use in sensors in a wide range of temperatures.

Acknowledgements The work was performed under financial support of the Ministry of Education and Science of the Russian Federation (state assignment Grant No. 3.5710.2017/8.9).

References

1. S.V. Zubkov, V.G. Vlasenko, J. Phys. Solid State **59**(12), 2325 (2017)
2. B. Aurivillius, Arkiv. Kemi. **1**, 463 (1949)
3. B. Aurivillius, Arkiv. Kemi. **1**, 499 (1949)
4. B. Aurivillius, Arkiv. Kemi. **2**, 512 (1950)
5. G.A. Smolensky, DAN USSR **76**(4), 519 (1951)
6. G.A. Smolensky, J. Phys. Solid State **1**, 1969 (1959)
7. I.G. Ismailzade, Vestn AS SSSR **24**, 1198 (1960)
8. B. Aurivillius, Phys. Rev. **126**, 893 (1962)
9. E.C. Subbarao, J. Am. Ceram. Soc. **45**, 166 (1962)
10. E.C. Subbarao, J. Chem. Phys. **34**, 695 (1961)
11. E.C. Subbarao, Phys. Rev. **122**, 804 (1961)
12. S.V. Zubkov, in *Advanced Materials—Proceedings of the International Conference on Physics and Mechanics of New Materials and Their Applications, PHENMA 2017*, ed. by A. Parinov, S-H. Chang, V.K. Gupta. Springer proceedings in physics, vol. 207 (Springer Cham, Heidelberg, New York, Dordrecht, London, 2018), p. 171
13. W. Kraus, G. Nolze, *Powder Cell for Windows, Version 2.3* (Federal Institute for Materials Research and Testing, Berlin, Germany, 1999)
14. L.A. Reznichenko, J. Inorg. Mater. **32**(4), 474 (1996)
15. V.A. Isupov, J. Inorg. Mater. **42**, 1353 (2006)
16. N.A. Lomanova, Nanosyst: Phys. Chem. Math. **2**(3), 93 (2011). (in Russian)
17. N.A. Lomanova, V.V. Gusarov, M.I. Morozov, V.L. Ugolkov, J. Inorg. Mater. **42**(2), 1 (2006)
18. Y. Shimakawa, Y. Kubo, Y. Nakagawa, S. Goto, T. Kamiyama, H. Asano, F. Izumi, J. Phys. Rev. B. **61**(10), 6559 (2001)
19. S. Borg, J. Solid State Chemistry. **157**, 160 (2001)
20. S. Borg, G. Svensson, J.-O. Bovin, J. Solid State Chem. **167**, 86 (2002)
21. W. Wong-Ng, Q. Huang, L.P. Cook, I. Levin, J.A. Kaduk, A.D. Mighell, J. Suh, J. Solid State Chem. **177**(10), 3359 (2004)
22. G. Nalini, T.N. Guru, Bul. Mater. Sci. **25**(4), 275 (2002)
23. I. Ismunandar, T. Kamiyama, A. Hoshikawa, Q. Zhou, B.J. Kennedy, Y. Kubota, K. Kato, J. Solid State Chem. **177**, 4188 (2004)

Chapter 18
Properties of Unipolarity Arising in an Unpolarized Ferroelectric Plate After Creating a Stationary Strain Gradient in the Interelectrode Space

Yu. N. Zakharov, V. P. Sakhnenko, I. P. Raevsky, I. A. Parinov, A. V. Pavlenko, V. A. Chebanenko, N. S. Filatova, M. A. Zaerko, E. I. Sitalo and L. I. Kiseleva

Abstract It has been established that after burning, the metal electrodes made of Ag into opposite surfaces of plates made of hot-pressed ferroelectric ceramics PZT-19 (T_c = 300 °C) with different depth of mechanical damage counter-directed stationary deformation gradients and, accordingly, internal displacement electric fields, are created. After replacing the Ag electrode with a valence of $V = 3$ for Cr with $V = 6$ from the side of the undamaged surface, a new heat-resistant polarization is created, directed from the damaged surface into the interelectrode space. Such plates have an asymmetric dielectric hysteresis loop, retain the pyro- and piezoelectric effect in the ferroelectric phase, and also the bolometric effect in the paraelectric phase, after repeated heating cycles up to 350 °C and cooling down to T_{norm}.

18.1 Introduction

The study was based on the consideration of the invention "A method for stabilizing the unipolarity of $BaTiO_3$ crystals" [1]. Unipolarity means that an internal electric field of displacement and polarization induced by this field exist in the

Yu. N. Zakharov · V. P. Sakhnenko · I. P. Raevsky · N. S. Filatova · M. A. Zaerko · E. I. Sitalo
Physics Faculty, Research Institute of Physics, Southern Federal University, Rostov-on-Don 344090, Russia

I. A. Parinov
Institute of Mathematics, Mechanics and Computer Sciences, Southern Federal University, Rostov-on-Don 344090, Russia

A. V. Pavlenko · V. A. Chebanenko (✉) · L. I. Kiseleva
South Scientific Center, Russian Academy of Sciences, Rostov-on-Don 344006, Russia
e-mail: valera.chebanenko@yandex.ru

I. A. Parinov et al. (eds.), *Advanced Materials*, Springer Proceedings in Physics 224, https://doi.org/10.1007/978-3-030-19894-7_18

interelectrode space of a single crystal. The main cause of the appearance of the internal field are stationary gradients of the volume strain and mechanical stresses directed from the "external" to the "internal" surface of the single crystal. They are formed in the process of specific crystal growth conditions. As a result, the single crystal exhibits pyro- and piezoelectric effects in the ferroelectric phase, as well as the bolometric effect in the paraelectric phase. These properties are retained after multiple phase transitions through the Curie point. The further use of different electrodes on the undamaged surfaces of the single crystal strengthens and stabilizes this unipolarity. To do this, an electrode from one metal, for example, Ag, Cu, Au, is deposited on the one of the surfaces of the crystal and on the opposite one—Cr, Al, Zn. The main feature of such unipolarity is the creation and maintenance of polarization in the entire volume of the interelectrode space.

18.2 Creation of Polarization in the Plate of Hot-Pressed Ferroceramics PZT-19 Without External Electric Field

Sample preparation for the study was divided into several stages:

(i) Plates 15 × 8 × 0.6 mm^3 in size were cut out of the hot-pressed PZT-19 block with a diamond saw. One of the large surfaces of the plate was damaged by laser scribing (see Fig. 18.1), or by abrasive powders with grain diameters of 12 and 22 μm.
(ii) Electrodes were deposited on both opposite surfaces using the method of reducing the silver nitrate at 730 °C.
(iii) After conducting preliminary studies, the electrode was removed from the undamaged side with ordinary grinding powder of 2–3 μm in diameter. Then, thin layers of Cr, and then Al, were successively deposited on this surface by evaporation in vacuum.

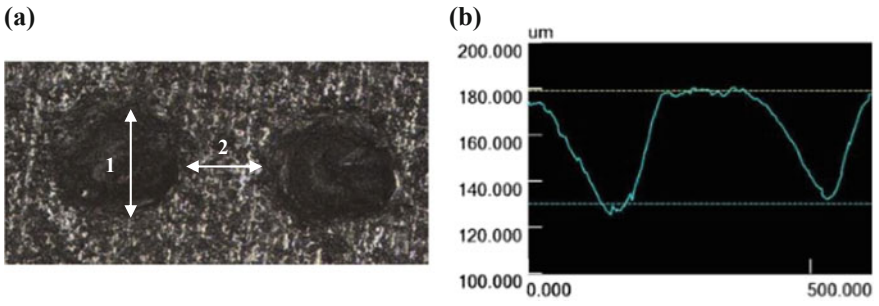

Fig. 18.1 Damaged surface of the plate: **a** surface of the central part of the plate, 1—diameter is 101–114 μm, 2—distance between adjacent pits is 135–160 μm; **b** depth of the damage is approximated

18.3 Investigation of the Spatially Inhomogeneous Distribution of Polarization in the Volume of a Ferroceramic Plate by the Dynamic Pyroelectric Method

It is known [2] that this method, by creating a temperature gradient in the inter-electrode volume of the sample, allows one to determine the polarity and amplitude of the electrical response of the ferroelectric sample along the thermal wave shown in Fig. 18.2. This makes it possible to obtain information on the spatially inhomogeneous distribution of polarization, when the plate is rotated to the radiation source on 180°.

With a smaller degree of resolution, similar studies can be carried out with sinusoidal modulation of the heat flux.

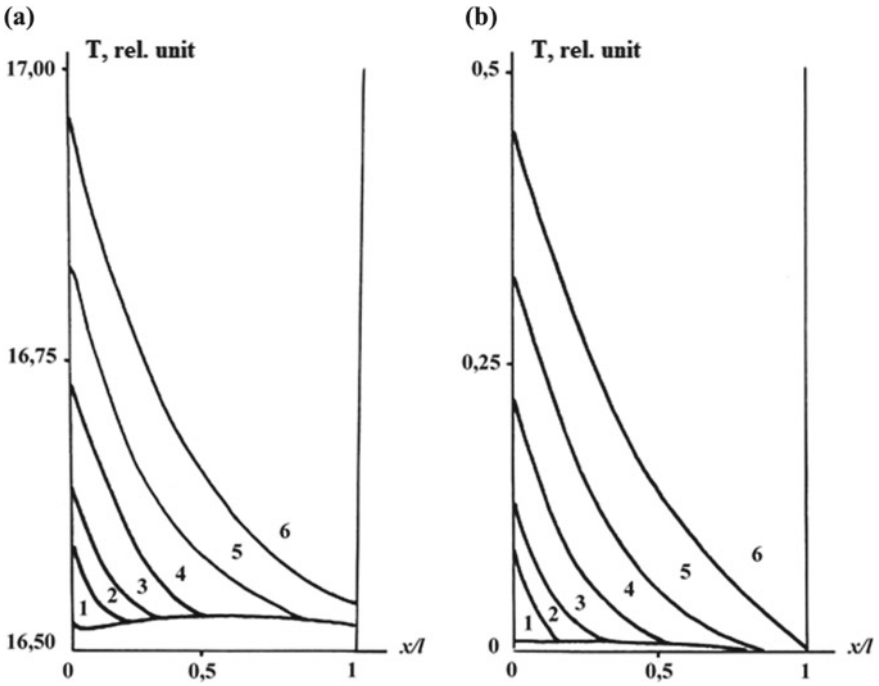

Fig. 18.2 The temperature distribution over the thickness of the $BaTiO_3$ plate, heated by rectangular heat pulses with $f = 10$ Hz and duty cycle $g = 10$: **a** without a heat sink on the opposite surface and **b** with a heat sink; the numbers indicate the sequence of changes in the distribution of T in the process of heating

18.3.1 Model Representation of the Polarization Distribution in the Interelectrode Space of Ferroelectric Plate Depending on the State of the Surfaces

When silver is fired into the surface of an unpolarized plate, a metal-ceramic layer is formed, in which the tangential compressive stresses σ create a stationary deformation gradient due to the difference in temperature coefficients of linear expansion of the electrode metal and ferroelectric ceramics after cooling from 730 °C.

Mechanical stresses in the near-electrode layers generate oppositely directed vectors of polarization and electric field displacement in the bulk of the plate.

Figure 18.3 shows a diagram of the oppositely directed polarization vectors $\mathbf{P_1}$ and $\mathbf{P_2}$ in the volume of the plate after surface treatment with grinding powder with a grain diameter of up to 10 μm and subsequent burning of the Ag-electrodes.

At equivalence of the near-electrode layers, the total polarization: $P_1 + P_2 = 0$. Hereinafter (+ or −) denote the sign of the Debye charge that screens.

The polarization distributions in the interelectrode space of the plate with nonequivalent surfaces are shown in Fig. 18.4. Index 1 refers to the surface subjected to conventional diamond cutting and grinding and index 2 corresponds to the surface after laser scribing by cells 30–40 μm deep, 60 μm in diameter and 100 μm in step. Electrodes from Ag are fired in the surface.

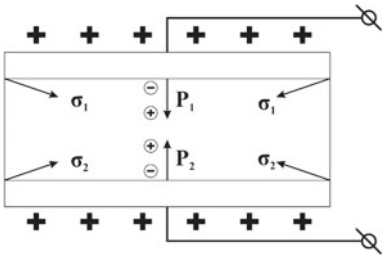

Fig. 18.3 Block diagram of the oppositely directed polarization vectors in the volume of the plate, where σ is the vector of tangential compressive stresses on surface and **P** is the polarization vector; the signs "+" and "−" indicate the polarity of the associated charges

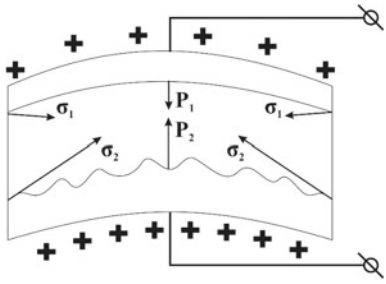

Fig. 18.4 Block diagram of the oppositely directed polarization vectors in the volume of the active element with nonequivalent surface layers; the vector P_2 is directed towards the undamaged surface

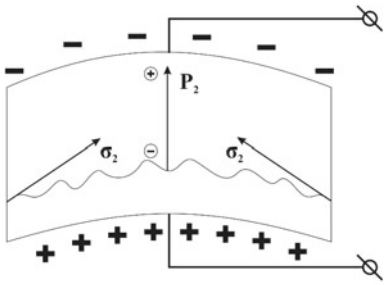

Fig. 18.5 Block diagram of the volume distribution of polarization P_2 after applying an electrode of Cr with $V = 6$ on the undamaged surface of the plate

The different magnitude and the opposite direction of the vectors of unipolarity in the interelectrode space show that the maximum value of unipolarity corresponds only to $P_2 - P_1$.

The block diagram of polarization distribution after replacing an Ag electrode with a valence of $V = 3$ to Cr with $V = 6$ on an undamaged surface directed from the damaged to undamaged surface is shown in Fig. 18.5.

18.3.2 Setup for Studying the Temperature Dependence of Pyroelectric Effect of the Samples in Dynamic Mode of Measurement in the Temperature Range from $\mathbf{T}_{norm}$ *up to 400 °C*

Figure 18.6 presents the block diagram of the setup for recording the temperature dependences of the components of the total conductivity and pyroelectric coefficient in a dynamic mode for measuring ferroelectric samples under the influence of the internal electric displacement field. Similar setup was successfully used for studying the effect of the external biasing field on the pyroelectric properties of ferroelectrics and relaxors [3–8].

The sample 1, placed in the heat chamber 2, through the focusing lens 3 is illuminated by the LED 4 with a sinusoidally intensity-modulated flux of infrared radiation. The modulation frequency and radiation intensity of the LED is set by the generator 5. A pyroelectric current i_p from the sample, excited in the result of such exposure, through the band-pass filter of device 6, is fed to the measuring input of a synchronous detector (SD) 8. To ensure the process of measuring the pyro-current, the common-mode voltage from generator 5 is connected to the input of the reference signal of the SD with the value specified by the SD passport.

The analog signal, detected in this way, is recorded by a PC through the ADC channel of the L-152 board. To register the dependence of $i_p(T)$ and the ranges of its change according to a linear law, a programmer-thermostat controller (PTC) 7 is used, which records the absolute value of temperature T according to thermocouple 2 in the heat chamber. The values of the boundaries of the ranges and the rate of

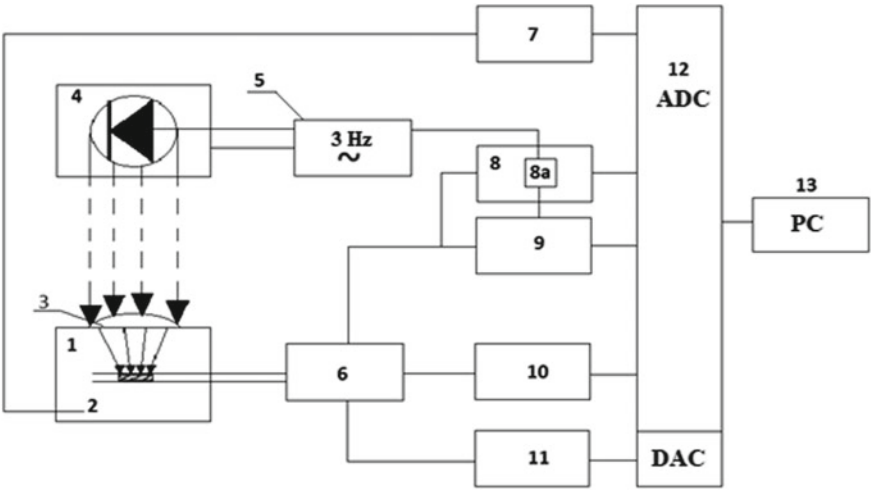

Fig. 18.6 Block diagram of the setup represents the following elements: 1—test sample; 2—thermostatically controlled chamber; 3—focusing lens; 4—LED; 5—LED startup generator; 6—block of active filters; 7—programmer-thermostat; 8—synchronous nanovoltmeter "Unipam"; 8a—phase shifter at 90°; 9—synchronous nanovoltmeter "Unipam"; 10—immittance meter E70-20; 11—controlled source of direct current (voltage); 12—specialized board for collecting and processing information L-152; 13—personal computer

change of T are programmatically set by the PC. The control of the PTC and the registration of changes in T is carried out through the corresponding L-152 ADC channel.

18.3.3 The Contribution of the Temperature Dependence of Dielectric Constant (Bolometric Effect) to Pyroelectric Response

According to thermodynamics in the absence of electric fields, the pyroelectric coefficient $\gamma \sim \varepsilon P$, (the product of the dielectric permittivity ε by the polarization P), then the extremum condition P is:

$$\varepsilon \frac{\mathrm{d}P}{\mathrm{d}T} + P\frac{\mathrm{d}\varepsilon}{\mathrm{d}T} = 0; \quad \frac{\mathrm{d}\varepsilon}{\mathrm{d}T} = -\frac{\varepsilon\gamma}{P} > 0, \quad \text{since } \gamma < 0$$

Consequently, the maximum of $\gamma(T)$ is below the maximum of $\varepsilon(T)$ in the rising region of $\varepsilon(T)$.

The presence of an electric field will lead to an additional relative shift of the maxima of $\varepsilon(T)$ and $\gamma(T)$ in the region of elevated temperatures. The source of the electric field can be the external electric field, contact fields (in our case, the field of

unipolarity) and the field of free charges, which screen polarization. The contribution of the component, $E\,d\varepsilon/dT$, as a rule, is considered small and is usually not taken into account in the calculations, and no comments are made on the direction E with respect to the direction P.

At the same time, the presence of a field E of any nature that does not coincide in direction with P can even lead to a change in the sign of $\gamma(T)$.

The additional contribution of temperature changes of the dielectric permittivity to the pyroelectric response is possible only when a constant electric field (external or internal) is applied to the ferroelectric sample.

18.3.4 The Results of the Study of Pyroelectric Effect

To interpret the results, we consider the features of the method for measuring the dynamic pyroelectric effect and the research samples.

When measuring the pyroelectric response to the amplitude-modulated thermal radiation in the sample volume (Fig. 18.2), a temperature gradient periodically occurs. As a result, the side of the plate that receives radiation per each period heats up more than the entire volume. The pyroelectric response illustrates the state of polarization of only this part of the plate. For completeness of the study, it is necessary to turn the sample to thermal radiation by 180°.

The pyroelectric response was measured by sinusoidally modulated thermal radiation from a laser LED at a frequency of 7.5 Hz. The study was performed in 2 stages.

Fist stage is devoted to the investigation of a $10 \times 6 \times 0.6$ mm^3 ferroelectric plate after laser scribing of one surface (A) and polishing to size with a grinding powder with a particle diameter of up to 10 μm of the opposite surface (B). Electrodes were deposited with Ag.

On the temperature dependences (Figs. 18.7, 18.8, 18.9 and 18.10) of the pyro-current in the ferroelectric phase—paraelectric phase, the arrows indicate

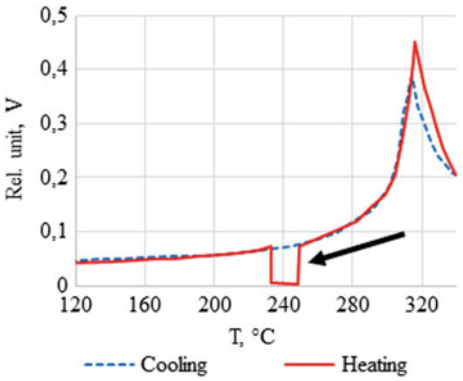

Fig. 18.7 Temperature dependences of the pyroelectric current, when the laser scribed surface is irradiated by the LED (A)

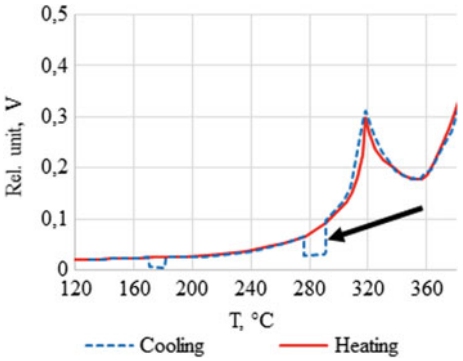

Fig. 18.8 Temperature dependences of the pyroelectric current when irradiated by the LED plate from the side (*B*)

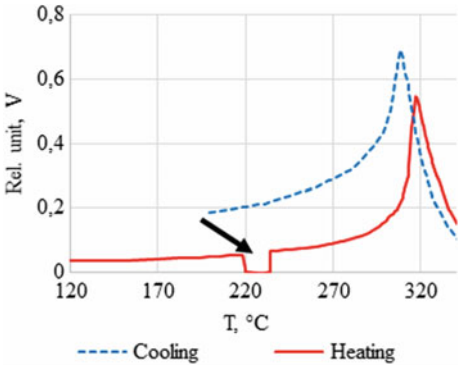

Fig. 18.9 Temperature dependence of the pyroelectric current when surface (*A*) is irradiated by the LED after changing the electrode on the surface (*B*)

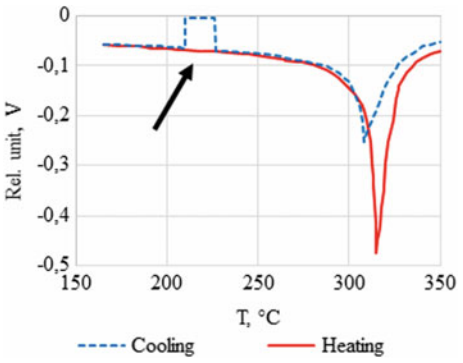

Fig. 18.10 Temperature dependences of the pyroelectric current when surface (*B*) is irradiated by the LED after changing the electrode to Cr, which has $V = 6$

the areas of stepwise reduction of the pyro-signal "plateau" on the plots where the thermal radiation flow was blocked. The presence of such a deviation indicates the polarization of the sample in the ferroelectric phase. The electrical response in the paraelectric phase is the bolometric effect.

Figure 18.7 shows the results of measuring the temperature dependences of the pyroelectric current (heating—cooling) when a heat wave is applied to the laser scribed surface (*A*). Similar measurements of the opposite surface after rotating the sample by 180° from the less defective side (*B*) are shown in Fig. 18.8. Figure 18.8 presents the measurement of the pyrosignal of the sample after turning to radiation by 180°.

Comparison of the results shows that laser scribing creates greater unipolarity of responses to the action of heat pulses in the ferro- and paraphase.

Analysis of the results of the study of opposite surfaces shows their good coincidence with the model representation of Fig. 18.5. Measurements of the pyroelectric effect confirm the existence of layers at the opposite surfaces of the plate with antiparallel polarization. In the ferroelectric phase, this is the pyroelectric current, which, like the bolometric effect in the paraphase, retains its direction after turning by 180°.

Second stage is devoted to the measurements of the pyro-effect in the dynamic mode for the previous sample after replacing the electrode at the surface (*B*) of Ag with a valence of $V = 3$ with chromium-aluminum, where Cr has $V = 6$.

Figure 18.9 presents the results of measuring the pyrosignals from the previous sample after replacing the electrode on the surface (*B*). Comparison of Figs. 18.9 and 18.10 shows that the replacement of the electrode at the surface (*B*) has led to the creation of unipolarity in the entire volume of the interelectrode space, directed from the side of laser scribing. The result obtained is consistent with studies of the unipolarity of single crystals of barium titanate [1]. It was noted there that the use of Ag and Cr electrodes on opposite surfaces of single crystals enhances their natural unipolarity due to recombination of electrons in the valence bands. In our case, the natural unipolarity is created by a stationary strain gradient directed from the surface into the volume of the plate.

18.4 Studies of the Dielectric Hysteresis of Samples of Unipolar Ferroelectric Plates

The temperature dependences of the coercive field U on the dielectric hysteresis loop of polarization $P(U)$ in the range of $T = (20–350)$ °C were measured to eliminate the effect of conductivity at a frequency $f = 300$ Hz. Hysteresis loops were recorded with a special setup consisting of the TF Analyzer 2000 and the Varta TP703 thermostat.

The loops of the dielectric hysteresis of the PZT-19 ceramics, measured at different temperatures, are present in Fig. 18.11.

Figure 18.11 shows that the asymmetry of the switching fields is maintained up to 310 °C. The result obtained is maintained after repeated heating cycles up to 350 °C and cooling to T_{norm}.

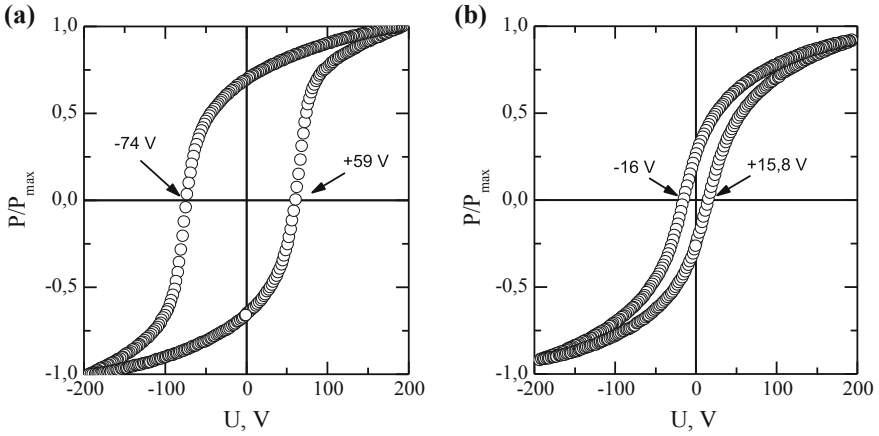

Fig. 18.11 Dielectric hysteresis loops of the PZT-19 ceramics, measured at a frequency of 300 Hz at different temperatures: **a** 248 °C (ΔU = 15 V), **b** 310 °C (ΔU = 0.2 V)

18.5 Study of the Piezoelectric Effect in Unipolar Plates After Repeated Thermal Cycling in the Range T_{norm}—400 °C

Heat treatment of the shorted samples was carried out at a rate of 10° per minute in a heat chamber with a temperature controller.

The d_{33} piezomodulus was measured by the quasistatic method in the direct piezoelectric effect mode. A wide-range piezo-tester with polarity, YE2730A (d_{33} m), manufacturer: APC International, Ltd. was used. The measurement results are presented in Table 18.1.

Table 18.1 Results of d_{33} measurement

No	Surface treatment *A* and *B* of the sample, electrodes	Piezo modulus d_{33}, pC/N
1	*A* is the grinding powder with diameter of d = 22 μm, electrode is the fired Ag	−9.0
	B is the grinding powder with a diameter of d = 2 μm, electrode is the Cr	+14.0
2	*A* is the laser scribing, fired Ag	−23.0
	B is the grinding powder with a diameter of d = 2 μm, electrode is the Cr	+24.0 (Ag)

18.6 Conclusion

It has been established that after burning the metal electrodes made of Ag into opposite surfaces of plates made of hot-pressed ferroelectric ceramics PZT-19 with different depth of mechanical damage counter-directed stationary deformation gradients and, accordingly, internal displacement electric fields are created. After replacing the Ag electrode with a valence of $V = 3$ for Cr with $V = 6$ from the side of the undamaged surface, a new heat-resistant polarization is created, directed from the damaged surface into the interelectrode volume. Such plates have an asymmetric dielectric hysteresis loop, retain the pyro- and piezoelectric effect in the ferroelectric phase, and also the bolometric effect in the paraelectric phase, after repeated heating cycles up to 350 °C and cooling down to T_{norm}.

Acknowledgements The work was supported by the grant of Russian Foundation for Basic Research, No. 19-08-00365, Ministry of Education and Science of the Russian Federation: project No. 3.5378.2017/VU (organization of the implementation of researches).

References

1. V.Z. Borodin, B.Ts. Spitalnik, B.F. Proskuryakov, L.M. Berberov, *Method of Stabilizing the Unipolarity of $BaTiO_3$ Crystals*. Description of the Invention to the Author's Certificate of the USSR, no. 501444, (1976). (in Russian)
2. V.Z. Borodin, S.G. Gach, Y.N. Zakharov, E.M. Pikalev, B.C. Shpitalnik, A.M. Blokhin, Ferroelectrics **6**(1), 83 (1973)
3. S.I. Raevskaya, Y.N. Zakharov, A.G. Lutokhin, A.S. Emelyanov, I.P. Raevski, M.S. Panchelyuga, V.V. Titov, S.A. Prosandeev, Appl. Phys. Lett. **93**(4), 042903 (2008)
4. Y.N. Zakharov, S.I. Raevskaya, A.G. Lutokhin, V.V. Titov, I. P. Raevski, V.G. Smotrakov, V. V. Eremkin, A.S. Emelyanov, A.A. Pavelko, Ferroelectrics **399**(1), 20 (2010)
5. S.I. Raevskaya, V.V. Titov, I.P. Raevski, A.G. Lutokhin, Y.N. Zakharov, V.Y. Shonov, A.V. Blazhevich et al., Ferroelectrics **475**(1), 31 (2015)
6. E.I. Sitalo, Y.N. Zakharov, A.G. Lutokhin, S.I. Raevskaya, I.P. Raevski, M.S. Panchelyuga, V. V. Titov et al., Ferroelectrics **389**(1), 107 (2009)
7. S.I. Raevskaya, A.G. Lutokhin, A.M. Pugachev, I.P. Raevski, V.V. Titov, Y.N. Zakharov, D. V. Suzdalev, E.M. Panchenko, S.A. Prosandeev, Ferroelectrics **440**(1), 59 (2012)
8. A.G. Lutokhin, E.A. Bikyashev, Y.N. Zakharov, E.A. Reshetnikova, I.P. Raevskii, N.A. Korchagina, Phys. Solid State **54**(5), 1021 (2012)

Chapter 19
The Changes in the Structure of PZT-Ceramics at Nano-, Mezo- and Microscopic Levels Under Morphotropic Phase Transitions

Sergei Titov, Inna Andryushina, Lydia Shilkina, Victor Titov, Konstantin Andryushin and Larisa Reznichenko

Abstract Ferroelectric ceramics of the $(1 - x)PbZrO_3$–$xPbTiO_3$ (PZT) system solid solutions (SSs) were obtained and comprehensively investigated in the full range of components' solubility. The processes occurring in the nano-, meso-, and microstructure of ceramics with changes in the ratio of the components were considered in detail. It is shown that the appearance of clusters of a new phase and their evolution when solid solutions approach the morphotropic regions of the system cause consistent changes in the structural ordering in the entire range of scales studied. X-ray studies of the crystal structure and multifractal parametrization of the grain landscape were carried out. Comprehensive studies have shown that changes in the crystal structure begin already far from morphotropic phase transitions areas. The role of crystallographic shear planes as a concentrator of mechanical stresses in the system was revealed. In a number of compositions, the appearance of phases with symmetry of the matrix and close but different cell parameters and the rate of their change is established. They were called phase states. It was shown that the multifractal parameters of a microstructure are a sensitive indicator of all mesostructural changes occurring in a ceramic object. The possibilities of the influence of the state of different structural levels on the formation of piezoelectric properties of the material are considered.

19.1 Introduction

The binary system $(1 - x)$ $PbZrO_3$–$xPbTiO_3$ is of great practical importance due to the unique electromechanical properties of solid solutions, which composition are close to the region of the morphotropic phase transition of the system from rhombohedral (R) to tetragonal (T) symmetry. A huge amount of research has been

S. Titov (✉) · I. Andryushina · L. Shilkina · V. Titov · K. Andryushin · L. Reznichenko
Research Institute of Physics, Southern Federal University, Rostov-on-Don, Russia
e-mail: svtitov@sfedu.ru

I. A. Parinov et al. (eds.), *Advanced Materials*, Springer Proceedings in Physics 224, https://doi.org/10.1007/978-3-030-19894-7_19

devoted to the study of the structure and properties of PZT system solid solutions. In this case, usually, the objects are only selected compositions, mainly belonging to the morphotropic and R-regions of the system (for example, the review [1]). The PZT system was studied in details [2–4]; the objects of study were monocrystals grown by the authors. However, in objects that are in different solid states, the piezoelectric, dielectric, and mechanical properties of solid solutions PZT may change significantly.

The methods of synthesis and the associated types and concentration of crystal lattice defects, mesostructural formations, and microstructural ordering have a significant effect. Thus, the real structure of the solid solution is described in the phase diagram of the system, which is more complex than the diagram presented in [4, 5]. It was found out [6, 7] that the rhombohedral (Rh) and tetragonal (T) regions in phase diagram of the system are not single-phase in the full sense of the word. They include structures with the same symmetry, but different cell parameters. And the rate of change of parameters with variations in the composition of such structures is different. Such structures were called phase states (PSs), the areas of coexistence of phase states (ACPSs) were defined. The detected periodicities in changes of the PSs and ACPSs, and, caused by this, periodic fluctuations in the electrophysical responses indicate that a change in the real structure of the solid solutions occurs in the system. Thus, with an increase of the titanium concentration in the crystal structure, oxygen vacancies are formed and accumulated. With increasing concentration, ordering and elimination of the planes of oxygen vacancies by crystallographic shift (CS) occur. The formation of local regions of the solid solutions of interstitial implantation in the crystallographic shear plane (CSP) takes place [8]. In this study the attention is drawn to the processes in the crystal structure of solid solutions obtained in the form of ceramics, to the processes occurring simultaneously at the nano-, meso- and microscopic levels of the structure of PZT system with different compositions.

19.1.1 Research Purpose

The objectives of this work: (i) to identify patterns of structure formation in solid solutions of PZT system, taking into account the defectiveness of their structure; (ii) to trace the influence of nanostructural changes in solid solutions on the meso- and microstructure of ceramics; (iii) to clarify the formation of dielectric, piezoelectric and ferroelastic properties in ceramics.

19.1.2 Research Scope

In this study, we consider the following frameworks of the problem:

(i) crystal structure of the $PbZr_{1-x}Ti_xO_3$ (PZT) solid solutions, phases and phase states;
(ii) mesoscopic scale defects in the structure of PZT solid solutions;
(iii) multifractal parameters of the grain structure (microstructure) of PZT solid solutions.

19.2 Research Method

19.2.1 Objects of the Study

The composition of the solid solutions studied corresponds to the formula $(1 - x)PbZrO_3$–$xPbTiO_3$ ($0.00 \leq x \leq 1.00$). Solid solutions were studied with a concentration step $\Delta x = 0.01$ in the intervals: $0.00 \leq x \leq 0.04$, $0.08 \leq x \leq 0.12$ and $0.30 < x < 0.36$; in the interval $0.04 < x < 0.06$ with a step $\Delta x = 0.0025$; in the interval $0.12 < x \leq 0.30$ with a step $\Delta x = 0.02$; in the interval $0.60 \leq x \leq 1.00$ with a step $\Delta x = 0.025$; in the intervals $0.36 \leq x \leq 0.42$ and $0.52 \leq x \leq 0.57$ with a step $\Delta x = 0.01$; in the interval $0.42 < x < 0.52$ with a step of 0.005. Samples were obtained by two-stage solid-phase synthesis at temperatures $T_1 = T_2 = 870$ °C, the durations of isothermal exposures $\tau_1 = \tau_2 = 7$ h, followed by conventional ceramic technology sintering at temperatures: $T_3 = 1220$–1240 °C (depending on the composition), $\tau_3 = 3$ h.

19.2.2 X-Ray Diffraction Studies

X-ray diffraction analysis (XRD) was performed by powder diffraction using a Dron-3 diffractometer (filtered $Co_{K\alpha}$-radiation, a Bragg-Brentano focusing scheme). The crushed objects were investigated, which made it possible to eliminate the influence of surface effects, stresses and textures arising during the preparation of ceramics. The perovskite cell parameters were calculated by the standard method [9]. The homogeneous deformation parameter, δ, characterizing the spontaneous deformation of oxides with the perovskite structure, was determined by the formula $\delta \approx \cos\alpha$ for the Rh-phase and $\delta \approx 2/3\ (c/a - 1)$ for the T-phase (c, a, α—parameters of the perovskite cell) [9]. The theoretical volume was calculated according to the formula [10]:

$$V_{\text{th}} = \left\{ \frac{n_{\text{Pb}}\sqrt{2}L_{\text{PbO}} + 2[n_{\text{Ti}}xL_{\text{TiO}} + n_{\text{Zr}}(1-x)L_{\text{ZrO}}]}{6} \right\}^3, \tag{19.1}$$

where L is the length of a non-stressed cation–oxygen bond, taking into account the coordination number of the cation in oxygen (for calculation of L, ionic radii according to Belov-Bokiyu [11] were used); n is the valence of cations.

The relative measurement errors of structural parameters have the following values: linear, $\delta a = \delta b = \delta c = \pm 0.05\%$; angular, $\delta\alpha = \pm 5\%$; volume, $\delta V = \pm 0.07\%$.

19.2.3 Microstructure Studies

The grain structure studies of ceramics for $0.00 < x < 0.80$ were carried out on an optical microscope Leica DMI5000M, with an increase from 305 to 1050. The visualization of the intercrystalline boundaries of ferroelectric ceramics was carried out by chemical etching. Etching times were selected for each material in the range from 0.5 to 10 min. A detailed study of the grain structures in the analyzed objects was carried out using the method of their multifractal parametrization [12]. During the study the black-and-white images of the objects surface were subjected to computer processing, as a result of which a mesh of grain boundaries of ceramics cleared of extraneous noise was detected. The $f(\alpha)$-spectra and spectra of the generalized dimensions D_q were analyzed for approximated black and white areas of microstructure regions images of the samples under study. Calculations were carried out on the cells that fall on the grain boundaries of the samples. These cells were assigned unit weight values. The spectra of generalized dimensions (Renyi dimensions) of the D_q and $f(\alpha)$-spectra were determined according to the standard interpretation of the multifractal formalism [12] as relations (19.2)–(19.5).

$\{\mu_i\}$ is the measure generated when equoring cells of the Euclidean space, covering the object studied, into N cells of size l.

$$\tau(q) = \lim_{l \to 0} \frac{\ln \sum_{i=1}^{N} \mu_i^q}{\ln l} \tag{19.2}$$

$$\alpha(q) = \frac{\mathrm{d}\tau}{\mathrm{d}q} \tag{19.3}$$

$$f(\alpha) = q\alpha - \tau \tag{19.4}$$

$$D_q = \frac{\tau}{q-1} \tag{19.5}$$

$$\sum_{i=1}^{N} \mu_i = 1 \tag{19.6}$$

Each cell, containing an element of the grain boundary, is assigned a weight value $\mu_i \neq 0$, so condition (19.6) is satisfied. The weight of a cell not containing the boundary $\mu_i = 0$. For parametrization we used the following parameters of canonical spectra [12] as the most informative: (I) fractal dimension, D_0, by definition it is related to the area of the grain boundary, and, according to our studies [13], to the degree of self-similarity of grain boundaries sections; (II) the "ordering" parameter $\Delta_\infty = D_1 - D_q$ for $q >> 1$ is the characteristic of the "width" of the multifractal spectrum of the structure studied. Here D_1 (the value of D_q with $q = 1$) is the value of the information dimension, determined by the formula:

$$D_1 = \lim_{l \to 0} \frac{\sum_{i=1}^{N} \mu_i \ln(\mu_i)}{\ln l} \tag{19.7}$$

as a result of uncovering the uncertainty in Formula (19.4) for $q \to 1$. The maxima of the "ordering" parameter, which, by the definition of the information dimension (D_1), is related to the entropy of the distribution of the grain boundary elements and the spatial correlation of the distribution of structure elements (D_∞), according to [12], correspond to the states with the most stable ceramic grain distributions of shape and size. In the calculations of D_q for $q >> 1$, the value of the parameter q was assumed equal to 40. The quantity $q = 40$ as $q >> 1$ was chosen to be optimal for calculations on the one hand, since the function D_q for a given value of q is already sufficient for the required accuracy, its asymptote, on the other hand, the number q in calculations acts as an exponent (19.1) and its increase leads to much more time and computational power in calculations; (III) the "homogeneity" parameter $f_\infty = f[\alpha(q)]$ for $q >> 1$ is an indicator of the character of the distribution of unit elements of the structure in Euclidean space embracing this structure. The minima of the "homogeneity" parameter correspond to the maximum values of microstrains in the crystal structure [14]. In the calculations of $f[\alpha(q)]$ for $q >> 1$, the value of the parameter q was also taken to be equal to 40. The parameters were determined with relative errors: $\delta D_q \pm 0.02\%$, $\delta\Delta\infty \pm 0.04\%$, $\delta f_\infty \pm 0.02\%$. For analysis, the average values of D_q, f_∞, Δ_∞ were used for 6–8 samples.

19.3 Results and Discussion

XRD data indicate that pure samples were obtained in all the studied concentration ranges of the system. Samples from different areas of the same sample and different samples of the same composition showed reproduction of their phase composition and density, which indicates a fairly high uniformity of ceramic objects.

19.3.1 Rhombic–Rhombohedral Phase Transition Region

The X-ray diffraction data show that solid solutions from the concentration region near to $PbZrO_3$, like pure $PbZrO_3$, possess rhombic (R) symmetry up to the value $x = 0.065$. Earlier it was reported about the boundary with $x = 0.057$ for single crystals [4]. Figure 19.1a shows the evolution of the diffraction pattern during the transition from rhombic (R) to the rhombohedral (Rh) phase. At $x = 0.040$, the lines correspond to the R symmetry of the cell. In solid solutions with $x = 0.045$, the intensity of the maxima of lines 240 and 004 (rhombic) already decreases significantly while their width increases. The single line 042 acquires asymmetry from the side of smaller angles θ. With a further increase of concentration x, there appears a maximum, which corresponds to the 111 reflection for the Rh-phase (indices of the Rh-phase refer to the perovskite axes). There is a splitting of the 240 line into two peaks, one of which remains the line 240 of the R-phase, and the second remains the line 200 of the emerging Rh-phase. At $x = 0.065$, traces of the R-phase lines are still visible. Thus, the morfotropic phase transition from R- to Rh-phase corresponds to $0.045 \leq x \leq 0.065$.

Figure 19.1b shows the dependences of the parameters of solid solutions crystalline cells at concentrations of $0.00 \leq x \leq 0.08$. Figure 19.2a shows the behavior of the multifractal parameters of the homogeneity of f_∞ and the ordering Δ_∞ of the grain structure of ceramics in the region of the morfotropic phase transition. Joint anomalies (min f_∞ and max Δ_∞) were observed, which are

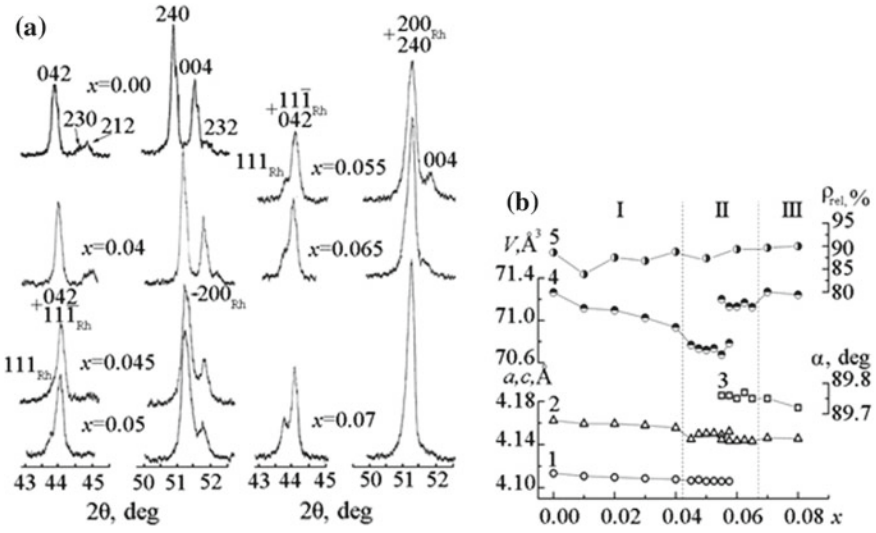

Fig. 19.1 **a** Fragments of diffractograms, g phase transition from rhombic to rhombohedral (Rh) phases of $PbZr_{1-x}Ti_xO_3$ solid solutions. **b** Crystalline cell parameters dependences 1—c, 2—a for R, 3—a for Rh, 4–cell volume V, 5–relative density $\rho_{rel}t$

characteristic of the phase transition regions in ceramic oxides of the perovskite structure. A decrease in f_∞, which is caused by an increase of mechanical stresses in the structure, stops, from the concentration $x > 0.040$. This corresponds to the appearance of nanoclusters of Rh-phase in the R-region. As the amount of Rh-phase regions increases, the stresses in the structure decrease. Mesoscopic inhomogeneity, reaches max at x close to 0.05 (max Δ_∞), and then decreases. Intercrystalline interaction becomes more homogeneous. Near the state with the maximum mechanical relaxation (at $x = 0.070$), during the parameters an anomaly is observed at $x \approx 0.060$ It may be caused by a sharp decrease in the number of residues of the R-phase and mesostructural rebuildings of the Rh-regions. The same effect can influence the emergence of new phase states of the Rh-phase, which will be described below.

19.3.2 Structure of the Solid Solutions of PZT Ceramics in Rhombohedral Region

PZT solid solutions at room temperature have Rh symmetry in the range of $0.07 \leq x \leq 0.36$. At the same time, diffractograms for different concentration ranges have differences (Fig. 19.3a). In some solid solutions ($0.065 < x \leq 0.20$, $0.22 < x \leq 0.24$, $0.26 < x \leq 0.28$, $0.30 < x \leq 0.34$, $0.35 < x \leq 0.36$),

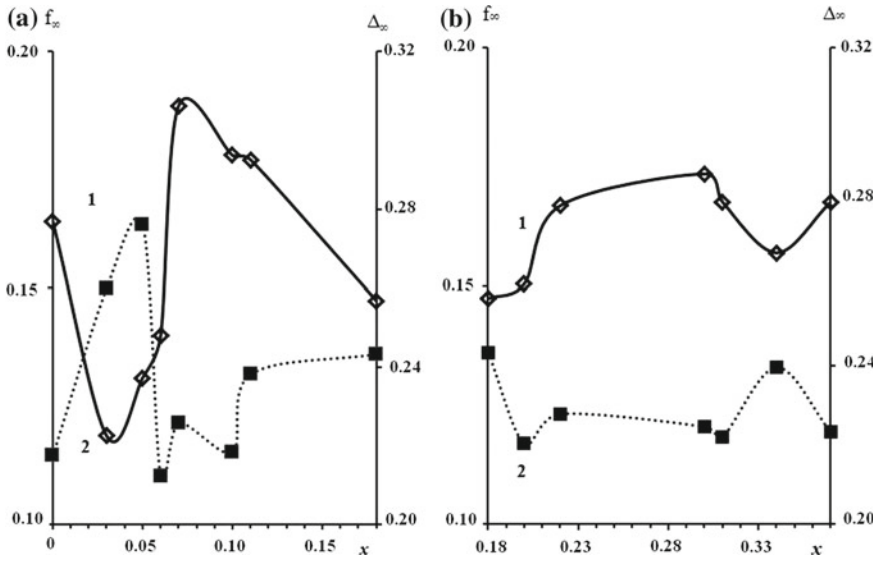

Fig. 19.2 Dependencies of the microstructure multifractal homogeneity parameters f_∞ (1) and the ordering parameter Δ_∞ (2) of the solid solutions $PbZr_{1-x}Ti_xO_3$ ceramics system on Ti-concentration in the intervals: **a** $0.0 < x < 0.18$, **b** $0.18 < x < 0.37$

multiplets with narrow sharp lines characteristic of rhombohedral cell distortion are observed. In other ranges ($0.20 < x \leq 0.22$, $0.24 < x \leq 0.26$, $0.28 < x \leq 0.30$, $0.34 < x \leq 0.35$), the splitting of single multiplet lines is recorded. This effect was also observed in [15] on single crystals. The analysis in [15] showed that double maxima cannot be associated with twinning or possible misorientations of 180° domains. The nature of the splitting and an increase in the width of the reflections in Fig. 19.3a shows that in compositions with $x = 0.22$, 0.30, 0.35, another phase arises with Rh symmetry and close values of the cell parameters. Thus, it can be concluded that within the rhombohedral region of the PZT system, periodic changes in phase states are observed. As the composition in the Rh region changes sequentially, the phase state of the system changes discretely. There are already, as was shown previously in [6, 7], five different phase states and four areas of coexistence of phase states (Fig. 19.3b).

The anomalies of the multifractal parameters observed in the Rh region (Fig. 19.2) show that transitions from one phase state to another have a significant effect on the microstructure of the ceramic samples. To a greater extent, mesostructural heterogeneities that cause "pre-transition" changes in multifractal parameters are manifested in regions with a single phase state ($0.31 < x \leq 0.34$,

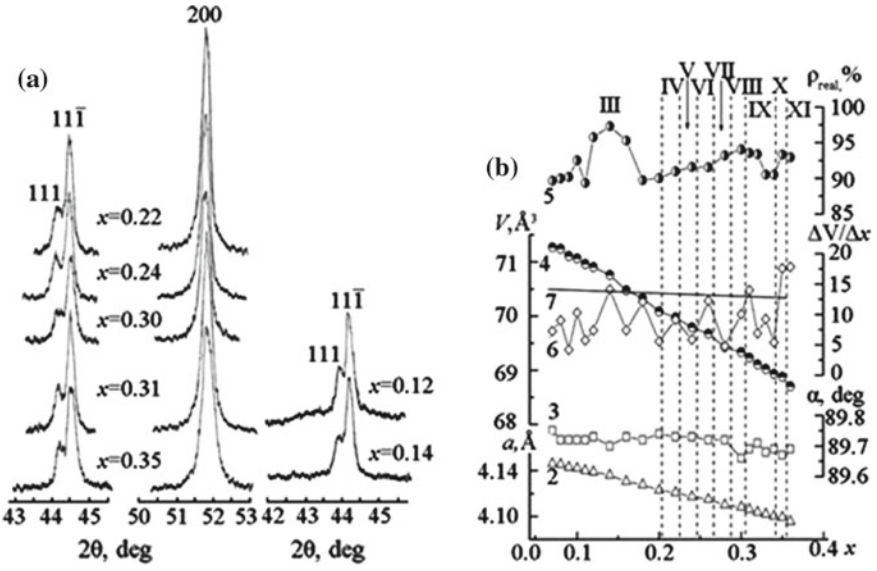

Fig. 19.3 **a** Fragments of diffraction patterns for solid solutions $PbZr_{1-x}Ti_xO_3$ in the Rh-phase: $x = 0.12$, 0.14, 0.24, 0.31—solid solutions in one phase state; $x = 0.22$, 0.30, 0.35—solid solutions from the areas of coexistence of phase states; **b** 2—structural parameter a, 3—angle α, 4—cell volume V, 5—relative density ρ_{rel}, 6—modulus of the rate of change of the experimental $|\Delta V_{exp}/\Delta x|$ and 7—theoretical $|\Delta V_{th}/\Delta x|$ volumes, in the range of $0.07 \leq x \leq 0.36$. The areas marked by Roman numerals correspond to [6, 7]: III—Rh_1 ($0.065 < x \leq 0.20$), IV—$Rh_1 + Rh_2$ ($0.20 < x \leq 0.22$), V—Rh_2 ($0.22 < x \leq 0.24$), VI—$Rh_2 + Rh_3$ ($0.24 < x \leq 0.26$), VII—Rh_3 ($0.26 < x \leq 0.28$), VIII—$Rh_3 + Rh_4$ ($0.28 < x \leq 0.30$), IX—Rh_4 ($0.30 < x \leq 0.34$)

$0.35 < x \leq 0.39$), while relative relaxation occurs in the areas of co-existence of phase states.

The intensity of the recorded microstructural responses is up to 30–50% of their intensity during phase transitions between phases, at which the symmetry of distortion of the perovskite cell changes. Attention is drawn to the absence in these regions of areas of constancy or a slight change in the multifractal parameters of the microstructure. This means that, not only the heterogeneities of the crystal structure, but also the mesoscopic inhomogeneities in crystallites arise almost constantly far from the points of the phase state change.

Figure 19.3b shows that the angle α is almost constant throughout the all concentration range of existence of the Rh-phase and decreases slightly at $x = 0.08$, 0.14, 0.30, and behaves unstably in the range of $0.30 < x \leq 0.36$. According to [16], the angle α decreases monotonically with increasing x in the interval $0.13 \leq x \leq 0.40$. Our data indicate that α decreases like a step only at certain concentrations of Ti. The density ρ_{rel} has three maxima corresponding the values of x, when jumps of α occur. Virtually the entire dependence $|\Delta V_{exp}/\Delta x|$ passes lower than $|\Delta V_{th}/\Delta x|$.

This means that the decrease in the V_{exp} cell is slower than it should be when replacing the larger Zr^{4+} ion with Ti^{4+}. On the $|\Delta V_{exp}/\Delta x|$ dependence on x, the maxima are noted at $x = 0.14$, 0.18, 0.22, 0.26, 0.31, 0.35, 0.36, in four of them, with $x = 0.14$, 0.31, 0.35, 0.36, $|\Delta V_{exp}/\Delta x|$ exceeds $|\Delta V_{th}/\Delta x|$. At the same x (Fig. 19.3b), there are jumps of the angle α and maxima of ρ_{rel}. The minima with proximity to the invar effect are observed at $x = 0.09$, 0.11, 0.20, 0.24, 0.28, 0.34. The presence of plots with invar effect indicates that, at certain concentration ranges, the structure ceases to be stable, that is contributes to its easy change [6, 7]. Invar effect in the range of $0.09 \leq x \leq 0.10$ is most likely due to the disappearance of R-phase clusters, and in the range of $0.11 \leq x \leq 0.12$ with the onset of the formation of a new phase. The structure changes affect the meso- and microstructural levels, which is reflected by anomalies on the multifractal parameters dependencies in this concentration x region. Against the background of the general trend towards an increase in stresses in crystallites (a monotonic decrease in the parameter of homogeneity f_∞ at $0.07 < x \leq 0.18$), phase changes occurring in the interval $0.10 \leq x \leq 0.12$ lead to their local stabilization. The growth of parameter Δ_∞ marks the weakening of multipoint correlations in the system of grain boundaries of the ceramic object, which also indicates a complication of the phase composition of the solid solution. The parameter Δ_∞ varies with significantly smaller amplitude than with the previous morfotropic phase transition and subsequent changes in the phase states therefore the effect of changes in the crystal structure on the microstructure level is much weaker. This indicates a small value, spatial localization, and weak interaction of altered regions. The line (111) on the X-ray pattern for the solid solution with $x = 0.12$ (Fig. 19.3a) has a halo at its base, which is a sign of the emergence of a new phase [16]. At this stage, the new phase represents only the packaging of certain planes, which transform into a three-dimensional structure with further changes in the composition of the solid solution. In the case of solid solution with $x = 0.14$ the halo is already absent at the

same line. In [17], during the study of the Rh region of the PZT system by transmission electron microscopy, the authors observed superstructural reflections of the types: ½ {*hkl*} and ½ {*hk*0} in the range of $0.06 \leq x < 0.12$. Satellites were recorded at ½ {*hk*0}. The authors of [17] showed that the occurrence of superstructure reflections of type ½ {*hk*0}, caused by anti-parallel displacements of lead ions, characteristic of $PbZrO_3$, and the satellites are associated with periodic antiphase boundaries. Superstructure reflections of type ½ {*hk*0} disappear at $x > 0.12$, and only superstructure reflections of type ½ {*hkl*} remain, which are associated with the antiphase slope of the oxygen octahedra. Our results are consistent with the data of [17]. In the first wide single-phase region, structural changes occur at the clusters level of the vanishing and nascent phases. They are not reflected in the diffraction patterns by the line splitting, but affect the volume of the unit cell. Crystal structure transformations lead to the formation of local mesostructural anomalies in crystallites, which are displayed by the multifractal parameters of the system of grain boundary. The processes of more significant changes in the microstructure, recorded at $x > 0.18$, for example, in the interval $0.18 \leq x \leq 0.20$ (Fig. 19.4b), significally different from the anomalies for $x \approx 0.6$ or $x \approx 0.11$. There are regions of Δ_∞ decrease, which indicates an increase in many-particle correlations. Significant amplitudes changes of Δ_∞ and f_∞ parameters show that mesostructural transformations occur in the volume occupied by the main phase. The regions of smooth changes in multifractal parameters seem to reflect the coexistence of nanoclusters of different phase states and beyond the area of coexistance of phase states. The areas of coexistence of phase states are located in the concentration intervals following minima $|\Delta V_{exp}/\Delta x|$, indicating structural changes starting from the concentration $x > 0.20$. In the concentration intervals following the maxima $|\Delta V_{exp}/\Delta x|$, the phase states regions are located. In those cases, when $|\Delta V_{exp}/\Delta x|$ is close to $|\Delta V_{th}/\Delta x|$, V_{exp} decreases with increasing x in accordance with the decrease in the average ionic radius of cation B. When $|\Delta V_{exp}/\Delta x|$ exceeds $|\Delta V_{th}/\Delta x|$, the structure sealing mechanism associated with the crystallographic shear plane. In oxides, with ions of variable valence, the compaction takes place according to the crystallographic shear plane [18]. An exception is the (110) type planes—antiphase boundaries that were found in the $PbZrO_3$ structure in [19]. At $x = 0.14$, the density of ceramics is the greatest (Fig. 19.3b), and $|\Delta V_{exp}/\Delta x|$ exceeds $|\Delta V_{th}/\Delta x|$. This suggests that the new phase, arising at $x \geq 0.11$, contains crystallographic shear planes that are different from the antiphase boundaries and has a real structure that differs from the Rh-phase. As shown in [18], in oxides containing cations with variable valency, the direction of cations and oxygen displacement is determined by the position of the crystallographic shear plane in the structure. Thus, the ion displacements in the emerging phase must differ from the displacements characteristic of the main rhombohedral crystal structure. In [20], when the structure of the solid solution was refined from the Rh region by neutron diffraction, it was established that the displacements of Pb^{2+} ions in the [111] direction and in the [100] directions are characteristic for Rh symmetry. The authors of [20] proposed to consider such states as those preceded by the appearance of the T-phase. A similar assumption concerning the existence of locally ordered regions

with a different symmetry in the Rh-phase was made for the solid solutions of the $PbZr_{1-x}Ti_xO_3$ system with $x = 0.04, 0.14, 0.23$ [21]. In view of the foregoing, it can be concluded that in the interval $x = 0.11$–0.12, already far from the region of the Rh–T morphotropic phase transition, nucleation of T-phase clusters occurs. The maximum $|\Delta V_{exp}/\Delta x|$, observed at $x = 0.31$, corresponds to the concentration of Ti-ions, at which the displacement values of the cations vary sharply according to [21]. At $x = 0.35$, 0.36 superstructural reflections of the type ½ $\{hkl\}$ disappear, which were recorded in [17]. Thus, in the region $x = 0.36$, there is a phase transition R3c → R3m, which is confirmed by other researchers [4]. The periodicity in the formation of phases and phase states can be explained by the accumulation of oxygen vacancies with an increase in the concentration of titanium, the ion with variable valence, their ordering and elimination at crystallographic shear. Crystallographic shear occurs at such values of x, when $|\Delta V_{exp}/\Delta x|$ becomes larger than $|\Delta V_{th}/\Delta x|$, that is, at $x = 0.14, 0.31, 0.35, 0.36$. In the same solid solution, the highest relative density is observed (Fig. 19.3b). Thus, the real structure of the PZT system solid solution in the Rh region includes nanoclusters of phases and various phase states, interphase and domain boundaries, as well as extended defects of the crystal structure of the crystallographic shear plane type. Changes in the size and position of the crystallographic shear plane with Ti concentration, lead to a change in the crystal structure, meso- and microstructural characteristics of solid solutions.

19.3.3 Structural Features of Tetragonal Solid Solutions Ceramics

The XRD data of the PZT system solid solutions from T region ($0.58 \leq x \leq 1.0$, Rh-phase) show that single-phase regions and regions of coexistence of phase states can be distinguished (Fig. 19.4a). Four regions with different phase states are located in the ranges: $0.58 \leq x \leq 0.65$, $0.725 < x \leq 0.75$, $0.775 < x \leq 0.925$, $0.95 < x \leq 1.0$. The other ranges: $0.65 < x \leq 0.725$, $0.75 < x \leq 0.775$, $0.925 < x \leq 0.95$ are areas of coexistence of phase states. Figure 19.4b shows dependencies of the parameter a, angle α, volume cell V, modulus of the rate of change $|\Delta V/\Delta x|$ for experimental and theoretical volumes, the relative density of solid solutions, ρ_{rel}, on x ($0.58 \leq x \leq 1.0$). Oscillations of $|\Delta V_{exp}/\Delta x|$ in the T-area is not as large as in Rh. The maxima at $x = 0.60$ and 0.95 are followed by phase states sections, and the minima at $x = 0.65$ and 0.75 are followed the regions of coexistence of phase states. The signs of a short-range order appear with an increase of x: diffuse maxima are shown by arrows on the wings of the lines in Fig. 19.4a, the width and position of the maxima change with increasing x. Thus, the principle of periodicity of phase formation processes, observed in the Rh region, is also preserved for solid solutions in the T-phase.

The f_∞ parameter of microstructure decreases in the phase state regions, indicating an increase in mechanical stresses (Fig. 19.5b). The overall multifractal trend

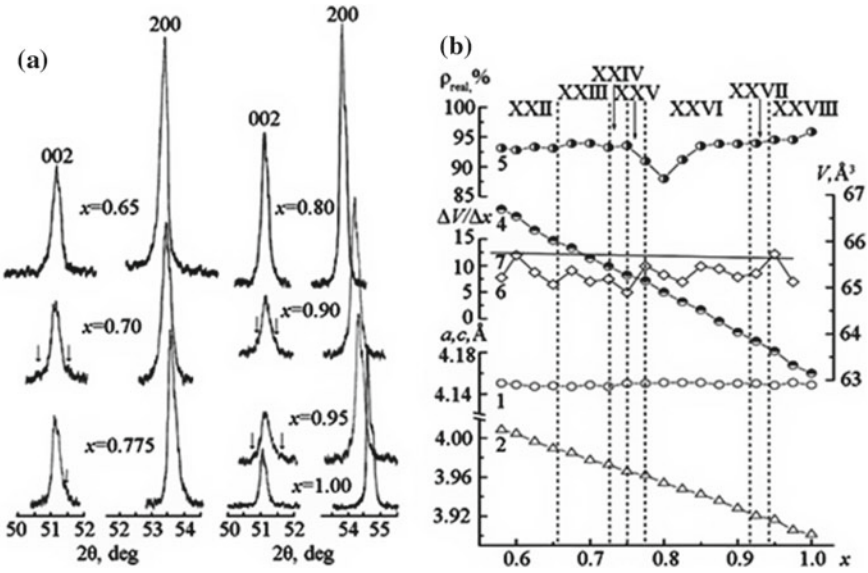

Fig. 19.4 **a** Fragments of X-ray diffractograms of $PbZr_{1-x}Ti_xO_3$ solid solutions system in the tetragonal phase: x = 0.65, 0.80, 0.90—single phase solid solutions; x = 0.70, 0.775, 0.95—solid solutions from the areas of coexistence of phase states; **b** dependencies of structural parameters, modulus of the rate of decrease of the experimental and theoretical volumes $|\Delta V/\Delta x|$, relative density ρ_{rel}, on x, where $0.58 \leq x \leq 1.00$: 1—c, 2—a, 4—V, 5—ρ_{rel}, 6—$\Delta V_{exp}/\Delta x$, 7—$\Delta V_{th}/\Delta x$. The areas designated by the Roman figures correspond to phase states and the areas of coexistence of phase states according [6, 7]: XXII—T_2 ($0.515 < x \leq 0.65$); XXIII—$T_2 + T_3$ ($0.65 < x \leq 0.725$); XXIV—T_3 ($0.725 < x \leq 0.75$); XXV—$T_3 + T_4$ ($0.75 < x \leq 0.775$); XXVI—T_4 ($0.775 < x \leq 0.925$); XXVII—$T_4 + T_5$ ($0.925 < x \leq 0.95$); XXVIII—T_5 ($0.95 < x \leq 1.00$)

for the microstructure of ceramics in the T-phase with increasing Ti content in solid solutions is the decrease in the number of multipoint correlations in the system, which reflects an increase in Δ_∞. Thus, the mesostructure of solid solutions in the Rh and T regions is significantly different. The relatively weak response of Δ_∞ is observed in the areas of change in mechanical stresses after shift the solid solutions to the right of the morphotropic region which is clearly marked by f_∞ maxima (Fig. 19.5a). This means that mechanical stresses are concentrated within small volumes of matter, the interaction between which weakens. Thus, significant changes occur in the T region in the defective subsystem of the object. They can be associated with a change in the number of arising crystallographic shear planes and their role as a mechanical stress concentrator in the system. In the areas of coexistence of phase states this role can be fulfilled by a part of coexisting clusters with different cell parameters or symmetry. The constancy of the parameter c for the entire concentration range is a feature of the cell of solid solutions from the T region of the system. We showed in [22] that $PbTiO_3$ is an autoisomorphic substance (internal solid solution), in which 2–3% of ions can be placed in elongated oxygen

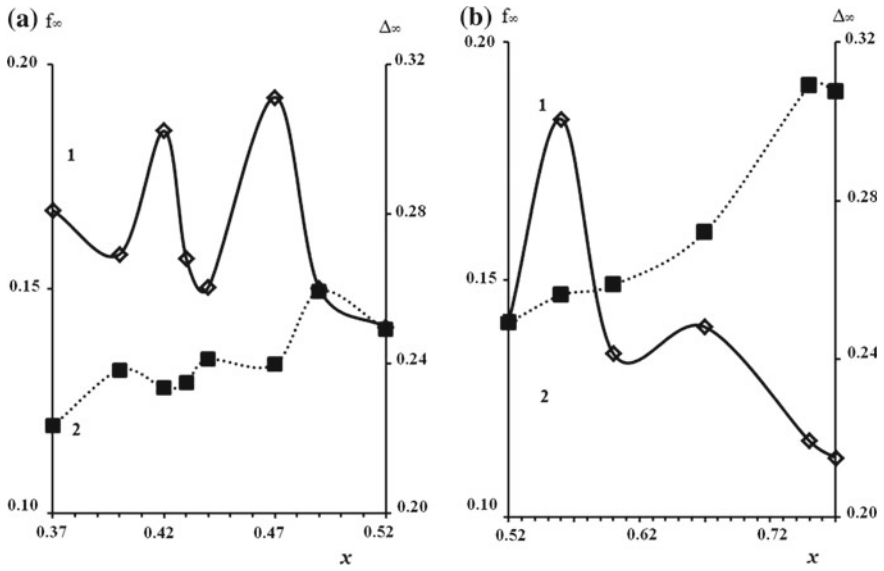

Fig. 19.5 Changes in multifractal homogeneity, f_{∞} (1) and ordering, Δ_{∞} (2) parameters of the microstructure of the $PbZr_{1-x}Ti_xO_3$ solid solutions ceramics with increasing Ti concentration in the ranges: **a** $0.37 \leq x \leq 0.52$, **b** $0.52 \leq x \leq 0{,}77$

octahedra along the plane. These planar defects were experimentally detected in $PbTiO_3$ in [19, 23]. The large size of Pb^{2+} ions causes the appearance of tensile stresses and an increase in the deformation of oxygen octahedra in the region of the crystallographic shear plane. The Pb^{2+} ions are displaced from ideal positions in the polar direction to the maximum possible value $\Delta z = 0.47$ Å in the result of the correlation. This explains both the large value of the *c*/*a* ratio and the constancy of the parameter *c*, regardless of the ionic radius of the *B*-cation. A solid solution with $x = 0.80$, in which the relative density is only 88% (Fig. 19.4b) attracts special attention. All attempts to vary the technological regimes for lifting ρ_{rel} did not lead to success.

The structure of this solid solution is very stable, which indicates the minimum number of crystallographic shear planes along which the compaction of ceramics can occur. Diffuse scattering is minimal at a given concentration in the region of the wings of the diffraction lines (Fig. 19.4a). V_{exp} and V_{th} become equal at $x = 0.83$ (see Fig. 19.4b). However, approximately 2–3% of Pb^{2+} ions can displace Ti^{4+} (Zr^{4+}) ions from the *B*-positions. Therefore, a solid solution with $x = 0.80$ actually has the least defective structure. Planar defects attract aliovalent dissolved ions. The role of these ions is performed by Pb^{2+}, Pb^{4+} [24] and Ti^{3+}, occupying the *B*-position in the cell along crystallographic shear planes, and leading to modulation of the structure, as can be seen from the appearance of satellite diffraction lines near the main ones (Fig. 19.4a). Since no modulation of the structure is observed at $x = 0.80$, it can be assumed that the amount of crystallographic shear planes in this

solid solution is minimized. Consequently, the values of the displacements of cations and oxygen associated with them should also become minimal [18]. This conclusion is confirmed by the results of studies [25], where it was found from the Raman spectra that the frequency of the soft mode E (1TO) decreases with decreasing x in the range of $0.75 < x < 1.00$ to "vanishingly small" values with a speed greater than temperature ferroelectric phase transition.

In the region of the T-phase, clusters with a symmetry different from the symmetry of the average crystal structure (T) at a certain concentration of Zr can be expected, by analogy with the Rh region. The existence of the Rh- and T-phases in $PbZr_{0.35}Ti_{0.65}O_3$ thin films was discovered by the authors [26]. The behavior of multifractal parameters (Fig. 19.5b) and the results of X-ray diffraction studies allow us to conclude that in the solid solution the nuclei of the Rh-phase appear in the interval $0.675 < x < 0.80$.

19.3.4 *Effect of Structural Features on the Formation of Properties of PZT Solid Solutions*

One of the main characteristics of the perovskite-type solid solutions structure is the characteristic of elongation of the reduced perovskite cell along the polar axis—the uniform deformation parameter δ [9]. It gives the possibility of an objective comparison of solid solutions with different symmetries. Stable correlations of δ with the dielectric, piezoelectric and ferroelastic parameters of the materials make it possible to explain and predict macroscopic responses of ferroelectric solid solutions systems. Due to a decrease in the mobility of the domain boundaries, $\varepsilon_{33}^{\mathrm{T}}/\varepsilon_0$, $\tan\delta$ and mechanical losses of $1/Q_{\mathrm{M}}$ should decrease with increasing δ. Accordingly, Q_{M}, Y_{11}^{E} and the sound velocity, V_1^{E}, should increase. There should also be a decrease in K_{p}, and a piezomodule, $|d_{31}|$, since $|d_{31}| \sim K_{\mathrm{p}}\sqrt{\varepsilon_{33}^{T}}$. In the T-phase, we observe just such trends in parameter changes. However, changes that are generally consistent with the change in δ have an important feature in the T-phase: a stepwise increase in δ and a decrease in $\varepsilon_{33}^{\mathrm{T}}/\varepsilon_0$ with the presence of invariance sites is observed not only, when the phase state changes, but in areas of coexistence of phase states (area XXIII), and even within a single phase state (area XXII). This indicates the existence of intraphase transformations, probably caused by changes in the defect subsystem of solid solutions. Mechanical stresses in ceramics of solid solutions from region XXII are so high that intraphase mesostructural changes affect the microstructure as much as morphotropic phase transitions cause a global restructuring of the entire structure of solid solutions. The changes in f_∞ (Fig. 19.5b) in the single-phase region reach the value observed only in the regions of phase transitions. The instability of the defect subsystem is manifested in the extreme instability of the profiles of a number of main diffraction lines. The crystalline lattice of solid solutions at high concentrations of Ti^{4+} becomes so sensitive to the appearance of additional vacancies that even X-ray

irradiation, which introduces some small amount of radiation defects, destabilizes the lattice defect system. The symbiotic behavior of $\varepsilon_{33}^{T}/\varepsilon_0$ and δ, the strong irregularity of the concentration dependences of the parameters $\varepsilon_{33}^{T}/\varepsilon_0$, Q_M, Y_{11}^{E} (without ranges of their constancy) are characteristic of solid solutions from the Rh region. The values of δ in the Rh region are small and the behavior of the electrophysical properties is determined by the degree of domain reorientations, other than 180°, occurring during the ceramics polarization.

19.4 Conclusion

A complete x–T phase diagram (for T = 25 °C) of the $PbZr_{1-x}Ti_xO_3$ system for $0.00 \leq x \leq 1.00$, and a multifractal scan of the ceramics microstructure for $0.00 \leq x \leq 0.77$ were obtained by X-ray diffraction studies and the multifractal parameterization of flat cross-sections of ceramics grain boundaries. It is revealed that the states with local loss of stability of the main phase consistently occur in $PbZr_{1-x}Ti_xO_3$ solid solutions when the composition changes. In this case, in the matrix phase, nanoscale cluster structures are formed—these are either nuclei of new phase states that retain the original symmetry, or nuclei of new phases. Clusters of new phases appear in solid solutions, significantly (by 20 molar % and more) remote from the regions of morphotropic phase transitions. The evolution of clusters of new phases and phase states affects the state of the mesostructure (configuration of the fields of defects inside the crystallites and at their boundaries) with changes in the composition. Mesostructural changes are directly recorded by X-ray diffraction (satellite lines) and affect the state of the microstructure, leading to changes in its multifractal homogeneity and ordering. The changes in the piezoelectric properties of PZT solid solutions follow the structure changes at the nano-, meso-, microscale levels, they are non-monotonic, spasmodic. The priority contribution to the formation of the system properties in the T region is due to the spontaneous deformation of the crystal cell, while in the Rh region, it is caused not by 180° domain reorientations.

Acknowledgements The work was supported by the Ministry of Education and Science of the Russian Federation: projects Nos. 3.6371.2017/8.9 (the basic part of the state task), Grant of Russian Foundation for Basic Research No. 18-32-00552. The equipment of the Center of Research Institute of Physics SFedU was used.

References

1. B. Noheda, Current Opinion Solid State. Mater. Sci. **6**, 27 (2002)
2. E.G. Fesenko, V.V. Eremkin, V.G. Smotrakov, Phys. Solid State **28**, 324 (1986). (in Russian)
3. E.G. Fesenko, V.V. Eremkin, V.G. Smotrakov, S.G. Shmalko, A.T. Kozakov, Crystallogr. Rep. **32**, 1049 (1987). (in Russian)

4. V.V. Eremkin, V.G. Smotrakov, E.G. Fesenko, Ferroelectrics **110**, 137 (1990)
5. B. Jaffe, W. Cook, G. Jaffe, *Piezoelectric Ceramics* (World Publishing House, Moscow, 1974), p. 288. (in Russian)
6. L.A. Reznichenko, L.A. Shilkina, O.N. Razumovskaya, E.A. Yaroslavtseva, S.I. Dudkina, O. A. Demchenko, A.A. Esis, I.N. Andrushina, YuI Yurasov, Phys. State **50**, 1469 (2008)
7. L.A. Reznichenko, L.A. Shilkina, O.N. Razumovskaya, E.A. Yaroslavtseva, S.I. Dudkina, O. A. Demchenko, YuI Yurasov, A.A. Esis, I.N. Andrushina, Phys. Solid State **51**, 958 (2009)
8. A.H. Meitzler, Ferroelectrics **11**, 503 (1975)
9. E.G. Fesenko. *Perovskite Family and Ferroelectricity* (Atomizdat, Moscow, 1972), p. 248. (in Russian)
10. N.V. Dergunova, V.P. Sakhnenko, E.G. Fesenko, Crystallogr. Rep. **23**, 94 (1978)
11. G.B. Bokiy. *Introduction in Crystallochemistry* (Moscow State University Press, Moscow, 1954), p. 490. (in Russian)
12. G.V. Vstovsky, A.G. Kolmakov, I.Z. Bunin. *Introduction in Multi-Fractal Parametrization of Material Structures* (NITs "Regul. Khaot. Din.," Izhevsk, 2001), p. 116. (in Russian)
13. V.V. Titov, S.V. Titov, L.A. Reznichenko, O.N. Razumovskaya, L.A. Shilkina, Bull. Russ. Acad. Sci. Phys **69**(7), 1173 (2005)
14. V.V. Titov, S.V. Titov, L.A. Reznichenko, Phys. Mesomech. Spec. **7**(1), 275 (2004). (in Russian)
15. V.V. Eryomkin, V.G. Smotrakov, E.S. Tsihotsky, V.A. Aleshin, E.G. Fesenko, Inorg. Mater. **23**, 284 (1987)
16. S.V. Titov, L.A. Shilkina, L.A. Reznichenko, S.I. Dudkina, O.N. Razumovskaya, S.I. Shevtsova, E.M. Kuznetsova, Tech. Phys. Lett. **26**(18), 9 (2000)
17. J. Ricote, D.L. Corcer, R.W. Whatmore, S.A. Impey, A.M. Glazer, J. Dec, K. Roleder, J. Phys.: Cond. Matter. **10**, 1767 (1998)
18. Y.D. Tretyakov. *Chemistry of Non-stoichiometric Oxides* (Moscow State University Press, Moscow, 1974), p. 364
19. A.A. Dobrikov, O.V. Presnyakova, Inorg. Mater. **17**, 2239 (1981)
20. D.L. Corcer, A.M. Glazer, R.W. Whatmore, A. Stallard, F.J. Fauth, J. Phys.: Cond. Matter. **10**, 6251 (1998)
21. B. Noheda, J.A. Gonzalo, M. Hagen, J. Phys.: Cond. Matter. **11**, 3959 (1999)
22. S.V. Titov, L.A. Shilkina, O.N. Razumovskaya, L.A. Reznichenko, V.G. Vlasenko, A.T. Shuvaev, S.I. Dudkina, A.N. Klevtsov, Inorg. Mater. **37**, 718 (2001)
23. A.A. Dobrikov, O.V. Presnyakova, V.I. Zaitsev, V.V. Prisedskii, G.F. Panko, Kristall. Technik. **15**(2), 207 (1980)
24. K. Sato, T. Miyanaga, S. Ikeda, D. Diop, Phys. Scr. **115**, 359 (2005)
25. Gerald Burns, Bruce A. Scott, Phys. Rev. Lett. **25**(17), 1191 (1970)
26. Maxim B. Kelman, Paul C. Mclntyre, Bryan C. Gruverman, J. Appl. Phys. **94**(8), 5210 (2003)

Chapter 20
Features of the Structural Model of the Low-Temperature Phase of Lead Magnesium Niobate—Relaxor Ferroelectric

Alla R. Lebedinskaya and Nonna G. Kasparova

Abstract In this work, we discuss a model of the behavior of the crystal lattice in lead magnoniobate (PMN) crystals, beeing the classical ferroelectric relaxor, according to X-ray diffraction at temperatures of 103, 183 and 203 K. We have analyzed changes in the electron density in different cross-sections using difference synthesis with a temperature change below the phase transition temperature (T_m = 240 K). The obtained results of atomic displacements in PMN at temperatures below the phase transition temperature in this method of analysis are explained. The results are explained, if it is assumed that the deviations from 180° of the angles between the Mg/Nb–O–Mg/Nb–O bonds exist and because of the occurrence of some rotation of the chains Mg/Nb–O–Mg/Nb–O relative to their positions in an ideal cubic structure. The corresponding changes in the positions of the atoms must lead to some distortion of the oxygen octahedra in the chain, owing to the difference in the lengths of the interatomic Mg–O and Nb–O bonds forming at the apices of the octahedra. The maps of the electron density cross-sections and the diagrams of its distribution along the bonds in the PMN reveal changes in the displacements of atoms with decreasing temperature, and a correlation is observed in the directions of these displacements. The possible structural models of the low-temperature PMN contingency corresponding to the obtained electron density distributions are discussed in this work.

20.1 Introduction

The discovery and study of innovative functional materials with special electrical and magnetic properties that form today the technological base of modern micro- and optoelectronics is one of the rapidly developing areas of condensed matter physics [1–3]. The emergence and development of modern experimental and

A. R. Lebedinskaya (✉) · N. G. Kasparova
Academy of Architecture and Art, Southern Federal University, Rostov-on-Don, Russia
e-mail: lebed1989@rambler.ru

I. A. Parinov et al. (eds.), *Advanced Materials*, Springer Proceedings in Physics 224, https://doi.org/10.1007/978-3-030-19894-7_20

computational research methods provide new opportunities for modeling their atomic structure, the directed formation of the necessary physical properties and their changes under the influence of temperature, electric and magnetic fields [4–6].

In recent years, partially disordered mixed perovskite-like materials have attracted increasing attention, in which two types of mesoscopic short-range order are observed: (i) compositional, associated with self-organized chemical ordering, and (ii) structural, associated with ionic displacements and arising, in particular, during phase transitions in such materials [7–9].

Relaxors-ferroelectrics were discovered more than half a century ago [1, 2]. Most relaxors are mixed cubic perovskite-like crystals, the specific properties of which are due to the structural disordering observed in them [7–9]. Lead magnoniobate $PbMg_{1/3}Nb_{2/3}O_3$ (PMN) is often considered as a model object for studying the properties of relaxors. Today, the microscopic mechanism of the processes occurring in the above systems, the influence of external conditions (temperature, external field), has not been fully studied and understood, which certainly makes it difficult to understand the physical properties of heterogeneous materials and prevents their wide practical application [10–12].

20.1.1 Research Purpose

The purpose of this work was to determine the structural features in lead magnoniobate at temperatures below the ferroelectric phase transition using X-ray structural data and to construct electron density maps at low temperatures.

20.1.2 Research Objects

Lead magnoniobate (PMN) crystals, which are promising technological materials, were taken as the object of study. In PMN the non-isovalent Mg^{2+} and Nb^{5+} ions with probabilities 1/3 and 2/3 are respectively distributed in crystallographically equivalent positions of the *B*-sublattice at the center of the oxygen octahedron, and the positions of the *A*-sublattice at the vertices of the cubic cell are occupied by Pb^{2+} ions. Currently, there is extensive experimental results related to the study of this and similar compounds, but the microscopic nature of the low-temperature phase is still the subject of wide discussion.

20.2 Research Method

20.2.1 Characteristics of Object, Subject and Method of Research

The studies were carried out on three PMN single crystals in the form of a parallelepiped with dimensions of $1.1 \times 0.6 \times 0.5$ mm^3 (283, 183, 103 K), $0.5 \times 0.6 \times 0.5$ mm^3 (283, 203 K), $0.3 \times 0.2 \times 0.1$ mm^3 (283 K), respectively. To eliminate the effect of machining on the structure of PMN crystals, they were not prepared in a spherical or cylindrical shape.

The subject of research in the work was the integral intensity of the Bragg reflections, the structural factor, the atomic scattering function, the distribution maps of the electron density of the object of study at room temperature and three low temperatures of 203, 183, 103 K.

The intensity of the Bragg reflections of PMN was measured on a CAD-4 automatic diffractometer (Enraf Nonius) using MoK_α radiation ($\sin\theta/\lambda < 1.01$ Å^{-1}) and graphite monochromator. In all cases, the parameters of the unit cell were determined by the least squares method using a series of 24 reflexes. This allowed us to compare the values of the parameters of the PMN cubic cell for the three investigated crystals at room temperature ("Round Robin"). The maximum error in determining the parameter of the unit cell was $\Delta a = 0.007$ Å. Modules of experimental values of structural amplitudes $|F(hkl)_{exp}|$ was determined after the usual consideration of the polarization factors, Lorentz and the absorption factor.

The measurements were carried out at temperatures of 283, 203, 183, 103 K, and the accuracy of the temperature determination was ±1 K. The full experimental conditions and the procedure for processing the results obtained were previously described in detail in [13].

20.2.2 Construction of Electron Density Maps

Experimental studies of the distribution of electron densities in crystals according to X-ray and neutron diffraction measurements have expanded significantly in recent years [14–17]. This is facilitated, firstly, by the fact that the obtained maps of the distribution of electron densities in crystals make it possible not only to judge the nature of the bond qualitatively, but also to quantify the physical properties of materials.

From classical structural analysis, it is known that

$$F(hkl) = \sum_{j=1}^{N} f_j \cdot e^{i2\pi\left(hx_j + ky_j + lz_j\right)}, \quad (1)$$

where f_j is the atomic scattering amplitude, and

$$F(hkl) = \int_{V_0} \rho(xyz) \cdot e^{i2\pi\left(hx_j + ky_j + lz_j\right)} dV, \tag{2}$$

where V_0 is the unit cell volume.

From the last expression, it follows that the electron density function can be represented as follows

$$\rho(xyz) = \frac{1}{V} \sum_h \sum_k \sum_l F(hkl) \cdot e^{-i2\pi\left(hx_j + ky_j + lz_j\right)}. \tag{3}$$

Using the obtained electron density maps, one can judge the distortion of the distribution of electrons, mainly valence, with respect to spherical symmetry during the formation of a chemical bond in a crystal. Directly from the experiment, we obtained reflection arrays containing the indices h, k, l, the values of the structural amplitudes $F(hkl)$ at room temperature 283 K and three low temperatures 183, 203, 103 K. The electron density (3) is dynamic, because it includes the effect of thermal movement. For infinite summation limits (idealized case), the function $\rho(xyz)$ is constant and normalized to the number of electrons in the cell. In the theory of the ground state in a crystal [14, 15], it was shown that such electron density satisfies the laws of quantum mechanics. The problem of synthesizing the electron density $\rho(xyz)$ according to X-ray diffraction data is reduced either to an approximation of the structural amplitude $F(hkl)$ with the help of some rather flexible model.

In reality, the summation in expression (3) is limited to some maximally available experimental measurement by the value h_{max}, k_{max}, l_{max}; therefore, when synthesizing $\rho(xyz)$ using X-ray diffraction data obtained using MoK_α radiation, a resolution of 0.2 Å is achieved [16]. This means that the details of the electron density much smaller than 0.2 Å cannot be reconstructed during syntheses of the electron density.

The final dimensions of the cell impose a restriction on the position in the reciprocal space of the first measured reflex. In addition, the structural amplitudes included in expression (1), even with adequate processing of experimental data, contain random errors.

To reduce the negative impact of the above factors, temperature changes in the structure of PMN were estimated using the difference synthesis of electron density:

$$\delta\rho(xyz) = \frac{1}{V} \sum_{h_{min}}^{h_{max}} \left[F_{exp}(hkl) - F_{mod}(hkl)\right] \cdot e^{-i2\pi\cdot(hx + ky + lz)} \tag{4}$$

where $F_{mod}(hkl)$ is the structural amplitude, corresponding to the computational model, calculated in the general form by formula (1).

Assuming the existence of an inversion center and placing the origin of coordinates in it, we obtain an expression to calculate $\delta\rho(xyz)$:

$$\delta\rho(xyz) = \frac{1}{V}\sum_{h_{\min}}^{h_{\max}} \left(F_{\exp}(hkl) - F_{\mathrm{mod}}(hkl)\right) \cdot \mathrm{Cos}(2\pi \cdot (hx + ky + lz))$$

The function $\delta\rho(xyz)$ is significantly weaker than the total electron density $\rho(xyz)$ and depends on the series termination effect: the corresponding error in $\delta\rho(xyz)$ manifests itself least in the internuclear space [17].

20.3 Results and Discussion

When determining the atomic parameters from the electron density distributions in perovskite structures, difficulties arise due to the small atomic displacements with a temperature change compared with the cell size, as well as due to the presence of heavy atoms (type *A* or *B*) along with light oxygen atoms. In addition, in the cross-sections of the electron density there is a partial overlap of the electron density of different atoms [14, 15].

Taking into account these features, we analyzed the changes in electron density in different sections using differential synthesis with temperature.

Figure 20.1a shows the obtained cross-sections of the electron density distributions in the vicinity of the lead atom at the temperatures studied. It was found that with a decrease in temperature to 203 K, there are significant redistributions of electron density in the *zx*-plane in the [110] direction.

On the obtained sections of the electron plane in the *zx*- and *xy*-planes at the indicated temperature, anisotropy of the electron density distribution $\rho(xyz)$ in the vicinity of the Pb atom is detected. The cross-section maps obtained by difference synthesis of the electron density distributions $\Delta\rho_{Pb}$ $(xyz, T) = \rho_{Pb}(xyz, T) - \rho_{Pb}(xyz, 293\ \mathrm{K})$ reveal small changes in $\Delta\rho_{Pb}$ (xyz, T) in the directions [101], [011].

From the analysis of the observed changes in $\Delta\rho_{Pb}(xyz, T)$, it follows that they can be explained by the perturbations of the electron density of the Pb atom caused by the displacement of its center from the ideal position (0,0,0) in the [110] direction.

With a further decrease in temperature to 103 K, an increase in the planned $\Delta\rho_{Pb}(xyz, T)$ changes of the lead atom is observed in the *zy*- and *xy*-planes.

Calculations of the synthesis of electron density showed that the smallest value of the reliability *R*-factor is achieved by introducing equal displacements of the Pb atom along the directions [110], [101], [011]. The nature of the distribution of $\rho(xyz)$ serves as a control of the correctness of the interpretation of the electron density—it reveals a reasonable arrangement of atoms, false maxima disappear. At each step of successive approximations of the electron density, the value of the

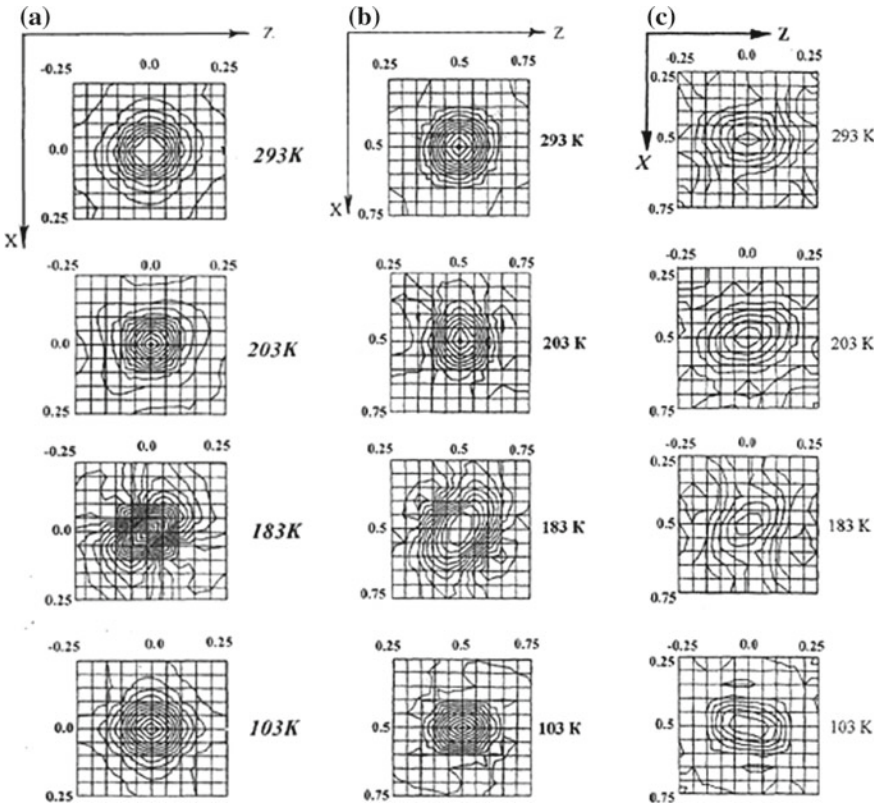

Fig. 20.1 Electron density cross-section in the vicinity of atoms in PMN at different temperatures: **a** atom of Pb, **b** atom of type *B* (Mg/Nb); **c** atom O

R-factor is calculated, which decreases as the parameters of the PMN atoms are refined [13].

The magnitudes of the obtained displacements are comparable with those obtained earlier [10] in the direct calculation of the positional and thermal parameters of the lead atom.

This result can be interpreted in favor of the appearance at low temperatures of the displacement of lead along one of the eight [111] directions in the cell. Such a result agrees well with the data given earlier in [10].

An analysis of the electron density distribution for other PMN atoms shows the following.

At a temperature of 203 K, asymmetry arises in the distribution of the electron density $\rho(T)$ of Mg/Nb atoms predominantly in the [100] direction in the *zx*-plane relative to the ideal positions (0.5, 0.5, 0.5) in the perovskite cell.

In other planes *zy* and *xy* no changes in the distribution of $\rho_{\mathrm{Mg/Nb}}$ (T) at this temperature were revealed.

As the temperature decreases to 183 K, asymmetry appears in the electron density distribution $\rho_{Mg/Nb}$ (T) in all three sections, however, the greatest changes are observed as in the case of a lead atom in the zx-plane.

The distribution of $\rho_{Mg/Nb}$ (T) becomes symmetric along the [110] direction.

With a further decrease in temperature to 103 K, symmetry arises with respect to the [010] direction relative to the ideal position (0.5, 0.5, 0.5) in the perovskite cell.

Calculations based on maps of electron density difference synthesis showed the occurrence of Mg/Nb atom mixing along one of the two indicated directions.

This result can be explained if one assumes the occurrence of deviations of the angles between the bonds—*B*–O–*B*–O—from 180° and the occurrence as a result of some rotation of the chains—*B*–O–*B*–O—in relation to their positions in an ideal cubic structure. Corresponding changes in the positions of atoms should result in some distortion of the oxygen octahedra in the chain, due to the difference in the lengths of the Mg–O and Nb–O interatomic bonds forming the octahedra at the vertices. Since the O atom belongs simultaneously to two neighboring oxygen octahedra, when a shortened *B*–O bond forms in one octahedron, an elongated *B*–O bond must appear in the adjacent octahedron, which in turn leads to the displacement of the *B* atom already in this oxygen octahedron from the center of the octahedron. As a result, the *B* atoms in the chain of octahedra will be displaced in the same way, which leads to an electrical ordering of the structure. These differences of distances were indeed found in [11, 12].

A feature of PMN is that two nonequivalent ions Mg^{2+} and Nb^{5+} are located in the *B* sublattice, which destroys the possible higher electrical ordering due to both the differences in the ionic radii of these atoms and the ability to form bonds with neighboring atoms. In addition, the Nb^{5+} ion belongs to the *ds*-elements, which at this oxidation state are generally considered to be ferroactive [18, 19].

Thus, electroneutrality and equivalence of cells in PMN due to the aforementioned reasons is absent, and therefore, the identified displacements in the *B* sublattice may be due to electron density perturbations due to displacements of Pb atoms [17].

An analysis of the condition of deviations of bond angles—sB–O–B–O—, causing a polar state, showed [19, 20] that the dipole moments of the unit cells in ferroelectrics are due to the asymmetry of atomic orbitals be due to ion displacement. The displacement of ions is only a side effect of the asymmetry of the electron cloud in the oxygen octahedron.

Earlier, the possibility of the existence of electron states with a dipole moment in a system of noninteracting octahedra without ion displacement was also shown [21, 22].

However, such states should be associated with an increase in the electron density concentration along one, two, or three bonds in the oxygen octahedron. It should lead to ion displacements and shortening of bonds along the corresponding directions. The observed changes in the electron density near the oxygen atoms fit into the picture of these changes.

Despite the fact that the oxygen atoms are “low-electron” and, therefore, possessing a weak scattering ability with respect to X-rays, we detected the following

temperature changes in the electron subsystem of oxygen atoms using, deformation electron density maps.

When the temperature drops below the phase transition temperature, a redistribution of electron density occurs in the *zx*-plane along the [110] direction at a temperature of 183 K and the [010] direction at a temperature of 103 K.

Within the framework of consideration of deviations from the ideal perovskite model, it was shown that the observed changes in the electron density could be interpreted from the point of view of the occurrence of disordered displacements of O atoms relative to ideal positions in the [110] direction at the temperature of 183 K and the direction of [010] at the temperature of 103 K.

Considering together the detected temperature changes in the electron density cross-sections, it can be concluded that the atomic displacements in the *B*-sublattice correlate with the displacements of O atoms. Figure 20.2 shows the scheme of the oxygen octahedra and lead atoms in PMN at 283 K.

The displacements of O atoms can correspond to the rotations/vibrations of oxygen octahedra as a whole, belonging to the chain—B–O–B–O—.

Figure 20.3 shows the scheme of rotations of the oxygen octahedra and the associated lead atoms in PMN at low temperatures.

In regions with an increased concentration of Nb atoms as compared to Mg atoms, electrical ordering may occur, associated with the displacements of atoms from the centers of octahedra along one of the Nb–O bonds. The results of the PMN study confirmed the presence of similar displacements of Nb atoms from the centers of oxygen octahedra [23].

These changes clearly reflect the correlations of thermal motion of atoms and statically disordered displacements of lead atoms.

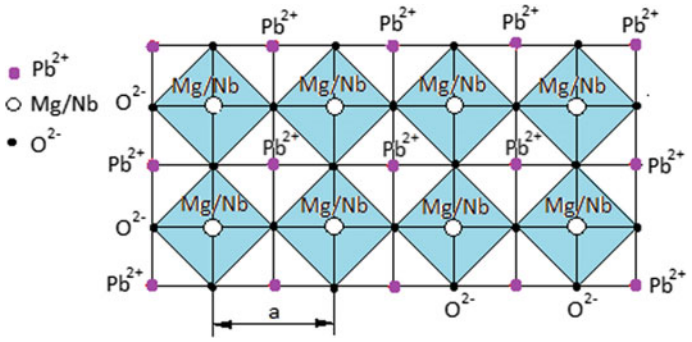

Fig. 20.2 Scheme of oxygen octahedra and lead atoms in PMN at the temperature of 283 K

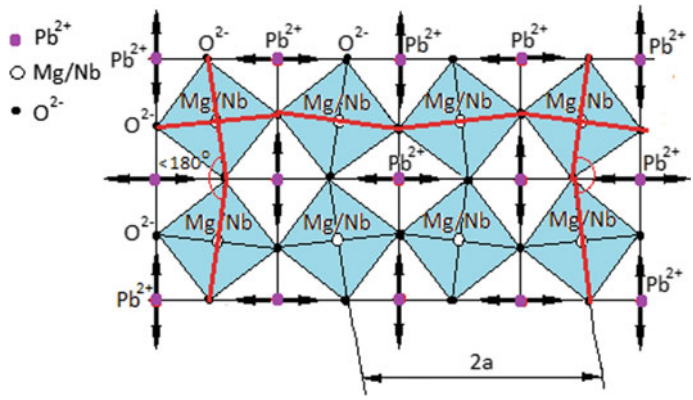

Fig. 20.3 Scheme of consistent rotations of oxygen octahedra and the related displacements of lead atoms in PMN at low temperatures

20.4 Conclusion

Thus, the electron density cross-section maps in PMN revealed changes in atomic displacements with decreasing temperature and a correlation in the directions of these displacements was noted.

References

1. G.A. Smolensky, V.A. Isupov, A.I. Agranovskaya, J.V. Popov. FTT **2**, 2906 (1960) (in Russian)
2. M.E. Lines, A.M. Glass, *Principles and Applications of Ferroelectrics and Related Materials* (Oxford University Press, Oxford, 1977), 679 p
3. L.E. Cross, Ferroelectrics **76**, 241 (1987)
4. K.L. Brown et al., J. Phys. Condens. Matter **30**, 125703 (2018)
5. A. Kania, E. Talik, M. Kruczek, A. Słodczyk, J. Phys. Condens. Matter **17**(42), 6737 (2005)
6. Yu.S. Kuzminov, *Ferroelectric Crystals for Controlling Laser Radiation* (Nauka, Moscow, 1982), 400 p (in Russian)
7. N. Setter, J. Appl. Phys. **51**, 4356 (1980)
8. D. Viehland, J.-F. Li, Ferroelectrics **158**, 381386 (1994)
9. N. Takesue, Y. Fujii, H. Chen, H. You, in *ISRF-III, Program and Abstract Book, Dubna, Russia*, 64 (2000)
10. A. Verbaere, Y. Piffard, Z.G. Ye, E. Husson, Mat. Res. Bull. **27**, 1227 (1992)
11. H. Idink, W.B. White, J. Appl. Phys. **76**(3), 1789 (1994)
12. H.D. Rosenfeld, T. Ecami., A. Bhalla. *IEEE Transactions on Ultrasonics, Ferroelectrics and Frequency Control* **38**(6), 559 (1991)
13. A.R. Lebedinskaya, M.F. Kupriyanov, Phase Transit. **75**(3), 289 (2002)
14. I. Lundqvist, N. March. *Theory of Inhomogeneous Electron Gas* (Mir, Moscow, 1987), 400 p
15. Y.G. Tsirelson, R.P. Ozerov. *Electron Density and Bonding in Crystals* (Bristol, Adam Hilger, 1993) 450 p (in Russian)

16. V.G. Tsirelson. Results of science and technology. VINITI. Ser. Crystal Chem. **27**, 267p (1992) (in Russian)
17. N.N. Lobanov, V.G. Tsirelson, B.N. Volkov, Z. Kristallogr. **35**, 589 (1990) (in Russian)
18. F. Brus, P. Cowley, *Structural Phase Transitions* (Mir, Moscow, 1984), 408p (in Russian)
19. E.A. Zhurova, V.E. Zavodnik, S.A. Ivanov, V.G. Tsirelson, in *Seminar Abstr. "Energy Structure of Nonmetallic Crystals with Different Types of Chemical Bonds"*. Uzhgorod, 80 (1991) (in Russian)
20. E.G. Fesenko *Perovskite Family and Ferroelectricity* (Atomizdat, Moscow, 1972), 248 p (in Russian)
21. S.B. Vakhrushev, A.A. Naberezhnov, N.M. Okuneva, B.N. Savenko. FTT **37**(12), 3621 (1995) (in Russian)
22. H.D. Rosenfeld, T. Egami, Ferroelectrics **150**, 183 (1993)
23. A. Bokov, B.J. Rodriguez, X. Zhao, J.-H. Ko, S. Jesse, X. Long, W. Qu, T.H. Kim, J.D. Budai, A.N. Morozovska, S. Kojima, X. Tan, S.V. Kalinin, Z.-G. Ye, Z. Kristallogr. **226**, 99 (2011)

Chapter 21
Fine Particularities of Structure and Optical Properties of Lithium Niobate Crystals Grown from Boron Doped Charge with Different Genesis

Nikolay V. Sidorov, Natalya A. Teplyakova, Roman A. Titov, Mikhail N. Palatnikov, Alexander V. Syuy and Nikolay N. Prokopiv

Abstract This work demonstrates that nonmetal boron is absent in the crystal structure thus it structures the melt and has a significant influence on the structure and physical characteristics of lithium niobate crystals. At this $LiNbO_3$:B crystals possess a structure uniformity (and it is higher than that of a congruent crystals), their Nb_{Li} defects amount is close to the amount in stoichiometric crystals though a photorefractive effect of $LiNbO_3$:B crystals is much lower than in stoichiometric crystals and the structure and an optical uniformity is higher in $LiNbO_3$:B crystals.

21.1 Introduction

A lithium niobate crystal ($LiNbO_3$) refers to the most important nonlinear optical materials applied in telecommunication technologies of an information transmission, a holographic recording of information and optical processes of amplification and conversion of an optical radiation [1]. Lithium niobate is a non-stoichiometric oxygen octahedral ferroelectric with a wide homogeneity area on the phase diagram (44.5–50.5 mol% Li_2O at 1460 K). $LiNbO_3$ should actually be considered as a solid solution $LiNbO_3$:Nb [2, 3]. Oxygen ions coordinate metals cations in oxygen octahedra in lithium niobate crystals. This fact permits doping of the crystals by a wide range of metal elements. At this a considerable distortions occur in the MeO_6 octahedra (Me = Li^+, Nb^{5+}, doping cation or a vacancy), but the symmetry stays intact [4–6]. All this provides a good base for the control of material physical

N. V. Sidorov (✉) · N. A. Teplyakova · R. A. Titov · M. N. Palatnikov
Tananaev Institute of Chemistry, Subdivision of the Federal Research Centre, "Kola Science Centre of the Russian Academy of Sciences", 26a, Akademgorodok, Apatity, Murmansk Region 184209, Russia
e-mail: sidorov@chemy.kolasc.net.ru

A. V. Syuy · N. N. Prokopiv
Far Eastern State Transport University, 47, Seryshev Str., Khabarovsk 680021, Russia

I. A. Parinov et al. (eds.), *Advanced Materials*, Springer Proceedings in Physics 224, https://doi.org/10.1007/978-3-030-19894-7_21

characteristics. A lithium niobate ferroelectric crystal being a various composition phase has a developed defect structure. A photorefractive effect is basically formed because of defects with a localized electron. Such defects form photoelectric fields. $LiNbO_3$ crystals are characterized by high values of the photoelectric field intensity and the photorefractive effect. The latter can be adjusted in a very wide range [4, 5, 7]. One of the ways to increase an optical damage resistance of congruent crystals is doping by non-photorefractive metallic cations.[1] The resulting crystals are $LiNbO_3$:*Me* (*Me* = Zn, Mg, In, etc.) [5]. The influence of non-photorefractive metallic dopants on $LiNbO_3$ properties is based on their ability to regulate the amount and the position of cation sublattice defects and molecular complexes connected with the defects [4, 5, 8–10]. At this defects Nb_{Li} (Nb^{5+} cations located in Li^+ sites of the perfect stoichiometric crystal structure with the composition R = Li/Nb = 1) together with transition metals impurities (for example, $Fe^{2+} \rightarrow Fe^{3+}$) are deep traps for electrons. The influence of these defects on the photorefractive effect is considerable [4, 5]. Despite Nb_{Li} defects, the lithium niobate structure contains a number of other defects such as shallow electron traps. The latter also influence the photorefractive effect in crystals with a low photorefractive effect [11]. Note that doping by metallic elements in high concentrations inevitably leads to a significant increase in an optical and a structural non-uniformity of a single crystal [4, 5, 8–10, 12].

Non-metal cations possess other than metal cations chemical bonding mechanisms. As a result, non-metal cations influence on physical characteristics of the melt-crystal system is different. These cations are unable to incorporate into oxygen octahedra of a $LiNbO_3$ crystal structure. Due to this fact influence of non-metal dopants on the structure and physical characteristics of a $LiNbO_3$ single crystal are rarely researched. Though there is a reason to believe that non-metal elements are able to change physical characteristics of the melt. This would lead to changes in thin particularities of the crystal structure. Papers [13, 14] have detected that the Curie temperature (T_c) increases by $\sim$47 K and the melting point increases by $\sim$10 K for $LiNbO_3$ crystals grown from the charge that contained boron compared to the same characteristics of a congruent crystal.

This paper considers a chemical interaction in a system Li_2O–B_2O_3–Nb_2O_5, and some particularities of a crystallization of $LiNbO_3$ crystals from the charge that contains non-metal dopants. Raman spectra are sensitive towards changes in a relation between structural units of a crystal. Thus we have used Raman spectra to study crystals $LiNbO_3$:B (0.55–1.24 mol% in the charge) in dependence of the dopant concentration and the charge genesis. An optical and a structural uniformity of crystals were researched by a photoinduced light scattering (PILS) and a laser conoscopy. Results on $LiNbO_3$:B crystals were compared with identical results on a nominally pure stoichiometric ($LiNbO_{3stoich}$) and congruent ($LiNbO_{3cong}$) crystals.

[1]Non-photorefractive cations do not change the charge in the crystals under an optical radiation (they do not provide extra electrons to the system) despite the photorefractive cations.

21.2 Method

Nominally pure congruent crystals $LiNbO_3$ and $LiNbO_3$:B (0.55–1.24 mol% in the charge) were grown from the congruent melt [15]. The doping was carried out both by a homogeneous doping of the precursor Nb_2O_5 [16] and a direct solid phase doping [14, 17]. A direct solid phase doping is a solid phase synthesis of a mixture of niobium pentoxide, lithium carbonate and boric acid. A granular charge appears during the annealing of the mixture in the pre-melting area temperature (1240–1250 °C). General disadvantage of the direct doping method is a possibility of appearance of growth bands and cracking of the $LiNbO_3$ crystals due to after-growth thermal stresses [17, 18]. Defects and the non-uniformity lead to a rejection of individual areas of crystals at creation of optical devices elements. Crystals $LiNbO_3$:B (0.55–0.83 mol% B_2O_3 in the charge) were grown by the direct single phase doping. At homogeneous doping, a reagent containing boron (boric acid) is added to a niobium re-extract. The re-extract is obtained during an extraction purification of the dirty niobium hydroxide (2 wt% impurities) to the pure niobium hydroxide (10^{-4}–10^{-6} wt% impurities). The doped niobium pentoxide is used as a precursor at the lithium niobate charge synthesis. A single crystal $LiNbO_3$:B (1.24 mol% B_2O_3 in the charge) was growth from this charge. Application of a homogeneous doping of a Nb_2O_5 precursor enables obtaining of crystals free of growth bands and other macro- and micro-defects. Due to mass-spectrometry data, concentration of nonmetal element boron in $LiNbO_3$:B crystals grown by both described methods is very low ($\sim 10^{-4}$ wt%). Impurities concentrations were: Pb, Ni, Cr, Co, V, Ti, Fe, Al less than 2×10^{-4}, Ca, Si, F less than 1×10^{-3} wt%. Growth of optically perfect crystals with a low photorefractive effect is possible when the boron concentration in the melt does not exceed ~ 0.1 wt% [13]. At a higher boron concentration, the melt viscosity considerably increases which results in appearance of macro-defects in the grown crystals. The latter worsens an optical quality of the crystals [13, 14].

$LiNbO_{3stoich}$ crystal was grown from a melt with 58.6 mol% Li_2O. Growth of congruent nominally pure crystals was carried out using the original granular charge of lithium niobate prepared in ICT KSC RAS. Such charge enables obtaining of water-white nominally pure single crystals $LiNbO_{3cong}$ [19]. All crystals were grown on air by the Czochralski method on an installation "Crystal-2" equipped with a system of an automatic control of the crystal diameter.

All grown crystals were brought to a single-domain state by a high temperature electro-diffuse annealing with applying a direct current at a constant cooling 20 °C/h in the temperature range 1240–880 °C. The control of a single domain state was carried out by the analysis of a frequency dependence of the electrical impedance and by the determining of a static piezoelectric coefficient (d_{333st}) of a crystal boule.

Samples for research had a shape of parallelepipeds ($\sim 7 \times 6 \times 5$ mm^3), edges of which coincided with crystallographic axes *X*, *Y*, *Z* (*Z* is the polar axis of a crystal). Sample faces were thoroughly polished.

Raman spectra were excited by the band 514.5 nm of an argon laser Spectra Physics (model 2018-RM) and were registered by a spectrograph T64000 by Horiba Jobin Yvon with a confocal microscope. Spectra were excited by a low power radiation to decrease the influence of a photorefractive effect on Raman spectra. An exciting laser power under the microscope was 3 mW. All spectra were registered with the resolution 1.0 cm^{-1}. The spectra treatment was carried out on the software package Horiba LabSpec 5.0 and Origin 8.1. The error in determination of frequencies, bandwidths and intensities was ±1.0, ±3.0 cm^{-1} and 5%, correspondingly. PILS and laser conoscopy methods are described in detail in [10, 12, 20]. In PILS and laser conoscopy experiments a Nd:YAG (MLL-100) laser with the wavelength 532 nm and a power from 1 to 160 mW was applied.

An absorption edge was determined by monochromator MDR-41. The crystal transmission spectrum was detected to find a band gap. After that an inverted spectrum was built. The result was an absorption spectrum. Deuterium lamp was a source of light. The linear part of this spectrum was approximated by a line to the point of crossing with the abscissa axis. This value on the abscissa axis in a wavelength corresponded to the absorption edge af a crystal. Band gap was determined due to a formulae $E = hc/\lambda$, where λ is a wavelength corresponding to the absorption edge af a crystal, h is a Planck's constant, c is the light speed in vacuum. The error in determination of an absorption edge was ±1.0 nm.

21.3 Results and Discussion

Raman spectra of crystals $LiNbO_3$:B (0.55–1.24 mol% B_2O_3 in the charge) were researched earlier in papers [21–24]. The attention was drawn to the influence of a cation sublattice disorder on $A_1(TO)$ symmetry type phonons in the $Y(ZZ)\bar{Y}$ scattering geometry and a manifestation of the photorefractive effect in Raman spectra. At this, oxygen octahedra O_6 distortions caused by the cation sublattice disorder were not considered. Table 21.1 demonstrates main parameters of Raman bands of single crystals $LiNbO_{3stoich}$, $LiNbO_{3cong}$, $LiNbO_3$:B (0.55–1.24 mol% B_2O_3 in the charge) registered in the $Y(ZX)\bar{Y}$ scattering geometry. Phonons $E(TO)$ symmetry type are active in this geometry. The crystal $LiNbO_{3stoich}$ is characterized by the most ordered cation sublattice structure. We have detected that Raman spectra of $LiNbO_{3stoich}$ registered in the $Y(ZX)\bar{Y}$ geometry contain all 9 bands corresponding to $E(TO)$ symmetry type phonons allowed by the selection rules (see Table 21.1).

Low intensity bands with frequencies 179 and 611 cm^{-1} do not appear in Raman spectra of crystals $LiNbO_{3cong}$ and $LiNbO_3$:B (0.55–1.24 mol% B_2O_3 in the charge) because they are masked by the structure disorder effects. Table 21.1 also demonstrates that $LiNbO_3$:B bandwidths, which correspond to vibrations of cations inside octahedra (150–300 cm^{-1}) are narrower than such bandwidths in a $LiNbO_{3cong}$ spectrum. Widths of bands 152 and 240 cm^{-1} in the $LiNbO_3$:B spectrum coincide within the error with the bandwidths in the $LiNbO_{3stoich}$ spectrum. At the same time the width of the 578 cm^{-1} band is much wider in the Raman spectra

Table 21.1 Basic parameters of bands appearing in Raman spectra of single crystals $LiNbO_{3stoich}$, $LiNbO_{3cong}$, and $LiNbO_3:B^{3+}$ (0.55–1.24 mol% B_2O_3 in the charge). The scattering geometry is $Y(ZX)\bar{Y}$ ($E(TO)$)

$LiNbO_{3stoich}$		$LiNbO_{3cong}$		$LiNbO_3$:B (0.55 mol%)		$LiNbO_3$:B (0.69 mol%)		$LiNbO_3$:B (0.83 mol%)		$LiNbO_3$:B (1.24 mol%)	
v	*S*	*v*	*S*	*v*	*S*	*v*	*S*	*v*	*S*	*v*	*S*
152	7	152	12	152	7	152	9	152	9	152	10
179	–	–	–	–	–	–	–	–	–	–	–
240	9	240	11	41	9	241	11	240	10	240	11
268	10	268	14	270	13	271	12	270	13	270	13
324	10	324	13	325	12	324	14	324	14	323	16
371	17	371	23	371	24	370	24	370	26	371	26
434	10	434	14	432	9	432	10	432	11	432	14
578	16	576	15	575	32	576	33	576	33	575	24
611	–	–	–	–	–	–	–	–	–	–	–
630[a]	20	626	25	626	41	628	42	626	46	626	28
876[a]	20	876	30	875	25	877	25	875	26	875	31

[a]*A remark* Bands with frequencies 630 and 876 cm^{-1} correspond to phonons of $A_1(TO)$ and $A_1(LO)$ symmetry type. The phonons are inactive in the scattering geometry $Y(ZX)\bar{Y}$. They manifest in this geometry due to the photorefractive effect. Widths of low-intensity bands with frequencies 180 and 610 cm^{-1} are absent from the table due to great errors in their determination

of crystals $LiNbO_3$:B (0.55–1.24 mol% B_2O_3 in the charge) than in spectra of crystals $LiNbO_{3stoich}$ and $LiNbO_{3cong}$ (see Table 21.1; Fig. 21.1a). This band corresponds to twice degenerate $E(TO)$ vibrations of oxygen atoms in O_6 octahedra. These data indicate that even little changes in a boron concentration in the charge (0.55–1.24 mol% B_2O_3) and thus, in the melt, lead to a considerable increase in the order of cations along the polar axis of $LiNbO_3$:B crystals. This effect does not depend on the doping method and is accompanied by the distortion of oxygen octahedra O_6. At the same time new bands are absent from the spectra area corresponding to oxygen octahedra vibrations. Such bands could indicate the change in the oxygen octahedra geometry.

Bands with frequencies of 578 and 630 cm^{-1} correspond to twice degenerate $E(TO)$ vibrations of oxygen atoms in O_6 octahedra and totally symmetric $A_1(TO)$[2] vibrations of oxygen octahedra. The 578 and 630 cm^{-1} bands are much wider in $LiNbO_3$:B (0.55–0.83 mol% B_2O_3 in the charge, direct doping) spectra than in a $LiNbO_3$:B (1.24 mol% B_2O_3 in the charge, homogeneous doping) spectrum. At the same time, bands with frequencies of 432 ($E(TO)$) and 875 cm^{-1} ($E(LO)$) bridge, stretching vibrations of oxygen atoms along the polar axis [5], are narrower in the spectra of $LiNbO_3$:B (direct doping) than in the spectrum of $LiNbO_3$:B (homogeneous doping), see Table 21.1. Obtained data indicate that the distortion of O_6 octahedra in $LiNbO_3$:B depends on the doping method.

[2]A band with frequency 630 cm^{-1} ($A_1(TO)$) is forbidden by the selection rules in the scattering geometry $Y(ZX)\bar{Y}$, it manifests in this geometry due to the photorefractive effect.

A 630 cm^{-1} band is forbidden in the Raman spectrum by the selection rules in the $Y(ZX)\bar{Y}$ scattering geometry [5, 25, 26]. This band corresponds to the vibration of oxygen octahedra of an $A_1(TO)$ symmetry type. A 630 cm^{-1} band is the most sensitive band towards the photorefractive effect. Literature usually considers this band as an analytical one for the evaluation of the photorefractive effect due to lithium niobate Raman spectra. Figure 21.1a, b, c demonstrates that the concentration behavior of the 630 cm^{-1} band intensity of crystals $LiNbO_3$:B (0.55–1.24 mol% B_2O_3 in the charge) correlate well with the concentration behavior of PILS opening angle θ. A good correlation with θ is also characteristic of 630 cm^{-1} ($A_1(TO)$), 576 cm^{-1} ($E(TO)$) bandwidths. This obviously indicates that both oxygen octahedra distortions and the photorefractive effect depend on the boron concentration in the charge of crystals $LiNbO_3$:B (0.55–1.24 mol% B_2O_3 in the charge). These data clearly demonstrate that boron structures the melt, which may cause growth of almost pure congruent crystals from a congruent melt doped by boron. Such crystals have obvious differences in the structure and physical characteristics from a congruent crystal grown from a pure congruent melt. These experimental results can be explained by the following reasoning.

It may be that the doping of a nominally pure $LiNbO_3$ charge by boron leads to such melt structuring that grown crystals possess a lower amount of Nb_{Li} defects. The defects are the deepest electron traps. Raman spectroscopy data confirm this fact. It has commonly been assumed that 120 cm^{-1} band corresponds to a two-particle state of acoustic phonons with a zero total wave vector.[3] The intensity of the band is zero in a spectrum of a perfect stoichiometric crystal, where Nb_{Li} defects are absent [5, 28–30]. At the same time, the intensity of this band is nonzero for non-stoichiometric crystals that contain Nb_{Li} defects [5, 29, 30]. Figure 21.1d demonstrates that the 120 cm^{-1} band intensity first decreases than increases with the rise in the boron concentration in the charge of $LiNbO_3$:B (0.55–1.24 mol% B_2O_3 in the charge) crystals Raman spectra. This band is divided into two components 112 and 123 cm^{-1} (Fig. 21.1d) both in spectra of $LiNbO_3$:B (1.24 mol% B_2O_3 in the charge, homogeneous doping) and highly ordered $LiNbO_{3cong}$, that contains Nb_{Li} defects. This indicates the structure perfection of both crystals. As long as the 120 cm^{-1} band intensity is zero in the spectrum of a highly ordered stoichiometric crystal [5, 28–30], than the decrease in its intensity may indicate a decrease in the number of Nb_{Li} defects in a crystal $LiNbO_3$:B. At this, two processes take place simultaneously. The cation sublattice structure units order, and this manifests in narrowing of widths of bands in the area 150–300 cm^{-1}, see Table 21.1. A decrease is also observed in an resonance anharmonic interaction between $A_1(TO)$ symmetry type fundamental bands with the lowest frequencies 254 and 274 cm^{-1} and two-particle acoustic excitations of a $A_1(TO)$ symmetry type. This interaction is discussed in detail in a review [31].

[3]For [27], a low-intensity band with frequency 120 cm^{-1} may also correspond to a mode of a pseudoscalar type A_2, forbidden by the selection rules for a point group C_{3v}. This vibration may appear in a Raman spectrum due to a lowering in a local point symmetry of lithium niobate crystals from C_{3v} to C_3 due to O_3 triangles turning because of impurities in real crystals [27].

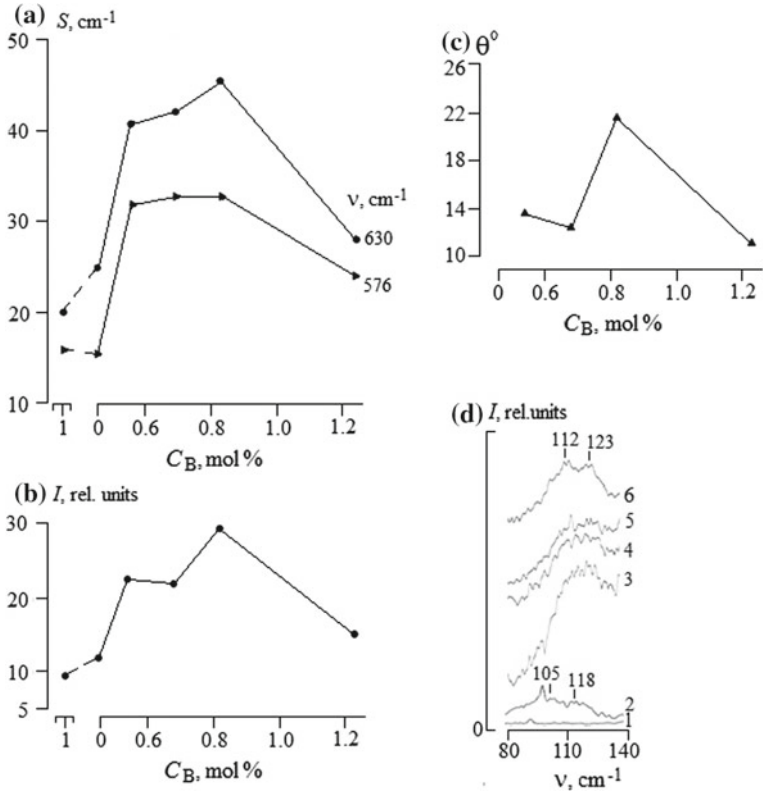

Fig. 21.1 Concentration dependencies of widths (S) (**a**), intensities (I) of bands with frequencies 576 and 630 cm^{-1} in Raman spectra (**b**) and PILS opening angle θ (**c**) of crystals $LiNbO_{3stoich}$, $LiNbO_{3cong}$, $LiNbO_3$:B; a fragment of a low-frequency Raman spectrum of crystals $LiNbO_{3stoich}$ (1), $LiNbO_{3cong}$ (2), $LiNbO_3$:B (0.55 (3), 0.69 (4), 0.83 (5), 1.24 (6) mol% B_2O_3 in the charge) in the scattering geometry $Y(ZX)\bar{Y}$ ($A_1(TO)$) (**d**)

It should be noted that 120 cm^{-1} band is sensitive towards changes in an acoustic Q-factor of a $LiNbO_3$ crystal due to the work [32]. The higher an acoustic Q-factor is, the smaller the band's intensity is. This could be explained by an increase in the structure perfection of a crystal due to a decrease in the basic structure defects Nb_{Li} amount. Thus, the data suggest a higher structural perfection of nominally pure $LiNbO_3$ crystals grown from a boron-doped charge compared to that of nominally pure congruent crystals. The most structurally perfect crystal is a single crystal $LiNbO_3$:B (1.24 mol% B_2O_3 in the charge, homogeneous doping).

Conoscopic pictures confirm high optical homogeneity of single crystals $LiNbO_3$:B (0.55–1.24 mol% B_2O_3 in the charge), Fig. 21.2.

A conoscopic picture of the only crystal $LiNbO_3$:B (0.83 mol% B_2O_3 in the charge), excited by a relatively high power laser beam (90 mW), contains a slight evidence of an anomalous biaxiality. The evidence could perhaps be connected with

increase in a photorefractive effect, Fig. 21.2. The crystal $LiNbO_3$:B (1.24 mol% B_2O_3 in the charge) has the best optical damage resistance due to PILS data. The indicatrix of the PILS speckle-structure of the crystal does not open even at the excitation by the laser radiation power 160 mW, Fig. 21.2. A comparative conoscopic analysis of the researched crystals using an excitation laser radiation with powers 1 and 90 mW and research of PILS allowed us to conclude that the structure uniformity of crystals $LiNbO_3$:B is comparative with that of a crystal $LiNbO_{3cong}$ and is higher than the optical uniformity of a crystal $LiNbO_{3stoich}$, Fig. 21.2. It should be noted that the photorefractive effect in a stoichiometric crystal is much higher than that in a congruent crystal and in crystals $LiNbO_3$:B (0.55–1.24 mol% B_2O_3 in the charge). An opening angle θ of a PILS speckle-structure is higher for $LiNbO_{3stoich}$ (56°). For crystals $LiNbO_3$:B (0.55–1.24 mol% B_2O_3 in the charge) θ does not exceed 22°, Fig. 21.1c, 2. A stoichiometric crystal $LiNbO_{3stoich}$ grown from a melt with 58.6 mol% Li_2O is characterized by a non-uniform refractive index along the polar axis, and a nominally pure congruent crystal has a uniform refractive index along the polar axis. Photorefractive effect is much stronger in a $LiNbO_{3stoich}$ than in a $LiNbO_{3cong}$ [5, 33]. It is a well-known fact that changes in a structure and properties of the melt, along with the crystal doping, influence thin particularities of the crystal structure. Thus, these factors also influence an appearance of additional impurity levels in the band gap, which changes photorefractive properties of a crystal. The crystal $LiNbO_3$:B (0.83 mol% B_2O_3 in the charge, direct doping) is photorefractive, has a clear PILS and a uniform refractive index along the polar axis. The latter is confirmed by a sharp conoscopic picture (see Fig. 21.2). At the same time the crystal $LiNbO_3$:B (1.24 mol% B_2O_3 in the charge, homogeneous doping) has a low photorefractive effect, its conoscopic picture is blurred. The latter results from fluctuations in a refractive index of a crystal along the polar axis (growth axis). The similar, but even more blurred conoscopic picture is observed for a crystal $LiNbO_{3stoich}$ (see Fig. 21.2). A $LiNbO_{3stoich}$ crystal also possesses an intermittent laser beam structure propagating along the polar axis (Fig. 21.3) which indicates a much higher non-uniformity of a refractive index along the polar axis compared to that in a crystal $LiNbO_3$:B (1.24 mol% B_2O_3 in the charge, homogeneous doping). $LiNbO_{3stoich}$ is the only crystal with an observed intermittent laser beam structure.

A decrease in the photorefractive effect could be caused by changes in a band structure and electro-optical properties of a crystal due to structuring of a melt by boron. Figure 21.4 demonstrates that the crystal $LiNbO_3$:B (1.24 mol% B_2O_3 in the charge, homogeneous doping) has a wider band gap than crystals $LiNbO_{3stoich}$, $LiNbO_{3cong}$, $LiNbO_3$:B (0.83 mol% B_2O_3 in the charge, direct doping). At the same time, the fundamental absorption edge of crystals $LiNbO_3$:B is much steeper than that of crystals $LiNbO_{3stoich}$, $LiNbO_{3cong}$. An increase in the steepness of the fundamental absorption edge indicates a high structural and compositional

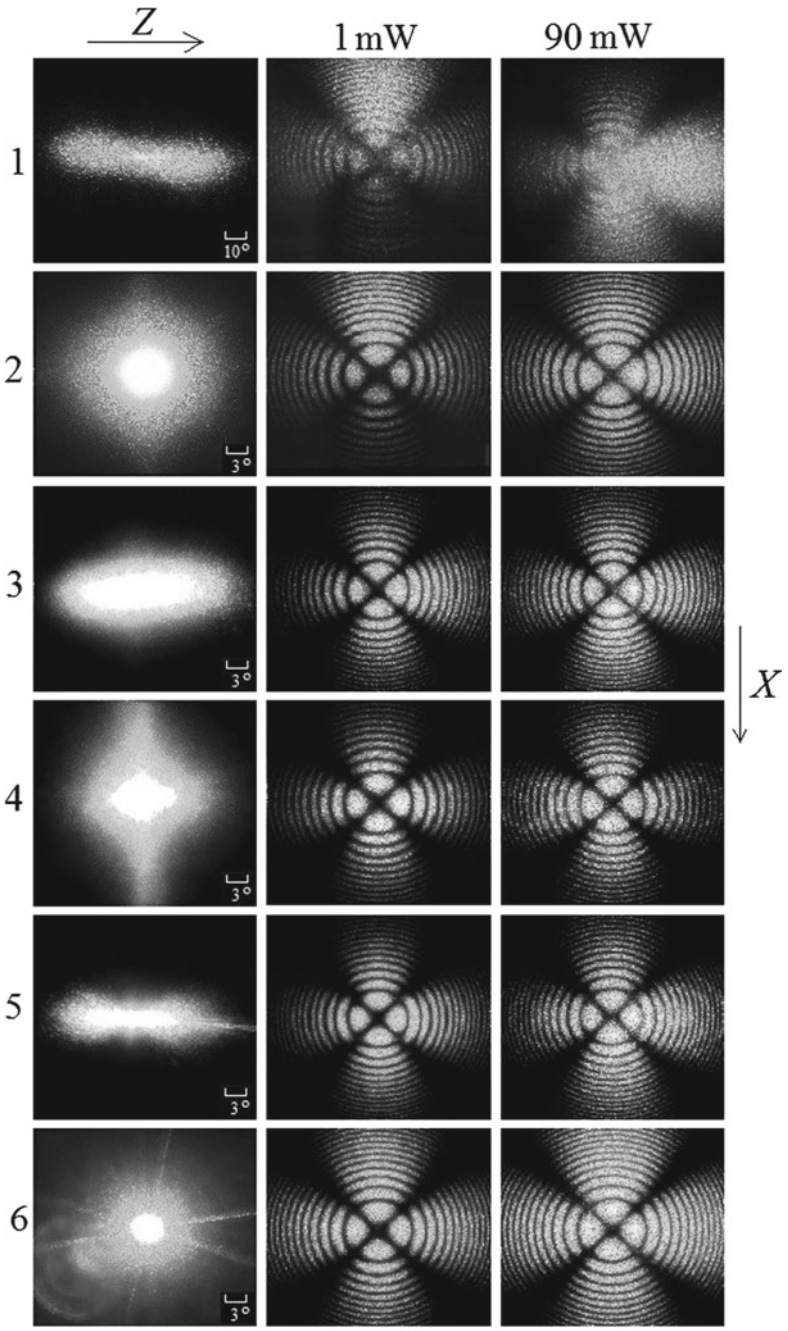

Fig. 21.2 Speckle-structure of the PILS indicatrix (P = 160 mW) and conoscopic pictures (P = 1 and 90 mW) of crystals $LiNbO_{3stoich}$ (1), $LiNbO_{3cong}$ (2), $LiNbO_3$:B (0.55 (3), 0.69 (4), 0.83 (5), 1.24 (6) mol% B_2O_3 in the charge). A complete PILS indicatrix opening time is 60 s for all researched crystals

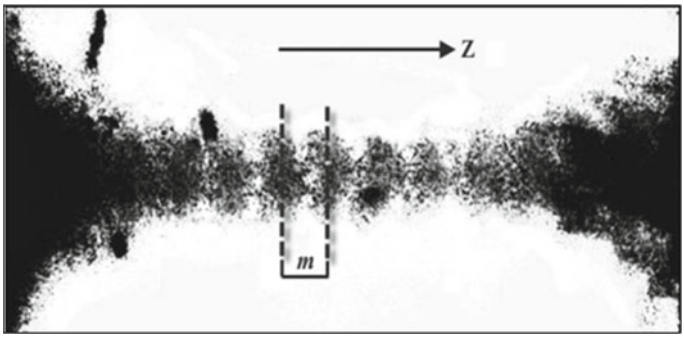

Fig. 21.3 Intermittent structure of a focused laser beam (λ = 514.5 nm) in a lithium niobate single crystal of a stoichiometric composition grown from the melt with 58.6 mol% Li_2O. The laser beam is directed along the crystal polar axis, the period $m \approx 0.33$ mm

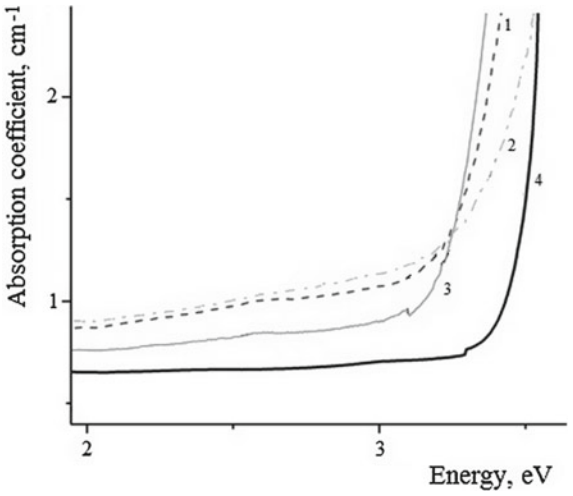

Fig. 21.4 An absorption spectrum of $LiNbO_3$ crystals: 1—$LiNbO_{3stoich}$, 2—$LiNbO_{3cong}$, 3—$LiNbO_3$:B (0.83 mol%), 4—$LiNbO_3$:B (1.24 mol%)

uniformity of the volume of crystals $LiNbO_3$:B [5]. A low photorefractive effect in the crystal $LiNbO_3$:B (1.24 mol% B_2O_3 in the charge, homogeneous doping) is explained by changes in electro-optical properties that are governed by the polarizability of the oxygen-octahedral clusters MeO_6 [34, 35]. The latter is determined by particularities in a distortion of oxygen octahedra O_6 and an order of the structure units of a cation sublattice along the polar axis. Due to authors of [34, 35], changes in electro-optical coefficients in nominally pure $LiNbO_3$ crystals at variation of the Li/Nb ratio leads to changes of an ion contribution to the magnitude of the electro-optic effect. We can assume that the addition of boron results in such a melt that produces a crystal with a more rigid crystal structure (compared to a nominally pure $LiNbO_3$ crystal). Oxygen octahedra MeO_6 of such a structure are less deformable.

According to mass spectrometry data, boron concentration in $LiNbO_3$:B crystals is close to traces ($\sim 10^{-4}$ wt%), because this boron is unable to influence the crystal structure, defectiveness and physical characteristics of crystals. Thus significant differences between $LiNbO_3$:B and $LiNbO_{3stoich}$, $LiNbO_{3cong}$, could be caused only by dopant influence on the melt structure. Solid-phase chemical reactions take place during a high-temperature charge synthesis in a system Li_2O–B_2O_3–Nb_2O_5. Different borates that appear at this process influence compound and physical characteristics of the melt.

$LiNbO_3$ has a high melting point ($\sim$1526 K) and a high chemical activity of a melt, which claims platinum crucibles. This is the main reason why papers on study of lithium niobate melt structure are scarce. In recent years, in connection with the need to obtain optically perfect single crystals the attention was drawn to an influence of the $LiNbO_3$ melt structure on the process of crystallization. It has commonly been assumed that the basic concept is existence of strongly bound groups of atoms or ions (clusters) in the melt. The groups have a certain composition [36]. Papers [37–39] considered the crystallization from the melt by a high-temperature Raman spectroscopy. A considerable change in the melt structure was detected in a pre-crystallization area due to Raman spectra. Anion motives did not coincide in the melt and in a grown lithium niobate crystal. This phenomenon existing near the melting point causes serious obstacles for the emergence of equilibrium structures [37–39]. Meta-stable phases obtain an advantage at crystallization in such conditions. The phases have a crystal lattice structure far from the short-range order structure of the melt. The mismatch (or the difference) of an anionic structure of the lithium niobate melt in the crystal arises growth of crystalline faces or creation of structure defects [37, 38].

The crystal structure of lithium niobate is a carcass made of close-packed oxygen octahedra O_6. The octahedra are connected via vertices and edges. Octahedra contain basic (Li^+ and Nb^{5+}) and doping cations. Bonds in octahedra occupied by niobium are mostly covalent [4]. At the same time, the lithium ion is connected with oxygen atoms only via an electrostatic interaction. Due to this niobium tends to form anion motives of NbO_4-tetrahedra in the melt. Thus during melting a niobium atoms coordination changes from octahedral to a tetrahedral one which Raman spectra confirm [37–39]. A strong covalent bond enables a possibility of preserving the oxianion structure in a melt. Thus, the melt may contain not only isolated tetrahedral groups but also complexes with a stable structure [37]. Indeed, Raman spectra of the system Li_2O–Nb_2O_5 revealed bands corresponding to the vibrations of the edge NbO_3- and middle NbO_2- groups (815–870 cm^{-1}) and also bands corresponding to symmetrical stretching bridge vibrations of bonds Nb–O–Nb (670–690 cm^{-1}). Such bonds are located at the point of connection of two tetrahedra [37, 38]. However, the melt in a pre-crystallization temperature range contains perhaps not only tetrahedra NbO_4 but also octahedra NbO_6. Raman spectra were researched in [40] for Nb_2O_5, used for synthesis of charge and growth of lithium niobate crystals. In the area of stretching bridge vibrations of oxygen atoms along the polar axis (800–1100 cm^{-1}) authors have detected five bands with frequencies 814, 845, 902, 965, 995 cm^{-1}. This indicates a diversity of island

structures in a niobium pentoxide, the structures most likely consist of octahedra and tetrahedra chains.

One of the basic boron properties as a dopant with a high chemical activity is a change in a crystallization temperature, the viscosity and the surface tension of melts [41]. We have detected an increase in a melt viscosity, the melting point by ~ 10 K, the Curie temperature by ~ 50 K compared to a nominally pure congruent crystal [13]. A crystal chemistry of boron oxide compounds is highly various. It is determined by a double hybridization possibility of boron atom, sp^2- and sp^3-, with appearance of $[BO_3]^{3-}$ triangles and $[BO_4]^{5-}$ tetrahedra [42]. Radius of a neutral boron atom is 0.88 Å; in the case of B^{3+}: 0.15 Å for $B^{(3)}$ and 0.25 Å for $B^{(4)}$. Boron atoms have a configuration $2s^2 2p^1$ in the ground state, with one unpaired electron and two vacant *p*-orbitals. A relatively small atom has vacant orbitals; this is a reason why boron is a very strong acceptor of unshared electron pairs. Use of these orbitals in a donor-acceptor interaction enables an increase in a boron coordination number to 4. Atoms and atom groups surrounding boron are located in three angles of a tetrahedron, the fourth angle stays unoccupied, and a positive electric field of a significant intensity appears in this fourth angle. This is the reason why boron is able to create strong molecular complexes. Triangles and tetrahedra of boron can exist separately or polymerize among themselves via a common oxygen atom [42]. A predisposition to the formation of bulky polyanions explains an increase in the melt viscosity [43].

It is a well-known fact that alkali metals oxides are modifiers of boron-oxygen grid in a melt and turn a boron atom into a four-coordinated state which leads to the appearance of tetrahedra $[BO_4]$ [43]. Absolute values of specific negative charges of complex anions monotonously decrease in a line ortho-, pyro-, meta- and polyborates at combining of boron-oxygen triangles and tetrahedra. This fact provides a necessary stability of numerous condensed compounds with monovalent, as well as large divalent elements. A paper [38] considers melts of lithium metaborates by temperature Raman spectra. The paper demonstrates the existence of a chain boron-oxygen anion in the melt. All the above-mentioned crystal chemical dependences determine a reaction potential of borate containing melts.

Papers [44, 45] research a triple system Li_2O–B_2O_3–Nb_2O_5. The authors considered more than 30 different molar ratios of components. Authors of [44] claimed appearance of six different lithium borates (LiB_3O_5, $Li_2B_4O_7$, $LiBO_2$, $Li_6B_4O_9$, $Li_4B_2O_5$, Li_3BO_3), one niobium borate (Nb_3BO_9) and three lithium niobates ($LiNb_3O_8$, $LiNbO_3$, Li_3NbO_4) in the system. According to this paper, lithium borates dissolve pretty well in lithium niobate at the temperature lower than 1100 °C. Thus, borates are able to be a flux at $LiNbO_3$ crystals growth. Moreover, the concentration area of lithium niobate crystallization, detected by a spontaneous nucleation, is quite wide in a system Li_2O–B_2O_3–Nb_2O_5.

There is a method of growing of stoichiometric lithium niobate single crystals with a low photorefractive effect from a congruent melt using flux K_2O (HTTSSG —High temperature top speed solution growth) [46–48]. Absence of potassium in the crystal structure becomes obvious at comparison of ions radii Li^+ and K^+ (0.68

and 1.38 Å, respectively). Such a great difference in ion radii makes an isomorph substitution of similar elements of an alkali group (of lithium by potassium) improbable. Thus, both potassium and boron fail to incorporate into the lithium niobate crystal structure. Such method enables obtaining of stoichiometric crystal with a constant refractive index along the polar axis from a congruent melt [49–51].

We may assume that polyanions containing boron form stable covalent bonds with polyanions containing niobium in the melt. This binds the excess of niobium and increases the ratio Li/Nb in the melt. As a result, the grown crystal approaches a stoichiometric one in a cation sublattice order. The same process takes place at using of a K_2O flux. Such crystal is characterized by a lower concentration of Nb_{Li} defects and lithium vacancies (V_{Li}). This assumption is confirmed by the increase in a Curie temperature (T_K) of a crystal $LiNbO_3$:B ([B] $\sim$0.1 wt% in the melt) by $\sim$47 K compared to that of a congruent crystal [13]. The same changes in T_C of $LiNbO_3$ crystals doped by metals dopants (Mg, Zn, etc.) claim much higher dopant concentrations ($\sim$2–3 wt%).

Moreover, [52] demonstrates that melts of inorganic polymers that tend to form chains and rings including ions of a solute (B_2O_3, $Na_2B_4O_7$, $Li_6B_4O_9$, etc.) and to form glasses are excellent solvents. For example, paper [53] reports formation of a high-temperature insoluble borate Al_5BO_9, which means that the melt loses a great amount of Al_2O_3. We may assume that metals cations existing in the melt, which usually introduce in the structure of lithium niobate crystal as uncontrollable impurities [46], will also be removed from the melt. As a result, grown crystal will be perfect.

According to Raman spectra data (see Table 21.1), oxygen octahedra in $LiNbO_3$:B crystals of homogeneous doping are less distorted in comparison with $LiNbO_3$:B crystals of direct doping. This is obviously caused by the ordering of Li^+, Nb^{5+} cations and vacancies along the polar axis. The ordering manifested in widening of bands with frequencies of 432 and 875 cm^{-1}. The bands correspond to deformation and stretching vibrations of oxygen atoms in a bridge *Me*–O–*Me* (*Me* = Li^+, Nb^{5+}, a vacancy). Note that parameters of 875 cm^{-1} band are sensitive towards changes in the value of a dipole moment and a spontaneous polarization of a crystal [5].

Paper [16] researches crystals of $LiNbO_3$:Mg obtained both by direct and homogeneous doping of a precursor Nb_2O_5. Raman spectra and optical methods revealed a higher structure order of homogeneously doped crystals compared to directly doped crystals. Magnesium incorporates directly into the niobium pentoxide structure at homogeneous doping. At this, it has coordination inside polyhedra and a uniform distribution in the melt volume. Clusters appearing in a melt at different doping methods have different structure and size and, consequently, melts should crystallize in different ways. This problem is discussed in details in [32, 54, 55]. It is connected with the appearance of quite stable clusters in a melt. The clusters structure and size depend on a melt composition and thermal pre-history. One of the conclusions of these papers is that the crystallization goes on by joining of clusters to a growing crystal.

$[BO_4]^{5-}$ tetrahedra could be both of perfect and distorted shape. Boron forms three covalent bonds with oxygen atoms and the fourth bond is formed due to a coordinate covalent mechanism. This is the reason why B–O bonds lengths vary from 1.462 to 1.512 Å and angle between <O–B–O> has values 104–115° in a tetrahedron [42]. Boron containing reagent was added to a niobium re-extract at the homogeneous doping. At this only one type of borates appear (Nb_3BO_9). Bonds B–O and Nb–O are less different in the length, than at direct doping. At direct doping the appearance of seven different borates is possible [44]. Due to this difference boron and niobium containing complexes will contain less distorted tetrahedra at homogeneous doping. Later in a pre-crystallization area, forming octahedra will also be less distorted. This is the reason why oxygen octahedra are more perfect in the structure of a crystal $LiNbO_3$:B (homogeneous doping) compared to a crystal $LiNbO_3$:B (direct doping). This was confirmed by Raman spectra.

21.4 Conclusion

Obtained results allow us to expand the term "doping". Usually doping is thought about as introduction of a doping element (or elements) into the crystal structure to change its physical properties. Nonmetal boron does not introduce into the lithium niobate crystal structure. Despite the high concentration of boron in the charge (up to 2.0 mol%), its concentration in the crystal is very low, comparable with traces. This is several orders of magnitude less than for metal dopants. The absence of boron in the structure is explained by its pretty small radius $\sim$0.2 Å (Li^+ and Nb^{5+} = 0.68 Å). This is a reason why octahedral coordination of B^{3+} ion (like Nb^{5+} ion) is impossible as well as an ion interaction with oxygen cannot occur (like Li^+ ion and doping ions Zn^{2+}, Mg^{2+}). Oxide compound of boron are strong complexing agents and solvents. That is the reason why they influence the structure and physical characteristics of a melt and a grown from this melt crystal. An increase in a melting point (1264 °C) is observed for $LiNbO_3$:B compared to that of a nominally pure congruent crystal. Boron addition decreases the amount of Nb_{Li} defects and probably of uncontrollable impurities by structuring of the melt. This leads to a decrease in a photorefractive effect value and an increase in the structure and the optical uniformity of lithium niobate crystals. Thus, it is the first time when $LiNbO_3$ crystals with the given properties are obtained by structuring of the melt by a chemically active dopant, but the dopant does not incorporate into the crystal structure. This approach allows us to obtain nominally pure $LiNbO_3$ crystals with properties as in a doped crystal but the cation sublattice units order and Nb_{Li} defects amount as in a stoichiometric crystal. At the same time, $LiNbO_3$:B crystals have a much lower photorefractive effect than a stoichiometric crystal. The distortion of oxygen octahedra O_6 and photorefractive properties of $LiNbO_3$:B crystals could be varied by the method of a charge doping.

References

1. P. Gunter, J.-P. Huidnard, *Photorefractive Materials and Their Applications*, vol. 1 (Springer, Berlin, 2007), p. 2
2. S.C. Abrahams, *Properties of Lithium Niobate* (Pergamon, New York, 1989)
3. S.C. Abrahams, J.M. Reddy, J.L. Bernstein, J. Phys. Chem. Solids **27**(6/7), 997 (1966)
4. Yu.S. Kuzminov, *Electro-optical and Nonlinear-optical Lithium Niobate Crystal* (Nauka, Moscow, 1987). (in Russian)
5. N.V. Sidorov, T.R. Volk, B.N. Mavrin, V.T. Kalinnikov, *Lithium Niobate: Defects, Photorefraction, Vibrational Spectra, Polaritons* (Nauka, Moscow, 2003). (in Russian)
6. T. Volk, M. Wohlecke, *Lithium Niobate. Defects, Photorefraction and Ferroelectric Switching* (Springer, Berlin, 2008)
7. M. Aillerie, P. Bourson, M. Mostefa, F. Abdi, M.D. Fontana, J. Phys. Conf. Ser. **416**, 012001 (2013)
8. N.V. Sidorov, M.N. Palatnikov, V.T. Kalinnikov, *Influence of the Secondary Structure on Optical Properties of Ferroelectric Crystals of Lithium Niobate with Low Photorefractive Effect* (Proc. KSC RAS. Chemistry and Materials, Apatity, 2015). (in Russian)
9. M.D. Fontana, P. Bourson, Appl. Phys. Rev. **2**, 046002 (2015)
10. N.V. Sidorov, O.Y. Pikoul, A.A. Kruk, N.A. Teplyakova, A.A. Yanichev, M.N. Palatnikov, Opt. Spectrosc. **118**(2), 273 (2015)
11. A.A. Blistanov, V.M. Lyubchenko, A.N. Goryunova, Kristallographija **43**(1), 86 (1998)
12. N.V. Sidorov, A.A. Yanichev, M.N. Palatnikov, A.A. Gabain, O.Y. Pikoul, Opt. Spectrosc. **117**(1), 76 (2014)
13. O.V. Makarova, M.N. Palatnikov, I.V. Biryukova, N.A. Teplyakova, N.V. Sidorov, Inorg. Mater. **54**(1), 53 (2018)
14. M.N. Palatnikov, I.V. Biryukova, O.V. Makarova, V.V. Efremov, O.E. Kravchenko, V.T. Kalinnikov, *Obtaining and Properties of Lithium Niobate Crystals Grown from the Melt of Congruent Composition Doped by Boron* (Proc. KSC RAS. Chemistry and Materials, Apatity, 2015). (in Russian)
15. M.N. Palatnikov, I.V. Biryukova, S.M. Masloboeva, O.V. Makarova, D.V. Manukovskaya, N.V. Sidorov, J. Cryst. Growth **386**, 113 (2014)
16. M.N. Palatnikov, I.V. Biryukova, S.M. Masloboeva, O.V. Makarova, O.E. Kravchenko, A.A. Yanichev, N.V. Sidorov, Inorg. Mater. **49**(7), 765 (2013)
17. S.M. Masloboeva, M.N. Palatnikov, L.G. Arutjunian, D.I. Ivanenko, Izv. Spb. Technol. Inst. **64**(38), 34 (2017)
18. M.N. Palatnikov, N.V. Sidorov, V.T. Kalinnikov, Nonferr. Met. (10), 54 (2000)
19. M.N. Palatnikov, N.V. Sidorov, I.V. Biryukova, O.B. Shcherbina, V.T. Kalinnikov, Perspekt. Mater. (2), 93 (2011) (in Russian)
20. O.Y. Pikoul, N.V. Sidorov, *Laser Conoscopy of Crystals* (KSC RAS Press, Apatity, 2014). (in Russian)
21. N.V. Sidorov, M.N. Palatnikov, A.A. Yanichev, R.A. Titov, N.A. Teplyakova, Opt. Spectrosc. **121**(1), 40 (2016)
22. N.V. Sidorov, M.N. Palatnikov, A.A. Yanichev, R.A. Titov, N.A. Teplyakova, J. Appl. Spectrosc. **83**(5), 707 (2016)
23. N.V. Sidorov, YuA Serebryakov, Ferroelectrics **160**, 191 (1994)
24. N.V. Sidorov, M.N. Palatnikov, N.A. Teplyakova, A.A. Yanichev, R.A. Titov, Proc. SPIE Asia-Pacific Conf. Fundam. Probl. Opto Microelectron. **10176** (2016). https://doi.org/10.1117/12.2268155
25. A.E. Semyonov, E.V. Cherkasov, J. Phys. Chem. **54**(10), 2600 (1980)
26. A.A. Kruk, N.V. Sidorov, A.A. Yanichev, M.N. Palatnikov, J. Appl. Spectrosc. **81**(1), 5 (2014)
27. V.S. Gorelik, P.P. Sverbil', Inorg. Mater. **51**(11), 1104 (2015)
28. M.R. Okamoto, W. Ping-Chu, J.F. Scott, Phys. Rev. **32B**(10), 6787 (1985)

29. N.V. Sidorov, B.N. Mavrin, P.G. Chufyrev, M.N. Palatnikov, *Phonon Spectra of Lithium Niobate Single Crystals*, V.T. Kalinnikov (ed.) (KSC RAS Press, Apatity, 2012) (in Russian)
30. N.V. Surovtsev, V.K. Malonovskii, A.M. Pugachev, A.P. Shebanin, Phys. Solid State **45**(3), 505 (2003)
31. A.A. Anikjev, Eng. J. Sci. Innov. **19**(7), 50 (2013)
32. M. Umarov, V. Gruzienko, A. Vtjurin, A. Hodgabaev, Compon. Technol. **107**(6), 138 (2010)
33. N.V. Sidorov, E.A. Antonycheva, A.V. Syui, M.N. Palatnikov, Kristallographija **55**(6), 1079 (2010)
34. M.D. Fontana, K. Laabidi, B. Jannot, M. Maglione, P. Jullien, Solid State Commun. **92**, 827 (1994)
35. F. Abdi, M. Aillerie, P. Bourson, M.D. Fontana, K. Polgar, J. Appl. Phys. **84**(4), 2251 (1998)
36. S. Uda, K. Shimamura, T. Fukuda, J. Cryst. Growth **155**, 229 (1995)
37. Yu.K. Voronko, S.B. Gessen, A.B. Kudrjavtsev, A.A. Sobol, E.V. Sorokin, S.N. Ushakov, L. I. Tsimbal, Spectroscopy of oxide crystals for quantum electronics, in *Proceedings of GFIRAS*, vol. 29 (Nauka, Moscow, 1991) (in Russian)
38. A.A. Sobol, *High-temperature Spectroscopy of Raman Scattering in Solid and Melted Dielectrics*, PhD thesis, Moscow, 2012 (in Russian)
39. Yu.K. Voronko, A.B. Kudrjavtsev, V.V. Osiko, A.A. Sobol, E.V. Sorokin, Phys. Solid State **29**(5), 1348 (1987)
40. S.M. Masloboeva, N.V. Sidorov, M.N. Palatnikov, L.G. Arutjunian, P.G. Chufyrev, J. Inorg. Chem. **56**(8), 1 (2011)
41. R.S. Bubnova, *Crystallochemical Design of Borate Materials with a Special Structure-Physical Properties, ICS RAS—80 Years. Modern Problems of Inorganic Chemistry*, V.Ya. Shevchenko (ed.) (Art-express, Saint-Petersburg, 2016) (in Russian)
42. T.B. Bekker, *Phase Formation and Growth of Crystals in a Quaternary Mutual System Na, Ba, B*, PhD thesis, Novosibirsk, 2015 (in Russian)
43. N.I. Leonjuk, L.I. Leonjuk, *Crystal Chemistry of Waterless Borates* (MSU, Moscow, 1983). (in Russian)
44. C. Huang, S. Wang, N. Ye, J. Alloys Compd. **502**, 211 (2010)
45. M.P.F. Graça, M.G. Ferreira da Silva, M.A. Valente, J. Non-Cryst. Solids **354**, 901 (2008)
46. M.N. Palatnikov, *Materials of Electron Techniques Based on Ferroelectric Materials and Ceramics Solid Solutions of Niobates-tantalates of Alkali Metals with Micro- and Nanostructures*, PhD thesis, Apatity, 2010 (in Russian)
47. R.N. Balasanjan, V.T. Gabrieljan, E.P. Kokanjan, Kristallographija **35**(6), 1540 (1990)
48. R.N. Balasanjan, V.T. Gabrieljan, L.M. Kazarjan, NAS RA Rep. Phys. **100**(2), 1 (2000)
49. O.F. Shirmer, O. Thiemann, M. Wohlecke, J. Phys. Chem. Solids **52**(1), 185 (1991)
50. D.M. Krol, G. Blasse, J. Chem. Phys. **73**, 163 (1980)
51. L. Redonta, M.F. Da Silva, J.C. Soares, J.A. Sanz-Garcio, E. Dieguez, Lopez F. Agalla, Ind. Instrum. Methods Phys. Res. **64**(1–4), 189 (1992)
52. L.M. Viting, *High Temperature Melts-Solutions* (Moscow State University Press, Moscow, 1991). (in Russian)
53. N.I. Leonjuk, Kristallographija **53**(3), 546 (2008)
54. Yu.K. Voronko, S.B. Gessen, A.B. Kudrjavtsev, A.A. Sobol, E.V. Sorokin, S.N. Ushakov, L. I. Tsimbal, High Temperature Raman Spectroscopy—A Method of Study of Phase Transitions in Laser Crystals, in *Proceedings of GFIRAS*, vol. 29 (Nauka, Moscow, 1991) (in Russian)
55. Yu.K. Voronko, A.B. Kudrjavtsev, V.V. Osiko, A.A. Sobol, E.V. Sorokin, Bull. Lebedev Phys. Inst. (2), 34 (1987) (in Russian)

Chapter 22
Optical Properties of the $Ba_{0.5}Sr_{0.5}Nb_2O_6$ Epitaxial Films on Al_2O_3 (001) and MgO (001) Substrates

Svetlana Kara-Murza, Nataliya Korchikova, Alexandr Tikhii, Anatoly Pavlenko and Gennady Tolmachev

Abstract The results of X-ray diffraction analysis, spectrophotometry, ellipsometry of thin films of the ferroelectric-relaxor $Ba_{0.5}Sr_{0.5}Nb_2O_6$ (SBN-50) deposited on Al_2O_3 (001) and MgO (001) crystal substrates are presented. It is established that the natural direction of film growth coincides with the direction of the optical axis in uniaxial crystals [001]. A method for determining optical parameters (the refractive index and the thickness of a film material, as well as the disturbed surface layers) of transparent films on transparent substrates by combination of the ellipsometric methods and spectrophotometric measurements is described. The results of calculations of the parameters of the films are present. It is shown that the values of the refractive indices n_0 and n_e SBN-films do not differ from the crystal ones.

22.1 Introduction

The headlong development of micro- and nanoelectronics in recent decades has led to a great deal of attention paid to obtaining and studying the properties of heterostructures based on thin films of ferroelectric materials in physical materials science [1]. It is known that the properties of ceramics, poly- and single ferroelectric crystals, is adjusted mainly by variation of the chemical composition: by changing the concentration of components in solid solutions or by modifying [2]. For nanoscale structures based on ferroelectric films, it is also possible to do this by

S. Kara-Murza (✉) · N. Korchikova · A. Tikhii
Lugansk Taras Shevchenko National University, Lugansk, Ukraine
e-mail: s.karamyrza@gmail.com

A. Pavlenko · G. Tolmachev
Southern Scientific Center of Russian Academy of Science, Rostov-on-Don, Russia

A. Pavlenko
Research Institute of Physics, Southern Federal University, Rostov-on-Don, Russia

I. A. Parinov et al. (eds.), *Advanced Materials*, Springer Proceedings in Physics 224, https://doi.org/10.1007/978-3-030-19894-7_22

changing the film growth mechanism, its thickness, and/or by creating sublayers [1, 3], which enable not only to vary the properties of the material within one chemical composition, but also to form new one, peculiar only to thin films. Among the most promising ferroelectric thin-film materials are the uniaxial $Sr_{1-x}Ba_xNb_2O_6$ solid solutions (SBNx) [4] due to the high values of dielectric, piezoelectric and optical characteristics. Literature analysis shows, that information about the optical properties of SBNx films is quite contradictory. Thus, the authors of [5] noted a decrease in the values n_0 and n_e of SBNx/MgO films (x = 0.25, 0.60, 0.75) in comparison with single crystals of similar compositions [4], while according to the data of [6] the optical characteristics of the $Ba_{0.5}Sr_{0.5}Nb_2O_6$/Pt(111)/Si(001) heterostructure corresponds to those in a single crystal of $(Ba_{0.5}Sr_{0.5})Nb_2O_6$. These contradictions indicate the need for further studies of the optical properties of SBNx films, depending on the method of their production.

This work is devoted to the study of the optical properties of $Sr_{0.50}Ba_{0.50}Nb_2O_6$ (SBN-50) films on Al_2O_3 and MgO substrates, and also to compare the properties of these films and single crystals.

22.2 Objects and Methods of Research

The SBN-50 films were obtained by high-frequency gas-discharge sputtering in an atmosphere of pure oxygen on the single-crystal Al_2O_3 (001) and MgO (001) substrates of the ceramic target of the stoichiometric composition of $Sr_{0.50}Ba_{0.50}Nb_2O_6$.

X-ray diffraction analysis of the films was carried out with a "DRON-4-07" diffractometer by the $\theta/2\theta$ method using $Cu_{K\alpha}$-radiation.

Ellipsometry is one of the most sensitive optical methods for studying the surface of solids. When an elliptically polarized electromagnetic wave reflected from the solid surface, the parameters of the polarization ellipse of the incident wave have changed. This change are described by ellipsometric angles ψ and Δ, determined by the results of the experiment. These angles are related to the amplitude reflection coefficients s- ($R^{(s)}$) and p- ($R^{(p)}$) by the fundamental equation of ellipsometry:

$$e^{i\Delta}\mathrm{tg}\psi = \frac{R^{(p)}}{R^{(s)}}. \tag{22.1}$$

The expressions for $R^{(s)}$ and $R^{(p)}$ are determined by the surface structure—the number and thickness of the layers, the optical parameters of these layers and the substructure. The solution of the problem of recovery the parameters of a transparent thin-film coating on a transparent substrate from the experimentally determined angles ψ and Δ (inverse problem of ellipsometry) using the optical transmission spectrum will be considered below.

Ellipsometric measurements were performed using a multi-angle reflective null-ellipsometer at the wavelength of a helium-neon laser (λ = 632.8 nm).

Transmission spectra were recorded for the wavelength range 200–1000 nm at room temperature using the Shimadzu UV-2450 spectrophotometer.

22.3 The Results of X-Ray Diffraction Analysis of the SBN-50 Films

On the X-ray patterns of the $\theta - 2\theta$ scan (Fig. 22.1), only reflections from the (00*l*) planes of the SBN-50 film and (0006) of the Al_2O_3 substrate were present.

It is established that the film is polycrystalline, textured, and there are no impurity phases in it. The film is formed with a predominant orientation of the crystallographic axis [001] parallel to the normal to the substrate (the [006] axis of the substrate). The unit cell parameter c = 0.3948 nm is determined from the position of the reflex maxima (00*l*) of the film. The obtained parameter slightly exceeds the parameter of the bulk SBN-50 (c = 0.3945 nm).

22.4 Optical Studies of SBN-50 Films

22.4.1 The Method of Processing the Results of Ellipsometric and Spectrophotometric Measurements

In the simplest case of a single-layer homogeneous and isotropic transparent film (refractive index n_2) on a transparent substrate (refractive index n_3), the problem of determining the film parameters from the results of ellipsometric and

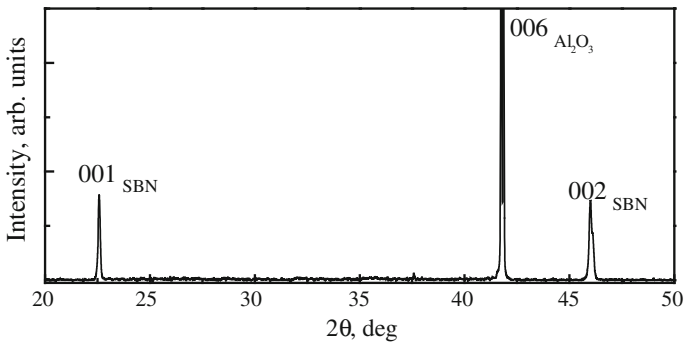

Fig. 22.1 $\theta - 2\theta$ X-ray patterns of SBN/Al_2O_3

spectrophotometric measurements is solved by the method described in [7, 8]. The method is based on the features of the dependences of ellipsometric angles $\psi(\varphi)$ and $\Delta(\varphi)$: when the incidence angle φ is equal to the principal angle φ_0, angle $\psi(\varphi)$ has a minimum and $\Delta(\varphi) = \pi/2$ or $3\pi/2$. Wherein

$$\mathrm{Re}\left\{\frac{R^{(p)}(\varphi_0)}{R^{(s)}(\varphi_0)}\right\} = 0, \tag{22.2}$$

and finding the thickness d and refractive index of the film reduces to solving the quadratic equation with respect to the quantity $X = \cos\alpha$ $\left(\alpha = \frac{4\pi}{\lambda} d\sqrt{n_2^2 - \sin^2\varphi_0}\right)$:

$$(B^p B^s + C^p C^s)X^2 + (A^p B^s + A^s B^p)X + (A^p A^s - C^p C^s) = 0. \tag{22.3}$$

The general form of the coefficients A, B and C for s- and p-polarizations is the same:

$$A = r_{12}\left(1 + r_{23}^2\right),\ B = r_{23}\left(1 + r_{12}^2\right) \text{ and } C = r_{23}\left(1 - r_{12}^2\right),$$

where r_{12} and r_{23} are the Fresnel amplitude reflection coefficients at the air-film and the film-substrate boundaries. The roots $|X| \leq 1$ of (22.3) give the values of the argument:

$$\begin{cases} \alpha = \arccos X + 2\pi m, \text{ if } \mathrm{Im}\left\{\dfrac{R^{(p)}(\varphi_0)}{E^{(s)}(\varphi_0)}\right\} = \dfrac{\pi}{2}, \quad \text{and} \\ \alpha = -\arccos X + 2\pi(m+1), \text{ if } \mathrm{Im}\left\{\dfrac{R^{(p)}(\varphi_0)}{E^{(s)}(\varphi_0)}\right\} = \dfrac{3\pi}{2}, (m_0 = 0, 1, 2, \ldots). \end{cases}$$

It is obvious that the solution of (22.3) is possible only when the value of the refractive index of the film n_2 is known. Moreover, even if value n_2 is known, the true thickness of film d can be determined only, if the order of the interference m is known, too. In turn, the order of interference can be found from the optical transmission spectrum by analyzing the interference extrema. Such an analysis makes it possible to estimate the $n_2 d$ value and then to agree the values of n_2 and d with (22.3) by the iteration method. In the case of ultrathin films, when there are no interference extrema on the transmission spectrum, $m = 1$.

The possible presentations of broken layer on the free surface of the film and the transition layer at the film-substrate interface account to correct the computational results for the best agreement between theory and experiment. The presence of boundaries is modeled by thin transition layers with effective values of thicknesses and refractive indices; amplitude reflection coefficients $R^{(s)}$ and $R^{(p)}$ are formed using the scattering matrix of such a three-layer system. The problem of finding the

values of the parameters of the layers is solved by an optimization method by minimizing the root-mean-square deviations of the ellipsometric angles ψ and Δ, calculated in accordance with (22.1) from experimentally found ones [9]. In this case, the results obtained by solving the inverse problem of ellipsometry within the framework of the single-layer coating model are used as the zeroth approximation.

22.4.2 The Results of Optical Measurements of SBN-50 Films

We present the results of studies of three SBN films—two of them have different thicknesses deposited on Al_2O_3 (001) substrates and one film has deposited on MgO (001) substrate (further these films will be referred to as samples No. 1, No. 2 and No. 3, respectively). The ellipsometric measurements of SBN-50/Al_2O_3 and SBN-50/MgO films showed that the studied films are epitaxial and characterized by a natural growth direction that coincides with the direction of the optical axis [001] of the uniaxial $Ba_{0.5}Sr_{0.5}Nb_2O_6$ crystal (the rotation of the plane of incidence of the probing beam does not change the values of ellipsometric angles ψ and Δ).

As an example of using the measurement and calculation methods, developed by us, we consider the procedure for determining the optical parameters of the SNB-50/Al_2O_3 (001) film—sample No. 1.

To interpret the results of ellipsometric measurements of sample No. 1, the single-layer model described above was used in the zeroth approximation. Ellipsometric measurements were supplemented by measurements of optical transmission (Fig. 22.2).

An analysis of the extrema has restored the order of the interference $m = 2$ at λ = 632.8 nm. The recovery procedure consists in finding such a minimum order of interference for the first observed long-wavelength extremum that provides the dispersion of the optical thickness $n_o d$ of the film to be the same as one characteristic for the crystalline material. The main angle $\varphi_0 = 60.5°$ is a peculiarity of the described SBN film because of $\mathrm{tg}\varphi_0 = 1.76 = n_s$ (n_s is the refractive index of the substrate), i.e. the probing beam "does not see" the film. In this case, the film have such thickness that the Fresnel amplitude reflection coefficients for air-film $r_{12}^{(p)}$, film-substrate $r_{23}^{(p)}$ and substrate-air $r_{31}^{(p)}$ interfaces satisfy condition $r_{12}^{(p)} + r_{23}^{(p)} = r_{31}^{(p)}$, $\cos\alpha = 1$ and $d\sqrt{n^2 - \sin^2\varphi_0} = \lambda$. So, in the zeroth approximation of homogeneous isotropic film with refractive index $n = n_o = 2.3$, the film thickness is $d = 297$ nm.

The fact that the probing beam "does not see" the film leads to trivial dependencies $\psi(\varphi)$ and $\Delta(\varphi)$, calculated in accordance with the basic equation of ellipsometry (22.1) for a model of an optically homogeneous isotropic film with $n = 2.3$ and $d = 297$ nm on a substrate with $n = 1.76$ (Fig. 22.3). It is seen that

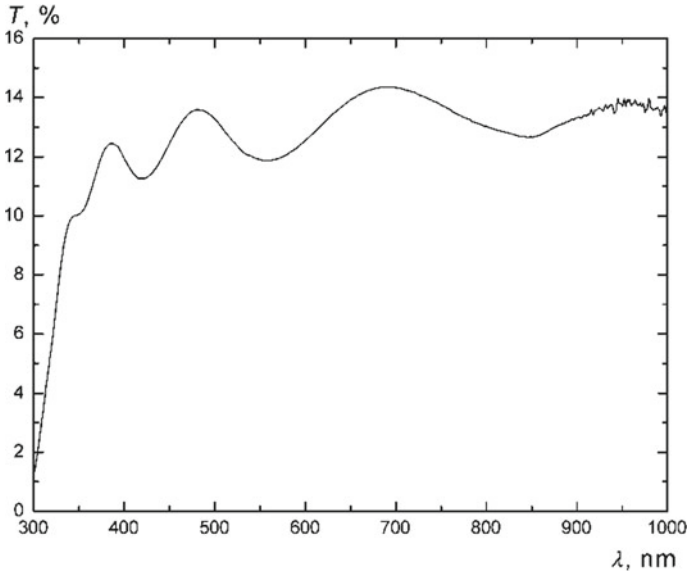

Fig. 22.2 Optical transmission of the $Ba_{0,5}Sr_{0,5}Nb_2O_6/Al_2O_3$ (001) film—sample No. 1

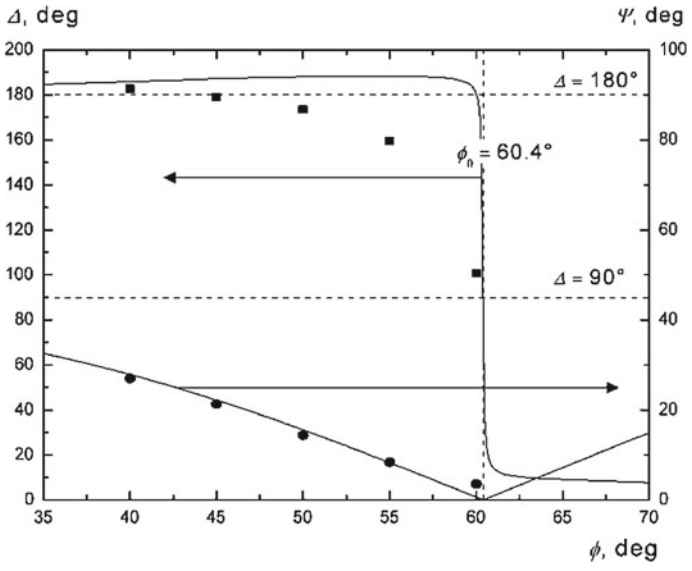

Fig. 22.3 Calculated dependences of the ellipsometric angles ψ and Δ on the angle of incidence φ within the framework of single-layer coating model and the experimental points for the SBN/Al_2O_3 (001) film

despite good agreement between theory and experiment for the angle ψ, the theoretical curve $\Delta(\varphi)$ deviates significantly from the experimental dependence. This can be due to both unaccounted anisotropy and the presence of disturbances at the substrate—film and the film—air interfaces.

These features of the film make it possible to estimate the effect of anisotropy on the interpretation of the results of ellipsometric measurements, quite simply. Because the phases of reflected *p*-polarized and *s*-polarized beams are

$$\delta^{(p)} = \frac{4\pi}{\lambda} d \frac{n_o}{n_e} \sqrt{n_e^2 - \sin^2 \varphi_0}, \ \delta^{(s)} = \frac{4\pi}{\lambda} \sqrt{n_o^2 - \sin^2 \varphi_0}. \tag{22.4}$$

It is sufficient to compare the phases of the *p*- and *s*-components of the reflected light, i.e. compare quantities $\sqrt{n_o^2 - \sin^2 \varphi_0}$ and $\frac{n_o}{n_e}\sqrt{n_e^2 - \sin^2 \varphi_0}$. For a single crystal of $Ba_{0.5}Sr_{0.5}Nb_2O_6$, $n_0 = 2.3{-}2.31$ and $n_e = 2.26{-}2.28$ [10, 11]. Then $\sqrt{n_o^2 - \sin^2 \varphi_0} = 2.129$ and $\frac{n_o}{n_e}\sqrt{n_e^2 - \sin^2 \varphi_0} = 2.124$. A small difference in the values of these quantities makes it possible to use the isotropic SBN-film model with $n = n_0 = 2.3$ for interpretation of the results of ellipsometric measurements. Thus, only the possible presence of transition layer at the film—substrate interface should be account to correct the theoretical model. This transition layer is due to the roughness of the film surface, which is also modeled by the surface layer. In this case, the surface layer can have an effective extinction coefficient, which reflects energy losses due to scattering by inhomogeneities of the surface of the film.

The correction of the theoretical model was performed by the optimization method described in Sect. 4.1: with five search parameters, two refractive indices for the film—substrate and film—air transition layers, two thicknesses of these layers, and an extinction coefficient for the surface layer. Our calculations showed that there is no transition layer at the film—substrate interface. The best agreement between theory and experiment was obtained by taking anisotropy into account and introducing a disturbed surface layer with 7.5 nm thickness with an effective refractive index $n_{ef} = 1.7$ and an effective extinction coefficient $\kappa_{ef} < 0.01$. The effective refractive index of the layer is related to the volume filling coefficient by the Lorentz-Lorentz ratio: $\frac{n_{ef}-1}{n_{ef}+2} = q\frac{n-1}{n+2}$, from which $q = 0.625$. The results are

Table 22.1 The experimental and calculated values of ellipsometric angles ψ and Δ of sample No. 1 for the different angles of incidence φ

Substrate n_s	Angle of incidence φ,°	Experiment		Theory	
		ψ,°	Δ,°	ψ,°	Δ,°
1.76	40	27.0125	182.7454	27.184	180.982
	45	21.3235	178.9224	21.575	179.155
	50	14.3796	173.4771	15.309	174.567
	55	8.3315	159.3511	8.817	161.635
	60	3.5288	100.6841	4.23	105.637

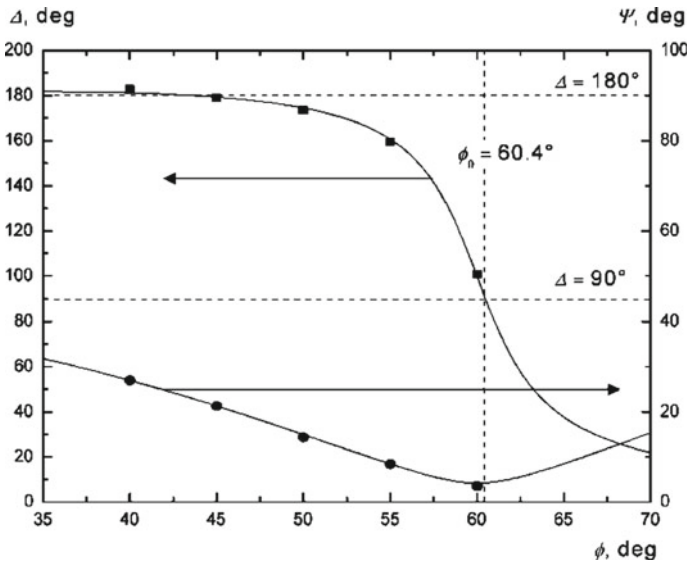

Fig. 22.4 Calculated dependences of the ellipsometric angles ψ and Δ on the angle of incidence φ and the experimental points for the SBN/Al_2O_3 film—sample No. 1 (layer: $d = 7.5$ nm, $n_{ef} = 1.7$, $\kappa_{ef} < 0.01$; film: $d = 290$ nm) $n_o = 2.3$, $n_e = 2.28$

shown in Table 22.1 and in Fig. 22.4, where the experimental and calculated dependences of ellipsometric angles ψ and Δ on the angle of incidence φ for sample No. 1 are presented.

The results of ellipsometric measurements of the SBN-50/Al_2O_3 film (sample No. 2) are significantly different from those for sample No. 1. So, the main angle for this film is $\varphi_0 = 65.6°$, $\Delta(\varphi_0) = 270°$. However, a similar calculation of the parameters of this sample led to the results presented in Fig. 22.4, which differ from the results of sample No. 1 practically only by the film thickness.

The film SBN-50/MgO (sample No. 3) is characterized by a much smaller thickness (d = 168 nm). Nevertheless, its optical parameters, measured at a wavelength of 632.8 nm, correspond to the parameters of a single crystal: $n_o = 2.3$ and $n_e = 2.28$.

The wavelength dependences n_o of all investigated films are determined from the transmission spectra using the found thicknesses. Figure 22.5 shows the dispersion for SBN/Al_2O_3 (sample No. 1) and SBN-50/MgO (sample No. 3) films; here we also show the experimental points for single crystals, given in [4, 10, 11]. These results confirm the identity of the properties of the investigated films and SBN-50 single crystals (Fig. 22.6).

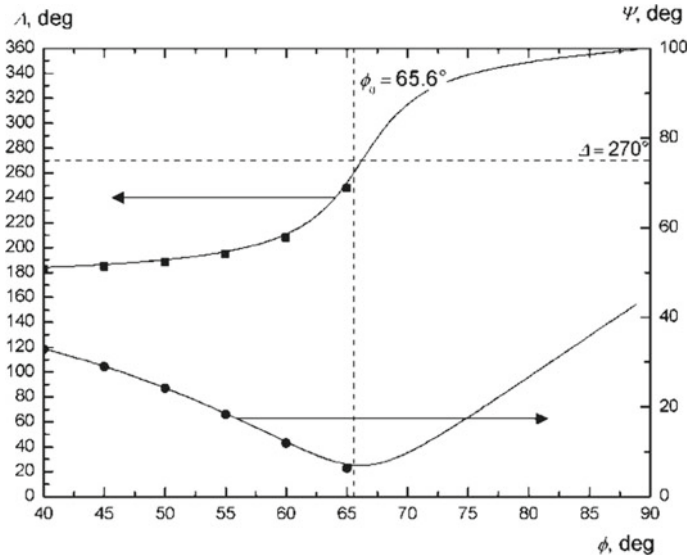

Fig. 22.5 Calculated dependences of ellipsometric angles ψ and Δ on the angle of incidence φ and experimental points of the film SBN/Al_2O_3—sample No. 2 (layer: $d = 5$ nm, $n_{ef} = 1.7$, $\kappa_{ef} < 0.01$; film: $d = 331$ nm), $n_o = 2.3$, $n_e = 2.28$

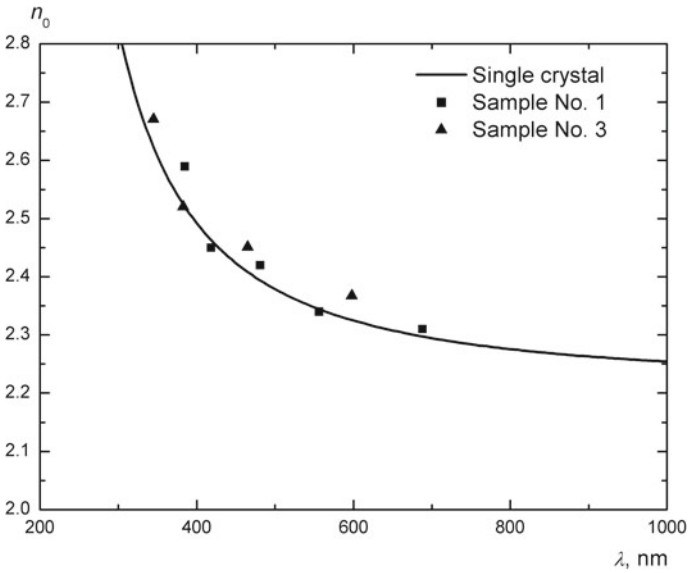

Fig. 22.6 The dispersion $n_o(\lambda)$ of SBN-50 single crystals and the films on the Al_2O_3 and MgO substrates

22.5 Conclusion

Films grown by the method of high-frequency ion-plasma sputtering of a ceramic target of the stoichiometric composition $Ba_{0,5}Sr_{0,5}Nb_2O_6$ on the Al_2O_3 (001) and MgO (001) crystal substrates in a pure oxygen atmosphere are characterized by a natural growth direction coinciding with the direction of the optical axis of the uniaxial crystal [001].

X-ray diffraction analysis revealed the presence of some deformation of the unit cell in polycrystalline textured SBN-50/Al_2O_3 films, which, however, does not lead to significant differences in the properties of films and monocrystals.

By using spectrophotometry and ellipsometry, it was established that the optical properties of films coincide with the optical properties of single crystals. At the film-substrate interface, the transition layer is absent, the disturbed surface layer has the thickness of 5–7 nm and characterized by an effective refractive index $n_{ef} = 1.7$, which corresponds to the coefficient of volume filling of this layer $q = 0.6$.

The obtained results are expedient for use in the fabrication of thin strontium barium niobate films on Al_2O_3 substrates and in the fabrication of functional structures based on them.

Acknowledgements The work was supported by the Ministry of Education and Science of the Russian Federation (project No. 3.6371.2017/8.9) and the grant of the President of the Russian Federation No. MK-4100.2018.2.

References

1. K.A. Vorotilov, V.M. Mukhortov, A.S. Sigov, *Integrated Ferroelectric Devices* (Energoatomizdat, Moscow, 2011), 175 p (in Russian)
2. E.G. Fesenko, *The Perovskite Family and Ferroelectricity* (Atomizdat, Moscow, 1972), 248 p (in Russian)
3. V.M. Mukhortov, Y.I. Golovko, S.V. Biryukov, A. Anokhin, Y.I. Yuzyuk, Tech. Phys. **61**, 91 (2016)
4. Y.S. Kuzminov, *Ferroelectric Crystals for Controlling Laser Radiation* (Nauka, Moscow, 1982), 400 p (in Russian)
5. J. Koo, E. Kang, B. Bae, J. Korean Phys. Soc. **42**, S1161 (2003)
6. A.P. Kovtun, S.P. Zinchenko, A.V. Pavlenko, G.N. Tolmachev, Tech. Phys. Let. **42**(6), 577 (2016)
7. V.A. Gritskikh, I.V. Zhikharev, S.V. Kara-Murza, N.V. Korchikova, Y.M. Nikolaenko, A.A. Tikhii, *Proceedings of the 7th International Symposium "Physics of Surface Phenomena, Interfaces Boundaries and Phase Transitions"* vol. 7, 16–21 Sept 2017 (Tuapse, Russia, 2017) p. 53 (in Russian)
8. A.A. Tikhii, V.A. Gritskikh, S.V. Kara-Murza, Y.M. Nikolaenko, I.V. Zhikharev, Opt. Spectrosc. **112**(2), 300 (2012)

9. A.A. Tikhii, V.A. Gritskikh, S.V. Kara-Murza, N.V. Korchikova, Y.M. Nikolaenko, V.V. Faraponov, I.V. Zhikharev, Opt. Spectrosc. **119**(2), 268 (2015)
10. D. Kip, S. Aulkevye, K. Buse, F. Mersch, R. Panlrath, E. Kratziom, Phys. Stat. Sol. (a) **151**, K3 (1996)
11. P.V. Lenzo, E.C. Spemcer, A.A. Baltman, Appl. Phys. Let. **11**(1), 23 (1997)

Chapter 23
Crystal Structure, Dielectric and Thermophysical Properties of Multiferroics $BiFeO_3$/*REE*

S. V. Khasbulatov, L. A. Shilkina, S. I. Dudkina, A. A. Pavelko, K. P. Andryushin, S. N. Kallaev, G. G. Gadjiev, Z. M. Omarov, M.-R. M. Magomedov, A. G. Bakmaev, I. A. Verbenko and L. A. Reznichenko

Abstract The effects of the modification of bismuth ferrite by various rare earth elements (*REE*) are considered: the results of the investigation of the influence of crystal-physical parameters of stoichiometrically introduced dopants on the form of the phase diagrams of $Bi_{1-x}REE_xFeO_3$ systems, the grain structure of ceramics, the dielectric spectra and thermal properties of samples over a wide range of temperatures are presented.

23.1 Introduction

In the next 10–15 years, the priorities of scientific and technological development of the leading countries of the world will be those areas that will allow to obtain scientific and technical results and create technologies that are the base for innovative development of the market of products and services, and also provide a transition to digital, technologies, new materials and methods of their design, to the creation of systems for storing, processing, transferring and reliable protection of information arrays, to environmentally friendly technologies and energy harvesting devices.

Among these materials, multiferroics are the most promising and attractive, representing an extensive class of materials combining ferroelectric, ferromagnetic

S. V. Khasbulatov (✉) · L. A. Shilkina · S. I. Dudkina · A. A. Pavelko · K. P. Andryushin · I. A. Verbenko · L. A. Reznichenko
Research Institute of Physics, Southern Federal University, Rostov-on-Don 344090, Russia
e-mail: said_vahaevich@mail.ru

S. N. Kallaev · G. G. Gadjiev · Z. M. Omarov · M.-R. M. Magomedov · A. G. Bakmaev
H.I. Amirkhanov Institute of Physics of Daghestanian Scientific Center of the Russian Academy of Sciences, Makhachkala 367010, Russia

I. A. Parinov et al. (eds.), *Advanced Materials*, Springer Proceedings in Physics 224, https://doi.org/10.1007/978-3-030-19894-7_23

and ferroelastic properties with the potential for use in new devices based on mutual control of magnetic and electric fields [1]: magnetic field sensors, information recording/reading devices, in spintronics, artificial intelligence systems, quantum heavy-duty computers, etc. At the same time, among them the most vocal is the bismuth ferrite, $BiFeO_3$, (BFO), which does not contain toxic elements and has high electrical temperatures (Curie temperature, $T_C \sim 1083$ K) and magnetic ordering (Néel temperature, $T_N \sim 643$ K), can be described as possible [2]. From the fundamental point of view, bismuth ferrite and its solid solutions are interesting in view of the strong interrelation of the crystal structure with magnetic and electrical properties, which is possible only under the condition of suppression of the spatially modulated magnetic (spin) structure of the cycloid type, characteristic of $BiFeO_3$. This can be achieved by deforming the crystal lattice due to the replacement of Bi by *REE* [3], which in recent years has been the subject of research by many world scientific schools.

However, despite the rapid dynamics of the publication activity of recent years concerning the mentioned media, there are practically no systematic detailed studies devoted to the establishment of correlation relations "the composition and the thermodynamic background (the conditions of preparation)—the crystal structure (phase diagrams of equilibria)—the microstructure (the grain landscape)—the electro/thermophysical properties". In connection with this, it seems relevant to fill this gap in the paper, which is devoted to the consideration of the effects of modifying ferrite of bismuth REE.

23.2 Objects and Methods

Ceramic solid solutions based on bismuth ferrite corresponding to the formula $Bi_{1-x}REE_xFeO_3$, conventionally divided into two groups, as a function of the ionic radius, *R*, *REE*: coarse grain (1st group) with 0.94 Å < *R* < 1.04 Å for La, Pr, Nd, Sm, Eu, Gd; medium and fine grain (2nd group) with *R* < 0.94 Å for Tb, Du, Ho, Er, Tu, Yb, Lu.

Samples obtained by two-stage solid-phase synthesis followed by sintering by conventional ceramic technology.

X-ray study of the objects was held by powder diffraction method using a DRON-3 diffractometer (CoKα-radiation, Bragg-Brentano focusing scheme). X-ray spectra smoothing algorithm and the corresponding software, used in the article, were contributed by A.P. Kovtun [4]. Symmetry and parameters of perovskite cell (for the convenience of the structural characteristics of the various phases comparison); microstrains; X-ray, experimental and relative densities of ceramics were calculated. Cell parameters were calculated by the standard technique [5]. Microstrains were calculated analytically by approximation of the two X-ray lines 100 and 200, which represent two different orders of reflection from a plane [6]. Microstrain $\Delta d/d$ calculations were conducted only in the R_h phase up to $x = 0.13$, at higher *x* line broadening is largely due to different phase reflections overlapping.

Experimental (ρ_{exp}) density of the samples was measured by hydrostatic weighing in octane; X-ray density (ρ_{XRD}) was calculated according to the formula: $\rho_{XRD} = 1.66 \times M/V$, where M is the weight of formula unit in grams; the relative density (ρ_{rel}) was calculated by the formula (ρ_{exp}/ρ_{XRD}) × 100%.

Investigation of polycrystalline (grain) structure of the samples was performed in reflected light on an optical microscope Neophot 21 and on the inverted high-precision microscope Leica DMI 5000M.

Temperature dependencies of relative dielectric permittivity, $\varepsilon/\varepsilon_0$, at frequencies $25 - 2 \times 10^6$ Hz were investigated in the range 300–900 K at the special setup with use of precision LCR meter Agilent E4980A. Thermal conductivity (λ) and thermal diffusivity (χ) were measured at the facility LFA-457 "MicroFlash" (NEZSCH), a heat capacity (C_p) was defined by means of the differential scanning calorimeter DSC-204 F1 (NEZSCH).

23.3 Results and Discussion

Figure 23.1a–f shows the dependencies of the structural characteristics and densities of the objects of the 1st group on the content (x) of the modifiers. It is clearly seen that in all cases, the state diagrams contain five concentration regions corresponding to the successive structural transformations $R_h \rightarrow R_h + R_1 \rightarrow R_h + R_2 + R_2$ with small variations of the phase filling, and Fig. 23.2 illustrates the dependence of the position of the existence boundaries of the pure R_h phase, its mixture with the R_1 and R_2 phases, the differences between R_{Bi} and R_{REE}, $V_{exp.}$ and $V_{theor.}$ from the radius R of *REE*.

The stabilization of the R_h phase upon the introduction of La, Pr, Nd (with $R \geq 0.99$ Å) is probably related to the creation of the most favorable (dimensional) conditions for the existence of $BiFeO_3$, as is known [5], the boundary position in the perovskite family. At lower R, the shift of the R_h boundary toward lower *REE* concentrations is obviously a consequence of a significant deviation of the conditions from the substitution needed for the formation of the solid solution (ΔR should be less than 15%). The latter is associated with the loss of stability of the coexistence region of *REE* and $R_{1,2}$-phases due to greater instability of the structure of multiphase TP compared with single-phase ones.

The reasonableness of the above assumption is confirmed by the behavior of the value of ΔV (Fig. 23.2a), which characterizes the structural non-stoichiometry of the $BiFeO_3$ compound with the valence ion ($Fe^{3+} \leftrightarrow Fe^{2+}$) and, as a consequence, the vacancy-saturated one, in which the defect situation is excluded by the crystallographic shift with development anionic and A-deficiency. At low *REE*-contents (Fig. 23.2b–d), their effect is minimal, and $\Delta V_{0.05}$ against the backdrop of an appreciable spread of ΔV values practically does not depend on R of *REE*.

For large x in the region with $R > 0.99$ Å, ΔV varies little, contributing to the stabilization of the R_h phase, and at $R < 0.99$ Å in the case of $x = 0.10$, $\Delta V_{0.10}$ naturally increases with decreasing R, destabilizing R_h and $R_h + R_{1,2}$ phases; in the

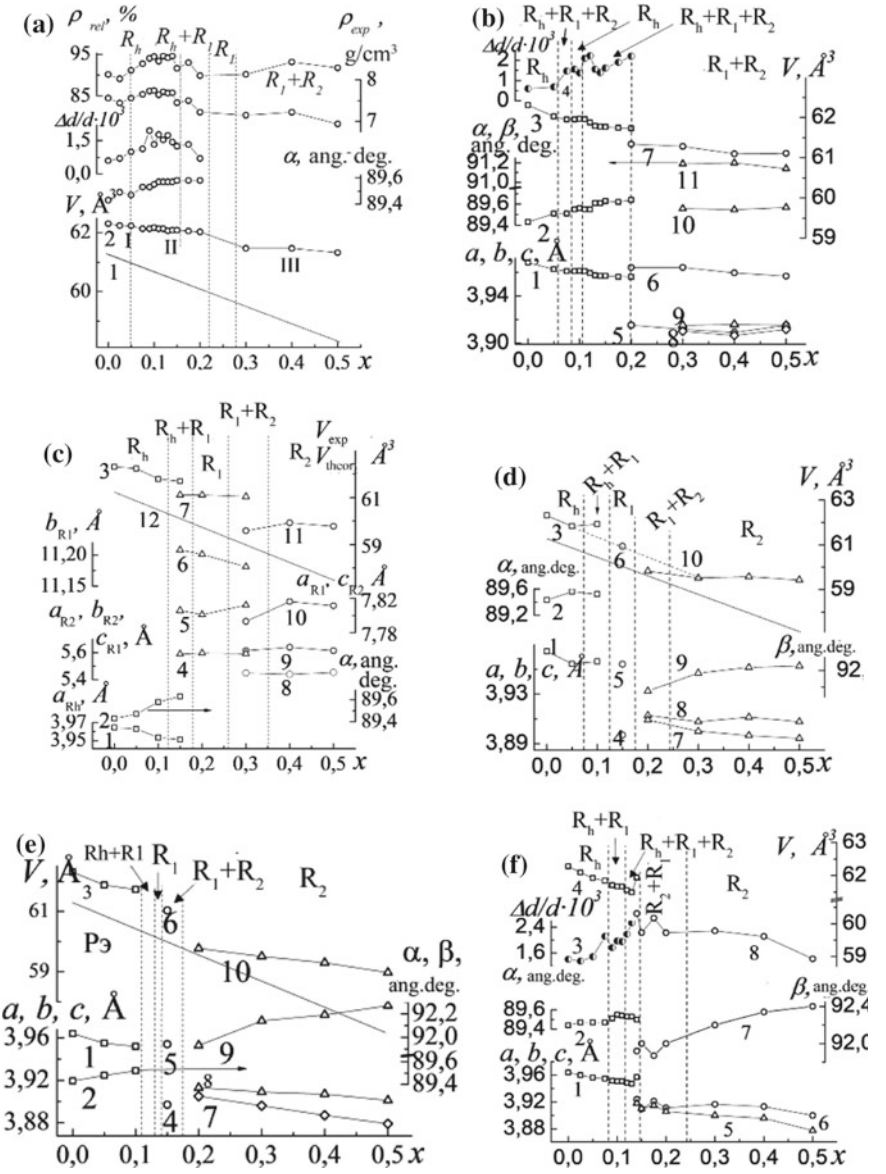
(a)
(b)
(c)
(d)
(e)
(f)
x

◂**Fig. 23.1** Dependences of the structural characteristics and densities of bismuth ferrite with La (**a**), Pr (**b**), Nd (**c**), Sm (**d**), Eu (**e**), Gd (**f**) on the concentration (x) of the modifier. Curves designations: **a** 1-theoretical, 2-experimental volumes of the perovskite cell; **b** 1, 2, 3—a, α parameters and V of R_h cell; 5, 6, 7—a, c parameters and V of pseudotetragonal cell (R_1 phase); 8, 9, 10, 11—b, a, β parameters and V of monoclinic cell (R_2 phase); 4—microstrain, $\Delta d/d$, respectively; **c** 1, 2, 3—a, α parameters and V of R_h cell; 4, 5, 6—c, a, b parameters of R_1 phase; 7—V of R_1 phase; 8, 9, 10, 11—a, b, c parameters and V of R_2 phase; 12—$V_{theor.}$ of perovskite cell, respectively; **d** 1, 2, 3—a, α parameters and V of R_h cell; 4, 5, 6—c, α parameters and V of R_1 cell; 7, 8, 9, 10—b, a, β parameters and V of R_2 cell, respectively; **e** a, α parameters and V of R_1 cell; 4, 5, 6—c, α parameters and V of R_1 cell; 7, 8, 9, 10—b, a, β parameters and V of R_2 cell, respectively; **f** 1, 2, 4—a, α parameters and V of R_h cell; 5, 6, 7, 8—b, a, β parameters and V of R_1 cell; 3—$\Delta d/d$, respectively. Straight lines without experimental points—dependence $V_{theor.}$ (x), calculated for substitution solid solutions in A-positions

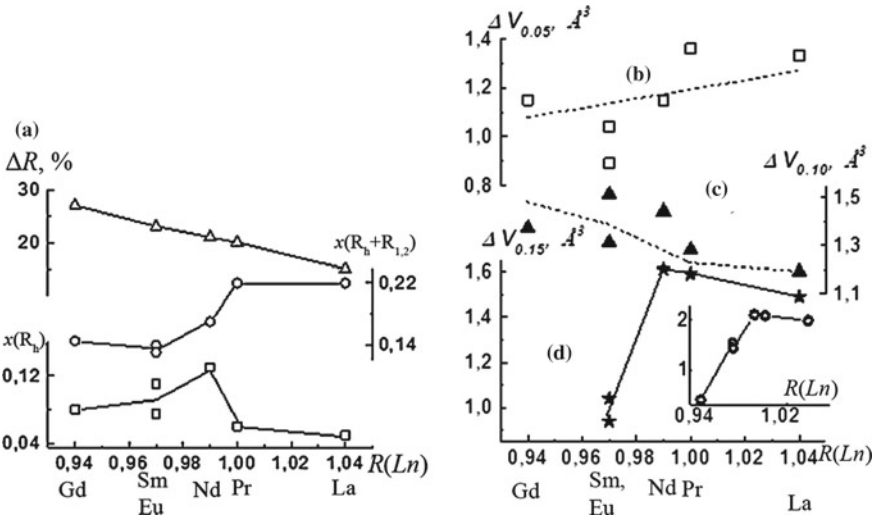

Fig. 23.2 **a** Dependence of the position (x) of the boundary of pure R_h phase existence, its mixture with $R_{1,2}$ phases, the relative difference between R_{Bi} and R_{REE} according to the radius, R, of *REE*; **b**–**d** dependence of the difference between $V_{exp.}$ and $V_{theor.}$ on the R in solid solutions with $x = 0.05$ (**b**); 0.10 (**c**); 0.15 (**d**)

case of $x = 0.15$, the decrease in structural nonstoichiometry is apparently due not so much to dimensional effects as to the specificity of other crystallographic characteristics of the *REE*s being introduced.

In the second group of the solid solutions, the R_h phase inherent in $BiFeO_3$ either remains in the whole range of REE concentrations (Ho, Tm, Yb, Lu) or coexists with the emerging R phase (Tb, Dy, Er). Such a simplification of phase pictures is due to the presence of a large number of Bi- and Fe-containing impurities, usually associated with the formation of $BiFeO_3$, and the ballast phases of the non-perovskite structure with the participation of *REE*, the number of which increases as the R of *REE* decreases, as is clearly seen in Fig. 23.3 with microphotographs of the

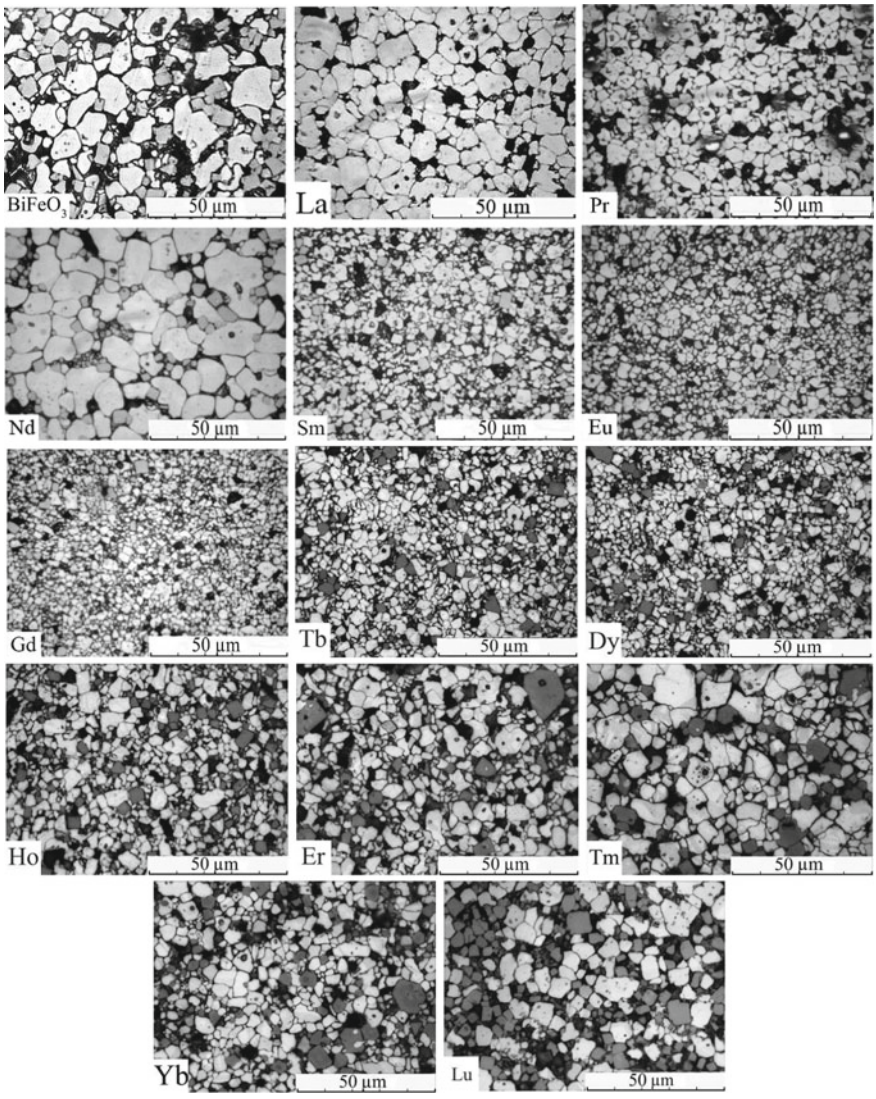

Fig. 23.3 Fragments of microstructures of $BiFeO_3$ and $B_{1-x}REE_xFeO_3$ ($x = 0.10$) ceramics

grain structures of the studied objects. Accumulation of such phases ("gray" grains) in the series La → Lu leads to loosening of the microstructure, thickening of the boundaries of crystallites, deformation of the grains of the main phase.

Figure 23.4 shows the dependences $\varepsilon'/\varepsilon_0(T)$, $\varepsilon''/\varepsilon_0(T)$, $\tan\delta(T)$ at different frequencies of the alternating electric field. The results show that in $BiFeO_3$ all large-sized REEs and some small-sized relaxation peaks $\varepsilon'/\varepsilon_0$ in the vicinity (400–450) K and the frequency-dependent maximum $\tan\delta$ near 600 K forms in

$BiFeO_3$, the position of the latter is shifted towards low temperatures as the $BiFeO_3$ enrichment is introduced by *REE*. With small-sized *REE*, the first maximum is localized near (550–600) K, the second maximum at (750–800) K.

To describe the process of low-temperature dielectric relaxation from the data obtained from the dependences $\varepsilon'/\varepsilon_0(\omega)$, the plots $\ln\omega(1/T_m)$, (where T_m is the extremum temperature for $\varepsilon'/\varepsilon_0$ measured at the frequency $f = \omega/2\pi$) were constructed. The obtained dependences satisfy the Arrhenius law with the activation energy, E_a, close to 1 eV (in $BiFeO_3$ $E_a = 1.007$ eV) and the mean time to

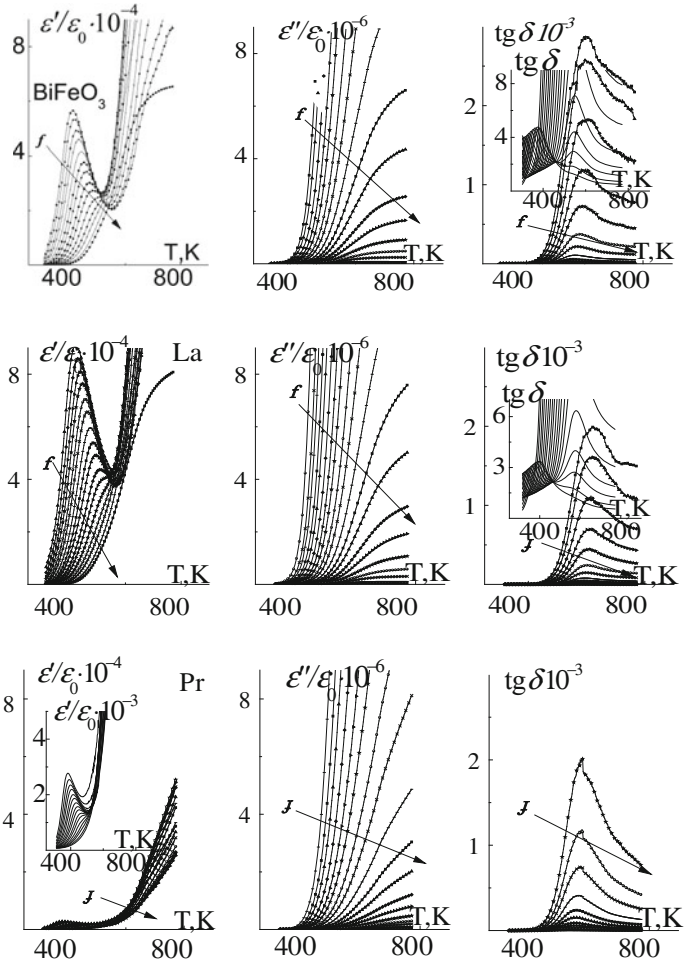

Fig. 23.4 Dependences of $\varepsilon'/\varepsilon_0(T)$, $\varepsilon''/\varepsilon_0(T)$, $\tan\delta(T)$ for $BiFeO_3$ and $Bi_{0.9}REE_{0.1}FeO_3$, at different frequencies of the ac electric field in the range of $25 - 1.5 \times 10^6$ Hz

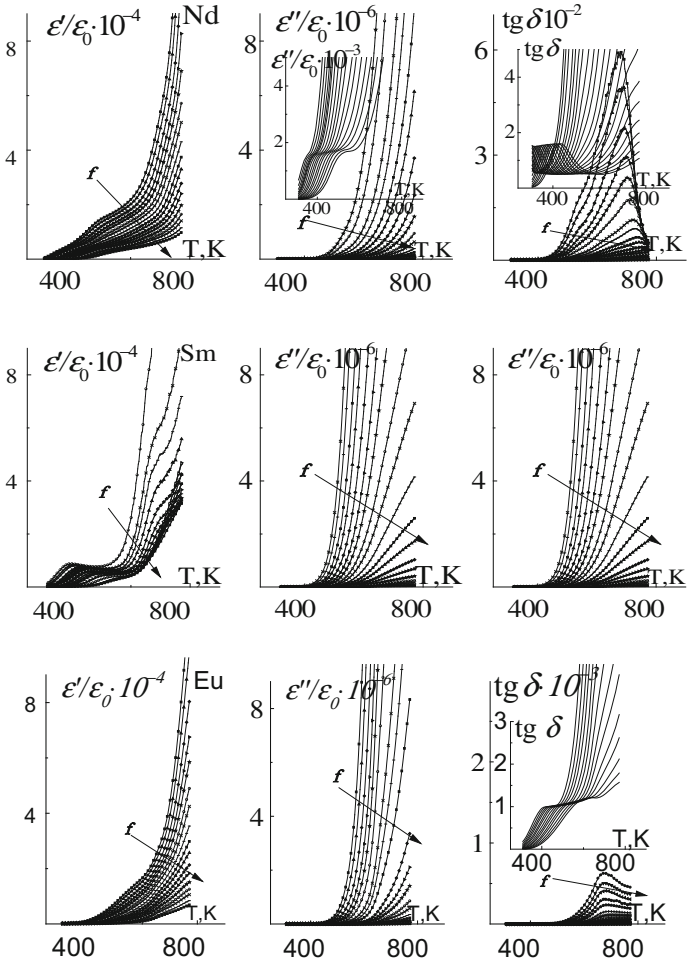

Fig. 23.4 (continued)

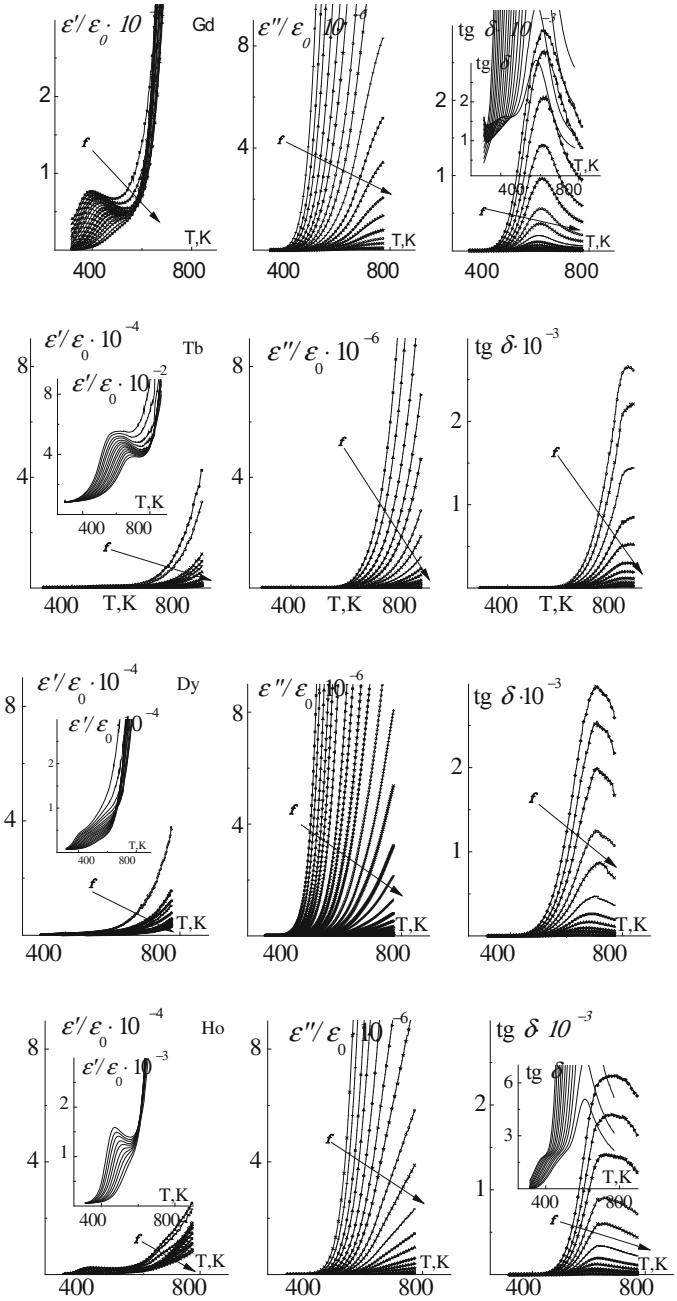

Fig. 23.4 (continued)

overcome the potential barrier is about 1.06×10^{-16} s, which is characteristic of Maxwell-Wagner relaxation [7] associated with accumulation of free charges on the interface of components in spatially inhomogeneous media against the background of interlayer, interphase and intraphase rearrangements. The reason for its development is the natural composite structure of $BiFeO_3$ and $BiFeO_3$/*REE*, which forms on the base of at least four (apart from sa $BiFeO_3$) Bi-, Fe-containing compounds (Bi_2O_3, Fe_2O_3, $Bi_{25}FeO_{40}$, $Bi_2Fe_4O_9$), almost always accompanying the formation of $BiFeO_3$, remaining in it (in different amounts) in the form of ballast phases and undergoing a series of bifurcations in the above-mentioned temperature ranges (Fig. 23.5).

Dependencies of thermal characteristics of all studied objects on temperature are present in Fig. 23.6. It is seen that the behavior of the characteristics is extremal in the vicinity of a temperature of about 640 K [8, 9], which belongs to the antiferromagnetic transition region [2]. An analysis of the data obtained allows us to conclude that T_N does not undergo significant shift at the changes of concentrations and type of *REE* that replace Bi.

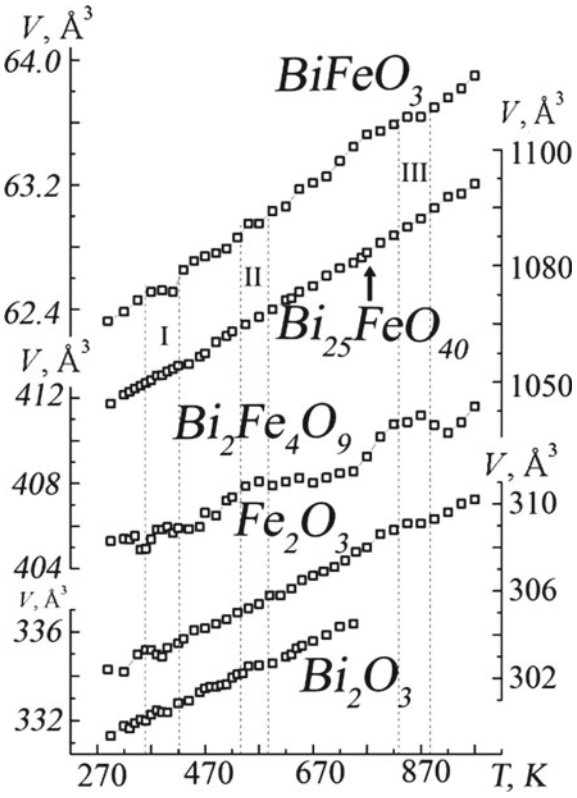

Fig. 23.5 Dependences of the volumes of unit cells of component compounds of the natural-composite structure of $BiFeO_3$ (I-III—invar effect regions)

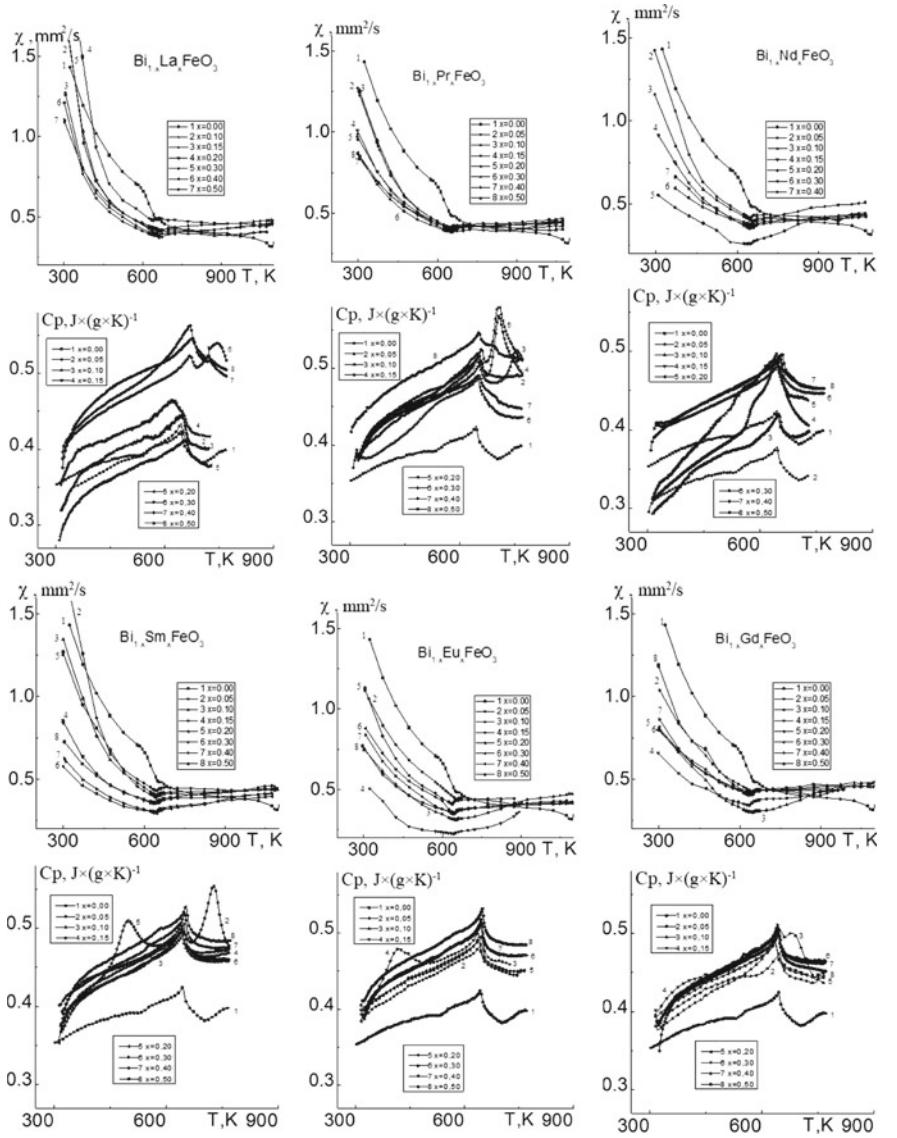

Fig. 23.6 Dependences of C_p, χ, λ of $Bi_{1-x}REE_xFeO_3$ ceramic solid solutions on temperature

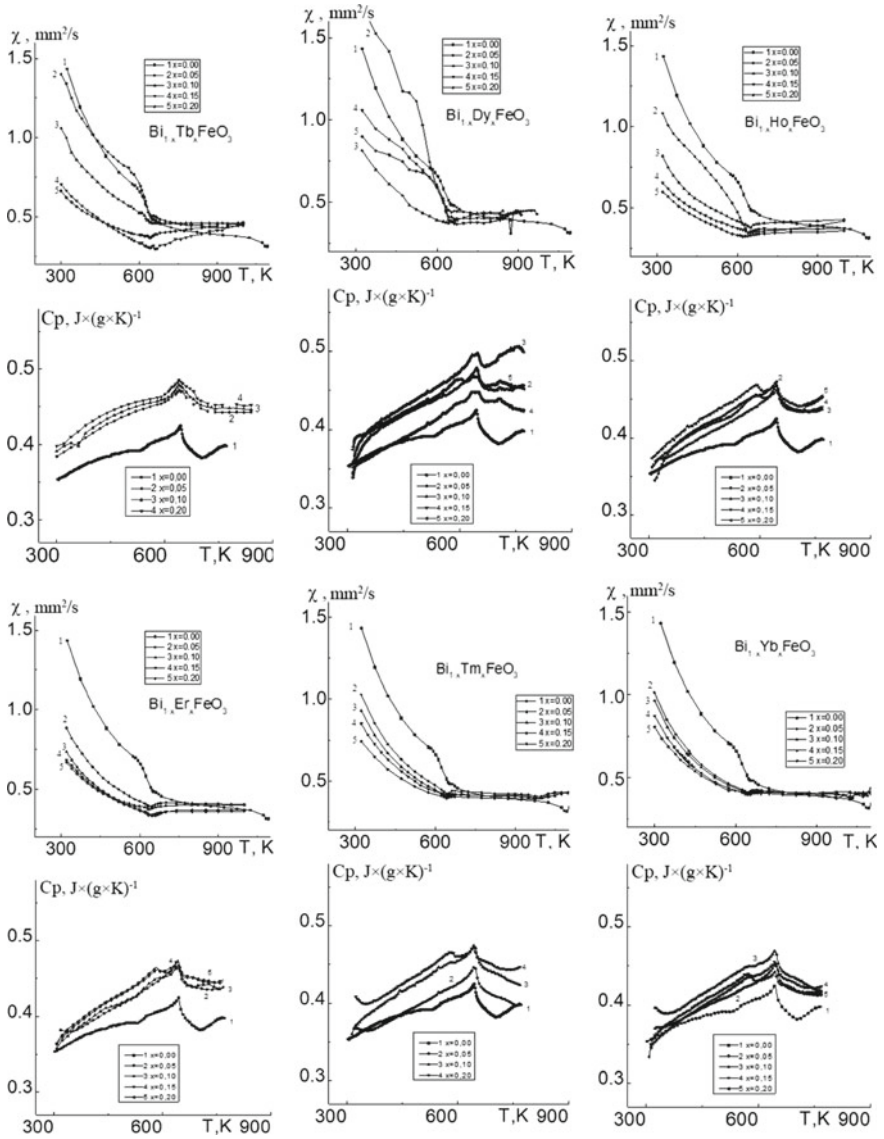

Fig. 23.6 (continued)

23.4 Conclusion

In the result of the studies carried out, it was established that during the synthesis of all the investigated solid solutions impurity phases $Bi_2Fe_4O_9$ and $Bi_{25}FeO_{40}$ are formed, the number of which increases with increasing x. In all solid solutions,

volume of the unit cell decreases with an increase in the amount of *REE*, which corresponds to the logic of decreasing the mean radius of the *A*-cation.

A feature of the dispersion maxima $\varepsilon/\varepsilon_0$ of the studied objects is a shift to the high-temperature region, a decrease and blurring of their peak values with increasing frequency, which is characteristic of Maxwell-Wagner relaxation. It is shown that T_N in the studied objects does not undergo significant displacement when the type of *REE* and its concentration change.

The results obtained in this paper should be taken into account when creating a new generation of multifunctional materials (combining ferroelectric, magnetic and ferroelastic properties), capable of finding promising applications in such areas as sensory technology, diagnostics, processing and storage of information and many others.

Acknowledgements This work was financially supported by the Ministry of Education and Science of the Russian Federation: Agreement No. 14.575.21.0007 (Federal Target Program); themes Nos. 1927, 213.01-2014/012-VG and 3.1246.2014/K (the basic and project parts of the State task).

The dielectric spectroscopy measurements were performed using the equipment of the Shared Research Facility Centre of Research Institute of Physics, Southern Federal University.

References

1. A.K. Zvezdin, A.P. Pyatakov, Phys. Usp. **47**, 416–421 (2004)
2. G.A. Smolenskii, I.E. Chupis, Sov. Phys. Usp. **25**, 415–448 (1982)
3. A.V. Zalesskiĭ, A.A. Frolov, T.A. Khimich, A.A. Bush, Phys. Solid State **45**, 141–145 (2003)
4. S.P. Zinchenko, A.P. Kovtun, G.N. Tolmachev, Technical Physics. The Russian J. Appl. Phys. **54**, 1689–1694 (2009)
5. E.G. Fesenko, *Perovskite Family and Ferroelectricity* (Atomizdat, Moscow, 1972)
6. V.P. Nagornov, Analytical determination of the parameters of the substructure of the deformed polycrystalline X-ray method of approximation using Cauchy functions, "Engineering". Apparatus and methods for X-ray analysis, Leningrad (1982)
7. A.V. Turik, G.S. Radchenko, Phys. Solid State **45**, 1060–1064 (2003)
8. A.A. Amirov, A.B. Batdalov, S.N. Kallaev, Z.M. Omarov, I.A. Verbenko, O.N. Razumovskaya, L.A. Reznichenko, L.A. Shilkina, Phys. Solid State **51**, 1189–1192 (2009)
9. S.N. Kallaev, A.G. Bakmaev, L.A. Reznichenko, JETP Lett. **97**, 470–472 (2013)

Chapter 24
Investigation of Micro-arc Discharge in Deep Sea Water at High Pressure

Vladislav Gamaleev, Hiroshi Furuta and Akimitsu Hatta

Abstract In this work, micro-arc discharges generated in sea water at high pressure were investigated. For generation of micro-arc discharges, electrodes were introduced into a high-pressure chamber and a current pulse was supplied to the electrodes by a custom pulse current source. By using pin-to-pin electrodes system, micro-arc discharges were successfully generated in highly conductive sea water at high pressure up to 17.5 MPa for the first time. Analysis of current and voltage waveforms showed that micro-arc discharge process at high pressure was same to the atmospheric pressure case and could be divided into three phases: pre-heating, micro-arc discharge and subsequent oscillation. A difference to atmospheric pressure was increase of power consumption during pre-heating phase with increase of pressure. Use of pin-to-pin electrode system with insulation of sides allowed us to generate micro-arc discharges with relatively low energy even at high pressure due to concentration of strong electric field between the electrodes in a small volume. Repetition number of reproducible discharges using the same electrodes was limited below 30 due to erosion of the electrodes caused by a high current during the discharge. A rod-to-rod electrode system consisting of two parallel metal rods aligned with a small gap was developed instead. In the case of rod-to-rod electrode system, due to increase of the surface of the facing electrodes, local erosion caused by high current did not have significant impact on the reproducibility of the discharges while the energy consumption increased by 33% compared to the pin-to-pin electrode system owing to increased volume between the electrodes in the gap. By using the rod-to-rod electrode system, it was succeeded to generate reproducible micro-arcs at high pressures up to 17.5 MPa. Repetition number was increased to more than 100 owing to improved durability of the electrodes.

V. Gamaleev (✉) · H. Furuta · A. Hatta
Department of Electronic and Photonic Systems Engineering,
Kochi University of Technology, Kami, Kochi 782-8502, Japan
e-mail: vlad.gamaleev@gmail.com

H. Furuta · A. Hatta
Center for Nanotechnology, Research Institute of KUT,
Kochi University of Technology, Kami, Kochi 782-8502, Japan

I. A. Parinov et al. (eds.), *Advanced Materials*, Springer Proceedings
in Physics 224, https://doi.org/10.1007/978-3-030-19894-7_24

24.1 Introduction

Currently, there is continuous contamination of available water resources by industry and agriculture, which makes pollution control and ecological monitoring necessary for saving water resources [1–3]. On the other hand, marine resources are taking growing role in the sustainable development of industry. With the growing needs in industrial resources, there is significant interest in new sources of materials that can meet the growing demands of the industry. The problem of limited resources available for industry can be solved partially by use of marine resources and underwater deposits [4, 5]. In both cases, for the exploration of marine resources and ecological monitoring, a high precision analysis of sea water is required. There are many methods of determining the composition of sea water, such as inductively coupled plasma (ICP) mass spectroscopy of sprayed liquid and optical absorption spectroscopy of examined liquid. However, most of these methods are operated in laboratory conditions and require sampling of water and transport of the samples. The necessity of sampling makes elemental composition analysis of deep sea water complicated and as result costly [6–10]. Most perspective way to solve mentioned problem is development of compact diagnostic tools which can provide on-site elemental composition analysis and contaminants detection. One of the promising methods of on-site identification of elemental composition of water is a spectral analysis of different types of plasmas generated in examined liquid [11–17]. By considering high pressure in deep sea, use of micro-arc discharges looks promising for analysis of elemental composition of deep sea water owing to increase of optical emission intensity from the arc with increase of pressure [18]. Recent research shows that it is possible to generate micro-arc directly in highly conductive sea water at atmospheric pressure; moreover, optical emission spectroscopy of micro-arc discharges was successfully applied to detection of Fe contaminants in sea water [3, 17, 19]. However, there is no research on generation of micro-arc discharges in highly conductive deep sea water at high pressure being conducted. For that reason, it is necessary to check possibility of generation of micro-arc discharges in such a condition and perform analysis of the discharge process, which could be used in development of compact diagnostic tools for on-site analysis of deep sea water and contaminants detection.

In this study, we successfully generated micro-arc discharges in highly conductive artificial sea water at high pressure using two types of electrodes and analyzed effect of pressure on generation of the discharge.

24.2 Experimental Setup

For the experiments, artificial sea water composed of 10 typical components (10ASW) was used. The chemical composition of 10ASW is shown in Table 24.1, the electrical conductivity of 10ASW was 45.1 mS/cm (at 20.3 °C).

Table 24.1 Elemental composition of 10ASW in grams for 1 kg of water

Ingredient	Mass (g)
NaCl	23,939
$MgCl_2 + 6H_2O$	10,849
Na_2SO_4	3.994
$CaCl_2$	1.123
KCl	0.667
$NaHCO_3$	0.196
KBr	0.098
H_3BO_3	0.027
$SrCl_2 + H_2O$	0.004
NaF	0.003

A schematic of the experimental setup is present in Fig. 24.1. High pressure chamber was filled with 10ASW, pressure was sustained by high pressure pump (Dual pump KP 22) and controlled by valve in a range of 0.1–17.5 MPa. Discharges were operated using two types of electrodes, which were introduced inside the chamber and connected to a custom-made pulse current source. The pulse current source, consisting of a capacitor (C = 440, 660 nF), inductor (L = 67, 100, 150 μH) and MOSFET switch was used to supply the discharge. The capacitor was charged by a regulated DC power supply through a resistor to resulting voltage of

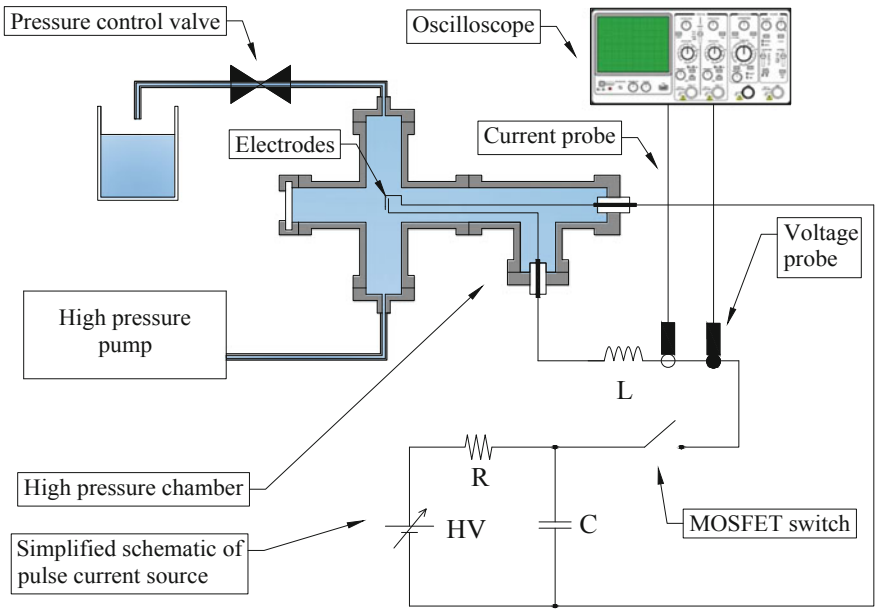

Fig. 24.1 Experimental setup for generation of micro-arc discharges at high pressure

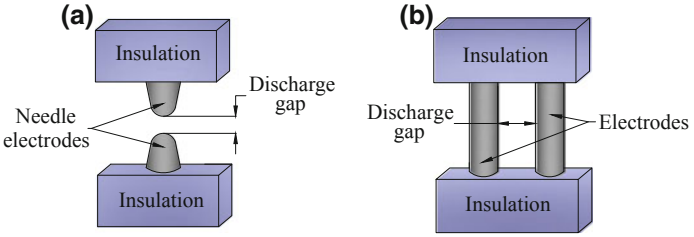

Fig. 24.2 Schematic of **a** pin-to-pin and **b** rod-to-rod electrode systems

650–750 V. During the discharge, the MOSFET switch was closed, in order to apply a current pulse to the gap between the electrodes. Current and voltage waveforms of the pulse were dependent on the parameters of C, L and the resistance (R) of the 10ASW between the electrodes. The pulse current source was manually operated using a single trigger, the MOSFET switch was kept closed for 500 μs to completely cover all discharge processes. Furthermore, to prevent excessive heating of water in the micro-gap and keep temperature same before each discharge, sufficient intervals (for more than 30 s) between the discharges were applied.

Schematics of two electrode systems used in experiments are present in Fig. 24.2. In the case of pin-to-pin electrode system (Fig. 24.2a), two needle electrodes (NPS Inc. P26-10-20 × 1″) were faced to each other with a fixed gap of 150 μm. To reduce current through the surrounding liquid, sides of the needle electrodes were insulated with polytetrafluoroethylene spray and torr seal, in result only the tips of 0.3 mm in length remained open. In the case of rod-to-rod electrodes (Fig. 24.2b), two parallel pieces of stainless-steel wire (Nilaco Company SUS304, 0.5 mm in diameter) were placed with the gap of 150 μm. To avoid current through the surrounding liquid, electrodes were insulated as shown in Fig. 24.2b, resulting in 1 mm length of open part of the wire.

The voltage and current waveforms were stored in a digital oscilloscope using a high voltage probe and a current probe (IWATSU SS 281). The maximum voltage and current for this setup were 800 V and 25 A, respectively.

24.3 Results and Discussion

24.3.1 Generation of Micro-arc Discharge Using Pin-to-Pin Electrodes

Voltage waveforms for micro-arc discharges generated in 10ASW using 150 μH inductor, 440 nF capacitor charged to voltages in a range of 650–800 V and various pressure in a range from atmospheric (0.1 MPa) to 17.5 MPa are shown in Fig. 24.3.

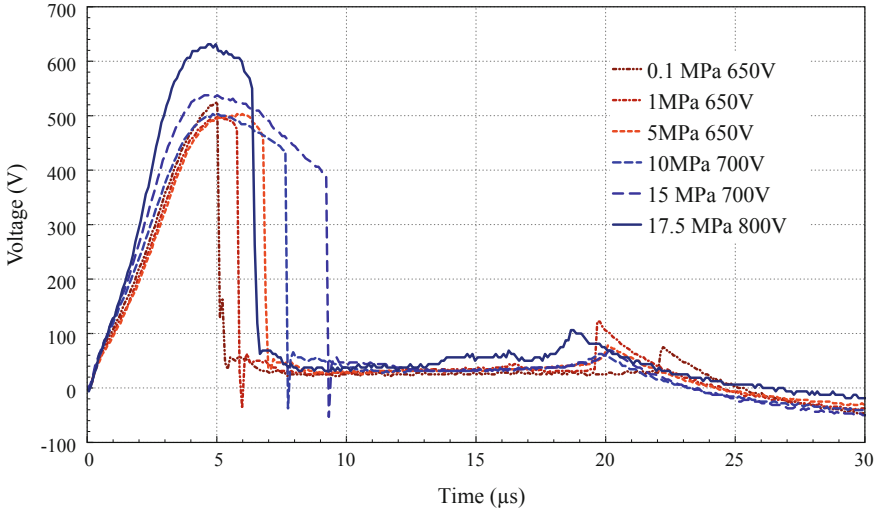

Fig. 24.3 Voltage waveforms for micro-arc discharges generated using 150 μH inductor, 440 nF capacitor and various values of charging voltage of capacitor and pressure

By using the pin-to-pin electrode system, micro-arc discharges were successfully generated in highly conductive sea water even at high pressures up to 17.5 MPa, which was equal to 1.75 km in depth, for the first time. It could be observed that discharge process for the case of high pressure follows the same scheme as for the atmospheric pressure case: pre-heating phase, micro-arc discharge and subsequent oscillation. Detailed information about generation of micro-arc discharge in highly conductive sea water at atmospheric pressure and the discharge process could be found elsewhere [3, 17, 19]. From voltage waveforms, it could be observed that micro-arc discharges could be generated in a range of pressure from 0.1 to 5 MPa using the capacitor charged to 650 V. However, increase of pressure results in increase of duration of pre-heating phase from 5 μs for atmospheric pressure to 7 μs for 5 MPa. Moreover, for generation of micro-arc discharge at higher pressure, it was necessary to charge the capacitor to 700 V for 10–15 MPa cases and to 800 V for 17.5 MPa case. It confirms that the pre-heating phase is having the key role in the discharge process at high pressures, in the similar way as for the atmospheric pressure case [3, 17, 19].

These results clearly show that for generation of micro-arc discharge at high pressure it was necessary to deliver more energy during pre-heating phase. By using the pin-to-pin electrode system, it has been found that the pre-heating energy depended on the pressure, however, it was difficult to perform statistical measurements due to erosion of the electrodes. Erosion of the needle electrodes resulted in increase of the discharge gap length, which limited number of discharges possible to generate using the same electrodes to 20–30, depending on the conditions.

24.3.2 *Generation of Micro-arc Discharge Using Rod-to-Rod Electrodes*

The problem of erosion of needle electrodes could be solved using the rod-to-rod electrode system, as it shown In Fig. 24.2b. Two-rod electrodes were placed parallel with micro-gap and discharge was generated in the gap. Usage of the rod-to-rod electrode system significantly increases the facing surface of the electrodes in the gap, which allows one to compensate damage caused by erosion due to high current during the discharge. Even if a part of the electrode locally damaged by the arc, the discharge gap length remained same owing to configuration feature. The next discharge generated in another place of the discharge gap, where electrodes remained not damaged. Moreover, due to larger size of the electrodes, comparing to the pin-to-pin case, heat transfer from the electrode surface to the bulk reduced damage caused by the high current. In the case of rod-to-rod electrode system, volume of the discharge gap was increased significantly comparing to the pin-to-pin electrodes with resulting in increase of energy required for pre-heating phase. To generate reproducible discharges at high pressure up to 17.5 MPa using the rod-to-rod electrode system, it was necessary to use 660 nF capacitor, which was 33% larger than that in the pin-to-pin electrodes case, charged to 750 V.

Current and voltage waveforms for three discharges generated in 10ASW at 17.5 MPa pressure using 150 μH inductor and 660 nF capacitor charged to 750 V are shown in Fig. 24.4. Rod-to-rod electrode system allowed us to generate reproducible micro-arc discharges even at high pressure up to 17.5 MPa, which is

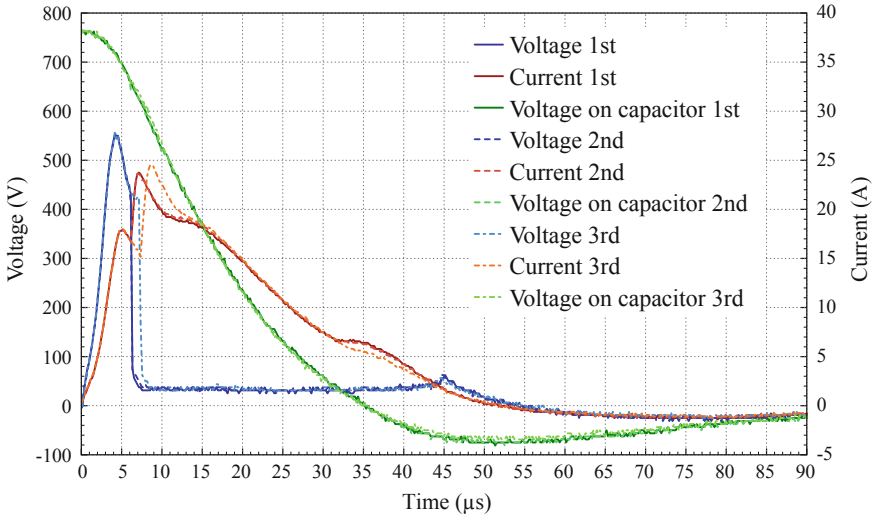

Fig. 24.4 Current and voltage waveforms for three micro-arc discharges generated in 10ASW at 17.5 MPa pressure using 150 μH inductor and 660 nF capacitor charged to 750 V

equal to 1.75 km depth. However, insignificant difference in duration of pre-heating phase could be observed. Possible reasons for that difference are fluctuations in bubble formation process and dynamics of the bubbles in the discharge gap.

Despite insignificant difference in duration of pre-heating phase, waveform of voltage on capacitor (which represents amount of energy stored in the capacitor) was same for all three presented discharges, which shows that small difference in duration of pre-heating phase has not significant effect on amount of energy stored in capacitor. Considering that in all three discharges the same energy remained for the micro-arc discharge phase, it could be concluded that mentioned variation of duration of pre-heating phase will not have significant effect on the optical emission spectrum of the plasma, which could be essential for analysis of composition of deep sea water using OES of microplasma.

In both cases, for pin-to-pin and rod-to-rod electrode systems, it was possible to generate micro-arc discharges in highly conductive sea water using small amounts of energy (below 200 mJ). Despite increase of power consumption with increase of pressure, power consumption for generation of micro-arcs in sea water at high pressure was relatively small, which looks promising for development of compact analytical tools for on-site measurements in deep sea. For generation of reproducible discharges with reduced power consumption, further improvements in electrode system and discharge circuit are required.

24.4 Conclusions

We investigated micro-arc discharges generated in highly conductive sea water at high pressure up to 17.5 MPa for the first time. For generation of micro-arc discharges, electrodes were introduced inside high-pressure chamber and discharges was generated using the custom made pulse current source. Using pin-to-pin electrodes system, micro-arc discharges were successfully generated in highly conductive sea water at high pressure up to 17.5 MPa. Analysis of current and voltage waveform revealed that process of generation of micro-arc discharge at higher pressure is same as that of the atmospheric pressure case and the phenomenon can be divided into three phases: pre-heating, micro-arc discharge and subsequent oscillation. The energy consumption on pre-heating phase increased with increase of pressure. By using the pin-to-pin electrode system, micro-arc discharge can be generated with a small amount of energy even at high pressures due to the strong electric field between the electrodes and the small volume of water in the discharge gap. Due to the erosion of electrodes was caused by the high current during the discharge. However, number of reproducible discharges generated using the same electrodes was limited below 30 times. The erosion was suppressed by using the developed rod-to-rod electrode system. In the case of rod-to-rod electrode system, due to increase of the surface of the electrodes, erosion caused by high current did not cause fatal damage while the volume of water in the gap increased with resulting in increase of energy consumption as compared to the

pin-to-pin electrode system. By using the developed rod-to-rod electrode system, it was possible to generate reproducible micro-arc discharges at high pressures up to 17.5 MPa. Moreover, repetition rate was increased to more than 100 times due to improved durability of the electrodes.

Acknowledgements This work was supported by JSPS KAKENHI Grant Number 26600129. The 10ASW was provided from Prof. Kei Okamura of Kochi University.

References

1. W.T. Bu, J. Zheng, T. Aono, J.W. Wu, K. Tagami, S. Uchida, Q.J. Guo, J. Nucl. Radiochem. Sci. **15**, 1 (2015)
2. W. Bu, J. Zheng, Q. Guo, T. Aono, K. Tagami, J. Chromatogr. A **1337**, 171 (2014)
3. V. Gamaleev, H. Furuta, A. Hatta, Jpn. J. Appl. Phys. **57**, 8 (2018)
4. K. Bostrom, H. Kunzendorf, Elsevier Oceanogr. Ser. Elsevier, Amsterdam. **41**, 21 (1986)
5. G.P. Glasby, Mar. Georesources Geotechnol. **20**, 161 (2002)
6. H. Kumagai, M. Yamanaka, T. Sakai, T. Yokoyama, J. Anal. At. Spectrom. **13**, 579 (1998)
7. Z. Wang, A.J. Schwartz, S.J. Ray, G.M. Hieftje, J. Anal. At. Spectrom. **28** (2013)
8. J.M. Lee, E.A. Boyle, Y. Echegoyen-Sanz, J.N. Fitzsimmons, R. Zhang, R.A. Kayser, Anal. Chim. Acta **686**, 93 (2011)
9. J.S. Oh, H. Yajima, K. Hashida, T. Ono, T. Ishijima, I. Serizawa, H. Furuta, A. Hatta, J. Photopolym. Sci. Technol. **29**, 427 (2016)
10. P. Lindahl, M.J. Keith-roach, P.J. Worsfold, Anal. Chim. Acta **671**, 61 (2010)
11. Y. Kohara, Y. Terui, M. Ichikawa, K. Yamamoto, T. Shirasaki, K. Kohda, T. Yamamoto, Y. Takamura, J. Anal. At. Spectrom. **30**, 2125 (2015)
12. Y. Kohara, Y. Terui, M. Ichikawa, T. Shirasaki, K. Yamamoto, T. Yamamoto, Y. Takamura, J. Anal. At. Spectrom. **27**, 1457 (2012)
13. N.H. Tung, M. Chikae, Y. Ukita, P.H. Viet, Y. Takamura, Anal. Chem. **84**, 1210 (2012)
14. A. Kitano, A. Iiduka, T. Yamamoto, Y. Ukita, E. Tamiya, Y. Takamura, Anal. Chem. **83**, 9424 (2011)
15. C.G. Wilson, Y.B. Gianchandani, I.E.E.E. Trans, Electron Devices **49**, 2317 (2002)
16. D. V. Khoai, T. Yamamoto, Y. Ukita, Y. Takamura, Jpn. J. Appl. Phys. **53**, 05FS01 (2014)
17. V. Gamaleev, Y. Okamura, K. Kitamura, Y. Hashimoto, J.-S. Oh, H. Furuta, A. Hatta, Jpn. J. Appl. Phys. **55**, 07LC03 (2016)
18. Y.P. Raizer, *Gas Discharge Physics*, 1st edn. (Springer, Berlin, 1991)
19. V. Gamaleev, J.-S. Oh, H. Furuta, A. Hatta, IEEE Trans. Plasma Sci. **45**, (2017)

Chapter 25
Hydrogen in Materials Obtained Using of Additive Technologies

Y. A. Yakovlev and D. A. Tretyakov

Abstract Mechanical characteristics of constructional materials depend on the presence of structure defects. The accumulation of hydrogen inside constructional materials takes place during widely differing stages of metallurgical production. Presence of hydrogen in materials is always fraught with deep-seated hazard. Due to diffusion, accumulation of the critical concentrations in local areas is possible. Such accumulation leads to formation of flaws and brittle fracture. The paper deals with experimental data determination of hydrogen concentration in alloy 718. Using hydrogen analyzer AV-1, the hydrogen concentrations in a sample of an alloy of metallurgical production and obtained with the help of additive technologies were measured. The processes of hydrogen accumulation in alloy 718 at cathodic charging are also investigated.

25.1 Introduction

One of the most important characteristics of metal casting from which are various mechanisms and machine parts are assembled is hydrogen concentration value. In spite of relatively low content, hydrogen provides strong influence on the mechanical properties of metal. As a rule, the excess of the initial concentration of hydrogen in only twofold brings to serious degradation of mechanical properties [1, 2]. Therefore, taking into account the influence of hydrogen on the mechanical characteristics of structural materials is an extremity important task.

Modern engineering approaches expect the use of materials with extreme mechanical properties. The share of new high-strength materials with extreme properties is increasing every year. For instance, the mass fraction of high-strength steels in the car body is more than 70%. Sensitivity to hydrogen is a feature of all

Y. A. Yakovlev (✉)
Institute for Problems in Mechanical Engineering RAS, Saint-Petersburg, Russia
e-mail: yura.yakovlev@gmail.com

D. A. Tretyakov
Peter the Great Saint-Petersburg Polytechnic University, Saint-Petersburg, Russia

I. A. Parinov et al. (eds.), *Advanced Materials*, Springer Proceedings in Physics 224, https://doi.org/10.1007/978-3-030-19894-7_25

these materials. Due to low initial hydrogen field concentration in high-strength material and a large diffuse activity of hydrogen, the accumulation time of critical concentrations decreases several fold. It is known that under influence of thermos-mechanical strains the diffusion of component alloys increases therefore the rapid increase of local concentration of hydrogen conditioned by as extreme operating conditions as diffusion from external environment. The yield surface of modern high-strength alloys reduced due to significant increase in strength, therefore the plastic flow itself can lead to destruction, and the oxygen influence can make the situation catastrophic due to the reduction of the limits of fatigue, fluidity and strength. Therefore, the hydrogen-induced destruction of high-strength materials proceeds quickly, without a long process of formation and development of main cracks.

The main mechanism of such destruction is the formation of areas of hydrogen embrittlement. Determining the life of the material accurately and diagnosing the condition of the product in such cases is very difficult problem. To provide indestructible diagnostics on spot is just impossible. Unfortunately, existing methods of testing of materials for resistance to hydrogen corrosion and cracking are not always usable for existing constructions that are working under loading. A feature of local hydrogen embrittlement is that it is poorly diagnosed before the time of destruction by standard methods (ultrasound, X-ray, chemical analysis, etc.). The only way to diagnose directly determination of hydrogen is to perform destructive testing. There are not reliable non-destructive methods at present for controlling hydrogen in metals.

Historically, in studies of the influence of hydrogen on the destruction of structural materials, saturation of these materials with hydrogen was used in four ways:

(i) in gaseous hydrogen;
(ii) in acid solution due to corrosion or stress corrosion;
(iii) cathodic hydrogen charging;
(iv) in electrolyte, associated with near-neutral pH.

All these methods are standardized, but because of the high degree of danger of experiments on hydrogen saturation, most often cathodic hydrogen charging is used. Annually dozens of works, devoted to researchers with this method, are published.

In our work, we investigated the distribution of hydrogen concentrations for samples of a nickel 718 alloy by using traditional way and with the help of additive technologies. We conducted experiments to determine the natural hydrogen concentration. The existing equipment allows one to extract and determine with a high accuracy natural hydrogen concentrations in any materials. The process of hydrogen storage in these materials with cathode charging was explored as well.

25.2 Experimental Equipment

The precision hydrogen analyzer AV-1 has been designed for hydrogen detection in metals and alloys under the plant laboratory conditions during the outgoing mouldings control with various alloys [3–6]. The operating principle of the analyzer is mass-spectrometric.

The sample processing, shown in Fig. 25.1, includes a vacuum extractor and a heater. The vacuum extractor is made of quartz glass and has three setoffs. The first setoff contains the samples before the test. The hydrogen content analysis takes place in the second setoff. The samples, which have been tested, are kept in the third setoff.

Before testing, the heater (4) with previously set temperature is placed upon the second setoff of the extractor. With the help of a magnetically push rod the test sample from the first setoff is thrown into the second analytic setoff of the extractor. During the test, the metal sample within the second setoff is subjected to gradual heating up to the extraction temperature. The extraction temperature for the sample is lower than its flowing temperature, as a rule, it is within the range of 400–900 °C. The fumes that have been emitted during heating are evacuated from the extractor before the pressure reaches 50 micro-Pascal and are analyzed with a mass-spectrometer which is located in the vacuum pumping pass customized for the hydrogen line. The end of the testing is identified with the help of background signal. The background signal remains constant from the beginning to the end of the testing. As soon as the level of the signal from the sample becomes equal to the background signal, the test stops and the sample from the analytical setoff 2 is placed into the setoff for the samples, which have been analyzed (3). For this purpose, the heater (4) is lowered down with the help of hoisting gear, and the extractor keeps turning about itself until the sample being tested falls down from setoff 2 into setoff 3 under gravity. After that, the extractor is returned to the original position, and the heater is placed on setoff 2 with the help of hoisting gear. After setting the background hydrogen value the test continues for the next sample from setoff 1. In such manner, the next sample is analyzed without vacuum failure. It should be emphasized, that the extraction temperature does not change during the test. This makes it possible to reach high stability of the background signal.

The time dependence of hydrogen flow $q(t)$ is recorded by the system of digital registration as an extraction curve. Figure 25.2 shows an extraction curve for aluminum alloy AMg-6, which is a simple example to describe.

Time integral from extraction curve (painted grey in Fig. 25.2) in reference to background hydrogen flow is proportional to hydrogen evolved from the sample. The proportionality factor is set during analyzer calibration.

Each peak of the extraction curve can be correlated with its hydrogen binding energy [4].

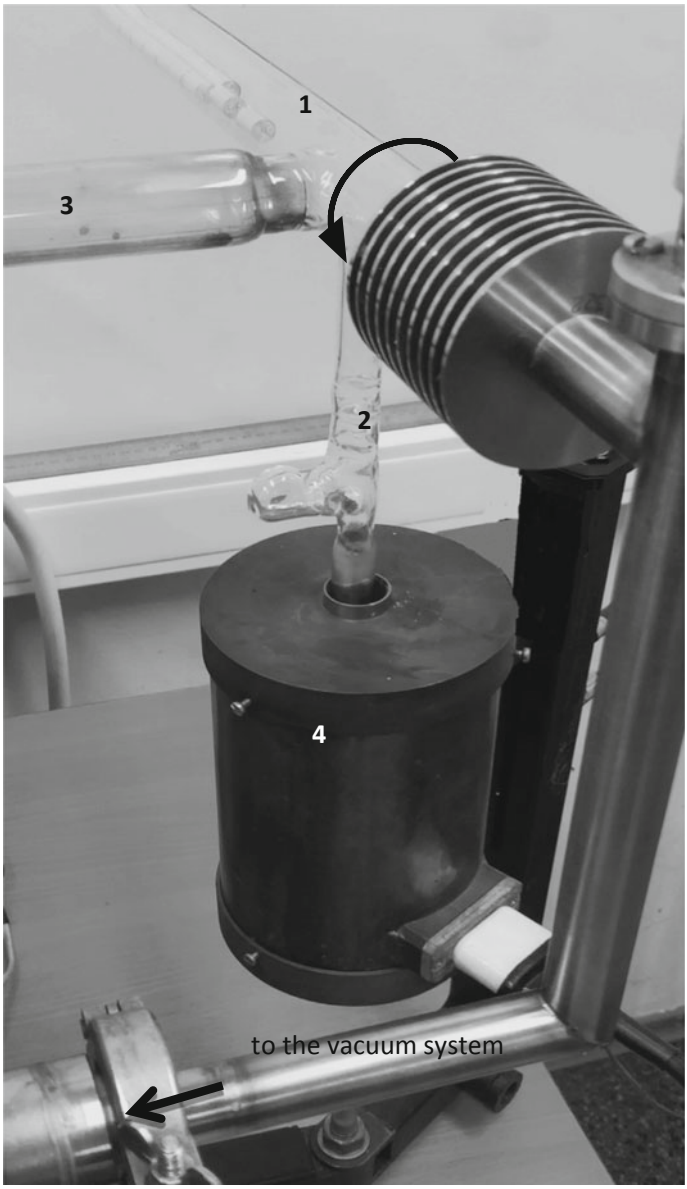

Fig. 25.1 Sample processing of hydrogen analyzer AV-1

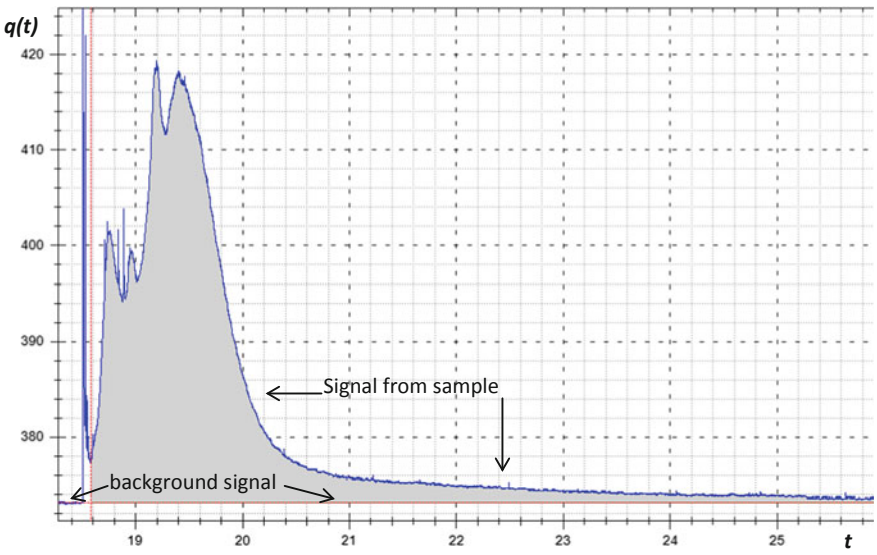

Fig. 25.2 Extraction curve for aluminum alloy AMg-6

25.3 Experimental Data

A series of experiments was conducted with materials obtained with the use of additive technologies. In particular, the high-temperature nickel alloy 718 was investigated. For comparison, samples obtained by metallurgical method and obtained using 3d-printing technology (Fig. 25.3) were studied.

The study of the distribution of hydrogen concentrations was carried out according to the method of discrete thermodesorption spectra [3]. This technique consists in that first extracting hydrogen from the test sample occurs at one temperature, then the sample cools down in a vacuum, and a new extraction temperature is set. After the background hydrogen fluxes are established, the sample is analyzed again. The studies were carried out in the temperature range from 200 to 800 °C in steps of 100 °C. Using this technique, three samples were analyzed:

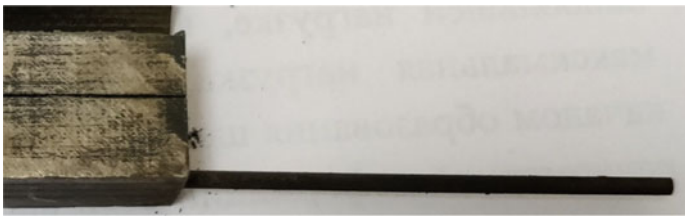

Fig. 25.3 3d-printed samples

(i) the initial sample, obtained by metallurgical method (initial sample); (ii) the sample, obtained by additive technologies (3d) and (iii) the sample, obtained by additive technologies after heat treating at 1038 °C and artificial ageing for 6 h at 782 °C (3d+HT). The result of this study, the hydrogen concentration values were obtained at different extraction temperatures. From the points obtained, the graphs shown in Fig. 25.4 were constructed.

The solid line denotes the specimen obtained by the metallurgical method. The dashed line denotes the specimen obtained using additive techniques. The dotted line denotes the specimen, obtained with the use of additive technologies and after quenching and aging. The analysis of the peaks on the curve (see Fig. 25.4) for the metallurgically produced specimen shows the presence of two energy states of hydrogen inside the metal at 400 °C and at 600 °C. The analysis of the results of studies of thermal-desorption spectra allows us to conclude that the temperature 400 °C is the limit for the first energy state of diffusive-mobile hydrogen, and the temperature 600 °C is the limit for the all diffusively mobile hydrogen. The temperature of 800 °C was chosen to extract the all the hydrogen from the metal. The peak at the extraction temperature of 400 °C refers to hydrogen with a low binding energy, and the peak at 600 °C refers to the strongly bound hydrogen with a higher energy state. The diffusive-mobile hydrogen has a strong influence on the mechanical properties of steels.

Discrete thermo-desorption spectra for specimens pre-saturated with hydrogen by the cathode charging method are shown in Fig. 25.4.

The black line in the graph refers to the initial specimen. The red line refers to the initial specimen after cathodic charging. The green line refers to a specimen obtained with the use of additive technologies after its cathodic charging. The blue

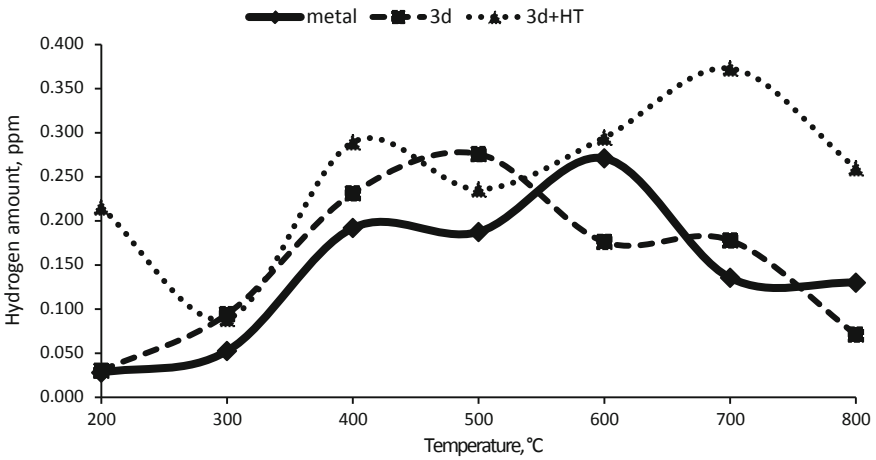

Fig. 25.4 Dependence of hydrogen concentration from extraction temperature for initial sample (solid line), 3d-printed sample (dashed line) and 3d-printed sample after heat treating and artificial ageing (dotted line)

Table 25.1 Resualts of hydrogen charging of samples

Sample	Hydrogen concentration (ppm)
Initial	0.997
Initial + charge	2.246
3d + charge	2.977
3d + HT + charge	4.219

line refers to a specimen, obtained using additive technologies after cathodic charging, hardening and aging.

The significant difference in the distributions is observed only in the region of low extraction temperatures up to 400 °C (see Fig. 25.4). It means that the accumulation of hydrogen occurs in traps with a low binding energy. Note that the specimens obtained with the use of additive technologies accumulate in two times more hydrogen than the metallurgically obtained specimens. Thus, the use of cathodic charging caused the general increase in hydrogen concentrations compared to the initial unsaturated specimen. The total hydrogen concentrations, measured after cathodic charging, are present in Table 25.1.

25.4 Discussion

Comparison of samples, obtained metallurgically (solid line) and using 3d-technologies (dashed line), shows that at approximately the same total hydrogen content of 0.9 and 1.05 ppm, its energy distribution differs significantly. In the sample obtained with the use additive technologies, the peak of diffusive-mobile hydrogen is much larger. It can talk about another internal structure of the material. The accumulation of hydrogen in a diffusely mobile state conceals a hidden danger, since under loading it is possible to accumulate a critical concentration of hydrogen, which will lead to embrittlement. Our data show that to substantially reduce the mechanical properties of the material, it is sufficient to increase the initial concentration of hydrogen by a factor of 2. Unfortunately, such accumulation can occur quickly.

For comparison, Fig. 25.4 shows one more graph for the 3d-sample after heat treatment and artificial ageing, a line of points. This curve is located above the rest, which means that the hydrogen content in the sample is much higher that is 1.8 ppm. In addition, under the influence of thermal loading and aging of the material, the accumulation of hydrogen in the region with low binding energy has begun (see an additional peak in the graph at 200 °C). Apparently, the applied load leads to the formation of additional diffusion channels and hydrogen traps. As a rule, with the “natural” aging of materials, hydrogen is redistributed from the region with a high binding energy into the diffusely mobile region. In this case, it is not observed.

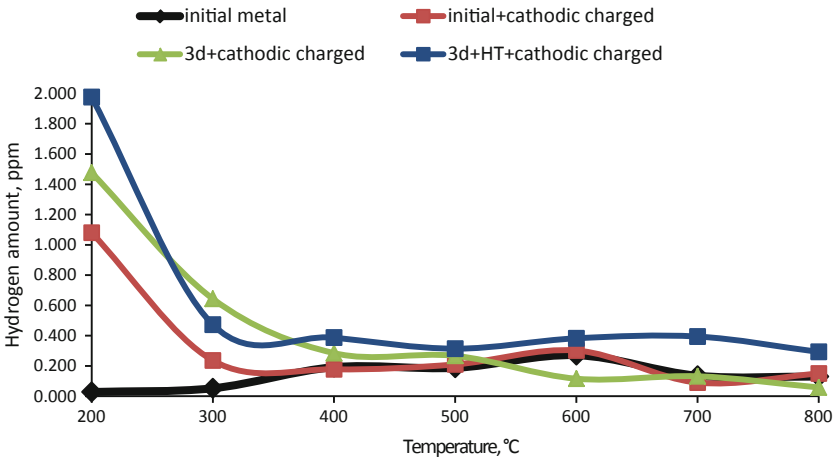

Fig. 25.5 Dependence of hydrogen concentration from extraction temperature for samples after hydrogen charging

Cathodic hydrogen charging (Fig. 25.5) showed that only hydrogen in a diffusely mobile state with a low binding energy increases. As a rule, diffusive-mobile hydrogen accumulates in thin surface layers and does not penetrate deep into the material. Thus, hydrogen charging leads only to the modification of the surface layer. We were unable to fix the tendency to increase the hydrogen concentration in the inner regions of the sample while increasing the charging time. Probably, this is due to the effect of the "screen", which creates a surface layer saturated with hydrogen.

25.5 Conclusion

We have experimentally determined the natural hydrogen concentrations in the heat-resistant nickel alloy 718. A comparison of the samples obtained by metallurgical means and by means of additive technologies has been carried out. It was found that at the same hydrogen concentration for a sample obtained using 3d-printing technology, the concentration of diffusively mobile hydrogen is substantially greater than the concentration of strongly bound hydrogen. For steels, the increased concentration of diffusive-mobile hydrogen has a strong effect on the mechanical properties

Saturation of samples with hydrogen by cathodic charging and artificial ageing of sample showed that hydrogen accumulation occurs only in the surface layer with low binding energies. The problem is that artificial saturation with hydrogen is widely used in research. Hydrogen fragility and other effects associated with hydrogen are often encountered in practice. It is not clear how the influence of the

surface saturation found by us is related to the actual accumulation of hydrogen and the development of hydrogen fragility.

Acknowledgements This research was performed into framework of financing RSF grant No. 18-19-00160.

References

1. H.P. Van Leeuwen, Eng. Fract. Mech. **6**(1), 141 (1974)
2. L.A. Konopel'ko, A.M. Polyanskii, V.A. Polyanskii, Y.A. Yakovlev. Meas. Tech. **60**(12), 1222 (2018)
3. J. Konar, N.G. Banerjee, NML Tech. J. **16**(1–2), 18 (1974)
4. A.K. Belyaev, A.M. Polyanskiy, V.A. Polyanskiy, Ch. Sommitsch, Y.A. Yakovlev, Int. J. Hydrogen Energy **41**(20), 8627 (2016)
5. A.M. Polyanskiy, V.A. Polyanskiy, Y.A. Yakovlev, Int. J. Hydrogen Energy **39**(30), 17381 (2014)
6. D.Y. Andronov, D.G. Arseniev, A.M. Polyanskiy, V.A. Polyanskiy, Y.A. Yakovlev, Int. J. Hydrogen Energy **42**(1), 699 (2017)

Chapter 26
New Method for Detecting Ultra Low Boron Concentration in Steel

Yuri F. Migal, Oleg V. Kudryakov and Vladimir I. Kolesnikov

Abstract To detect boron in steel we propose a method, based on the possibility to increase sharply the boron concentration at grain boundaries of a studied sample. This takes place when the sample is heated to the phase transition temperature at which the boride eutectic is formed. At high temperatures, the grain size increases many times. Due to appeared eutectic, the sample becomes brittle and can be easily destroyed. The increased boron concentration at the fracture surface under such conditions can be detected by standard X-ray methods.

26.1 Introduction

One of the effective methods for increasing the wear resistance of steel is the boriding method, which is one of the options for chemical heat treatment (CHT) of metals [1]. This method was first proposed by Chizhevsky [2]. It allows us to improve many characteristics of steel, including hardness, wear resistance, corrosion resistance, surface tension, etc. The drawback of this method is the increase of surface brittleness. This phenomenon is undesirable and sometimes unacceptable when mechanical or thermal loads rapidly change. The reason for increase in brittleness is the formation of iron borides FeB and Fe_2B in surface layers. These compounds inevitably appear at temperatures above 800 °C, at which classical CHT-boriding is carried out.

To avoid the appearance of iron borides, we develop boriding procedures at $t < 800$ °C. Their main purpose is to create a durable and not brittle surface. At such temperatures, iron borides are not formed and, as we expect, the brittleness of the surface does not increase.

Y. F. Migal (✉) · V. I. Kolesnikov
Rostov State Transport University, Rostov-on-Don, Russia
e-mail: ymigal@mail.ru

O. V. Kudryakov
Don State Technical University, Rostov-on-Don, Russia

I. A. Parinov et al. (eds.), *Advanced Materials*, Springer Proceedings in Physics 224, https://doi.org/10.1007/978-3-030-19894-7_26

The methods of diffusion introduction of boron into steel, studied by our group, are discussed in [3]. The schemes developed are based on that at low temperatures, boron is practically insoluble in the bulk of metallic grains and locates on grain boundaries. Due to this circumstance and also because of the high strength of the chemical bond Fe–B in such system [4], the boron atoms strengthen the bonds between grains in surface layers of metal. This is accompanied by a general increase in wear resistance. Such facts were demonstrated in [3–5].

When developing new methods of boriding, it is important to be able to control the presence of boron in steel and to determine the possible changes in its concentration. In this connection, there arises a problem of detecting boron in a metal. In this paper, we propose a method for detecting diffused boron in the surface layers of steel in the case of its extremely low concentrations.

26.2 Relationship Between Grain Size and Boron Concentration in Steel

As it was noted above, at low concentrations and temperatures, boron does not dissolve in the bulk of grains in steel, and locates on grain boundaries. Figure 26.1 shows a simplified scheme of the arrangement of atoms at a boundary between grains. Here the detail most important for us is reflected, that boron configuration is approximately a monatomic layer between the grains of iron (we used earlier this model for quantum chemical calculations of the binding energy of boron atoms with iron [5]).

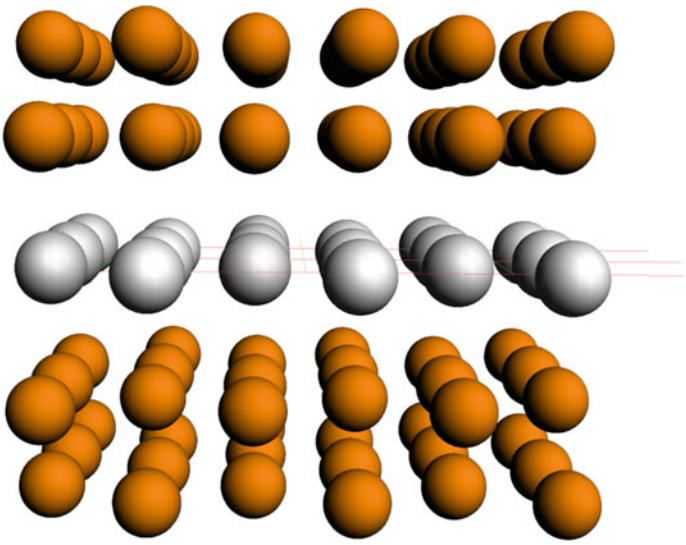

Fig. 26.1 Simplified model of a boundary between iron grains; the middle layer consists of boron atoms [5]

Further, for a theoretical analysis of the situation, we need to evaluate the relationship between grain sizes and boron concentration in steel. Let us consider for this purpose the simplest model of the grain in the form of a cube. The boron atoms in our model locate only on the surface of the cube. Taking into account that these atoms are simultaneously locate on surfaces of neighboring grains, we assume that only half of each boron atom belongs to the grain chosen by us.

Let us consider the case when the linear size of a grain in steel is of the order of 3 μm. Taking into account that the dimensions of atoms of boron and iron are of the order of 0.1 nm, it is easy to determine that in this case the number of Fe atoms within the cube is equal to 27×10^{12}, and the number of B atoms, belonging to this cube and located on its all six lateral surfaces, is equal to 27×10^{8}. So, we have approximately one boron atom per 10^4 iron atoms. Correspondingly, the concentration of boron atoms in the iron is 0.01%. For a grain size of about 30 μm, the concentration of boron atoms decreases by a factor of 10 and becomes 0.001%, and for a grain size of about 300 μm, the boron concentration is 0.0001%.

At such concentrations, the signal from boron fixed by X-ray electron and Auger spectroscopy methods becomes too weak, which makes it impossible to obtain reliable information with these methods not only on the concentration, but in some cases even on the presence of boron in the steel sample.

At present, for the element analysis of results of HTO-boriding, the wave-dispersion analysis (WDA) method is used, which has a lower accuracy than Auger electron spectroscopy. For this reason, in the case of low concentrations of the elements under investigation, the reliability of the WDA analysis is also not high and it does not always give correct results.

Mass-spectrometric methods could be an alternative to methods based on X-ray radiation. However, mass-spectrometric equipment, which is usually used in materials science laboratories, is primarily applicable for volumetric analysis of substances. In our case, when we investigate the composition of a thin surface layer having a thickness of the order of 10 μm and its fraction in the total bulk of substance is very small, the results of volumetric analysis are also of little use.

In this connection, it is necessary to create effective methods for detecting diffused boron within the surface layers of steel in the case of its ultra-low concentrations. In this paper, we propose a method that allows us to increase many times the possibility of fixing boron in the surface layers of steel.

26.3 Analysis of the Phase Equilibrium Diagram

The starting point in developing such approach is the analysis of the phase equilibrium diagram of the Fe–B system [6–8] (Fig. 26.2).

Let us consider some features of this diagram, important for us. The diagram shows that at a temperature of 1174 °C the eutectic transformation takes place in the system and a heterogeneous structure (eutectic) Fe_γ–Fe_2B with a boron content of ~17 at.% is formed. It is also known that a triple eutectic Fe_γ–Fe_2B–Fe_3C is

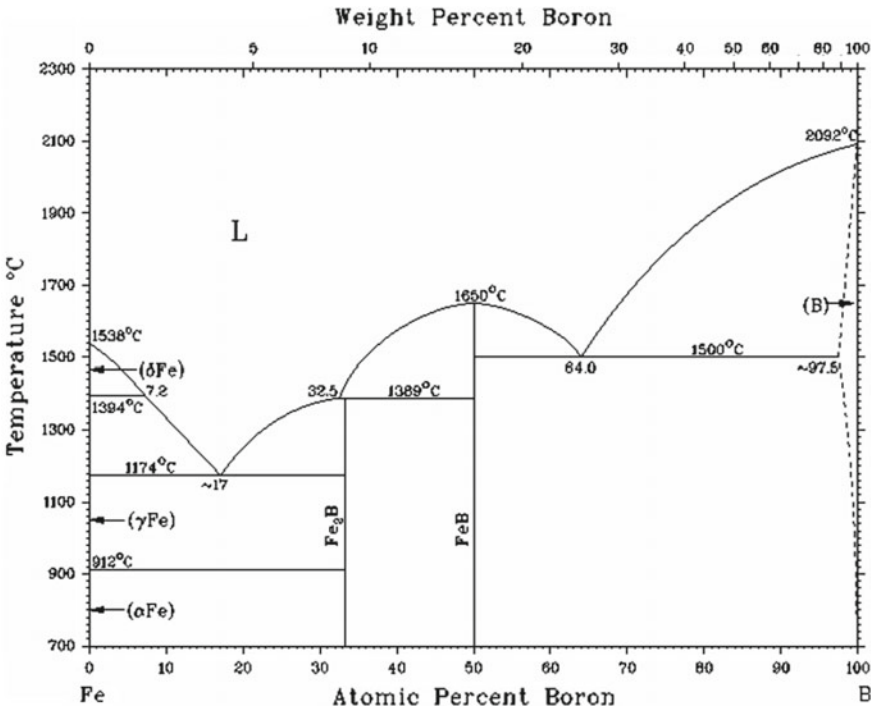

Fig. 26.2 Phase equilibrium diagram of the Fe–B system [8]

formed in the three-component system Fe–C–B (steel) at a temperature of 1100 °C. This eutectic contains 1.5% by weight of carbon and 2.9% by weight of boron (such boron content approximately corresponds to 17 at.% in the Fe_γ–Fe_2B system).

Using the above facts, it is possible to propose the following method for detecting boron introduced into the surface layers of steel at $t < 800$ °C.

26.4 Method for Detection of Ultra-Low Concentrations of Boron

It is assumed that boron diffuses into a steel sample with a fine-grained structure. Such a structure is usually created in industrial steels to ensure a certain level of wear resistance. If boron is introduced into such a structure, it will be distributed over a very large grain boundary area in the form of an irregular layer approximately one atom thick. The volume concentration of boron will remain small enough, and it will be very difficult to detect boron with Auger electron spectroscopy.

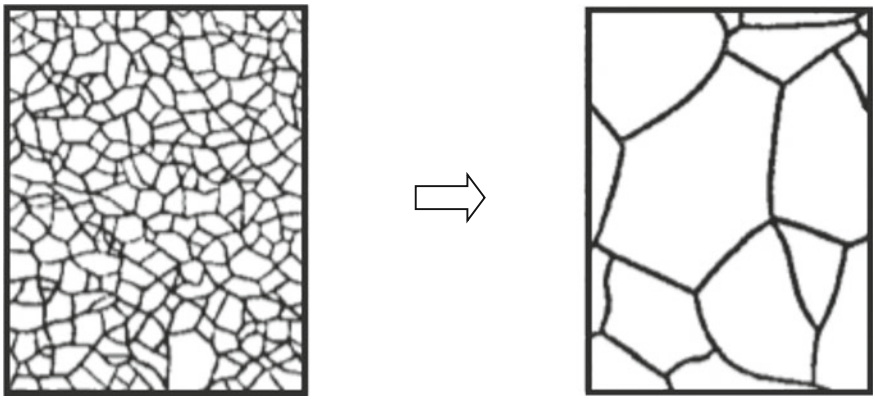

Fig. 26.3 Growth of grains upon transition from sample 1 to sample 2; here the average grain size increases 6.5 times, the total surface area of grains decreases many times, and the boron concentration on them sharply increases

If then the borided sample is heated to temperatures of 1150–1200 °C, two phenomena will be observed: grain growth and fusion of their boundaries due to the formation of a eutectic (either double Fe_γ–Fe_2B or triple Fe_γ–Fe_2B–Fe_3C). The growth of grains reduces the total area of grain boundaries saturated with boron, so if the total amount of boron is not changed, its concentration at the boundaries sharply increases (Fig. 26.3).

On the other hand, steel is strongly embrittled, so the sample can be easily fractured for example by impact loads. In this case, the fracture mechanism is brittle, and the crack surface is an intergranular fracture, i.e., it passes along grain boundaries. Therefore, the determination of boron content on such a surface actually gives its concentration at the grain boundaries. Hence, we can propose the following methodological sequence for the detection of boron.

First, boriding should be carried out at temperatures required for this process ($t < 800$ °C). Then it is necessary to raise the temperature up to 1200 °C and expose the samples at this temperature for grain growth. The exposure time is determined by standard methods, depending on the size and configuration of the samples. Under conditions of high-temperature exposure, atomic rearrangements in iron crystallites, leading to grain growth, occur according to the mechanism of migration and confluence of boundaries. In this case, the practically zero solubility of boron in iron (Fig. 26.2) ensures its presence only at grain boundaries (mainly in the eutectic composition).

To fix a coarse-grained structure of iron or steel at room temperature, it is necessary to suppress the diffusion process of phase recrystallization that inevitably occurs during cooling in iron-based alloys. For this purpose, the samples should be cooled quickly, that is, they should be hardened.

In practice, hardening is carried out by cooling in water. As a result, the phase transition $\gamma \rightarrow \alpha$ in iron occurs through a diffusionless mechanism, and the crystallites of the resulting α-phase (ferrite, martensite) take an acicular shape. In this case, the hereditary boundaries of coarse-grained γ-phase are preserved and become faceted, that is, their morphology is characterized by steps, ledges, teeth.

Under the influence of external loads such boundaries become places of facilitated origin and propagation of cracks. Quickly performed cooling suppresses the possible diffusion of boron and its presence is retained only on the inherited boundaries of the former γ-phase (austenite), mainly in the form of a boride eutectic.

Then it is necessary to carry out the destruction of the sample. As a result, a fracture surface will be obtained. Just this surface with the boride eutectic located on it is subject to analysis. The concentration of boron on such a surface significantly exceeds its concentration at the boundaries of the initial grains. We expect it will be sufficient for the detection of boron by various methods of spectrometry. It should be noted that for reliable identification of boron by these methods its concentration of the order of tenths of a mass% is necessary.

Currently, this method is being tested.

26.5 Conclusion

The proposed method, which makes it possible to detect boron at its extremely low concentrations in the surface layers of steel, can be effectively used in the development of new technologies for hardening of steel.

Acknowledgements This work was supported by the Russian Science Foundation (RSF) (grant No. 16-19-10467 provided to the Rostov State Transport University).

References

1. H. Kunst, B. Haase, J.C. Malloy, K. Wittel, M.C. Nestler, A.R. Nicoll, U. Erning, G. Rauscher, *Ullmann's Encyclopedia of Industrial Chemistry* (Wiley-VCH, Weinheim, 2006)
2. N.P. Chizhevski. J. Russ. Metall. Soc. **4**(19), 645 (1915) (In Russian)
3. Y.F. Migal, V.I. Kolesnikov, in *Advanced Materials*, I.A. Parinov, S.-H. Chang, V.K. Gupta. Springer Proceedings in Physics, vol. 207, no. 101 (2018)
4. V.I. Kolesnikov, YuF Migal, I.V. Kolesnikov, E.S. Novikov, J. Fric. Wear **36**(1), 1 (2015)
5. YuF Migal, V.I. Kolesnikov, I.V. Kolesnikov, Comput. Mater. Sci. **111**, 503 (2016)
6. Y. Khan, E. Kneller, M.Z. Sostarich, Metallkunde **73**(10), 624 (1982)
7. T.B. Massalski et al. (ed.), *Binary Alloy Phase Diagrams*, vol. 1 (American Society for Metals. Metals Park. OH, 1986)
8. *Phase Diagrams of Binary Systems: Phase Diagram of the B-Fe System*. http://www.himikatus.ru/art/phase-diagr1/B-Fe.php

Part III
Mechanics of Advanced Materials

Chapter 27
Harmonic Vibrations of Nanosized Magnetoelectric Bodies with Coupled Surface and Interphase Effects: Mathematical Models and Finite Element Approaches

Victor A. Eremeyev and Andrey V. Nasedkin

Abstract The harmonic problems for piezomagnetoelectric nanosized bodies with taking into account the coupled damping and surface effects are considered on the base of the generalized Gurtin-Murdoch model. In the development of previous investigations, the coupled mechanical, electric and magnetic surface effects with surface inertial terms are introduced into the model. For a homogeneous model, the composite material is considered as homogeneous with the suitable effective material properties. The weak or generalized formulation of the steady-state oscillation problem is given together with the suitable formulation of the modal problem. For numerical solution of these problems, the finite element approximations, leading to a symmetric structure of finite element matrices, are present. The procedures of homogenization of piezomagnetoelectric nanostructured composite materials with piezoelectric and piezomagnetic phases are described on the base of the methods of effective moduli and finite elements.

27.1 Introduction

The models for nanoscale bodies differ from the classical models for bodies of ordinary size, since they must reflect the effect of nanoscale. This effect, among other things, leads to a change in the material moduli of nanoobjects in comparison with the corresponding moduli of ordinary materials. A number of different size effect models have been developed. We can mention, for example, models based on

V. A. Eremeyev
Faculty of Civil and Environmental Engineering, Gdańsk University of Technology, 80-233 Gdańsk, Poland

V. A. Eremeyev · A. V. Nasedkin (✉)
I. I. Vorovich Institute of Mathematics, Mechanics and Computer Sciences, Southern Federal University, Rostov-on-Don, Russia
e-mail: nasedkin@math.sfedu.ru

I. A. Parinov et al. (eds.), *Advanced Materials*, Springer Proceedings in Physics 224, https://doi.org/10.1007/978-3-030-19894-7_27

the methods of molecular dynamics, non-local models, models of surface elasticity and their generalization. Among the models of surface elasticity, one of the most popular for elastic nanoscale bodies is the Gurtin-Murdoch model with the introduction of surface stresses [1–6]. Recently, this model was extended to piezoelectric [1–12] and magnetoelectric [13–15] nanoscale and nanostructured bodies. Examples of investigations of various nanomechanics problems for piezoelectric and magnetoelectric bodies with surface effects can be found in [16–26] etc.

In this paper, in the development of approaches [11, 12, 14, 15], a model of steady-state oscillations for a nanoscale piezomagnetoelectric body is proposed, in which surface stresses and surface electric and magnetic fluxes are introduced with coupled constitutive equations for surface mechanical, electric and magnetic fields. Similar to [11, 12, 14, 15], the model takes into account the damping properties, and for numerical solutions a finite element approach is presented, leading to symmetric structures of finite element matrices.

It is noted that the proposed model can be used in the homogenization problems of two-phase composites [27], consisting of piezoelectric and piezomagnetic phases with nanoscale interface boundaries.

27.2 Boundary Problems for Magnetoelectric Bodies

Let $\Omega \in \mathrm{R}^3$ be a region occupied by a magnetoelectric (piezomagnetoelectric) material; $\mathbf{x} = \{x_1, x_2, x_3\}$ is the vector of Cartesian coordinates; $\Gamma = \partial\Omega$ is the boundary of Ω; $\mathbf{n}$ is the external unit normal to Γ; ω is the circular frequency; $\mathbf{u} = \mathbf{u}(\mathbf{x})$ is the vector of complex vibration amplitude (mechanical displacement); $\varphi = \varphi(\mathbf{x})$ is the function of complex amplitude of electric potential; $\phi = \phi(\mathbf{x})$ is the function of complex amplitude of magnetic potential. The system of differential equations for magnetoelectric body occupying the volume Ω considering damping effects can be present in the following form in the vector-matrix notation:

$$\mathbf{L}^{\mathrm{T}}(\nabla)\cdot\mathbf{T} + \rho\mathbf{f} = \rho(-\omega^2 + j\alpha_d\omega)\mathbf{u}, \quad \nabla\cdot\mathbf{D} = q_\Omega, \quad \nabla\cdot\mathbf{B} = 0, \tag{27.1}$$

$$\mathbf{T} = (1 + j\beta_d\omega)\mathbf{c}\cdot\mathbf{S} - \mathbf{e}^{\mathrm{T}}\cdot\mathbf{E} - \mathbf{h}^{\mathrm{T}}\cdot\mathbf{H}, \tag{27.2}$$

$$(1 + j\zeta_d\omega)\mathbf{D} = (1 + j\zeta_d\omega)\mathbf{e}\cdot\mathbf{S} + \boldsymbol{\kappa}\cdot\mathbf{E} + \boldsymbol{\alpha}\cdot\mathbf{H}, \tag{27.3}$$

$$(1 + j\gamma_d\omega)\mathbf{B} = (1 + j\gamma_d\omega)\mathbf{h}\cdot\mathbf{S} + \boldsymbol{\alpha}^{\mathrm{T}}\cdot\mathbf{E} + \boldsymbol{\mu}\cdot\mathbf{H}. \tag{27.4}$$

$$\mathbf{S} = \mathbf{L}(\nabla)\cdot\mathbf{u}, \quad \mathbf{E} = -\nabla\varphi, \quad \mathbf{H} = -\nabla\phi, \tag{27.5}$$

$$\mathbf{L}^{\mathrm{T}}(\nabla) = \begin{bmatrix} \partial_1 & 0 & 0 & 0 & \partial_3 & \partial_2 \\ 0 & \partial_2 & 0 & \partial_3 & 0 & \partial_1 \\ 0 & 0 & \partial_3 & \partial_2 & \partial_1 & 0 \end{bmatrix}, \quad \nabla = \begin{Bmatrix} \partial_1 \\ \partial_2 \\ \partial_3 \end{Bmatrix}. \tag{27.6}$$

Here $\mathbf{T} = \{\sigma_{11}, \sigma_{22}, \sigma_{33}, \sigma_{23}, \sigma_{13}, \sigma_{12}\}$ is the array of the mechanical stress components σ_{ij}; $\mathbf{D}$ is the electric flux density vector or called also the vector of electric displacement; $\mathbf{B}$ is the magnetic flux density vector; $\mathbf{S} = \{\varepsilon_{11}, \varepsilon_{22}, \varepsilon_{33}, 2\varepsilon_{23}, 2\varepsilon_{13}, 2\varepsilon_{12}\}$ is the array of the strain components ε_{ij}; $\mathbf{E}$ is the electric field intensity vector; $\mathbf{H}$ is the magnetic field intensity vector; $\mathbf{f}$ is the vector of mass density forces; q_Ω is the density of free electric charges (as a rule, $q_\Omega = 0$); $\mathbf{c} = \mathbf{c}^{E,H}$ is the 6×6 matrix of elastic stiffness moduli at constant electric and magnetic fields; $\mathbf{e} = \mathbf{e}^H$ is the 3×6 matrix of piezoelectric moduli at constant magnetic field; $\mathbf{h} = \mathbf{h}^E$ is the 3×6 matrix of magnetostriction (piezomagnetic) moduli at constant electric field; $\boldsymbol{\kappa} = \boldsymbol{\kappa}^{S,H} = \boldsymbol{\varepsilon}^{S,H}$ is the 3×3 matrix of dielectric permittivity moduli at constant strains and magnetic field; $\boldsymbol{\alpha} = \boldsymbol{\alpha}^S$ is the 3×3 matrix of magnetoelectric coupling coefficients at constant strains; $\boldsymbol{\mu} = \boldsymbol{\mu}^{S,E}$ is the 3×3 matrix of magnetic permeability moduli at constant strains and electric field; α_d, β_d, ς_d, γ_d are the damping coefficients for different physical fields; $(\ldots)^{\mathrm{T}}$ is the transpose operation, and $(\ldots) \cdot (\ldots)$ is the scalar or internal product operation.

In (27.2)–(27.4), the material moduli have the usual symmetry properties: $c_{\alpha\beta} = c_{\beta\alpha}$, $\kappa_{kl} = \kappa_{lk}$, $\mu_{kl} = \mu_{lk}$. The requirement of positive definiteness of the volumetric intrinsic energy density $U(\mathbf{S}, \mathbf{E}, \mathbf{H})$ of the magnetoelectric medium leads to the following inequality, valid for all six-dimensional array $\mathbf{S}$, and for all vectors $\mathbf{E}$ and $\mathbf{H}$:

$$2U(\mathbf{S}, \mathbf{E}, \mathbf{H}) = \mathbf{S}^{\mathrm{T}} \cdot \mathbf{c} \cdot \mathbf{S} + \mathbf{E}^{\mathrm{T}} \cdot \boldsymbol{\kappa} \cdot \mathbf{E} + 2\mathbf{E}^{\mathrm{T}} \cdot \boldsymbol{\alpha} \cdot \mathbf{H} + \mathbf{H}^* \cdot \boldsymbol{\mu} \cdot \mathbf{H} \geq c_U^{\Omega}(\mathbf{S}^{\mathrm{T}} \cdot \mathbf{S} + \mathbf{E}^{\mathrm{T}} \cdot \mathbf{E} + \mathbf{H}^{\mathrm{T}} \cdot \mathbf{H}), \tag{27.7}$$

where c_U^{Ω} is a positive constant.

To take into account the nanoscale factors, we assume that on the boundary Γ of nanosized magnetoelectric body the surface stresses $\mathbf{T}^s$, the surface strains $\mathbf{S}^s$, the surface electric and magnetic fluxes $\mathbf{D}^s$ and $\mathbf{B}^s$, and the surface electric and magnetic field intensities $\mathbf{E}^s$ and $\mathbf{H}^s$ exist. For these quantities, we accept the following extended Gurtin–Murdoch model:

$$\mathbf{L}^{\mathrm{T}}(\mathbf{n}) \cdot \mathbf{T} = \mathbf{L}^{\mathrm{T}}(\nabla^s) \cdot \mathbf{T}^s + \rho^s(-\omega^2 + j\alpha_d\omega)\mathbf{u}^s + \mathbf{p}, \tag{27.8}$$

$$\mathbf{n} \cdot \mathbf{D} = \nabla^s \cdot \mathbf{D}^s - q, \quad \mathbf{n} \cdot \mathbf{B} = \nabla^s \cdot \mathbf{B}^s, \tag{27.9}$$

$$\mathbf{T}^s = (1 + j\beta_d\omega)\mathbf{c}^s \cdot \mathbf{S}^s - \mathbf{e}^{s\mathrm{T}} \cdot \mathbf{E}^s - \mathbf{h}^{s\mathrm{T}} \cdot \mathbf{H}^s, \tag{27.10}$$

$$(1 + j\zeta_d\omega)\mathbf{D}^s = (1 + j\zeta_d\omega)\mathbf{e}^s \cdot \mathbf{S}^s + \boldsymbol{\kappa}^s \cdot \mathbf{E}^s + \boldsymbol{\alpha}^s \cdot \mathbf{H}^s, \tag{27.11}$$

$$(1 + j\gamma_d\omega)\mathbf{B}^s = (1 + j\gamma_d\omega)\mathbf{h}^s \cdot \mathbf{S}^s + \boldsymbol{\alpha}^{s\mathrm{T}} \cdot \mathbf{E}^s + \boldsymbol{\mu}^s \cdot \mathbf{H}^s. \tag{27.12}$$

$$\mathbf{S}^s = \mathbf{S}^s(\mathbf{u}) = \mathbf{L}(\nabla^s) \cdot \mathbf{u}^s, \quad \mathbf{u}^s = \mathbf{A} \cdot \mathbf{u}, \quad \mathbf{A} = \mathbf{I} - \mathbf{n} \otimes \mathbf{n}, \tag{27.13}$$

$$\mathbf{E}^s = -\nabla^s \varphi, \quad , \mathbf{H}^s = -\nabla^s \phi, \quad \nabla^s = \nabla - \mathbf{n}(\partial/\partial n), \tag{27.14}$$

where ∇^s is the surface gradient operators; ρ^s is the surface mass density; $\mathbf{c}^s$, $\mathbf{e}^s$, $\boldsymbol{\kappa}^s$, $\mathbf{h}^s$, $\boldsymbol{\alpha}^s$, $\boldsymbol{\mu}^s$ are the matrices of surface elastic stiffness moduli, piezoelectric moduli, dielectric permittivity moduli, magnetostriction moduli, magnetoelectric coupling coefficients, and magnetic permeability moduli, respectively; $\mathbf{p}$ is the traction vector; q is the surface electric charge density; $\mathbf{I}$ is the identity matrix.

Here the properties of the matrices of surface material moduli $\tilde{\mathbf{c}}^s$, $\tilde{\kappa}^s$, $\tilde{\alpha}^s$, $\tilde{\mu}^s$, represented in local coordinate system $\tilde{O}\tilde{x}_1\tilde{x}_2\tilde{x}_3$, associated with the center $\tilde{O}$ in the point $\mathbf{x} \in \Gamma$, with tangent orts $\tilde{\mathbf{e}}_1 = \boldsymbol{\tau}_1$, $\tilde{\mathbf{e}}_2 = \boldsymbol{\tau}_2$ and normal $\tilde{\mathbf{e}}_3 = \mathbf{n}$ to Γ, are similar to the corresponding properties of the matrices of volume material moduli. Thus, the symmetry properties take place both the local coordinate system and in the initial Cartesian coordinate system, i.e. $c^s_{\alpha\beta} = c^s_{\beta\alpha}$, $\kappa^s_{kl} = \kappa^s_{ik}$, $\mu^s_{kl} = \mu^s_{ik}$, $\tilde{c}^s_{\alpha\beta} = \tilde{c}^s_{\beta\alpha}$, $\tilde{\kappa}^s_{kl} = \tilde{\kappa}^s_{ik}$, $\tilde{\mu}^s_{kl} = \tilde{\mu}^s_{ik}$, and $\exists c^\Gamma_U > 0$, $\forall \tilde{\mathbf{S}}^s = \{\tilde{S}^s_1, \tilde{S}^s_2, 0, 0, 0, \tilde{S}^s_6\}$, $\tilde{\mathbf{E}}^s = \{\tilde{E}^s_1, \tilde{E}^s_2, 0\}$, $\tilde{\mathbf{H}}^s = \{\tilde{H}^s_1, \tilde{H}^s_2, 0\}$:

$$\tilde{\mathbf{S}}^{s\mathrm{T}} \cdot \tilde{\mathbf{c}}^s \cdot \tilde{\mathbf{S}}^s + \tilde{\mathbf{E}}^{s\mathrm{T}} \cdot \tilde{\kappa}^s \cdot \tilde{\mathbf{E}}^s + 2\tilde{\mathbf{E}}^{s\mathrm{T}} \cdot \tilde{\alpha}^s \cdot \tilde{\mathbf{H}}^s + \tilde{\mathbf{H}}^{s\mathrm{T}} \cdot \tilde{\mu}^s \cdot \tilde{\mathbf{H}}^s \geq c^\Gamma_U (\tilde{\mathbf{S}}^{s\mathrm{T}} \cdot \tilde{\mathbf{S}}^s + \tilde{\mathbf{E}}^{s\mathrm{T}} \cdot \tilde{\mathbf{E}}^s + \tilde{\mathbf{H}}^{s\mathrm{T}} \cdot \tilde{\mathbf{H}}^s), \tag{27.15}$$

that follow from the condition of the positive definiteness of the surface energy density

$U^s(\tilde{\mathbf{S}}^s, \tilde{\mathbf{E}}^s, \tilde{\mathbf{H}}^s) = (\tilde{\mathbf{S}}^{s\mathrm{T}} \cdot \tilde{\mathbf{c}}^s \cdot \tilde{\mathbf{S}}^s + \tilde{\mathbf{E}}^{s\mathrm{T}} \cdot \tilde{\kappa}^s \cdot \tilde{\mathbf{E}}^s + 2\tilde{\mathbf{E}}^{s\mathrm{T}} \cdot \tilde{\alpha}^s \cdot \tilde{\mathbf{H}}^s + \tilde{\mathbf{H}}^{s\mathrm{T}} \cdot \tilde{\mu}^s \cdot \tilde{\mathbf{H}}^s)/2.$

It is important to note, that in (27.8), (27.9) $\mathbf{p}$ and q are the surface quantities, which can be known (active) or unknown (reactive) according to the assumed boundary conditions.

For completeness of the statement of the magnetoelectric problem, we have to add the boundary conditions for the system of differential equations (27.1)–(27.6). These boundary conditions are of three types: mechanical, electric and magnetic.

To formulate the basic mechanical boundary conditions we suppose that the boundary Γ is subdivided into two parts Γ_σ and Γ_u ($\Gamma = \Gamma_\sigma \cup \Gamma_u$). On the part Γ_σ the surface stress $\mathbf{T}^s$, the surface inertial and damping effects are presented and the traction vector $\mathbf{p}_\Gamma$ is specified

$$\mathbf{L}^{\mathrm{T}}(\mathbf{n}) \cdot \mathbf{T} = \mathbf{L}^{\mathrm{T}}(\nabla^s) \cdot \mathbf{T}^s + \rho^s(-\omega^2 + j\alpha_d\omega)\mathbf{u}^s + \mathbf{p}_\Gamma, \quad \mathbf{x} \in \Gamma_\sigma, \tag{27.16}$$

On the part Γ_u, we suppose that the mechanical displacement vector $\mathbf{u}_\Gamma$ is known:

$$\mathbf{u} = \mathbf{u}_\Gamma, \quad \mathbf{x} \in \Gamma_u \tag{27.17}$$

To set the electric boundary conditions, we consider other partition of the external surface Γ into two subsets: Γ_D and Γ_φ ($\Gamma = \Gamma_D \cup \Gamma_\varphi$).

The region Γ_D is free from electrodes, and on Γ_D the surface density of electric charge q_Γ is known, i.e. in the first formula from (27.9) $q = q_\Gamma$, and therefore we have:

$$\mathbf{n} \cdot \mathbf{D} = \nabla^s \cdot \mathbf{D}^s - q_\Gamma, \quad \mathbf{x} \in \Gamma_D, \tag{27.18}$$

where usually $q_\Gamma = 0$.

The part Γ_φ is the sum of L sets $\Gamma_{\varphi i}$ ($i \in J_V \cup J_Q$, $J_V = \{1, 2, \ldots, l\}$, $J_Q = \{l+1, l+2, \ldots, L\}$, $l \geq 1$, i.e. $\Gamma_{\varphi 0} \neq \wedge$), which do not border on each other and are covered with infinitely thin electrodes. On these surface regions, we pose the following boundary conditions:

$$\varphi = \Phi_i, \quad \mathbf{x} \in \Gamma_{\varphi i}, \quad \int\limits_{\Gamma_{\varphi i}} q \, d\Gamma = Q_i, \quad I_i = \pm j\omega Q_i, \quad i \in J_Q, \tag{27.19}$$

$$\varphi = V_i, \quad \mathbf{x} \in \Gamma_{\varphi i}, \quad i \in J_V, \tag{27.20}$$

where the quantities Φ_i, V_i of electric potentials on the electrodes do not depend on $\mathbf{x}$, i.e. electrodes are the equipotential surfaces; the values Φ_i are not initial known, in contrast to the input known values V_i; Q_i is the overall electric charge on electrode $\Gamma_{\varphi i}$, the sign "+" or "−" in (27.19) is chosen according to the used direction of the current I_j in the external electric circuit.

For magnetic boundary condition we assume that the second equality from (27.9) holds on the boundary Γ, except for the arbitrary point $\mathbf{x}_*$, where some value ϕ_0 of magnetic potential is specified, i.e.

$$\mathbf{n} \cdot \mathbf{B} = \nabla^s \cdot \mathbf{B}^s, \quad \mathbf{x} \in \{\Gamma \backslash \mathbf{x}_*\}; \quad \phi(\mathbf{x}_*) = \phi_0. \tag{27.21}$$

Formulas (27.1) and (27.21) represent the harmonic problem definition for magnetoelectric body with the generalized Rayleigh damping and with coupled surface effects for mechanical, electric and magnetic fields. From these formulas, we can also obtain the corresponding statements of static and modal piezomagnetoelectric problems with coupled generalized Gurtin–Murdoch surface effects.

In models (27.1)–(27.21) we use a special method of damping evaluation, which is extended the known Rayleigh damping method for the magnetoelectric material with coupled surface effects.

It has been shown that the model (27.1)–(27.21) with $\beta_d = \varsigma_d = \gamma_d$ satisfies the properties of the dissipation of volume and surface energies and has the possibility of splitting the weak statement and the finite element system into independent equations for the separate vibration modes.

We can also consider the particular statements of this model without taking into account the connectivity between some physical volume and surface fields. Thus, we can obtain the model for piezoelectric material with coupled damping and surface effects, if we assume $\mathbf{h} = 0, \boldsymbol{\alpha} = 0, \mathbf{h}^s = 0, \boldsymbol{\alpha}^s = 0$, and if we ignore the equations for magnetic fields. We can also reduce these models to the models with uncoupled surface effects, if we assume that some surface connectivity moduli are equal to zero.

27.3 Weak or Generalized Statement of Harmonic Problem

In order to obtain the weak or generalized formulation of harmonic problem for magnetoelectric solid with surface effects, we scalar multiply (27.1) by some sufficiently differentiable projection vector-function $\mathbf{v}(\mathbf{x})$ and functions $\chi(\mathbf{x})$ and $\eta(\mathbf{x})$, which satisfies homogeneous and constant essential boundary conditions, corresponding to (27.17), (27.19)–(27.21), i.e.

$$\mathbf{v} = 0, \quad \mathbf{x} \in \Gamma_u, \tag{27.22}$$

$$\chi = X_i, \quad \mathbf{x} \in \Gamma_{\varphi i}, \quad i \in J_Q, \tag{27.23}$$

$$\chi = 0, \quad \mathbf{x} \in \Gamma_{\varphi i}, \quad i \in J_V, \tag{27.24}$$

$$\eta = 0, \quad \mathbf{x} = \mathbf{x}_*, \tag{27.25}$$

where X_i are the arbitrary constant values on $\Gamma_{\varphi i}$, $i \in J_Q$. Further we describe the mathematical restrictions imposed on the functions $\mathbf{v}(\mathbf{x})$, $\chi(\mathbf{x})$ and $\eta(\mathbf{x})$ more precisely.

By integrating the obtained equations over the volume Ω and by using the standard technique of the integration by parts, with (27.1)–(27.12), (27.22)–(27.24) and with the relations for surface fields, we obtain:

$$-\omega^2 \rho(\mathbf{v}, \mathbf{u}) + j\omega d(\mathbf{v}, \mathbf{u}) + c(\mathbf{v}, \mathbf{u}) + e_u(\varphi, \mathbf{v}) + h_u(\phi, \mathbf{v}) = \tilde{L}_u(\mathbf{v}), \tag{27.26}$$

$$-(1 + j\varsigma_d \omega) e_\varphi(\chi, \mathbf{u}) + \kappa(\chi, \varphi) + \alpha_\varphi(\chi, \phi) = (1 + j\varsigma_d \omega)\tilde{L}_\varphi(\chi), \tag{27.27}$$

$$-(1 + j\gamma_d \omega) h_\phi(\eta, \mathbf{u}) + \alpha_\phi(\varphi, \eta) + \mu(\eta, \phi) = 0, \tag{27.28}$$

where

$$\rho(\mathbf{v}, \mathbf{u}) = \rho_\Omega(\mathbf{v}, \mathbf{u}) + \rho_\Gamma(\mathbf{v}, \mathbf{u}), \quad c(\mathbf{v}, \mathbf{u}) = c_\Omega(\mathbf{v}, \mathbf{u}) + c_\Gamma(\mathbf{v}, \mathbf{u}), \tag{27.29}$$

$$d(\mathbf{v}, \mathbf{u}) = \alpha_d \rho(\mathbf{v}, \mathbf{u}) + \beta_d c(\mathbf{v}, \mathbf{u}), \tag{27.30}$$

$$e_u(\varphi,\mathbf{v}) = e_\Omega(\varphi,\mathbf{v}) + e_{\Gamma\sigma}(\varphi,\mathbf{v}), \quad h_u(\phi,\mathbf{v}) = h_\Omega(\phi,\mathbf{v}) + h_{\Gamma\sigma}(\phi,\mathbf{v}), \tag{27.31}$$

$$e_\varphi(\chi,\mathbf{u}) = e_\Omega(\chi,\mathbf{u}) + e_{\Gamma D}(\chi,\mathbf{u}), \quad \kappa(\chi,\varphi) = \kappa_\Omega(\chi,\varphi) + \kappa_\Gamma(\chi,\varphi), \tag{27.32}$$

$$\alpha_\varphi(\chi,\phi) = \alpha_\Omega(\chi,\phi) + \alpha_{\Gamma D}(\chi,\phi), \quad h_\phi(\eta,\mathbf{u}) = h_\Omega(\eta,\mathbf{u}) + h_\Gamma(\eta,\mathbf{u}), \tag{27.33}$$

$$\alpha_\phi(\varphi,\eta) = \alpha_\Omega(\varphi,\eta) + \alpha_\Gamma(\varphi,\eta), \quad \mu(\eta,\phi) = \mu_\Omega(\eta,\phi) + \mu_\Gamma(\eta,\phi), \tag{27.34}$$

$$\rho_\Omega(\mathbf{v},\mathbf{u}) = \int\limits_\Omega \rho\,\mathbf{v}^{\mathrm{T}}\cdot\mathbf{u}\,d\Omega, \quad \rho_\Gamma(\mathbf{v},\mathbf{u}) = \int\limits_\Gamma \rho^s\,\mathbf{v}^{s\mathrm{T}}\cdot\mathbf{u}^s\,d\Gamma, \quad \mathbf{v}^s = \mathbf{A}\cdot\mathbf{v}, \tag{27.35}$$

$$c_\Omega(\mathbf{v},\mathbf{u}) = \int\limits_\Omega \mathbf{S}^{\mathrm{T}}(\mathbf{v})\cdot\mathbf{c}\cdot\mathbf{S}(\mathbf{u})\,d\Omega, \quad c_\Gamma(\mathbf{v},\mathbf{u}) = \int\limits_{\Gamma_\sigma} \mathbf{S}^{s\mathrm{T}}(\mathbf{v})\cdot\mathbf{c}^s\cdot\mathbf{S}^s(\mathbf{u})\,d\Gamma, \tag{27.36}$$

$$e_\Omega(\varphi,\mathbf{v}) = \int\limits_\Omega (\nabla\varphi)^{\mathrm{T}}\cdot\mathbf{e}\cdot\mathbf{S}(\mathbf{v})\,d\Omega, \quad e_{\Gamma\sigma}(\varphi,\mathbf{v}) = \int\limits_{\Gamma_\sigma} (\nabla^{\mathrm{s}}\varphi)^{\mathrm{T}}\cdot\mathbf{e}^s\cdot\mathbf{S}(\mathbf{v})\,d\Gamma, \tag{27.37}$$

$$h_\Omega(\phi,\mathbf{v}) = \int\limits_\Omega (\nabla\phi)^{\mathrm{T}}\cdot\mathbf{h}\cdot\mathbf{S}(\mathbf{v})\,d\Omega, \quad h_{\Gamma\sigma}(\phi,\mathbf{v}) = \int\limits_{\Gamma_\sigma} (\nabla^{\mathrm{s}}\phi)^{\mathrm{T}}\cdot\mathbf{h}^s\cdot\mathbf{S}^s(\mathbf{v})\,d\Gamma, \tag{27.38}$$

$$e_{\Gamma D}(\chi,\mathbf{u}) = \int\limits_{\Gamma_\sigma} (\nabla^{\mathrm{s}}\chi)^{\mathrm{T}}\cdot\mathbf{e}^s\cdot\mathbf{S}^s(\mathbf{u})\,d\Gamma, \quad \alpha(\chi,\phi) = \int\limits_\Omega (\nabla\chi)^{\mathrm{T}}\cdot\boldsymbol{\alpha}\cdot\nabla\phi\,d\Omega, \tag{27.39}$$

$$\alpha_{\Gamma D}(\chi,\phi) = \int\limits_{\Gamma_D} (\nabla^{\mathrm{s}}\chi)^{\mathrm{T}}\cdot\boldsymbol{\alpha}^s\cdot\nabla^{\mathrm{s}}\phi\,d\Gamma, \tag{27.40}$$

$$\kappa_\Omega(\chi,\varphi) = \int\limits_\Omega (\nabla\chi)^{\mathrm{T}}\cdot\boldsymbol{\kappa}\cdot\nabla\varphi\,d\Omega, \quad \kappa_\Gamma(\chi,\varphi) = \int\limits_{\Gamma_D} (\nabla^{\mathrm{s}}\chi)^{\mathrm{T}}\cdot\boldsymbol{\kappa}^s\cdot\nabla^s\varphi\,d\Gamma, \tag{27.41}$$

$$h_\Gamma(\eta,\mathbf{u}) = \int\limits_\Gamma (\nabla^{\mathrm{s}}\eta)^{\mathrm{T}}\cdot\mathbf{h}^s\cdot\mathbf{S}^s(\mathbf{u})\,d\Gamma, \quad \alpha_\Gamma(\varphi,\eta) = \int\limits_\Gamma (\nabla^{\mathrm{s}}\varphi)^{\mathrm{T}}\cdot\boldsymbol{\alpha}^s\cdot\nabla^{\mathrm{s}}\eta\,d\Gamma, \tag{27.42}$$

$$\mu_\Omega(\eta,\phi) = \int\limits_\Omega (\nabla\eta)^{\mathrm{T}}\cdot\boldsymbol{\mu}\cdot\nabla\phi\,d\Omega, \quad \mu_\Gamma(\eta,\phi) = \int\limits_\Gamma (\nabla^{\mathrm{s}}\eta)^{\mathrm{T}}\cdot\boldsymbol{\mu}^s\cdot\nabla^s\phi\,d\Gamma, \tag{27.43}$$

$$\tilde{L}_u(\mathbf{v}) = \int\limits_{\Omega} \mathbf{v}^{\mathrm{T}} \cdot \rho \mathbf{f}\, d\Omega + \int\limits_{\Gamma_\sigma} \mathbf{v}^{\mathrm{T}} \cdot \mathbf{p}_\Gamma\, d\Gamma, \tag{27.44}$$

$$\tilde{L}_\varphi(\chi) = \int\limits_{\Omega} \chi \sigma_\Omega\, d\Omega + \int\limits_{\Gamma_D} \chi \sigma_\Gamma\, d\Gamma + \sum_{j \in J_Q} X_j Q_j. \tag{27.45}$$

In order to remove the heterogeneity in the essential boundary conditions, we will present the functions $\mathbf{u}$ and φ as

$$\mathbf{u} = \mathbf{u}_0 + \mathbf{u}_b, \quad \varphi = \varphi_0 + \varphi_b, \tag{27.46}$$

where $\mathbf{u}_0$, φ_0 satisfy homogeneous mechanical boundary conditions and homogeneous or constant electric boundary conditions, and $\mathbf{u}_b$, φ_b are the known (specially chosen) functions satisfying the inhomogeneous boundary conditions, i.e.

$$\mathbf{u}_0 = 0, \quad \mathbf{u}_b = \mathbf{u}_\Gamma, \quad \mathbf{x} \in \Gamma_u. \tag{27.47}$$

$$\varphi_0 = \Phi_{0i}, \quad \varphi_b = \Phi_{bi}, \quad \Phi_{0i} + \Phi_{bi} = \Phi_i, \quad \mathbf{x} \in \Gamma_{\varphi i}. \quad i \in J_Q, \tag{27.48}$$

$$\varphi_0 = 0, \quad \varphi_b = V_i, \quad \mathbf{x} \in \Gamma_{\varphi i}, \quad i \in J_V. \tag{27.49}$$

Using (27.46), we modify the system (27.26)–(27.28) to the following form:

$$-\omega^2 \rho(\mathbf{v}, \mathbf{u}_0) + j\omega d(\mathbf{v}, \mathbf{u}_0) + c(\mathbf{v}, \mathbf{u}_0) + e_u(\varphi_0, \mathbf{v}) + h_u(\phi, \mathbf{v}) = L_u(\mathbf{v}), \tag{27.50}$$

$$-(1 + j\varsigma_d \omega) e_\varphi(\chi, \mathbf{u}_0) + \kappa(\chi, \varphi_0) + \alpha_\varphi(\chi, \phi) = L_\varphi(\chi), \tag{27.51}$$

$$-(1 + j\gamma_d \omega) h_\phi(\eta, \mathbf{u}_0) + \alpha_\phi(\varphi_0, \eta) + \mu(\eta, \phi) = L_\phi(\eta), \tag{27.52}$$

where

$$L_u(\mathbf{v}) = \tilde{L}_u(\mathbf{v}) - \omega^2 \rho(\mathbf{v}, \mathbf{u}_b) - j\omega d(\mathbf{v}, \mathbf{u}_b) - c(\mathbf{v}, \mathbf{u}_b) - e_u(\varphi_b, \mathbf{v}), \tag{27.53}$$

$$L_\varphi(\chi) = (1 + j\varsigma_d \omega)(\tilde{L}_\varphi(\chi) + e_\varphi(\chi, \mathbf{u}_b)) - \kappa(\chi, \varphi_b), \tag{27.54}$$

$$L_\phi(\eta) = (1 + j\gamma_d \omega) h_\phi(\eta, \mathbf{u}_b) - \alpha_\phi(\varphi_b, \eta). \tag{27.55}$$

We introduce the Hilbert vector space H_u^1 as the closure of the set of vector functions $\mathbf{v} \in \mathrm{C}^1$, satisfying homogeneous essential boundary condition (27.22), with the norm determined by the bilinear form $c(\mathbf{v}, \mathbf{u})$ from the second formula in (27.29) and (27.36).

We also introduce the Hilbert space H_φ^1 as the closure of the set of functions $\chi \in \mathrm{C}^1$, satisfying boundary condition (27.23) and (27.24), in the norm determined by the bilinear form $\kappa(\chi, \varphi)$ from the second formula in (27.32) and (27.41).

Finally, we introduce the Hilbert space H^1_ϕ as the closure of the set of functions $\eta \in \mathrm{C}^1$, $\chi \in \mathrm{C}^1$, satisfying boundary condition (27.25), in the norm determined by scalar production $\mu(\eta, \phi)$ from (27.34) and (27.43).

Using these functional spaces, we can define weak or generalized solution of harmonic problem (27.1)–(27.21).

Definition *The functions* $\mathbf{u} = \mathbf{u}_0 + \mathbf{u}_b$, $\mathbf{u}_0 \in H^1_u$; $\varphi = \varphi_0 + \varphi_b$, $\varphi_0 \in H^1_\varphi$; $\phi \in H^1_\phi$ *are the weak or generalized solution of harmonic problem for the magnetoelectric body with damping and coupled surface effects, if* (27.50)–(27.52) *with* (27.53)–(27.55), (27.29)–(27.45) *are satisfied for* $\forall \mathbf{v} \in H^1_u$, $\chi \in H^1_\varphi$, $\eta \in H^1_\phi$.

Note that after transfer from (27.26)–(27.28) to (27.50)–(27.52), the following important equalities hold:

$$e_{\Gamma\sigma}(\varphi_0, \mathbf{v}) = e_{\Gamma\sigma D}(\varphi_0, \mathbf{v}) = \int\limits_{\Gamma_{\sigma D}} (\nabla^{\mathrm{s}}\varphi_0)^{\mathrm{T}} \cdot \mathbf{e}^s \cdot \mathbf{S}(\mathbf{v})\, d\Gamma, \tag{27.56}$$

$$e_{\Gamma D}(\chi, \mathbf{u}_0) = e_{\Gamma\sigma D}(\chi, \mathbf{u}_0) = \int\limits_{\Gamma_{\sigma D}} (\nabla^{\mathrm{s}}\chi)^{\mathrm{T}} \cdot \mathbf{e}^s \cdot \mathbf{S}^s(\mathbf{u}_0)\, d\Gamma, \tag{27.57}$$

$$h_\Gamma(\eta, \mathbf{u}_0) = h_{\Gamma\sigma}(\eta, \mathbf{u}_0) = \int\limits_{\Gamma_\sigma} (\nabla^{\mathrm{s}}\eta)^{\mathrm{T}} \cdot \mathbf{h}^s \cdot \mathbf{S}^s(\mathbf{u}_0)\, d\Gamma, \tag{27.58}$$

$$\alpha_\Gamma(\varphi_0, \eta) = \alpha_{\Gamma D}(\varphi_0, \eta) = \int\limits_{\Gamma_D} (\nabla^{\mathrm{s}}\varphi_0)^{\mathrm{T}} \cdot \boldsymbol{\alpha}^s \cdot \nabla^{\mathrm{s}}\eta\, d\Gamma, \tag{27.59}$$

where $\Gamma_{\sigma D} = \Gamma_\sigma \cap \Gamma_D$, as far as $\nabla^{\mathrm{s}}\varphi_0 = 0$ for $\forall \mathbf{x} \in \Gamma_\sigma \backslash \Gamma_{\sigma D}$ and $\forall \mathbf{x} \in \Gamma_\varphi = \Gamma \backslash \Gamma_D$, $\mathbf{S}^s(\mathbf{u}_0) = 0$ for $\mathbf{x} \in \forall \Gamma_D \backslash \Gamma_{\sigma D}$ and $\forall \mathbf{x} \in \Gamma_u = \Gamma \backslash \Gamma_\sigma$.

These equations allow us to obtain later for the case $\varsigma_d = \gamma_d$ the symmetric systems, because from (27.56)–(27.59) with (27.31)–(27.34) it is follow that

$$e_u(\varphi_0, \mathbf{v}) = e_\varphi(\varphi_0, \mathbf{v}), \quad e_\varphi(\chi, \mathbf{u}_0) = e_u(\chi, \mathbf{u}_0), \tag{27.60}$$

$$h_u(\phi, \mathbf{v}) = h_\phi(\phi, \mathbf{v}), \quad h_\phi(\eta, \mathbf{u}_0) = h_u(\eta, \mathbf{u}_0), \tag{27.61}$$

$$\alpha_\varphi(\chi, \phi) = \alpha_\phi(\chi, \phi), \quad \alpha_\phi(\varphi_0, \eta) = \alpha_\varphi(\varphi_0, \eta). \tag{27.62}$$

27.4 Eigenvalue Problem

The eigenfrequencies or natural frequencies $f_k = \omega_k/(2\pi)$ for magnetoelectric solids under consideration can be found from the solution of the weak eigenvalue

problem or modal problem, obtained from (27.50)–(27.52) without damping effects and without any nonzero external influences, i.e. with $\alpha_d = \beta_d = \varsigma_d = \gamma_d = 0$, $L_u(\mathbf{v}) = 0$, $L_\varphi(\chi) = 0$, $L_\phi(\eta) = 0$. In this situation $\mathbf{u}_0 = \mathbf{u} \in H_u^1$, $\varphi_0 = \varphi \in H_\varphi^1$, and the system (27.50)–(27.52) with taking into account (27.60)–(27.62) has the form:

$$c(\mathbf{v}, \mathbf{u}) + e_u(\varphi, \mathbf{v}) + h_u(\phi, \mathbf{v}) = \omega^2 \rho(\mathbf{v}, \mathbf{u}), \tag{27.63}$$

$$e_u(\chi, \mathbf{u}) + \kappa(\chi, \varphi) + \alpha_\varphi(\chi, \phi) = 0, \tag{27.64}$$

$$h_u(\eta, \mathbf{u}) + \alpha_\varphi(\varphi, \eta) + \mu(\eta, \phi) = 0, \tag{27.65}$$

Definition *We call the quarter of quantities* ω^2, $\mathbf{u} \in H_u^1$, $\varphi \in H_\varphi^1$, $\phi \in H_\phi^1$, *which satisfy* (27.63)–(27.65) *for* $\forall \mathbf{v} \in H_u^1$, $\chi \in H_\varphi^1$, $\eta \in H_\phi^1$, *a generalized or weak solution of eigenvalue problem for magnetoelectric body with coupled surface effects.*

This eigenvalue problem can be investigate similar to [11, 28], and therefore the following theorem holds.

Theorem *The eigenvalue problem for magnetoelectric body with coupled surface effects has a discrete real spectrum:* $0 < \omega_1^2 \le \omega_2^2 \le \cdots \le \omega_k^2 \le \cdots$; $\omega_k^2 \to \infty$ as $k \to \infty$, *the corresponding eigenvectors* $\mathbf{u}^{(k)}$ *form a system that is complete in the spaces* H_u^1, *and the triple of eigenfunctions* $\mathbf{u}^{(k)}$, $\varphi^{(k)}$, $\phi^{(k)}$ *has the orthogonality properties:*

$$\rho(\mathbf{u}^{(m)}, \mathbf{u}^{(k)}) = 0, \tag{27.66}$$

$$c(\mathbf{u}^{(m)}, \mathbf{u}^{(k)}) + e_u(\varphi^{(k)}, \mathbf{u}^{(m)}) + h_u(\phi^{(k)}, \mathbf{u}^{(m)}) = 0, \tag{27.67}$$

$$e_u(\varphi^{(m)}, \mathbf{u}^{(k)}) + \kappa(\varphi^{(m)}, \varphi^{(k)}) + \alpha_\varphi(\varphi^{(m)}, \phi^{(k)}) = 0, \tag{27.68}$$

$$h_u(\phi^{(m)}, \mathbf{u}^{(k)}) + \alpha_\varphi(\varphi^{(k)}, \phi^{(m)}) + \mu(\phi^{(m)}, \phi^{(k)}) = 0, \tag{27.69}$$

where $k \ne m$.

27.5 Finite Element Approximations

27.5.1 Harmonic Analysis

For solving the magnetoelectric problems (27.50)–(27.52) with (27.53)–(27.55), (27.29)–(27.45), we use classical finite element technique. Let Ω_h be the region filled by the finite element mesh, $\Omega_h \subseteq \Omega$, $\Omega_h = \cup_k \Omega^{ek}$, where Ω^{ek} is a separate

magnetoelectric finite element with the number k. Let also Γ_h be a finite element mesh from surface elements conformable with the volume mesh: Ω_h, $\Gamma_h = \partial\Omega_h$, $\Gamma_h \approx \Gamma$, $\Gamma_h = \cup_m \Gamma^{em}$, Γ^{em} is a separate magnetoelectric surface finite element with number m, and the elements Γ^{em} are the edges of the suitable volume elements Ω^{ek}, located on the external boundary. We will use the classic Lagrangian or serendipity volume finite elements with nodal degrees of freedom of displacements, electric and magnetic potentials. Note that due to structure of surface fields, the shell elements Γ^{em} have the structure of elastic membrane stresses, and so the shell elements have also only nodal degrees of freedom of displacements, electric and magnetic potentials.

We will find the approximate solution $\{\ \mathbf{u}_h \approx \mathbf{u}_0,\ \varphi_h \approx \varphi_0,\ \phi_h \approx \phi_0\ \}$ at the finite element mesh Ω_h in the form:

$$\mathbf{u}_h(\mathbf{x}) = \mathbf{N}_u^{\mathrm{T}}(\mathbf{x}) \cdot \mathbf{U}, \quad \varphi_h(\mathbf{x}) = \mathbf{N}_\varphi^{\mathrm{T}}(\mathbf{x}) \cdot \mathbf{\Phi}, \quad \phi_h(\mathbf{x}) = \mathbf{N}_\phi^{\mathrm{T}}(\mathbf{x}) \cdot \mathbf{\Psi}, \tag{27.70}$$

where $\mathbf{N}_u^{\mathrm{T}}$ is the matrix of the basic or form functions for displacements, $\mathbf{N}_\varphi^{\mathrm{T}}$ is the row vector of the basic functions for the electric potentials, $\mathbf{N}_\phi^{\mathrm{T}}$ is the row vector of the basic functions for the magnetic potentials, $\mathbf{U}$ is the vector of nodal displacements, $\mathbf{\Phi}$ is the vector of nodal electric potentials, and $\mathbf{\Psi}$ is the vector of nodal magnetic potentials.

According to usual approach we approximate the continuum weak formulation of the magnetoelectric problem in finite-dimensional spaces related to the system of basic functions $\mathbf{N}_u^{\mathrm{T}}$, $\mathbf{N}_\varphi^{\mathrm{T}}$, $\mathbf{N}_\phi^{\mathrm{T}}$. We present the projecting functions $\mathbf{v}$, χ, η in finite-dimensional spaces by the formulae:

$$\mathbf{v}(\mathbf{x}) = \mathbf{N}_u^{\mathrm{T}}(\mathbf{x}) \cdot \delta\,\mathbf{U}, \quad \chi(\mathbf{x}) = \mathbf{N}_\varphi^{\mathrm{T}}(\mathbf{x}) \cdot \delta\,\mathbf{\Phi}, \quad \eta(\mathbf{x}) = \mathbf{N}_\phi^{\mathrm{T}}(\mathbf{x}) \cdot \delta\,\mathbf{\Psi}, \tag{27.71}$$

Substituting (27.70) and (27.71) into the weak statement of the magnetoelectric problem for Ω_h, $\Gamma_h = \partial\Omega_h$, $\Gamma_{h\sigma}$, Γ_{hD}, $\Gamma_{h\sigma D}$, we obtain the following finite element system:

$$-\omega^2 \mathbf{M}_{uu} \cdot \mathbf{U} + j\omega \mathbf{C}_{uu} \cdot \mathbf{U} + \mathbf{K}_{uu} \cdot \mathbf{U} + \mathbf{K}_{u\varphi} \cdot \mathbf{\Phi} + \mathbf{K}_{u\phi} \cdot \mathbf{\Psi} = \mathbf{F}_u, \tag{27.72}$$

$$-(1 + j\varsigma_d\omega)\mathbf{K}_{u\varphi}^{\mathrm{T}} \cdot \mathbf{U} + \mathbf{K}_{\varphi\varphi} \cdot \mathbf{\Phi} + \mathbf{K}_{\varphi\,\phi} \cdot \mathbf{\Psi} = \mathbf{F}_\varphi, \tag{27.73}$$

$$-(1 + j\gamma_d\omega)\mathbf{K}_{u\phi}^{\mathrm{T}} \cdot \mathbf{U} + \mathbf{K}_{\varphi\,\phi}^{\mathrm{T}} \cdot \mathbf{\Phi} + \mathbf{K}_{\phi\,\phi} \cdot \mathbf{\Psi} = \mathbf{F}_\phi, \tag{27.74}$$

where

$$\mathbf{M}_{uu} = \mathbf{M}_{\Omega uu} + \mathbf{M}_{\Gamma uu}, \quad \mathbf{K}_{uu} = \mathbf{K}_{\Omega uu} + \mathbf{K}_{\Gamma uu}, \quad \mathbf{C}_{uu} = \alpha_d \mathbf{M}_{uu} + \beta_d \mathbf{K}_{uu}, \tag{27.75}$$

$$\mathbf{K}_{u\varphi} = \mathbf{K}_{\Omega u\varphi} + \mathbf{K}_{\Gamma u\varphi}, \quad \mathbf{K}_{u\phi} = \mathbf{K}_{\Omega u\phi} + \mathbf{K}_{\Gamma u\phi}, \quad \mathbf{K}_{\varphi\varphi} = \mathbf{K}_{\Omega\varphi\varphi} + \mathbf{K}_{\Gamma\varphi\varphi}, \tag{27.76}$$

$$\mathbf{K}_{\varphi\phi} = \mathbf{K}_{\Omega\varphi\phi} + \mathbf{K}_{\Gamma\varphi\phi}, \quad \mathbf{K}_{\phi\phi} = \mathbf{K}_{\Omega\phi\phi} + \mathbf{K}_{\Gamma\phi\phi}, \tag{27.77}$$

Here $\mathbf{M}_{\Omega uu} = \sum^a \mathbf{M}^{ek}_{\Omega uu}$, $\mathbf{M}_{\Gamma uu} = \sum^a \mathbf{M}^{ek}_{\Gamma uu}$, $\mathbf{K}_{\Omega uu} = \sum^a \mathbf{K}^{ek}_{\Omega uu}$, $\mathbf{K}_{\Gamma uu} = \sum^a \mathbf{K}^{ek}_{\Gamma uu}$, etc., are the global matrices, obtained from the operation of corresponding finite element matrices ensemble ($\sum^a$).

According to (27.35)–(27.43), (27.56)–(27.62), the element matrices have the form:

$$\mathbf{M}^{ek}_{uu} = \int\limits_{\Omega^{ek}} \rho\, \mathbf{N}^e_u \cdot \mathbf{N}^{e\mathrm{T}}_u d\Omega, \quad \mathbf{M}^{ek}_{uu} = \int\limits_{\Gamma^{ek}} \rho^s\, \mathbf{N}^e_u \cdot \mathbf{N}^{e\mathrm{T}}_u d\Gamma, \tag{27.78}$$

$$\mathbf{K}^{ek}_{\Omega uu} = \int\limits_{\Omega^{ek}} \mathbf{B}^{e\mathrm{T}}_u \cdot \mathbf{c} \cdot \mathbf{B}^e_u d\Omega, \quad \mathbf{K}^{ek}_{\Gamma uu} = \int\limits_{\Gamma^{ek}_{\sigma}} \mathbf{B}^{e\mathrm{T}}_{su} \cdot \mathbf{c}^s \cdot \mathbf{B}^e_{su} d\Gamma, \tag{27.79}$$

$$\mathbf{K}^{ek}_{\Omega u\varphi} = \int\limits_{\Omega^{ek}} \mathbf{B}^{e\mathrm{T}}_u \cdot \mathbf{e}^{\mathrm{T}} \cdot \mathbf{B}^e_{\varphi} d\Omega, \quad \mathbf{K}^{ek}_{\Gamma u\varphi} = \int\limits_{\Gamma^{ek}_{\sigma D}} \mathbf{B}^{e\mathrm{T}}_{su} \cdot \mathbf{e}^{s\mathrm{T}} \cdot \mathbf{B}^e_{s\varphi} d\Gamma, \tag{27.80}$$

$$\mathbf{K}^{ek}_{\Omega u\phi} = \int\limits_{\Omega^{ek}} \mathbf{B}^{e\mathrm{T}}_u \cdot \mathbf{h}^{\mathrm{T}} \cdot \mathbf{B}^e_{\phi} d\Omega, \quad \mathbf{K}^{ek}_{\Gamma u\phi} = \int\limits_{\Gamma^{ek}_{\sigma}} \mathbf{B}^{e\mathrm{T}}_{su} \cdot \mathbf{h}^{s\mathrm{T}} \cdot \mathbf{B}^e_{s\phi} d\Gamma, \tag{27.81}$$

$$\mathbf{K}^{ek}_{\Omega\varphi\varphi} = \int\limits_{\Omega^{ek}} \mathbf{B}^{e\mathrm{T}}_{\varphi} \cdot \boldsymbol{\kappa} \cdot \mathbf{B}^e_{\varphi} d\Omega, \quad \mathbf{K}^{ek}_{\Gamma\varphi\varphi} = \int\limits_{\Gamma^{ek}_{D}} \mathbf{B}^{e\mathrm{T}}_{s\varphi} \cdot \boldsymbol{\kappa}^s \cdot \mathbf{B}^e_{s\varphi} d\Gamma, \tag{27.82}$$

$$\mathbf{K}^{ek}_{\Omega\varphi\phi} = \int\limits_{\Omega^{ek}} \mathbf{B}^{e\mathrm{T}}_{\varphi} \cdot \boldsymbol{\alpha} \cdot \mathbf{B}^e_{\phi} d\Omega, \quad \mathbf{K}^{ek}_{\Gamma\varphi\varphi} = \int\limits_{\Gamma^{ek}_{D}} \mathbf{B}^{e\mathrm{T}}_{s\varphi} \cdot \boldsymbol{\alpha}^s \cdot \mathbf{B}^e_{s\phi} d\Gamma, \tag{27.83}$$

$$\mathbf{K}^{ek}_{\Omega\phi\phi} = \int\limits_{\Omega^{ek}} \mathbf{B}^{e\mathrm{T}}_{\phi} \cdot \boldsymbol{\mu} \cdot \mathbf{B}^e_{\phi} d\Omega, \quad \mathbf{K}^{ek}_{\Gamma\phi\phi} = \int\limits_{\Gamma^{ek}} \mathbf{B}^{e\mathrm{T}}_{s\phi} \cdot \boldsymbol{\mu}^s \cdot \mathbf{B}^e_{s\phi} d\Gamma, \tag{27.84}$$

$$\mathbf{B}^e_u = \mathbf{L}(\nabla) \cdot \mathbf{N}^{e\mathrm{T}}_u, \quad \mathbf{B}^e_{su} = \mathbf{L}(\nabla^s) \cdot \mathbf{A} \cdot \mathbf{N}^{e*}_u, \quad \mathbf{B}^e_{(s)\varphi} = \nabla^{(s)} \mathbf{N}^{e\mathrm{T}}_{\varphi}, \quad \mathbf{B}^e_{(s)\phi} = \nabla^{(s)} \mathbf{N}^{e\mathrm{T}}_{\phi}, \tag{27.85}$$

where Γ^{ek}, Γ^{ek}_{σ}, Γ^{ek}_{D}, $\Gamma^{ek}_{\sigma D}$, are the edges of finite elements facing the regions Γ_h, $\Gamma_{h\sigma}$, Γ_{hD}, $\Gamma_{h\sigma D}$, that approximate the corresponding boundaries Γ, Γ_{σ}, Γ_D, $\Gamma_{\sigma D}$; $\mathbf{N}^{e\mathrm{T}}_u$, $\mathbf{N}^{e\mathrm{T}}_{\varphi}$, $\mathbf{N}^{e\mathrm{T}}_{\phi}$ are the matrix and the row vectors of approximating form functions, respectively, defined at separate finite elements. The vectors $\mathbf{F}_u$, $\mathbf{F}_{\varphi}$, $\mathbf{F}_{\phi}$ in right part of (27.73)–(27.74) are obtained from the corresponding right parts of the system

(27.50)–(27.52) with (27.44), (27.45), (27.53)–(27.55) and the finite element representations (27.71).

We note that in (27.78)–(27.85) the matrices with subscript Ω are the same matrices as in finite element analysis of magnetoelectric bodies of usual sizes. Surface effect generates additional surface elements with finite element matrices with a subscript Γ. Such matrices are absent in the standard software, and therefore the finite element analysis of magnetoelectric problems with surface effects require the creation of new surface magnetoelectric elements. On variant of the special surface or interphase, finite elements with the coupled physical and mechanical fields can be obtained from the corresponding volume elements in the form of bricks or wedges by the procedure of collapse of opposing nodes.

If $\varsigma_d = \gamma_d$ we can transform the system (27.72)–(27.74) to the symmetric form:

$$(-\omega^2 \mathbf{M}_{uu} + j\omega \mathbf{C}_{uu} + \mathbf{K}_{uu}) \cdot \mathbf{U} + \mathbf{K}_{ub} \cdot \mathbf{b} = \mathbf{F}_u, \tag{27.86}$$

$$\mathbf{K}_{ub}^{\mathrm{T}} \cdot \mathbf{U} - (1 + j\varsigma_d \omega)^{-1} \mathbf{K}_{bb} \cdot \mathbf{b} = -(1 + j\varsigma_d \omega)^{-1} \mathbf{F}_b, \tag{27.87}$$

where

$$\mathbf{K}_{bb} = \begin{bmatrix} \mathbf{K}_{\varphi\varphi} & \mathbf{K}_{\varphi\phi} \\ \mathbf{K}_{\varphi\phi}^{\mathrm{T}} & \mathbf{K}_{\phi\phi} \end{bmatrix}, \quad \mathbf{K}_{ub}^{\mathrm{T}} = \begin{Bmatrix} \mathbf{K}_{u\varphi}^{\mathrm{T}} \\ \mathbf{K}_{u\phi}^{\mathrm{T}} \end{Bmatrix}, \quad \mathbf{b} = \begin{Bmatrix} \mathbf{\Phi} \\ \mathbf{\Psi} \end{Bmatrix}, \quad \mathbf{F}_b = \begin{Bmatrix} \mathbf{F}_\varphi \\ \mathbf{F}_\phi \end{Bmatrix}. \tag{27.88}$$

27.5.2 Static Analysis

In the case of static problems, all time dependencies are absent, and the system (27.72)–(27.74) with $\omega = 0$ can be reduce to the following form:

$$\mathbf{K} \cdot \mathbf{a} = \mathbf{F}, \tag{27.89}$$

where

$$\mathbf{K} = \begin{bmatrix} \mathbf{K}_{uu} & \mathbf{K}_{ub} \\ \mathbf{K}_{ub}^{\mathrm{T}} & -\mathbf{K}_{bb} \end{bmatrix}, \quad \mathbf{a} = \begin{Bmatrix} \mathbf{U} \\ \mathbf{b} \end{Bmatrix}, \quad \mathbf{F} = \begin{Bmatrix} \mathbf{F}_u \\ -\mathbf{F}_b \end{Bmatrix}, \tag{27.90}$$

and the matrices $\mathbf{K}_{bb}$, $\mathbf{K}_{ub}$ and the vectors $\mathbf{b}$ and $\mathbf{F}_b$ were defined in (27.88).

The matrix $\mathbf{K}$ in (27.89) with (27.90), (27.88) is symmetric and has the quasi-definite properties [29], because the matrices $\mathbf{K}_{uu}$ and $\mathbf{K}_{bb}$ are positive defined. Thus, the static problem (27.86) possesses the basic calculating properties of finite element system for the theories of piezomagnetoelectricity or

piezoelectricity for the bodies of usual sizes, and therefore it can be solved by the same effective algorithms as the similar problems for ordinary magnetoelectric or piezoelectric media. For example, we can use the set of algorithms for finite element analysis with quasi-definite symmetric matrices presented in ACELAN package [30–32]: the rotations of finite element coordinate systems, the setting of boundary conditions, LDL^{T}-factorization or iterative methods from [29] for solving the system of linear algebraic equations (27.89), and others.

27.5.3 Modal Analysis

The resonance frequencies $f_k = \omega_k/(2\pi)$ for magnetoelectric body with surface effects can be found using the finite element approach from the generalized eigenvalue problem, obtained from (27.86) and (27.87) with $\mathbf{C}_{uu} = 0$, $\varsigma_d = 0$, $\mathbf{F}_u = 0$, $\mathbf{F}_b = 0$. In this case, we obtain the finite element system:

$$\mathbf{K}_{uu} \cdot \mathbf{U} + \mathbf{K}_{ub} \cdot \mathbf{b} = \omega^2 \mathbf{M}_{uu} \cdot \mathbf{U}, \tag{27.91}$$

$$\mathbf{K}_{ub}^{\mathrm{T}} \cdot \mathbf{U} - \mathbf{K}_{bb} \cdot \mathbf{b} = 0. \tag{27.92}$$

The generalized eigenvalue problem (27.91) and (27.92) can be rewritten in the form:

$$\overline{\mathbf{K}}_{uu} \cdot \mathbf{U} = \lambda \mathbf{M}_{uu} \cdot \mathbf{U}, \quad \lambda = \omega^2, \tag{27.93}$$

where

$$\overline{\mathbf{K}}_{uu} = \mathbf{K}_{uu} + \mathbf{K}_{ub} \cdot \mathbf{K}_{bb}^{-1} \cdot \mathbf{K}_{ub}^{\mathrm{T}}, \quad \mathbf{b} = \mathbf{K}_{bb}^{-1} \cdot \mathbf{K}_{ub}^{\mathrm{T}} \cdot \mathbf{U}, \tag{27.94}$$

Since the intrinsic bulk and surface energies have positive definiteness properties (27.7), (27.15), then the generalized stiffness matrix $\overline{\mathbf{K}}_{uu}$ is positive defined ($\overline{\mathbf{K}}_{uu} > 0$), and the mass matrix $\mathbf{M}_{uu}$ is also positive defined ($\mathbf{M}_{uu} > 0$), because $\rho(\mathbf{x}) \geq \rho_0 > 0$. Then, in accordance with theorem from the Sect. 27.4 and by analogy with the eigenvalue problems for elastic body, the eigenvalues $\lambda_k = \omega_k^2$ ($k = 1, 2, \ldots, n$; n is the order of matrices in (27.93) $\overline{\mathbf{K}}_{uu}$) are real and positive. We will denote the eigenvector, corresponding to the eigenvalue λ_k, by $\mathbf{U}_k = \mathbf{W}_k$. The system of these eigenvectors $\mathbf{W}_k$ form the basis in R^n, and we can select them orthonormal with respect to the matrix $\mathbf{M}_{uu}$ and orthogonal with respect to the matrix $\overline{\mathbf{K}}_{uu}$:

$$\mathbf{W}_k^{\mathrm{T}} \cdot \mathbf{M}_{uu} \cdot \mathbf{W}_m = \delta_{km}, \quad \mathbf{W}_k^{\mathrm{T}} \cdot \overline{\mathbf{K}}_{uu} \cdot \mathbf{W}_m = \omega_m^2 \delta_{km}. \tag{27.95}$$

Extended variant of the orthogonality relations in compliance with (27.66)–(27.69) have the form:

$$\mathbf{U}_m^{\mathrm{T}} \cdot (\mathbf{M}_{uu} \cdot \mathbf{U}_k + \mathbf{K}_{uu} \cdot \mathbf{U}_k + \mathbf{K}_{u\varphi} \cdot \mathbf{\Phi}_k + \mathbf{K}_{u\phi} \cdot \mathbf{\Psi}_k) = 0,$$

$$\mathbf{\Phi}_m^{\mathrm{T}} \cdot (\mathbf{K}_{u\varphi}^{\mathrm{T}} \cdot \mathbf{U}_k - \mathbf{K}_{\varphi\varphi} \cdot \mathbf{\Phi}_k - \mathbf{K}_{\varphi\,\phi} \cdot \mathbf{\Psi}_k) = 0,$$

$$\mathbf{\Psi}_m^{\mathrm{T}} \cdot (\mathbf{K}_{u\phi}^{\mathrm{T}} \cdot \mathbf{U}_k - \mathbf{K}_{\varphi\,\phi}^{\mathrm{T}} \cdot \mathbf{\Phi}_k - \mathbf{K}_{\phi\,\phi} \cdot \mathbf{\Psi}_k) = 0,$$

where $\mathbf{b}_k = \mathbf{K}_{bb}^{-1} \cdot \mathbf{K}_{ub}^{\mathrm{T}} \cdot \mathbf{U}_k$, $\mathbf{b}_k = \{\mathbf{\Phi}_k, \mathbf{\Psi}_k\}$.

Thus, the modal problems (27.91) and (27.92) with respect to the triple $\{\omega, \mathbf{U}, \mathbf{b}\}$ are the form of usual generalized eigenvalue problems (27.93), (27.94) with respect to the circular frequency ω and oscillation mode $\mathbf{U}$. For solving this problem, we can use the several block algorithms, described in [30].

27.5.4 Mode Superposition Method for Harmonic Analysis

For the case of the same structural damping coefficients $\beta_d = \varsigma_d = \gamma_d$ the problem of steady-state oscillations (27.86) and (27.87) takes the form standard for the finite element method in the dynamic theory of elasticity:

$$(-\omega^2 \mathbf{M}_{uu} + j\omega\,\overline{\mathbf{C}}_{uu} + \overline{\mathbf{K}}_{uu}) \cdot \mathbf{U} = \overline{\mathbf{F}}_u, \tag{27.96}$$

where

$$\overline{\mathbf{C}}_{uu} = \alpha_d \mathbf{M}_{uu} + \beta_d \overline{\mathbf{K}}_{uu}, \tag{27.97}$$

$$\overline{\mathbf{F}}_u = \mathbf{F}_u - \mathbf{K}_{ub} \cdot \mathbf{B}_{st}, \tag{27.98}$$

$$\mathbf{b} = \mathbf{B}_{st} + (1 + j\omega\beta_d)\mathbf{K}_{bb}^{-1} \cdot \mathbf{K}_{ub}^{\mathrm{T}} \cdot \mathbf{U}, \quad \mathbf{B}_{st} = \mathbf{K}_{bb}^{-1} \cdot \mathbf{F}_b. \tag{27.99}$$

If in (27.17) $\mathbf{u}_\Gamma = 0$, we can find the solution of problem (27.96) as series expansion of vibration modes (eigenvectors) $\mathbf{W}_k$ of eigenvalue problem (27.93) with the same zero essential boundary conditions:

$$\mathbf{U} = \sum_{k=1}^{n} z_k \mathbf{W}_k. \tag{27.100}$$

If we substitute (27.100) into (27.96), multiply the obtained equation by $\mathbf{W}_m^{\mathrm{T}}$ and take into account the relations of orthogonality (27.95) and (27.97), we find the coefficient z_k of mode contribution:

$$z_k = \frac{1}{\omega_k^2 - \omega^2 + 2j\xi_k\omega\omega_k} Q_k, \quad Q_k = \mathbf{W}_k^{\mathrm{T}} \cdot \overline{\mathbf{F}}_u, \quad \xi_k = \alpha_d \frac{1}{2\omega_k} + \beta_d \frac{\omega_k}{2}. \tag{27.101}$$

Thus, using the mode superposition method, the solutions of the steady-state vibration problems are determined by (27.100) and (27.101) and (27.97)–(27.99). Note that the efficiency of the mode superposition method decreases as compared with the purely elastic problem, since here it is necessary to find the inverse matrix $\mathbf{K}_{bb}^{-1}$, or to solve additional systems of finite element equations for determination $\mathbf{B}_{st}$ and $\mathbf{b}$ in (27.99).

27.6 Homogenization of Two-Phase Composites with Interface Effects by the Method of Efficient Moduli

Model (27.1)–(27.21) describes the steady-state oscillations of a piezomagneto-electric nanoscale body. However, in reality, the piezomagnetoelectric body is a composite consisting of the piezoelectric and piezomagnetic phases. Therefore, for such body, it is necessary to pre-determine its effective material moduli $c_{\beta\gamma}^{\mathrm{eff}}$, $e_{i\beta}^{\mathrm{eff}}$, $h_{i\beta}^{\mathrm{eff}}$, $\kappa_{ij}^{\mathrm{eff}}$, $\alpha_{ij}^{\mathrm{eff}}$, μ_{ij}^{eff}; $\beta, \gamma = 1, 2, \ldots, 6$, $i, j = 1, 2, 3$. For this, in the homogenization problem, the region Ω must be considered as a representative volume, including parts Ω^p and Ω^m ($\Omega = \Omega^p \cup \Omega^m$) filled with materials of the piezoelectric and piezomagnetic phases, respectively. In the case of nanostructured interphase boundaries, $\Gamma^s = \partial\Omega^p \cap \partial\Omega^m$, on this boundary the interface conditions can be considered:

$$\mathbf{L}^{\mathrm{T}}(\mathbf{n}) \cdot [\mathbf{T}] = \mathbf{L}^{\mathrm{T}}(\nabla^s) \cdot \mathbf{T}^s, \quad \mathbf{n} \cdot [\mathbf{D}] = \nabla^s \cdot \mathbf{D}^s, \quad \mathbf{n} \cdot [\mathbf{B}] = \nabla^s \cdot \mathbf{B}^s, \quad \mathbf{x} \in \Gamma^s, \tag{27.102}$$

where $[\mathbf{T}] = \mathbf{T}^p - \mathbf{T}^m$, $[\mathbf{D}] = \mathbf{D}^p - \mathbf{D}^m$ and $[\mathbf{B}] = \mathbf{B}^p - \mathbf{B}^m$ are the jump of the corresponding fields when passing through the interface.

On the external boundary $\Gamma = \partial\Omega$ of the representative volume, one can accept standard boundary conditions for the effective moduli method:

$$\mathbf{u} = \mathbf{L}^{\mathrm{T}}(\mathbf{x}) \cdot \mathbf{S}_0, \quad \varphi = -\mathbf{x} \cdot \mathbf{E}_0, \quad \phi = -\mathbf{x} \cdot \mathbf{H}_0, \quad \mathbf{x} \in \Gamma, \tag{27.103}$$

where $\mathbf{S}_0$, $\mathbf{E}_0$ and $\mathbf{H}_0$ are some not depended from $\mathbf{x}$ arrays (vectors) of the sizes 6 and 3.

In the case of piezomagnetoelectric composite of arbitrary anisotropic class, in order to determine all its effective moduli, it is enough to solve twelve static boundary problems (27.1)–(27.6), (27.102), (27.10)–(27.14), (27.103) with $\omega = 0$

and with various values of $\mathbf{S}_0$, $\mathbf{E}_0$ and $\mathbf{H}_0$, having set only one of the components: $S_{0\gamma}$, E_{0k}, H_{0k} ($\gamma = 1, 2, \ldots, 6$, $k = 1, 2, 3$) in the boundary conditions (27.103) not equal to zero:

(i) problems I–VI ($\varsigma = 1, 2, \ldots, 6$)

$$S_{0\gamma} = S_0\delta_{\varsigma\gamma}, E_{0k} = 0, H_{0k} = 0 \Rightarrow c^{\text{eff}}_{\beta\varsigma} = \langle T_\beta \rangle / S_0, e^{\text{eff}}_{i\varsigma} = \langle D_i \rangle / S_0, h^{\text{eff}}_{i\varsigma} = \langle B_i \rangle / S_0, \tag{27.104}$$

(ii) problems VII–IX ($j = 1, 2, 3$)

$$S_{0\varsigma} = 0, E_{0k} = E_0\delta_{jk}, H_{0k} = 0 \Rightarrow e^{\text{eff}}_{j\beta} = -\langle T_\beta \rangle / E_0, \kappa^{\text{eff}}_{ij} = \langle D_i \rangle / E_0, \alpha^{\text{eff}}_{ji} = \langle B_i \rangle / E_0, \tag{27.105}$$

(iii) problems X – XII ($j = 1, 2, 3$)

$$S_{0\varsigma} = 0, E_{0k} = 0, H_{0k} = H_0\delta_{jk} \Rightarrow h^{\text{eff}}_{j\beta} = -\langle T_\beta \rangle / H_0, \alpha^{\text{eff}}_{ij} = \langle D_i \rangle / H_0, \mu^{\text{eff}}_{ij} = \langle B_i \rangle / H_0, \tag{27.106}$$

where $\beta = 1, 2, \ldots, 6$; $i = 1, 2, 3$;

$$< (\ldots) > = \frac{1}{|\Omega|} \left(\int\limits_{\Omega} (\ldots) d\Omega + \int\limits_{\Gamma^s} (\ldots)^s d\Gamma \right). \tag{27.107}$$

Thus, as we can see, the boundary value problems (27.1)–(27.6), (27.102), (27.10)–(27.14), (27.103) with $\omega = 0$ and with (27.104)–(27.106) differ from the usual problems of linear piezomagnetoelectricity by the presence of the interface boundary conditions (27.102) with (27.10)–(27.14) and average quantities (27.107) with integration not only over the volume, but also over the interface surfaces, which are typical for the Gurtin – Murdoch model of surface stresses for nanosized bodies [33, 34]. Since the interface boundaries complicate the internal structure of the representative volume, it is possible to solve the homogenization boundary value problems only numerically, for example, using the finite element method described above.

27.7 Concluding Remarks

Thus, in this paper the harmonic problems for magnetoelectric (piezomagnetoelectric or electromagnetoelastic) nanosized bodies with account for coupled damping and surface effects are studied. At the beginning, we assume that magnetoelectric composite body can be modelled as homogeneous material with appropriate effective material moduli. For the considered problems, we propose the mathematical models, which generalize the models of the elastic and piezoelectric media with damping in sense of the Rayleigh approach and the generalized Gurtin-Murdoch model of surface effects for the cases of magnetoelectric materials. Our model of energy dissipation and surface effects has coupling of anisotropic properties between mechanical, electric and magnetic fields, both for the damping terms and constitutive equations for magnetoelectric materials on the surface. We formulate the system of differential equations with damping properties, the special boundary conditions with taking into account the coupled piezomagnetoelectric surface effects and damping for magnetoelectric nanosized bodies. Further, we expand these approaches to the analogous problems for magnetoelectric bodies composed of nanosized piezoelectric and magnetoelectric phases. For these composites, we assume the imperfect interphase conditions similar to the boundary conditions with taking into account the coupled surface effects.

We present the weak or generalized formulations of the harmonic and modal problems. For solving these and static problems, we suggest the finite element approximations with Lagrangian or serendipity volume elements and suitable conformal surface elements. A set of effective finite element schemes is examined for finding numerical solutions of weak statements for steady-state vibrations and for modal and static problems within the framework of modelling of magnetoelectric nanosized materials with damping and surface or interphase effects. For harmonic problems, we also demonstrate that the proposed models with the equal structural damping coefficients allow us to apply the mode superposition method, which is efficient tool for the analysis of the influence of individual vibration modes.

Acknowledgements This work was supported by the Russian Science Foundation (grant number 15-19-10008-P).

References

1. M.E. Gurtin, A.I. Murdoch, Arch. Ration. Mech. An. **57**, 291 (1975)
2. M.E. Gurtin, A.I. Murdoch, Int. J. Solid. Struct. **14**, 431 (1978)
3. J.C. Hamilton, W.G. Wolfer, Surf. Sci. **603**, 1284 (2009)
4. V.A. Eremeyev, Acta Mech. **227**, 29 (2016)
5. J. Wang, Z. Huang, H. Duan et al., Acta Mech. Solida Sin. **24**, 52 (2011)
6. T. Chen, Acta Mech. **196**, 205 (2008)

7. V.A. Eremeyev, A.V. Nasedkin, In: *Wave Dynamics and Composite Mechanics for Microstructured Materials and Metamaterials. Advanced Structured Materials*, M.A. Sumbatyan (Ed.), **59**, 1 (Springer, Singapore, 2017)
8. S.-T. Gu, J.-T. Liu, Q.-C. He, Comput. Mat. Sci. **94**, 182 (2014)
9. S.-T. Gu, L. Qin, Int. J. Eng. Sci. **78**, 89 (2014)
10. G.Y. Huang, S.W. Yu, Phys. Status Solidi B **243**(4), R22 (2006)
11. A.V. Nasedkin, V.A. Eremeyev, ZAMM **94**(10), 878 (2014)
12. A.V. Nasedkin, V.A. Eremeyev, *Problems of Strength and Plasticity*, **79**(4) 375 (2017) (In Russian)
13. S.-T. Gu, J.-T. Liu, Q.-C. He, Int. J. Eng. Sci. **85**, 31 (2014)
14. A. Nasedkin, Ferroelectrics **509**, 57 (2017)
15. A.V. Nasedkin, V.A. Eremeyev, In: *Advanced Materials—Manufacturing, Physics, Mechanics and Applications*, ed. by I.A. Parinov, S.-H. Chang, V.Y. Topolov. Springer Proceedings in Physics, vol. **175** (Springer, 2016), p. 373
16. H.-Y. Kuo, K.-H. Wang, Int. J. Solids Struct. **106–107**, 164 (2017)
17. E. Pan, X. Wang, R. Wang, Appl. Phys. Lett. **95**, 181904 (2009)
18. X.H. Pan, S.W. Yu, X.Q. Feng, Science China: Physics. Mech. Astron. **54**(4), 564 (2011)
19. A. Sahoo, D. Bhattacharya, J. Alloys Comp. **772**, 193 (2019)
20. Y. Shi, Compos. Struct. **185**, 474 (2018)
21. Y. Shi, Y. Gao, J. Alloys Comp. **762**, 706 (2018)
22. Y. Wang, Y Su., J. Li, G.J. Weng, J. Appl. Phys. **117**, 164106 (2015)
23. Z. Wang, J. Zhu, X.Y. Jin, W.Q. Chen, Ch. Zhang, J. Mech. Phys. Solids **65**, 138 (2014)
24. Z. Yan, L.Y. Jiang, J. Phys. D Appl. Phys. **44**(36), 365301 (2011)
25. Z. Yan, L.Y. Jiang, J. Phys. D Appl. Phys. **45**(25), 255401 (2012)
26. G.L. Yu, H.W. Zhang, Y.-X. Li, Compos. Struct. **132**, 65 (2015)
27. A. Nasedkin, in *VIII ECCOMAS Thematic Conference Smart Structure Materials—SMART 2017*, ed. by A. Guemes, et al., 5–8 June 2017, Madrid, Spain (CIMNE, Barcelona, 2017), p. 1137
28. V.A. Eremeev, A.V. Nasedkin, Mech. Solids **50**(5), 495 (2015)
29. M. Benzi, G.H. Golub, J. Liesen, Acta Numerica **14**, 1 (2005)
30. A.V. Belokon, V.A. Eremeyev, A.V. Nasedkin, A.N. Soloviev, J. Appl. Math. Mech. (PMM) **64**, 367 (2000)
31. A.V. Belokon, A.V. Nasedkin, A.N. Soloviev, J. Appl. Math. Mech. (PMM) **66**(3), 481 (2002)
32. A.V. Nasedkin, in *Piezoceramic Materials and Devices*, ed. by I.A. Parinov, vol. 177 (Nova Science Publishers, N.-Y., 2010)
33. G. Chatzigeorgiou, A. Javili, P. Steinmann, Math. Mech. Solids. **20**(9), 1130 (2015)
34. A. Javili, S. Kaessmair, P. Steinmann, Comput. Methods Appl. Mech. Engrg. **275**, 76 (2014)

Chapter 28
Elastic Properties of CNT-Reinforced Silver Nanocomposites Using FEM

Lakshya Khurana, Ashish Kumar Srivastava and Dharmendra Tripathi

Abstract In the present study, at the outset, a three-phase model of carbon nanotube (CNT)-reinforced silver (Ag) nanocomposite is proposed. The proposed model constitutes CNT (i.e., reinforcement); Ag (i.e., matrix material) and a third phase representing the interphase zone between CNT and Ag. The thickness and elastic modulus of the proposed interphase zone are computed with the aid of cohesive zone model. Finite element method (FEM) based study is conducted using COMSOL Multiphysics to characterize the nanocomposite in terms of its elastic properties. The method of representative boundary element (RVE) is used to model the unit cell of the CNT-Ag nanocomposite along with interphase zone. Periodic boundary and various loading conditions are applied on the RVE in order to predict the elastic moduli of nanocomposite. The results obtained through the FEM analysis are validated by analytical approaches viz. rule of mixtures (ROM). The influence of the length and volume fraction of CNT on the elastic properties of nanocomposite is discussed. It is observed that, in contrast to CNT-polymer nanocomposites, in CNT-Ag nanocomposites, the interphase zone poses a negative effect on the effective elastic properties of the nanocomposite.

28.1 Introduction

Carbon nanotubes are cylindrical structures made of carbon atoms arranged hexagonally, the diameter of which is in the nanometre scale. They exhibit exceptional mechanical properties and possess very high ratio of length to diameter. Such a very significant use of carbon nanotubes is in the form of reinforcements in nanocomposites. There is a significant increase in the strength of a material with the use of CNTs as reinforcements as compared to the pure material. The simulations

L. Khurana (✉) · A. K. Srivastava
Department of Mechanical Engineering, Manipal University Jaipur, Jaipur, India
e-mail: lakshyak894@gmail.com

D. Tripathi
Department of Mathematics, NIT Uttarakhand, Srinagar, India

I. A. Parinov et al. (eds.), *Advanced Materials*, Springer Proceedings in Physics 224, https://doi.org/10.1007/978-3-030-19894-7_28

done in this paper are based on the LJ (Lennard-Jones) potential parameters as focused on the interaction of silver and carbon atoms at the interphase. The LJ potential provides us the cohesive energy of the interaction between two non-bonding atoms or molecules at a given distance and gives information regarding the equilibrium distance at which the cohesive energy is minimised. The force interaction between these atoms or molecules is van der Wall in nature. At the equilibrium distance obtained from LJ potential considerations, it is possible to determine the elastic modulus of the interphase. The interphase behaves in a manner of possessing its own unique mechanical properties that have a significant effect on the properties of the nanocomposite as a whole. It, hence, has to be determined for undertaking the simulations accurately.

The cohesive energy (ϕ) between two non-bonding atoms or molecules as given by the LJ potential [2, 3, 6] at the equilibrium distance is given by

$$\phi = \frac{2\pi^2}{3}\rho_m\rho_c\sigma_1^3\varepsilon_1\left\{2R\left[\left(\frac{2\sigma_1}{15r}\right)^9-\left(\frac{\sigma_1}{r}\right)^3\right]+\frac{3}{2}\sigma_1\left[\frac{1}{10}\left(\frac{\sigma_1}{r}\right)^8-\left(\frac{\sigma_1}{r}\right)^2\right]\right\} \quad (28.1)$$

where ρ_m is the density of matrix material (Ag), ρ_c is the density of the CNT, σ_1 is the $v\mathrm{d}W$ radius at equilibrium, ε_1 is the bond energy at equilibrium distance, r is the variable distance between a point in the matrix from the surface of CNT.

The value of the elastic modulus of the interphase is derived from the cohesive energy by differentiating it with the strain as follows;

$$E = \frac{\partial^2\phi}{\partial^2 S} \quad (28.2)$$

where S is the strain $\left(=\frac{r-h_0}{h_0}\right)$

This gives us the interphase modulus for the CNT reinforced nanocomposite as

$$E = \frac{2}{3}\pi^2 h_0\rho_m\rho_c\sigma_1\varepsilon_1\left\{24R\left[\left(\frac{\sigma_1}{r}\right)^{11}-\left(\frac{\sigma_1}{r}\right)^5\right]+9\sigma_1\left[\frac{6}{5}\left(\frac{\sigma_1}{r}\right)^{10}-\left(\frac{\sigma_1}{r}\right)^4\right]\right\} \quad (28.3)$$

The equation for elastic modulus obtained here is in the units of force per unit length and needs to divided by the average circumference of the CNT $\left[=2R\left(R+\frac{h_0}{2}\right)\right]$ to give the correct solution.

The thickness of the interphase (h_0) is a function of the equilibrium van der Wall radius of the LJ potential and is derived by evaluating $\frac{\partial\phi}{\partial r}=0$. It is given as

$$h_0 = 0.8584\sigma_I \quad (28.4)$$

28.2 Modelling

The nanocomposite is modelled in the form of a representative volume element (RVE) (see Fig. 28.1). The RVE is a volume with a square cross-section such that a particular volume fraction of the CNT is maintained [5, 7]. In the case of this paper, the volume fractions used are 1, 2, 3 and 4 in %. The volume fraction of the CNT and interphase is given as follows:

$$V_N = \frac{\pi\left(r_o^2 - r_i^2\right)}{a^2 - \pi r_i^2} \tag{28.5}$$

$$V_I = \frac{\pi n\left(r_I^2 - r_o^2\right)}{a^2 - \pi n r_i^2} \tag{28.6}$$

where a is the RVE side and n is the number of CNTs (5 or 9).

Equations (28.5) and (28.6) are for volume fraction of CNT and interphase, respectively. Calculating the volume fraction from these two equations, we get the value for side of the RVE cross-section (square) for the nanocomposite as follows:

$$a = \sqrt{\left[\pi r_i^2 + \left(\frac{\pi}{V_N}\right)\left(r_o^2 - r_i^2\right)\right]} \tag{28.7}$$

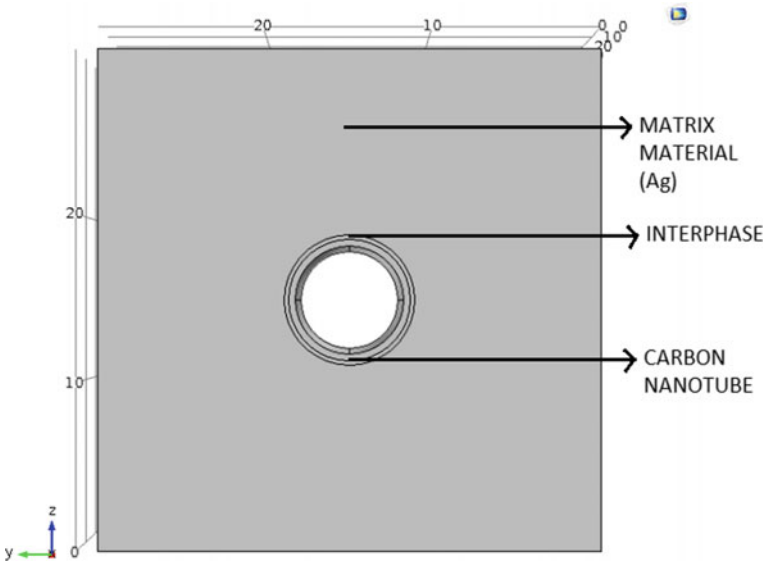

Fig. 28.1 Representative Volume Element (RVE) showing material geometry and placement

Table 28.1 LJ potential parameters for CNT reinforced silver nanocomposite

Material	Bonding	σ (nm)	ε (eV)
Silver	Ag–Ag	0.2644	0.3447
Carbon	C–C	0.3369	0.00263
Silver–Carbon	Ag–C	0.3006	0.0301

$$a = \sqrt{\left\{ n\pi \left[r_i^2 + \frac{\left(r_o^2 - r_i^2\right)}{V_N} \right] \right\}} \tag{28.8}$$

Equations (28.7) and (28.8) are for single CNT reinforced RVE and multiple CNT reinforced RVE, respectively.

The LJ potential parameters for bonding between atoms of the same elements are available from online resources. These parameters are used to calculate the potential parameters of bonding between two atoms of different elements (see Table 28.1). LB (Lorentz-Berthelot) mixing rule [8, 9] is used to calculate these parameters [1, 2, 4, 8] and is given as follows:

$$\sigma_I = \frac{\sigma_N + \sigma_m}{2} \tag{28.9}$$

$$\varepsilon_I = \sqrt{\varepsilon_N \varepsilon_m} \tag{28.10}$$

28.3 Methodology

Model nanocomposite RVEs are present in Fig. 28.2. The simulations performed in this paper are done by applying periodic boundary conditions to the RVE [2]. Orthogonal moduli in all three dimensions are hence obtained. The simulations were performed using FEM package COMSOL Multiphysics. The values for stress and strain in the required direction are obtained by using the volume integration feature in COMSOL. This method is based upon the homogenisation method (numerical homogenisation procedure [2]) used to obtain the average values of stress and strain for the nanocomposite. The value for elastic constant of carbon nanotube is obtained by finding the slope of stress strain curve for CNT [10].

3.1. For calculating E_x (Normal Loading), the boundary conditions are given as

$$u_{11}(0, y, z) = u_{22}(x, 0, z) = u_{33}(x, y, 0) = 0; u_{11}(L, y, z) = \delta_1$$

where u_{11}, u_{22} and u_{33} are the displacement components in x, y and z directions, respectively and δ_1 is the displacement applied in the $x = L$ face in x-direction.

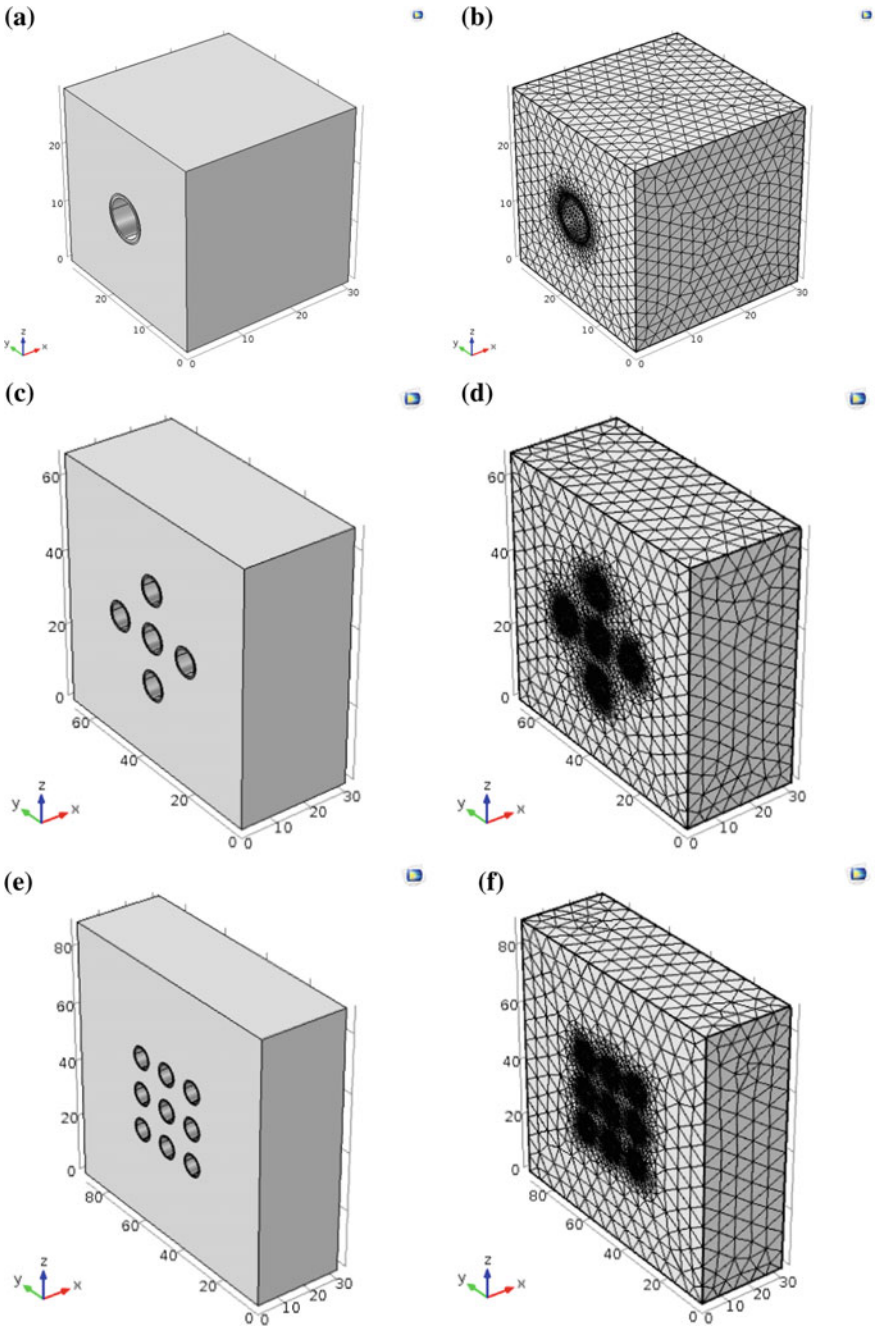

Fig. 28.2 Nanocomposite RVE with length of 30 nm, reinforced with: **a** a single (Unmeshed), **b** a single CNT (Fine Mesh), **c** 5 CNTs (Unmeshed), **d** 5 CNTs (Fine Mesh), **e** 9 CNTs (Unmeshed) and **f** 9 CNTs (Fine Mesh)

3.2. For calculating E_y (Normal Loading), the boundary conditions are given as

$$u_{11}(0, y, z) = u_{22}(x, 0, z) = u_{33}(x, y, 0) = 0; u_{22}(x, a, z) = \delta_2$$

where δ_2 is the displacement applied on the $y = a$ face in y-direction.

3.3. For calculating E_z (Normal Loading), the boundary conditions are given as

$$u_{11}(0, y, z) = u_{22}(x, 0, z) = u_{33}(x, y, 0) = 0; u_{33}(x, y, a) = \delta_3$$

where δ_3 is the displacement applied on the $z = a$ face in z-direction.

3.4. For calculating G_{12} (Longitudinal Shear Loading), the boundary conditions are given as

$$u_{11}(x, y, 0) = u_{22}(x, y, 0) = u_{33}(x, y, 0) = 0; u_{11}(x, y, a) = \delta_4$$

where δ_4 is the displacement applied in the $z = a$ face in x-direction.

3.5. For calculating G_{13} (Longitudinal Shear Loading), the boundary conditions are given as

$$u_{11}(x, 0, z) = u_{22}(x, 0, z) = u_{33}(x, 0, z) = 0; u_{11}(x, a, z) = \delta_5$$

where δ_5 is the displacement applied in the $y = a$ face in x-direction.

3.6. For calculating G_{23} (Transverse Shear Loading), the boundary conditions are given as

$$u_{11}(x, y, 0) = u_{22}(x, y, 0) = u_{33}(x, y, 0) = 0; u_{11}(x, y, a) = \delta_6$$

where δ_6 is the displacement applied in the $z = a$ face in y-direction.

28.4 Validation

The validation of the results of the simulation is done by comparing them with the analytical solutions for the same geometrical RVE with the same boundary conditions. The analytical method used, called the rules of mixture (ROM), is given as

$$E_1 = V_N E_N + V_I E_I + (1 - V_N - V_I) E_m \tag{28.11}$$

where E_1 is the elastic modulus in the x-direction; V_N and V_I are the volume fractions of the CNT and the interphase, respectively; E_I, E_m and E_N are the elastic moduli for the interphase, matrix material and CNT, respectively.

The deviation of FEM results from the analytical (true) results is calculated by a simple error formula. The error is relative to the analytical results derived from the rule of mixture (ROM) method. The error is given by

$$\text{Error}(e) = \frac{(A - F) \cdot 100}{A} \tag{28.12}$$

where A represents the analytical value and F represents the FEM (simulation) value.

28.5 Results and Discussion

In this section, the results of the FEM simulations are tabulated. They include the stiffness constants for various number of CNTs (see Tables 28.2, 28.3, 28.4, 28.5, 28.6, 28.7, 28.8, 28.9 and 28.10), various volume fractions of CNT and different RVE lengths. The numbers of CNTs used are 1, 5 and 9. The CNTs are arranged in a pattern to observe the effect of the arrangement on the mechanical properties (see Figs. 28.3 and 28.4). The volume fractions used are 1, 2, 3 and 4 in %. The RVE lengths used are 30, 50 and 100 in nm.

Table 28.2 Stiffness constants for 30 nm RVE nanocomposite reinforced with 1 CNT

Stiffness constants (GPa)	Volume fraction of CNT (%)			
	1	2	3	4
E_x	101.804	118.613	135.414	152.217
E_y	88.725	92.329	95.823	99.207
E_z	88.725	92.329	95.823	99.207
G_{12}	34.649	36.656	38.69	40.753
G_{13}	34.6495	36.655	38.6915	40.7525
G_{23}	34.1205	35.643	37.266	39.0055

Table 28.3 Stiffness constants for 50 nm RVE nanocomposite reinforced with 1 CNT

Stiffness constants (GPa)	Volume fraction of CNT (%)			
	1	2	3	4
E_x	101.804	118.613	135.414	152.217
E_y	88.819	92.466	95.978	99.367
E_z	88.819	92.466	95.978	99.367
G_{12}	34.689	36.722	38.78	40.862
G_{13}	34.687	36.7215	38.7795	40.862
G_{23}	34.12	35.639	37.2605	39

Table 28.4 Stiffness constants for 100 nm RVE nanocomposite reinforced with 1 CNT

Stiffness constants (GPa)	Volume fraction of CNT (%)			
	1	2	3	4
E_x	101.804	118.613	135.414	152.217
E_y	88.891	92.569	96.094	99.49
E_z	88.891	92.569	96.094	99.49
G_{12}	34.7125	36.76	38.831	40.9245
G_{13}	34.7125	36.758	38.831	40.9245
G_{23}	34.1195	35.639	37.2595	38.997

Table 28.5 Stiffness constants for 30 nm RVE nanocomposite reinforced with 5 CNTs

Stiffness constants (GPa)	Volume fraction of CNT (%)			
	1	2	3	4
E_x	101.803	118.617	135.414	152.219
E_y	88.568	92.107	95.539	98.796
E_z	88.568	92.107	95.539	98.796
G_{12}	34.617	36.625	38.7245	40.9055
G_{13}	34.6165	36.624	38.7245	40.9055
G_{23}	34.1275	35.45	36.6095	37.6065

Table 28.6 Stiffness constants for 50 nm RVE nanocomposite reinforced with 5 CNTs

Stiffness constants (GPa)	Volume fraction of CNT (%)			
	1	2	3	4
E_x	101.803	118.617	135.414	152.217
E_y	88.869	92.273	95.73	99.002
E_z	88.689	92.273	95.73	99.002
G_{12}	34.65	36.69	38.7915	40.963
G_{13}	34.65	36.688	38.7195	40.963
G_{23}	34.127	35.4475	36.601	37.5925

Table 28.7 Stiffness constants for 100 nm RVE nanocomposite reinforced with 5 CNTs

Stiffness constants (GPa)	Volume fraction of CNT (%)			
	1	2	3	4
E_x	101.803	118.617	135.414	152.219
E_y	88.796	92.414	95.874	99.168
E_z	88.796	92.414	95.874	99.168
G_{12}	34.6945	36.7515	38.8505	41.0135
G_{13}	34.696	36.7515	38.851	41.0135
G_{23}	34.1725	35.446	36.5965	37.587

Table 28.8 Stiffness constants for 30 nm RVE nanocomposite reinforced with 9 CNTs

Stiffness constants (GPa)	Volume fraction of CNT (%)			
	1	2	3	4
E_x	101.805	118.609	135.415	152.214
E_y	88.449	91.893	95.315	98.716
E_z	88.449	91.893	95.315	98.716
G_{12}	31.5705	31.4885	32.513	34.098
G_{13}	34.5955	36.557	38.6025	40.7205
G_{23}	34.214	35.662	36.987	38.1785

Table 28.9 Stiffness constants for 50 nm RVE nanocomposite reinforced with 9 CNTs

Stiffness constants (GPa)	Volume fraction of CNT (%)			
	1	2	3	4
E_x	101.805	118.609	135.415	152.213
E_y	88.564	92.074	95.519	99.065
E_z	88.564	92.074	95.519	99.065
G_{12}	32.172	33.311	34.9415	39.361
G_{13}	34.623	36.6285	38.6995	40.9135
G_{23}	34.2115	35.658	36.982	38.178

Table 28.10 Stiffness constants for 100 nm RVE nanocomposite reinforced with 9 CNTs

Stiffness constants (GPa)	Volume fraction of CNT (%)			
	1	2	3	4
E_x	101.805	118.608	135.415	152.213
E_y	88.692	92.242	95.682	99.065
E_z	88.692	92.242	95.682	99.065
G_{12}	33.532	35.357	37.313	39.361
G_{13}	34.6735	36.7185	38.7995	40.9135
G_{23}	34.2125	35.661	38.9855	38.178

Tables 28.11, 28.12 and 28.13 show very low error value between the analytical and FEM results and hence verify that the results derived from the simulations are correct.

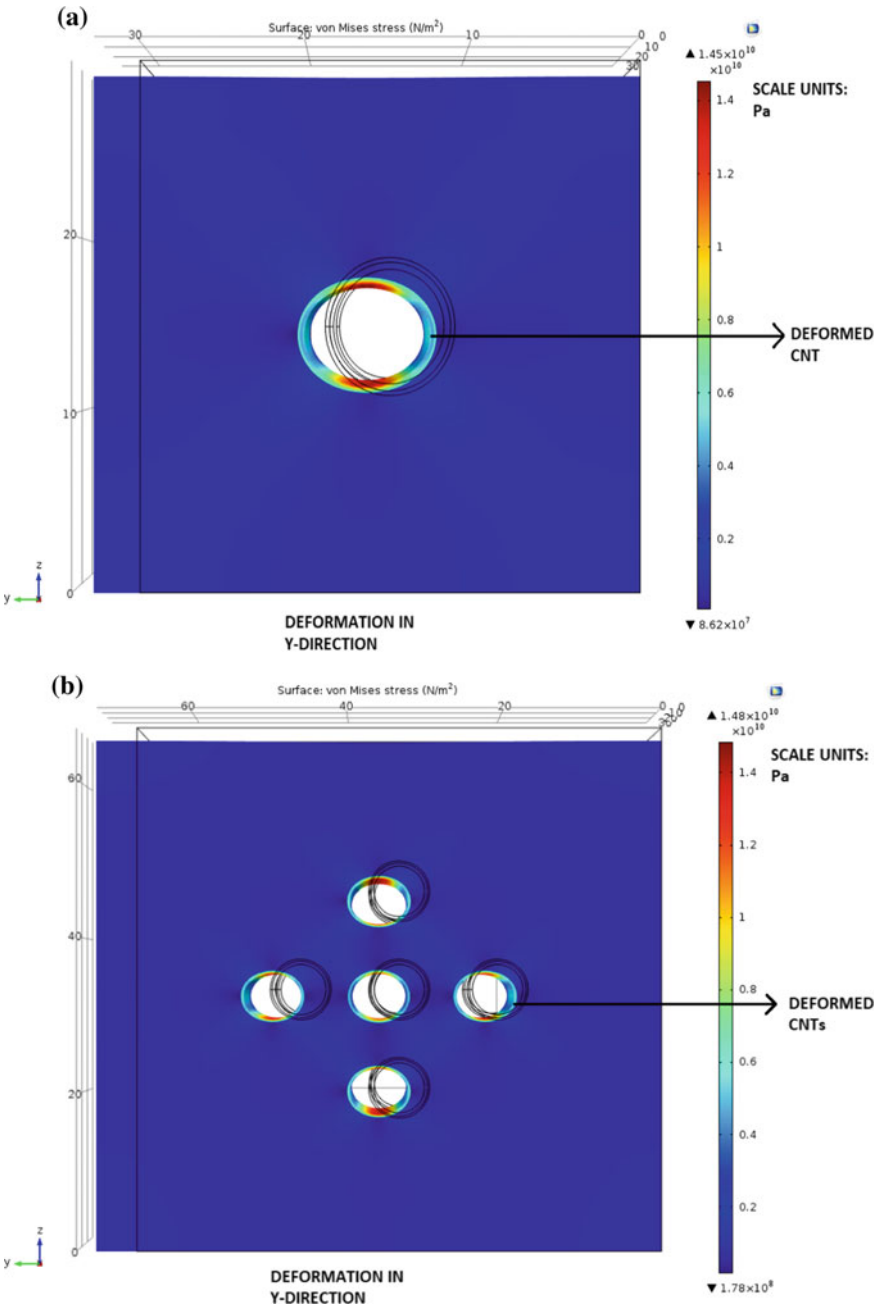

Fig. 28.3 Deformation of nanocomposite in y-direction nanocomposite RVE with length of 30 nm for reinforced with **a** a single CNT, **b** 5 CNTs and **c** 9 CNTs

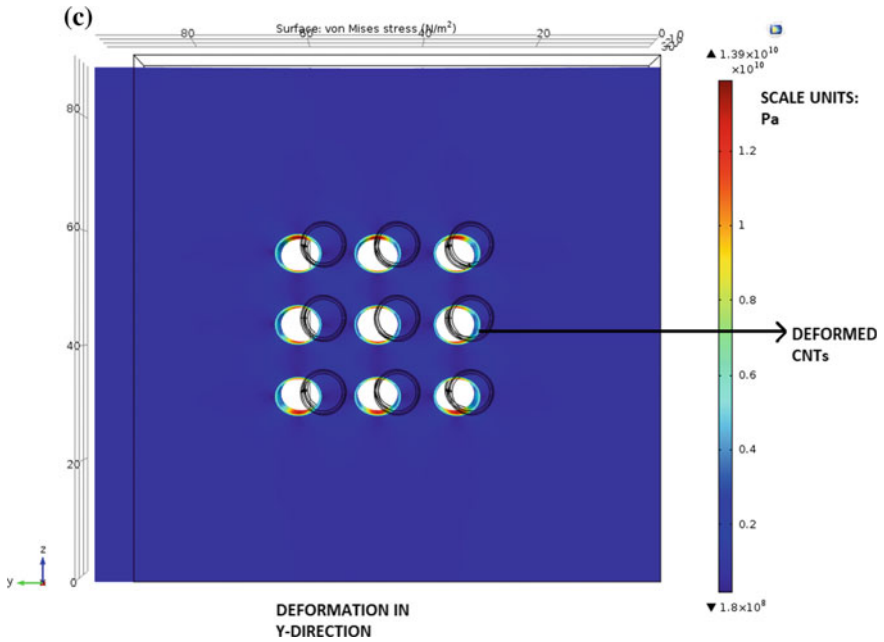

Fig. 28.3 (continued)

28.6 Conclusions

The simulations conducted for this paper have the range of 1–4% for the volume fraction of the CNT relative to the RVE and for RVE lengths of 30, 50 and 100 nm. The boundary conditions applied to the RVE are periodic in nature and the following conclusions can be derived from the results:

(i) the orthogonal moduli of the nanocomposite increase linearly with the increase of the volume fraction of the CNT. This is attributed to increase in the high-strength CNT fibre relative to the matrix material;
(ii) the orthogonal moduli are independent of the length of the RVE and only depend on the volume fraction of CNT;
(iii) the orthogonal moduli are heavily dependent on the number of the CNTs present in an RVE with significant increase in the strength of the nanocomposite with the number density of CNTs.

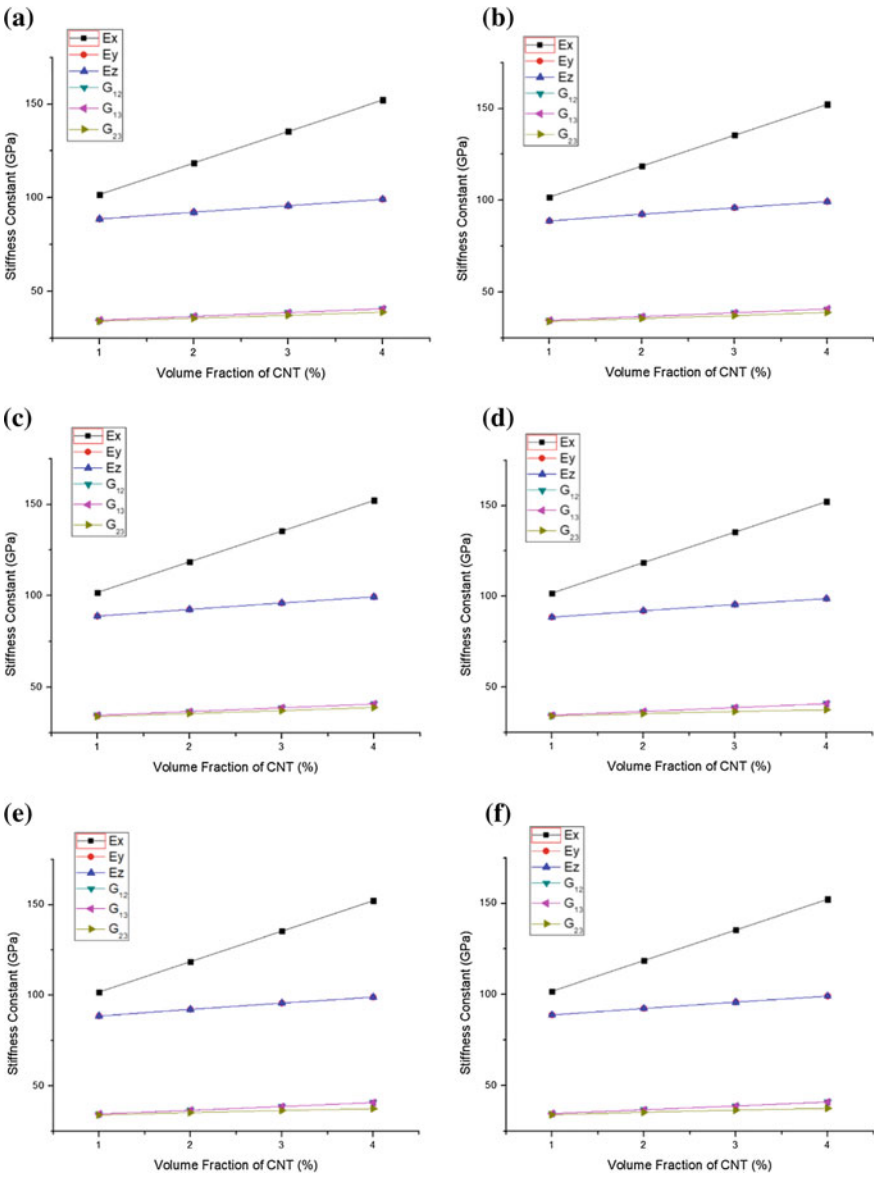

Fig. 28.4 Modulus of elasticity *vs* volume fraction of CNT for **a** single CNT nanocomposite (30 nm), **b** single CNT nanocomposite (50 nm), **c** single CNT nanocomposite (100 nm), **d** multiple CNTs (5) nanocomposite (30 nm), **e** multiple CNTs (5) nanocomposite (50 nm), **f** multiple CNTs (5) nanocomposite (100 nm), **g** multiple CNTs (9) nanocomposite (30 nm), **h** multiple CNTs (9) nanocomposite (50 nm), **i** multiple CNTs (9) nanocomposite (100 nm)

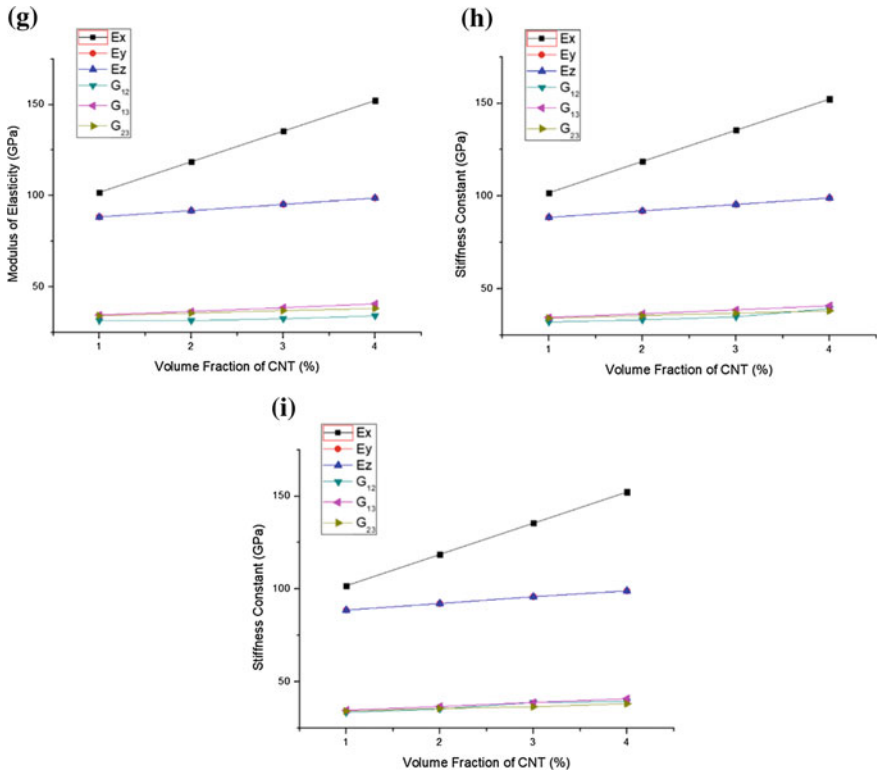

Fig. 28.4 (continued)

Table 28.11 Error (%) for nanocomposite reinforced with a single CNT for given volume fraction of CNT

Length of RVE (nm)	Volume fraction of CNT (%)			
	1	2	3	4
30	−0.00393	−0.00253	−0.00295	0.00197
50	−0.00393	−0.00253	−0.00295	0.00197
100	−0.00295	−0.002530	−0.00295	0.00197

Table 28.12 Error (%) for nanocomposite reinforced with 5 CNTs for given volume fraction of CNT

Length of RVE (nm)	Volume fraction of CNT (%)			
	1	2	3	4
30	−0.00295	−0.0059	−0.00295	0.000657
50	−0.00295	−0.0059	−0.00295	0.00197
100	−0.00295	−0.0059	−0.00295	0.000657

Table 28.13 Error (%) for nanocomposite reinforced with 9 CNTs for given volume fraction of CNT

Length of RVE (nm)	Volume fraction of CNT (%)			
	1	2	3	4
30	−0.00491	0.000843	−0.00369	0.00394
50	−0.00491	0.000843	−0.00369	0.00459
100	−0.00491	0.00169	−0.00295	0.00459

References

1. H. Akbarzadeh, H. Yaghoubi, J. Colloid Interface Sci. **418**, 178–184 (2014)
2. A. Srivastava, D. Kumar, Mat. Res. Expr. **4**(2), 025036 (2017)
3. A.K. Srivastava, V.K. Pathak, M.K. Dixit, in *National Conference on Advanced Materials, Manufacturing and Metrology (NCAMMM - 2018)*, vol. 74, ed. by Dr. S. Dutta, Dr. S.S. Chakraborty (2018)
4. M. Neek-Amal, R. Asgari, M.R. Tabar, Nanotechnology **20**(13), 135602 (2009)
5. X.L. Chen, Y.J. Liu, Comput. Mater. Sci. **29**(1), 1 (2004)
6. L.Y. Jiang, Y. Huang, H. Jiang, G. Ravichandran, H. Gao, K.C. Hwang, B. Liu, J. Mech. Phys. Solids **54**(11), 2436 (2006)
7. I.M. Gitman, H. Askes, L.J. Sluys, Eng. Fract. Mech. **74**(16), 2518 (2007)
8. D. Boda, D. Henderson, Mol. Phys. **106**(20), 2367 (2008)
9. A. White. *Intermolecular Potentials of Mixed Systems: Testing the Lorentz-Berthelot Mixing Rules with Ab Initio Calculations* (No. DSTO-TN-0302). Defence Science and Technology Organisation Melbourne, Australia (2000)
10. M.F. Yu, B.S. Files, S. Arepalli, R.S. Ruoff, Phys. Rev. Lett. **84**(24), 5552 (2000)

Chapter 29
Thermoelastic Instability in Coupled Thermoelastic Sliding Wear Problem

Vladimir B. Zelentsov, Boris I. Mitrin, Igor A. Lubyagin and Sergei M. Aizikovich

Abstract Thermoelastic instability is considered in the case of the rigid semi-infinite body sliding over the coating surface, exposing it to abrasive wear and frictional heating. The solution of the formulated quasi-static coupled thermoelasticity problem is represented in the form of integrals of the inverse Laplace transform, which are found to be dependent on four dimensionless parameters. Analysis of the integrand poles with respect to these parameters reveals four types of stability and instability regions. Expressions for temperature, contact stresses and wear of the coating are obtained in form of series over integrands poles. Numerical analysis of the solution is carried out with respect to the dimensionless and dimensional parameters of the problem. Particular attention is paid to the effect of the thermoelastic coupling parameter.

29.1 Introduction

Interaction of deformation and temperature fields was started from [1, 2] as a coupled thermoelasticity theory. These basic results were generalized in [3–5]. To solve coupled thermoelastic problems, different methods was developed since then, both analytical [4, 5] and numerical [6]. In [6], a finite element scheme was developed to solve a coupled thermoelasticity problem. Further investigations on coupled elasticity also heavily used the finite element method, for example [7–11]. Analytical methods for these problems have not gained such wide development as numerical. Intermediate results on analytical methods was summarized in [12].

Starting from [13–18], uncoupled thermoelasticity problems were considered accounting for friction, frictional heating and abrasive wear of the coating. Due to large number of parameters in the sliding thermoelastic contact problems [15–19], one-dimensional quasi-static problems were mostly considered. Solutions of

V. B. Zelentsov · B. I. Mitrin (✉) · I. A. Lubyagin · S. M. Aizikovich
Research and Education Center “Materials”, Don State Technical University, Rostov-on-Don, Russia
e-mail: bmitrin@dstu.edu.ru

I. A. Parinov et al. (eds.), *Advanced Materials*, Springer Proceedings in Physics 224, https://doi.org/10.1007/978-3-030-19894-7_29

uncoupled problems in [15–19] were constructed by the Laplace integral transform in the form of functional series over poles of integrands of contour integrals of the inverse Laplace transform. This method of the uncoupled thermoelastic problems solutions allowed one to obtain parametric boundaries of sliding contact thermoelastic instability and to investigate properties of the obtained solutions. In [20–22] a new directions were developed for the model of sliding of two elastic bodies against each other accounting for friction, frictional heating and wear, based on the virtual energy principle and main laws of thermodynamics. To solve problems based on this model, the finite element method is adopted [22].

The present works addresses effect of the dimensionless parameter of thermal and elastic fields coupling on the main parameters of sliding contact and on the thermoelastic instability occurrence.

29.2 Statement of the Coupled Problem of Wear

To investigate the effect of thermoelastic coupling on the occurrence of thermoelastic instability in sliding contact problems, the contact problem of coupled thermoelasticity on sliding with a constant velocity V of a rigid heat-insulated half-plane I $(h \le x < \infty)$ over the upper $(x = h)$ surface of an elastic thermal-conducting coating of thickness h $(0 \le x \le h)$, is considered. The lower surface of the coating is rigidly coupled to a non-deformable non-heat-conducting substrate in the form of a half-plane II $(\infty < x < 0)$. Sliding of the half-plane I along the surface of the elastic coating takes into account Coulomb friction and abrasive wear of the coating surface [15–19]. The heat flux generated at the contact due to friction is directed into the coating. From the initial time moment, the half-plane I moving along the axis y deforms the surface $(x = h)$ of the elastic coating, moving in the direction opposite to the x-axis, according to the law $\Delta(t)$. Until the initial moment, the coating was at rest, and its temperature was equal to T_0.

The formulation of the problem assumes that the distributions of temperature, stresses and displacements in the coating do not depend on the choice of the horizontal coordinate along the y-axis parallel to the direction of the half-plane I sliding, and are functions of only the coordinate x and time t [15–19]. The displacements and temperature in the coating are governed by quasi-static coupled thermoelasticity equations [23]:

$$\frac{\partial^2 u}{\partial x^2} = \frac{1+\nu}{1-\nu}\alpha\frac{\partial T}{\partial x}, \quad \frac{\partial^2 w}{\partial x^2} = 0, \quad 0 \le x \le h, \quad t > 0 \tag{29.1}$$

$$\frac{\partial^2 T}{\partial x^2} - \frac{1}{\kappa}\frac{\partial T}{\partial t} = \alpha\frac{3\lambda + 2\mu}{K}T_0\frac{\partial^2 u}{\partial x \partial t} \quad 0 \le x \le h, \quad t > 0 \tag{29.2}$$

where $T(x,t)$ is the temperature distribution in the coating, $u(x,t)$, $w(x,t)$ are the vertical and horizontal displacements in the coating, α is a coefficient of linear

expansion of coating material, κ is a coefficient of thermal diffusivity, λ, μ are Lamé coefficients, K is a coefficient of thermal conductivity, T_0 is the initial temperature in the coating.

The boundary conditions of the problem for the differential equations (29.1) and (29.2) are:

mechanical $(t > 0)$

$$x = h \quad u(h,t) = -\Delta(t) + u_w(t) \tag{29.3}$$

$$\sigma_{xy}(h,t) = -f\sigma_{xx}(h,t) \tag{29.4}$$

$$x = 0 \quad u(0,t) = 0 \tag{29.5}$$

$$w(0,t) = 0 \tag{29.6}$$

temperature $(t > 0)$

$$x = h \quad K\frac{\partial T(h,t)}{\partial x} = Q(t) \tag{29.7}$$

$$x = 0 \quad K\frac{\partial T(0,t)}{\partial x} = k(T(0,t) - T_0) \tag{29.8}$$

where f is a coefficient of friction, k is a coefficient of heat transfer, $u_w(t)$ is the half-plane I displacement due to the wear of the coating, $Q(t) = fV(-\sigma_{xx}(h,t))$ is the heat generated by friction at the contact interface [24]; $\sigma_{xx} = \sigma_{xx}(x,t)$, $\sigma_{xy} = \sigma_{xy}(x,t)$ are the normal and tangential stresses in the coating, defined by a form of the Hooke's law:

$$\sigma_{xx} = (\lambda + 2\mu)\frac{\partial u}{\partial x} - (3\lambda + 2\mu)\alpha(T - T_0), \quad \sigma_{xy} = \mu\frac{\partial w}{\partial x} \tag{29.9}$$

Further, the abrasive wear model [25] is used, according to which the amount of wear is

$$u_w(t) = -fVK^* \int_0^t \sigma_{xx}(h,\tau)\mathrm{d}\tau \quad t > 0 \tag{29.10}$$

where K^* is a coefficient of proportionality between the work of friction al forces and the amount of material removed from the contact. In addition, according to (29.7), it is assumed that all the heat at the contact is formed due to friction.

The initial conditions for displacement in the coating are zero:

$$u(x,0) = w(x,0) = 0 \tag{29.11}$$

while initial temperature is set to T_0:

$$T(x,0) = T_0 \tag{29.12}$$

Thus, the solution of the formulated problem is reduced to solution the system of differential equations (29.1) and (29.2) with the boundary (29.3)–(29.8) and initial conditions (29.11) and (29.12). It should be noted that the vertical displacements $u(x,t)$, normal stresses $\sigma_{xx}(x,t)$ and temperature $T(x, t)$ in the coating are determined independently from the horizontal displacements $w(x, t)$, while latter are determined from (29.1), (29.4) and (29.6) through $\sigma_{xx}(x,t)$.

29.3 Exact Solution of the Problem

The solution of the coupled contact thermoelasticity problem given in Sect. 29.2 is constructed using the Laplace integral transformation [27]:

$$u^L(x,p) = \int_0^\infty u(x,t)e^{-pt}\mathrm{d}t, \quad u(x,t) = \frac{1}{2\pi i}\int_{-i\infty+c}^{i\infty+c} u^L(x,p)e^{pt}\mathrm{d}p, \tag{29.13}$$
$$\mathrm{Re}\, p < c, \quad c > 0$$

The index L in (29.13) denotes the transform of the Laplace transformation.

The Laplace transformation (29.13) is applied to the differential equations (29.1) and (29.2) taking into account the initial conditions (29.11) and (29.12) and the existence conditions for the Laplace integrals (29.13) [27]. As a result, a system of ordinary differential equations is obtained with respect to the transforms $u^L(x,p)$ and $T^L(x,p)$:

$$\frac{\mathrm{d}^2u^L}{\mathrm{d}x^2} = \frac{1+\nu}{1-\nu}\alpha\frac{\mathrm{d}T^L}{\mathrm{d}x}, \quad 0 \le x \le h \tag{29.14}$$

$$\frac{\mathrm{d}^2T^L}{\mathrm{d}x^2} - \frac{p}{\kappa}T^L - \frac{1}{\kappa}T_0 = \frac{2\mu(1+\nu)}{1-2\nu}\frac{\alpha}{K}T_0 p\frac{\mathrm{d}u^L}{\mathrm{d}x}, \quad 0 \le x \le h \tag{29.15}$$

Differentiating (29.15) and substituting the second derivative of $u^L(x,p)$ from (29.14) into the resulting relation, the following differential equation is obtained with respect to $T^L(x,p)$:

$$\frac{\mathrm{d}}{\mathrm{d}x}\left(\frac{\mathrm{d}^2T^L}{\mathrm{d}x^2}-\frac{\beta^2}{\kappa}pT^L\right)=0 \quad 0\le x\le h \tag{29.16}$$

$$\beta^2=1+\hat{T}, \quad \hat{T}=\frac{2\mu(1+\nu)^2}{(1-\nu)(1-2\nu)}\frac{\kappa\alpha^2}{K}T_0$$

The general solution of the differential equation (29.16) has the form:

$$T^L(x,p)=A_1+A_2\,\mathrm{sh}\left(\sqrt{\frac{p}{\kappa}}\beta x\right)+A_3\,\mathrm{ch}\left(\sqrt{\frac{p}{\kappa}}\beta x\right) \tag{29.17}$$

in which A_1, A_2, A_3 are arbitrary constants.

Substituting $T^L(x,p)$ from (29.17) into (29.14), an inhomogeneous differential equation with respect to $u^L(x,p)$ is obtained. Its double integration gives the general solution:

$$u^L(x,p)=\frac{1+\nu}{1-\nu}\alpha\frac{1}{\sqrt{\frac{p}{\kappa}}\beta}\left(A_2\,\mathrm{ch}\left(\sqrt{\frac{p}{\kappa}}\beta x\right)+A_3\,\mathrm{sh}\left(\sqrt{\frac{p}{\kappa}}\beta x\right)\right)+A_4x+A_5 \tag{29.18}$$

where A_2, A_3 are from (29.17), A_4, A_5 are new unknown values depending on p.

Substituting (29.17) and (29.18) into (29.15), a dependence between A_1 and A_4 is found:

$$A_1=\frac{T_0}{p}-\frac{1-\nu}{1+\nu}\frac{\hat{T}}{\alpha}A_4 \tag{29.19}$$

Replacing A_1 by A_4 in (29.17) according to (29.19), the general solution for $T^L(x,p)$ from (29.14), (29.15) is obtained as

$$T^L(x,p)=\frac{T_0}{p}+A_2\,\mathrm{sh}\left(\sqrt{\frac{p}{\kappa}}\beta x\right)+A_3\,\mathrm{ch}\left(\sqrt{\frac{p}{\kappa}}\beta x\right)-\frac{1-\nu}{1+\nu}\frac{\hat{T}}{\alpha}A_4 \tag{29.20}$$

Thus, $u^L(x,p)$ from (29.18) and $T^L(x,p)$ from (29.20) with constants A_2–A_5 are general solutions of the system (29.14) and (29.15), and the constants A_2–A_5 are found from the boundary conditions (29.3), (29.5), (29.7) and (29.8), after applying the integral Laplace transform to them:

mechanical

$$x = h \quad u^L(h,p) = -\Delta^L(p) + u_w^L(p) \tag{29.21}$$

$$x = 0 \quad u^L(x,p) = 0 \tag{29.22}$$

temperature

$$x = h \quad K\frac{dT^L(h,p)}{dx} = -fV\sigma_{xx}^L(h,p) \tag{29.23}$$

$$x = 0 \quad K\frac{dT^L(0,p)}{dx} = k\left(T^L(0,p) - \frac{T_0}{p}\right) \tag{29.24}$$

in which $u_w^L(p) = -fVK^*\frac{\sigma_{xx}^L(h,p)}{p}$

$$\sigma_{xx}^L(x,p) = \frac{2\mu(1-\nu)}{1-2\nu}\frac{du^L(x,p)}{dx} - \frac{2\mu(1+\nu)}{1-2\nu}\alpha\left(T^L(x,p) - \frac{T_0}{p}\right) \tag{29.25}$$

Substituting (29.18) and (29.20) into the boundary conditions (29.22) and (29.24) gives relations for A_4 and A_5 which, after being itself substituted to (29.18) and (29.20), allow us to obtain $u^L(x,p)$ and $T^L(x,p)$ in the new form, depending only on A_2 and A_3:

$$\begin{aligned} u^L(x,p) = {} & \frac{1+\nu}{1-\nu}\frac{\alpha h}{\sqrt{\frac{p}{\kappa}}\beta h}\left(A_2\left(\operatorname{ch}\sqrt{\frac{p}{\kappa}}\beta x - 1\right) + A_3 \operatorname{sh}\sqrt{\frac{p}{\kappa}}\beta x\right) \\ & - \frac{1+\nu}{1-\nu}\frac{\alpha}{\hat{T}\mathrm{Bi}}\left(\sqrt{\frac{p}{\kappa}}\beta h A_2 - \mathrm{Bi}A_3\right)x \end{aligned} \tag{29.26}$$

$$T^L(x,p) = A_2\frac{1}{\mathrm{Bi}}\left(\sqrt{\frac{p}{\kappa}}\beta h + \mathrm{Bi}\operatorname{sh}\sqrt{\frac{p}{\kappa}}\beta x\right) + A_3\left(\operatorname{ch}\sqrt{\frac{p}{\kappa}}\beta x - 1\right) + \frac{T_0}{p} \tag{29.27}$$

The constants A_2 and A_3 are determined by substituting (29.26) and (29.27) into the boundary conditions (29.21) and (29.23), after which a system of linear algebraic equations is formed with respect to A_2 and A_3:

$$\sum_{j=1}^{2} a_{ij}A_{j+1} = b_i \quad i = 1,2 \tag{29.28}$$

where b_i, a_{ij} $i,j = 1,2$ are calculated from the formulas:

$$a_{11} = \sqrt{z}\left(\hat{T}\mathrm{Bi}\ (\mathrm{ch}\sqrt{z} - 1) - z - \hat{V}k_w\beta^2\right), \quad a_{12} = \mathrm{Bi}\left(\hat{T}h\sqrt{z}\,\mathrm{sh}\,\sqrt{z} + z + \hat{V}k_w\beta^2\right)$$

$$a_{21} = \sqrt{z}\left(\hat{T}\mathrm{Bi}\,\mathrm{ch}\sqrt{z} - \hat{V}\beta^2\right), \quad a_{22} = \mathrm{Bi}\left(\hat{T}\sqrt{z}\,\mathrm{ch}\,\sqrt{z} + \hat{V}\beta^2\right)$$

$$b_1 = -\frac{1-v}{1+v}\frac{\hat{T}\mathrm{Bi}}{\alpha h}z\Delta^L(p), \quad b_2 = 0$$

$$z = \frac{p}{\kappa}\beta^2h^2, \quad \hat{V} = \frac{fV\alpha}{K}\frac{2\mu(1+v)h}{1-2v}, \quad k_w = \frac{1-v}{1+v}\frac{KK^*}{\alpha\kappa}\beta^2, \quad \mathrm{Bi} = \frac{kh}{K} \tag{29.29}$$

By solving the equation system (29.28) with respect to the constants A_2, A_3, and substituting them into (29.25)–(29.27), the Laplace images of temperature, displacements and stresses are obtained (not given here).

After inversion of the resulting images: $T^L(x,p)$, $u^L(x,p)$, $\sigma^L_{xx}(x,p)$, with the help of the inverse Laplace transform (29.13), it is convenient to write down the considered problem solution $T(x,t)$, $u(x,t)$, $\sigma_{xx}(x,t)$ in the form of convolutions:

$$T(x,t) - T_0 = \frac{1-v}{1+v}\frac{1}{\alpha h}\int_0^t \Delta(\tau)f_T^0(x,t-\tau)d\tau, \quad 0 \le x \le h, \quad t > 0 \tag{29.30}$$

$$f_T^0(x,t) = \frac{1}{2\pi i}\int_\Gamma \frac{N_T^0(x,z)}{t_\kappa R(z)}e^{z\tilde{t}}\mathrm{d}z, \quad \tilde{t} = \frac{t}{t_\kappa}, \quad t_\kappa = \frac{h^2}{\kappa} \tag{29.31}$$

$$N_T^0(x,z) = \hat{V}\beta^2\sqrt{z}\left(\mathrm{Bi}\,\mathrm{sh}\sqrt{z}\frac{x}{h} + \sqrt{z}\,\mathrm{ch}\,\sqrt{z}\frac{x}{h}\right) + \hat{T}z\left(r(z) - \mathrm{Bi}\,\mathrm{ch}\,\sqrt{z}\frac{h-x}{h}\right) \tag{29.31}$$

$$R(z) = zr(z) - \hat{V}\beta^2((1-k_w)r(z) - \mathrm{Bi}) + \hat{T}\mathrm{Bi}\sqrt{z}\,\mathrm{sh}\,\sqrt{z} \tag{29.32}$$

$$r(z) = \mathrm{Bi}\,\mathrm{ch}\,\sqrt{z} + \sqrt{z}\,\mathrm{sh}\,\sqrt{z}$$

$$u(x,t) = -\int_0^t \Delta(\tau)f_u^0(x,t-\tau)\mathrm{d}\tau, \quad 0 \le x \le h, \quad t > 0 \tag{29.33}$$

$$f_u^0(x,t) = \frac{1}{2\pi i}\int_\Gamma \frac{N_u^0(x,z)}{t_\kappa R(z)}e^{z\tilde{t}}\mathrm{d}z, \quad \tilde{t} = \frac{t}{t_\kappa} \tag{29.34}$$

$$N_u^0(x,z) = zr(z)\frac{x}{h} - \hat{V}\beta^2\left(\mathrm{Bi}\,\mathrm{ch}\,\sqrt{z}\frac{x}{h} + \sqrt{z}\,\mathrm{sh}\,\sqrt{z}\frac{x}{h} - \mathrm{Bi}\right) - \hat{T}\mathrm{Bi}\sqrt{z}\left(\mathrm{sh}\,\sqrt{z}\frac{h-x}{h} - \mathrm{sh}\,\sqrt{z}\right) \tag{29.35}$$

$$\sigma_{xx}(x,t) = -\frac{2\mu(1-\nu)}{(1-2\nu)h}\int_0^t \Delta(\tau) f_\sigma^0(x, t-\tau)\mathrm{d}\tau, \quad 0 \le x \le h, \quad t > 0 \tag{29.36}$$

$$f_\sigma^0(x,t) = \frac{1}{2\pi i}\int_\Gamma \frac{N_\sigma^0(x,z)}{t_\kappa R(z)} \mathrm{e}^{z\tilde{t}}\mathrm{d}z, \quad \tilde{t} = \frac{t}{t_\kappa} \tag{29.37}$$

$$N_\sigma^0(x,z) = (1+\hat{T})zr(z), \tag{29.38}$$

where the integration contour $\Gamma = \{z : -i\infty + \mathrm{d}t_\kappa, +i\infty + \mathrm{d}t_\kappa\}$ represents a straight line in the complex plane of the variable of integration z parallel to the imaginary axis and spaced from it by an amount $\mathrm{d}t_\kappa$ that is selected so that the integration contour passes to the right of all isolated singular points of the integrands.

The wear $u_w(t)$ calculation formula can be obtained from (29.3):

$$u_w(t) = k_w\hat{V}\beta^2\int_0^t \Delta(\tau) f_w^0(x, t-\tau)\mathrm{d}\tau, \quad t > 0 \tag{29.39}$$

$$f_w^0(x,t) = \frac{1}{2\pi i}\int_\Gamma \frac{N_w^0(x,z)}{t_\kappa R(z)} e^{z\tilde{t}}\mathrm{d}z, \quad \tilde{t} = \frac{t}{t_\kappa} \tag{29.40}$$

where $N_w^0(z) = r(z)$, and $r(z)$ is from (29.32).

The obtained formulas for $T(x,t)$, $u(x,t)$, $\sigma_{xx}(x,t)$, $u_w(t)$ contain contour quadratures (29.30), (29.34), (29.37) and (29.40). In the complex plane of the integration variable z, the integrands of the contour quadratures (29.30), (29.34), (29.37) and (29.40) are meromorphic functions that contain a countable set of poles. Along the axis of integration, when $|z| \to \infty$ and $\arg z = \pi/2$, the integrands in (29.30), (29.34), (29.37) and (29.40) behave as follows:

$$N_T^0(x,z)R^{-1}(z) = \hat{T} + O\left(z^{-1/2}\right), \quad 0 < x < h$$

$$N_u^0(x,z)R^{-1}(z) = \frac{x}{h} + O\left(z^{-1/2}\right), \quad 0 < x < h \tag{29.41}$$

$$N_{\sigma}^{0}(x,z)R^{-1}(z) = 1 + \hat{T} + O\left(z^{-1/2}\right), \quad 0 < x < h$$

$$N_{w}^{0}(z)R^{-1}(z) = O\left(z^{-1}\right).$$

The asymptotics (29.41) show that the quadratures (29.30), (29.34) and (29.37) do not exist in the common sense, but are understood as generalized [26]. To calculate the quadratures in (29.30), (29.34) and (29.37), regularization of the integrands at infinity (when $|z| \to \infty$) is performed with the estimates (29.41) taken into account. As a result, the quadratures are represented as a superposition of the regular part of the generalized component and the quadrature existing in the common sense:

$$T(x,t) - T_0 = \frac{1-\nu}{1+\nu}\frac{1}{\alpha h}\left(\hat{T}\Delta(t) + \int_0^t \Delta(\tau) f_T(x, t-\tau)\mathrm{d}\tau\right), \quad 0 \le x \le h, \ t > 0 \tag{29.42}$$

$$f_T(x,t) = \frac{1}{2\pi i}\int_{\Gamma} \frac{N_T(x,z)}{t_{\kappa} R(z)} \mathrm{e}^{z\tilde{t}}\mathrm{d}z, \quad N_T(x,z) = N_T^0(x,z) - \hat{T}R(z) \tag{29.43}$$

$$u(x,t) = -\Delta(t)\frac{x}{h} - \int_0^t \Delta(\tau) f_u(x, t-\tau)\mathrm{d}\tau, \quad 0 \le x \le h, \ t > 0 \tag{29.44}$$

$$f_u(x,t) = \frac{1}{2\pi i}\int_{\Gamma} \frac{N_u(x,z)}{t_{\kappa} R(z)} \mathrm{e}^{z\tilde{t}}\mathrm{d}z, \quad N_u(x,z) = N_u^0(x,z) - \frac{x}{h}R(z) \tag{29.45}$$

$$\sigma_{xx}(x,t) = -\frac{2\mu(1-\nu)}{(1-2\nu)h}\left((1+\hat{T})\Delta(t) - \int_0^t \Delta(\tau) f_{\sigma}(x, t-\tau)\mathrm{d}\tau\right), \quad 0 \le x \le h, t > 0 \tag{29.46}$$

$$f_{\sigma}(x,t) = \frac{1}{2\pi i}\int_{\Gamma} \frac{N_{\sigma}(x,z)}{t_{\kappa} R(z)} \mathrm{e}^{z\tilde{t}}\mathrm{d}z, \quad N_{\sigma}(x,z) = N_{\sigma}^0(x,z) - (1+\hat{T})R(z) \tag{29.47}$$

where $N_T^0(x,z)$, $N_u^0(x,z)$, $N_{\sigma}^0(x,z)$, $R(z)$ are from the formulas (29.31), (29.35), (29.38) and (29.32).

To calculate the integrals in (29.43), (29.45) and (29.47), in which the integrand functions are meromorphic and decreasing at infinity along the axis of integration, according to estimates:

$$N_a(x,z)R^{-1}(z) = O\left(z^{-1/2}\right) \quad |z| \to \infty, \quad 0 \le x \le h, \quad a = T, u, \sigma \tag{29.48}$$

the methods of the theory of functions of a complex variable [28] can be used. When implementing these methods, it becomes necessary to determine the poles of the integrands in (29.43), (29.45) and (29.47) in the complex plane of the integration variable.

29.4 Poles of Integrands

The poles of the integrands in (29.43), (29.45) and (29.47) coincide with the zeros $R(z)$ of (29.32) except for those zeros that are removable singular points of the integrands. To determine the zeros $R(z)$ in the complex plane $z = \xi + i\eta$, the equation is solved:

$$R(z) = zr(z) - \hat{V}\beta^2((1-k_w)r(z) - \mathrm{Bi}) + \hat{T}\mathrm{Bi}\sqrt{z}\,\mathrm{sh}\,\sqrt{z} = 0 \tag{29.49}$$

where β^2, Bi, $\hat{T}$, $\hat{V}$, k_w are from (29.29), $r(z)$ is from (29.32).

In (29.49), the zeros $R(z)$ depend on four dimensionless parameters of the problem $\hat{V}$, k_w, $\hat{T}$,Bi, since the fifth parameter β^2 is expressed in terms of $\hat{T}$ in (29.29). Using the approach of [19, 29, 30], we will investigate the behavior of the zeros from (29.49) for fixed k_w, $\hat{T}$, Bi and variable parameter $\hat{V}$, which varies from 0 to ∞. Assuming $\hat{V} = 0$ and $\mathrm{Bi} = 0$ in (29.49), we obtain a simplified equation to determine the zero approximations $\zeta_k^0 = \zeta_k(0)$, $k = 0, 1, 2, \ldots$ of the roots $\zeta_k(\hat{V})$ $k = 0, 1, 2, \ldots$ of (29.49). It was found that all zero approximations of zeros $R(z)$ from (29.49) are located on the negative part of the real axis or at zero. Nevertheless, when changing $\hat{V}$ from 0 to ∞ for fixed k_w, Bi, $\hat{T}$, the first two poles ζ_0 and ζ_1 can be located: I—on the negative part of the real axis (at $0 < \hat{V} < \hat{V}_{\mathrm{I}}$); II—in the left half-plane ($\hat{V}_{\mathrm{II}} < \hat{V} < \hat{V}_{\mathrm{III}}$); III—in the right half-plane ($\hat{V}_{\mathrm{II}} < \hat{V} < \hat{V}_{\mathrm{III}}$); IV—on the positive part of the real axis ($\hat{V}_{\mathrm{III}} < \hat{V} < \infty$). Figure 29.1 shows the trajectories of the poles $\zeta_0(\hat{V})$ and $\zeta_1(\hat{V})$ with change of $\hat{V}$ from 0 to ∞. The closed points indicate the location of the poles $\zeta_0(\hat{V})$ and $\zeta_1(\hat{V})$ at $\hat{V} = 0$, while open ones correspond to $\hat{V} \to \infty$. The crossed-out square marks the point of the trajectory, with the passage of which with the increasing of $\hat{V}$ the real poles $\zeta_0(\hat{V})$ and $\zeta_1(\hat{V})$ become a pair of complex conjugate poles, and vice versa.

It should be noted that even a small change in the coefficient k_w, containing the ratio of the dimensional parameters K^* and α, regulating respectively the wear and thermal expansion of the strip, leads to significant changes in the trajectories of $\zeta_0(\hat{V})$ and $\zeta_1(\hat{V})$ and, to a lesser extent, of the others $\zeta_k(\hat{V})$ $k = 2, 3, 4, \ldots$. When wear prevails (Fig. 29.1, curves ***5***, ***6***), then ζ_0, ζ_1 and even more ζ_k $k = 2, 3, 4, \ldots$ at $k_w > 1$ are in regions I, II. The prevalence of the expansion of the strip from the

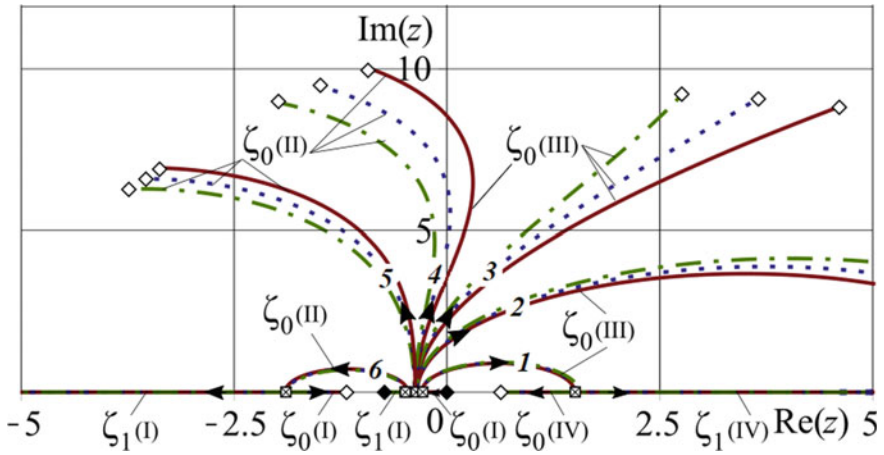

Fig. 29.1 Location of $R(z)$ (29.49) zeros ζ_0, ζ_1 in the upper part of the complex plane z and their movement when $\hat{V}$ increases from 0 to ∞ (lower part is symmetrical), when $\mathrm{Bi} = 1$ is fixed for three values of $\hat{T} = 0$ (solid lines); 0.01 (dashed lines); 0.02 (dash-dotted lines) and different $k_w = 0.5$ (set of curves ***1***), 0.9 (***2***), 1.0 (***3***), 1.35 (***4***), 5.0 (***5***)

incoming heat over wear $0 < k_w < 1$ (curves ***1–4***) leads to the fact that ζ_0 and ζ_1 go to the right half-plane to the regions III, IV (Fig. 29.1).

Note than when a neighboring pair of poles is located in the complex plane, they are complex conjugant, i.e. $\zeta_1 = \overline{\zeta_0}$ and $\zeta_0 = \overline{\zeta_1}$ in regions II, III.

It is important that, in contrast to quasi-static problems with friction and heat generation from friction, but without wear, when the poles ζ_0 and ζ_1 at $\hat{V} \in [0, \infty)$ always remained on the real axis and did not come out into the complex plane [31], in the corresponding problems, which take into account wear, friction and heat release from friction, the poles ζ_0 and ζ_1 move into the complex plane at $\hat{V} \in \left(\hat{V}_{\mathrm{I}}, \hat{V}_{\mathrm{II}}\right)$.

29.5 Formulas for the Exact Solution of the Problem

Let the poles of the integrands ζ_k $k = 0, 1, 2, \ldots$ in (29.43), (29.45) and (29.47) are known. The calculation of the quadratures in (29.43), (29.45) and (29.47) in this case is reduced to calculating the sum of the residues at the poles of the integrands. Assuming that the poles ζ_k, $k = 0, 1, 2, \ldots$ are simple, we obtain the following formulas for calculating the quadratures (29.43), (29.45) and (29.47):

$$\frac{1}{2\pi i}\int\limits_{\Gamma}\frac{N_a(x,z)}{t_\kappa R(z)}\mathrm{e}^{z\tilde{t}}\mathrm{d}z=\sum_{k=0}^{\infty}B_a(x,\zeta_k)\mathrm{e}^{\zeta_k\tilde{t}},\quad \tilde{t}=\frac{t}{t_\kappa} \tag{29.50}$$

$$B_a(x,z)=\frac{N_a(x,z)}{t_\kappa R'(z)} \tag{29.51}$$

where $R'(z)$ is derivative of $R(z)$. Replacing index a in (29.50) and (29.51) with T, u, σ gives the formula for computing integral in (29.43), (29.45) and (29.47), respectively. If ζ_k and ζ_{k+1}, $k=0,1,2,\ldots$ represent a complex conjugate pair $\zeta_{k+1}=\overline{\zeta_k}$, $k=0,1,2,\ldots$, then

$$B_a(x,z)\mathrm{e}^{z\tilde{t}}=2\mathrm{Re}\frac{N_a(x,z)}{t_\kappa R'(z)}\mathrm{e}^{z\tilde{t}} \tag{29.52}$$

and the summation in (29.50) can be carried out over even numbers $k=2n$, $n=0,1,2,\ldots$ for complex conjugates ζ_k, $k=0,1,2,\ldots$. Taking into account (29.42)–(29.47) and (29.51), integration formula is obtained as

$$f_a(x,t)=\frac{1}{2\pi i}\int\limits_{\Gamma}\frac{N_a(x,z)}{t_\kappa R(z)}\mathrm{e}^{z\tilde{t}}\mathrm{d}z=\sum_{k=0}^{\infty}B_a(x,\zeta_k)\mathrm{e}^{\zeta_k\tilde{t}},\quad a=T,u,\sigma \tag{29.53}$$

The solutions of the problem are written in the following series:

$$T(x,t)-T_0=\frac{1-\nu}{1+\nu}\frac{1}{\alpha h}\left(\hat{T}\Delta(t)+\sum_{k=0}^{\infty}B_T(x,\zeta_k)D(\zeta_k,t)\right),\quad 0\le x\le h,\quad t>0 \tag{29.54}$$

$$u(x,t)=-\frac{x}{h}\Delta(t)+\sum_{k=0}^{\infty}B_u(x,\zeta_k)D(\zeta_k,t),\quad 0\le x\le h,\quad t>0 \tag{29.55}$$

$$\sigma_{xx}(x,t)=-\frac{2\mu(1-\nu)}{(1-2\nu)h}\left((1+\hat{T})\Delta(t)-\sum_{k=0}^{\infty}B_\sigma(x,\zeta_k)D(\zeta_k,t)\right),\quad 0\le x\le h,\quad t>0 \tag{29.56}$$

where $B_a(x,z)$ are calculated according formulas (29.51) or (29.52), $D(z,t)$ uses the formula:

$$D(z,t)=\int\limits_0^t\Delta(\tau)\exp(z(t-\tau)/t_\kappa)\mathrm{d}\tau\quad t>0 \tag{29.57}$$

After calculation of $f_w^0(t)$ in (29.40) by using the formula:

$$f_w^0(x,t) = \frac{1}{2\pi i}\int_\Gamma \frac{N_w(z)}{t_\kappa R(z)} e^{z\tilde{t}} dz = \sum_{k=0}^{\infty} B_w(\zeta_k) e^{\zeta_k \tilde{t}}, \quad B_w = \frac{N_w(z)}{t_\kappa R'(z)} \tag{29.58}$$

and substituting it in (29.39), the expression is obtained for calculating the wear $u_w(t)$ of the coating material on the contact:

$$u_w(t) = \sum_{k=0}^{\infty} B_w(\zeta_k) D(\zeta_k, t), \quad t > 0 \tag{29.59}$$

The horizontal displacements $w(x,t)$ are determined from (29.1), (29.4) and (29.6) and after integration in (29.1), the following formula is obtained:

$$w(x,t) = -f\mu^{-1}\sigma_{xx}(h,t)x, \quad 0 \le x \le h, \quad t > 0 \tag{29.60}$$

29.6 Analysis of the Problem Solution: Domains of Stable and Unstable Solutions

Investigation of the solutions of the problem $T(x,t)$, $u(x,t)$, $\sigma_{xx}(x,t)$, represented by formulas (29.54)–(29.56), shows that if $\mathrm{Re}(\zeta_k) < 0$ $k = 0, 1, 2, \ldots$ the solutions of the problem are stable and tend to a stationary state with increasing time t. If at least one ζ_k, $k = 0, 1, 2, \ldots$ has $\mathrm{Re}(\zeta_k) > 0$, then the amplitude of the solution increases indefinitely at $t \to \infty$ and is oscillating with frequency $\mathrm{Im}(\zeta_k) \neq 0$, which indicates the instability of the solution of the problem. If we assume that the law of penetration $\Delta(t)$ is a bounded function:

$$m < \Delta(t) < M \quad m, M > 0, \quad 0 < t < \infty$$

then for the integral (29.57), the following estimate takes place:

$$|D(\zeta_k, t)| \ge m \left| \frac{1 - e^{\zeta_k \tilde{t}}}{\zeta_k} \right|, \quad \text{when} \quad \mathrm{Re}(\zeta_k) > 0, \quad k = 0, 1, 2, \ldots, \quad t = \frac{t}{t_\kappa}$$

In the complex z-plane, the pole trajectories $\zeta_k(\hat{V})$, $k = 0, 1, 2, \ldots$, $\hat{V} \in [0, \infty)$ in the left half-plane represent stable solutions $(\mathrm{Re}(\zeta_k) < 0)$, and the regions *I* and *II* themselves are called the regions of stable solutions. Regions *III* and *IV* in the right half-plane $(\mathrm{Re}(\zeta_k) > 0\, k = 0, 1)$ are regions of unstable solutions of the problem, since in region *III* the limits $\lim_{t\to\infty} T(h,t)$ and $\lim_{t\to\infty} \sigma_{xx}(h,t)$ do not exist because of $\mathrm{Im}(\zeta_k) \neq 0$ $k = 0, 1$, and in region *IV* $\lim_{t\to\infty} T(h,t) = \lim_{t\to\infty} \sigma(h,t) = \infty$, since $\mathrm{Im}(\zeta_k) = 0$ $k = 0, 1$.

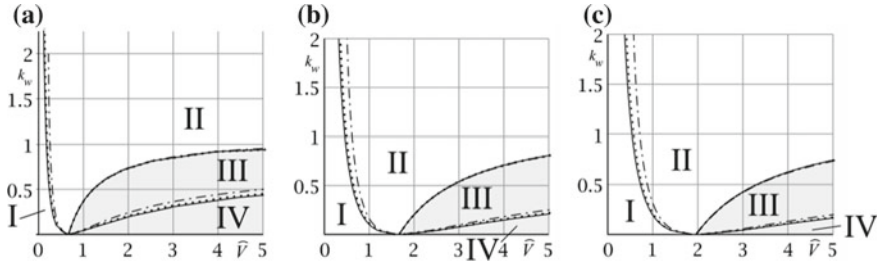

Fig. 29.2 Boundaries of stable (I, II) and unstable (III, IV) solution domains at **a** Bi = 1, **b** Bi = 10, **c** Bi = 100 (Bi $\to \infty$); different values of $\hat{T}$ are represented by solid lines ($\hat{T} = 0$), dotted lines ($\hat{T} = 0.1$), and dash-dotted lines ($\hat{T} = 0.5$); unstable solution domains are shaded

Parametric boundaries of stable and unstable solutions of the problem in the space of dimensionless parameters $\hat{V}$, k_w, Bi, $\hat{T}$ present theoretical and practical interest. Figure 29.2 shows the domains of stable *I*, *II* and unstable *III*, *IV* solutions on the $(\hat{V}, k_w)$ plane for different values of Bi and $\hat{T}$. The analysis of the graphs in Fig. 29.2 shows the significant influence of the parameters $\hat{V}$, k_w, Bi on the change in the boundaries of regions *I–IV*. When $k_w \to 0$ for Bi = 1 and Bi = 100, the boundaries of regions *I–IV* converge on the axis $\hat{V}$ to a point $\hat{V} = 2\text{Bi}/(2 + \text{Bi})$ that does not depend on $\hat{T}$. This means that thermomechanical coupling in heat equation have no effect on stability in the considered case but without wear.

It is worth to note that dimensionless thermomechanical coupling coefficient $\hat{T}$ does not significantly affect the stable (*II*) and unstable (*III*) solutions domains boundary, except narrow range of dimensionless wear rates $k_w \in [1, 1.14]$ (at Bi = 100). At $k_w = 1.120$, change of $\hat{T}$ from 0 to 0.5 leads to 1.5 times change in critical dimensionless speed $\hat{V}_*$ (from 33.532 to 51.143); at $k_w = 1.222$ to 1.7 times change (from 35.164 to 60.065). At $k_w = 1.124$ and $\hat{T} = 0$ there is critical value of $\hat{V}_* = 37.051$, whereas for all $k_w \geq 1.124$ at $\hat{T} = 0.05$ there are no unstable solution domain, and thermoelastic stability is kept in all dimensionless speed range.

29.7 Asymptotic and Numerical Analysis of the Obtained Solutions

It is necessary to determine the effect of dimensionless coupling parameter $\hat{T}$ and other parameters on behavior of obtained solutions. For this purpose, the asymptotic analysis of the solutions $T(x,t)$, $u(x,t)$, $\sigma_{xx}(x,t)$, $u_w(t)$ for small values of t was performed. The separated principal terms $T(x,t) - T_0$ in (29.42), $u(x,t)$ in (29.44), $\sigma_{xx}(x,t)$ in (29.46), taking into account the convolution integral formula, allow us to obtain following asymptotic relations:

$$T(x,t) - T_0 = \frac{1-v}{1+v}\frac{\hat{T}}{\alpha}\cdot\frac{\Delta(t)}{h} + O\left(t^{3/2}\Delta(t)\right), \quad t \to 0 \tag{29.61}$$

$$u(x,t) = -x\frac{\Delta(t)}{h} + O\left(t^{3/2}\Delta(t)\right), \quad t \to 0 \tag{29.62}$$

$$\sigma_{xx}(x,t) = -\frac{2\mu(1-v)}{1-2v}(1+\hat{T})\frac{\Delta(t)}{h} + O\left(t^{3/2}\Delta(t)\right), \quad t \to 0 \tag{29.63}$$

Note that at differentiation of $u(x,t)$ in (29.62) according to x and t, rate of deformation on the contact (when $x = h$) is written as

$$\dot{\varepsilon}_{xx} = \frac{\partial^2 u}{\partial x \partial t} = -\frac{\dot{\Delta}(t)}{h} + O\left(t^{3/2}\Delta(t)\right), \quad t \to 0 \tag{29.64}$$

Differentiation of the relations (29.61) and (29.63) on t shows that the rate of temperature $\dot{T}(x,t)$ and contact stresses $\dot{p}(t) = -\dot{\sigma}_{xx}(x,t)$ at small values of t is proportional to the rate of deformation $\dot{\varepsilon}_{xx}$, and coefficients:

$$-\frac{1-v}{1+v}\frac{\hat{T}}{\alpha h} \text{ and } -\frac{2\mu(1-v)}{(1-2v)h}(1+\hat{T})$$

indicate decreasing of temperature and contact stresses, respectively, with increasing of coupling parameter. These relations also show effect of the other parameters of the problem contained in them. Rate of wear $\dot{u}_w(t)$ on the contact is deduced from (29.39) and (29.40) by separating principal term in (29.40) and subsequent differentiating the result, and its final form is given by

$$\dot{u}_w(t) = k_w \hat{V}\beta^2\frac{\kappa}{h}\cdot\frac{\dot{\Delta}(t)}{h} + O(t\Delta(t)) \quad t \to 0 \tag{29.65}$$

where ratio between $\dot{u}_w(t)$ and $\dot{\varepsilon}_{xx}$ depends on $\hat{T}$ and other parameters of the problem.

Numerical analysis of the solutions of the considered coating wear problem is carried out by the formulas (29.54), (29.56) and (29.59). Suppose that the maximum level of penetration of the rigid half-plane I into an elastic coating is given by Δ_0, and its penetration law $\Delta(t)$, consisting of the active and the passive penetration phase, is described by the formulas:

$$\Delta(t) = \Delta_0\begin{cases} -1 + e^{\varepsilon t} & 0 < t < t_\varepsilon \\ 1 & t_\varepsilon < t < \infty \end{cases} \tag{29.66}$$

where $t_\varepsilon = \varepsilon^{-1}\ln 2$ is the active penetration duration, ε is the penetration law parameter.

The nature of the loss of stability of solutions $T(h,t)$, $u_w(t)$, $\sigma_{xx}(h,t)$ of the uncoupled problem of sliding contact thermoelasticity depending on the parameters of the problem $\hat{V}$, k_w, Bi was described in detail in [15, 19, 29, 30]. Here we study the effect of the parameters V (m/s), K^* (m^2/N), T_0 (K) of the considered coupled thermoelastic sliding friction al wear contact problem on the main contact parameters: temperature $T(h,t)$ from (29.54), contact stresses $p(t) = -\sigma_{xx}(h,t)$ from (29.56) that arise and develop in time on the contact interface between the rigid half-plane I and the coating, wear of the coating $u_w(t)$ from (29.59), and wear rate of the coating $\dot{u}_w(t)$ from (29.59). The material of the coating is aluminum alloy with the following thermomechanical characteristics: $\mu = 24.8$ GPa, $\nu = 0.34$, $\kappa = 88.1 \times 10^{-6}$ m^2/s, $\alpha = 22.9 \times 10^{-6}$ 1/K, $K = 209.3$ W/(m K), $f = 0.47$, $h = 25$ mm, $\Delta_0 = 0.01h = 0.25$ mm. Wear of the coating surface ends at $t = t_w$, when the contact stresses turn to zero: $p(t_w) = -\sigma_{xx}(h,t_w) = 0$. The time t_w is called *the coating wear time*.

The effect of the wear coefficient K^* and the initial temperature T_0 on the solutions of the problem under consideration is illustrated in Figs. 29.3, 29.4, 29.5 and 29.6, which show the graphs $T_*(h,t) = T(h,t) - T_0$, $p(t)$, $u_w(t)$, $\dot{u}_w(t)$, respectively for the following task parameters: $V = 3.22$ mm/s ($\hat{V} = 0.86085$), Bi = 11.9446. $V = 3.22$ mm/s ($\hat{V} = 0.86085$), Bi = 11.9446. The graphs denoted by ***1*** are constructed at $K^* = 7.5 \cdot 10^{-12} m^2/N$ ($k_w = 0.3833$); those denoted by ***2*** are constructed at $K^* = 1.5 \cdot 10^{-11} m^2/N$ ($k_w = 0.7665$); those denoted by ***3*** correspond to $K^* = 2.25 \cdot 10^{-11} m^2/N$ ($k_w = 1.1498$). The solid lines in Figs. 29.3, 29.4, 29.5 and 29.6 represent the graphs of the solution of the present coupled thermoelastic problem at $T_0 = 0$ K ($\hat{T} = 0$), which coincide with the graphs for the solution of the corresponding uncoupled problem; the dashed line shows the solution graphs at $T_0 = 300$ K ($\hat{T} = 0.0279$), the dash-dotted line shows the solution graphs at $T_0 = 525$ K ($\hat{T} = 0.0489$).

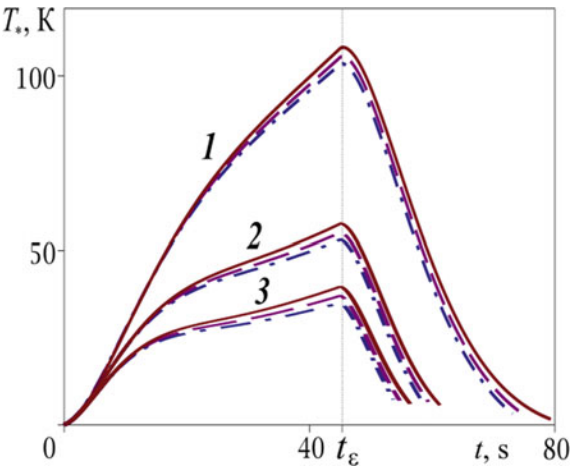

Fig. 29.3 Temperature $T(h,t)$ at the contact interface

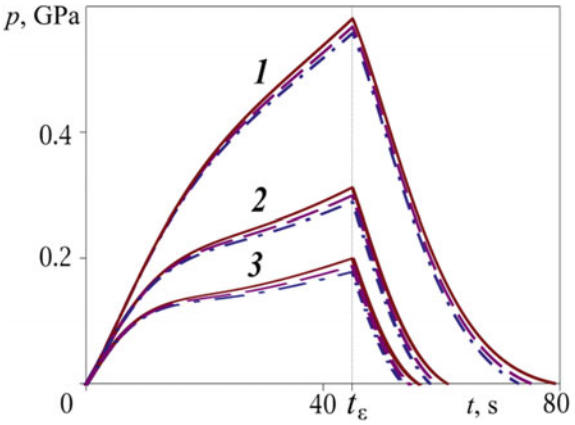

Fig. 29.4 Contact pressure $p(t) = -\sigma_{xx}(h, t)$

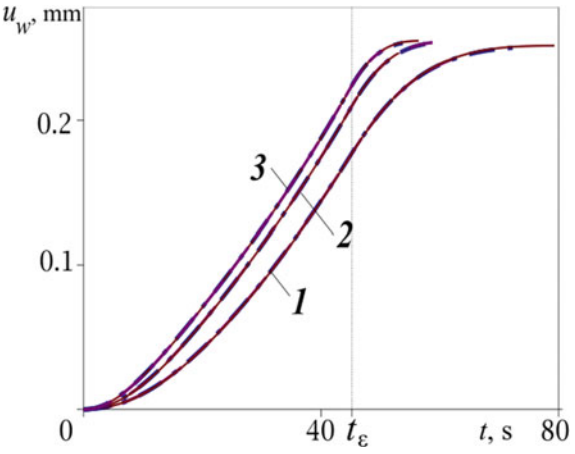

Fig. 29.5 Wear amount $u_w(t)$

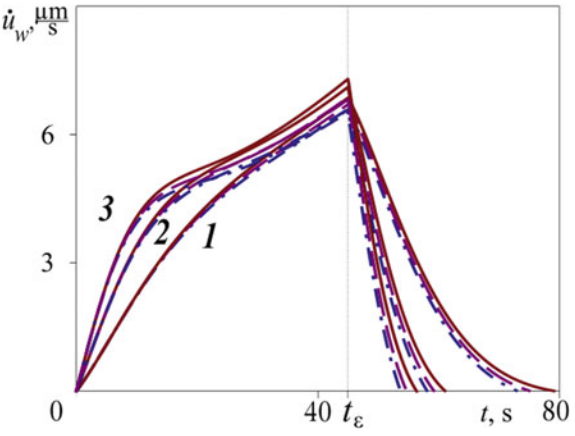

Fig. 29.6 Wear rate $\dot{u}_w(t)$

From Figs. 29.3, 29.4 and 29.5, it follows that the values of $p(t)$ and $T_*(h,t)$ decrease with increasing of wear coefficient K^* and initial temperature T_0 (curves 3), while wear is accelerating.

29.8 Conclusion

An analysis of the exact solution of the coupled quasi-static thermoelasticity problem of wear by a rigid body of an elastic coating on a sliding thermofriction al contact makes it possible to draw the following conclusions:

(i) the boundary between the region of stable (*I*, *II*) and unstable (*III*, *IV*) solutions of the problem remains unchanged for any values of the thermomechanical coupling parameter;
(ii) the eigenvalues of the problem essentially depend on the thermomechanical coupling parameter of the problem;
(iii) an increase in the thermomechanical coupling parameter of the problem, as well as an increase in the wear coefficient, leads to a decrease in both the temperature and the stresses at the contact.

The obtained solutions of the coupled quasi-static problem of wear allow one to solve inverse problems. These problems are devoted to control the parameters of a sliding contact due to a special selection of the law of penetration of a rigid body into an elastic coating, as well as monitoring problems of sliding contact parameters using buried sensors. The sensor readings then can be recalculated to contact parameter values using the obtained formulas.

Acknowledgements The work was carried out within the framework of the State Assignment of the Ministry of Education and Science of the Russian Federation Nos. 9.1481.2017/4.6, 9.4761.2017/6.7 and Russian Foundation for Basic Research grants Nos. 18-07-01397-a, 18-57-00015-Bel_a.

References

1. M.A. Biot, J. Appl. Phys. **27**(3), 240 (1956)
2. H. Deresiewicz, *Proceedings of the 3rd U.S. National Congress Applied Mechanics* (Brown University, Providence, 1958), p. 287
3. P. Chadwick, in *Progress in Solid Mechanics*, ed. by I.N. Sneddon, R. Hill (North-Holland Publishing Company, Amsterdam, 1960), p. 263
4. B.A. Boley, J.H. Weiner, *Theory of Thermal Stresses* (Wiley, New York, 1960)
5. W. Nowacki, *Dynamic Problems of Thermoelasticity* (Springer Science & Business Media, Noordhoff, Gronigen, 1975)
6. R.E. Nickell, J.L. Sackman, J. Appl. Mech. **35**(2), 255 (1968)
7. J.T. Oden, Nucl. Eng. Des. **10**(4), 465 (1969)
8. J.H. Prevost, D. Tao, J. Appl. Mech. **50**(4a), 817 (1983)

9. J.P. Carter, J.R. Booker, Comput. Struct. **31**(1), 73 (1989)
10. A. Hacquin, P. Montmitonnet, J.P. Guillerault, J. Mater. Process. Technol. **60**(1), 109 (1996)
11. M. Repka, A. Lion, Thermochim. Acta **581**, 62 (2014)
12. V.F. Gribanov, N.G. Panichkin, *Coupled and Dynamic Problems of Thermoelasticity* (Mashinostroenie, Moscow, 1984). (in Russian)
13. V.M. Alexandrov, G.K. Annakulova, J. Friction Wear **11**(1), 24 (1990)
14. V.M. Alexandrov, G.K. Annakulova, J. Friction Wear **13**(1), 154 (1992)
15. A.A. Evtushenko, Y.A. Pyryev, Izvestiya Rossiyskoy Akademii Nauk. Mekhanika Tverdogo Tela (1), 114 (1997)
16. YuA Pyryev, D.V. Grilitsky, Appl. Math. Tech. Phys. **37**(6), 99 (1996)
17. Y.A. Pyryev, Phys.-Chem. Mech. Mat. **36**(3), 53 (2000) (in Russian)
18. J. Awrejcewicz, Yu. Pyryev, Int. J. Eng. Sci. **40**(10), 1113 (2002)
19. V.B. Zelentsov, B.I. Mitrin, I.A. Lubyagin, Comput. Mech. Continuous Media **9**(4), 430 (2016)
20. N. Strömberg, L. Johansson, A. Klarbring, Int. J. Solids Struct. **33**(13), 1817 (1996)
21. K.T. Andrews, M. Shillor, S. Wright, A. Klarbring, Int. J. Eng. Sci. **35**(14), 1291 (1997)
22. N. Strömberg, Comput. Methods Appl. Mech. Eng. **177**(3–4), 441 (1999)
23. A.D. Kovalenko, *Thermoelasticity: Basic Theory and Applications* (Wolters-Noordhoff, Groningen, 1970)
24. F.P. Bowden, D. Tabor, *The Friction and Lubrication of Solids* (Oxford, London, 1950)
25. J.F. Archard, J. Appl. Phys. **24**(8), 981 (1953)
26. YuA Brychkov, A.P. Prudnikov, *Integral Transformations of Generalized Functions* (Nauka, Moscow, 1977). (in Russian)
27. V.A. Ditkin, A.P. Prudnikov, *Operational Calculus* (Vishaya Shkola, Moscow, 1975). (in Russian)
28. A. Hurwitz, R. Courant, *Theory of Functions* (Nauka, Moscow, 1968). (in Russian)
29. V.B. Zelentsov, B.I. Mitrin, S.M. Aizikovich, L.L. Ke, Mat. Phys. Mech. **23**, 14 (2015)
30. V.B. Zelentsov, B.I. Mitrin, I.A. Lubyagin, J. Friction Wear **38**(4), 265 (2017)
31. V.B. Zelentsov, B.I. Mitrin, S.M. Aizikovich, J. Friction Wear **37**(3), 213 (2016)

Chapter 30
Homogenization of Dispersion-Strengthened Thermoelastic Composites with Imperfect Interfaces by Using Finite Element Technique

Andrey Nasedkin, Anna Nasedkina and Amirtham Rajagopal

Abstract The paper describes the homogenization procedure for a two-phase mixture composite that consists of two isotropic thermoelastic materials. It is assumed that the special interface conditions are held on the boundary between the phases, where the stress and the thermal flux jump over the interphase boundary are equal to the surface stresses and thermal flux at the interface. Such boundary conditions are used to describe the nanoscale effects in thermoelastic nanodimensional bodies and nanocomposites. The homogenization problems are solved using the approach of the effective moduli method, the finite element method and the algorithm for generating the representative volume of cubic finite elements with random distribution of element material properties. As a numerical example, a mixture wolfram-copper composite is considered, where the interface conditions are simulated by surface membrane and thermal shell elements.

30.1 Introduction

At present, the models of surface elasticity and thermal conductivity are widely used to describe well-known effect of the material moduli changing for the nanoscale thermoelastic bodies. Among these models, the Gurtin-Murdoch models

A. Nasedkin · A. Nasedkina (✉)
Institute of Mathematics, Mechanics and Computer Science,
Southern Federal University, 8a, Milchakova Street, 344090 Rostov-on-Don, Russia
e-mail: anasedkina@sfedu.ru

A. Nasedkin
e-mail: nasedkin@math.sfedu.ru

A. Rajagopal
Department of Civil Engineering, Indian Institute of Technology,
Hyderabad 502205, India
e-mail: rajagopal@iith.ac.in

I. A. Parinov et al. (eds.), *Advanced Materials*, Springer Proceedings
in Physics 224, https://doi.org/10.1007/978-3-030-19894-7_30

of surface or interface stresses [1–3] and the models of highly thermal conducting boundaries are the most popular ones. The hypothesis of surface stresses in deformable bodies has been suggested long time ago [4]. However, essential development of this idea was performed later in [1–3, 5–9]. It was also shown, that the model of surface stresses can be considered as a special case of the models with imperfect interfaces.

Nowadays, the Gurtin-Murdoch theory of surface elastic stresses has been become widely used for describing nanoscale effects for elastic solids. Reviews of research in the framework of this theory and its generalizations can be found, for example, in [10, 11]. In a range of papers, this theory was extended for the modelling of nanosized thermoelastic composite materials. For example, in [12–15] the effective properties of thermoelastic composites with spherical nanoinclusions or with nanopores and effective properties of nanofiber composites were investigated using models of thermal stresses with surface energies. The finite element technique was employed for thermoelastic materials with surface or interface boundaries in [16–21].

Models of lowly and highly thermal conducting interfaces [22, 23] were used to determine the effective thermal conductivity of the composites with imperfect interface boundaries. The lowly conducting interface, which includes Kapitsa contact thermal resistance, allows for the model with discontinuous temperature field. Generalizations of this model for a thermoelastic interface boundaries were presented in [24], and a related review was presented in [18]. The high conductivity model with continuous temperature field and with surface thermal fluxes on the interphase surfaces from a mathematical point of view is analogous to the Gurtin-Murdoch model for elastic fields. The problems on the determination of the effective thermal conductivity moduli for composites with imperfect boundaries, including micro- and nanoscale effects, were studied in [25–31] and others.

In the present paper we consider mixture composites that consist of two isotropic thermoelastic phases. We assume that the inclusions have nanoscale sizes, and therefore at the interphase boundaries of the composite we adopt the interface conditions for the stresses and thermal flux. We solve the homogenization problems using general technique described in [19–21, 32, 33] for anisotropic thermoelastic composites with interface effects. This approach includes the effective moduli method, the representative volumes generation with stochastically distributed particles and the finite element solutions of the set of static thermoelastic and thermal problems.

We used the representative volume made of cubic finite elements. At the first stage, we built cubic array of thermoelastic cubic finite elements. Further, by means of the simple random algorithm, we chose certain elements and changed their material properties to the properties of inclusions. The most challenging stage was finding the edges of contact between elements of different phases. After this stage, all edges of contact between the elements of different phases were covered by thermoelastic shell elements with the option of membrane stresses or by thermal shell elements. Numerical solution of homogenization thermoelastic problems and uncoupled thermal problems in the representative volume was obtained in ANSYS

finite element software. Further, in the ANSYS postprocessor the averaged stresses and the average heat fluxes were calculated, both by using the volume and surface finite elements. Finally, the effective moduli were calculated by using the obtained averaged characteristics.

As an example, we present the finite element solutions of the homogenization problems for a wolfram-copper composite with surface effects and provide analysis of the effective moduli behaviour depending on the values of the interface moduli, the inclusion percentage and the number of finite elements in the representative volumes. The results of solving test problems enabled us to estimate the influence of the imperfect interfaces on the values of the effective moduli.

30.2 Effective Moduli Method for Homogenization of Thermoelastic Two-Phase Isotropic Nanocomposites

Let V be a representative volume of two-phase mixed or bulk thermoelastic composite body with nanodimensional inclusions; $V = V^{(1)} \cup V^{(2)}$; $V^{(1)}$ is the region occupied by the main materials of the first phase (matrix); $V^{(2)}$ is the aggregate of the regions occupied by the materials of the second phase (inclusions); $S = \partial V$ is the external boundary of the body V; S^i is the set of frontier surfaces of regions with different phases ($S^i = \partial V^{(1)} \cap \partial V^{(2)}$); $\mathbf{n} = \{n_1, n_2, n_3\}$ is the external unit normal vector to the boundary, outward with respect to the region $V^{(1)}$ occupied by the material of the matrix; $\mathbf{x} = \{x_1, x_2, x_3\}$ is the vector of the spatial coordinates. We assume that the volumes $V^{(1)}$ and $V^{(2)}$ are filled with different isotropic thermoelastic materials. Then in the framework of linear static theory of thermoelasticity we have the following system of equations:

$$\partial_l \sigma_{kl} = 0, \quad \sigma_{kl} = \lambda \varepsilon_{mm} \delta_{kl} + 2\mu \varepsilon_{kl} - \beta\theta, \quad \varepsilon_{kl} = (\partial_l u_k + \partial_k u_l)/2, \tag{30.1}$$

$$\partial_l q_l = 0, \quad q_l = -k\partial_l \theta, \tag{30.2}$$

where $\sigma_{kl}, \varepsilon_{kl}$ are the components of the stress tensor and the strain tensor, respectively; λ, μ are the Lamé coefficients; $\mu = G$ is also called the shear modulus; β is the thermal stress coefficient; q_l is the component of the heat flux vector; k is the thermal conductivity.

As we can see, an elastic material is described by four independent material moduli: λ, μ, β and k. The most frequently used material parameters are the Young's modulus E, the Poisson's ratio ν, and the coefficient of thermal expansion α. Then the Lamé coefficients $\lambda, \mu = G$, the bulk modulus K, the stiffness moduli c_{11}, c_{12}, c_{44}, and the thermal stress coefficient β can be expressed in terms of the material parameters E, ν, and α by well-known formulas:

$$\lambda = \frac{vE}{(1+v)(1-2v)}, \quad \mu = G = \frac{E}{2(1+v)}, \quad K = \frac{E}{3(1-2v)}, \quad \beta = 3K\alpha, \tag{30.3}$$

and $c_{11} = \lambda + 2\mu,\ c_{12} = \lambda,\ c_{44} = G$.

For a two-phase composite body these moduli differ for each phase: $E = E^{(j)}, v = v^{(j)}$, for $\mathbf{x} \in V^{(j)}$, $j = 1, 2$ and so on.

In accordance with the Gurtin-Murdoch model, we assume that at the nanoscale interphase boundaries S^i the following condition is held:

$$n_l[\sigma_{kl}] = \partial_l^s \sigma_{kl}^i, \quad \mathbf{x} \in S^i, \tag{30.4}$$

where $[\sigma_{kl}] = \sigma_{kl}^{(1)} - \sigma_{kl}^{(2)}$ are the stress jumps over the interface between the phases; $\partial_l^s = \partial_l - n_l(n_m\partial_m)$ are the components of the surface gradient operator. Here σ_{kl}^i are the components of the tensor of interface stresses, which are related to the interface strains ε_{kl}^i by the "interface" Hook's law:

$$\sigma_{kl}^i = \lambda^i \varepsilon_{mm}^i \delta_{kl} + 2\mu^i \varepsilon_{kl}^i - \beta^i \theta, \quad \varepsilon_{kl}^i = \left(\partial_l^s u_k^i + \partial_k^s u_l^i\right)/2, \quad u_k^i = (\delta_{km} - n_k n_m) u_m, \tag{30.5}$$

where λ^i, μ^i are the Lamé coefficients for the interface; β^i is the thermal stress coefficient for the interface. We note that instead of λ^i, μ^i and β^i other moduli can be used to formulate the Hooks's law. For example, we can use the material parameters E^i, v^i and α^i, through which we can express the Lamé coefficients and the thermal stress coefficient using the plane stress formulas: $\lambda^i = v^i E^i/[1-(v^i)^2],\ \mu^i = E^i/[2(1+v^i)],\ \beta^i = \alpha^i E^i/(1-v^i) = 2\alpha^i(\lambda^i + \mu^i)$.

Similarly, for the interphase boundaries S^i, we accept the equation of highly thermal conducting boundaries:

$$n_l[q_l] = \partial_l^s q_l^i, \quad q_l^i = -k^i \partial_l^s \theta, \quad \mathbf{x} \in S^i, \tag{30.6}$$

where k^i is the surface thermal conductivity.

Thus, a two-phase composite consisting of two isotropic thermoelastic phases with interface boundaries is characterized by 12 material moduli, for example, $E^{(1)}, v^{(1)}, \alpha^{(1)}, k^{(1)}, E^{(2)}, v^{(2)}, \alpha^{(2)}, k^{(2)}, E^i, v^i, \alpha^i$ and k^i. If the representative volume does not have a pronounced anisotropy in the components distribution, then a such called "equivalent" homogeneous material will also be isotropic and will be described by only four independent moduli, for example, $c_{11}^{\text{eff}}, c_{12}^{\text{eff}}, \beta^{\text{eff}}$ and k^{eff}. It is important to observe, that $\theta = \theta_0 = \text{const}$ for $\mathbf{x} \in V$; (30.2), (30.6) are satisfied identically, because $q_l = 0,\ q_l^i = 0$. Therefore the pure thermal problem (30.2), (30.6) is not actually used for solving the mechanical problem with thermal stresses

(30.1), (30.4), (30.5), and therefore the moduli $c_{11}^{\text{eff}}, c_{12}^{\text{eff}}, \beta^{\text{eff}}$ and the modulus k^{eff} can be found from separate problems.

In order to determine the effective moduli c_{11}^{eff} and c_{12}^{eff}, it is enough to solve only one problem (30.1), (30.4), (30.5) in the representative volume of the composite with the boundary condition ($\varepsilon_0 = \text{const}$):

$$u_k = x_1 \varepsilon_0 \delta_{1k}, \quad \theta = 0, \ \mathbf{x} \in S, \tag{30.7}$$

where θ is identically equal to zero in the volume V.

Then, from the solution of problem (30.1), (30.4), (30.5), (30.7) similarly to [6, 7] we can find:

$$c_{11}^{\text{eff}} = \langle \sigma_{11} \rangle / \varepsilon_0, \quad c_{12}^{\text{eff}} = \langle \sigma_{22} \rangle / \varepsilon_0, \tag{30.8}$$

where the angle brackets denote the averaged by the volume V and by the interface S^i values:

$$\langle (\ldots) \rangle = \frac{1}{|V|} \left(\int\limits_V (\ldots) \mathrm{d}V + \int\limits_{S^i} (\ldots)^s \mathrm{d}S^i \right). \tag{30.9}$$

If instead of (30.7) we use the boundary condition:

$$u_k = 0, \quad \theta = \theta_0, \ \mathbf{x} \in S, \tag{30.10}$$

where $\theta_0 = \text{const} \neq 0$, θ is identically equal to θ_0 in the volume V, then from boundary-value problem (30.1), (30.4), (30.5), (30.10), the thermal stress effective modulus β^{eff} can be obtained:

$$\beta^{\text{eff}} = -\langle \sigma_{11} \rangle / \theta_0. \tag{30.11}$$

As it was mentioned above, in order to determine the effective coefficient k^{eff}, it is sufficient to consider thermal conductivity equation (30.2) and interface relation (30.6). For the formulation of the corresponding boundary-value problem, we adopt the boundary conditions in the following form ($G_0 = \text{const}$):

$$\theta = x_1 G_0, \quad \mathbf{x} \in S. \tag{30.12}$$

Having solved problem (30.2), (30.6), (30.12) for heterogeneous medium, we get computational formulas for the effective thermal conductivity coefficient:

$$k^{\text{eff}} = -\langle q_1 \rangle / G_0. \tag{30.13}$$

We can check that the homogenized material is isotropic in respect to its elastic properties, if the solution of the problem (30.1), (30.4), (30.5), (30.7) also gives:

$c_{12}^{\text{eff}} \approx \langle\sigma_{33}\rangle/\varepsilon_0; \langle\sigma_{km}\rangle \approx 0, k \neq m$. For additional control of the quality of the representative volume, it makes sense to solve problem (30.1), (30.4), (30.5) with a shear boundary condition: $u_k = \varepsilon_0(x_3\delta_{2k} + x_2\delta_{3k})/2, \theta = 0, \mathbf{x} \in S$. If we obtain $c_{44}^{\text{eff}} = \langle\sigma_{23}\rangle/\varepsilon_0$ from the solution of this problem, then this value should be approximately equal to $c_{44}^{\text{eff}} \approx (c_{11}^{\text{eff}} - c_{12}^{\text{eff}})/2$, where the moduli c_{11}^{eff}, c_{12}^{eff} are determined from the solution of problem (30.1), (30.4), (30.5), (30.7).

We can also note that the homogenized material is isotropic in respect to the thermal stress properties, if the solution of the problem (30.1), (30.4), (30.5), (30.10) gives: $\beta^{\text{eff}} \approx -\langle\sigma_{22}\rangle/\theta_0 \approx -\langle\sigma_{33}\rangle/\theta_0; \langle\sigma_{km}\rangle \approx 0, k \neq m$. Finally, the homogenized material is isotropic in respect to the thermal conductivity properties, if the solution of the problem (30.2), (30.6), (30.12) gives: $\langle q_2\rangle \approx \langle q_3\rangle \approx 0$.

In conclusion of this section we can note that taking into account the interface surface effects for nanostructured composites leads to the appearance of special boundary conditions (30.4)–(30.6) on the surface S^i and to the necessity of calculating the averaged stresses and heat fluxes in (30.9) not only by the volume V, but also by the surface S^i.

30.3 Numerical Results

The elastic problem (30.1), (30.4), (30.5), (30.7), the thermal stress problem (30.1), (30.4), (30.5), (30.10) and thermal problem (30.2), (30.6), (30.12) have been solved numerically in the finite element software package ANSYS using the technique similar to the one described in [6]. The representative volume V was chosen as a cube with the side L, which was evenly divided into smaller geometrically identical cubes. These cubes represented twenty node hexahedral finite elements SOLID226 with thermoelastic option for elastic and thermal stress problems, and twenty node hexahedral finite elements SOLID90 for thermal problem. As a result, for a separate problem in the volume V there were $n_V = n^3$ finite elements, where n was the number of elements along one of the axis. For the simulation of a two-phase composite, the finite elements had properties of one of the phases. At the beginning, all elements had the properties of the first phase. Then, based on the required percentage of the material of the second phase p_a, for randomly chosen $n_p = \text{NINT}(n_V p_a/100)$ finite elements their material properties were changed to the material properties of the second phase (here NINT is the rounding function to nearest integer in ANSYS APDL programming language). Note that the resulting percentage of inclusions $p = 100n_p/n_V$ can differ from the expected value p_a, although this difference is usually negligibly small.

Further, the boundaries of the elements with different material properties were automatically covered [6] by eight-node shell elements SHELL281 with the option of only membrane stresses for mechanical problems or by eight-node shell elements SHELL132 without temperature variation through shell layer for thermal problem.

At the end all interface edges were covered by membrane elastic elements or by thermal shell finite elements, which simulated the presence of interface stresses (30.4), (30.5) or high thermal conductivity (30.6) on the boundaries S^i. At the next stage, for the generated representative volume we solved the described above problems, and after that in ANSYS postprocessor we calculated the averaged stresses or the averaged thermal fluxes by both volume and surface elements using the element table ANSYS procedure. Lastly, using formulas (30.8), (30.11) or (30.13) we calculated the effective moduli of the composite, taking the interface effects into account.

We note that for the same size L of the volume V, depending on the number of elements n along the axes, the size $l = L/n$ of finite elements can be different, hence, the size of inclusions can be different. Therefore, for a fixed percentage of inclusions p and increasing n, the size of inclusions will be smaller, but the total number of the elements of inclusions n_p will increase, and thus the total area of the boundary S^i will increase [6].

As an example, we consider the problem of finding the effective moduli of a two-phase composite, where the first (main) phase is wolfram and the second (inclusion) phase is copper. As it is known, both phases can be adopted as isotropic materials. For numerical results, we took the following values of bulk material moduli of the first and second phases: $E^{(1)} = 4 \times 10^{11}\,\mathrm{N/m^2}$; $\nu^{(1)} = 0.28$; $\alpha^{(1)} = 4.4 \times 10^{-6}\,\mathrm{K^{-1}}$; $k^{(1)} = 163.3\,\mathrm{W/(m\,K)}$; $E^{(2)} = 1.1 \times 10^{11}\,\mathrm{N/m^2}$; $\nu^{(2)} = 0.34$; $\alpha^{(2)} = 16.4 \times 10^{-6}\,\mathrm{K^{-1}}$; $k^{(2)} = 385\,\mathrm{W/(m\,K)}$. It is easy to note that the material of the first phase is almost four times stiffer than the material of the second phase. However, the Poisson's ratio, the coefficient of thermal expansion and the thermal conductivity of the material of the first phase are smaller than those of the second phase.

As the interface stresses and the interface thermal conductivity were simulated by the elastic membrane and thermal shell finite elements, for them it was necessary to set the thickness h^i. The surface Young's modulus and the surface coefficient of thermal conductivity were taken proportional to the difference between the corresponding volumetric quantities of two phases: $\widetilde{E}^i = k^s\left|E^{(1)} - E^{(2)}\right|$, $\widetilde{k}^i = k^s\left|k^{(1)} - k^{(2)}\right|$, where k^s is a dimensionless factor. Moreover, the Poisson's ratio and the coefficient of thermal expansion were determined by the formulas: $\nu^i = (\nu^{(1)} + \nu^{(2)})/2$, $\alpha^i = (\alpha^{(1)} + \alpha^{(2)})/2$. Such approach leads to the taking into account the surface stresses (30.4), (30.5) with the Young's modulus $E^i = h^i\widetilde{E}^i = h^i k^s\left|E^{(1)} - E^{(2)}\right|$ and the surface thermal fluxes with the surface coefficient of thermal conductivity $k^i = h^i\widetilde{k}^i = h^i k^s\left|k^{(1)} - k^{(2)}\right|$. It means that in these cases the values h^i and k^s are not considered independently, but their product $h^i k^s$ is important. In connection to this, in further numerical calculations the thickness h^i was fixed: $h^i = 1$ m, and for the analysis of the interface stresses and the interface thermal fluxes influence we varied only the coefficient k^s from 10^{-4} to 1.

Figures 30.1, 30.2 and 30.3 show the dependencies of the effective moduli with respect to the factor k^s in the logarithmic scale ($\lg \equiv \log_{10}$): the Young's modulus

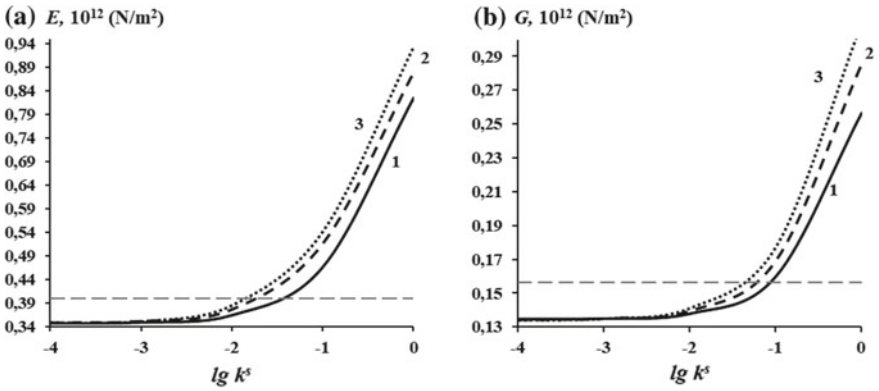

Fig. 30.1 Dependencies of the effective moduli E^{eff} (**a**) and G^{eff} (**b**) versus the factor k^s for $p = 15\%$: curve 1 is for $n = 10$; curve 2 is for $n = 15$; curve 3 is for $n = 20$

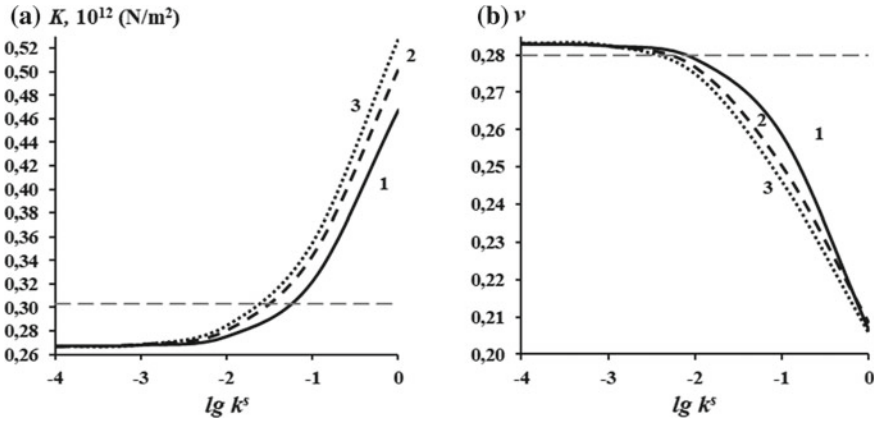

Fig. 30.2 Dependencies of the effective moduli K^{eff} (**a**) and ν^{eff} (**b**) versus the factor k^s for $p = 15\%$: curve 1 is for $n = 10$; curve 2 is for $n = 15$; curve 3 is for $n = 20$

E^{eff} (Fig. 30.1a), the shear modulus G^{eff} (Fig. 30.1b), the bulk modulus K^{eff} (Fig. 30.2a), the Poisson's ratio ν^{eff} (Fig. 30.2b), the coefficient of thermal expansion α^{eff} (Fig. 30.3a), and the thermal conductivity k^{eff} (Fig. 30.3b). Here the percentage of inclusions (material of the second phase) remains unchanged $p = 15\%$, and the curves 1, 2, 3 correspond to the values $n = 10$, $n = 15$, and $n = 20$, respectively.

As we can see, the behaviours of the effective moduli E^{eff}, G^{eff}, K^{eff}, and k^{eff} depending on the interface moduli values, qualitatively coincide, but the effective thermal conductivity increases the most rapidly. For $k^s \leq 5 \times 10^{-3}$ the surface effects have only a slight influence on the values of the material moduli.

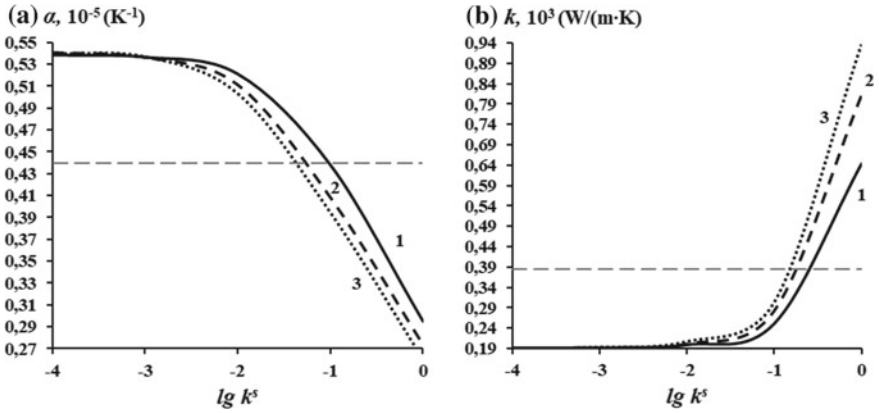

Fig. 30.3 Dependencies of the effective moduli α^{eff} (**a**) and k^{eff} (**b**) versus the factor k^s for $p = 15\%$: curve 1 is for $n = 10$; curve 2 is for $n = 15$; curve 3 is for $n = 20$

Approximately starting from the values of the factor $k^s \leq 10^{-2}$, the stiffness moduli and the thermal conductivity begin to grow quite rapidly. Thus, for the fixed percentage of inclusions $p = 15\%$ with increasing $n = 10$, 15, 20 the size of inclusions decrease, but the number of inclusions and their total area increase. As a result, the interface effects are manifested in a greater extent, therefore the stiffness moduli (Figs. 30.1 and 30.2a) and the thermal conductivity (Fig. 30.3b) increase (curves 1 are located lower than curves 2, and curves 2 are located lower than curves 3).

It should be noted that for large values of the interface stiffness moduli the overall effective stiffness moduli of composite nanomaterials with interfaces may exceed the moduli of the stiffest phase in the composite. In Figs. 30.1 and 30.2a, this effect is observed when the values of the moduli are larger than the moduli of the stiffest material in the composite (dashed lines). Similarly, the effective thermal conductivity coefficient for larger values of the interface conductivity moduli can exceed the value of the maximal coefficient among the thermal conductivity coefficients of separate materials of the composite (see Fig. 30.3b, dashed line for values of maximal thermal conductivity of the second phase).

Figures 30.2b and 30.3a show that the behaviour of the Poisson ratio and the behaviour of the coefficient of thermal expansion with increasing interface modulus is opposite to the behaviour of the moduli E^{eff}, G^{eff}, K^{eff} and k^{eff}. This can be explained by an increase in the overall stiffness of the composite material.

In order to analyse the influence of the interface effect on the effective properties with different percentage of inclusions, we have calculated the effective moduli with the fixed number of elements $n = 10$, but for different percentage of inclusions and different values of the factor k^s. The results of these calculations are shown in Figs. 30.4, 30.5 and 30.6, where the curves 1, 2, 3, 4 correspond to the values $k^s = 0.1$, $k^s = 0.05$, $k^s = 0.01$, and $k^s = 0.001$, respectively.

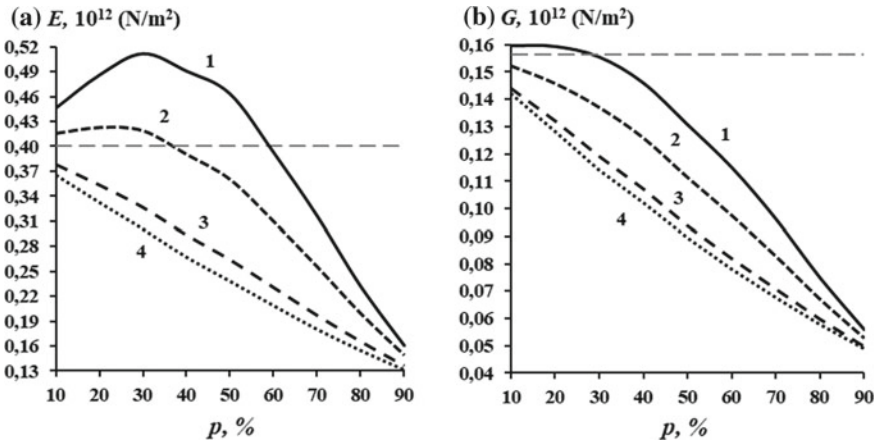

Fig. 30.4 Dependencies of the effective moduli E^{eff} (**a**) and G^{eff} (**b**) versus the percentage of inclusions for $n = 10$ and for the factor k^s: curve 1 is for $k^s = 0.1$; curve 2 is for $k^s = 0.05$; curve 3 is for $k^s = 0.01$; curve 4 is for $k^s = 0.001$

As Figs. 30.4, 30.5 and 30.6 demonstrate, for small values of the factor k^s (curves 3 and 4) the interface effects do not affect the material moduli except for the Poisson's ratio. However, for any percentage of inclusions the interface stresses are larger than the effective stiffness of the composite material. Moreover, as it was mentioned earlier, there are cases when the composite material with interfaces can have greater stiffness than the stiffest material in the composite. This situation takes place, when $k^s = 0.1$ for the Young's modulus E^{eff}, if $p \leq 63\%$, for the shear modulus G^{eff}, if $p \leq 32\%$, and for the bulk modulus K^{eff}, if $p \leq 45\%$, (see curves 1, which are located higher that the dashed lines in Figs. 30.4 and 30.5a). On the contrary, the Poisson's ratio of the composite structure can be smaller than the Poisson's ratio of the main material for large values of k^s in a wide range of p (Fig. 30.5b).

We note that the percentage of softer inclusions and the interface stresses have the opposite influence on the effective stiffness: a simple increase of the percentage of softer inclusions leads to a decrease in the stiffness moduli, however, the interface stresses increase the stiffness. The growth of the percentage of the softer inclusions for nanocomposite materials with interphase effects entails an increase of the boundary areas with interface stresses. Therefore, with the increase of the percentage of softer inclusions, the stiffness moduli of nanocomposite materials with interface may increase. For example, for large values of interface moduli, an increase of the percentage of inclusions for no very large p ($p \leq 32\%$ for $k^s = 0.1$ and $p \leq 22\%$ for $k^s = 0.05$) leads to a growth of the effective Young's modulus, and with further increase of p the effective Young's modulus starts to decrease. The effects mentioned also take place for the effective bulk modulus K^{eff} (Fig. 30.5a), but to a less extent.

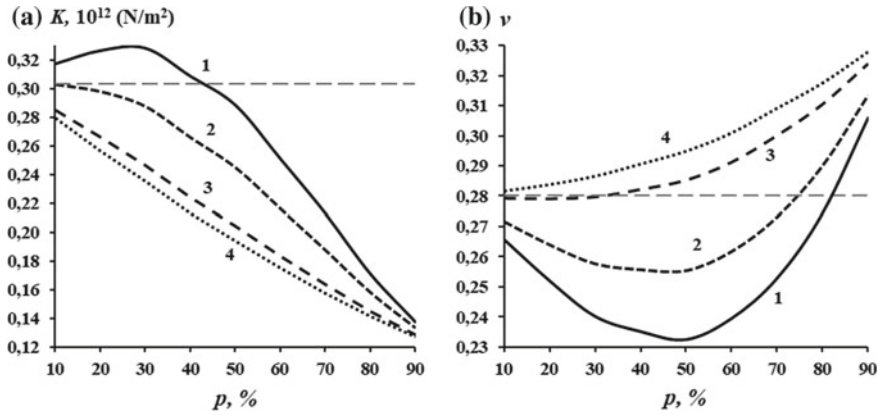

Fig. 30.5 Dependencies of the effective moduli K^{eff} (**a**) and ν^{eff} (**b**) versus the percentage of inclusions for $n = 10$ and for the factor k^s: curve 1 is for $k^s = 0.1$; curve 2 is for $k^s = 0.05$; curve 3 is for $k^s = 0.01$; curve 4 is for $k^s = 0.001$

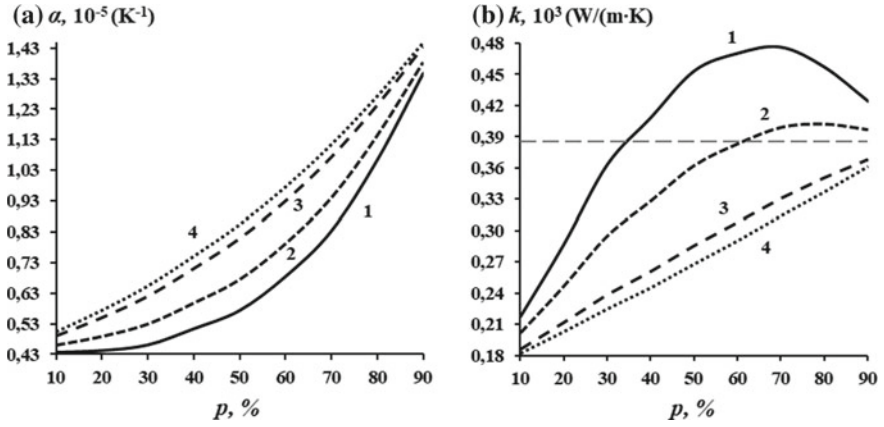

Fig. 30.6 Dependencies of the effective moduli K^{eff} (**a**) and ν^{eff} (**b**) versus the percentage of inclusions for $n = 10$ and for the factor k^s: curve 1 is for $k^s = 0.1$; curve 2 is for $k^s = 0.05$; curve 3 is for $k^s = 0.01$; curve 4 is for $k^s = 0.001$

When analysing the values of the thermal conductivity coefficient, it is important to take into account that the thermal conductivity coefficient of the second phase material is considerably larger than the thermal conductivity coefficient of the first phase material $(k^{(1)} < k^{(2)})$. Therefore, the dependencies of the effective coefficient of thermal conductivity k^{eff} in Fig. 30.6b are inverted with respect to the percentage of inclusions p compared to the behaviours of the moduli E^{eff} and K^{eff}. However, also here the values of the interface moduli $(k^s = 0.1$ and $k^s = 0.05)$ lead to non-monotonous behaviour of k^{eff} with respect to p and to larger values of k^{eff} in comparison with $k^{(2)}$ at $p \geq 35\%$ for $k^s = 0.1$ and $p \geq 63\%$ for $k^s = 0.05$.

30.4 Conclusions

The homogenization model was described for a two-phase thermoelastic isotropic composite with surface stresses and surface thermal fluxes at the interphase boundaries, which reflected the nanoscale effects for nanostructured composites. This model was applied for the calculation of the effective moduli of a wolfram-copper composite with interphase boundary conditions. The solutions of the homogenization problems were obtained by the finite element method in ANSYS finite element package for a cubic representative volume with mapped meshing in hexahedral finite elements and random distribution of inclusions. In order to take into account the interface effects, shell finite elements were added to the finite element mesh at the boundaries between the composite phases. For the considered composite with stiffer skeleton and softer inclusions, it was noted that the effective moduli were dependent on the percentage of inclusions, their configuration and size. These dependencies appear to be similar to the known dependencies for nanoporous composites [10, 19, 32–35] and others. Analogous but inverted dependencies were also observed for the thermal conductivity coefficients, which were induced by larger values of the thermal conductivities for the material of inclusion.

Acknowledgements This research was performed in the framework of the Russian-Indian RFBR-DST Collaborative project with RFBR grant number 16-58-48009 IND_omi and DST grant number DST/INT/RFBR/IDIR/P-11/2016.

References

1. M.E. Gurtin, A.I. Murdoch, Arch. Ration. Mech. An. **57**, 291 (1975)
2. M.E. Gurtin, A.I. Murdoch, Int. J. Solid. Struct. **14**, 431 (1978)
3. A.I. Murdoch, Q.J. Mech, Appl. Math. **29**, 245 (1976)
4. R. Shuttleworth, Proc. Phys. Soc. A. **63**, 444 (1950)
5. J.C. Hamilton, W.G. Wolfer, Surf. Sci. **603**, 1284 (2009)
6. A. Javili, P. Steinmann, Int. J. Solid. Struct. **47**, 3245 (2010)
7. R.J. Needs, M.J. Godfrey, M. Mansfield, Surf. Sci. **242**, 215 (1991)
8. Y.Z. Povstenko, J. Mech. Phys. Solids **41**, 1499 (1993)
9. D.J. Steigmann, R.W. Ogden, Proc. R. Soc. A **455**, 437 (1999)
10. V.A. Eremeyev, Acta Mech. **227**, 29 (2016)
11. J. Wang, Z. Huang, H. Duan et al., Acta Mech. Solida Sin. **24**, 52 (2011)
12. T. Chen, G.J. Dvorak, C.C. Int, J. Solids Struct. **44**, 941 (2007)
13. H. Le Quang, Q.-C. He, J. Mech. Phys. Solids. **55**, 1889 (2007)
14. H. Le Quang, Q.-C. He, Arch. Appl. Mech. **79**, 225 (2009)
15. H.L. Duan, B.L. Karihaloo, J. Mech. Phys. Solids **55**, 1036 (2007)
16. A. Javili, P. Steinmann, Int. J. Solids Struct. **47**, 3245 (2010)
17. A. Javili, P. Steinmann, Comput. Methods Appl. Mech. Eng. **200**, 1963 (2011)
18. A. Javili, A. McBride, P. Steinmann, Appl. Mech. Rev. **65**, 010802 (2013)
19. A.V. Nasedkin, A.A. Nasedkina, A.S. Kornievsky, A.I.P. Conf, Proc. **1798**, 020110 (2017)

20. A.V. Nasedkin, A.A. Nasedkina, A.S. Kornievsky, in *Coupled Problems 2017—Proceedings of the VII International Conference on Coupled Problems in Science and Engineering*, 12–14 June 2017, Rhodes Island, Greece, ed. by M. Papadrakakis, E. Oñate, B.A. Schreflers, (CIMNE, Barcelona, Spain, 2017), p. 1140
21. A.A. Nasedkina, A. Rajagopal, Mater. Phys. Mech. **37**, 34 (2018)
22. H. Le Quang, T.-L. Phan, G. Bonnet, Int. J. Therm. Sci. **50**, 1428 (2011)
23. H. Le Quang, D.C. Pham, G. Bonnet, Q.-C. He, Int. J. Heat Mass Transf. **58**, 175 (2013)
24. S. Kaessmair, A. Javili, P. Steinmann, Arch. Appl. Mech. **84**, 1409 (2014)
25. S. Graham, D.L. McDowell, J. Heat Transfer **125**, 389 (2003)
26. V.I. Kushch, I. Sevostianov, V.S. Chernobai, Int. J. Eng. Sci. **83**, 146 (2014)
27. H. Le Quang, Int. J. Heat Mass Transf. **95**, 162 (2016)
28. J.T. Liu, S.T. Gu, E. Monteiro, Q.-C. He, Comput. Mech. **53**, 825 (2014)
29. L. Wu, Int. J. Eng. Sci. **48**, 783 (2010)
30. J. Xiao, Y. Xu, F. Zhang, Compos. Struct. **189**, 553 (2018)
31. J. Yvonnet, Q.-C. He, Q.-Z. Zhu, J.-F. Shao, Comp. Mater. Sci. **50**, 1220 (2011)
32. A.V. Nasedkin, A.S. Kornievsky, Comput. Contin. Mech. **10**, 375 (2017). (in Russian)
33. A.V. Nasedkin, A.S. Kornievsky, in *Methods of Wave Dynamics and Mechanics of Composites for Analysis of Microstructured Materials and Metamaterials. Advanced Structured Materials*, ed. by M.A. Sumbatyan, vol. 59 (Springer, Singapore, 2017), p. 107
34. H.L. Duan, J. Wang, B.L. Karihaloo, Z.P. Huang, Acta Mater. **54**, 2983 (2006)
35. V. Eremeyev, N. Morozov, Dokl. Phys. **55**(6), 279 (2010)

Chapter 31
Dynamic Analysis of the Poroviscoelastic Halfspace with a Cavity Under Vertical Load Using BEM

Leonid Igumnov, Aleksandr Ipatov and Svetlana Litvinchuk

Abstract The present work is dedicated to three dimensional poroviscodynamic problems and numerical technique for solving such problems. Our numerical technique is based on Boundary Element Method usage. Boundary-value problem of poroviscoelastic halfspace with a cavity under vertical load is considered. Theory of poroviscoelasticity is based on Biot's equations of fluid saturated porous media under the assumption that the skeleton is viscoelastic. Viscoelastic effects of solid skeleton are modeled by means of elastic-viscoelastic correspondence principle. The standard viscoelastic solid model is employed. In order to study the boundary-value problem boundary integral equations method is applied, and boundary element method for obtaining numerical solutions is used. The solution of the original problem is constructed in Laplace transforms, with the subsequent application of the algorithm for numerical inversion. To introduce BE-discretization, we consider the regularized boundary-integral equation. Mixed boundary element discretization is introduced to obtain discrete analogues. Modified Durbin's algorithm of numerical inversion of Laplace transform is applied to perform solution in time domain.

31.1 Introduction

Wave motion in porous media is an important issue in several branches of engineering science, such as geophysics, geomechanics, seismic prospecting, bioengineering etc. All of this requires the development of effective tools, methods and models. Thus, the problem of mathematical methods development and their application in wave propagation investigation in viscoelastic, poroelastic and poroviscoelastic solids appears. Mathematical modeling is one of the main tools to analyze and optimize the development of oil and gas fields, to solve the problems of

L. Igumnov · A. Ipatov (✉) · S. Litvinchuk
Research Institute for Mechanics, Lobachevsky State University of Nizhni Novgorod, 603950 Nizhny Novgorod, Russia
e-mail: ipatov@mech.unn.ru

I. A. Parinov et al. (eds.), *Advanced Materials*, Springer Proceedings in Physics 224, https://doi.org/10.1007/978-3-030-19894-7_31

seismic construction and bioengineering [1–4]. The model of poroelastic medium, allowing one to describe fluid filtration in pores in together with a full-scale mechanical model of the stress-strain state of medium is usually used to describe the "solid–fluid" system.

Study of wave propagation processes in saturated porous media originates from Frenkel [5] and Biot [6, 7]. It is assumed that the space containing poroelastic medium is filled with a two-phase material, and one phase corresponds to the elastic skeleton, and the another one to the fluid in pores. Both phases are present at each point of the physical space, and the phase distribution in space is described by macroscopic quantities such as porosity. Biot's model correctly describes processes of elastic porous medium deformation and fluid flow in that medium. The implementation of the solid viscoelastic effects in the theory of poroelasticity was first introduced by Biot [8]. The coexistence of poroelastic and viscoelastic phenomena has been observed in the laboratory and in the field for a range of rock types [9, 10].

It is known that drilling difficulties are mainly associated with shales and tuffaceous sediments. Typical problems while drilling is tool sticking and creep or swelling in the borehole wall. These problems may be caused both by chemical and mechanical nature of sediments. Part of the difficulty can be attributed to mechanical effects of poroelastic and viscoelastic origin [11]. A poroviscoelastic solution can help elucidate these phenomena and the associated creep events.

Dealing with wave propagation in a halfspace, surface waves are one of most interesting effects, especially the Rayleigh wave. Although Biot's model allows solving a number of particular problems connected with wave propagation in poroelastic halfspaces [12–15], there is still a problem of increasing complexity of computational schemes for boundary value problems, especially considering infinite and semi-infinite domains.

Wave propagation phenomena are often observed in semi-infinite media, for example propagation of machine foundation excitations in the soil, earthquake motion and their effect on buildings, so the Boundary Element Method (BEM) is a very reasonable approach dealing with such kind of problems. Also classical formulations for boundary integral equation (BIE) method with boundary element schemes are successful approaches for solving three-dimensional problems of dynamic elasticity. Extension of BIE method and BEM to anisotropic problems, visco- and poroelastic material models needs development of new numerical schemes. Nowadays there are two fundamentally different approaches for constructing such numerical scheme: direct solving in time domain [16, 17], or solving in Laplace or Fourier domain [18, 19]. Durbin [20] developed an approach, namely fast Laplace inverse transform for numerical evaluation of the integrals. Some modifications were recently proposed by Zhao [21] in order to overcome a drawback of constant integration step in FLIT. In present paper we employ a modified Durbin's algorithm with variable integrating step and linear approximation.

The first BEM formulations for Biot's poroelastodynamics was performed with Laplace transform usage. Fundamental solutions and BIE of the dynamic theory of poroelasticity were obtained in [22–24]; in [25, 26] different variants of boundary element schemes for the solution of problems in porodynamics are presented and

results of numerical experiments are provided. Boundary element solutions for dynamic problems of poroelastic halfspaces are presented in [27, 28].

The viscoelastic behavior of poroelastic medium can be due to the viscoelastic properties of the skeleton [29, 30]. Some results of simulation of wave processes in poroelastic solids with the use of BIE, BEM and various models of viscoelastic behavior of the skeleton are presented in [31, 32].

In present paper we consider an extension of Biot poroelastic model by means of correspondence principal in order to take into the account viscoelastic behavior of porous media. Correspondence principal is applied to a skeleton of porous material, viscoelastic properties are described by means of standard linear solid model. The modeling of wave propagation in homogeneous poroviscoelastic halfspace with cavity is presented. The influences of cavity form and viscosity parameter are studied.

31.2 Mathematical Model

Basic poroelastic material is a two-phase material consisting of an elastic skeleton and compressible fluid or gas filler. Porous material of a volume V can be constructed as follows:

$$V = V^{\mathrm{f}} + V^{\mathrm{s}}$$

where V is the total volume, V^{f} is the summary pore volume and V^{s} is the volume of the skeleton. It is assumed that filler can openly seep through the pores and all closed pores are assumed as a part of the skeleton.

After formal applying of Laplace transform we obtain a statement for a boundary-value problem for Biot's model of fully saturated poroelastic continuum in Laplace domain. Then it can be rewritten for four unknowns (displacements $\bar{u}_i$ and pore pressure $\bar{p}$). The final set of differential equations in Laplace transform takes the following form [22]:

$$\begin{aligned} &G\bar{u}_{i,jj} + \left(K + \tfrac{G}{3}\right)\bar{u}_{j,ij} - (\psi - \beta)\bar{p}_{,i} - s^2(\rho - \beta\rho_f)\bar{u}_i = -\bar{F}_i, \\ &\tfrac{\beta}{s\rho_{\mathrm{f}}}\bar{p}_{,ii} - \tfrac{\phi^2 s}{R}\bar{p} - (\psi - \beta)s\bar{u}_{i,i} = -\bar{a}, \quad x \in \Omega, \end{aligned} \tag{31.1}$$

Boundary conditions:

$$\begin{aligned} &\bar{u}(x,s) = f(x,s), \quad x \in \Gamma^u, \quad \bar{u} = (\bar{u}_1, \bar{u}_2, \bar{u}_3, \bar{p}), \\ &\bar{t}(x,s) = g(x,s), \quad x \in \Gamma^\sigma, \quad \bar{t} = (\bar{t}_1, \bar{t}_2, \bar{t}_3, \bar{q}), \end{aligned}$$

where Γ^u and Γ^σ denote boundaries for boundary conditions of 1st and 2nd kind, respectively, G, K are the elastic moduli, $\phi = V^{\mathrm{f}}/V$ is the porosity, $\bar{F}_i, \bar{a}$ are the bulk body forces.

$$\beta = \frac{\kappa\rho_{\mathrm{f}}\phi^2 s}{\phi^2 + s\kappa(\rho_{\mathrm{a}} + \phi\rho_{\mathrm{f}})}, \quad \psi = 1 - \frac{K}{K_{\mathrm{s}}} \quad \text{and} \quad R = \frac{\phi^2 K_{\mathrm{f}} K_{\mathrm{s}}^2}{K_{\mathrm{f}}(K_{\mathrm{s}} - K) + \phi K_{\mathrm{s}}(K_{\mathrm{s}} - K_{\mathrm{f}})}$$

are constants reflecting interaction between skeleton and filler, κ is permeability. Further, $\rho = \rho_{\mathrm{s}}(1-\phi) + \phi\rho_{\mathrm{f}}$ is a bulk density, $\rho_{\mathrm{s}}, \rho_{\mathrm{a}}, \rho_{\mathrm{f}}$ are solid, apparent mass density and filler density, respectively, $K_{\mathrm{s}}, K_{\mathrm{f}}$ are elastic bulk moduli of the skeleton and filler, respectively. Apparent mass density $\rho_{\mathrm{a}} = C\phi\rho_{\mathrm{f}}$ was introduced by Biot to describe dynamic interaction between fluid and skeleton, C is a factor depending on the pores geometry and excitation frequency.

Then the elastic-viscoelastic correspondence principle is applied to the skeleton, so we extend poroelastic formulation to poroviscoelasticity. Poroviscoelastic solution is obtained from poroelastic solution by replacing to skeleton's moduli K and G in Laplace domain with material creep functions $\bar{K}(s)$ and $\bar{G}(s)$.

In present paper we employ standard linear solid model:

$$\bar{K}(s) = K^{\infty} \cdot \left[(\chi - 1)\frac{s}{s+\eta} + 1 \right]$$
$$\bar{G}(s) = G^{\infty} \cdot \left[(\chi - 1)\frac{s}{s+\eta} + 1 \right]$$

The equilibrium and instantaneous values of the relaxation function associated with material modules are connected as follows:

$$\chi = K^0/K^{\infty} = G^0/G^{\infty}$$

Equilibrium and instantaneous values are denoted by ∞ and 0, respectively.

31.3 Boundary-Element Approach

Following regularized BIE system corresponding boundary-value problem (31.1) is considered:

$$\frac{1-\alpha_{\Omega}}{2} v_i(\mathbf{x}, s) + \int_{\Gamma} \left(T_{ij}(\mathbf{x}, \mathbf{y}, s) v_i(\mathbf{y}, s) - T^0_{ik}(\mathbf{x}, \mathbf{y}, s) v_i(\mathbf{x}, s) - U_{ij}(\mathbf{x}, \mathbf{y}, s) t_i(\mathbf{y}, s) \right) \mathrm{d}\Gamma = 0, \quad \mathbf{x}, \mathbf{y} \in \Gamma$$

where U_{ij}, T_{ij} are the fundamental and singular solutions, T^0_{ij} contains the isolated singularities, $\mathbf{x} \in \Gamma$ is an arbitrary point. Coefficient α_{Ω} equals 1 in the case of finite domain and -1 in the case of infinite domain.

Boundary surface of our homogeneous solid is discretized by quadrangular and triangular elements and triangular elements are assumed as singular quadrangular elements. The Cartesian coordinates of an arbitrary point of the element are expressed through the coordinates of the nodal points of this element, using shape

functions of the local coordinates. Shape functions are quadratic polynomials of interpolation. We use reference elements: square $\xi = (\xi_1, \xi_2) \in [-1, 1]^2$ and triangle $0 \le \xi_1 + \xi_2 \le 1,\ \xi_1 \ge 0,\ \xi_2 \ge 0$, and each boundary element is mapped to a reference one by the following formula:

$$y_i(\xi) = \sum_{l=1}^{8} N^l(\xi) y_i^{\beta(k,l)}, \quad i = 1, 2, 3,$$

where l is the local node number in element k, $\beta(k, l)$ is the global node number, $N^l(\xi)$—shape functions. Goldshteyn's displacement-stress mixed model is performed. To discretize the boundary surface eight-node biquadratic quadrilateral elements are used, generalized displacements and tractions are approximated by linear and constant shape functions, respectively.

Subsequent applying of collocation method leads to the system of linear equations. As the collocation nodes, we take the approximation nodes of boundary functions. Gaussian quadrature are used to calculate integrals on regular elements. But if an element contains a singularity, algorithm of singularity avoiding or order reducing is applied. When singularity is excluded we use an adaptive integration algorithm. An appropriate order of Gaussian quadrature is chosen from primarily known necessary precision, if it is impossible, the element is subdivided to smaller elements recursively.

31.4 Laplace Transform Inversion

The poroviscoelastic solution in time domain is obtained with the help of the Laplace transform inversion. Durbin's algorithm [20] is used for numerical inversion of Laplace transform. The inverse Laplace transform is defined as the following contour integral

$$L^{-1}\left\{\bar{f}(\mathbf{x}, s)\right\} = f(\mathbf{x}, t) = \frac{1}{2\pi i} \int_{\alpha - i\infty}^{\alpha + i\infty} \bar{f}(\mathbf{x}, s) \mathrm{e}^{st} \mathrm{d}s, \tag{31.2}$$

where $\alpha > 0$ is the arbitrary real constant greater than the real parts of all singularities in $\bar{f}(\mathbf{x}, s)$. When values of $\bar{f}(\mathbf{x}, s)$ are available only at the sample points, analytical evaluation of integral in (31.2) is impossible. Supposing $s = \alpha + \mathrm{i}\omega$, we have the following expressions (variable $\mathbf{x}$ is omitted hereinafter for convenience):

$$f(0) = \frac{1}{\pi} \int_0^{\infty} \mathrm{Re}[\bar{f}(\alpha + \mathrm{i}\omega)] \mathrm{d}\omega, \tag{31.3}$$

$$f(t) = \frac{e^{\alpha t}}{\pi} \int_0^{\infty} \left\{ \mathrm{Re}[\bar{f}(\alpha + i\omega)] \cos \omega t - \mathrm{Im}[\bar{f}(\alpha + i\omega)] \sin \omega t \right\} d\omega \quad t > 0. \tag{31.4}$$

Let R be large real number so we can rewrite (31.3) and (31.4) as follows:

$$f(0) = \frac{1}{\pi} \lim_{R \to \infty} \int_0^{R} \mathrm{Re}[\bar{f}(\alpha + i\omega)] d\omega, \tag{31.5}$$

$$f(t) = \frac{e^{\alpha t}}{\pi} \lim_{R \to \infty} \int_0^{R} \left\{ \mathrm{Re}[\bar{f}(\alpha + i\omega)] \cos \omega t - \mathrm{Im}[\bar{f}(\alpha + i\omega)] \sin \omega t d\omega \right\}, \quad t > 0. \tag{31.6}$$

Defining the nodes as $0 = \omega_1 < \omega_2 < \cdots < \omega_n < \omega_{n+1} = R$, we approximate (31.5) and (31.6) as

$$f(0) = \frac{1}{\pi} \sum_{k=1}^{n} \int_{\omega_k}^{\omega_{k+1}} \mathrm{Re}[\bar{f}(\alpha + i\omega)] d\omega, \tag{31.7}$$

$$f(t) = \frac{e^{\alpha t}}{\pi} \sum_{k=1}^{n} \int_{\omega_k}^{\omega_{k+1}} \left\{ \mathrm{Re}[\bar{f}(\alpha + i\omega)] \cos(\omega t) - \mathrm{Im}[\bar{f}(\alpha + i\omega)] \sin(\omega t) \right\} d\omega, \quad t > 0. \tag{31.8}$$

In each segment $[\omega_k, \omega_{k+1}]$, $k = \overline{1, n}$, the real and imaginary parts of $\bar{f}(s)$ are approximated with linear functions as follows

$$\mathrm{Re}[\bar{f}(\alpha + i\omega)] \approx F_k + \frac{F_{k+1} - F_k}{\omega_{k+1} - \omega_k} (\omega - \omega_k), \tag{31.9}$$

$$\mathrm{Im}[\bar{f}(\alpha + i\omega)] \approx G_k + \frac{G_{k+1} - G_k}{\omega_{k+1} - \omega_k} (\omega - \omega_k), \tag{31.10}$$

where $F_k = \mathrm{Re}[\bar{f}(\alpha + i\omega_k)]$, $G_k = \mathrm{Im}[\bar{f}(\alpha + i\omega_k)]$.

Substituting (31.9), (31.10) into (31.7), (31.8) and providing direct integration we obtain:

$$f(0) \approx \sum_{k=1}^{n} \left[\frac{(F_{k+1} - F_k)\Delta_k}{2\pi} \right],$$

$$f(t) \approx \frac{e^{\alpha t}}{\pi t^2} \sum_{k=1}^{n} \left[\frac{F_{k+1} - F_k}{\Delta_k} (\cos(\omega_{k+1} t) - \cos(\omega_k t)) + \frac{G_{k+1} - G_k}{\Delta_k} (\sin(\omega_{k+1} t) - \sin(\omega_k t)) \right],$$

where $t > 0$, $\Delta_k = \omega_{k+1} - \omega_k$.

31.5 Inversion Algorithm Tests

In order to study the efficiency of proposed BEM formulation and inversion algorithms the following problem is solved (Fig. 31.1): three-dimensional anisotropic elastic prismatic body is clamped at its left end, and subjected to uniaxial and uniform impact loading $t_2 = t_2^* H(t)$, $t_2^* = -1$ N/m^2 at the right end, $H(t)$ is a Heaviside step function. The remaining surfaces are traction free. Poroelastic material parameters are: $K = 8 \times 10^9$ N/m^2, $G = 6 \times 10^9$ N/m^2, $\phi = 0.66$, $\rho = 2458$ kg/m^3, $K_s = 3.6 \times 10^{10}$ N/m^2, $\rho_f = 1000$ kg/m^3, $K_f = 3.3 \times 10^9$ N/m^2, $k = 1.9 \times 10^{-10}$ m^4/(N s),

In this example, we consider different ways of Durbin's method modification. Use of the modifications makes it possible to reduce the number of discretization points required for providing an assigned accuracy.

Figures 31.2 and 31.3 show the displacement $u_2(t)$ at the center point of the loaded end and tractions $t_2(t)$ at the center point of the clamped end. Following inversion algorithms are considered:

1. Constant integration step: $\Delta_k = 0.5$, $k = 1, 2, \ldots, 600$, $\omega_{\max} = 300$.
2. Variable integration step: from 0 to 10, $\Delta_k = 0.1$; from 10 to 100, $\Delta_k = 0.5$; from 100 to 300, $\Delta_k = 1$, $k = 1, 2, \ldots, 480$, $\omega_{\max} = 300$.

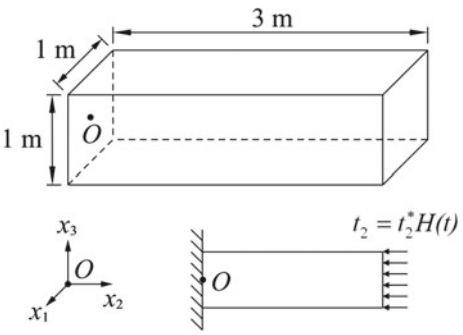

Fig. 31.1 Problem statement

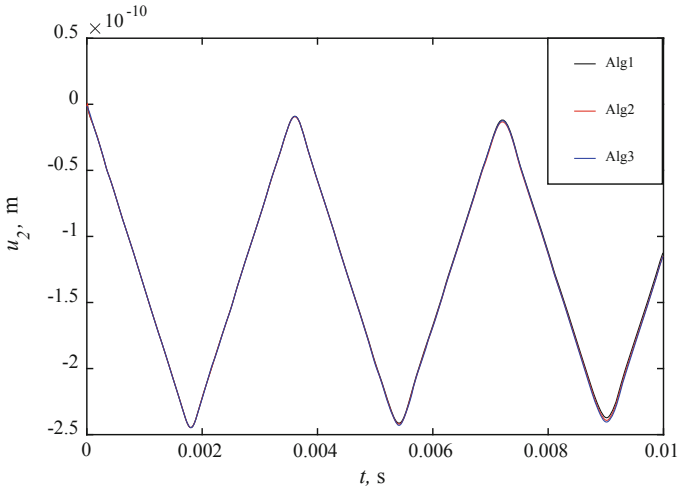

Fig. 31.2 Displacements u_2 in case of different Laplace transform inversion algorithms

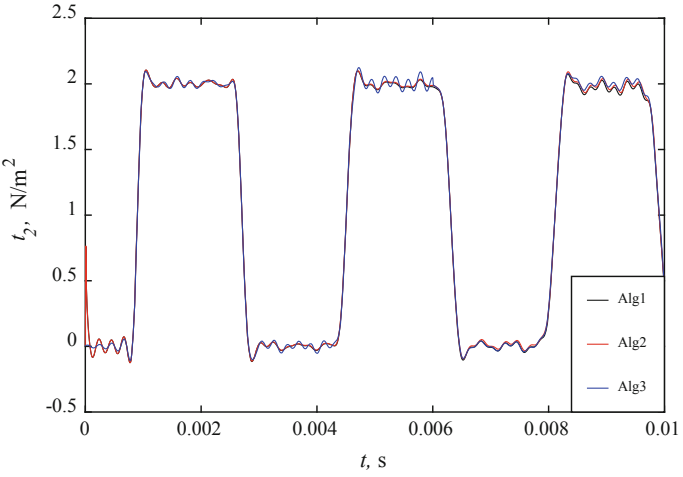

Fig. 31.3 Tractions t_2 in case of different Laplace transform inversion algorithms

3. **Integration** steps are calculated with following relation $\Delta_k = \omega_{k+1} - \omega_k$ in Zhao's algorithm:

$$\omega_k = \mathrm{e}^{(kx)^m} - 1,$$

where $m = 0.8$, $k = 1, 2, \ldots, 480$ and $x = (\ln(\omega_{\max} + 1))^{1/m}/k$, with $\omega_{\max} = 300$.

It can be observed in Figs. 31.2, 31.3 that Algorithm 3 gives the most appropriate results. Further computations are made with Algorithm 3.

31.6 Numerical Results and Discussion

Problem of a vertical Heaviside-type load acting on a poroelastic halfspace is considered. Two types of cavities are considered: cubic and spherical. Force $P(t)$ acting on a square $S = 1$ m^2 on a surface of the halfspace:

$$P(t) = P_0 f(t), \quad f(t) = H(t), \quad P_0 = 1000 \text{ N/m}^2.$$

There is a spherical cavity inside the halfspace: the center of the cavity is located at depth $h = 7.5$ m, radius of the spherical cavity is $R = 5$ m (Fig. 31.4). We study the displacements on the boundary surface of the halfspace at the distance of 15 m away from loading square.

Boundary element discretization is performed with taking into account two planes of symmetry. Boundary element mesh parameters: 864 elements for quarter of the halfspace and 150 elements for quarter of the cavity (see Fig. 31.5).

The next considered problem is a halfspace with a cubic cavity under Heaviside-type load (see Fig. 31.6). Center of the cavity is located at depth $h = 7.5$ m, the edge of the cubic cavity is 10 m long.

Boundary element mesh parameters: 864 elements for quarter of the halfspace and 150 elements for quarter of the cavity (see Fig. 31.7).

Basic poroelastic material parameters are: $K = 8 \times 10^9$ N/m^2, $G = 6 \times 10^9$ N/m^2, $\rho = 2458$ kg/m^3, $\phi = 0.66$, $K_s = 3.6 \times 10^{10}$ N/m^2, $\rho_f = 1000$ kg/m^3, $K_f = 3.3 \times 10^9$ N/m^2, $k = 1.9 \times 10^{-10}$ m^4/(N s)

The reference point is 15 m away from loading square and has coordinates (15, 0, 0). Results of the study of the cavity form influence on displacements at reference point in case of poroelastic material are present in Figs. 31.8 and 31.9.

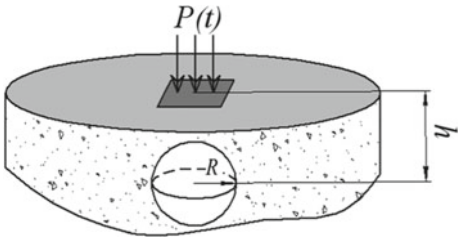

Fig. 31.4 Problem statement

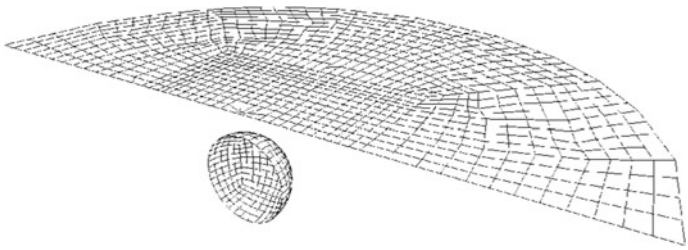

Fig. 31.5 Boundary element mesh visualization

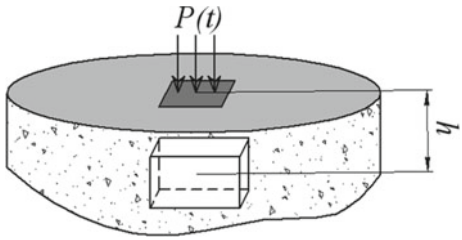

Fig. 31.6 Problem statement

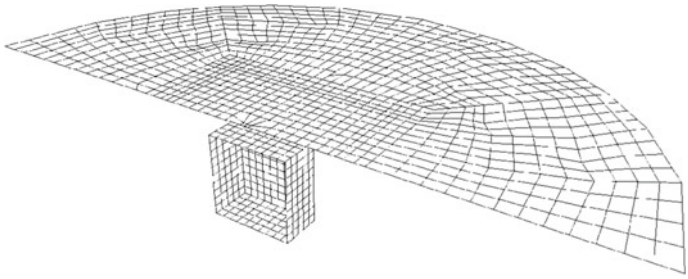

Fig. 31.7 Boundary element mesh visualization

Poroviscoelastic solutions are obtained by using standard linear solid model:

$$\bar{K}(s) = K^{\infty} \cdot \left[(\chi - 1) \frac{s}{s+\gamma} + 1 \right], \quad \bar{G}(s) = G^{\infty} \cdot \left[(\chi - 1) \frac{s}{s+\gamma} + 1 \right],$$
$$\chi = K^0 / K^{\infty} = G^0 / G^{\infty}.$$

Parameters of standard model: $\chi = 4$, $\gamma = 1000, 100, 1$ and 0.1.

In Figs. 31.10, 31.11, 31.12 and 31.13, the Rayleigh wave is demonstrated. We can observe the decrease of Rayleigh wave amplitude depending on viscosity.

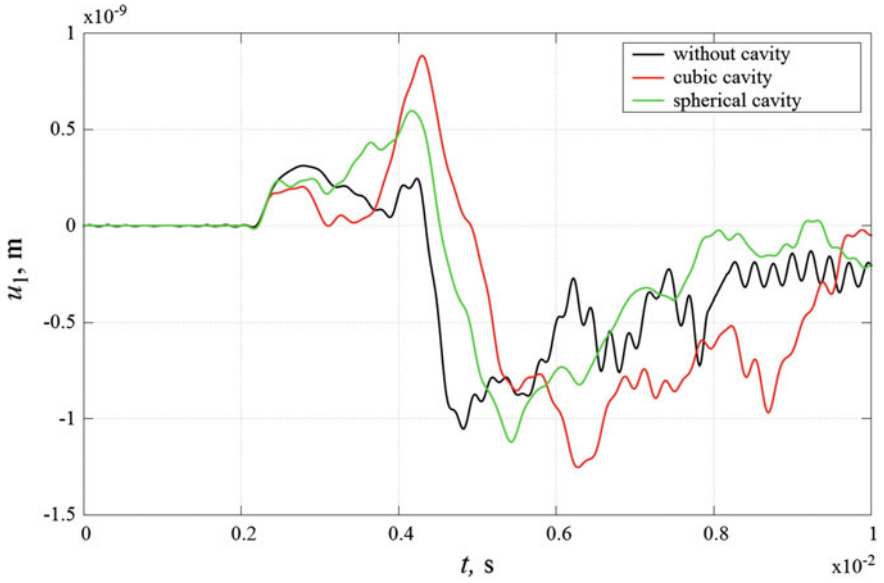

Fig. 31.8 Comparison of displacements u_1 in case of different cavity forms

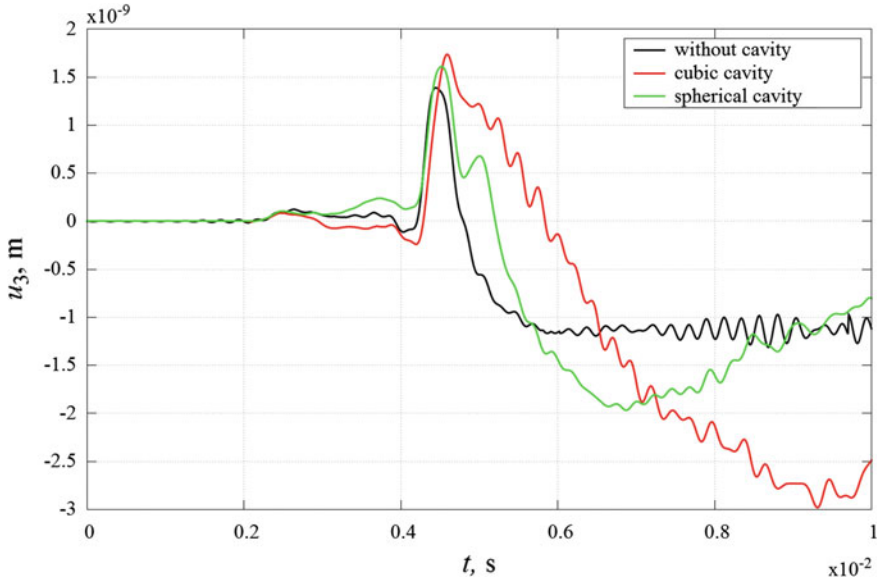

Fig. 31.9 Comparison of displacements u_3 in case of different cavity forms

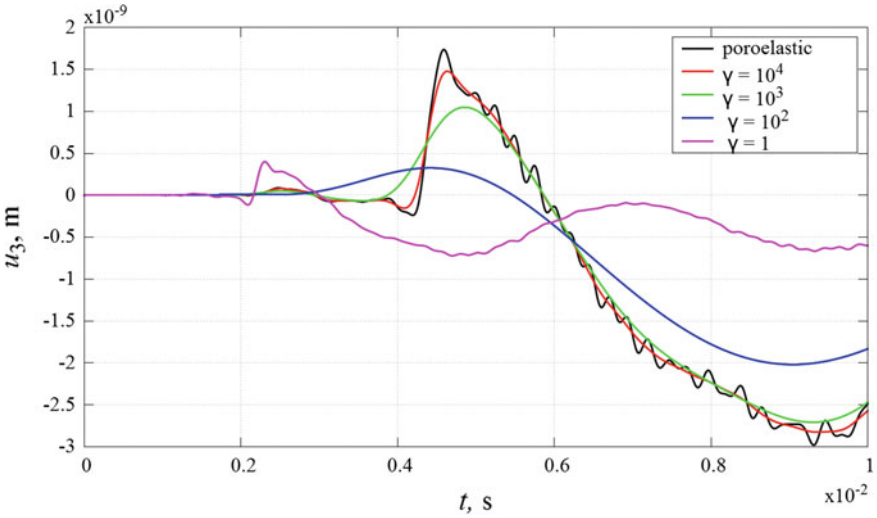

Fig. 31.10 Displacements u_1 in case of cubic cavity for various viscosity parameters

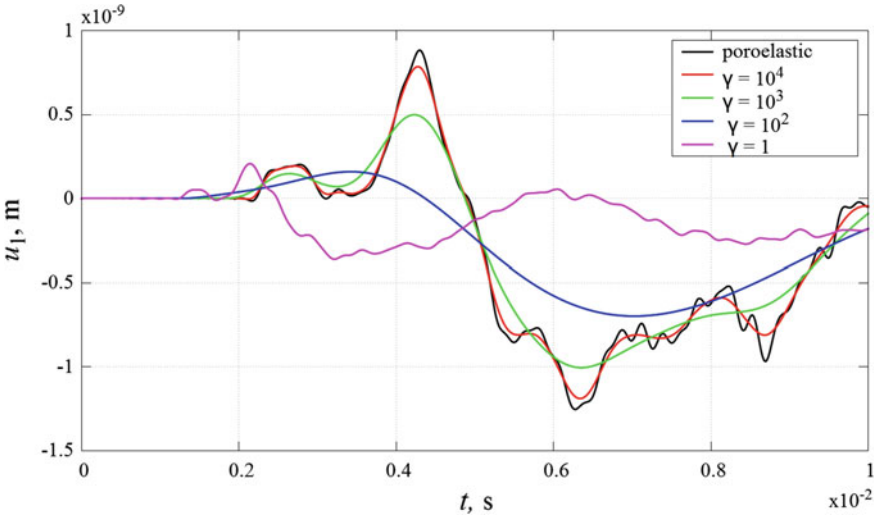

Fig. 31.11 Vertical displacements u_3 in case of cubic cavity for various viscosity parameters

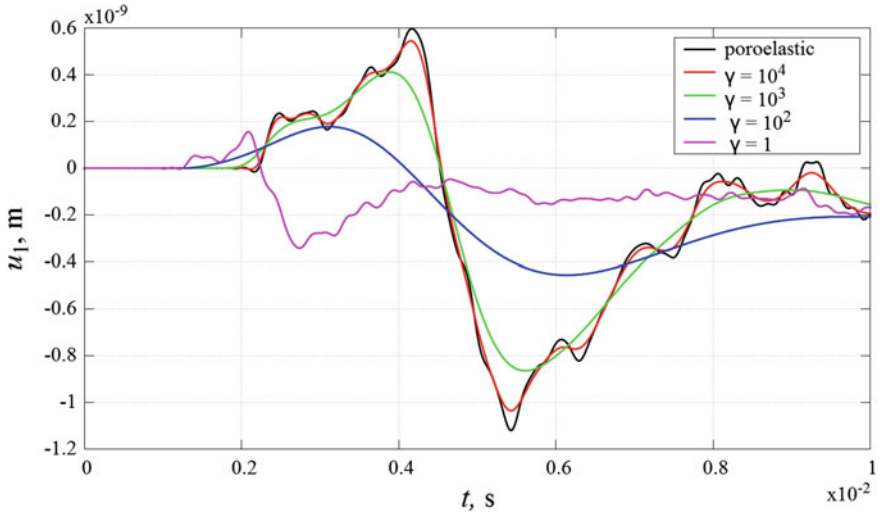

Fig. 31.12 Displacements u_1 in case of spherical cavity with various viscosity parameters

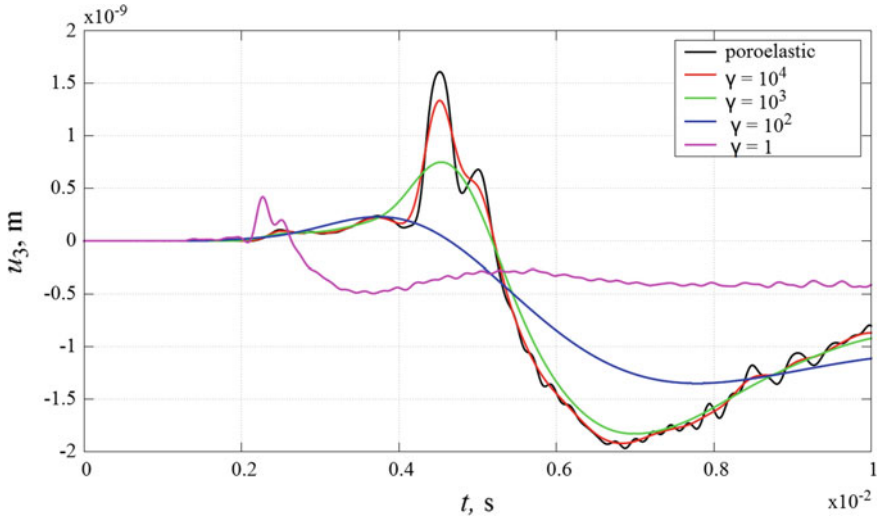

Fig. 31.13 Vertical displacements u_3 in case of spherical cavity for various viscosity parameters

31.7 Conclusion

Theory of poroviscoelasticity based on Biot's poroelastic model is performed. Boundary integral equation s method and boundary element method are applied in order to solve three-dimensional boundary-value problems. The development of

known numerical technique for solving such problems is presented. A Laplace domain BEM approach for the transient analysis of the three-dimensional linear poroviscoelastic solids based on the correspondence principle is applied. The standard viscoelastic solid model is employed to take into the account viscoelastic behavior of porous media.

To introduce BE-discretization, we consider the regularized boundary-integral equation. Mixed boundary element discretization is introduced to obtain discrete analogues. We used the modified Durbin's method to invert solution to the time domain is proved to be an accurate and efficient method particularly well suited for the dynamic problems of the linear poroviscoelasticity.

Problem of a vertical Heaviside-type load acting on a poroelastic halfspace with a cavity is considered. Comparison of displacements in case of different cavity forms is present. Viscous parameter influence is studied. An influence of viscoelastic parameter on Rayleigh wave is demonstrated.

Acknowledgements The work was financially supported by Russian Foundation for Basic Research (RFBR), grant No. 18-08-00895.

References

1. P.J. Phillips, M.F. Wheeler, Comput. Geosci. **11**, 131 (2007)
2. P.J. Phillips, M.F. Wheeler, Comput. Geosci. **11**, 145 (2007)
3. P. Causin, G. Guidoboni, A. Harris, D. Prada, R. Sacco, S. Terragni, Math. Biosci. **257**, 33 (2014)
4. D. Chapelle, J.-F. Gerbeau, J. Sainte-Marie, I.E. Vignon-Clementel, Comput. Mech. **46**, 91 (2010)
5. J. Frenkel, J. Appl. Phys. **8**, 230 (1944)
6. M.A. Biot, J. Appl. Phys. **12**, 155 (1941)
7. M.A. Biot, J. Appl. Phys. **26**, 182 (1955)
8. M.A. Biot, J. Appl. Phys. **27**(5), 459 (1956)
9. A.W.El Rabaa, in *Proceedings of ISRM International Symposium* 1017 (1989)
10. A.W. El Rabaa, Meadows D.L. *Proceedings of SPE 56th California Regional Meeting*, 259 (1986)
11. F.K. Mody, A.H. Hale, J. Pet. Technol. **45**(11), 1093 (1993)
12. S. Paul, Pure Appl. Geophysics **114**(4), 605 (1976)
13. G. Gazetas, E. Petrakis, *Proceedings of International Conference on Recent Advances in Geotechnical Earthquake Engineering and Soil Dynamics*, 381 (1981)
14. B. Jin, H. Liu, Soil Dyn. Earthquake Eng. J. **19**(4), 269 (2000)
15. B. Jin, H. Liu, Soil Dyn. Earthquake Eng. J. **19**(7), 469 (2000)
16. D. Nardini, C.A. Brebbia, in *Boundary Element Methods in Engineering*, ed. by C.A. Brebbia (Springer, Berlin, 1982)
17. W. J. Mansur, in *A Time-Stepping Technique to Solve Wave Propagation Problems Using the Boundary Element Method*. Ph.D. thesis, University of Southampton (1983)
18. T.A. Cruze, F.J. Rizzo, J. Math. Anal. Appl. **22**(1), 244 (1968)
19. V.A. Babeshko, Proc. USSR Acad. Sci. **284**, 73 (1985)
20. F. Durbin, Comput. J. **17**, 371 (1974)
21. X. Zhao, Int. J. Solids Struct. **41**, 3653 (2004)

22. M. Schanz, *Wave Propagation in Viscoelastic and Poroelastic Continua* (Springer, Berlin, 2001)
23. M. Schanz, Appl. Mech. Rev. **62**, 030803 (2009)
24. B. Gatmiri, M. Kamalian, Int. J. Geomech. **2**(4), 381 (2002)
25. S. Seyerafian, B. Gatmiri, A. Nourzad. Int. J. Comput. Methods Eng. Sci. **15**(2), 115 (2006)
26. B. Gatmiri, H. Eslami, Int. J. Geomech. **7**(5), 371 (2007)
27. L.A. Igumnov, A.N. Petrov, I.V. Vorobtsov, IOP Conf. Ser. Earth Environ. Sci. **87**(8), 082022 (2017)
28. L. Igumnov, A. Ipatov, A. Belov, A. Petrov, EPJ Web Conf. **94**, 04026 (2015)
29. W. Ehlers, B. Markert, Granular Matter **2**(3), 153 (2000)
30. A.F. Mak, J. Biomech. Eng. **108**, 123 (1986)
31. A.A. Ipatov, L.A. Igumnov, A.A. Belov, in *Advanced Materials—Techniques, Physics, Mechanics and Applications*, ed. by I.A. Parinov, S.-H. Chang, M.A. Jani. Springer Proceedings in Physics, vol. 193 (Springer Cham, Heidelberg, 2017), 331
32. F. Wuttke, P. Dineva, I.-K. Fontara, J. Theor. Appl. Mechanics. **47**(2), 34 (2017)

Chapter 32
Block Element with a Circular Boundary

Evgeniya Kirillova and Pavel Syromyatnikov

Abstract The block element method (Babeshko in Ecol Bull Res Centers Black Sea Econ Coop (BSEC) 2:13, 2014, [1]), which was elaborated by V. A. Babeshko and developed by his disciples, makes it possible to solve boundary-value problems stated for arbitrary convex domains and described in terms of arbitrary linear systems of differential equations in finite-order partial derivatives. The boundary-value problems are assumed to be properly stated. The domains can be bounded, semi-bounded and unbounded. Moreover, the method can be applied to the finite aggregate of domains, which interact over shared boundaries. According to the block element method, the boundary-value problem is set in the topological space and reduced to the system of functional equations using external analysis tools. From the pseudo-differential equations obtained due to differential factorization and automorphism, integral equations are extracted, which correspond to certain boundary conditions. A large number of variations of the block element method have been developed so far for the three-dimensional setting of boundary-value problems for various mathematical physics equations. The method is highly versatile, however, it requires the knowledge of topology, differential geometry, multidimensional complex analysis, external analysis, i.e. the disciplines, which are normally not included in the standard mathematics curricular at the university level. To increase the comprehension of the method, it is necessary for scientific and methodological purposes to study in detail how comparatively simple problems are solved by this method. The research provides a detailed algorithm of the block element for the model boundary-value problem, which is described by the Bessel equation for the circular domain.

E. Kirillova (✉)
RheinMain University of Applied Sciences, Wiesbaden, Germany
e-mail: evgenia.kirillova@hs-rm.de

P. Syromyatnikov
Southern Research Center of Russian Academy of Sciences, Rostov-on-Don, Russia

I. A. Parinov et al. (eds.), *Advanced Materials*, Springer Proceedings in Physics 224, https://doi.org/10.1007/978-3-030-19894-7_32

32.1 Statement and Analytical Solution of the Boundary-Value Problem

Let us consider for the circular domain Ω with the radius $r_0 > 0$, the equation:

$$\frac{\partial^2 \varphi}{\partial x_1^2} + \frac{\partial^2 \varphi}{\partial x_2^2} - k^2 \varphi = 0, \quad (x_1, x_2) \in \Omega. \tag{32.1}$$

Hereinafter, we will consider the boundary-value solutions:

$$\varphi|_{r=r_0} = f_1, \frac{\partial \varphi}{\partial r}\bigg|_{r=r_0} = f_2, \tag{32.2}$$

which depend only on the radius $r = \sqrt{x_1^2 + x_2^2}$. Equation (32.1) for the function, which depends only on the radius r, can be written as follows:

$$\frac{\partial^2 \varphi}{\partial \mathrm{r}^2} + \frac{1}{r}\frac{\partial \varphi}{\partial \mathrm{r}} - k^2 \varphi = 0. \tag{32.3}$$

The general solution of the problem (32.3), (32.2) is written in terms of modified Bessel functions I_0, K_0 [2] as

$$\varphi(r) = C_1 I_0(kr) + C_2 K_0(kr). \tag{32.4}$$

Considering the known properties of functions I_0, K_0 [2]:

$$I_0'(z) = I_1(z), I_0(z) = J_0(iz), I_1(z) = -iJ_1(iz),$$
$$K_0'(z) = -K_1(z), K_0(z) = \frac{i\pi}{2} H_0^{(1)}(iz), K_1(z) = \frac{-\pi}{2} H_1^{(1)}(iz),$$

with respect to C_1, C_2, we obtain the equation system:

$$C_1 I_0(kr_0) + C_2 K_0(kr_0) = f_1, C_1 k I_1(kr_0) - C_2 k K_1(kr_0) = f_2,$$

whence it follows that

$$C_1 = \frac{-f_1 k K_1(kr_0) + f_2 K_0(kr_0)}{\Delta}, \quad C_2 = \frac{-f_1 k I_1(kr_0) + f_2 I_0(kr_0)}{\Delta},$$
$$\Delta = \Delta(k, r_0) = -k(I_0(kr_0) K_1(kr_0) + K_0(kr_0) I_1(kr_0)).$$

It is easily to show that

$$\Delta = k\left(\frac{\pi}{2}\right)\left(J_0(ikr_0)H_1^{(1)}(ikr_0) - J_1(ikr_0)H_1^{(1)}(ikr_0)\right) \equiv -\frac{1}{r_0}.$$

In this case, we obtain:

$$C_1 = r_0\left(\frac{i\pi}{2}\right)\left(f_1 ikH_1^{(1)}(ikr_0) + f_2 H_0^{(1)}(ikr_0)\right), C_2 = r_0(-f_1 ikJ_1(ikr_0) - f_2 J_0(ikr_0)).$$

The general representation of solving a boundary-value problem (32.3), (32.2) takes the form:

$$\begin{aligned}\varphi(r) = J_0(ikr)\left(\frac{i\pi r_0}{2}\right)\left(f_1 ikH_1^{(1)}(ikr_0) + f_2 H_0^{(1)}(ikr_0)\right)\\ + H_0^{(1)}(ikr)\left(\frac{i\pi r_0}{2}\right)(-f_1 ikJ_1(ikr_0) - f_2 J_0(ikr_0)).\end{aligned} \tag{32.5}$$

Solution (32.5) consists of two summands:

$$\varphi(r) = \varphi^{(1)}(r) + \varphi^{(2)}(r).$$

Solution $\varphi^{(1)}$ is bounded by

$$\varphi^{(1)}(r) = C_1 J_0(ikr) = J_0(ikr)\left(\frac{i\pi r_0}{2}\right)\left(f_1 ikH_1^{(1)}(ikr_0) + f_2 H_0^{(1)}(ikr_0)\right). \tag{32.6}$$

Solution $\varphi^{(2)}$ is not bounded, because it has a singularity at zero due to properties of Hankel function:

$$\varphi^{(2)}(r) = C_2 H_0^{(1)}(ikr) = H_0^{(1)}(ikr)\left(\frac{i\pi r_0}{2}\right)(-f_1 ikJ_1(ikr_0) - f_2 J_0(ikr_0)). \tag{32.7}$$

Expression (32.5) provides a general representation of the solution for an internal problem with boundary conditions (32.2), as well as for the corresponding external problem at $r \geq r_0$, which is stated below.

Let us additionally restrict the solution of the boundary-value problem (32.3), (32.2). For the internal problem, this restriction leads to $\varphi^{(2)}(r) \equiv 0 \leftrightarrow C_2 \equiv 0$, which is equal to the condition

$$\frac{f_1}{f_2} = \frac{i}{k}\frac{J_0(ikr_0)}{J_1(ikr_0)}. \tag{32.8}$$

Whereas $\lim_{kr_0\to\infty}\frac{J_0(ikr_0)}{J_1(ikr_0)}=-i$, then, at $k>>1$

$$\frac{f_1}{f_2}\approx\frac{1}{k},\quad 0\le r\le r_0, \tag{32.9}$$

which is equivalent to the boundary conditions:

$$\varphi|_{r=r_0}=f,\frac{\partial\varphi}{\partial r}\Big|_{r=r_0}=kf,\quad f=\text{const}\neq 0. \tag{32.10}$$

Similarly, in order to restrict the external problem, the condition $\varphi^{(1)}(r)\equiv 0\leftrightarrow C_1\equiv 0$ should be satisfied, then:

$$\frac{f_1}{f_2}=\frac{i}{k}\frac{H_0^{(1)}(ikr_0)}{H_1^{(1)}(ikr_0)}. \tag{32.11}$$

Taking into account that

$$\lim_{kr_0\to\infty}\frac{H_0^{(1)}(ikr_0)}{H_1^{(1)}(ikr_0)}=i, \tag{32.12}$$

then, at $k>>1$

$$\frac{f_1}{f_2}\approx-\frac{1}{k},\quad 0<r_0\le r, \tag{32.13}$$

Therefore, at $k>>1$, it is possible to use the expressions (32.10) as approximated boundary conditions for the internal problem, and relations:

$$\varphi|_{r=r_0}=f,\frac{\partial\varphi}{\partial r}\Big|_{r=R_0}=-kf,\quad 0<r_0\le r, \tag{32.14}$$

for the external problem. The restriction requirement results in the fact that the values f_1,f_2 cannot be arbitrary and must satisfy (32.8) or (32.11). At large k, exact terms (32.8) and (32.11) can be replaced by approximated conditions (32.10) and (32.14), respectively.

32.2 Block Element with a Circular Boundary

According to the general algorithm of the block element method [1] in the case of a two-dimensional domain Ω, we introduce the double forward and inverse Fourier transforms:

$$\begin{aligned}\Phi(\alpha_1,\alpha_2) &= \iint\limits_{\Omega} \varphi(x_1,x_2)\ \exp(i(\alpha_1 x_1+\alpha_2 x_2))\mathrm{d}x_1\mathrm{d}x_2\\ \varphi(x_1,x_2) &= \frac{1}{4\pi^2}\int\limits_{-\infty}^{+\infty}\int\limits_{-\infty}^{+\infty}\Phi(\alpha_1,\alpha_2)\exp(-i(\alpha_1 x_1+\alpha_2 x_2))\mathrm{d}x_1\mathrm{d}x_2\end{aligned} \tag{32.15}$$

Let us apply the forward transform (32.15) to the (32.1) and the Stokes formula [3] to the surface integral, and obtain the functional equation:

$$-\left(\alpha_1^2+\alpha_2^2+k^2\right)\Phi(\alpha) = \iint\limits_{\Omega}\mathrm{d}\omega = \int\limits_{\partial\Omega}\omega, \{x_1,x_2\}\in\partial\Omega. \tag{32.16}$$

Here $\partial\Omega$ is the boundary of the domain Ω, ω is the external differential form. As a result, we obtain:

$$\left(\alpha_1^2+\alpha_2^2+k^2\right)\Phi(\alpha_1,\alpha_2) = \int\limits_{\partial\Omega}\left\{\left[\frac{\partial\varphi}{\partial x_2}-i\alpha_2\varphi\right]\mathrm{e}^{(i\alpha_1 x_1+i\alpha_2 x_2)}\mathrm{d}x_1+\left[\frac{\partial\varphi}{\partial x_1}-i\alpha_1\varphi\right]\mathrm{e}^{(i\alpha_1 x_1+i\alpha_2 x_2)}\mathrm{d}x_2\right\}. \tag{32.17}$$

Let us introduce the following coordinates:

$$\begin{aligned}&\xi_1 = r_0\cos\psi,\quad \xi_2 = r_0\sin\psi,\quad r_0=\sqrt{\xi_1^2+\xi_2^2},\quad \psi = arctg(\xi_2/\xi_1),\\ &x_1 = r\cos\theta,\quad x_2 = r\sin\theta,\quad r=\sqrt{x_1^2+x_2^2},\quad \theta = arctg(x_2/x_1),\\ &\alpha_1 = u\cos\gamma,\quad \alpha_2 = u\sin\gamma,\quad u=\sqrt{\alpha_1^2+\alpha_2^2},\quad \gamma = arctg(\alpha_2/\alpha_1).\end{aligned} \tag{32.18}$$

After some uncomplicated transformations, we obtain

$$\begin{aligned}\left(u^2+k^2\right)\Phi(u,\gamma) = &\int\limits_{\partial\Omega}\exp(iur_0\cos(\psi-\gamma))\times\\ &\times\left(\frac{\partial\varphi}{\partial r}r_0\mathrm{d}\psi-\frac{1}{r_0}\frac{\partial\varphi}{\partial\psi}\mathrm{d}r-iur_0\cos(\gamma-\psi)\varphi\mathrm{d}\psi+iu\sin(\gamma-\psi)\varphi\mathrm{d}r\right).\end{aligned} \tag{32.19}$$

Integrals over dr in (32.19) are equal to zero, while when the circle d$r = 0$, only integrals remain over dψ. As a result, we obtain:

$$\begin{aligned}&\left(u^2+k^2\right)\Phi(u,\gamma)\\&=\int\limits_{\partial\Omega}\exp(ir_0u\cos(\gamma-\psi))\left[r_0\frac{\partial\varphi(r_0,\psi)}{\partial r}-iur_0\cos(\gamma-\psi)\varphi(r_0,\psi)\right]\mathrm{d}\psi.\end{aligned}\tag{32.20}$$

Let us write the formula (32.20) as follows:

$$\Phi(\alpha_1,\alpha_2)=\int\limits_{\partial\Omega}\frac{\exp(i(\alpha_1\xi_1+\alpha_2\xi_2))}{(\alpha_1^2+\alpha_2^2+k^2)}\left[r_0\frac{\partial\varphi(r_0,\psi)}{\partial r}-iur_0\cos(\gamma-\psi)\varphi(r_0,\psi)\right]\mathrm{d}\xi_1\mathrm{d}\xi_2.\tag{32.21}$$

Next, let us apply the inverse Fourier transform (32.15) to the expression (32.21) and obtain

$$\begin{aligned}\varphi(r,\theta)&=\frac{1}{4\pi^2}\int\limits_{-\infty}^{\infty}\int\limits_{-\infty}^{\infty}\int\limits_{\partial\Omega}\frac{\omega}{(u^2+k^2)}\exp(-i(\alpha_1x_1+\alpha_2x_2))\mathrm{d}\xi_1\mathrm{d}\xi_2\mathrm{d}\alpha_1\mathrm{d}\alpha_2\\&=\frac{1}{4\pi^2}\int\limits_{-\infty}^{\infty}\int\limits_{-\infty}^{\infty}\int\limits_{\partial\Omega}\frac{\exp(-i(\alpha_1(x_1-\xi_1)+\alpha_2(x_2-\xi_2)))}{(u^2+k^2)}\\&\quad\times\left[r_0\frac{\partial\varphi(r_0,\psi)}{\partial r}-iur_0\cos(\gamma-\psi)\varphi(r_0,\psi)\right]\mathrm{d}\xi_1\mathrm{d}\xi_2\mathrm{d}\alpha_1\mathrm{d}\alpha_2.\end{aligned}\tag{32.22}$$

The transformations of the integral (32.22), which are described below in Appendix, result in

$$\varphi(r)=r_0\int\limits_0^{\infty}\frac{J_0(ur)u}{(u^2+k^2)}(J_0(ur_0)f_2+J_1(ur_0)uf_1)\mathrm{d}u.\tag{32.23}$$

The expression (32.23) is an integral representation of the restricted solution of the problem (32.3), (32.2), which can be used for calculations, when f_j are known. Using the contour unfolding operation [4], we can calculate this integral accurately applying the residues theory. Let us write the integral (32.23) as follows:

$$\varphi(r) = \int_0^\infty (J_0(ur_0)F_0(u) + J_1(ur_0)F_1(u))u\mathrm{d}u$$
$$= \int_0^\infty J_0(ur_0)uF_0(u)\mathrm{d}u + \int_0^\infty J_1(ur_0)uF_1(u)\mathrm{d}u,$$

where $F_0(u) = f_2\frac{J_0(ur)r_0}{(u^2+k^2)}, F_1(u) = f_1\frac{J_1(ur)ur_0}{(u^2+k^2)}$. Functions F_0, F_1 have the property: $F_n(-u) = (-1)^n F_n(u), n = 0, 1$. When we put down the Bessel functions $J_0(z), J_1(z)$ as a sum of the Hankel functions $J_n(z) = \frac{1}{2}\left(H_n^{(1)}(z) + H_n^{(2)}(z)\right)$ and apply the contour unfolding operation, we obtain:

$$\varphi(r) = \frac{1}{2}\int_{-\infty}^\infty \frac{H_0^{(1)}(ur_0)}{(u^2+k^2)}uJ_0(ur)f_2r_0\mathrm{d}u + \frac{1}{2}\int_{-\infty}^\infty \frac{H_1^{(1)}(ur_0)}{(u^2+k^2)}uJ_0(ur)uf_1r_0\mathrm{d}u. \quad (32.24)$$

The exponential decrease of the Hankel functions $H_j^{(1)}$ makes it possible to close the contour of integration upwards in the upper half-plane and obtain the integral value (32.24) through the residue in the pole $u = ik$ as

$$\varphi(r) = J_0(ikR)\left(\frac{i\pi r_0}{2}\right)\left(f_1 ikH_1^{(1)}(ikr_0) + f_2H_0^{(1)}(ikr_0)\right) = \varphi^{(1)}(r), \quad 0 \le r \le r_0 \quad (32.25)$$

It is obvious that the latter expression agrees closely with the bounded solution of the inner problem (32.6). Let us show that at $0 < r_0 < r$, the integral (32.23) is equal to zero. In fact, it is possible to put down the function $J_0(ur)$ as a sum of the Hankel functions and turn the contour as shown above. By closing the contour at $0 < r_0 < r$ in the upper half-plane and by calculating the integral through residue in the pole $u = ik$, we obtain:

$$\varphi(r) = \frac{r_0}{2}\int_{-\infty}^{+\infty} \frac{H_0^{(1)}(ur)u}{(u^2+k^2)}(J_0(ur_0)f_2 + J_1(ur_0)uf_1)\mathrm{d}u =$$
$$= H_0^{(1)}(ikr)\left(\frac{i\pi r_0}{2}\right)\left(-f_1 ikJ_1(ikr_0) - f_2J_0(ikr_0)\right). \quad (32.26)$$

The factor at the function $H_0^{(1)}$ in (32.26) is equal to zero according to the condition (32.8). In the case of an approximate solution (32.9), the right-hand side of (32.26) will be also equal to zero, approximately. Since $H_0^{(1)}(ikr)$ decreases exponentially with the growth of r, then $\varphi(r) \approx \exp(-k(r - r_0))$ at large r. Moreover, it is obvious that integral (32.26) describes the restricted solution

(32.7) of the corresponding external problem, where f_1, f_2 and k are bounded by the relations (32.11) or (32.13). The estimations for the internal problem, which are shown below, are identical with the estimations for the external problem, therefore, we do not consider them separately.

The integrals (32.23), (32.24) represent the block element for the boundary-value problem (32.3), (32.2). After the values f_1, f_2 are found accurately or approximately, the integral (32.23) can be calculated numerically with a high accuracy, e.g. by means of the integrating algorithms of strongly oscillating functions [5]. In this case, the integral (32.23) using the contour unfolding procedure, which is described above, can be calculated accurately using the theory of residues.

32.3 Approximate Solutions

In the case under consideration, we obtain boundary values f_1, f_2 by applying an analytical solution (32.8), which is not, understandably, always possible. When the second value is given, the block-element method makes is possible to find (accurately or approximately) one of the boundary values $\left(\varphi \text{ or } \frac{\partial \varphi}{\partial r}\right)$ from the solutions of corresponding equations, which are described further.

Let us decompose the unity and introduce local coordinate systems α^μ, x^μ [6]. As a result, the integrals over $\mathrm{d}x_2$ will retreat, and only integrals over $\mathrm{d}x_1$ will remain in the integral (32.17). We then obtain

$$\int\limits_{\partial\Omega} \left[\frac{\partial \varphi}{\partial x_2} - i\alpha_2 \varphi\right] \mathrm{e}^{(i\alpha_1 x_1 + i\alpha_2 x_2)} \mathrm{d}x_1 = \sum_\mu \varepsilon_\mu \left[\frac{\partial \varphi_\mu}{\partial x_2^\mu} - i\alpha_2^\mu \varphi_\mu\right] \exp\left(i\alpha_1^\mu x_1^\mu + i\alpha_2^\mu x_2^\mu\right) \Delta x_1^\mu$$

The characteristic equation in Fourier terms takes the form $(\alpha_1^2 + \alpha_2^2 + k^2) = 0$. In any new coordinates, we obtain $\left(\alpha_1^\mu\right)^2 + \left(\alpha_2^\mu\right)^2 + k^2 = 0$. Let us indicate the roots of the characteristic polynomial $\alpha_{2\pm}^\mu$, where «+» stands for the upper half-plane and «−» stands for the lower one. Then

$$\alpha_{2+}^\mu = +i\sqrt{\left(\alpha_1^\mu\right)^2 + k^2}, \quad \alpha_{2-}^\mu = -i\sqrt{\left(\alpha_1^\mu\right)^2 + k^2}.$$

The integral equation set to determine the unknown quantities $\frac{\partial \varphi_\mu}{\partial x_2^\mu}, \varphi_\mu$, which are constant in any coordinate system, can be written as follows:

$$\int\limits_{-\varepsilon}^{\varepsilon} \left(\frac{\partial \varphi_\mu}{\partial x_2^\mu} - i\alpha_{2-}^\mu \varphi_\mu\right) \exp\left(i\alpha_1^\mu x_1^\mu\right) \mathrm{d}x_1^\mu = 0$$

When $\varphi_\mu = f$, the degenerate solution of the integral equation can be written as

$$\frac{\partial \varphi_\mu}{\partial x_2^\mu} - \sqrt{\left(\alpha_1^\mu\right)^2 + k^2} \cdot f = 0, \quad \alpha_1^\mu = 0.$$

It follows that

$$\frac{\partial \varphi_\mu}{\partial x_2^\mu} = f\sqrt{k^2} = f \cdot k. \tag{32.27}$$

Thus, we obtain approximate solutions of the function $\varphi_\mu = f$ and the derivative $\frac{\partial \varphi_\mu}{\partial x_2^\mu} = kf$. It is possible to obtain a more accurate solution of the integral equation by using the Fourier transform, i.e.

$$\int_{-\varepsilon}^{\varepsilon} \frac{\partial \varphi_\mu}{\partial x_2^\mu} \exp\left(i\alpha_1^\mu x_1^\mu\right) \mathrm{d}x_1^\mu = i\alpha_{2-}^\mu \cdot f \cdot \frac{\mathrm{e}^{i\alpha_1^\mu \varepsilon} - \mathrm{e}^{-i\alpha_1^\mu \varepsilon}}{i\alpha_1^\mu}.$$

We therefore obtain approximately:

$$\frac{\partial \varphi_\mu}{\partial x_2^\mu} = \frac{1}{2\pi} \int_{-\infty}^{+\infty} i\alpha_{2-}^\mu \cdot f \cdot \frac{\mathrm{e}^{i\alpha_1^\mu \varepsilon} - \mathrm{e}^{-i\alpha_1^\mu \varepsilon}}{i\alpha_1^\mu} \exp\left(-i\alpha_1^\mu x_1^\mu\right) \mathrm{d}\alpha_1^\mu. \tag{32.28}$$

In Table 32.1, the solutions of (32.8) $f_2^{(1)}$, approximated solution of the integral equation (32.28) $f_2^{(2)}$, and the degenerate solution (32.27) $f_2^{(3)}$ are compared depending on $1 \le k \le 10$ at $r_0 = 1, f_1 = 1$. It should be noted that solutions of (32.27) and (32.28) are obtained without using analytical solution.

Table 32.1 Values $f_2^{(j)}(k)$ at $1 \le k \le 10$

k	Solution of (32.8) $f_2^{(1)}$	Solution of (32.28) $f_2^{(2)}$	Solution of (32.27) $f_2^{(3)}$
1	0.4463900	0.7176216	1.0
2	1.395549	1.689416	2.0
3	2.429956	2.686028	3.0
4	3.454090	3.685591	4.0
5	4.466916	4.685533	5.0
6	5.474156	5.685527	6.0
7	6.478725	6.685524	7.0
8	7.481884	7.685526	8.0
9	8.484209	8.685524	9.0
10	9.485998	9.685521	10.0

Figure 32.1a shows an example of the bounded solution of the internal boundary-value problem (32.3), (32.2): $\varphi^{(1)}(r,k)$ depending on r and k, $(f_1 = 1, r_0 = 1)$. The difference between the exact solution (32.6) and the numerical calculation of the integral (32.23) are unobservable within the scale of the picture.

Let us show that the integral representation (32.23) is numerically stable. Let f_1 be set exactly, while f_2 is set approximately and $\tilde{f}_2 = f_2 - \varepsilon_2$, where ε_2 is the absolute error of the solution f_2. Then, the absolute error is as follows:

$$\varepsilon(r,k) = \varphi(r) - \tilde{\varphi}(r) = \int_0^\infty \frac{J_0(ur)u}{(u^2+k^2)}\varepsilon_2 J_0(ur_0)\mathrm{d}u = \varepsilon_2 J_0(ikr)\left(\frac{i\pi r_0}{2}\right)H_0^{(1)}(ikr_0).$$

At large $k >> 1$

$$\varepsilon(r,k) \approx \varepsilon_2 \exp[-k(r_0 - r)], \quad 0 < r < r_0. \tag{32.29}$$

The relative error δ

$$\delta(k) = \left(1 - \frac{\tilde{\varphi}(r)}{\varphi(r)}\right) = \frac{H_0^{(1)}(ikr_0)\varepsilon_2}{\left(f_1 ikH_1^{(1)}(ikr_0) + f_2 H_0^{(1)}(ikr_0)\right)} = \frac{\varepsilon_2}{f_1 ik\frac{H_1^{(1)}(ikr_0)}{H_0^{(1)}(ikr_0)} + f_2}.$$

Since the properties of (32.27), (32.12) we obtain at $k >> 1$:

$$\delta(k) \approx \frac{\varepsilon_2}{f_1 k + f_1 k} \approx \frac{\varepsilon_2}{2fk}. \tag{32.30}$$

The obtained estimations of the absolute and relative errors (32.29), (32.30) mean the stability of the solution (32.23) at non-zero errors of derivative f_2, which was obtained by formula (32.28) or (32.27). These estimations are obtained by assuming that the integral (32.23) can be calculated accurately. In practice, when we calculate the integral (32.23) numerically, the mean absolute and relative errors will be unavoidably higher, since any computing algorithm leads to additional errors. Let us introduce relative errors $\delta^{(n)}$ as

$$\delta^{(n)}(k) = \frac{1}{r_0}\int_0^{r_0} |1 - \varphi_n(r,k)/\varphi(r,k)|\mathrm{d}r. \tag{32.31}$$

Here, φ_1 corresponds to the accurate solution (32.6) with a mean absolute error $\varepsilon_2^{(1)} \approx 10^{-6}$, φ_2 corresponds to the approximate solution of the integral equation (32.28) with $\varepsilon_2^{(2)} \approx 0.23$, φ_3 corresponds to the degenerate solution of the integral equation (32.27) with $\varepsilon_2^{(3)} \approx 0.54$.

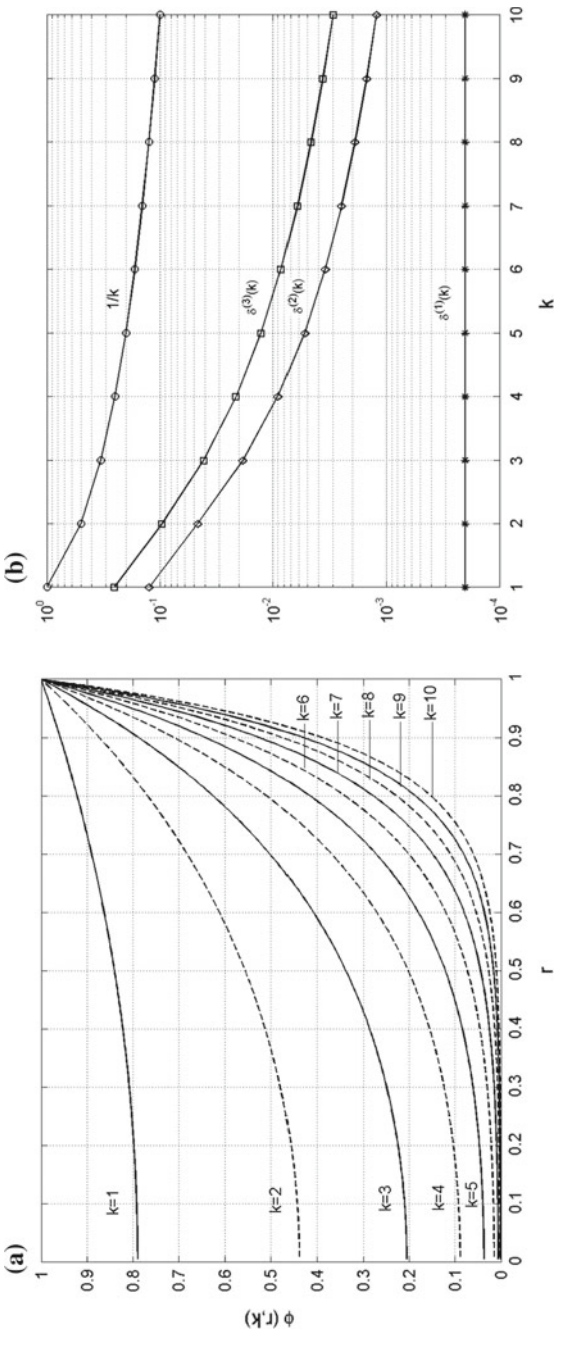

Fig. 32.1 **a** Solutions $\varphi^{(1)}(k,r), (f_1 = 1, r_0 = 1)$; **b** average relative errors $\delta^{(n)}(k)$ from (32.31)

In Fig. 32.1b, the values $\delta^{(n)}$ are shown on the logarithmical scale in comparison with the value $1/k$. As is obvious, at small $k \leq 10$ the average relative errors (32.31) decrease with the growth of k even more rapidly than the asymptotic estimation (32.30).

32.4 Conclusion

The work describes the algorithm for solving a model boundary-value problem, which corresponds to the Bessel equation for the circular domain, using the block element method. The boundary-value problem has a simple analytical solution, which makes it possible to compare the accurate and approximate solution, which is obtained using the block element method. The solution is represented as an improper integral of the Bessel functions, which can be easily calculated in quadratures and can be calculated exactly using the residues theory. The unknown coefficients of the exterior form can be found by solving the integral equation. The results of the numerical solution of the integral equation are demonstrated in the work, as well as practical and theoretical estimations of absolute and ratio solution errors obtained using the block element method and their solution stability.

Acknowledgements The work was carried out within the framework of the State task for Southern Scientific Center of the Russian Academy of Sciences, State Registration No. 01201354241, and has been supported by RheinMain University of Applied Sciences.

Appendix

In the appendix, transformations of a multidimensional integral:

$$\varphi(r,\theta) = \frac{1}{4\pi^2} \int\limits_{-\infty}^{\infty} \int\limits_{-\infty}^{\infty} \int\limits_{\partial\Omega} \frac{\exp(-i(\alpha_1(x_1-\xi_1)+\alpha_2(x_2-\xi_2)))}{(u^2+k^2)} \times \left[r_0 \frac{\partial\varphi(r_0,\psi)}{\partial r} - iur_0\cos(\gamma-\psi)\varphi(r_0,\psi) \right] \mathrm{d}\xi_1 \mathrm{d}\xi_2 \mathrm{d}\alpha_1 \mathrm{d}\alpha_2, \tag{32.32}$$

into the integral of a single variable are present. Despite the awkwardness of the stated expressions, the transformations are in principle simple. The relations:

$$\exp(-iz\cos\tau) = \sum_{k=-\infty}^{+\infty} \exp\left(-ik\left(-\tau - \frac{\pi}{2}\right)\right) J_{-k}(-z)$$
$$= \sum_{k=-\infty}^{+\infty} \exp\left(ik\left(-\tau - \frac{\pi}{2}\right)\right) J_k(z) = \sum_{k=-\infty}^{+\infty} \exp\left(ik\left(\tau - \frac{\pi}{2}\right)\right) J_k(z), \tag{32.33}$$

are used further. When we transform the exponent in formula 32.32), we obtain a product of series, which can be written down as a two-fold series:

$$\exp(-i[\alpha_1(x_1 - \xi_1) + \alpha_2(x_2 - \xi_2)]) = \exp(-iur\cos(\gamma - \theta))\exp(iur_0\cos(\gamma - \psi))$$
$$= \sum_{m=-\infty}^{+\infty} \exp(im(\theta - \gamma - \frac{\pi}{2}))J_m(ur) \sum_{n=-\infty}^{+\infty} \exp(in(\psi - \gamma + \frac{\pi}{2}))J_n(ur_0)$$
$$= \sum_{m=-\infty}^{+\infty} \sum_{n=-\infty}^{+\infty} \exp(im(\theta - \gamma - \frac{\pi}{2}))J_m(ur)\exp(in(\psi - \gamma + \frac{\pi}{2}))J_n(ur_0). \tag{32.34}$$

Then

$$\varphi(r,\theta) = \frac{1}{4\pi^2} \int_0^{\infty} \int_0^{2\pi} \int_0^{2\pi} \sum_{m=-\infty}^{+\infty} \sum_{n=-\infty}^{+\infty} \frac{}{(u^2+k^2)} \exp(im(\theta - \gamma - \tfrac{\pi}{2}))J_m(ur)\exp(in(\psi - \gamma + \tfrac{\pi}{2}))J_n(ur_0)$$
$$\times \left[r_0 \frac{\partial\varphi(r_0,\psi)}{\partial r} - \frac{iur_0}{2}(\exp i(\gamma - \psi) + \exp(-i(\gamma - \psi)))\varphi(r_0,\psi) \right] u\mathrm{d}\psi\mathrm{d}\gamma\mathrm{d}u. \tag{32.35}$$

We further assume that:

$$\varphi(r_0,\psi) = \varphi(r_0)\exp(i\lambda\psi). \tag{32.36}$$

We obtain:

$$\varphi(r,\theta) = \frac{1}{4\pi^2} \int_0^{\infty} \int_0^{2\pi} \int_0^{2\pi} \sum_{m=-\infty}^{+\infty} \sum_{n=-\infty}^{+\infty} \frac{}{(u^2+k^2)} \exp\left(im\left(\theta - \gamma - \tfrac{\pi}{2}\right)\right)J_m(ur)\exp(i\psi(n+\lambda))\exp\left(in\left(-\gamma + \tfrac{\pi}{2}\right)\right)$$
$$\times J_n(ur_0)\left[r_0 \frac{\partial\varphi(r_0)}{\partial r} - \frac{iur_0}{2}(\exp(-i\psi)\exp(i\gamma) + \exp(i\psi)\exp(-i\gamma))\varphi(r_0) \right] u\mathrm{d}\psi d\gamma\mathrm{d}u. \tag{32.37}$$

Let us write down this integral as a sum of three integrals:

$$\begin{aligned}\varphi(r,\theta) = &\frac{1}{4\pi^2}\int_0^{\infty}\int_0^{2\pi}\int_0^{2\pi}\sum_{m=-\infty}^{+\infty}F_m\sum_{n=-\infty}^{+\infty}\exp(i\psi(n+\lambda))\\ &\times\exp\left(in\left(-\gamma+\frac{\pi}{2}\right)\right)J_n(ur_0)\left[R_0\frac{\partial\varphi(r_0)}{\partial r}\right]u\mathrm{d}\psi\mathrm{d}\gamma\mathrm{d}u\\ &+\frac{1}{4\pi^2}\int_0^{\infty}\int_0^{2\pi}\int_0^{2\pi}\sum_{m=-\infty}^{+\infty}F_m\sum_{n=-\infty}^{+\infty}\exp(i\psi(n+\lambda-1))\\ &\times\exp\left(in\left(-\gamma+\frac{\pi}{2}\right)\right)J_n(ur_0)\left[-\frac{iur_0}{2}\exp(i\gamma)\varphi(r_0)\right]u\mathrm{d}\psi\mathrm{d}\gamma\mathrm{d}u\\ &+\frac{1}{4\pi^2}\int_0^{\infty}\int_0^{2\pi}\int_0^{2\pi}\sum_{m=-\infty}^{+\infty}F_m\sum_{n=-\infty}^{+\infty}\exp(i\psi(n+\lambda+1))\\ &\times\exp\left(in\left(-\gamma+\frac{\pi}{2}\right)\right)J_n(ur_0)\left[-\frac{iur_0}{2}\exp(-i\gamma)\varphi(r_0)\right]u\mathrm{d}\psi\mathrm{d}\gamma\mathrm{d}u.\end{aligned} \tag{32.38}$$

The coefficients at ψ in exponents can be set to zero, since the final solution should not depend on ψ. Thus, we obtain for the first integral $n=-\lambda$, for the second integral $n=-\lambda+1$, and for the third one $n=-\lambda-1$. As a result, the integral 32.38) can be written as:

$$\begin{aligned}\varphi(r,\theta) = &\frac{1}{4\pi^2}\int_0^{\infty}\int_0^{2\pi}\int_0^{2\pi}\sum_{m=-\infty}^{+\infty}F_m\exp\left(i(-\lambda)\left(-\gamma+\frac{\pi}{2}\right)\right)\\ &\times J_{-\lambda}(ur_0)\left[r_0\frac{\partial\varphi(r_0)}{\partial r}\right]u\mathrm{d}\psi\mathrm{d}\gamma\mathrm{d}u\\ &+\frac{1}{4\pi^2}\int_0^{\infty}\int_0^{2\pi}\int_0^{2\pi}\sum_{m=-\infty}^{+\infty}F_m\exp\left(i(-\lambda+1)\left(-\gamma+\frac{\pi}{2}\right)\right)\\ &\times J_{-\lambda+1}(ur_0)\left[-\frac{iur_0}{2}\exp(i\gamma)\varphi(r_0)\right]u\mathrm{d}\psi\mathrm{d}\gamma\mathrm{d}u\\ &+\frac{1}{4\pi^2}\int_0^{\infty}\int_0^{2\pi}\int_0^{2\pi}\sum_{m=-\infty}^{+\infty}F_m\exp\left(i(-\lambda-1)\left(-\gamma+\frac{\pi}{2}\right)\right)\\ &\times J_{-\lambda-1}(ur_0)\left[-\frac{iur_0}{2}\exp(-i\gamma)\varphi(r_0)\right]u\mathrm{d}\psi\mathrm{d}\gamma\mathrm{d}u.\end{aligned} \tag{32.39}$$

While developing type F_m in integrals and summing up the terms in exponents, we obtain:

$$\begin{aligned}\varphi(r,\theta) = {} & \frac{1}{4\pi^2}\int_0^{\infty}\int_0^{2\pi}\int_0^{2\pi}\frac{\sum_{m=-\infty}^{+\infty}J_m(ur)}{(u^2+k^2)}\exp\left(i\gamma(\lambda-m)+im\left(\theta-\frac{\pi}{2}\right)+i(-\lambda)\frac{\pi}{2}\right)\\ & \times J_{-\lambda}(ur_0)\left[r_0\frac{\partial\varphi(r_0)}{\partial r}\right]u\mathrm{d}\psi\mathrm{d}\gamma\mathrm{d}u\\ & + \frac{1}{4\pi^2}\int_0^{\infty}\int_0^{2\pi}\int_0^{2\pi}\frac{\sum_{m=-\infty}^{+\infty}J_m(ur)}{(u^2+k^2)}\exp\left(i\gamma(\lambda-m)+im\left(\theta-\frac{\pi}{2}\right)+i(-\lambda+1)\frac{\pi}{2}\right)\\ & \times J_{-\lambda+1}(ur_0)\left[-\frac{iur_0}{2}\varphi(r_0)\right]u\mathrm{d}\psi\mathrm{d}\gamma du\\ & + \frac{1}{4\pi^2}\int_0^{\infty}\int_0^{2\pi}\int_0^{2\pi}\frac{\sum_{m=-\infty}^{+\infty}J_m(ur)}{(u^2+k^2)}\exp\left(i\gamma(\lambda-m)+im\left(\theta-\frac{\pi}{2}\right)+i(-\lambda-1)\frac{\pi}{2}\right)\\ & \times J_{-\lambda-1}(ur_0)\left[-\frac{iur_0}{2}\varphi(r_0)\right]u\mathrm{d}\psi\mathrm{d}\gamma\mathrm{d}u.\end{aligned} \tag{32.40}$$

Since the Fourier term $\Phi(u,\gamma)$ is axially symmetric, we set the coefficients at γ to zero and obtain $m=\lambda$. Then:

$$\begin{aligned}\varphi(r,\theta) = {} & \frac{1}{4\pi^2}\int_0^{\infty}\int_0^{2\pi}\int_0^{2\pi}\frac{J_{\lambda}(ur)}{(u^2+k^2)}\exp\left(i\lambda\left(\theta-\frac{\pi}{2}\right)+i(-\lambda)\frac{\pi}{2}\right)\\ & \times J_{-\lambda}(ur_0)\left[-r_0\frac{\partial\varphi(r_0)}{\partial r}\right]u\mathrm{d}\psi\mathrm{d}\gamma\mathrm{d}u\\ & + \frac{1}{4\pi^2}\int_0^{\infty}\int_0^{2\pi}\int_0^{2\pi}\frac{J_{\lambda}(ur)}{(u^2+k^2)}\exp\left(i\lambda\left(\theta-\frac{\pi}{2}\right)+i(-\lambda+1)\frac{\pi}{2}\right)\\ & \times J_{-\lambda+1}(ur_0)\left[-\frac{iur_0}{2}\varphi(r_0)\right]u\mathrm{d}\psi\mathrm{d}\gamma\mathrm{d}u\\ & + \frac{1}{4\pi^2}\int_0^{\infty}\int_0^{2\pi}\int_0^{2\pi}\frac{J_{\lambda}(ur)}{(u^2+k^2)}\exp\left(i\lambda\left(\theta-\frac{\pi}{2}\right)+i(-\lambda-1)\frac{\pi}{2}\right)\\ & \times J_{-\lambda-1}(ur_0)\left[-\frac{iur_0}{2}\varphi(r_0)\right]u\mathrm{d}\psi\mathrm{d}\gamma\mathrm{d}u.\end{aligned} \tag{32.41}$$

Let us now set λ in the expression (32.36) equal to zero $\lambda = 0$. Then

$$\begin{aligned}\varphi(r) = &\frac{1}{4\pi^2}\int_0^{\infty}\int_0^{2\pi}\int_0^{2\pi}\frac{J_0(ur)}{(u^2+k^2)}J_0(ur_0)\left[r_0\frac{\partial\varphi(r_0)}{\partial r}\right]u\mathrm{d}\psi\mathrm{d}\gamma\mathrm{d}u\\ &+\frac{1}{4\pi^2}\int_0^{\infty}\int_0^{2\pi}\int_0^{2\pi}\frac{J_0(ur)}{(u^2+k^2)}J_1(ur_0)\left[\frac{ur_0}{2}\varphi(r_0)\right]u\mathrm{d}\psi\mathrm{d}\gamma\mathrm{d}u\\ &+\frac{1}{4\pi^2}\int_0^{\infty}\int_0^{2\pi}\int_0^{2\pi}\frac{J_0(ur)}{(u^2+k^2)}J_{-1}(ur_0)\left[-\frac{ur_0}{2}\varphi(r_0)\right]u\mathrm{d}\psi\mathrm{d}\gamma\mathrm{d}u.\end{aligned} \tag{32.42}$$

Let us simplify:

$$\begin{aligned}\varphi(r) = &\frac{1}{4\pi^2}\int_0^{\infty}\int_0^{2\pi}\int_0^{2\pi}\frac{J_0(ur)u}{(u^2+k^2)}\left\{J_0(ur_0)\left[r_0\frac{\partial\varphi(r_0)}{\partial r}\right]\right.\\ &\left.+(J_1(ur_0)-J_{-1}(ur_0))\left[\frac{ur_0}{2}\varphi(r_0)\right]\right\}\mathrm{d}\psi\mathrm{d}\gamma\mathrm{d}u.\end{aligned} \tag{32.43}$$

Let us integrate over ψ, γ:

$$\varphi(r) = \int_0^{\infty}\frac{J_0(ur)u}{(u^2+k^2)}\left\{J_0(ur_0)\left[r_0\frac{\partial\varphi(r_0)}{\partial r}\right]+(J_1(ur_0)-J_{-1}(ur_0))\left[\frac{ur_0}{2}\varphi(r_0)\right]\right\}\mathrm{d}u. \tag{32.44}$$

Taking into consideration that:

$$J_{-1}(u) = (-1)^1 J_1(u) = -J_1(u), \tag{32.45}$$

we finally obtain:

$$\varphi(r) = r_0\int_0^{\infty}\frac{J_0(ur)u}{(u^2+k^2)}(J_0(ur_0)f_2 + J_1(ur_0)uf_1)\mathrm{d}u. \tag{32.46}$$

References

1. V.A. Babeshko, O.V. Evdokimova, O.M. Babeshko, E.M. Gorshkova, I.B. Gladskoi, D.V. Grishenko, I.S. Telatnikov, Ecol. Bull. Res. Centers Black Sea Econ. Coop. (BSEC) **2**,13 (2014)
2. M. Abramovits, I. Stigan (Eds.) *Guidebook on Special Functions* (Nauka, Moscow, 832) (1979) (in Russian)
3. U. Rudin, *Fundamentals of Mathematical Analysis*. (Mir, Moscow, 216 p) (1982) (in Russian)
4. V.A. Babeshko, E.V. Glushkov, Zh. F. Zinchenko, *Dynamics of Heterogeneous Linear-elastic Media* (Nauka, Moscow, 346 p) (1989) (in Russian)
5. *D01AKF Subroutine. The NAG Fortran Library, The Numerical Algorithms Group (NAG)*, Oxford, United Kingdom, www.nag.com
6. V.A. Rokhlin, D.B. Fuchs, *Introductory to Topology* (Nauka, Moscow, 488 p) (1977) (in Russian)

Chapter 33
The Nonstationary Contact Problem of Thermoelasticity for a Ring in the Presence of a Reinforcing Layer on the Friction Surface

V. I. Kolesnikov, M. I. Chebakov and S. A. Danilchenko

Abstract The present paper deals with the spatial thermoelastic contact problem of the brake shoe pressing into the rotating roller with provision for friction and heat generation due friction and taking into account the reinforcing layer with other mechanical and thermophysical properties on the roller surface. The results of calculations of equivalent stresses and temperature fields are presented in relation to the thickness of the surface layer, its elasticity modulus and the rotation time. The simulation and calculation were performed by using the finite element method and the ANSYS software package. It is shown that the main changes of the temperature and the equivalent stresses take place at the depth of up to 1 mm from the friction surface. The presence of the reinforcing layer leads to decrease of the temperature on the surface. It is important to note that at the certain values of parameters the maximum value of temperature is achieved not on the friction surface out of the contact area, but at a certain depth.

33.1 Introduction

In the contact interaction between machine parts and mechanisms, the temperature in the contact area plays an important role. Hot temperatures can lead to arising degradation and to life loss of construction elements or even to their destruction. The main contribution to heat generation in such constructions is made by friction in the contact area. A lot of works are devoted to the study of thermophysical processes in tribocontacts, for example [1–4]. This matter is essential to braking systems of railway vehicles; there are works that are devoted to modeling the

V. I. Kolesnikov · M. I. Chebakov · S. A. Danilchenko
Rostov State Transport University, Rostov-on-Don, Russia

M. I. Chebakov (✉) · S. A. Danilchenko
I. I. Vorovich Mathematics, Mechanics and Computer Sciences Institute, Southern Federal University, Rostov-on-Don, Russia
e-mail: chebakov@math.sfedu.ru

I. A. Parinov et al. (eds.), *Advanced Materials*, Springer Proceedings in Physics 224, https://doi.org/10.1007/978-3-030-19894-7_33

thermoelastic interaction in various friction nodes of the railway transport [5, 6]. For this reason, the problem of how to strengthen the surface layers of friction bodies still continues to be relevant at the present time [7].

The present paper deals with the spatial thermoelastic contact problem of the brake shoe pressing into the rotating roller with provision for friction and heat generation due friction and taking into account the reinforcing layer with other mechanical and thermophysical properties on the roller surface.

33.2 Formulation

The elastic inhomogeneous roller $\Omega_r = (R_3 \leq \rho \leq R_1;\ 0 \leq \varphi \leq \varphi_1;\ -d/2 \leq z \leq d/2)$ is considered in a cylindrical coordinate system ρ, φ, z. A brake shoe $\Omega_p = (R_1 \leq \rho \leq R_2;\ \varphi_2 \leq \varphi \leq \pi - \varphi_2;\ -d/2 \leq z \leq d/2)$, loaded by a normal force P, evenly distributed on the surface $S_p = (\rho = R_2;\ \varphi_2 \leq \varphi \leq \pi - \varphi_2;\ -d/2 \leq z \leq d/2)$, is forced against the frontal surface of the roller (Fig. 33.1). The surface S_p is fixed in Ox and Oz axes. The roller rotates with a constant angular velocity ω, and herewith there are Coulomb friction forces with the coefficient k between the roller and the brake shoe. The heat flow distribution coefficient f is given between the contact surfaces of the roller and the brake shoe. The interaction free surfaces of the roller are assigned by the convective heat transfer with a heat transfer coefficient α. For the reason of the symmetry of the regarded problem in respect to the plane Oxy the half of the model $(0 \leq z \leq d/2)$ has been considered in calculation, whereupon the symmetry condition is given on the boundary $z = 0$.

33.3 Solution

To solve the given problem, the finite element method and the special ANSYS software were used. The finite element mesh is built by using 20-node coupled elastic SOLID226 elements, for which the option of the thermoelastic analysis is

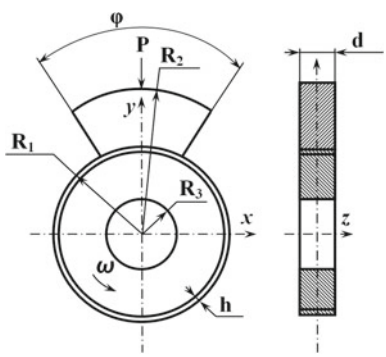

Fig. 33.1 Statement of the problem

applied. By using the special APDL ANSYS macros these elements received the different fixed values of Young's modulus.

For modelling the contact interaction between the roller and the brake shoe, the contact pair was constructed that was determined by the CONTA174 and TARGE170 elements. The CONTA174 contact elements covered the boundary $S_{\text{cont}} = (\rho = R_1;\ \varphi_2 \leq \varphi \leq \pi - \varphi_2;\ -d/2 \leq z \leq d/2)$, and the TARGE170 responding elements covered the boundary $S_{\text{targ}} = (\rho = R_1;\ 0 \leq \varphi \leq \varphi_1;\ 0 \leq z \leq d/2)$. For the roller rotation, the additional contact pair was constructed regarding the "node point – surface" concept. The pilot node $N_\omega = (\rho = 0;\ \varphi = 0;\ z = 0)$ was determined, which all nodal degrees of freedom were equal to 0, except the rotation in the Oz-axis. The given node was rigidly coupled with the surface $S_\omega = (\rho = R_3;\ 0 \leq \varphi \leq \varphi_1;\ 0 \leq z \leq d/2)$, that was covered with the CONTA174 contact elements.

To solve the nonstationary problem, the minimal and maximal time steps are set, and the settings are defined that allow the ANSYS software to choose the optimal time step during the calculations.

33.4 Results

The numerical calculations were carried out for two variants of the problem: (1) the initial roller made of the homogenous material; (2) along the outer radius of the roller there was a thin surface layer of the thickness h, which properties were different in comparison with the core material. In both cases, the identical geometrical parameters of the roller and the brake shoe, the roller rotation velocity, the load and the friction coefficient were used.

As materials, which the roller and the brake shoe were made, we used the steel 45 and TIIR 300, respectively. The physical properties of these materials are present in Table 33.1.

The values of the geometrical parameters of the problem are as follows: $R_1 = 20$ mm, $R_2 = 34$ mm, $R_3 = 9$ mm, $d = 9$ mm, $\varphi_1 = 2\pi$, $\varphi_2 = \pi/3$.

The roller rotation velocity $\omega = 189$ rpm, the applied load $P = 500$ N, the friction coefficient $k = 0.45$, the heat flow distribution coefficient $f = 0.5$, the heat

Table 33.1 Physical properties of materials of roller and brake shoe

Parameter	Value for roller	Value for brake shoe
Density ρ, kg/m^3	7800	2100
Elasticity modulus E, MPa	2×10^5	5×10^4
Poisson's constant υ	0.3	0.36
Coefficient of thermal expansion a, 10^{-5} 1/deg	1.1	3.9
Coefficient of heat conductivity λ, W/(m deg)	50.2	1.4
Heat capacity C, J/(kg deg)	473	1480

transfer coefficient $\alpha = 50$ W/(m^2·K). A special attention was paid to the influence of the thickness value and mechanical properties of the surface reinforcing layer on the distribution of temperature fields in the roller and the value of the equivalent stresses.

According to the calculation results, the plots, showing the distribution of the temperature and the equivalent stresses along two selected sections, were constructed (Fig. 33.2). The first section is the line ***AB***, where the point ***A*** had coordinates ($\rho = R_1$; $\varphi = \varphi_3$; $z = 0$), and the point ***B*** ($\rho = R_3$; $\varphi = \varphi_3$; $z = 0$). The angle $\varphi_3 = \varphi_2 - \pi/36$. The second section is the line ***CD***, where the point ***C*** has coordinates ($\rho = R_1$; $\varphi = \varphi_3$; $z = d/2$), and the point ***D*** ($\rho = R_3$; $\varphi = \varphi_3$; $z = d/2$); $l = R_1 - R_3$.

The presented plots show, that the temperature and the equivalent stresses in the middle cross-section of the roller are higher than at the side surface. It is important to note that the maximum value of the temperature is achieved not on the friction surface out of the contact area, but at a certain depth, which agrees with [8]. Figure 33.3 presents the pictures of the distribution of the temperature fields and the equivalent stresses in the initial roller (without the reinforcing layer).

Figure 33.4 shows the distributions of the temperatures and the equivalent stresses, if there is a 100 μm deep reinforcing layer with another values of elasticity modulus. The values of density, the Poisson's constant, the coefficient of thermal expansion, the coefficient of heat conductivity and the heat capacity of the layer coincide with the values for steel 45 from Table 33.1.

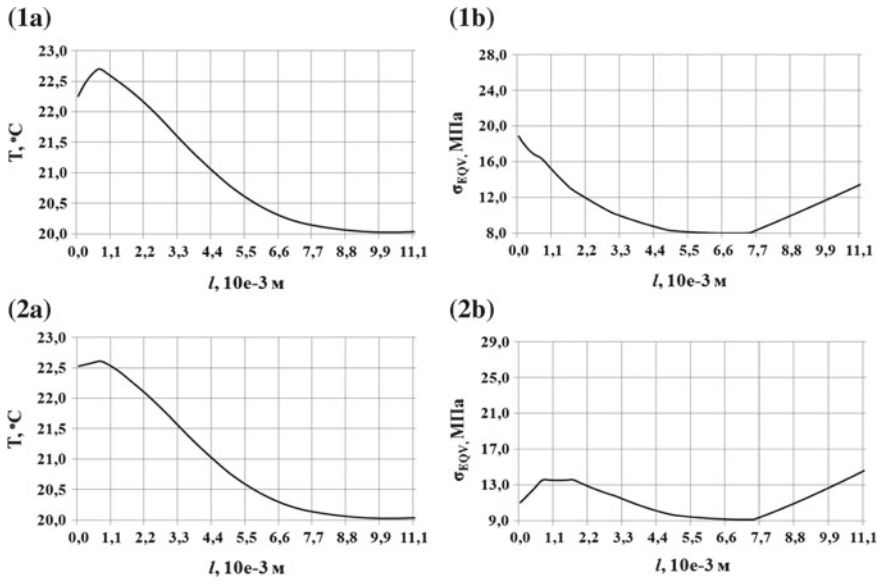

Fig. 33.2 Distributions of the temperature (**a**) and the equivalent stress (**b**) in the initial roller (without the reinforcing layer) along the lines ***AB*** (**1**) and ***CD*** (**2**), $t = 1$ s (3.15 rotations)

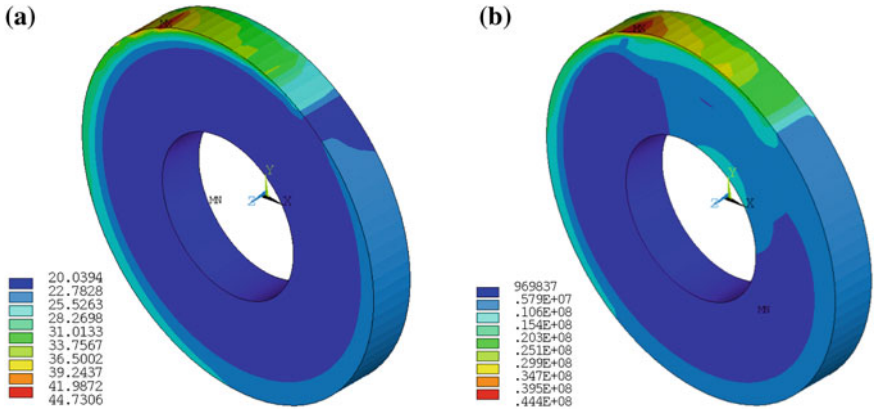

Fig. 33.3 Distributions of the temperature fields (**a**) and the equivalent stresses (**b**) in the initial roller (without the reinforcing layer), t = 1 s (3.15 rotations)

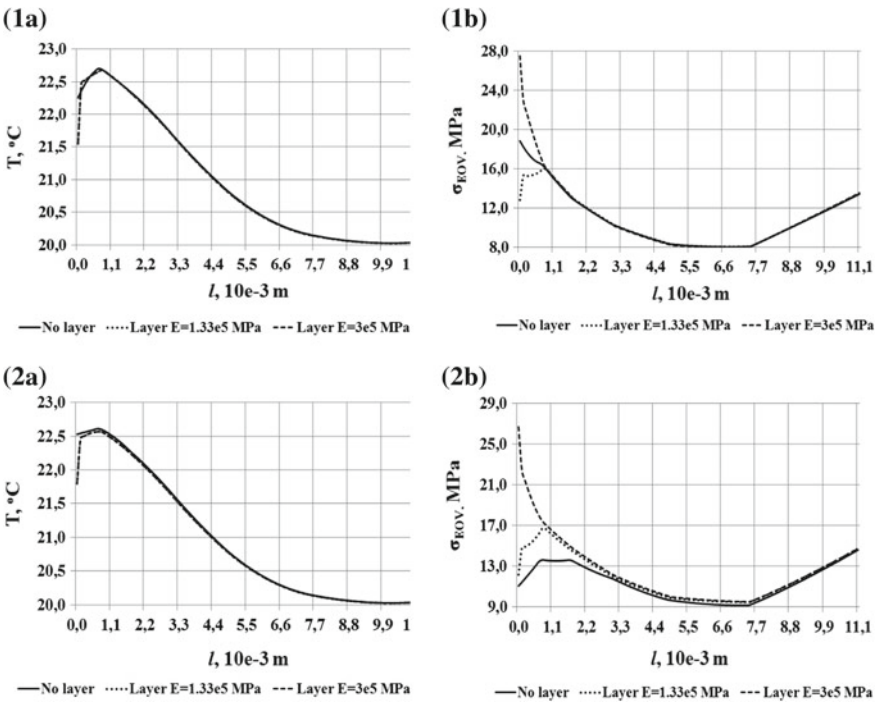

Fig. 33.4 Distributions of the temperatures (**a**) and the equivalent stress (**b**) in the roller along the lines ***AB*** (**1**) and ***CD*** (**2**) depending on the value of the elasticity modulus of the surface layer, t = 1 s (3.15 rotations)

As it can be seen from the plots, the main changes take place at the depth of up to 1 mm from the rolling surface. The presence of the layer has led to the temperature fall at the rolling surface. It should be also mentioned, that the change of the elasticity modulus of the layer leads to the directly proportional change of the equivalent stresses and does not influence the temperature.

Then, the distributions of the temperature and the equivalent stresses at the depth of up to 1.1 mm from the rolling surface of the roller are present on the plots of Fig. 33.5.

Figures 33.6 and 33.7 show distributions of the temperature and the equivalent stresses depending on the thickness of the surface layer. The results for the layer with the elasticity modulus $E = 3 \times 10^5$ MPa are present. The values of other physical properties of the layer coincide with the corresponding values for the roller (Table 33.1).

It follows from the obtained results, that when the thickness of the layer increases, the temperature decreases at the rolling surface and increases on the boundary between the layer and the core material. The values of the equivalent stresses increase.

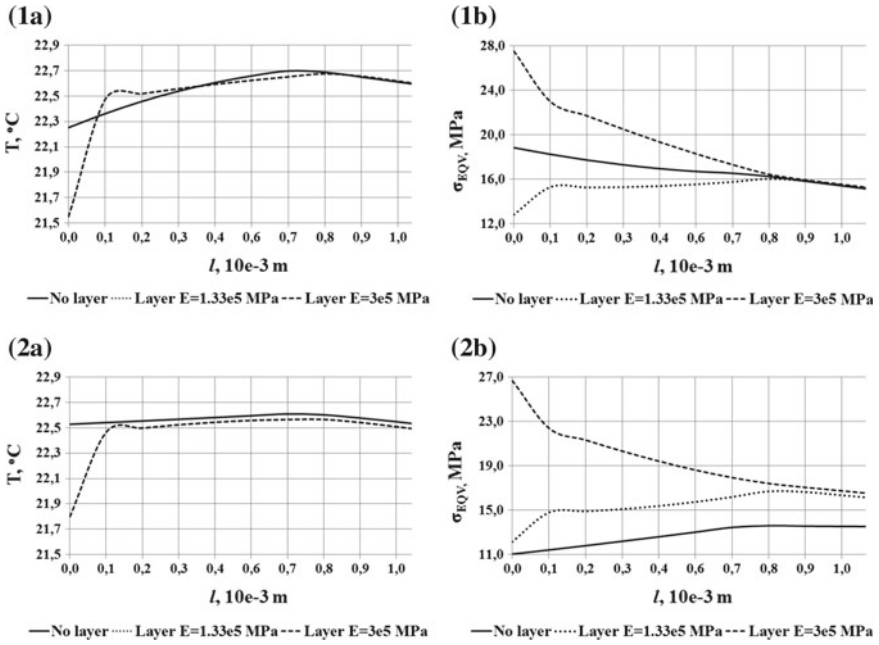

Fig. 33.5 Distributions of the temperature (**a**) and the equivalent stress (**b**) in the roller along the lines ***AB*** (**1**) and ***CD*** (**2**) at the depth of up to 1.1 mm depending on the value of the elasticity modulus of the surface layer, $t = 1$ s (3.15 rotations)

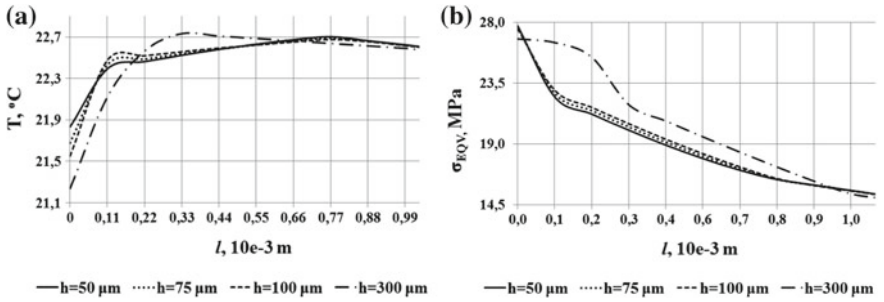

Fig. 33.6 Graphs of the distribution of the temperature (**a**) and the equivalent stress (**b**) in the roller along the lines ***AB*** at the depth of up to 1.1 mm depending on the thickness of the surface layer h, t = 1 s (3.15 rotations)

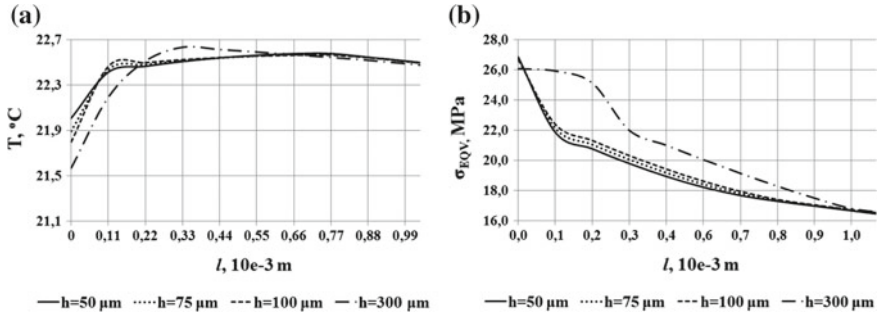

Fig. 33.7 Distributions of the temperature (**a**) and the equivalent stress (**b**) in the roller along the lines ***CD*** at the depth of up to 1.1 mm depending on the thickness of the surface layer h, t = 1 s (3.15 rotations)

Figure 33.8 presents the plots of the distribution of the temperature and the equivalent stresses at the rotation time t = 5 s (15.75 rotations). The results are given for the layer with the elasticity modulus $E = 3 \times 10^5$ MPa and the thickness of 100 μm. The values of other physical properties of the layer coincide with the corresponding values for the roller (Table 33.1). It follows from the obtained results, that when the rotation time increases, the temperature maximum moves to the friction surface, while the shape of the distribution of the equivalent stresses does not practically change, only the numerical values change.

Figure 33.9 presents the graphs of the temperature changes at the points ***A*** and ***C*** at the rotation time t = 5 s (15.75 rotations).

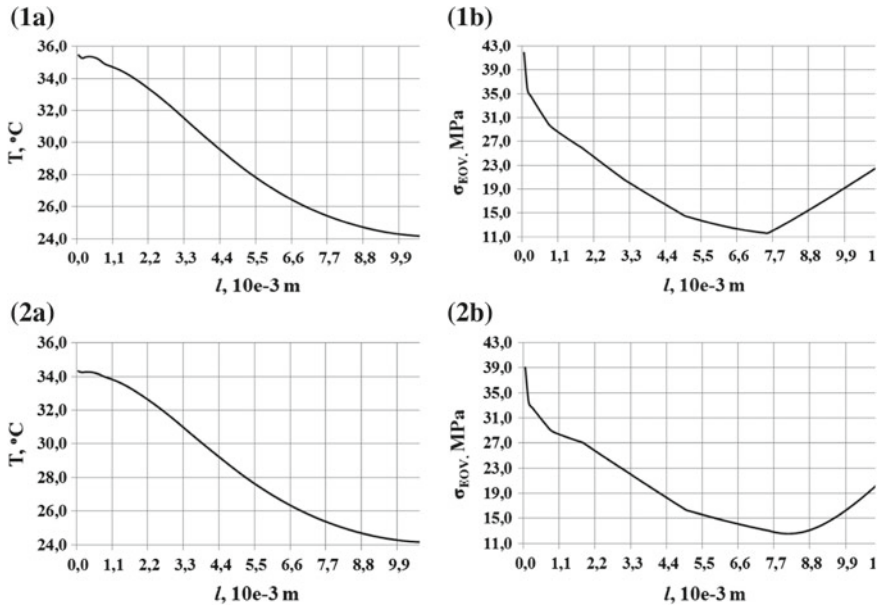

Fig. 33.8 Distributions of the temperature (**a**) and the equivalent stress (**b**) in the roller along the lines ***AB*** (**1**) and ***CD*** (**2**), t = 5 s (15.75 rotations)

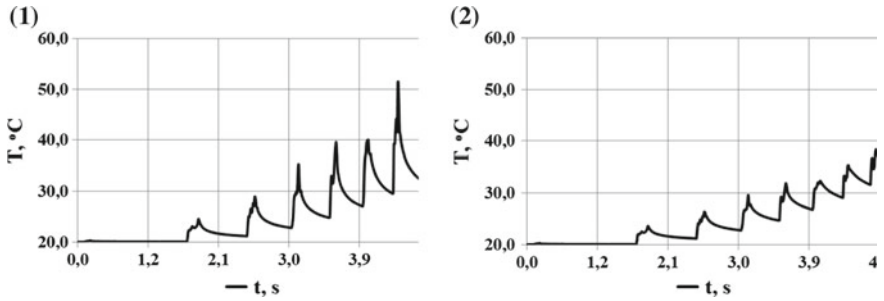

Fig. 33.9 Plots of the temperature changes at the points ***A*** (**1**) and ***C*** (**2**), t = 5 s (15.75 rotations)

33.5 Conclusions

By using the finite element ANSYS software package, the calculations of the temperature fields and the equivalent stresses are carried out for the given problem of the interaction between the roller and the brake shoe depending on the geometric and physical-mechanical parameters of the problem. It is stated that the main changes of the temperature and the equivalent stresses take place at the depth of up to 1 mm from the friction surface. The presence of the reinforcing layer leads to

decrease of the temperature on the surface. It is important to note that at the certain values of parameters, the maximum value of the temperature is achieved not on the friction surface out of the contact area, but at a certain depth. It should be also noticed, that the increase of the elasticity modulus leads to the increase of the equivalent stresses and does not influence the temperature. When the size of the layer changes, the following effect can be seen: the thickness increases, the temperature decreases on the friction surface, and increases at the boundary between the layer and the core material, the values of the equivalent stresses increase.

Acknowledgements This work is supported by the Russian Science Foundation under grant No. 16-19-10467, performed in Rostov State Transport University.

References

1. A.A. Yevtushenko, M. Kuciej, O. Yevtushenko, Int. J. Heat Mass Transf. **81**, 915 (2015)
2. A.V. Chichinadze, E.D. Braun, A.G. Ginsburg, Z.V. Ignat'eva, *Calculation, Test and Selection of Frictional Couples* (Nauka, Moscow, 1979), 267p (in Russian)
3. M. Conte, B. Pinedo, A. Igartua, Tribol. Int. **74**, 1 (2014)
4. W. Nowacki, *Dynamic Problems of Thermoelasticity* (Springer, New York, 1975)
5. V.I. Kolesnikov, M.I. Chebakov, I.V. Kolesnikov, A.A. Lyapin, Transp. Sci. Equip. Manage. **1**, 6 (2015). (in Russian)
6. V.I. Sakalo, V.S. Kosov, *Contact Problems in Rail Transport* (Mechanical Engineering, Moscow, 2004), 160p (in Russian)
7. V.I. Kolesnikov, M.I. Chebakov, I.V. Kolesnikov, A.A. Lyapin, in *Advanced Materials: Manufacturing, Physics, Mechanics and Applications*, ed. by I.A. Parinov, S.-H. Chang, V.Y. Topolov. Springer Proceedings in Physics, vol. 175 (Springer Cham, Heidelberg, 2016), 527
8. V.I. Kolesnikov, *Thermophysical Processes in Metal Polymeric Tribosystems* (Nauka, Moscow, 2003), 280p (in Russian)

Chapter 34
Mathematical Modeling of Indentation Process for Layered Sample Taking into Account Plastic Properties of Material Layers

A. A. Lyapin, M. I. Chebakov, E. M. Kolosova, A. Alexiev and E. Barkanov

Abstract The problem on indentation of elastic area with layered coating by cone shaped indenter is studied. Corresponding layers as well as material area are described using different models such as bilinear and Drucker-Prager model. As a result, the study covers materials of different nature described by completely different mechanical behavior under hydrostatic load. Various cases of elastoplastic properties for each layer are considered including the phenomena of residual stresses appearing after unloading and delaminating defects caused by stress concentration at the interface between layers.

34.1 Introduction

Mechanical properties of coating are usually unknown and require detailed studies and characterization [1, 2]. The methods for creating coating also have influence on final mechanical properties [3]. Another well-known factor as residual stresses in coatings, arising from various technological operations, also is under the view of numerous research groups [4]. A large group of articles available is devoted to numerical study of coatings including finite element analysis [5]. The special phenomena like nanoscale effect [6] and delaminating [7], as well as great difference in mechanical properties of coating and basic body [8] are presented in scientific literature.

A. A. Lyapin · M. I. Chebakov (✉) · E. M. Kolosova
I. I. Vorovich Institute of Mathematics, Mechanics and Computer Sciences, Southern Federal University, Rostov-on-Don, Russia
e-mail: chebakov@math.sfedu.ru

A. Alexiev
Institute of Mechanics, Bulgarian Academy of Sciences, Sofia, Bulgaria

E. Barkanov
Riga Technical University, Riga, Latvia

I. A. Parinov et al. (eds.), *Advanced Materials*, Springer Proceedings in Physics 224, https://doi.org/10.1007/978-3-030-19894-7_34

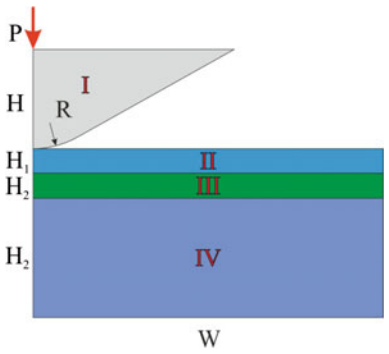

Fig. 34.1 Schematic picture of the problem

The object of study is the area of width W, consisting of three subareas with thicknesses H_1 (area II), H_2 (area III), H_3 (area IV). Areas II and III form double-layer coating with mechanical properties, which will be studied. The area is indented by the body I, which has the form of cone with rounded tip of radius R. The problem is studied in terms of axisymmetrical statement allowing one to reduce significantly the calculation time. The schematic view of problem is demonstrated in Fig. 34.1.

The simulation is realized using ANSYS software. The area, coating and indenter are modeled using PLANE 182 element type used for solid structures simulations in framework of plane strain, plane stress and axisymmetrical cases. The element is determined with four nodes, each having two degrees of freedom (horizontal and vertical displacements). The element supports various physical properties of the material, including plasticity and viscoelasticity. The contact interaction between coating and indenter is realized using TARGE169 and CONTA172 element types.

It is sufficient to distinct the object being studied using indentation technique on the base of their nature. The point is such materials as soils, rocks, coals etc. differ valuably with corresponding mechanical properties from, for example, metals. Such difference is based on various behavior of corresponding material under the hydrostatic loading. In particular, metals do not reach yield surface in terms of principal stresses under hydrostatic loading in comparison with soils. Graphically such distinctions could be demonstrated via various forms of yield surface (see Fig. 34.2): for metals such surface is presented by cylinder as for von Misses criteria, at the same time soils represented by cone-like surface, and mechanical behavior for such materials could be described with Drucker-Prager model.

The material properties of the areas under study are described by the classical Drucker-Prager model [9], which is applicable to granular materials such as soil, stone, concrete and other materials, whose elastoplastic properties depend on hydrostatic pressure. The model uses the approximation of the yield surface in the form of a cone according to the Drucker-Prager law:

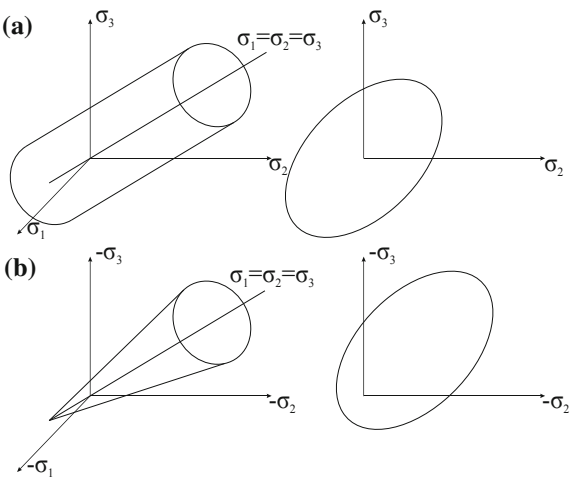

Fig. 34.2 Various yield surfaces for materials: **a** surface for von Misses criteria, **b** surface for Drucker-Prager model

$$f(I_1, J_2) = aI_1 + \sqrt{J_2} - \sigma_y \tag{34.1}$$

where I_1 is the hydrostatic-dependent first principal invariants of stress, a characterizes the dependence on hydrostatic pressure, J_2 is the non-zero principal invariant of the deviatoric stress, σ_y is the critical stress value.

The von Misses criterion could be described with following equation:

$$(\sigma_1 - \sigma_2)^2 + (\sigma_2 - \sigma_3)^2 + (\sigma_3 - \sigma_1)^2 = 2\sigma_y^2 \tag{34.2}$$

Deformation of the indenter is described in terms of the linear elastic model with Young's modulus of 865 GPa and Poisson's ratio of 0.32.

34.2 Homogeneous Problem: Demonstration of Different Natures for Materials While Indentation Technique

Consider the problem for homogeneous body without coating. The elastoplastic properties are described using two models: bilinear model, corresponding to von Misses criteria, and Drucker-Prager model. The Young's modulus for the area is 86 GPa, Poisson's ratio is 0.17, yield stress limit is 4 GPa. Figure 34.3 demonstrates the vertical stresses σ_y distribution for two models of elastoplastic behavior. It could be seen, that the hydrostatic pressure zone is localized in the neighborhood of indenter tip, leading to different indentation results for materials of different nature and properties under hydrostatic loading.

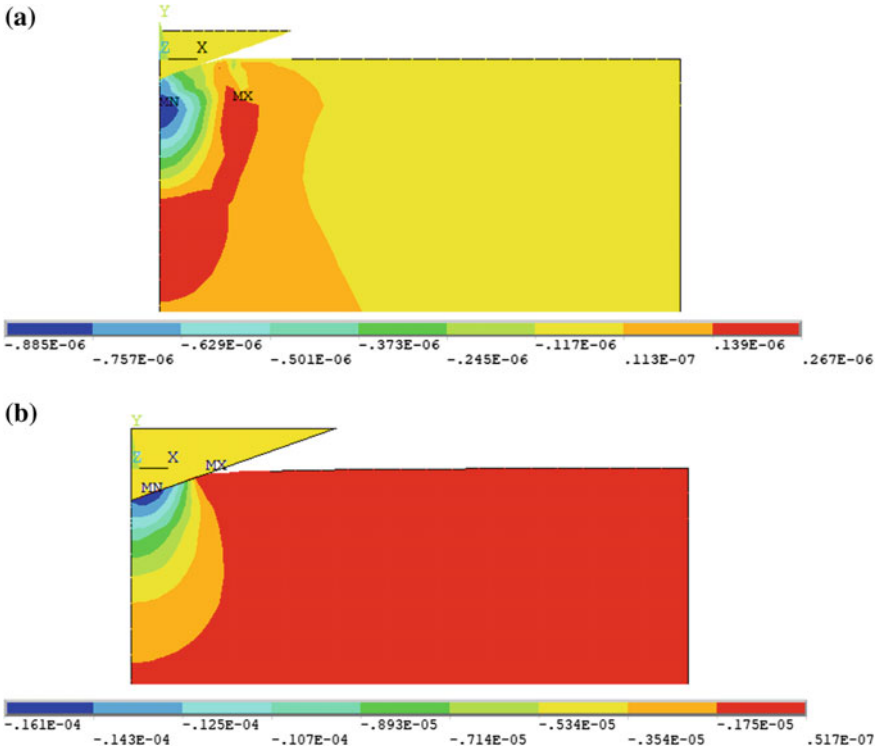

Fig. 34.3 Vertical stresses σ_y distribution for bilinear model (**a**) and Drucker-Prager model (**b**)

34.3 Elastic Coating Placed on Elastoplastic Body

Let us treat the problem for an area with coating at different mechanical properties in the considered parts. In particular, the coating reaches the yield stress in terms of the indentation process while area does not. In such a case, after the unloading the residual deformations do not allow the coating to restore the initial condition, as a result, both the area and coating are under the action of residual stresses. Corresponding plastic deformation $\varepsilon_y^{\text{plastic}}$ and vertical residual stresses σ_y distributions are present in Fig. 34.4.

It should be mentioned, that interface zone between coating and area includes the stress concentration (see Fig. 34.4b). It could be the reason of delaminating.

In this way, it is possible to study such phenomena by introducing contact elements in the zone of possible delaminating. Figure 34.5 demonstrates the plastic deformation $\varepsilon_y^{\text{plastic}}$ (a) and vertical residual stresses σ_y (b) distributions after unloading taking into account delaminating zone.

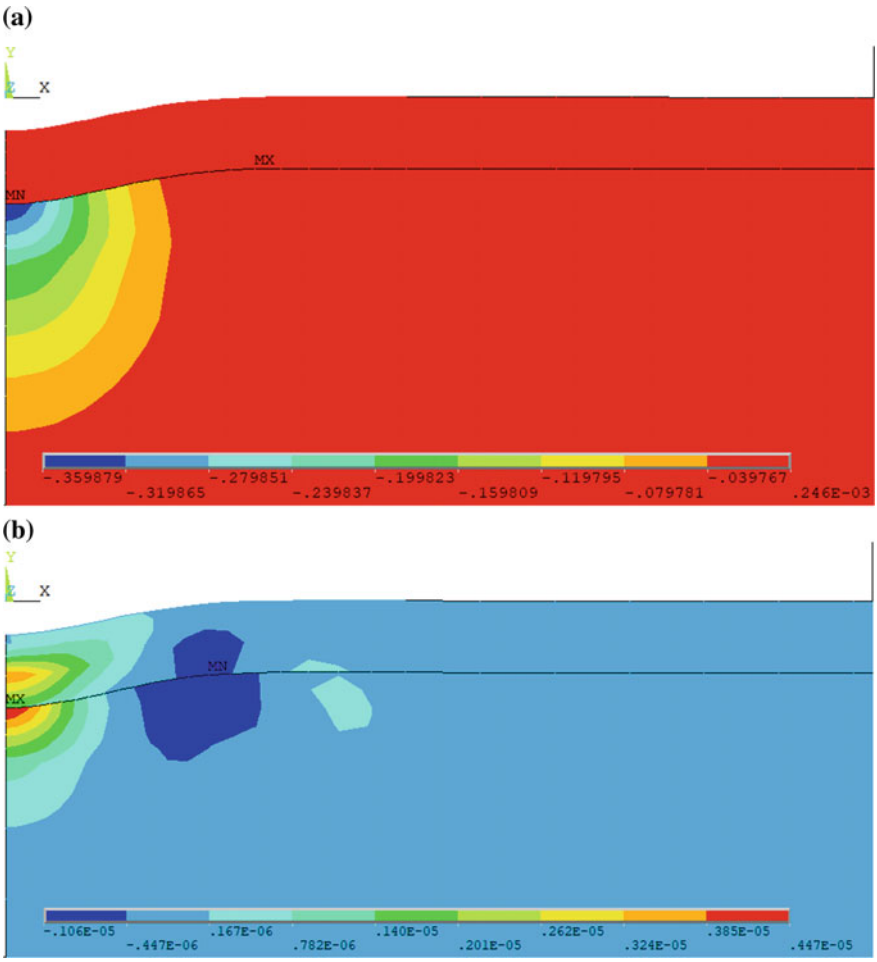

Fig. 34.4 Plastic deformation $\varepsilon_y^{\text{plastic}}$ (**a**) and vertical residual stresses σ_y (**b**) distributions in the problem with coating

34.4 Double-Layered Elastoplastic Coating Placed on Elastic Body

Similar results are achieved for the case of double-layered coating with second layer reaching yield stresses at indentation process. As a result, after unloading the structure is under action of residual stresses (see Fig. 34.6).

Such a case is valid for different complex coatings made of materials with different characteristics. Another application is including additional layer between coating and body in the way to decrease the stress concentration at the interface and, as a result, avoid the delaminating consequences.

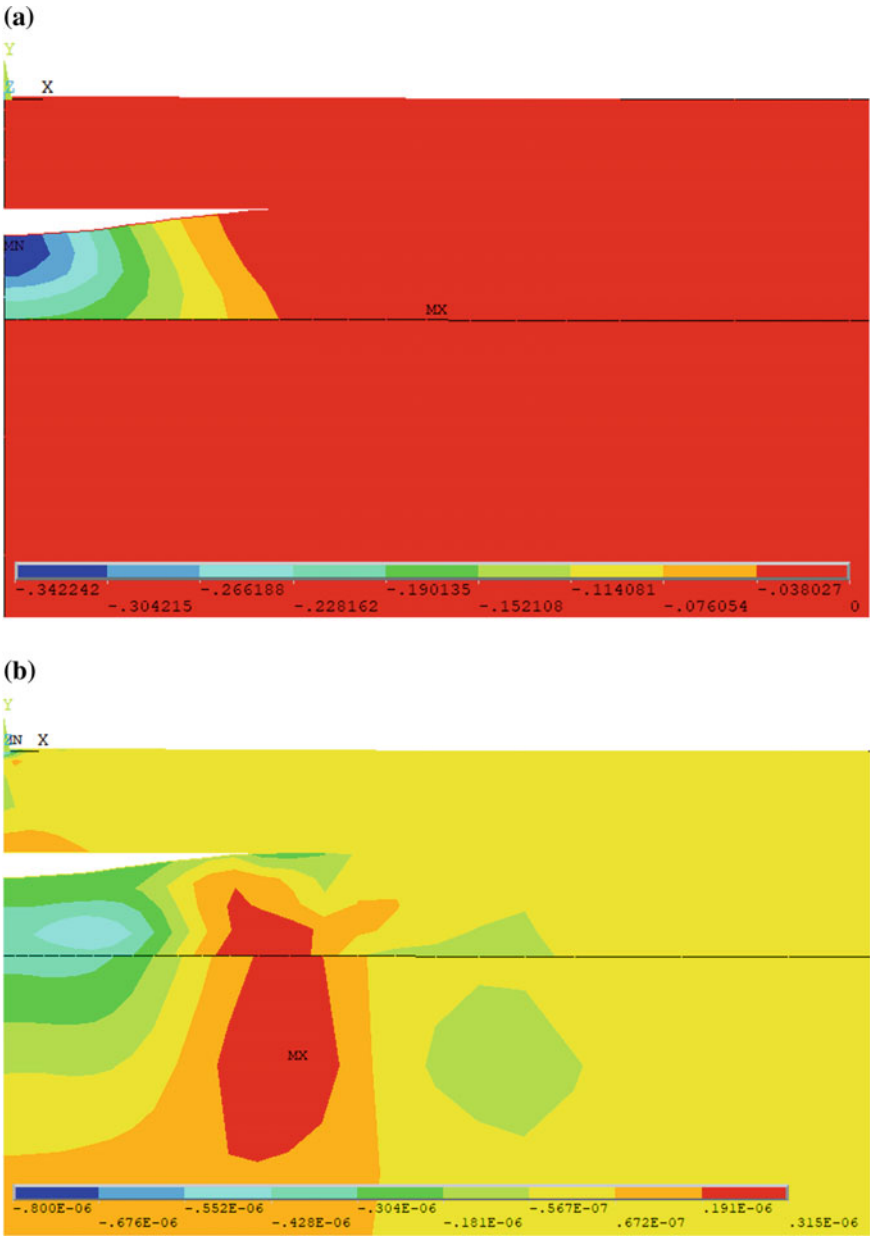

Fig. 34.5 Hydrostatic pressure zone under the tip

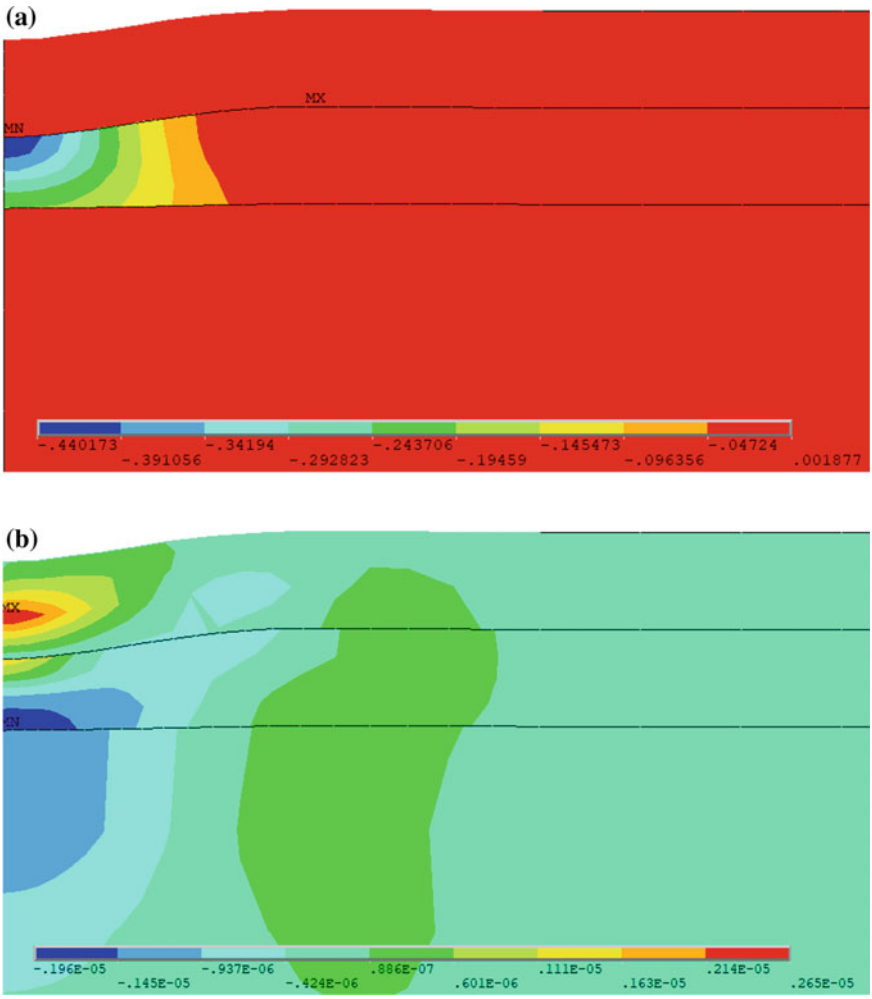

Fig. 34.6 Hydrostatic pressure zone under the tip

34.5 Conclusion

The study demonstrates various opportunities and simulation results on the problems of coatings indentation. Due to various differences in mechanical characteristics, in particular elastoplastic properties, a coating could be under the action of residual stresses after possible contact with other bodies or indentation technique. Such stresses could lead to delaminating and, as a result, damage of coating.

Another aspect is mechanical behavior under hydrostatic load. Since the most popular characterization technique is the indentation, this property for corresponding material is vital for getting correct and valid results of experiment.

The simulation demonstrates sufficient differences in stress-strain state of the sample tested for various models describing elastoplastic behavior. Therefore, corresponding assumptions should be taken for engineering methods on material characterization using indentation technique.

Acknowledgements This work is supported by Ministry of Education and Science of Russian Federation (project No. 9.4726.2017/8.9).

References

1. W. Chuhong, F. Zoheir, J. George, K.H. Mohamed, A. Aboubakr, Wear **376–377**, 1630 (2017)
2. W. Chuhong, F. Zoheir, J. George, K.H. Mohamed, A. Aboubakr, Surf. Coat. Technol. **334**, 526 (2018)
3. A. Mejias, R.T. Candidato, L. Pawłowski, D. Chicot, Surf. Coat. Technol. **298**, 93 (2016)
4. W.M. Seidl, M. Bartosik, S. Kolozsvári, H. Bolvardi, P.H. Mayrhofer, Surf. Coat. Technol. **347**, 92 (2018)
5. S. Bigelow, Y. Shen, Surf. Coat. Technol. **350**, 779 (2018)
6. A.S. Alaboodi, Z. Hussain, J. King Saud Univ.—Eng. Sci. 9 p (2017)
7. Y. Xiao, W. Shi, J. Luo, Vacuum **122**, 17 (2015)
8. J.L. He, S. Veprek, Surf. Coat. Technol. **163–164**, 374 (2003)
9. D.C. Drucker, W. Prager, Q. Appl. Math. **10**(2), 157 (1952)

Chapter 35
Nonsymmetrical Forced Oscillations of a Combined Polymeric Composite Shell of Revolution

V. G. Safronenko

Abstract Development and updating of mathematical models describing dynamics of stationary composite shells with the complex physical and mechanical properties takes one of the central places in the mechanics of thin-walled structures. The problem of reducing vibration levels and improving vibroacoustic and dissipative characteristics of shell structures is crucial for a wide range of applications in advanced technologies. Modern shell structures are, as a rule, geometrically complex and can be made up of the sections representing different shells of revolution. Mathematical and computer models for the stationary dynamics of multilayered combined composite shells of revolution under vibration load are proposed. The Timoshenko model is used, which takes into account the deformation of transverse displacement and rotation inertia. Constitutive equations of polymeric binding are applied, taking into account nonlinear and non-monotone dependence of physical and mechanical properties on both load frequency and temperature. For the numerical solution of the problem, the Fourier factorization method is used. The resulting system of equations of the normal type is solved with the sweep method. Non-symmetric forced oscillations of a combined cones-cylindrical polymeric composite shell are studied. Amplitude-frequency characteristics, forms of vibration and coordinates of points on the surface, at which transverse displacements have their maximum values, are numerically defined.

35.1 Introduction

The problem reducing vibration levels of shell structures is efficiently solved, when composite materials with high coefficients of internal dissipation of vibration energy are used.

V. G. Safronenko (✉)
I. I. Vorovich Mathematics, Mechanics and Computer Sciences Institute, Southern Federal University, Rostov-on-Don, Russia
e-mail: safron@math.sfedu.ru

I. A. Parinov et al. (eds.), *Advanced Materials*, Springer Proceedings in Physics 224, https://doi.org/10.1007/978-3-030-19894-7_35

It is well known that the anisotropy of physical and mechanical properties, increased compliance to transverse shear and high-nonlinear dependence of thermoviscoelastic properties of the polymer binding on the frequency, temperature and load are typical for polymer composites. Modern shell structures are usually geometrically complex and can be composed of sections, each representing different shells of revolution. The asymmetric nature of the external vibration load leads to the need to determine the areas of the greatest vibration activity in order to reduce it. The method of mathematical modeling and the experiment are the main methods of investigation, efficiently and economically feasible in the design of advanced thin-walled structures.

35.2 Methods

Let us consider forced oscillations of a combined shell made of a fiber composite, which depend on the type of boundary conditions as well as the volumetric fiber content and direction of reinforcement.

As the base for further calculations we shall use the Timoshenko type theory according to which the kinematic and strain ratio, recorded for the rotation shells, in conventional notation have the form [1, 2]:

$$
\begin{aligned}
&U(\alpha_1,\alpha_2,Z)=u(\alpha_1,\alpha_2)+z\varphi_1(\alpha_1,\alpha_2), V(\alpha_1,\alpha_2,z)=v(\alpha_1,\alpha_2)+z\varphi_2(\alpha_1,\alpha_2);\\
&W(\alpha_1,\alpha_2,z)=w(\alpha_1,\alpha_2);\\
&\varepsilon_{11}(\alpha_1,\alpha_2,z)=E_{11}(\alpha_1,\alpha_2)+zK_{11}(\alpha_1,\alpha_2);\quad (1\leftrightarrow 2)\\
&\varepsilon_{13}(\alpha_1,\alpha_2,z)=E_{13}(\alpha_1,\alpha_2);\quad (1\leftrightarrow 2)\\
&\varepsilon_{12}(\alpha_1,\alpha_2,z)=E_{12}(\alpha_1,\alpha_2)+zK_{12}(\alpha_1,\alpha_2);\varepsilon_{33}(\alpha_1,\alpha_2,z)=0.\\
&E_{11}=\frac{1}{A_1}\frac{\partial u}{\partial\alpha_1}+k_1w;\quad E_{22}=\frac{1}{A_2}\frac{\partial v}{\partial\alpha_2}+\psi u+k_2w;\\
&E_{13}=\varphi_1-\theta_1;\quad E_{23}=\varphi_2-\theta_2;\quad E_{12}=\frac{1}{A_1}\frac{\partial v}{\partial\alpha_1}+\frac{1}{A_2}\frac{\partial u}{\partial\alpha_2}-\psi v;\\
&K_{11}=\frac{1}{A_1}\frac{\partial\varphi_1}{\partial\alpha_1};\quad K_{22}=\frac{1}{A_2}\frac{\partial\varphi_2}{\partial\alpha_2}+\psi\varphi_1;\quad K_{12}=\left(\frac{1}{A_1}\frac{\partial\varphi_2}{\partial\alpha_1}\right)+k_1\left(\frac{1}{A_2}\frac{\partial u}{\partial\alpha_2}-\psi v\right)\\
&\quad+\left(\frac{1}{A_2}\frac{\partial\varphi_1}{\partial\alpha_2}-\psi\varphi_2\right)+k_2\left(\frac{1}{A_1}\frac{\partial v}{\partial\alpha_1}\right);\quad \theta_1=k_1u-\frac{1}{A_1}\frac{\partial w}{\partial\alpha_1};\quad \theta_2=k_2v-\frac{1}{A_2}\frac{\partial w}{\partial\alpha_2};
\end{aligned}
\tag{35.1}
$$

where $\psi=\frac{1}{A_1A_2}\frac{\partial A_2}{\partial\alpha_1}$.

Equations of harmonic oscillations, obtained from the Hamilton variational principle in conventional notation have the following form:

$$\begin{aligned}
&\frac{\partial T_{11}}{A_1\partial\alpha_1}+\psi(T_{11}-T_{22})+\frac{\partial S}{A_2\partial\alpha_2}+k_1Q_{11}+\Omega^2\rho_{11}u+q_1=0;\\
&\frac{\partial S}{A_1\partial\alpha_1}+2\psi S+\frac{\partial T_{22}}{A_2\partial\alpha_2}+k_2Q_{22}+\Omega^2\rho_{11}v+q_2=0;\\
&\frac{\partial Q_{11}}{A_1\partial\alpha_1}+\psi Q_{11}+\frac{\partial Q_{22}}{A_2\partial\alpha_2}-k_1T_{11}-k_2T_{22}+\Omega^2\rho_{11}w+q_3=0;\\
&\frac{\partial M_{11}}{A_1\partial\alpha_1}+\psi(M_{11}-M_{22})+\frac{\partial H}{A_2\partial\alpha_2}-\frac{1}{\varepsilon_1}Q_{11}+\Omega^2\rho_{12}\varepsilon_1\varphi_1=0;\\
&\frac{\partial H_{11}}{A_1\partial\alpha_1}+2\psi H+\frac{\partial M_{22}}{A_2\partial\alpha_2}-\frac{1}{\varepsilon_1}Q_{22}+\Omega^2\rho_{12}\varepsilon_1\varphi_2=0;
\end{aligned}\tag{35.2}$$

For combined shells of rotation, the conditions of conjugation of adjacent sections must be satisfied:

$$\begin{aligned}
&T_{11}^+=Q_1^-\cos\gamma^++T_3^-\sin\gamma^+;S^+=S^-;M_{11}^+=M_{11}^-;\\
&Q_{11}^+=Q_1^-\sin\gamma^+-T_3^-\cos\gamma^+;H^+=(\sin\gamma^-/\sin\gamma^+)H^-;\\
&u^+=u_1^-\cos\gamma^++u_3^-\sin\gamma^+;v^+=v^-;\varphi_1^+=\varphi_1^-;\\
&w^+=u_1^-\sin\gamma^+-u_3^-\cos\gamma^+;\varphi_2^+=\psi_2^-\sin\gamma^+-\psi_1^-\cos\gamma^+;\\
&u_1^-=u^-\cos\gamma^-+w^-\sin\gamma^-;u_3^-=u^-\sin\gamma^--w^-\cos\gamma^-;\\
&Q_1^-=T_{11}^-\cos\gamma^-+Q_{11}^-\sin\gamma^-;T_3^-=T_{11}^-\sin\gamma^--Q_{11}^-\cos\gamma^-;\\
&\psi_1=\varphi_2^-\cos\gamma^-;\psi_2=\varphi_2^-\sin\gamma^-.
\end{aligned}\tag{35.3}$$

Efficient physical and mechanical properties of a composite are determined by the properties of the isotropic components that make up this composite.

In the case of fiber-laminated composite, let E_f, v_f, G_f, V_f are the shear modulus, Poisson's ratio, shear modulus and volumetric fiber content of high modulus; E_m, v_m, G_m, are the complex analogs of the polymer matrix, respectively.

For a monolayer composite with the fibers arranged along the axis of symmetry (the winding angle $\beta = 0$) effective characteristics are present in [3]:

Longitudinal modulus: $E_1^k = E_fV_f + E_mV_m$;

Cross module: $E_2^k = \frac{eE_1^k}{(V_f+eV_m)(V_m+eV_f)-(ev_f-v_m)^2V_fV_m}$

Poisson's ratio: $v_1^k = v_fV_f + v_mV_m$

Shear moduli:

$$G_{12}^k=\frac{g(1+V_f)+V_m}{gV_m+1+V_f}G_f;\quad G_{23}^k=\frac{gG_m}{V_f+gV_m};\tag{35.4}$$

where $e=\frac{E_f}{E_m}$, $g=\frac{G_f}{G_m}$.

If we admit a sufficiently high saturation of the composite with the reinforcing fibers, we can claim with high accuracy that each monolayer is an orthotropic body, that is

$$\begin{aligned}&\sigma_{11}^k = C_{11}^k\varepsilon_{11}^k + C_{12}^k\varepsilon_{22}^k, \sigma_{22}^k = C_{12}^k\varepsilon_{11}^k + C_{22}^k\varepsilon_{22}^k;\\ &\sigma_{12}^k = 2C_{66}^k\varepsilon_{12}^k, \sigma_{23}^k = 2C_{44}^k\varepsilon_{23}^k; \sigma_{13}^k = 2C_{55}^k\varepsilon_{13}^k,\end{aligned} \tag{35.5}$$

where $\sigma_{ij}^k, \varepsilon_{ij}^k$ are the amplitudes of the corresponding stresses and strains; C_{ij}^k are the components of a complex matrix with the average hardness of the reinforced layer:

$$\begin{aligned}&C_{11}^k = \frac{E_1^k}{1-\nu_1\nu_2}; \quad C_{22}^k = \frac{E_2^k}{1-\nu_1\nu_2};\\ &C_{12}^k = \frac{\nu_1 E_2}{1-\nu_1\nu_2} = \frac{\nu_2 E_1}{1-\nu_1\nu_2};\\ &C_{44}^k = G_{23}^k; \quad C_{55}^k = G_{13}^k; \quad C_{66}^k = G_{12}^k.\end{aligned}$$

These equations are valid: $G_{12}^k = G_{13}^k$; $\nu_1^k E_2^k = \nu_2^k E_1^k$.

Constitutive correlations for stress and moments can be written as

$$\begin{aligned}&T_{11} = B_{11}E_{11} + B_{12}E_{22} + A_{11}K_{11} + A_{12}K_{22};\\ &T_{22} = B_{12}E_{11} + B_{22}E_{22} + A_{12}K_{11} + A_{22}K_{22};\\ &M_{11} = A_{11}E_{11} + A_{12}E_{22} + D_{11}K_{11} + D_{12}K_{22};\\ &M_{22} = A_{12}E_{11} + A_{22}E_{22} + D_{12}K_{11} + D_{22}K_{22};\\ &S = B_{33}E_{12} + 2A_{33}K_{12}; \quad H_{-} = A_{33}E_{12} + 2D_{33}K_{12};\\ &Q_{11} = G_{13}E_{13}; \quad Q_{22} = G_{23}E_{23};\end{aligned} \tag{35.6}$$

Here A_{ij}, B_{ij}, D_{ij} are the compliance stiffness defined by the formulae:

$$B_{ij} = h\sum_{k=1}^{m} C_{ij}^k; \quad A_{ij} = h\sum_{k=1}^{m} C_{ij}^k z_k; \quad D_{ij} = h\sum_{k=1}^{m} C_{ij}^k z_k^2; \quad i,j = 1,2;$$

$$B_{33} = h\sum_{k=1}^{m} C_{66}^k; \quad A_{33} = h\sum_{k=1}^{m} C_{66}^k z_k; \quad D_{33} = h\sum_{k=1}^{m} C_{66}^k z_k^2;$$

where m is the number of monolayers in the composite material; z_k is the coordinate of the gravity center of the monolayer section.

The stiffness matrix in the case of symmetric reinforcement for $\beta \neq 0$, is defined with the formulae of the coordinate system transformation [3]:

$$\begin{aligned}&C'_{11} = C_{11}c^4 + 2(C_{12}+2C_{66})c^2s^2 + C_{22}s^4;\\ &C'_{22} = C_{11}s^4 + 2(C_{12}+2C_{66})c^2s^2 + C_{22}c^4;\\ &C'_{12} = (C_{11}+C_{22}-4C_{66})c^2s^2 + \left(c^4+s^4\right)C_{12};\\ &C'_{66} = (C_{11}+C_{22}-2C_{12})c^2s^2 + 2C_{22}\left(c^2-s^2\right)cs + C_{66}\left(c^2-s^2\right)^2;\\ &C'_{44} = C_{44}c^2 + C_{55}s^2; \quad C'_{55} = C_{55}c^2 + C_{44}s^2;\end{aligned} \tag{35.7}$$

where C'_{ij} are the components of the transformed matrix; $c = \cos\beta$; $s = \sin\beta$; β is the angle of rotation around the z-axis of the new coordinate system with respect to the old one.

Further constitutive relationships for polymer binder are used [4]. Components of the complex compliance under I', I'' shear are represented by the functions of the cyclic frequency $\omega = 2\pi f$.

$$I'(\omega, T) = \int_{r_1}^{r_2} \frac{C(r)}{G(r, \upsilon, T)} \left(1 - H(r) \frac{\omega^2}{(\varphi(r, \upsilon, T))^2 + \omega^2}\right) \mathrm{d}r,$$

$$I''(\omega, T) = \int_{r_1}^{r_2} \frac{C(r)H(r)}{G(r, \upsilon, T)} \left(\frac{\varphi(r, \upsilon, T)\omega}{(\varphi(r, \upsilon, T))^2 + \omega^2}\right) \mathrm{d}r.$$

For the numerical study, an approach associated with the representation of required functions in the form of expansions in the Fourier series is used:

$$X(\alpha_1, \alpha_2) = \sum_{n=0}^{N} (X_{+n}(\alpha_1)\cos(n\alpha_2) + X_{-n}(\alpha_1)\sin(n\alpha_2).$$

After the district coordinate being separated and the ratios reset to a dimensionless form, a complex-valued system of the normal 10th order is obtained, which is solved by the orthogonal sweep method.

35.3 Numerical Experiment

As an example, consider the forced oscillations of a combined shell consisting of two sections. The first section has a cylindrical shape, the second section, coupled with it a conical shell. The load on the surface of the shell is located asymmetrically, according to the scheme shown in Fig. 35.1.

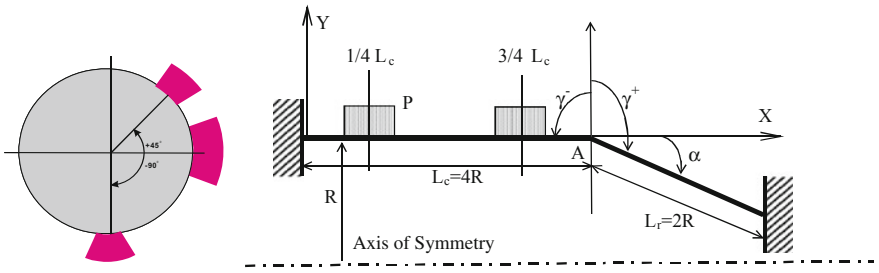

Fig. 35.1 Location of loading areas and combined shell profile

In our numerical experiment, forced oscillations of a combined shell of fiber composite with a polymer matrix were considered. The boundary conditions at the ends of the shells corresponded to those of the clamped edges and the hinged ones.

A variant of a five-layer composite with laying fibers along the generatrix and with a volume fiber content $V_f = 0.8$ is considered. Numerical results are obtained with a temperature $T = 290$ K and amplitude of loading $P = 10$ kPa. In the numerical solution of the problem, an algorithm for finding points at each frequency with the largest transverse deflection W_{max} was implemented. Figure 35.2 presents the cumulative amplitude-frequency characteristics of W_{max}. For Figs. 35.3 and 35.4 the coordinates of the greatest deflection points are given. The forms of forced vibrations of the structure calculated at the first resonance frequency $\Omega = 0.044$ in the longitudinal and transverse sections passing through the point of the greatest deflection, as well as a three-dimensional image of the deformed structure are shown in Fig. 35.5.

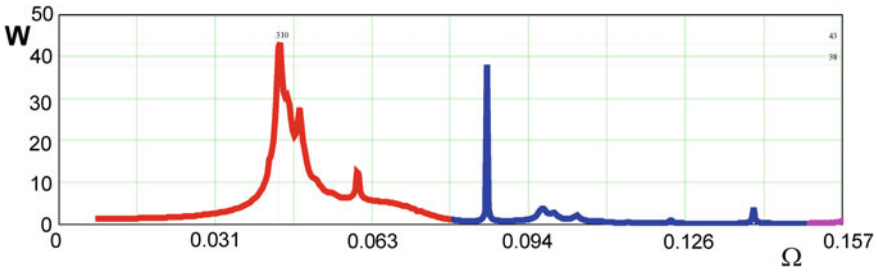

Fig. 35.2 Amplitude-frequency response $|W|_{max}$

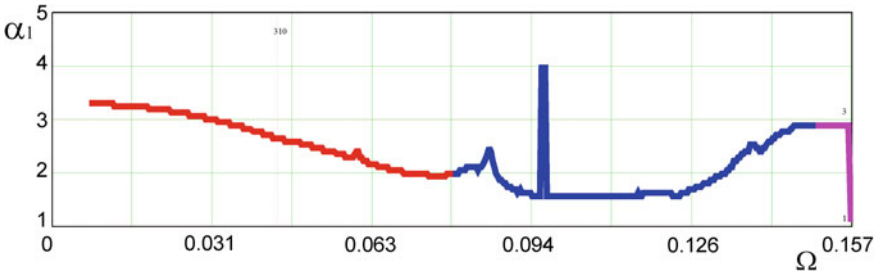

Fig. 35.3 Coordinate α_1 of maximum deflection

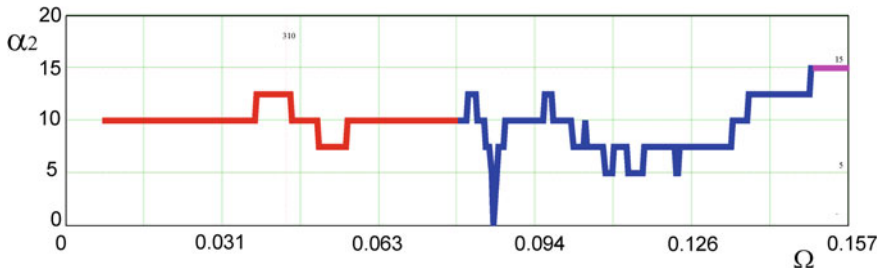

Fig. 35.4 Coordinate α_2 of maximum deflection

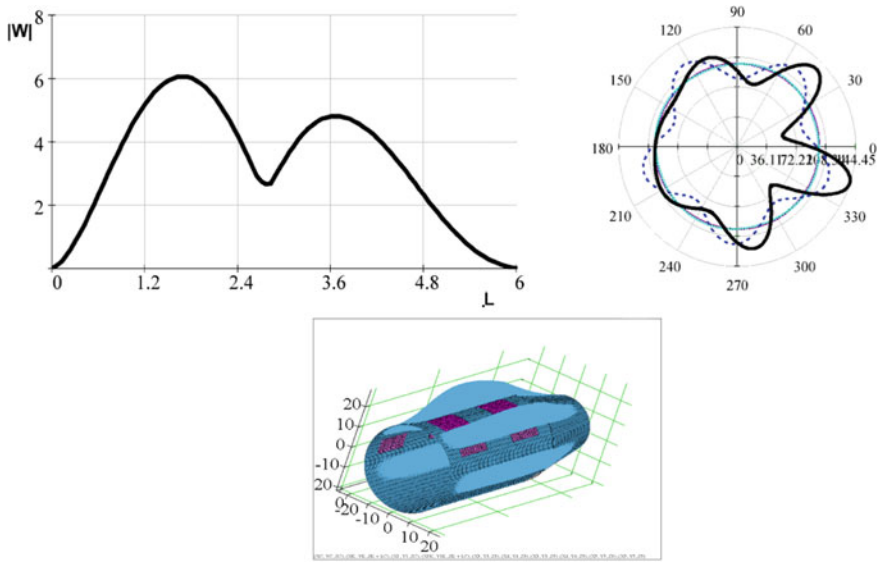

Fig. 35.5 Forms of forced oscillations and the image of the deformed construction

35.4 Conclusion

Mathematical and computer models for multilayered composite polymeric shells of revolution under the influence of vibration loadings have been developed. Non-symmetric forced oscillations of a combined cones-cylindrical polymeric composite shell is studied.

In particular, numerical and analytical approaches, based on the Fourier-series method, as well as the sweep method, were used. Amplitude-frequency characteristics, forms of vibration and coordinates of points on the surface, at which transverse displacements have their maximum values, are numerically defined.

References

1. E.I. Grigolyuk, G.M. Kulikov, *Multilayer Reinforced shell*s (Mashinostroenie, Moscow, 1988) 288 p (in Russian)
2. A.S. Yudin, V.G. Safronenko, *Vibroacoutics of Structurally-nongomogeneous Shells* (Southern Federal University Press, Rostov-on-Don, 2013) 424 p (in Russian)
3. R.M. Cristensen, *Mechanics of Composite Materials* (Mir, Moscow, 1982). 336 p (in Russian)
4. Y.P. Stepanenko, K.V. Isaev, A.D. Azarov, Modern problems of continuum mechanics, in *Proceedings of II International Conference*, vol. 1 (Rostov-on-Don, 1996) p. 118 (in Russian)

Chapter 36
Stress-Strain State of Transversally Isotropic Plane-Layer Constructions Under Pulse Loading

I. P. Miroshnichenko, I. A. Parinov and V. P. Sizov

Abstract The paper proposes the governing equations for determining the stress-strain state in plane-layer constructions made of transversely isotropic materials. They are obtained on the base of applying tensor relations for displacements, stresses and deformations of the generalized method of scalarization of dynamic elastic fields in transverse isotropic media. They allow us to calculate the stress-strain state in certain areas of the constructions under consideration, both during the pulse loading and after its completion. The effect of the anisotropy of the materials of the layers on the stress-strain state in the structures under consideration is studied, taking into account the features of the propagation of elastic waves in transverse isotropic materials.

36.1 Introduction, Original Relationships

At present, composite materials with the properties of transverse isotropic media are widely used in constructions for various purposes. This makes it relevant to develop scientific and methodological grounds for analyzing their stress-strain state under pulse loading in the process of quality control during manufacturing and for diagnostics of a condition during operation.

In [1], a generalized method for the scalarization of dynamic elastic fields in transverse isotropic media was proposed. According to [1], for a transverse isotropic medium, the tensor fields of displacements, stresses and strains can be expressed in terms of three scalar functions, φ, w, v describing quasi-longitudinal, quasi-transverse and transverse waves, respectively.

I. P. Miroshnichenko (✉) · V. P. Sizov
Don State Technical University, Rostov-on-Don, Russia
e-mail: ipmir@rambler.ru

I. A. Parinov
Southern Federal University, Rostov-on-Don, Russia

I. A. Parinov et al. (eds.), *Advanced Materials*, Springer Proceedings in Physics 224, https://doi.org/10.1007/978-3-030-19894-7_36

The general scheme for solving boundary problems of the dynamic theory of elasticity for transverse isotropic materials in this case remains the same as in the case of isotropic media.

Functions φ, w and v are the solutions of the Helmholtz wave equation with wave numbers $\overset{(L)}{g}$, $\overset{(T)}{g}$ and χ, respectively, for quasi-longitudinal, quasi-transverse and transverse waves (the index L refers to quasi-longitudinal waves, and the index T refers to quasi-transverse waves).

The full displacement field U_i for a transverse isotropic medium according to [1], taking into account all types of waves, through potential functions φ, w, v is written as follows:

$$U_i = \left(\overset{(L)}{D}_1 \nabla_i + \delta_i^J \overset{(L)}{D}_2 \nabla_J\right)\varphi + \left(\overset{(T)}{D}_1 \frac{1}{\overset{(T)}{g}} \nabla_i \nabla_J + \overset{(T)}{g}\, \delta_i^J\right) w + \sqrt{g}\left(\delta_i^K \nabla^N - \delta_i^N \nabla^K\right) v. \tag{36.1}$$

The full stress field σ_{ij} for a transverse isotropic medium according to [1], taking into account all types of waves, through potential functions φ, w, v, has the form:

$$\begin{aligned}\sigma_{ij} = &\left(\overset{(L)}{d}_1 g_{ij} + \overset{(L)}{d}_2 \delta_i^J \delta_j^J + \overset{(L)}{d}_3 \delta_{(i}^J \nabla_{j)} \nabla_J + \overset{(L)}{d}_4 \nabla_i \nabla_j\right)\varphi \\ &+ \left(\overset{(T)}{d}_1 g_{ij} \nabla_J + \overset{(T)}{d}_2 \delta_i^J \delta_j^J \nabla_J + \overset{(T)}{d}_3 \delta_{(i}^J \nabla_{j)} + \overset{(T)}{d}_4 \nabla_i \nabla_J \nabla_j\right) w \\ &+ 2\sqrt{g}\left[a_2\left(\nabla_{(i}\delta_{j)}^K \nabla^N - \nabla_{(i}\delta_{j)}^N \nabla^K\right) + a_4\left(\delta_{(i}^J \delta_{j)}^K \nabla^N - \delta_{(i}^J \delta_{j)}^N \nabla^K\right)\nabla_J\right] v,\end{aligned} \tag{36.2}$$

The full field of deformations U_{ij} for a transverse isotropic medium according to [1], which takes into account all types of waves, through potential functions φ, w, v is presented in the following form:

$$U_{ij} = \left(\overset{(L)}{D}_1 \nabla_i \nabla_j + \overset{(L)}{D}_2 \nabla_{(i}\delta_{j)}^J \nabla_J\right)\varphi + \left(\overset{(L)}{D}_1 \frac{1}{\overset{(T)}{g}} \nabla_i \nabla_j \nabla_J + \overset{(T)}{g}\, \nabla_{(i}\delta_{j)}^J\right) w + \sqrt{g}\left(\nabla_{(i}\delta_{j)}^K \nabla^N - \nabla_{(i}\delta_{j)}^N \nabla^K\right) v. \tag{36.3}$$

In relations (36.1)–(36.3) the notations are entered:

$$\overset{(L)}{D}_1 = \frac{\overset{(L)}{g^2}\, b_4}{b_3 - \left(\overset{(L)}{g^2} - \overset{(L)}{h^2}\right)(1 - b_4)}; \quad \overset{(L)}{D}_2 = \frac{\overset{(L)}{g^2}}{\overset{(L)}{h^2}} \frac{b_3 - \left(\overset{(L)}{g^2} - \overset{(L)}{h^2}\right) - b_4 \overset{(L)}{h^2}}{b_3 - \left(\overset{(L)}{g^2} - \overset{(L)}{h^2}\right)(1 - b_4)}; \tag{36.4}$$

$$\overset{(T)}{D}_1 = -\frac{\overset{(T)}{g^2}\, b_4}{b_3 - \left(\overset{(T)}{g^2} - \overset{(T)}{h^2}\right) - b_4 \overset{(T)}{h^2}}; \tag{36.5}$$

$$b_3 = \left(\omega^2 \rho - h^2 C_{44}\right)/C_{11}; \quad b_4 = (C_{13} + C_{44})/C_{11}; \tag{36.6}$$

$$\begin{aligned}
&\overset{(L)}{d}_1 = -\overset{(L)}{g^2}\, a_1 - h^2 a_3 \left(\overset{(L)}{D}_1 + \overset{(L)}{D}_2\right); \\
&\overset{(L)}{d}_2 = -\overset{(L)}{g^2}\, a_3 - h^2 \left(2a_4 \overset{(L)}{D}_2 + a_5 \overset{(L)}{D}_1 + a_5 \overset{(L)}{D}_2\right); \\
&\overset{(L)}{d}_3 = 2a_2 \overset{(L)}{D}_2 + 2a_4 \left(2\overset{(L)}{D}_1 + \overset{(L)}{D}_2\right); \quad \overset{(L)}{d}_4 = 2a_2 \overset{(L)}{D}_1;
\end{aligned} \tag{36.7}$$

$$\begin{aligned}
&\overset{(T)}{d}_1 = a_1 \overset{(T)}{g} \left(1 - \overset{(T)}{D}_1\right) + a_3 \left(\overset{(T)}{g} - \frac{\overset{(T)}{h^2}}{\overset{(T)}{g}} \overset{(T)}{D}_1\right); \\
&\overset{(T)}{d}_2 = a_3 \overset{(T)}{g} \left(1 - \overset{(T)}{D}_1\right) + 2a_4 \overset{(T)}{g} + a_5 \left(\overset{(T)}{g} - \frac{\overset{(T)}{h^2}}{\overset{(T)}{g}} \overset{(T)}{D}_1\right); \\
&\overset{(T)}{d}_3 = 2a_2 \overset{(T)}{g} + 2a_4 \left(\overset{(T)}{g} - 2\overset{(T)}{D}_1 \frac{\overset{(T)}{h^2}}{\overset{(T)}{g}}\right); \quad \overset{(T)}{d}_4 = 2a_2 \overset{(T)}{D}_1 \frac{1}{\overset{(T)}{g}};
\end{aligned} \tag{36.8}$$

$$\begin{aligned}
&a_1 = C_{12}; \quad a_2 = (C_{11} - C_{12})/2; \quad a_3 = C_{13} - C_{12}; \\
&a_4 = C_{44} - (C_{11} - C_{12})/2; \quad a_5 = C_{11} + C_{33} - 2(C_{13} + 2C_{44});
\end{aligned} \tag{36.9}$$

the constants C_{ij} are the elements of the matrix of elastic constants written according to the convolved index [2]; δ_i^J is the Kronecker symbol.

Wave numbers $\overset{(L)}{g}$, $\overset{(T)}{g}$ and χ are defined as follows:

$$g^2 = A_1 \pm \sqrt{A_1^2 - A_2^2}; \tag{36.10}$$

$$\chi^2 = 2\left(\omega^2\rho - C_{44}h^2\right)/(C_{11} - C_{12}) + h^2, \tag{36.11}$$

where ρ is the medium density and ω is the angular frequency;

$$A_1 = \left\{(C_{11} + C_{44})\omega^2\rho - [C_{11} - (C_{33} - 2C_{44}) - C_{13}(C_{13} + 2C_{44})]h^2\right\}/(2C_{11}C_{44});$$
$$A_2 = [C_{13}(C_{13} + C_{44}) + C_{44}(C_{11} + C_{13}) + C_{33}(C_{44} - C_{11})]h^4$$
$$- (C_{33} - C_{11})h^2\omega^2\rho + \omega^4\rho^2/(C_{11}C_{44}).$$

The sign of minus in expression (36.10) refers to the wave number $\overset{(L)}{g}$ of quasi-longitudinal waves, and sign of plus refers to the wave number $\overset{(T)}{g}$ of quasi-transverse waves.

To solve a specific problem, it is necessary to find a particular solution that corresponds to a given boundary conditions (see [4]).

36.2 Relationships to Determine the Stress-Strain State in Plane-Layer Constructions with Transverse Isotropic Layers

For plane-layer constructions with layers made of transverse isotropic materials, if the material symmetry axis of the layer materials coincides with the normal to their surface (the z-axis of the Cartesian coordinate system also coincides with the pointed normal), the displacement and stress components are expressed through scalar functions φ, w, v as follows:

$$U_z = \left(\overset{(L)}{D}_1 + \overset{(T)}{D}_1\right)\frac{\partial}{\partial z}\varphi + \left(-\overset{(T)}{D}_1\frac{\overset{(T)}{h^2}}{\overset{(T)}{g}} + \overset{(T)}{g}\right)w;$$

$$U_x = \overset{(L)}{D}_1\frac{\partial}{\partial x}\varphi + \overset{(T)}{D}_1\frac{1}{\overset{(T)}{g}}\frac{\partial^2}{\partial z\partial x}w + \frac{\partial}{\partial y}v;$$

$$U_y = \overset{(L)}{D}_1\frac{\partial}{\partial y}\varphi + \overset{(T)}{D}_1\frac{1}{\overset{(T)}{g}}\frac{\partial^2}{\partial z\partial y}w - \frac{\partial}{\partial x}v;$$

$$\sigma_{zz} = -\overset{(L)}{g}{}^2 C_{13} - \overset{(L)}{h}{}^2 (C_{33} - C_{13}) \left(\overset{(L)}{D}_1 + \overset{(L)}{D}_2 \right) \varphi$$
$$+ \left[\overset{(T)}{g} C_{13} \left(1 - \overset{(T)}{D}_1 \right) + (C_{33} - C_{13}) \left(\overset{(T)}{g} - \frac{\overset{(T)}{h}}{\overset{(T)}{g}} \overset{(T)}{D}_1 \right) \right] \frac{\partial}{\partial z} w;$$
$$\sigma_{zx} = C_{44} \left(2\overset{(L)}{D}_1 + \overset{(L)}{D}_2 \right) \frac{\partial^2}{\partial z \partial x} \varphi + C_{44} \left(\overset{(T)}{g} - \frac{\overset{(T)}{h}{}^2}{\overset{(T)}{g}} 2 \overset{(T)}{D}_1 \right) \frac{\partial}{\partial x} w + C_{44} \frac{\partial^2}{\partial z \partial y} v;$$
$$\sigma_{zy} = C_{44} \left(2\overset{(L)}{D}_1 + \overset{(L)}{D}_2 \right) \frac{\partial^2}{\partial z \partial y} \varphi + C_{44} \left(\overset{(T)}{g} - \frac{\overset{(T)}{h}{}^2}{\overset{(T)}{g}} 2 \overset{(T)}{D}_1 \right) \frac{\partial}{\partial y} w + C_{44} \frac{\partial^2}{\partial z \partial x} v. \tag{36.12}$$

From physical considerations we can put $\frac{\partial}{\partial y} = 0$ in relations (36.12), without limiting the generality. Then using the expansion of scalar functions φ, w, v in plane waves, relations (36.12), and considering only quasi-longitudinal and quasi-transverse waves, we can write the matrix $C(z)$ in the form:

$$C(z) = \begin{pmatrix} \widetilde{C_1} & \widetilde{C_2} \\ \widetilde{C_3} & \widetilde{C_4} \end{pmatrix} \widetilde{\Im}(z), \tag{36.13}$$

where

$$\widetilde{C_1} = \begin{pmatrix} i \overset{(L)}{h} \left(\overset{(L)}{D}_1 + \overset{(T)}{D}_1 \right) & -\overset{(T)}{D}_1 \frac{\overset{(T)}{h}{}^2}{\overset{(T)}{g}} + \overset{(T)}{g} \\ i\beta \overset{(L)}{D}_1 & -\overset{(T)}{h}\, \beta \overset{(T)}{D}_1 \frac{1}{\overset{(T)}{g}} \end{pmatrix};$$

$$\widetilde{C_3} = \begin{pmatrix} -\overset{(L)}{g}{}^2 C_{13} - \overset{(L)}{h}{}^2 (C_{33} - C_{13}) \left(\overset{(L)}{D}_1 + \overset{(L)}{D}_2 \right) & i \overset{(T)}{h} \left[\overset{(T)}{g}{}^2 C_{13} \left(1 - \overset{(T)}{D}_1 \right) + (C_{33} - C_{13}) \left(\overset{(T)}{g} - \frac{\overset{(T)}{h}{}^2}{\overset{(T)}{g}} \overset{(T)}{D}_1 \right) \right] \\ -\overset{(L)}{h}\, \beta C_{44} \left(2\overset{(L)}{D}_1 + \overset{(L)}{D}_2 \right) & i\beta C_{44} \left(\overset{(T)}{g} - \frac{\overset{(T)}{h}{}^2}{\overset{(T)}{g}} 2 \overset{(T)}{D}_1 \right) \end{pmatrix};$$

matrix blocks $\widetilde{C_2}$ and $\widetilde{C_4}$ coincide with $\widetilde{C_1}$ and $\widetilde{C_3}$, respectively, if the elements of the main diagonal $\widetilde{C_1}$ of the matrix and the secondary diagonal $\widetilde{C_3}$ of the matrix change the signs to the opposite;

$$\widetilde{\Im}(z) = \begin{pmatrix} e^{i\overset{(L)}{h}z} & 0 & & \\ & e^{i\overset{(T)}{h}z} & & \\ 0 & & e^{-i\overset{(L)}{h}z} & \\ & & & e^{-i\overset{(T)}{h}z} \end{pmatrix};$$

$\overset{(L)}{g}{}^2 = \overset{(L)}{h}{}^2 + \beta^2$; $\overset{(T)}{g}{}^2 = \overset{(T)}{h}{}^2 + \beta^2$.

For plane-layer constructions with the layers made of transverse isotropic materials, if the material symmetry axis of the layer materials is perpendicular to the normal to their surface (the z-axis of the Cartesian coordinate system coincides with the pointed normal), the displacement and stress components are expressed through scalar functions φ, w, v in the following way:

$$\begin{aligned}
U_z &= \overset{(L)}{D}_1 \frac{\partial}{\partial z}\varphi + \overset{(T)}{D}_1 \frac{1}{\overset{(T)}{g}} \frac{\partial^2}{\partial z \partial x} w - \frac{\partial}{\partial y} v; \\
U_x &= \left(\overset{(L)}{D}_1 + \overset{(T)}{D}_1\right) \frac{\partial}{\partial z}\varphi + \left(-\overset{(T)}{D}_1 \frac{\overset{(T)}{h}{}^2}{\overset{(T)}{g}} + \overset{(T)}{g}\right) w; \\
U_y &= \overset{(L)}{D}_1 \frac{\partial}{\partial y}\varphi + \overset{(T)}{D}_1 \frac{1}{\overset{(T)}{g}} \frac{\partial^2}{\partial y \partial x} w + \frac{\partial}{\partial z} v; \\
\sigma_{zz} &= \left(\overset{(L)}{d}_1 + \overset{(L)}{d}_4 \frac{\partial^2}{\partial z^2}\right)\varphi + \left(\overset{(T)}{d}_1 + \overset{(T)}{d}_4 \frac{\partial^2}{\partial z^2}\right) \frac{\partial}{\partial x} w - 2a_2 \frac{\partial^2}{\partial z \partial y} v; \\
\sigma_{zx} &= \left(\frac{1}{2}\overset{(L)}{d}_3 + \overset{(L)}{d}_4\right) \frac{\partial^2}{\partial z \partial x}\varphi + \left(\frac{1}{2}\overset{(T)}{d}_3 - \overset{(T)}{h}{}^2 \overset{(T)}{d}_4\right) \frac{\partial}{\partial x} w - (a_2 + a_4) \frac{\partial^2}{\partial x \partial y} v; \\
\sigma_{zy} &= \overset{(L)}{d}_4 \frac{\partial^2}{\partial z \partial y}\varphi + \overset{(T)}{d}_4 \frac{\partial^3}{\partial x \partial y \partial z} w + a_2 \left(\frac{\partial^2}{\partial z^2} - \frac{\partial^2}{\partial y^2}\right) v.
\end{aligned} \tag{36.14}$$

In the case of a two-dimensional problem $\left(\frac{\partial}{\partial y} = 0\right)$, for the quasi-longitudinal and quasi-transverse waves, we obtain the following expressions of matrices $C(z)$:

$$C_1 = \begin{pmatrix} i\overset{(L)}{\beta}\overset{(L)}{D_1} & -\overset{(T)}{D_1}h\overset{(T)}{\beta}/\overset{(T)}{g} \\ ih\left(\overset{(L)}{D_1}+\overset{(L)}{D_2}\right) & -\overset{(T)}{D_1}h^2/\overset{(T)}{g}+\overset{(T)}{g} \end{pmatrix};$$

$$C_{(3)} = \begin{pmatrix} \overset{(L)}{d_1}-\overset{(L)}{d_4}\overset{(L)}{\beta}^2 & ih\left(\overset{(T)}{d_1}-\overset{(T)}{d_4}\overset{(T)}{\beta}^2\right) \\ -\left(\frac{1}{2}\overset{(L)}{d_3}+\overset{(L)}{d_4}\right)\overset{(L)}{\beta}h & i\overset{(T)}{\beta}\left(\frac{1}{2}\overset{(T)}{d_3}-h^2\overset{(T)}{d_4}\right) \end{pmatrix}; \tag{36.15}$$

$$F = F(z) = \begin{pmatrix} \Im & 0 \\ 0 & \Im^{-1} \end{pmatrix}; \quad \Im = \begin{pmatrix} \exp(i\overset{(L)}{\beta}z) & 0 \\ 0 & \exp(i\overset{(T)}{\beta}z) \end{pmatrix}; \tag{36.16}$$

$$\overset{(L)}{h} = \overset{(T)}{h} = h; \quad \overset{(L)}{g}^2 = \overset{(L)}{\beta}^2 + h^2; \quad \overset{(T)}{g}^2 = \overset{(T)}{\beta}^2 + h^2. \tag{36.17}$$

Further, the solution of specific problems is performed according to the well-known method described in [4]. For example, to calculate the stress-strain state in a three-layer construction from [4], we have:

$$\begin{aligned} B_3 &= C_3\Im_{23}\psi_3; \\ B_2 &= C_2C_2^{\uparrow -1}C_3^{\downarrow}\Im_{23}\psi_3; \\ B_1 &= C_1C_1^{\uparrow -1}C_2^{\downarrow}C_2^{\uparrow -1}C_3^{\downarrow}\Im_{23}\psi_3, \end{aligned} \tag{36.18}$$

where B_n is a state vector-column composed of the components of displacements and stresses included in the boundary conditions for a specific problem (see [4]); n is the number of the layer in the construction (1, 2, 3, for this example); $\Im_{23} = \exp(ihx)$; ψ_3 is the vector-column of the amplitudes of scalar functions for waves traveling in the forward and reverse directions in the third layer of the construction (see [4]); the arrow $\uparrow$ indicates the outer boundary of the layer, and the $\downarrow$ presents inner boundary.

In the one-dimensional case, when waves propagate along the axis of the material symmetry of the materials of the layers, we obtain:

$$\overset{(L)}{g}^2 = \omega^2\rho/C_{33}; \quad \overset{(T)}{g}^2 = \omega^2\rho/C_{44}; \tag{36.19}$$

$$\overset{(L)}{D_1} = 1; \quad \overset{(T)}{D_1} = 1; \quad \overset{(L)}{D_2} = 0. \tag{36.20}$$

In the one-dimensional case of wave propagation along the normal to the surface of the layers, we obtain:

$$\overset{(L)}{g}{}^2 = \omega^2\rho/C_{11}; \quad \overset{(T)}{g}{}^2 = \omega^2\rho/C_{44}; \tag{36.21}$$

$$\begin{gathered}\overset{(L)}{D}_1 = 1; \quad \overset{(L)}{h}\,\overset{(L)}{D}_2 \to 0; \quad \overset{(T)}{D}_1 = \frac{b_4\,\overset{(T)}{g}{}^2}{\overset{(L)}{g}{}^2 - \overset{(T)}{g}{}^2}; \\ \overset{(L)}{d}_1 - \overset{(L)}{d}_4\,\beta^2 = -\overset{(L)}{g}{}^2\,C_{11}; \quad \frac{1}{2}\overset{(T)}{d}_3 - \overset{(T)}{h}\,\overset{(T)}{d}_4 = \overset{(T)}{g}\,C_{44}.\end{gathered} \tag{36.22}$$

Hence, the matrix (36.15) and its inverse matrix can be written as follows:

$$\begin{aligned}C = &\begin{pmatrix} i\overset{(L)}{g} & 0 & i\overset{(L)}{g} & 0 \\ 0 & \overset{(T)}{g} & 0 & -\overset{(T)}{g} \\ -\overset{(L)}{g}{}^2 C_{11} & 0 & -\overset{(L)}{g}{}^2 C_{11} & 0 \\ 0 & i\overset{(T)}{g}{}^2 C_{44} & 0 & i\overset{(T)}{g}{}^2 C_{44} \end{pmatrix} \\ &\times \begin{pmatrix} \exp\left(i\overset{(L)}{g}\,z\right) & 0 & 0 & 0 \\ 0 & \exp\left(i\overset{(T)}{g}\,z\right) & 0 & 0 \\ 0 & 0 & \exp\left(-i\overset{(L)}{g}\,z\right) & 0 \\ 0 & 0 & 0 & \exp\left(-i\overset{(T)}{g}\,z\right) \end{pmatrix};\end{aligned} \tag{36.23}$$

$$\begin{aligned}C^{-1} = &\begin{pmatrix} \exp\left(-i\overset{(L)}{g}\,z\right) & 0 & 0 & 0 \\ 0 & \exp\left(-i\overset{(T)}{g}\,z\right) & 0 & 0 \\ 0 & 0 & \exp\left(i\overset{(L)}{g}\,z\right) & 0 \\ 0 & 0 & 0 & \exp\left(i\overset{(T)}{g}\,z\right) \end{pmatrix} \\ &\times \begin{pmatrix} \frac{i}{2\overset{(L)}{g}} & 0 & \frac{1}{2\overset{(L)}{g}{}^2 C_{11}} & 0 \\ 0 & \frac{1}{2\overset{(T)}{g}} & 0 & \frac{i}{2\overset{(T)}{g}{}^2 C_{44}} \\ \frac{i}{2\overset{(L)}{g}} & 0 & \frac{1}{2\overset{(L)}{g}{}^2 C_{11}} & 0 \\ 0 & \frac{1}{2\overset{(T)}{g}} & 0 & \frac{i}{2\overset{(T)}{g}{}^2 C_{44}} \end{pmatrix}.\end{aligned} \tag{36.24}$$

By using these relations, we obtain the equations of eigenfrequencies in explicit form for one anisotropic layer of thickness H:

$$F^{-}\left(z_{s1}z_{s2}\right) = F^{+}\left(z_{s2}z_{s1}\right) = \begin{pmatrix} \exp\left(i \overset{(L)}{g} H\right) & 0 \\ 0 & \exp\left(i \overset{(T)}{g} H\right) \end{pmatrix};$$

$$\overset{(1)}{\Gamma} = \overset{(2)}{\Gamma} = -C_{(4)}^{-1}C_{(3)} = -E; \quad Q = \begin{pmatrix} \exp\left(i2 \overset{(L)}{g} H\right) & 0 \\ 0 & \exp\left(i2 \overset{(T)}{g} H\right) \end{pmatrix}.$$

The equation of natural frequencies has the form:

$$\left[1 - \exp\left(i2 \overset{(L)}{g} H\right)\right]\left[1 - \exp\left(i2 \overset{(T)}{g} H\right)\right] = 0, \tag{36.25}$$

where

$$\overset{(L)}{g}{}^2 = \omega^2\rho/C_{11}; \quad \overset{(T)}{g}{}^2 = \omega^2\rho/C_{44}.$$

As we can see, the resonant frequency spectrum is equidistant, which should be for a single layer. Note, however, that since in all cases we have:

$$\begin{aligned} C_{(1)} &= \begin{pmatrix} C_{11} & C_{12} \\ C_{21} & C_{22} \end{pmatrix}; \quad C_{(2)} = \begin{pmatrix} -C_{11} & C_{12} \\ C_{21} & -C_{22} \end{pmatrix}; \\ C_{(3)} &= \begin{pmatrix} C_{31} & C_{32} \\ C_{41} & C_{42} \end{pmatrix}; \quad C_{(4)} = \begin{pmatrix} C_{31} & -C_{32} \\ -C_{41} & C_{42} \end{pmatrix}, \end{aligned} \tag{36.26}$$

then for the reflection coefficients from the free boundary, the expression is true:

$$\Gamma_{св} = -\frac{1}{\Delta}\begin{pmatrix} C_{31}C_{42} + C_{41}C_{32} & 2C_{42}C_{32} \\ 2C_{31}C_{41} & C_{31}C_{42} + C_{41}C_{32} \end{pmatrix}, \tag{36.27}$$

where $\Delta = C_{31}C_{42} - C_{41}C_{32}$,

but from the hard border:

$$\Gamma_{жс} = \frac{1}{\Delta}\begin{pmatrix} C_{11}C_{22} + C_{12}C_{21} & 2C_{22}C_{12} \\ 2C_{11}C_{21} & C_{11}C_{12} + C_{12}C_{21} \end{pmatrix}, \tag{36.28}$$

where $\Delta = C_{11}C_{22} - C_{12}C_{21}$.

Moreover, for $\det\Gamma$ we have:

$$\begin{aligned}\det\Gamma_{св} &= -\det C_{(4)}^{-1}\cdot\det C_{(3)} = -1;\\ \det\Gamma_{ж} &= -\det C_{(1)}^{-1}\cdot\det C_{(2)} = 1.\end{aligned} \tag{36.29}$$

Expressions (36.29) are in accordance with the law of energy conservation, when there are no active energy losses and radiation losses.

Matrices C can be used to study various degenerate cases when the energy of elastic waves propagates along the interface of the conjugation of layers. In particular, it is possible to obtain the dispersion relations that determine the wave numbers of surface waves. The components of the field in this case are also determined by the matrix C. In order to find the dispersion equation, it is sufficient to equate Δ to zero. So for the free boundary we have:

$$\Delta = C_{31}C_{42} - C_{41}C_{32} = 0. \tag{36.30}$$

For the case when the axis of the main symmetry coincides with the normal to the surface of the structure we obtain:

$$\begin{aligned}&-\left(\overset{(T)}{g} - \frac{\overset{(T)}{h^2}}{\overset{(T)}{g}} 2\overset{(T)}{D_1}\right)\left[\overset{(L)}{g^2}C_{13} + \overset{(L)}{h^2}\left(C_{33} - C_{13}\right)\left(\overset{(L)}{D_1} + \overset{(L)}{D_2}\right)\right]\\ &+ \overset{(L)}{h}\,\overset{(T)}{h}\left(2\overset{(L)}{D_1} + \overset{(L)}{D_2}\right)\left[\overset{(T)}{g}C_{13}\left(1 - \overset{(T)}{D_1}\right) + \left(C_{33} - C_{13}\right)\left(\overset{(T)}{g} - \frac{\overset{(T)}{h^2}}{\overset{(T)}{g}}\overset{(T)}{D_1}\right)\right] = 0.\end{aligned} \tag{36.31}$$

Substituting the values of $\overset{(L)}{h^2} = \overset{(L)}{g^2} - \beta^2$ and $\overset{(T)}{h^2} = \overset{(T)}{g^2} - \beta^2$ into this expression find the equation for the definition β. Real roots at $\beta > g$ correspond to surface waves in an anisotropic half-space, when the axis of principal symmetry coincides with the normal to the surface of the construction.

As an example, we consider the nonstationary problem of internal stresses in a semi-infinite elastic transverse isotropic medium arising under the action of a pulse loading with a given space-time distribution applied to a part of its surface.

In the Cartesian coordinate system, when the axis of the main symmetry of the transverse isotropic medium is parallel to the plane of the boundary $z = 0$ and coincides with the x-axis, it is possible to obtain the design relations for stresses in an explicit form:

$$\sigma_{zz} = \frac{1}{(2\pi)^2}\iint_{-\infty}^{\infty}\left[\left(\overset{(l)}{d}_1 - \overset{(l)}{d}_4\beta_{(l)}^2\right)e^{i\beta_{(l)}z}\varphi_1 + ih\left(\overset{(\tau)}{d}_1 - \overset{(\tau)}{d}_4\beta_{(\tau)}^2\right)e^{i\beta_{(\tau)}z}W_1\right]e^{ihx}e^{-i\omega t}dhd\omega;$$

$$\sigma_{zx} = \frac{1}{(2\pi)^2}\iint_{-\infty}^{\infty}\left[\left(\frac{1}{2}\overset{(l)}{d}_3 + \overset{(l)}{d}_4\right)h\beta_{(l)}^2e^{i\beta_{(l)}z}\varphi_1 - i\beta_{(\tau)}\left(\frac{1}{2}\overset{(\tau)}{d}_3 - h^2\overset{(\tau)}{d}_4\right)\right.$$
$$\left.\times e^{i\beta_{(\tau)}z}W_1\right]e^{ihx}e^{-i\omega t}dhd\omega;$$

$$\sigma_{xx} = \frac{1}{(2\pi)^2}\iint_{-\infty}^{\infty}\left[\left(\overset{(l)}{d}_1 + \overset{(l)}{d}_2 - \overset{(l)}{d}_3h^2 + \overset{(l)}{d}_4h^2\right)e^{i\beta_{(l)}z}\varphi_1 + ih\left(\overset{(\tau)}{d}_1 + \overset{(\tau)}{d}_2 + \overset{(\tau)}{d}_3 - \overset{(\tau)}{d}_4h^2\right)\right.$$
$$\left.\times e^{i\beta_{(\tau)}z}W_1\right]e^{ihx}e^{-i\omega t}dhd\omega; \tag{36.32}$$

where

$$\varphi_1 = \frac{\beta_{(\tau)}\left(\frac{1}{2}\overset{(\tau)}{d}_3 - \overset{(\tau)}{d}_4h^2\right)\sigma_0(\xi,\omega)}{\left(\overset{(l)}{d}_1 - \overset{(l)}{d}_4\beta_{(l)}^2\right)\beta_{(\tau)}\left(\frac{1}{2}\overset{(\tau)}{d}_3 - \overset{(\tau)}{d}_4h^2\right) + h^2\beta_{(l)}\left(\frac{1}{2}\overset{(l)}{d}_3 + \overset{(l)}{d}_4\right)\left(\overset{(\tau)}{d}_1 - \beta_{(\tau)}^2\overset{(\tau)}{d}_4\right)};$$

$$W_1 = \frac{-i\xi\beta_{(l)}\left(\frac{1}{2}\overset{(l)}{d}_3 + \overset{(l)}{d}_4\right)\sigma_0(\xi,\omega)}{\left(\overset{(l)}{d}_1 - \overset{(l)}{d}_4\beta_{(l)}^2\right)\beta_{(\tau)}\left(\frac{1}{2}\overset{(\tau)}{d}_3 - \overset{(\tau)}{d}_4h^2\right) + h^2\beta_{(l)}\left(\frac{1}{2}\overset{(l)}{d}_3 + \overset{(l)}{d}_4\right)\left(\overset{(\tau)}{d}_1 - \beta_{(\tau)}^2\overset{(\tau)}{d}_4\right)};$$

$\sigma_0(\xi,\omega)$ is the angle-frequency spectrum of pulse loading.

36.3 Example of the Calculation of the Stress-Strain State in Plane-Layer Constructions with Transverse Isotropic Layers

Using the described calculation relationships we calculated the stresses in the plates, made of two different transverse isotropic materials, when exposed to a single pressure pulse (time dependence as a Gaussian function with duration τ). The pressure distribution over the surface was also represented in the form of a Gaussian function (with width a).

The characteristics of material *I* were set as follows: C_{11} = 6.43 GPa; C_{12} = 1.95 GPa; C_{13} = 0.563 GPa; C_{33} = 1.48 GPa; C_{44} = 0.5 GPa; ρ = 1650 g/m^3.

The characteristics of material *II* differed by value of C_{11} = 3 GPa.

For the material *I* with more pronounced anisotropy, the ratio of the propagation speeds of quasi-longitudinal waves in two mutually perpendicular directions $\overset{(l)}{V}(90°)/\overset{(l)}{V}(0°) = 2.07$, for the material *II* this ratio is equal to 1.42.

Figure 36.1 shows the stress levels σ_{zz} (dashed line) and σ_{zx} at time $t = 0$, when the pressure on the surface reaches its maximum value.

Figure 36.2 shows the results of the calculation of stresses σ_{zz} in the material *I* (dashed line) and in the material *II* at $t = 0.4\tau$.

Analysis of the results, shown in Fig. 36.2, demonstrates that the pressure pulse expands by spreading in the material and its amplitude decreases. In the material *II*, the expansion along the *x*-axis is greater than in the material *I*.

Figure 36.3 shows the distribution of tangential stresses σ_{zx} in materials *I* and *II* over the depth of the plates under the middle of the area of application of the pressure pulse ($x = 0$) at $t = 0$.

In accordance with [3], in the isotropic elastic half-space, the highest shear stress arises at a depth of $0.25a$.

As can be seen from Fig. 36.2, in the considered anisotropic materials, the maximum σ_{zx} is at a distance $(0.3–0.4)a$ from the surface, while in a material with a smaller anisotropy, the maximum σ_{zx} is closer to the surface.

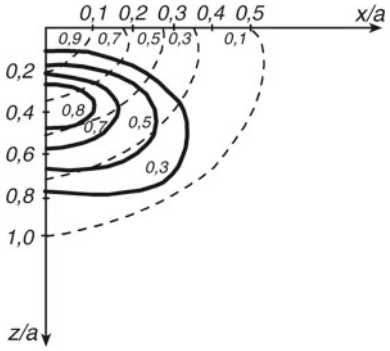

Fig. 36.1 Stress levels σ_{zz} and σ_{zx} at time $t = 0$

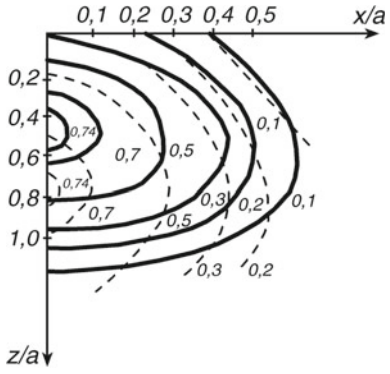

Fig. 36.2 Stress distributions σ_{zz} in materials *I* and *II* at $t = 0.4\tau$

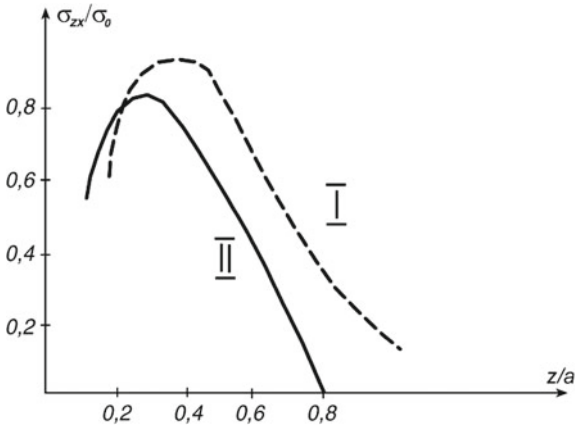

Fig. 36.3 Distributions of tangential stresses σ_{zx} in materials *I* and *II* on the depth of the plates

36.4 Conclusion

The calculation relationships have been proposed for determining the stress-strain state in plane-layer constructions made of transverse isotropic materials. These relationships were obtained on the base of applying tensor relations for displacements, stresses and strains of the generalized method of scalarization of dynamic elastic fields in transverse isotropic media [1]. They allow us to calculate the stress-strain state in specified areas of the structures under consideration, both during the pulse loading and after its completion. For example, the effect of the anisotropy of layer materials on the stress-strain state in the constructions under consideration is studied, taking into account the peculiarities of the propagation of elastic waves in transverse isotropic materials.

The described results expand and complement the scientific and methodological grounds for determining the stress-strain state in layered constructions made of transverse isotropic materials proposed in [4–9]. The results obtained are most appropriate to use in the development of new designs of products for various purposes in mechanical engineering, shipbuilding, and aircraft manufacturing. These results can also be used to control the quality of plane-layer constructions during production and diagnostics of their state during operation.

Acknowledgements The work was supported by the grant of Russian Foundation for Basic Research, No. 19-08-00365, Ministry of Education and Science of the Russian Federation: projects Nos. 3.5378.2017/VU (organization of the implementation of researches), 9.9770.2017/BCh (the basic part of the state task).

References

1. V.P. Sizov, Izv. SSSR AS Mech. Solids **5**, 55 (1988)
2. F.I. Fedorov, *Theory of Elastic Waves in Crystals* (Nauka, Moscow, 1965), p. 386
3. J.A. Zukas, T. Nikolas, H.F. Swift, L.B. Greszczuk, D.R. Curran, *Impact Dynamics* (Wiley, N. Y., 1982), 452 p.
4. V.P. Sizov, I.P. Miroshnichenko, *Excitation of Elastic Waves in Layered Anisotropic Constructions* (LAP LAMBERT Academic Publishing, Saarbrucken, Germany, 2012), 270 p. (in Russian)
5. V.P. Sizov, I.P. Miroshnichenko, in *Physics and Mechanics of New Materials and Their Applications*, ed. by I.A. Parinov, S.-H. Chang (Nova Science Publishers, New York, 2013), p. 203
6. I.P. Miroshnichenko, in *Advanced Materials. Physics, Mechanics and Applications*, ed. by S.-H. Chang, I.A. Parinov, V.Y. Topolov. Springer Proceedings in Physics, vol. 152 (Springer International Publishing, Switzerland, 2014), p. 163
7. I.P. Miroshnichenko, V.P. Sizov. in *Advanced Materials. Studies and Applications*, ed. by I.A. Parinov, S.-H. Chang, S. Theerakulpisut (Nova Science Publishers, New York, 2015), p. 353
8. I.P. Miroshnichenko. in *Proceedings of the 2015 International Conference on "Physics, Mechanics of New Materials and Their Applications"*, ed. by I.A. Parinov, S.-H. Chang, V.Y. Topolov (Nova Science Publishers, New York, 2016), p. 509
9. I.P. Miroshnichenko. in *Advanced Materials—Techniques, Physics, Mechanics and Applications*, ed. by I.A. Parinov, S.-H. Chang, M.A. Jani. Springer Proceedings in Physics, vol. 193 (Springer, Cham, Heidelberg, New York, Dordrecht, London, 2017), p. 435

Chapter 37
On the Wave Propagating Along the Plate-like Waveguide

Lyubov I. Parinova

Abstract Wave processes in an elastic plate-like waveguide were studied. The functional was obtained on the base of the Hamilton–Ostrogradsky variational principle. The theory of plates with variable stiffness was applied. The approximate Ritz method was used. Results were obtained for two materials. One material is isotropic, and the second material is orthotropic. A comparison of the wave number values for a wave of a plate waveguide propagating along the edge and a Konenkov's wave was carried out in the isotropic case.

37.1 Introduction

The study of vibration processes in elastic bodies with extended boundaries is important for mechanics and acoustics. New methods of non-destructive testing are being developed based on the study of the propagation of elastic waves. These technologies allow us to detect hidden defects in various structures. The results of solving the problems of natural oscillations are used in aerospace engineering, shipbuilding and instrument making.

An important part of this research is the study of the characteristics of the surface acoustic wave propagation. A body with extended boundaries can be considered as a topographic waveguide with infinite length. The properties of elastic waves propagating along a waveguide depend on the geometric characteristics of this elastic structure.

The first surface acoustic waves were described by Lord Rayleigh (J. Strett) in 1885. He considered a solid elastic half-space bordering with a vacuum. Lord Rayleigh studied waves that ran along the surface of the globe, but did not penetrate

L. I. Parinova (✉)
I. I. Vorovich Mathematics, Mechanics and Computer Sciences Institute, Southern Federal University, Rostov-on-Don, Russia
e-mail: parinovali@mail.ru

I. A. Parinov et al. (eds.), *Advanced Materials*, Springer Proceedings in Physics 224, https://doi.org/10.1007/978-3-030-19894-7_37

deep into it. It was theoretically demonstrated that the amplitude of waves propagating in the near-surface layer along the formed boundary coincides with the depth.

In 1960, the propagation of a bending wave along the free edge of a semi-infinite plate was investigated by Konenkov [1]. It is shown that this elastic wave attenuates, when it propagates away from the edge. It is interesting to note that the studies of the Soviet scientist were not known in other countries. Similar results were repeated by another scientists only in 1974.

The first studies of waves propagating in topographic elastic waveguides were carried out in the early 1970s. These wave processes were investigated by Lagasse. For the first time, wedge waves were described. At that time, the finite element method was used to calculate the surface wave velocities. Special attention was paid to investigation of the isotropic medium. In this particular case, there is no dispersion. In the result of calculations, the localization of the wave field was shown near the edge of the wedge.

The propagation of an acoustic wave along the edge of an infinite triangular waveguide made from orthotropic material was studied in 2005. In [2], the velocities of wedge waves were calculated by using a variational approach. The obtained results were compared with the data, obtained by the geometric-acoustic theory.

The study of wave processes in a rigidly clamped wedge of finite height was performed in [3]. By using a variational approach, a waveguide with a triangular cross-section was explored. A more general case was observed in [4], where a waveguide of finite height with a trapezoidal cross-section was considered. The special cases were investigated and a solution of the problem explored in [3] was confirmed.

The purpose of the present work is to study the propagation of an acoustic wave along the edge of a plate-like infinite waveguide. The study is based on the Ritz method and the Hamilton–Ostrogradsky variational principle. A comparison is made between the wavenumbers of the elastic wave, propagating along the edge of a plate-like waveguide, and the Konenkov's bending wave. Dispersion dependences are constructed in the orthotropic case.

37.2 Mathematical Problem Formulation

The topographic waveguide is a rather extended elastic structure with inhomogeneities on the surface. The geometry of the surface affects the properties of the waveguide of this type. Topographic waveguides are characterized by a strong localization of the wave field energy, a weak dispersion and insignificant losses.

Let us consider the surface acoustic wave propagating along the plate-like waveguide (see Fig. 37.1a). The orthotropic material and the isotropic material are considered. The elastic symmetry axes coincide with the coordinate axes in these materials. The length of the finite plate of the plate-like waveguide is equal to $2l$.

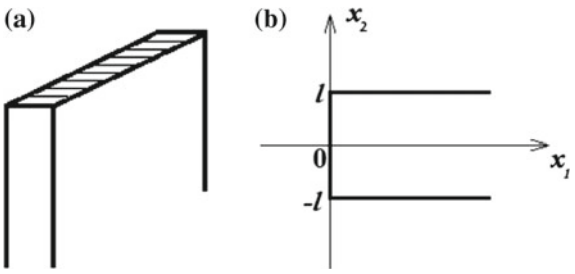

Fig. 37.1 **a** Topographic waveguide with a rectangular cross-section, **b** the waveguide section in Ox_1x_2-plane

This waveguide can be considered as a semi-infinite plate. The waveguide section in Ox_1x_2-plane is shown in Fig. 37.1b.

Boundaries of the plate are free from stresses. The method presented in the papers [2–4] is used to solve the problem. The presentation of the functional was obtained in these papers. We search the solution of the problem as a displacement vector in the form:

$$u_m(x_1, x_2, x_3, t) = U_m(x_1, x_2)\mathrm{e}^{i(\gamma x_3 - \omega t)}, \quad j = 1, 2, 3 \tag{37.1}$$

where γ is the wavenumber, ω is the oscillation frequency, $U_m(x_1, x_2)$ are the wave amplitudes.

Let us introduce the following dimensionless parameters:

$$\begin{aligned} &\frac{C_{11}}{C_{55}} = \gamma_1, \quad \frac{C_{22}}{C_{55}} = \gamma_2, \quad \frac{C_{33}}{C_{55}} = \gamma_3, \quad \frac{C_{12}}{C_{55}} = \gamma_5, \\ &\frac{C_{23}}{C_{55}} = \gamma_7, \quad \frac{C_{13}}{C_{55}} = \gamma_8, \quad \frac{\rho\omega^2 l^2}{C_{55}} = \kappa^2, \quad \gamma l = \gamma_0 \end{aligned} \tag{37.2}$$

where C_{ij} are elastic constants for orthotropic media, ρ is the material density, γ_0 is a dimensionless wavenumber and κ is a frequency parameter, for which the homogeneous boundary-value problem has a non-zero solution.

Based on the Hamilton–Ostrogradsky principle, it was shown in the works [2, 3] that the study of wave processes in the waveguide can be reduced to finding the stationary value of a certain quadratic functional M, and in this case:

$$M[U_i] = \int_S M_0 \mathrm{d}S \tag{37.3}$$

and the integrand has the form:

$$\begin{aligned} M_0 = {} & (\gamma_1 U_{1,1} + \gamma_5 U_{2,2} + i\gamma\gamma_8 U_3)\overline{U_{1,1}} + (\gamma_5 U_{1,1} + \gamma_2 U_{2,2} + i\gamma\gamma_7 U_3)\overline{U_{2,2}} \\ & + (\gamma_8 U_{1,1} + \gamma_7 U_{2,2} + i\gamma\gamma_3 U_3)\overline{iU_3} + \gamma_5 (U_{1,2} + U_{2,1})\overline{(U_{1,2} + U_{2,1})} \\ & + \gamma_8 (i\gamma U_1 + U_{3,1})\overline{(i\gamma U_1 + U_{3,1})} + \gamma_7 (i\gamma U_2 + U_{3,2})\overline{(i\gamma U_2 + U_{3,2})} \\ & - \kappa^2 (U_1^2 + U_2^2 + U_3^2) \end{aligned} \tag{37.4}$$

From the condition of stationarity of the functional, we have $\delta M[U_i] = 0$, and it is necessary to find the value of γ_0 on κ, for which the variational equation has a non-zero solution.

With this aim, we introduce the new variables:

$$\frac{x_1}{l} = z, \gamma_0^2 = \mu, \tag{37.5}$$

Based on the generalized hypotheses of the theory of anisotropic plates with variable stiffness, the constructing problem of dispersion relation reduces to the finding stationary value of a functional [4]:

$$M[W] = \int_0^\infty M_0 \mathrm{d}z, \tag{37.6}$$

where in the considered case of the waveguide

$$M_0 = \left(\gamma_1 W_{,zz}^2 - 2\gamma_8 \mu W_{,zz} W + \gamma_3 W^2 \mu^2 + 4\mu W_{,z}^2\right) - \kappa^2 \left(W_{,z}^2 - W^2 \mu + 3W^2\right). \tag{37.7}$$

To find the stationary value of the functional $M[W]$, we will use one of the approximate methods, namely the Ritz method [5]. In accordance with the requirements for coordinate functions, the solution $W(z)$ will be sought in the class of functions that are bounded at $z = 0$. These functions decrease rapidly for $z \to +\infty$, too.

We search the solution $W(z)$ in the form:

$$W = \exp(-\alpha z) \cdot \sum_{j=1}^{N} c_j \phi_j(z), \tag{37.8}$$

and as functions, it is chosen the system of coordinate functions $\phi_j(z) = z^{j-1}$, $j = 1, 2, \ldots, \alpha$ is a constant. Then functional (37.6) takes the form of a quadratic function of N variables:

$$M(c_1, c_2 \ldots c_N) = \int_0^\infty M_1 \mathrm{d}z, \quad \text{where } M_1 = M_1(c_1, c_2 \ldots c_N, z). \tag{37.9}$$

From the condition of stationarity of functional M, a homogeneous system of linear algebraic equations is found in respect to the factors c_k, $k = 1, 2, \ldots, N$. By equating the determinant of this system of linear equations to zero, we obtain an approximate dispersion algebraic equation connecting κ with γ_0.

37.3 Results and Discussion

We studied a convergence of the Ritz method in the dependence on the number of coordinate functions. Computational experiments were performed for two materials. The first material was isotropic (namely, carbon steel) and had the dimensionless parameters: $\gamma_1 = 3$, $\gamma_3 = 3$, $\gamma_8 = 1$. The second material was orthotropic (namely, barite) and had dimensionless parameters: $\gamma_1 = 3.15$, $\gamma_3 = 3.72$, $\gamma_8 = 0.96$.

A comparison of the wavenumber of an elastic wave, propagating along the edge of a plate-like waveguide, and corresponding known parameter of the Konenkov's edge bending wave was made in isotropic case.

The first approximation for the quadratic function (37.9) with $\alpha = \gamma_0$ in (37.8) was considered; in this case $N = 1$.

Then the dispersion dependence had the form:

$$\gamma_0^4(\gamma_1 - 2\gamma_8 + \gamma_3 + 4) - 3\kappa^2 = 0, \tag{37.10}$$

where the wavenumber parameter was present as

$$\gamma_0 = \sqrt[4]{\frac{3\kappa^2}{\gamma_1 - 2\gamma_8 + \gamma_3 + 4}} \tag{37.11}$$

The elastic constants in the isotropic case are present as

$$\begin{aligned} C_{11} &= C_{22} = C_{33} = \lambda + 2\mu \\ C_{12} &= C_{13} = C_{23} = \lambda \\ C_{55} &= C_{66} = C_{44} = \mu \end{aligned} \tag{37.12}$$

From (37.10)–(37.12), we obtained in the isotropic case:

$$\gamma_0 = d_1 \cdot \sqrt{\kappa}, \tag{37.13}$$

where $d_1 = \sqrt[4]{\frac{3}{8}}$.

In this notation, the wavenumber for the Konenkov's bending edge wave, described in the paper [1], is found in the form:

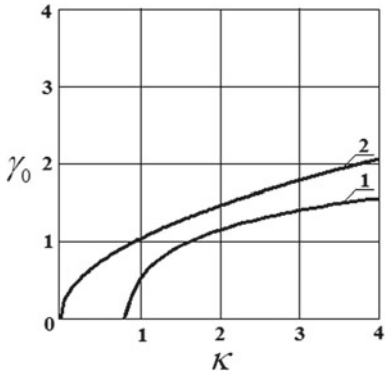

Fig. 37.2 Dispersion dependences of the wavenumber γ_0 on the parameter κ for carbon steel

$$\gamma_0 = d_2\sqrt{\kappa}, \tag{37.14}$$

where $d_2 = \sqrt[4]{\frac{3(1-\nu)}{2}}$, ν is Poisson's ratio.

Then we consider the case of $\alpha = 0$. To compare the acoustic wave, propagating along the edge of the plate-like waveguide, with the Konenkov's bending edge wave, the corresponding dependences of the wavenumber γ_0 on the parameter κ are plotted in isotropic case in Fig. 37.2. Curves 1 and 2 correspond to the dispersion dependence for the acoustic wave propagating along the edge plate-like waveguide and the Konenkov's wave, respectively.

The dependence $\gamma_0(\kappa)$ is shown in Table 37.1, too. The different numbers of coordinate functions are studied and the results for the Konenkov's wave are present. A monotonic increase of the characteristic values of the Ritz method with the rise of the number of coordinate functions is stated. The relative difference of the values for the Konenkov's wave and the wave, propagating along the waveguide edge, corresponding to $N = 6$, is shown in the last column of Table 37.1.

Table 37.1 Values of γ_0 for carbon steel

κ	Konenkov's wave	γ_0 depending on the number of coordinate functions						The relative difference (%)
		$N = 1$	$N = 2$	$N = 3$	$N = 4$	$N = 5$	$N = 6$	
1	1.030	0.514	0.860	0.902	0.913	0.917	0.920	10.7
2	1.456	1.144	1.194	1.204	1.207	1.207	1.208	17.0
3	1.784	1.399	1.400	1.402	1.402	1.402	1.402	21.4
4	2.060	1.554	1.588	1.605	1.617	1.617	1.617	21.5
5	2.303	1.659	1.815	1.815	1.844	1.862	1.866	19.0

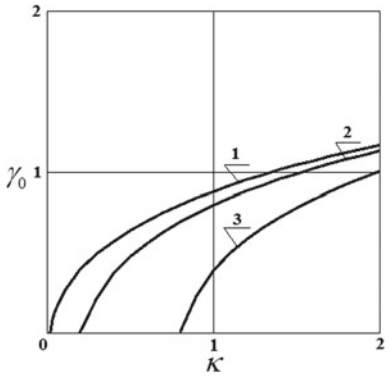

Fig. 37.3 Dispersion relations for the plate-like waveguide $(N = 5)$ for case of barite

Table 37.2 Values of the locking point depending on the number of coordinate functions

Number of coordinate functions	$N = 1$	$N = 2$	$N = 3$	$N = 4$	$N = 5$
Value of the locking point	0.888	0.230	0.101	0.056	0.036

Based on the constructed algorithm, the natural oscillations of the orthotropic plate-like waveguide were investigated, too. Dispersion dependencies were constructed by using five coordinate functions. They are shown in Fig. 37.3 and curves 1, 2, 3 correspond to the first, second and third modes of oscillation, respectively.

The dispersion curve, corresponding to the first mode does not go out from the coordinate origin point. For different coordinate functions, so-called locking points were found. These points define the values of the frequency parameter κ for $\gamma_0 = 0$ (the points of intersections of the curves with κ-axis). Values of the locking points are present in Table 37.2.

It can be seen that the value of the smallest locking point approaches the coordinate origin point with increasing number of coordinate functions. The dependence $\gamma_0(\kappa)$ for barite is present in Table 37.3. The results show a monotonous relation.

To obtain sufficiently accurate results for the first and the second dispersion curve it is sufficient to use three and four coordinate functions, respectively.

Table 37.3 Values γ_0 for wave propagating along the plate-like waveguide made of barite

No. mode	κ	Number of coordinate functions			
		$N = 1$	$N = 2$	$N = 3$	$N = 4$
The first mode	1	0.468	0.827	0.863	0.863
	2	1.102	1.152	1.160	1.161
	3	1.355	1.356	1.360	1.360
	4	1.513	1.543	1.564	1.577
	5	1.621	1.768	1.769	1.801
The second mode	1	–	–	0.411	0.714
	2	–	–	1.013	1.103
	3	–	0.784	1.292	1.312
	4	–	1.288	1.494	1.428
	5	–	1.463	1.507	1.519
The third mode	2	–	–	–	0.673
	3	–	–	–	1.168
	4	–	–	–	1.401
	5	–	–	0.757	1.504

37.4 Conclusion

By using the variational approach and the Ritz method, taking into account the theory of plates of variable stiffness, a method for the studying wave processes in plate-like orthotropic waveguides has been developed. The obtained results are compared with similar values of the Konenkov's edge bending wave. Dispersion curves are investigated and the features of their construction are revealed.

Acknowledgements The author is very grateful to Prof. A. O. Vatulyan for constant attention to this research.

References

1. Yu.K. Konenkov. Acoust. J. **6**(1), 124 (1960) (In Russian)
2. A.O. Vatulyan, L.I. Parinova. Vestnik DGTU **5**(4), 491 (2005) (In Russian)
3. A.O. Vatulyan, L.I. Parinova, in *Advanced Materials—Techniques, Physics, Mechanics and Applications*, Springer Proceedings in Physics, ed. by I.A. Parinov, S.-H. Chang, M.A. Jani, vol. 193, (Springer Cham, Heidelberg, New York, Dordrecht, London, 2017), p. 309
4. A.O. Vatulyan, L.I. Parinova, News of Higher Educational Institutions. North-Caucasus Region **3**, 10 (2018) (In Russian)
5. V.S. Blistanov, V.S. Bondarenko, N.V. Peremolova et al., in *Acoustic Crystals: Handbook*, ed. by M.P. Shaskol'skaya (Moscow, Nauka, 1982), 632 p (In Russian)

Chapter 38
Identification of Zones of Local Hydrogen Embrittlement of Metals by the Acoustoelastic Effect

Kseniya Frolova, Vladimir Polyanskiy, Dmitriy Tretyakov and Yuri Yakovlev

Abstract In this paper, we present the results of the investigation of statistical correlations between local plastic deformation distributions, the acoustic anisotropy magnitude, and concentrations of hydrogen dissolved in corset samples. Pirson's correlation coefficients with values up to 0.95 were obtained. These coefficients designate the relationship between large hydrogen concentrations in the local areas of the samples and the acoustic anisotropy magnitude. The obtained results make it possible to establish that contribution of concentrations of the dissolved hydrogen to the acoustic anisotropy is much greater than contribution of the nonlinear elasticity (acoustoelastic effect). The obtained data allow one to develop new methods for the destructive control of hydrogen embrittlement.

38.1 Introduction

The share of new materials used in industry is permanently increasing. For example, mass fraction of high-strength steels in the body of a modern car is about 70%. Usually the effect of hydrogen existence on these materials is significant. Mass concentration of hydrogen equal to 0.2 ppm leads to decrease of the tensile strength of new high-strength steels by one and a half to two times [1]. In its turn, this entails a critical effect of hydrogen at a concentration of six atoms per million atoms of the metal matrix.

High hydrogen sensitivity leads to the changing of a role of the hydrogen embrittlement. In traditional metals, it was necessary to accumulate dozens of ppm of hydrogen [2]. The concentrations were equalized in the metal volume due to diffusion [2]. As a rule, large cracks propagated [3].

V. Polyanskiy (✉) · D. Tretyakov
Peter the Great Saint-Petersburg Polytechnic University, St. Petersburg, Russia
e-mail: vapol@mail.ru

K. Frolova · V. Polyanskiy · Y. Yakovlev
Institute for Problems in Mechanical Engineering RAS, St. Petersburg, Russia

I. A. Parinov et al. (eds.), *Advanced Materials*, Springer Proceedings in Physics 224, https://doi.org/10.1007/978-3-030-19894-7_38

The critical concentrations of hydrogen in modern materials are so small that they can accumulate locally. This fact significantly complicates the diagnostics of hydrogen embrittlement. Spectral analysis of ultrasonic signals [4, 5], sound velocity measurement [5] as well as ultrasonic scanning [6] do not have sufficient sensitivity. The hydrogen embrittlement detecting method based on measurement of the absolute sound velocity has another drawback. Namely, this velocity depends on many factors, and therefore in practice it is impossible to separate the influence of temperature, microstructure and hydrogen on its value [7, 8].

Our investigations allow one to consider the acoustoelasticity method [9–11] as one of methods for monitoring the metal damage under loading [12, 13]. An important feature of this method is that the measured data of the value of acoustic anisotropy depend only on the initial anisotropy of the material, mechanical stresses, plastic deformations and damage [11, 13, 14]. We obtained the relation between the acoustic anisotropy magnitude and the residence time of hydrogen charging of the sample in a corrosive solution.

The problem of local nature of the acoustic anisotropy method remains important from practical point of view, since according to the theory of this method [9, 10], the acoustic anisotropy magnitude is affected by the metal mechanical characteristics averaged along the path of the sound wave.

38.2 Research Method

38.2.1 Acoustic Experiments

The acoustoelasticity method, based on measurement of the acoustic anisotropy, makes it possible to evaluate mechanical stresses occurring in structures. In this sense, it is an alternative method to the tensometric ones. It is standardized [4] and widely used in modern technical diagnostics [5]. Unlike diagnostic methods using electro-magnetic properties of metals, the method of acoustoelasticity is standardized precisely as a method for monitoring internal mechanical stresses. The method is provided with serial measuring equipment.

In this regard, it is enough to have a reference sample or an unloaded section of a structure made of the same material. A great advantage of this method is the possibility to obtain mechanical stresses averaged along the material thickness. In this case, the thickness of the metal can be 5 mm or more. Thus, it is one more reason indicating that this method advantageously differs from the tensometry, since the last allows one to measure only deformations of the material surface. Measuring sensors are easily installed by using special grease. Measurements can be carried out quickly, in the express mode.

The essence of the method is to measure the relative difference of the propagation velocities of a transverse acoustic ultrasonic wave with different polarizations v_1 and v_2:

$$\Delta a = 2(v_1 - v_2)/(v_1 + v_2).$$

Parameter Δa is called the acoustic anisotropy.

In the basic work [6], it was theoretically explained and experimentally confirmed that in the case of pure elastic deformations the acoustic anisotropy Δa is proportional to the difference of the principal stresses $\sigma_1 - \sigma_2$.

At the same time, the constructions use metal rolling. Consequently, the metal of the structure is preliminarily subjected to plastic deformation. Plastic deformations contribute to the value of the acoustic anisotropy. In [7–9] it was experimentally obtained that in this case the following expression holds:

$$\Delta a = a_0 + a_1 \cdot \left(\varepsilon_1^p - \varepsilon_2^p\right) + C_A(\sigma_1 - \sigma_2), \tag{38.1}$$

where $\varepsilon_1^p, \varepsilon_2^p$ are the principal plastic deformations, σ_1 and σ_2 are the principal stresses, C_A is an experimentally obtained value, $a_0 + a_1\left(\varepsilon_1^p - \varepsilon_2^p\right)$ is interpreted as the contribution of the anisotropic microstructure of the metal to the value Δa.

The effect of elastic deformations is described by the term $C_A(\sigma_1 - \sigma_2)$, which is physically related to the displacement of the atoms of the crystal lattice from the equilibrium position under the action of internal mechanical stresses.

According to our investigations [14, 15], the formation of a microcracks system can lead to appearance of an additional contribution to (38.1), which can be rewritten in the following way:

$$\Delta a = a_0 + a_1\left(\varepsilon_1^p - \varepsilon_2^p\right) + C_A(\sigma_1 - \sigma_2) + a_2 \tag{38.2}$$

where the term a_2 is associated with the formation of microcracks.

No every plastic deformation leads to metal cracking. At the same time, elastic deformations also are not related for the microcracks formation. So, the term a_2 cannot be included in other components of the equation and must be considered separately.

Acoustic anisotropy was measured by a IN5101A device, which realized the shock generation of ultrasonic waves in the tested body and received the reflected signal by piezotransducers. The three-component piezotransducer radiates and receives one longitudinal wave and two transverse waves polarized in mutually perpendicular directions. Appropriate software permits carrying out precision measurements of the time of propagation of the ultrasonic wave through the body thickness. The time lags between several reflected pulses are measured and averaged to increase the accuracy. The value of the acoustic anisotropy is calculated as the ratio of the difference between time lags of the reflected pulse of polarized transverse wave to the half-sum of these times. In this case, the first wave is polarized along of the line of the load application direction and the second wave is polarized in the perpendicular direction.

We used flat corset samples cut from industrial rolled metal to realize the experiments. Samples from commercially pure aluminum and three grades of steels,

Fig. 38.1 Measurement of acoustic anisotropy: 1—corset sample in the test machine, 2—IN5101A device with piezotransducers

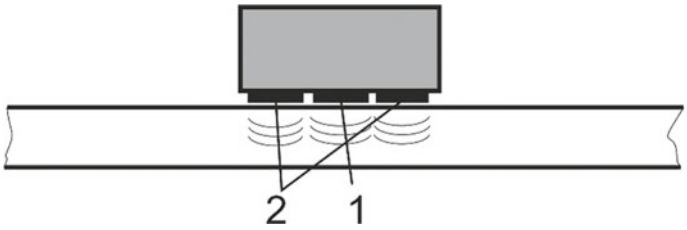

Fig. 38.2 Scheme of the piezotransducers of IN5101A device; 1—piezotransducer of a longitudinal wave, 2—piezotransducers of transverse waves

namely, A192, 5L Gr X-6, F-522, VNS-5 were investigated. The thickness of the samples is varied from 5 to 20 mm. Measurement of acoustic anisotropy is shown in Fig. 38.1.

In case of standard measurements, plates emitting three different types of waves are spaced approximately one centimeter apart, as shown in Fig. 38.2.

It makes difficult to look for local anomalies with the magnitude of the acoustic anisotropy. To increase the resolution, the device with the piezotransducers moved

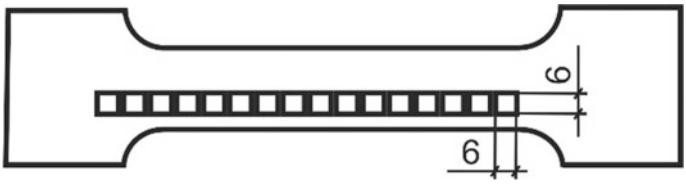

Fig. 38.3 Scheme of the samples cutting for hydrogen testing

along a special grid, as shown in Fig. 38.1. The grid spacing was the same as the spacing between the piezoelectric plates. Thus, resolution for detection of local anomalies of the order of 10 mm was obtained by data imposing measured for different positions of the piezotransducers.

38.2.2 Hydrogen Experiments

We carried out different mechanical tests for corset samples, namely, static stretching and cyclic loading. Measurement of hydrogen concentration was carried out by using the standard industrial mass spectrometric analyzer of hydrogen AB-1. The analyzer operation is based on the Vacuum Hot Extraction (VHE) method [16, 17]. The measurement process is described in detail in [18, 19].

In order to measure the volumetric distribution of hydrogen concentrations in corset samples, they were cut into small prismatic samples with a cross-section equal to 6×6 mm^2. The cutting scheme is shown in Fig. 38.3.

The samples cutting was performed by a handsaw, so that the metal did not overheat and the hydrogen concentration was not changed.

A mass spectrometric analyzer of hydrogen allows one to realize measurements at various temperatures of hot vacuum extraction. In terns, it allows one to specify several temperature points for Vacuum Hot Extraction. Such points make it possible to separate hydrogen with different binding energies and to isolate diffusively-mobile hydrogen from the entire volume of hydrogen dissolved in the sample.

38.2.3 Mechanical Testing

Mechanical tests were carried out by applying the INSTRON machines.

One of the machines is present in Fig. 38.1. The load parameters were chosen in such a way that plastic deformation of the samples was occurring during the whole loading or one loading cycle. Some samples were loaded up to destruction, whereas some of them were not destroyed. Measurements of the distribution of the acoustic

anisotropy were made directly under the loading and after the destruction of the samples.

Measurements of the hydrogen concentration distribution were carried out for unloaded samples after measurements of the acoustic anisotropy.

In addition to the distribution of the acoustic anisotropy and hydrogen concentration, the thickness of the sample was measured in the site of location of the sensor. In case of the plastic flow, the thickness of the sample varies non-uniformly and the characteristic Lüder's bands are observed. Within these bands the deformation value is much bigger than the average one. The measurements were realized by an electronic micrometer with accurate to 0.01 mm.

38.3 Results and Discussion

The acoustic anisotropy distributions along the sample, made of technically pure aluminum and underwent significant plastic deformation equal to 28%, were obtained. Herewith, an appreciable non-uniformity of the plastic deformation magnitude was observed. Lüder's bands observable on the surface had a width of about 2–3 cm and were oriented perpendicular to the tensile forces applied to the specimen.

Distribution of the acoustic anisotropy in the sample is shown in Fig. 38.4. Values of the acoustic anisotropy were measured for two or three points placed at the same distance x from the origin of the working part of the sample.

Distribution of the thickness of the sample is shown in Fig. 38.5. The corresponding measurements were made in the middle of the site on which the acoustic anisotropy sensor plate was positioned.

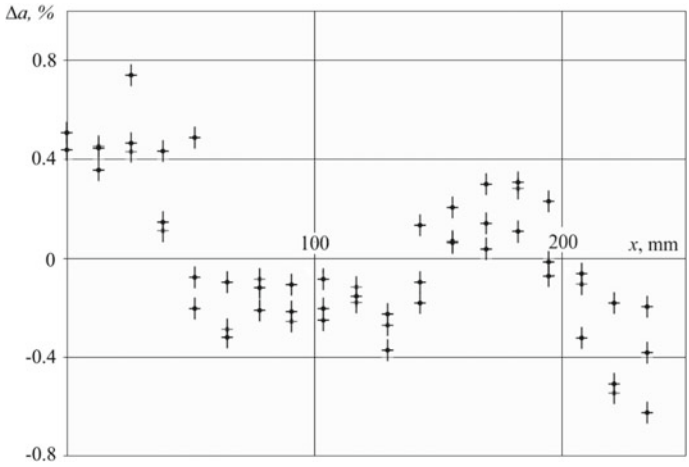

Fig. 38.4 Acoustic anisotropy versus coordinate x along the sample

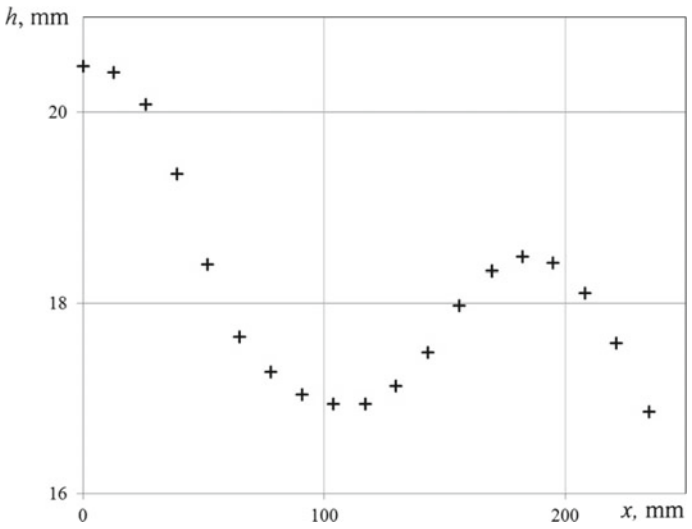

Fig. 38.5 Thickness of the sample after plastic deformation versus coordinate x along the sample

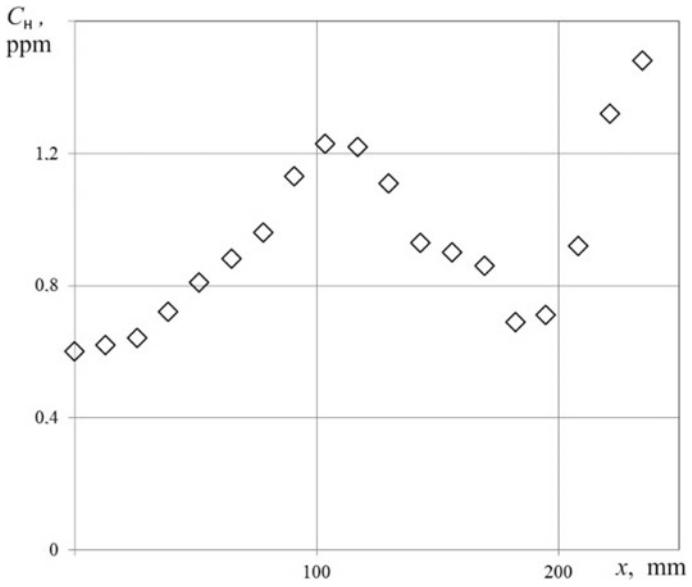

Fig. 38.6 Average concentration of dissolved hydrogen after plastic deformation versus coordinate x along the sample

Distribution of the average hydrogen concentrations in the same sample is shown in Fig. 38.6.

Pearson's correlation coefficients between the acoustic anisotropy and the sample thickness and between the acoustic anisotropy and hydrogen concentration are 0.83 and 0.79, respectively. In its turn, this makes it possible to assume a linear correlation of these quantities.

Similar results characterized by a correlation coefficient ranging from 0.72 to 0.78 were obtained for various steel samples.

It turned out that correlation between distribution of the acoustic anisotropy and distribution of the average concentration of dissolved hydrogen is better in case of aluminum alloys. For several samples, the correlation coefficient reached a value of 0.95.

Comparison of hydrogen concentrations before and after the plastic deformation showed that during the plastic deformation the average concentration of dissolved hydrogen increases.

We conducted an additional investigation. We manually ground the surface layer of the experiment samples to a depth of the order of 0.5–1 mm for aluminum samples and 60–100 μm for steel ones before measuring of hydrogen concentration. Removal of the surface layer led to the average hydrogen concentration decrease, as well as to the correlation coefficient drop to values of the order of 0.07–0.1.

Thus, an almost linear relationship between the hydrogen concentration in the surface layer and the value of the acoustic anisotropy takes place.

We would like to note that the acoustic anisotropy variations caused by the saturation of the thin surface layer of the metal with hydrogen are significantly (from 2 to 6 times) greater than the variations associated with the direct acoustoelastic effect arising due to mechanical stresses.

This makes it possible to establish reliable correlation dependencies between local areas of a metal with an increased hydrogen concentration and leaps observed for the acoustic anisotropy distribution over the metal surface.

This important result is in some measure confirmed by the data presented in [7]. In contrast with these findings, our measurements made for a hydrogenated material allow us to obtain the magnitude of the acoustic anisotropy, which is less subjected to temperature fluctuations and practically unrelated to the metal heat treatment method, as in case of large plastic deformations. Our results makes it possible to indicate the range of this magnitude variation associated with mechanical stresses for whole groups of metals [15, 20].

38.4 Conclusion

Multipurpose investigations consisting of mechanical tests, measurements of the acoustic anisotropy magnitude distribution and measurement of the distribution of hydrogen concentrations in metallic samples after mechanical testing were performed. We got a set of distributions of quantities along the axis of mechanical loading of the sample.

Statistical analysis of Pearson's correlation coefficients corresponding to the obtained distributions allows one to conclude that the value of the acoustic anisotropy correlates well with the concentration of hydrogen dissolved in a thin surface layer of the samples.

The correlation coefficient of several samples takes the value 0.95. This fact indicates availability of a linear dependence of the magnitude of acoustic anisotropy on the local hydrogen concentration. This dependence makes it possible to perform non-destructive testing of local hydrogen embrittlement by the acoustoelasticity method.

Acknowledgements The financial support by the Siemens scholarship program is acknowledged.

References

1. A.N. Solovyev, Y. Nie, Y. Kimura, T. Inoue et al., Metall. Mater. Trans. A **43**(5), 1670 (2012)
2. J.P. Hirth, Metall. Trans. A **11**(6), 861 (1980)
3. J.E. Costa, A.W. Thompson, Metall. Trans. A **13**(7), 1315 (1982)
4. S.E. Krüger, J.M.A. Rebello, P.C. De Camargo, NDT & E Int. **32**(5), 275 (1999)
5. P. Senior, J. Szilard, Ultrasonics **22**(1), 42 (1984)
6. J. Kittel, V. Smanio, M. Fregonese, L. Garnier, X. Lefebvre, Corros. Sci. **52**(4), 1386 (2010)
7. A.M. Lider, V.V. Larionov, G.V. Garanin, M.K. Krening, Tech. Phys. **58**(9), 1395 (2013)
8. S.K. Lawrence, B.P. Somerday, M.D. Ingraham, D.F. Bahr, Ultrasonic methods. JOM **1** (2018)
9. D.S. Hughes J.L. Kelly, Phys. Rev. **92**(5), 1145 (1953)
10. M. Hirao, Y.H. Pao, J. Acoust. Soc. Am. **77**(5), 1659 (1985)
11. Y.H. Pao, *Solid Mechanics Research for Quantitative Non-destructive Evaluation* (Springer, Netherlands, 1987), p. 257
12. A.K. Belyaev et al., Mech. Solids **51**(5), 606 (2016)
13. A.K. Belyaev et al., Procedia Struct. Integrity **6**, 201 (2017)
14. E.L Alekseeva, et al., Stroitel'stvo Unikal'nyh Zdanij i Sooruzenij **12**, 33 (2016) (In Russian)
15. E.L. Alekseeva et al., AIP Conf. Proc. **1915**(1), 030001 (2017)
16. E. Petushkov, A. Tserfas, T. Maksumov, in *Secondary Emission and Structural Properties of Solids*, ed. by U. Arifov (Springer US, 1971), p. 107
17. J. Konar, N. Banerjee, NML Tech. J. **16**(1–2), 18 (1974)
18. A. Polyanskiy, V. Polyanskiy, Y.A. Yakovlev, Int. J. Hydrogen Energy **39**(30), 17381 (2014)
19. A. Polyanskiy, D. Popov-Diumin, V. Polyanskiy, in *Hydrogen Materials Science and Chemistry of Carbon Nanomaterials*, ed. by T. Veziroglu, S. Zaginaichenko, D. Schur, B. Baranowski, A. Shpak, V. Skorokhod, A. Kale, NATO Security through Science Series A: Chemistry and Biology (Springer, Netherlands, 2007) p. 681
20. A.G. Lunev, M.V. Nadezhkin, S.A. Barannikova, L.B. Zuev, AIP Conf. Proc. **1909**(1), 020121 (2017)

Part IV
Applications of Advanced Materials

Chapter 39
Geometric and Physical Parameters Influence on the Resonant Frequencies of Ultrasonic Vibrations of a Medical Scalpel

A. S. Skaliukh, T. E. Gerasimenko, P. A. Oganesyan, A. N. Soloviev and A. A. Solovieva

Abstract Resonance frequencies of the longitudinal oscillations are investigated for a system consisting of diverse geometrical and physical elements—piezoceramic, elastic, and acoustic ones. The results are compared in COMSOL and ACELAN packages. The dependence of the first eigenfrequency value on the geometric parameters is evaluated. The dynamic viscosity effect on the longitudinal oscillations near the first resonance frequency (FRF) is studied. The system of elastic and acoustic elements, which allows describing the operation of an ultrasonic cutting device, is selected for the study. The oscillator is a piezoelectric transducer, which oscillates in thickness. An oscillation concentrator and a rod element are specified as elastic elements. They are made from stainless steel. Possible model of the human body soft tissues is an acoustic fluid. Modal and harmonic analysis of a complex system consisting of diverse physical elements is carried out. Axisymmetric and three-dimensional finite element models of the investigated system are constructed. Various types of curvature and thickness of the link with changeable surface shape are proposed for the oscillation concentrator. The first eigenfrequencies of the longitudinal vibrations of the rod element contacting with the acoustic liquid are obtained. Good agreement with the results of the ACELAN finite-element package is established. The amplitude-frequency characteristics of the end oscillations near the first resonance frequency are obtained. It is notable that the acoustic medium viscosity has little effect on the oscillation amplitude of the elastic rod and does not affect the resonance frequency at all. Harmonic and modal analysis has shown that the high-frequency longitudinal vibrations of the rod element depend significantly on the dissipation factor of the

A. S. Skaliukh · T. E. Gerasimenko · P. A. Oganesyan
I. I. Vorovich Mathematics, Mechanics and Computer Sciences Institute, Southern Federal University, Rostov-on-Don, Russia

A. N. Soloviev (✉) · A. A. Solovieva
Department of Theoretical and Applied Mechanics, Don State Technical University, Rostov-on-Don, Russia
e-mail: solovievarc@gmail.com

I. A. Parinov et al. (eds.), *Advanced Materials*, Springer Proceedings in Physics 224, https://doi.org/10.1007/978-3-030-19894-7_39

elastic elements and depend weakly on the viscosity of the contacting acoustic medium. The results obtained may be of interest under designing ultrasonic cutting medical devices.

39.1 Introduction

Harmonic scalpels allow us to perform not only dissection, but also coagulation of soft tissues, which helps to prevent bleeding [1–4]. Structurally, such devices consist of a chain of elastic and electroelastic (piezoceramic) elements assembled into a single system, creating maximum longitudinal oscillations to the cutting element at frequencies from 20 to 50 kHz. The most effective mode is when the cutting element performs longitudinal oscillations at the resonant frequency. Under the influence of cavitation of the cellular structure of the tissue layers adjacent to the blade, dry friction turns into a semi-dry or even liquid friction. These results in a significant reduction in both the normal and tangential cutting forces, but the maximum amplitude of the oscillations and the resonance frequency vary. Therefore, the fundamental frequency of the oscillations, ignoring the load on the cutting element, indicated in the instructions to the ultrasonic scalpels, is unlikely to be resonant. On the other hand, in the chain of elastic elements contains an oscillation concentrator, which allows increasing the amplitude of longitudinal oscillations of the dissecting element, the shape and size of which affect the amplitude-frequency characteristics of the scalpel. Another important element is a piezoceramic transducer, which can be multi-sectional, and may also have an inhomogeneous pre-polarization [5–7].

To model the operation of an ultrasonic cutting device, a finite element model of a composite system of piezoceramic and elastic elements was considered, one of which has a longitudinal dimension prevailing over the others, to study the effect of physical and geometric parameters on its longitudinal oscillations. Such a system is close to the design of a medical ultrasonic scalpel and can be used to model its operation.

Among the factors that affect the eigenfrequencies of the oscillations under study, three main groups can be distinguished: geometric parameters, material properties, and inhomogeneous polarization of the piezoelectric element. In addition, the calculation of performance characteristics considers the environment with which the cutting element is in contact. To this end, a viscous acoustic fluid model was used. To analyze the behavior of the scalpel in different types of tissues, the parameters of this liquid (for example, viscosity and density) can be varied. Different approaches to modeling the properties of living tissues of the body, including acoustic fluids, are present in [8, 9].

In this paper, parametrized geometry of the model is constructed, a series of numerical experiments is carried out, and changes in the natural frequencies are determined depending on the dimensions of the individual elements of the system. In addition, the amplitude-frequency characteristics of the system at frequencies close to resonance were analyzed, depending on the physical properties of the acoustic fluid medium.

39.1.1 Research Purpose

Optimal design of ultrasonic scalpel can lead to more energy effective and light-weight tools. Developing of finite element model allows one to perform computer simulation both with simplified 2D-model and full 3D-model with parametrized geometry.

39.1.2 Research Scope

At this study, we consider the following frameworks of the problem:

(i) Mathematical models of the device with elastic and piezoelectric parts;
(ii) Soft tissues modeling;
(iii) Finite element models in 2D and 3D;
(iv) Numerical experiments and possible optimization of the scalpel design.

39.2 Research Method

39.2.1 Models of the Device and Tissue

For the study, a system, consisting of a chain of elastic and electroelastic elements, is shown in Fig. 39.1.

Here the sections AB, BD, DG are the piezoceramic element, the oscillation concentrator and the rod element, respectively. All elements have an axisymmetric structure. The piezoelectric element is a cylindrical piezoceramic transducer with a

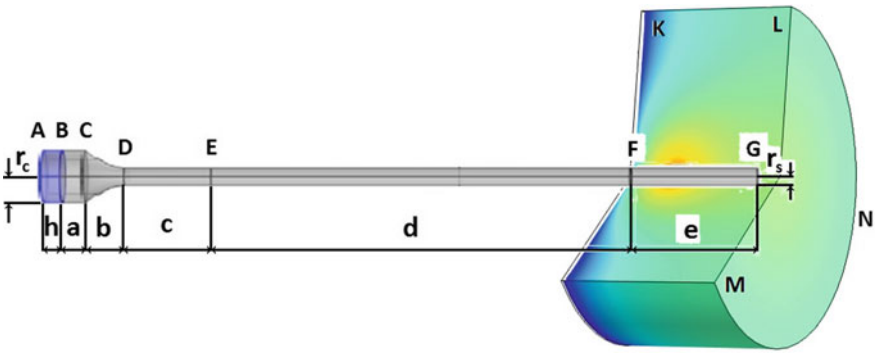

Fig. 39.1 Parametrized scalpel model geometry in axisymmetric and three-dimensional setting in COMSOL package

thickness h and a preliminary polarization directed along the thickness. Electrodes are applied to the faces of a piezoceramic cylinder. They are fed a potential difference, varying according to the harmonic law in time. The material of the vibration concentrator and the rod element is stainless steel. The contact interaction between the transducer and the oscillation concentrator, and between the concentrator and the rod is non-disruptive. Section A of the converter is fixed; on the lateral surface, there is a smooth rigid contact. The last condition is satisfied for the stress concentrator in the section BC of length a. The remaining lateral surface of length b is free of mechanical stresses. For the rod, the condition of smooth rigid contact in the section DE of length c was adopted. In the section EF with length d, zero voltages were assumed. In the section FG of length e and at its end section G, conjugation with the acoustic medium KLNM takes place. In the section FG of length e and at its end section G there is a contact with the acoustic medium KLNM. It was assumed that on the front surface passing through the point K, the sound pressure is zero, on the lateral surface KL the condition of the impedance type takes place. The front surface LNM is an impenetrable plane.

Each of the parts mentioned above is described by linear models, which for simplicity are represented in vector form.

Piezoceramic solid:

$$\begin{aligned} &\nabla \cdot \boldsymbol{\sigma} = \rho\,\omega^2\,\mathbf{u}; \qquad \boldsymbol{\sigma} = \mathbf{C} : \boldsymbol{\varepsilon} - \mathbf{e}^{\mathrm{T}} \cdot \mathbf{E}; \qquad \boldsymbol{\varepsilon} = 1/2(\nabla \mathbf{u} + \nabla \mathbf{u}^{\mathrm{T}}); \\ &\nabla \cdot \mathbf{D} = 0; \qquad \mathbf{D} = \mathbf{e} : \boldsymbol{\varepsilon} + \mathfrak{э} \cdot \mathbf{E}; \qquad \mathbf{E} = -\nabla \varphi; \end{aligned} \tag{39.1}$$

in which $\boldsymbol{\sigma}$, $\boldsymbol{\varepsilon}$, $\mathbf{D}$, $\mathbf{E}$, $\mathbf{u}$, $\mathbf{C}$, $\mathbf{e}$, $\mathfrak{э}$, ρ, ω are the stress tensor, strain tensor, electric displacement vector, electric field vector, displacement vector, electric potential, tensor of elastic constants, tensor piezoelectric constants, the permittivity tensor, the density of the ceramic material and the circular frequency, respectively.

Elastic solid:

$$\nabla \cdot \boldsymbol{\sigma} = \rho_{\mathrm{k}}\,\omega^2\,\mathbf{u}; \quad \boldsymbol{\sigma} = \lambda_{\mathrm{k}} tr\,\boldsymbol{\varepsilon}\,\mathbf{I} + 2\,\mu_{\mathrm{k}}\,\boldsymbol{\varepsilon}; \quad \boldsymbol{\varepsilon} = 1/2(\nabla \mathbf{u} + \nabla \mathbf{u}^{T}); \tag{39.2}$$

in which $\boldsymbol{\sigma}$, $\boldsymbol{\varepsilon}$, $\mathbf{u}$, $\mathbf{I}$, λ_{k}, μ_{k}, ρ_{k} are the stress tensor, strain tensor, displacement vector, unit tensor, Lame coefficients and material density of the oscillation concentrator and rod, respectively (k = 1,2). The attenuation in these materials is modeled with the help of complex Lamé coefficients, and the tangent of the loss angle is 0.0001.

Acoustic medium:

$$\begin{aligned} &\nabla \cdot \left(-\frac{1}{\rho_{\mathrm{c}}} \nabla \mathrm{p} \right) - \frac{k_{\mathrm{eq}}^2\,\mathrm{p}}{\rho_{\mathrm{c}}} = 0; \quad k_{\mathrm{eq}}^2 = \left(\frac{\omega}{c_{\mathrm{c}}} \right)^2; \\ &c_{\mathrm{c}} = c \left(1 + i\,\omega \frac{\left(\frac{4\mu}{3} + \mu_{\mathrm{b}} \right)}{\rho\,c^2} \right)^{0.5}; \quad \rho_{\mathrm{c}} = \frac{\rho\,c^2}{c_{\mathrm{c}}^2}; \end{aligned} \tag{39.3}$$

in which p, ρ, c, μ_a, μ_b are the acoustic pressure, the fluid density, the sound velocity in it, the dynamic viscosity and the second viscosity coefficient of the medium, respectively.

The boundary conditions and conjugation conditions have been described in detail above, they are obvious, so mathematical formulae for them will not be issued. We add only that if heterogeneously polarized ceramic tablets are considered, the elastic, piezoelectric (electroelastic) and dielectric characteristics of such media will represent the functions of the coordinates of the area occupied by the ceramic.

To describe the geometry of all elements of the system, three finite element models were developed. Two axisymmetric models were built in the ACELAN and COMSOL packages. The third model is built in the COMSOL package for the 3D case.

At the base of each model, there is parametrized geometry, shown in Fig. 39.1, which also indicates the independent parameters that are responsible for the geometry of the model. On the left side of the system, there is a piezoceramic cylinder marked with a darker color. The next element is a steel concentrator, consisting of two geometric components: a cylinder and a cone-shaped adapter. In real designs of surgical instruments, the thickness of the transducer and the radii of the end sections of the concentrator are related to the lengths of propagating waves. In the proposed variant, we abandoned additional constraints on geometric parameters able to obtain more general results. At the same time, the model can change the diameter of the conical part in a functional manner. To this end, the generator of the cone in global coordinates in the yz-plane is described by a quadratic equation:

$$\begin{gathered} y(z) = kz^2 + k_1 z + k_2; \quad k_1 = \frac{rs - rc + k(z_0^2 - z_2^2)}{z_2 - z_0}; \\ k_2 = rc - k_1 z_0^2; \quad z_0 = hc + a; \quad z_1 = z_0 + b, \end{gathered} \tag{39.4}$$

which makes it possible to carry out numerical experiments for concave and convex profiles of the guide, changing only one parameter k, as shown in Fig. 39.2.

The next in the chain of elastic elements is a rod, simulating the body of the dissector. The rod is divided into three parts, each of which is given its own boundary conditions, as mentioned above. The acoustic part is also shown in Fig. 39.1 in green and locates on the right hand. For convenience, an incision was made in this medium, which makes it possible to evaluate its effect on the longitudinal oscillations of the rod structure.

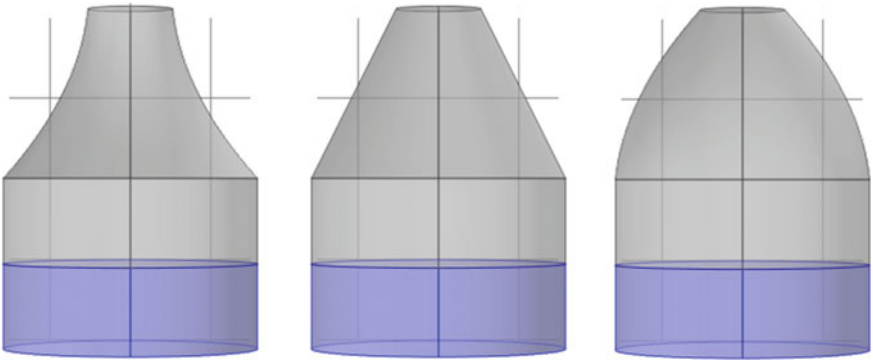

Fig. 39.2 Various forms of the adapter between the piezoelectric cell and the rod (the shape is determined by the parameter k)

39.3 Results and Discussion

39.3.1 2D Models and Optimum Frequency Analysis

The indicator of the efficiency of converting the electric energy, supplied to the piezoelectric element into the mechanical energy of the cutting tool, is K, named electromechanical coupling coefficient, which can be estimated from the formula:

$$K = \sqrt{\left(1 - \left(\frac{f_r}{f_a}\right)^2\right)} \tag{39.5}$$

where f_r, f_a are the resonance and antiresonance frequencies, respectively.

So, in Table 39.1, the frequencies of resonances, antiresonances and their electromechanical coupling coefficients are present. Computations were made with ACELAN package [10]. It can be concluded that the first longitudinal mode is not

Table 39.1 Frequencies of resonances, antiresonances and their electromechanical coupling coefficient

No	F_r (kHz)	F_a (kHz)	Output potential (V)
1	5.0240	5.0397	0.081
2	15.0610	15.1135	0.084
3	25.0585	25.1690	0.094
4	34.9591	35.1871	0.114
5	44.5936	45.1319	0.154
6	53.3122	54.9172	0.240
7	60.1792	64.2813	0.352
8	67.8420	72.4783	0.352

excited efficiently by electric means, the most effective are the 7 and 8 modes. In Table 39.3 are presented the frequencies of resonances, antiresonances and their electromechanical coupling coefficients, from which it is seen that the first longitudinal mode is not electrically energized, the most effective are the 7 and 8 modes.

Figure 39.3 shows the distribution of the axial displacement in the first, seventh and eighth modes (a), (b) and (c), respectively. It should be noted that the maximum amplitude at the end of the rod is observed in the first and seventh modes. Analysis of Figs. 39.8 and 39.9 shows that the seventh mode is the most effective.

Figure 39.4 shows the frequency response of the axial displacement of the end of the rod at the 7th and 8th modes, and in Fig. 39.5, it is the same with a smaller step in frequency.

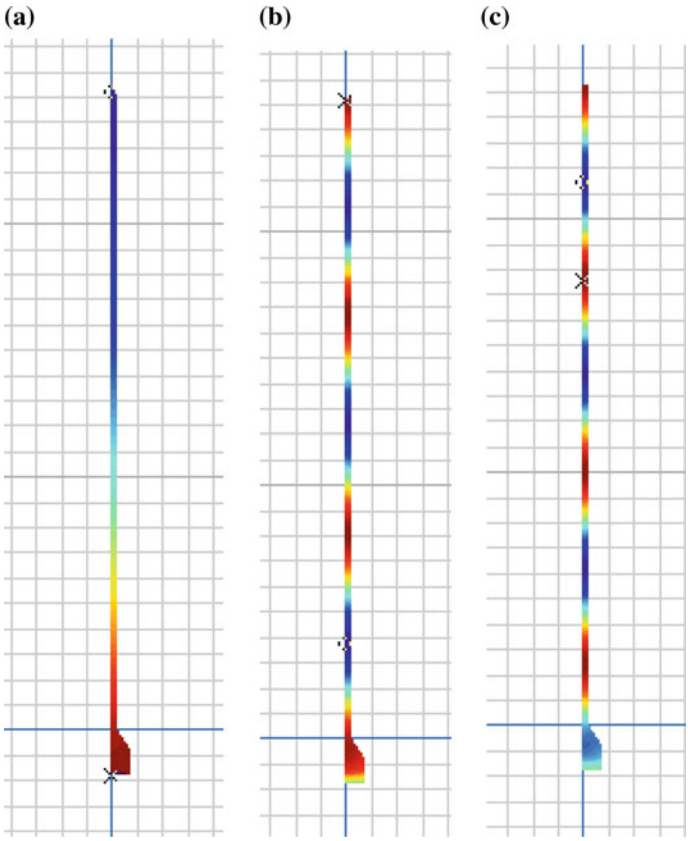

Fig. 39.3 Distribution of the axial displacement in the first, seventh and eighth modes: (**a**), (**b**) and (**c**), respectively

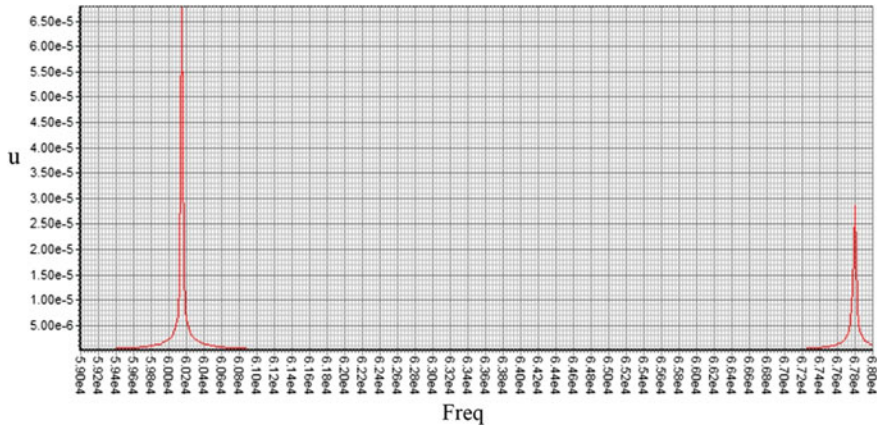

Fig. 39.4 Frequency response of the axial displacement of the end of the rod at the 7th and 8th modes

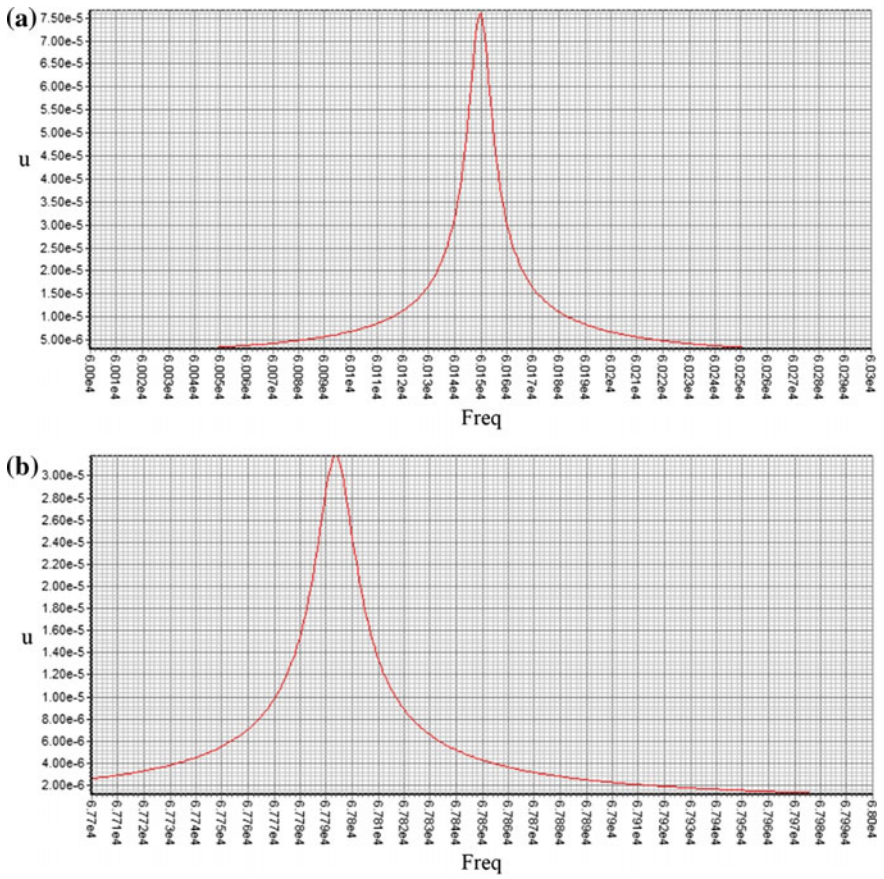

Fig. 39.5 Frequency response of the axial displacement in the seventh (**a**) and eighth mode (**b**)

39.3.2 Analysis of the Oscillations of the Device in the Shell Housing

Above, the analysis of the dynamics of the working tool of the device was performed, provided, that its left end is fixed along its normal, but a model more approximate to practice assumes the presence of some case and the connection of the left end of the piezoelement with it. In this section, we consider such a scalpel model (Fig. 10) with an external electric oscillation source. Figure 39.6 shows the half of the axial section of the left side of the scalpel, placed in shell housing.

Table 39.2 shows resonance, antiresonance frequencies and ECC for axisymmetric scalper model in the shell housing made from stainless steel. Substrate was made with ebonite.

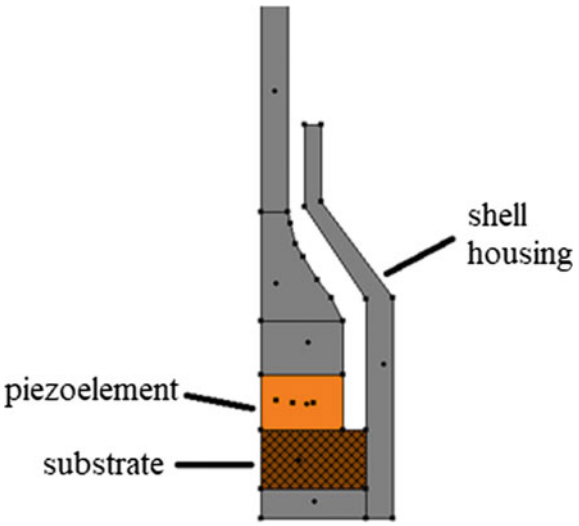

Fig. 39.6 Frequency response of the axial displacement of the end of the rod at the 7th and 8th modes

Table 39.2 Frequencies of resonances, antiresonances and their electromechanical coupling coefficient

No.	Frequencies of resonances, f_r (kHz)	Frequencies of antiresonances, f_a (kHz)	Electromechanical coupling coefficient, K
1	5.9707	5.9777	0.0480
2	15.2974	15.3269	0.0620
3	24.6355	24.7498	0.0960
4	31.0581	31.4241	0.1522

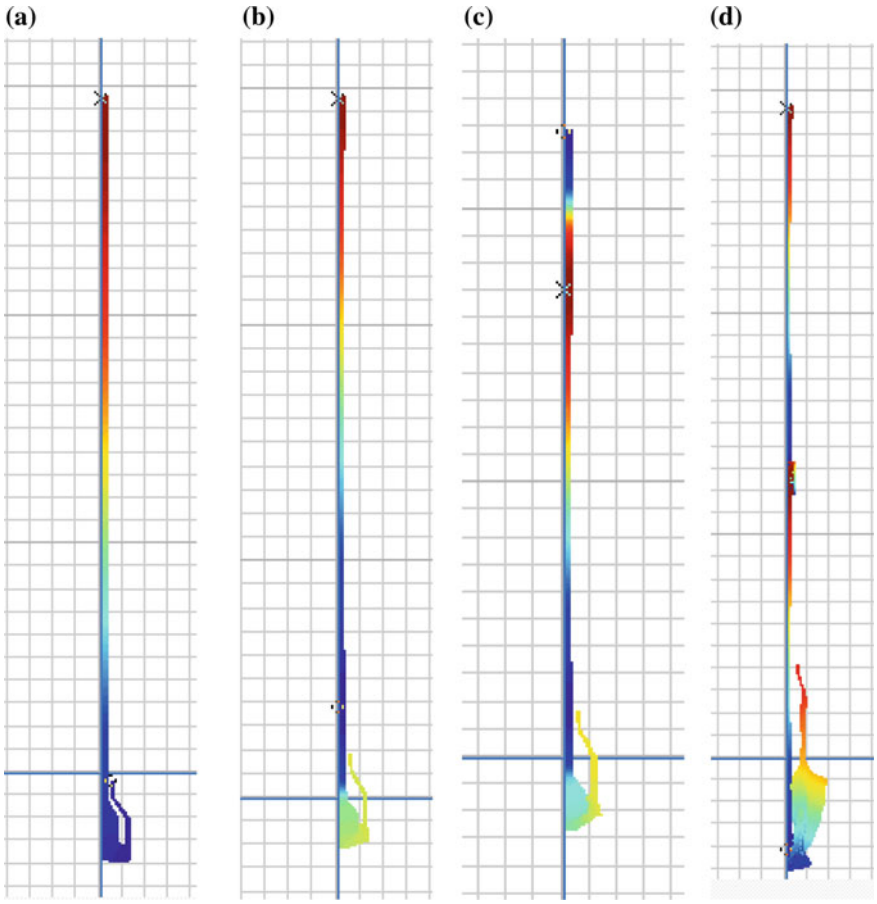

Fig. 39.7 Distribution of axial displacement at first **a**, second **b**, third **c** and fourth **d** modes

Figure 39.7 shows the eigenmodes of the oscillations at the first four modes. The analysis of the electromechanical coupling coefficient and the eigenmodes of the oscillations at the first four modes shows that the highest ECC is at the fourth mode, however, at this frequency, intensive movements of the case itself are observed, this can lead to a loss of precision in the cuts. Most preferable are the second and third modes of oscillations, on which the movements of the case are not significant, while in the third mode the oscillations are concentrated at the cutting end of the tool.

39.3.3 2D and 3D Models Comparison

Complete list of geometrical parameters for 3D model is given in Table 39.3.

Table 39.3 Frequencies of resonances, antiresonances and their electromechanical coupling coefficient

Name	Initial value	Description
r_c	7.5 mm	Radius of the ceramic disc
h	5 mm	Ceramic disc thickness
a	5 mm	Metal layer thickness
b	10 mm	Adapter thickness
r_s	2.5 mm	Rod radius
k	−80	Dimensionless parameter of curvature of cone adapter generatrix
c	0.02 m	Length of the initial segment of the rod
d	0.2 m	Length of the middle segment of the rod
e	0.03 m	Length of a rod segment immersed in a liquid
μ	1 Pa s	Liquid viscosity
ρ	1500 kg/m^3	Liquid density
c_s	1900 m/s	Speed of sound in liquid

Table 39.4 Mesh analysis results

	2D		3D	
Element size [min, max] (m)	f_1 (Hz)	Degrees of freedom	f_1 (Hz)	Degrees of freedom
[6.8 × 10^{-4}, 0.034]	4900.8	827	5050.0	3300
[1.02 × 10^{-4}, 0.0228]	4900.3	1059	5011.4	6316
[1.02 × 10^{-4}, 0.018]	4900.1	1095	4934.7	22,960
[4.25 × 10^{-5}, 0.0126]	4900.1	1559	4932.1	178,816

Axisymmetric and three-dimensional models were used to evaluate the quality of finite element meshes. The eigenvalue problem was solved by using grids with different sizes. The refinement of the finite element meshes continued until the further decrease in size did not begin to affect the result for a given computational error. In our case, the first eigenvalue resonance frequency of the longitudinal oscillations was chosen as the result of the investigation. Longitudinal oscillations were selected by sampling their own modes of oscillation.

Table 39.4 shows the results of calculations, based on the results, when optimal grid sizes are determined, which allow obtaining reliable results with a minimum number of elements.

The presented results allow us to conclude that to achieve a given accuracy, an axisymmetric model allows us to use a much smaller number of degrees of freedom. Thus, with an error of $\delta = 0.6\%$ in an axisymmetric model, we can take 115 times less finite elements, which is important in solving optimization problems in terms of parameters. However, in the future there will be a need to use a three-dimensional model, when the non-axisymmetric type of the rod tip and the non-axisymmetric form of external influences will be considered.

The first stage of the numerical experiment in COMSOL consisted in validating the models by comparing different implementations, when solving the eigenvalue problem. A technique was developed for determining the first three operating frequencies of the device, which correspond to longitudinal oscillations of the rod (the value of only the first of them is indicated in Table 39.2).

The next step in numerical experiments was the comparison of the results of calculating the eigenvalue frequencies of longitudinal oscillations, obtained by different models and different finite-element complexes.

In particular, in the package ACELAN, an axisymmetric model of this system was constructed. Table 39.5 shows the results of calculating the first two eigenvalue frequencies.

Comparison of the results shows that axisymmetric models are consistent with very high accuracy. The difference between the three-dimensional model and the axisymmetric model can be caused by the complexity of constructing a three-dimensional grid on the thinnest sections of geometry. The capabilities of the postprocessor package COMSOL allow us to build a three-dimensional image based on the results of solving the axisymmetric problem. Here and in the following work, results of processing of solutions to the axisymmetric problem are presented.

Next, we estimated the effect of geometric parameters on eigenfrequencies. Figure 39.7 shows the dependence of eigenfrequencies on different geometric parameters.

It can be seen from the figures that with an increase in the thickness of the converter and with an increase in the length of the rod part, the first eigenfrequency decreases. This decrease will be significant when it is necessary to increase the length of the rod part but is practically absent with a small change in the thickness of the converter. It is characteristic that the curvature of the stress concentrator and its length are also practically unaffected by the eigenfrequency (Fig. 39.8).

Another important characteristic is the amplitude-frequency characteristic of longitudinal oscillations near resonant frequencies. Thus, Fig. 39.9 shows the results of calculating the amplitude-frequency characteristics of longitudinal oscillations near the first resonant frequency (FRF) for certain values of independent physical and geometric parameters.

Calculations were carried out taking into account the acoustic fluid into which the end of the rod part is inserted. The effect of an acoustic fluid leads to damping, at which the resonance frequency varies depending on the properties of the acoustic medium. Figure 39.9 shows the amplitude-frequency characteristics of longitudinal oscillations for different values of dynamic viscosity *mu*. The second viscosity coefficient was assumed to be zero.

Table 39.5 Results of solving eigenvalue problem on optimal grids in various packages

Model	f_1 (Hz)	f_2 (HZ)
ACELAN	4907.0	14,711
COMSOL (2D)	4900.1	14,691
COMSOL (3D)	4932.1	14,782

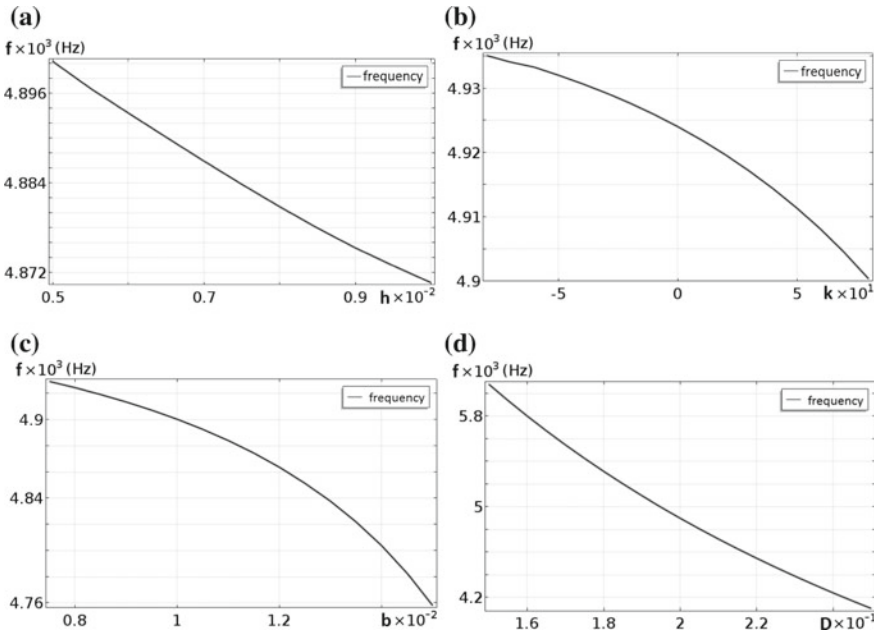

Fig. 39.8 Effect on eigenfrequency of geometric parameters: thickness h of piezoelectric transformer (**a**); curvature parameter k of oscillation concentrator guide (**b**); thickness b of oscillation concentrator (**c**); rod length D (**d**)

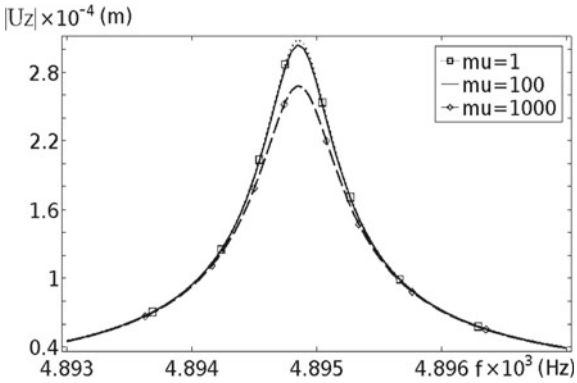

Fig. 39.9 FRF of forced scalpel oscillations at various values of viscosity

It is interesting to note that with changes in the viscosity of an acoustic medium over a large range, FRF varies insignificantly. It can be concluded that the main factor affecting the amplitude of oscillations near the first resonance of longitudinal oscillations is damping in an elastic medium. Thus, an increase in the viscosity of the acoustic medium by more than an order of magnitude does not lead to a significant decrease in the amplitude of the vibrations of the rod link. It is also

interesting to note that viscosity affects the amplitude of the oscillations but does not affect the frequency. This may be due to the small cross-sectional area of the scalpel.

39.4 Conclusion

In the present work, resonant frequencies of longitudinal oscillations of a system consisting of a chain of elements different in physical parameters: piezoceramic, elastic and acoustic, were investigated. For this purpose, axisymmetric and three-dimensional finite element models were constructed. For comparison, two finite element COMSOL and ACELAN packages were selected. A good agreement is found between the results for eigenfrequencies for an axisymmetric problem. The influence of geometric parameters on the value of the first eigenfrequency is estimated. In particular, options are considered in which the following parameters varied: the thickness of the piezoelectric transducer; curvature and thickness of the oscillation concentrator; length of the rod link. Calculations are made with the following changing parameters: piezoelectric transducer thickness; curvature and thickness of the oscillation concentrator; length of the rod link.

Another important parameter of the study was the amplitude-frequency response of longitudinal oscillations near the first resonant frequency. It is noted that a small change in the dynamic viscosity of an acoustic medium has little effect on this characteristic. A noticeable increase in this viscosity leads only to a decrease in the amplitude of the oscillations, but practically does not change the resonance frequency. The results obtained may be of interest in the design of ultrasonic cutting medical devices.

Acknowledgements This research was performed into framework of financing RFBR grant number 17–08–00860–a.

References

1. V.I. Loshilov, S.M. Volkov. *Proceedings of the Moscow Higher Technical School*. vol. **165**, 29 (1973) (In Russian)
2. V.B. Akopyan, Yu. A. Ershov, in: *Ultrasound in Medicine, Veterinary Medicine and Biology*. 2nd edn. ed. by S.I. Shchukin (Moscow, Yurayt, 2017), 223 p (In Russian)
3. V.I. Dubrovsky, V.N. Fedorova. *Biomechanics*. (VLADOS-Press, Moscow, 2003), 672 p (In Russian)
4. A. Carovac, F. Smajlovic, D. Junuzovic, Acta Informatica. Medica. **19**(3), 168 (2011)
5. S. Dong, J. Adv. Dielectr. **2**(1), 1230001 (2012)
6. D.-K.-C. Liu, J. Friend, L. Yeo, Acoust. Sci. Technol. **31**(2), 115 (2010)
7. A. Skaliukh, G. Li, in: *Advanced Materials—Manufacturing, Physics, Mechanics and Applications*, Springer Proceedings in Physics, vol. 175, ed. by I.A. Parinov, S.-H. Chang, V. Yu. Topolov (Heidelberg, New York, Dordrecht, London: Springer Cham, 2016), 393 p

8. N.I. Vykhodtseva, K. Hynynen, C. Damianou, Ultrasound Med. Biol. **20**(9), 987 (1994)
9. F.-A. *Duck, Physical Properties of Tissue: A Comprehensive Reference Book* (Academic Press, London, 1990), 336 p
10. A.V. Belokon, A.V. Nasedkin, A.N. Soloviev, J. Appl. Math. Mech. **66**(3), 491 (2002)

Chapter 40
Layers of Composite Nanomaterials as Prototype of a Tensoresistor Sensor

Levan Ichkitidze, Alexander Gerasimenko, Dmitry Telyshev, Vladimir Petukhov, Evgeny Kitsyuk, Vitali Podgaetski and Sergei Selishchev

Abstract The layers of various materials are discussed. They include nanomaterials containing carbon nanotubes with tensoresistive properties. The investigated layers are divided into two groups: without (group I) and with carbon nanotubes (group II). From materials of group I, the most suitable for the manufacture of strain sensors for medical purposes is an elastomer with microchannels, filled with a conductive liquid. Such a strain sensor can detect small bends of parts of the human body with an error of 8%. In group II, carbon nanotubes, located between layers of natural rubber or between flexible layers of polydimethylsiloxane, showed acceptable values of strain sensitivity and maximum deformation of ~ 40 and $\sim 500\%$, respectively. Based on layers (thickness ~ 0.5–1.5 μm) of biocompatible composite nanomaterials in bovine serum albumin or microcrystalline cellulose and carbon nanotubes (concentration ≤ 2 wt%), prototypes of deformation sensors (tensoresistors) showed high positive characteristics. In particular, bipolar behavior, strain sensitivity ~ 160, small hysteresis ($\leq 3\%$) after training cycles (deformation/deformation) more than 25 times, the possibility of applying an aqueous dispersion of nanomaterials to the human skin by the 3-D printer. Further improvement (in particular, an increase in the linear deformation region and a decrease in deformation, a decrease in hysteresis) of the parameters of composite nanomaterials in a matrix of biological materials and a filler made of carbon nanotubes will allow the use of deformation sensors, both non-invasive and invasive medical applications.

L. Ichkitidze (✉) · A. Gerasimenko · D. Telyshev · V. Petukhov · V. Podgaetski · S. Selishchev
National Research University of Electronic Technology, Zelenograd, Moscow 124498, Russia
e-mail: ichkitidze@bms.zone; leo852@inbox.ru

L. Ichkitidze · A. Gerasimenko · D. Telyshev
I.M. Sechenov First Moscow State Medical University, Moscow 119991, Russia

E. Kitsyuk
Scientific Manufacturing Complex "Technological Centre", Zelenograd, Moscow 124498, Russia

I. A. Parinov et al. (eds.), *Advanced Materials*, Springer Proceedings in Physics 224, https://doi.org/10.1007/978-3-030-19894-7_40

40.1 Introduction

Deformation sensors (strain gauges) are among the ones claimed in practical applications. Close attention is paid to research, development and creation advanced characteristics, as well as new types of sensors. For example, in the database of the Scopus system, about a thousand documents of information on new developments of load cells, reflected every year, tens of percent are occupied by sensors for medical purposes.

Indeed, recently in medical practice there has been an interest in strain gauges that could easily be attached to clothing or directly to the body of a person. Monitoring of human body movements can be classified into two categories: detection of large-scale (for example, movement of hands, feet) and small-scale movements (for example, blinking, swallowing). In the first category, it is important to monitor the condition: limbs, joints, chest, as well as tumors, deformation of muscle tissue in the postoperative therapy, etc. In the second category, for diagnostic purposes, it is necessary to detect signs of: damaged vocal cords, respiratory diseases, angina pectoris, changes in the spatial gap between the bones, Parkinson's disease, etc. For such purposes, numerous and varied strain sensors are required that must meet the requirements: high elongation (>10%), flexibility (>10%), strain sensitivity ($S \gg 10$), durability, rapid reaction/recovery rate and biocompatibility.

The simplest and most widespread strain gauges are based on the phenomenon of resistance variation under strain, and call tensoresistors. The strain sensitivity of these devices is determined as $S = \delta R/\varepsilon$, where $\delta R = \Delta R/R_0$, R_0 is the initial resistance, ΔR is the absolute resistance variation under strain, $\varepsilon = \Delta l/l$, l is the initial length of a sensitive element, and Δl is the absolute variation in its length.

Conventional tensoresistors are fabricated from metal or semiconductor materials. Meander-shaped tensoresistors, formed from a metallic foil, have the low-temperature resistance coefficient ($\alpha \leq 10^{-5}$ K^{-1}) and relatively wide strain measurement range ($\varepsilon = \pm 5\%$), but the low strain sensitivity ($S \leq 10$). Semiconductor tensoresistors are characterized by the high sensitivity ($S \sim 100$–200), very low strain ($\varepsilon \leq 0.2\%$), and high-temperature resistance coefficient ($\alpha \geq 10^{-3}$ K^{-1}) [1]. Note that both the metal and semiconductor tensoresistors have insufficient elasticity and strongly restrict movements of a biological object, because their moduli of elasticity E exceed the value characteristic of a human skin by several orders of magnitude ($E \sim 25$–220 kPa, $\varepsilon >> 1\%$) [2].

In this work, we briefly describe different layers with the tensoresistive properties (hereinafter, tensoresistors) that were designed using original methods and/or materials and their potential applications in medicine. The investigated devices are divided into two groups. Group I is formed from the tensoresistors that do not contain carbon nanotubes (CNTs) and group II, from the tensoresistors containing CNTs or based on nanocomposites with CNTs.

40.2 Layers—Group I

A great number of tensoresistors have been developed and fabricated using nanoparticles and nanotechnologies. However, the high strain sensitivity ($S \geq 100$) is often attained in a very narrow strain range ($\varepsilon \leq 1\%$), which is not suitable for medical applications. Indeed, to control movements of human body parts, a strain of $\varepsilon \geq 10\%$ is usually required. In [3], the materials, based on ZnO nanowires and characterized by $S \approx 1250$ and $\varepsilon \leq 1\%$, were reported. In a hybrid material, consisting of ZnO nanowires fixed on polystyrene nano- and microfibers, the high ε values ($\leq 50\%$) and relatively low S values (~ 100) were established [4]. A tensoresistor is encapsulated in a polydimethylsiloxane (PDMS) film and has the high moisture resistance. However, the excessively high resistance ($\geq 10^9$ Ω) and, consequently, high intrinsic noise level of the material significantly restrict the strain measurement accuracy.

The parameters $S \sim 10$ and $\varepsilon \sim (20–80)\%$ were obtained in a tensoresistor, based on the thermoplastic elastomer, containing ~ 50 wt% of soot [5]. The proposed sensor, however, rapidly loses its strain sensitivity ($S \leq 0.1$) at $\varepsilon \leq 10\%$ and can probably be used to detect fabric strain.

The graphite layers deposited onto natural rubber substrates exhibit the tensoresistive effect with the high parameters: $S \sim 12–346$ and $\varepsilon \leq 246\%$ [6]. Nevertheless, their $\delta R(\varepsilon)$ dependences are strongly nonlinear, especially in the range of $\varepsilon \geq 100\%$. The strong nonlinearity of the $\delta R(\varepsilon)$ dependence is caused mainly by the behavior of pure rubber, i.e., by the strong nonlinearity of the stress induced during straining the rubber. Hence, the use of such layers as tensoresistors is complicated by the difficulty of brining the $\delta R(\varepsilon)$ curves to the linear shape with good accuracy.

In [7], an original tensoresistor, consisting of a silicone elastomer with microchannels, filled with a conductive liquid, was developed to control movements of different human body parts. The strain (tension) increases the length and decreases the width of a microchannel and, thus, leads to the corresponding increase in its resistance. Testing of the tensoresistor showed that it has a strain of $\varepsilon \leq 300\%$ and a sensitivity of $S \leq 3$ at bending angles of $\theta < 120°$; the strain measurement error was $\sim 8\%$. Obviously, this sensor is inapplicable to detecting movements of human body parts, where the angles can be in the range of $\theta \geq 120°$, e.g., in total finger, knee, or elbow flextions.

40.3 Layers—Group II

40.3.1 Carbon Nanotubes

Carbon nanotubes (CNTs) have the unique properties, including high strength, heat and electric conductivity, and optical transparency. Nanocomposites with even

minor (<10%) CNT additions acquire special characteristics. Depending on a fabrication technique used and nanomaterial composition, the tensoresistive effect in the CNT-based layers is either enhanced or suppressed. Indeed, the layers, consisting of multiwalled CNTs (MWCNTs), added with $AgNO_3$ in a concentration of 2–10 g/l, deposited onto PDMS substrates, exhibit a stable resistance upon multiple bending in the angle range from −180° to +180° and have almost no tensoresistive properties [8].

Study of the MWCNT films used as tensoresistors showed the almost linear $\delta R(\varepsilon)$ dependence and absence of the hysteresis under loading and unloading in combination with the high stability of a signal detected for 2-hour testing at $\varepsilon \leq 10$ [9]. Such a tensoresistor, however, appeared highly sensitive to various gases, moisture, and working temperature, i.e., it should be protected against environmental factors.

The tensoresistors in the form of thin films containing aligned single-walled CNTs (SWCNTs) on flexible substrates exhibit the excellent elasticity ($\varepsilon \sim 280\%$), but the very low sensitivity ($S \leq 0.8$), high hysteresis, and insufficient strain measurement accuracy [10]. A MWCNT film placed between natural rubber layers showed the higher strain sensitivity ($S \sim 43$) at $\varepsilon \sim 620\%$ [6]. However, the $\delta R(\varepsilon)$ dependence for this film is approximately linear only at $\varepsilon \leq 100\%$.

A new type of the tensoresistor, based on SWCNTs encapsulated in the PDMS layers, was proposed in [11]. The parameters of $S \leq 6.3$ and $\varepsilon \leq 10\%$ and the moisture resistance higher than that of the tensoresistor without a protective layer were reported. For the MWCNT film-based tensoresistor, the linear $\delta R(\varepsilon)$ portions were observed at $\varepsilon \leq 0.1\%$ and $S \leq 0.35$ [12]. A similar tensoresistor based on graphene, encapsulated between the PDMS films, showed the high sensitivity ($S \sim 30$), but the low ($\leq 1\%$) ε value [13]. Such a tensoresistor can apparently be used for fragile (rigid) objects, but not in medicine, where the high strain ($\varepsilon \geq 10\%$) is needed.

The parameters suitable for monitoring the strain of human organs were obtained in different CNT/PDMS tensoresistor structures [14, 15]. However, these devices demonstrate the high nonlinear responses and hysteresis in combination with the insufficient elasticity. For these structures, we have $E \sim 0.4$–3.5 MPa [16–18], whereas epidermal applications require the materials with $E \sim 25$–220 kPa [2]). The modulus of elasticity of PDMS increases after adding CNTs; therefore, the discrepancy between elasticity values for human skin and the tensoresistor grows. In addition, absorption of water (moisture) by PDMS leads to the enhancing rigidity and aging. The material becomes fragile and its E value significantly increases over the modulus of elasticity of human skin. Indeed, to exactly detect human skin movements, it is necessary to use high-efficiency strain gauges containing more elastic (soft) materials than PDMS. Many drawbacks of the tensoresistor based on the CNT-containing film encapsulated in the PDMS layers were eliminated using the modified PDMS (the so-called Ecoflex silicone rubber). The CNT/Ecoflex PDMS tensoresistor is characterized by $\varepsilon \sim 500\%$, broad $\delta R(\varepsilon)$ linearity portions, and negligible hysteresis ($\varepsilon < 150\%$), as well as high stability and repeatability of a detected signal during multiple (~ 2000) loading/unloading cycles [19].

Both in the CNT/PDMS and CNT/Ecoflex PDMS structures, PDMS is polymerized by heat treatment at a temperature of 70°C for 2 h. Certainly, this procedure complicates fabrication of the devices.

40.3.2 Composite Nanomaterials with Carbon Nanotubes

The thin (<100 nm) SWCNT-containing films on flexible polyethylene naphthalate substrates exhibited the optical transparency and resistance variation with the bending angle θ [20]. The bending sensitivity $S_\theta = \delta R/\delta\theta$ was found to be $\sim$0.08%/deg. at $\theta = \pm 180°$. Here, θ is the bending angle and $\delta\theta$ is the θ increment; at $\theta = 0$, there was no film bending.

The composite nanomaterials containing CNTs deserve high attention. For example, the films, consisting of polimethyl methacrylate (PMMA) matrix, filled with MWCNTs, exhibited a linear strain of $\varepsilon \leq 1\%$ at 0.75 wt% of MWCNTs [21]. In [22], a 80-μm-thick buckypaper was fabricated from thermoplastic polyurethane (TPU) and MWCNTs and the value of $\varepsilon \approx 180\%$ at a ratio of 80:20 between TPU and CNTs was attained. The tensoresistor, however, had a very narrow region of the linear strain dependence of the output signal ($\varepsilon \leq 1\%$) and the low strain sensitivity ($S \leq 2$).

Study of many nanocomposites, included in epoxy polymers and CNTs, showed that with an increase in the MWCNT concentration in the range of $1 - 10$ wt% the conductivity σ increases from 10^{-2} to 10^2 S/m and the S value decreases from $\sim$22 to $\sim$3 [23–25].

The layers consisting of the carboxymethyl cellulose (CMC) matrix filled with $\sim$5 wt% of MWCNTs demonstrate the high conductivity ($\sigma \sim 10^4$ S/m), $\alpha \leq 10^{-5}$ K^{-1}, and $S \sim 10$ [26, 27]. Laser techniques and nanotechnologies make it possible to control the characteristics of a tensoresistor in wide ranges; in particular, the main parameter, i.e., conductivity, can be changed within $\sigma \sim 10^{-1}$–10^4 S/m. The degradation testing of the CMC/MWCNT layers showed no significant σ variations upon multiple bending of flexible substrates. In particular, upon layer bending by $\theta = \pm 180°$ with a bending radius of 1 mm for up to 10 cycles, the conductivity hysteresis was no larger than 20% relative to its initial value. The hysteresis decreased with increasing number of measurement cycles and was no larger than 8% after 300 cycles. The high strain sensitivity ($S_\theta \sim 0.80\%$/grad) was demonstrated on the CMC/MWCNT nanocomposite layers with thicknesses of 0.2–10 μm. This is higher than the parameter of $S_\theta \sim 0.08\%$/grad, reported in [20]. The layers did not exfoliate from substrates upon multiple bending, did not damage, and kept their initial exterior.

Various strain gauges containing CNTs were reviewed in [28–31]. Their operation is based on the measurements of resistance or capacitance of strained layers. In the first case, these are tensoresistors and the presented examples can be added with our group-II sensors. In the second case, the gauges are capacitive and usually

consist of three layers; the flexible layer is placed between two MWCNT layers. Despite the acceptable parameters ($S_\theta \sim 0.2\%$/grad and $\varepsilon \leq 100\%$), the repeatability of the characteristics is complicated.

Above we described some tensoresistors that are promising for medical applications. Of special importance is their use as miniature epidermic strain or pressure gauges for controlling the recovery after complex surgery and tactile sense recovery. The authors of [32] carried out investigations in this direction: they formed miniature skin pressure gauge prototypes using a 3D printer [32]. However, the direct contact of the strain gauge with the human skin surface is allowed only at the high biocompatibility. Certainly, this approach is valid for the above-mentioned tensoresistors, including those based on CNTs.

Since CNTs and CNT-based nanocomposites are relatively new materials, the health and ecology risks have been thoroughly investigated. Numerous experiments with CNTs revealed both positive and negative effects. The positive effects of CNTs are the possibility of vector drug delivery to different (including brain) organism parts [33–36] and neuron and neurite growth assistance [37, 38]. The negative effects are acceleration of the destruction of duplex DNA fragments [39] and blood thrombocyte aggregation [40].

By now, the following aspects concerning CNTs have been established [41–45]: (i) pure CNTs are more dangerous than functionalized ones; (ii) the CNT toxicity significantly weakens in a composite nanomaterial; (iii) the CNT toxicity is lower than the toxicity of asbestos particles; (iv) in a biological medium, oxidative fermentation and biodegradation of CNTs occur; and (v) citrullination in cells can be indicative of cytotoxicity of CNTs at the early diagnostic stages [46]. The bovine serum albumin molecules are adsorbed and uniformly cover the SWCNT surface layer by layer; bovine fibrinogen molecules behave similarly. Thus, the modified SWCNTs appear almost non-toxical [47–49].

40.3.3 Biocompatible Composite Nanomaterial with Carbon Nanotubes

In [50] we proposed a strain gage, based on layers of biocompatible composite nanomaterials. An aqueous dispersion of composite nanomaterials, consisting of a matrix of bovine serum albumin (BSA) or microcrystalline cellulose (MCC) and filler (MWCNT), is prepared. The components in aqueous dispersions have the following ratios: 20% by weight BSA/0.5% by weight MWCNT; 3% by weight MCC/0.2% by weight MWCNT.

The procedure for preparation of aqueous dispersion is typical for all materials considered in previous works [50]. In particular, in order to obtain an aqueous dispersion of 20% by weight BSA/0.5% by weight MWCNT, the following steps are taken:

(1) MWNT is added to the distilled water and the dispersion is stirred in a magnetic stirrer for 30 min and then dispersed in an ultrasonic disperser at a temperature of ≤ 30 °C for 30 min until a homogeneous black dispersion is obtained. The concentration of MWCNTs is selected in the range 0.5–1% by weight.
(2) BSA powder is introduced into the aqueous dispersion of MWNT in a concentration of 20–25% by weight, so that the ratio of 20% by weight of BSA/2% by weight of MWCNT and water is the rest. The dispersion is then placed in an ultrasonic bath and dispersed at a temperature of ≤ 40 °C for 60 min until a homogeneous BSA/MWCNT dispersion of black color is obtained.
(3) BSA/MWCNT dispersion is decanted within 24 h, filtered and poured into another vessel. Further, the film of the BSA/MWNT aqueous dispersion is silk-screened onto a substrate. In this case, layers of paper, or textiles, or polyethylene terephthalate (PET) with thicknesses up to 50 μm serve as a flexible substrate. After drying at room temperature, the 0.05–0.5 μm thick layers on a flexible substrate appear as a prototype of a strain gauge with a strain-sensitive layer of the BSA/MWCNT composite nanomaterial. On the free surface of the film, i.e. electrical measurements are carried out on the surface bordering the air. In the same way, aqueous dispersions of 3% by weight MCC/0.2% by weight MWCNTs are made, and prototypes of the strain gauge are also generated on their base.

The composite materials used in the preparation of aqueous dispersions of composite nanomaterials are biocompatible. Some of their characteristics are described below.

Biomaterial BSA from AMRESCO with code 0332-100G and CAS# 9048-46-8 was used as the matrix of the composite BSA/MWCNT nanomaterial. As filler in the composite nanomaterial, MWCNT of the "Taunit-MD" type is used. The main parameters of these carbon nanotubes are: outer diameter is 30–80 nm; internal diameter is 10–20 nm; length is $\geq$ 0 μm; total amount of impurities after purification is $\leq 1\%$; bulk density is 0.0 3–0.5 g/cm^3; specific surface area is 180–200 m^2/g; thermal stability in air is ≤ 600 °C.

After drying the moisture, the composite concentration of the constituent parts of the composite nanomaterial changes. In fact, if the aqueous dispersion was 20% by weight of BSA/0.5% by weight of MWCNT, then after deposition on the substrates and drying, a composite nanomaterial layer composed of BSA/$\sim$2 wt% MWCNT is formed.

Figure 40.1 shows the appearance of a typical layer with a thickness $d \sim 0.5$ μm, made of a composite BSA/MWNT nanomaterial, deposited on a calico. Usually, the layers were strips with 5–7 mm wide and 25–30 mm long. Figure 40.2 shows a photo of the mechanical part of the installation, allowing measurements of the sensor parameters for bending deformations (concavity, curvature). The following parameters are recorded: number of cycles, number of steps, resistance, operating temperature, measurement time of each step. The bending radius r is adjustable in the range of 0.5–10 mm. In all cases, we used $r = 2$ mm.

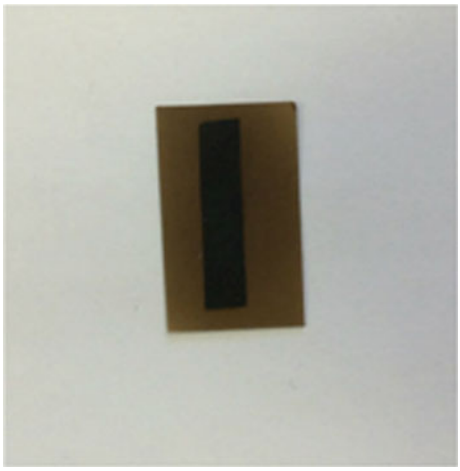

Fig. 40.1 Typical layers of BSA/MWCNT composite nanomaterial on a chintz substrate

Fig. 40.2 Photo of the mechanical part f the installation, in the middle (between the "paws") of which he sample is fixed

In Fig. 40.2, electrodes are seen from aluminum and getinax rods with cuts in which the ends of the sensor are fixed. One step corresponds to an angle $\theta = 2°$ of the electrode rotation, i.e. bending the sensor. The step speed (bending) is adjustable in the range of 0.2–2 step/s. The bending range can be $\Delta\theta = \pm 180°$. At $\theta = 0$, the sensor is not deformed; at $\theta > 0$, the sensor is concave (the free surface is concave); at $\theta < 0$, the sensor is bent (the free surface is bent). In our experiment, one complete cycle contained about 280 steps, i.e. the sensor received bends in the range $\Delta\theta = \pm 140°$. The bending speed is $\sim$0.5 step/s, i.e. 1°/s, one measurement cycle lasted $\sim$560 s. For some sensors, the total number n of measurement cycles reached $n \sim 50$, and the number of steps $\sim$200,000.

Figure 40.3 shows a typical dependence of the resistance R on the angle θ for a sensor, based on a film of the BSA/MWNT composite nanomaterial for a number of measurement cycles $n = 30$. It can be seen that the curve $R(\theta)$ is continuous and practically linear for small ranges of $\Delta\theta$, for example, $\Delta\theta = 20°$. At initial cycles (n = 1–10), hysteresis is observed on $R(\theta)$, which gradually decrease with

increasing n, and at $n \geq 25$ practical disappear. For example, for $n = 1$ and fixed $\theta = 0$, the hysteresis range for R reaches 10–15%, and for a fixed R the hysteresis range for θ is 30%. However, as the cycles increase and at $n \geq 25$, the hysteresis values decrease significantly and they do not exceed 1–2% in one measurement cycle. With an increase in n, the absolute value of R is insignificantly increased. In particular, for the case shown in Fig. 40.3, with $\theta = 0$, the sensor resistance varies from 56.5 to 57.1 kΩ, with registration cycles $n = 1$ and $n = 30$, respectively.

According to Fig. 40.3, the strain gage considered is a bipolar strain gauge. The physical mechanism of the bipolar behavior of the strain sensor is related to the following: compression (concavity) increases, and stretching (curvature) reduces the density of contacts between CNTs at bending points of the film. Accordingly, during compression, the electrical conductivity increases, and decreases with stretching.

From $R(\theta)$, the sensitivity was calculated: $S_\theta \sim 2\times10^{-3}$ deg^{-1} and $S \sim 40$. They have acceptable order and exceed the values, achieved in the prototype. The value of S was determined taking into account the bending radius $r = 2$ mm and the thickness $d \approx 0.5$ μm, as $S = (\Delta R/R_0)/(d/r)$ according to the geometry of the film.

Similar $R(\theta)$ curves were recorded for films of the composite nanomaterial MCC/MWCNT. Some parameters of the sensors, obtained by processing $R(\theta)$, are given in Table 40.1. The specific resistivity $R(\theta)$ of the layers is determined in the absence of deformation, i.e. at $\theta = 0$.

Table 40.1 shows the measured sensor data (accuracy in order of magnitude), from which the correlation follows: high bend strain sensitivity is realized on thinner films having relatively low resistivity. We note that the obtained values of $S_\theta \sim (13–17)\times10^{-3}$ deg^{-1} and $S \sim 100–160$ exceed by more than an order of magnitude those in the strain gauges based on metal films and have the same order for strain gages on the base of semiconductors.

We note some important properties of the proposed sensor:

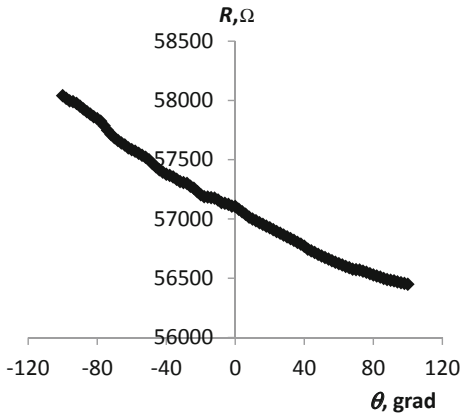

Fig. 40.3 Typical dependence $R(\theta)$ for layers of composite nanomaterial BSA/MWCNT

Table 40.1 Some parameters of strain sensors

Composite nanomaterial	d (μm)	ρ (mΩ m)	S_θ (deg^{-1})	S
BSA/MWCNT	~0.5	~60	$\sim 2\times10^{-3}$	~40
	~0.2	~80	$\sim 5\times10^{-3}$	~100
MCC/MWCNT	~0.4	~20	$\sim 13\times10^{-3}$	~150
	~0.1	~40	$\sim 17\times10^{-3}$	~160

(i) bipolar strain gauge has a high tensile sensitivity with respect to bending, 10^{-2} deg^{-1}; low resistivity ≤ 1 Ω;
(ii) the sensor is a film with a thickness of ≤ 0.5 μm from a composite nanomaterial, consisting of a matrix of biological material (bovine serum albumin or microcrystalline cellulose) and multilayered carbon nanotubes in small amounts ($\leq 3\%$ by weight);
(iii) the ability to form on the human skin with a 3-D printer;
(iv) a simple technology for preparing films on the surface of a flexible substrate that does not require heat treatment;
(v) the sensor can be applied directly to the human skin;
(vi) due to the high sensitivity and small mass-dimensions, the proposed sensor is promising as a pressure sensor and as a sensor of tactile sensation;
(vii) for a large number (more than 25) of the bending cycles, the hysteresis for the resistive characteristics is negligible ($\leq 1\%$).

The advantage of the deformation sensors described on the base of the layers of composite BSA/MWNT and CMC/MWCNT nanomaterials is the possibility to vary the consistency, hardness, modulus of elasticity, strain sensitivity and specific electrical conductivity in dependence on the preparation conditions and the concentration composition of the material. Moreover, these composite nanomaterials are biocompatible materials and on their base, it is possible to realize strain gages, both non-invasive and invasive medical applications. Therefore, for each specific task, we can select the necessary parameters of the sensor, in particular, the modulus of elasticity for its formation not only on the skin of a person, but also on the skin of various biological objects. Considered composite nanomaterials because of their biocompatibility, electrical conductivity and the possibility of application to the skin surface, are promising for the rapidly developing direction of "Skin Electronics".

Thus, the task has been accomplished. A bipolar strain sensor based on biocompatible nanomaterials with increased sensitivity and the possibility of its formation on the surface of human skin is proposed.

40.4 Conclusions

The overwhelming majority of diagnostic and therapeutic devices and systems require various sensors, including strain gauges. In particular, they are used to control the recovery after surgical operations or test thigmesthesia. In this work, we discussed some types of the layers with the tensoresistive properties and possibility of designing original medical tensoresistors on their base. The analyzed materials were divided in two groups: without CNTs (group I) and with them (group II).

(i) The group-I device the most promising for medical applications is an original tensoresistor, which represents a silicone elastomer, containing microchannels, filled with a conductive liquid [7]. Such a tensoresistor detects small bending ($\theta < 120°$) of human body parts with an error of 8%.

(ii) The group-II tensoresistors, which are based on thin films, containing aligned SWCNTs on flexible substrates, exhibit the excellent elasticity ($\varepsilon \sim 280\%$), but very low strain sensitivity ($S \leq 0.8$), high hysteresis, and low strain measurement accuracy [10]. The MWCNT film, placed between the natural rubber layers, demonstrated the highest strain sensitivity ($S \sim 43$) at $\varepsilon \sim 620\%$ [6]. However, their $\delta R(\varepsilon)$ dependences are approximately linear only at $\varepsilon \leq 100\%$.

(iii) In many cases, the CNT films were encapsulated between flexible PDMS layers. The tensoresistors of this type exhibit the highest parameters, including the maximum strain of $\varepsilon \sim 500\%$ and the approximately linear dependence of the relative resistance variation on ε in the range of $\varepsilon < 150\%$, as well as the stability and repeatability of the detected signal upon multiple loading/unloading cycles ($\sim$2000) [19].

(iv) Nevertheless, the above-mentioned gauges cannot be directly laminated onto a complex curvilinear human skin surface to control the skin surface dynamics with high accuracy. This limitation is related to the fact that the PDMS polymerization requires heat treatment at a temperature of 70 °C for 2 h.

(v) In epoxy nanocomposites, the high strain sensitivity ($\sim$22) is implemented at the low MWCNT concentration ($\sim$1 wt%) [23–25].

(vi) The layers based of a nanocomposite, consisting of CMC and MWCNTs, showed the quite acceptable parameters, i.e., the high electrical conductivity (10^{-1}–10^{-4} S/m) and a bending sensitivity of $\sim$0.80%/grad.

Based on the layers of composite BSA/MWCNT and MCC/MWCNT nanomaterials, prototype tensoresistors of bipolar behavior and tensor sensitivity values of $\sim$ 100–160 are realized [50]. The bipolar strain sensor has a high tensile sensitivity with respect to bending (10^{-2} deg^{-1}), low specific resistance ($\leq$ 1 Ω m) and small hysteresis ($\leq$3%) after training cycles (deformation increases/deformation decreases) more than 25 times. The aqueous dispersion of the proposed nanomaterials contains biocompatible materials (matrix) and a small amount of carbon nanotubes (filler $\leq$3 wt%). Water dispersions can be applied by a

3D-printer on human skin, which is very promising in the development of the direction of “Skin Electronics”.

In most cases, the region of tensoresistor linearity should be broadened, which is a complex problem. To do this, it is necessary to take into account not only the substrate elasticity, but also transparency of tunnel contacts at the points of nanotube adjustment in the CNT-containing layers [50, 51]. In some cases, the above-described tensoresistors have the characteristics suitable for applications in medicine. However, their safety at the lamination onto the human skin has still been investigated and the results of these investigations are of crucial importance [32]. In addition, it should be taken into account that the tensoresistors need to be protected from moisture, temperature, gases, and other effects during their operation.

Thus, the results obtained yield a promising outlook of fabrication of the tensoresistors containing carbon nanotubes or nanocomposites based on them.

Acknowledgements The study was carried out with the financial support of the Russian Foundation for BasicResearch and the German research community in the framework of the research project No. 19-51-12005. The work was done with the involvement of the Center by the collective use of “Microsystem technology and electronic component base MIET” and the Center for Technological Initiative MIET “Sensory”.

References

1. http://www.hbm.ru/pic/pdf/1372416324.pdf
2. X. Liang, S.A. Boppart, IEEE Trans. Biomed. Eng. **57**(4), 953 (2010)
3. J. Zhou, Y. Gu, P. Fei et al., Nano Lett. **8**(9), 3035 (2008)
4. X. Xiao, L.Y. Yuan, J.W. Zhong et al., Adv. Mater. **23**, 5440 (2011)
5. C. Mattmann, F. Clemens, G. Tröster, Sensors. **8**(6) (2008)
6. S. Tadakaluru, W. Thongsuwan, P. Singjai, Sensors. **14** (2014)
7. Y. Menguc, Y.-L. Park, E. Martinez-Villalpando et al., in *IEEE International Conference on Robotics and Automation*, p. 5309, Karlsruhe, Germany, 6–10 May 2013
8. D. Jiang, *EMSL Department of Microtechnology and Nanoscience (MC2).* (Chalmers University of Technology, SE-412 96 Gothenburg, Sweden, 2015), p. 55
9. D. Jung, G.S. Lee, J. Sens. Sci. Technol. **22**(5), 315 (2013)
10. T. Yamada, Y. Hayamizi, Y. Yamamoto et al., Nat. Nanotechnol. **6**, 296 (2011)
11. Y. Liu, Q. Sheng, S. Muftu et al., *Transducers*, p. 1091. (Barcelona, Spain, 16–20 June 2013)
12. S.M. Vemuru, R. Wahi, S. Nagarajaiah, P.M. Ajayan, J. Strain Analysis. **44**, 555 (2009)
13. Y. Wang, L. Wang, T. Yang et al., Adv. Funct. Mater. **24**, 4666 (2014)
14. A. Mata, A.J. Fleischman, S. Roy, Biomed. Microdevices **7**(4), 281 (2005)
15. Q. Qin, Y. Zhu, ACS Nano **5**(9), 7404 (2011)
16. Q. Fan, Z. Qin, S. Gao et al., Carbon **50**(11), 4085 (2012)
17. A. Mata, A.J. Fleischman, S. Roy, Biomed. Microdevices **7**, 281 (2005)
18. J. Lu, M. Lu, A. Bermak, Y-K., in *7th IEEE Conference on Nanotechnology*, p. 1240. (Hong Kong, China, 2–5 August 2007)
19. M. Amjadi, Y.J. Yoon, I. Park, Nanotechnology **26**, 375501 (2015)
20. K.F. Akhmadishina, I.I. Bobrinetskii, R.A. Ibragimov et al., Inorg. Mater. **50**(1), 23 (2014)
21. K. Grabowski1, P. Zbyrad, A. Wilmanski, T. Uhl, in *7th European Workshop on Structural Health Monitoring*, vol. 1, p. 1768. (La Cite, Nantes, France, 8–11 July 2014)

22. B. Ashrafi, K. Laqua, Y. Martinez-Rubi, et al. in *31st Annual Technical Conference of the American Society for Composites*. vol. 1, p. 307. (Williamsburg, Virginia, USA, 19–22 September 2016)
23. N. Hu, Y. Karube, M. Arai et al., Carbon **48**, 680 (2010)
24. G. Yin, N. Hu, Y. Karube et al., Compos. Mater. **45**, 1315 (2011)
25. N. Hu, T. Itoi, T. Akagi et al., Carbon **51**, 202 (2013)
26. L. Ichkitidze, V. Podgaetsky, S. Selishchev et al., Mater. Sci. Appl. **4**(5A), 1 (2013)
27. L.P. Ichkitidze, V.M. Podgaetsky, A.S. Prihodko et al., Biomed. Eng. **47**(2), 68 (2013)
28. L. Weiwei, in *FIU Electronic Theses and Dissertations*. 2016, p. 3025
29. X. Li, C. Levy, Sens. Transducers J. **7**(Special Issue), 5 (2009)
30. Yu. Liu, *Electrical Engineering Dissertations*, 2012, p. 156
31. A.A. Krechetov, Vestnik Mashinostroenia. **8**, 50 (2015). (in Russia)
32. S-Z. Guo, K. Qiu, F. Meng et al., Adv. Mater. 1701218 (2017)
33. E. Andreoli, R. Suzuki, A.W. Orbaek et al., J. Mater. Chem. B. **2**(29), 4740 (2014)
34. E. Dillon, M.S. Bhutani, A.R. Barron, J. Mater. Chem. B. **1B**, 1461 (2013)
35. H. Kafa, J.T.W. Wang, N. Rubio et al., Biomaterials **53**, 437 (2015)
36. J. Liu, F. Appiax, O. Bibari et al., Nanotechnology **22**(19), 195101 (2011)
37. I. Bobrinetsky, A. Gerasimenko, L. Ichkitidze et al., Am. J. Tissue Eng. Stem Cell **1**(1), 27 (2014)
38. N. Alegret, E. Santos, A. Rodriguez-Fortea et al., Chem. Phys. Lett. **525–526**, 120 (2012)
39. S.H. Lacerda, J. Semberova, K. Holada et al., ACS Nano **5**(7), 5808 (2011)
40. B.M. Mohamed, D. Movia, A. Knyazev et al., Sci. Rep. **3**, 1124 (2013)
41. B.L. Allen, G.P. Kotchey, Y. Chen et al., J. Am. Chem. Soc. **31**, 17194 (2009)
42. C. Farrera, K. Bhattacharya, B. Lazzaretto et al., Nanoscale **6**, 6974 (2014)
43. F.T. Andon, A.A. Kapralov, N. Yanamala et al., Small **9**, 2721 (2013)
44. J.M. Tan, P. Aruselvan, S. Fakurazi, et al., J. Nanomater. **2014**, Article ID 917024 (2014)
45. Y. Zhang, Y. Bai, B. Yan, Drug Discovery Today **15**(11/12), 429 (2010)
46. B.M. Mohamed, D. Movia, A. Knyazev et al., Sci. Rep. **3**, 1241136 (2013)
47. H. Haniu, N. Saito, Y. Matsuda et al., Int. J. Nanomed. **9**, 1979 (2014)
48. AYu. Gerasimenko, A.A. Dedkova, L.P. Ichkitidze et al., Opt. Spectrosc. **115**, 283 (2013)
49. L.P. Ichkitidze, M.S. Savelev, E.A. Bubnova et al., Biomed. Eng. **49**(1), 36 (2015)
50. L.P. Ichkitidze, V.A. Petukhov, A.Y. Gerasimenko, V.M. Podgaetsky, S.V. Selischev, Patent RF, No. 2662060
51. http://www.amresco-inc.com/ALBUMIN-BOVINE-0332.cmsx

Chapter 41
Optimization of $Zn_{1-x-y}Mg_xAl_yO$ Film Properties to Use in Deep UV SAW Photodetector

M. E. Kutepov, V. E. Kaydashev, G. Ya. Karapetyan, D. A. Zhilin, T. A. Minasyan, A. S. Anokhin, A. V. Chernyshev, K. G. Abdulvakhidov, E. V. Glazunova, V. A. Irkha and E. M. Kaidashev

Abstract The maximum of spectral sensitivity of ZnO based photodetectors can be shifted to deep UV photon range of ~250 to 300 nm by Mg dosing [1, 2]. However heavily Mg doped ZnO shows very poor conductance and optical properties, which limits its use as a sensitive element of deep UV SAW photodetector. The simultaneously doped ZnO by Mg and Al atoms may assist in tuning electrical, optical and structural properties of ZnO in wide range and opens the possibility to use $Zn_{1-x-y}Mg_xAl_yO$ films for deep UV detector integrated to SAW device. Apart from dopant related aspects the structural and optical quality of a film prepared by PLD method is heavily influenced by the film/nanostructure growth temperature and oxygen pressure. We study optical, structural, lattice vibration modes and photoelectric properties of $Zn_{1-x-y}Mg_xAl_yO$ films on $LiNbO_3$ substrates designed by PLD method at different oxygen pressure and growth temperatures to optimize their properties for using as a deep-UV-sensitive element of surface acoustic wave (SAW) photodetector. The optical absorption band edge for optimized $Zn_{0.52}Mg_{0.19}Al_{0.007}O/LiNbO_3$ film was shifted to 320 nm and the corresponding photodetector demonstrates high sensitivity and fast photoelectric response towards 248 nm laser light.

M. E. Kutepov · V. E. Kaydashev (✉) · G. Ya.Karapetyan · D. A. Zhilin · T. A. Minasyan · A. V. Chernyshev · K. G. Abdulvakhidov · E. M. Kaidashev
Southern Federal University, Stachki 200/1, Rostov-on-Don 344090, Russia
e-mail: kaydashev@gmail.com

A. S. Anokhin
Southern Scientific Center of the RAS, Chekhova 41, Rostov-on-Don 344006, Russia

E. V. Glazunova
Southern Federal University, Stachki, 194/1, Rostov-on-Don 344090, Russia

V. A. Irkha
Don State Technical University, Gagarina 1, Rostov-on-Don 344002, Russia

I. A. Parinov et al. (eds.), *Advanced Materials*, Springer Proceedings in Physics 224, https://doi.org/10.1007/978-3-030-19894-7_41

41.1 Introduction

The band gap of ZnO can be gradually enlarged from 3.37 to ~4.05 eV by Mg doping up to 49 at. mol% [1]. This results in ZnO UV light sensitivity shift to the range of 220–260 nm [2]. However a high Mg content in ZnO provokes a formation of defects in crystalline structure, which causes the degradation of its optical properties. The conductance of ZnO is dramatically decreased upon Mg dosing, which limits the use of such material in many photonic applications. In opposite case, a doping of ZnO by Al results in lower resistance making the ZnO properties similar to those of metal.

The optical, electrical and structural properties of ZnO may be widely tuned when it is simultaneously doped by Mg and Al atoms, which provides great flexibility for design of deep UV photodetector integrated to SAW device.

In particular, the band gap is enlarged by the increase of the Mg content and the conductivity can be controlled by the variation of the *x*/*y*-ratio in $Zn_{1-x-y}Mg_xAl_yO$ oxide. Namely, $Zn_{0.96-x}Mg_xAl_{0.04}O$ ($x = 0.25$) films show both a band gap as wide as 4.5 eV and a resistance as low as 6×10^{-3} Ω·cm [4].

The minor structural strains are desired to obtain a highly UV light sensitive photodetector with fast photoresponse/relaxation. Interesting, that the structural defects amount is also regulated by the *x*/*y*-ratio. Indeed the lattice constant of Al_2O_3 is larger and of MgO is smaller than the lattice constant of ZnO [3]. Therefore $Zn_{1-x-y}Mg_xAl_yO$ and ZnO may possess the similar lattice constant when the *x*/*y*-ratio is ~2.8, even if the needed Mg content is chosen arbitrary [3].

It was found that the crystalline quality of $Zn_{1-x-y}Mg_xAl_yO$ with 10 at. mol% of Mg and Al content less than ~4 to 5 at. mol% remains good [4] and is degraded when Mg content is increased to ~30 at. mol% [3]. Indeed, the best crystallinity and minimal structural stress of $Zn_{1-x-y}Mg_xAl_yO$ films are expected at Mg and Al content less than ~30 at. mol. and ~4 to 5 at. mol%, respectively. However it does not mean that those structures are best for photoelectric applications, i.e. have low amount of long living trap states in the band gap. Moreover, as we will show below, sometimes, amorphous films show better photoelectric performance compared to crystalline counterparts.

The design of a UV photodetector based on a photosensitive ZnMgAlO film located in the channel of propagation of surface acoustic waves (SAWs) is even more challenging task then the design of resistive type photodetector. The permissible range of conductivity of a photosensitive ZnMgAlO film in "dark"/illumination regimes is dictated by the features of attenuation of an acoustic wave in a film due to acoustoelectric interaction. In particular, heavy doping of ZnO by Mg results to gradual decrease of the film conductance, which eliminates the acoustoelectric interaction. The acoustic wave passes the film almost without attenuation and the illumination induced conductivity changes cannot be monitored. On the contrary, at high Al concentrations the ZnO conductivity is increased, which causes a high native ("dark") attenuation of the propagating SAW. The dynamic range ("amplitude") of the conductivity change in the "light on/off" regime in this case is

also low. Therefore, the UV "light on/off" conductivity of ZnMgAlO film should be not too low and not high to meet requirements needed for successful integration of film to SAW device.

Apart from the above-mentioned dopant related aspects, the structural, optical and photoelectric properties are influenced by the film growth temperature and by the ambient oxygen pressure. For PLD and CVD techniques the energetics of atomic/molecular species near the substrate surface and material flux velocity also influence the material quality. In particular for films prepared by PLD method the used laser wavelength, laser fluence, pulse repetition rate, the ambient gas pressure and corresponding plasma plume stopping distance define the energetics of species in plasma and influence the amount of structural defects and electronic states.

Therefore the wavelength photosensitivity of the designed $Zn_{1-x-y}Mg_xAl_yO$, its conductance and UV light sensitivity and photo-response time may be optimized by varying the Mg and Al content and films deposition conditions.

In this paper, we study the optical, structural and photoelectric properties of ZnMgAlO films *YX*-128° $LiNbO_3$ substrates prepared by pulsed laser deposition method at varied growth temperatures. We explore the deposition regimes, which are best to design fast and highly sensitive deep UV SAW photodetector.

41.2 Synthesis

A series of ZnMgAlO films was deposited on a central part of $LiNbO_3$ *YX*-cut 1×2 cm^2 substrates using pulsed laser deposition method (PLD). Laser ablation was performed by focusing a KrF (248 nm) laser beam at a rotating $Zn_{0.52}Mg_{0.19}Al_{0.007}O$ ceramic target to give a fluence of 2 J/cm^2. The target to substrate distance was set to be 5 cm and a $\sim$250 nm thick film was deposited for 4000 laser pulses. The films were deposited at oxygen ambient pressure of 10^{-1} mBar and at substrate temperatures of 400–600 °C.

The optical transmission of prepared films was characterized by depositing similar films onto double side polished fused silica substrates, which were positioned near the ZnMgAlO/$LiNbO_3$ samples and were prepared simultaneously.

41.3 Experiments and Discussion

Transmittance spectra (Fig. 41.1) showed a considerable shift of light absorption edge into UV region up to $\sim$260 nm. For comparison, absorption edge of pure ZnO is equal to 365 nm. The optical band gap energy (E_g) was determined by plotting $(\alpha h\nu)^2$ against $h\nu$. The band gap is increased for more than 1.5 eV compared to the pure ZnO (3.37 eV) and shows a maximum at 5.034 eV for sample grown at 500 °C (Fig. 41.2).

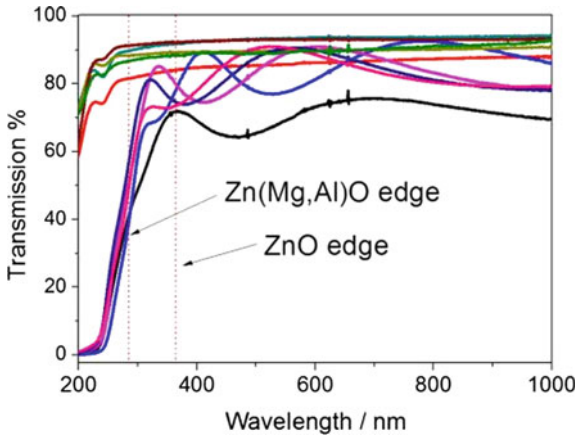

Fig. 41.1 Transmittance spectra of ZnMgAlO samples

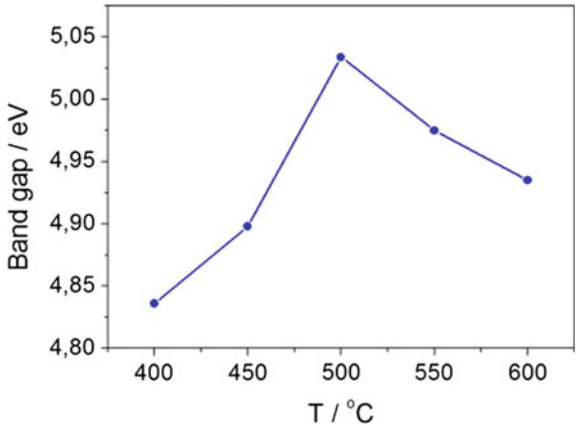

Fig. 41.2 Band gaps of ZnMgAlO films prepared at different growth temperatures

Structural properties of the samples were investigated by means of X-ray diffraction (XRD) analysis. Substitution of the larger Zn_{2+} ions (0.60 Å) by the smaller Mg_{2+} ions (0.57 Å) results in shift of (0002) reflex to larger angles. Indeed for samples grown at elevated temperature of 550–600 °C, the ZnMgO (0002) reflex was revealed at 34.7°, which is shifted compared to (0002) reflex of ZnO, observed in reference sample at 34.5°.

The samples, grown at lower temperatures of 400–500 °C, showed a considerable decrease of the (0002) ZnMgO reflex (Fig. 41.3). As the (0002) ZnMgO did not show a detectable shift for samples, grown at different temperatures, we believe that the Mg content in ZnO lattice was not strongly changed. However the considerable decrease of (0002) ZnMgO reflex for samples, obtained at lower temperatures, claims that the overall degradation of ZnMgO crystalline structure occurs and the amorphous phase content increases at lower temperatures. The former statement is supported by the appearance of additional MgO peak at 42.55° for the samples grown at temperature of 400–500 °C.

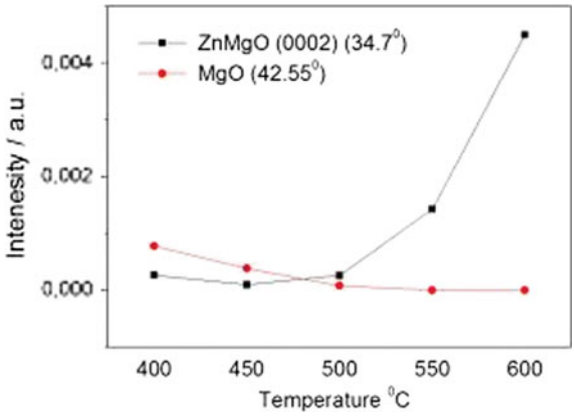

Fig. 41.3 Dependence of (200) MgO and (0002) ZnMgO XRD peak intensity on the synthesis temperature

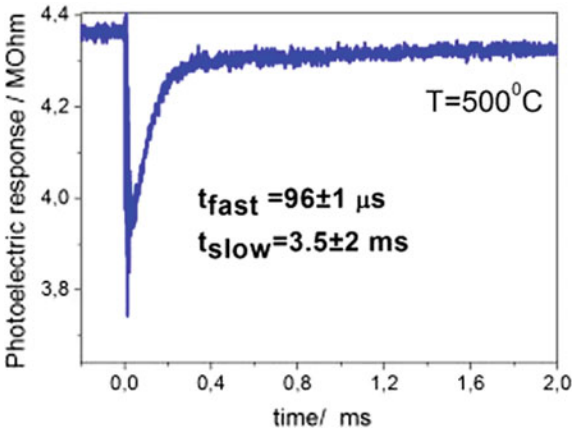

Fig. 41.4 Photo-electric response of Zn(Mg, Al)O films upon exposure by 15 ns pulse of KrF laser at 248 nm

The samples, grown at elevated temperature, show also higher conductivity and larger band gap compared to those prepared at 400–500 °C. Indeed, ZnMgO crystalline structures are known to have much lower conductivity compared to the pure ZnO.

Photoelectrical characteristics were investigated under 15 ns KrF pulsed laser (248 nm) irradiation and energy of ~100 μJ per pulse.

Having poor crystal structure, the ZnMgAlO films, grown at low temperatures, show however much better photoelectrical characteristics. The amount of defect states, which trap the recombining carriers, is lowered which results in very fast (0.1–0.2 ms) photo-response to nanosecond 248 nm laser pulses with absent or minor slow (~ms) photo-response component (see Fig. 41.4).

On the other hand, samples grown at higher temperatures possessed slow photo-response even having better structure and much higher conductivity. This can

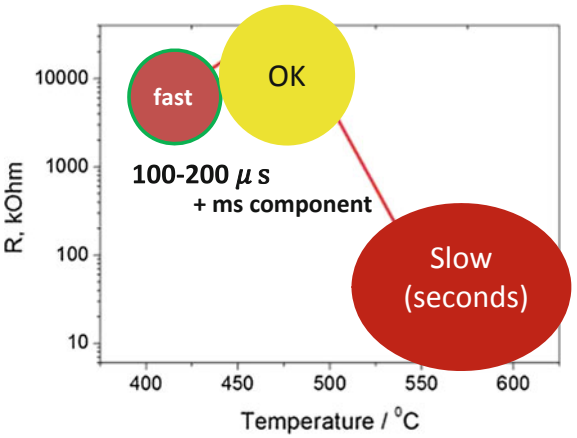

Fig. 41.5 Dependence of the samples resistance on the synthesis temperature

Table 41.1 Times of fast and slow components of electric photoresponse

Temperature of growth	Photo-electric response (t_1), μs	Photo-electric response (t_2), ms
400	126 ± 5	–
450	208 ± 3	23.5 ± 0.7
500	96 ± 1	3.5 ± 2
550	–	1361 ± 12
600	13 ± 0.5	1092 ± 18

be explained by the presence of long-living states in the film material, which hinder the rapid recombination of carriers and significantly increase the recovery time of the detector.

Besides response speed, the samples made at a temperature of 400–500 °C also showed higher sensitivity to 248 nm (see Fig. 41.5 and Table 41.1). For comparison, ΔR (UV on/off) for low-temperature samples was ~15%, and for samples with an increased synthesis temperature, ΔR was only ~1%.

41.4 Conclusions

In summary, we synthesized a series of ZnMgAlO samples using PLD method at different temperatures (400–600 °C). In spite of poor crystallinity, the samples grown at lower temperatures (400–500 °C) showed high and fast photoelectric response. Further rise of a growth temperature resulted in improvement of structure and degradation of sensing properties of the samples. We believe that ZnMgAlO films, prepared at 400–500 °C with fast and deep UV sensitive photoelectric films,

may replace previously designed ZnO films in previously proposed by us multiple acoustic reflection type SAW photodetector [5], however much shifting its UV sensitivity range.

Acknowledgements This research work is supported by Russian Education and Science Ministry project No. 16.5405.2017/8.9 and RFBR according to the research project No. 16-58-52013 MNT_a.

References

1. W.I. Park, G.C. Yi, H.M. Jang, Appl. Phys. Lett. **79**, 2022 (2001)
2. H. Endo, M. Kikuchi, M. Ashioi, Y. Kashiwaba, K. Hane, Y. Kashiwaba, Appl. Phys. Express **1**, 051201 (2008)
3. I.S. Kim, B.T. Lee, Cryst. Growth Des. **10**, 3273 (2010)
4. C. Yang, X.M. Li, X.D. Gao, X. Cao, R. Yang, Y.Z. Li, Solid State Commun. **151**, 264 (2011)
5. G.Y. Karapetyan, V.E. Kaydashev, D.A. Zhilin, T.A. Minasyan, K.G. Abdulvakhidov, E.M. Kaidashev, Smart Mater. Struct. **26**(3), 035029 (2017)

Chapter 42
Study of Archimedes Wave Swing Harvester for Indian Ocean

Rommel Nath, P. K. Kankar and V. K. Gupta

Abstract Ocean waves are one of the great sources of energy. Researchers have explored various ways to extract energy from these ocean waves. Tides generated due to gravitational force between earth and moon and partly between earth and sun help in generating high heads of water to harness pollution free energy. The objective of this paper is to model Archimedes Wave Swinger (AWS) for Indian Ocean application for energy harvesting. The AWS is a submerged air-filled piston that expands and contracts in response to wave pressures. Relative movement of the two parts of the device (floater and stator) is converted directly to electricity by a linear generator. A Simulink model is developed for the purpose. Mechanical and electrical systems are coupled through floater velocity and operation condition is determined based on bode plot.

42.1 Introduction

Ocean energy is highly concentrated energy per square meter. It is considered as one of the economical form of renewable energy. The Indian coastal line of 7516.5 km has great potential to fulfill the energy requirement of India as well as nearby countries [1]. In this paper, a mathematical model for conversion of ocean wave energy into electrical energy has been derived. Various devices having the capability of conversion of such energy have been developed [2]. These devices works on different principals developed based on different environmental

R. Nath (✉) · P. K. Kankar · V. K. Gupta
Discipline of Mechanical Engineering, PDPM Indian Institute of Information Technology, Design and Manufacturing, Jabalpur, Jabalpur, Madhya Pradesh, India
e-mail: emailtorommel@gmail.com

P. K. Kankar
e-mail: kankar@iiitdmj.ac.in

V. K. Gupta
e-mail: vkgupta@iiitdmj.ac.in

I. A. Parinov et al. (eds.), *Advanced Materials*, Springer Proceedings in Physics 224, https://doi.org/10.1007/978-3-030-19894-7_42

conditions and type of external force. A comparison of such devices has been summarized in Table 42.1.

Indian Ocean is considered as low tide region (less than 2 m height) and hence AWS is best suited for the conversion in such cases. Maximum average height of Indian Ocean waves (near India) is observed as 0.64 m as per BD14 Moored Buoy device [1]. AWS works on the principal of resonance and can produce large displacement. Hence, in this paper AWS as developed by Breugel and Gardner [6] has been considered for study. The working principle of the device is simple and is shown in Fig. 42.1.

Table 42.1 Comparison of different devices developed

Sr. no	Device name	Place of installation	Installed capacity	Developer	Year of development
1	Pelamis Waves [3]	Aguçadoura Wave Farm	2.25 MW	Pelamis Wave Power	2008
2	Wavestar [4] Hanstholm prototype	Hanstholm west coast Denmark	6.877 MWh	Wavestar and EnergiNet.dk	2010
3	Tidal Barrages [5]	Kislaya Guba, Russia	1.7 MW	RusHydro	1968
4	Archimedes wave swing [6]	Portuguese coast	2 MW	AWS Ocean Energy Ltd	2004
5	Oscillating Water Column [7]	Isle of Islay	500 kW	Wavegen and Queen's University Belfast	2000
6	Wave Dragon [8]	Wales	7 MW	Wave Dragon	2009

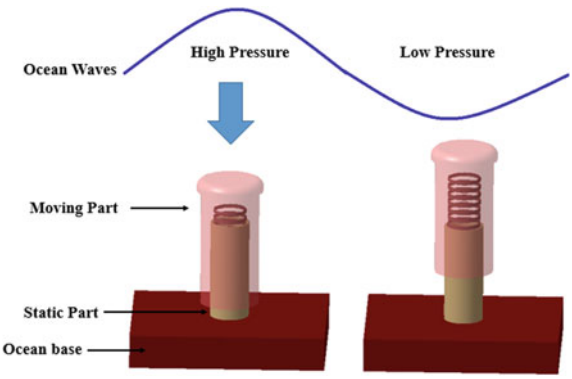

Fig. 42.1 Working principle of AWS

AWS consists of two parts:

- upper movable part is called a floater;
- the lower part is fixed in the sea bed and is called stator.

The entire device is submerged under the ocean. A chamber is placed between the fixed and floater part and contains air. The ocean waves have crust and trough as shown in Fig. 42.1. When trough part of ocean wave comes over AWS, floater moves upwards. Similarly, when crust part of the wave comes over AWS, floater moves downwards. During these movements, the lower part does not have any movement. The floater contains permanent magnet, which moves up and down due to movement of waves. The fixed part contains stator winding in a closed loop. Due to movement of magnet inside stator, electric field is generated due to Electro Magnetic Force (EMF). It works similar to a linear generator.

For achieving higher velocity and stroke length, system frequency can be matched with the average ocean wave frequency i.e. the system can be operated near resonance. This system is unique as it is fully submerged in the ocean. It will not have any danger of exposure to tsunami, human disturbance, hurdle for ships and submarines. Pacific Northwest National Laboratory specifies that these devices have negligible effect on marine life.

The AWS device pilot plant was assembled in Portuguese coast in 2001 [8]. Indian waves do not have waves similar to Portuguese wave. This research is focussed on implementing AWS system for Indian coastal system and modifying the system for generation of economical and renewal energy.

42.2 Modeling of AWS

42.2.1 Mechanical Model of AWS

The AWS system encounters forces such as-

- radiation force, F_{RAD}
- friction of bearing, F_{BEAR}
- horizontal force, F_{HOR}
- drag force-F_{DRAG}
- generator force due to electronic convertor, F_{GEN}
- water brakes damping force, F_{WB}
- air pressure inside AWS, F_{AIR}
- force due to N_2, F_{NITRO}
- gravity force, F_{GRAV}
- hydrostatic pressure force, F_{HS}
- total dynamic pressure field acting force (exciting force), F_{WAVE}.

These forces guide the motion of the AWS floater and are responsible for AWS wall strength and controls the device output.

By applying Newton second law, we obtain:

$$F_{\mathrm{WAVE}} + F_{\mathrm{RAD}} + F_{\mathrm{BEAR}} + F_{\mathrm{DRAG}} + F_{\mathrm{HOR}} + F_{\mathrm{GEN}} + F_{\mathrm{WB}} + F_{\mathrm{AIR}} + F_{\mathrm{NITRO}} + F_{\mathrm{GRAV}} + F_{\mathrm{HS}} = m\vec{a} \tag{42.1}$$

By substituting forces at their respective place and simplifying as proposed by Prado et al. [6], Eq. (42.1) can be written as

$$(m_{\mathrm{f}} + m_{\mathrm{add}\infty})\ddot{x} + \beta_{\mathrm{GEN}}\dot{x} + \beta_{\mathrm{WB}}\dot{x}|\dot{x}| + kx = F_{\mathrm{WAVE}} \tag{42.2}$$

In the above equation

- m_f = 0.4 Mkg, it includes all the weights moving part of AWS it also includes the generator translator of the device;
- m_{add} = 0.2 Mkg, it is taken from hydrodynamic software AQUADYN from reference Sarmento and A Luis;
- $\beta_{\mathrm{GEN}} = 275$ kN s/m, it is calculated from the above mentioned formula of force generation;
- $\beta_{\mathrm{WB}} = 1.42 \times 10^6\,\mathrm{N} \times \mathrm{s}^2/\mathrm{m}^2$; it is given by standard hydraulic discharge and coefficient water brakes geometric dimensions of the water brakes;
- k = 0.55 MN/m; it is calculated here from stiffness formula mentioned above.

In (42.2), third term corresponds to force of water brake and is a function of direction. One can consider one direction positive and its opposite direction as negative. In this work, upward motion is considered as negative (−) and downward motion as positive (+). The equation is solved by ODI23 of MATLAB®. Time period for Portugal sea conditions is taken from reference paper Prado et al. [6], and is equal to 11.5 s. Corresponding angular frequency comes out to be $\omega = 0.5463$.

For F_{WAVE}, amplitude of wave force F_0 is calculated by applying boundary conditions. The calculated output matches with the data of prototype pilot plant created in Portuguese in 2001. This ensures that the mathematical model is working correctly.

After verifying the model with the reference [6], same model is used to calculate output power for Indian Ocean waves. Indian Ocean data is taken from Indian National Centre for Ocean Information Services [1].

For the Portugal Ocean conditions:

$$F_{\mathrm{WAVE}} = 7.569 \times 10^6 \cos 0.5463\,\mathrm{t} \tag{42.3}$$

The equilibrium condition of AWS at which all the forces balance each other is at 0.7 m.

In AWS nitrogen in cylinder, air in chamber and hydrostatic forces act as a spring. Their stiffness changes with respect to temperature of device. The floater of

the device is considered to move fast enough to behave like adiabatic process. The γ is the adiabatic coefficient, considered in this case equal to ~ 1.4.

Polinder et al. [9] mentioned the stiffness of nitrogen, air and hydrostatic forces as $k_a = 1.16 \times 10^6, k_n = 9 \times 10^4$, $k_h = -7 \times 10^5$ N/mm^2.

By substituting all terms into (42.2) of ocean waves we obtain:

$$0.6 \times 10^6 \ddot{x} + [275 \times 10^3 \dot{x} + 1.42 \times 10^6 \dot{x}|\dot{x}| + 5.5 \times 10^5 x = 7.569 \times 10^6 \cos 0.5463\,t \tag{42.4}$$

For safe running of device, a range is defined based on Bode diagram and it is observed to operate the device on a frequency ratio, which gives the best power as suggested by Valerio et al. [10].

42.2.2 Electrical Model of AWS

Electrical model is the power generation model of AWS is simulated in Simulink and works on the principle of electromagnetic induction. AWS generator system has three phases. AWS has a quasi-flat linear generator with the linear machine. In this analysis, the variable is velocity. The velocity varies sinusoidally with respect to the ocean wave current. From Simulink, the input and output powers of the generator at a rated speed of 2.2 m/s are 40 and 34 kW, respectively, corresponding to load resistance of 7.5 Ω. The combination of mechanical and electrical parts of AWS model can be simply defined in Fig. 42.2.

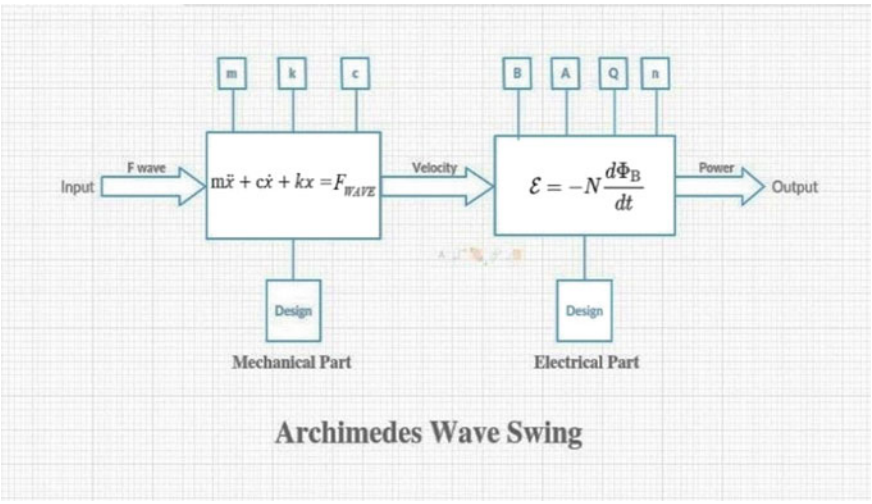

Fig. 42.2 Combined electrical and mechanical model of AWS

42.3 Result of AWS

42.3.1 Model Result for Indian Ocean Waves

The information for Indian Ocean waves are taken from INCOIS (Indian National Centre for Ocean Information Services) and used for analyzing the power output from Indian Ocean waves. The required parameter detail such as wave height and wave period are measured by the government of India using device named as Moored Buoy. These Buoys are placed at a set of places and some of them are represented in Table 42.2.

The installation locations of these devices are chosen near Indian coast to minimize the electricity transmission cost. For better results, data are taken in such a way that two devices AD09 and BD14 are recording the data of waves from Indian Ocean at two different location. Other two devices are chosen in such a way that BD11 device is located in the Bay of Bengal and AD07 device in the Arabian Sea. These data enable to observe device output across the entire Indian Ocean as well as two nearby seas. Figure 42.3 represents average wave data of Buoy BD14 for one year.

Table 42.3 represents minimum and maximum wave height and wave period of different Moored Buoy devices located at different locations of Indian coastline.

The data needed in the mechanical model as depicted by (42.2) is wave period corresponding to angular frequency of the oscillation of the ocean wave. Second data required is the force of wave. This force plays a key role in AWS working. It is known as exciting force. Calculation of this force requires assumption of linear wave characteristics.

Table 42.2 Moored Buoy Indian Ocean devices

Buoy ID	Latitude:Longitude	Device location
BD14	6.19:85.87	Indian Ocean (near Sri Lanka)
AD09	8.26:73.3	Indian Ocean (near Lakshadweep)
BD11	14.2:82.9	Bay of Bengal (near Andhra Pradesh)
AD07	14.99:68.89	Arabian Sea (near Maharashtra)

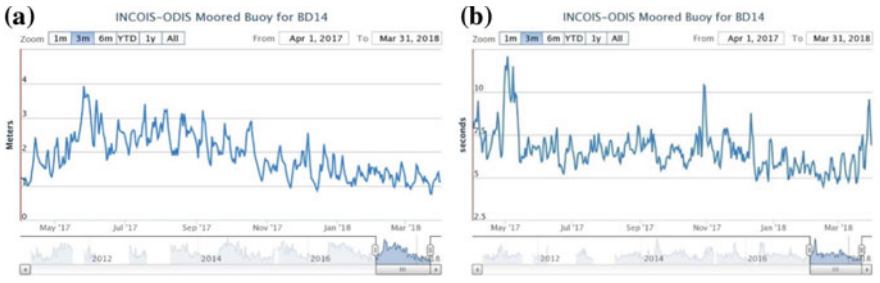

Fig. 42.3 **a** Moored Buoy BD14 wave height; **b** Moored Buoy BD14 wave period

Table 42.3 Moored Buoy Indian Ocean data

Buoy ID	Max:Min wave height (m)	Wave period (s)
BD14	2.70:1.42	6.78
AD09	1.52:0.90	6.55
BD11	2.29:1.16	6.93
AD07	2.15:1.16	6.24

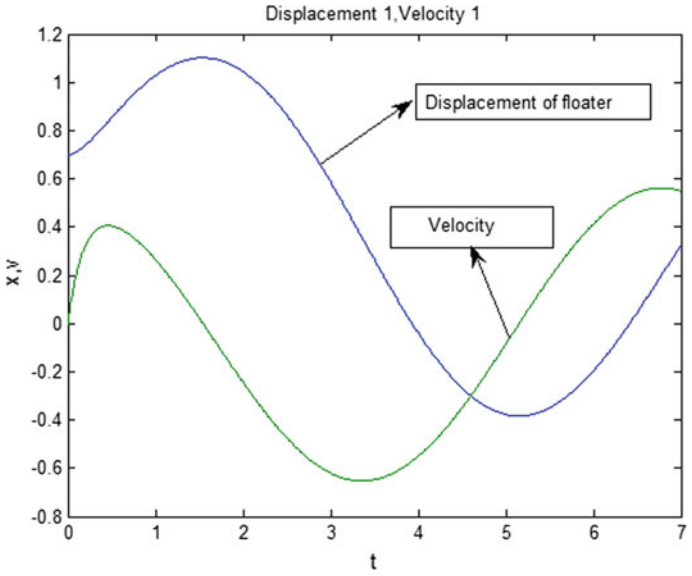

Fig. 42.4 Output velocity and displacement of AWS as per Indian Ocean wave

Table 42.3 indicates that BD14 Moored Buoy has maximum wave height out of considered regions of Indian Ocean. The wave force for this region is considered maximum on an average for throughout the year performance. By calculating angular frequency from wave period, it comes out to be 0.92 s. Wave amplitude is equal to 2.018×10^6. Therefore wave force (excitation force), calculated for height 0.64 m, is $2.018 \times 10^6 \cos 0.9267t$. By using this force in a mechanical model and basing on Ph.D thesis of Prasad [11], F_{WAVE} is calculated by using the relation obtained by Khalil [12]. Figure 42.4 shows output velocity and displacement of AWS. The output results for Indian Ocean waves are maximum stroke length 1.4853 m and maximum amplitude of floater velocity is equal to 0.5621 m/s.

Using the above output parameters in the electrical model in Simulink program, various outputs are calculated and shown in Fig. 42.5.

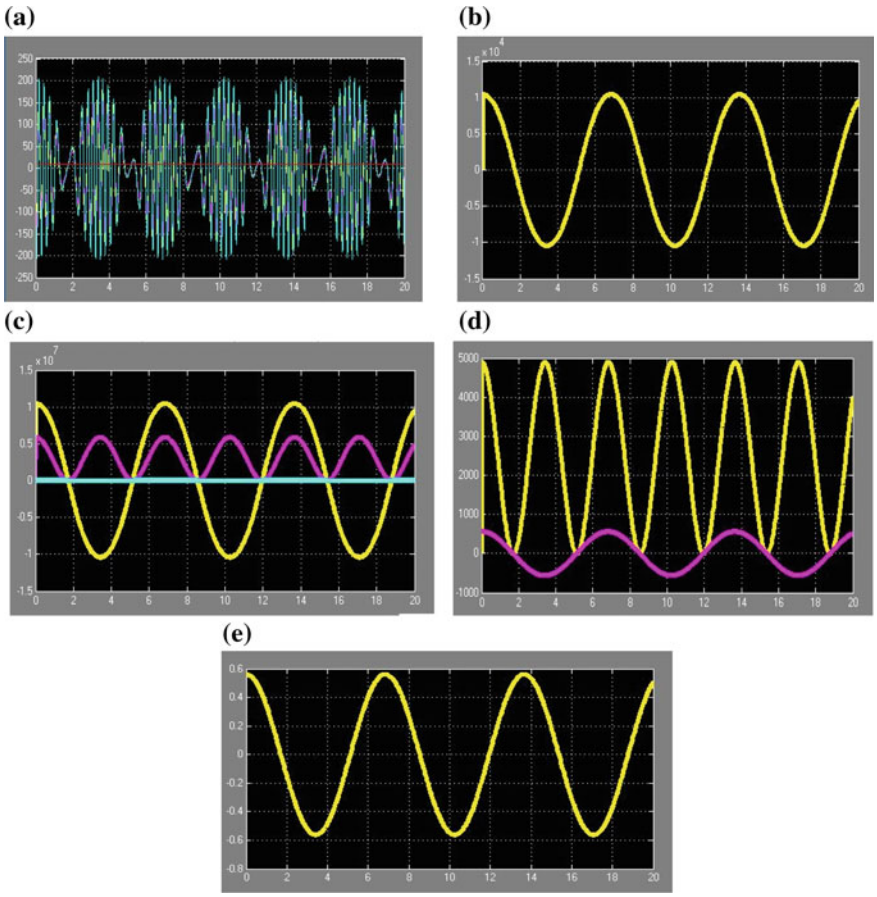

Fig. 42.5 **a** Voltage, current, load resistance, induced EMF, **b** electromagnetic force, **c** input power, **d** output power, **e** sinusoidal velocity

In Fig. 42.5, color notations of figures are as follows: in Fig. 42.5a yellow color presents induced EMF, blue color presents terminal voltage, purple color presents phase current, red color presents load resistance; in Fig. 42.5b, yellow color presents electromagnetic force; in Fig. 42.5c, yellow color presents electromagnetic force, pink color presents input power, blue color presents velocity; in Fig. 42.5d, yellow color presents output power, pink color presents sinusoidal velocity; in Fig. 42.5e, yellow color presents sinusoidal velocity.

These outputs data represent performance of AWS in Indian Ocean.

Table 42.4 Comparison between AWS on Portuguese and Indian Ocean waves

Variable	Portugal	India Ocean
Wave period	11.5 s	6.78 s
Wave height	2.4 m	0.64 m
Stock of AWS	7.797 m	1.4853 m
AWS velocity	2.2 m/s	0.5621 m/s
Voltage	770 V	194 V
Current	48.93 A	12.32 A
Power	37.67 kW	2.39 kW

42.3.2 Comparison Between Indian and Portugal Results

By comparing Indian with Portugal Ocean waves, it is observed that Indian Ocean waves amplitude are small in size as compared to Portugal Ocean waves. Table 42.4 shows the comparison of different parameters.

From above table it can concluded that Indian Ocean waves offer less height of oscillating kinetic energy as compared to Portugal ocean waves. For acceptable output production, there are two possible ways. First external modification (modifying surroundings), second internal modification (Modifying system-device).

External modification. There is no modification in device but the surrounding is changed to extract acceptable amount of energy. Few of those changes are use of multiple devices. External mechanical amplification system is employed and wide energy area absorbing system is employed.

Internal modification. This modification deals with modifying and redesigning of device by changing different device affecting parameters like to damping, stiffness, mass, magnetic intensity, no of wires in winding and so on.

42.4 Improvement for Indian Ocean Waves Output

Forces responsible for damping are: $F_{\mathrm{BEAR}} + F_{\mathrm{DRAG}} + F_{\mathrm{HOR}} + F_{\mathrm{GEN}} + F_{\mathrm{WB}}$. In this sum, it is observed that the maximum contribution for damping contribution is of F_{WB} (force of water brake) and F_{GEN} (generator force), other three damping forces have negligible values as compare to these forces therefore neglecting other three damping forces. Water brake force can be express as

$$F_{\mathrm{WB}} = -\beta_{\mathrm{WB}}\dot{x}|\dot{x}|, \quad \beta_{\mathrm{WB}} = \rho S_{\mathrm{WB}}\left(\frac{S_{\mathrm{WB}}}{C_v S_o}\right)^2, \tag{42.5}$$

where, β_{WB} is a damping coefficient, ρ is the mass density, S_{WB} is the cross-section area of water brake, C_{v} is a discharge coefficient of orifice, S_{o} is the orifice area for water flow, c is a damping, $\dot{x}$ is the velocity.

By increasing orifice area for water flow, damping can be reduces. From (42.5), it is observed that force due to water brake is inversely proportional to orifice area. Force due to damping can be expressed as $F = c\dot{x}$. From these two equation following conclusion can be made.

$$F_{WB} \propto \text{Constant}\left(\frac{1}{S_o}\right)^2 \dot{x} = c\dot{x}. \tag{42.6}$$

The equation for Indian wave is:

$$\begin{aligned} &0.6 \times 10^6 \ddot{x} + 33.99 \times 10^5 \dot{x} + 5.5 \times 10^5 x \\ &= 2.018 \times 10^6 \cos 0.9267\,t. \end{aligned} \tag{42.7}$$

By calculating the value of damping ratio ξ, we obtain:$\xi = 2.958$ (overdamped system). Therefore the basic idea to improve output for Indian Ocean waves is by making system underdamped. The value of ξ is defined as $\xi = \frac{c}{\sqrt{4 \times k \times m}}$. In the case of Indian ocean, damping is reducing in such a way that ξ value become <1 (underdamped system).

For the reduced damping, the new area of the orifice is calculated. The new value of water brake damping is optimized by modifying the damping value. The optimized damping becomes c = 1.09 N s/m. The corresponding value of ξ is 0.948 (underdamped system). For this new value of damping, the corresponding orifice area for water flow is calculated by using ratio law. By considering all other

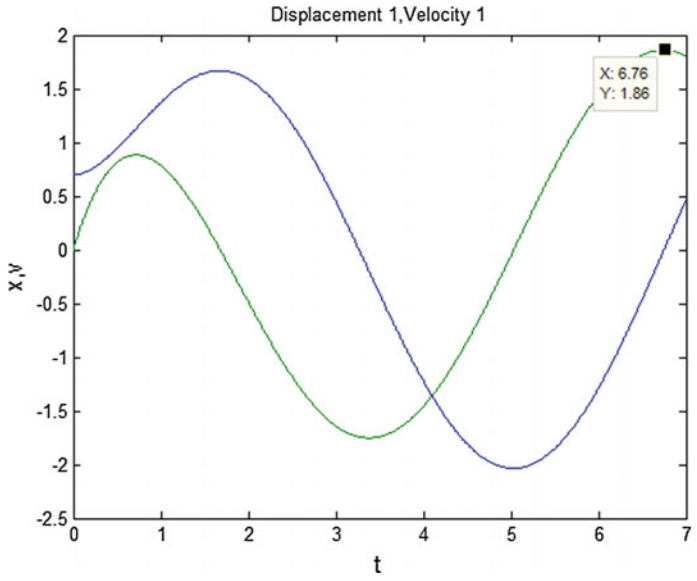

Fig. 42.6 Mechanical output of Indian wave after modification

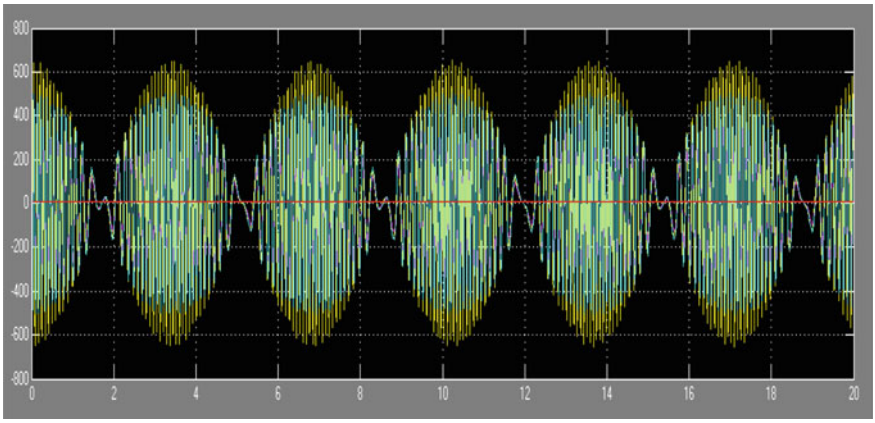

Fig. 42.7 Electrical output of Indian wave after modification

variable parameters constant, we obtain: $S_o|_{new} = 1.9578\ S_o|_{old}$. By increasing area by 95%, it is observed that output power of the electrical model increases from 2.39 to 26.50 kW. Figure 42.6 represents the mechanical output for Indian Ocean waves after modification and Fig. 42.7 represents electrical output. Maximum stroke length in this case is observed as 3.704 m and floater velocity as 1.86 m/s.

42.5 Conclusion

In this work, mathematical model of AWS is developed by combining electrical and mechanical models. The working of AWS for Indian Ocean is studied and damping was adjusted to suit the Indian Ocean conditions. By increasing orifice area by 95%, it is observed that output power of the electrical model increases from 2.39 to 26.50 kW.

References

1. *Indian National Centre for Ocean Information Services*, website: www.incois.gov.in/geoportal/OON/index.html
2. Alireza Khaligh, O.C. Onar, *Solar, Wind, and Ocean Energy Conversion Systems* (Taylor and Francis, Energy Harvesting, 2010)
3. *Wave Energy Contract Goes Abroad*. BBC Scotland. 2005–05–19. Retrieved 2008–08–06. https://en.wikipedia.org/wiki/Pelamis_Wave_Energy_Converter
4. *Wavestar Prototype at Roshage Performance Data for ForskVE Project No. 2009- 1-10305 January 2013*. http://wavestarenergy.com/sites/default/files/Wavestar.pdf
5. *Tidal Barrages and Tidal Turbines*. Retrieved 2 November 2010. https://en.wikipedia.org/wiki/Tidal_barrage

6. M.G. de Sousa Prado, F. Gardner, M. Damen, H. Polinder, Proc. Inst. Mech. Eng. Part A. J. Power Energy **220**(8), 855 (2006)
7. *LIMPET at Queen's University Belfast, Wave Power Device*. https://web.sbe.hw.ac.uk/staffprofiles/bdgsa/shsg/Documents/2004sem/limpet.PDF
8. *Wave Dragon*. www.wavedragon.co.uk
9. H. Polinder, M.E.C. Damen, F. Gardner, Euro. Trans. Electr. Power **15**(3), 245 (2005)
10. D. Valérioa, P. Beirãob, J. Sá da Costaa, Optimisation of wave energy extraction with the Archimedes Wave Swing. Ocean Eng. **34**, 2330 (2007)
11. S. Prasad, *Wave Impact Forces on Horizontal Cylinder*. Ph.D. Thesis. The University of British Columbia, 1994
12. G.M. Khalil, Indian J. Eng. Mater. Sci, **8**, 59 (2001)

Chapter 43
Propagation Behaviour of Acoustic Waves Excited by a Circular PZT-Actuator in Thin CFRP Plate with an Orthotropic Symmetry

M. S. Shevtsova, E. V. Kirillova, E. V. Rozhkov, V. A. Chebanenko, I. E. Andzhikovich and S.-H. Chang

Abstract The article investigates the Lamb wave generation by the bonded piezoelectric (PZT) actuator and its travel within the orthotropic Carbon Fiber Reinforced Plastic (CFRP) plate. We consider the anisotropy of the plate elastic and damping properties, existence of the adhesive layer and dependence of the interfacial stress distribution on the surface between host plate and actuator on the anisotropy of the plate's material, on the excited frequency, wavelength and plate's thickness. Our investigation includes experimental determination of the elastic properties of CFRP, the wave attenuation, on the base of which the models of anisotropic material damping and the Finite Element (FE) implementation of transient wave generation, propagation and attenuation have been proposed. The proposed results can be used at the design of Structural Health Monitoring (SHM) for the composite structures with the structural anisotropy and damping, to make a reasonable choice of the frequency, type, dimensions and optimum placement of the actuators and sensors.

M. S. Shevtsova (✉) · E. V. Kirillova
RheinMain University of Applied Sciences, Wiesbaden, Germany
e-mail: maria.shevtsova@hs-rm.de

E. V. Kirillova
e-mail: evgenia.kirillova@hs-rm.de

E. V. Rozhkov
Southern Federal University, Rostov on Don, Russia
e-mail: rozhkov@math.rsu.ru

V. A. Chebanenko · I. E. Andzhikovich
South Center of Russian Academy of Science, Rostov on Don, Russia
e-mail: valera.chebanenko@yandex.ru

S.-H. Chang
National Kaohsiung University of Science and Technology, Kaohsiung city, Taiwan
e-mail: stephenshchang@me.com

I. A. Parinov et al. (eds.), *Advanced Materials*, Springer Proceedings in Physics 224, https://doi.org/10.1007/978-3-030-19894-7_43

43.1 Introduction

This paper is motivated by the goal of developing improved technique for the Nondestructive Evaluation (NDE) and the Structural Health Monitoring (SHM) of the load carrying composite structures, which usually have the orthotropic structural symmetry, using Lamb waves generated by the surface mounted piezoelectric transducers. The Lamb waves are used in the active SHM systems because they can propagate over large distances in the thin walled composite parts, interact directly with the potential defects that is allow us to estimate the state of health and reliability of the modern aircrafts, rotorcrafts and another machines. The most interesting benefits of guided Lamb waves use is their abilities to detect such defects in composites as delaminations, inclusions, porosity, undesirable local changes of the material's mechanical properties, and, sometimes, a possibility to control the waves directivity, i.e. beam steering. These aspects of the Lamb waves use in the active SHM system are outlined and considered in the monographs [1, 2], in the papers [3–7] and many others. The Lamb waves can be produced in a structure by a variety of different techniques, including piezoelectric transducers, made of monolithic ceramics in the forms of circular [8–11] and annular tablets [12, 13] or rectangular PZT patches [12, 14]. They also can be generated by PZT wedge transducers [15, 16], piezoelectric wafer active systems (PWASs), macro-fiber composite (MFC) actuators [17–20], and by laser beam excitation [21]. At the same time, to sensing the waves, which are reflected or scattered on the defects, the small piezoelectric transducers [7, 22, 23] or non-contact Laser Doppler Vibrometry (LDV) [9, 14, 16, 19, 24–26] are most often used.

Typically, every full-featured SHM, including Lamb waves based, involves four functional levels referred as:

(i) detection of the occurrence of an unsafe event;
(ii) identification of the geometric location of the event;
(iii) determination of the magnitude or severity of the event;
(iv) estimation of the remaining service life/strength (prognosis).

As the first phase of such SHM technique should be surely fulfilled, it assumes the proper choice of the wavelength, its intensity and availability of reliable information about wave attenuation, which depends on the distance, on the material structural anisotropy and damping determining the propagation and attenuation of the traveling wave.

Most articles, in which the theory of the excitation and propagation of Lamb waves is presented applying them to the problems of SHM, assumes the elastic composite material as ideally elastic and non-dissipating. When a Lamb wave propagates in a defect-free and non-dissipating 3D waveguide, amplitude of the wave reduces with distance of propagation. This reduction in amplitude of Lamb wave is due to geometrical attenuation of the 3D waveguide. In reality, besides geometrical attenuation, Lamb wave undergoes attenuation due to material damping as well. Shape of the wave front depends on lay-up for a given Lamb mode of

propagation and also on the shape of the stress generation source [21, 27]. However, the cyclically deformed multilayered fiber reinforced polymeric composites are characterized by the mechanical energy dissipation, and the nature of this damping can be classified as follows [6, 28, 29]:

(i) viscoelastic nature of matrix and/or fiber materials; the major contribution to composite damping is due to matrix, but the fiber damping also give its contribution to the common material damping ;
(ii) damping due to interphase (the region adjacent to fiber surface along the fibers length);
(iii) damping due to some damage (delamination, matrix crack etc.);
(iv) viscoplastic damping (damping due to the presence of high stress and strain concentration that exists in local regions between fibers);
(v) thermo-elastic damping due to cyclic heat flow from the region of compressive stress to the region of tensile stress in the composite.

The dynamic response of composites is complicated by their anisotropic behavior, which is inherent both elastic and dissipative properties of the composite materials with different structural symmetry. Due to the complexity of micro- and mezostructure of multilayered composites, they are considered as homogenized on the approach of "effective moduli", which is most use at the experimental study of composites mechanics. It is important to note that the criterion for the use of the effective modulus theory was that the scale of the inhomogeneity, d, had to be much smaller than the characteristic structural dimension, L, over which the averaging is performed. Since we consider the dynamic behavior of the composite structure, another criterion related to the dynamic effect should be added. That is, the scale of the inhomogeneity, d, must also be much smaller than the characteristic wavelength, λ, of the dynamic stress distribution. Thus, both these inequalities $d << L$ and $d << \lambda$ should be satisfied [30]. In order to estimate the damping properties of the laminate for the different stress orientation, Hashin [31] has developed a general theory of complex moduli of viscoelastic composites, which indicated that the macroscopic dynamic behavior may be approximated by classical continuum dynamics for relatively low frequencies. According to the proposed concept, the composite viscoelastic response can then be determined by replacing the elastic moduli with the identical phase geometry by the effective complex moduli. This procedure utilizes as input the characteristics of lamina loss factor to determine the effective laminate loss factor. The fibers are assumed elastic and the matrix is assumed linearly viscoelastic. As such, the composite behaves macroscopically as a linearly viscoelastic body.

The accessible results of the numerous experimental studies demonstrate dependencies of the material damping characteristics on the angle of acting strain relative to the lamina and laminate orientation, on the relative fiber volume, on the properties of the fibers and matrix material and on the frequency [32–35]. Comparison of these data is very difficult, especially, because these results were obtained by using different experimental technique for the same material.

Concluding the few results concerning the experimental studies of composites damping it is worth to note the following remarks.

In most practical cases, the damping in polymeric composites should be taken into account. This damping depends on the composite structure (relative fiber volume), on the damping property of the matrix material, on the frequency and the orientation of the acting strain relative to the main coordinate system of the orthotropic or transverse symmetry.

At the case of the unidirectional lamina, the largest damping is when the acting strain is oriented normal to the fiber direction, whereas the damping at the excitation along the fiber is minimal.

The damping of both unidirectional lamina and laminate grows with the frequency excitation above 10 kHz, then it stabilizes at frequencies up to 50 kHz.

At the excitation of laminated composites with the different lay-up sequence, there are orientations where the damping parameters change, taking the maximum and minimum values that depend on the lay-up stacking, on the components properties, on the acting stress and excitation frequency. The range of the varied loss factor is typically 0.001–0.025.

At the known values of the lamina damping properties, the angular dependencies of the damping for laminate can be estimated using the Hashin theory, which is based on the classical laminate theory and complex representation of elastic moduli of the lamina.

The value of every chosen damping parameter sufficiently depends on the specimen's shape (beam, plate, shell) and on the vibration mode at which this parameter is monitored [36]. These considerations justify the need for an experimental study of the damping properties of the composites under investigation in each case.

A further important feature of the PZT excited Lamb waves is an influence of the shear stress distribution on the interface between piezoelectric actuator and anisotropic host structure on the frequency, actuator's size and structure's stiffness. All surface bonded transducers excite and sense the Lamb waves in the structure directly through in-plane strain coupling. The author [17] comes to the right conclusion, which approves that a comprehensive modeling of the interaction between the transducer, the structure, and the Lamb waves traveling at ultrasonic frequencies through the structure is needed as an essential design tool.

For the quasi-static low frequency vibrations it was shown by many authors that a simple hypothesis about linear displacement for flexural motion lead to the representing the shear stress on interface in terms of hyperbolic functions. This relationship demonstrates that relatively thick bonding layer produces a slow shear transfer over the entire span, whereas a thin bonding layer produces a very rapid transfer [37–40]. In the case of ideal bonding, this solution converges to the simplest pin force model, in which all the load transfer takes place over an infinitesimal

region at the ends of transducer. This model assumes that the shear stress distribution along the interface can be expressed using Dirac function $\delta(x)$, i.e.

$$\tau_a(x) = a\tau_0[\delta(x-a) - \delta(x+a)], \tag{43.1}$$

where a is the half length of the transducer, and $a\tau_0$ is the pin force applied at the ends of transducers. The similar models were used by the most authors. In the paper [9], where the directivity of Lamb wave in thin CFRP plate was studied, the action of annular piezoelectric transducer has been simulated by a surface load **q** taken in the form of δ-like distribution along the transducer edges.

The authors of [9, 12, 17, 19] at the modeling Lamb wave generation in composite plates by the rectangular and annular transducer use similar simple models. For the ring-shaped actuator located at the center of the coordinate system, the actuation components f_i, $i = 1, 2, 3$ are given by

$$\begin{cases} f_1 = \tau_0[\delta(r-A_o) - \delta(r-A_i)]\cos\theta \\ f_2 = \tau_0[\delta(r-A_o) - \delta(r-A_i)]\sin\theta \\ f_3 = 0 \end{cases}, \tag{43.2}$$

where A_i and A_o are the outer and inner radii of annular actuator, respectively, r and θ are the polar coordinates. So, according to the assumption that a circular piezoceramic can be modelled as producing a uniform shear distribution located on its circumference, independent of the frequency generated or the host structure.

Both these last representations of the forcing functions are only valid for infinitely thin PZTs, assuming a weak coupling between the PZT and the host structure, and when the wavelength generated is larger than the PZT size (below the first electro-mechanical resonances). In practice, these assumptions are only verified at the low frequencies [11, 12]. Above-mentioned works use some analytical approach to the problem of the Lamb wave generation and propagation along the composite plates. Such approach requires the maximum simplification of the forms, which define the stress generated by the transducers. Meanwhile, mechanics of interaction between e.g., piezoelectric actuator and thin walled composite host structure is very complex. These difficulties are due to many reasons. Most piezoelectric ceramics used in the actuators structures have the transverse isotropic structural symmetry, whereas the composite materials can have quasi-isotropic or even much more complex orthotropic symmetry. However, the spatial (angular) distribution of interfacial shear stress depend on the correspondence of mechanical stiffness of both interacted bodies: PZT actuator and composite plate. Moreover, the longitudinal and flexural stiffness of these relatively thin bodies depend on their thickness. The elastic, damping property and thickness of adhesive layer also modify the transfer of the stress to the composite plate [17, 37–40].

Most important results, which refute the assumption justified the pin-force and other simple models are the following [11]: the in-plane shear stresses (i) vary in amplitude over the frequency range of interest, (ii) depend on the orientation, and

(iii) do not only locate at the edge of the PZT. The results of [11] demonstrate that accurate consideration of the transducer dynamics, where the shear stress distribution under the transducer is taken into account, allow us to reproduce much more precisely the generation of guided waves on composite structures.

This paper content is organized as follows. In the first part of the article, we report on the structure of the studied composite material and its mechanical properties, which were obtained experimentally. On this base, we calculate the dispersion curves for both symmetric and anti-symmetric Lamb wave in the chosen frequency range. These dispersion relations for the phase and group velocities are determined by two analytical methods by using the FE analysis and have been confirmed experimentally. They are used to estimate a type of the wave that can be excited to determine the structural imperfections in a composite part with given material properties and sizes. The next part of the article sets forth the technique of the experiment aimed at studying the propagation of waves in a CFRP plate, and on the determination of the material damping with its inherent anisotropy. The last part considers the dependence of the interfacial shear stress distribution under circular PZT actuator on its dimension, the material properties and the excited frequency. To perform this, we used the FE model of the system that takes into account the coupled piezoelectric phenomena, structural dynamics of dissipating CFRP material, and simulates the Lamb wave propagation in the time domain. Comparison of the numerical results with obtained LDV-based experimental data allowed us to estimate a contribution of the considered phenomena in forming and attenuation of excited Lamb waves. It allows also one to propose some recommendations for the optimal choice of the transducer destined to excite the desired type of the Lamb waves, to estimate the wave directivity and effectively monitor the zone of orthotropic plate.

43.2 The Studied CFRP Panel and the Elastic Properties of Its Material

The square CFRP panel for research was assembled using unidirectional carbon-fiber epoxy based prepreg KMKY-2m.120 (tape width 250 mm, thickness 0.12 mm). In order to obtain a symmetric balanced orthotropic laminate the stacking sequence [0; −30; 30; 90; 90; 30; −30; 0] was used. The final panel thickness was 1 mm with the overall dimensions 700 × 700 mm^2. It has been cured in autoclave according to the manufacturer recommendations. Mechanical properties of the lamina are the followings: E_x = 120 GPa; $E_y = E_z$ = 9.5 GPa; $\nu_{xy} = \nu_{xz}$ = 0.3; ν_{yz} = 0.48; $G_{xy} = G_{xz}$ = 4.5 GPa; G_{yz} = 3.2 GPa; ρ = 1510 kg/m^3.

Mechanical testing of the laminate elastic properties has been carried out according to standards ASTM D 3039-95 (longitudinal E_1, transversal E_2 Young moduli and Poisson ratio ν_{12}) and ASTM D 5379-93 (Iosipescu test of in-plane

shear module G_{12}) with further numerical processing for the refinement of the measured data [41]. Two interlaminar shear modules G_{23} and G_{31} were determined numerically by using the FE models, which simulate a shear loading of rectangular specimens, and shear moduli were calculated by averaging over the points with pure shear state. All calculated values of the modules were checked for consistency using the relationships [30]:

$$\begin{aligned} &(1-\nu_{23}\nu_{32}), (1-\nu_{13}\nu_{31}), (1-\nu_{12}\nu_{21}), (1-\nu_{12}\nu_{21}-\nu_{13}\nu_{31}-\nu_{23}\nu_{32}-2\nu_{21}\nu_{32}\nu^{13}) > 0; \\ &\nu_{ij} \le (E_i/E_j)^{1/2}; \\ &\nu_{21}\nu_{23}\nu_{13} < \tfrac{1}{2}. \end{aligned} \tag{43.3}$$

Four confidence intervals for some modules are present in Fig. 43.1, and three angular distributions of the modules used in the classic laminate theory are shown in Fig. 43.2. Stiffness matrix that has been constructed using nine calculated moduli was inserted into the FE models of the studied CFRP panel.

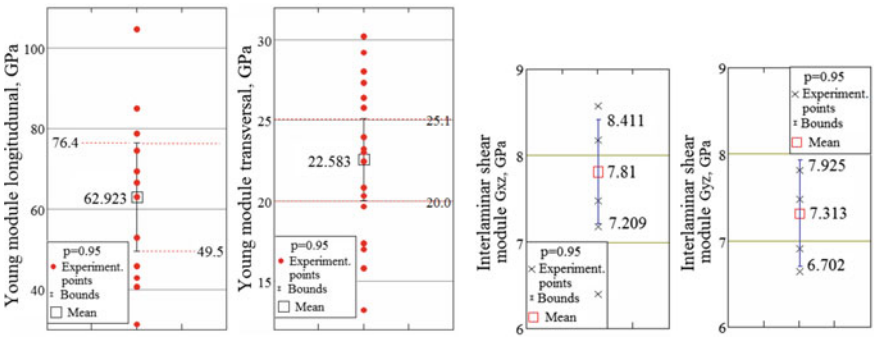

Fig. 43.1 Confidence intervals for determined elastic modules of CFRP

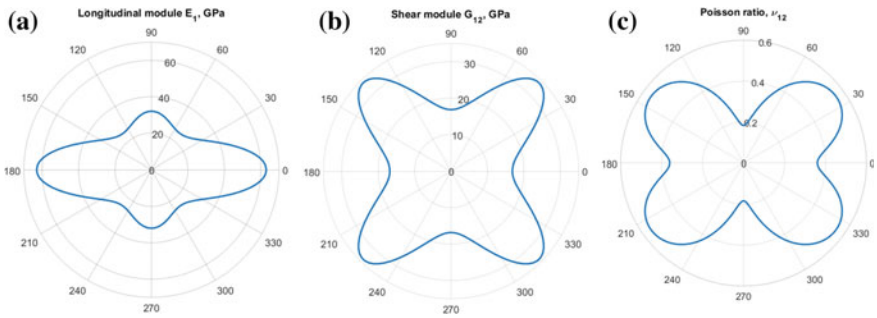

Fig. 43.2 Angular distributions of Young's module (**a**), in-plane shear module (**b**) and Poisson ratio (**c**) of CFRP

43.3 Dispersion Relations for the Phase and Group Velocities of the Lamb Waves

In order to estimate, what kinds of the Lamb waves can be excited in the studied CFRP plate with the given elastic properties and sizes, the dispersion relations for the phase and group velocities were determined. With this aim, we used the equations, which are based on the effective moduli of composites [42], on the 3D elasticity of multilayered composites [43], experimentally and used the FE model of transient process of Lamb and SH waves propagation.

43.3.1 Dispersion Relations for the Phase Velocity on the Base of Effective Moduli of Composite

For the symmetric, antisymmetric modes of the Lamb waves and shear horizontal (SH) waves, the equations [42] have been transformed to the form:

$$\left(q^2 - k^2\right)^2 \cdot \sin(qh) \cdot \cos(ph) + 4k^2 pq \cdot \sin(ph) \cdot \cos(qh) = 0 \tag{43.4a}$$

$$\left(q^2 - k^2\right)^2 \cdot \sin(ph) \cdot \cos(qh) + 4k^2 pq \cdot \sin(qh) \cdot \cos(ph) = 0 \tag{43.4b}$$

$$\frac{4k^2h^2}{\pi^2}\left[\left(\frac{c}{c_T}\right)^2 - 1\right] = n^2 \tag{43.4c}$$

and solved numerically. In (43.4a–c)

$$p^2 = \omega^2/c_L^2 - k^2; \quad q^2 = \omega^2/c_T^2 - k^2, \tag{43.5}$$

where $k = \omega/c$ is the wavenumber, ω is the angular frequency, c is the wave speed, $c_L^2 = (\lambda + \mu)/\rho$ and $c_T^2 = \mu/\rho$ are the pressure (longitudinal) and shear (transverse) wave speeds, λ and μ are the Lamé constants, h is the half-thickness of the elastic layer, and ρ is the mass density. Transcendental feature of these equations do not allows one to obtain the quantitative representation of the Lamb wave dispersion for the specific material at the use well known plots [17] for the dimensionless wave speed dependence on the dimensionless frequency. Therefore (43.4a–c) were solved numerically for both longitudinal and transverse directions of the orthotropic material of the panel under investigation. Figure 43.3 demonstrates that in a frequency range up to 1 MHz only two Lamb waves propagating across the main direction of orthotropic CFRP panel can be excited at these frequencies, whereas

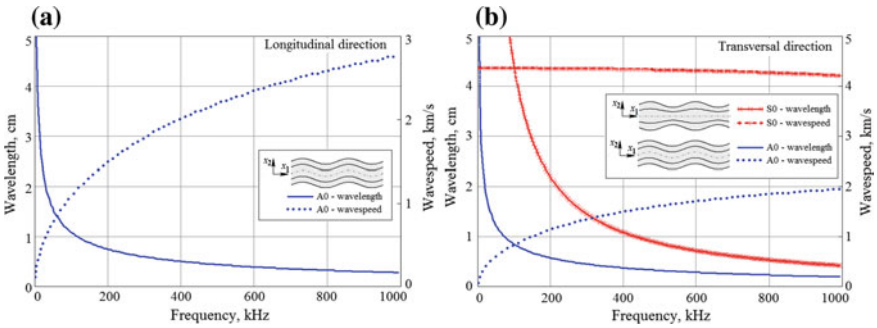

Fig. 43.3 Dependencies of the wave speed and wavelength on the frequency for the Lamb waves, which propagate along (**a**) and across (**b**) the main direction of CFRP panel

only one antisymmetric type Lamb wave can be excited along the main direction of this panel. The dependency of the wavelength of the symmetric SH wave on the frequency is present in Fig. 43.4.

Due to the relatively small size of the studied CFRP plate (length of the wave trajectory is limited by 35 cm), elevated experimental noise at the high frequencies, and due to the limiting frequency range of experimental setup, the propagation of anti-symmetric Lamb waves mode A_0 has been verified by another methods.

Our experimental study of the waves propagation in the studied plate has been carried out in the frequency range 5–100 kHz, and calculated dispersion relations determine the wavelengths 1–5 cm that can be registered in a plate with given dimension. This requirement constrains the wave type that can be generated and detected.

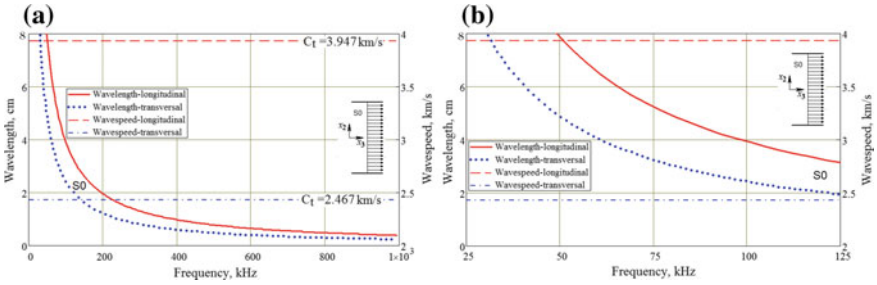

Fig. 43.4 Dependencies of the wave speed and wavelength on the frequency for SH waves, which propagate along and across the main direction of CFRP panel

43.3.2 Dispersion Relations for the Phase and Group Velocities on the Base of 3D Elasticity of Multilayered Composites

This part of investigation uses a problem statement, proposed by Wang and Yuan [43], where the elastodynamic equations of motion in each layer with respect to a rectangular Cartesian system are represented as follows

$$\begin{aligned}
&\partial\sigma_x^{(n)}/\partial x+\partial\tau_{xy}^{(n)}/\partial y+\partial\tau_{xz}^{(n)}/\partial z=\rho^{(n)}\partial^2u_x^{(n)}/\partial t^2\\
&\partial\sigma_y^{(n)}/\partial y+\partial\tau_{xy}^{(n)}/\partial x+\partial\tau_{yz}^{(n)}/\partial z=\rho^{(n)}\partial^2u_y^{(n)}/\partial t^2\,,\\
&\partial\sigma_z^{(n)}/\partial z+\partial\tau_{xz}^{(n)}/\partial x+\partial\tau_{yz}^{(n)}/\partial y=\rho^{(n)}\partial^2u_z^{(n)}/\partial t^2
\end{aligned} \tag{43.5}$$

where $\mathbf{u}^{(n)}=\left(u_x^{(n)},u_y^{(n)},u_z^{(n)}\right)^T$ and $\rho^{(n)}$ are the displacement vector and the mass density of n-th layer, respectively. If the laminate does not contain defects, the normal stresses and displacements are continuous on the layers interfaces:

$$\sigma_{j3}^{(n)}=\sigma_{j3}^{(n+1)};\quad u_j^{(n)}=u_j^{(n+1)};\quad \text{at}\quad n=1,\ldots,N-1;\quad j=1,2,3 \tag{43.6}$$

Let us assume that lower boundary is free of stress:

$$\left(\sigma_{13}^{(N)},\sigma_{23}^{(N)},\sigma_{33}^{(N)}\right)\big|_{z=z_{N+1}}=0 \tag{43.7}$$

and upper boundary $z=z_1$ of the domain Ω is experienced the excitation force:

$$\sigma_{j3}^{(1)}=\begin{cases}V(t)\cdot q_j(x,y), & (x,y)\in\Omega\\ 0, & (x,y)\notin\Omega\end{cases}\quad j=1,2,3\,. \tag{43.8}$$

Then the solution of wave (43.5) can be written using the harmonic wave representation as follows

$$\mathbf{u}^{(n)}(x,y,z,t)=\breve{\mathbf{u}}^{(n)}\mathrm{e}^{i\left(k_xx+k_yy+k_zz-\omega t\right)} \tag{43.9}$$

where $\breve{\mathbf{u}}^{(n)}$ is an amplitude of the wave, $\mathbf{k}=\left(k_x,k_y,k_z\right)$ is a wave vector.

A semi-analytical approach of deriving the dispersion equation based on the integral representation and the calculation of the Green's matrix for the n-th layered composite is described in detail in [6, 43]. The equality of determinant of the matrix resulting from boundary and interfaces conditions to zero, relates the wavenumbers k_x,k_y of plane waves to their material properties and to frequency ω. This relation is

the dispersion equation and for a multi-layered structure, it can be present only in the implicit form:

$$\Delta\left(\omega, k_x, k_y\right) = 0 \,\text{or}\, \Delta(\omega, k, \theta) = 0, \tag{43.10}$$

if the wave vector is represented in polar coordinates as $k_x = k\cos\theta$, $k_y = k\sin\theta$. The dispersion (43.5)–(43.10) were solved numerically for wavenumbers k in dependence on circular frequency ω and propagation direction θ taking into account plate symmetry with respect to mid-plane and antisymmetric motion (AS modes), which does not produce the vertical stress and in-plane displacement at the mid-plane: $u_x = u_y = \sigma_z \equiv (0, 0, 0) \quad \text{at} \quad z = 0$.

The wavelength of Lamb waves $\lambda(\omega, \theta)$, phase $c_p(\omega, \theta)$ and group $c_g(\omega, \theta)$ velocities are calculated as follows

$$\lambda(\omega, \theta) = 2\pi/k(\omega, \theta); c_p(\omega, \theta) = \omega/k(\omega, \theta); c_g(\omega, \theta) = \mathrm{d}\omega/\mathrm{d}k(\omega, \theta) \tag{43.11}$$

43.3.3 Dispersion of the Phase and Group Velocities: Experimental Determination

At the experimental determination of the phase and group velocities, their values were calculated according to their definitions. The phase velocity of a wave is the rate, at which the phase of the wave propagates in space, whereas the group velocity of a wave is the velocity with which the overall shape of the wave's amplitudes (known as the modulation or envelope of the wave) propagates through space.

The studied panel was marked to measure the out-of-plane displacement in two point placed along the radial lines in one quadrant. The circular piezoelectric actuators were placed in the geometrical center of the panel, which was surrounded by the absorbing layer to eliminate the reflection of waves.

Two small piezoelectric sensors were placed along the radial lines at 15 cm distances from the circular actuator's center (first sensor) and 25 cm (second sensor), respectively, distance between sensors was 10 cm. The main difficulty of used technique is a possibility to monitor the wave propagation in the time, not in the space, because both sensors are in the fixed position (Fig. 43.5).

At the experiments implementation and during FE simulation too, the electric potential applied to the conductive surface of PZT actuator had a form of symmetric tone-burst:

$$A \cdot \sin\left(\frac{2\pi(t - nT_\mathrm{r})}{T_\mathrm{en}} N\right) \cdot \begin{cases} \sin^2\left(\frac{2\pi(t-n)}{T_\mathrm{en}}\right) & \text{if} \quad (t - nT_\mathrm{r} \geq 0) \cap (t - nT_\mathrm{r} \leq T_\mathrm{en}/2) \\ 0 \quad \text{if} \quad (t - nT_\mathrm{r} < 0) \cup (t - nT_\mathrm{r} > T_\mathrm{en}/2) \end{cases} \tag{43.12}$$

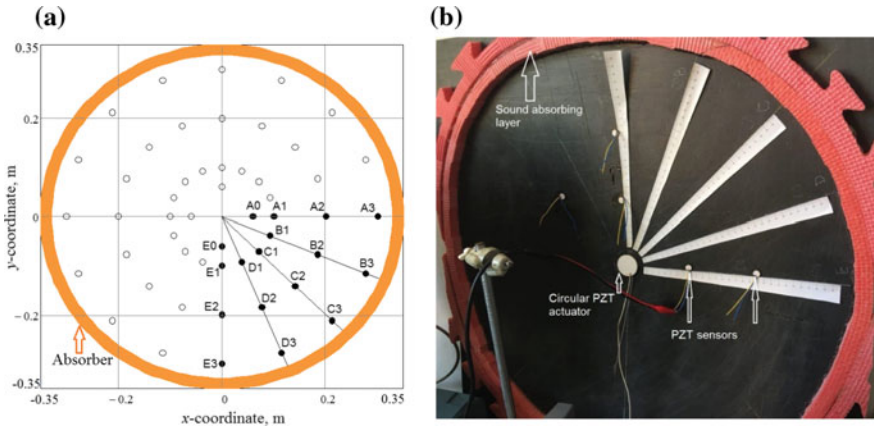

Fig. 43.5 Experimental setup to measure the phase and group velocities in CFRP panel: **a** Schematic view; **b** Photo of experimental panel with bonded circular actuator and two radially placed piezoelectric sensors

where T_r is a period of repetition; $n = 0, 1, 2, ..$ is a number of pulse; $T_{en}/2$ is the pulse duration; $N = 1, 3, ..$ is the odd number of sine waves inside the pulse and A is the signal amplitude (see Fig. 43.6).

The electronic equipment for the wave generation and sensing consists of a signal generator Tektronix AFG 3022B, which output signal form can be programmed using ArbExpress AXW 100 soft tool, piezodrivers PA 94 (Apex Co., USA), the power supplies TDK Lambda, and oscilloscope LeCroy 422. This equipment allowed one to investigate the processes of the waves generation and propagation in a frequency range up to 125 kHz.

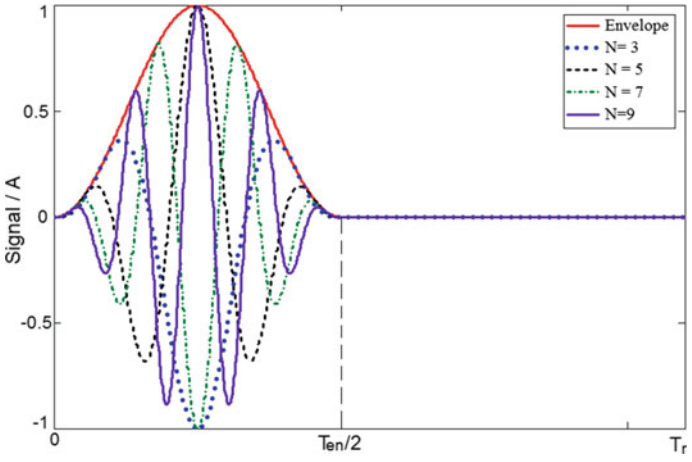

Fig. 43.6 Time pulses for electric potential applied to the piezoelectric actuator

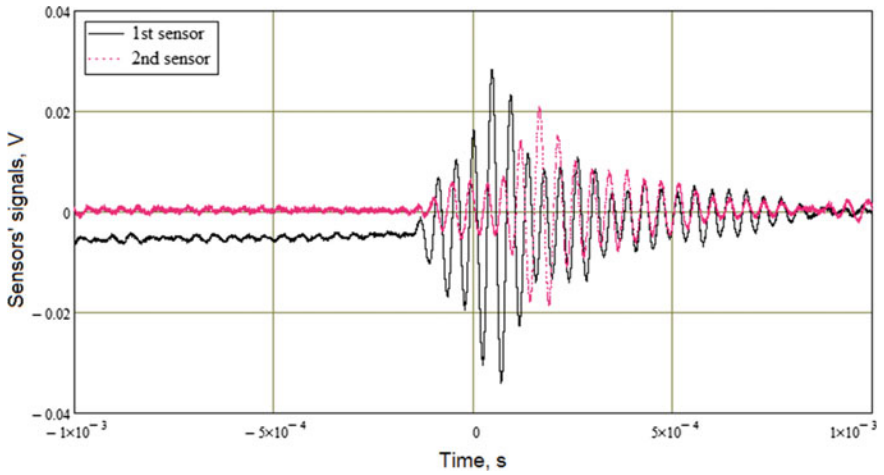

Fig. 43.7 Sensors' responses on the out-of-plane oscillation caused by propagated wave packet

Because both sensors are fixed, only time lag between two signals can be used to estimate the wave speed propagation. Processing of the output signals starts from their time histories that are registered by oscilloscope and saved in a text file (see Fig. 43.7).

Next stage of the sensors' response processing is their symmetrization relative to the zero value of signals and selection of time interval, at which the sensors experience the out-of-plane oscillations. Symmetrized sensors' response at this time interval is present in Fig. 43.8, where one can see some secondary fluctuations,

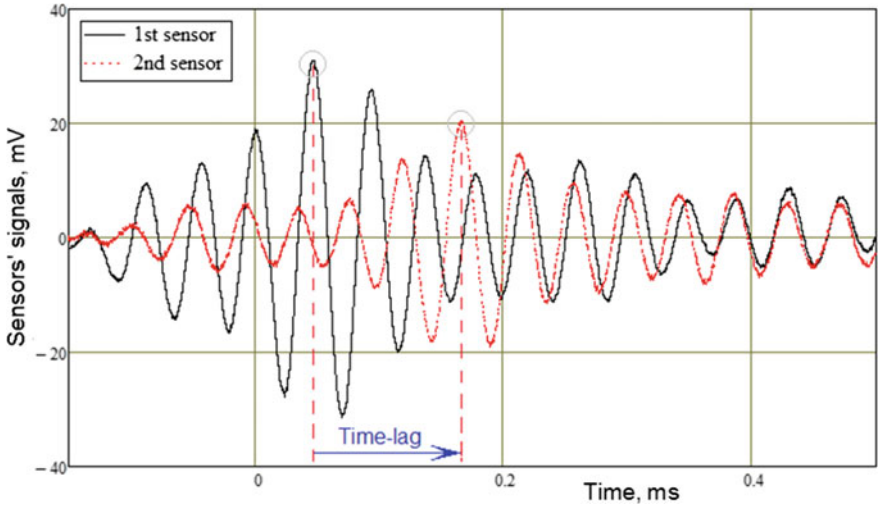

Fig. 43.8 Determination of time lag using signals from both sensors

namely oscillating tail. Time lags between signals of sensors, excited by a propagating sine wave, are measured.

In order to eliminate an influence of experimental noise, both signals are approximated by the second order polynomials:

$$s^{1,2}(t) = a^{1,2}\left(t - t_m^{1,2}\right)^2 + b^{1,2} \tag{43.13}$$

in the vicinities of their maximum and minimum values as it is demonstrated in Fig. 43.9. The phase velocity is calculated by averaging the values $c_p = \Delta r/\left(t_m^2 - t_m^1\right)$, which should be determined for 3…4 maxima and minima. An example of scattering of the measured wavespeeds and corresponding wavelengths is present in Fig. 43.10. For the known excited frequencies f_{ex} the wavelengths were calculated as $\lambda = c_p/f_{\text{ex}}$.

Technique for experimental evaluation of the group velocities is similar. The difference is that time lag should be measured between two crests of the envelopes of signals incoming from both sensors after these signals symmetrization (see Fig. 43.11). Location of these crests on the time axis is determined after numerical approximation of the envelopes by the function:

$$S_{\text{env}}^{1,2} = A_{\text{en}}^{1,2} \cdot \sin^2\left(\frac{\pi}{T_{\text{en}}^{1,2}} \cdot \left(t - t_{\text{cr}}^{1,2} - T_{\text{en}}^{1,2}/2\right)\right). \tag{43.14}$$

After identification of all approximants parameters $A_{\text{en}}^{1,2}, T_{\text{en}}^{1,2}, t_{\text{cr}}^{1,2}$ a group velocity is calculated as $c_g = \Delta r/\left(t_{\text{cr}}^2 - t_{\text{cr}}^1\right)$. Unlike the numerical procedure for determination of a phase velocity, there is no possibility for averaging in this case. The value of a group velocity is a result of only one measurement at the chosen frequency. Therefore, the accuracy and reliability of such determination technique is sufficiently lower comparing to technique of the phase velocity measurement.

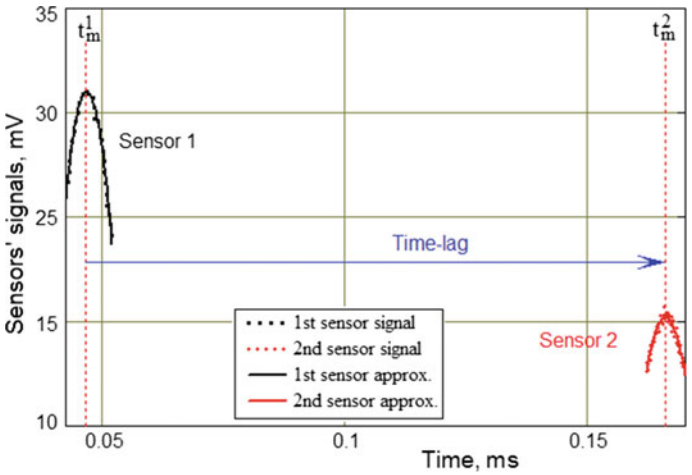

Fig. 43.9 Calculation of time lag between approximated signals from the first and second sensors

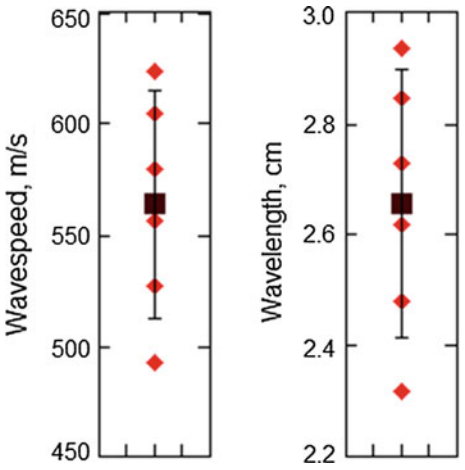

Fig. 43.10 Example of scattered values of calculated wave speeds and wavelengths with corresponding confidence intervals (p = 95%)

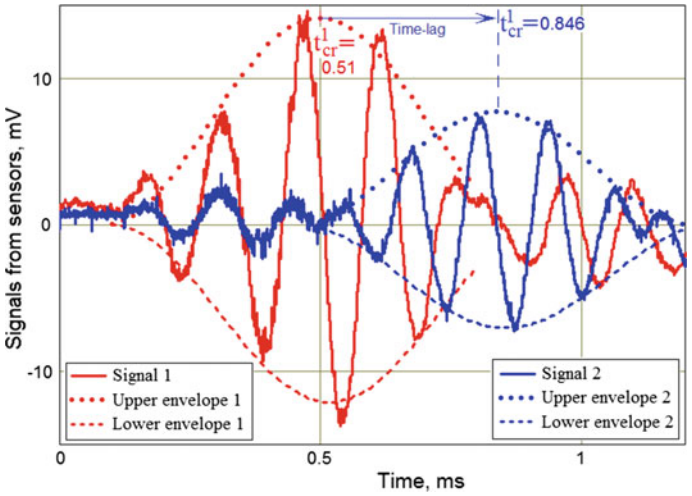

Fig. 43.11 Calculation of time lag between approximated envelopes for determination a group velocity

43.3.4 Determination of Phase and Group Velocities of the Lamb Waves in CFRP Laminate Using FE Modeling

The greatest advantage of the finite element method over the above described experiment technique is that there is a possibility to monitor the propagation of the wave and its modulated packet both in a space and in time. All finite element simulations were implemented using nine-count tone-burst, i.e. N = 9 (see Fig. 43.6).

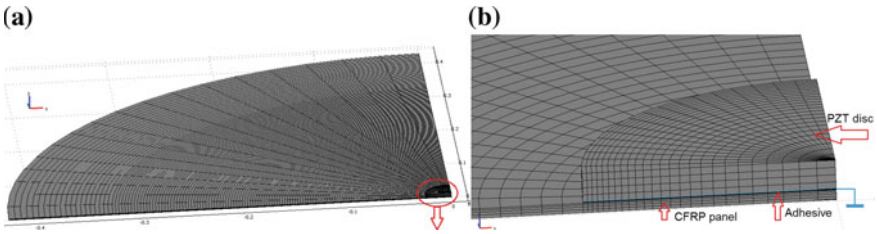

Fig. 43.12 Finite element mesh of the plate's model: **a** Full view; **b** Magnified view on the part of the model with PZT tablet

The FE model includes one quarter of the circular CFRP plate with bonded PZT actuator. This plate is surrounded by the absorbing region. One sector of the modeled plate was selected taking into account orthotropic symmetry of composite material (see Fig. 43.12).

At the phase velocity determination, some phase of the wave was selected and its propagation in space was monitored with small step on time (see Fig. 43.13). Each position of these phases is denoted by the points in Fig. 43.13. The value of a slope of the line, which approximates these points, is a phase velocity. This time step was taken equal to the time integration step, which was accepted at the transient problem solving. One FE model of the orthotropic CFRP plate (see Fig. 43.12) was used for determination of the phase velocity along the different directions at the wave excitation on unchanged amplitude and frequency generated by PZT actuator.

The FE simulation results allow us to monitor propagation of the wave packet envelope along the chosen direction. The shape of this envelope can be approximated

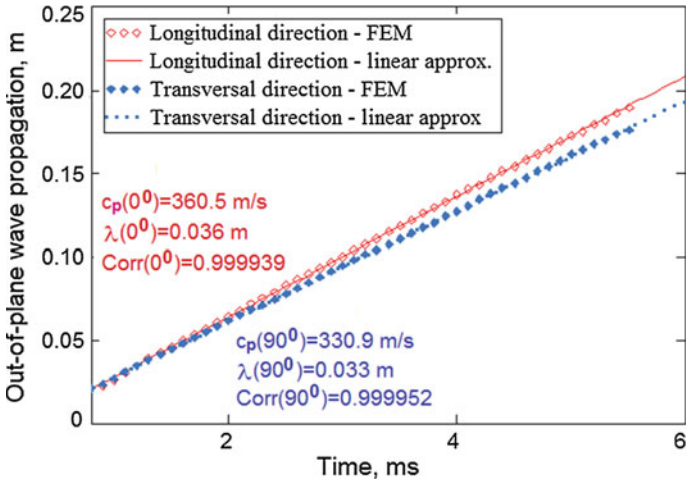

Fig. 43.13 Calculation of the phase velocities as the slope of the lines, which approximate the propagations of some fixed phases of the waves in the space and in time

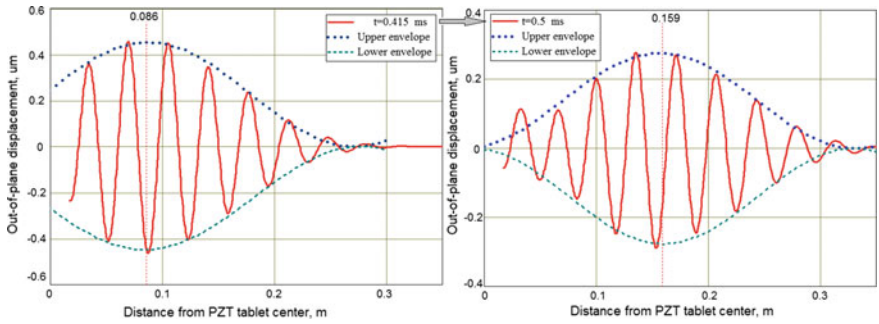

Fig. 43.14 Monitoring of the wave envelope propagation by using FE simulation results

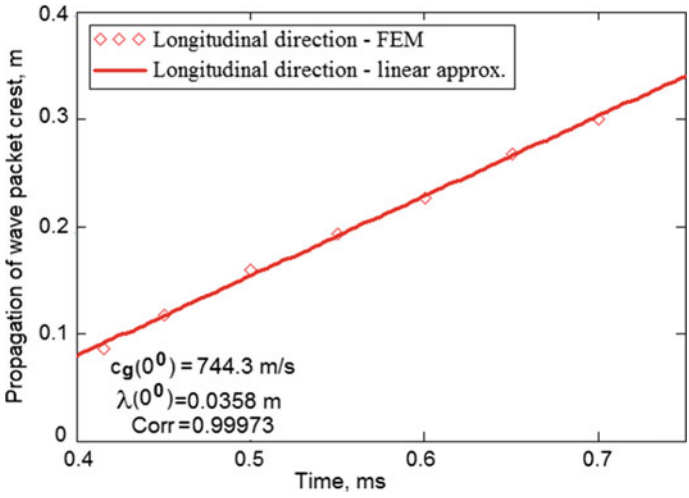

Fig. 43.15 Calculation of the group velocity using FE simulation results

as described above; and positions of crest of moving envelope at the different time instants can be used to calculate a group velocity (see Figs. 43.14 and 43.15). Unlike the experimental case, the FE model allows one to obtain some set of the group velocity values, and average them. Due to this ability, the simulation results of the correct FE model are more reliable comparing with the experimental results.

The frequency dependencies of the phase velocity for the anti-symmetric Lamb wave AS0 propagation and wave lengths, which were determined by calculation the dispersion curves solving the (43.3a, b) for the laminate with effective moduli, (43.5)–(43.11) for the multilayered CFRP laminate, by the FE method, and experimentally, are present in Figs. 43.16 and 43.17.

The dispersion curves for the group velocity of anti-symmetric Lamb wave AS0 have been calculated by solving the (43.5)–(43.11) for the multilayered CFRP laminate, and compared with the experimental data and results of FE analysis

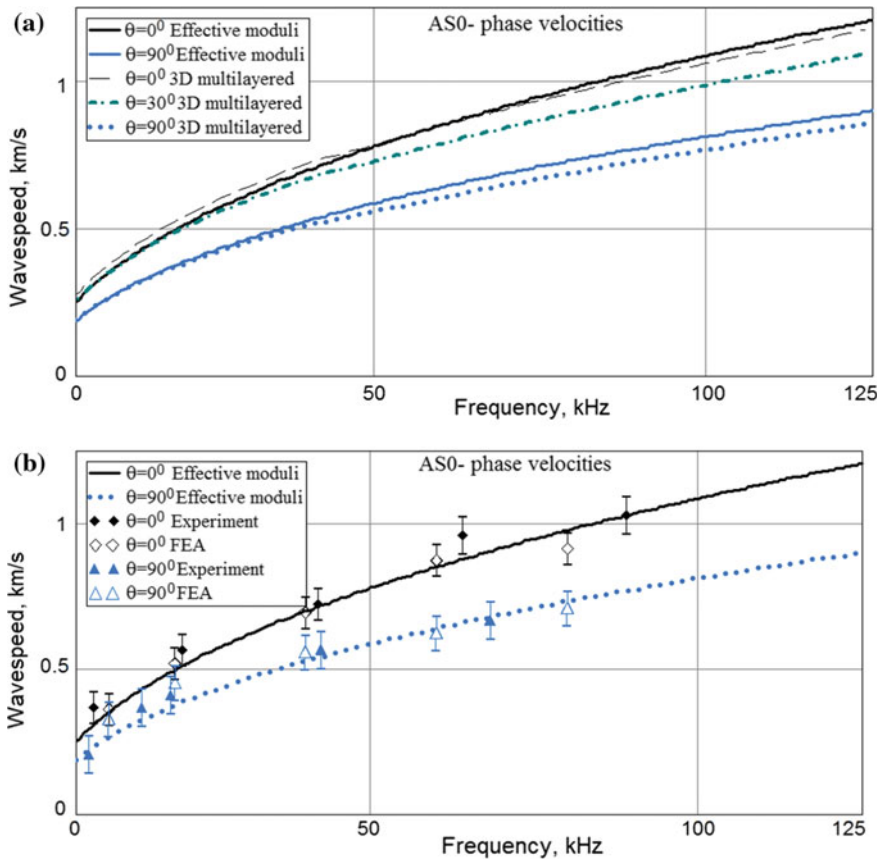

Fig. 43.16 Dispersion curves for the phase velocity of anti-symmetric Lamb wave AS0: **a** Calculated by solving (43.4a, b) for the laminate with effective moduli and (43.5)–(43.11) for the multilayered CFRP laminate; **b** Those compared with the results of experimental study and FE analysis

obtained for directions $\theta = 0°, 90°$. The curves, which are present in Figs. 43.16, 43.17 and 43.18, demonstrate a very good coincidence that confirms their feasibility and workability for further wave propagation analysis.

43.4 Identification of Anisotropic Material Damping and Lamb Waves Attenuation

As noted above the damping property of anisotropic layered composites depends on the stress/strain direction relative to the layers or coordinate systems of orthotropic material orientation, and also, on the frequency of the excitation [6, 27–31]. Our

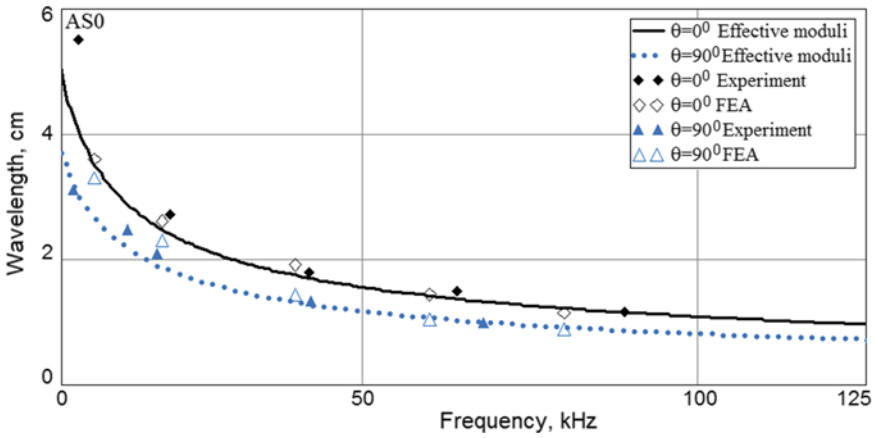

Fig. 43.17 Dispersion curves for the wavelength of anti-symmetric Lamb wave AS0, calculated by solving (43.4a, b) and compared with the results of experimental study and FE analysis

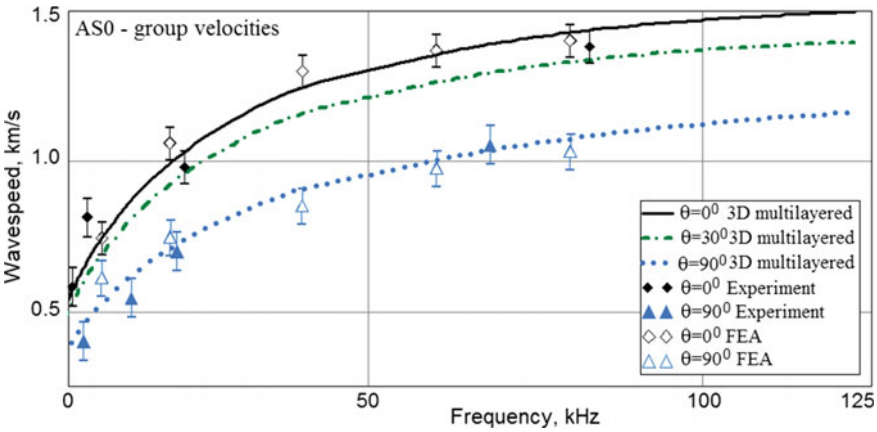

Fig. 43.18 Dispersion curves for the group velocity of anti-symmetric Lamb wave AS0, calculated by solving (43.5)–(43.10) for the multilayered CFRP laminate compared with the results of experimental study and FE analysis

research is devoted to the study of Lamb waves generation by the circular piezoelectric transducer and their propagation in thin walled CFRP plate. Consequently, the quantitative data about material damping should be obtained using the similar conditions of experimental technique, that is, the needed experiment should be implemented using the same actuator, plate, amplitudes and frequencies of excited strains.

If the medium of propagation is non-dissipating, then the amplitude of the wave can be expressed as [21, 27]

$$W(r,t) = \frac{A_0}{\sqrt{r}} \exp[i(kr - \omega t)]; \quad r \neq 0 \tag{43.15}$$

where W is the amplitude at time instant t and at position r from source of excitation; k is the wave number vector, ω is circular frequency, A_0 is peak amplitude and i is the imaginary unit. In this equation the wave amplitude $A(r)$ at a distance r from the point or circular source of excitation is

$$A(r) = A_0/\sqrt{r}. \tag{43.16}$$

$A(r)$ can be normalized with respect to amplitude A_0 at the source as

$$A(r)/A_0 = 1/\sqrt{r}. \tag{43.17}$$

The decline of the wave amplitude with the distance from the point excitation source is because the wave propagates as a cylindrical wave, covering increasing volumes of the plate's material. This attenuation is termed as "geometrical attenuation". When Lamb wave is propagating in an attenuating (dissipating) medium, then wave number becomes a complex number, which can be expressed as follows [6, 27].

$$k = k_r + ik_i \tag{43.18}$$

which imaginary part characterizes the dissipative properties of the material. In this case, the resulting relative wave amplitude attenuation $h(r)$ is described by the equation:

$$h(r) = A(r)/A_0 = \exp(-k_i r)/\sqrt{r}. \tag{43.19}$$

In the experimental investigation, vibration deflection shapes, obtained by using the Laser Doppler Vibrometer (LDV), are used for characterizing the wave attenuation parameters by measuring the vibratory response using the LDV. The laser beam can be focused into any specified area or points on the structure and the data (typically velocity histories) at these points are acquired and post processed to determine the location and extent of possible damage, wave source directivity etc. [14, 19, 24, 44–46].

Due to the orthotropic symmetry only one quarter of panel was studied (see Fig. 43.5b). In order to accurately positioning of the measuring points, five rulers have been placed on the surface of panel radially with an angular step 22.5°. These rulers were oriented relative to the main material coordinate systems with the angles: 0° (A), 22.5° (B), 45° (C), 67.5° (D), 90° (E). Along these tracks the out-of-plane displacement speeds has been measured by using Polytec PDV-100

laser vibrometer. The studied circular area of the panel was surrounded by an absorbing layer, made of the porous rubbery belt, which simulated a perfectly matched layer. Use of the similar absorbers to avoid reflection of the traveling waves and formation of the standing waves are reported in [11, 23, 47, etc.] (see Fig. 43.5). It is efficient both at the experimental studies and the finite-element modeling.

As a source of acoustic wave excitation, the piezoelectric disc STEMINC SMD50T21F45R with dimensions 50×2.1 mm^2 and the resonance frequency 45 kHz was used. Its material properties corresponded to PZT-4. Sine wave voltage with amplitude 100 V was applied on the piezoelectric transducer by the high-voltage piezodriver PA94 (Apex Co., USA), which is controlled by the wide frequency range generator Tektronix.

Reported experiment was implemented at the fixed frequencies within a range 5–110 kHz. Steering of vibrometer to desired position has been carried out manually by moving it along the vertical rod of a tripod with a step of 5 mm. Distance between vibrometer and vertically installed panel was near 80 cm, at which diameter of the laser beam spot was approximately 2.5–3 mm. Preliminary, laser vibrometer has been calibrated to establish the relationship between output voltage, registered by oscilloscope LeCroy, and displacement speed of a certified vibration source. The corresponding coefficient was found as $k_V = 1.878 \times 10^{-3}\text{m}/(\text{s V})$. In order to obtain the values of vibration amplitudes (in μm) the measured potential has been multiplied by the coefficient $1.878 \times 10^3/(2\pi f_0)$ μm/V.

All measurements data in the form of voltage amplitude, received from the laser vibrometer, were stored in the text files, which correspond to the tracks A, B, C, D and E (see Fig. 43.5b). One example of these results is present in Fig. 43.19. The similar dependencies have been obtained for another tracks B, C, D, and E.

It is important to note that experimental data are distorted by the strong noise. This fact led to filter the measured data to reduce the influence of experimental noise. Therefore, a further numerical processing has been carried out using the modification of the method proposed in [27]. This method assumes that reduction in wave amplitude near to the circular excitation source is independent of the material attenuation. When moved away from the excitation source, the reduction in amplitude also depends on the material properties. In this region, the reduction in amplitude is due to both geometry and material, but latter dominates. The methodology proposed in [27] suppose approximation of the relative wave amplitude attenuation $h(r)$ by the exponential curve $f(r)$:

$$f(r) = P \cdot \exp(-\gamma r), \tag{43.20}$$

which should supply a better correspondence to the experimental data far from the excitation source. The parameter, γ in (43.20) characterizes the combined attenuation of geometry and material. Hence, it is called ‘effective attenuation coefficient’. Parameter P is the amplitude at $r = 0$.

Method [27] for identification effective attenuation coefficient γ is applicable to the distances from the source, when material attenuation prevails over the

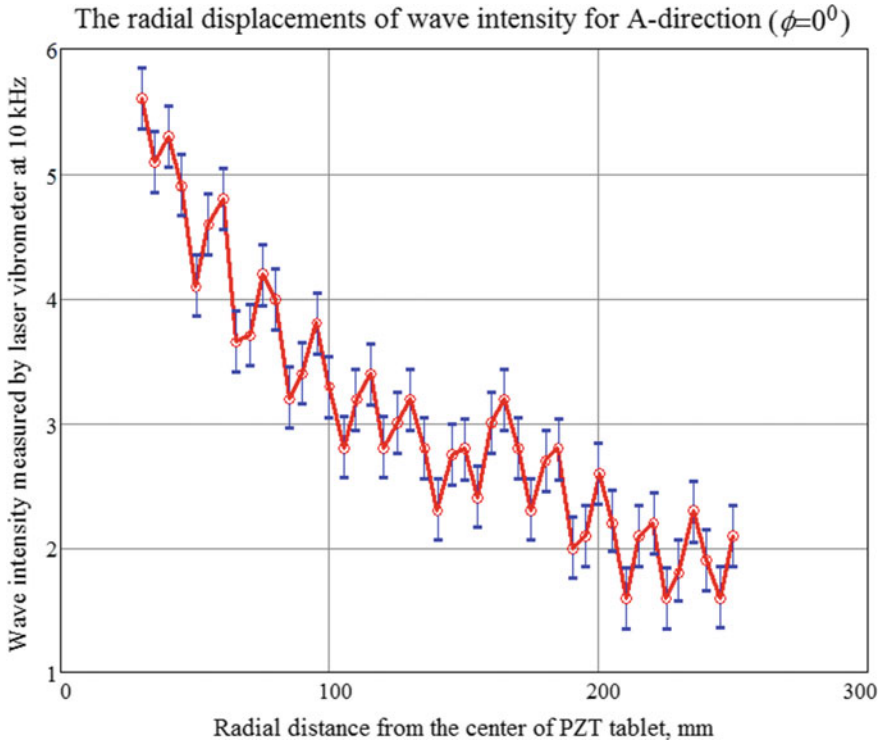

Fig. 43.19 Radial distribution of the wave intensity along A-track (the principal axis of orthotropic symmetry)

geometrical attenuation, but in the experimental practice dimensions of the studied specimens often are limited. In such cases, we cannot neglect geometric attenuation, and we should determine the parameter k_i of material attenuation using full relationship (43.19). To illustrate difference between the models (43.17), (43.19) and (43.20), let us consider the experimentally obtained radial distribution of the wave amplitude along the principal axis of orthotropic symmetry (see Fig. 43.20) with these three imposed models, whose parameters were determined by using the Levenberg–Marquardt algorithm of optimization. One can see that difference between all these curves grows both at the vicinity of the source and far from it.

When we move start point for the approximation (43.19) far from the excitation source, the value of the parameter k_i converges to the stable value. In the considered case, this is $k_i \approx 1.2$ Np/m. Corresponding dependence of the wave amplitude is located below to the pure geometric attenuation, thereby demonstrating the presence of the material attenuation (see Fig. 43.21). The similar plots for the wave amplitude distribution along all five tracks were built and coefficients k_i were

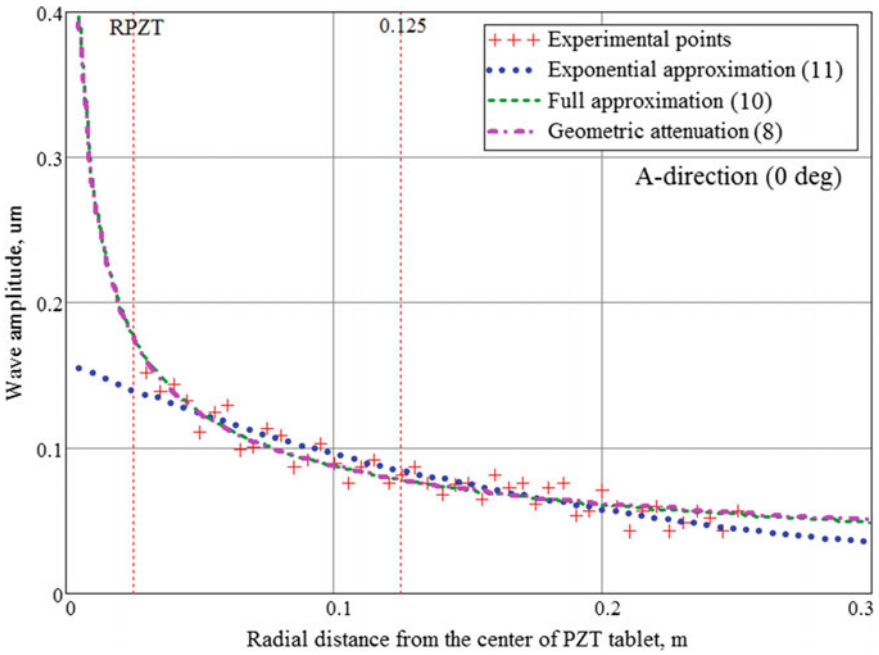

Fig. 43.20 Experimentally observed radial distribution of the wave amplitude along A-track and its different approximations

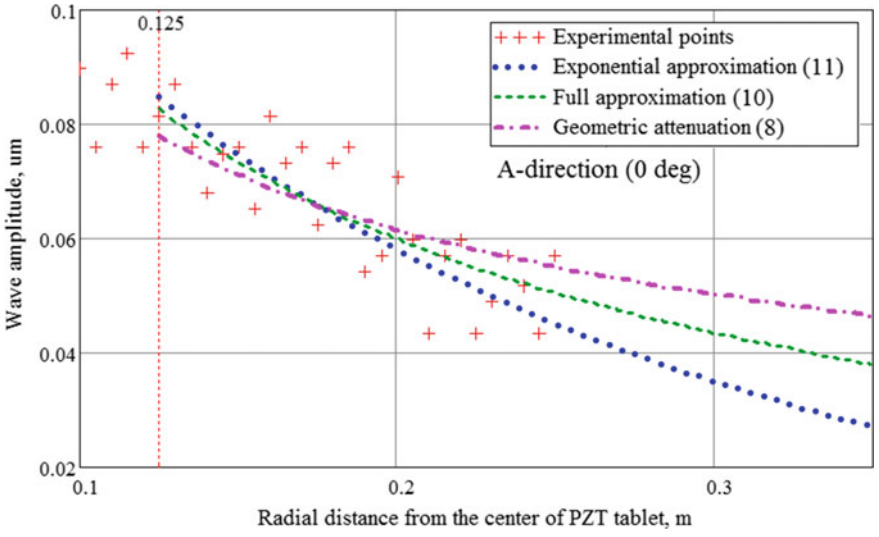

Fig. 43.21 Different approximations for the experimental points, located at $r \geq 125$ mm

calculated. In particular, B-direction is characterized by the value of $k_i \approx 3.3\,\mathrm{Np/m}$ that converges at $r \geq 150$ mm.

It is worth to note two important features of the obtained results. These are dependencies of both geometric and material attenuations on the wave propagation orientation relative to the main coordinate system of orthotropic plate. Although the simple relationship between the material attenuation parameter k_i and any material damping parameter cannot be established due to dependence of k_i on the waveguide's structure and wave type, its change with the orientation of the wave propagation should be taken into account to provide an adequate and valid mathematical modeling of the wave process.

In order to describe the angular dependence of the attenuation coefficient a polynomial of 5th order approximation was used. With a viewpoint of simplifying its description, we used the relative change of the attenuation coefficient, accepting its value for A-track (along the main direction of the studied CFRP) as 1. This polynomial is defined on the angle range 0–90°. To supply the ability to use this polynomial at the finite-element modeling, we constructed this polynomial as a function of cosine of angle between the main axis of CFRP and arbitrary direction inside $\theta \in [0°; 90°]$. The constraints imposed to the approximating polynomial $\bar{k}_i^{\mathrm{appr}}(\theta)$ are

$$\begin{cases} \mathrm{d}\bar{k}_i^{\mathrm{appr}}(\theta)/\mathrm{d}\theta\big|_{\theta=0} = \mathrm{d}\bar{k}_i^{\mathrm{appr}}(\theta)/\mathrm{d}\theta\big|_{\theta=\pi/2} = \mathrm{d}\bar{k}_i^{\mathrm{appr}}(\theta)/\mathrm{d}\theta\big|_{\theta=\pi/3} = 0 \\ \bar{k}_i^{\mathrm{appr}}(0) = 1 \\ \bar{k}_i^{\mathrm{appr}}(\pi/2) = 1.5 \\ \bar{k}_i^{\mathrm{appr}}(\pi/3) = 3 \end{cases} \tag{43.21}$$

First three conditions determine the values of the attenuation coefficient, which correspond to the main CFRP axis, the normal to it, and to the orientation of maximum attenuation $\theta = \pi/3$, respectively, whereas the last three conditions are due to C^1-continuity at the bounds of each pair of quadrants. These six conditions allow us to determine all six coefficients of approximating polynomial:

$$\bar{k}_i^{\mathrm{appr}}(\cos\theta) = \sum_{i=0}^{5} a_i \cdot (\cos\theta)^{5-i}. \tag{43.22}$$

The graphical representation of this polynomial, tabulating (43.22) by 19 equidistant points together with the values of experimentally measured relative attenuations is plotted in Fig. 43.22. At the finite-element implementation in Comsol Multiphysics soft tool of the Lamb wave propagation in the studied thin CFRP panel, this polynomial approximation was used in the form of piecewise cubic interpolation, based on the set of these 19 equidistant points. Spreading this dependence on the angle 2π with considering the orthotropic symmetry of the

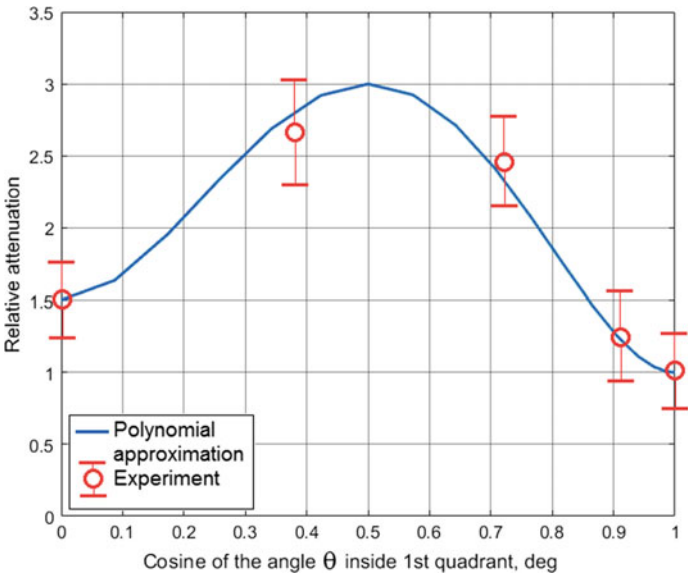

Fig. 43.22 Angular dependence of the relative attenuation coefficient for the studied CFRP panel in 1st quadrant

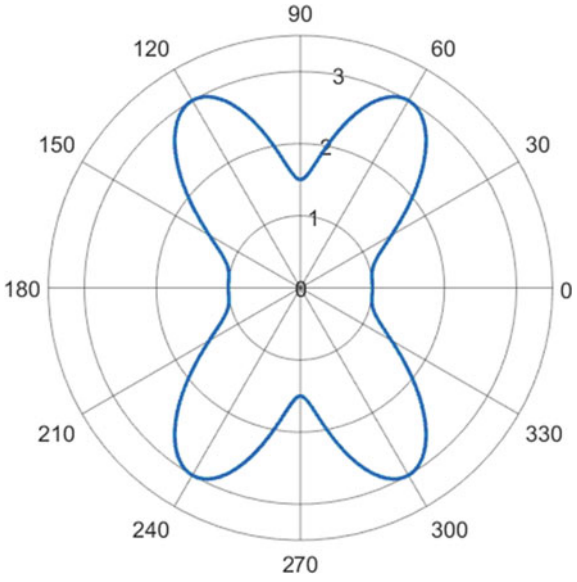

Fig. 43.23 Angular dependence of the relative attenuation coefficient for the studied CFRP panel in polar coordinates

plate's material allows one to represent the angular distribution of the relative attenuation for the Lamb wave, excited by the omnidirectional circular transducer (see Fig. 43.23).

In our numerical study of Lamb wave generation and propagation in plate, we used the Raylegh damping rheological model, which contains two parameters α and β, expressed through the wave speed c_g, angular frequency ω and attenuation coefficient k_i according to relationship [6]:

$$\left(\alpha + \beta\omega^2\right) = 2k_i c_g. \tag{43.23}$$

To determine the parameters α and β, we solved a linear system, constructed using (43.23) by the least square method with the values of k_i^j that have been determined experimentally at the frequencies ω_j, whereas the wave speeds c_g^j were calculated from the dispersion curves for the different orientations relative to the main axis of orthotropic CFRP panel. In the FE model described below the used Rayleigh damping is active inside the whole modeled CFRP domain. The C^2-continuity is supplied on the boundary, which separates the modeled area of CFRP plate with propagating wave and absorbing region, added to avoid the wave reflection from this border. When moving outside from this border, the relative attenuation coefficient and corresponding Raylegh damping parameters grow as a second order polynomial (see Fig. 43.24).

43.5 Shear Stress Distribution on the Interface Between Circular PZT Actuator and Host Orthotropic Panel

This study has been carried out to determine dependence of the interfacial shear stress generated by transducer on the excitation frequency and on the properties of the host structure, and also to determine the scope of simple forcing functions like pin-force. Due to experimental difficulties of such analysis, we use the numerical approach, which is based on the FE models (see Fig. 43.12) that take into account anisotropy of both effective elastic and damping properties of composite material, plate thickness and interaction of host structure with PZT transducer through adhesive layer.

Our preliminary study, which used the isotropic (Y = 63 GPa, ν = 0.36, ρ = 1510 kg/m^3) plate of 1 mm thickness, excited by the circular PZT actuator, showed that at the frequencies 1 kHz, the interfacial shear stresses are distributed as axially symmetric delta-function. However, at the frequencies above 10 kHz, the stress distribution is badly distorted. Our next, more detailed simulations were performed at the frequencies 10, 30, 100 kHz with two PZT tablet-like actuators that correspond to STEMINC actuators, used in our experiments, SMD50T30F45R

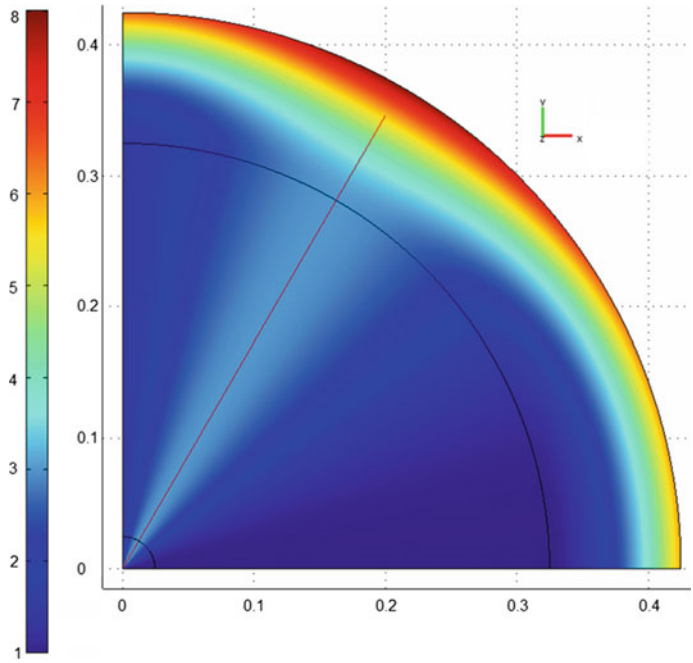

Fig. 43.24 Spatial dependency of the relative attenuation coefficient within the studied CFRP panel and absorbing region (the sector of one quarter of the panel is shown); two circular arcs with radii 0.025 and 0.325 m, depicted by the solid black lines, represent the side of PZT transducer (r = 0.025 m) and border, which separates CFRP plate and absorbing region (r = 0.325 m), respectively

(D = 50 mm, f_{rez} = 45 kHz) and SMD10T2R111WL (D = 10 mm, f_{rez} = 215 kHz), bonded through an adhesive layer of 100 μm thickness. In order to identify the interfacial shear stress distribution on the plate thickness, which depends the mechanical stiffness of excited structure, we modeled the plates of three different thickness: 1, 2, and 4 mm. The results of modeling the Lamb waves propagation in a plate with the smallest thickness were compared with experiment. The radial shear stress distributions at some simulation conditions are present in the forms of 3D plots (see Figs. 43.25 and 43.26), 2D plots for the shear stress distribution along the radial lines, which are differently oriented relative to the axis of orthotropic symmetry of the plate's material, and in the form of polar plot of shear stress along the border of PZT tablets.

These plots demonstrate three very important features. All figures confirm a significant deviation of calculated stress distributions from the simple delta-like

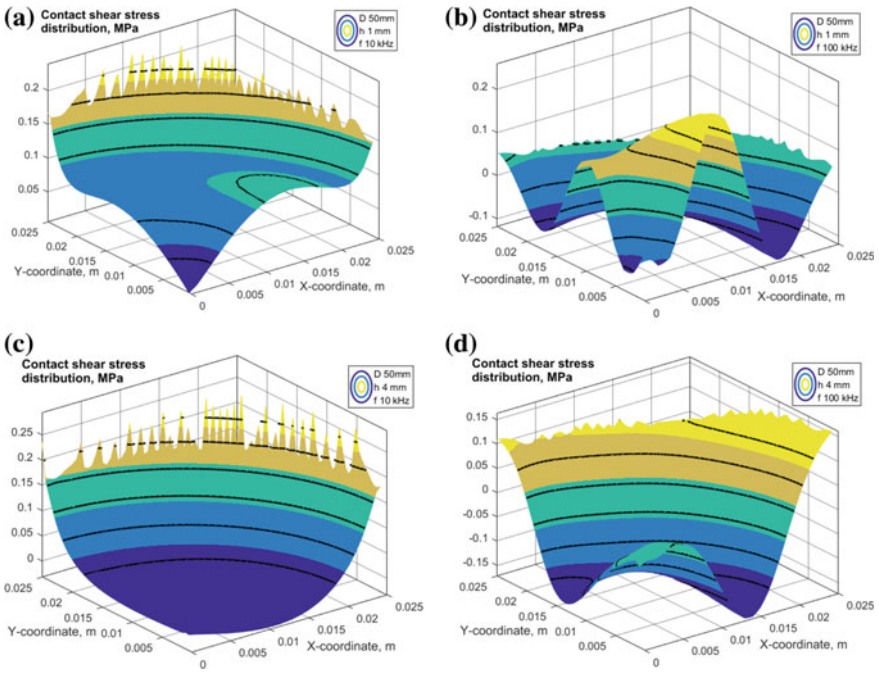

Fig. 43.25 3D maps for the radial shear stress distribution on the interface between circular PZT actuator (D = 5 cm) and host orthotropic panel with thickness of 1 mm (**a**, **b**) and 4 mm (**c**, **d**) at excitation frequencies 10 kHz (**a**, **b**) and 100 kHz (**c**, **d**)

circular distribution even at the relatively low frequency 10 kHz. These distributions are specifically anisotropic. The interaction between actuator and excited host structure grows with the frequency and structure's compliance, which depends on the plate thickness. The dependence of the stress distribution on the plate thickness holds even for the structurally anisotropic material of this plate.

The radial stress distributions, calculated for the transducer of 1 cm diameter (see Fig. 43.26), demonstrate the significantly less distortion comparing to the transducer of 5 cm diameter. This result can be explained by the fact that bigger actuator's dimension is comparable to the excited wavelength.

The plots in Figs. 43.27 and 43.28 allow us to estimate an influence of the structural anisotropy and the adhesive layer on the shear lag and on the circular PZT tablets border. However, this anisotropy is more visible on the polar plots for the radial shear stress along the circular PZT borders, which are present in Figs. 43.29 and 43.30.

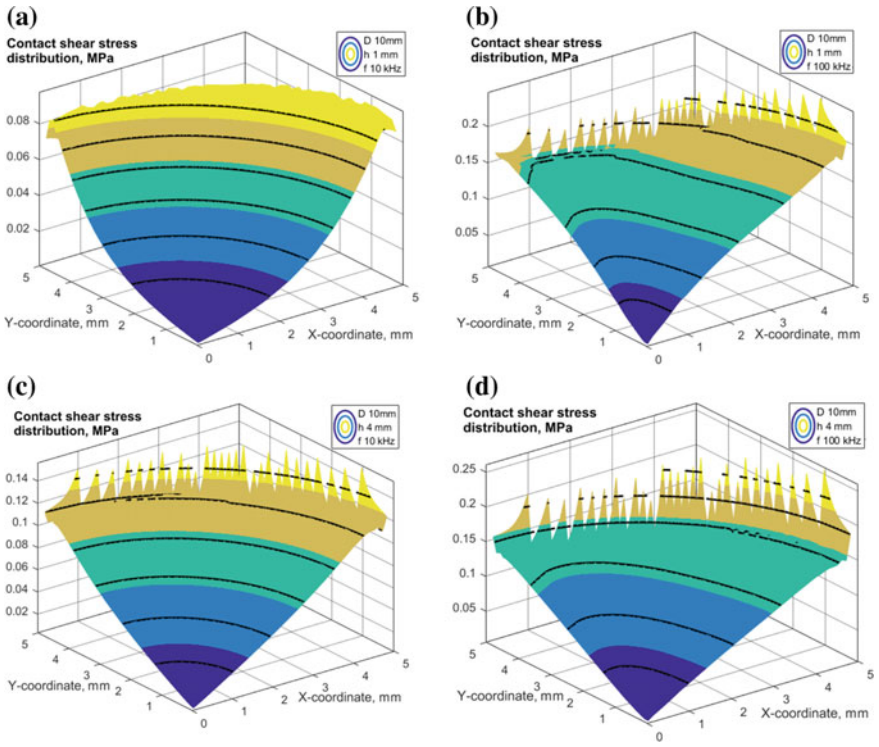

Fig. 43.26 3D maps for the radial shear stress distribution on the interface between circular PZT actuator (D = 1 cm) and host orthotropic panel with thickness of 1 mm (**a**, **b**) and 4 mm (**c**, **d**) at excitation frequencies 10 kHz (**a**, **b**) and 100 kHz (**c**, **d**)

Last two figures demonstrate a much stronger dependence of the anisotropy for the generated shear stress along the actuators border on the larger actuator's dimensions, generated wave frequency and host structure compliance.

43.6 Comparison of Two Model Approaches

In order to compare the Lamb waves propagation in the PZT excited plate with and without above considered anisotropic material damping, and also the interface shear stress dependencies, we constructed two FE models implemented in Comsol

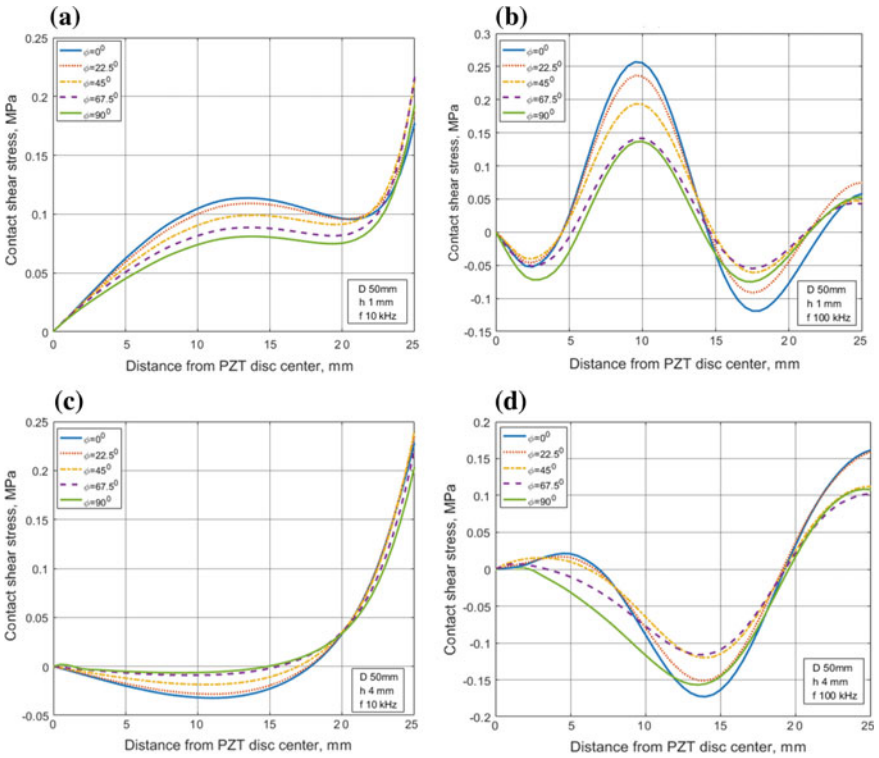

Fig. 43.27 Radial shear stress distribution in MPa along the radial lines on the interface between circular PZT actuator (D = 5 cm) and host orthotropic panel of thickness 1 mm (**a**, **b**) and 4 mm (**c**, **d**) at excitation frequencies 10 kHz (**a**, **b**) and 100 kHz (**c**, **d**)

software. The first model, which is present in Fig. 43.12, consists of one quarter of CFRP plate with inherent elastic properties and structural damping, and a circular piezoelectric actuator bonded at the central point of the plate. The second FE model represents the plate of same dimensions with pure elastic properties, which is excited by the sinusoidally varied delta-like radial shear stress (see Fig. 43.31).

The sinusoidally varying function as a source of excitation with δ-like amplitude is defined in the vicinity of the circular line on the plate surface:

$$\hat{\delta}(r,n) = \frac{n}{\pi \cdot \cosh[n \cdot (r-R)]}; \quad n \to \infty. \tag{43.24}$$

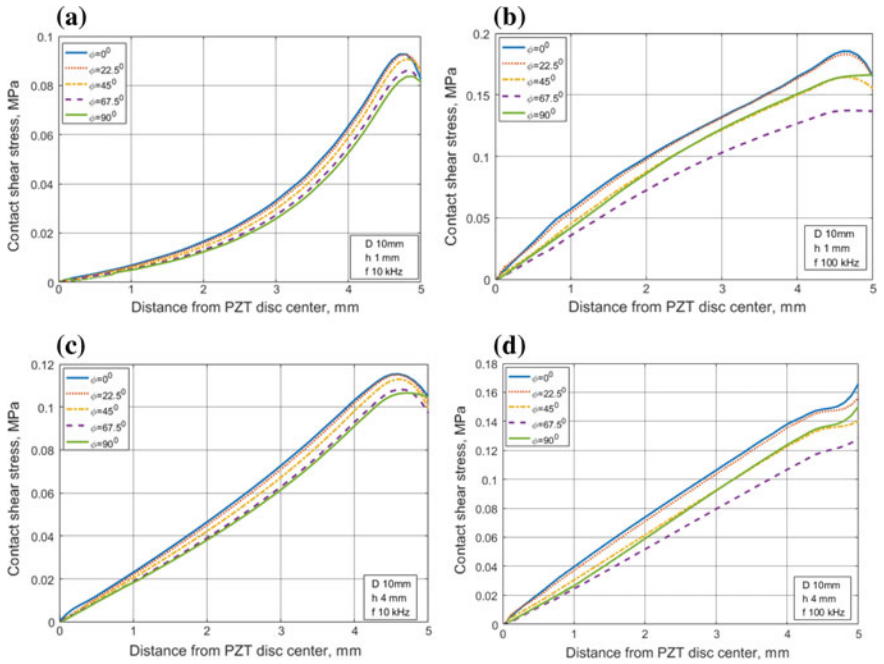

Fig. 43.28 Radial shear stress distribution in MPa along the radial lines on the interface between circular PZT actuator (D = 1 cm) and host orthotropic panel of thickness 1 mm (**a**, **b**) and 4 mm (**c**, **d**) at excitation frequencies 10 kHz (**a**, **b**) and 100 kHz (**c**, **d**)

In our numerical experiments, n was accepted equal to 7500 that provide the width of the annular excitation area near 0.5 mm.

The transient analysis of first FE model included a smooth increase and subsequent stabilization of the sinusoidally varying control potential up to 100 V. In order to match the excitation of both compared FE models, we equalized the wave amplitudes at a distance 5 cm from the PZT actuator's center. Some post-processing of the simulations results are present in Fig. 43.32, which demonstrates two important features of the wave process, caused by anisotropy of elastic properties and structural damping. These features are the dependencies of the wavelength and its attenuation on the wave path orientation. Two left plots relate to the orthotropic plate without any structural damping, where a wave attenuates due to geometry of the plate only. Comparison of the left and right plots show that wavelength in the

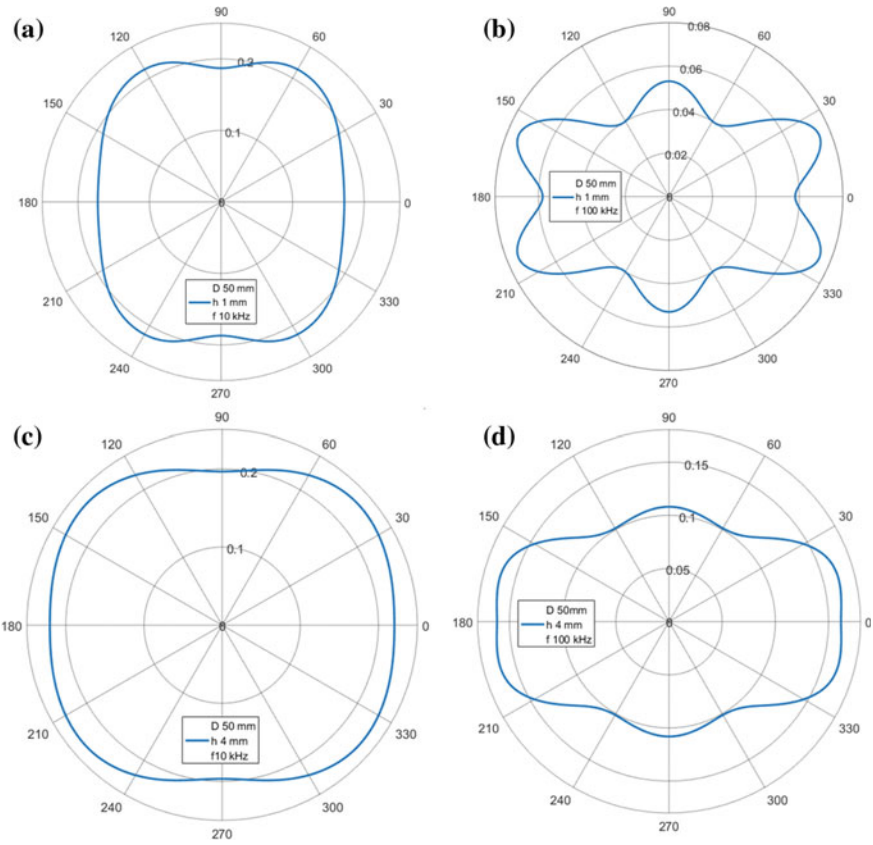

Fig. 43.29 Radial shear stress distribution in MPa along the circular PZT borders on the interface between actuator (D = 5 cm) and host orthotropic panel of thickness 1 mm (**a**, **b**) and 4 mm (**c**, **d**) at excitation frequencies 10 kHz (**a**, **b**) and 100 kHz (**c**, **d**)

plate does not depends on the material damping, whereas angular distribution of the wave amplitude sufficiently depends on the Rayleigh damping anisotropy that is considered in FE model. Results of this model simulation are in good agreement with the experimentally observed by LDV out-of-plane displacements in the plate that confirms the need to consider the studied CFRP damping and its anisotropy. These results suggest that the simple delta-like shear stress distribution can be permissible

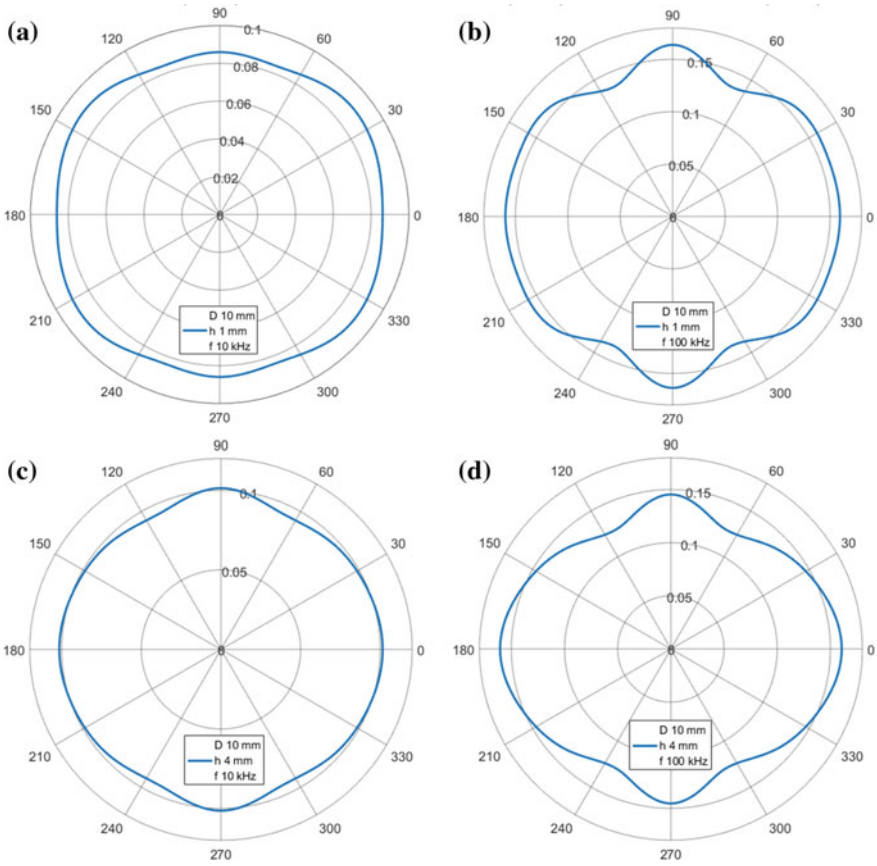

Fig. 43.30 Radial shear stress distribution in MPa along the circular PZT borders on the interface between actuator (D = 1 cm) and host orthotropic panel of thickness 1 mm (**a**, **b**) and 4 mm (**c**, **d**) at excitation frequencies 10 kHz (**a**, **b**) and 100 kHz (**c**, **d**)

at the modeling of the wave propagation in the low compliance structures made of anisotropic material only when actuator's dimensions are less than the wavelength excited. Otherwise, the dynamic of structure-actuator should be correctly considered. This derivation confirms the results of article [11].

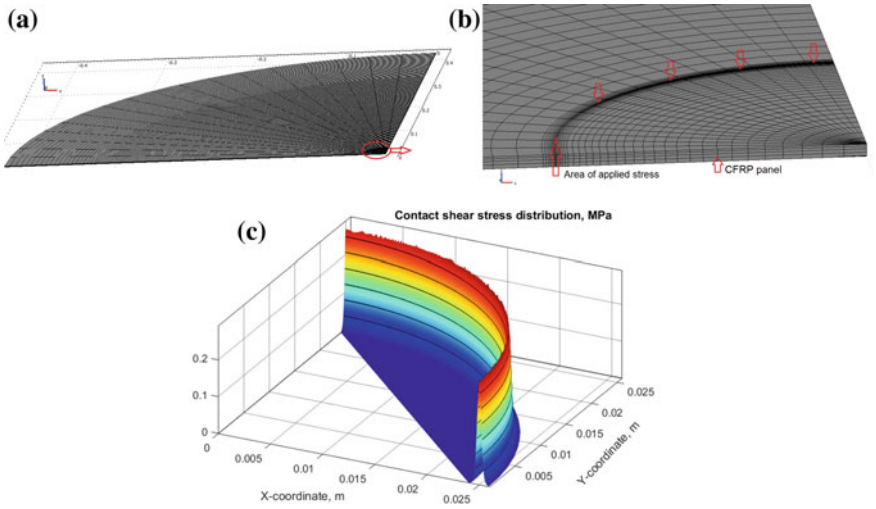

Fig. 43.31 FE model that simulates the wave propagation in the pure elastic orthotropic plate, excited by the sinusoidally varied delta-like radial shear stress: **a** Full view; **b** Magnified view on the central part of the plate; **c** Spatial distribution of applied shear stress amplitude

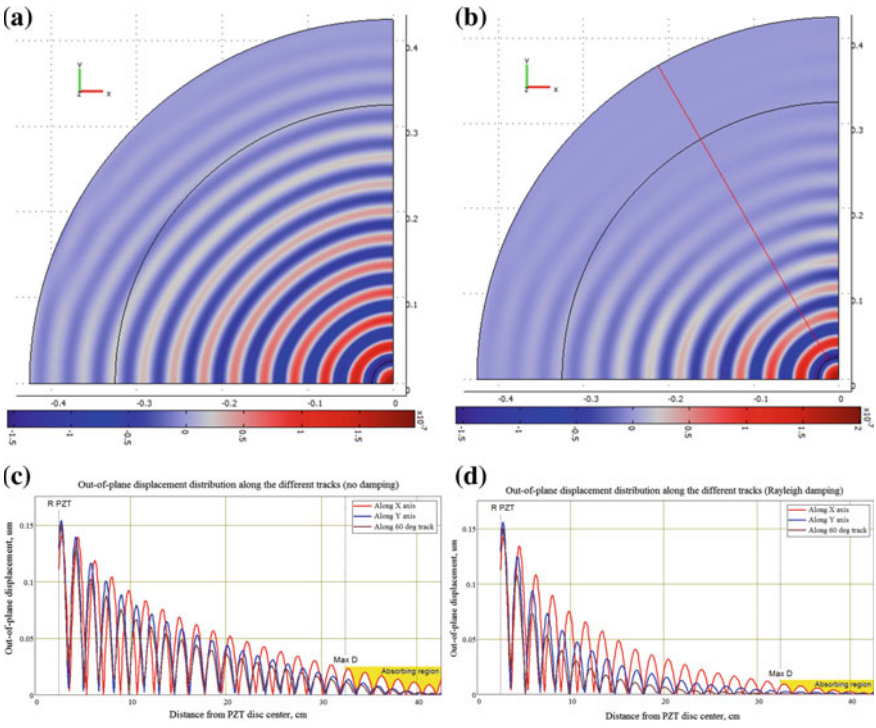

Fig. 43.32 FE modeling results of the out-of-plane displacement of thin CFRP plate excited by the circular PZT actuator of 5 cm diameter: **a**, **c** Without considering the material damping; **b**, **d** The anisotropic material damping was taken into account; **a**, **b** 3D maps; **c**, **d** The radial distributions along the different directions

43.7 Conclusion

We present the methods and solution results of the problem of the modeling the Lamb waves excitation by piezoelectric transducer and propagation of these waves in a strongly anisotropic CFRP panel with dissipating material. The proposed approach and solution method require:

(i) experimental determination of the structurally anisotropic CFRP elastic properties;
(ii) reconstruction of the dispersion curves for the symmetric/anti-symmetric waves that can be excited in the studied and in a given frequency range that depends on the possible defects' sizes;
(iii) experimentally obtained angular distribution of the wave attenuation;
(iv) the identification of anisotropic material damping model.

These data allow us to build a finite-element model, which takes into account all listed phenomena and accurately simulates the system dynamics, including interaction between PZT actuator and excited composite structure through the adhesive. We established the dependencies of the generated interfacial stress between actuator and host structure on the exciting frequency, the thickness and mechanical properties of adhesive layer, on actuator type and dimensions, on the anisotropic elastic and damping properties of the material, and also on thickness of the excited CFRP panel. These abilities can be effectively used at the SHM of composite structures with structural anisotropy and damping to make a justified choice of the frequency, type, dimensions and optimum placement of the actuators and sensors, taking into account size and possible location of the verifiable defects.

Acknowledgements The authors wish to acknowledge the valuable financial support from the German Federal Ministry of Education and Research (BMBF) (Grant No. 13FH009IX5), Russian Foundation for the Basic Research (Grants No. 16-58-52013 and 18-38-00912) and from Russian Academy of Science (project A16-116012610052-3).

References

1. D. Royer, T. Dieulesaint, *Elastic Waves in Solids I. Free and Guided Propagation* (Springer, 1999)
2. J.L. Rose, *Ultrasonic Guided Waves in Solid Media* (Cambridge University Press, 2014)
3. T. Kundu, P. Kapur, T.E. Matikas, P.D. Nicolau, Rev. Prog. Q. **15**, 231 (1996)
4. S.S. Kessler, S.M. Spearing, C. Soutis, Smart Mater. Struct. **11**, 269 (2002)
5. J.L. Rose, Key Eng. Mater. **270–273**, 14 (2004)
6. M. Gresil, V. Giurgiutiu, J. Intel. Mat. Syst. Str. **26**(16), 19 (2015)
7. V. Jawali, P. Parasivamurthy, A. Nagesh, Mat. Sci. Forum. **783–786**, 2296 (2014)
8. Z. Su, I. Ye, Proc. Inst. Mech. Engrs. Part L: J. Mater. Design and Appl, **218**, 95 (2004)
9. E. Glushkov et al., J. Acoust. Soc. Am. **132**(2), 119 (2012)
10. I. Kim, A. Chattopadhyay, J. Intel. Mat. Syst. Str. **26**(8), 2515 (2015)

11. P.-C. Ostiguy, N. Quaegebeur, M. Bilodeau, P. Masson, in *Proceeding SPIE 9438, Health Monitoring of Structural and Biological Systems 2015*, (Mar 23, 2015), p. 14
12. A. Raghavan, C.E.S. Cesnik, *Proceedings of the 48th AIAA/ASME/ASCE/AHS/ASC Structures, Structural Dynamics, and Materials conference,* (Honolulu, Hawaii, 23–26 Apr 2007), p. 15
13. S.K. Parashar, J. Intel. Mat. Syst. Str. **24**(13), 1572 (2013)
14. A. Ghoshal et al., J. Intel. Mat. Syst. Str. **14**, 521 (2003)
15. K.-H. Im et al., AIP Conf. Proc. **1096**, 1033 (2009)
16. Z. Sun, B. Rocha, K.-T. Wu, N. Mrad. Int. J. Aero. Eng. **2013**, 22 (2013)
17. V. Giurgiutiu, J. Intel. Mat. Syst. Str. **16**, 291 (2005)
18. N. Hu, Y. Liu, X. Peng, B. Yan, J. Compos. Mater. **44**, 1643 (2010)
19. D. Kim, M. Philen, J. Intel. Mat. Syst. Str. **21**, 1011 (2010)
20. T. Stepinski, M. Manka, A. Martowicz, NDT&E Int. **86**, 199 (2017)
21. H. Kim, K. Jhang, M. Shin, J. Kim, NDT&E Int. **39**(4), 312 (2006)
22. F. Yan, R.L. Royer Jr., J.L. Rose, J. Intel. Mat. Syst. Str. **20**, 377 (2010)
23. K.J. Schubert, C. Brauner, A.S. Herrmenn, Struct. Health Monit. **13**(2), 158 (2014)
24. G. Giridhara et al., in *Proceeding of the 48th AIAA/ASME/ASCE/AHS/ASC Structures, Structural Dynamics, and Materials Conference* (Honolulu, Hawaii, 23–26 Apr 2007), p. 12
25. L. Yu, Z. Tian, Struct. Health Monit. **12**(5–6), 469 (2013)
26. Z. Tian, L. Yu, C. Leckey, J. Intel. Mat. Syst. Str. **26**(3), 1723 (2014)
27. C. Ramadas, J. Reinf. Plast. Comp. **33**, 824 (2014)
28. S. Lonne et al., Rev. Prog. Q. **23**, 875 (2004)
29. A.M. Kamal, I. Taha, Key Eng. Mat. **425**, 179 (2010)
30. R.G. Gibson, *Principles of Composite Material Mechanics* (McGrave Hill Inc., 1994)
31. R.M. Crane, *Vibration Damping Response of Composite Materials* (David Taylor Research Center Report, 1991), p. 302
32. R.D. Adams et al., J. Compos. Mater. **3**, 594 (1969)
33. R.D. Adams, D.G.C. Bacon, J. Compos. Mater. **7**, 402 (1973)
34. Y. Gao, Y. Li, H. Zhang, X. He. Polym. Polym. Compos. **19**(2, 3), 119 (2011)
35. M.R. Adams, M.R. Maheri, Key Eng. Mater. **50**, 497 (1994)
36. D.A. Saravanos, C.C. Chamis. *Computational Simulation of Damping in Composite Materials* (NASA Tech. Report TM-102567, 1989)
37. O. Rabinovitch, J.R. Vinson, J. Intel. Mat. Syst. Str. **13**, 689 (2002)
38. L. Yu, G. Bottai-Santoni, V. Giurgitiutiu, Int. J. Eng. Sci. **48**, 848 (2010)
39. K.R. Mulligan et al., Struct. Health Monit. **13**(1), 68 (2014)
40. S. Kapuria, J.K. Agrahari, J. Intel. Mat. Syst. Str. **29**(4), 585 (2018)
41. L. Chinchan et al., Advanced materials-physics, mechanics and applications, in *Springer Proceedings in Physics*, vol. 152, eds. by S.-H. Chang, I.A. Parinov, V.Y. Topolov (Springer, Heidelberg, New York, Dordrecht, London, Springer Cham, 2014), p. 201
42. J.D. Achenbach, *Wave Propagation in Elastic Solids* (North-Holland Publishing Company, Inc., New-York)
43. L. Wang, F.G. Yuan, Compo. Sci. Technol. **67**, 1370 (2007)
44. V.K. Sharma, et al., in *Proceeding of the 48th AIAA/ASME/ASCE/AHS/ASC Structures, Structural Dynamics, and Materials Conference* (Honolulu, Hawaii, 23–26 Apr 2007), p. 12
45. L. Yu, Z. Tian, Struct. Health. Monit. **12**(5–6), 469 (2013)
46. D.D. Mandal, D. Wadadar, S. Banerjee, J. Vib. Control **24**(12), 2464 (2018)
47. P. Hora, O. Červená, Appl. Comp. Mech. **6**, 5 (2012)

Chapter 44
Experimental Studies of Cantilever Type PEG with Proof Mass and Active Clamping

A. V. Cherpakov, I. A. Parinov, A. N. Soloviev and E. V. Rozhkov

Abstract It is considered experimental simulation of a cantilever piezoelectric generator (PEG) with an active clamping. The generator has two types of piezoelectric elements: (i) elements located on a substrate in the form of a bimorph, and (ii) piezoelectric elements of cylindrical shape fixing the base plate. The considered PEG is a part of the energy generation system, designed to convert mechanical energy from the environment into electrical energy, followed by its accumulation. The results of the analysis of forced oscillations in the vibration excitation of the PEG base are presented. The analysis of PEG output parameters was carried out under vibration loading of PEG base.

44.1 Introduction

One of the priority tasks of the world research is the development of efficient generator and energy harvesting devices. One of the types of generators are piezoelectric converters of mechanical energy into electrical energy. This type of converters is called piezoelectric generators (PEG). Basic information about PEG, as well as problems arising at the stages of development of energy harvesting devices, were given in review works [1–4], as well as in fundamental monographs [5, 6].

In the literature, a number of analogs of PEG are considered, as an example, a piezoelectric transducer of the cantilever type of mechanical energy into electrical [7], which contains a cantilever, which is a thin cantilever beam or a plate of elastic material on which piezoelectric elements are glued, one end of which is clamped at the base, the other is free. The disadvantage of the analog is its low power and low conversion efficiency.

A. V. Cherpakov (✉) · I. A. Parinov · A. N. Soloviev · E. V. Rozhkov
Southern Federal University, Rostov-on-Don, Russia
e-mail: alex837@yandex.ru

A. V. Cherpakov · A. N. Soloviev
Don State Technical University, Rostov-on-Don, Russia

I. A. Parinov et al. (eds.), *Advanced Materials*, Springer Proceedings in Physics 224, https://doi.org/10.1007/978-3-030-19894-7_44

Known PEG of cantilever type, adopted for the prototype, which contains the cantilever, consists of a cantilever beam of elastic material, which is glued to the piezoelectric elements or one side (unimorph), or from both sides (bimorph), one end of which is fixed at the base and at the free end is stiffened by additional proof mass [8]. The proof mass converts the input external acceleration into an effective inertial force deflecting the cantilever beam, which causes an increase in the mechanical stress in the piezoelectric layer of the cantilever, which is converted into additional useful power.

Depending on the field of application, PEGs of various types have been created, in which a direct piezoelectric effect is used when excitation in the sensitive element is mainly longitudinal (d_{33}) [9–12] or bending (d_{31}) [13–17] oscillations.

The problem of evaluating the energy efficiency of cantilever type PEG was previously considered in the works [3, 5, 6, 14, 15, 17]. It was shown that the output power of PEG depends not only on the electrical characteristics of piezoceramic materials (PCM) of PEG sensing elements, but also on the method of measuring their output characteristics, as well as the parameters of the electrical circuit [18].

As an example of calculations and the use of PEG can be the use of finite-element (FE) software ANSYS, whose examples of calculations are present in the papers [19, 20].

The relevance of the results is to develop a device that produces electrical energy using piezoelectric bending and clamping edges.

44.2 Problem Statement

In this paper, we descrie an experimental approach in the evaluation of the output parameters of the cantilever-type piezoelectric generator, which has active elements in the shape of a bimorph on the base, and in the form of symmetrically fixed at the base of the cantilever piezoelectric cylinders.

44.3 Description of Model Parameters

The cantilever-type piezoelectric transducer of mechanical energy into electrical energy contains a cantilever beam made of an elastic material on which piezoelectric elements are glued on one side (unimorph) or on both sides (bimorph). One end of the cantilever beam is fixed at the base. On the free end, an additional proof mass is located. Moreover, four piezoelectric elements, two above and two below in respect to the beam, having either opposite or identical directions of the polarization vector, are installed at the base. The planes of their electrodes are pressed with the help of the base elements to the conductive layers of thin metallic elastic pads on one side (see Fig. 44.1).

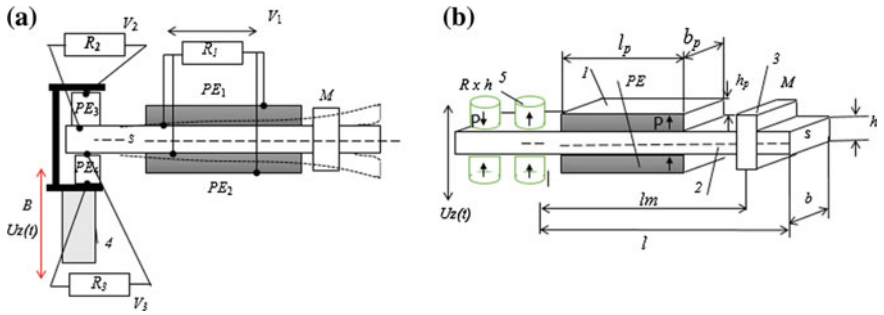

Fig. 44.1 a Electric scheme of compound PEG under active load and b structure scheme of PEG with proof mass: 1—piezoelectric element; 2—substrate; 3—proof mass; 4—place of fixing PEG (B is the movable base); 5—piezoelectric cylinders

Thin symmetrical piezoelectric elements (PEs) are polarized in thickness. PEs are glued to the console base. The geometric dimensions of the PEG are shown in Fig. 44.1b. Characteristics of the dimensions of PEG elements are present in Table 44.1, the properties of the elements are present in Table 44.2. Tables 44.3 and 44.4 demonstrate the mechanical properties of relevant materials of PE piezoceramic plates of a material PCR-7M, and piezocrystal of material PZT-19. Description of material parameters is given in [21]. The electrical diagram of the joining the PEG with active load is shown in Fig. 44.1a. The value of the proof mass can vary from 3 to 25 g. The experiment used M = 17.6 g.

Table 44.1 Characteristics of the dimensions of PEG elements

Piezoelements			Piezocylinder	
l_p, mm	b_p, mm	h_p, mm	R, mm	H, mm
50	10	0.45	10	10
Substrate			Proof mass	
l, mm	b, mm	h, mm	M, g	l_m, mm
160	13.2	1.5	17.6	65–150

Table 44.2 Mechanical properties of the structural materials

No.	Element of PEG	Material	ρ, kg/m^3	$E\times10^{11}$, Pa	v
1	Base	Duralumin	2800	0.33	0.33
2	Substrate	Duralumin	2800	0.33	0.33
3	Proof mass	Steel	7700	2.1	0.33
4	Piezoelements	PCR-7M	7280	–	0.33
5	Piezocylinder	PZT-19	7280	–	0.33

Table 44.3 Elastic modulus C_{pq}^{E} (in 10^{10} Pa), piezoelectric coefficients e_{kl} (in C/m^2) and relative permittivity $\varepsilon_{kk}^{\xi}/\varepsilon_0$ of piezoceramics (based on measurements at room temperature)

PE type	C_{11}^{E}	C_{12}^{E}	C_{13}^{E}	C_{33}^{E}	C_{44}^{E}	e_{31}	e_{33}	e_{15}	$\frac{\varepsilon_{11}^{\xi}}{\varepsilon_0}$	$\frac{\varepsilon_{33}^{\xi}}{\varepsilon_0}$
PZT-19	10.9	6.1	5.4	9.3	2.4	−4.9	14.9	10.6	820	840
PCR-7M	13.3	9.2	9.1	12.5	2.28	−9.5	31.1	20.0	1980	1810

Table 44.4 Elastic compliance S_{pq}^{E} (10^{-12} Pa), piezoelectric modules d_{fp} (in pC/N) and relative permittivity $\varepsilon_{kk}^{\sigma}/\varepsilon_0$ of piezoceramics (based on measurements at room temperature)

PE type	s_{11}^{E}	s_{12}^{E}	s_{13}^{E}	s_{33}^{E}	s_{44}^{E}	d_{31}	d_{33}	d_{15}	$\frac{\varepsilon_{11}^{\sigma}}{\varepsilon_0}$	$\frac{\varepsilon_{33}^{\sigma}}{\varepsilon_0}$
PZT-19	15.1	−5.76	−5.41	17.0	41.7	−126	307	442	1350	1500
PCR-7M	17.5	−6.7	−7.9	19.6	43.8	−350	760	880	3990	5000

44.3.1 Description of Model

Figure 44.2 shows a model sample of the cantilever-type PEG of transformation of mechanical energy into electrical energy. The cantilever beam 3 (generator substrate) of PEG (Fig. 44.2) consists of an elastic material, on which the piezoelectric elements 5 are glued on both sides (bimorph), one end of the console 3 is clamped in the base 1, and the proof mass 4 is fixed on the free end, the base additionally has four piezoelectric elements 8, two at the top and two at the bottom in respect to the cantilever beam 4 having the polarization vector directions according to the shown scheme in Fig. 44.1b. The planes of the electrodes are pressed with the help of the elements 9 of the base 1 to the conductive layers of thin metallized elastic pads 6 on one side. Upper piezocylinders have polarization vectors with different directions, the lower piezocylinders have polarization vectors directed in the same direction along the *y*-axis.

The proposed device operates as follows. Under the influence of external mechanical forces of the impact-type and vibrations due to base excitation of the vibration table 2 on the base of pezogenerator 1 in cantilever beam 3, the flexural vibrations occur. They jointly influence on the piezoelectric elements 8, in which the variables strain arise due to the reaction forces of the supports with the frequency of external forces of impacts and vibrations. Moreover, due to the direct piezoelectric effect, AC voltage generates on the electrodes of an additional piezoelectric elements 6 and, therefore, additional electric energy. The combined use of such elements can increase the output power and conversion efficiency of the . This alternating voltage and additional electrical energy can be converted by means of bridge rectifiers into a constant voltage, which is accumulated in the batteries by means of energy harvesting and storage systems. The excitation of oscillations in the cantilever beam can be performed by mechanical loading both on the base 1, in which the cantilever beam 3 is clamped, and on the free end of the cantilever beam 3. Then the maximum output power is achieved when the frequency of the external mechanical action coincides, or is close to the natural frequency of the layered cantilever, i.e., has a resonance value.

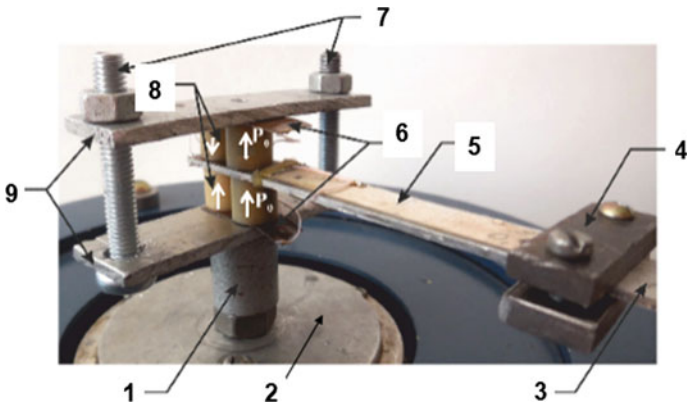

Fig. 44.2 Cantilever-type PEG of transformation of mechanical energy into electrical energy: 1—support stand; 2—base of the vibrating table; 3—plate of PEG base; 4—proof mass; 5—piezoplate (bimorph); 6—elastic insulating pads; 7—tightening bolts; 8—piezo-cylinders at the PEG base; 9—pressure plates

Piezoelectric elements can be connected in parallel, in series or have a separate connection. The choice between the types of connection elements depends on the device that we want to power. If it is required more output voltage, we should choose a series connection, and if we need more output current, then the parallel connection is necessary.

Figure 44.3 presents a vibration setup for the study of oscillatory processes of PEG. As the defining movements of elements, we used laser displacement sensors optoNSDT (3) and the RF603 (6). The sensor (3) was used to record the movements of the PEG base. The sensor (6) was used to record the movements of the proof mass fixed to the free end of the PEG cantilever. The following parameters were recorded: voltage supplied to the base plug of the vibration table 1, output voltage from PEG piezoelements (8) and (9) coming in from the electrical circuit (5) to the ADC, and signals on base vibrations from the sensors optoNSDT (3) and RF603 (6).

Figure 44.4 schematically shows a measuring system for the research of output parameters of PEG under vibration excitation.

The work of the complex was carried out as follows. Vibrations and output characteristics of PEG were investigated in stationary vibration excitation of vibration table with obtaining the frequency response of PEG. The first resonance frequency of the generator was $\sim$22 Hz. Then the signal in the form of a sine wave with a frequency of the first resonance was excited on the generator AFG3022. Vibrating table (2) with a PEG, attached to it, was actuated through the amplifier (9). In this case, all piezoelectric elements, according to the scheme of Fig. 44.1, were loaded with active resistance. Through matching devices (4), (6), (8) the ADC (7) received signals, generated by PEG and laser motion sensors, and they were recorded by using software in computer (11).

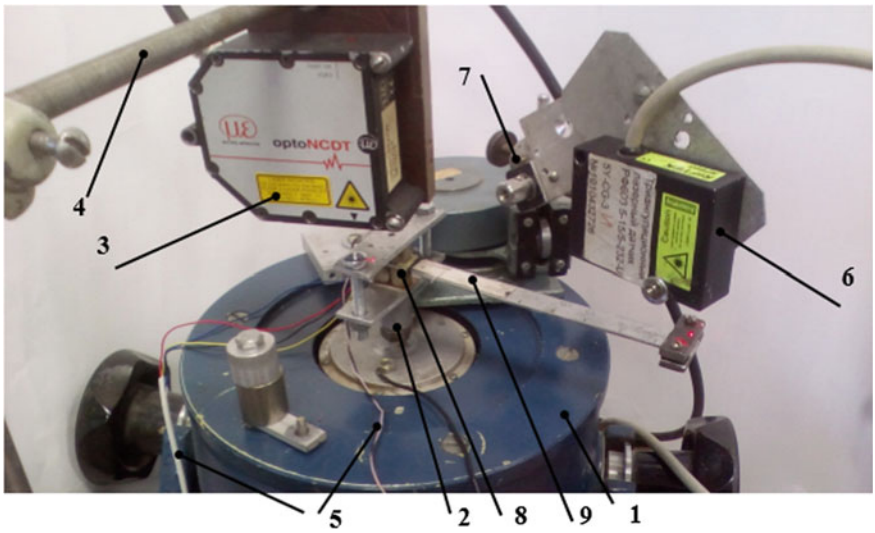

Fig. 44.3 Vibration set up of PEG: 1—vibrating table; 2—PEG; 3—laser displacement sensor optoNSDT; 4—mounting of the laser sensor (3); 5—electric tract of *PEG*; 6—triangulation laser meter RF603 of displacements; 7—support column of the sensor (6); 8—PEs of cylindrical type, located at the base of the PEG; 9—PEs in the form of plates

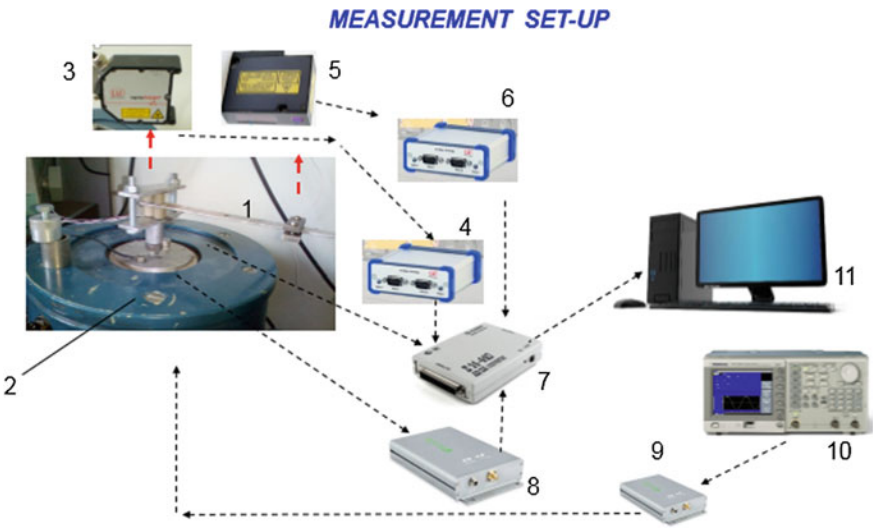

Fig. 44.4 Measurement set-up: 1—PEG; 2—vibration exciter; 3—optical sensor of linear displacement; 4—controller of the optical sensor (3); 5—optical sensor of linear displacement; 6—controller of the optical sensor (3); 7—external ADC/DAC module; 8—matching device of the acceleration sensor; 9—power amplifier; 10—sets of the signal generator; 11—computer

44.4 Results and Discussion

Analysis of the voltage dependence on the active load shows that the voltage increases smoothly to the value of $U_{\text{Bim}} = 5.13$ V at a load equal to 2 MΩ for PE in the form of plates located on the substrate (Fig. 44.5). For the top piezocrystal with mixed polarization, the magnitude of the generated voltage is greater than the lower piezocrystal with the polarization directed in one direction, and is under active load 2 MΩ: $U_{\text{PCup}} = 3.66$ V and $U_{\text{PCdn}} = 2.61$ V, respectively (Fig. 44.5).

Analysis of these power values shows that for this construction and fixing of PEG elements by fixing the proof mass at the end right position $L_m = 150$ mm, peak power values are achieved at the active load equal to $R = 270$ kΩ and are $P_{\text{Bim}} = 41.8$ μW; the output voltage is $U_{\text{Bim}} = 3.36$ V. The value of the oscillations of the PEG base was 0.022 mm. In this case, the value of the cantilever end

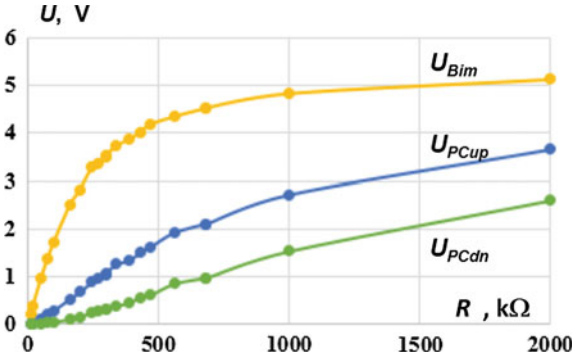

Fig. 44.5 Dependence of voltage on the load impedance for the first four modes of oscillation: U_{Bim} is the voltage on the bimorph, located on the cantilever PEG; U_{PCup}, U_{PCdn} are the voltages on the electrodes for upper and lower piezocylinders, respectively, located at the PEG base

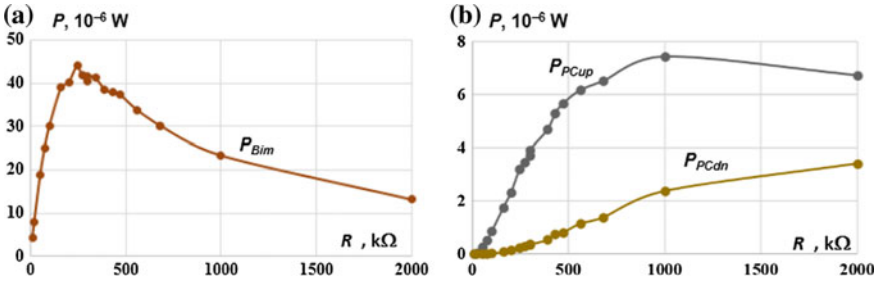

Fig. 44.6 Dependence of power from the load impedance for the first four modes of oscillation: P_{Bim} is the removable power on the bimorph, located on the cantilever PEG;, P_{PCup}, P_{PCdn} are the removable power on the electrodes for upper and lower piezocylinders, respectively, located at the *PEG* base

oscillation with the proof mass reaches 0.67 mm at the first resonance 22 Hz. Peak power for the upper piezocrystal is achieved at a load R_{PCup} = 1 MΩ and the output voltage U_{PCup} = 4.83 V and is P_{PCup} = 7.42 μW. For the lower piezocylinders, the peak value is P_{PCdn} = 3.41 μW at a load of R_{PCdn} = 2 MΩ and an output voltage U_{PCdn} = 2.61 V (Fig. 44.6).

44.5 Conclusions

We described full-scale experimental modeling of the cantilever-type PEG with a proof mass, and an active base of piezocrystal. The proof mass was located in the region of free edge of the PEG cantilever at L_m = 150 mm. Analysis of the amplitude—frequency characteristics showed that the first resonance frequency of PEG has a value of 22 Hz. Vibration tests of PEG at the first resonance frequency were performed. The displacement of the PEG base was 0.022 mm, the displacement of the free edge of the piezogenerator with the proof mass was 0.67 mm. The maximum output power, taken from the piezoelectric plates, was 41.8 μW at an active load of 270 kΩ and output voltage of 3.36 V. Peak power for the upper piezocylinders achieved 7.42 μW at a load of 1 MΩ, when the output voltage was equal to 4.83 V. For the lower piezocylinders, the peak value was 3.41 μW at a load of 2 MΩ and the output voltage of 2.61 V.

A more detailed analysis of the output power of PEG requires calculations for the cases of different variations of proof mass and account of other properties of the substrate material and the dimensions of the piezoelectric elements.

Acknowledgements The research was partially supported by the proposal of the Russian Department of Education and Science No. 11.6767.2017/BCh and 3.5378.2017/VU (organization of the implementation of researches), and also the Russian Foundation for Basic Research (grants No. 16-08-00740-a, 19-08-00365-a).

References

1. A. Erturk, D.J. Inman, *Piezoelectric Energy Harvesting* (John Wiley & Sons, 2011)
2. S.R. Anton, *Multifunctional Piezoelectric Energy Harvesting Concepts. PhD Thesis* (Virginia Polytechnic Institute and State University, Blackburn, Virginia, USA, 2011), 190 p
3. A. Badel, D. Guyomar, E. Lefeuvre, C. Richard, J. Intell. Mater. Syst. Struct. **16**(10), 889 (2005)
4. A.V. Cherpakov, V.A. Chebanenko, I.A. Parinov, S.-H. Chang, M.A. Jani, in *Proceedings of the International Symposium "Physics of Lead-free Piezoactive and Relative Materials » (Analysis of Current State and Prospects of Development), LFPM-2016"*, vol. 2, Tuapse, Russia, 12–15 Sept, 2016, p. 265
5. D. Guyomar, M. Lallart, Micromachines **2**(2), 274 (2011)
6. S.N. Shevtsov, A.N. Soloviev, I.A. Parinov, A.V. Cherpakov, V.A. Chebanenko, *Piezoelectric Actuators and Generators for Energy Harvesting. Research and*

Development. Series: Innovation and Discovery in Russian Science and Engineering (Springer Cham, Switzerland, 2018)
7. Y. Liao, H.A. Sodano, J. Intell. Mater. Syst. Struct. **21**(2), 149 (2010)
8. Wahied G. Ali, Sutrisno W. Ibrahim, Energy Power Eng. **4**, 496 (2012)
9. S. Shevtsov, V. Akopyan, E. Rozhkov, V. Chebanenko, C.-C. Yang, C.-Y. Jenny Lee, C.-X. Kuo, in *Advanced Materials—Manufacturing, Physics, Mechanics and Applications*, eds. by I.A. Parinov, S.-H. Chang, V.Y. Topolov, vol. 175 (Springer, Heidelberg, New York, Dordrecht, London, 2016), p. 534
10. A.N. Soloviev, V.A. Chebanenko, I.A. Parinov, in: *Analysis and Modelling of Advanced Structures and Smart Systems*. eds. by H. Altenbach, E. Carrera, G. Kulikov (Heidelberg, New York, Dordrecht, London, Springer, 2018)
11. S. Zhao, A. Erturk, Sens. Actuators, A **214**, 58 (2014)
12. J. Wang, Z. Shi, Z. Han, J. Intell. Mater. Syst. Struct. **24**(13), 1626 (2013)
13. A.N. Soloviev, I.A. Parinov, A.V. Cherpakov, V.A. Chebanenko, E.V. Rozhkov, L.V. Duong, in *Proceedings of International Conference Structural Integrity Conference and Exhibition (SICE-2016) (July 4–6, 2016, Bangalore, India)* (Springer, Heidelberg, New York, Dordrecht, London, 2017)
14. V.A. Akopyan, Y.N. Zakharov, I.A. Parinov, E.V. Rozhkov, S.N. Shevtsov, V.A. Chebanenko. in *Nano- and Piezoelectric Technologies, Materials and Devices*, ed. by I.A. Parinov (Nova Science Publishers, New York 2013), p. 111
15. V.A. Akopyan, I.A. Parinov, Y.N. Zakharov, V.A. Chebanenko, E.V. Rozhkov. in *Advanced Materials-Studies and Applications*, eds. I.A. Parinov, S.H. Chang, S. Theerakulpisut (Nova Science Publishers, New York, 2015), p. 417
16. A. Erturk, D.J. Inman, Smart Mater. Struct. **18**(2), 025009 (2009)
17. N.E. Dutoit, B.L. Wardle, S.G. Kim, Integr. Ferroelectrics **71**(1), 121 (2005)
18. A.A. Gusev, E.G. Avvakumov, V.P. Isupov, L.A. Reznichenko, I.A. Verbenko, A.I. Miller, A.V. Cherpakov. in *Piezoelectric Materials and Devices*, ed. by I.A. Parinov (Nova Science Publishers, New York, 2011), p. 189
19. A.N. Soloviev, I.A. Parinov, A.V. Cherpakov, V.A. Chebanenko, E.V. Rozhkov, Mater. Phys. Mech. **37**(2), 168 (2018)
20. A.N. Soloviev, I.A. Parinov, A.V. Cherpakov, YuA Chaika, E.V. Rozhkov, Mater. Phys. Mech. **37**(2), 192 (2018)
21. A.A. Panich, M.A. Marakhovskii, D.V. Motin. *Electronic Scientific Journal "Engineering Journal of Don*", No. 1, (2011) (In Russian)

Chapter 45
A Novel Design for Piezoelectric Based Harvester for Rotating Objects

Tejkaran Narolia, V. K. Gupta and I. A. Parinov

Abstract In this work, a novel rotating hub piezoelectric energy harvester has been proposed. This harvester converts the magnetic force of attraction in electric charge. The magnetic force is induced between the magnets mounted on the hub and a lever mounted directly below it. The magnetic force on the lever is magnified at the other end where a piezoelectric bar is mounted. Due to rotation, the magnetic force on piezoelectric bar varies continuously and generates charge due to piezoelectric effect. A mathematical model is formulated to compute root mean square of the power. Effects of various parameters such as thickness of magnets, thickness and length of piezoelectric bar, ratio of moment arms and structural stiffness of lever on the power and natural frequency of system have been studied. The maximum power of 113.6684 W is obtained in the current system.

45.1 Introduction

Use of piezoelectric materials in the area of energy harvesting from kinetic energy has been increased during the last decade. Such kinds of harvester have low cost, simple design and easy manufacturing process. The main aim of this work is to convert rotary motion into vibratory motion and subsequent generation of electric charge with the help of piezoelectric materials [1]. There are two ways of harvesting energy from piezoelectric material viz. compression (d_{33}) mode and bending (d_{31}) mode. In d_{33}-mode, periodic compressive force is applied on the piezoelectric material while in d_{31} mode, the piezoelectric patch is mounted on a cantilever beam and a periodic force is applied at the end of the beam to produce the bending strain in the piezoelectric patch [2]. A simple mathematical model for voltage generation by a unimorph piezoelectric cantilever beam, based on classical beam analysis, was

T. Narolia (✉) · V. K. Gupta
PDPM IIITDM Jabalpur, Jabalpur, India
e-mail: tejkaran.narolia@iiitdmj.ac.in

I. A. Parinov
Southern Federal University, Rostov-on-Don, Russia

I. A. Parinov et al. (eds.), *Advanced Materials*, Springer Proceedings in Physics 224, https://doi.org/10.1007/978-3-030-19894-7_45

proposed by Nechibvute et al. They reported that the proposed model simulations were in good agreement with the experimental results [3]. A simple model of piezoelectric generator in the form of bending mode was developed using Euler-Bernoulli beam theory by Tangerino et al. They observed that maximum power of 6.5 mW was generated across 29 kΩ resistance [4]. Efforts have been made to increase the harvested power by various researchers. By modifying the magnitude and orientation of the magnetic force, the piezoelectric cantilever's frequency response can be adequately altered in such a way that provides a useful method to harvest off-resonance vibrations [5]. Harvested energy from rotating magnets can be enhanced by increasing the broadband frequency range [6]. Use of multiple cantilever beams for the output harvesting power can be increased up to 55.6% [7]. Manla et al. used deformation of pre-stressed piezoelectric beam due to interaction with a magnet. This harvester was used in tire pressure monitoring system [8]. A hybrid energy harvester combining piezoelectric and electromagnetic generators was developed for electronic devices, wireless system. Approximate 10.7 mW power was harvested, which was 81.4% higher than single electromagnetic harvester [9]. Sirohi et al. [10] used galloping cantilever beam for energy harvesting. The beam has a D-shaped cross section piezoelectric sheet bonded in the form of bimorph. Rezaei-Hosseinabadi et al. [11] developed a topology for PZT energy harvesting made up of a lift-based wind turbine and a PZT beam without contact vibration mechanism. Wu et al. [12] developed a cantilever harvester for crosswind and were able to generate 2 W power at resonant frequency. Xie et al. [13] presented a ring PZT harvester excited by attractive magnetic forces at high excitation frequencies. They reported that 5274.8 W of power can be harvested using their mechanism. Most of the literature discusses use of piezoelectric in d_{31} mode for energy harvesting. Weinstein et al. [14] constructed a novel cantilever piezoelectric beam harvester, excited by flow produced for heating, ventilation and air conditioning. They increased excitation by attaching an aerodynamic fin at the end of beam. Approximately 3 mW power was generated at flow velocity 5 m/s. Zhang et al. [15] used impact of a turn table on piezoelectric (PVDF) beam to generate electricity. A simple analytical model was developed and simulation was carried out by using finite element method. Tao et al. [16] developed a harvester based on scotch yoke mechanism to convert the rotational motion into linear vibrations of two piezoelectricity-levers through springs. They reported that power of the order of 150 W can be harvested for at an angular velocity of 50 rad/s. Narolia et al. [17] proposed a simple configuration of parallel plate coaxial piezoelectric energy harvester. A mathematical model was developed for RMS power generation and effect of various design parameters on energy harvesting was studied. Optimal harvested power of 1.3572 W was obtained at 1600 rps.

In this chapter, an energy harvester based on magnetic attractive force excitation, with magnification of force by lever mechanism is designed and developed. Magnets of same properties and dimensions are mounted on the periphery of vertical axis hub and tip of lever, with opposite pole in front of each other. Rotation of hub produces impulse attractive force on the tip of lever, which is magnified at the other end. d_{33} mode is used to convert this force into charge. To calculate the

generated RMS power from the harvester, a simple mathematical model is developed and the effect of various parameters on the RMS power analyzed and studied.

45.2 Modeling and Design

Figure 45.1 shows basic components of the proposed "vertical axis hub rotary energy harvester" for extracting power. The main components of the harvester are, a rotating hub of radius r, 8 lever mechanisms with piezoelectric bar, 16 magnetic slabs of length l_m, width w_m and thickness t_m. The capacity of harvester can be enhanced by increasing the radius of hub and number of levers according to the requirement of power. The rotation of hub about its axis generates periodic magnetic force of attraction, $F_M \sin(\omega t)$ between the magnet slabs, at a distance d mounted on periphery of the hub and end of the lever.

The attractive force F_M between two permanent magnets of thickness t_m can be expressed as [18, 19]

$$F_M = l_m w_m t_m^{1/3} B_r |B(d)| f(d), \tag{45.1}$$

where, B_r is the residual flux density of the magnet, $B(d)$ is the magnitude of the magnetic flux density field, and $f(d)$ is an empirical function, representing the decay of the attractive force between two magnets.

For a rectangular magnet, the relation for calculation of $B(d)$ and $f(d)$ can be expressed as [18, 19]

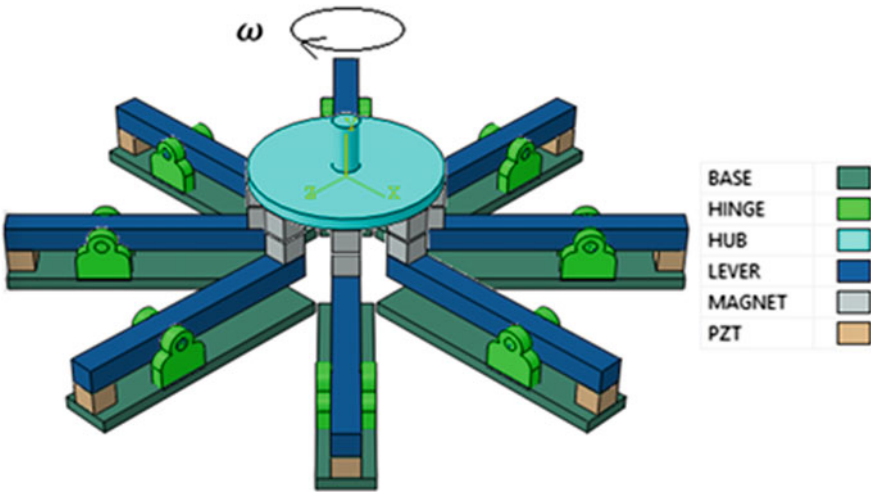

Fig. 45.1 Simple configuration of rotary hub energy harvester

$$B(d) = \frac{B_r}{\pi}\left[\tan^{-1}\left\{\frac{l_m w_m}{2d\sqrt{4d^2 + l_m^2 + w_m^2}}\right\} - \tan^{-1}\left\{\frac{l_m w_m}{2(t_m + d)\sqrt{4(t_m + d)^2 + l_m^2 + w_m^2}}\right\}\right], \tag{45.2}$$

$$f(d) = [1.749 + 1.145e^{\left(-\frac{d}{d_0}\right)}] \times 10^6 \left(\frac{\text{kg}}{\text{s}^4\text{m}^{\left(\frac{4}{3}\right)}}\right), \tag{45.3}$$

where $d_0 = 1$ mm.

The magnetic force, calculated using (45.1), is magnified with help of a lever mechanism as shown in Fig. 45.2. The other end of the lever is rigidly fixed to a piezoelectric bar.

The lever mechanism has piezoelectric bar of length l_p, width w_p and thickness t_p, and also a lever having the long and short moment arms (l_2 and l_1, respectively) and a fixed hinge. Due to rotation of hub and magnetic coupling between the lever and hub, a harmonic force is produced at point A and is magnified by n ($=l_2/l_1$) times at point C on the piezoelectric bar due to leverage action.

In order to determine the time response of end A of the lever, we consider this system as damped single degree of freedom (damper-spring-mass) system, shown in Fig. 45.3 [20, 21]. The equivalent mass m_e, spring stiffness k_e and damping coefficient c can be calculated using the dimensions and material properties of lever and PZT bar.

The lever is assumed rigid. The equivalent mass m_e can be written as the sum of mass of magnetic slab on lever at point A and 33/140 part of the mass of the lever (at site AB). Hence:

$$m_e = m_m + \left(\frac{33}{140}\right)m_l = \rho_m t_m w_m l_m + \left(\frac{33}{140}\right)\rho_l A_l l_1 n, \tag{45.4}$$

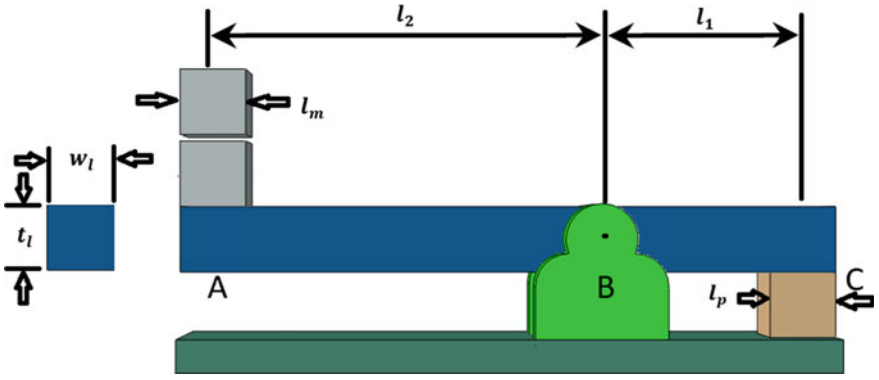

Fig. 45.2 Schematic view of leverage system

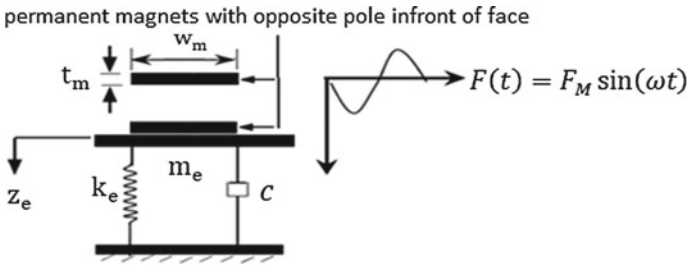

Fig. 45.3 Equivalent mass-spring-damper model

where ρ_m is the mass density of magnet and ρ_l and A_l are the mass density and cross-section area of the lever, respectively. The cross-section of lever is rectangular shape of width w_l and height t_l. Material of lever is assumed to be aluminum.

Since, the elastic deformation of the cantilever at site AB and axial deformation of the PZT bar are produced by applied force at point A, the equivalent spring stiffness k_e in Fig. 45.3 can be determined as [22]:

$$k_e = k_l k_p / \left(k_l + k_p\right), k_l = E_l w_l t_l^3 / 4(l_1 n)^3, k_p = E_p l_p w_p / \left(n^2 t_p\right), \tag{45.5}$$

where k_l, E_l, k_P and E_P are the spring constant and Young's modulus of the cantilever and PZT bar, respectively.

The equivalent damping coefficient, as shown in Fig. 45.3, is the sum of the electrical and mechanical damping coefficients:

$$c = c_e + c_m. \tag{45.6}$$

The electrical damping in the PZT bar is due to the electrical resistance when the work done by the magnetic force is converted into electricity [23]. Electrical damping coefficient c_e, can be written as [24]

$$c_e = n^2 d_{33}^2 k_e^2 / \left(\pi^2 c_v f\right), \tag{45.7}$$

where d_{33} is the piezoelectric strain coefficient in the direction of polling, c_v is the electric capacity of the PZT bar, f is the natural frequency of vibration of the single-degree-of-freedom system.

Internal structural damping force [25] and the friction between the cantilever surfaces and viscous air induce the mechanical damping in the cantilever beam during the vibration, which is given as

$$c_m = 2\xi\sqrt{k_l m_l}, \tag{45.8}$$

where ξ is the damping ratio.

Now, the equation of motion of mass m_e can be written by using Newton's second law of motion as

$$m_e\ddot{z}_e + c\dot{z}_e + k_e z_e = F_M \sin(\omega t), \tag{45.9}$$

where z_e is the displacement of the mass m_e.

The displacement of equivalent mass m_e is assumed as

$$z_e(t) = X\sin(\omega t - \phi), \tag{45.10}$$

where X is the maximum amplitude of $z_e(t)$ and ϕ is the phase angle, which can be defined as [26]

$$X = \frac{F_M}{\sqrt{(k_e - m_e\omega^2)^2 + (c\omega)^2}}, \quad \tan\phi = \frac{c\omega}{k_e - m_e\omega^2}. \tag{45.11}$$

Equivalent magnified force $F_m(t)$ at the PZT bar can be calculated as

$$F_m(t) = n[k_e.z_e(t) - c\dot{z}_e(t)]. \tag{45.12}$$

The generated periodic charge, voltage and current on the PZT patch can be deduced as

$$Q(t) = d_{33}F_m(t) = d_{33}n[k_e.z_e(t) - c\dot{z}_e(t)]; \tag{45.13a}$$

$$V(t) = d_{33}n[k_e z_e(t) - c\dot{z}_e(t)]/c_v; \tag{45.13b}$$

$$I(t) = d_{33}n[k_e\dot{z}_e(t) - c\ddot{z}_e(t)], \tag{45.13c}$$

where the electric capacity of the piezoelectric material is calculated as [12]

$$c_v = 0.0001c_v' l_p w_p/\big(0.01\cdot 0.01\cdot t_p\big). \tag{45.14}$$

The electric power produced by each PZT bar of the generator can be expressed as

$$P_e(t) = V(t)I(t). \tag{45.15}$$

There are eight sets of lever and PZT bar; hence, the total generated electric power would be

$$P_T(t) = 8P_e(t). \tag{45.16}$$

The expression of RMS of the electric power generated from 0 to t can be expressed as

$$P_T^{rms} = 8\sqrt{\frac{1}{\tau}\int_0^{\tau} P_e^2(t)\mathrm{d}t} \tag{45.17}$$

45.3 Validation of Harvester for Sustainability

The harvester was first validated for sustainability viewpoint. Following design parameters are considered:

(i) von Mises stress of the system;
(ii) pattern of magnetic force between two magnets;
(iii) torsion about the neutral axis of lever due to magnetic force;
(iv) maximum twisting of lever about its neutral axis.

The induced maximum shear stress computed using torsion equation for rectangular cross-section bar is 0.150 MPa, which is much less as compared to von Mises stress (84.97 MPa) of the material.

The plots of attractive magnetic force and torque about the neutral axis of lever having the cross-section area 10 mm × 10 mm and magnet dimensions 10 mm × 10 mm × 10 mm are shown in the Figs. 45.4 and 45.5.

From Figs. 45.4 and 45.5, it is confirmed that the maximum attractive force is applied at the point, where both magnets just overlap each other and maximum twisting moment 12.77 mN is obtained at a distance of 2 mm from the neutral axis

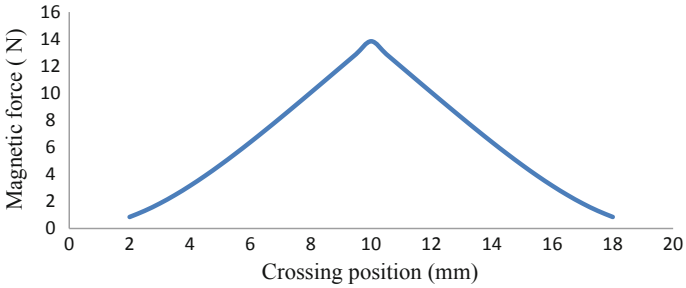

Fig. 45.4 Attractive magnetic force versus crossing length of magnets

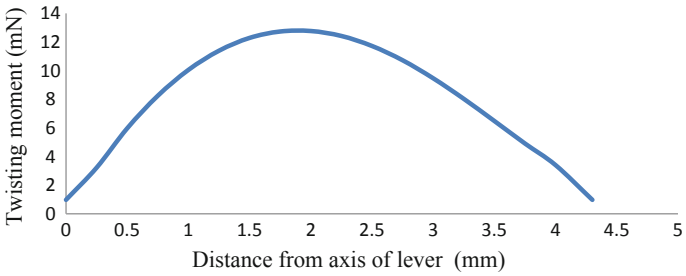

Fig. 45.5 Twisting moment versus distance from neutral axis

of the lever. The maximum twisting angle on the base of maximum twisting moment after calculation about neutral axis of lever is 0.02889°, which is very small. Hence, it can be claimed that the system is sustainable for the working conditions.

45.4 Results and Analysis

After developing the relation of RMS power due to rotation, effects of various parameters of harvester on generated power are studied. For the simulation, it is assumed that the PZT bars, magnets, levers and hub are made of PZT-4 (lead zirconate titanate), N5311 (neodymium iron boron) and aluminum, respectively. The dimensions and materials properties of the PZT bar, magnetic patch, hub and leverage system are given in Tables 45.1, 45.2 and 45.3.

Table 45.1 Material properties and dimensions of piezoelectric patches (PZT-4)

K_{33}	d_{33}(C/N)	E_p (N/m^2)	l_p(mm)	w_p (mm)	t_p (mm)
0.70	3×10^{-10}	53×10^9	10–22	10	2–24
C_v'	0.375 for the piezoelectric patch with the geometry of $w = 0.01$ m, $l = 0.01$ m, $t_p = 0.0001$ m[12]				

Table 45.2 Material properties and dimensions of magnets (neodymium iron boron, N5311)

ρ (kg/m^3)	B_r(T)	d (mm)	l_m(mm)	w_m (mm)	t_m (mm)
7500	1.45	10	10	10	10–20

Table 45.3 Material properties and dimensions of hub and lever (Al)

E_{al} (N/m^2)	ρ (kg/m^3)	r (mm)	l_1 (mm)	t_l (mm)	w_l(mm)	ξ	n
7×10^{10}	2700	36	10–100	9–18	10	0.0017	1–19

The frequency of the rotation of hub is set equivalent to the natural frequency of the lever system in order to extract maximum energy. First, effect of thickness of magnetic slabs on the extracting power has been studied. Following parameters are considered for the analysis: ratio of moment arms $n = 3$, thickness of lever $t_l = 10$ mm, width of lever $w_l = 10$ mm, length and width of magnets $l_m = w_m = 10$ mm and length, width and thickness of PZT bar $l_p = w_p = t_p = 10$ mm. When the thickness of magnetic slabs increases, then the equivalent mass M_e and sinusoidal magnetic attractive force F_M increase, too. The effect of variation of thickness on power is shown in Fig. 45.6. From Fig. 45.6, it is clear that the RMS power varies linearly with thickness. At the same time, increasing in equivalent mass decreases the natural frequency of the system, consequently decreases in angular velocity of hub. The maximum RMS power of 206.3799 W is obtained at angular velocity of 182.2605 rad/s (1740.45 rpm).

In order to capture the effect of thickness of piezoelectric bar during rotation, the thickness of PZT bar was varied between 1 and 24 mm. In the result of increasing the thickness, the overall damping coefficient decreases before 8 mm thickness of PZT bar but after that it starts increasing. The variation in power with increasing

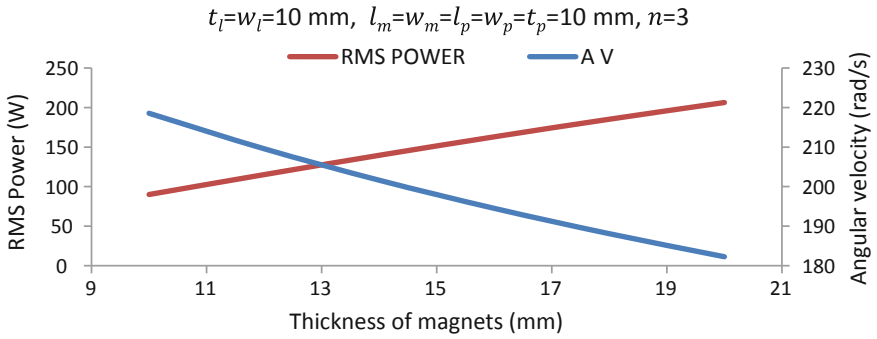

Fig. 45.6 RMS power and resonant angular velocity versus thickness of magnets

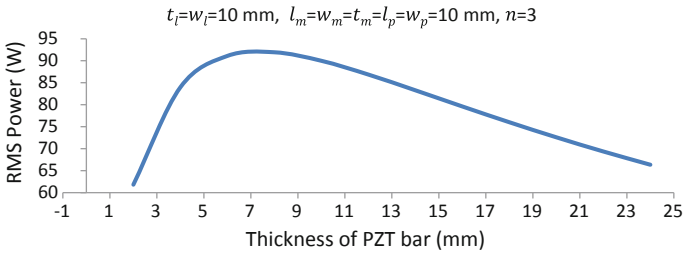

Fig. 45.7 Variation in RMS power with thickness of PZT bar

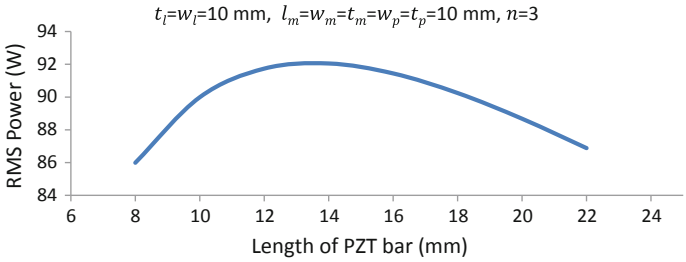

Fig. 45.8 RMS power versus length of PZT bar

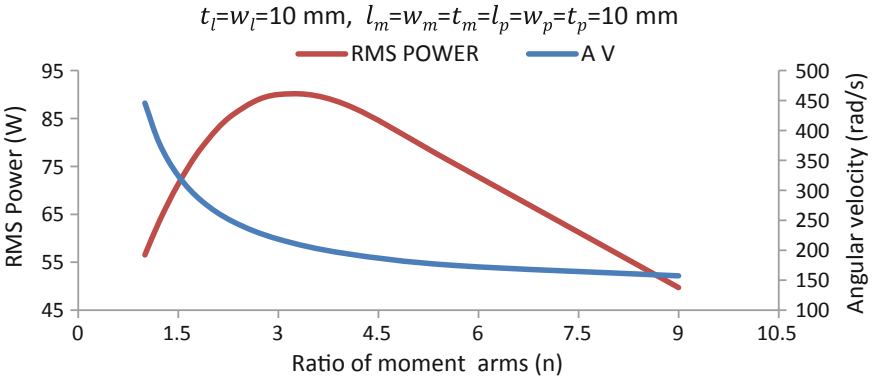

Fig. 45.9 Effects of moment arms ratio on RMS power and resonant angular velocity

thickness is shown in Fig. 45.7. The maximum power of 92.0105 W is observed at 7 mm thickness.

Figure 45.8 illustrates that, if the length of piezoelectric bar is increased from 8 to 22 mm the capacitance of PZT bar increases and more charge is generated on the plate, resulting in nonlinear increase in RMS power. Power starts decreasing after 13.5 mm of optimum length of bar. Corresponding power is 92.0720 W.

Then, the effect of moment arm ratio on output power angular velocity is studied. As shown in Fig. 45.9, increasing moment arms ratio n decreases deflection of lever end.

It is clear from (45.12) that the magnified force $F_m(t)$ increases with moment arms ratio, n, and consequently RMS power increases up to a certain limit. At higher values of moment arms ratio, the equivalent damping coefficient c dominates and decreases with power according to (45.6) and (45.7). This is due to the fact that the equivalent mass of lever site AB increases, thus reducing angular velocity as shown in Fig. 45.9. Hence, the optimum value of power is calculated as 89.989 W.

According to the relation expressed in (45.5), the structural stiffness is proportional to the cube of the lever thickness. It has been observed that the slight

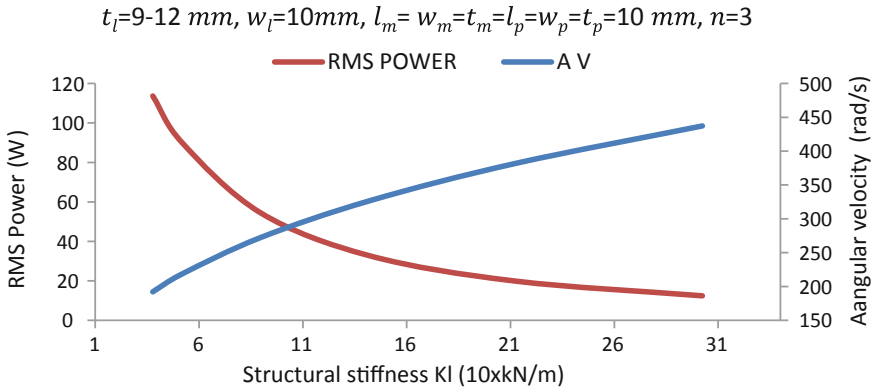

Fig. 45.10 Effects of structural stiffness of lever on RMS power and resonant velocity

increment in the lever thickness, significantly enhanced the structural stiffness k_l, which corresponded less deflection of lever at end A. Subsequently not much magnification is observed at the piezoelectric bar. On the other hand, if the thickness of lever decreases, the harvested power increases drastically due to increase in deflection. Below 9 mm thickness of the lever, the deflection of the end A is more and sticking take place between the magnets faces. As we know, the natural frequency of system is proportional to the square root of equivalent stiffness, in the result the angular velocity increases nonlinearly as shown in Fig. 45.10. Finally the RMS power varies nonlinearly and the maximum output power of harvester is obtained as 113.6684 W.

45.5 Conclusions

In this chapter a rotating hub piezoelectric energy harvester based on leverage system, excited by magnetic force has been developed. Rotating objects such as water turbine or wind turbine can be coupled to the shaft of the hub to harvest the ambient energy. The angular motion of hub exerts a periodic attractive magnetic force at the end of lever mechanism, which is magnified at the piezoelectric bar. This magnified periodic force generates periodic voltage and hence electrical power. In this configuration, eight piezoelectric bars have been considered. A mathematical model based on single mass-spring-damper system has been developed to calculate root mean square of the output electric power. The maximum power of 113.6684 W is calculated at $n = 3$, $l_m = l_p = t_m = t_p = 10\,\text{mm}$, $w_m = w_p = w_l = 10\,\text{mm}$, $t_l = 9\,\text{mm}$, $d = 10\,\text{mm}$ and angular velocity of 1834.5917 rpm. Depending on the available ambient energy, more and more power can be harvested by optimizing dimensions and size of the harvester.

Acknowledgements The study is supported partially by the Russian Foundation for Basic Research (Grant No. 19-08-00365); IAP thanks the Russian Department of Science and High Education for grant No. 3.5378.2017/VU.

References

1. T. Hehn, Y. Manoli, Springer Series in Adv. Microelectron. **38**, 33 (2015)
2. D.J. Leo, *Engineering Analysis of Smart Material Systems* (John Wiley & Sons, Inc., Hoboken, NJ, 2007)
3. A. Nechibvute, A.R. Akande, P.V.C. Luhanga, J. Pertanika, J. Sci. Technol. **19**(2), 259 (2011)
4. A.T. Mineto, M.P.S. Braun, H.A. Navarro, P.S. Varoto, *Proceedings of the 9th Brazillian Conference on Dynamics Control and Their Applications*, 07–11 June 2010
5. Ji-T. Lin, B. Lee, B. Alphenaa, Smart Mater. Struct. **19**, 045012 (2010)
6. S. Zhou, J. Cao, A. Erturk, J. Lin, Appl. Phys. Lett. **102**, 173901 (2013)
7. J. Yang, Y. Wen, P. Li, X. Bai, M. Li, *IEEE*. 978-1-4244-9289 (2011)
8. G. Manla, M.W. Neil, M.J. Tudor, IEEE Sens. J. **12**(6) (2012)
9. Y. Sang, X. Huang, H. Liu, P. Jin, IEEE Trans. Magn. **48**(11) (2012)
10. J. Sirohi, R. Mahadik, J. Vibr. Acoust. **134**(1), 011009 (2012)
11. N. Rezaei-Hosseinabadi, A. Tabesh, R. Dehghani, A. Aghili, IEEE Trans. Ind. Electron. **62** (6), 3576 (2012)
12. N. Wu, Q. Wang, X.D. Xie, Smart Mater. Struct. **21**, 095023 (2012)
13. X.D. Xie, Q. Wang, N. Wu, Int. J. Eng. Sci. **77**, 71 (2014)
14. L.A. Weinstein, M.R. Cacan, P.M. So, P.K. Wright, Smart Mater. Struct. **22**, 045003 (2013)
15. J. Zhang, Z. Fang, C. Shu, Z. Jia, Zhang, C. Li, Sens. Actuators **262**, 123 (2017)
16. J.X. Tao, N.V. Viet, A. Carpinteri, Q. Wang, Eng. Struct. **133**, 74 (2017)
17. T. Narolia, V.K. Gupta, I.A. Parinov, in *International Conference on Physics and Mechanics of New Materials and Their Applications*, Jabalpur, India (2017)
18. K&J Magnetics, www.kjmagnetics.com/calculator.asp (2011)
19. A.A. Waleed, H. Matthias, H. Tobias, W. Walter, Smart Mater. Struct. **21**, 035019 (2012)
20. N.V. Viet, X.D. Xie, K.M. Liew, N. Banthia, Q. Wang, J. Energy **112**, 1219 (2016)
21. S.O. Oyadiji, S. Qi, R. Shuttleworth, *Proceedings of the 4th World Congress on Engineering Asset Management Athens, Greece*, 28–30 Sept 2009
22. R.D. Blevins, R. Plunkett, J. Appl. Mech. **47**, 461 (1980)
23. P.D. Mitcheson, E.M. Yeatman, G.K. Rao, A.S. Holmes, T.C. Green, Proc. IEEE **96**(9), 1457 (2008)
24. X.D. Xie, Q. Wang, J. Energy **86**, 385 (2015)
25. J. Woodhouse, J. Sound Vibr. **215**(3), 547 (1998)
26. S.S. Rao, F.F. Yap, *Mechanical Vibrations*, vol 4 (Addison-Wesley, New York, 1995)

Chapter 46
Identification of Defects in Pavement Images Using Deep Convolutional Neural Networks

Arcady Soloviev, Boris Sobol and Pavel Vasiliev

Abstract A model of deep convolutional neural network for the identification of defects on the road surface images is proposed. The model is implemented as a simplified and optimized version of the most popular, at present, fully connected networks. Techniques for building the training set and learning the two-stage network are proposed, with respect to the specific nature of the problem being solved. The work done showed that it was possible to successfully apply such architectures in conditions of a small amount of initial data. The proposed model has a high degree of repeatability and can be used in various segmentation problems.

46.1 Introduction

Public infrastructure is subject to a natural ageing process. In connection with this, more frequent control procedures are required. Effective monitoring strategies can help engineers in the proper planning of maintenance and repair of road surfaces. This will result in a significant reduction in the maintenance costs of the road surface life cycle. Timely detection of problem areas and effective management of maintenance services ensure the continued availability of infrastructure. Assessment of the critical state of the road surface has passed many stages from the application of manual methods of photo-fixation to the use of high-speed digital technology [1].

A. Soloviev
Department of Theoretical and Applied Mechanics, Don State Technical University, Gagarin Square 1, Rostov-on-Don 344010, Russia

A. Soloviev
Institute of Mathematics, Mechanics and Computer Sciences, Southern Federal University, 8a Milchakova Str, Rostov-on-Don 344000, Russia

B. Sobol · P. Vasiliev (✉)
Department of Information Technologies, Don State Technical University, Gagarin Square 1, Rostov-on-Don 344010, Russia
e-mail: lyftzeigen@mail.ru

I. A. Parinov et al. (eds.), *Advanced Materials*, Springer Proceedings in Physics 224, https://doi.org/10.1007/978-3-030-19894-7_46

Russia is one of the five countries with the largest length of roads and Federal highways. Long-haul infrastructure requires monitoring systems that combine ease of use, high speed, reliability and quality of operation.

Photo and video surveillance systems can be used to monitor the condition of the road surface. The manual evaluation and analysis of the data collected can take a very long time. Therefore, the time required for the actual inspection and further assessment of the state of the objects of control may exceed their service life.

In this paper, we propose an approach that uses machine-learning technology. This allows us to automate the process of assessing the quality of the road surface. The proposed approach is to train a convolutional neural network based on data marked up manually. Thus, the system will learn to recognize the main types of damage for the objects of control and assess them. This will significantly increase the speed of inspection of the roadway and reduce material costs.

46.2 Related Work

In recent years, many researchers have focused their efforts on the improvement of algorithms for detection of defects and the development of methods for automatic detection of cracks in the parts of structures and infrastructure. As practice has shown, the field of computer vision, aimed at detecting defects, is constantly evolving with steady progress in sensing technology, hardware and software. Despite this, there are still limitations to existing methods and approaches. In the field of determining defects on the road surface, such restrictions may be, for example, the heterogeneity of the defects, a wide variety of surface types, the complexity of the background, various adjacencies, and so on.

Much attention in the published works was paid to the research and development of automated methods for detecting cracks in images [2–9]. Some of the considered works are more specific, for example [10, 11], in the field of road transport infrastructures [12, 13], in the field of bridges and structures.

Before the global spread of neural network technologies and machine learning, supported by the processing power of graphics processors, the main trend was the use of manual techniques such as morphological operations [13], extraction of geometric features [6], application of Gabor filters [14], wavelet transforms [15], histograms of oriented gradients (HOG) [16], textural analysis and machine learning [17].

Convolutional neural network (CNN) is the architecture of artificial neural network, specially designed to work with images [18]. SNN is a multilayer neural network architecture that implements local receptive fields through convolutional layers and invariance of relatively small geometric deformations through a pooling layer.

This architecture shows outstanding results in the classical problem of recognition of handwritten digits [19], in recognition of the house numbers on the base of

the Google StreeView house number (SVHN) data set [20] and in the problem of recognition and classification of road signs [21].

Recent discoveries in the field of artificial convolutional neural networks have given researchers a unique tool and a number of advantages. With the increase of computing power of graphic processors, it became possible to apply deeper architectures of machine learning models [22]. Modern technologies, such as increase of data, regularization, and others gave the opportunity to avoid overfitting [23].

With the development of convolutional neural networks, it became possible to more effectively study and generalize the features of images. This has been applied to areas such as image classification [24], object search [25], vehicle detection [26].

Flexibility and prospects of application of deep learning in problems of automatic detection of cracks in the road surface are shown in [27–29].

In work [30] the approach of automatic detection of cracks on asphalt and their classification with use of neural networks is considered. The authors proposed an approach in which they divide the image into fragments, and then each cell is classified as a crack, using the mean and variance of the grayscale values. It was shown that deflectometers with a falling weight (FWD) are useful tools for assessment of cracks in asphalt layer. In 98% of the cases, the system was able to detect the crack image effectively.

In [31] the authors considered the use of neural network for defect detection. They found that compared to other methods, clustering pixels as objects is a good way to increase identification accuracy and reduce noise.

In [32], the authors used a deep learning architecture that includes a pre-trained VGG-16 model. The pre-trained model VGG-16 has learned how to extract features from images that can distinguish one class of images from another. It showed excellent recognition quality even when working with images from previously unaffected areas. The stripped-down DCNN VGG-16 is used as a deep feature generator for road surface images. The authors taught only the last layer of the classifier. The authors conduct extensive experiments with various machine-learning models and show their strengths and weaknesses.

The paper [33] presents the application of CNN in an applied problem in the field of robotics. The objective of the system is autonomous detection and assessment of cracks and damages in the sewer pipe. CNN performs data filtering, localizing cracks, which allows them to obtain a subsequent characteristic of its geometric parameters.

The aim of [34] was to develop an integrated model based on image processing and machine-learning methods to automate the sequential detection of chips and the numerical representation of fracture in subway networks. The integrated model consists of a hybrid algorithm, interactive 3D representation and is supported by regression analysis to predict the depth of chips.

The paper [35] provides an overview and assessment of some promising approaches based on the concept of automatic detection of cracks and corrosion in civil infrastructure systems.

The paper [36] presents an effective architecture based on CNN for the detection of cracks in the pavement on the three-dimensional surface of asphalt. CrackNet

architecture provides high accuracy of data processing, using the original method of representing the geometry of the road surface. CrackNet consists of five layers and includes more than a million parameters that are trained in the learning process. Experiments using 200 test with 3D images have shown that CrackNet can achieve high accuracy (90.13%).

46.3 Proposed Method

To carry out identification of defects on pavement images, it is necessary to determine what is defect and what is not. In other words, we need to segment the image and define the appropriate classes. This type of problems is effectively solved with the help of specially developed architectures of convolutional neural networks, such, for example, as SegNet [37] and U-Net [38].

Images of the road surface have their own specifics. It consists of a small range of gray and a small difference between the background and the target of the image. In addition, images may contain a large amount of noise and foreign objects. Images can contain different types of defects with different sizes and shapes.

At present, there are a large number of datasets, on the base of which, it is possible to train a neural network [39, 40]. These data sets include the original road surface images and their corresponding mask images showing the presence or absence of defects. Since images with defects on the road surface have their own specifics, the authors propose their own simplified model of deep convolutional neural network. For image segmentation is proposed fully convolutional neural network [41] with the structure of the Encoder-Decoder. At the input of the system, we have an image of the road surface, and a binary image exists at the output. Thus, as a result, a segmented image is obtained, showing the presence and absence of defects.

46.4 Network Architecture

Figure 46.1 shows the architecture of the proposed deep convolutional neural network. The neural network consists of two parts, namely convolutional and de-convolutional ones. The convolution network is the extracting features mechanism. It converts the input image into a multidimensional representation of characteristics. The de-convolutional network plays the role of a generator that creates a segmented image based on the characteristics obtained from the convolutional network. The last convolutional network layer with a sigmoid activation function generates a segmented image, in other words, a probability map of the presence of a defect. The generated image has the same size as the input image.

The first part of the network consists of five convolutional layers with filter sets (256, 128, 64, 64, 64). The batch normalization (BN) [42] is used. The rectified

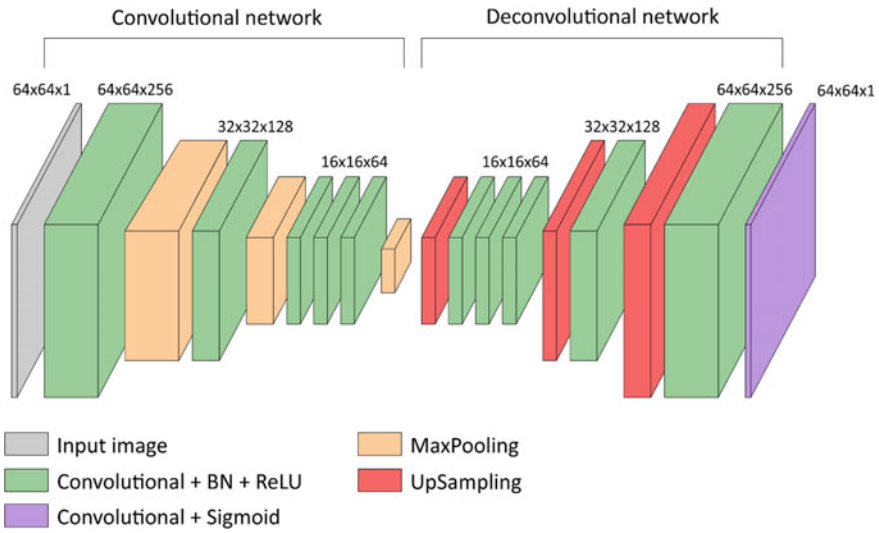

Fig. 46.1 Architecture of proposed network

linear unit (ReLU) is used as activation function. Next, there are the layers of the sub-sampling (pooling) with the window 2 × 2, thus the image is reduced by two times after its passage through this layer. The second part of the network is a mirror image of the first part. In order to restore the image size to the original image and generate a probability map, based on the characteristics of the input image, up sampling layers are used in combination with convolutional layers. The proposed neural network has 10 convolutional layers and 929,665 trainable parameters.

46.5 Training Set Preparation

The CrackForest [39] dataset is used for neural network training. The augmentation (artificial increase of a data) is carried out. So, training and operation of a neural network are based on Path-based approach. The dataset consists of 117 images. It is divided into training, test and validation sets. For each image from the training and test sets randomly selected fragments of size 64 × 64. It was established that in the framework of the task, gamma-correction of images increases the quality of the work of the neural network. Each image fragment is subject to rotation, reflection, and deformation. It was found that the most effective ratio of fragments with a defect (the defect occupies at least 5% of the image area) to the case without of defect is 95–5%. The sample size affects the learning process and the quality of the network. It was found that the optimal ratio is 15,200 fragments of the training sample and 3968 fragments of the test sample. Figure 46.2 shows the images and the corresponding masks used to train the neural network.

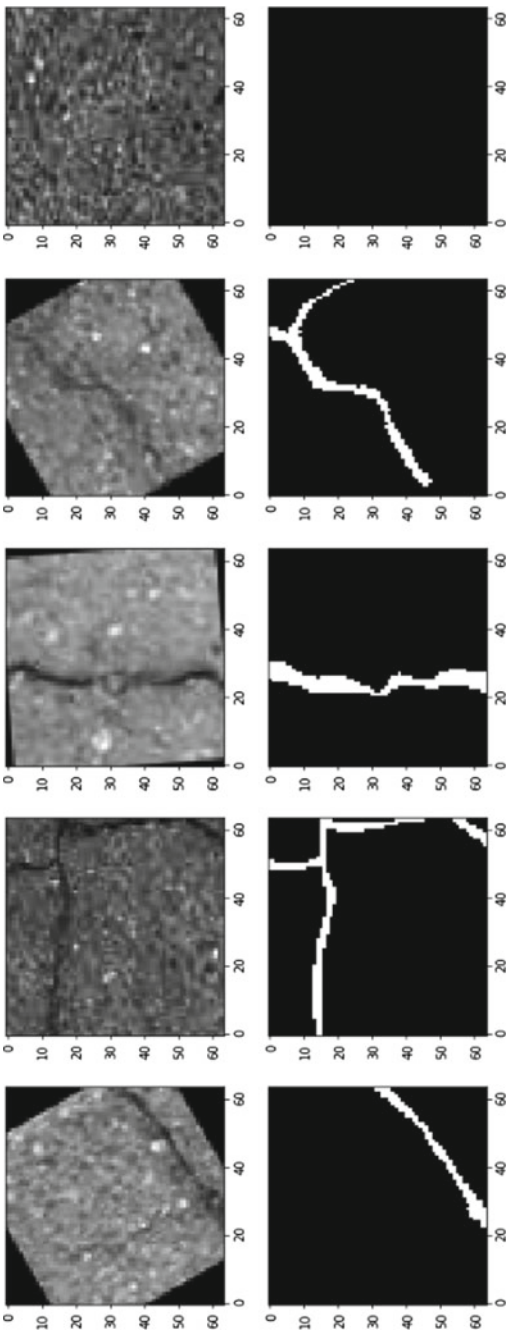

Fig. 46.2 Images and corresponding binary masks obtained in the result of data augmentation

46.6 Neural Network Training

In connection with the specificity of the area under study, the intersection over union metrics (IoU, the Jacquard coefficient) and the equivalent binary measure of similarity (Dice, the Sørensen measure) are used to train and evaluate the performance of the neural network. As a loss function, the function $1 - J$ is used.

$$J(A,B) = \frac{|A \cap B|}{|A \cup B|}, S(A,B) = \frac{2|A \cap B|}{|A| + |B|}$$

Initialization of weights in the layers of the neural network is carried out using the Glorot method [43]. Batch normalization is performed to reduce the internal covariance shift by normalizing the input distributions of each layer. For training, the Adam optimization algorithm (Method for Stochastic Optimization) is used [44].

Training of neural network is carried out in several stages. At the first stage, the network is trained on a small amount of data (30% of the main set), 5 epochs. At the second stage, the network is trained on the full amount of data required number of eras. The learning rate parameter changes with each epoch, according to the established dependency, as shown in Fig. 46.3. Within the framework of the task, the optimal number of training epochs was established equal to 25 (5 epochs at the first stage and 20 epochs at the second stage of training). With more number of epochs, the accuracy of the neural network remained largely unchanged.

To implement the developed architecture, DCNN uses frameworks Keras and Tensorflow.

46.7 Results

After training the neural network, validation is performed on the prepared dataset. Each image fragment is fed to the input of the neural network, and the output is a generated map of the probability of a defect. Figure 46.4 shows the results of the

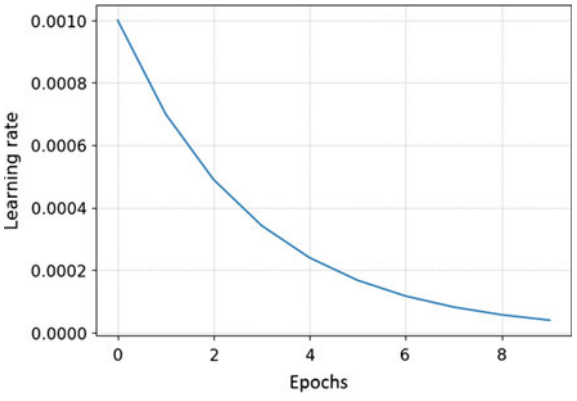

Fig. 46.3 Images and corresponding binary masks obtained in the result of data augmentation

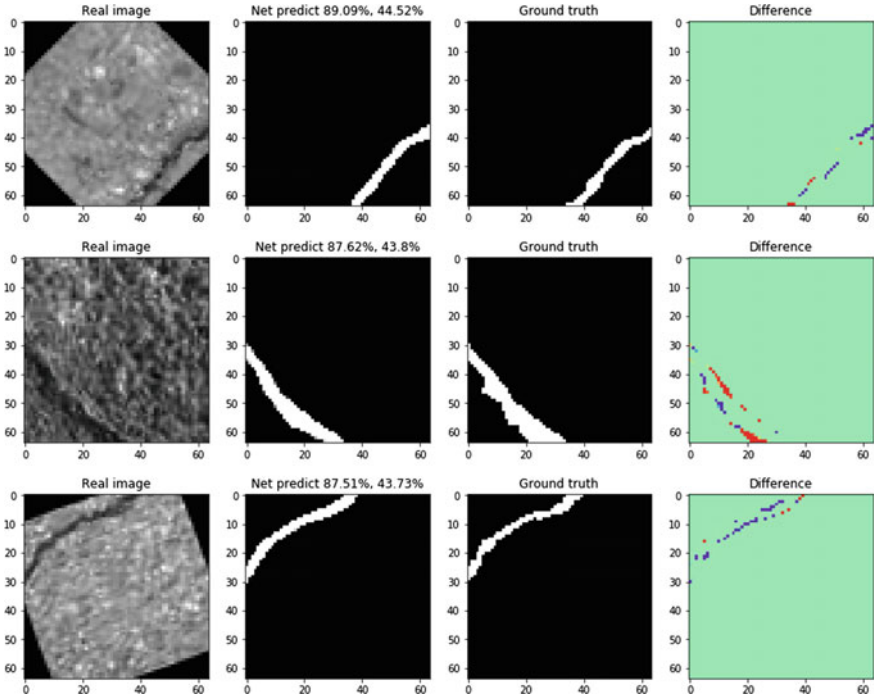

Fig. 46.4 Results of the trained neural network: first column shows the image under study, second column shows the result of the neural network, third column shows the defect, marked by human, and the fourth column shows their difference

trained network and their comparison with the true values from the test sample. The resulting network assumption is compared with the true value. Due to the specific ratio of the defect area to the area of the entire image, as well as the binary (one-bit) mask and the actual (4-byte) generated image, the values of the IoU and Dice metrics have specific values. It is worth noting that when using the IoU metric for fragments that do not have a defect, the metric values are 0, as shown in Fig. 46.5.

The quality of the prepared data set has a great influence on the training and the result of the neural network. In some cases, due to the neural network, there is a defect, although the true image defect is absent (markup error) or vice versa. This affects the overall assessment of the quality of the presented model. In general, the evaluation of the accuracy of the neural network by the proposed metrics can be subjective. Therefore, do not take these values as absolute (Fig. 46.4).

As part of this work, some models of FCN neural networks were evaluated. The results are shown in Table 46.1. The number of filters in the first part of the network is indicated in brackets. The number of filters on the second part of the network is mirrored (Fig. 46.1).

To process high-resolution images, a sliding window method with a specified step is used. It regulates processing speed and detail. Thus, the resulting map of the

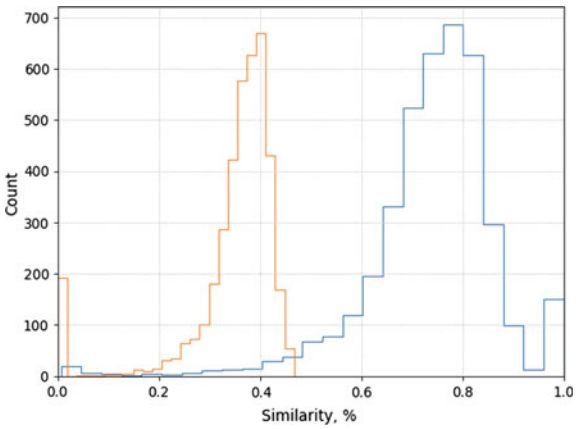

Fig. 46.5 Number of images identified with a certain accuracy: left (orange) tower represents the IoU metric and right (blue) tower represents the Dice metric

Table 46.1 Accuracy of some models of neural networks

Network structure	Accuracy
10 layers (256, 128, 64, 64, 64, …); 929,665 parameters	Dice: 73.81%, IoU: 34.88%
16 layers (32, 32, 16, 16, 16, 8, 8, 8, …); 43,441 parameters	Dice: 70.40%, IoU: 33.24%
12 layers (32, 32, 16, 16, 8, 8, …); 37,537 parameters	Dice: 67.57%, IoU: 32.12%

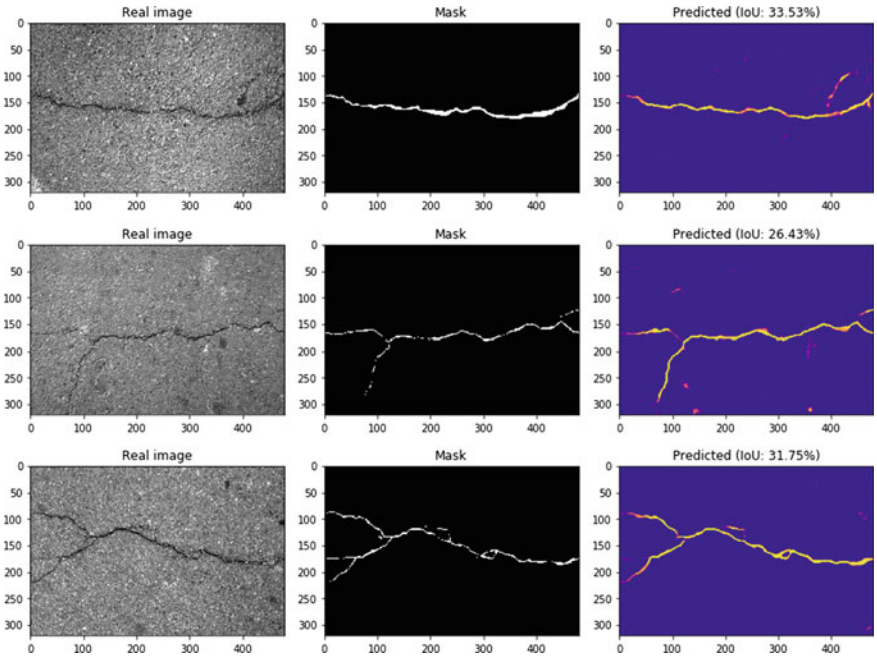

Fig. 46.6 Validation images processed by a trained neural network

probability of a defect for the entire image is formed. Several images from the validation set and the result of their processing by the neural network are shown in Fig. 46.6.

46.8 Conclusion

In this work, authors proposed an effective model of deep convolutional neural network for the identification of defects on the pavement images. The model is implemented as a simplified and optimized version of the most popular, at present, fully connected networks. Techniques for building the training set and learning the two-stage network are proposed with respect to the specific nature of the problem being solved. The work done has shown that it is possible to successfully apply such architectures in conditions of a small amount of initial data. The proposed model has a high degree of repeatability and can be used in various segmentation problems. As a result, according to the metrics used, FCN shows the following results: IoU = 0.3488, Dice = 0.7381.

Acknowledgements This work was supported by the Russian Foundation for Basic Research in the framework of projects No. 18-31-00024, No. 19-08-00074, No. 18-01-00017.

References

1. *National Academies of Sciences, Engineering, and Medicine. Quality Management of Pavement Condition Data Collection*. Washington, D.C.: The National Academies Press (2009)
2. D.S. Mahler, Z.B. Kharoufa, E.K. Wong, L.G. Shaw, Comput.-Aided Civ. Infrastruct. Eng. **6**, 1 (1991)
3. H.R. Tizhoosh, G. Krell, B. Michaelis, in *Computational Intelligence Theory and Applications. Fuzzy Days 1997*, vol. 1226, ed. by B. Reusch, Lecture Notes in Computer Science (Springer, Heidelberg, 1997)
4. Q. Zou, Y. Cao, Q. Li, Q. Mao, S. Wang, Pattern Recogn. Lett. **33**(3), 227 (2012)
5. W. Xu, Z. Tang, J. Zhou and J. Ding, in *2013 IEEE International Conference on Image Processing*, Melbourne, VIC, 4093 (2013)
6. H. Oliveira, P. Correia, in *2014 IEEE International Conference on Image Processing*, ICIP (2014)
7. Y. Shi, L. Cui, Z. Qi, F. Meng, Z. Chen, IEEE Trans. Intell. Transp. Syst. **17**, 1 (2016)
8. B.J. Lee, H. Lee, Comput.-Aided Civ. Infrastruct. Eng. **19**, 105 (2004)
9. B.-C. Sun, Y. Qiu, in *Automatic Identification of Pavement Cracks Using Mathematic Morphology* (2007)
10. S. Chambon, in *International Joint Conference on Computer Vision Theory and Applications*, VISAPP (2010)
11. L. Zhang, F. Yang, Z. Yimin, Z. Julie, Ying. *Road Crack Detection Using Deep Convolutional Neural Network* (2016)
12. P. Prasanna, K. Dana, N. Gucunski, B. Basily, H. La, R. Lim, H. Parvardeh, IEEE Trans. Autom. Sci. Eng. **1** (2014)

13. M.R. Jahanshahi, S.F. Masri, C.W. Padgett et al., Mach. Vis. Appl. **24**, 227 (2013)
14. R. Medina, J. Llamas, E. Zalama, J. Gómez-García-Bermejo, *2014 IEEE International Conference on Image Processing*, ICIP 2014, 778 (2015)
15. S. Chanda, et al., in *Artificial Neural Networks in Pattern Recognition*. vol. 8774, ed. by N. El Gayar, F. Schwenker, C. Suen (Springer, Cham, 2014), ANNPR 2014. Lecture Notes in Computer Science
16. R. Kapela, P. Rydzewski, W. Michał, A. Błoch, P. Śniatała, A. Pożarycki, A. Rybarczyk, A. Turkot, *Asphalt Surfaced Pavement Cracks Detection Based on Histograms of Oriented Gradients* (2015)
17. Q. Zou, Y. Cao, Q. Li, Q. Mao, S. Wang, Pattern Recogn. Lett. **33**(3), 227 (2012)
18. Y. Le Cun, L. Bottou, Y. Bengio, P. Haffner, Proc. IEEE **86**(11), 2278 (1998)
19. D. Ciresan, U. Meier, J. Schmidhuber, in *Proceedings of Conference on Computer Vision and Pattern Recognition (CVPR)*, 3642, (June 2012)
20. I.J. Goodfellow, Y. Bulatov, J. Ibarz, S. Arnoud, V. Shet, In: *Proceedings of International Conference on Learning Representations (ICLR)* (April 2014)
21. D. Ciresan, U. Meier, J. Masci, J. Schmidhuber, in *Proceedings of International Joint Conference on Neural Networks (IJCNN)*, 1918 (July 2011)
22. I. Arel, D.C. Rose, T.P. Karnowski, IEEE Comput. Intell. Mag. **5**(4), 13 (2010)
23. P.Y. Simard, D. Steinkraus, J.C. Platt, in *Proceedings of International Conference on Document Analysis and Recognition (ICDAR)*, 958 (2003)
24. C. Szegedy, et al., *2015 IEEE Conference on Computer Vision and Pattern Recognition (CVPR)*, Boston, MA, 1 (2015)
25. R. Girshick, J. Donahue, T. Darrell, J. Malik, in *2014 IEEE Conference on Computer Vision and Pattern Recognition*, Columbus, OH, 580 (2014)
26. X. Chen, S. Xiang, C. L. Liu, C. H. Pan, IEEE Geosci. Remote Sens. Lett. **11**(10), 1797 (2014)
27. L. Some, *Automatic Image-Based Road Crack Detection Methods* (KTH Royal Institute of Technology, Stockholm, Sweden, 2016)
28. D. Xie, L. Zhang, L. Bai, Appl. Comput. Intell. Soft Comput. (2017)
29. D. Xie, L. Zhang, L. Bai, Appl. Comput. Intell. Soft Comput. **2017**, 1320780 (2017)
30. T. Saar, O. Talvik, in *12th Biennial Baltic Electronics Conference*, Tallinn, 345 (2010)
31. D. Meignen, M. Bernadet, H. Briand, in *Proceedings Eighth International Workshop on Database and Expert Systems Applications*, Toulouse, France, 459 (1997)
32. K. Gopalakrishnan, S.K. Khaitan, A. Choudhary, A. Agrawal, Constr. Build. Mater. **157**, 322 (2017)
33. M. Browne, S.S. Ghidary, in *Advances in Artificial Intelligence (AI 2003)*, vol. 2903, ed. by T. D. Gedeon, L.C.C. Fung. Lecture Notes in Computer Science (Springer, Heidelberg, 2003)
34. T. Dawood, Z. Zhu, T. Zayed, Autom. Constr. **81**, 149 (2017)
35. M.R. Jahanshahi, J.S. Kelly, S.F. Masri, G.S. Sukhatme, Struct. Infrastruct. Eng. Maintenance Manage. Life-Cycle Des. Perform. **5**(6), 455 (2009)
36. A. Zhang, K.C. Wang, B. Li, E. Yang, X. Dai, Y. Peng, Y. Fei, Y. Liu, J.Q. Li, C. Chen, Comput.-Aided Civ. Infrastruct. Eng. **32**, 805 (2017)
37. V. Badrinarayanan, A. Kendall, R. Cipolla, in IEEE Trans. Pattern Anal. Mach. Intell. **39**(12), 2481 (2017)
38. O. Ronneberger, P. Fischer, T. Brox, in *Medical Image Computing and Computer-Assisted Intervention (MICCAI 2015)*, vol. 9351, ed. by N. Navab, J. Hornegger, W. Wells, A. Frangi. Lecture Notes in Computer Science (Springer, Cham, 2015)
39. Y. Shi, L. Cui, Z. Qi, F. Meng, Z. Chen, in IEEE Trans. Intell. Transp. Syst. **17**(12), 3434 (2016)
40. M. Eisenbach, R. Stricker, D. Seichter, K. Amende, K. Debes, M. Sesselmann, D. Ebersbach, U. Stöckert, H.-M. Gross, in *International Joint Conference on Neural Networks (IJCNN)*, Anchorage, USA, 2039 (2017)
41. E. Shelhamer, J. Long, T. Darrell, IEEE Trans. Pattern Anal. Mach. Intell. **39**(4), 640 (2017)

42. S. Ioffe, C. Szegedy, arXiv:1502.03167v3 (2015)
43. X. Glorot, B. Yoshua, *Understanding the Difficulty of Training Deep Feedforward Neural Networks*. AISTATS (2010)
44. D. Kingma, J. Ba, in *International Conference on Learning Representations* (2014)

Chapter 47
Effect of Heat Treatment on the Density and Surface Roughness Aluminum Alloy-Coal Bottom Ash Particle (5 Wt%) Composites for Bolts and Nuts Applications

Mastuki, Harjo Seputro and Muslimin Abdulrahim

Abstract Metal composite or better known as Metal Matric Composite (MMC) is a combination of two or more materials, in which the metal as a matrix and ceramic as an amplifier exist to obtain the desired characteristics. To produce solid components and fine microstructure in its manufacture, the squeeze casting process has an approximate capability. In the manufacture of aluminum matrix composite, to obtain better mechanical properties such as hardness and strength, it is required existence of T6 heat treatment process. The purpose of this research is to analyze the influence of pouring temperature and pouring time variation on squeeze casting process to density and surface roughness of 6061 coal bottom ash composite. The research method consists in casting aluminum 6061 to melt at 660 °C and then adding coal bottom ash electroless plating and magnesium, the temperature is increased with variation of casting temperature 675, 700 and 725 °C. Pouring is performed for 60, 90, 120 s with following pressing under a 20 kgf load. Then we carry out T6 heat treatment. The tests include density testing and surface roughness testing. The results of the research on the density test showed that the value of density after the T6 heat treatment is greater. This shows the presence of expansion and shrinkage during the T6 heat treatment process. Based on the results of the surface roughness testing, the grown value of the roughness after T6 treatment is between 5 and 10% of the initial roughness value before T6.

Mastuki (✉) · H. Seputro
Department of Mechanical Engineering, 17 Agustus 1945 University, Surabaya, Indonesia
e-mail: mastuki@untag-sby.ac.id

M. Abdulrahim
Department of Industrial Engineering, 17 Agustus 1945 University, Surabaya, Indonesia

I. A. Parinov et al. (eds.), *Advanced Materials*, Springer Proceedings in Physics 224, https://doi.org/10.1007/978-3-030-19894-7_47

47.1 Introduction

Bolt and nut components are very widely used, because the function of the bolt is as a means of connecting or binding components with each other in order to become a solid unity and form according to the desires of the designer. Connection techniques using bolts and nuts are relatively safer, as they are easier to install and disassemble when necessary to do things like maintenance, repair and more. The choice of bolts and nuts as a means of attachment or binder in this case for bridge construction should be done carefully and thoroughly to obtain the quality or strength of bolts and nuts corresponding to the construction. Bolts and nuts for bridge construction should have several conditions in order to be used, namely have high strength with low weight, corrosion resistance, wear resistance, and controlled strength. The eligible material is composite [1–3].

Material selection plays an important role in the quality of bolts and nuts. Bolts and nuts are made of metal composite material is one of the alternatives for consideration. Metal composites are in the most degree applied in bridge construction. The use of aluminum as a matrix is the most popular in the manufacture of metal composite, due to its light weight and high corrosion resistant properties. However, its application in such areas as transport and construction is limited due to low strength, stiffness and wear out resistance.

The composite material is a material system, composed of a combination of two or more different micro- or macro-elements in the form of chemical composition, essentially insoluble in each other. One of these elements is called matrix and the other is filler. The fill phase is embedded into matrix to provide the desired characteristics. Aluminum 6061 is the 6xxx Aluminum alloy containing magnesium and silicon as the main alloying element. Its density is 2.7 g/cm^3 and it melts at a temperature of about 630 °C. The last two digits of aluminum 6061 present the group of different aluminum alloys [5, 7]. The second number shows the modification of the alloy. A zerous second digit indicates the original alloy and integers from 1 to 9 indicate the modifications of successive alloys. Coal bottom ash is one of the oxide materials composed of more than 70% coal bottom ash, SiO_2 and Fe_2O_3, which has a high hardness value and a melting point up to above 2000 °C. The main problem in the manufacture of reinforced composite materials with oxide materials is wettability. Therefore, to increase the wetness on the surface of coal base ash particles, it is necessary to add Mg to the wetting agent by passing through the coating process of coal bottom ash powder using electroless plating method.

One of the methods that can be used in manufacture of MMC is the squeeze casting method. There are several factors that influence on the squeeze casting process such as casting temperature and time. However, the results of squeeze casting process will affect the density and surface roughness of the bolts and nuts. Squeeze casting is also called liquid metal forging, a process whereby the metal in

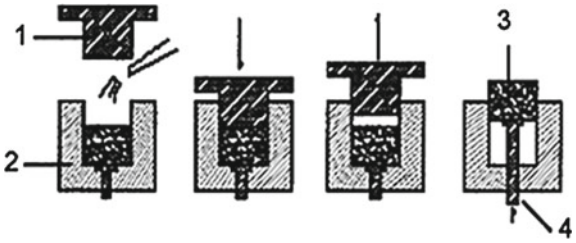

Fig. 47.1 Squeeze casting process

liquid condition is cooled and also subjected to compression (see Fig. 47.1). This process essentially combines the advantages of forging and casting processes [4–7].

In the manufacture of aluminum matrix composite, to obtain better mechanical properties such as: hardness and strength, a T6 heat treatment process is required. T6 heat treatment is a heat treatment process above the solvus line, then saturated for a while and continued by quenching. The T6 heat treatment process combines heating and cooling to solid metal over a period of time in order to obtain certain mechanical properties. This heat treatment process depends on its usage, because it can be used to tighten, soften, remove residual stress, and to improve engine capability. The following stages are taken during the aging process (see Fig. 47.2): (i) solution treatment at 530 °C for 120 s; (ii) quenching in water at 80 °C; (iii) stabilization at room temperature for 30 s; (iv) aging at 180 °C with different time variations starting from 120 s.

After quenching is performed and then heated again to the solvus line, the specimen is held for long period of time and then the cooling treatment is conducted slowly in the air. However, the often constraints of the heat treatment process are distortion and dimensional changes (shape and size). The heat treatment of the material can change its dimensional shape and microstructure so that it will affect its mechanical properties. First, before the creation of specimens of nuts and bolts, it is necessary to review the experimental materials, used for improvements.

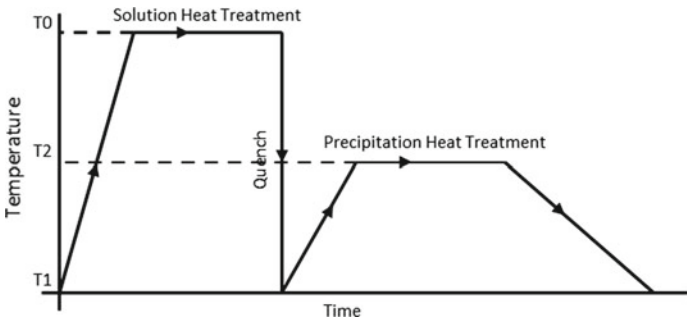

Fig. 47.2 T6 heat treatment process

47.1.1 Research Purpose

The effects of the variation of temperature and time casting at squeeze casting process on density and surface roughness of nut and bolt made of aluminum 6061 coal bottom ash composite are studied. Aluminum 6061 is used as matrix and coal bottom ash—as reinforcement.

47.1.2 Research Scope

In this study, we consider the following frameworks of the problem:

(i) Applied technology of squeeze casting method in the manufacture of MMC on the base of aluminum;
(ii) Applied technology of T6 heat treatment for "aluminum 6061—coal bottom ash" composite to obtain effective mechanical properties;
(iii) Measurement and analysis of density before and after T6 heat treatment for "aluminum 6061—coal bottom ash" composite;
(iv) Measurement and analysis of surface roughness before and after T6 heat treatment for "aluminum 6061—coal bottom ash" composite.

47.2 Research Method

47.2.1 Research Flowchart

Research flowchart is present in Fig. 47.3.

47.2.2 Description of Test/Measurement

The density size of a substance is expressed by the amount of matter or mass per unit volume. Density is used in determining the type of substance. Each substance has a different density [1, 3]. A substance with any mass regardless of its volume will have the same density. Any object, submerged partially or completely into the fluid, is subject to pushing force of the weight of the fluid transferred by the object, satisfying the Archimedes law. By immersing in water, there are three states of the experienced object, which is floating, being pushed out from water or drowned. The object is said to float in liquid when some part of object partly appears in the air,

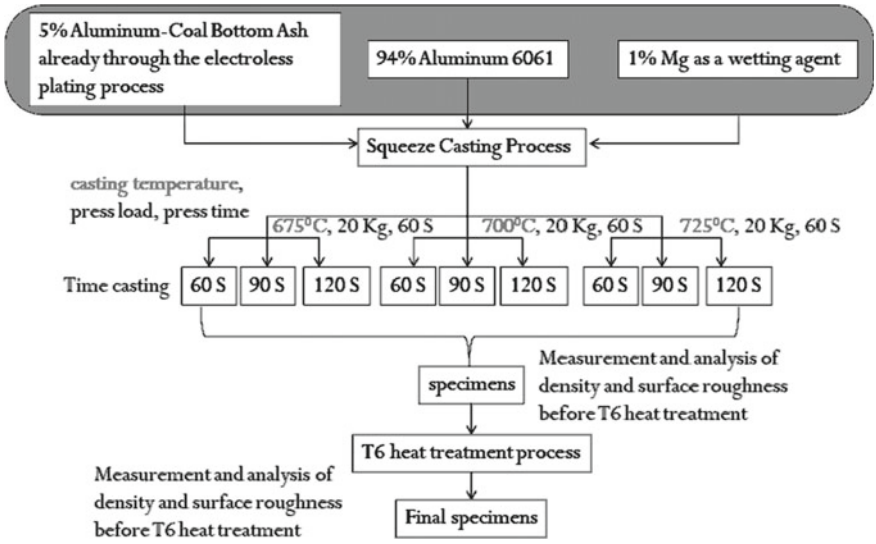

Fig. 47.3 Research flowchart

because the density of the object is less than the density of the liquid. In this case, the law of Archimedes applies so that the equations used to calculate the density are as follows:

$$\rho = \frac{\rho_{\text{air}} \times m_{\text{k}} \times \text{g}}{W_{\text{k}} - W_{\text{b}}} \tag{47.1}$$

where ρ is the mass density (kg/m^3), ρ_{air} is the density of water (1000 kg/m^3), m_{k} is the dry mass of the specimen (kg), W_{k} is the wet weight of the specimen (N = kg m/s^2), W_{b} is the weight of dry specimen (N = kg m/s^2), and g is the gravity acceleration (9.8 m/s^2).

In industry, the surface of the workpiece has a different surface roughness level, appropriate to the needs of the tool. Surface roughness has a different quality (N). The surface roughness quality has been classified by ISO: lowest value is N1 which has a surface roughness (R_{a}) of 0.025 μm and the highest values is N12, which has a roughness of 50 μm.

Surface roughness measuring instrument used is Mitutoyo surface roughness, this tool can be used to observe or measure surface roughness with ISO standards. Some of the data that this surface roughness tool can show are the values of the surface roughness and graphs of the surface roughness. Surface roughness is defined by several parameters: (i) total roughness (R_{t}) is the distance between the reference line and the base line; (ii) roughness grading (R_{p}) is the distance between the reference line and the measured line; (iii) roughness arithmetic average (R_{a}) is the arithmetic value of the measured midline and line.

The working mechanism of the surface roughness tester is to put the sensor needle (Styus), attached to the test equipment with following aligning the surface of measuring instrument with the material tested. At the time of the process, the measuring instrument must not move because it will disturb the sensor in reading of surface roughness of the material. The measurement values obtained will appear on the display that is compatible with four standards including ISO world, SIN, ANSI and JIS, so no doubt the precision and accuracy in the measurement accuracy.

47.3 Results and Discussion

47.3.1 Density Testing

Table 47.1 presents the results of density testing before and after the T6 heat treatment process.

In Fig. 47.4, it can be seen that there is a difference in the density of the specimen before and after T6 heat treatment. It can be said that the T6 heat treatment affects the density of a specimen. In Fig. 47.4, it can also be seen that the squeeze casting process parameters greatly influences the density. The parameters used are pouring temperature 675, 700, 725 °C and pouring time 60, 90 and 120 s. Based on the pouring temperature variation and the time of pouring in the squeeze casting process, the density of the test specimen is greater after T6 heat treatment. The pouring temperature of 725 °C with the time of pouring 60 s after T6 heat treatment produces the largest density compared to the other cases of temperature and time of pouring in the squeeze casting process after T6 heat treatment. This is because of the effectiveness of the time of pouring and the temperature that is far above the melting point of the specimen makes the castings solid the best during the squeeze casting process.

Table 47.1 Results of density testing before and after the T6 heat treatment process

Squeeze casting process	Density (kg/m^3)		
	Before	After	Difference
675 °C, 60 s	2637.09	2735.09	98
700 °C, 60 s	2690.54	2752.91	62.37
725 °C, 60 s	2708.36	2770.73	62.37
675 °C, 90 s	2619.27	2699.45	80.18
700 °C, 90 s	2663.82	2726.18	62.36
725 °C, 90 s	2681.64	2744.01	62.37
675 °C, 120 s	2592.54	2663.82	71.28
700 °C, 120 s	2646.02	2681.64	35.62
725 °C, 120 s	2654.91	2708.37	53.46

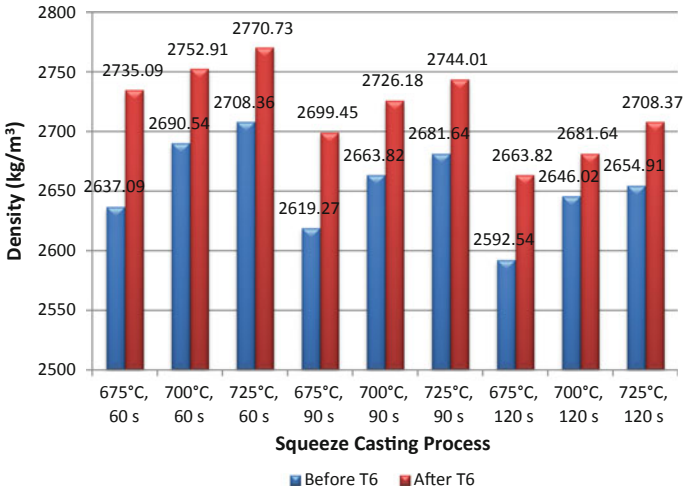

Fig. 47.4 Density graphs before and after T6 heat treatment

47.3.2 Surface Roughness Testing

Surface roughness testing is carried out on the upper surface of the specimen. Table 47.2 presents the results of surface roughness before and after T6 heat treatment.

In Fig. 47.5, it can be seen that there is a large difference in the surface roughness of the specimen before and after T6 heat treatment. After T6 heat treatment the surface of the specimen becomes coarser. It can also be seen that the squeeze casting process parameters greatly affect the value of surface roughness. The parameters used are pouring temperature 675, 700, 725 °C and pouring time 60, 90 and 120 s. Based on the pouring temperature variation and the time of pouring in the squeeze casting process, the surface roughness of the test specimen

Table 47.2 Results of surface roughness before and after T6 heat treatment

Squeeze casting process	Surface roughness (μm)		
	Before	After	Difference
675 °C, 60 s	2.87	3.49	0.62
700 °C, 60 s	2.18	2.42	0.24
725 °C, 60 s	1.69	1.79	0.1
675 °C, 90 s	3.03	3.74	0.71
700 °C, 90 s	2.32	2.84	0.52
725 °C, 90 s	1.8	1.93	0.13
675 °C, 120 s	3.26	3.83	0.57
700 °C, 120 s	2.5	3.33	0.83
725 °C, 120 s	2.08	2.33	0.25

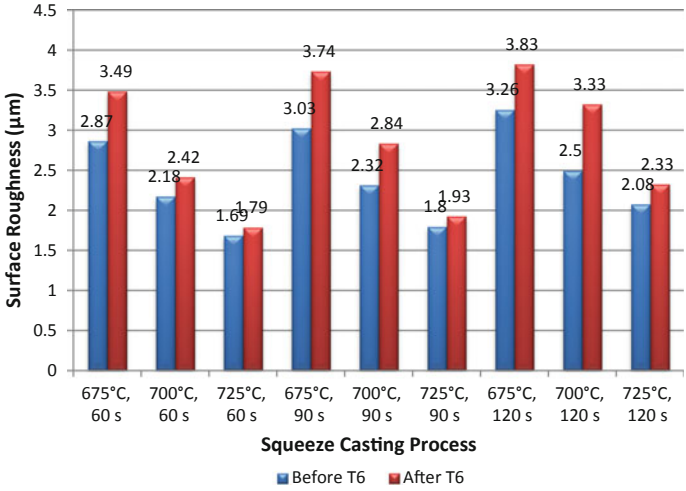

Fig. 47.5 Surface roughness graph before and after T6 heat treatment

increased after T6 heat treatment. The pouring temperature of 725 °C with 60 s of pouring time before T6 heat treatment results in the smallest/smoothest surface roughness compared to the other cases of temperature and time of pouring in the squeeze casting process after T6 heat treatment. This is because of the effectiveness of the time of pouring and the temperature that is far above the melting point of the specimen. The faster pouring provides the less air that enters, so that a little air bubbles stick to the surface of the specimen and make the surface of the specimen smoother.

47.4 Conclusion

Aluminum MMCs with Aluminum 6061 as a matrix and coal bottom ash as filler have been manufactured. The results of the analysis of density showed a significant change in the density of the test specimens after the T6 heat treatment process. The largest density is 2770.73 kg/m^3 for casting temperature at 725 °C for 60 s. The surface roughness analysis showed an increase in surface roughness values in the test specimens after the T6 heat treatment process. The increasing surface roughness after T6 heat treatment is relatively the same without sharp differences. However, the smallest surface roughness, obtained at the temperature of 725 °C, is equal to 1.69 µm and the largest surface roughness is equal to 3.83 µm at 675 °C.

Acknowledgements This research was partially supported by "Hibah PKAPT" research grant provided by Simlitabmas, Ristekdikti Indonesia, 2018.

References

1. A. Kumar, K. Kumar, S. Saurav, R. Siva Sankar Raju, Imperial J. Interdisc. Res. (IJIR) **2**(5), 151 (2016)
2. S. Attar, M. Nagaral, H.N. Reddappa, V. Auradi, J. Emerg. Technol. Innovative Res. (JETIR) **2** (2), 225 (2015)
3. P. Kittali, J. Satheesh, G. Anil Kumar, T. Madhusudhan, Int. Res. J. Eng. Technol. (IRJET) **3** (4), 2412 (2016)
4. G.C. Manjunath Patel, R. Mathew, P. Krishna, M.B. Parappagoudar, Proc. Technol. **14**, 149 (2014)
5. A.M. Dhanashekar, V.S. Senthil Kumar, Proc. Eng. **97**, 412 (2014)
6. M. Habibur Rahman, H.M.M.A. Rashed, Int. J. Sci. Eng. Res. **5**(3), 1210 (2014)
7. J. Xue, Y.F. Han, J. Wang, B.D. Sun, J. Mater. Sci. Technol. **29**(11), 1373 (2013)

Chapter 48
Analysis of the Effect of the Hardened Surface Layer Properties of the Tribocontact Parts on Their Wear and Stress-Strain State

V. I. Kolesnikov, M. I. Chebakov and S. A. Danilchenko

Abstract The present paper is aimed at scrutinizing the contact interaction between the brake shoe and the railway wheel, taking into account the contacting surfaces friction and wear. The Archard's model was used as a model describing the wear process. The solution to the problem was carried out applying the finite element method and the ANSYS software. The paper contains the results of calculations of wear and contact pressure intensity in the presence of a thin hardened layer on the shoe base, the survey of the influence of the mechanical properties of a layer on these values, as well as on the equivalent stress intensity at the boundary of the base material and the hardened layer. The performed calculations manifest that an entire set parameters must be considered when creating a hardened surface to increase the wear resistance of tribocontact parts.

48.1 Introduction

As it is widely known, the wear process affects mainly the surface layers of the tribocontact parts. This process characterized by the destruction and removal of part of the material, which ultimately leads to a malfunction or even failure of machines and mechanisms. A great number of factors, including friction in the contact area, contact pressure, etc., influences the wear intensity [1, 2]. Currently, various methods are applied to reduce wear on rubbing parts. For instance, the use of lubricants and antifriction materials can significantly reduce friction [3, 4].

Hardening of the surface layers located right in the tribocontact is also one of the most effective ways to increase the durability of working units [5, 6]. However, the

V. I. Kolesnikov · M. I. Chebakov · S. A. Danilchenko
Rostov State Transport University, Rostov-on-Don, Russia

M. I. Chebakov (✉) · S. A. Danilchenko
I. I. Vorovich Mathematics, Mechanics and Computer Sciences Institute, Southern Federal University, Rostov-on-Don, Russia
e-mail: michebakov@yandex.ru

I. A. Parinov et al. (eds.), *Advanced Materials*, Springer Proceedings in Physics 224, https://doi.org/10.1007/978-3-030-19894-7_48

main difficulty of this approach is essentially connected with obtaining the optimal parameters of each unit's strengthened surface.

The given paper is aimed at scrutinizing the contact interaction between the brake shoe and the railway wheel, taking into account the contacting surfaces friction and wear. The Archard's model [7] was used as a model describing the wear process. The choice of the abovementioned model can be explained by its ability to describe quite well the mechanical wear of the contacting surfaces in terms of the linear theory of elasticity [8, 9]. The paper contains the results of calculations of wear and contact pressure intensity in the presence of a thin hardened layer on the shoe base, the survey of the influence of the mechanical properties of a layer on these values, as well as on the equivalent stress intensity at the boundary of the base material and the hardened layer.

48.2 Formulation of the Research Problem

We consider the contact interaction between the railway wheel and the brake shoe. The wheel geometry is constructed according to the scheme presented in Figure A.1, Appendix A of 10791-2011 Russian National Standards Regulations. The geometry of the brake shoe is designed in accordance with 720.31.44.157.1 brake shoe drawing scheme. Figure 48.1 demonstrates the finite-element model of a wheel-shoe tribocontact.

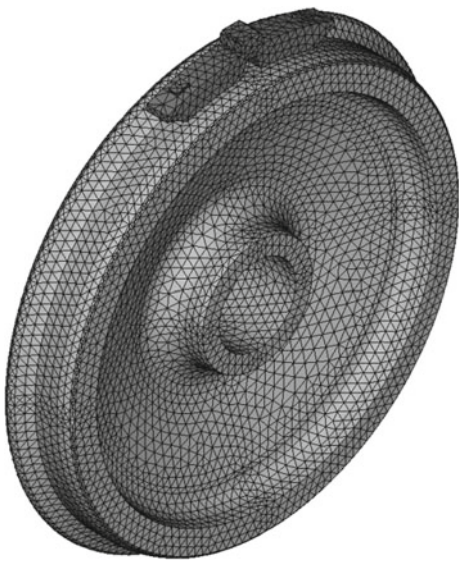

Fig. 48.1 Finite element model of a wheel-shoe tribocontact

The wheel rotates with a constant angular velocity ω around x-axis. Displacements relative to the other axes are prohibited. The force F presses the brake shoe against the wheel rolling surface, thus it can only move along the applied force direction. Coulomb friction with coefficient k is set between the wheel rolling surface and the shoe base.

Analyzing the given tribocontact, we consider the non-stationary elastic contact problem of the theory of elasticity about the brake shoe wear during friction interaction with a rotating wheel, taking into account the presence of the hardened layer on the shoe base.

The solution of the problem was carried out applying the finite element method and the ANSYS software. The finite-element mesh was built using 20-node elastic elements SOLID186. The shoe base strengthening was simulated on the base of shell element SHELL181, which allows describing thin or relatively thick shell structures. The element has four nodes, having six degrees of freedom per node: movement and rotation about three axes. Solution of the problem does not takes into account neither inertial effects nor material plastic properties. The possibility of exploiting shell elements for modeling bodies with a layered structure is shown in [10].

To determine the initial contact and the best convergence of the calculations, the solution consisted of two stages by analogy with [11]. The Archard's model was applied to calculate the wear intensity. Since the wear rate of the brake shoe is significantly higher than the wear rate of the wheel, the latest was not taken into account in the calculations.

48.3 Calculation Results

When modeling the brake shoe and the wheel, the following material properties were assigned for them: steel with Young modulus parameters $E_1 = 2 \times 10^{11}$ Pa, Poisson ratio $\upsilon_1 = 0.3$ and density $\rho_1 = 7826$ g/m^3 for the wheel; material with Young modulus parameters $E_2 = 5 \times 10^9$ Pa, Poisson ratio $\upsilon_2 = 0.36$, density $\rho_2 = 2100$ g/m^3 and hardness $H = 2.5 \times 10^7$ Pa. While simulating the hardened layer, three variants of material properties were used (Table 48.1). Layer thickness is $h = 0.5$ mm.

Table 48.1 Material properties of the hardened layer

Parameter	Set of material properties 1	Set of material properties 2	Set of material properties 3
Density ρ (kg/m^3)	4000	2100	4000
Modulus of elasticity E (Pa)	1×10^{10}	5×10^9	1×10^{10}
Poisson ratio υ	0.32	0.36	0.32
Hardness H (Pa)	2.5×10^7	5×10^7	5×10^7

The angular velocity of the wheel rotation is $\omega = 5.85\ c^{-1}$, the applied load $F = 10$ kH, the coefficient of friction between the wheel and the shoe was set constant and equal to $k = 0.38$.

The calculations of intensity of vertical wear and contact pressure on the shoe base were made for four problem options: (i) the brake shoe without the hardened layer; (ii–iv) the brake shoe base is coated with the hardened layer with various mechanical properties described in Table 48.1.

The obtained results manifest that hardness has a greater effect on the wear intensity than the modulus of elasticity. It is explained by the fact that the hardness is a term of the Archard wear equation, whereas the modulus of elasticity affects only the contact pressure. Figure 48.2 presents the plots, revealing the dependence of the vertical wear intensity and the contact pressure on the brake shoe base on time for: 1—the brake shoe without the hardened layer; 2—the brake shoe base is coated with the hardened layer with set of material properties 2, described in Table 48.1.

The plots (Fig. 48.2) prove that the presence of the hardened layer with a greater hardness leads to a decrease in wear intensity, while the contact pressure changes slightly.

In addition to the wear and contact pressure intensity, the investigation is focused on analyzing the stresses in the base material of a shoe under the hardened

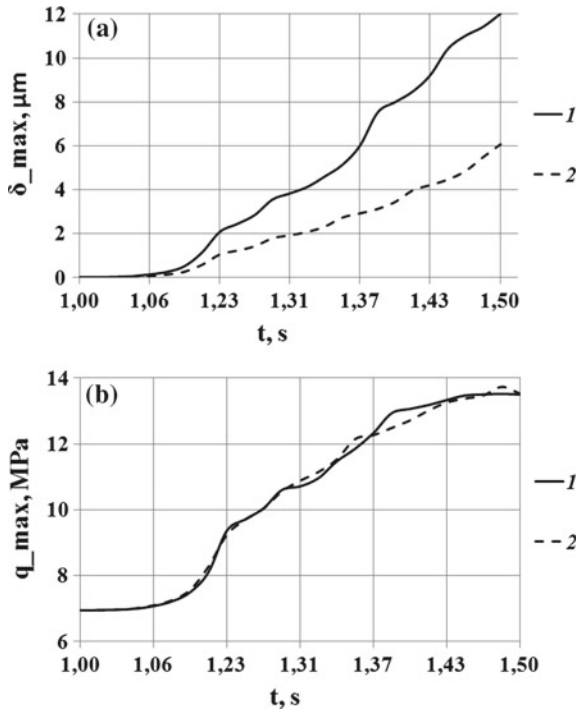

Fig. 48.2 Dependences of the vertical wear (**a**) and the contact pressure (**b**) intensity on the brake shoe base on time

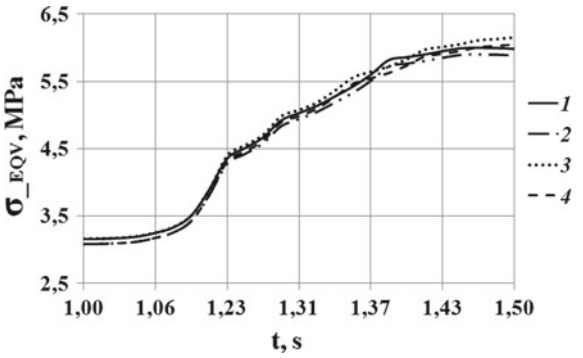

Fig. 48.3 Dependences of equivalent stress on time at the boundary of the base material and the hardened layer for four cases: *1*—the initial brake shoe; *2*—there is the hardened layer with set of material properties 1 depicted in Table 48.1; *3*—there is the hardened layer with set of material properties 2 described in Table 48.1; *4*—there is the hardened layer with set of material properties 3 presented in Table 48.1

layer. Figure 48.3 shows a dependence of equivalent stress on time at the boundary of the base material and the hardened layer.

The obtained results indicate that the equivalent stresses at the boundary of the base material and the hardened layer enlarge with an increase in the hardness of the hardened layer. Based on this, we can conclude that the growth of wear resistance due to an increase in the contacting surface hardness is not the optimal solution, since it leads to an increase in stresses under the surface layer.

Further calculations were carried out taking into account diverse thicknesses of the hardened layer. The results evidence that the increase in the hardened layer thickness cause a slight growth of wear (less than 2%), but the contact stresses remain almost unchanged. The layer thickness has a more significant effect on the stresses at the boundary of the base material and the hardened layer. A decrease in equivalent stress values is observed while thickness increasing. Figure 48.4 shows

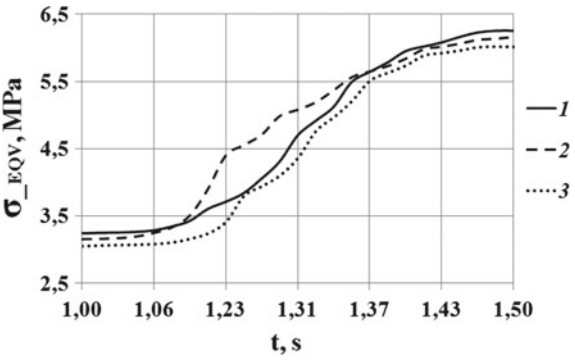

Fig. 48.4 Dependences of equivalent stress on time at the boundary of the base material and the strengthened layer at diverse layer thicknesses: *1*—h = 0.1 mm; *2*—h = 0.5 mm; *3*—h = 1 mm

dependences of equivalent stress on time at the boundary of the base material and the hardened layer at different layer thicknesses. The layer is characterized by a set of material properties 2, depicted in Table 48.1.

48.4 Conclusions

The performed calculations manifest that an entire set parameters must be considered when creating a strengthened surface to increase the wear resistance of tribocontact parts. Thus, despite that the increase in the surface layer hardness contributes to increasing wear resistance, it leads to an increase in the equivalent stresses intensity at the boundary with the base material. At the same time, the layer thickness layer has not a significant impact on the intensity, yet affects the equivalent stresses values right under the layer. Therefore, it is necessary to conduct a wide range of theoretical and experimental studies to obtain optimal properties of strengthened surface structures.

Acknowledgements The research is carried out in accordance with the Federal Target Program "Research and Development in the Priority Areas of Development of the Russian Scientific and Technological Complex for 2014-2020" and is supported by the Government of the Russian Federation represented by the Ministry of Higher Education and Science of Russia (Agreement No. 14.607.21.0203, Project identifier RFMEFI60718X0203).

References

1. M. Gee, J. Nunn, Wear **376–377**, Part B, 1866 (2017)
2. T. Dyck, P. Ober-Wörder, Wear **368–369**, Supplement C, 390 (2016)
3. T.W. Scharf, S.V. Prasad, J. Mater. Sci. **48**(2), 511 (2013)
4. V.I. Kolesnikov, Yu.F. Migal, N.A. Myasnikova, Vestnik of the Southern Scientific Center RAS, Pilot issue, 45 (2004) (in Russian)
5. A.V. Byeli, G.D. Karpenko, N.K. Myshkin, *Structure and Methods of Formation of Wear Resistant Surface Layers*. Mashinostroenie, Moscow, 208p (1991) (in Russian)
6. D. Panfil, M. Kulka, P. Wach, J. Michalski, J. Achievements Mater. Manuf. Eng. **85**(1), 12 (2017)
7. J. Archard, J. Appl. Phys. **24**(8), 981 (1953)
8. T. Telliskivi, Wear **256**(7), 817 (2004)
9. M.I. Chebakov, S.A. Danilchenko, A.A. Lyapin, Izvestiya Vuzov Severo-Kavkazskii Region. Nat. Sci. **2**, 32 (2017) (in Russian)
10. M.I. Chebakov, A.A. Lyapin, *Vestnik Rostovskogo Gosudarstvennogo Universiteta Putey Soobshcheniya*, No. 3, 27 (2018) (in Russian)
11. M.I. Chebakov, S.A. Danilchenko, A.A. Lyapin, Izvestiya Vuzov Severo-Kavkazskii Region. Nat. Sci. **4**, 51 (2017) (in Russian)

Chapter 49
Fracture Prediction of the Self Adjusting File Using Force and Vibration Signature Analysis

Ankit Nayak, P. K. Kankar, Prashant K. Jain and Niharika Jain

Abstract The self-adjusting file (SAF) is the most popular endodontic file of the latest generation. Unique properties of the SAF like adjustable, adaptable, thin-walled, hollow pointed cylindrical lattice-like structure and shaping ability, makes it different from other endodontic files. Endodontist can easily shape oval or flat root canals using the SAF. The SAF has abrasive particles on the lattice structure. It performs transline motion in the root canal at 83.33 Hz. In the transline motion of the SAF, abrasive particles dislodge material from the inner wall of the root canal. During root canal shaping, the endodontic instruments may get fractured which is one of the iatrogenic error involved with root canal instrumentation. Continuous monitoring of the endodontic file may help to avoid such fracture of the SAF. In this work, force and vibration signatures of the SAF were analyzed to predict the fracture of the SAF. For force and vibration analysis simulated root canals (Endo Training Bloc-J) were held in a vice which was connected with the accelerometer and dynamometer to acquire force and vibration signature of root canal shaping. The features from force and vibration signatures were calculated. On the analysis of these features, the failure of the SAF was predicted. It was concluded that the vibration signature of the simulated root canal can be used to predict the fracture of the SAF to prevent the treatment from iatrogenic errors related to instrument failure.

A. Nayak (✉) · P. K. Kankar · P. K. Jain
CAD/CAM Lab, Mechanical Engineering Discipline, PDPM, Indian Institute of Information Technology, Design and Manufacturing Jabalpur, Jabalpur 482005, Madhya Pradesh, India
e-mail: ankitnayak@iiitdmj.ac.in

N. Jain
Department of Conservative Dentistry and Endodontics, Hospital and Research Centre, Triveni Institute of Dental Science, Bilaspur 495001, Chhattisgarh, India

I. A. Parinov et al. (eds.), *Advanced Materials*, Springer Proceedings in Physics 224, https://doi.org/10.1007/978-3-030-19894-7_49

49.1 Introduction

The root canal treatment (RCT) is an endodontic treatment process to restore the infected tooth. RCT process starts from diagnosis of the tooth to locate the root of the infection. In RCT, the disinfection of canal is carried out and the root canal is reshaped using endodontic files; this is known as root canal shaping [1, 2]. Root canal cavity filled using filler materials followed by sealing of root canal access cavity, using photocurable resin. To strengthen the restored tooth, a crown has been placed over it.

Root canal shaping is the primary factor of successful RCT. First root canal shaping was performed with the help of a watch spring by Edwin Manynard of Washington, DC in 1838 [3]. From the results of that revolutionary experiment, endodontists, designers, and manufacturer get influenced and designed and fabricated new endodontic files [4–6]. These files were based on the principle of helical motion of cutting edge in the root canal. Further, the designs of endodontic files were updated into the next generation of endodontic filing system. Shaping kinematics and protocols of use were also transformed according to the design of endodontic files.

File separation during root canal shaping is one of the severe iatrogenic error as it may be complicated to recover the separated part from the root canal [7–10]. Prediction of the fracture of the endodontic file may be one of the solutions to this problem. Force and vibration signature may help to predict the fracture of endodontic instruments. There is a strong linear correlation between force and vibration amplitude of the SAF, produced during the shaping of simulated root canals [4]. In this study, the features of force and vibration signatures were analyzed which can be used to predict the file separation during the root canal shaping.

49.2 Materials and Methods

In the present study, the force and vibration signatures of the SAF file were analyzed. The motion of SAF is one of the source of vibration [11]. The principal design feature of the SAF is its hollow lattice-like adaptable structure. The SAF can adjust itself automatically as per the shape of the root canal. The unique feature of shape flexibility marks the SAF more efficient among the other endodontic files [12]. The adaptable lattice structure of the SAF shrinks and expands in each cycle to retain the shape as per the geometry of the root canal. The abrasive particles placed over the lattice structure of the SAF remove material from the wall of the root canal. In each stroke of the SAF, small grainy elements of the SAF surface got stuck with particles of root canal wall and pulled them from their original position; hence small particles from the inner wall of the root canal are dislodged. In each stroke, the forces are exerted on the wall of the root canal which is also the cause of vibration

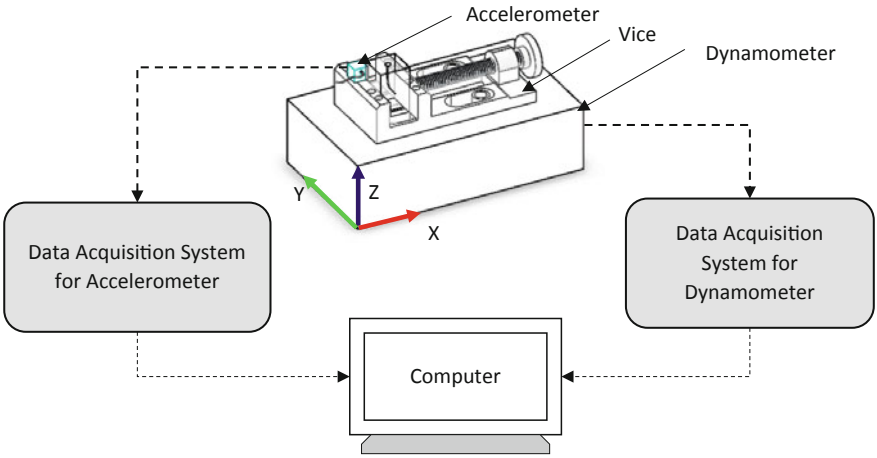

Fig. 49.1 Graphical representation of the experimental setup

due to material dislodging. The FFT plots of forces and vibrations showed that the major amplitudes of force and vibrations occur at the frequency of filing ω_f (83.33 Hz) and its harmonics [4].

To maintain similar geometry, anatomy and to avoid the sample related errors J-shape, square pillars, endodontic training blocks (Endo Training Bloc-J, Dentsply Maillefer) were used. A vice was used to provide a rigid support to endodontic block. Vice was equipped with an accelerometer (Dytran 3093B) for measurement of the vibration signature and mounted on the Kistler dynamometer for cutting force measurement as shown in Fig. 49.1. The data sampling frequency for accelerometer and dynamometer were set at 51,200 and 7142 Hz, respectively. Dynamometer and accelerometers were connected to a data acquisition system. Data acquisition system decodes the voltage and current signals into the force and vibration signals further these signals were monitored on a computer monitor. Further stored signals were processed in MATLAB to know their characteristics.

The root canal shaping was performed by an experienced endodontist. Before root canal shaping, the glide path for easy move of endodontic file was verified or prepared with the help of #15 K file. After that root canal shaping was performed using the SAF. The WaveOne motor (WOM, Dentsply Maillefer) along with a vibrating hand-piece head (RDT3: ReDent-Nova Reanana, Israel) was used to actuate the SAF.

The SAF performs transline oscillations at the frequency (ω_f) of 83.33 Hz and 0.4 mm amplitude. The root canal was continuously irrigated using distilled water. During root canal shaping pecking motion was performed as per the protocol suggested by the file manufacturer (ReDent-Nova Reanana, Israel).

In this study, a single file was used for the shaping of different endodontic blocks to study the changes in vibration signature throughout the life of the endodontic file. The recorded signature was processed in MATLAB and features of vibration and

force signature were calculated to identify the significant difference between the healthy condition of file and condition of the file just before fracture.

Following features of force and vibration signature were calculated.

(i) Mean
(ii) Root Mean Square
(iii) Standard Deviation
(iv) Kurtosis
(v) Skewness
(vi) Crest Factor
(vii) Clearance Indicator
(viii) Shape Indicator
(ix) Impulse Indicator.

49.3 Results and Discussion

It was observed from Figs. 49.2 and 49.3 that there was significant variation in a 4th sample which was just before the fracture of the endodontic file. This shows that the vibration signature can be used for prediction of the SAF separation. It was found that clearance indicator, crest factor and skewness of the signature may help to predict the file fracture in the more precise way.

It was observed that the SAF separated after the gradual decay in RMS values of the force and vibration amplitude in initial experiments. It was perceived from the graph that the RMS values of force and vibrations increase before the separation of the SAF. Measurement of this force during root canal shaping is a challenging task during the root canal treatment. Since there is a strong linear correlation between force and vibration [4]; so vibration signature can be used to predict the file separation. Due to continuous oscillatory motion and material dislodging, abrasive particles of the SAF were also ground. Due to continuous grinding of the abrasive particle the SAF gets blunt [13]. Blunt SAF applies less material removal and vibration excitation forces [3]. This phenomenon can be observed in the graph of RMS value as it is continuously decreasing. After that bulging on the lattice of the SAF was initiated, this caused a significant increment in the force and vibration signature. After further use of the SAF, lattice joints are fractured. Before fracture, an increment in RMS values of vibration and force was sighted in responses as shown in Fig. 49.2. Bulging is the primary sign of the fracture. The significant decrement in the RMS value appeared before bulging. This decrement can be used to predict the bulging. A further increment of the RMS value can be used to predict the file separation.

Some studies revealed that the SAF has a lifespan of 27 min [12] before any failure but this conclusion regarding lifespan cannot be considered for each case of endodontic shaping. Moreover, the life of file also depends on the operating conditions, geometry, and anatomy of the root canal [12, 14]. Instrument separation

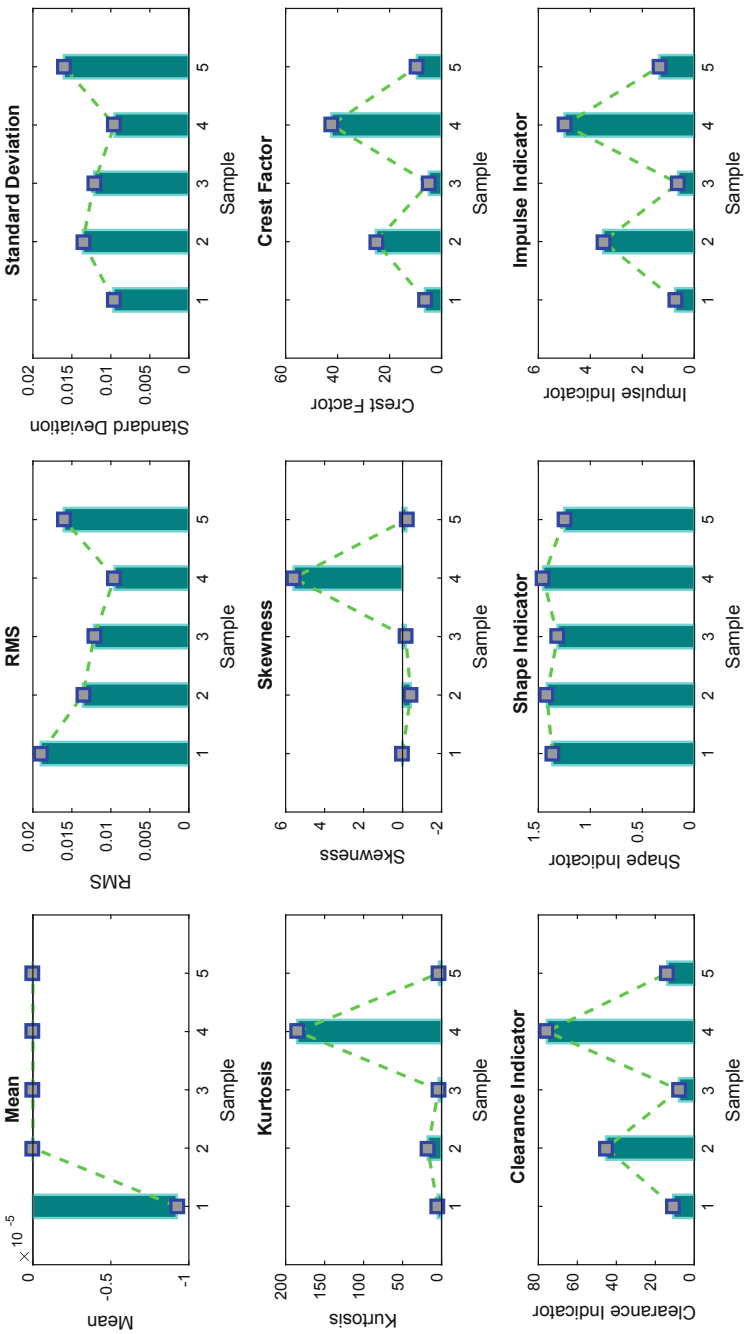

Fig. 49.2 Feature extraction of force signature

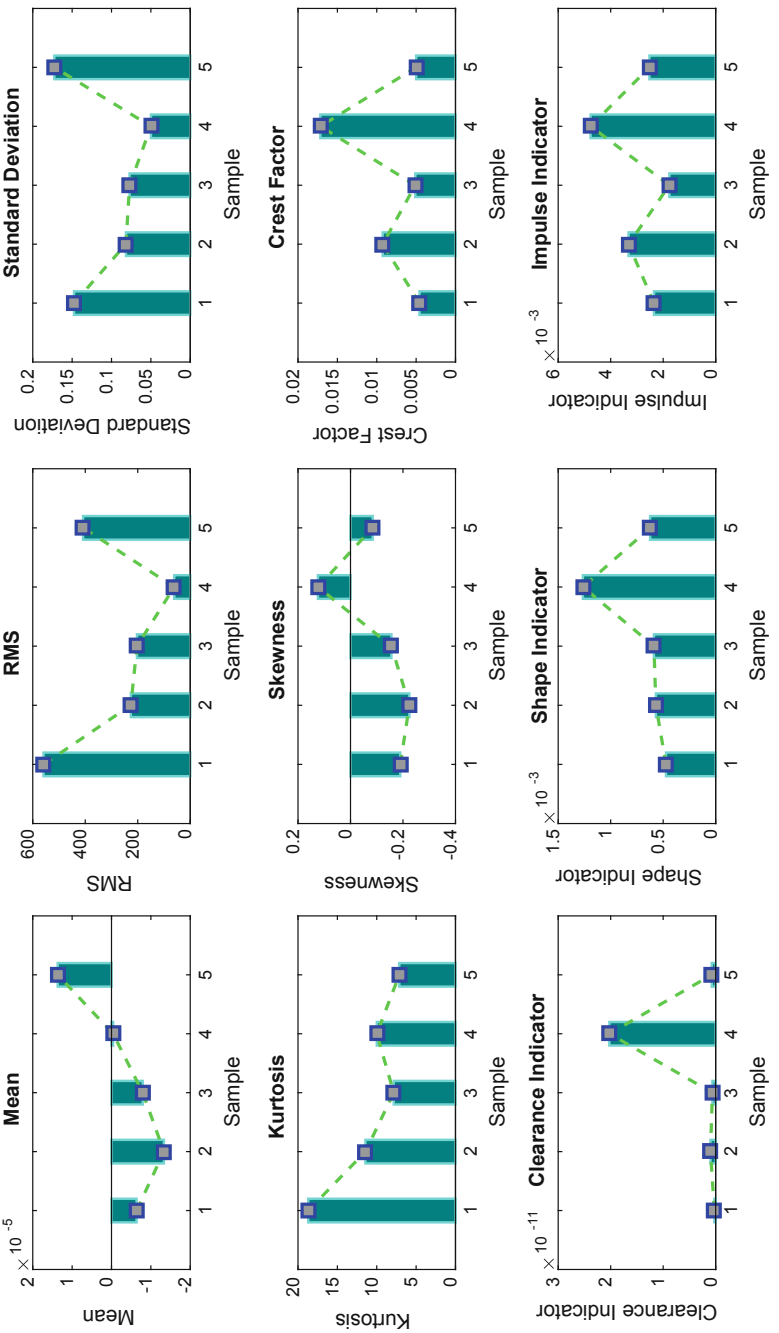

Fig. 49.3 Feature extraction of vibration signature

cannot be neglected. Akcay et al. [14] revealed that the single SAF may not be enough for curved canal enlargement, particularly for molar tooth with curved root canals and extra root canal, mesio buccal second or distal buccal second. The dentist may need to change the instrument in between root canal shaping to avoid instrument separation. Other than special cases the instrument separation cannot be avoided in normal cases and clinical practice. This study presents a remedy to prevent the instrument separation during the root canal treatment. Different features of vibration will help to know to predict the instrumentation separation more precisely and vibration signature analysis might be a helpful method to estimate the structural deformities and related forces which are the causes of file separation.

49.4 Conclusion

For more precise prediction of the file separation, the various features of the signal can be used. From Figs. 49.2 and 49.3, it is concluded that the clearance indicator, crest factor and skewness can be used to predict the file fracture. In operating condition, the endodontic file applies excitation forces on the root canal and therefore system excites on the frequency of filing. This study suggests that the vibration signature analysis can be used to predict the instrument separation. But it is still a challenge to predict the instrument life during root canal shaping and is one of the limitations of this study. Further the statistical features of the force and vibration signature can be used to predict the root fracture, root perforation, and external tooth resorption.

References

1. A. Nayak, P.K. Jain, P. Kankar, N. Jain, Proc. Inst. Mech. Eng. Part H, J. Eng. Med., p. 095441191878810, July (2018)
2. R.C. Therapy, *Endodontic Treatment Procedures*
3. L.I. Grossman, J. Endod. **8**(suppl), 1 (1982)
4. A. Nayak, P.K. Kankar, N. Jain, P.K. Jain, J. Dent. Sci. Mar (2018)
5. S.E. Elsaka, A.M. Elnaghy, A.E. Badr, Int. Endod. J. **50**(11), 1077 (2016)
6. Y. Shen, H.M. Zhou, Y.F. Zheng, B. Peng, M. Haapasalo, J. Endod. **39**(2), 163 (2013)
7. H.C. Kim, S.Y. Sung, J.H. Ha, M. Solomonov, J.M. Lee, C.J. Lee, B.M. Kim, J. Endod. **39**(12), 1572 (2013)
8. S.E.D.M. Saber, M.M. Nagy, E. Schafer, Int. Endod. J. **48**(1), 109 (2015)
9. G. Gavini, C.L. Caldeira, E. Akisue, G.T.D.M. Candeiro, D.A.S. Kawakami, J. Endod. **38**(5), 684 (2012)
10. J. Ha, S.W. Kwak, S.K. Kim, J. Endod. **43**(3), 443 (2016)
11. R. Hof, V. Perevalov, M. Eltanani, R. Zary, Z. Metzger, J. Endod. **36**(4), 691 (2010)
12. Z. Metzger, E. Teperovich, R. Zary, R. Cohen, R. Hof, J. Endod. **36**(4), 679 (2010)
13. Z. Metzger, E. Teperovich, R. Cohen, R. Zary, F. Paqué, M. Hülsmann, J. Endod. **36**(4), 697 (2010)
14. I. Akay, S. Yiğit-Özer, Ö. Adigüzel, S. Kaya, Oral Surg., Oral Med Oral Pathol. Oral Radiol. Endod. **112**(5), 12 (2011)

Chapter 50
Direct Mapping FBMC Based Underwater Transmission Scheme for Audio Signals

Chin-Feng Lin, Chun-Kang Li, Shun-Hsyung Chang, Ivan A. Parinov and Sergey Shevtsov

Abstract This paper proposes a direct mapping (DM) filter bank multicarrier (FBMC) based underwater transmission scheme for audio signals. Figure 50.1 schematically shows the proposed FBMC scheme, and DM transmission technology, low-density parity-check (LDPC) channel coding, adaptive binary phase shift keying (BPSK) modulation or offset quadrature amplitude modulation (OQAM), FBMC transmission technology, and a power assignment mechanism are integrated into an underwater audio transmission system. The BER performances of the proposed scheme in an underwater channel were explored through simulations, and the power saving ratios for the underwater transmissions of audio signals were discussed.

50.1 Introduction

Orthogonal frequency division multiplexing (OFDM) is an important high speed multicarrier communication scheme. One of the shortcomings of OFDM is relatively large side lobes [1]. Filter bank multicarrier (FBMC) uses a filtering mechanism with small side lobes to minimize the interference compared to OFDM

C.-F. Lin (✉) · C.-K. Li
Department of Electrical Engineering, National Taiwan Ocean University, Keelung, Taiwan, ROC
e-mail: lcf1024@mail.ntou.edu.tw

S.-H. Chang
Department of Microelectronic Engineering, National Kaohsuing University of Science and Technology, Kaohsiung, Taiwan, ROC

I. A. Parinov
I. I. Vorovich Mathematics, Mechanics, and Computer Science Institute, Southern Federal University, Rostov-on-Don, Russia

S. Shevtsov
Head of Aircraft Systems and Technologies Laboratory at the South Center of Russian Academy of Science, Rostov-on-Don, Russia

I. A. Parinov et al. (eds.), *Advanced Materials*, Springer Proceedings in Physics 224, https://doi.org/10.1007/978-3-030-19894-7_50

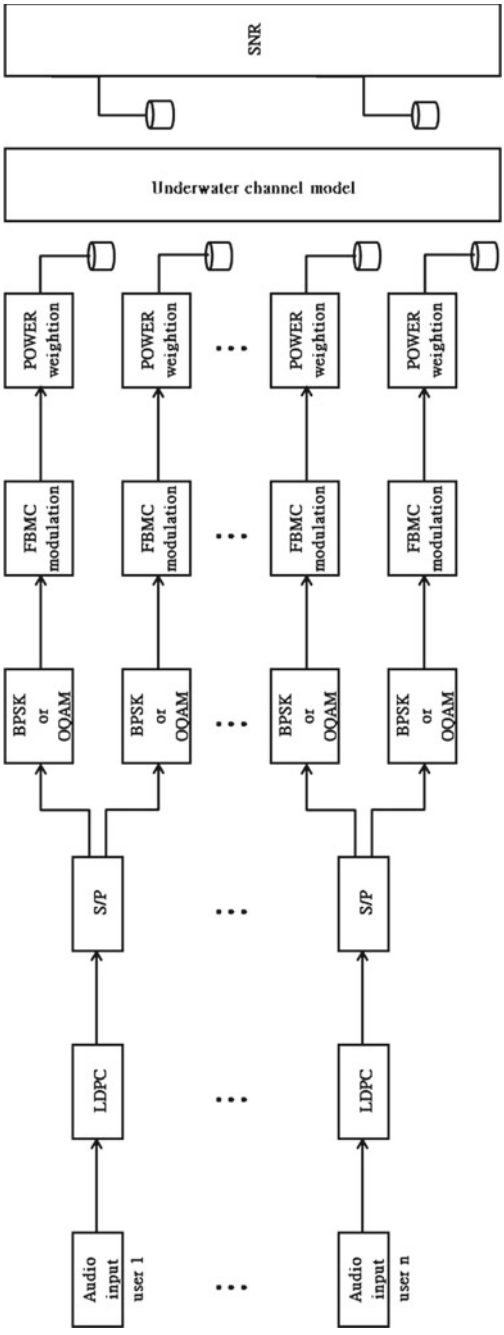

Fig. 50.1 Proposed DM FBMC-based underwater transmission scheme for audio signals

technology, and is more complex than OFDM. FBMC is a modified OFDM technology that improves bandwidth efficiency of subcarrier signals. The performance evaluation of FBMC technology with multiple inputs and multiple outputs (MIMOs) as well as channel estimation is explored for future mobile communications [2]. The FBMC increased symbol density, and time-frequency localization compare to OFDM. The FBMC transmission technique presents a new insight for multicarrier modulators [3], and the FBMC scheme includes inverse Fast Fourier transform (IFFT), and a finite impulse response (FIR) filter bank (FB). The intersub-channel interference frequency response was analyzed, and the FB based transmitter architecture was illustrated. An overview of the fifth generation (5G) requirement, massive MIMO communications, and FBMC modulation were demonstrated [4].

Amini et al. [5] demonstrated the FBMC communication scheme for the doubly dispersive underwater acoustic channels. In addition, the performances of transmission bit error rates (BERs) and signal-to-interference plus noise ratios were investigated. Lin et al. [6] proposed the FBMC-based technology for the underwater voice and image transmission system, and the performances of these signals were investigated.

50.2 Research Method

The proposed direct mapping (DM) FBMC-based underwater transmission scheme for audio signals is shown in Fig. 50.1. The DM transmission mechanism, the 2×2 multi-input multi-output (MIMO) scheme, the PHYDYAS FBMC solution with a 64-point IFFT and two polyphase networks [3], adaptive modulation through binary phase shift keying (BPSK) or 4-offset quadrature amplitude modulation (4-OQAM), (2000, 1000) low-density parity-check (LDPC) code encoder with a code rate of 1/2; serial-to-parallel (S/P) schemes, and a power assignment mechanism are integrated in the proposed architecture. The frequency domain prototype filter coefficients of the FBMC technology are 1, 0.971960, $\sqrt{2/2}$, and 0.235147, and the overlapping factor is 4 [3]. Audio data were input into an LDPC code encoder, and LDPC audio data bit streams were extracted as outputs. The LDPC audio data bit streams were then input into the serial-to-parallel mechanism, which output LDPC audio data bit streams 1 and 2. The transmission speed was twice the single input signal of the FBMC-based system by using 2 adaptive BPSK and 4OQAM modulators, 2 FBMC modulators, 2 power assignment mechanisms, and 2 transmission and receiver antenna. With the multipath fading and AWGN noise increased, the transmission power weighting increased, and with the multipath fading and AWGN noise decreased, the transmission power weighting decreased. The low power transceiver design was achieved using the dynamic power assignment mechanism.

50.3 Simulation Results

Figure 50.2 shows the BER performance of the DM FBMC underwater transceiver architecture (UTA) scheme with a perfect channel estimation (PCE), and channel estimation errors (CEEs) of 5 and 10%. The underwater channel model with a carrier central frequency of 11.5 kHz, an underwater channel bandwidth of 3.9 kHz, and a transmission distance of 1 km were used [7]. The solid and dashed lines, in Figs. 50.2, 50.3 and 50.4, denote the BPSK modulation, and the 4OQAM, respectively. The symbols '○', '△', and '□', in Figs. 50.2, 50.3 and 50.4, denote the modulation with a PCE, the modulation with a CEE of 5%, and the modulation with a CEE of 10%, respectively.

The audio signals received using the BPSK modulation with a PCE for signal to noise ratios (SNRs) of 5.37, 7.21 and 10.45 dB, with the corresponding BERs of the received audio signals were 1.4×10^{-3}, 0.4×10^{-3} and 7.69×10^{-6}, respectively. The audio signals received using the BPSK modulation with a CEE of 5% for signal to noise ratios (SNRs) of 5.37, 7.21 and 10.45 dB, with the corresponding BERs of the received audio signals were 0.0019, 0.0005 and 1.54×10^{-5}, respectively. The audio signals received using the BPSK modulation with a CEE of 10% for signal to noise ratios (SNRs) of 5.37, 7.21 and 10.45 dB, with the corresponding BERs of the received audio signals were 0.0024, 0.0007 and 4.62×10^{-5}, respectively. The BER performances increased as the CEE decreased.

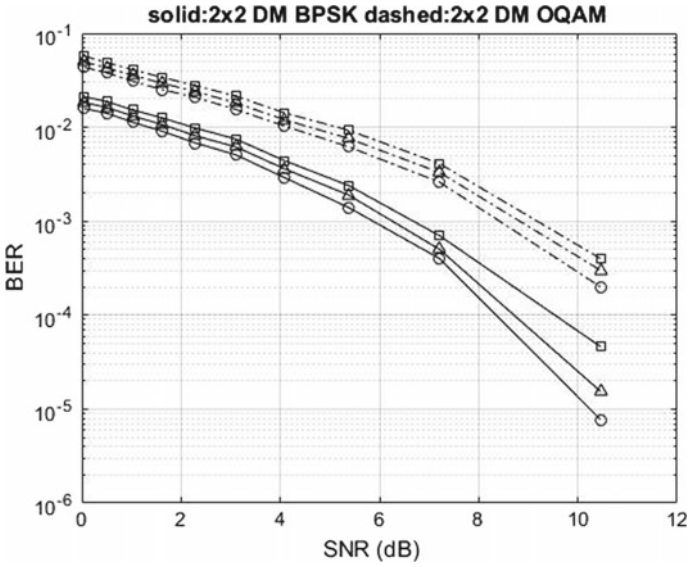

Fig. 50.2 BER performances of the DM FBMC UTA scheme with a PCE and CEEs of 5 and 10%

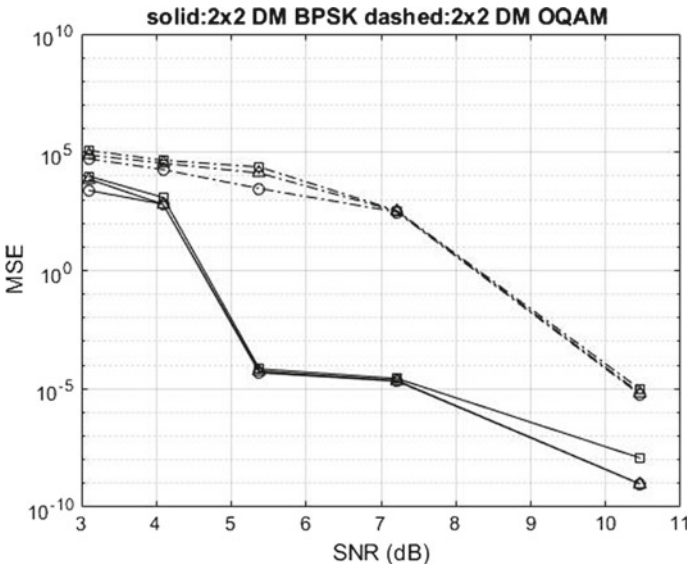

Fig. 50.3 MSE performances of the DM FBMC UTA scheme with a PCE and CEEs of 5 and 10%

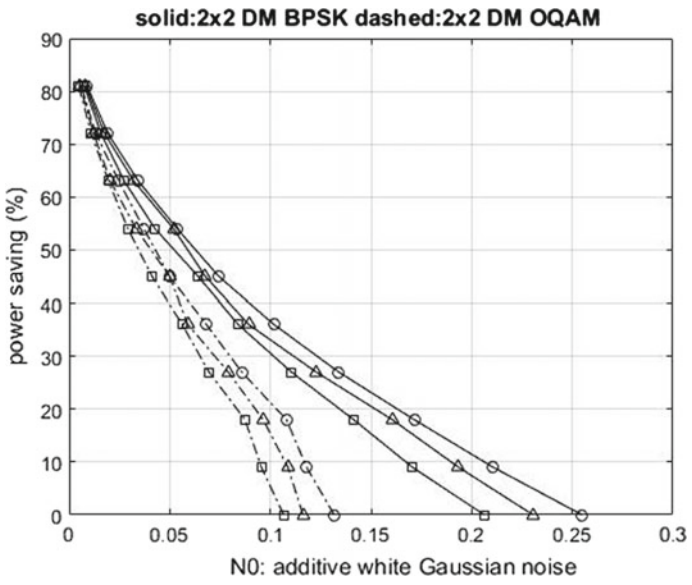

Fig. 50.4 Power saving ratios of the DM FBMC UTA scheme with a BER of 0.001, for PCE and CEEs of 5 and 10%

The audio signals received using the 4OQAM with a PCE for SNRs of 5.37, 7.21 and 10.45 dB, with the corresponding BERs of the received audio signals were 6.2×10^{-3}, 2.6×10^{-3} and 2×10^{-4}, respectively. The audio signals received using the 4OQAM with a CCE of 5% for SNRs of 5.37, 7.21 and 10.45 dB, with the corresponding BERs of the received audio signals were 0.0076, 0.0033 and 0.0003, respectively. The audio signals received using the 4OQAM with a CCE of 10% for SNRs of 5.37, 7.21 and 10.45 dB, with the corresponding BERs of the received audio signals were 0.0093, 0.0041 and 0.0004, respectively. In the proposed DM FBMC-based UTA, the BER performance of the BPSK modulation is better than that of the 4OQAM, at the same SNRs. Figure 50.3 shows the mean square error (MSE) performance of the DM FBMC UTA scheme with PCE. The MSE of the original and received voice signals is defined as follows:

$$\mathrm{MSE} = \frac{1}{N}\sum_{i=1}^{N}\left(V_i - \hat{V}_i\right)^2, \tag{50.1}$$

where N, V_i, $\hat{V}_i$ denote the length of the audio voice signal, the original audio signal, and the received audio signal, respectively. The audio signals received using the BPSK modulation with a PCE for SNRs of 5.37, 7.21 and 10.45 dB, with the corresponding MSEs of the received voice signals were 4.83×10^{-5}, 2.11×10^{-5} and 9.39×10^{-10}, respectively. The audio signals received using the BPSK modulation with a CEE of 5% for SNRs of 5.37, 7.21 and 10.45 dB, with the corresponding MSEs of the received voice signals were 5.52×10^{-5}, 2.23×10^{-5} and 9.43×10^{-10}, respectively. The audio signals received using the BPSK modulation with a CEE of 10% for SNRs of 5.37, 7.21 and 10.45 dB, with the corresponding MSEs of the received voice signals were 6.90×10^{-5}, 2.71×10^{-5} and 1.2×10^{-8}, respectively. The corresponding MSEs of the received voice signals with a PCE, CEEs of 5 and 10% using BPSK modulation were approximate for SNRs of 5.37, 7.21 and 10.45 dB. The audio signals received using 4OQAM with a PCE for SNRs of 5.37, 7.21 and 10.45 dB, respectively, with the corresponding MSEs of the received audio signals were 2930, 300 and 5.81×10^{-6}, respectively.

The audio signals received using 4OQAM with a CCE of 5% for SNRs of 5.37, 7.21 and 10.45 dB, respectively, with the corresponding MSEs of the received audio signals were 13194, 320 and 6.71×10^{-6}, respectively. The audio signals received using 4OQAM with a CCE of 10% for SNRs of 5.37, 7.21 and 10.45 dB, respectively, with the corresponding MSEs of the received audio signals were 23719, 338 and 9.73×10^{-6}, respectively. The corresponding MSEs of the received voice signals with a PCE, CEEs of 5 and 10% using 4OQAM were approximate for SNRs of 7.21 and 10.45 dB.

The audio signals received using the BPSK modulation with a PCE for an SNR of 7.21 dB, with the corresponding BER and MSE of the received voice signals were 4×10^{-4} and 2.11×10^{-5}, respectively. The audio signals received using the BPSK modulation with a CEE of 5% for an SNR of 7.21 dB, with the

corresponding BER and MSE of the received voice signals were 5×10^{-4} and 5.25×10^{-5}, respectively. The audio signals received using the BPSK modulation with a CEE of 10% for an SNR of 7.21 dB, with the corresponding BER and MSE of the received voice signals were 7×10^{-4} and 2.71×10^{-5}, respectively; The audio signals received are clear.

The audio signals received using 4OQAM with a PCE for an SNR of 10.45 dB, with the corresponding BER and MSE of the received audio signals were 2×10^{-4} and 5.81×10^{-6}, respectively. The audio signals received using 4OQAM with a CEE of 5% for an SNR of 10.45 dB, with the corresponding BER and MSE of the received audio signals were 3×10^{-4} and 6.71×10^{-6}, respectively. The audio signals received using 4OQAM with a CEE of 10% for an SNR of 10.45 dB, with the corresponding BER and MSE of the received audio signals were 4×10^{-4} and 9.73×10^{-6}, respectively. The audio signals received are clear. The power saving ratios of the DM FBMC UTA scheme is defined as follows:

$$PS = (1 - E_b) \times 100\%; \quad E_b \leq 1 \tag{50.2}$$

where E_b is the transmission power weighting for the audio signals. The power saving ratios of the DM FBMC UTA scheme with a BER of 0.001, for PCE and CEEs of 5 and 10%, are shown in Fig. 50.4. The maximum acceptable transmission BER value for the voice signal is 0.001. The audio signals received using the BPSK modulation with a PCE for the power saving ratios of 63, 72 and 81%, with the corresponding additive white Gaussian noises (AWGNs, N_0) of the received audio signals were 0.0344, 0.0193 and 0.0089, respectively. The audio signals received using the BPSK modulation with a CEE of 5% for the power saving ratios of 63, 72 and 81%, with the corresponding AWGNs of the received audio signals were 0.0322, 0.0176 and 0.0082, respectively. The audio signals received using the BPSK modulation with a CEE of 10% for the power saving ratios of 63, 72 and 81%, with the corresponding AWGNs of the received audio signals were 0.0274, 0.0159 and 0.0075, respectively. With the CEE increases, the AWGN decreases at the same power saving ratio for a BER of 0.001. The audio signals received using 4OQAM with a PCE for the power saving ratios of 63, 72 and 81%, with the corresponding AWGNs of the received audio signals were 0.0247, 0.0132 and 0.0060, respectively. The audio signals received using 4OQAM with a CEE of 5% for the power saving ratios of 63, 72 and 81%, with the corresponding AWGNs of the received audio signals were 0.0205, 0.0122, and 0.0055, respectively. The audio signals received using 4OQAM with a CEE of 10% for the power saving ratios of 63, 72 and 81%, with the corresponding AWGNs of the received audio signals were 0.0196, 0.0110 and 0.0048, respectively. At the same power saving ratio and underwater channel multipath fading, the BPSK modulation demonstrated better performance to combat the AWGNs than that of 4OQAM. Figure 50.5 shows the audio signal received using the BPSK modulation with a PCE in the DM FBMC

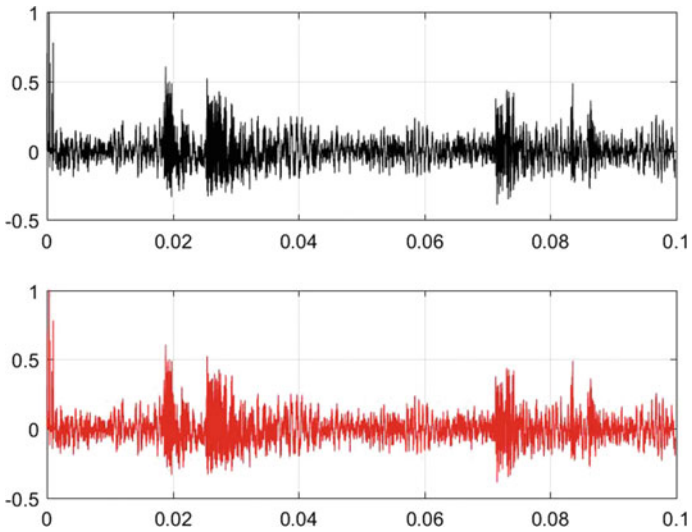

Fig. 50.5 Audio signal received using BPSK modulation in the DM FBMC UTA scheme with a BER of 0.001, for PCE

UTA scheme with a BER of 0.001, for PCE. The above and below figures are the original and received audio signals, respectively, and the MSE of the original and received audio signals is 4.83×10^{-5}. The received voice signal is clear, and can be used for underwater voice communication.

50.4 Conclusion

In this paper, the DM FBMC-based underwater audio transmission scheme with LDPC error-correcting mechanism was proposed. Adaptive BPSK modulation and 4OQAM, and a power assignment mechanism were integrated into the proposed system. The transmission speed of the DM FBMC-based scheme was twice that of the SISO FBMC-based system. In the proposed DM FBMC-based UTA, the BER performance of the BPSK modulation is better than that of the 4OQAM, at the same SNRs. The BER performances increased as the CEE decreased. The corresponding MSEs of the received audio signals with a PCE, CEEs of 5 and 10% were approximate for SNRs of 5.37, 7.21 and 10.45 dB. The corresponding MSEs of the received audio signals with a PCE, CEEs of 5 and 10% using 4OQAM were approximate for SNRs of 7.21 and 10.45 dB. With the CEE increases, the AWGN decreases at the same power saving ratio and a BER of 0.001. From simulation results, the BER, MSE, and power saving performances for the DM FBMC-based scheme were explored, and the simulation results show that the DM FBMC-based communication technology is suitable for underwater audio transmission.

Acknowledgements The authors acknowledge the support of the grant from The Ministry of Science and Technology of Taiwan, under contracts No. MOST 107-2221-E-992-027, MOST 105-2923-E-992-302-MY3, and the valuable comments of the reviewers.

References

1. B. Farhang-Boroujeny, IEEE Sig. Process. Mag. **28**(3), 92 (2011)
2. R. Nissel, S. Schwarz, M. Rupp, IEEE J. Sel. Areas Commun. **35**(8), 1768 (2017)
3. M. Bellanger et. al., FBMC physical layer: a primer. PHYDYAS (2010)
4. W. Xinag, K. Zheng, X. Shen, *5G Mobile Communications* (Springer, 2017)
5. P. Amini, R.R. Chen, B. Farhang-Boroujeny, IEEE J. Oceanic Eng. **40**(1), 115 (2015)
6. C.F. Lin, Y.T. Hung, H.W. Lu, S.H. Chang, I.A. Parinov, S. Shevtsov, J. Mar. Sci. Technol. **26** (3), 327 (2018)
7. J. Zhang, Y.R. Zheng, C. Xiao, in *Proceedings of the MIT/IEEE Ocean International Conference* (IEEE Publishers, USA, 2008)

Index

I. A. Parinov et al. (eds.), *Advanced Materials*, Springer Proceedings in Physics 224, https://doi.org/10.1007/978-3-030-19894-7